PROCEEDINGS OF THE EIGHTEENTH INTERNATIONAL SYMPOSIUM ON ARTIFICIAL LIFE AND ROBOTICS

(AROB 18th '13)

Jan. 30-Feb. 1, 2013

Daejeon Convention Center, Daejeon, KOREA

Publication Date: January 30, 2013
ISBN 978-4-9902880-7-5

Proceedings of the Eighteenth International Symposium on

ARTIFICIAL LIFE AND ROBOTICS

(AROB 18th '13)

January 30 - February 1, 2013

Daejeon Convention Center, Daejeon, Korea

Artificial Life and Robotics

We invite you to publish your paper

in this journal full of inventive scientific findings and state-of-the art technologies.

Two types of papers from the world are

I. Contributed papers

II. Recommended papers presented at **the International Symposium on Artificial Life and Robotics (ISAROB),**

Contribution fee:

4 pages or Under **¥19,950 / page** (¥19,000 + 5 % consumption tax: only in Japan)

Extra page charge **¥16,800 / page** (¥16,000 + 5% consumption tax: only in Japan)

(Pages are counted on double-columns basis as they appear in the journal.)

Shipping Cost:

domestic **¥735 / delivery** (¥700 + 5 % consumption tax)

overseas **¥3,000 / delivery**

We deliver every corresponding author (or sponsor) one copy of journal in which his/her paper is included. We would like to thank authors for their support in the form of contribution fee payable before publication, which funds the production of this journal contracted by Springer Japan.

Order:

I. Price for co-authors

¥ 5,250 (¥5,000 + 5 % consumption tax: only in Japan) **per copy (for every co-author)**

If necessary, please order extra copies for co-authors to the Journal Office.

II. Subscription fee

	domestic	**overseas**
Annual subscription rate	**¥21,000*/year**	**¥20,000/year**
Shipping Costs	**free**	**¥2,000/year**

*including consumption tax

III. Purchase price for single issue

¥ 8,400 (¥8,000 + 5 % consumption tax: only in Japan) **per issue**.

AROB Journal Office : journal@isarob.org

© ISAROB 2013

Artificial Life and Robotics

Our Review System

For contributed papers,

1. Duration:

   Two months is our target time of the whole review process, however, we are trying our best to make it as short as possible.

2. Review results:

   Every contributed paper will be reviewed by three assigned reviewers with score ranging from 1 (highest mark) to 4 (lowest mark);

   1. publish with no revision,
   2. publish with minor revisions,
   3. possibly publish with revision and re-review,
   4. reject.

   Review results, a total score of the three evaluation scores, would be read as;.

3 or 4	:	accepted and to be published as it is,
4, 5, or 6	:	accepted and to be published after minor revisions,
7, 8, or 9	:	acceptable but subject to rewriting and re-review,
10, 11, or 12	:	rejected

For recommended papers,

The recommended papers are ones that the chair of each session and reviewers read before the symposium that year and recommend to AROB Journal Office using the same evaluation score above. Therefore, the quality of recommended papers is apparent at the time of recommendation.

We express our heartfelt gratitude to chairs and reviewers of ISAROB for their support and sincere voluntary work without which this journal never exists.

AROB Journal Office : journal@isarob.org

© ISAROB 2013

Artificial Life and Robotics

We invite you to advertise your company

in this international journal financed by **ISAROB (International Symposium on Artificial Life and Robotics)** and produced by a renowned publisher, Springer Japan.

Merits:

- **Connectivity with ambitious academic circles in the rapidly-advancing fields**,
- **Expanded publicity through toll electronic circulation by Springer-Japan**,
- **Reasonable advertising fee**

  1 page = ¥ 90,000, 2 pages = ¥ 150,000

  (Fee+ 5 % consumption tax: only in Japan)

For further details please contact

AROB Journal Office

AROB Secretariat
International Society on Artificial Life and Robotics
A-101, 8-7 Hatakenaka, Oita, 870-0856, Japan

Tel: +81-97-594-0181
Fax: +81-97-547-9242
Email: journal@isarob.org
Home Page：http://isarob.org/

© ISAROB 2013

THE EIGHTEENTH INTERNATIONAL SYMPOSIUM ON ARTIFICIAL LIFE AND ROBOTICS

(AROB 18th '13)

ORGANIZED BY

International Organizing Committee of International Symposium on Artificial Life and Robotics (AROB)

CO-OPERATED BY

The Society of Instrument and Control Engineers (SICE, Japan)
The Robotics Society of Japan (RSJ, Japan)
The Institute of Electrical Engineers of Japan (IEEJ, Japan)
The Institute of Systems, Control and Information Engineers (ISCIE)
The Institute of Electronics, Information and Communication Engineers (IEICE)
IEEE Japan Council (IEEE Robotics and Automation Society Japan Chapter)
Japan Robot Association (JARA)
Institute of Control, Robotics and Systems (ICROS, Korea)
Chinese Association for Artificial Intelligence (CAAI, China)

© ISAROB 2013

GENERAL CHAIR

Ju-Jang Lee (KAIST, Korea)
Masanori Sugisaka (Alife Robotics Co., Ltd., Japan)

PROGRAM CHAIR

Hiroshi Tanaka (Tokyo Medical & Dental University, Japan)

VICE CHAIR

John L. Casti (International Institute for Applied Systems Analysis, Austria)
Yingmin Jia (Beihang University, China)
Henrik Hautop Lund (Technical University of Denmark, Denmark)
Hiroshi Tanaka (Tokyo Medical & Dental University, Japan)
Yong-Guang Zhang (Academia Sinica, China)

ADVISORY COMMITTEE CHAIR

F. Harashima (Tokyo Metropolitan University, Japan)

ASSISTANT GENERAL CHAIRMAN

Takao Ito (Ube National College of Technology, Japan)

ADVISORY COMMITTEE

Bruce Eisenstein (Drexel University, Former IEEE President, USA)
Robert Fischl (Drexel University, USA)
Toshio Fukuda (Nagoya University, Japan)
Fumio Harashima (Tokyo Metropolitan University, Japan)
Paul Kalata (Drexel University, USA)
Moshe Kam (Drexel University, IEEE President, USA)
Hidenori Kimura (RIKEN, Japan)
Paul Oh (Drexel University, USA)
Masayoshi Tomizuka (University of California Berkeley, USA)

INTERNATIONAL ORGANIZING COMMITTEE

Hussein Abbass (University of New South Wales, Australia)
Kazuyuki Aihara (The University of Tokyo, Japan)
Takaya Arita (Nagoya University, Japan)
Christopher L. Barrett (Virginia Polytechnic Institute and State University, USA)
Mark A. Bedau (Reed College, USA)
Malachy Eaton (University of Limerick, Ireland)
Joshua M. Epstein (The Johns Hopkins University, USA)
Adam Grzech (Wroclaw University of Technology, Poland)
Hideki Hashimoto (Chuo University, Japan)
Yoshiteru Ishida (Toyohashi University of Technology, Japan)
David John Glyndwyr James (Coventry University, UK)
Takashi Kohno (The University of Tokyo, Japan)
Kazuo Kyuma (Mitsubishi Electric Corporation, Japan)
Man Hyung Lee (Pusan National University, Korea)
Kenneth James Mackin (Tokyo University of Information Sciences, Japan)
Fumitoshi Matsuno (Kyoto University, Japan)
Masatoshi Nakamura (Research Institute of Systems Control, Japan)
Marion Oswald (Vienna University of Technology, Austria)

© ISAROB 2013

Steen Rasmussen (University of Southern Denmark, Denmark)
Thomas S. Ray (University of Oklahoma, USA)
Shinichi Sagara (Kyushu Institute of Technology, Japan)
Katsunori Shimohara (Doshisha University, Japan)
Hideyuki Suzuki (The University of Tokyo, Japan)
Jerzy Świątek (Wroclaw University of Technology, Poland)
Charles Taylor (University of California-Los Angeles, USA)
Toshio Tsuji (Hiroshima University, Japan)
Jiwu Wang (Beijing Jiaotong University, China)
Keigo Watanabe (Okayama University, Japan)
Kazuko Yamasaki (Tokyo University of Information Sciences, Japan)
Masao Yokota (Fukuoka Institute of Technology, Japan)
Changshui Zhang (Tsinghua University, China)

INTERNATIONAL PROGRAM COMMITTEE

Richard K. Belew (University of California-San Diego, USA)
Shyi-Ming Chen (National Taichung University of Education, Taiwan)
Young Im Cho (The University of Suwon, Korea)
Mo-Yuen Chow (North Carolina State University, USA)
Fengzhi Dai (Tianjin University of Science & Technology, China)
Yueyue Fan (University of California-Davis, USA)
Takayasu Fuchida (Kagoshima University, Japan)
Ivan Godler (The University of Kitakyushu, Japan)
Sung Hyun Han (Kyungnam University, Korea)
Noriyasu Homma (Tohoku University, Japan)
Zunaidi bin Ibrahim (TATi University College, Malaysia)
Seiji Ishikawa (Kyushu Institute of Technology, Japan)
Takashi Iwamoto (Mitsubishi Electric Corporation, Advanced Technology R&D Center, Japan)
Kiyotaka Izumi (Saga University, Japan)
Jeff Johnson (The Open University, UK)
Sanjay S. Joshi (College of Engineering University of California, USA)
Hiroshi Kinjo (University of the Ryukyus, Japan)
Kentarou Kurashige (Muroran Institute Technology, Japan)
Hee-Hyol Lee (Waseda University, Japan)
Yong Liu (University of Aizu, Japan)
Kathryn Elizabeth Merrick (University of New South Wales and ADFA, Australia)
Chris Mi (University of Michigan-Dearborn, USA)
Kazushi Nakano (The University of Electro-Communications, Japan)
Tomoharu Nakashima (Osaka Prefecture University, Japan)
Walter Nistico (University of Dortmund, Germany)
Harutoshi Ogai (Waseda University, Japan)
Shigeru Omatu (Osaka Institute of Technology, Japan)
Luigi Pagliarini (Technical University of Denmark, Denmark)
Rolf Pfeifer (University of Zurich-Irchel, Switzerland)
Mohd Rizon (University of Malaysia Perlis, Malaysia)
Peter S. Sapaty (National Academy of Sciences of Ukraine, Ukraine)
Jeong-Yon Sim (Kangnam University, Korea)
Ken Sugawara (Tohoku Gakuin University, Japan)
Mikhail Svinin (Kyushu University, Japan)
Ivan Tanev (Doshisha University, Japan)
Hiroshi Umeo (Osaka Electro-Communication University, Japan)
Katsuji Uosaki (Fukui University of Technology, Japan)
Mutsumi Watanabe (Kagoshima University, Japan)
Hidekazu Yanagimoto (Osaka Prefecture University, Japan)
Ikuo Yoshihara (University of Miyazaki, Japan)
Yong Yu (Kagoshima University, Japan)
Tao Zhang (Tsinghua University, China)

© ISAROB 2013

Huailin Zhao (Shanghai Institute of Technology, China)

LOCAL ARRANGEMENT COMMITTEE

Sung Hyun Han (Kyungnam University, Korea)
Jang Myung Lee (Pusan National University, Korea)
Jin Bae Park (Yonsei University, Korea)
Jeong Yon Shim (Kangnam University, Korea)

HISTORY

The AROB was founded in 1996 under the support of Science and International Affairs Bureau, Ministry of Education, Culture, Sports, Science and Technology, Japanese Government. Since then, the symposium organized by the AROB has been held every year at B-Con Plaza, Beppu, Japan except AROB 5th '00 (Oita) and AROB 6th '01 (Tokyo). The eighteenth symposium will be held on January 30–February 1, 2013, at Daejeon Convention Center, Daejeon, Korea.

OBJECTIVE

This symposium will bring together researchers to discuss development of new technologies concerning *artificial life and robotics* based on computer simulations and hardware designs of state-of-the-art technologies, and to share findings on how advancements in artificial life and robotics technologies that relate to artificial intelligence, virtual reality, and computer science are creating the basis for exciting new research and applications in various fields.

COPYRIGHTS

Accepted papers will be published in the proceeding of AROB and some of high quality papers in the proceeding will be requested to re-submit their papers for the consideration of publication in an international journal ARTIFICIAL LIFE AND ROBOTICS. All correspondence related to the symposium should be addressed to AROB Secretariat.

AROB Secretariat

AROB Secretariat
International Society on Artificial Life and Robotics
A-101, 8-7 Hatakenaka, Oita, 870-0856, Japan

Tel: +81-97-594-0181
Fax: +81-97-547-9242
Email: arobsecr@isarob.org
Home Page : http://isarob.org/

© ISAROB 2013

GENERAL SESSION TOPICS

Artificial intelligence
Artificial life and complexity
Artificial living
Control techniques
Human - machine cooperative systems
Human - welfare robotics
Image processing
Intelligent control & modeling
Learning
Mobile vehicles
Multi agent system
Neural networks
Pattern recognition
Robotics
Virtual reality

ORGANIZED SESSION TOPICS

Applications and Theories of Advanced Technology
Artificial Life and Control
Bio-inspired Theory and Applications
Biomimetic Machines and Robots
Complexity and Diversity
Computer-Supported Learning Systems
Control in Mechatronics and Power Electronics
Control of Mechatronic System
Facial Expression Recognition, Speech Synthesis of Emotions, and Music Recommendation
Information Technology for Environmental Research
Intelligent control and applications
Intelligent control and implement
Intuitive Human-System Interaction
Kansei Engineering and its Applications

© ISAROB 2013

MESSAGES

Ju-Jang Lee

General Chair of AROB

Professor, KAIST

The Eighteenth International Symposium on Artificial Life and Robotics (AROB) will be held in Daejeon, Korea from Jan 30th to Feb. 1st, 2013. This year's Symposium will be held amidst the high expectation of the increasingly important role of the new interdisciplinary paradigm of science and engineering represented by the field of artificial life and robotics that continuously attracts wide interests among scientist, researchers, and engineers around the globe.

Since the time of the very first AROB meeting in 1996, each year, distinguished researchers and technologists from around the world are looking forward to attending and meeting at AROB. AROB is becoming the annual excellent forum that represents a unique opportunity for the academic and industrial communities to meet and assess the latest developments in this fast growing artificial life and robotics field. AROB enables them to address new challenges, share solutions, discuss research directions for the future, exchange views and ideas, view the results of applied research, present and discuss the latest development of new technologies and relevant applications.

In addition, AROB offers the opportunity of hearing the opinions of well known leading experts in the field through the keynote sessions, provides the bases for regional and international collaborative research, and enables to foresee the future evolution of new scientific paradigms and theories contributed by the field of artificial life and robotics and associated research area. The twenty-first century will become the century of artificial life and intelligent machines in support of humankind and AROB is contributing through wide technical topics of interest that support this direction.

It is a great for me as the General Chairman of the 18th AROB 2013 to welcome everyone to this important event. Also, I would like to extend my special thanks to all authors and speakers for contributing their research works, the participants, and the organizing team of the 18th AROB.

Looking forward to meeting you at the 18th AROB in Dajeon, Korea and wishing you all the best.

© ISAROB 2013

Masanori Sugisaka

General Chair of AROB

ALife Robotics Corporation, Ltd. , Japan

It is my great pleasure to invite you all to the Eighteenth International Symposium on Artificial Life and Robotics (AROB 18th '13).

The symposium from the first (1996) to the Thirteenth (2008) were organized by Oita University and Nippon Bunri University (NBU) and the Symposium from the Fourteenth (2009) to the Seventeenth (2012) were organized by Nippon Bunri University (NBU) and ALife Robotics Corporation Ltd. under the sponsorship of the Science and Technology Policy Bureau, the Ministry of Education, Science, Sports, and Culture (Monbusho), presently, the Ministry of Education, Culture, Sports, Science, and Technology (Monkasho), Japanese Government, Japan Society for the Promotion of Science (JSPS), The Commemorative Organization for the Japan World Exposition ('70), Air Force Office of Scientific Research, Asian Office of Aerospace Research and Development (AFOSR/AOARD), USA. I would like to express my sincere thanks to not only Monkasho, JSPS, the Commemorative Organization for the Japan World Exposition ('70), AFOSR/AOARD but also Japanese companies (Mitsubishi Electric Corporation, Advanced Technology R&D Center, Oita Gas Co., Ltd., ME System Co. LTD, and Sanwa Shurui Co., LTD.) for their repeated supports.

This symposium is organized by International Organizing Committee of AROB and is sponsored by ALife Robotics Co., Ltd., and technically co-sponsored by IEEE Robotics and Automation Society Japan Chapter, JARA, SICE, ISCIE, IEICE and CAAI (P.R. China).

I hope that the new technologies presented in this symposium bring happiness to human society and will facilitate the establishment of an international research Institute of Artificial Life and Robotics.

Welcome and enjoy your stay in Daejeon.

Conference Rooms

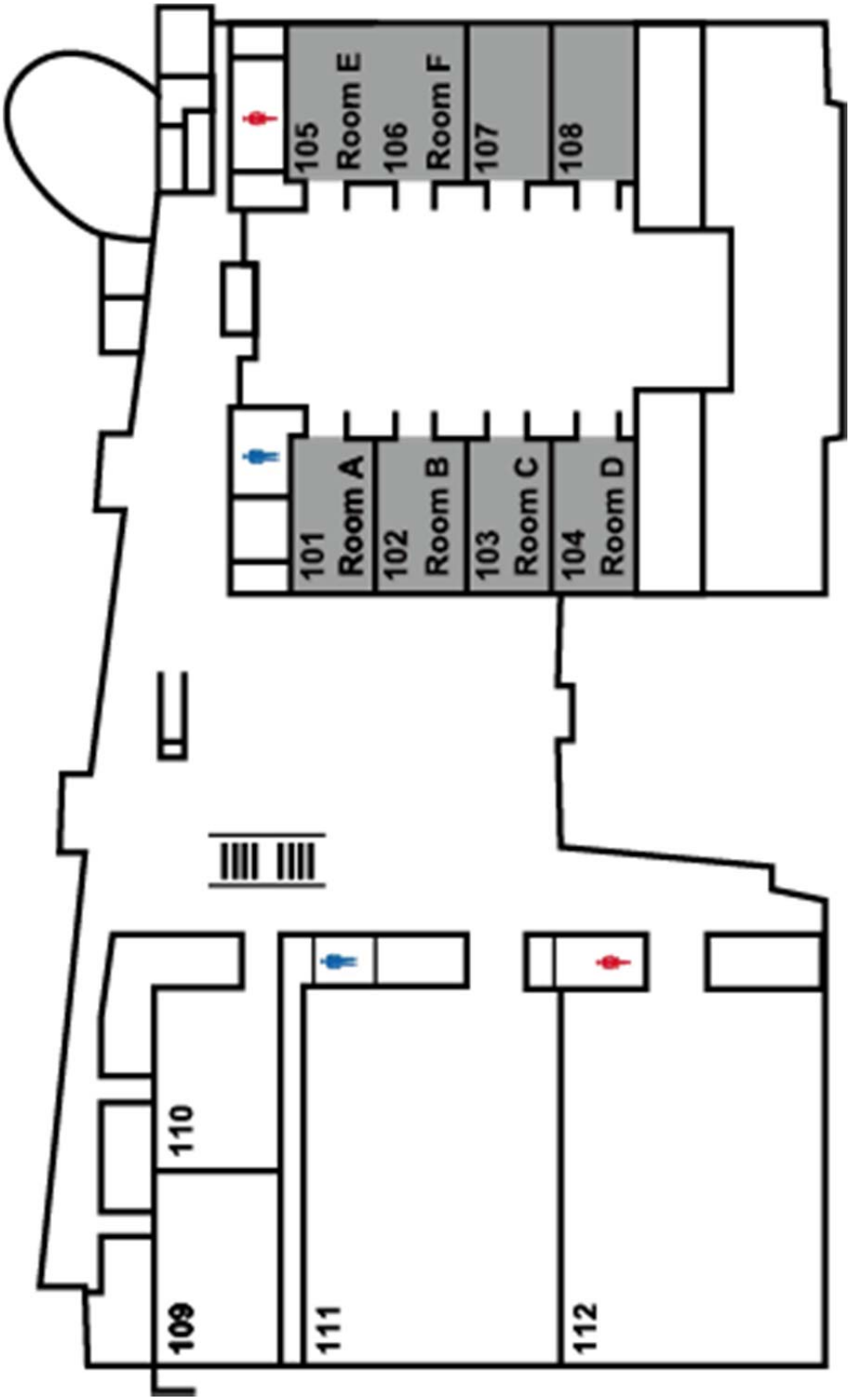

1F-101: Room A
1F-102: Room B
1F-103: Room C
1F-104: Room D
1F-105: Room E
1F-105+1F-106: Room F
1F-107: Computer Room
1F-108: VIP Meeting Room

Daejeon Convention Center 1F

Time Table (January 30, 2013)

	Room A	Room B	Room C	Room D
09:00 –	Registration (Registration Desk)			
10:00 – 11:45	OS6 Control in Mechatronics and Power Electronics Chair: K. Higuchi	OS3 Biomimetic Machines and Robots Chair: K. Watanabe	OS4 Complexity and Diversity Chair: K. Naitoh	OS10 Intelligent control and applications Chair: K.-L. Su
11:45 – 12:35	Lunch			
12:35 – 13:00	Opening Ceremony (Room F)			
13:00 – 15:30	**Invited Session on Playware** (Room F) Chair H.H. Lund			
15:30 – 16:00	Coffee Break			
16:00 – 17:15	OS9 Information Technology for Environmental Research Cair: T. Yamaguchi	GS14 Robotics I	GS1 Artificial intelligence	OS11 Intelligent control and implement Chair: C.-W. Hung

OS: Organized Session GS: General Session PS: Poster Session

© ISAROB 2013

Time Table (January 31, 2013)

	Room A	Room B	Room C	Room D
09:00 –	Registration (Registration Desk)			
10:00 – 11:00	GS8 Intelligent control & modeling	GS15 Robotics II	GS5 Human-machine	GS12 Neural networks
11:00 – 11:15	Coffee Break			
11:15 – 12:15	Poster Session			
12:15 – 13:15	Lunch			
13:15 – 14:15	**Invited Speech** (Room F) **Dr. Peter S. Sapaty**			
14:15 – 14:30	Coffee Break			
14:30 – 15:30	GS4 Control techniques	GS10 Mobile vehicles	GS2 Artificial life and complexity	GS7 Image processing
15:30 – 15:45	Coffee Break			
15:45 – 17:00	GS9 Learning	OS13 Kansei Engineering and its Applications Chair: T. Hattori	OS1 Artificial Life and Control Chair: H.-H. Lee	GS11 Multi agent system

OS: Organized Session **GS: General Session** **PS: Poster Session**

© ISAROB 2013

Time Table (February 1, 2013)

	Room A	Room B	Room C	Room D	Room E
08:00 –	Registration (Registration Desk)				
08:30 – 10:15	OS5 Computer-Supported Learning Systems Chair: K.J. Mackin	OS7 Control of Mechatronic System Chair: S. Sagara	OS8 Facial Expression Recognition, Speech Synthesis of Emotions, and Music Recommendation Chair: Y. Yoshitomi	GS17 Virtual reality will end at 09:30	GS6 Human-welfare robotics
10:15 – 10:30	Coffee Break				
10:30 – 11:30	GS13 Pattern recognition	GS16 Robotics III	GS3 Artificial living	9:45-10:45 Bio-inspired Theory and Applications Chair: K. Yamamori 11:00-11:30 Applications and Theories of Advanced Technology Chair: T. Ito	OS12 Intuitive Human-System Interaction Chair: M. Yokota

OS: Organized Session **GS: General Session** **PS: Poster Session**

© ISAROB 2013

Technical paper index

January 30 (Wednesday), 13:00-15:30

Room F

Invited Session on Playware

Chair: Henrik Hautop Lund (Center for Playware, Technical University of Denmark, Denmark)

ISP1 *Effect of Playful Balancing Training - A Pilot Randomized Controlled Trial*

Henrik Hautop Lund, Jari Due Jessen (Centre for Playware, Technical University of Denmark, Denmark)

ISP2 *Engaging through her eyes Embodying the perspective of a robot companion*

Patrizia Marti (Social, Political and Cognitive Science Department, University of Siena, Italy)

Jelle T. Stienstra (Department of Industrial Design, Eindhoven University of Technology, Netherlands)

ISP3 *Fable: Socially Interactive Modular Robot*

Arnþór Magnússon, Moises Pacheco, Mikael Moghadam, Henrik H. Lund, David J. Christensen (Technical University of Denmark, Denmark)

ISP4 *bioToys: biofeedback device for physiotherapy using building blocks*

Tomoya Shimokakimoto, Asaki Miura, Kenji Suzuki (University of Tsukuba, Japan)

January 31 (Thursday), 13:15-14:15

Room F

Invited Speech

IS1 Future Technology and Market Developments for Unmanned Maritime Vehicles

Peter S. Sapaty (National Academy of Sciences of Ukraine, Ukraine)

January 30 (Wednesday), 10:00-11:45

Room A

OS6 Control in Mechatronics and Power Electronics

Chair: Kohji Higuchi (The University of Electro-Communications, Japan)

Co-Chair: Kazushi Nakano (The University of Electro-Communications, Japan)

OS6-1 *Robust Digital Control for Interleave PFC Boost Converter*

Yuto Adachi, Kohji Higuchi, Tatsuyoshi Kajikawa (The University of Electro-Communications, Japan)

Tomoaki Sato (C&C SYSTEMS CENTER Hirosaki University, Japan)

Kosin Chamnongthai (King Mongkut's University of Technology Thonburi, Thailand)

OS6-2 *Synthesis of continuous-time dynamic quantizers for LFT type quantized feedback systems*
Kenji Sawada, Seiichi Shin (The University of Electro-Communications, Japan)

OS6-3 *Optimal scheduling of automatic guided vehicle transportation system based on MLD system modeling*
Kenji Sawada, Seiichi Shin (The University of Electro-Communications, Japan)

OS6-4 *Direct Multivariable PI Controller Tuning from Closed-Loop Response Data*
Yosihiro Matsui, Hideki Ayano (Tokyo National College of Technology, Japan)
Kazushi Nakano (The University of Electro-Communications, Japan)

OS6-5 *On inhibition of premature convergence in Genetic Algorithms for mobile robot control*
Satoshi Shintaku, Kazushi Nakano (The University of Electro-Communications, Japan)

OS6-6 *Digital PI control for Interleave PFC boost converter*
Yuto Adachi, Kohji Higuchi, Tatsuyoshi Kajikawa (The University of Electro-Communications, Japan)
Tomoaki Sato (Hirosaki University, Japan)
Kosin Chamnongthai (King Mongkut's University of Technology Thonburi, Thailand)

Room B

OS3 Biomimetic Machines and Robots

Chair: Keigo Watanabe (Okayama University, Japan)

Co-Chair: Akimasa Otsuka (Tokyo University of Science, Yamaguchi, Japan)

OS3-1 *A new solution to the SLAM problem by using an unscented smoother*
Keigo Watanabe, Shoichi Maeyama (Okayama University, Japan)
Satoshi Funamoto (Shin Nippon Koki Co., Ltd., Japan)

OS3-2 *Kinodynamic motion planning and control using anisotropic damping forces*
Kimiko Motonaka, Keigo Watanabe, Shoichi Maeyama (Okayama University, Japan)

OS3-3 *Application of variable search space GAs to fine gain tuning of model-based robotic servo controller*
Akimasa Otsuka, Fusaomi Nagata (Tokyo University of Science, Yamaguchi, Japan)

OS3-4 *Propulsive force analysis of a pectoral fin for rajiform type fish robots from fluid dynamic aspects*
Masaaki Ikeda, Shigeki Hikasa, Keigo Watanabe, Isaku Nagai (Okayama University, Japan)

OS3-5 *Underactuated control for a blimp with four-propellers by a logical switching method*
Yoshikazu Nakamura, Keigo Watanabe, Isaku Nagai (Okayama University, Japan)

OS3-6 *Continuous shape-grinding experiment based on model-independent force / position hybrid control method with spline approximation*
Akira Yanou, Mamoru Minami, Hiro Tanimoto (Okayama University, Japan)

Room C

OS4 Complexity and Diversity

Chair: Ken Naitoh (Waseda University, Japan)

Co-Chair: Hiroshi Tanaka (Tokyo Medical and Dental University, Japan)

OS4-1 *Catastrophic chaos theory: predicting the edge between health and death*

Ken Naitoh, Hirofumi Inoue (Waseda University, Japan)

OS4-2 *Supercomputing of transition to turbulence in pipe with adit flow*

Tsuyoshi Nogami, Takahiro Tobe, Ken Naitoh (Waseda University, Japan)

OS4-3 *Stock market dynamics derived from a cognitive bias*

Moto Kamiura, Yu Murata (Tokyo Denki University, Japan)

OS4-4 *Fusion visualization of surface and volume on AVS/Express*

Hideo Miyachi (CYBERNET SYSTEMS CO.,LTD., Japan)

Koji Koyamada, Naohisa Sakamoto (Kyoto University, Japan)

OS4-5 *Autonomous polymer actuators*

Yusuke Hara (The National Institute of Advanced Industrial Science and Technology (AIST), Japan)

OS4-6 *Cyanobacterial circadian clock is nullified under low temperature via Hopf bifurcation*

Yoriko Murayama, Hideo Iwasaki (Waseda University, Japan)

Hiroshi Kori (Ochanomizu University, Japan)

Takao Kondo (Nagoya University, Japan)

Hiroshi Ito (Kyushu University, Japan)

OS4-7 *Molecular robotics for artificial cell-model construction*

Shin-ichiro M. Nomura, Yusuke Sato (Tohoku University, Japan)

Kei Fujiwara (JSPS Research Fellow, Japan)

Room D

OS10 Intelligent control and applications

Chair: Kuo-Lan Su (National Yunlin University of Science and Technology, Taiwan)

Co-Chair: Chia-Nan Ko (Nan Kai University of Technology, Taiwan)

OS10-1 *Adaptive learning neural networks for system identification of a magneto-rheological damper*

Chia-Nan Ko, Guan-Yu Liu, Yu-Yi Fu (Nan-Kai University of Technology, Taiwan)

Pi-Yun Chen (National Chin-Yi University of Technology, Taiwan)

OS10-2 *Identification of RBFNs with SVR under censored data*

Yu-Yi Fu, Chia-Nan Ko, Jhih-Cheng Chang (Nan Kai University of Technology, Taiwan)

Yu-Fen Fu (China University of Technology, Taiwan)

Kuo-Lan Su (National Yunlin University of Science and Technology, Taiwan)

© ISAROB 2013

OS10-3 *Drift algorithm second order sliding mode control for a synchronous reluctance motor*

Wen-Bin Lin (National Yunlin University of Science and Technology and Far East University, Taiwan)

Huann-Keng Chiang, Yi-Chang Chang (National Yunlin University of Science and Technology, Taiwan)

OS10-4 *Development of the multi-detection system using multi-sensor fusion algorithms*

Ying-Yao Ting, Huan-Sheng Wang (National Kaohsiung First University of Science of Technology, Taiwan)

OS10-5 *Design a feasible docking station for mobile robots*

Yi-Lin Liao, Kuo-Lan Su, Jr-Hung Guo (National Yunlin University of Science and Technology, Taiwan)

Li-Chun Lai (National Pingtung University of Education, Taiwan)

OS10-6 *A PSO method for time-optimal motion planning of a mobile robot*

Li-Chun Lai, Sheau-Wen Lin, Chia-Hung Shih (National Pingtung University of Education, Taiwan)

Kuo-Lan Su,(National Yunlin University of Science and Technology, Taiwan)

Chia-Nan Ko (Nan Kai University of Technology, Taiwan)

OS10-7 *The Implementation of Driving anti-sleep Safety warning system*

Yi-Yu Lu, Kuo-Kung Chen, Po-Yu Chen, Wen-Bin Lin (Far East University, Taiwan)

January 30 (Wednesday), 16:00-17:15

Room A

OS9 Information Technology for Environmental Research

Chair: Takashi Yamaguchi (Tokyo University of Information Sciences, Japan)

Co-Chair: Kenneth J. Mackin (Tokyo University of Information Sciences, Japan)

OS9-1 *Study on the efficient use of satellite image data analysis system*

Hayao Mori, Seiji Tsukamoto, Takashi Yamaguchi, Masaki Hanada, Jong Geol Park, Eiji Nunohiro (Tokyo University of Information Sciences, Japan)

OS9-2 *Administrative division based data segmentation for autonomous paddy field classifier modeling*

Takashi Yamaguchi, Shinya Iwasaki, Kazuma Mori, Kenneth J. Mackin, Masaki Hanada, Eiji Nunohiro (Tokyo University of Information Sciences, Japan)

OS9-3 *Analysis of seasonal variability of methane over global land area*

Jonggeol Park, Sooyoung Park, Eiji Nunoriho, Takashi Yamaguchi (Tokyo University of Information Sciences, Japan)

Youngjoo Kwak (International Centre for Water Hazard and Risk Management (ICHARM), Japan)

OS9-4 *Estimating a floodwater from MODIS time series and DEM data using the self-organizing map*

Youngjoo Kwak, Kazuhiko Fukami (International Centre for Water Hazard and Risk Management (ICHARM), Japan)

Jonggeol Park (Tokyo University of Information Sciences, Japan)

Room B

GS14 Robotics I

GS14-1 *A simple wall-climbing mechanism for a window cleaning robot*

Takafumi Soeda, Nobuhiro Okada, Kazuo Kiguchi (Kyushu University, Japan)

GS14-2 *Topological Graph Based Boundary Coverage Path Planning for a Mobile Robot*

Bong Keun Kim, Hideyuki Tanaka, Yasushi Sumi (Intelligent Systems Research Institute, AIST, Japan)

GS14-3 *Arc/line segments extraction from unknown indoor environment with laser sensor*

Rui-Jun Yan, Jing Wu, Ming-Lei Shao, Ji-Yeong Lee, Chang-Soo Han (Hanyang University, Korea)

GS14-4 *Study on the development of an open motion control platform for a differential mobile robot based on ROS*

Jiwu Wang, Fangbo Liao (Beijing Jiaotong University, China)

Sugisaka Masanori (Alife Robotics Corporation Ltd., Japan)

Room C

GS1 Artificial intelligence

GS1-1 *A proposition of addition and integration of q-values in Q-Learning*

Kathy Thi Aung, Takayasu Fuchida (Kagoshima University, Japan)

GS1-2 *Recipe search engine inspired by ant colony's foraging*

Jinwook KIM, Kazuyuki Ito (Hosei University, Japan)

Katsunori Tachibana (NEC Communication Systems, Ltd., Japan)

GS1-3 *Phase Scaling Effect of Adiabatic Quantum Computation in Deutsch-Jozsa Problem (withdrawal)*

Shigeru Nakayama (Kagoshima University, Japan)

Ichiro Iimura (Prefectural University of Kumamoto, Japan)

Gang Peng (Huizhou University, China)

GS1-4 *Constructing Obstacle-Based Triangularized Roadmap*

Jeong Hyeon Wang, Ju Jang Lee (Korea Advanced Institute of Science and Technology, Korea)

Room D

OS11 Intelligent control and implement

Chair: Chung-Wen Hung (National Yunlin University of Science and Technology, Taiwan)

Co-Chair: Kuo-Hsien Hsia (Far East University, Taiwan)

OS11-1 *Motion planning of the multi-robot based chess game*

Yung-Chin Lin (National Yunlin University of Science and Technology, WuFeng University of Science of Technology, Taiwan)

Yi-Lin Liao, Cheng-Yun Chung, Kuo-Lan Su (National Yunlin University of Science and Technology, Taiwan)

OS11-2 *An Indoor Autonomous Surveillance Robot via Humanoid Vision System*
Kuo-Hsien Hsia (Far East University, Taiwan)
Shao-Fan Lien, Juhng-Perng Su, Wei-Yi Ciou (National Yunlin University of Science and Technology, Taiwan)

OS11-3 *Autonomous robot localization based on 3D pose estimation approach (withdrawal)*
Chien-Chou Lin, Ben-Zhong Lin, Chang-Hong Wu (National Yunlin University of Science and Technology, Taiwan)

OS11-4 *An ultra-high speed motor driver with hybrid modulations*
Chung-Wen Hung (National Yunlin University of Science and Technology, Taiwan)

OS11-5 *A current balance strategy for multi channel interleaved power converters*
Jhih-Han Chen, Chung-Wen Hung (National Yunlin University of Science and Technology, Taiwan)

January 31 (Thursday), 10:00-11:00

Room A
GS8 Intelligent control & modeling

GS8-1 *Modeling and robust decoupling control for hypersonic scramjet vehicle*
Xiaofeng Su, Yuefei Jiang, Yingmin Jia (Beihang University, China)

GS8-2 *Flocking control of multi-agent systems in a limited space*
Sharu Jiang, Yingmin Jia, Shichen Long (Beihang University, China)

GS8-3 *Inverse kinematics in Hyper-redundant robot using Adaptive Neural Network*
Chatklaw Jareanpon (Polar lab, Department of Computer Science, Faculty of Informatics, Mahasarakham University, Thailand)

GS8-4 *Reduction of Impact when a Humanoid Robot Lands on the Ground*
Homare Fujieda, Shingo Okamoto, Jae Hoon Lee (Ehime University, Japan)

Room B
GS15 Robotics II

GS15-1 *Study on the remote and high accurate measurement of micro-cracks on the bottom of a bridge*
Jiwu Wang, Shaodong Do, Fangbo Liao (Beijing Jiaotong University, China)
Masanori Sugisaka (ALife Robotics Co., Ltd., Japan)

GS15-2 *The small eye and tongue module for an android robot head*
Dongwoon Choi, Dongwook Lee, Duckyeon Lee, Byeong-kyu Ahn, Hogil Lee (Korea Institute of Industrial Technology, Korea)

GS15-3 *Design of a robotic arm's behavior in imitation of animal consciousness: development of altruistic behavior*
Kyoko Tanaka, Eiji Hayashi (Kyushu Institute of Technology, Japan)

GS15-4 *Network Based Multiple Mobile Robots with Subsumption Architecture Supporting Swarm Behaviors*

Maki K. Habib (American University in Cairo, Egypt)

Fusaomi Nagata, Akimasa Otsuka (Tokyo University of Science, Yamaguchi, Japan)

Keigo Watanabe (Okayama University, Japan)

Room C

GS5 Human-machine cooperative systems

GS5-1 *Design of a user support system for event addition based on route search using schedule information*

Hiroki Imamura, Hiroyuki Nishiyama (Tokyo University of Science, Japan)

GS5-2 *The study of walking control with plural cylinder leg robots*

Jihao Cao, Feifei Zhang, Masanori Ito, Takumi Yaginuma (Tokyo University of Marine Science and Technology, Japan)

GS5-3 *The Ground Reaction Force generation algorithm for tracking the wearer's*

Sukwoo Lee, Jongwon Lee (University of Science and Technology, Korea)

Hyogon Kim, Jaeho Jang, Sangdeok Park (Korea Institute of Industrial Technology, Korea)

Room D

GS12 Neural networks

GS12-1 *Epilepsy Diagnosis Using PSO based ANN*

Nesibe Yalçın, Cihan Karakuzu (Bilecik Şeyh Edebali University, Turkey)

Gülay Tezel (Selçuk University, Turkey)

GS12-2 *The effect of the internal parameters on association performance of a chaotic neural network*

Shun Watanabe, Takashi Kuremoto, Masanao Obayashi (Yamaguchi University, Japan)

Kunikazu Kobayashi (Aichi Prefectural University, Japan)

GS12-3 *An estimating method for missing values by using multiple SOMs*

Yuui Kikuchi, Nobuhiro Okada, Yasutaka Tsuji, Kazuo Kiguchi (Kyushu University, Japan)

GS12-4 *Proposal and Evaluation of information gathering methods that considers the MANET's load in a desaster*

Keisuke Gohara, Hiroyuki Nishiyama (Tokyo University of Science, Japan)

January 31 (Thursday), 11:15-12:15

Poster Session

PS1-1 *Application of the actor-critic method to a robot using state representation based on distance between distributions*

Manabu Gouko (Tohoku Gakuin University, Japan)

PS1-2 *Color Halftoning Using the Error Diffusion Method by the Edge Adjustment and the False Colored Limit*

Kazuya Kadoya, Ken-ichi Tanaka (Meiji University, Japan)

PS1-3 *The Three Optimization Methods of Searching The Effective Combination Dither Matrix*
Shohei Niinuma, Kenichi Tanaka (Meiji University, Japan)

PS1-4 *Inverse halftoning of color image using unsharp mask*
Hiroki Matsuo, Ken-ichi Tanaka (Meiji University, Japan)

PS1-5 *Development of mobile robot navigation system using simplified map based on place recognition*
Satoshi Yamanaka, Kazuyuki Morioka (Meiji University, Japan)

PS1-6 *Robots from printer: the prospect of using printed electronics technologies for producing robots and creating objects of electronic artificial life*
Sergey N. Orlov, Evgeny S. Gornev, Nikolay A. Zaytsev, Sergey I. Yanovich, Andrey G. Krasnikov, Ilya A. Khomyakov (Molecular Electronics Research Institute JSC, Russia)

PS1-7 *Teaching method for the industrial dual-arm robot*
Taeyong Choi (KIMM, Korea)

PS1-8 *Real-time 3D-Shape Reconstruction System in Intelligent Space Based on Networked Vision Sensors*
Takashi Ishimaru, Kazuyuki Morioka (Meiji University, Japan)

PS1-9 *Using a GA-based extension recognized method for fault diagnosis in car engines*
Meng-Hui Wang, Pi-Yun Chen (National Chinyi University of Technology, Taiwan)

PS1-10 *Design of a rehabilitation robot suit with hardware-based safety devices: Proposal of the basic structure*
Yoshihiro Kai, Satoshi Kitaguchi (Tokai University, Japan)
Wenlong Zhang, Masayoshi Tomizuka (University of California, Berkeley, USA)

PS1-11 *Through-Wall Imaging for a Metallic Cylinder by Dynamic Differential Evolution*
Chung-Hsin Huang (Taipei College of Maritime Technology, Taiwan)
Chi-Hsien Sun, Ping-Chieh Chiang (National Taiwan University of Science and Technology, Taiwan)
Lung-Fai Tuen, Ching-Lieh Li, Pin-Ru Lai (Tamkang University, Taiwan)

PS1-12 *Analysis of Effects of Exercises on Middle-aged and Elderly Arthritics by Thermal Imagery and Automatic Auxiliary Diagnosis*
Chin-Lun Lai, Tung-Lin Yang (Oriental Institute of Technology, Taiwan)
Tsung-Ching Lin (Far Eastern Memorial Hospital, Taiwan)

PS1-13 *Enhancing electrical communication through reconstructed nanowire electrodes for implantable enzymatic biofuel cell (EBFC)*
Deby Fapyane, Soo-Jin lee, In seop Chang (Gwangju Institute of Science and Technology (GIST), Korea)
DuHyun Lim, Jou-Hyeon Ahn (Gyeongsang National University, Korea)

PS1-14 *Object tracking based on adaboost classifier and particle filter*
Chin-Lun Lai, Li-Yin Lee (Oriental Institute of Technology, Taiwan)

PS1-15 *A metaheuristic for huge scale quadratic assignment problems*
Hatsumi Nakaura, Fubito Toyama, Hiroshi Mori, Kenji Shoji, Juichi Miyamichi (Utsunomiya University, Japan)

PS1-16 *Competition-based Particle Swarm Optimizer for solving Numerical Optimization Problems*
Sheng-Ta Hsieh, Bo-Han Chen (Oriental Institute of Technology, Taiwan)

© ISAROB 2013

PS1-17 *Elitist Differential Evolution for solving Numerical Optimization Problems*
Sheng-Ta Hsieh, Huang-Lyu Wu, Tse Su (Oriental Institute of Technology, Taiwan)

PS1-18 *Artificial Bee Colony Algorithm with Crossover Strategy for Global Numerical Optimization*
Sheng-Ta Hsieh, Jhih-Sian Chen (Oriental Institute of Technology, Taiwan)

PS1-19 *Microwave Imaging of Dielectric Cylindrical Target Using Dynamic Differential Evolution and Self-Adaptive Dynamic Differential Evolution*
Ching-Lieh Li, Lung-Fai Tuen, Huang-Wei Wong (Tamkang University, Taiwan)
Chi-Hsien Sun (National Taiwan University of Science and Technology, Taiwan)
Chung-Hsin Huang (Taipei College of Maritime Technology, Taiwan)

PS1-20 *Application of Natural Language Processing for Information Retrieval*
Su Mei Xi (Shandong Polytechnic University, China)
Dae Jong Lee (Chungbuk National University, Korea)
Young Im Cho (Suwon University, Korea)

January 31 (Thursday), 14:30-15:30

Room A
GS4 Control techniques

GS4-1 *Self-triggered optimal control based on optimization with prediction horizon one*
Koichi Kobayashi, Kunihiko Hiraishi (Japan Advanced Institute of Science and Technology, Japan)

GS4-2 *H∞ controller with graphical LMI region profile for gantry crane system*
Mohd Zaidi Bin Mohd Tumari, Muhammad Salihin Bin Saealal, Mohd Riduwan Bin Ghazali, Yasmin Binti Abdul Wahab (Universiti Malaysia Pahang, Malaysia)

GS4-3 *Optimized Walking Control of a Biped Walking Robot Considering Theory of a Pendulum*
Hisashi Koike, Jae Hoon Lee, Shingo Okamoto (Ehime University, Japan)

GS4-4 *Sliding mode control of a quad rotor helicopter using nonlinear sliding surface*
Bambang Sumantri (Toyohashi University of Technology, Electronic Engineering Polytechnic Institute of Surabaya, Indonesia)
Naoki Uchiyama, Shigenori Sano, Yuma Kawabata (Toyohashi University of Technology, Japan)

Room B
GS10 Mobile vehicles

GS10-1 *Development of Outdoor Mobile Robot for Human Following Navigation*
Jae Hoon LEE, Kei OKAMOTO, Masumi OUE, Shingo OKAMOTO (Ehime University, Japan)

GS10-2 *Parameter Estimation Experiment and Development of Decentralized Caster Modules*
Kazuyoshi Ohara, Jae Hoon Lee, Shingo Okamoto (Ehime University, Japan)

GS10-3 *Parameter optimization for decoupling controllers of 4WS vehicles*
Mingxing Li, Haijing Xu, Yingmin Jia (Beihang University, China)

GS10-4 *A method of sharing for common coordinate system by using relative position among the swarm*
Koji Makino (Tokyo University of Technology, Japan)

Room C

GS2 Artificial life and complexity

GS2-1 *Non-uniform Cellular Automata based on Open-ended Rule Evolution*
Noritsugu Sughimura, Reiji Suzuki, Takaya Arita (Nagoya University, Japan)

GS2-2 *A Procedure for Constructing Social Network Using Web Search Engines: The Case for Japanese Automotive Industry*
Yuchi Kubota, Reiji Suzuki, Takaya Arita (Nagoya University, Japan)

GS2-3 *Statistical Analysis for Price Changes of Carbon European Union Allowances*
zeyu zheng, Kazuko yamasaki (Tokyo University of information sciences, Japan)
Jun Yang (Chongqing University, China)

Room D

GS7 Image processing

GS7-1 *A describing method of latency tolerant hardware for a pure ANSI-C/C++ based high-level synthesis technology*
Akira Yamawaki, Seiichi Serikawa (Kyushu Institute of Technology, Japan)

GS7-3 *A Research on State Recognition in Wide Area by Aerial Images Analysis*
Ganwen Jiang, Masayuki Kashima, Kiminori Sato, Mutsumi Watanabe (Kagoshima University, Japan)

GS7-4 *Semantic Segmentation in Manhattan-like Environments from 2.5D data*
Sven Olufs, Markus Vincze (University of Technology / Automation and Control Institute, Austria)

January 31 (Thursday), 15:45-17:00

Room A

GS9 Learning

GS9-1 *Cell-production parts layout by virtual factory system using reinforcement learning and MTM*
Hidehiko Yamamoto, Tsuyoshi Sugimoto, Takayoshi Yamada (Gifu University, Japan)
Masahiro Nakamura (Lexer Research Inc, Japan)

GS9-2 *Gait motion of a six legged real robot employing associatron*
Masashi Sakai, Tomo Ishikawa, Masato Hashimoto, Tomo Ishikawa, Koji Makino, Jin-Hua She, Yasuhiro Ohyama (Tokyo University of Technology, Japan)

GS9-3 *Modified Neural Q-Learning for Two-Wheeled Inverted Pendulum balancing Control*
Yeon-Seob Kim, Ju-Jang Lee (Korea Advanced Institute of Science and Technology, Korea)

GS9-4 *Reinforcement learning for dynamic environment: a classification of dynamic environments and a detection method of environmental changes*
Masato Nagayoshi (Niigata College of Nursing, Japan)
Hajime Murao, Hisashi Tamaki (Kobe University, Japan)

Room B

OS13 Kansei Engineering and its Applications
Chair: Tetsuo Hattori (Kagawa University, Taiwan)
Co-Chair: Yoshiro Imai (Kagawa University, Japan)

OS13-1 *On a relation between feeling Impression and 3PACF of sound signal*
Yusuke Kawakami, Tetsuo Hattori (Kagawa University, Japan)
Hiromichi Kawano (NTT Advanced Technology, Japan)
Tetsuya Izumi (Micro Technica Co., Ltd., Japan)

OS13-2 *Color image arrangement by elastic transform based on histogram matching*
Daisuke Kutsuna, Tetsuo Hattori, Yusuke Kawakami, Haruna Matsushita, Yoshiro Imai (Kagawa University, Japan)
Tetsuya Izumi (Micro Technica Co., Ltd., Japan)

OS13-3 *Face identification insensitive to facial expression in the crowded people scene*
Qingyu Shu, Tetsuo Hattori, Saki Masunari (Kagawa University, Japan)
Tetsuya Izumi (Micro Technica Co., Ltd., Japan)
Hiromichi Kawano (NTT Advanced Technology, Japan)
Bahram Javidi (University of Connecticut, USA)

OS13-4 *Kansei Engineering based evaluation for distance learning on distributed multiple servers*
Yoshio Moritoh (Kagawa Junior College, Japan)
Yoshiro Imai, Tetsuo Hattori (Kagawa University, Japan)

OS13-5 *An application of Kansei Engineering to community-based collaboration*
Masatoshi Imai (Kagawa Junior College, Japan)
Yoshiro Imai, Tetsuo Hattori (Kagawa University, Japan)

Room C

OS1 Artificial Life and Control
Chair: Hee-Hyol Lee (Waseda University, Japan)

OS1-1 *A Micro-Simulator for Traffic Signal Control Based on A Modified Cellular Automaton Traffic Flow Model*
Hu Jin, Chengyou Cui, Hee-hyol Lee (Waseda University, Japan)

OS1-2 *Real-Time Stochastic Optimal Control for Traffic Signals of Multiple Intersections*
Chengyou Cui, Hee-hyol Lee (Waseda University, Japan)

OS1-3 *Decouple PID Control of Compact Binary Power Generation*
Kun-Young Han, Lu Li, Hee-Hyol Lee (Waseda University, Japan)

OS1-4 *Decouple Sliding Mode Control of Compact Binary Power Generation*
Kun-Young Han, Hee-Hyol Lee (Waseda University, Japan)

Room D

GS11 Multi agent system

GS11-1 *Evaluation of efficiency of the symmetry bias in grammar acquisition*
Ryuichi Matoba, Hiroki Sudo, Shingo Hagiwara (Toyama National College of Technology, Japan)
Satoshi Tojo (Japan Advanced Institute of Science and Technology, Japan)

GS11-2 *The Evolution of Pre-play Communication in the Interactive Minority Game*
Keita Nishimoto, Reiji Suzuki, Takaya Arita (Nagoya University, Japan)
Ivan Tanev, Katsunori Shimohara (Doshisha University, Japan)

GS11-3 *A new decision-making system of an agent based on emotional models in multi-agent system*
Shogo Watada, Masanao Obayashi, Takashi Kuremoto, Shingo Mabu (Yamaguchi University, Japan)
Kunikazu Kobayashi (Aichi Prefectural University, Japan)

GS11-4 *Design of a user-support system for finding the other person talking on smart Phones*
Hiroyuki Nishiyama, Fumio Mizoguchi (Tokyo University of Science, Japan)

February 1 (Friday), 08:30-10:15

Room A

OS5 Computer-Supported Learning Systems
Chair: Kenneth J. Mackin (Tokyo University of Information Sciences, Japan)
Co-Chair: Takashi Yamaguchi (Tokyo University of Information Sciences, Japan)

OS5-1 *Development of entertainment based learning features in programming learning support system*
Eiji Nunohiro, Masanori Ohshiro, Takashi Yamaguchi (Tokyo University of Information Sciences, Japan)

OS5-2 *Programming learning support systems focused on structures of programming language and code*
Masanori Ohshiro, Takashi Yamaguchi, Eiji Nunohiro (Tokyo University of Information Sciences, Japan)

OS5-3 *Individual student support system for teacher and TAs using mobile devices in exercise classes*
Masaki Hanada, Takashi Yamaguchi, Yasuo Nagai (Tokyo University of Information Sciences, Japan)

OS5-4 *Research on XP approach using The Personal Software Process Practices*
Daisuke Yamaguchi (Toin University of Yokohama, Japan)

OS5-5 *Non-event driven graphics API for programming education*

Kenneth J. Mackin (Tokyo University of Information Sciences, Japan)

OS5-6 *An Education of Social Media Literacy to High School Students in Social Media Times*

Yoshihiro Kawano, Takuya Miya, Naoki Furuya (Tokyo University of Information Sciences, Japan)

Yuka Obu (Unicast Inc., Japan)

OS5-7 *Syntax structure based typing tool for source code writing*

Takashi Yamaguchi, Shinya Iwasaki, Kazuma Mori, Kenneth J. Mackin, Masaki Hanada, Eiji Nunohiro (Tokyo University of Information Sciences, Japan)

Room B

OS7 Control of Mechatronic System

Chair: Shinichi Sagara (Kyushu Institute of Technology, Japan)

Co-Chair: Masahiro Oya (Kyushu Institute of Technology, Japan)

OS7-1 *Adaptive steering controller for vehicles with driving/braking force distribution*

Bo Zhou, Masahiro Oya, Jinxin Zhuo, Panfeng Shu (Kyushu Institute of Technology, Japan)

OS7-2 *Oscillation Control of a Contact Scanning Scanners System*

Hideki Wada (Sin-Nippon Nondestructive Inspection co., Japan)

Hiroyuki Koga, Masahiro Oya (Kyushu Institute of Technology, Japan)

Katuhiro Okumura (Fukuoka Industrial Technology Center, Japan)

OS7-3 *Rollover Prevention Control of Driver-Heavy Vehicle Systems*

Yusuke Suetake, Masahiro Oya, Pangfeng Shu, Jinxin Zhou (Kyushu Institute of Technology, Japan)

OS7-4 *Development of a dual-shaft propeller thruster equipped with rotational speed sensor for UVMS control*

Radzi Bin Ambar, Shinichi Sagara, Takuya Yamaguchi (Kyushu Institute of Technology, Japan)

OS7-5 *Control of a dual arm underwater robot*

Shinichi Sagara, Radzi Bin Ambar, Kenichi Imaike (Kyushu Institute of Technology, Japan)

Room C

OS8 Facial Expression Recognition, Speech Synthesis of Emotions, and Music Recommendation

Chair: Yasunari Yoshitomi (Kyoto Prefectural University, Japan)

Co-Chair: Taro Asada (Kyoto Prefectural University, Japan)

OS8-1 *Speech synthesis of emotions using vowel features of a speaker*

Kanu Boku, Taro Asada, Yasunari Yoshitomi, Masayoshi Tabuse (Kyoto Prefectural University, Japan)

OS8-2 *A system for facial expression recognition of a speaker using thermal image processing and feature vector space characteristics*

Taro Asada, Yasunari Yoshitomi, Yuu Nakanishi, Masayoshi Tabuse (Kyoto Prefectural University, Japan)

© ISAROB 2013

OS8-3 *Facial expression recognition of a speaker using thermal image processing and reject criteria in feature vector space*

Yuu Nakanishi, Yasunari Yoshitomi, Taro Asada, Masayoshi Tabuse (Kyoto Prefectural University, Japan)

OS8-4 *Music recommendation hybrid system for improving recognition ability using collaborative filtering and impression words*

Saya Yoshizaki (Works Applications Co., Ltd., Japan)

Yasunari Yoshitomi, Taro Asada (Kyoto Prefectural University, Japan)

Chikoto Koro (ISI Software Corp., Japan)

February 1 (Friday), 08:30-09:30

Room D

GS17 Virtual reality

GS17-1 *Estimating the clothes characteristics with image and depth sensors for developing virtual fitting room*

Yuka Matsuba, Hiroyuki Funaya, Kazushi Ikeda (Nara Institute of Science and Technology, Japan)

Jehan Jung, Rammohan Mallipeddi, Minho Lee (Kyungpook National University, Korea)

GS17-2 *Spatial operation using skeletal recognition for virtual 3D work space*

Yusuke Saito, Hiroyuki Nishiyama (Tokyo University of Science, Japan)

GS17-3 *Breast Cancer Palpation Training System Using Five-Fingered Haptic Interface Robot and GPGPU*

Takamitsu Kawai, Tetsuya Mouri, Takahiro Endo, Haruhisa Kawasaki (Gifu University, Japan)

GS17-4 *ALife approach for body-behavior predator-prey coevolution: body first or behavior first?*

Takashi Ito, Marcin L. Pilat, Reiji Suzuki, Takaya Arita (Nagoya University, Japan)

February 1 (Friday), 08:30-10:15

Room E

GS6 Human-welfare robotics

GS6-1 *A study on the communication system using electrooculogram signals for persons with disabilities*

Sou GO, Mingmin Yan, Hiroki Tamura, Koichi Tanno (University of Miyazaki, Japan)

GS6-2 *A study on the electric wheelchair hands-free control system using the laser range scanner*

Takayuki Murata, Hiroki Tamura, Koichi Tanno (University of Miyazaki, Japan)

GS6-3 *On driving assistance using forearm vibrotactile feedback for wheelchair drivers*

Aydin Tarik Zengin, Kazuki Nabekura, Hiroshi Okajima, Nobutomo Matsunaga (Kumamoto University, Japan)

GS6-4 *Measurement and analysis of upper-limb essential tremor motion for tremor suppression with an exoskeleton robot*

Yosuke Ono, Kazuo Kiguchi, Nobuhiro Okada (Kyushu University, Japan)

© ISAROB 2013

February 1 (Friday), 10:30-11:30

Room A
GS13 Pattern recognition

GS13-1 *Simultaneous Recognition of Multiple Actions using CHLAC features*
Kyosuke Masumitsu, Takayasu Fuchida (Kagoshima University, Japan)

GS13-2 *Hand gesture recognition using subunit-based dynamic time warping*
Yanrung Wang, Atsushi Shimada, Rin-ichiro Taniguchi (Kyushu University, Japan)
Takayoshi Yamashita (OMRON Corporation, Japan)

GS13-3 *Mathematical modeling of mirror based passive moiré target for orientation sensing*
Md. Mahbub Hasan, Satoshi Tanemura, Kenbu Teramoto(Saga University, Japan)

GS13-4 *A study about interactive musical editing system for automatic piano : Inferring performance expression by considering tempos*
Tomohiro Inoue, Eiji Hayashi (Kyushu Institute of Technology, Japan)

Room B
GS16 Robotics III

GS16-1 *A precision position arrangement of the SCARA robot by H∞ robust control*
Yasuyuki Hirofuji, Feifei Zhang, Masanori Ito (Tokyo University of Marine Science and Technology, Japan)

GS16-2 *Hybrid control with adaptive and state feedback control for Robot Hand*
Kazuma Funahashi, Hiroki Goto, Feifei Zhang, Masanori Ito (Tokyo University of Marine Science and Technology, Japan)

GS16-3 *Hexa-Quad Transformation Control for Hexapod Robot Based on Support Polygon Pattern*
Addie Irawan, Yee Yin Tan, Mohd Syakirin Ramli, Mohd Riduwan Ghazali (University Malaysia Pahang, Malaysia)
Kenzo Nonami (Chiba University, Japan)

GS16-4 *Design of a special cam-based high speed manipulator system*
Jing Wu, Rui-Jun Yan, Kyoosik Shin, Chang-Soo Han (HanYang University, Korea)

Room C
GS3 Artificial living

GS3-1 *A Real-Coded Genetic Algorithm Taking Account of the Weighted Mean of the Population*
Naotoshi Nakashima, Yuichi Nagata, Isao Ono (Tokyo Institute of Technology, Japan)

© ISAROB 2013

GS3-2 *Diesel Engine Fuel Injection Control with DDVC Hydraulic System*

Xing Jin, Feifei Zhang, Masanori Ito, Kyoko Narukawa (Tokyo University of Marine Science and Technology, Japan)

GS3-3 *The Complex Network Study of Money and CO2 Emission Flows between Industrial Sectors in Asian Countries using Input-Output Table*

Xiang Gao, Takeshi Fujiwara, Kousuke Yoshizawa, Shuhei Miyake, Zeyu Zheng, Naoko Sakurai, Kazuko Yamasaki (Tokyo University of Information Sciences, Japan)

GS3-4 *On a serendipity oriented recommender system based on folksonomy*

Hisaaki Yamaba, Michihito Tanoue, Kayoko Takatsuka, Naonobu Okazaki, Shigeyuki Tomita (University of Miyazaki, Japan)

February 1 (Friday), 9:45-10:45

Room D

OS2 Bio-inspired Theory and Applications

Chair: Kunihito Yamamori (University of Miyazaki, Japan)

OS2-1 *Diffusion model analysis of OneMax problem*

QinLian Ma, Kiminobu Koga, Kunihito Yamamori, Makoto Sakamoto, Hiroshi Furutani (University of Miyazaki, Japan)

Yu-an Zhang (Qinghai University, China)

OS2-2 *Study of factor IX gene using regional structure*

Hiroshi Furutani, Kenji Sueyoshi, Kenji Aoki, Kunihito Yamamori, Makoto Sakamoto (University of Miyazaki, Japan)

OS2-3 *Remarks on Recognizability of Four-Dimensional Topological Components*

Makoto SAKAMOTO, Makoto NAGATOMO, Tatsuma KUROGI, Satoshi IKEDA, Masahiro YOKOMICHI, Hiroshi FURUTANI (University of Miyazaki, Japan)

Takao ITO, Yasuo UCHIDA (Ube National College of Technology, Japan)

Tsunehiro YOSHINAGA (Tokuyama College of Technology, Japan)

OS2-4 *Power Consumption Reduction by Dynamic Core-counts Control with Power Gating*

Kazuyuki Tamoto, Kunihito Yamamori, Masaru Aikawa (University of Miyazaki, Japan)

February 1 (Friday), 11:00-11:30

Room D

OS14 Applications and Theories of Advanced Technology
Chair: Takao Ito (Ube National College of Technology, Japan)

OS14-1 *Bottom-Up Pyramid Cellular Acceptors with n-Dimensional Layers*
Makoto SAKAMOTO, Tatsuma KUROGI, Makoto NAGATOMO, Satoshi IKEDA, Masahiro YOKOMICHI, Hiroshi FURUTANI, (University of Miyazaki, Japan)
Takao ITO, Yasuo UCHIDA (Ube National College of Technology, Japan)
Tsunehiro YOSHINAGA (Tokuyama College of Technology, Japan)

OS14-2 *Homogeneous Systolic Pyramid Automata with n-Dimensional Layers*
Makoto SAKAMOTO, Tatsuma KUROGI, Makoto NAGATOMO, Satoshi IKEDA, Masahiro YOKOMICHI, Hiroshi FURUTANI, (University of Miyazaki, Japan)
Takao ITO, Yasuo UCHIDA (Ube National College of Technology, Japan)
Tsunehiro YOSHINAGA (Tokuyama College of Technology, Japan)

February 1 (Friday), 10:30-11:30

Room E

OS12 Intuitive Human-System Interaction
Chair: Masao Yokota (Fukuoka Institute of Technology, Japan)
Co-Chair: Kaoru Sugita (Fukuoka Institute of Technology, Japan)

OS12-1 *Automatic identification of 3-D shape of head for wig manufacture*
Yonghu Zhu, Yoshiaki Adaniya, Kazuhiro Tsujino, Cunwei Lu (Fukuoka Institute of Technology, Japan)

OS12-2 *Retrieval method for augmented reality objects based on color impression*
Kazunori Nakamura, Kaoru Sugita, Masao Yokota (Fukuoka Institute of Technology, Japan)

OS12-3 *Preparatory data analysis for customer servicing interface of Buddhism statue ordering system*
Tzu-Hsuan Huang, Kaoru Sugita, Masao Yokota (Fukuoka Institute of Technology, Japan)

OS12-4 *Toward multimodal user interface for intuitive interaction with Buddhism statue ordering system*
Tzu-Hsuan Huang, Kaoru Sugita, Masao Yokota (Fukuoka Institute of Technology, Japan)

© ISAROB 2013

The Eighteenth International Symposium on Artificial Life and Robotics 2013 (AROB 18th '13),
Daejeon Convention Center, Daejeon, Korea, January 30-February 1, 2013

Effect of Playful Balancing Training – A Pilot Randomized Controlled Trial

Henrik Hautop Lund Jari Due Jessen

Centre for Playware, Technical University of Denmark, 2800 Kgs. Lyngby, Denmark

hhl@playware.dtu.dk
www.playware.dk

Abstract

We used the modular playware in the form of modular interactive tiles for playful training of community-dwelling elderly with balancing problem. During short-term play on the modular interactive tiles, the elderly were playing physical, interactive games that were challenging their dynamic balance, agility, endurance, and sensor-motoric reaction. A population of 12 elderly (average age: 79) with balancing problems (DGI average score: 18.7) was randomly assigned to control group or tiles training group, and tested before and after intervention. The tiles training group had statistical significant increase in balancing performance (DGI score: 21.3) after short-term playful training with the modular interactive tiles, whereas the control group remained with a score indicating balancing problems and risk of falling (DGI score: 16.6). The small pilot randomized controlled trial suggests that the playful interaction with the modular interactive tiles has a significant effect even after a very short time of play. The average total training time to obtain the statistical significant effect amounted to just 2h45m.

Introduction

Research into playware [1] and modular playware [2] puts emphasis on the design of (modular) intelligent hardware and software that creates play and playful experiences. Often, it is believed that such playware can mediate other actions, for instance actions such as social interaction and physical movement. It has been outlined how the playware may act as a play force that pushes the user into play dynamics [3]. When you are in such play dynamics, you may feel transformed from the normal state of being and feel as if forgetting about time and place. Sometimes we may feel being able to perform more or better when in play, which is interesting if such performance may have a desired side effect. Indeed, Vygotsky puts it like "Play creates a zone of proximal development in the child. In play, the child always behaves beyond his average age, above his daily behavior; in play it is as though he were a head taller than himself. As in the focus of a magnifying glass, play contains all developmental tendencies in a condensed form and is itself a major source of development." [4].

We believe that this quality of play may translate to many different groups of people. However, often accounts for the potential benefit of play e.g. on cognitive learning or physical abilities remain of a descriptive nature. Therefore, in this study, we engage in making a quantitative study of the effect of play, and we perform the study with a user group with whom play is often not attributed. In particular, to make such a study, our objective became to test for dynamic balancing of community-dwelling elderly as a result of short-term training playing with a specific playware, namely the modular interactive tiles [5].

Equipment - Modular Interactive Tiles

For the effect test of playful training, we used the modular interactive tiles as the training equipment. The modular tiles have been described before in details, e.g. [5, 6]. This is a fully distributed system made up of a number of tiles that can connect to each other to form a surface, on which people can play different games, either by themselves or by competing with each other. Each tile contains a microprocessor, battery, IR communication, an FSR sensor, and 8 coloured LEDs in a circle. The FSR sensor can sense a step or a hit on a tile, and the LEDs can shine up in different coloured patterns. This is used to create interactive games on the modular interactive tiles. Currently, there are more than 20 different games for the modular interactive tiles. The games used for the intervention are described later.

The tiles can easily be taken apart and put together to create different forms, which will demand different

© ISAROB 2013

interaction patterns by the users when playing the games, e.g. the tiles can be changed from a 3*3 square to a horse-shoe shape in less than a minute.

Figure 1: Left: The interior of the modular interactive tiles. Right: Assembling of a tile play field.

Intervention

We prepared a small randomized controlled trial as a pilot study of dynamic balancing of elderly training with modular interactive tiles, with the objective to evaluate the effect of short-term playful training.

Twelve community-dwelling elderly people (average age: 79 (66-88)) with balancing problems were recruited from the waiting list for voluntary balancing training amongst elderly in Lyngby-Taarbaek Municipality in Copenhagen, Denmark. The population of elderly with balancing problems was randomly assigned to control group (CG) or tiles training group (TTG). The random assignment was done by lottery tickets picked by a third person blinded to the intervention.

The population from both the tiles training group and the control group was tested for dynamic balancing using the Dynamic Gait Index test before (pretest) and after (posttest) the intervention. The tests were performed by two physiotherapists from Lyngby-Taarbaek Municipality, who were both blinded to the intervention and who did not take part in the intervention.

The Dynamic Gait Index (DGI) contains 8 different tests of balancing. The DGI was developed by Shumway-Cook and Woollacott [7] as a clinical tool to assess gait, balance and fall risk, and it is viewed as an especially sensitive task, since it evaluates not only usual steady-state walking, but also walking during more challenging tasks. The eight abilities assessed are: steady-state walking, walking while changing gait speed, walking while moving the head vertically and horizontally, walking while stepping over and around an obstacle, pivoting during walking, and stair climbing (each ability is scored 0-3). A DGI score lower than 19 points has been associated with impairment of gait and fall risk [7, 8].

DGI was collected before and after a 2-months period, during which the tiles training group performed an average of 12.5 group training sessions on the modular interactive tiles. On average, each individual performed 13 minutes of playful training on the modular interactive tiles at each of the group sessions (Fig. 2). The control group continued their normal daily activities during the 2-months period.

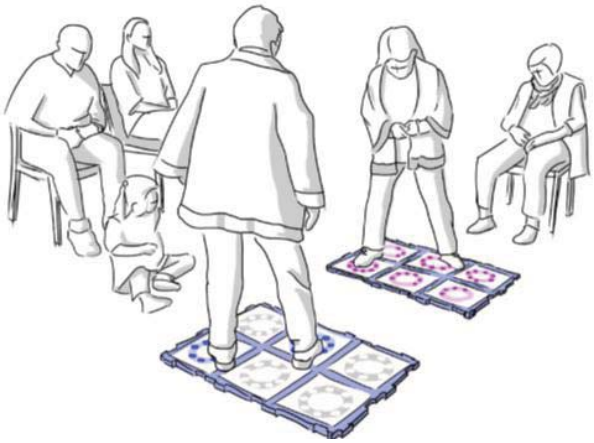

Figure 2: The group session for playful training in the tiles training group.

The training sessions with the elderly group was planned in cooperation with physiotherapists from Lyngby-Taarbaek Municipality. In order to secure a valid result, a protocol for the intervention was designed, in which 4 games were chosen that the elderly should try out: "Color Race", "Final Countdown", "Island" and "Concentration Color" (see Fig. 3 for the protocol). "Color Race" is a game where one of the tiles will light up in red. When stepped on, the tile will go black and another will light up. The player needs to step on as many tiles as possible within 30 seconds. In "Final Countdown" all the tiles will light up in purple and each tile will start counting down by turning off one of its 8 LED's every second. When the player steps on a tile, the countdown will restart. If any of the tiles gets all its LED's turned off, the game is lost. "Island" can be compared to the children game "The Floor is Made of Lava". Here, the player needs to move from green tile to green tile or island to island, without stepping on the other tiles. Once stepped on, the tile will start counting down and the player has to go on to the next before the tile turns off. This game will automatically adjust the speed according to the player's performance. The last game "Concentration Color" is a

© ISAROB 2013

memory game where all tiles turn white but they are hiding a colour 'underneath'. When stepped on, a tile will show the color it is "hiding". The object of the game is then to find all the matching color pairs (red, green, blue, yellow, purple, light blue).

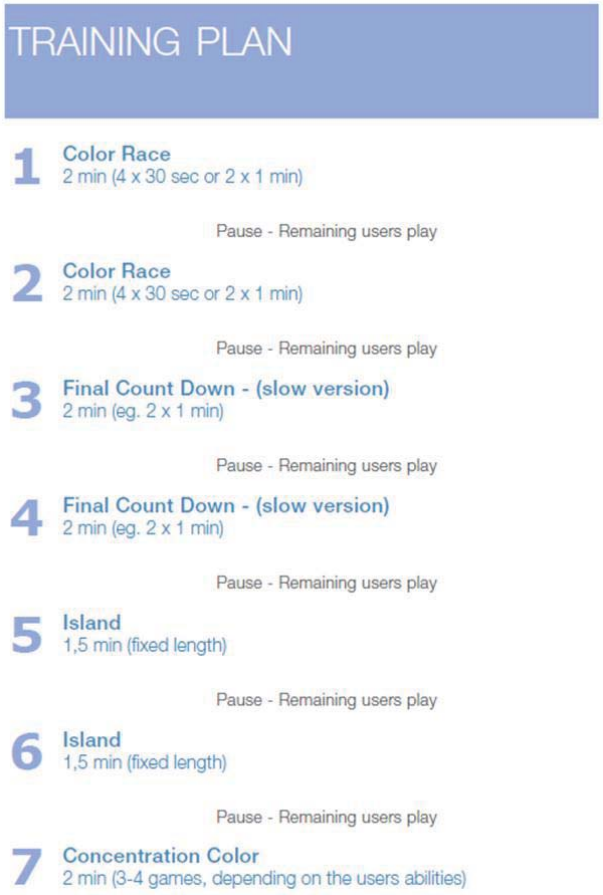

Figure 3: The training protocol for the tiles training group.

The training group was put into two groups where each group had one hour of training. The group was placed around the tiles that to begin with were placed in a group of 3x3 tiles. This setup of the tiles was changed before playing the game "Concentration Color" where the platform was changed to a "horse shoe" formation.

The sessions was built up of small "rounds" of play, where each participant played two minutes (though only 1,5 minutes for the game Island) of each game before having a small break while the rest of the group played.

Each training session was organized like this: 2 rounds of "Color Race", 2 rounds of "Final Countdown", 2 rounds of "Island" and 1-2 rounds of "Concentration Color" depending on the time available (see Fig 3).

Results

The population of elderly with balancing problems was tested with the DGI, and had an average score of 18.7. In the DGI test, below 19 is viewed as the threshold for having balancing problems and risk of falls. The population was randomly assigned to control group or tiles training group. Data were analyzed for statistical significant differences between the control group and the tiles training group, and for increase of mean score on DGI.

After the random division into the two groups, the control group and the tiles training group did not differ at baseline (DGI mean score: 18.3 vs. 19.0). After the 2-months period, there was significant difference in change of DGI score period with the control group decreasing DGI score by 9.3% and tiles training group increasing DGI score by 12.3% on average. A two way repeated measures ANOVA (Student Newman-Keuls method) resulted in no statistical significant differences at baseline. Also, there was no statistical significant difference in the control group's performance over time. There was statistical significant increase in performance of the tiles training group over time ($p<0.05$). Also, there was statistical significant difference between the control group and the tiles training group after intervention ($p<0.05$). DGI mean score after intervention was 16.6 for the control group, and 21.33 for the tiles training group, or an average decrement of 9.3% for the control group and an increase of 12.3% for the tiles training group.

The score for control group and intervention group is presented in table 1.

Table 1. Results of the DGI pre-test and post-test after two months of the 12.5 sessions training with modular interactive tiles.

	Pre-test	Post-test	Improve-ment	Significance
Control group	18.3	16.6	-9.3%	NS
Training group	19.0	21.3	12.3%	P<0.05

The community dwelling elderly with balancing problems seemed to be at high risk of falling if not subject to any training, whereas those who performed training increased their dynamic balancing abilities. A DGI score of <19 is associated with impairment of gait and fall risk [7, 8], so the statistical significant difference

© ISAROB 2013

between DGI score of 16.6 of the control group and DGI score of 21.33 of the tiles training group is important.

During the sessions the elderly expressed an increase in their abilities and endurance in normal day activities. At the posttest one participant expressed that others had told her that they could see and feel an increase in her general movements, endurance and balance.

Discussion and Conclusion

Despite the limited sample set, the trend of the pilot study is clear: there is statistical significant effect from short-term playful training with the modular interactive tiles. The community dwelling elderly with balancing problems seemed to be at high risk of falling if not subject to any training, whereas those who performed training increased their dynamic balancing abilities. A DGI score of <19 is known to signify risk of falling, so the significant difference between DGI score of 16.6 of CG and DGI score of 21.33 of TTG is important, as it indicates that it may be possible to ensure that such a test population may reduce risk of falling by training on the modular interactive tiles.

The study also shows how playful hardware (playware) can be used to create a quantifiable effect on people by using play as a motivator for engagement and training.

The study has certain, clear limitations. First and foremost, the study was performed as a pilot study with only 12 subjects. A larger randomized control trial (RCT) should be performed based upon the indications of this small pilot study. Despite such limitations, it is interesting that the effect of training with the modular interactive tiles amongst the community-dwelling elderly with balancing problems was obtained after just 13 minutes of training per session for an average of 12.5 training sessions. Hence, the average total training time to obtain this statistical significant effect amounts to just around 2h45m, which is very little training time.

Acknowledgement

The work is partly sponsored by the project Patient @ Home. The authors would like to thanks participating elderly in the intervention group and control group, therapists from Lyngby-Taarbaek Municipality, and colleagues from the Center for Playware, DTU.

References

[1] H. H. Lund, T. Klitbo, and C. Jessen, C. Playware Technology for Physically Activating Play, Artificial Life and Robotics Journal, 9:4, 165-174, 2005.
[2] H. H. Lund, and P. Marti. Designing Modular Robotic Playware. In Proc. of 18th IEEE Int. Symposium on Robot and Human Interactive Communication (Ro-Man 2009), IEEE Press, 115-121, 2009.
[3] C. Jessen and H. H. Lund. On play forces, play dynamics, and playware. Unpublished manuscript.
[4] L. S. Vygotsky, L.S. Mind in society: The development of higher mental processes. Eds. and trans. M. Cole, V. John-Steiner, S. Scribner and E. Souberman. Cambridge, MA: Harvard University Press, 1930-35/1978.
[5] H. H. Lund. Modular Robotics for Playful Physiotherapy, in Proceedings of IEEE Int. Conference on Rehabilitation Robotics, IEEE Press, 571-575, 2009.
[6] C. B. Nielsen and H. H. Lund. Adapting Playware to Rehabilitation Practices. *International Journal of Computer Science in Sport, 11:1*, 2012.
[7] A. Shumway-Cook and M. Woollacott. Motor Control: Theory and Applications. Baltimore, MD: Wilkins & Wilkins; 1995.
[8] A. Shumway-Cook, M. Baldwin, N. L. Polissar, and W. Gruber. Predicting the probability for falls in community-dwelling older adults. *Phys Ther.* 1997;77:812–819.

© ISAROB 2013

Engaging through her eyes
Embodying the perspective of a robot companion

Patrizia Marti[1], Jelle T. Stienstra[12]

[1]Social, Political and Cognitive Science Department, University of Siena, Italy
[2]Department of Industrial Design, Eindhoven University of Technology, Netherlands
(Tel: +390577234743, Fax: +390577234754)

patrizia.marti@unisi.it, j.t.stienstra@tue.nl

Abstract: In response to a change in the use of computers and interactive technologies, traditional Human-Computer Interaction concepts of usability, efficiency and productivity have progressively been enriched with other concepts such as curiosity, empathy, playfulness and affection [1]. Korhonen et al. [2] state that the acceptance of a product depends not only on its utilitarian properties but also on non-utilitarian ones including playfulness. However, even if there seems to be near consensus on the importance of designing interactive systems beyond rational and functional requirements, the way in which this can be achieved is still an open research issue. In this paper we describe our design approach to develop an embodied and playful mobile interface to control a robot companion in a smart home environment.
A major challenge of the research is to engage an older person in rich, empathic and playful interaction with a robot to encourage a prolonged, subtle, and stimulating effect beyond the initial encounter [3]. This challenge is explored through the design of innovative concepts of playful interaction embodying the perspective of the robot companion.

Keywords: embodied interaction, graphical user interface. playful interaction,

1 INTRODUCTION

Embodied interaction describes how meaning in interaction emerges from a bodily and contextual experience. It refers to the way our perception of physical and social phenomena develops in interplay with the world around us. Dourish defines embodied interaction as "the creation, manipulation and sharing of meaning through engaged interaction with artefacts" [4] (p. 126). Since its original definition, the concept of embodied interaction has inspired a number of design approaches considering "embodiment" as the bridge between the physical and digital. In particular this concept emphasises the opportunities of action that the physical world offers and that should not be neglected in the design of digital interactive products.

With this approach as a source of inspiration for the design, this paper explores the possibilities of embodied interaction in controlling a robot companion, namely Care-O-Bot, by an older person in the home environment. Following the principles of designing for embodiment, a graphical user interface (GUI) has been developed exploiting perspective taking to engage in playful interaction modalities with the robotic system.

In this context, the concept of playful interaction explores and expands the range of interaction modes between the digital and the physical enabled by the GUI.

In the following we first describe the theoretical framework that inspired our design. Later we illustrate the GUI and the interaction modalities. Finally we discuss the characteristics of the playful experience associated to embodying the robot's perspective. For doing this, we apply the Playful Experience Categories as defined by Korhonen et al. [2]. These researchers studied the pleasures of play with the aim to understand the underlying fundamental elements of pleasure or play and inform designers. They developed a framework elaborating and expanding the model defined by Costello and Edmonds [5] who derived thirteen categories of pleasure: Creation, Exploration, Discovery, Difficulty, Competition, Danger, Captivation, Sensation, Sympathy, Simulation, Fantasy, Camaraderie and Subversion.

Since these categories focus on pleasurable playful interfaces in interactive artworks, the model has been expanded by Korhonen et al. to address the design of utilitarian products that elicit playful experiences. More design practical notions to achieve playful interaction can be found in the work of Bekker et al. [6]. Together with direct motivational feedback and open-endedness Bekker et al. [7] use social player-interaction patterns as one of their three design values for creating playful interactions. The social player-interactions exploited in their approach is by collaborative and competitive richness of interaction.

The whole framework is fully illustrated in the final section of the paper and applied to our concept of embodied

© ISAROB 2013

perspective taking. The objective is to evaluate if the application of embodied principles (continuity, intersubjectivty, contextuality and personalization), might help in engendering playful and engaging interactions.

2 DESIGN

A context dependent and personalized interaction capitalized within perspective taking is one of the concepts of social behaviour that we have been developing in the project. It emerges in an active interplay in context where the elderly takes on the robot's point of view by looking through its eyes. The concept is based on the notion of intersubjectivity, a phenomenological notion that emphasizes that shared contextual activity and consensus is essential in shaping empathic relationships. Our graphical user interface containing context depending action-possibilities, is further build upon philosophical perspectives derived from ecological psychology [8] and phenomenology of perception of Merleau-Ponty [9] An affordance, in Gibsonian sense, is an action-possibility that is enabled by our bodies action-possibilities in relation to those of the 'bodies' in the environment. In the context of the graphical user-interface we approach action-possibilities in the relation the robot has towards objects in the environment.

By extending the reciprocal character of affordance with the subjective experience of context following Merleau-Ponty's thought, we approach action-possibilities in context depending yet embodied manner. Thus action-possibilities are relations between actors and objects or environment. In this case the Care-O-Bot towards objects and environment, therefore the graphical user-interface requires information about states of the objects to be handled by the Care-O-Bot, about the states of the Care-O-Bot himself, the environment as well as the states of the user and its unique approach to its world.

In other words we require a larger picture of context. Lets say, an action-possibility 'making coffee with sugar' requires to know where the user is located (to bring the coffee to), whether the user is thirsty (not to provide coffee over and over again). It further needs from the environment and objects involved whether there are empty and clean cups, as well as sufficient coffee, a clean coffee machine and so on. The likelihood of an action-possibility is also defined by previous preferences and rituals between the robot and the elderly, that can hold in interaction in the long term. We thus utilize desires and factual states of the actors (Care-O-Bot and user(s)) and physical states of the tangible objects and environment.

2.1 Interaction dynamics

Through a tablet interface, the person can see and execute action-possibilities that can be performed by or with the robot at the moment of interaction. The action-possibilities are organized by relevance. In time, the elderly's usage of action-possibilities will influence their relevance with respect to a specific context of use.

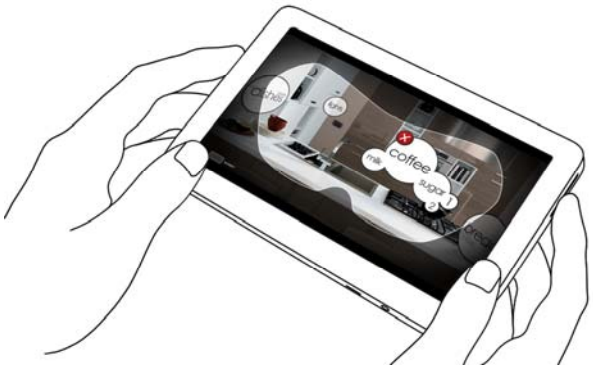

Fig. 1. Seeing through the eyes of the robot, including context depending action possibilities, varying in size depending on their likelihoods.

While selecting a desired action-possibility through clicking the Care-O-Bot will start performing. The elderly persons can see how the task is performed from the Care-O-Bots eyes. On completion of the task, the displayed action-possibilities are updated as the context has changed through the task executed by the Care-O-Bot (e.g. after closing the door, 'closing the door' is most likely not actionable anymore and has been substituted by another action-possibility namely 'open the door').

The robot-view displays what the Care-O-Bot is looking at. This view is covered with a mask indicating a clear vision in the centre and cloudy one outside the centre. As if looking through the eyes of the robot.

While looking the action-possibilities are displayed on the actual objects in the environment. In other words what is behind the robot can not be selected. In order to turn the robot, to look around, the robot can be controlled with a swipe movement. A direct action-perception loop is applied in the interaction, while swiping has started, the vision displayed on the screen starts moving (even before the robot does) using the full image that is used. In other words,

© ISAROB 2013

the mask hides part of the view, which will appear on direct interaction.

Fig. 2. By swiping, the elderly person can look through the eyes of the robot and see around. It allows for exploring action-possibilities.

The robot-view contains a perspective from the Care-O-Bot on the environment as elaborated before. This is extended with certain expressions of how the robot feels. When the Care-O-Bot is sleepy (due to performing many tasks) the vision (and thereby mask) will express this to the user besides the 'tired' movement of the executed task, mimicking blinking eyelids.

3 DISCUSSION

As anticipated in the introduction, we conclude our paper by discussing the Playful Experience Categories applying the framework by Korhonen et al. [2]. Our aim is to evaluate if embodied interaction realised through the application of continuity, intersubjectivty, contextuality and personalization principles, might help in engendering playful and engaging interactions.

The categories Captivation (the experience of forgetting one's surroundings), Control (the experience power, mastery, control or virtuosity) and Challenge (the experience of having to develop and exercise skills in a challenging situation) are closely related to Csikszentmihalyi's flow theory [10]. He describes the experience of being in the Flow as being constituted by a balance between one's skills and the challenge; a thin line between boredom and difficultness. Even though we consider captivation to be an objective, evidence of such achievement is yet to be found. As we do not intend to vary the challenge, we hope to achieve this experience through the engagement or embodiment of context the elderly person has with seeing through the eyes of the robot.

Our GUI design deliberately chooses collaboration over Competition (the experience of victory-oriented competition against oneself, opponent or system). The elderly person can together with the robot achieve things that would be impossible without its help. The experience of Completion, finishing and closure, in relation to an earlier task or tension as category is thus addressed in the collaborative making things work. The nature of this collaborative relationship is of Fellowship (the experience of friendship, fellowship, communality or intimacy) and Nurture (the experience of nurturing, grooming or caretaking)

Collaborative Discovery (the experience of discovering a new solution, place or property) and Exploration (the experience of exploring or investigating a world, affordance, puzzle or situation) can be considered as core values of our contextual action-possibility interface design. The embodiment of context, achieved through the eyes of the robot enables the older person to discover action-possibilities and thereby the opportunities the robot provides within the independent live of the elderly person. Seeing what is possible by collaboration, and exploring the world that is shared between elderly person and robot highly provokes playful interaction.

Expression (experience of creating something or expressing oneself in a creative fashion) might occur when action-possibilities emerge through use. But till this happens, action-possibilities are straightforward embodied in the actual possibilities the robot has with its environment. This further limits the Fantasy (the experience of make-believe involving fantastical narratives, worlds or characters) one can have when not considering the explorative element of finding action-possibilities by playing with the eyes.

Sensation (a meaningful sensory experience) is stimulated as the robot is part of the direct world of the elderly person. Even though the movements of performing action-possibilities are stiff and 'robot'-like, the robot is actually there to be part of life. The graphical-user-interface as a tablet filled with 'representational action-possibility labels' is flat and does not allow for meaningful sensory experience)

The category Simulation, an experience of perceiving a representation of everyday life, is rooted in gaming where things are to be done that can normally not be done. This category profoundly contradicts our approach as we intend to achieve an embodiment within a direct interaction with the real world. Therefore we attempt to bypass any representation and utilize the direct sensorial world as it is

© ISAROB 2013

to the elderly person and robot and not address digital abstractions.

Subversion, the experience of breaking social roles, rules and norms, might be achieved as meaning emerges in interaction. Though we did not specifically design for this matter.

Sympathy, described as an experience of sharing emotional feelings, is addressed in our embodied perspective interface. Perhaps we have to be more nuanced in this as could argue that the robot does not have feelings, we consider a limitation of an action-possibility informed by the robots properties a feeling of the robot. In other words, in case the robot is not able to perform a difficult task informed by a low battery and overused motors, the graphical-user-interface does reflect these inner states by not showing action-possibilities.

The Thrill category, defined as an experience of thrill derived from an actual or perceived danger or risk, the Eroticism category (the experience of sexual pleasure or arousal), the Sadism category (the experience of destruction and exerting power over others), Relaxation (the experience of unwinding, relaxation or stress relief. Calmness during play), and the Suffering category (experience of frustration, anger, boredom and disappointment typical to playing) are being purposely avoided. The Suffering category, in our view, contradicts with the Captivation category in which the above mentioned experiences are ought to be avoided by a dynamic challenge that matches the elderly person's skills.

The playful interaction design values by Bekker et al [7] as introduced before can be found in our work as well. The direct motivational feedback design value is addressed via continuous-sustained action-perception loops as well as the collaborative achievement of action-possibilities. Here thus we approach the social player-interaction pattern by interactions of collaborative nature between elderly person and robot. The open-endedness design value is provided by the context and the action-possibilities of the robot itself, yet this can be seen as a limiting factor more than an opening. Open-endedness concerns the opportunity to create interaction paradigms in contrast to predefined rules and objectives. To come forth to this design value not only the meaning should emerge within interaction between elderly person and robot but also the growth of action-possibilities from the robots side.

The novelty of the approach relies on an innovative concept of interaction, based on perspective taking. The robot control is addressed via the resonation of older person and robot through shared viewpoints; providing the older person with insights of what is possible for the robot to do in a continuous flow of interaction.

ACKNOWLEDGEMENTS

The research leading to these results has received funding from the EU-FP7 ACCOMPANY project under grant agreement n°287624. We thank Ernesto Di Iorio for his support with implementing the GUI and Michele Tittarelli for his collaboration with the graphical design.

REFERENCES

[1] Marti, P., Overbeeke, C.J. (2010), "Il bello dell'interazione". In S. Bagnara, M. Mattioda (ed) *Index: Un percorso di specializzazione in Interaction Design Experience*, Franco Angeli, Milano, 2010, ISBN 978-88-568-3206-8.

[2] Korhonen, H. Montola, M. Arrasvuori, J. (2009), Understanding Playful User Experience Through Digital Games In *Designing Pleasurable Product and Interfaces, DPPI09*, 13- 16 October 2009, Compiegne University of Technology, Compiegne, France.

[3] Stienstra J.T., Marti P., (2012), Squeeze Me: Please gently. *Proceedings of the 7th Nordic Conference on Human-Computer Interaction NordiCHI 2012*, Copenhagen, 14-17 October 2012, pp. 746-750.

[4] Dourish P. (2001), *Where The Action Is: The Foundations of Embodied Interaction***.** MIT Press, 2001.

[5] Costello, B. Edmonds, E. (2007), A Study in Play, Pleasure and Experience Design. In *Designing Pleasurable Products and Interfaces conference, DPPI'07*, 2007 (ACM Press), pp.76-91.

[6] Bekker M.M., Sturm J and Eggen B. (2010), Designing playful interactions for social interaction and physical play. *Personal Ubiquitous Comput.* 14, 5 (July 2010), 385-396. DOI=10.1007/s00779-009-0264-1

[7] Bekker M.M., Sturm J, Barakova E (2008), Designing for social interaction through physical play, In: *Extended abstracts of conference on fun and games 2008*, pp 62–67

[8] Gibson, J.J. (1986), *An ecological approach to vis ual perception*. London, UK: Lawrence Erlbaum Associ ates.

[9] Merleau-Ponty, M. (1962), Phenomenology of Perc eption (C. Smith, Trans.). New York: Humanities Press. (Original work published in 1945)

[10] Csikszentmihalyi, M. (1990), *Flow: The Psychology of Optimal Experience*. New York, NY: Harper & Row.

The Eighteenth International Symposium on Artificial Life and Robotics 2013 (AROB 18th '13),
Daejeon Convention Center, Daejeon, Korea, January 30-February 1, 2013

Fable: Socially Interactive Modular Robot

Arnþór Magnússon, Moises Pacheco, Mikael Moghadam, Henrik Hautop Lund, and David Johan Christensen

Technical University of Denmark, Center for Playware, DTU Electrical Engineering, Elektrovej, building 325, DK-2800 Kgs. Lyngby, Denmark
{arnma, mpac, mikm, hhl, djchr}@elektro.dtu.dk

Abstract: Modular robots have a significant potential as user-reconfigurable robotic playware, but often lack sufficient sensing for social interaction. We address this issue with the Fable modular robotic system by exploring the use of smart sensor modules that has a better ability to sense the behavior of the user. In this paper we describe the development of a smart sensor module which includes a 3D depth camera, and a server-side software architecture featuring user tracking, posture detection and a near-real-time facial recognition. Further, we describe how the Fable system with the smart sensor module has been tested in educational and playful contexts and present experiments to document its functional performance.

Keywords: human-robot interaction, modular robots, playware, vision

1 INTRODUCTION

Fable is a modular robotic platform under development, aimed at enabling non-expert users to design and develop socially interactive robotic creatures from various types of modules. A user can create their own Fable robots by assembling its modules into some configuration and programming it with the desired behavior based on a simple programming language. We explore the use of smart sensors modules, which are needed to achieve social interaction between a human and a robot. The smart sensor enables the robot to sense the user's behavior and respond accordantly. Smart sensors modules could for example be cameras or microphones combined with appropriate processing and mechanical encapsulation able to recognize the face or voice of the user. Mixing smart sensors and modularity introduces a set of challenges due to high bandwidth and processing beyond what a low power microcontroller, as typically used in modular robots, can handle.

This paper presents the design and tests of a smart sensor module for the Fable platform. The module contains a 3D camera, Asus Xtion Pro Live (similar to Kinect by Microsoft) and is equipped with connectors for compatibility with other Fable modules. The smart sensor module and corresponding software architecture provides the user with a simple programming interface for user tracking, posture detection and facial recognition. Our working hypothesis is that smart sensor modules will enable non-expert users to construct socially interactive and playful Fable robots and that this will be more motivating for the user than a system with no or only primitive sensors.

In the rest of this paper we first describe related work in Sec. 2. The Fable system is described in Sec. 3 and the software architecture for smart sensor modules is described in Sec. 4. Sec. 5 describes tests performed to study the system performance and the use of the system in an educational and an playful context.

2 RELATED WORK

Modular robots are comprised of independent robotic modules that can be attached and detached from one another, being able to construct various robot morphologies depending on the scenario [1]. Some modular robotic systems are able to self-reconfigure [2, 3] which allows the robots to shift their own shape by rearranging the connectivity of their parts to adapt to circumstances [4] [5], form needed tools [6] or furniture [7].

In this paper we explore user-reconfigurable robots, which allow non-expert users to physically construct their own robots from different types of modules (such as passive, actuators and sensors). This type of robots are particular suited for applications such as rapid robot prototyping [8], play [9, 10], rehabilitation [11, 12], composing music [13], and education (e.g. Mobot, Barobo, Inc. or LEGO Mindstorms). The modularity and open-endedness of these systems motivates the user to be creative, reflect, and iterate on their creations whereby they learn, train, or simply enjoy themselves.

In this paper we are considering modular robots for playful social interaction. Social interaction is being widely utilized for non-modular robots [14]. The interactive and animated iCat [15] is a type of user interface for controlling various media in a more natural way. Probo [16] [17] is a huggable robot designed to improve the living conditions of children in hospitals as a tele-interface for entertainment, communication and medical assistance. MeBot [18] is a telerobot that allows people in different places to feel present and to allow for social expressions, not only from video and audio, but also expressive gestures and body pose. Playware technology [19] has also been developed as a mediator for playful social interaction for over long distances.

© ISAROB 2013

3 FABLE: MODULAR ROBOTIC PLATFORM

3.1 Concept

The vision of the Fable project is to build a novel modular robotic platform, which enables non-expert users to assemble innovative robotic solutions from user-friendly building blocks. A robot is assembled by connecting two or more modules together where each module provides functionality to perform a specific task, such as sensing users, environment or actions, moving or manipulating its surroundings. With an easy-accessible software tool-kit provided, the user can create custom functionality and eventually we plan to make it easy to share their creations online with other users to try out, for inspiration, or as a starting point for their own creations. The objective is to develop this platform to enable users to realize their own innovative ideas.

3.2 Hardware

The Fable is a heterogeneous chain-based modular robotic system which consist of various modules, such as different types of joint, branching and termination modules [20]. Joint modules are actuated robotic modules used to enable locomotion and interaction with the environment. Branching modules connects several modules together in tree-like configurations. Termination modules may add structure, a visual expression, additional sensors, or actuators (e.g. grippers or wheels).

Every module, depending on its type has one or more mechanical magnetic connectors. The connectors are designed to allow rapid and solid attachment and detachment between modules. Further, the connectors are scalable to allow modules of different sizes to be combined and designed to allow neighbor-to-neighbor communication. Flanges mechanically lock the connection against twisting and bending and only allow disconnection by pulling on the axis perpendicular to the connecting surfaces.

Each module will be equipped with an onboard battery and an electronic board with an Atmel Atmega2561 microcontroller. Each board has four IR channels for communicating with neighboring modules and in addition, have the possibility to connect a ZigBee chip for wireless communication between modules or a PC. All modules have an onboard accelerometer and a gyroscope. The actuator modules have in addition a connector to power and can control several daisy chained AX-12A Dynamixel servos. These custom made electronic boards are in the process of being integrated into the system. Meanwhile we have used a compatible embedded system, CM-510, for centralized control of the modules.

The Fable system is still being extended with new module types to allow a wide range of different robots to be created. Fig. 1 shows examples of humanoid, snake and walking robots constructed with the current Fable system.

(a) Humanoid.

(b) Four legged robot.

(c) Snake.

Fig. 1: Example configurations with the Fable system.

3.3 Sensor Module Design

The Fable system is designed to include primitive and smart sensors:

Primitive Sensors sense simple signals, often from the environment, that can be processed by the small 8-bit microcontroller, also controlling the module, to extract meaningful low-level features (e.g. brightness, distance and temperature).

Smart Sensors sense simple or complex signals and process them to extract higher-level information about the user, the robot or its environment. Possible example includes, emotion categorization based on audio signals, gesture recognition based on accelerations, and posture detection based on 3D depth signals.

The design of smart sensor modules should preferably be fully embedded to make the robot system self-contained and independent of external devices. This is however challenged by the limited space, processing power and battery capacity which can be embedded inside a module. Another option is to offload the sensor outputs to a server through a wireless transport to have maximum processing power, but that also introduce challenges, such as the capability to transfer large amount of data wireless, potential delays in the system, and a higher hardware complexity. At this stage of the development we have chosen to use a server-based solution with a software architecture that can be ported to an embedded device in the future. The smart sensor module presented in this paper is therefore connected using

© ISAROB 2013

a tether to a server for processing and feature extraction. This high-level information is then offered as services to the modules wirelessly and can be accessed by the user application (as explained in Sec. 4).

4 FABLE SOFTWARE ARCHITECTURE

The section describes the software architecture of the Fable system with special focus on the server-side architecture to process smart sensor signals and provide them as services. The architecture is split into three main components: the user computer, the embedded device(s), and the server (see the diagram in Fig. 2.).

4.1 User Computer Architecture

To enable non-expert users to program their own Fable robots, we provide the LOGO programming language for user application development. LOGO is an educational programming language coming from Seymour Papert's constructionism tradition [21] and gives a more natural English-like syntax than C (e.g. no braces). We use a restricted version of LOGO, called PicoLOGO [22], which has a reduced instruction set and limited data types. An application is created by the user, which is then compiled into a byte-code representation and uploaded through a serial connection or a USB flash drive. This architecture makes it simple for the user to program the robot and easy for us, the developers, to add new Fable specific primitives to the PicoLOGO instruction set.

Listings 1.1 depicts an example LOGO program where the 3D depth camera is utilized to detect the angle of the left elbow joint of a user and maps it to a specific motor of the robot. Note that the symbol ';' starts a comment line and that the program will start on the function `onstart`.

Listing 1.1: Example PicoLOGO application.

```
constants [
  [userId 1]
  [left_elbow 0]
  [motorId 1]
]

to mirror_elbow
  ; Define a variable
  let [angle 0]

  ; Assigns the variable with elbow angle
  make "angle get_joint_angle userId left_elbow

  ; Set the motor position to angle
  set_motor_pos motorId :angle

  wait 1
end
```

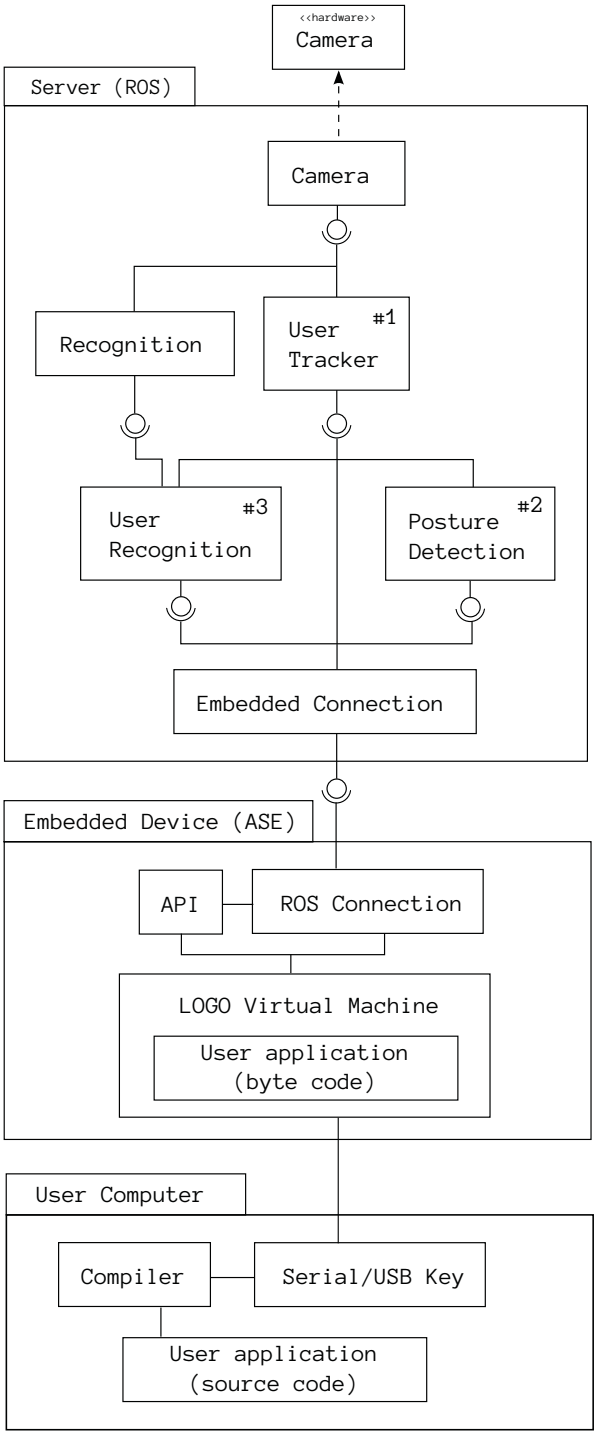

Fig. 2: Diagram of software architecture.

© ISAROB 2013

```
to onstart
  ; Requests for left elbow data
  use_user_joint left_elbow

  ; Infinite loop
  forever [mirror_elbow]
end
```

4.2 Embedded Architecture

Every module is controlled by an embedded device containing a small microcontroller. The microcontroller runs the Assemble-and-Animate framework (ASE) [23]. ASE is a flexible and extendible control framework targeted for modular robots, it provides high level of abstraction, libraries of algorithms, components and an asynchronous event-driven system. A virtual machine (VM) able to execute PicoLOGO code compiled into byte-code [22] is included as a process in ASE. Hence, the user application is executed by the VM, which may call functions that use smart sensor services from the server-side. The VM abstracts many of the system resources away, such as low level details of sensors, motors and distributed processing. This enables users to more quickly develop applications and upload them to the robot.

4.3 Server Architecture

The server architecture is designed to process signals from smart sensors and offer them as services to the user application. We utilize the Robot Operating System (ROS) [24] on the server, offering graph node structure, to create loosely coupled components which allows for task abstraction and code re-use. ROS provides a messaging framework for communication between components and also offers access to large sets of software libraries such as OpenCV and many community created components. The components role can vary from receiving sensor inputs, extract features or offering services to the user application running on the modules. The following subsections will describe some of these components and example applications.

User tracker component The robot must be able to sense users and their movements in order to enable interaction based on body language.

As a basis for tracking and detecting users we utilize OpenNI[1] user tracker module and Asus Xtion Live Pro (similar to Kinect from Microsoft). It allows for user detection and tracking by providing coordinates for all major limbs of the body as well the angles of the joints. The component is placed on the server, as seen in Fig. 2, component #1.

[1] OpenNI (Open Natural Interaction) is a framework created for sensor devices published under LGPL license. http://openni.org

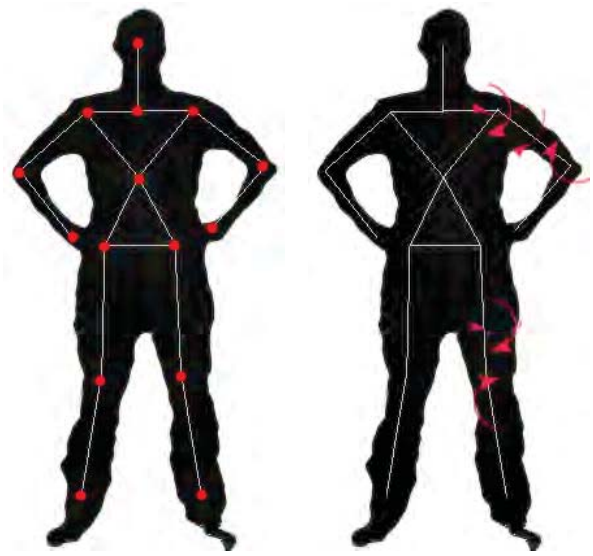

(a) Red dots showing joint positions available for each user.

(b) Showing different angles of arms and legs that could be calculated from the joint positions.

Fig. 3: Image showing joint positions and angles available for each user.

These features form the basis for other components for further processing but are also offered as a service for the user application layer. An example application we have developed with this component is a Fable robot configured as a humanoid torso with the 3D camera module on top. The robot then mimics or mirrors the users shoulders and elbow movements with its two degree of freedom joint modules (the application is an extension of Listings 1.1).

Posture detection component An efficient way for humans to communicate is verbally, but in many cases it is supported by body language, such as body posture, gestures, facial expression and eye movements. Body language can provide clues to attitude or state of mind of a person, or simply to give commands or descriptions.

To enable such a communication between a robot and the user, we implemented a posture detection system where the robot can detect pre-defined postures stored in a database. A posture is a set of labeled angles, where each angle represents a joint on the user, gathered from previously described user tracking component. The user's posture is continuously being compared to the database, detection is considered when the Euclidean distance between two sets are below a certain threshold, and then an event is triggered. This component #2 can be seen in Fig. 2.

This functionality allows for a simple interaction between users and the Fable system. As an example we have developed

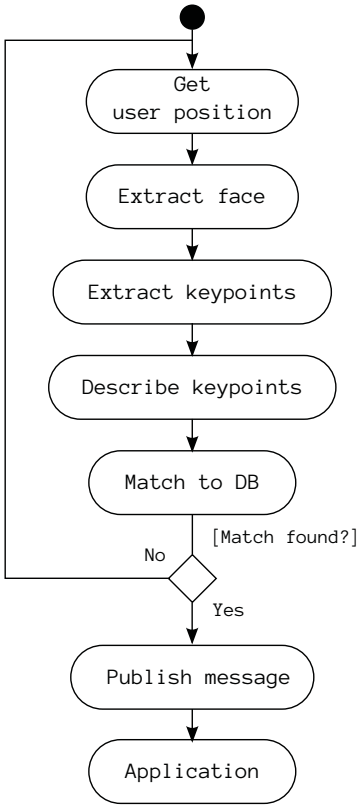

Fig. 4: Facial recognition process.

another mimic application, again with the modules configured into a humanoid torso and the 3D camera module on top. In this game the robot does a certain posture with its arms and then the user mimics that posture, when the robot detects the correct posture it makes a new one, and so on.

Facial recognition component A facial recognition service (see component #3 in Fig. 2) is provided in order to make the robot's behavior dependent on which person it is interacting with. For example a user developing an interactive robot application might want the robot to greet and speak the name of the user's family members whenever it sees them.

The facial recognition is performed in several steps, depicted in Fig. 4. First, the users face is extracted from an image with help from the user tracker component. Keypoints are extracted from these images with the FAST [25] algorithm, which are then given a description with the SIFT [26] algorithm. The descriptors are compared to the database with Fast library approximate nearest neighbor (FLANN) [27] matcher and on a match an event is sent. OpenCV's implementations of the algorithms were used.

5 TESTS

5.1 Playful User Test

The Fable system is designed to enable the construction of playful interactive robots. As a proof-of-concept, a pilot user test was performed with a 6 year old girl who interacted with a simple upper humanoid torso. The robot was pre-programmed with a LOGO application and pre-assembled from Fable modules. The robot was equipped with a smart sensor module, the 3D depth camera, directly connected to a server which was running the software architecture described in Sec. 4. An embedded controller, the CM-510, was running the LOGO application to control the robot's actuators based on the services provided by the server. Specifically, the LOGO application would use the user tracking service to mirror the girl's movement of hers shoulders and elbows. Two special postures, identified with the posture detection service, would start and end application.

We observed the girl's reactions during the pilot test (see Fig. 5). She was given the basic instructions about how a specific posture would trigger the mimicking. As soon as the robot started moving she reacted with positive excitement. Soon she realized the connection between the movement of her hands and the robots. As the play progressed she tried to go beyond the limits of the movements the robot can perform, for example, try to make the robot clap its hands and dance, but still appearing to be enjoying herself. In the end (after around 5 min.) she started to complain about her tired arms, as she had been moving them the whole time. The system was not glitch-free; there were occurrences where an unintended posture was detected, which resulted in ending the mimicking. Overall, this pilot-test confirmed that it was possible with the system to construct robotic application that would trigger play dynamics and interaction between a child and the robot. Further testing is needed to explore this in greater detail.

5.2 Educational User Test

One of the objectives of the Fable system is that it can be used as an educational tool. By tinkering with constructing robots, the user will be motivated to learn something about programming, mathematics, robotics, sensors, actuators, etc. in order to build better robots.

To test the Fable system's potential as an educational platform we have performed a user test with seven high school students. The students had little or no programming experience. They participated in a 2-hour programming exercise where they should create an application for a robot configured as a humanoid torso using the LOGO programming language. The robot should do a posture with its arms and the user is supposed to perform the same posture, then the robot does another posture and so on. This would require the participants to create functions, loops and use pre-defined functions that involve the robot moving its arms

© ISAROB 2013

Fig. 5: The Fable robot mimicking a 6 year old girl.

in certain positions and detecting users and their postures. A manual was supplied with the problem broken down into smaller steps and a presentation was given explaining the tools to program, compile, and upload the code to the robot.

We observed that the students quickly realized how to use the tools, while the actual programming, understanding functions and loops had a small learning curve. Most grasped the concepts quickly while others needed some extra help. By studying the manual they learned how to create functions for the different postures that the robot was supposed to perform. Some parts required extra effort, e.g. the part of detecting a user's posture. We observed that the students seemed highly motivated to understand the programming in order to make the robot do as requested. Clearly the students learned something about robotics and programming from this exercise. By letting the students define their own projects and create robots that makes sense to them, we anticipate that it will motivate the students to work concentrated for long time periods. In this process we hope that the students will learn useful skills, but the extent to which the Fable system allows for such open-ended creation and learning is a topic which we will explore more in future work.

5.3 Posture Detection

A test was performed in order to determine the detection rate of the posture detection algorithm. 9 test subjects, all male ranging from ages 25-35, were asked to perform a set of nine postures twice. No feedback was given from the system if a posture was detected or not. The camera was placed about 3 meters from the subject at 1.5 meters height.

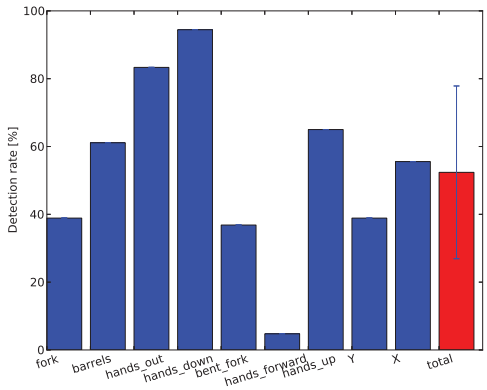

Fig. 6: Showing individual detection rates by postures, while the rightmost (red bar) shows the average detection rate.

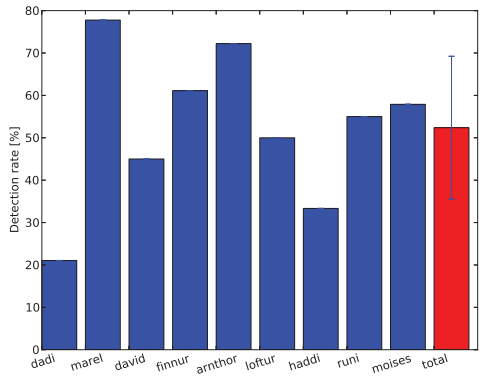

Fig. 7: Showing individual detection rates by subjects, while the rightmost (red bar) shows the average detection rate.

Fig. 6 shows the detection rates for each posture performed, while Fig. 7 depicts the detection rate per user. The accuracy (true positives / total detection) of performed postures was 95 %, where we observed false positives being recorded while the users were moving to the final posture. Note that one posture (`hands_forward`) had a very low detection rate. It turned out that since the hands were directed straight to the camera, it made the camera unable to correctly detect the positions of the hands. If the camera would have been placed lower this would not have affected the test. In summary the posture detection system is generally fairly capable to detect between the nine different postures, but it varies highly depending on the particular user. Further work is needed to make the posture detection component more robust.

© ISAROB 2013

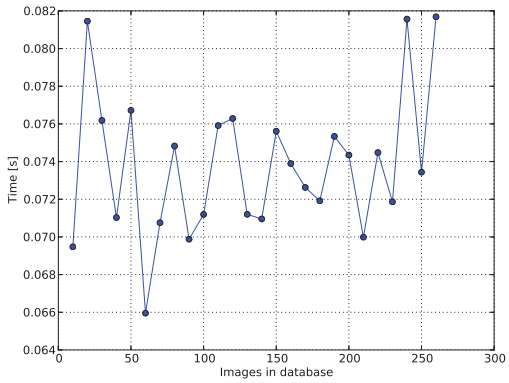

Fig. 8: Average time to match a face to database with varying database size.

5.4 Facial recognition

The facial recognition systems detection rate is highly dependent on the number of images in the database and specially the variation of image types, such as different illumination, face angles and distances. As the system is supposed to work in near real-time the speed of detections is a crucial factor and is therefore tested here in terms of the number of images in the database.

The test was performed on a database containing faces in different scales, distances and orientation of 5 subjects, all male ranging from the ages 25 - 35. Ten random images were incrementally added to the database at a time until 260 images had been reached, each time comparing 50 random images to the current database while recording the average time.

Fig. 8 depicts the average time to match a face to the database with varying database size. As one can see the average time is almost constant at 0.072 s or approximately 14 faces/sec, which is sufficient for most purposes. The corresponding detection rate is 75.8 % and the accuracy is 99.3 % (true positives / (true + false positives)). We anticipate that these results are sufficient for practical applications utilizing facial recognition but this has yet to be tested.

6 CONCLUSION

This paper presented a smart sensor module with corresponding server-side software architecture for the Fable modular robotic system. The sensor module is based on a 3D depth camera providing user tracking, posture detection and a near-real-time facial recognition. We tested the functional performance of these services and found them sufficient for our purpose although there is still room for improvements. Further, a pilot user test was described that demonstrated a playful and interactive robot build from the system. In addition, we described a user test with high-school students who used the system to program a robot and thereby learn about programming and robotics. In conclusion we anticipate that the Fable system equipped with smart sensor modules is a step towards a new type of user-reconfigurable robotic playware that motivate its users to be creative and learn while creating socially interactive robotic applications.

In future work a more integrated/embedded version of the smart sensor module will be developed (not tethered to the server). Further, the developments of new smart sensor modules are being explored and more thoroughly tested. In addition, the Fable system is being improved to be more user-friendly and include more module types.

7 ACKNOWLEDGEMENTS

This work was performed as part of the "Modular Playware Technology" project funded by the Danish National Advanced Technology Foundation. Many thanks to Brian Silverman who is the developer of the PicoLOGO virtual machine and compiler used to program the Fable robot.

8 REFERENCES

[1] T. Fukuda and S. Nakagawa. Dynamically reconfigurable robotic system. In *Proceedings of the IEEE International Conference on Robotics & Automation (ICRA'88)*, pages 1581–1586, 1988.

[2] M. Yim, W-M Shen, B Salemi, Daniela Rus, M. Moll, H Lipson, and E Klavins. Modular self-reconfigurable robot systems: Challenges and opportunities for the future. *IEEE Robotics & Automation Magazine*, 14(1):43–52, March 2007.

[3] K. Stoy, D. Brandt, and D. J. Christensen. *Self-Reconfigurable Robots: An Introduction*. Intelligent Robotics and Autonomous Agents series. The MIT Press, 2010.

[4] S. Murata, E. Yoshida, A. Kamimura, H. Kurokawa, K. Tomita, and S. Kokaji. M-tran: self-reconfigurable modular robotic system. *Mechatronics, IEEE/ASME Transactions on*, 7(4):431 –441, dec. 2002.

[5] E. H. Østergaard, K. Kassow, R. Beck, and H. H. Lund. Design of the atron lattice-based self-reconfigurable robot. *Auton. Robots*, 21(2):165–183, September 2006.

[6] K. W. Gilpin, A. N. Knaian, and D. L. Rus. Robot pebbles: One centimeter modules for programmable matter through self-disassembly. *IEEE*, 2010.

[7] A. Sproewitz, A. Billard, P. Dillenbourg, and A. J. Ijspeert. Roombots-mechanical design of self-reconfiguring modular robots for adaptive furniture. *IEEE International Conference on Robotics & Automation (ICRA)*, pages 4259–4264, 2009.

© ISAROB 2013

[8] A. Lyder, R. F. M. Garcia, and K. Stoy. Mechanical design of odin, an extendable heterogeneous deformable modular robot. In *Proceedings of the IEEE/RSJ International Conference on Intelligent Robots and Systems (IROS'2008)*, pages 883–888, Nice, France, September 2008.

[9] H. S. Raffle, A. Parkes, and H. Ishii. Topobo: a constructive assembly system with kinetic memory. In *Proceedings of the SIGCHI conference on Human factors in computing systems*, CHI '04, pages 647–654, New York, NY, USA, 2004. ACM.

[10] E. Schweikardt and M. D. Gross. roblocks: a robotic construction kit for mathematics and science education. In *Proceedings of the 8th international conference on Multimodal interfaces*, ICMI '06, pages 72–75, New York, NY, USA, 2006. ACM.

[11] P. Marti, L. Giusti, and H. H. Lund. The role of modular robotics in mediating nonverbal social exchanges. *IEEE Transactions on Robotics*, 25(3):602–613, June 2009.

[12] C. B. Nielsen and H. H. Lund. Adapting playware to rehabilitation practices. In *Serious Games - Theory, Technology & Practice: Proceedings GameDays 2011*, 2011.

[13] H. H. Lund, N. K. Bærendsen, J. Nielsen, C. Jessen, and K. Falkenberg. Robomusic with modular playware. In *Proceedings of International Symposium on Artificial Life and Robotics (AROB'10)*, 2010.

[14] C. L. Breazeal. *Designing sociable robots*. The MIT Press, 2004.

[15] A. J. N. van Breemen. Bringing robots to life: Applying principles of animation to robots. In *Proceedings of the CHI2004 Workshop on Shaping Human-Robot Interaction - Understanding the Social Aspects of Intelligent Robotic Products*, Vienna, 2008.

[16] K. Goris, J. Saldien, I. Vanderniepen, and D. Lefeber. The huggable robot probo, a multi-disciplinary research platform. *Communications in Computer and Information Science*, 33 CCIS:29–41, 2009.

[17] J. Saldien, K. Goris, S. Yilmazyildiz, W. Verhelst, and D. Lefeber. On the design of the huggable robot probo. *Journal of Physical Agents*, 2(2), 2008.

[18] S. Sigurdur O. Adalgeirsson and C. Breazeal. Mebot: A robotic platform for socially embodied presence. In *Proceedings of the 5th ACM/IEEE international conference on Human-robot interaction (HRI '10)*, pages 15–22, 2010.

[19] H. H. Lund and T. Thorsteinsson. Social playware for mediating tele-play interaction over distance. *Artificial Life and Robotics*, 16:435–440, 2012.

[20] M. Pacheco, M. Moghadam, A. Magnusson, B. Silverman, H. H. Lund, and D. J. Christensen. Fable: Design of a modular robotic playware platform. In *Proceedings of IEEE International Conference on Robotics and Automation*, 2013. (to appear).

[21] S. Papert. *Mindstorms: children, computers, and powerful ideas*. Basic Books, Inc., New York, NY, USA, 1980.

[22] Playful invention company. http://www.picocricket.com/picopeople.html. Developers of PicoLOGO.

[23] D. J. Christensen, U. P. Schultz, and M. Moghadam. The assemble and animate control framework for modular reconfigurable robots. In *Proceedings of the IROS Workshop on Reconfigurable Modular Robotics: Challenges of Mechatronic and Bio-Chemo-Hybrid Systems*, 2011.

[24] M. Quigley, B. Gerkey, K. Conley, J. Faust, T. Foote, J. Leibs, E. Berger, R. Wheeler, and A. Ng. Ros: an open-source robot operating system. In *ICRA workshop on open source software*, 2009.

[25] E. Rosten and T. Drummond. Machine learning for high-speed corner detection. In *Computer Vision ECCV 2006*, volume 3951 of *Lecture Notes in Computer Science*, pages 430–443. Springer Berlin / Heidelberg, 2006.

[26] D. G. Lowe. Object recognition from local scale-invariant features. In *Proceedings of the International Conference on Computer Vision-Volume 2 - Volume 2*, ICCV '99, pages 1150–, Washington, DC, USA, 1999. IEEE Computer Society.

[27] M. Muja and D. G. Lowe. Fast approximate nearest neighbors with automatic algorithm configuration. In *International Conference on Computer Vision Theory and Application VISSAPP'09)*, pages 331–340. INSTICC Press, 2009.

© ISAROB 2013

The Eighteenth International Symposium on Artificial Life and Robotics 2013 (AROB 18th '13),
Daejeon Convention Center, Daejeon, Korea, January 30-February 1, 2013

bioToys: biofeedback device for physiotherapy using building blocks

Tomoya Shimokakimoto[1], Asaki Miura[1], and Kenji Suzuki[1,2]

[1] Artificial Intelligence Laboratory, University of Tsukuba, Japan
[2] Japan Science and Technology Agency, Japan

{shimokakimoto, asaki}@ai.iit.tsukuba.ac.jp, kenji@ieee.org

Abstract: In the field of physiotherapy for children with impaired motor functions or congenital loss of limbs, physical therapists (PT) assist children to recover motor functions or to adapt to the use of artificial limbs controlled by Electromyography. However, children easily give up training to use artificial limbs because it becomes rapidly boring. Also, PT are required to perform many operations on the biofeedback system. It is important for children to feel excited about therapeutic activities and the system used should be easy to handled by the PT. In this research, we propose a building block based biofeedback toys called "*bioToys*". This system enables the use of biological or physiological signals in input blocks and generates various outputs. This building block system also allows users to program biofeedback systems. We show that the developed system is capable to control toys and to record muscle activities in real time.

Keywords: Playware, biofeedback, Tangible User Interfaces, toy, children, education.

1 INTRODUCTION

Electromyography (EMG) biofeedback is one of the methods of physiotherapy for augmented motor function [1]. EMG biofeedback therapy is widely used in the training for patient with impaired motor function or congenital loss of limbs. Physical therapists (PT) assist patient to recover the motor function and several biofeedback devices have been proposed so far such as presenting a waveform on the LCD display (i.e. MyoBoy, Ottobock, Inc.), converting EMG to the sound tone [2], or displaying the shape and brightness on the specific muscle on the body skin [3]. Also, these treatments are used for the training of EMG prosthesis. Although the rehabilitation trainings generally consist of simple tasks such as picking up and moving small objects,, some adults patients endure this training because of their strong motivation to go back to their daily life. However, children often refuse the training because it becomes boring after a while or become they just dislike it. Also, biofeedback systems require the PT to perform many operations including setting of instrumentation, parameters tuning, and maintenance of prosthesis. In addition, it is needed to observe the patient's activity, check the output from the biofeedback system, and instruct the patient the next action to be performed all at the same time. Then, it is also important for children to feel excited with the therapeutic activities to keep their motivation and this causes strong affects the therapeutic achievements. Since the therapist needs to handle the system and paid less attention to the therapeutic activity itself and also it is difficult to observe the child activity while handling the system.

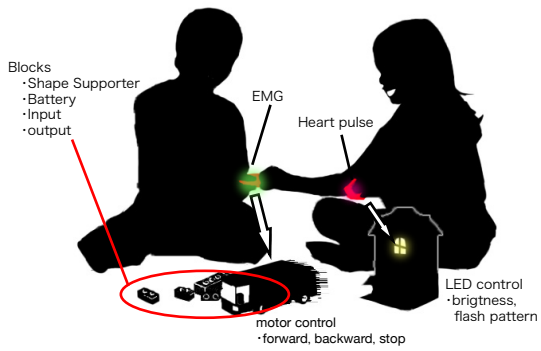

Fig. 1. Concept of bioToys

Many works have reported about the benefit of tangible user interfaces [4] which offer educational benefits to children. Especially, building blocks system have been a proposed as a tool for learning programing language [5,6,7]. These building blocks systems allows user to freely build system, and the system produces outcome under the combination of properly built blocks with a particular function. We consider that building blocks systems are an effective education tool for children to learn about system procedure, and also could encourage child to learn in voluntary and creative manners. .

In this study, we first introduce a building blocks like biofeedback toys called "bioToys" as shown in Fig.1 . Promising applications include a creative tool for physiotherapy. In this application, this system is designed for users to understand the causality between biosignal and system

© ISAROB 2013

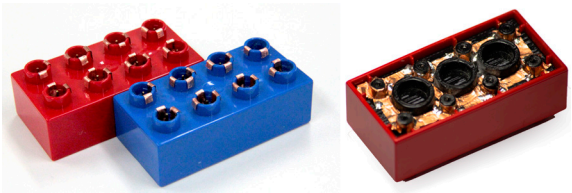

Fig. 2. Overview of the developed blocks.

output in an intuitive manner, and could encourages children to self initiate playing and training. Also it is easy for the PT and children to handle it.

2 BUILDING BLOCKS SYSTEM

2.1 Device Specification

Figure 2 shows an overview of the developed blocks. We implemented the system on the DUPLO(LEGO Group) and four types of block devices are constructed such as shape supporter, battery, input and output. These block-type devices are modified from the normal blocks and are added two connectors. On the upper side, each connecting parts has two electrodes. The inner and outer pins are used as a power and ground lines, respectively. On the lower side, in opposite, the connecting hole is used as a ground and the outer as a power. Since these electrodes are designed like coaxial socket, the devices shape are almost the same as the one of normal blocks and they can connect not only to modified block devices but also to regular DUPLO® blocks in a traditional way.

On the proposed system, power to each block is provided by a single master supply from the battery block. Recharging only the battery block is therefore adequate for maintenance. In order to reduce the number of cables between the blocks and also increase the flexibility of the system, power line communications have been used to share information between the blocks. Therefore, although the developed blocks have an electrical connection and function, physical connection between blocks are not limited. This mechanism allows the user to use and handle the developed blocks in the same way as normal building blocks.

Table 1 shows an example of block types and their functions. The developed blocks are classified in four different types. (i) *Link Block* is used to connect or disconnect the circuit and also used to determine the physical shape. Normal blocks are used to create shapes and separate electrical connections between blocks. Bridge blocks are used not only to create the shape but also to provide electrical connectivity and data communication between blocks through the in-built circuit between the upper and lower side. (ii) *Processing block* equipped with an electronic circuit with microcontroller (LPC1113/302, NXP) has different functions. These blocks are performed to obtain and transmit data to other blocks. Wireless receiver block is implemented to obtain biosignal or physical motion data form the wearable sensor via Bluetooth connection. Since biosignals and human motions are measured on body skin, each receiver block is paired with a wearable sensor. It then receives those messages from a pair of signal processing block and broadcasts to other blocks in the network. Parameter Tuner block has a gain adjuster for tuning data for the output. (iv) *Action Blocks* interpret the message from other blocks and convert the signal for providing several actions such as motion, vibrations, sounds and illuminations.

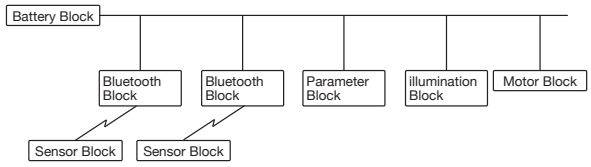

Fig. 3. Network structure of blocks

2.2 System Configuration

Figure 3 shows an example of a network structure between the connected blocks. Note that data communication is solely done on a power line. This network topology is a bus-network. When the battery block is switched on, blocks connected to the power line start to work according to their functions. Any blocks connected to the network broadcast data and share the circuit by serial communication. These data consist of a header, data length, its own specific type, signal data value/command and CRC. To avoid conflicts or

Table. 1. Example of the block type

Category	Specific type	Functions
Link Block	Normal	Disconnection between blocks
	Bridge	Connection between blocks
Power Block	Battery	Supply voltage to the blocks and monitoring power line
Processing Block	Signal Processing	AD conversion, processing of sensor signal and transmitting to received block
	Wireless Reciever	Receiving data from sensor and transmitting data to power line
	Parameter Tuner	AD conversion of a volume voltage and transmitting data to power line
Action Block	Motor	Get data form power line and interpret the data then gen-erate output for driving each element
	LEDs	
	Sound	

© ISAROB 2013

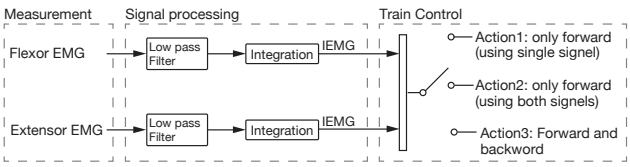

Fig. 4. Train system flow

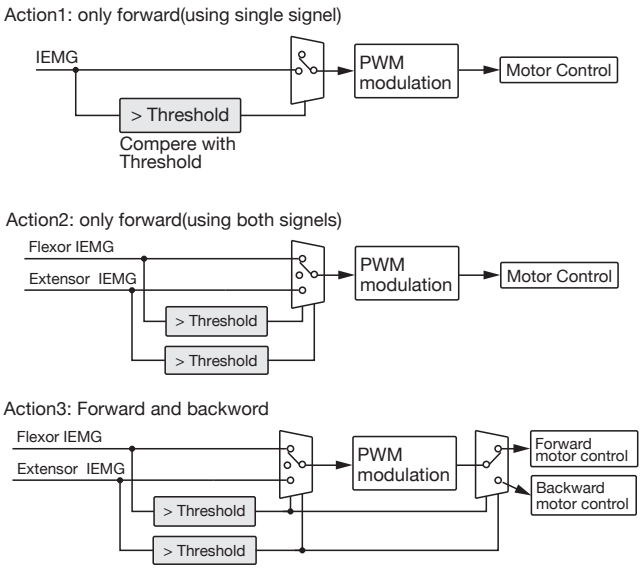

Fig. 5. variations of the train action

a crunch of the bandwidth, signal processing blocks compute AD converting data to meaningful and low frequency data depending on measurement signal feature before transmission. For example, EMG signals are obtained from the electrodes attached with a human skin and sampled at a rate around 1kHz. The resulting Integrated EMG(IEMG) signals are transmitted at a rate around 100Hz. On the other hand, in the case of changing parameters such as the parameter tuner, a rate of about 10Hz would be sufficient. When action blocks obtain data from the power line, the specific type of these data are checked and processed.

2.3 Action Blocks and Block Assembly

We have developed the train-toy system based on motor action block. Figure 4, 5 and 6 show the system overview and data flow. The train has two kinds of connectors, the connectors placed at the front and back sides on the roof are assigned for forward and backward motor control, respectively.. A set of a battery, block wireless receiver and parameter tuner are assembled to the train on the different side of the roof, the train moves forward or backward according to the given block assembly. In a simple case, when data values are above the given threshold determined by the parameter tuner (Action1). Then, when another block set is added, the train moves forward when either of the data values are above the threshold (Action2)(See Figure 6). On the other hand, when each set of blocks are assembled on each side of the roof, the train moves frontward or backward when either data value are above the threshold (Action3). These biofeedback systems are designed to manipulate blocks by simply arranging and rearranging them without consideration about the block order with the aid of communication on the battery line.

Fig. 6. Overview of the train system

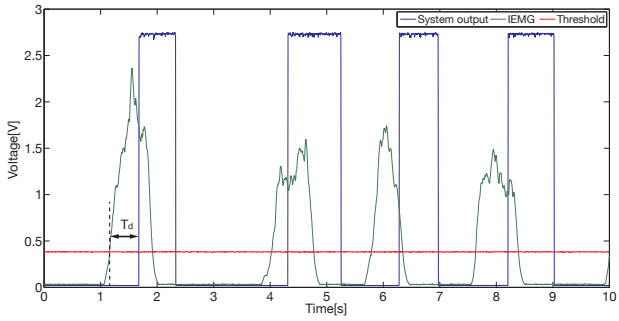

Fig. 7. IEMG, threshold and generated output Waveforms

3 Experiment

3.1 System Evaluation

In order to evaluate the performance of the proposed system, we conduct an evaluation experiment to verify the latency of the system. We prepared a basic system that is composed by a EMG wearable sensor, a wireless receiver, a parameter tuner and an action blocks. In this experiment, the biosignal data are transmitted at 1kHz and the parameter tuner block is transmitted data at 10Hz. Figure 7 shows a scene during the experiment. The train is controlled according to the measured EMG signal attached with the elbow of the subject. We measured T_d[s] is the system latency sixteen times and the averaged result is 0.454s. This includes a time required for wireless communication, and converting power line communication. We consider that this latency does not cause a problem for inferring the causality between bodily action and train movement.

© ISAROB 2013

Fig. 8. The scene in the physiotherapy using train system

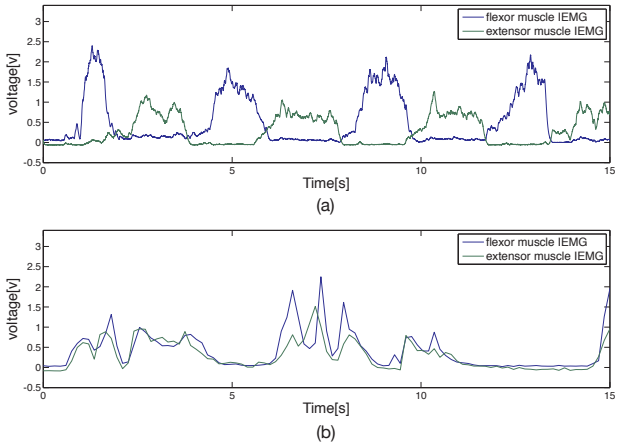

Fig. 9. Flexor and extensor IEMG (a) healthy participant (b) the child with congenital loss of left arm

3.2 Case-Study: Therapeutic Activities for Children

We used the train system with a child suffering from a congenital loss of the left arm.Children with forearm impaired motor functions or a congenital loss of limbs are trained to generate proper EMG signals for the use of prosthesis limb and hand. The participant is being trained to use flexor and extensor muscle for opening and closing the prosthesis hand. We describe such training can be achieved using the proposed biofeedback system. Before this experiment, the participant were not likely to wear cosmetic artificial hand and he was uncooperative even for the EMG measurement.. We then introduced a prototype setup as shown in Figure 8, which shows the scene in therapeutic activity using the train system. We observed that the participant was motivated and willing to play with the train toy. He was more cooperative to have its EMG measured. Physiotherapist attended to the session switched the action mode, and measured the EMG signals.

The proposed system is capable not only to control the train but also to record muscle activities in real time. Figure 9 shows the flexor and extensor IEMG wave form. We asked the participant to move the flexor and extensor muscles in turn during playing with the toys. The train system made the participant realize that he still does not control the two muscles separately. The system showed the possibility to help therapist to monitor the children's physiological activity while playing with toys.

4 CONCLUSIONS

In this paper we proposed a unique biofeedback toys called bioToys based on normal and modified building blocks. In the field of physiotherapy for children, therapists are struggling to design therapeutic programs and methods according to the response of patients. They encounter the problem that some children easily give up training to use prosthesis because such training become boring after a while, since the rehabilitation training contents comprise only simple tasks.

We developed special building blocks that can be used in a traditional way, although they are embedded with a fully functioned electronic circuit. We verified that these blocks can be utilized for a biofeedback training that enables the use of biological or physiological signals in processing blocks and can generates various actions. The system are constructed by arranging and rearranging these building blocks easily in real time. Further investigation will also include the design of different types of blocks.

REFERENCES

[1] Wolf S. L. (1983), Electromyographic biofeedback applications to stroke patients. A critical review. *Physical Therapy*, **63**(9): 1448–1459

[2] Tsubouchi, Y., and Suzuki, K. (2010), Biotones: A Wearable Device for EMG Auditory Biofeedback, *Proc. of Annual Intl. Conf. of the IEEE EMBS*, pp. 6543-6546

[3] Igarashi, N., Suzuki, K., Kawamoto, H., and Sankai, Y. (2010), Biolights: Light Emitting Wear for Visualizing Lower-Limb Muscle Activity, *Proc. of Annual Intl. Conf. of the IEEE EMBS*, pp. 6393-6396.

[4] Hiroshi, I., Brygg, U. (1997), Tangible Bits: Towards Seamless Interfaces between People, Bits and Atoms, *Proc. of the ACM CHI*, pp. 234-241.

[5] Lund.H.H. (2003), Intelligent Artefacts, *Proc. of 8th Intl. Symp. on Artificial Life and Robotics*, pp. 11-14.

[6] Horn, M.S., Jacob, R.J.K. (2007), Designing tangible programming languages for classroom use, *Proc. of the 1st Intl. Conf. on Tangible and Embedded Interaction*, pp.159-162.

[7] Schweikardt, E., Gross, M.D. (2008), The robot is the program: interacting with roBlocks, *Proc. of the 2nd Intl. Conf. on Tangible and Embedded Interaction*, pp.167-168.

© ISAROB 2013

The Eighteenth International Symposium on Artificial Life and Robotics 2013 (AROB 18th '13),
Daejeon Convention Center, Daejeon, Korea, January 30-February 1, 2013

A Micro-Simulator for Traffic Signal Control Based on A Modified Cellular Automaton Traffic Flow Model

Hu Jin[1], Cheng-You Cui[1], and Hee-Hyol Lee[1]

[1]Graduate School of Information, Production and Systems, Waseda University, Japan
(Tel: 81-93-692-5164, Fax: 81-93-692-5164)
[1]kinko@akane.waseda.jp

Abstract: In recent years, many traffic signal control methods have been proposed to reduce traffic jams. However, the experiments of the methods were difficult to perform in real road networks. In order to prove the effectiveness of the methods, traffic simulations by using a traffic simulator were required. Although various traffic simulators have been developed, the most of simulator was not specified for simulation of traffic signal control. A micro traffic simulator for simulation of traffic signal control is introduced in this paper. The micro-simulator is based on a Cellular Automaton (CA) model, which is a model of artificial life. Furthermore, the CA traffic model is modified according to features of traffic flows at intersections in order to reproduce the traffic situation of urban area. The usability of the proposed CA traffic model is evaluated through the analysis of relationship between traffic density, average speed, and traffic flows. Moreover, the micro-simulator is applied to evaluate traffic signal control methods.

Keywords: Traffic model, Cellular Automaton, Traffic Flow, Simulation.

1 INTRODUCTION

In recent years, many traffic signal control methods have been proposed to reduce traffic jams. However, the experiments of the methods were difficult to perform in real road networks. In order to prove the effectiveness of the methods, traffic simulations by using a traffic simulator were required. On the other hand, many traffic simulators were developed such as the TRANSIMS, SUMO, and VISSIM and so on. However, the most of simulator was not specified for simulation of traffic signal control. A micro traffic simulator for simulation of traffic signal control is introduced in this paper. The micro-simulator is based on a Cellular Automaton (CA) model, which is a model of artificial life. Furthermore, the CA traffic model is modified according to features of traffic flows at intersections in order to reproduce the traffic situation of urban area. The usability of the proposed CA traffic model is evaluated through the analysis of relationship between traffic density, average speed, and traffic flows. Moreover, the micro-simulator is applied to evaluate traffic signal control methods.

2 MODIFIED CELLULAR AUTOMATON TRAFFIC FLOW MODEL

Cellular Automaton (CA) models are conceptually simple, thus a set of simple CA rules can be used to produce complex behavior. Through the use of powerful computers, these models can encapsulate the complexity of the real world traffic behavior and produces clear physical patterns that are similar to those we see in everyday life. The proposed CA urban traffic model is built based on the SchCh model (highway traffic model).

2.1 Road setting and movement rule

In the proposed CA traffic model the default size of a cell is 7.5m, and an example is shown in Fig.1. The lane number is determined according to the real road and, right-turn only lane also considered in the model.

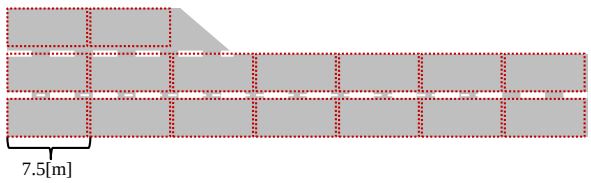

Fig. 1. Cell setting of road

2.2 Rules of Inflows and outflows

A vehicle will be created according to the inflow rate, and the travel direction will be determined according to the ratio of different travel direction. Here, the travel direction is the road's number, and a vehicle pass the intersection to move designated road according to the travel direction. An example is shown Fig.2.

The rules of inflows as follows:

Rule 1: *if* $\boldsymbol{inR} < rand()$,
than create a vehicle.

Rule 2: *if* $\boldsymbol{Dir}_d < rand() < \boldsymbol{Dir}_{d+1}$,
than set the travel direction to *d*.

© ISAROB 2013

Here, ***inR*** is the inflow rate, $\boldsymbol{Dir}_d$ is the ratio of the travel direction, *rand*() is random number within [0, 1]. The ***inR*** and $\boldsymbol{Dir}_d$ is determined according the equation (1), (2) with the measured traffic data. In the equations, *k* and m is the cycle number, *Ct* is the cycle length, *Ln* is the lane number, *d* is the different road number, *I* is the traffic volume of inflows, *O* is the traffic volume of outflows.

$$InR = \frac{\sum_{m=1}^{m=k-1} I_m}{\sum_{m=1}^{m=k-1} Ct_m \bullet Ln} \tag{1}$$

$$Dir_d = \frac{\sum_{m=1}^{m=k-1} Od_m}{\sum_{m=1}^{m=k-1} O_m} \tag{2}$$

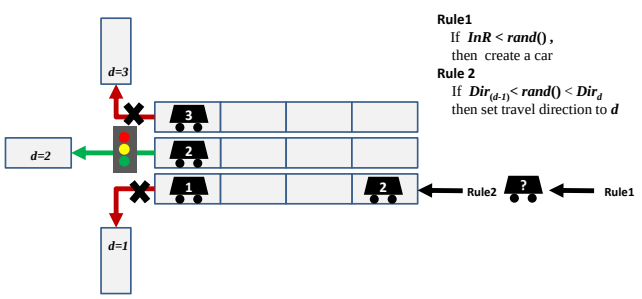

Fig. 2. Inflow and outflow

2.2 Rules of movements

In proposed CA traffic model, a vehicle can be accelerated up to maximum speed, and can change the road lane. In addition, particular rule will be used at the right-turn only lane. Specific rules are as follows:

Step 1: check cell
if the cell *i*+1 is empty,
than go to step 2;
else go to step 4.

Step 2: move one cell
Move the vehicle to i+1 cell.
if i+2 is the empty,
than go to step 3,
else stop.

Step 3: random accelerate
if $\boldsymbol{P}_{acc} < rand()$,
than move to cell i+2
else stop.

Step 4: check multi-lane
if the road is the multi-lane
than go to step 5.
else stop.

Step 5: move to parallel lane
if the parallel cell j, j+1, j-1,j-2 are empty,
than move the vehicle to cell j+1.
else stop.

Here, $\boldsymbol{P}_{acc}$ is determined by equation (3). P_0 is the set value; *Td* is the traffic density of the road.

$$P_{acc} = P_0 - Td \bullet rand() \bullet 0.1 \tag{3}$$

If the travel direction of a vehicle is right-turn, the vehicle moves to the right turn exclusive lane, even when there is no obstacle. As an example, the rule of movements is shown in Fig.3.

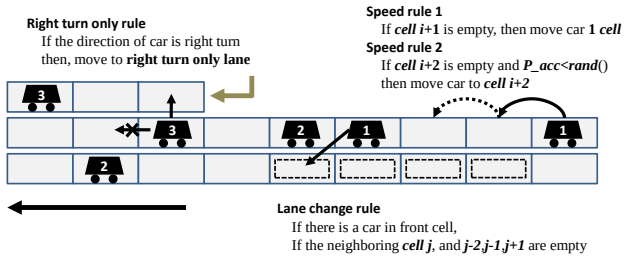

Fig. 3. Movements

3 MICRO SIMULATOR

A micro traffic simulator is developed based on the modified CA traffic flow model. The procedure of the simulator is shown Fig.4.

Step 1: Initialization
To set the intersection, and road length, lane number, inflow rate, ratio of different travel direction at each road. The traffic signal of each intersection can be obtained by using the empirical equations (Webster's formulations), also it can be changed by an interface.

Step 2: initial parameter
To set the simulation time (St), set the count time of each intersection (Ct), and set the cycle (k) of each intersection. Here, each intersection has respective Ct and k.

Step 3: Step check
If reach the simulation time, than go to step 15,
else continue next step.

Step 4: CA (1/2)
Move the vehicles according to CA rules (in/outflows)

Step 5: CA (2/2)

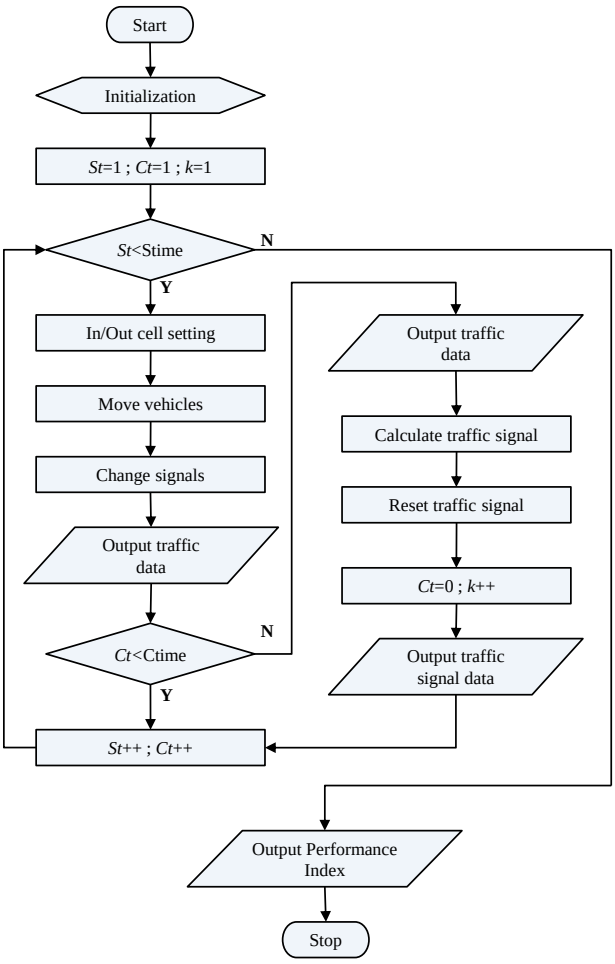

Fig. 4. Procedure of micro traffic simulator

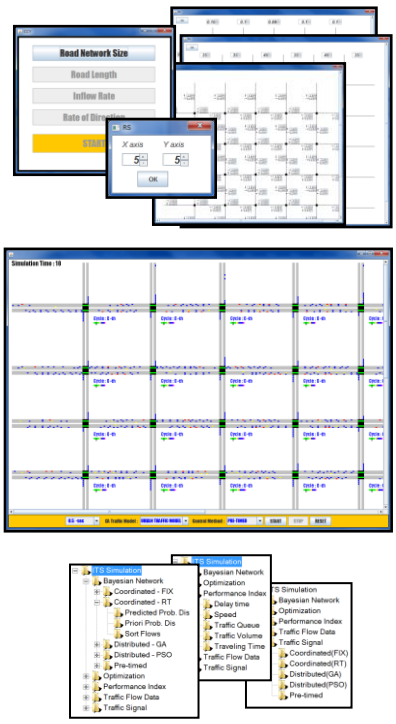

Fig. 5. Initial settings, Frame of simulator, and file structure

Move the vehicles according to CA rules (movements)

Step 6: Change signals

To change the signal phases of each intersection, according to the Ct with the parameters of traffic signals.

Step 7: Record 1

To record moved cells

Step 8: Cycle check

If reach the cycle time, than go to step 10,
else continue next step.

Step 9: Count

To counts simulation time (St) and cycle time (Ct) of each insertion, go to step 3.

Step 10: Record 2

To record traffic volume data of each intersection, and cycle number, intersection number.

Step 11: Calculation of Signal

To calculates the traffic signal of next cycle. If there no calculation algorithm is implemented the pre-timed signal will be used continued.

Step 12: Traffic signal reset

Reset the traffic signals of intersection.

Step 13: Parameter reset

Set the Ct to 0, and count the cycle k.

Step 14: Record 3

To record updated traffic signals.

Step 15: Record 4

To record PI(Performance Index). The PI will be calculated with the recorded data.

The frame of initialization and simulation are shown in Fig.5 as an example.

4 SIMULATION

To evaluate the usability of proposed CA traffic model, two kinds of the simulation were carried out. The first simulation is that analyze the relationship between traffic density, average speed, and traffic flows. Here, a diagram of relation between the traffic flux and the traffic density called the fundamental diagram of traffic flow. Generally, the fundamental diagram of traffic flow has some characteristics as follows;

1) When the density is 0, flow will also be 0, since there are no vehicles on the road.
2) When the number of vehicles gradually increases the density as well as flow increases.
3) When more and more vehicles are added, it reaches a situation where vehicles can't move. This is referred to as the jam density or the

© ISAROB 2013

maximum density. At jam density, flow will be 0 because the vehicles are not moving.

On the other hand, the average speed generally maintains 30-40[km/h], and when the average speeds smaller than 20[km/h] the road will be considered as a traffic jam in urban area

Fig.6 shows the fundamental diagram of proposed CA traffic model, and the Fig.7 is the relation between traffic density and speed, the Fig.8 is the relation between traffic flow and speed.

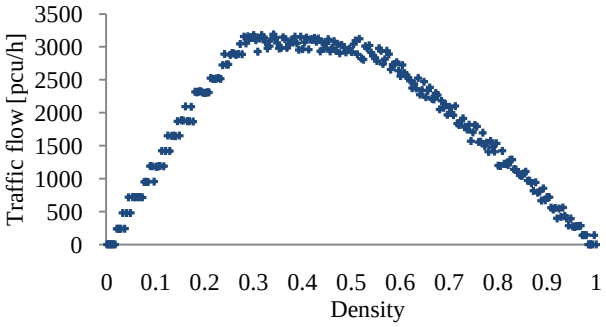

Fig. 6. Fundamental diagram of traffic flow

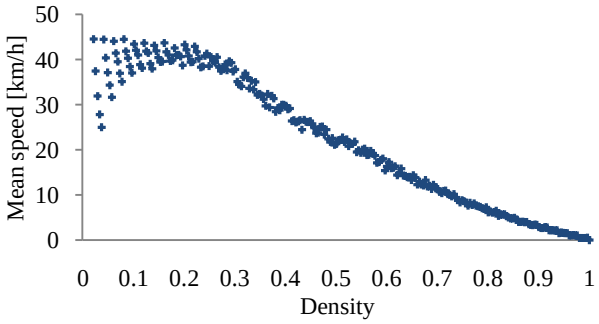

Fig. 7. Relation between traffic density and speed]

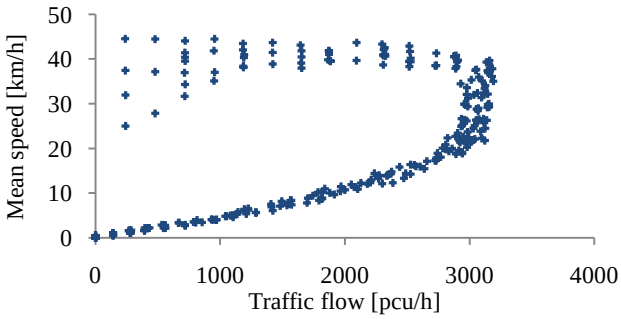

Fig. 8. Relation between traffic flow and speed

Table 1. Comparison of traffic flows

Traffic flows	Actual Data [pcu/h]	By simulator Mean(10times)	Mean error
In	2,325	2,362.7	0.7 %
Out	2,229	2,212.9	-1.6 %

The second simulation is comparison of the actual traffic flow data and simulated traffic data by using the micro simulator. The results are listed in table 1. These figures and the table can prove that, the modified CA traffic model can reproduce the traffic flows of urban areas very well.

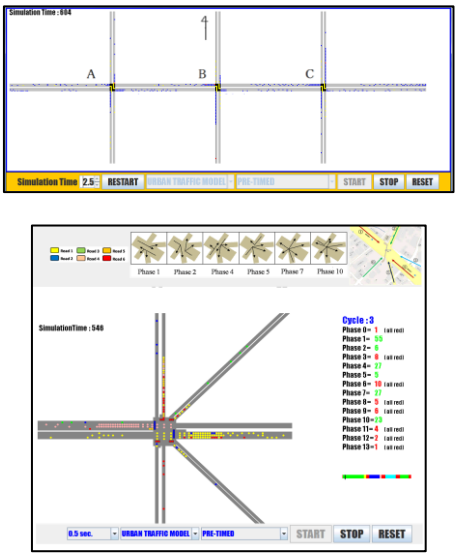

Fig. 9. Example of simulations

The micro simulator has been applied to evaluate several traffic signal control methods. Examples of the crossroad intersection and multi-way intersection are shown in Fig.9.

5 CONCLUSION

A micro traffic simulator is built up based on a modified CA traffic model. Through simulations the usability of the proposed CA traffic model is evaluated. As the future work, first is to improve the GUI, second is to add the vehicle category.

REFERENCES

[1] K. Nagel, M. Schereckenberg, "A Cellular automaton model for freeway traffic", Journal de Physique I, Vol.2, No.12, pp.1868-1870, 1996.

[2] Michał MACIEJEWSKI, "A comparison of microscopic traffic flow simulation systems for an urban area", Transport Problems: an International Scientific Journal, Vol.5, No.4, pp.27-38, 2010.

[3] Pedro Fernandes, Urbano Nunes, "Platooning of Autonomous Vehicles with Intervehicle Communications in SUMO Traffic Simulator", 13-th International IEEE Annual Conference on Intelligent Transportation Systems, pp.1313-1318, 2010.

© ISAROB 2013

The Eighteenth International Symposium on Artificial Life and Robotics 2013 (AROB 18th '13),
Daejeon Convention Center, Daejeon, Korea, January 30-February 1, 2013

Real-Time Stochastic Optimal Control for Traffic Signals of Multiple Intersections

Cheng-You Cui[1], Hee-Hyol Lee[1]

[1]Graduate School of Information, Production and Systems, Waseda University, Japan
(Tel: 81-93-692-5164, Fax: 81-93-692-5164)
[1]cuichengyou@ruri.waseda.jp

Abstract: Traffic congestion has become a serious problem with exponential increase of vehicles recently. In urban area, almost all of traffic jams occur at intersections. In such cases, traffic signal control is a reasonable method to reduce the traffic jams. Traffic signal control can be divided into two types: one is off-line (Pre-timed) control and the other is on-line (Adaptive) control. In the pretimed control, empirical formulas were used to calculate the traffic signals off-line using historical traffic data, but it cannot handle the variation of traffic flows. The adaptive control can overcome this limitation by adjusting the traffic signals on-line in the various traffic flows. The adaptive control can also be divided into two types: centralized and distributed systems. However, the centralized system requires the extensive data processing and computational time to calculate optimal traffic signals. On the other hand, the distributed system can achieve a real time control. In this paper, a real time stochastic optimal control method of traffic signal is proposed. A modified Cellular Automaton (CA) traffic model and Bayesian Network (BN) model are used to predict the traffic jams. In addition, H-GA-PSO algorithm is used to search optimal traffic signals based on the stochastic model. The H-GA-PSO algorithm is a modified Hierarchical Particle Swarm Optimization (H-PSO) method based on Genetic Algorithm (GA). Finally, the effectiveness of the proposed method is shown through simulations at multiple intersections using a micro traffic simulator.

Keywords: Traffic signal, Stochastic Optimal Control, Cellular Automaton Traffic model, H-GA-PSO algorithm.

1 INTRODUCTION

Traffic jam has become a serious problem with exponential increase of vehicles recently. In urban area, almost all traffic congestion occurs at intersections. One of the ways to solve this problem is road-expansion, but it is difficult to realize in urban areas. In such cases, traffic signal control is a reasonable method to reduce traffic-jam. Traffic signal control can be divided into two types. One is off-line (Pre-timed) control and the other is on-line (Adaptive) control. In the pre-timed control, Webster's formula is used to calculate the traffic signals off-line using historical traffic data, but it cannot handle the variation of traffic flows. On the other hand, the adaptive control can overcome this limitation by adjusting the traffic signals on-line in the various traffic flows. SCOOT and SCATS have been implemented on urban traffic networks using the centralized systems. However, the centralized systems require the extensive data processing and computational time for calculating optimal traffic signals. The distributed system can achieve the real time control.

In this paper, a real time stochastic optimal control method of traffic signal is proposed. A modified Cellular Automaton (CA) traffic model and Bayesian Network (BN) model are used to predict the probabilistic distributions of standing vehicles of the intersection roads. In addition, a hierarchical H-GA-PSO is proposed to search the optimal traffic signals to minimize traffic-jam probabilities using an optimal probabilistic model. Finally, the effectiveness of the proposed method is shown through simulations at multiple intersections using a micro traffic simulator.

2 STOCHASTIC MODEL FOR TRAFFIC JAM

2.1 Prediction of probabilistic distribution for standing vehicles at intersection

In order to predict the traffic jam probability, a Bayesian Network (BN) model is built to predict probabilistic distributions of standing vehicles at crossroad according to the relationship between traffic flows and standing vehicles.

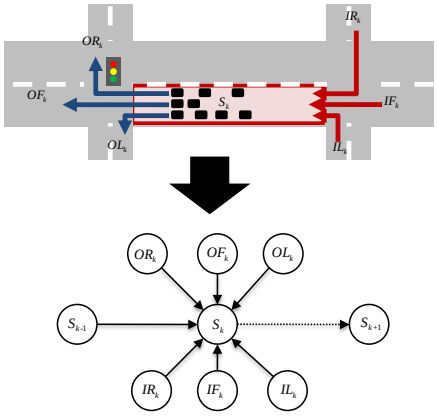

Fig. 1. Crossroad and BN model

© ISAROB 2013

Here, we consider a crossroads as shown in Fig.1. The random variables of the inflows and the outflows of the crossroad and the standing vehicles between the two intersections are represented as nodes. The Bayesian network model of the standing vehicles is shown in Fig.1. The number of the standing vehicles of k-th cycle can be calculated as equation (1). The probabilistic distribution of the standing vehicles is obtained by summing over all joint probability distribution of the other variables.

$$S_k = S_{k\text{-}1} + IR_k + IF_k + IL_k - OR_k - OF_k - OL_k \tag{1}$$

$$P(S_k) = \sum_{S_{k\text{-}1}}\sum_{IF_k}\sum_{IL_k}\sum_{IR_k}\sum_{OF_k}\sum_{OL_k}\sum_{OR_k} P(S_k, S_{k\text{-}1}, IF_k, IL_k \cdots, IR_k, OF_k, OL_k, OR_k) \tag{2}$$

$$\begin{aligned} P(S_k, S_{k\text{-}1}, IF_k, IL_k, IR_k, OF_k, OL_k, OR_k) = \\ & P(S_k \mid S_{k\text{-}1}, IF_k, IL_k, IR_k, OF_k, OL_k, OR_k) \\ & \times P(S_{k\text{-}1} \mid IF_k, IL_k, IR_k, OF_k, OL_k, OR_k) \\ & \times P(IF_k \mid IL_k, IR_k, OF_k, OL_k, OR_k) \\ & \times P(IL_k \mid IR_k, OF_k, OL_k, OR_k) \\ & \times P(IR_k \mid OF_k, OL_k, OR_k) \\ & \times P(OF_k \mid OL_k, OR_k) \\ & \times P(OL_k \mid OR_k) \\ & \times P(OR_k) \end{aligned} \tag{3}$$

With the chain rule, the joint probabilistic distribution is represented as the product of conditional probability as equation (3). Then, according to the d-separation and the relationship between traffic flows and standing vehicles the equation (2) can be represented as

$$P(S_k) = \sum_{S_{k\text{-}1}}\sum_{IF_k}\sum_{IL_k}\sum_{IR_k}\sum_{OF_k}\sum_{OL_k}\sum_{OR_k} P(S_k)P(S_{k\text{-}1})P(IF_k) \cdots, P(IL_k)P(IR_k)P(OF_k)P(OL_k)P(OR_k) \tag{4}$$

In order to calculate the probabilistic distribution of the standing vehicle at intersection road, the prior probabilities of traffic inflow and outflows must be updated. Generally, the priori probability of the traffic flows is variable under the different traffic signal. Hence, we use the CA traffic model to estimate the traffic flow of the different traffic signals. And then, according to the estimated traffic flows the priori probabilistic distributions will be updated. The updating process is as following:

Step1: Using the CA traffic model to estimate the traffic inflow I_k^e and outflow O_k^e of the different traffic signal of the k-th cycle.

Step2: Using the observed traffic data of before the k-th cycle to calculate the probabilistic distribution of inflow $\sum_i P(I_{k\text{-}1} = i)$ and outflow $\sum_i P(O_{k\text{-}1} = i)$.

Step3: Using the estimated traffic flow data and probabilistic distribution to calculate the prior probabilities of traffic inflow and outflows according to the equations (5) – (8).

$$\hat{P}(I_k^e) = P(\hat{I}_{k\text{-}1}^e) - \frac{\gamma}{E\text{-}1} \qquad (\hat{I}_{k\text{-}1}^e \neq \hat{I}_k) \tag{5}$$

$$\hat{P}(I_k^e) = P(\hat{I}_{k\text{-}1}^e) + \frac{\gamma.n}{E\text{-}1} \qquad (\hat{I}_{k\text{-}1}^e = \hat{I}_k) \tag{6}$$

$$\hat{P}(O_k^e) = P(\hat{O}_{k\text{-}1}^e) - \frac{\gamma}{E\text{-}1} \qquad (\hat{O}_{k\text{-}1}^e \neq \hat{O}_k) \tag{7}$$

$$\hat{P}(O_k^e) = P(\hat{O}_{k\text{-}1}^e) + \frac{\gamma.n}{E\text{-}1} \qquad (\hat{O}_{k\text{-}1}^e = \hat{O}_k) \tag{8}$$

$$e \in (0,1,2\cdots,E) \qquad \gamma = 5\%$$

Here, the CA traffic model is built based on the SchCh model (highway traffic model). The rules of movements for the vehicles on road network are shown in Fig.3 as an example. A vehicle can be accelerated up to maximum speed (Maximum speed = move 2 cell; 1cell=7.5m/1 step [1sec]) when there is no obstacle. According to the conditions of the road, the speed can be changed randomly. In multi lanes road, a vehicle can move to parallel lanes. If the direction of travel is right turn, the vehicle moves to the right turn exclusive lane.

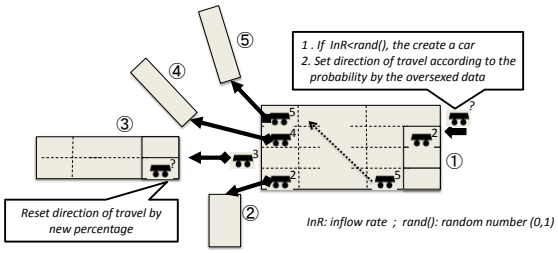

Fig. 2. CA traffic model

2.2 Traffic jam probability optimization problem

The objective of proposed method is to search an optimal traffic signal to minimize the traffic jam probabilities. Here, we formularized the traffic jam probability optimization problem as equation (9) according to the probabilistic distributions of the standing vehicles at crossroad intersection.

$$F(t_k^1, t_k^2, \ldots, t_k^i) = a \bullet \sum_{S_k = S_{\max}}^{S_k = +\infty} \hat{P}_{\text{main}}(S_k) + \beta \bullet \sum_{S_k = S_{\max}}^{S_k = +\infty} \hat{P}_{\text{minor}}(S_k)$$

Subject to (9)

$$t_{\min}^n \leq t_k^n \leq t_{\max}^n \qquad i = 1,2,\ldots,n$$

Here, t_k^n is the time length of signal phase n, and $t_{\min}^n$ and $t_{\max}^n$ indicates the adjustable range of the signal phase n, $\hat{P}_{\text{main}}(S_k)$ is the probabilistic distributions of the main road $\hat{P}_{\text{minor}}(S_k)$ is the probabilistic distributions of the minor road, a and β are weight value.

3 H-GA-PSO ALGORITHM AND REAL-TIME CONTROL

In order to achieve the real-time control, an H-GA-PSO algorithm is proposed based on the Hierarchical-PSO. In H-GA-PSO a particle is influenced by its own so far best position and by the best position of the particle that is directly above it in the hierarchy. All particles are arranged in a tree that forms the hierarchy so that each node of the tree contains exactly one particle. Fig.3 shows the structure of H-GA-PSO.

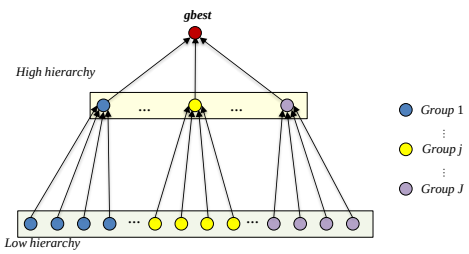

Fig. 3. Structure of H-GA-PSO algorithm

$$v_{ij}^{itr+1} = w_l \cdot v_{ij}^{itr} + c_{l1} \cdot rand() \cdot (pbest_{ij}^{itr} - x_{ij}^{itr}) + c_{l2} \cdot rand() \cdot (lbest_i^{itr} - x_{ij}^{itr}) + c_{l3} \cdot rand() \cdot (gbest^{itr} - x_{ij}^{itr}) \quad (10)$$

$$x_{ij}^{itr+1} = x_{ij}^{itr} + v_{ij}^{itr+1} \quad (11)$$

$$v_{ij}^{itr+1} = w_h \cdot v_{ij}^{ir} + c_{h1} \cdot rand() \cdot (pbest_{ij}^{itr} - x_{ij}^{ir}) + c_{h2} \cdot rand() \cdot (gbest^{itr} - x_{ij}^{ir}) \quad (12)$$

$$x_{ij}^{itr+1} = x_{ij}^{itr} + v_{ij}^{itr+1} \quad (13)$$

In the H-GA-PSO, the particles in low hierarchy are updated using equations (10) and (11), and the particles in high hierarchy are updated using equations (12) and (13). In equation (10), *lbest* is the position with the best fitness found so far by the corresponding group.

Also, Genetic Algorithm (GA) and a rule of particle's initialization are used to avoid the local minimum problem. The GA is used to update a selected particle's position and basic concepts of initialization for particles are shown in Fig.4. The crossover processing is used to exchange two particles from different group. The mutation processing is used to reset a particle around *gbest* or *lbest*. The initial particles can keep a certain distance by using the rules.

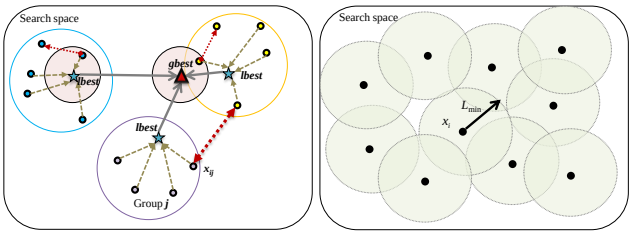

Fig. 4. Structure of H-GA-PSO

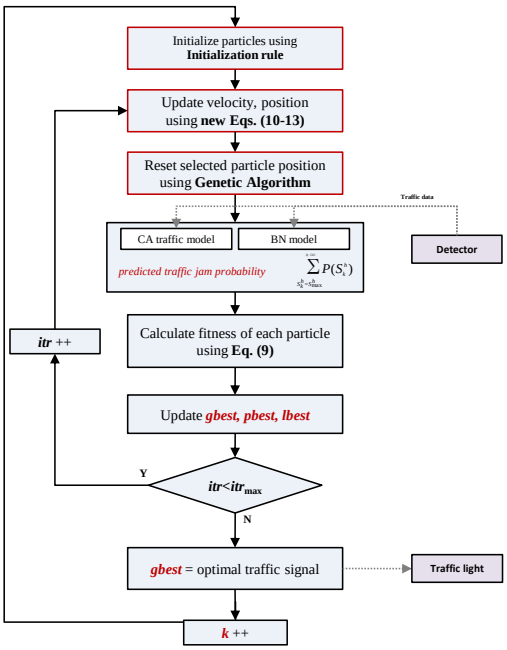

Fig. 5. GA operation and initialization of particles

The H-GA-PSO algorithm is used to search a opti mal traffic signal with traffic jam probability optimal model. The procedure is shown in Fig.5.

4 SIMULATION

To prove the effectiveness of the proposed method, a si mulation was carried out with a micro-traffic simulator. The micro-traffic simulator is developed based on the CA traffic model. We assume a road network and detector systems.

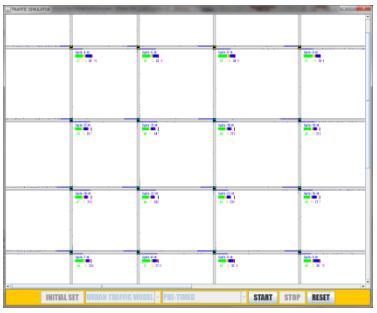

Fig. 6. Frame of micro simulator

The road network of the experiment includes 16 intersections, and all traffic data of the intersections can be observed by the detector systems. The simulator frame is shown in Fig.6. The conditions of the traffic flows and road networks are shown in table 1. Each pre-timed signal of the intersections are calculated according to the Webster's formula.

Table 1. Conditions of traffic flows

Direction	Road length	Lane	direction of ravel straight	right	left	No.	Inflows (pcu/h)
West to East	80 [cell]	3	90%	4%	6%	**1**	1300
						2	1100
						3	1400
						4	1500
East to West	80 [cell]	3	90%	4%	6%	**5**	1400
						6	1300
						7	1000
						8	900
South to North	70 [cell]	2	60%	10%	30%	**9**	600
						10	400
						11	500
						12	500
North to South	70 [cell]	2	60%	20%	20%	**13**	400
						14	500
						15	500
						16	600

* pcu : passenger car unit ; 1 cell=7.5m

The traffic signals of the intersection 1 suggested by the proposed method are shown in Fig.6. Compared with pre-time signals, the signals by the proposed method are updated according to the changing traffic flows.

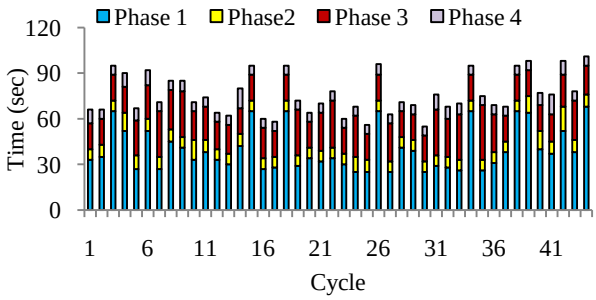

Fig. 7. Optimal Traffic signals of intersection1

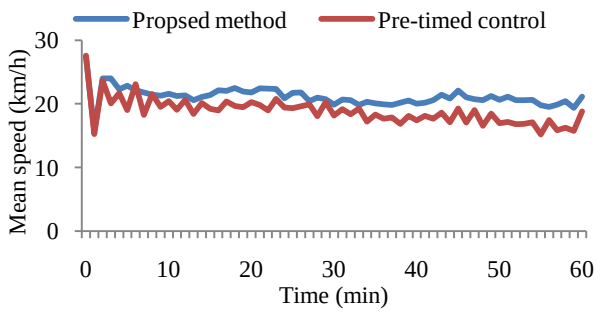

Fig. 8. Comparison of mean speed

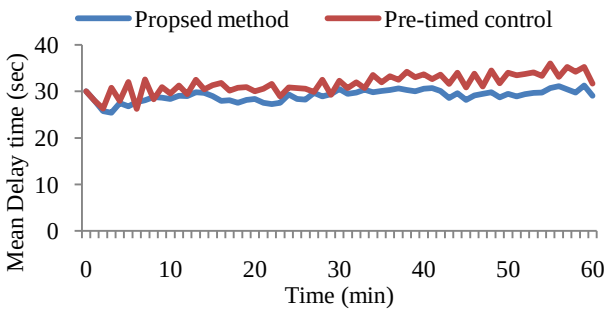

Fig. 9. Comparison of mean delay time

By the proposed the total delay time is decreased about 18.3% compared with pre-timed control, and the result is shown in Fig.9. And, the comparison of mean speed of proposed method and pre-timed control is shown Fig.8. By the proposed method, the mean speed is increased.

5 CONCLUSION

A real-time traffic signals stochastic optimal control was proposed based on the optimization model of traffic-jam probability and the H-GA-PSO algorithm to calculate the optimal signals. Through a simulation with the micro simulator the effectiveness of the proposed method was shown.

REFERENCES

[1] F. V. Webster and B. M. Cobbe, Traffic Signals, "Road Research Technical Report 39", Her Majesty's Stationery Office (London), 1958.

[2] Dennis I. Robertson and R.David Bretherton, "Optimizing Networks of Traffic Signals in Real Time The SCOOT Method", IEEE Transactions on Vehicular Technology, Vol.40, No.1, pp.11-15, 1991.

[3] A. G. SIMS and K. W. DOBINSON, "The Sydney Coordinated Adaptive Traffic (SCAT) System Philosophy and Benefits", IEEE Transactions on Vehicular Technology, Vol.29, No.2, pp.130-137, 1980.

[4] K. Nagel, M. Schereckenberg, "A Cellular automaton model for freeway traffic", Journal de Physique I, Vol.2, No.12, pp.1868-1870, 1996.

[5] J. Kennedy, R, Eberhart, "Particle Swarm Optimization", Proceedings IEEE International Conference on Neural Networks, pp.19842-1948, 1995.

[6] Janson S., Middendorf M., "A hierarchical particle swarm optimizer and its adaptive variant", IEEE Transactions on Systems, Man, and Cybernetics, Vol.35, No.6, pp.1272-1282, 2005.

[7] Cheng-You Cui, Hee-Hyol Lee, "Distributed Traffic Signal Control Using PSO Based on Probability Model for Traffic Jam", Intelligent Autonomous Systems 12 Advances in Intelligent Systems and Computing, Vol. 193, pp. 629-639, 2013.

© ISAROB 2013

Decouple PID Control of Compact Binary Power Generation

Kun-Young Han[1], Lu Li, and Hee-Hyol Lee

Graduate School of Information, Production and Systems, Waseda University, Japan
(Tel: 81-93-692-5164, Fax: 81-93-692-5164)

[1]kyhan@akane.waseda.jp

Abstract: A compact binary power generation using low-temperature difference thermal energy can be produce electric power by utilizing low temperature difference between hot water and cold water. In this study, a reduced transfer function model of whole transfer function model for the compact binary power generation pilot plant is constructed. A decouple PID control system is also designed to control the power generation pilot plant using a pseudo diagonalization, gershgorin bands, and multi-stage pre-compensators.

Keywords: power generation, renewable energy, evaporator, condenser, non-interacting, pre-compensator, PID

1 INTRODUCTION

A compact binary power generation is to convert thermal energy into electric power using temperature difference between heat and cooling source such as heat of hot springs, or waste heat of factories, and ocean thermal energy, which are enormous quantitatively. Thermal power plant that uses fossil fuels such as oil, coal, and natural gas, but the compact binary power generation is an environment-friendly and semi permanent energy source. In this respect, the compact binary power generation using renewable energy has been attracted. However, the temperature difference of compact binary power generation system is much lower than that of the other commercialized steam power plants. Furthermore, controlled variables and manipulated variables of the system interact on each other in general. If a control system is designed without consideration of such case, it is possible to make worse the control performance, because a control loop exerts harmful influence to other control loop through the interaction. For that reason, an appropriate control system is required to obtain the stable electric power.

In this paper, a reduced transfer function model of whole transfer function model is built for a power generation pilot plant and a decouple PID control system is designed to control the plant.

2 MODELING OF COMPACT BYNARY POWER GENERATION SYSTEM

2.1System structure and experiment Conditions

The block diagram of the power generation pilot plant by low- temperature difference is illustrated in Fig.1. The whole system consists of seven components: evaporator, condenser, separator, regenerator, turbine part (turbine and absorber), reducing valve, and working fluid pump.

1)Experimental conditions*:*

The pressure of the inlet and outlet of the turbine are measured by using amount of hot water as step input. At that time, Amount of cold water and working fluid is fixed. Next, amount of cold water is used as step input to measure the pressure of inlet and outlet of the turbine. At that time, amount of hot water and working fluid is fixed. The sampling time is 3[sec], the number of data is 100 samples.

A compact binary power generation system is modeled based on measured data.

2.2Transfer function models based on step response

The transfer function models for the compact binary power generation system using low-temperature difference are drawn by approximate methods using 1st time delay transfer function and 2nd order transfer functions is used to express oscillating component.

1) Transfer function model for evaporator

A block diagram of an evaporator is shown in Fig.2.The working fluid and hot water are used as input in the evaporator. The transfer function models of the evaporator are drawn as shown in Eq.(1)-(3).

$$G_{Ev}1(s) = \frac{1}{0.81s+1} \cdot \frac{15}{s^2+0.02s+15} \tag{1}$$

$$G_{Ev}2(s) = \frac{0.0875}{5s+1} \cdot \frac{15}{s^2+0.02s+15}e^{-s} \tag{2}$$

$$G_{Ev}3(s) = \frac{77.2}{1.1s+1} \cdot \frac{6}{s^2+0.07s+6}e^{-s} \tag{3}$$

© ISAROB 2013

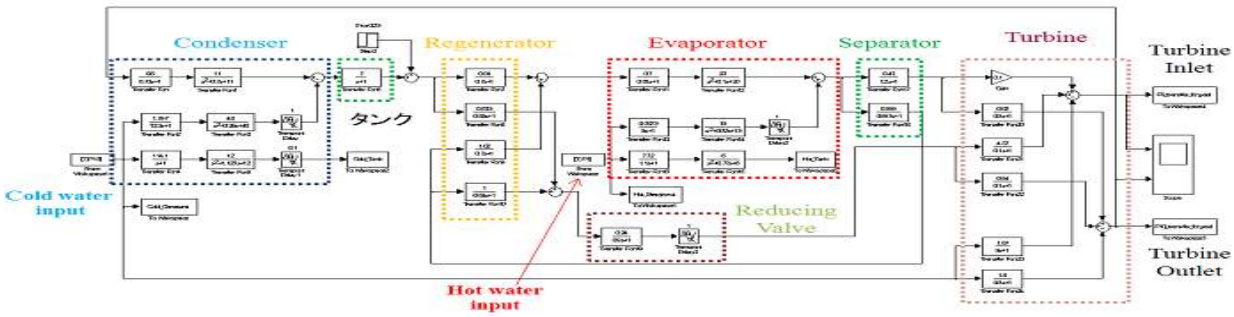

Fig.1. Block diagram of whole system

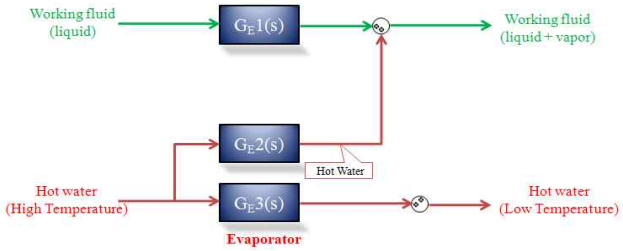

Fig.2. Block diagram of the Evaporator

In order to verify the transfer function models, the outputs from the evaporator of transfer function model are compared with the real data measured from the experimental plant. The simulation results are shown in Fig.3, Fig4respectively.

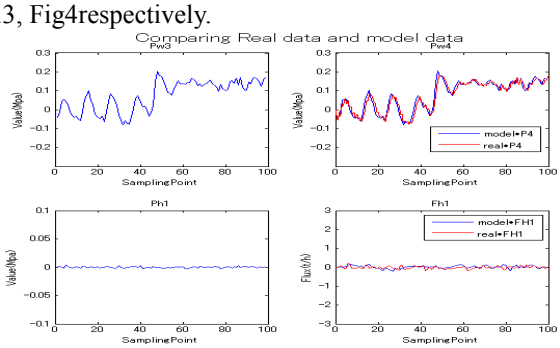

Fig.3. Input of working fluid, and outputs of hot water and working fluid for evaporator

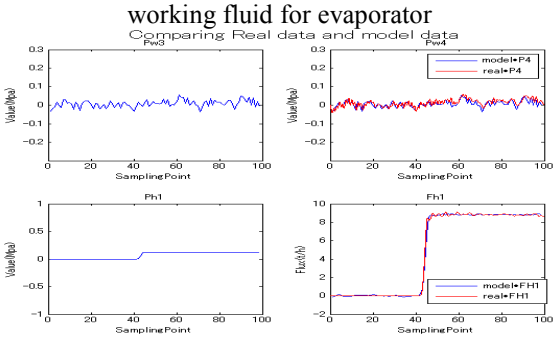

Fig.4. Input of hot water, and outputs of hot water and working fluid for evaporator

3) Transfer function models for additional components

A condenser, separator, regenerator, turbine part (turbine and absorb), reducing valve, and working fluid pump are modeled[1].

4) Deduction of total transfer function model for two inputs- two outputs system

For the total system, two inputs-two outputs transfer functions model that is regarded revolutions per minute of hot and cold water pump as manipulated values is modeled by using each of components of transfer function models. Fig.5 shows the block diagram of two inputs-two outputs transfer function model.

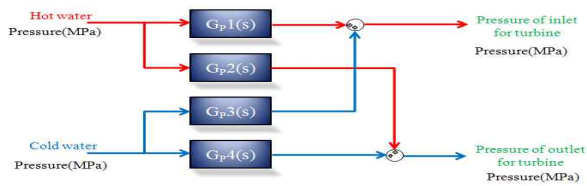

Fig.5. Transfer function model of two inputs two outputs

2.3Reduced order model

Obtained the transfer function models have a high order. In this paper, two inputs-two outputs transfer function model is represented as follows.

$$Gp11(s)=\frac{-0.002411s^3+0.004986s^2-0.003498s+0.001086}{s^4+0.6342s^3+0.3208s^2+0.05245s+0.002724}$$

$$Gp12(s)=\frac{0.1791s^3+0.08403s^2+0.02325s+0.004264}{s^4+0.4987s^3+0.2156s^2+0.02792s+0.00116}$$

$$Gp21(s)=\frac{-0.0005017s^3+0.001038s^2-0.0007492s+0.0002311}{s^4+0.6331s^3+0.319s^2+0.05208s+0.002703}$$

$$Gp22(s)=\frac{0.188s^3+0.07508s^2+0.02937s+0.001672}{s^4+0.4868s^3+0.2062s^2+0.02276s+0.0007496} \quad (4)$$

The simulation results of the reduced transfer functions are compared with transfer functions that are calculated by connection of the overall transfer functions as shown in Fig.6 and Fig.7, respectively.

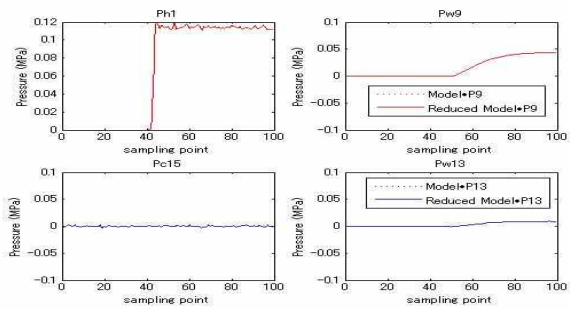

Fig.6. Input of cold water, outputs of working fluid, and cold water for condenser

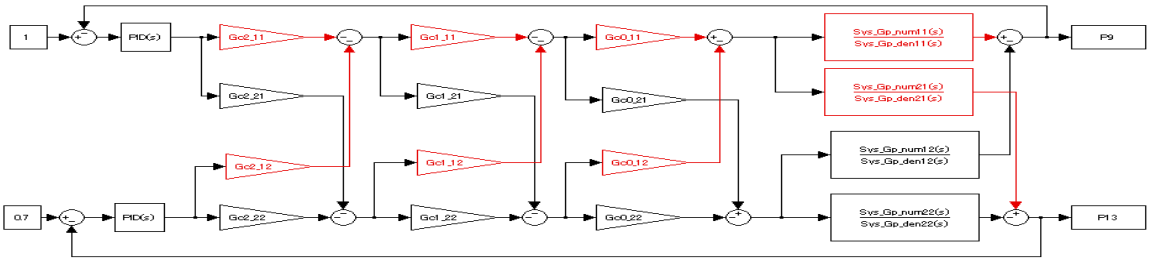

Fig.11. Block diagram of Decouple PID control system

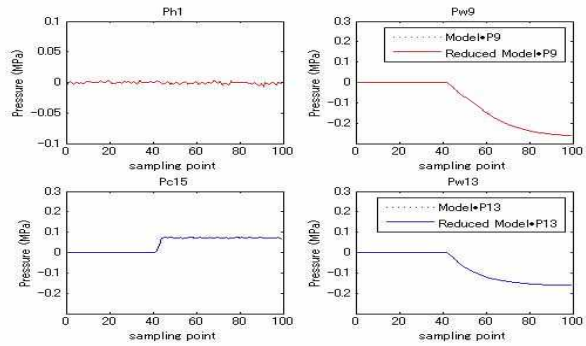

Fig.7. Input of cold water, outputs of working fluid, and cold water for condenser

3 MUITI-STAGECONNECTED NON-INTERACTING PRE-COMPENSATOR

3.1Pre-compensator based on generalized pseudo digonalization method and diagonal dominance

For the transfer function matrix *Gp(s)*, if G_{c0} is expressed by Eq.(5), there is no interaction each other in frequency region at nearby *s=0* from *G(0) = Gp(0)*G_{c0}*=I*[2].

$$G_{c0} = Gp(0)^{-1} = \begin{bmatrix} 3.8813 & -6.3958 \\ 0.1488 & -0.6936 \end{bmatrix} \quad (5)$$

The inverse nyquist array and the gershgorin bands of the system *G(s)=Gp(s)*G_{c0} are shown in Fig.8.

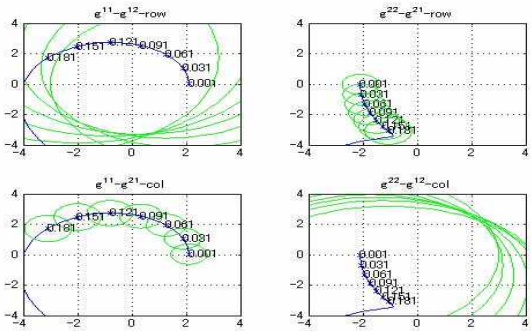

Fig.8. Inverse nyquist array, gershgorin band of *Gp(s)* G_{c0}

A pre-compensator $G_{c1}$is designed at *w*= 0.241 because the origin is included in a large number of gershgorin bands.

$$G_{c1} = \begin{bmatrix} -0.9998 & -0.9903 \\ -0.0222 & -0.1386 \end{bmatrix} \quad (6)$$

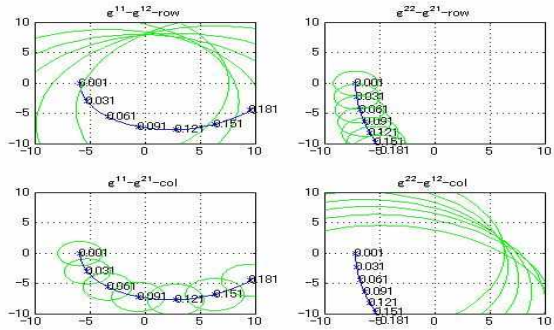

Fig.9. Inverse nyquist array and gershgorin bands by Gc_1

The origin is still included in the gershgorin bands as shown Fig.9 so that the multi-stage connection is considered [3].

3.2Multi-stage connection of Non-interacting pre-compensators

New pre-compensators G_{c1}, G_{c2} are designed to remove the interaction by using the multi-stage connection method and they are connected to three-stage series. Where G_{c1}, G_{c2} are designed at *w*= 0.241, *w*= 0.211, respectively.
The pre-compensators are calculated as

$$G_c(s) = G_{c0} \times G_{c1} \times G_{c2} = \begin{bmatrix} 2.9742 & -0.1376 \\ 0.0482 & -0.2590 \end{bmatrix} \quad (7)$$

The inverse nyquist array and the gershgorin bands are shown in Fig.10.

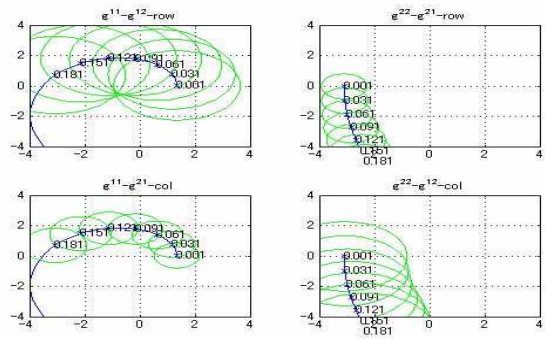

Fig.10. Inverse Nyquist array and Gershgorin band by $G_{c0}G_{c1}$ Gc_2

The gershgorin bands do not include the origin any longer, so the diagonal column dominace is realized by 3-stage series connection.

© ISAROB 2013

4DESIGN OF DECOUPLE PID CONTROL SYSTEM

The goal of this control system is to design a controller to make the pressure difference between the inlet and outlet of turbine by 0.3[MPa]. The decouple PID control system of two inputs-two outputs system which controls the pressure at inlet-outlet for the turbine was designed by using pre-compensators as shown Fig.11.

4.1Design of PID control system

For the controlled system $G_p(s)$, PID parameters are designed by using the ultimate sensitivity method. The PID parameters and the result of PID control are shown in Table1and Fig.12, respectively.

Table1.PID Parameters

	Hot water pump	***Cold water pump***
K_p	5.136	-120
T_i	16.2	0.261
T_d	4.05	0.065

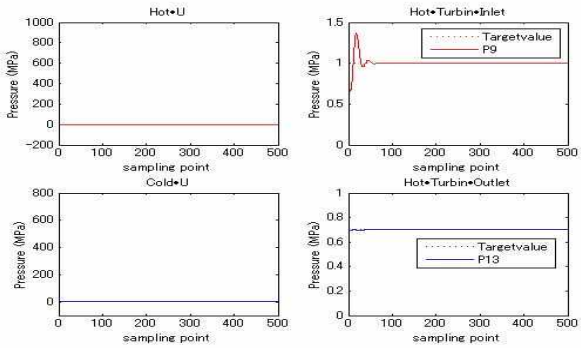

Fig.12. Result of PID control

4.2Design of Decouple PID control system

When the non-interacting pre-compensator *Gc* is used by three pre-compensator, the PID parameters of the decoupling control system are shown in Table2.

Table2.PID Parameters

	Hot water pump	***Cold water pump***
K_p	2.11	600
T_i	15.87	14.15
T_d	3.97	3.54

The modified PID parameters by trial and error and the result of the decoupling PID control system are shown in Table3 and Fig.13, respectively.

Table3.Modified PID Parameters

	Hot water pump	***Cold water pump***
K_p	0.0071	0.845
T_i	0.1914	22.54
T_d	1.3945	0.012

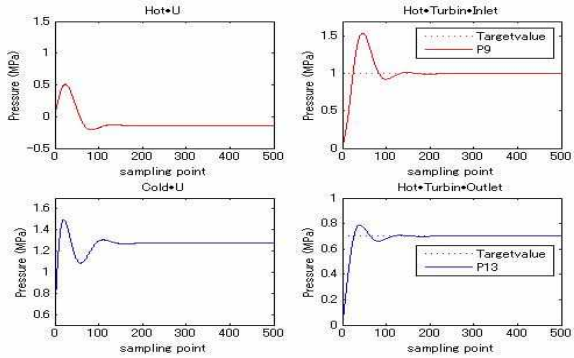

Fig.13. Result of decouple PID control

The control performance is improved by using 3-stage series connection of pre-compensators.

5CONCLUSION

The transfer function models of each of components for a compact binary power generation pilot plant using low-temperature difference thermal energy were built and they were integrated into the whole system. The reduced order transfer function model of two inputs-two outputs system which controls the pressure at inlet-outlet for the turbine was built, and the decoupling PID control system was designed. Also, the effectiveness of the transfer function models and the decoupling PID control system was confirmed through the simulation.

REFERENCES

[1] K-Y Han, ARITA M, H-H Lee, "Decoupling PID control System for Power Generation by Low-Temperature Difference", International conference on Humanized systems, pp.306-311,2012.

[2] H-H Lee, W-K Choi, J-Y Song, S-G Lee, Akizuki K, Noninteracting PID Control of a Fluid Temperature and Liquid Level Interacting System, Trans. IEE of Japan, vol.119-C. no.8/9, pp.1035-1041,1999.

[3] H-H Lee, Nagamachi M, W-K Choi, J-Y Song, Miyazaki M, Akizuki K, Noninteracting Multi-Stage Noninteracting PID Control by Pre compensators with Series-Parallel Connection, Trans. IEE of Japan, vol.123,no.1, pp.43-49,2003.

© ISAROB 2013

Decouple Sliding Mode Control of Compact Binary Power Generation

Kun-Young Han[1], Hee-Hyol Lee

Graduate School of Information, Production and Systems, Waseda University, Japan
(Tel: 81-93-692-5164, Fax: 81-93-692-5164)

[1]kyhan@akane.waseda.jp

Abstract: This paper presents a Decouple Sliding Mode Control(DSMC) of a compact binary power generation using low-temperature difference thermal energy. First, a state equation model based on the transfer function model is deduced. Then, a Sliding Mode Control system with decoupler is designed to control the pressure difference between inlet and outlet of a turbine by high pressure steam of working fluid. The validity of the proposed model is confirmed by a comparison between simulation and experimental result and the control simulation results show the effectiveness of the decouple Sliding Mode Control.

Keywords: power generation, low temperature thermal energy, optimum servo system, decoupling control, sliding mode control(SMC), decoupling Sliding Mode control(DSMC)

1 INTRODUCTION

A compact binary power generation uses the temperature differential between hot and cold waters to produce electric power. In the closed cycle concept, a secondary working fluid(e.g., ammonia or Hydro-chlorofluoro-carbon) is vaporized and recondensed in a closed loop to drive a turbine. The working fluid is vaporized by hot water that is pumped by hot water pump and passed through heat exchangers. This working fluid expands, emerging as a high pressure steam which derives a turbine. The vapor is condensed by passing it through a second set of heat exchangers containing cold water pumped by cold water pump.

The compact binary power generation is an effective method of power generation, which has small impact on environment and can be semi-permanently utilized. Therefore, if the power generation using enormous thermal energy is commercialized it is expected that huge change can be brought to energy supply. However, compared with the thermal power generation using fossils or nuclear energy, whose temperature difference between heat source and cooling source is very low. Also, this kind of the system controlled variables and manipulated variables interact on each other in general.Therefore, for an efficiency and stable operation of the compact binary power generation plant, a robust control system that is suitable for the environmental factor or disturbance is required[1].

In our recent study, a transfer function model and a control system of the compact binary power generation was developed to control the pilot plant in frequency domain.This paper deals with a modeling and designing control system in time domain. A state equation model based on a transfer function model is developed and a Decouple Sliding Model Control system is also designed to control the pressure difference between the inlet and outlet of turbine to keep 0.3[Mpa] by the high pressure steam of working fluid. The simulation model is compared experimental data that measured from the compact binary power generation pilot plant and the control simulation results show the effectiveness of the DSMC.

2MODELING OF COMPACT BYNARY POWER GENERATION SYSTEM

The schematic diagram of the compact binary power generation pilot plant using low temperature difference thermal energy is illustrated in Fig.1. A feature of this pilot plant uses ammonia/water mixed working fluid.

2.1Experiment Conditions

- Hot water pump: 60[Hz], Cold water pump: 60[Hz], Working fluid pump: 70[Hz].
- Sampling period: 3 [sec], measured data: 100 samples.
- These data was measured under a steady sate of compact binary power generation pilot plant

2.2two inputs-two outputs system state equation model

In our previous study[2], the transfer function model is already drawn as shown Eq.(1). It was modeled by using approximated method using 1st and 2nd order time delay transfer function.

© ISAROB 2013

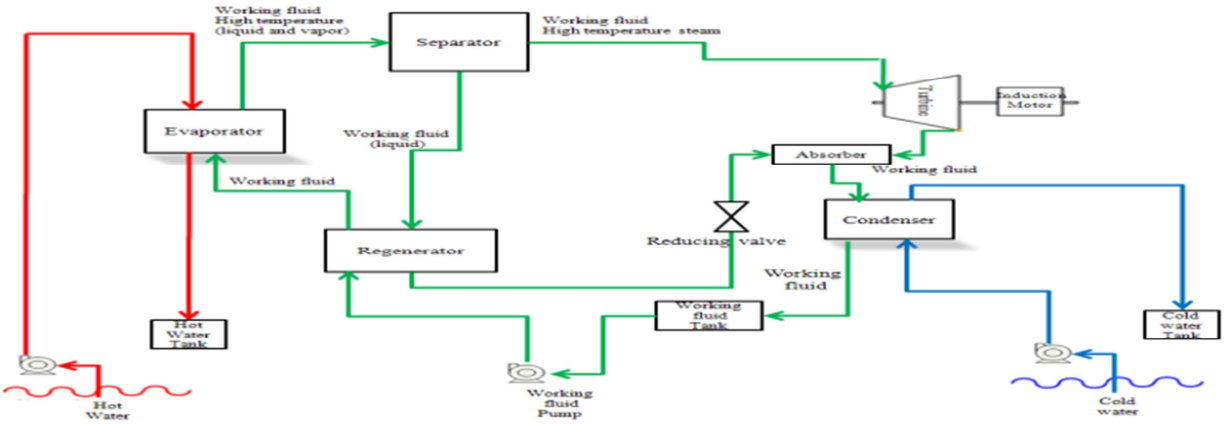

Fig.1. Schematic diagram of compact binary power generation system

$$\begin{bmatrix} y_1 \\ y_2 \end{bmatrix} = \begin{bmatrix} \dfrac{0.0435}{5s^3+1.5s^2+5.1s+1}e^{-0.01s} & -\dfrac{1.6}{11s^3+1.99s^2+11.09s+1}e^{-s} \\ \dfrac{0.01}{9.8s^3+1.98s^2+1.08s+0.1}e^{-0.5s} & -\dfrac{1.9}{15s^3+1.15s^2+15.01s+1}e^{-s} \end{bmatrix} \begin{bmatrix} u_h \\ u_c \end{bmatrix} \tag{1}$$

Where, y_1, y_2 are the pressure of inlet and outlet of turbine and u_h, u_c are the manipulated value of hot and cold water respectively. In this paper, a state equation model based on two inputs-two outputs transfer function model is drawn by using matlab as shown in Eq(2).

The simulation results of the state equation model are compared as shown in Fig.3, Fig.4, respectively.

$$A = \begin{bmatrix} -0.463 & -1.2481 & 0.3076 \\ 0.9677 & 0.4546 & 0.0315 \\ -0.0095 & -0.0012 & -0.0639 \end{bmatrix}, \quad B = \begin{bmatrix} -0.0009 & -0.3899 \\ 0.0025 & 0.1181 \\ 0.0081 & -0.1584 \end{bmatrix}$$

$$C = \begin{bmatrix} -0.0713 & -0.0655 & 0.7009 \\ -0.3024 & -0.2924 & 0.8361 \end{bmatrix}, \quad D = \begin{bmatrix} 0 & 0 \\ 0 & 0 \end{bmatrix} \tag{2}$$

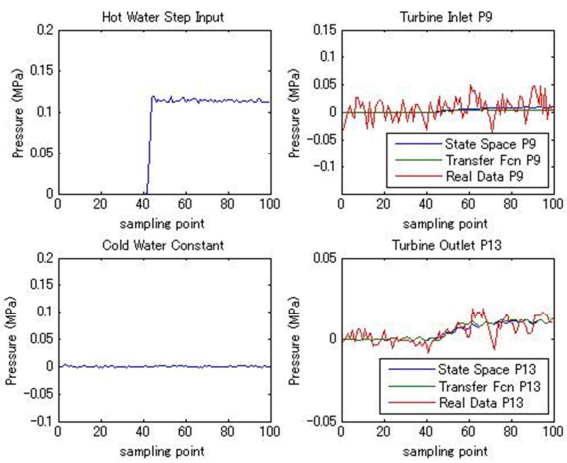

Fig.2. Input of hot water, outputs of inlet of turbine

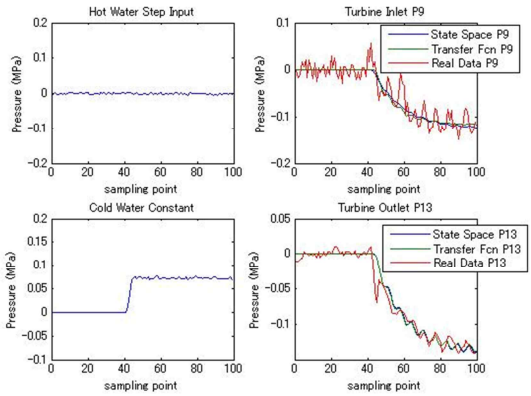

Fig.3. Input of cold water, outputs of inlet of turbine

3DECOUPLE SLIDING MODE CONTROL

Sliding Mode control is a robust control scheme based on the concept of changing with structures states of the system in order to obtain a desired response[3]. The biggest advantage of SMC is its robustness to variation in parameters, external disturbance and modeling errors, therefore, SMC with a decoupler is designed in this study.

3.1EquivalentControlSystem&Switching Hyper PlaneDesign

Let us consider as follows system,

$$\frac{d}{dt}\mathbf{x}(t) = (\mathbf{A} - \mathbf{B}\,\mathbf{F})\,\mathbf{x}(t) + \mathbf{B}\,\mathbf{G}\,\mathbf{u}(t)) \tag{3}$$
$$\mathbf{y}(t) = \mathbf{C}\,\mathbf{x}(t)$$

where, $\mathbf{x} \in R^3, \mathbf{u} \in R^2, \mathbf{y} \in R^2$

The error and switching hyper plane is defined as Eq.(4).

$$\mathbf{e}(t) \equiv \mathbf{r}(t) - \mathbf{y}(t)$$
$$\boldsymbol{\psi}_1 \equiv S_1\mathbf{e} + S_2\int \mathbf{e}dt \tag{4}$$

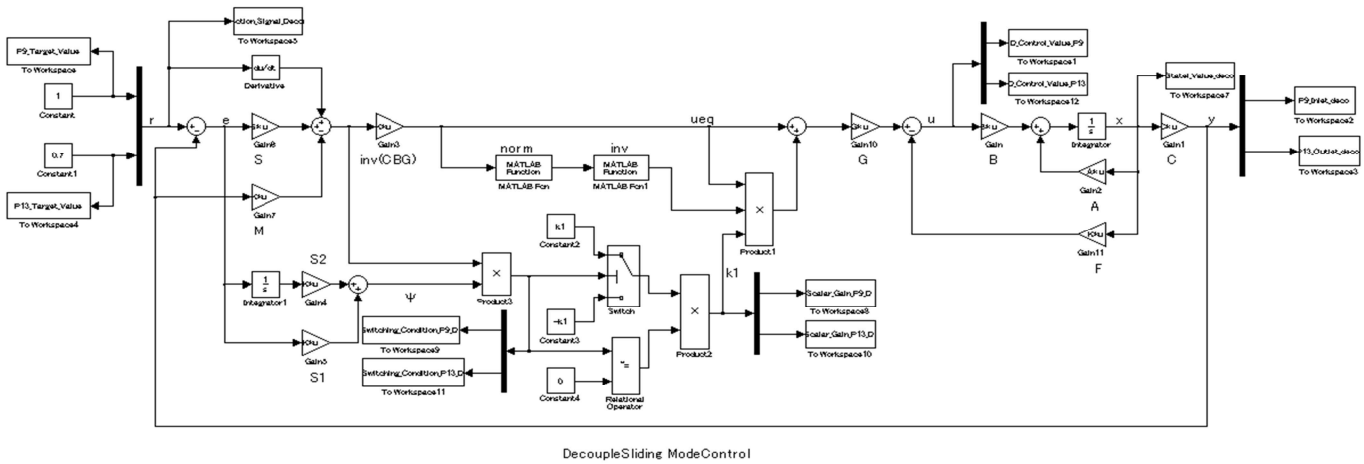

Fig.4. Block diagram of DSMC

When the state is restricted on a hyperplane, the equivalent control input U_{eq} can be obtained by Eq.(5) when $|S_1| \neq 0$,

$$\mathbf{CBGu}_{eq} = S_1^{-1} S_2 \mathbf{e} + \dot{\mathbf{r}}(\mathbf{A} - \mathbf{BF})\mathbf{x} \tag{5}$$

Also, the equivalent control input is obtained by Eq.(6) when *CBG* is nonsingular matrix.

$$\mathbf{u}_{eq} = (\mathbf{CBG})^{-1}(S_1^{-1} S_2 \mathbf{e} + \dot{\mathbf{r}} - \mathbf{My}) \quad (\mathbf{r} = \mathbf{m}) \tag{6}$$

Where, *M* satisfy,

$$\mathbf{C}(\mathbf{A} - \mathbf{BF}) = \mathbf{MC} \tag{7}$$

Eq.(7) may be rearranged as Eq.(8) by multiplying the transpose matrix of *C*.

$$\mathbf{M} = \mathbf{C}(\mathbf{A} - \mathbf{BF})\mathbf{C}'(\mathbf{CC}')^{-1} \tag{8}$$

In this paper, matrix *M* is obtained as Eq.(9).

$$\mathbf{M} = \begin{bmatrix} 0.2194\times10^{-16} & 0.4922\times10^{-16} \\ 0.1935\times10^{-16} & 0.1332\times10^{-16} \end{bmatrix} \tag{9}$$

Substituting for U_{eq} from Eq.(6) into Eq.(4) gives

$$\dot{\mathbf{e}} = S_1^{-1} S_2 \mathbf{e} \tag{10}$$

where, let $S_1 = I, S_2 = S$, then

$$\dot{\mathbf{e}} = -S\mathbf{e} \tag{11}$$

A Switching matrix *S* can be designed by setting an arbitrary eigenvalues.

3.2Sliding Mode Controller Design

Sliding mode controller is designed by using eventually hierarchy control law for the state of system to reach to switching hyper plane from arbitrary initial state x_0.

Let us define the Lyapunov function **V** with respect to Ψ_1 as Eq.(12),

$$\mathbf{V} \equiv \frac{1}{2}\boldsymbol{\psi}_1^T \boldsymbol{\psi}_1 \tag{12}$$

the condition of derivative time $\dot{\mathbf{V}}$ of the **V** is then given by Eq.(13),

$$\dot{\mathbf{V}} < 0 \tag{13}$$

This condition result in $\boldsymbol{\Psi}_1$ belong to the switching hyper plane.

Derivative time $\dot{\mathbf{V}}$ is rewritten as Eq.(14),

$$\dot{\mathbf{V}} = \boldsymbol{\psi}_1^T \dot{\boldsymbol{\Psi}}_1 = \boldsymbol{\Psi}_1^t (S\mathbf{e} + \dot{\mathbf{r}} - \mathbf{My}) - \boldsymbol{\Psi}_1^T \mathbf{CBu} \tag{14}$$

where, eventually hierarchy control input *u*, the equivalent control input as a linear control term, the unit input as a nonlinear control input and $k_1$as scalar gain is defined as Eq.(15),

$$\mathbf{u} \equiv \mathbf{u}_{eq} + k_1 \frac{\mathbf{u}_{eq}}{\|\mathbf{u}_{eq}\|} \tag{15}$$

where, $\|\bullet\|$ is norm.

Substituting Eq.(15) into Eq.(14), $\dot{\mathbf{V}}$ is rewritten as Eq.(16),

$$\begin{aligned} \dot{\mathbf{V}} &= \boldsymbol{\psi}_1^T (S\mathbf{e} + \dot{\mathbf{r}} - \mathbf{My}) - \boldsymbol{\psi}_1^T \mathbf{CBG}(\mathbf{U}_{eq} + k_1 \frac{\mathbf{u}_{eq}}{\|\mathbf{u}_{eq}\|} \\ &= k_1 \frac{\boldsymbol{\Psi}_1^T \mathbf{CBGu}_{eq}}{\|\mathbf{u}_{eq}\|} \end{aligned} \tag{16}$$

© ISAROB 2013

Hence, the switching condition scalar gain k_1 is obtained as Eq.(17).

$$k_1 \underset{>}{\overset{\leq}{}} 0: \quad if \ \mathbf{\Psi}_1^T \mathbf{CBGu}_{eq} \underset{>}{\overset{\leq}{}} 0 \tag{17}$$

3.3DSMC Control Simulation Result

A simulation is carried out using MATALB to verify the performance of the designed DSMC as shown in Fig.4.The results of DSMC are compared with SMC. In this paper, S_2, K_1 is configured 1000, 0.01 respectively. The goal of this control system is to make maintain the pressure difference between the inlet and outlet of turbine by 0.3[Mpa].

Fig.5 shows the comparative result of outputs.

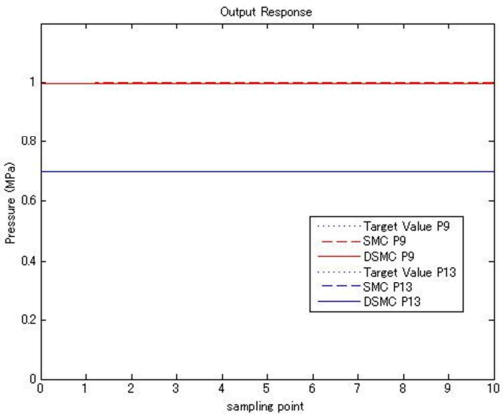

Fig.5. The result of outputs

Fig.6 shows the comparative result of control value.

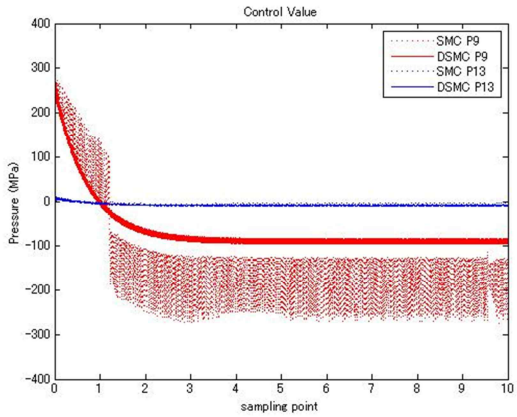

Fig.6. The result of control value

Fig.7 shows the comparative result of switching conditions.

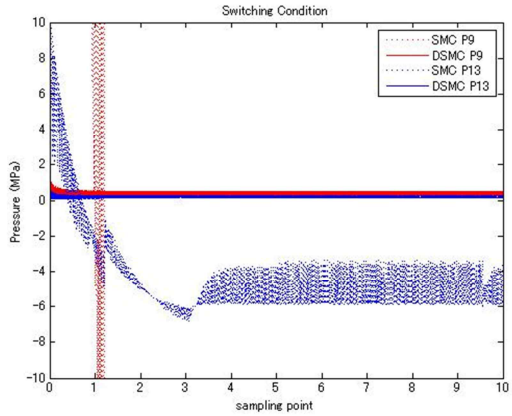

Fig.7. The result of switching condition

Fig.8 shows the comparative result of outputs of k_1.

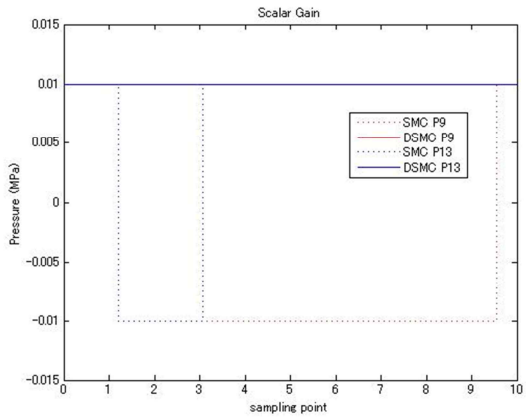

Fig.8. The result of k_1

4CONCLUSION

The state equation for two inputs-two outputs for a compact power generation pilot plant using low temperature difference is drawn. DSMC is designed to control the pressure at inlet-outlet of the turbine.

Also, the validity of the state equation model and the effectiveness of decoupler are confirmed through the simulation.

REFERENCES

[1] Kun-Young Han,Hee-Hyol Lee, "Neuro PID control of power generation using a low temperature gap", Artificial Life and Robotics, Vol.16.No.2,pp.178-184,2011.

[2] K-YHan, ARITAM,H-HLee,"Decoupling PID control System for Power Generation by Low-Temperature Difference", International conference on Humanized systems,pp.306-311,2012.

[3] H-HLee, SHOJI.F, TSURUOKAH, MIYAZAKI M, AKIZUKI K,"Frequency-ShapedSliding Mode Control Using Output Feedback and Application to Follow-up Control of Process System" ,SICE, vol.38,no.2, pp.186-192,2002.

The Eighteenth International Symposium on Artificial Life and Robotics 2013 (AROB 18th '13),
Daejeon Convention Center, Daejeon, Korea, January 30-February 1, 2013

Diffusion model analysis of OneMax problem

QingLian Ma[1], Kiminobu Koga[2], Kunihito Yamamori[3], Makoto Sakamoto[3], Hiroshi Furutani[3], and Yu-an Zhang[4]

[1] Interdisciplinary Graduate School of Agriculture and Engineering, University of Miyazaki, Japan
[2] Graduate School of Engineering, University of Miyazaki, Japan
[3] Faculty of Engineering, University of Miyazaki, Japan
[4] Department of Computer Science and Technology, Qinghai University, China

e-mail: furutani@cs.miyazaki-u.ac.jp

Abstract: A mathematical study is carried out for Genetic Algorithm (GA) on OneMax function within the framework of diffusion model. By using a partial differential equation, we obtain a distribution of the first order schema frequency. We consider the probability that a population includes the optimum solution by applying Markov chain model. We call this probability as the success probability of GA. Effects of mutation on the success probability were studied analytically and experimentally.

Keywords: genetic algorithms, schema theory , OneMax problem, Wrihgt-Fisher model, diffusion model

1 INTRODUCTION

Genetic algorithms are stochastic optimization techniques that simulate the biological evolution. We have studied the effects of stochastic fluctuation in the process of GA evolution. In the analysis, we applied the Wright-Fisher model and the diffusion model. In the diffusion model, we derived an analytical expression of the distribution of the first order schema frequency.

In the previous work, we showed that GA on the OneMax problem is equivalent to the asymmetric mutation, and proposed the method to predict the convergence time of OneMax GA [1, 2]. This paper treats the method for calculating the probability that a population includes the optimum solution, which we call the success probability.

In general, mutation plays an important role in computation of GAs. This paper reports the comparison of numerical experiments and the theoretical calculations. We found that mutation is a very important factor determining the work of stochastic fluctuation.

2 MATHEMATICAL MODEL

We treat the evolution process of a population with N individuals. The individuals are represented by binary strings of length ℓ, and there are $n = 2^\ell$ genotypes,

$$i =< i(\ell), \cdots, i(1) >, \quad i(k) \in \{0, 1\}.$$

We use the relative frequency $x_i(t)$ for describing the evolution

$$x_i(t) = N_i(t)/N,$$

where $N_i(t)$ is the number of individuals of genotype i at generation t.

The process of fitness proportionate selection is

$$x_i(t+1) = f_i x_i(t)/\bar{f}(t), \tag{1}$$

where $\bar{f}(t)$ is the average fitness of the population at generation t

$$\bar{f}(t) = \sum_{i=0}^{n-1} f_i\, x_i(t). \tag{2}$$

The OneMax fitness function f_i is defined as

$$f_i = \sum_{k=1}^{\ell} i(k). \tag{3}$$

Thus the string of all ones $< 1, 1, \ldots, 1 >$ is the optimum solution of this function.

2.1 Linkage Equilibrium

We derive here the evolution equation for the first order schema frequency. To do this, we introduce the notion of linkage equilibrium. Linkage means the correlation between the different loci in a chromosome, and if there is some correlation we call this state as linkage disequilibrium [3]. Crossover and mutation have the effect of making the population in linkage equilibrium.

The distribution of a population in linkage equilibrium is given by

$$x_i(t) = \prod_{k=1}^{\ell} h_{i(k)}(t), \tag{4}$$

where $h_{i(k)}(t)$ is a frequency of the first order schema at position k, and $i =< i(\ell), \ldots, i(1) >$. We also use the notation of $h_0^{(k)}$ and $h_1^{(k)}$ for the first order schema frequencies of bit 0 and bit 1, respectively.

© ISAROB 2013

2.2 Evolution Equation of the First Order Schema

In the deterministic schema theory, the evolution of the first order schema in linkage equilibrium is given by [4, 5]. The relative frequency of the first order schema at position k is determined by

$$h_1^{(k)}(t+1) = a h_1^{(k)}(t) + b, \tag{5}$$

where constants a and b are

$$a = (1 - \frac{1}{\ell})(1 - 2\mu), \quad b = \frac{1}{\ell}(1 - 2\mu) + \mu.$$

The solution is given in terms of a,

$$b_0 = 1 - \frac{\mu}{2\mu + (1 - 2\mu)/\ell},$$

and the initial value $h_1(0)$

$$h_1(t) = a^t \{h_1(0) - b_0\} + b_0. \tag{6}$$

Since $a < 1$, this solution converges to

$$t \to \infty \quad h_1(t) \to b_0.$$

3 MARKOV MODEL

3.1 Wright-Fisher Model

The stochastic model like Markov model explicitly treats the number of schemata. We consider the frequencies of two alleles at some locus. Two alleles are denoted by A and a, and the number of individuals having allele A and a are N_0 and N_1, respectively. Since $N = N_0 + N_1$ is constant, we consider N_1 in this analysis.

The probability $Q(j|i)$ that $N_1 = i$ at generation t becomes $N_1 = j$ at generation $t+1$ is given by the binomial distribution.

The probability $q_i(t)$ of $N_1 = i$ at generation t obeys the evolution equation

$$q_j(t+1) = \sum_{i=0}^{N} Q(j|i)\, q_i(t). \tag{7}$$

This equation is represented by using $(N+1)$-dimensional vector $\mathbf{q}(t)$

$$\mathbf{q}(t) = (q_0(t), \ldots, q_N(t))^T,$$

where T is transversion, and the matrix $Q = [Q(j|i)]$

$$\mathbf{q}(t+1) = Q\, \mathbf{q}(t), . \tag{8}$$

This model is called as the Wright-Fisher model[3].

Next, we derive the transition matrix on the OneMax fitness. Replacing

$$h_1(t) \to i/N$$

in the evolution equation of the first order schema (5), we have the transition matrix

$$\begin{aligned} Q(j|i) &= \binom{N}{j} u(y)^j \{1 - u(y)\}^{N-j}, \\ u(y) &= ay + b = a\frac{i}{N} + b, \end{aligned} \tag{9}$$

where $y = i/N$.

3.2 Diffusion Model

In genetics, the approximation of Markov model by the diffusion equation is used frequently [3, 6], and we have derived the diffusion approximation for OneMax problem [4].

Using two functions of y

$$M(y) = (a-1)y + b, \quad V(y) = u(y)\{1 - u(y)\}/N,$$

the diffusion approximation of Markov process in OneMax problem is given by

$$\frac{\partial \phi(y,t)}{\partial t} = \frac{1}{2}\frac{\partial^2}{\partial y^2}\{V(y)\phi(y,t)\} - \frac{\partial}{\partial y}\{M(y)\phi(y,t)\}. \tag{10}$$

The function $\phi(y,t)$ stands for the probability density function of the relative frequency y at time t.

We derive the solution of Kolmogorov forward equation (10). Approaching $t \to \infty$, $\phi(y,t)$ converges to the stationary solution $\psi(y)$. At this, $\partial\phi(y,t)/\partial t = 0$, and $\psi(y)$ satisfies

$$\frac{\mathrm{d}^2}{\mathrm{d}y^2}\{V(y)\psi(y)\} - 2\frac{\mathrm{d}}{\mathrm{d}y}\{M(y)\psi(y)\} = 0.$$

The solution is

$$\psi(y) = \frac{C}{V(y)} \exp\left\{2\int^y \frac{M(x)}{V(x)}\mathrm{d}x\right\}, \tag{11}$$

where C is the normalization constant.

$$\int_0^1 \psi(y)\,\mathrm{d}y = 1.$$

By integrating this equation, we have

$$\psi(y) = C\,(ay+b)^{2c_1-1}\,(1 - ay - b)^{2c_2-1} \tag{12}$$

where C is a normalization constant, and c_1 and c_2 are

$$c_1 = Nb/a^2, \quad c_2 = N(1-a-b)/a^2.$$

3.3 Success Probability

In condition of mutation existing, the GA becomes an ergodic Markov chain, and it drifts among all of placement states of population. Therefore, if there is enough time, it can get the transition state which contain optimum solution. We discuss the convergence between stationary distribution and stationary state by ergodic Markov chain. In other words, we

© ISAROB 2013

repeat the same calculation with different random numbers and examine distribution state of convergence.

Now we consider some partial bit string from l bit to $\ell - 1$ bite. The string in which all bits are $1, < 1, 1, \ldots, 1, 1 >$, has $\ell - 1$ bit partial optimum solution.

In population, partial string of length is X_ℓ, the probability of having j units of optimum solution is expressed by

$$S_j^{(\ell)} = \Pr\{X_\ell = j\}. \tag{13}$$

We have defined success probability and failure probability before, it can be calculated

$$S = \sum_{j=1}^{N} S_j^{(L)}, \quad F = S_0^{(L)}. \tag{14}$$

For obtain S and F, it is necessary to solve $S_j^{(\ell)}$.

$S_j^{(\ell)}$ can be calculated by regression, the initial condition is

$$S_j^{(1)} = \pi_j^{(1)}, \quad (0 \le j \le N). \tag{15}$$

when the number of $\ell - 1$ bit partial optimum solution is i, in the string length X_ℓ, the probability of having j units of optimum solution is

$$Q_{i,j}^{(\ell)} = \Pr X_\ell = j | X_{\ell-1} = i. \tag{16}$$

Transition probability $Q_{i,j}^{(\ell)}$ use the distribution of first order schemata in the ℓth bit,

1. if $j > i$

$$Q_{i,j}^{(\ell)} = 0, \tag{17}$$

2. if $j \le i$

$$Q_{I,J}^{(\ell)} = \sum_{m=j}^{N-i+j} \binom{N}{m}^{-1} \binom{i}{j} \binom{N-i}{m-j} \pi_m^{(\ell)}. \tag{18}$$

The probability $S_j^{(\ell)}$ of having j units of ℓ- bit partial optimum solution can be calculated by this equation

$$S_j^{(\ell)} = \sum_{i=0}^{N} S_i^{(\ell-1)} Q_{i,j}^{(\ell)}. \tag{19}$$

4 NUMERICAL EXPERIMENT

In this section, we compare results of the theoretical prediction with GA experiments. We use the fitness proportionate selection and uniform crossover. The length of string is $L = 20$, and population size $N = 100$. We performed 10000 runs for each parameter set, and averaged over them. The success probability S of the GA is calculated by summing the number of run, where the optimum solution appears in the population, and deviding it by 10000.

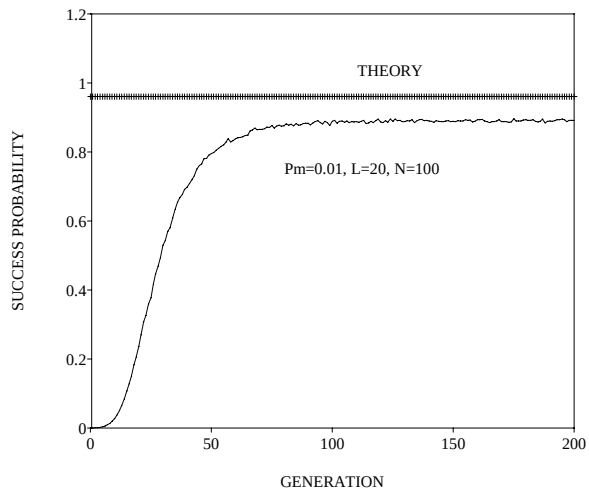

Fig. 1. Generation dependence of the success probability S with $L = 20$, $N = 100$ and $p_m = 0.01$. The thin line is the result of the GA calculation. The thick line is the theoretical prediction.

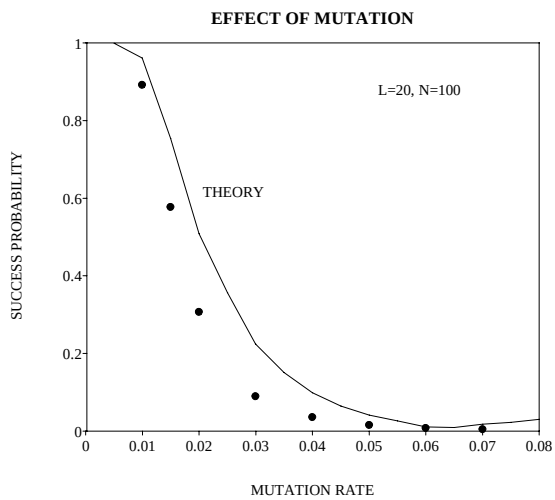

Fig. 2. Dependence of the success probability S on the mutation rate p_m. Calculation with $N = 100$ and $L = 20$. The solid line shows the theoretical prediction, and black circles are GA calculations.

© ISAROB 2013

Figure 1 shows the time dependence of the success probability S. The thin line is the result of GA calculation. The thick line is the theoretical prediction, which slightly overestimates the numerical calculation.

Figure 2 is the mutation rate p_m dependence of the success probability S. We observe that the theoretical prediction can reproduce the p_m dependence quite well. It should be noted that the success probability decreases sharply as p_m increases.

5 SUMMARY

In this paper, we demonstrate that the stochastic methods, Wright-Fisher model and its diffusion approximation, can reproduce the success probability S of GA on the OneMax function. Our next aim is to predict the first-appearing time T of the optimum solution in a population by applying the sotochastic methods used in this study.

REFERENCES

[1] Ma, Q., Zhang, Y., Koga, K., Yamamori, K., Sakamoto, M., and Furutani, H. (2012): Analysis of first order schema for OneMax problem, Proceedings of the 17th International Symposium on Artificial Life and Robotics

[2] W. Y. Tan (2002), *Stochastic Models with Applications to Genetics, Cancers, AIDS and Other Biomedical Systems*, World Scientific, Singapore.

[3] J. W. J. Ewens (2004), *Mathematical Population Genetics. I. Theoretical Introduction*, Second Edition. Springer-Verlag, New York.

[4] H. Furutani, S. Katayama, M. Sakamoto, M. Ito,(2007), Stochastic Analysis of Schema Distribution in a Multiplicative Landscape, Artificial Life and Robotics 11:101–104

[5] H. Furutani (2003), Schema Analysis of OneMax Problem –Evolution Equation for First Order Schemata. in Foundations of Genetic Algorithms 7, Morgan Kaufmann, San Francisco, 9–26

[6] J. F. Crow and M. Kimura (1970), *An Introduction to Population Genetics Theory*, Harper and Row, New York.

© ISAROB 2013

The Eighteenth International Symposium on Artificial Life and Robotics 2013 (AROB 18th '13),
Daejeon Convention Center, Daejeon, Korea, January 30-February 1, 2013

Study of factor IX gene using regional structure

Hiroshi Furutani[1], Kenji Sueyoshi[2], Kenji Aoki[3]
Kunihito Yamamori[1], and Makoto Sakamoto[1]

[1] Faculty of Engineering, University of Miyazaki, Japan
[2] Graduate School of Engineering, University of Miyazaki, Japan
[3] Information Technology Center, University of Miyazaki, Japan

e-mail: furutani@cs.miyazaki-u.ac.jp

Abstract: There have been reported a variety of defects in the factor IX gene, which is responsible for hemophilia B, and these are summarized in the hemophilia B database. We analyzed amino acid changing mutations, or missense mutations in the database described with factor IX activity values. We have carried out several kinds of theoretical studies to predict the effect of a missense mutations in Factor IX gene. In this paper, we report results of the analysis using Support Vector Machine. We applied the method of transfer learning, which uses the knowledge of some domain to predict the properties of other domains. As a training set, we use mutations of one of seven regions, and test the obtained parameters by the prediction of mutations in remaining regions.

Keywords: hemophilia, missense mutation , factor IX, SVM

1 INTRODUCTION

As an advance of genome science, there appear many reports describing the analysis of mutations in genes responsible for diseases. Foe example, the Human Gene Mutation Database includes mutations causing or associated with human inherited disease [1]. However, even in recent days, it has been difficult to characterize a genetic disorder, such as hemophilia, in which affected individuals have various types of mutations. It is a time consuming, laborious and expensive task to distinguish a causative mutation from neutral ones. Therefore, it becomes very important to study mutations in genes responsible for diseases by using computer.

We have applied a multiple regression model to predict the effect of a missense mutation in Factor IX gene of hemoplilia B patient [2]. As an extension of this work, we also carried out the same type of analysis using Support Vector Machine [3].

In this study, we apply the method of transfer learning, which uses the knowledge of some domain to predict the properties of other domains.

Genetic defects in blood coagulation proteins are associated with a bleeding disorder known as hemophilia. There are two types of hemophilia, Hemophilia A and Hemophilia B. Hemophilia B is a hereditary, X-linked, recessive hemorrhagic disorder, caused by various types of mutations in factor IX gene. Factor IX (or Christmas factor) is one of the serine proteases of the coagulation system [4, 5]. Mutation in factor IX is made up of a majority of point mutations. Substitution of amino acid sequence is the most common form of point mutations. In general, substitution in important site and substitution to different character from original amino acid are supposed to drastic decrease in activity of factor IX. There have been reported a variety of defects in the factor IX gene from hemophilia B patients, and these are summarized in the hemophilia B database [6].

We analyzed amino acid changing mutations, or missense mutations in the database described with factor IX activity values. We have introduced distances between 20 amino acids by using the following four physical-chemical properties: molecular volume, hydropathy, polar requirement, and isoelectric point. We carried out an analysis of missense mutations in the database by using SVM. We apply the theory of transfer learning for the analysis of these setting.

2 HEMOPHILIA B DATABASE

We used Hemophila B Mutation Database in this analysis [6]. The latest version of the database is the 13th edition.

There are 2,891 entries in this database, and 34 double mutations and 1 triple mutation are included. Of the 2,891 patients listed, 962 show unique molecular events probably causing the disease. Most of them are point mutations, and the database contains 561 different amino acid substitutions. One hundred and forty-eight residues of factor IX show two or more amino acid substitutions and 99 only one. Among them, the cases of double and triple mutations and female patients were excluded. We adopted 1494 cases as total.

The gene for factor IX contains eight exons and seven introns with an overall size of 33k base pairs[5]. Factor IX is a glycoprotein of 461 amino acids essential for blood coagulation, and made up of seven regions:

© ISAROB 2013

Table 1. Used data in database

Domain	Location	Number of mutants
Signal peptide	-46 to -18	18
Propeptide	-17 to -1	107
Gla	1 to 46	99
EGF(1st)	47 to 84	138
EGF(2nd)	85 to 127	95
Activation	128 to 195	241
Catalytic	196 to 415	795

(a) Signal peptide,

(b) Propeptide,

(c) Gla,

(d) EGF(1st),

(e) EGF(2nd),

(f) Activation,

(g) Catalytic.

Signal peptide and propeptide are removed during biosynthesis, and remaining protein circulates in the blood as a mature factor IX.

Activity of factor IX in a patient's blood depends on a position of the substitution and combination of original and substituting amino acids. Classification of the disease is given by in vitro clotting activity,

(i) Severe hemophilia B: <1 % factor IX

(ii) Moderate hemophilia B: 1 % – 5 % factor IX

(iii) Mild hemophilia B: > 5 % factor IX.

3 METHOD

We define the distance of amino acid. For each amino acid parameter, the distance D_{ij} between amino acid i and j is defined by the next expression,

$$D_{ij} = |f_i - f_j|.$$

Here, f_i and f_j are one of four amino-acid parameter of i and j, respectively.

3.1 Support Vector Machine

Support vector machine (SVM)[7][8] can classify the samples $\boldsymbol{x}_i$ $(i = 1, \cdots, n)$ belonging to unknown class into two classes C_1 or C_2. The classification function $f(\boldsymbol{x})$ is defined as the Equation (1).

$$f(\boldsymbol{x}) = sign\left(g(\boldsymbol{x})\right) = sign(\boldsymbol{w}^t\boldsymbol{x} + b), \tag{1}$$

where $\boldsymbol{w}$ and b are parameters.

Let $\boldsymbol{x}_i$ belong to the class y_i $(= \{1, -1\})$, and if all the samples are correctly classified, Equation (2) will be satisfied.

$$\forall i,\ y_i \cdot \left(\boldsymbol{w}^t\boldsymbol{x}_i + b\right) - 1 \geq 0. \tag{2}$$

When Equation (2) is satisfied, no samples exist between the $H_1 : (\boldsymbol{w}^t\boldsymbol{x} + b) = 1$ and the $H_2 : (\boldsymbol{w}^t\boldsymbol{x} + b) = -1$, and the distance between H_1 and H_2, called as *margin*, becomes $\frac{2}{||\boldsymbol{w}||}$. To obtain the maximum margin, we minimize $\frac{1}{2}||\boldsymbol{w}||^2$. In SVM, it is solved by a Lagrange-multiplier method. To maximize the margin, we rewrite the objective function as Equation (3) in subject to Equation (2),

$$L\left(\boldsymbol{w}, b, \boldsymbol{\alpha}\right) = \frac{1}{2}||\boldsymbol{w}||^2 - \sum_{i=1}^{n} \alpha_i \left[y_i\left(\boldsymbol{w}^t\boldsymbol{x} + b\right) - 1\right]. \tag{3}$$

where $\alpha \geq 0$ denotes Lagrange-multiplier. Partial differentiations of Equation (3) by $\boldsymbol{w}$ and b are substituted for Equation (3), we obtain Equation (4).

$$L(\boldsymbol{\alpha}) = \sum_{i=1}^{n} \alpha_i - \frac{1}{2}\sum_{i,j=1}^{n} \alpha_i\alpha_j y_i y_j \boldsymbol{x}_i^t\boldsymbol{x}_j, \tag{4}$$

in subject to

$$\forall_i,\ \alpha_j \geq 0,\ \sum_{i=1}^{n} \alpha_i y_i = 0. \tag{5}$$

Here we denote α_i to maximize Equation (4) as α_i^*. The sample $\boldsymbol{x}_i$ with $\alpha_i^* > 0$ is called as Support Vector (SV), it exists on H_1 or H_2. The optimum of $\boldsymbol{w}$ denoted as $\boldsymbol{w}^*$ is obtained from the partial differentiations of Equation (3) and α_i^* by Equation (6).

$$\boldsymbol{w}^* = \sum_{i=1}^{n} \alpha^* y_i \boldsymbol{x}_i. \tag{6}$$

The optimum of b denoted as b^* is obtained from the Equation (7) with any $\boldsymbol{x}_s$ $(s \in SV)$.

$$b^* = y_s - \boldsymbol{w}^{*t}\boldsymbol{x}_s. \tag{7}$$

Finally, we obtain the discriminant function of SVM for linearly separable problem as Equation (8).

$$f(\boldsymbol{x}) = sign\left(\sum_{i \in SV} \alpha_i^* y_i \boldsymbol{x}_i^t\boldsymbol{x} + b^*\right). \tag{8}$$

4 NUMERICAL EXPERIMENTS

In this discrimnant analysis, we adoped the software package SVM-Light developed by Joachims [9]. Patients' data are devided into two classes, (i) severe and moderate hemophilia, and (ii) mild hemophilia. We carried out two types of experiments, and compared their results. One is

© ISAROB 2013

the SVM analysis of learning phase in some region A (self-learning). Another is the SVM learning using data of other region B, and applied the obtained parameters to the discrimnant analysis of region A. We showed the results in the form of Reciever Operating Characteristic (ROC) curve.

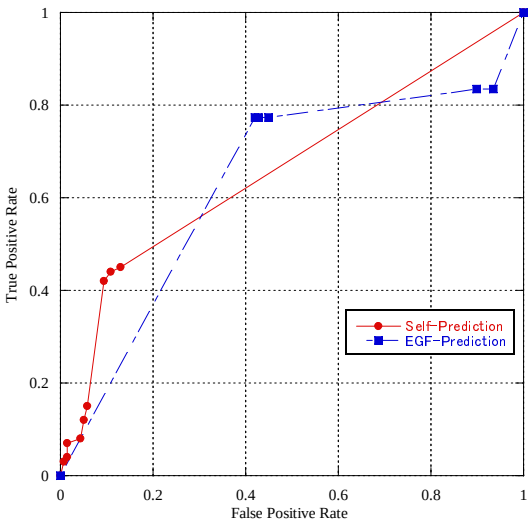

Fig. 1. ROC curves for the discrimination of severity of hemophilia B in EGF region. The solid line shows the SVM result of self-learning in EFF region. The dotted line for SVM learning in ACT region.

Figure 1 shows ROC curves for the discrimination of severity of hemophilia B in EGF region. The solid line shows the SVM result of self-learning. The dotted line shows the ROC curve of EGF data using the parameters obtained by the SVM learning in Activation (ACT) region. Two calculations have almost the same degree of discriminating power of patients' data.

Figure 2 presents two ROC curves in ACT region. The solid line is the results of self-learning, while the dotted line shows SVM learning in EGF region. In this case, the transfer-learning is better than the self-learning.

Figure 3 presents two ROC curves in GLA region. The solid line shows the SVM prediction of self-learning in GLA region. The dotted line is the result of SVM learning in ACT region. This figure presents that the transfer-learning has little power of discrimination.

5 SUMMARY

We applied the method of transfer learning, which uses the knowledge of some domain to predict the properties of other domains. As a training set, we use the clotting activity of mutations in one of seven regions, and test the obtained parameters by the discrimination of mutations in other regions. In some cases, the transfer-learning has the almost the same

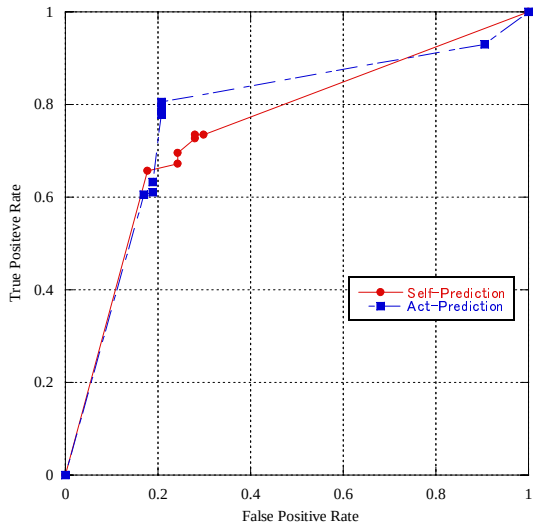

Fig. 2. ROC curves for the discrimination of severity of hemophilia B in ACT region. The solid line shows the SVM result of self-learning in ACT region. The dotted line for SVM learning in EGF region.

power of the discrimination of patients' data. However, there are many cases that the transfer-learning has no power of discrinimination. Thus the next step of this research is to study the mechanism why some transfer-learning has a discrimination power.

REFERENCES

[1] Sternson, P.D., Mort, M., Ball, E. V., Howells, K., Phillips, A.D., Thomas, N.S., Cooper, D.N.: The Human Gene Mutation Database: 2008 update. Genome Medicine, **1:13**, (2009).

[2] Utsunomiya, M., Sakamoto, M., Furutani, H.: Regression Analysis of Amino Acid Substitutions and Factor IX Activity in Hemophilia B. Artificial Life and Robotics, **13** (2008) 531–534

[3] Aoki, K., Yamamori K., Sakamoto. M., Furutani H.: Analysis of Genetic Disease Hemophilia B by Using Support Vector Machine. Proceedings of the 19th International Conference on Neural Information Processing, Lecture Notes in Computer Science, Vol.7666(4), (2012) 476–483

[4] Furie, B., Furie, B.C.: The Molecular Basis of Blood Coagulation. Cell, **53** (1988) 505–518

[5] Yoshitake, S., Schach, B. G., Foster D. C., Davie, E. W. and Kurachi, K.: Nucleotide Sequence of the Gene for Human Factor IX. Biochemistry. **24** (1985) 3736–3750

© ISAROB 2013

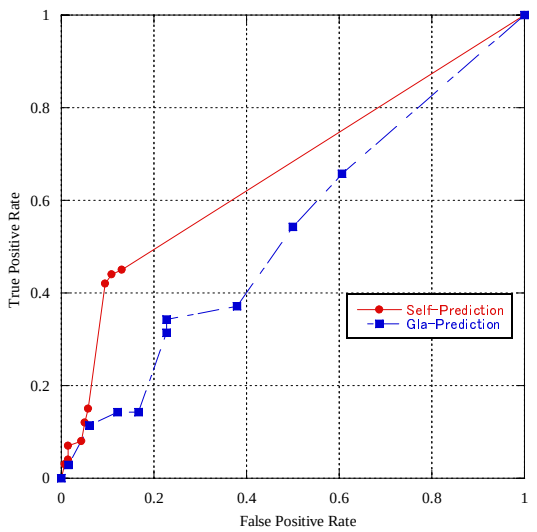

Fig. 3. ROC curves in GLA region. The solid line shows the SVM result of self-learning in GLA region. The dotted line for SVM learning in ACT region.

[6] Hemophilia B Mutation Database: A database of point mutations and short additions and deletions in the factor IX gene. version 13 (2004).

[7] Schölkopf B., Burges, C.J.C., Smola, A.J.: Advances in Kernel Methods, The MIT Press, London (1999)

[8] Schölkopf B., Tsuda K., Vert J.P.: Kernel Methods in Computational Biology, A Bradford Book, The MIT Press, London (2004)

[9] Joachims, T.: Making large-Scale SVM Learning Practical, in Advances in Kernel Methods - Support Vector Learning, The MIT Press, London (1999)

© ISAROB 2013

The Eighteenth International Symposium on Artificial Life and Robotics 2013 (AROB 18th '13),
Daejeon Convention Center, Daejeon, Korea, January 30-February 1, 2013

Remarks on Recognizability of Four-Dimentuonal Topological Components

Makoto SAKAMOTO[1], Makoto NAGATOMO[1], Tatsuma KUROGI[1], Takao ITO[2], Yasuo UCHIDA[2]
Tsunehiro YOSHINAGA[3], Satoshi IKEDA[1], Masahiro YOKOMICHI[1], and Hiroshi FURUTANI[1]
[1]Dept. of Computer Science and Systems Engineering, University of Miyazaki, Miyazaki 889-2192, JAPAN
[2]Dept. of Business Administration, Ube National College of Technology, Ube 755-8555, JAPAN
[3]Dept. of Computer Science and Systems & Electronic Enginieering, Tokuyama College of Technology, Shunan 745-8585,JAPAN

Abstract

The study of four-dimensional automata as the computational model of four-dimensinal pattern processing has been meaningful. However, it is conjectured that the three-dimensional pattern processing has its our difficulties not arising in two- or three-dimensional case. One of these difficulties occurs in recognizing topological properties of four-dimensional patterns because the four-dimensional neighborhood is more complicated than two- or three-dimensional case. Generally speaking, a property or relationship is topological only if it is preserved when an arbitrary ' rubber-sheet ' distortion is applied to the pictures . For example, adjacency and connectedness are topological ; area, elongatedness, convexity, straightness, etc. are not. In recent years, there have been many interesting papers on digital topological properties. For example, an interlocking component was defined as a new topological property in multi-dimensional digital pictures, and it was proved that no one marker automaton can recognize interlocking components in a three-dimensional digital picture. In this paper, we deal with recognizability of topological components by four-dimensional Turing machines, and investigate some properties.

KeyWords : digital geometry,interlocking component, one marker automaton, three-dimensional automaton, topological component, Turing machine.

1 Introduction

Digital geometry has played an important role in computer image analysis and recognition[3]. In particular, there is a well-developed theory of *topological* properties such as *connectedness* and *holes* for two-dimensional arrays[4]. On the other hand, three-dimensional information processing has also become of increasing interest with the rapid growth of computed tomography, robotics, and so on. Thus it has become desirable to study the geometrical properties such as *interlocking components* and *cavities* for three-dimensional arrays[2,5]. In[2], interlocking components was proposed as a new topological property of three-dimensional digital pictures : Let S_1 and S_2 be two subsets of the same three-dimensional digital picture. S_1 and S_2 are said to be interlocked when they satisfy the following conditions:

(1) S_1 and S_2 are *toruses*,
(2) S_1 goes through a *hole* of S_2,
(3) S_2 goes through a *hole* of S_1.

By the way, the question of whether processing four-dimensional degital pattern in much difficult than three-dimensional ones is of great interest from the theoretical and practical standpoints both. In recent years, due to the advances in many application areas much as computer animation, motion image processing, and so both, the study of four-dimentional pattern processing has been of crucial importance. Thus, it is very interesting to deal with the geometrical propertises such as interlocking components and cavities in a four-dimensional digital picture.

The interlocking of S_1 and S_2 in a four-dimentional tape is illustrated in Fig.1. This relation may be considered as a chainlike connectivity.

It is proved that no one marker automaton can recognize interlocking components in a three-dimensional digital picture in [2]. In this paper, we investigate recognizability of topological properties such as interlocking components by three-dimensional Turing machines.

2 Preliminaries

Definition 2.1. Let Σ be a finite set of symbols. A *four-dimensional tape* over Σ is a four-dimensional array of elements of Σ. The set of all four-dimensional tapes over Σ is denoted by $\Sigma^{(4)}$. Given a tape $x \in \Sigma^{(4)}$, for each $j(1 \leq j \leq 4)$, we let $l_j(x)$ be the length of x along the jth axis. When $1 \leq i_j \leq l_j(x)$ for each $j(1 \leq j \leq 4)$, let $x(i_1, i_2, i_3, i_4)$ denote the symbol in x with coordinates

© ISAROB 2013

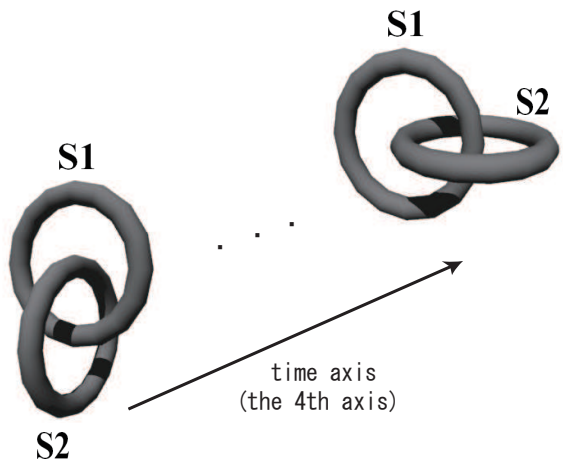

Fig. 1: Interlocking components in a four-dimensional tape.

(i_1, i_2, i_3, i_4), as shown in Fig. 2. Furthermore, we define

$$x[(i_1, i_2, i_3, i_4), (i'_1, i'_2, i'_3, i'_4)],$$

when $1 \leq i_j \leq i'_j \leq l_j(x)$ for each integer $j(1 \leq j \leq 4)$, as the four-dimensional tape y satisfying the following :

(i) for each $j(1 \leq j \leq 4)$, $l_j(y) = i'_j - i_j + 1$;

(ii) for each r_1, r_2, r_3, r_4 $(1 \leq r_1 \leq l_1(y),\ 1 \leq r_2 \leq l_2(y),\ 1 \leq r_3 \leq l_3(y),\ 1 \leq r_4 \leq l_4(y),\ y(r_1, r_2, r_3, r_4) = x(r_1 + i_1 - 1, r_2 + i_2 - 1, r_3 + i_3 - 1, r_4 + i_4 - 1)$.

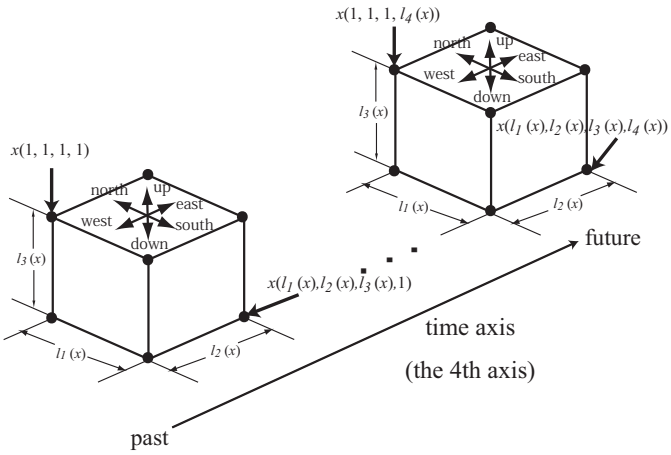

Fig. 2: Four-dimensional input tape.

Definition 2.2. *A four-dimensional nondeterministic one-marker automaton* 4-NM_1 is defined by the six-tuple

$$M = (Q, q_0, F, \Sigma, \{+, -\}, \delta),$$

where

(1) Q is a finite set of *states*;

(2) $q_0 \in Q$ is the *initial state*;

(3) $F \subseteq Q$ is the set of *accepting states*;

(4) Σ is a finite input alphabet ($\sharp \notin \Sigma$ is the *boundary symbol*);

(5) $\{+,-\}$ is the pair of signs of presence and absence of the marker; and

(6) δ: $(Q \times \{+,-\}) \times ((\Sigma \cup \{\sharp\}) \times \{+,-\}) \rightarrow 2^{(Q \times \{+,-\})} \times ((\Sigma \cup \{\sharp\}) \times \{+,-\}) \times \{$east,west,south, north,up,down,future,past,no move$\}$) is the *next-move function*, satisfying the following: For any $q, q' \in Q$, any $a, a' \in \Sigma$, any $u, u', v, v' \in \{+,-\}$, and any $d \in \{$east,west,south,north,up,down,future,past,no move$\}$, if $((q',u'),(a',v'),d) \in \delta((q,u),(a,v))$ then $a = a'$, and $(u,v,u',v') \in \{(+,-,+,-),(+,-,-,+),(-,+,-,+),(-,+,+,-),(-,-,-,-)\}$.

We call a pair (q,u) in $Q \times \{+,-\}$ an *extended state*, representing the situation that M holds or does not hold the marker in the finite control according to the sign $u = +$ or $u = -$, respectively. A pair (a,v) in $\Sigma \times \{+,-\}$ represents an input tape cell on which the marker exists or does not exsit according to the sign $v = +$ or $v = -$, respectively.

Therefore, the restrictions on δ above imply the following conditions. (A) When holding the marker, M can put it down or keep on holding. (B) When not holding the marker, and (i) if the marker exists on the current cell, M can pick it up or leave it there, or (ii) if the marker does not exist on the current cell, M cannot create a new marker any more.

Definition 2.3. Let Σ be the input alphabet of 4-NM_1 M. An *extended input tape* $\tilde{x}$ of M is any four-dimensional tape over $\Sigma \times \{+,-\}$ such that

(i) for each $j(1 \leq j \leq 4)$, $l_j(\tilde{x}) = l_j(x)$,

(ii) for each $i_1(1 \leq i_1 \leq l_1(\tilde{x}))$, $i_2(1 \leq i_2 \leq l_2(\tilde{x}))$, $i_3(1 \leq i_3 \leq l_3(\tilde{x}))$, and $i_4(1 \leq i_4 \leq l_4(\tilde{x}))$, $\tilde{x}(i_1, i_2, i_3, i_4) = x(i_1, i_2, i_3, i_4, u)$ for some $u \in \{+, -\}$.

Definition 2.4. A configuration of 4-NM_1 $M = (Q, q_0, F, \Sigma, \delta)$ is an element of

$$((\Sigma \cup \{\sharp\}) \times \{+, -\})^{(4)} \times (Q \times \{+, -\}) \times N^4,$$

where N denotes the set of all nonnegative integers. The first component of a configuration $c = (\tilde{x}, (q, u), (i_1, i_2, i_3, i_4))$ represents the extended input tape of M. The second component (q, u) of c represents the extended state. The third component

© ISAROB 2013

(i_1, i_2, i_3, i_4) of c represents the input head position. If q is the state associated with configuration c, then c is said to be an *accepting configuration* if q is an accepting state. The *initial configuration* of M on input x is

$$I_M(x) = (x^-, (q_0, +), (1, 1, 1, 1)),$$

where x^- is the special extended input tape of M such that $x^-(i_1, i_2, i_3, i_4)=(x(i_1, i_2, i_3, i_4), -)$ for each i_1, i_2, i_3, i_4 ($1\leq i_1\leq l_1(\tilde{x})$,$1\leq i_2\leq l_2(\tilde{x})$,$1\leq i_3\leq l_3(\tilde{x})$,$1\leq i_4\leq l_4(\tilde{x})$). If M moves determinately, we call M a *four-dimensional deterministic one-marker automaton* 4-DM_1.

Definition 2.5. A *seven-way four-dimensional Turing machine* is defined by the six-tuple

$$M = (Q, q_0, F, \Sigma, \Gamma, \delta),$$

where

(1) Q is a finite set of *states*;

(2) $q_0\in Q$ is the *initial state*;

(3) $F\subseteq Q$ is the set of *accepting states*;

(4) Σ is a finite *input alphabet* ($\sharp\notin\Sigma$ is the *boundary symbol*);

(5) Γ is a finite *storage-tape alphabet* ($B\in\Gamma$ is the *blank symbol*); and

(6) $\delta\subseteq(Q\times(\Sigma\cup\{\sharp\})\times\Gamma)\times(Q\times(\Gamma-\{B\})\times\{$east,west, south,north,up,down,future,no move$\}\times\{$right,left, no move$\})$.

If M moves determinately (nondeterminately), we call M a *seven-way four-dimensional deterministic* (*nondeterministic*) *Turing machine* $SV4$-DTM ($SV4$-NTM).

Let L: $\boldsymbol{N}\rightarrow\boldsymbol{R}$ be a function. A seven-way four-dimensional Turing machine M is said to be $L(m)$ *space bounded* if for all $m\geq1$ and for each x with $l_1(x)=l_2(x)=l_3(x)=l_4(x)=m$, if x is accepted by M, then there is an *accepting computation path* of M on x in which M uses no more than $L(m)$ cells of the storage tape. We denote an $L(m)$ space-bounded $SV4$-DTM ($SV4$-NTM) by $SV4$-$DTM(L(m))$ ($SV4$-$NTM(L(m))$).

Definition 2.6. Let $T(M)$ be the set of four-dimensional tapes accepted by a machine M, and let $\pounds[4\text{-}DM_1]=\{T|T(M)$ for some 4-DM_1 $M\}$. $\pounds[4\text{-}NM_1]$, etc. are defined in the same way as $\pounds[4\text{-}DM_1]$.

We can easily derive the following theorem by using ordinary technique[6].

Theorem 2.1. *For any function* $L(m) \geq \log m^3$, $\pounds[SV4\text{-}NTM(L(m))]\subseteq U_{c>0}\ \pounds[SV4\text{-}DTM(2^{c(L(m))})]$.

3 Simulation of four-dimensional one-marker automata by four-dimensional Turing machines

In this section, we show the algorithms described in the previous section are optimal in some sense. We can get the following Theorems any using the same technique as in the proof of Lemmas 6.2 and 6.3 in [6].

Theorem 3.1. *To simulate* $4-DM_1$*'s,* (1) $SV4$-NTM*'s require* $\Omega(m^3\log(m^3))$ *space and* (2) $SV4$-DTM*'s require* $2^{\Omega(m^3\log(m^3))}$ *spacespace*$(m\geq1)$.

Theorem 3.2. *To simulate* 4-NM_1*'s,*

(1) $SV4$-NTM*'s require* $\Omega(m^6)$ *space, and*
(2) $SV4$-DTM*'s require* $2^{\Omega(m^6)}$ *space*$(m\geq1)$.

4 Recognizability of interlocking components in four-dimensional images

In this paper, we show that interlocking components are not recognized by any space-bounded four-dimensional Turing machines.

First of all, we consider a four-dimensional input tape T_3 that is 7 units in thickness. So, for some m, $T_3=\{\ (i_1,i_2,i_3,i_4)\ |\ 1\leq i_1,i_2,i_3\leq\ m+2, 1\leq i_4\leq 7\ \}$. Fig.3(a)represents T_3. Now we define two different 5×5×5 patterns as shown in Fig.3(b)(c). Then we consider an arbitrary n-by-n matrix of those 5×5×5 patterns (see Fig.3).

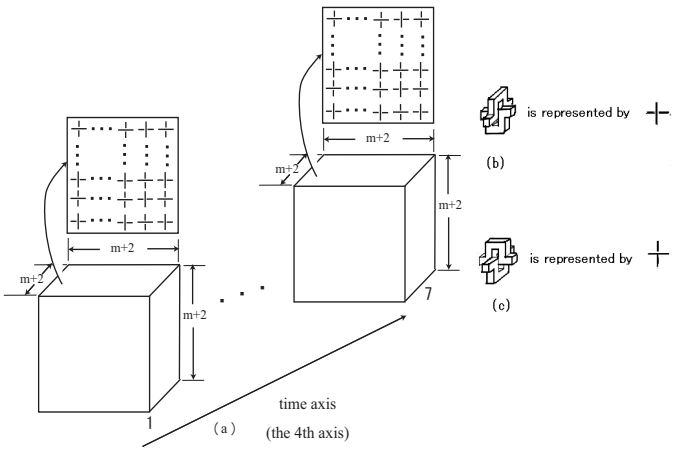

Fig. 3: Four-dimensional input tape including interlocking components T_3[2].

Then, we can get the following lemma from Lemma 2.1 in [2].

Lemma 4.1. 4-DM, *cannnot recognize interlocking components of an arbitrary given digital picture.*

From Theorem 3.1 and Lemma 4.1, we can get the following.

Theorem 4.1. *Interlocking components are not accepted by any* $SV4$-DTM $(L(m))$($SV4$-$NTM(L(m))$) *for any function* $L(m)$ *such that* $\lim_{m\to\infty}[L(m)/2^{m^3 log m^3}] = 0$ $(\lim_{m\to\infty}[L(m)/m^3 log\ m^3] = 0)(m\geq 1)$.

Next, we can get the following lemma by using a technique similar to that in the proof of Lemma 2.1 in [2].

Lemma 4.2. 4-ND_1 *cannnot recognize interlocking components of an arbitrary given digital picture.*

From Theorem 3.2 and Lemma 4.2, we can get the following.

Theorem 4.2. *Interlocking components are not accepted by any* $SV4$-$DTM(L(m))$ ($SV4$-$NTM(L(m))$) *for any function* $L(m)$ *such that* $\lim_{m\to\infty}[\mathrm{L(m)}/2^{m^6}] = 0$ $(\lim_{m\to\infty}[L(m)/m^6]=0)(m\geq 1)$.

5 Conclusion

In this paper, we dealt with recognizability of topological components by four-dimensional automata, and showed that interlocking components are not recognized by any space-bounded four-dimensional deterministic or nondeterministic Turing machines. By the way, what is the situation for a two or three marker automata, or for alternation (see [1])? This question seems very intersting. We will investigate the problem in further papers.

References

[1] A.K. Chandra , D.C. Kozen, and L.J. Stockmeyer, Alternation, *J. of ACM*, 28(1):114-133(1981).

[2] A.Nakamura and K.Aizawa, Detection of ic interlocking components in three-dimensional digital pictures, Imformation Sciences 40:143-153(1986).

[3] A.Rosenfeld and K.C. Kak, Digital Picture Processing, Academic Press, New York(1976).

[4] A.Rosenfeld, Picture Languages, Academic Press, New York(1979).

[5] A.Rosenfeld, Three-dimensionl digital topology, Information and Control 50:119-127(1981).

[6] M.Sakamoto, Three-dimensional alternating Turing machines, *Ph. D. Thesis*, *Yamaguchi University* (1999).

© ISAROB 2013

The Eighteenth International Symposium on Artificial Life and Robotics 2013 (AROB 18th '13),
Daejeon Convention Center, Daejeon, Korea, January 30-February 1, 2013

Power Consumption Reduction by Dynamic Core-Counts Control with Power Gating

Kazuyuki TAMOTO[1], Kunihito YAMAMORI[2], Masaru AIKAWA[3]

[1]Graduated school of Engineering, University of Miyazaki
[2]Faculty of Engineering, University of Miyazaki
[3]Technical Center, Faculty of Engineering, University of Miyazaki
(Tel: +81 985 58 7589, Fax: +81 985 58 7589)

[2]yamamori@cs.miyazaki-u.ac.jp

Abstract: Power Gating (PG) technology is known that it reduces static power consumption by leakage current. Linux operating system on multi-core processor evenly assigns processes to each core. Linux scheduler assigns processes to the core which has the fewest number of processes even if the core is idle. It makes an idle core in PG state change to active state, and avoids reducing power consumption. In this paper, we propose a method to reduce electric power consumption by effective use of PG. Our method modify linux kernel to change number of active cores in system dynamically, and apply PG to idle cores immediately. The number of active cores is changed according to the system load. Experimental results show that our proposed method reduces about 8kWh electric power consumption from the original kernel with keeping performance.

Keywords: Power Management, Power Gating, Linux Kernel

1 INTRODUCTION

Recent computers are required low electric power consumption in terms of thermal problem, running cost, and environmental problems. Fine process rule improves performance of CPU, and reduces total electric power consumption. However, increasing of leakage current becomes as a large problem. Leakage current is a flow through insulator of transistor when transistor is in off state, and it causes unnecessary power consumption. So many researchers try to reduce it.

To reduce electric power consumption of CPU, Clock Gating[1] (CG) is used in long time. As shown in Figure 1, CG technology stops to supply a clock signal for a CPU core and reduces power consumption. CG is easy to implement and efficient to reduce power consumption. However, leakage current remains in the clock circuit. Recently, Power Gating[2] (PG) is attracted in attention. PG technology stops to supply electric power for cores as shown in Figure 2. Thus, PG prevents to appear leakage current and reduces power consumption by leakage current. PG is now replacing with CG, and implementing in many kinds of CPUs.

CG and PG can work when cores are in idle state only. Current linux system on multi-core processor evenly assigns processes to each core. A new process is assigned to the core which has the fewest number of processes even if the core is in idle state. It means PG cannot work effectively.

In this paper, we propose a method to use PG effectively by modifying linux kernel on multi-core processor. Proposed method dynamically changes the number of active cores in order to load of linux system, and immediately apply PG for idle cores. While the system load is low, our method does not assign a new process to the idle cores to avoid interrupting PG state. As a result, power consumption of CPU is reduced. Our method also changes the number of active cores according to current load of system to keep system performance.

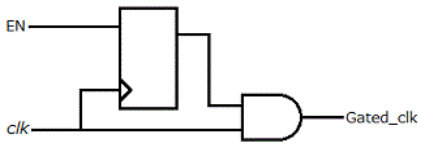

Fig. 1. A model of Clock Gating

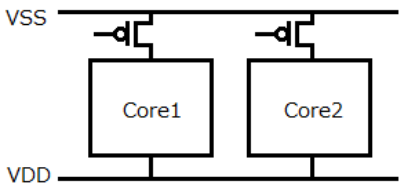

Fig. 2. A model of Power Gating

2 RELATED WORKS

Some works have been reported for effective use of PG to reduce electric power consumption. When CPU switches its state from active/PG to PG/active, additional electric power is consumed. It means that frequently change of CPU state affect power consumption. Kimura et al.[3] point out that additional electric power depends on CPU temperature, and they proposed a method that changes CPU state according to CPU temperature when processes frequently stay in WAIT state.

When CPU switches its state from active to PG, CPU must save the internal conditions such as program counter

© ISAROB 2013

to low level memory, and it takes additional time. Otomo et al.[4] propose a method that CPU can quickly switch from active to PG by use of an additional memory. By using of the additional memory, CPU does not need to save its internal conditions to low level memory.

These studies assume to use original CPU or FPGA, there are few researches for general CPUs.

3 IMPROVEMENT OF LINUX KERNEL

We modify a linux kernel to achieve a system that effectively uses PG on general multi-core processor. The system periodically watches load of CPU. When the load of system is low, kernel turns a CPU core off, and applies PG immediately. Meanwhile the load of system becomes high, our method wake core in PG state up. Thus, the system reduces power consumption with keeping system performance.

3.1 Environments

We implement proposed method in linux kernel 2.6.32 [5], and evaluate our method on Intel core i7 Nehalem architecture processor [6] which equips PG technology. Hyper-threading and DVFS is not used.

3.2 Dynamic Core-Counts Control

Linux kernel 2.6.32 controls on/off of core by bitmask and scheduling domain. If a bit in bitmask is 0, corresponding core is in off state. Scheduling domain manages cores with hierarchical group. If a process should move other core, it is preferentially moved to the core belonging to the same group. Figure 3 illustrates a concept of scheduling domain of hyper-threading dual core processor. If a process in core0 should move, preferential destination is core2. When system switches on/off of a core, those groups are reconstructed. In this paper, all cores belong to the same group.

Our proposed method controls the state of cores by bitmask, and reconstructs group of scheduling domain. We make original daemon process that watches the load of system and changes the number of active cores at fixed interval. In linux kernel, the lowest number of active core is one. Thus, core0 is always online, and our daemon process always works on core0.

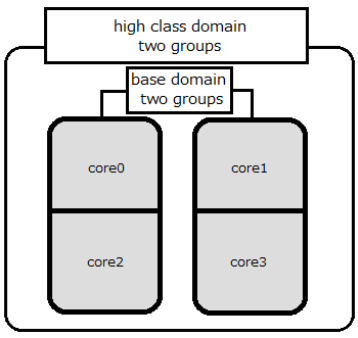

Fig. 3. Scheduling domain of dual core processor with Hyper-threading technology

3.3 Load of CPU

Our method changes the number of active cores according to the load of system. Thus, we implement a new function to get the load of system in linux kernel.

Equation (1) defines the load of the system. Linux kernel manages CPU time as the sum of system time t_s, user time t_u, idle time t_i and others t_o. The load of k-th core is defined as the ratio of active time to total time.

$$Load_k = \frac{t_s + t_u + t_o}{t_s + t_u + t_i + t_o} \times 100(\%) \qquad (1)$$

3.4 PG management through ACPI

Linux kernel manages CG and PG by C-states of ACPI [6]. C-states show power states when CPU core is in idle state. C-states consist of four level states, C0 means that the core is in active state, and C3 means in PG state. The core in deep level consumes low electric power. Meanwhile, the core in deep level needs large latency when the core changes its state from PG to active. Figure 4 illustrates relations between electric power consumption and latency in each C-state level. While a core is in idle state, system changes the state from C0 to C1, C2, and C3. If a process is assigned to a core, the core returns to C0.

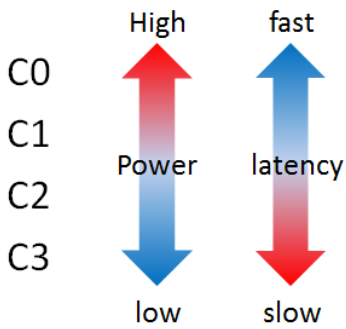

Fig. 4. Power stat and latency of each state

To reduce electric power consumption on multi-core CPU, it is important to keep the idle core in C3 state. However, linux scheduler evenly assigns a process to the core with the fewest number of processes, so C3 state is frequently interrupted. To avoid this situation, we logically removed the idle core from system as described in Section 3.2 since linux operating system cannot detect the logically removed core, no process is assigned to the removed core, and the core can keep C3 state. On the other hand, the remaining cores have to work harder because the number of cores is decreased, and it may make electric power consumption of remaining cores increase. If the load of system is high, this increasing of electric power consumption can ignore because the cores work hard and they already consume all the required electric power. If the load of system is low, increasing of electric power consumption of remaining cores may become a problem since logical removing of a core prevents remaining cores staying C1, C2 or C3.

Here we investigate the relations between the system

© ISAROB 2013

load and electric power consumption according to the number of active cores. Figure 5 and Figure 6 show that transition of load and power consumption of each number of active cores when initial average load is about 40%, 30%, 20% and 10% in four active cores. In both figures, bars denote the electric power consumption corresponding to the left vertical axis, and lines denote the average load of the system corresponding to the right vertical axis.

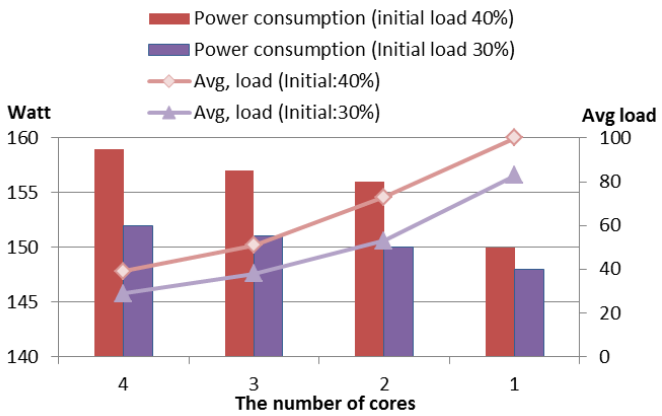

Fig. 5. Average load and power consumption when initial load is 40% and 30%.

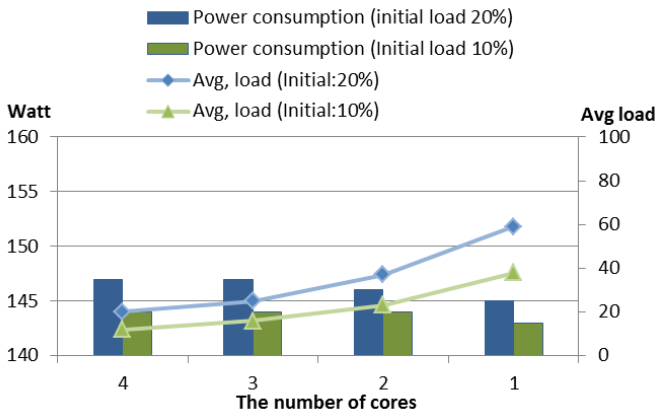

Fig. 6. Average load and power consumption when initial load is 20% and 10%.

Figure 5 shows that power consumption is clearly reduced when turn CPU cores off although the load of remaining cores is increasing. This means that logical removing of cores gives us reducing electric power consumption even if it increases the load of the remaining cores when the initial load of system is high. On the other hand, reducing of electric power consumption is not clear when the initial load of system is low as shown in Figure 6. But electric power consumption continues to be down even if the initial average load is 10%.

From experimental results, power consumption is actually reduced when cores are turned off.

3.5 Threshold for core state switching

Figure 5 and Figure 6 show that system can run with fewer cores even if load is moderately high. However, if high load leads poor performance, system should increase the number of active cores.

Threshold to turn the core on/off is not clear. Since early switching from off to on leads high electric power consumption, this switching is desirable near to 100% of system load. Figure 5 and Figure 6 shows that the average load of system is increased when a core is logically removed because the processes assigned to the removed core are distributed to other remaining cores. Therefore the threshold to turn the core on/off should be decided by the load of remaining cores. Suppose N denotes the number of remaining cores, the average load is defined by Equation (2).

$$Avg_{load} = \frac{\sum Load_k}{N-1} \ (N \geq 2) \qquad (2)$$

When the Avg_{load} becomes near to100%, it means the system performance may down. In the following experiments, we use Avg_{load} = 90% to switch the core state on/off.

4 EXPERIMENTS AND DISCUSSIONS

4.1 Experimental conditions

We evaluate electric power consumption and execution time by comparing our proposed method with original linux kernel 2.6.32. Our modified kernel watches the load of system at every two seconds, and decides to make a core remove or return. Test programs change Avg_{load} at random by forking small programs in many times, so system changes the number of active cores. We measure elapse time until the test programs have finished. Moreover, we evaluate performance of a floating-point matrix calculation under the modified kernel.

4.2 Results and Discussion

Figure 7 shows electric power consumption at every second of proposed method and original kernel. The horizontal axis is seconds, and vertical axis is actual power consumption of whole system. Figure 7 says that our method globally reduces power consumption. At the beginning, the number of active cores is one in our proposed method. Since our proposed method uses only a few cores for several seconds from the beginning, electric power consumption stays low. As shown in Figure 7, electric power consumption of our kernel is lower than that of the original kernel after 109 seconds since our kernel finishes test programs faster than the original kernel. Figure 7 also shows that our method is effective in the case which the electric power consumption by original kernel is more than 165W. Our kernel employs a hard threshold to decide on/off of a core, the curve of our kernel sometimes waves around 40 seconds and 65 seconds.

Table 1 shows mathematical total electric power consumption by our proposed kernel and the original kernel calculated from Figure 7. As shown in Table 1, our method can reduce about 8kWh from original kernel.

Table 2 shows executing time of test programs. It shows our method is faster than original system. It is because

© ISAROB 2013

migration mechanism of linux kernel. Linux kernel keeps load balance through this migration mechanism to move the process from busy core to idle core. This migration itself becomes overhead for execution of processes. Our test program forks many small processes, and the kernel assigns these processes into online cores. Since our kernel makes some cores stay offline, migration over cores is rare case and it reduce overhead by migration. Therefore execution time on our kernel becomes shorter than that of the original kernel.

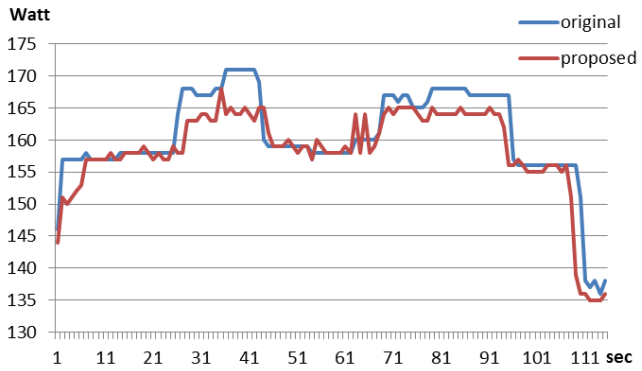

Fig. 7. Comparison with electric power consumption

Table 1. Average of power consumption

Original(kWh)	Proposed(kWh)
578.22	570.30

Table 2. Execution time of test programs

Original(sec)	Proposed(sec)
109.20	106.11

We also evaluate execution time of floating-point calculation by inverse matrix calculation whether our modified kernel affects the performance of scientific calculation. Table 3 shows the execution time of floating-point inverse matrix calculation. "Number of processes" denotes the number of floating-point calculation process simultaneously executed. Table 3 says that our kernel is about 3% slower than the original kernel. It is because the daemon process to decide on/off of the core described in Section 3.2. This daemon process always stays in core0. In the case of one floating-point calculation is executed, only the core0 is the active core. The core0 has to execute daemon process at every two seconds, it disturbs floating-point calculation. When we throw two floating-point calculations simultaneously, the one finishes about 6 seconds faster than the other. It means that the process assigned into core0 is affected by the daemon process. The number of active cores is the same between the original kernel and our modified kernel, so the electric power consumption is almost the same.

From the experiments, our method is suitable for the systems that execute many small processes or threads with high load. In that case, our method copes with both low electric power consumption and faster execution.

Table 3. Processing time of floating-point calculation

Number of Processes	Original(sec)	Proposed(sec)
1	133.26	139.68
2	132.99	134.81
	133.99	141.09

5 CONCLUSIONS

In this paper, we propose a method to reduce electric power consumption on linux servers. Our method dynamically manages the number of active cores, and immediately applies PG for idle cores. In addition, our method logically removes the idle cores from the system, and makes no process assign into idle cores to keep the core in PG state. When the system load is over threshold, our method return the cores in PG state to active. Experimental results show that our method copes with both low electric power consumption and good performance for the system executing many small processes with high load. It remains future works to employ "soft" threshold to stable electric power consumption and improve algorithm for core state switching.

REFERENCES

[1] Wu Q, Pedram M, Wu X (1997), Clock-Gating and its application to low power design of sequential circuits. Custom Integrated Circuits Conference, 1997, Proceedings of the IEEE 1997, pp.479-482

[2] Pakbaznia E, Fallah F, Pedram M (2008), Charge Recycling in Power-Gated CMOS Circuits. Computer-Aided Design of Integrated Circuits and Systems, Vol.27, Issue.10, pp.1798-1811

[3] Kimura K, Kondo M, Amano H (2011), Fine Grain Power Gating Control Adapting to a Change in Core Temperature with Operating System, Vol.2011-ARC-195 No.30, pp.1-8

[4] Otomo T, Kurihara K, Teranishi Y (2012), High-reliabillity, Low-power and High-performance Implementation by Memory Redundancy and Power Gating, Vol.2012-ARC-199 No.14,pp.1-8

[5] http://www.kernel.org/

[6] Intel(R) Turbo Boost Technology in Intel(R) Core(TM) Microarchitecture (Nehalem) Based Processors (2008) Intel White Paper

© ISAROB 2013

The Eighteenth International Symposium on Artificial Life and Robotics 2013 (AROB 18th '13),
Daejeon Convention Center, Daejeon, Korea, January 30-February 1, 2013

A new solution to the SLAM problem by using an unscented smoother

Keigo Watanabe[1], Satoshi Funamoto[2], and Shoichi Maeyama[1]

[1] Department of Intelligent Mechanical Systems, Division of Industrial Innovation Sciences,
Graduate School of Natural Science and Technology, Okayama University
3-1-1 Tsushima-naka, Kita-ku, Okayama 700-8530, Japan
Tel & Fax: +81-86-251-8064
E-mail: {watanabe, maeyama}@sys.okayama-u.ac.jp
[2] Shin Nippon Koki Co., Ltd., 4-1, Kita-Kyuhoji-Machi 2-chome, Chuo-ku, Osaka, Japan

Abstract: As a solution to the SLAM problem, the extended Kalman filter or unscented Kalman filter (UKF) is often used up to now. In the case of an offline use of estimated results, a fixed-interval smoother is available and it is expected to give much more high accuracy. In this paper, a solution to the SLAM problem is proposed with the unscented Rauch-Tung-Striebel (RTS) smoother (URTSS) and several experimental results are given to show the improvement of the estimation accuracy due to the present method. In particular, the superiority of our method over the conventional UKF based method is demonstrated by evaluating the estimated accuracy of both methods through some simulations using a mobile robot.

Keywords: SLAM, Unscented Kalman filter, Unscented RTS smoother, Mobile robots.

1 INTRODUCTION

For the solution to the Simultaneous Localization and Mapping (SLAM) problem [1], [2], two kinds of information are generally used for the estimation method. One is the self-position obtained from internal sensors such as encoders and inertial sensors. This information is called "control inputs". The other is relative position to the landmarks obtained from external sensors such as camera, laser range finder, etc. This information is called "measurements". However, the both information include noises and the exact position is not acquired. Therefore, probabilistic methods to integrate the both are applied for localization and map building.

Up to now, as a solution to the SLAM problem, extended Kalman filter (EKF) that is one of probabilistic estimation methods, is mainly used. However, the EKF has two problems: one is less-accuracy in the case of the system with any strong nonlinearity because of linearization by Taylor expansion, and the other is that the derivative of model must be calculated for linearization. To overcome these weak points, Julier et al. [3] proposed a novel method so-called Unscented Kalman Filter (UKF). The UKF based on using Unscented Transform (UT) excludes the derivative of model to improve the problems of the EKF and can estimate the state of nonlinear systems accurately.

The SLAM solutions using the EKF and the UKF are available online estimation. That is, it is possible to estimate the latest self-position and the optimal map while capturing the data. On the other hand, it is sometimes considered that there needs a precise trajectory and map information after completing the exploration. For instance, in the case of the exploration of planetary or disaster environments, the offline estimation is applicable.

In the case of offline use of estimation results, a fixed-interval smoother is available and expected to give much higher accuracy. A Rauch–Tung–Striebel (RTS) smoother, which is one of fixed interval smoothers proposed by Rauch et al. [4], was applied to various applications. Recent years, Terejanu et al. [5] and Särkkä [6]proposed an unscented RTS smoother (URTSS) with UT in order to apply it to a model that has strong nonlinearities.

The SLAM problem is one of nonlinear estimation problems so that the URTSS is expected to contribute the improvement of the accuracy on this problem. Therefore, in this paper, the solution to the SLAM problem with the URTSS is proposed and the experimental results are given to demonstrate the effectiveness of the present method by evaluating the estimated accuracy through some simulations.

2 URTSS–SLAM

The objective in the URTSS–SLAM is to simultaneously estimate the self-position and direction of the robot and the landmark position, which are described in a composite state vector $\boldsymbol{x}_t$ such as

$$\begin{aligned}\boldsymbol{x}_t =&(x,\, y,\, \theta,\, \mu_{1,x},\, \mu_{1,y},\, \ldots \\ &\mu_{j,x},\, \mu_{j,y},\, \ldots,\, \mu_{N,x},\, \mu_{N,y})^T\end{aligned} \tag{1}$$

where x, y and θ are the robot position and the direction (or azimuth), which are called the posture collectively in this paper. $\mu_{j,x}$ and $\mu_{j,y}$ denote the absolute position of the j-th landmark, and the N denotes the number of landmarks.

The action model used here and the measurement model are respectively described by

$$\boldsymbol{x}_t = g(\boldsymbol{u}_{t-1} + \boldsymbol{\rho}_{t-1},\, \boldsymbol{x}_{t-1}) \tag{2}$$

$$\boldsymbol{z}_t = h(\boldsymbol{x}_t) + \boldsymbol{\varepsilon}_t \tag{3}$$

where $\boldsymbol{u}_{t-1}$ is the "control" input. The action model transfers the state $\boldsymbol{x}_{t-1}$ to $\boldsymbol{x}_t$ through the action function g and the control input is affected by the noise $\boldsymbol{\rho}_{t-1}$. The measurement model produces the measurement $\boldsymbol{z}_t$ through the measurement function h and this model is also affected by the noise $\boldsymbol{\varepsilon}_t$.

In this paper, the estimate for $\boldsymbol{x}_t$ is represented by using the mean $\boldsymbol{m}_t$ and the covariance $\boldsymbol{P}_t$. The URTSS–SLAM is manly composed by the following two-steps:

© ISAROB 2013

Table 1. Simulation conditions

Meaning	Variable and parameter	Value	Unit
Simulation time	T	76	[s]
Sampling interval	Δt	0.5	[s]
Control noise const.	a_1	0.02	
	a_2	0.02	
	a_3	0.02	
	a_4	0.02	
Measurement noise S.D. for relative distance	σ_r	0.05	[m]
Measurement noise S.D. for relative angle	σ_ϕ	2.0	[deg]

1. Using the UKF-SLAM algorithm for the time interval $[0\ T]$, memorize the estimates for the self-position and direction of the robot and for the landmark position.

2. Re-estimate the states using the URTSS–SLAM algorithm backward in time from time T.

The UT technique and both the UKF–SLAM and the URTSS-SLAM algorithms are not described here, but see e.g., Terejanu et al. [5] and Särkkä [6] for the detailed explanations.

3 SIMULATIONS

Simulation experiments are presented to check the estimation accuracy of the proposed method, where the present URTSS–SLAM is compared with the conventional UKF–SLAM.

3.1 Simulation conditions

Assume that the robot navigates with a constant velocity along the path depicted in Fig. 1, where the robot moves from the coordinate $(0,\ 0)$ counterclockwise and the landmarks are assigned every 1.3 [m] in a 4 [m]×6.5 [m] rectangular area. The estimation accuracy is evaluated with 100 trials, where the action and measurement models are given by the previous sections. It is assumed that the measurement rage of the landmarks is restricted such as ± 120 [deg] measured from the centerline of the direction of movement and 4 [m] in maximum detection distance. Furthermore, following the results of Julier et al. [3] and Kim et al. [7], the parameters used in the UT were set to $\alpha = 0.002, \beta = 2$, and $\kappa = 3 - n$, where note that other simulation conditions are shown in Table 1.

3.2 Action model

An odometric model [8] is used for the action model, where the input to the model is the amount of the robot posture change obtained from the odometry. Note that the odometry is a measurement rigorously, so that velocity information should be added to the state, if the odometry is used as a measurement. If it is regarded as an input in general, then it is possible to reduce the number of states. The present paper follows such an approach.

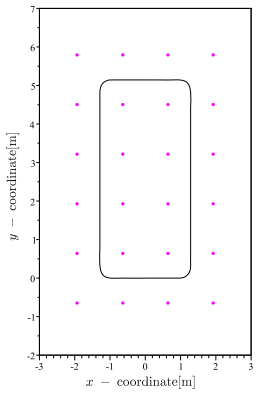

Fig. 1. Simulation environment

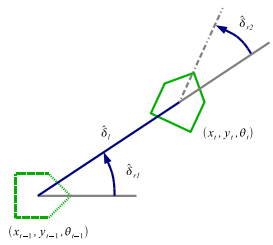

Fig. 2. Motion Model

The robot posture is defined as follows. Let us consider a robot moving on a plane, and its posture is described by

$$\boldsymbol{p} = \begin{pmatrix} x & y & \theta \end{pmatrix}^T \tag{4}$$

where x and y are the robot position, and θ is the azimuth of the robot. Assume that the robot moved from $\boldsymbol{p}_{t-1}$ to $\boldsymbol{p}_t$. Then, the odometry returns noisy $\hat{\boldsymbol{p}}_{t-1} = \begin{pmatrix} \hat{x}_{t-1} & \hat{y}_{t-1} & \hat{\theta}_{t-1} \end{pmatrix}^T$ and $\hat{\boldsymbol{p}}_t = \begin{pmatrix} \hat{x}_t & \hat{y}_t & \hat{\theta}_t \end{pmatrix}^T$. The control input can be obtained as a noisy value that includes noises as shown in Fig. 2, which is given by

$$\hat{\boldsymbol{u}}_{t-1} = \begin{pmatrix} \hat{\delta}_{r1,\,t-1} & \hat{\delta}_{l,\,t-1} & \hat{\delta}_{r2,\,t-1} \end{pmatrix}^T \tag{5}$$

Here, each component of the control input $\hat{\boldsymbol{u}}_{t-1}$ is as follows: $\hat{\delta}_{r1,\,t-1}$ is the amount of rotation before moving, $\hat{\delta}_{l,\,t-1}$ is the amount of movement, and $\hat{\delta}_{r2,\,t-1}$ is the amount of rotation after moving. $\hat{\boldsymbol{u}}_{t-1}$ can be then calculated as below:

$$\hat{\boldsymbol{u}}_{t-1} = \begin{pmatrix} \mathrm{atan2}(\hat{y}_t - \hat{y}_{t-1},\ \hat{x}_t - \hat{x}_{t-1}) - \hat{\theta}_{t-1} \\ \sqrt{(\hat{x}_t - \hat{x}_{t-1})^2 + (\hat{y}_t - \hat{y}_{t-1})^2} \\ \hat{\theta}_t - \mathrm{atan2}(\hat{y}_t - \hat{y}_{t-1},\ \hat{x}_t - \hat{x}_{t-1}) \end{pmatrix} \tag{6}$$

Equation (2) representing the action model is reduced to

$$\begin{aligned} \boldsymbol{x}_t &= g(\boldsymbol{u}_{t-1} + \boldsymbol{\rho}_{t-1},\ \boldsymbol{x}_{t-1}) \\ &= g(\hat{\boldsymbol{u}}_{t-1},\ \boldsymbol{x}_{t-1}) \\ &= \boldsymbol{x}_{t-1} + \begin{pmatrix} \hat{\delta}_{l,\,t-1}\cos(\theta_{t-1}) \\ \hat{\delta}_{l,\,t-1}\sin(\theta_{t-1}) \\ \hat{\delta}_{r1,\,t-1} + \hat{\delta}_{r2,\,t-1} \\ \mathbf{0} \end{pmatrix} \end{aligned} \tag{7}$$

© ISAROB 2013

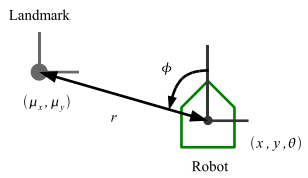

Fig. 3. Measurement model

in which $\boldsymbol{\rho}_{t-1}$ is the action noise defined by

$$\boldsymbol{\rho}_{t-1} = \begin{pmatrix} \mathcal{N}(0,\ a_1\delta^2_{r1,\,t-1} + a_2\delta^2_{l,\,t-1}) \\ \mathcal{N}(0,\ a_3\delta^2_{l,\,t-1} + a_4(\delta^2_{r1,\,t-1} + \delta^2_{r2,\,t-1})) \\ \mathcal{N}(0,\ a_1\delta^2_{r2,\,t-1} + a_2\delta^2_{l,\,t-1}) \end{pmatrix} \quad (8)$$

where a_1 to a_4 are the parameters that determine the amount of noises.

3.3 Measurement model

A rangefinder model is used for the measurement model. This model uses the measurements consisting of the relative distance r between the robot and a landmark, and the relative angle ϕ. When defining the robot posture as $(x,\ y,\ \theta)^T$, the j-th landmark position as $(\mu_{j,x},\ \mu_{j,y})$, and the measurements as $\boldsymbol{z} = (r, \phi)$, the measurement model in Eq. (3) can be rewritten by (see Fig. 3)

$$\begin{aligned} \boldsymbol{z} =& h(\boldsymbol{x}) + \boldsymbol{\varepsilon} \\ h(\boldsymbol{x}) =& \begin{pmatrix} \sqrt{(\mu_{j,x} - x)^2 + (\mu_{j,y} - y)^2} \\ \mathrm{atan2}(\mu_{j,y} - y,\ \mu_{j,x} - x) - \theta \end{pmatrix} \\ \boldsymbol{\varepsilon} =& \begin{pmatrix} \mathcal{N}(0, \sigma_r^2) \\ \mathcal{N}(0, \sigma_\phi^2) \end{pmatrix} \end{aligned} \quad (9)$$

where σ_r denotes the standard deviation for the relative noise and similarly σ_ϕ denotes one for the relative angle.

3.4 Results and considerations

Figures 4 and 5 show the estimation results of one trial for both methods, where in the figures the red dot denotes the landmark position, the black solid line is the movement trajectory of the robot, the light-blue broken line denotes the odometry value, and the blue $\times$ and solid line are the estimation results. For the estimation of self-position, it is found that both the URTSS-SLAM and UKF-SLAM methods have a high accuracy, compared to a method of using only the odometry. In particular, the estimate produced by using only the odometry displays a large deviation around the terminal point, whereas the both estimation methods give good estimates that reach the goal point. This is attributed to the fact that the both methods estimate the self-position by using the information on landmarks. It is seen that they also give all the landmark positions, i.e., the correct map estimate.

Figures 6 to 8 shows the time variation of the rms error in each axis of the robot posture. The broken line denotes the rms error for the UKF–SLAM, whereas the solid line is the rms error for the URTSS–SLAM. The rms error for the URTSS-SLAM is smaller in most of time durations than that for the UKF-SLAM. It is seen from Fig. 6 that the rms error in x-coordinate is gradually improved in its accuracy for the latter half of estimation: i.e., its accuracy recovers closely to that of around $t = 10$ [s].

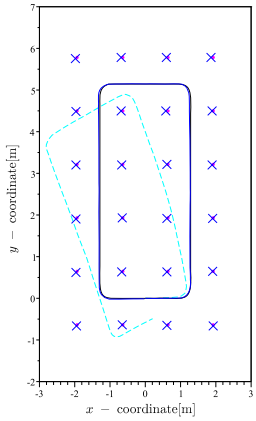

Fig. 4. Estimated robot paths and landmarks (UKF–SLAM)

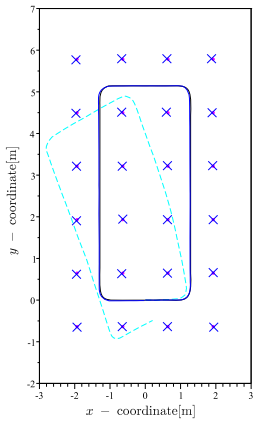

Fig. 5. Estimated robot paths and landmarks (URTSS–SLAM)

Table 2 shows the time average of the rms error for each axis of the self-position. It is seen that the URTSS-SLAM has about 5.6 [%]smaller rms error in the average of each axis, compared to the UKF-SLAM, so it is claimed that an improved accuracy has been obtained for the self-position estimate in the SLAM problem.

Figures 9 and 10 shows the rms error for the landmark position. It is found from Fig. 9 that the rms error is relatively large because the landmark is estimated with less number of measurements at start, but it becomes gradually small and

Table 2. Simulation results of localization

Algorithm	RMS error		
	x [mm]	y [mm]	θ [rad]
UKF–SLAM	36.233	23.145	0.018659
URTSS–SLAM	35.289	21.159	0.017063

© ISAROB 2013

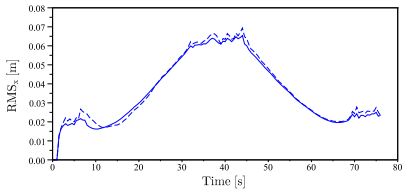

Fig. 6. RMS error for x coordinate

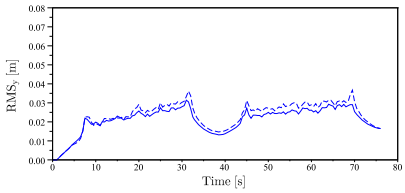

Fig. 7. RMS error for y coordinate

converges as time goes and the number of measurements increases. Two rms errors, related to the landmarks denoted by blue and yellow lines, become large once at about 10 [s] and 12 [s], decrease at about 53 [s], and after that they converge to small values. This is based on the fact that the robot measured those landmarks several times at about 10 [s] and 12 [s], moved out from the measurable range, returned to the original position at about 53 [s], and finally started to re-measure such landmarks. The rms error of the URTSS–SLAM is small and constant approximately, as seen from Fig. 10, because from the property of the URTSS the landmarks are estimated by using all the information for the estimation interval.

Table 3 shows the estimation error for the landmarks, where a landmark error was extracted when the minimum estimation covariance was achieved, and was also averaged by the number of landmarks and trials. The estimation error of the landmarks with the URTSS–SLAM is small about 6.8 [%], compared to that with the UKF-SLAM, so that it is claimed that the map accuracy has been improved, as well as the estimation accuracy of the self-position for the robot.

4 CNCLUSIONS

In this paper, the URTSS has been applied to the SLAM problem and a URTSS–SLAM has been proposed. The URTSS–SLAM is the technique of having aimed at the improvement in accuracy by reprocessing the estimation result

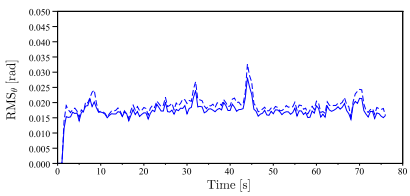

Fig. 8. RMS error for θ coordinate

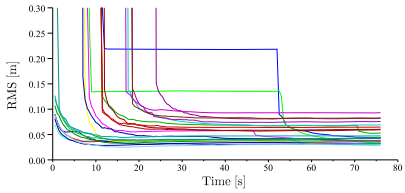

Fig. 9. RMS error for landmark location (UKF–SLAM)

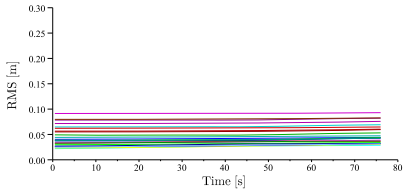

Fig. 10. RMS error for landmark location (URTSS–SLAM)

Table 3. Simulation results of landmark locations

Algorithm	error of landmark locations [mm]
UKF–SLAM	41.049
URTSS–SLAM	38.254

due to the UKF–SLAM by the URTSS. Then, the estimation accuracy of the proposed URTSS–SLAM and the conventional UKF–SLAM was compared through the simulation experiment. As a result, compared to the conventional technique, the estimation accuracy for both the self-position and the map was improved, so it can be said that the URTSS–SLAM is effective in an off-line SLAM problem.

REFERENCES

[1] Durrant-Whyte H, Bailey T (2006), Simultaneous localization and mapping Part I. IEEE Robotics & Automation Magazine 13(2): 99–110

[2] Durrant-Whyte H, Bailey T (2006), Simultaneous localization and mapping Part II. IEEE Robotics & Automation Magazine 13(3): 108–117

[3] Julier SJ, Uhlmann JK, Durrant-Whyte HF (1995), A new approach for filtering nonlinear systems. Proc. of American Control Conference, pp. 1628–1632

[4] Rauch HE, Tung F, Striebel CT (1965), Maximum likelihood estimates of linear dynamic systems. AIAA Journal 3(8): 1445–1450

[5] Terejanu G, Singh T, Scott PD (2007), Unscented Kalman filter/smoother for a CBRN Puff-based dispersion model, Proc. of the 10th Int. Conf. on Information Fusion

[6] Särkkä S (2008), Unscented Rauch–Tung–Striebel smoother. IEEE Trans. on Automatic Control 53(3), 845–849

[7] Kim C, Sakthivel R, Chung W (2008), Unscented fastSLAM: A robust and efficient solution to the SLAM problem. IEEE Trans. on Robotics 24(4), 808–820

[8] Thrun S, Burgard W, Fox D (2005), Probabilistic Robotics. The MIT Press

© ISAROB 2013

The Eighteenth International Symposium on Artificial Life and Robotics 2013 (AROB 18th '13),
Daejeon Convention Center, Daejeon, Korea, January 30-February 1, 2013

Kinodynamic motion planning and control using anisotropic damping forces

[1]Kimiko Motonaka, [1]Keigo Watanabe and [1]Shoichi Maeyama

[1]Department of Intelligent Mechanical Systems,
Division of Industrial Innovation Sciences,
Graduate School of Natural Science and Technology,
Okayama University,
3-1-1 Tsushima-naka, Kita-ku, Okayama 700-8530, Japan
E-mail: k.motonaka@usm.sys.okayama-u.ac.jp; {watanabe, maeyama}@sys.okayama-u.ac.jp
Tel&Fax: +81-86-251-8064

Abstract: We deal with gain optimization in kinodynamic motion planning by using NADFs (Nonlinear, Anisotropic, Damping Forces) and HPF (Harmonic Potential Field). The NADFs are a kind of controller which has been proposed by Masoud, and it has the effect of canceling the force in unnecessary direction (e.g. any external force or the inertial force). The NADFs have two gains, but optimizing them was not mentioned at all. In this paper, it is assumed that a mass with Kinodynamic Motion Planning is controlled in simulation. The effectiveness of NADFs is verified by comparing the control that uses only the gradient of HPF with the control that introduces the NADFs. At the same time, we apply a method called "Clamping Control" to the aforementioned situation, and accomplish a reliable convergence. It is reported through experiments that there exists a possibility of accomplishing more accurate motion planning by optimizing the gains of NADFs.

Keywords: Motion planning, Kinodynamic planning, Potential field

1 INTRODUCTION

Kinodynamics is a discipline dealing with the kinematics and dynamics simultaneously. Kinodynamic motion planning aims at synthesizing the kinematic motion planning like obstacle avoidance, and the dynamic motion planning which is needed in actual control. In this research, we deal with gain optimization in kinodynamic motion planning by using NADFs (Nonlinear, Anisotropic, Damping Forces) and HPF (Harmonic Potential Field). An HPF is a smooth potential field which has no stationary points [1]. It is guaranteed that a kinematic trajectory, which is generated by using the gradient of HPF, can reliably reach a target point. Thus, if a controlled object moves along the gradient of HPF, then such an object can reliably reach the target point. However, its trajectory deviates from the kinematic trajectory in the consequence of the inertia or an external force, even if a controller directly gives the controlled object the gradient of HPF as the control input. Then, we apply the NADFs to a controller. The NADFs is a kind of controller which has been proposed by Masoud [2], and it has the effect of canceling the force in unnecessary direction (e.g. any external force or the inertial force). By applying NADFs, the controlled object can reach the target point quickly without being affected by external forces or inertial forces. The NADFs introduced by Masoud has two gains, but he did not at all mention optimizing these gains. In this paper, it is assumed that a point mass with Kinodynamic Motion Planning is controlled in simulation. The effectiveness of NADFs is verified by comparing the control that uses only the gradient of HPF with the control that introduces the NADFs. At the same time, by changing the gains manually, the trend in the behavior of the controlled object is confirmed according to the change of the gains. We also prove the efficacy of introducing the NADFs in the environment where an external force exists. It is found in simulations that the NADFs are able to cope with the applied external force, but its posture diverges sometimes after the controlled object reaches the target point. Therefore, we apply a method called "Clamping ontrol" to the aforementioned situation, and accomplish a reliable convergence. "Clamping control" is a control method proposed by Masoud, which makes an attractive force in around the target point to confine the controlled object to the target point. It is reported through the experiments that the NADFs can be applied in an environment where external forces exist; the convergence time and trajectory are changed by tuning the gains; and there exists a possibility of accomplishing accurate motion planning by optimizing the gains.

2 MOTION PLANNING USING HPF

Kinodynamic motion planning using NADFs is based on the motion planning using HPF. In the motion planning using HPF, a controlled object is controlled by control input based on the gradient of HPF. HPF is generated from the boundary information on the environment. In what follows, a generation method of HPF and the motion planning using only the gradient of HPF are described.

2.1 Generation method of HPF and the calculation of gradient vector

An HPF is a smooth potential field which has no stationary points. For generating an HPF, an environment is at first segmented into small grids, and the potential at each grid (i, j) is calculated. In initial states, potential is set to 1 for the bound

© ISAROB 2013

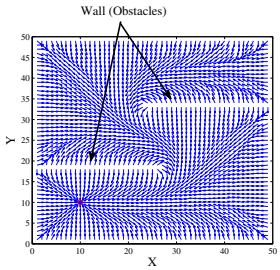

Fig. 1. Normalized gradient field

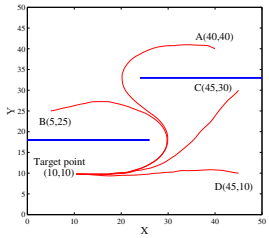

Fig. 2. Path generation by using gradient of HPF

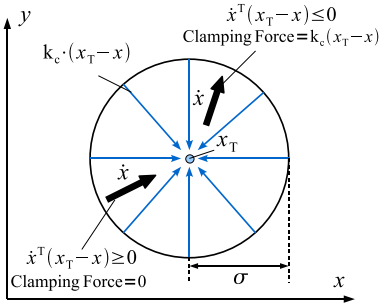

Fig. 3. The clamping control

of obstacles and the environment, and set to 0 for an intended target point. Then, to compute the potential in each grid, the following equation is calculated iteratively:

$$U(i,j) = \frac{1}{4}(U_{i,j-1} + U_{i,j+1} + U_{i-1,j} + U_{i+1,j}) \tag{1}$$

Note that, $U(i,j)$ is the value of the potential at an (i,j) grid in the environment field. By calculating Eq. (1) iteratively, the surface of the generated HPF becomes smooth, because the average of potentials in the four neighborhood grids is saved as the potential at the center grid.

Then, a gradient in each position is calculated by using the generated HPF. Fig. 1 shows gradient vectors calculated from HPF. Note that these vectors have been normalized by the grid size. The position circled in Fig. 1 shows the configured target point. Using this gradient vector, a kinematic trajectory can reliably reach a target point from anywhere in the field while avoiding obstacles. Letting $V(\boldsymbol{x})$ be a potential value in position $\boldsymbol{x} = [x\ y]^{\mathrm{T}}$, a gradient on the surface of HPF in position $\boldsymbol{x}$ can write $-\nabla V(\boldsymbol{x})$. Using gradient $-\nabla V(\boldsymbol{x})$, a kinematic trajectory can be generated from the following equation:

$$\dot{\boldsymbol{x}} = -\nabla V(\boldsymbol{x}) \tag{2}$$

As an example, Fig. 2 shows the calculated kinematic trajectories from four configured start positions to the target point. Configured start positions A to D and the target point were set as shown in Fig. 2. It is confirmed from Fig. 2 that a kinematic trajectory using the gradient of HPF can reach a target point from anywhere in the field while avoiding obstacles.

2.2 Control of a point mass based on the gradient of HPF

When controlling an object having a mass, dynamics including object mass, inertial force and external force should be considered. Koditschek et al. [3] proposed a method for designing a control input that considers dynamics by adding both the gradient of HPF and a damping force linearly proportional to the velocity. In this method, when controlling a point mass with 1 [kg], the control input $\boldsymbol{u}$ is given as follow:

$$\boldsymbol{u} = -b \cdot \dot{\boldsymbol{x}} - \nabla V(\boldsymbol{x}) \tag{3}$$

where b denotes a damping coefficient and also is positive constant. In Eq. (3), control input consists of the gradient of the current position, $-\nabla V(\boldsymbol{x})$, and the damping force linearly proportional to the velocity, $-b \cdot \dot{\boldsymbol{x}}$. This damping force increases in proportion to increasing of the damping coefficient or velocity, and suppresses the acceleration of a point mass.

3 MOTION PLANNING USING NADFS

The method described in previous section, which is based on only the gradient of HPF, does not work well under an environment where an external force exists. Masoud [2] proposed a control method that can cancel out the effect of external forces by combining the gradient of HPF with NADFs. The following equation is the controller proposed by Masoud [2]:

$$\boldsymbol{u} = -b_d \cdot h(\boldsymbol{x}, \dot{\boldsymbol{x}}) - k \cdot \nabla V(\boldsymbol{x}) \tag{4}$$

where b_d and k denote positive constant gains, and $h(\boldsymbol{x}, \dot{\boldsymbol{x}})$ is the proposed NADFs, which is given by

$$h(\boldsymbol{x}, \dot{\boldsymbol{x}}) = \left[\boldsymbol{n}^{\mathrm{T}}\dot{\boldsymbol{x}}\boldsymbol{n} + \left(\frac{V(\boldsymbol{x})^{\mathrm{T}}}{\|\nabla V(\boldsymbol{x})\|} \cdot \dot{\boldsymbol{x}} \cdot \Phi(\nabla V(\boldsymbol{x})^{\mathrm{T}}\dot{\boldsymbol{x}})\right)\frac{V(\boldsymbol{x})^{\mathrm{T}}}{\|\nabla V(\boldsymbol{x})\|}\right] \tag{5}$$

Here, $\boldsymbol{n}$ is a unit vector orthogonal to ∇V and $\Phi(\nabla V(\boldsymbol{x})^{\mathrm{T}}\dot{\boldsymbol{x}})$ is the unit step function. The function Φ takes 0 if $\nabla V(\boldsymbol{x})^{\mathrm{T}}\dot{\boldsymbol{x}}$ is negative, and otherwise takes 1. The function $\Phi(\nabla V(\boldsymbol{x})^{\mathrm{T}}\dot{\boldsymbol{x}})$ is prepared to check the consistency between the direction of current velocity of the controlled onject and the direction of gradient of HPF. If the direction of the current velocity matches the gradient direction, then $\nabla V(\boldsymbol{x})^{\mathrm{T}}\dot{\boldsymbol{x}}$ takes a positive value and $\Phi(\nabla V(\boldsymbol{x})^{\mathrm{T}}\dot{\boldsymbol{x}})$ takes 1, thus, a force toward the current velocity direction is increased. By contrast, if their directions are not matched, then $\nabla V(\boldsymbol{x})^{\mathrm{T}}\dot{\boldsymbol{x}}$ takes a negative value and $\Phi(\nabla V(\boldsymbol{x})^{\mathrm{T}}\dot{\boldsymbol{x}})$ takes 0, thus, a force canceling the current velocity is added. At the same time, a force toward the gradient direction is added, and the controlled object is returned to the kinematic trajectory. Thus, this method is also applicable to the control of an object in an environment where external forces exist.

4 CLAMPING CONTROL

The control using NADFs can guide a controlled object to a target point while cancelling external forces. However,

© ISAROB 2013

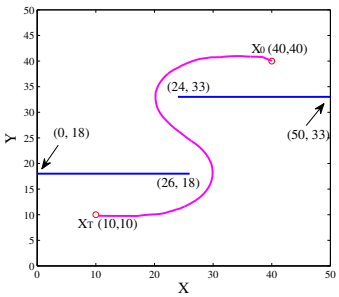

Fig. 4. Simulation environment

after reaching to the target point, the controlled object sometimes cannot maintain any states and therefore it oscillates and/or diverges. Therefore, we apply "clamping control". Fig. 3 shows the schematic structure of the clamping control. The clamping control is applied in a circle area as shown in Fig. 3. The center point of the region is a target point and its radius is σ. In this area, if a controlled object moves toward the target point, then the clamping control is not applicable. By contrast, if a controlled object moves against the target point in the area, then the clamping control adds a force $(\boldsymbol{x}_{\mathrm{T}} - \boldsymbol{x})$ in a direction toward the target point, and converges a controlled object on the target point. Appending the clamping control to the control input based on NADFs given in Eq. (4), it follows that

$$\boldsymbol{u} = -b_d \cdot h(\boldsymbol{x}, \dot{\boldsymbol{x}}) - k \cdot \nabla V(\boldsymbol{x}) - k_{\mathrm{C}} \cdot \boldsymbol{F}_{\mathrm{C}}(\boldsymbol{x}, \dot{\boldsymbol{x}}) \quad (6)$$

where k_{C} denotes a positive constant gain related to the clamping control and $\boldsymbol{F}_{\mathrm{C}}$ is clamping control given by

$$\boldsymbol{F}_{\mathrm{C}}(\boldsymbol{x}, \dot{\boldsymbol{x}}) = (\mathbf{x}_{\mathrm{T}} - \mathbf{x}) \cdot \Phi(\sigma - |\boldsymbol{x}_{\mathrm{T}} - x|) \cdot \Phi(\dot{x}^{\mathrm{T}}(\boldsymbol{x}_{\mathrm{T}} - x) \quad (7)$$

Here, the unit step function $\Phi(\sigma - |x_{\mathrm{T}} - x|)$ is set to check whether the controlled object is in the region, and $\Phi(\dot{x}^{\mathrm{T}}(x_{\mathrm{T}} - x))$ is prepared to check whether the direction of current velocity of the controlled object consists with the direction of the target point.

5 SIMULATION EXPERIMENT

In this section, we made a simulation experiment for comparing three methods as described above (using gradient of HPF only, applying NADFs, and combining NADFs and clamping control). Fig. 4 shows an experimental environment, where there are two obstacles. In this experiment, it is aimed at guiding a point mass with 1 [kg] from the initial position $x_0(40, 40)$ to the target point $x_{\mathrm{T}}(10, 10)$. The trajectory drawn in Fig. 4 is a kinematic trajectory calculated from the gradient of HPF. This kinematic trajectory is set to an ideal trajectory.

5.1 A point mass control in the absence of external forces

At first, we compared three different types control in the absence of external forces. The point mass has the mass of 1 [kg], so that the equation of motion with the controller based on only using the gradient of HPF is given by

$$\ddot{\boldsymbol{x}} = -b \cdot \dot{\boldsymbol{x}} - \nabla V(\boldsymbol{x}) \quad (8)$$

Similarly, one based on using the gradient and NADFs and that based on additionally applying clamping control are given as follows:

$$\ddot{\boldsymbol{x}} = -b_d \cdot h(\boldsymbol{x}, \dot{\boldsymbol{x}}) - k \cdot \nabla V(\boldsymbol{x}) \quad (9)$$

$$\ddot{\boldsymbol{x}} = -b_d \cdot h(\boldsymbol{x}, \dot{\boldsymbol{x}}) - k \cdot \nabla V(\boldsymbol{x}) - k_{\mathrm{C}} \cdot \boldsymbol{F}_{\mathrm{C}}(\boldsymbol{x}, \dot{\boldsymbol{x}}) \quad (10)$$

In this simulation, the gains k and k_{C} are set to $k = 1$ and $k_{\mathrm{C}} = 10$ constantly, and we compared the results when changing the gains b and b_d.

Figs. 5–7 show the trajectory of the point mass and the convergence time with each controller when the gains b and b_d are set to 0.1, 1.0 and 10.0. The trajectory of the point mass came closer to the kinematic trajectory (Fig. 4) in proportion to increasing gains. This is because the controller based on only the gradient of HPF suppresses the velocity with an increase in gain b. On the other hand, in the case of the controller including NADFs, a force canceling the velocity except the matched direction of the gradient is increased with an increase in gain. As a result, the both controllers can guide the mass point to a target point with high accuracy. As long as looking at the trajectory, there exist no big difference between the controller using NADFs and that not using NADFs, but there is a big difference in convergence time. In Fig. 5, the convergence time is increased particularly with an increase in gain b. By contrast, in Fig. 6, convergence time is shorter with an increase in gain b_d. This is because the NADFs consider the direction of the velocity and suppress unnecessary force only. In addition, when using the controller including the clamping control (Fig. 7), the trajectory and the convergence time are almost the same as those using NADFs, but the overshoot was suppressed after the point mass reached the target point.

In this experiment, it is confirmed that all controllers can guide the point mass to the target point by tuning the gains b and b_d. In particular, the controller using NADFs can guide the point mass quickly with a high accuracy. Moreover, we also confirmed that the overshoot is suppressed by applying the clamping control.

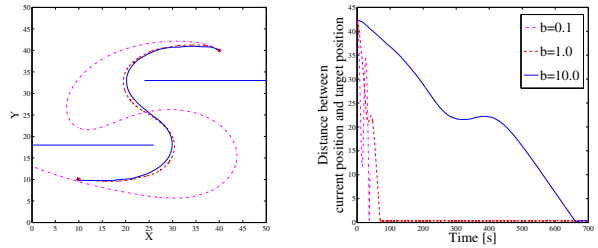

Fig. 5. Simulation results using formula (8) in static environment (gains $b = 0.1$, 1.0 and 10.0)

© ISAROB 2013

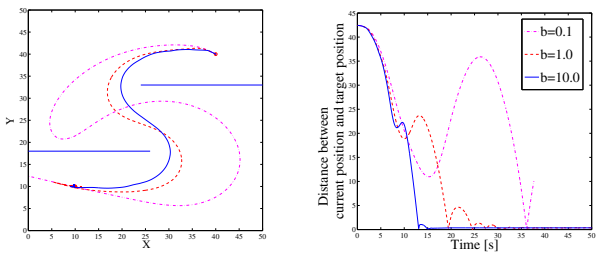

Fig. 6. Simulation results using formula (9) in static environment (gains $b_d = 0.1$, 1.0 and 10.0)

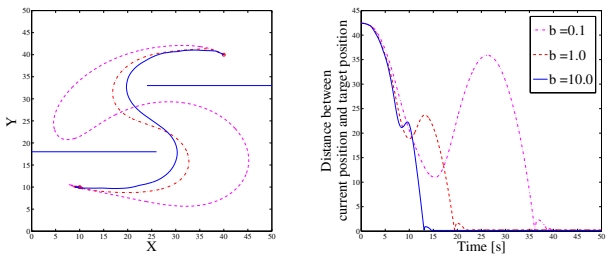

Fig. 7. Simulation results using formula (10) in static environment (gains $b_d = 0.1$, 1.0 and 10.0)

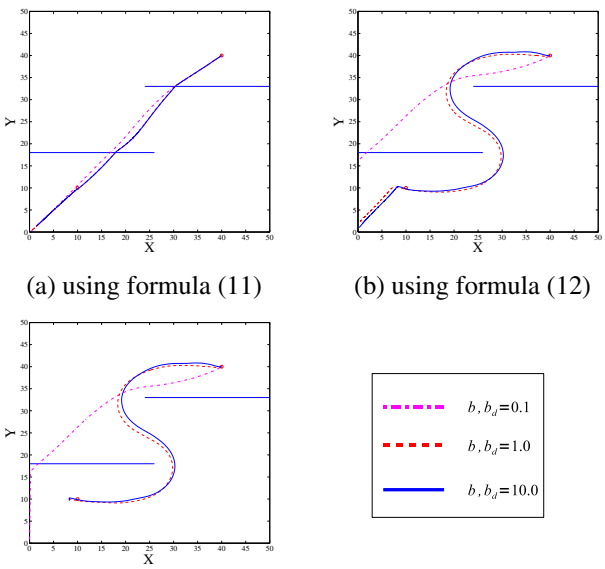

(a) using formula (11) (b) using formula (12)

(c) using formula (13)

Fig. 8. Simulation results where external forces exist (gains $b, b_d = 1.0$, 5.0 and 10.0)

5.2 A point mass control in the environment where external forces exist

Next, assume that external forces $\boldsymbol{f}_{\mathrm{g}} = [4\ 4]^{\mathrm{T}}$ exist in the environment. Behavioral models of the point mass with each controller are as follows, respectively:

$$\ddot{\boldsymbol{x}} = -b \cdot \dot{\boldsymbol{x}} - \nabla V(\boldsymbol{x}) - \boldsymbol{f}_{\mathrm{g}} \tag{11}$$

$$\ddot{\boldsymbol{x}} = -b_d \cdot h(\boldsymbol{x}, \dot{\boldsymbol{x}}) - k \cdot \nabla V(\boldsymbol{x}) - \boldsymbol{f}_{\mathrm{g}} \tag{12}$$

$$\ddot{\boldsymbol{x}} = -b_d \cdot h(\boldsymbol{x}, \dot{\boldsymbol{x}}) - k \cdot \nabla V(\boldsymbol{x}) - k_{\mathrm{C}} \cdot \boldsymbol{F}_{\mathrm{C}}(\boldsymbol{x}, \dot{\boldsymbol{x}}) - \boldsymbol{f}_{\mathrm{g}} \tag{13}$$

In this simulation, the gains k and k_{C} are set to $k = 1$ and $k_{\mathrm{C}} = 10$ constantly, and we compared the results of when changing the gains b and b_d.

Fig. 8 shows the trajectory of the point mass using each controller when the gains b and b_d are set to 1.0, 5.0 and 10.0. As shown in Fig. 8(a), the controller using only the gradient of HPF cannot suppress the external forces, and the point mass entirely deviated from the route. By contrast, the controller including NADFs suppressed the external forces, and guided the point mass to the target point by amplifying the gains (Fig. 8(b)). However, the point mass could not keep the state at the target point. The controller including NADFs and clamping control can guide the point mass, and kept the state at the target point (Fig. 8(c)). In this experiment, it is confirmed that the controller based on NADFs can also apply in the environment where external forces exist, and a controlled object can keep its state at the target point by adding the clamping control .

6 CONCLUSIONS

In this paper, we have compared three controllers: the controller by using only the gradient of HPF; the controller including NADFs; and the controller including NADFs and clamping control. At the same time, by changing the gains manually, the trend in the behavior of the controlled object is confirmed according to the change of the gains. As a result, kinodynamic motion planning by using NADFs can guide the controlled object to the target point quickly, and it is robust against external forces. Moreover, by applying the clamping control, the secure convergence to the target point was able to be realized. In future work, we will optimize gains for NADFs by using GA and validate the associated behavior.

REFERENCES

[1] Jan V (2007), Navigation of mobile robots using potential fields and computational intelligence means. Acta Polytechnica Hungarica, 4(1):63–74.

[2] Masoud A (2010), Kinodynamic motion planning. IEEE Robotics & Automation Magazine, 17(1):85–99.

[3] Elon R, Daniel E K (1995), Exact robot navigation using artificial potential fields. IEEE Trans. on Robotics and Automation, 8(5):501–518.

© ISAROB 2013

The Eighteenth International Symposium on Artificial Life and Robotics 2013 (AROB 18th '13),
Daejeon Convention Center, Daejeon, Korea, January 30-February 1, 2013

Application of variable search space GAs to fine gain tuning of model-based robotic servo controller

A. Otsuka[1], and F. Nagata[2]
Tokyo University of Science, Yamaguchi, Japan
(Tel: 0836-88-3500 Fax: 0836-88-3400)
[1]otsuka_a@rs.tus.ac.jp [2]nagata@rs.tus.ac.jp

Abstract: In this paper, genetic algorithms with a variable search space function are proposed for fine gain tuning of a resolved acceleration controller which is one of model based robotic servo controllers. Genetic algorithms proposed in this paper have a variable search space function which is activated if the optimal solution is not updated for fixed generations. The function is terminated if the optimal solution is updated, or if the optimal solution is not updated within certain generations. This proposed method is evaluated through a trajectory following control problem in simulation. Simulations for sine curve trajectories are conducted using the dynamic model of PUMA560 manipulator. The result shows the improvement of optimal solution and its convergence.

Keywords: Fine Gain Tuning, Genetic Algorithms, PUMA560.

1 Introduction

At designing a control system, feedback gains tuning is the complicated problem. Conventionally, the gains have been experimentally and instinctively tuned by trial and error based on known model information and an operator's skill. For articulated-type industrial robots, this problem tends to become more complicated. Recently, the computing power is increased significantly, so that the gains in a control system can be numerically tuned through computer simulations by using the target dynamic model. Gain tuning problem is a typical non-convex optimization problem, so that genetic algorithms have been applied to efficiently solve this problem. For example, Deris et al. [1] considered the stabilization of an inverted pendulum which can be controlled by moving a car in an intelligent way. Ya and Meng [2] proposed a genetic algorithm-based optimized hybrid controller which is suitable for controlling both linear and nonlinear systems. Also, Nagata et al. [3] proposed an effective fine gain tuning method for a computed torque controller, in which genetic algorithms were applied to obtain more suitable feedback gains after manual turning process.

Genetic algorithms proposed in this paper have a variable search space function which is activated if the optimal solution is not updated for fixed generations. The function is terminated if the optimal solution is updated, or if the optimal solution is not updated within certain generations. The propose method is evaluated through a trajectory following control problem using sine curves. Simulations are conducted by using the dynamic model of PUMA560 manipulator. Two types of the desired trajectories are designed with sine curves on x-y plane and x-z plane. The results of the simulations showed the improvement of optimal solution and its convergence. The simulation environment used is called Robotics Toolbox and was developed by Corke [4].

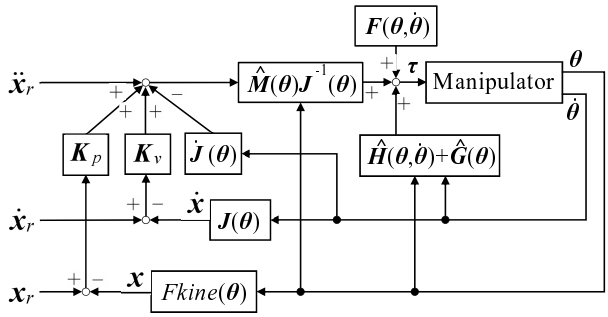

Fig. 1. Block diagram of resolved acceleration control

2 Robotic servo controller

The dynamic model of an industrial manipulator without friction torque is generally given by

$$\boldsymbol{M}(\boldsymbol{\theta})\ddot{\boldsymbol{\theta}} + \boldsymbol{H}(\boldsymbol{\theta},\dot{\boldsymbol{\theta}}) + \boldsymbol{G}(\boldsymbol{\theta}) = \boldsymbol{\tau} \tag{1}$$

where $\boldsymbol{M}(\boldsymbol{\theta}) \in \Re^{6\times6}$, $\boldsymbol{H}(\boldsymbol{\theta},\dot{\boldsymbol{\theta}}) \in \Re^{6\times1}$ and $\boldsymbol{G}(\boldsymbol{\theta}) \in \Re^{6\times1}$ are the inertia term, Coriolis/centrifugal force term and gravity term in joint space, respectively. $\boldsymbol{\theta}=[\theta_1, ..., \theta_6]^T$, $\dot{\boldsymbol{\theta}} \in \Re^{6\times1}$, $\ddot{\boldsymbol{\theta}} \in \Re^{6\times1}$, are the vector of joint angular position, velocity and acceleration. $\boldsymbol{\tau} \in \Re^{6\times1}$ is the joint driven torque vector. **Fig. 1.** shows the block diagram of the resolved acceleration controller, which is known as one of model based robotic servo controllers. Where $\boldsymbol{F}(\boldsymbol{\theta},\dot{\boldsymbol{\theta}}) \in \Re^{6\times1}$ is the frictional torque term. Desired position, velocity and acceleration in Cartesian coordinate system must be given to the reference of the servo system in order to apply the controller to a trajectory fol-

© ISAROB 2013

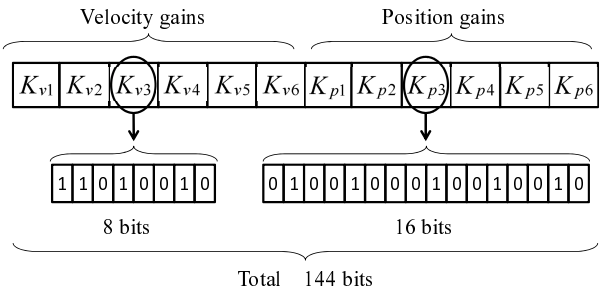

Fig. 2. Example of chromosome of an individual

Table 1. Initial parameters of genetic algorithms

Population size	100
Number of elite	6
Selection	Tournament selection and elitism
Crossover	Uniform crossover (rate=87.5%)
Mutation	Random mutation (rate=1.0 %)
Search space of K_{vi}	$50 \leq K_{vi} \leq 220$
Search space of K_{pi}	$1000 \leq K_{pi} \leq 35000$
Maximum generation	200

lowing control problem. The resolved acceleration controller generates the joint driven torque as given by

$$\boldsymbol{\tau} = \hat{\boldsymbol{M}}(\boldsymbol{\theta})\boldsymbol{J}^{-1}(\boldsymbol{\theta})\Big[\ddot{\boldsymbol{x}}_r + \boldsymbol{K}_v\{\dot{\boldsymbol{x}}_r - \dot{\boldsymbol{x}}\} + \boldsymbol{K}_p\{\boldsymbol{x}_r - \boldsymbol{x}\} - \dot{\boldsymbol{J}}(\boldsymbol{\theta})\dot{\boldsymbol{\theta}}\Big] + \hat{\boldsymbol{H}}(\boldsymbol{\theta}, \dot{\boldsymbol{\theta}}) + \hat{\boldsymbol{G}}(\boldsymbol{\theta}) \quad (2)$$

where the hat symbol means the estimated term obtained by computing inverse dynamics via recursive Newton-Euler formulation. $\boldsymbol{x} \in \Re^{6\times 1}$ consists of position vector $[x, y, z]^T$ and orientation vector $[\alpha, \beta, \gamma]^T$. $\dot{\boldsymbol{x}} \in \Re^{6\times 1}$ and $\ddot{\boldsymbol{x}} \in \Re^{6\times 1}$ are the velocity and acceleration vectors, respectively. $\boldsymbol{x}_r$, $\dot{\boldsymbol{x}}_r$ and $\ddot{\boldsymbol{x}}_r$ are the desired vectors of position, velocity and acceleration, respectively. $\boldsymbol{\theta}$, $\dot{\boldsymbol{\theta}}$, $\boldsymbol{x}$ and $\dot{\boldsymbol{x}}$ are actual controlled values. $Fkine(\boldsymbol{\theta})$ is the function of forward kinematics given by $\boldsymbol{x}$=$Fkine(\boldsymbol{\theta})$. $\boldsymbol{K}_v$=diag$(K_{v1}, ..., K_{v6})$. $\boldsymbol{K}_p$=diag$(K_{p1}, ..., K_{p6})$ are the feedback gains of velocity and position respectively, each of which is set to a positive definite diagonal matrix. $\hat{\boldsymbol{M}}(\boldsymbol{\theta})$, $\hat{\boldsymbol{H}}(\boldsymbol{\theta}, \dot{\boldsymbol{\theta}})$ and $\hat{\boldsymbol{G}}(\boldsymbol{\theta})$ are called nonlinear compensation terms, which act on the cancellation of nonlinearity of manipulator. The nonlinear compensation terms are effective to achieve a stable trajectory following control. If the estimate error dose not exist at all, then the second order error equation of this system described in Eq. (3) is derived from Eqs. (1) and (2).

$$\ddot{\boldsymbol{e}} + \boldsymbol{K}_v\dot{\boldsymbol{e}} + \boldsymbol{K}_p\boldsymbol{e} = \boldsymbol{O} \quad (3)$$

where $\boldsymbol{e} = \boldsymbol{x}_r - \boldsymbol{x}$, $\dot{\boldsymbol{e}} = \dot{\boldsymbol{x}}_r - \dot{\boldsymbol{x}}$, $\ddot{\boldsymbol{e}} = \ddot{\boldsymbol{x}}_r - \ddot{\boldsymbol{x}}$. Accordingly, a nominal response is obtained by adjusting $\boldsymbol{K}_v$ and $\boldsymbol{K}_p$ suitably considering the following equation based on critically damped condition.

$$K_{vi} = 2\sqrt{K_{pi}} \qquad (i = 1, ..., 6) \quad (4)$$

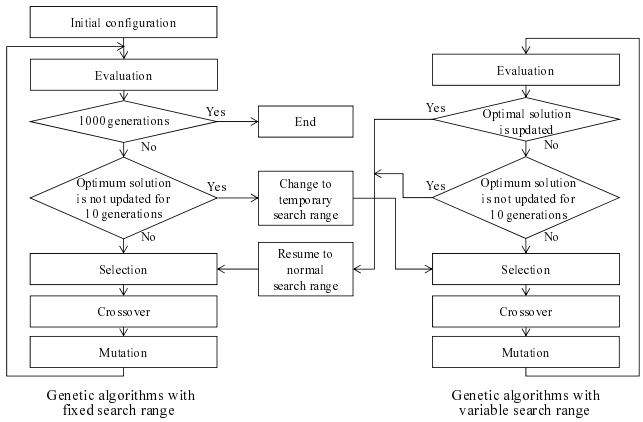

Fig. 3. Flowchart of proposed genetic algorithms

If $\boldsymbol{K}_v$ and $\boldsymbol{K}_p$ are selected based on Eq. (4), the stability is guaranteed and the errors convergence to zero.

3 Fine gain tuning by genetic algorithms

In this section, genetic algorithms are used to optimize $\boldsymbol{K}_v$ and $\boldsymbol{K}_p$. In order to apply genetic algorithms, $\boldsymbol{K}_v$ and $\boldsymbol{K}_p$ are transformed into a digit binary string as chromosome. Diagonal elements of them are encoded into 8 bits and 16 bits codes respectively, so that an individual chromosome is composed of 144 (=8 × 6+16 × 6) bits as shown in **Fig. 2.**. A population has 100 individuals and each individual in initial population is generated within the expectable values. The parameters of GAs are defined as shown **Table 1**. In our study, variable search space GAs are proposed and applied. **Fig. 3.** shows the flowchart of the proposed variable search space GAs, in which if the optimal gain is unchanged for 10 generations then the search space is varied. This means that the search spaces are redefined temporarily based on the optimal gains at the generation.

$$K_{pi\min} = K_{pi\text{best}} - 10000 \quad (5)$$

$$K_{pi\max} = K_{pi\text{best}} + 10000 \quad (6)$$

Each individual is evaluated through the following evaluation function.

$$E_v = \sqrt{\sum_{k=1}^{500} ||\boldsymbol{e}(k)||} \quad (7)$$

where k is the sampled discrete-time number in simulation. Note that, this evaluation function also represents the position errors.

4 Simulations

4.1 Desired trajectory

In this section, to evaluate the effectiveness of the proposed method, simulations are carried out by us-

© ISAROB 2013

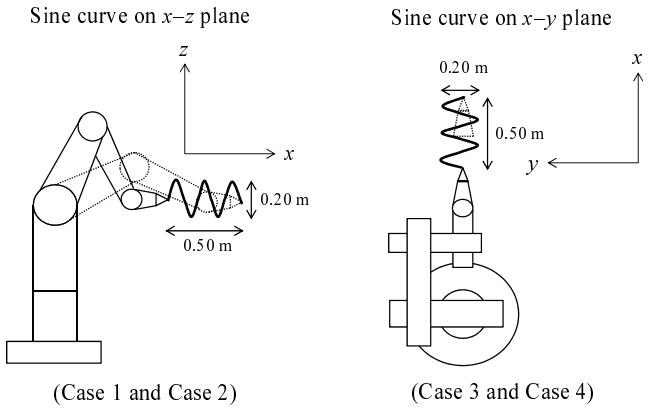

Fig. 4. Illustration of desired trajectory

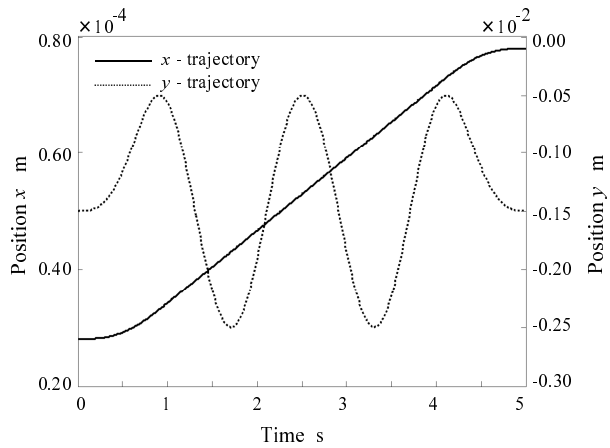

Fig. 5. Desired trajectory using Eq. (8)

ing the dynamic model of PUMA560 manipulator on MATLAB system [4]. First of all, in order to apply the resolved acceleration control method to PUMA560 manipulator, the desired trajectory in Cartesian coordinate system must be prepared. Discrete values of desired position, velocity and acceleration are generated for each sampling period in advance. Four type trajectories are prepared to be compared for each and set as below.

$$\text{Case 1.} \quad z = 0.1\sin(10\pi x) \tag{8}$$

$$\text{Case 2.} \quad z = 0.1\sin(20\pi x) \tag{9}$$

$$\text{Case 3.} \quad y = 0.1\sin(10\pi x) - 0.15 \tag{10}$$

$$\text{Case 4.} \quad y = 0.1\sin(20\pi x) - 0.15 \tag{11}$$

Fig. 4. is the overview of the desired manipulator movement. The desired positions given by Eq. (8) and (9) are designed with sinusoidal waves on x-z plane. Also, the desired positions given by Eqs. (10) and (11) are generated with sinusoidal waves on x-y plane. As an example, **Fig. 5.** illustrates the desired trajectory of Eq. (10) in x and y directions. The position x of desired trajectory is generated with a 4-1-4 order polynomial equation. The initial and final position/orientation vectors are set to $\boldsymbol{x}_{init} = (0.28, -0.15, 0.00, 0.00, \pi/2, 0.00)$, $\boldsymbol{x}_{fin} = (0.78, -0.15, 0.00, 0.00, \pi/2, 0.00)$, respectively.

In this simulation, we set them such that the total simulation time is 5.00 sec, the sampling width is 0.01 sec, the acceleration and deceleration time is 1.00 sec. To obtain satisfactory and safe control performance with avoiding singularities, $\boldsymbol{K}_v$ and $\boldsymbol{K}_p$ are roughly tuned with trial and error, considering the critically damped condition.

4.2 Dynamic model

In this simulation experiment, it is assumed that the friction is composed of viscous friction and Coulomb friction. Therefore, robotic dynamic model considering friction can be rewritten by

$$\boldsymbol{M}(\boldsymbol{\theta})\ddot{\boldsymbol{\theta}} + \boldsymbol{H}(\boldsymbol{\theta}, \dot{\boldsymbol{\theta}}) + \boldsymbol{G}(\boldsymbol{\theta}) + \boldsymbol{F}(\boldsymbol{\theta}, \dot{\boldsymbol{\theta}}) = \boldsymbol{\tau} \tag{12}$$

$\boldsymbol{F}(\boldsymbol{\theta},\dot{\boldsymbol{\theta}})$ is composed of viscous friction and Coulomb friction and given by

$$\boldsymbol{F}(\boldsymbol{\theta}, \dot{\boldsymbol{\theta}}) = \boldsymbol{B}\boldsymbol{G}_r^2\dot{\boldsymbol{\theta}} + \boldsymbol{G}_r\boldsymbol{\tau}_c\{\mathrm{sign}(\dot{\boldsymbol{\theta}})\} \tag{13}$$

where $\boldsymbol{B} \in \Re^{6\times 6}$ is the coefficient matrix of viscous friction at each motor, $\boldsymbol{G}_r \in \Re^{6\times 6}$ is the reduction gear ratio matrix which represents the motor speed to joint speed, and $\boldsymbol{\tau}_c\{\mathrm{sign}(\dot{\boldsymbol{\theta}})\}$ is the Coulomb friction torque appeared at each motor. If $\mathrm{sign}(\dot{\boldsymbol{\theta}})$ is positive/negative, then $\boldsymbol{\tau}_c = \boldsymbol{\tau}_c^+/\boldsymbol{\tau}_c = \boldsymbol{\tau}_c^-$, respectively. The friction parameters of PUMA560 manipulator such as $\boldsymbol{B}$, $\boldsymbol{G}_r$, $\boldsymbol{\tau}_c^+$ and $\boldsymbol{\tau}_c^-$ are technically available to engineers[4].

It is confirmed through preliminary simulations that this friction term, which works as disturbance as shown in **Fig. 1.**, causes undesirable error even in critically damped condition. Also, in actual robot systems there inevitably exists the modeling error with respect to $\hat{\boldsymbol{M}}(\boldsymbol{\theta})$, $\hat{\boldsymbol{H}}(\boldsymbol{\theta},\dot{\boldsymbol{\theta}})$ and $\hat{\boldsymbol{G}}(\boldsymbol{\theta})$. That is the reason why the fine gain turning after manual gain tuning is important for robotic servo system in order to realize more accurate trajectory following control.

4.3 Result and discussions

Fig. 6. shows the minimum E_v values at every generation searched by the proposed GAs. It is observed that optimal solutions of each case are almost converged before 50 generations. In **Fig. 7.**, the curved line is critical damping condition, and the plotted points are the optimal gains of each case. It is observed that most of gains lie on under-damping condition. **Table 2** tabulates each best fitness E_{vbest} which is obtained using the four optimal gains.

At first, E_{vbest} in case of using the trajectories in x-y and x-z planes are compared. **Table 2** indicates that

Table 2. Best fitness comparison for each case

	Case 1	Case 2	Case 3	Case 4
Ev_{best}	0.0630	0.0874	0.0672	0.1147

© ISAROB 2013

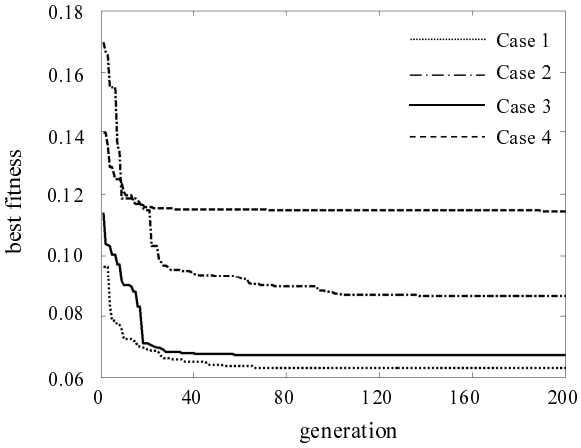

Fig. 6. Evolutionary histories of best fitness

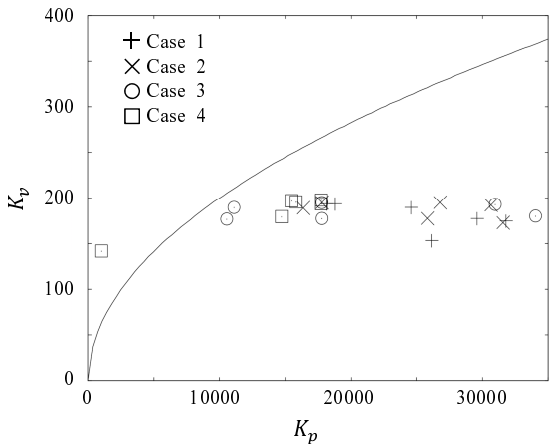

Fig. 7. Best gains and critical damping condition

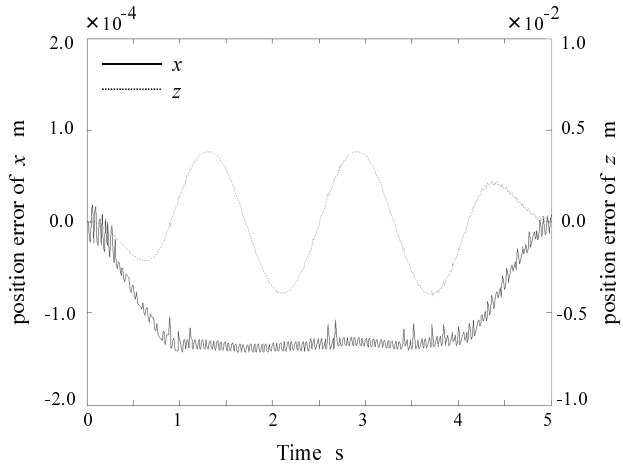

Fig. 8. Position error in Case 1

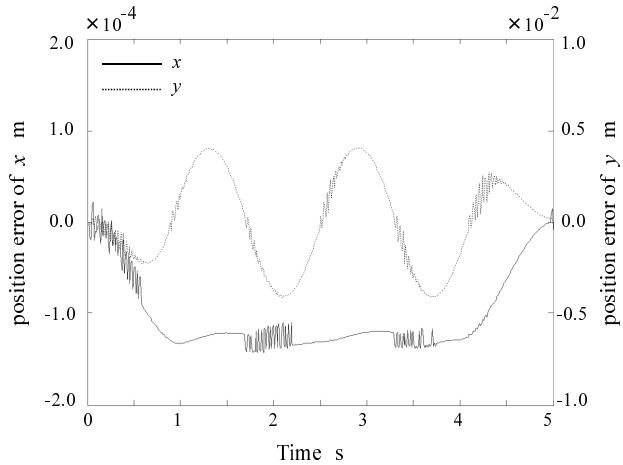

Fig. 9. Position error in Case 3

the position error of Case 3 was larger than Case 1. The similar tendency was observed from E_{vbest} of Case 2 and Case 4. The reason is supposed that only three joints must be driven to track the desired trajectories given by Eq. (8) and (9), whereas all joints must be driven when Eq. (10) and (11) are applied.

Next, E_{vbest} in case of using two kinds of frequencies are further compared. E_{vbest} of Case 1 is smaller than the one of Case 2. The reason is supposed that the desired velocity of Case 1 is slower than the one of Case 2. In other words, the desired trajectories shown in **Fig. 4.** are calculated within the range $0.28 \leq x \leq 0.78$, so the higher the frequency becomes, the longer the moved distance becomes. The similar tendency can be observed between Case 3 and Case 4. **Fig. 8.** and **Fig. 9.** are two examples of simulation when E_{vbest} shown in Table 2 are applied.

5 Conclusions

In this paper, genetic algorithms with a variable search space function has been proposed for fine gain tuning of a resolved acceleration controller. The proposed GAs are applied for a trajectory following control based on several sine curves using dynamic model of PUMA560 manipulator. It has been confirmed that the proposed GAs effectively can reduce the generations for convergence and search better optimal gains.

References

[1] S. Deris, S. Omatu and K. Kitagawa, "Stabilization of inverted pendulum by the genetic algorithm, " Proceedings of 1995 IEEE International Conference on Systems, Man and Cybernetics, pp. 4372–4377, 1995.

[2] L. S. Ya and J. E. Meng, "Optimal hybrid control of linear and nonlinear systems, " Proceedings of the 40th IEEE Conference on Decision and Control, pp. 1669–1674, 2001.

[3] F. Nagata and K. Watanabe, "Fine Gain Tuning for Model-Based Robotic Servo Controllers Using Genetic Algorithms, " Advances in Computer Science and Engineering, Vol. 2, No. 3, pp. 201–219, 2008.

[4] P. I. Corke, "A robotics toolbox for MATLAB, " IEEE Robot Automation Magazine, Vol. 3, No. 1, pp. 24–32, 1996.

© ISAROB 2013

The Eighteenth International Symposium on Artificial Life and Robotics 2013 (AROB 18th '13),
Daejeon Convention Center, Daejeon, Korea, January 30-February 1, 2013

Propulsive force analysis of a pectoral fin for rajiform type fish robots from fluid dynamic aspects

Masaaki Ikeda[1], Shigeki Hikasa[1], Keigo Watanabe[1], and Isaku Nagai[1]

[1] Okayama University, Okayama, Okayama 700-8530, Japan
(Tel: +81-86-251-8064, Fax: +81-86-251-8064)
(ikeda-m@usmm.sys.okayama-u.ac.jp)

Abstract: In this paper, we analyze the propulsive force generated from pectoral fins for a rajiform type fish robot from fluid dynamic aspects. A pectoral fin of the rajiform type fish robot is constructed by multiple fin-rays, which move independently, and a film of pushing water. Then, the propulsive force of the fish robot is analyzed from the momentum of the fluid surrounding for every fin between fin-rays. The total propulsive force for one pectoral fin is the sum of these momenta. The propulsion speed of a fish robot is determined from the difference of the propulsive force generated from pectoral fins, and the resistance force that the fish robot receives from the water when moving forward. The effectiveness of the calculated propulsive force is examined through numeric simulation results.

Keywords: Fish robot, Rajiform type swimming, Propulsive force analysis

1 INTRODUCTION

Oceanographic investigation for investigating mineral resources at sea bottom and an aquatic life is carried out actively. Autonomous (unmanned) underwater vehicles called AUVs are needed for such oceanographic investigation [1] [2]. Furthermore, an application to search activities in the shoal, where the introduction of any AUV is not easy, is also attractive. The conventional AUV has a common mechanism for propulsion using screw propellers. The underwater propulsion using screw propellers is good at performing a long-distance cruise and keeping a maximum speed. On the other hand, any screw propeller is not suitable for sudden acceleration or rapid turning.

When observing underwater living things, they hide themselves from an underwater foreign enemy, or have captured foods in the crevice of reefs, and manipulate sudden acceleration and rapid turning easily [3]. Fishes are in the aquatic life that can manipulate such things. It is known [4] that fishes can produce propulsive forces by oscillating the various kinds of fins and the body. The propulsion induced by oscillating fins and the body can change the propulsive force and direction easily by changing the oscillatory situation. Fishes are divided into some types, depending on every motion that produces propulsive forces. Among such motion types, a ray such as Manta is classified into a rajiform swimming type. Such type fishes can control underwater position and posture by using only one pair of right and left pectoral fins. Therefore, since there are few portions to be operated, compared to other swimming types, and it need not necessarily operate all fins cooperatively, it is easy to realize mechanical reappearance and mimicking in motion.

In this paper, we propose a diving method for a rajiform type fish robot, and examine the usefulness of the proposal technique by calculating the propulsive force by a pectoral fin. Then, the effectiveness of the diving method proposed here is checked by numeric simulations.

2 RAJIFORM TYPE FISH ROBOT

A rajiform type fish robot has a central float and a pectoral fin on each side, as shown in Fig. 1. The float is designed so that the specific gravity of the fish robot may be set to 1. A pectoral fin has six structures, each of which is called a fin-ray. The fin-ray has mounted a fin-ray driving unit, and each fin-ray can be driven independently. The film for pushing out water is mounted between fin-rays. The control circuit and power supply for controlling the pectoral fin of the fish robot are arranged by expanding electric wiring to the outside of water.

2.1 Fin-ray driving unit

The fin-ray driving unit is composed of a waterproofed box and a gear part, as shown in Fig. 2. The waterproofed box has one RC servo-motor in inside. The transfer part of driving force to a fin-ray is waterproofed by taking out the driving force of a motor using a stan-tube. A gear part is used to change the rotation axis from a motor 90 deg, and it is realized using a bevel gear.

2.2 Waveform with fin-rays

A pectoral fin of the rajiform type fish robot generates a propulsive force by driving the fin as a traveling wave. When the form of the traveling wave formed at a pectoral fin is a sinusoidal wave form, the angular velocity ω_k of the k-th fin

© ISAROB 2013

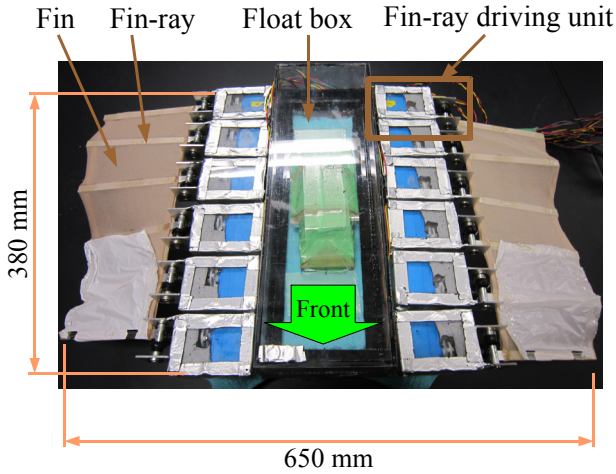

Fig. 1. Rajiform type fish robot

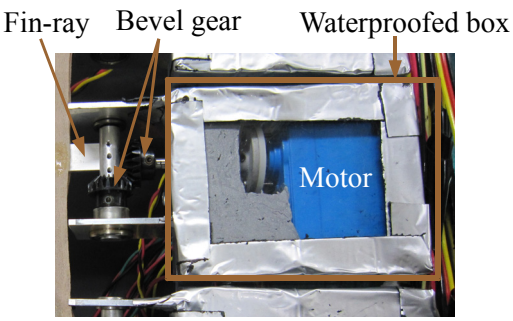

Fig. 2. Fin-ray driving unit

ray from a front side is expressed by the following equation:

$$\omega_k = \frac{2\pi\theta_{\max}}{T}\cos\left(\frac{2\pi t}{T} + (k-1)\phi\right) \tag{1}$$

Here, t [s] is time, $\theta_{\max}$ [rad] is amplitude, T [s] is a period, and ϕ [rad] is the phase difference between adjacent fin-rays. The waveform of a sinusoidal wave is changeable by changing these values.

3 DIVING METHOD

A diving method is proposed for a rajiform type fish robot using a forward propulsion speed. As shown in Fig. 3, two front fin-rays and the partial fin between them are fixed, where the fixed partial fin tilts with a fixed angle ψ. The propulsive force to the forward direction in this fish robot is obtained by making a traveling wave using other remaining fin-rays. When the robot moves forward by the propul-

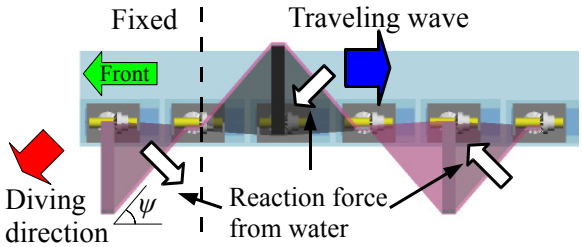

Fig. 3. Diving motion

sive force obtained from the traveling wave, the propulsive force to the diving direction occurs, according to the resistance force that the fixed partial fin receives from water. The propulsive force to the diving direction generated in this way is used in order that this fish robot may dive.

4 ANALYSIS OF PROPULSIVE FORCE

In this section, the equation for calculating the forward propulsion speed and diving speed of a rajiform type fish robot is derived. First, the equation for the forward speed of a rajiform type fish robot is derived from a forward propulsive force and a resistance force. Next, the equation for diving speed of a rajiform type fish robot is derived from the resistance added to the fixed partial fin. Two assumptions are set to derive these equations. One assumption is that the whole body of this fish robot is in static water. This means that the wave or the vortex does not occur in the water around this fish robot. When a rajiform type fish robot moves propulsively, the fish robot receives a resistance force by wave or vortex generated from itself, and a profile drag force with water by the profile. However, it is difficult to analyze the resistance force by wave or vortex. Therefore, the resistance force by wave and vortex is included by setting a profile drag coefficient as a larger value. The other assumption is to set the profile drag coefficient for this fish robot to 2.0. This value was decided based on the fact that the profile drag coefficient in a cube was 1.07, and that the maximum of a profile drag coefficient was 2.0.

4.1 Propulsive force between fin-rays

A pectoral fin has several fin-rays. Any two adjacent fin-rays and the fin existing between them are considered. The forces which this partial fin receives from water are shown in Fig. 4 as f_x and f_y. The way of the water on the considered partial fin is set as control volume (CV). Assume that the stream of the circumference of CV flows in from A_1 side in Fig. 4, and flows out of A_2 side. The momenta for the inflow and outflow per unit time are calculated from the area and the flow velocity that flows into CV, and the area and the

© ISAROB 2013

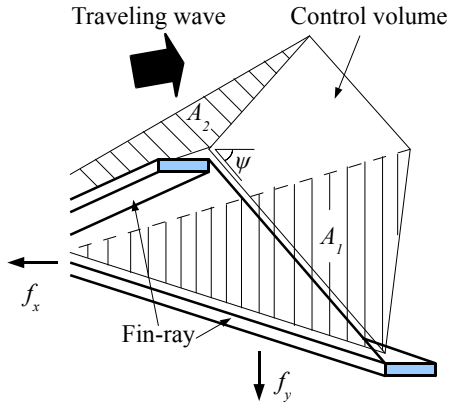

Fig. 4. Generated forces by two fin-rays

flow velocity that flows out of CV. The force that the considered partial fin receives from water is calculated from the difference between the momenta, which are produced when the surrounding water of CV flows in and flows out. The mean angular velocity of a fin-ray ω, the speed of a traveling wave u, the slant of a partial fin ψ, the inflow area A_1 and the outflow area A_2 of CV are expressed respectively by

$$\omega = \frac{4\theta_{\max}}{T} \tag{2}$$

$$u = \frac{\omega a}{\theta_{\max}\sin\phi} \tag{3}$$

$$\psi = \mathrm{atan}\frac{L\sin(\theta_{\max}\sin\phi)}{a} \tag{4}$$

$$A_1 = L^2\sin(\theta_{\max}\sin\phi)/2 \tag{5}$$

$$A_2 = A_1\cos\psi \tag{6}$$

where a is a distance between fin-rays and L is the length of a fin-ray. f_x which is the force of the forward direction, and f_y which is the force of the dive direction are expressed by the following equations:

$$f_x = \rho(v_x - u)^2 A_1(1-\cos\psi) \tag{7}$$

$$f_y = \rho(v_x - u)^2 A_2\sin\psi \tag{8}$$

where ρ is the density of water.

4.2 Forward velocity

A rajiform type fish robot has a pectoral fin in right and left, respectively. Only the surface projected on the direction of motion of a traveling wave pushes water, and generates propulsive force. Therefore, the forward propulsive force F_x generated from one pectoral fin of a fish robot is $2\pi/\phi$ times the force to the motion direction f_x generated from between fin-rays. Thus, F_x is expressed by the following equation:

$$F_x = \frac{2\pi}{\phi}\rho(v_x - u)^2 A_1(1-\cos\psi) \tag{9}$$

However, the forward propulsive force receives a constraint by the number of fin-rays n for making a traveling wave. Therefore, when $\pi/\phi > n$, π/ϕ is set to n. The resistance force D_x that a rajiform type fish robot receives from water is the sum of the profile-drag force for the body and the oscillating fin, and the resistance force for the fixed fin. D_x is expressed by the following equation:

$$D_x = \frac{1}{2}C_D\rho v_x^2 S_1 + 2\rho v_x^2 A_1(1-\cos\psi) \tag{10}$$

where the projected area of the propulsion direction is S_1. When the forward propulsive force F_x and the resistance force D_x are equal, the forward propulsion speed v_x is expressed by the following equation:

$$v_x = \frac{-\beta + \sqrt{\beta^2 - 4\alpha\gamma}}{2\alpha} \tag{11}$$

where α, β and γ are defined respectively as follows:

$$\alpha \triangleq \frac{1}{2}C_D S_1 + 2A_1(1-\cos\psi)(1-\frac{\pi}{\phi})$$

$$\beta \triangleq \frac{4\pi}{\phi}A_1(1-\cos\psi)u$$

$$\gamma \triangleq -\frac{2\pi}{\phi}A_1(1-\cos\psi)u^2$$

4.3 Diving speed

Since fin-rays of a fish robot are oscillated symmetrically with respect to the horizon, it is considered that the average propulsive force to the diving direction generated by the pectoral fin is 0. Therefore, the propulsive force to the diving direction is only a propulsive force to the dive direction generated by the fixed partial fins. In other words, the propulsive force F_y to the diving direction is the sum of f_y's generated by the fixed partial fins. Since the fixed partial fins may not make a traveling wave, u that is a speed of a traveling wave is 0. From equation (8), F_y is expressed by the following equation:

$$F_y = 2\rho v_x^2 A_2\sin\psi \tag{12}$$

When a rajiform type fish robot advances in the diving direction, the profile-drag force D_y which it receives is expressed by the following equation:

$$D_y = \frac{1}{2}C_D\rho v_y^2 S_2 \tag{13}$$

Here, the projected area to the diving direction is S_2. When the propulsive force F_y and the resistance force D_y to the diving direction are equal, the diving speed v_y is expressed by the following equation:

$$v_y = \sqrt{\frac{4v_x^2 A_2\sin\psi}{C_D S_2}} \tag{14}$$

© ISAROB 2013

5 NUMERICAL SIMULATION

When a rajiform type fish robot is diving by the method proposed in Section 3, the propulsion speed is changed by the phase difference ϕ [rad] between adjacent fin-rays, the amplitude $\theta_{\max}$ [rad] and the period T [s], associating with the oscillating fins. Change of a diving speed is examined by a numeric simulation by fixing two design parameters and changing one of the three above parameters using the equation derived in Section 4. Other parameters are set to n =4, C_D =2, L =150 [mm], a =60 [mm], ρ =1 [g/cm^3], S_1 =28000 [mm^2] and S_2 =250000 [mm^2].

The result of a numeric simulation is shown in Fig. 5. Fig. 5(a) shows the change of diving speed when changing $\theta_{\max}$ while T =2 [s] and ϕ =0.52 [rad] (=30 [deg]). Fig. 5(b) shows the change of a diving speed when changing T while $\theta_{\max}$ =0.52 [rad] and ϕ =0.52 [rad]. Fig. 5(c) shows the change of a diving speed when changing ϕ while $\theta_{\max}$ =0.52 [rad] and T=2 [s]. Fig. 5(a) shows that the diving speed of a fish robot becomes so speedy that the amplitude of the oscillating fin is large. Fig. 5(b) shows that the diving speed of a fish robot is so fast that the period of the oscillating fin is small. In Fig. 5(c), the diving speed of a fish robot is the fastest, when the phase difference between fin-rays is approximately set around 0.69 to 0.87 [rad] (=40 to 50 [deg]). This is because it becomes $\pi/\phi = n$ at the time of $\pi/\phi > n$, so it is restricted as the forward propulsive force of the fish robot stated in Section 4.2. Since the rajiform type fish robot used in this paper is n=4, a diving speed displays the maximum at the time of phase difference 0.79 [rad] (=45 [deg]). Therefore, this result is appropriate.

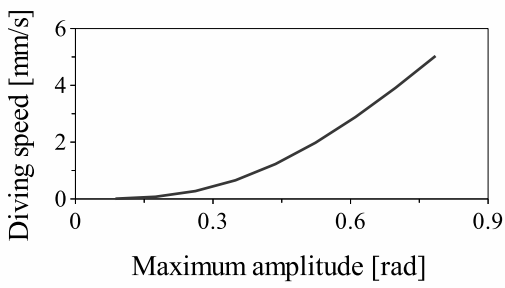

(a) Diving speed vs. maximum amplitude

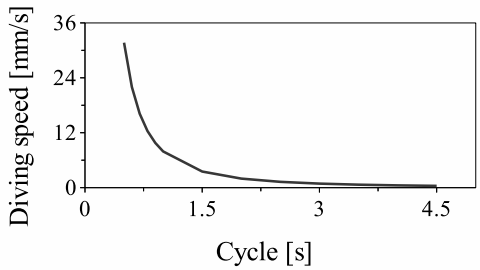

(b) Diving speed vs. cycle

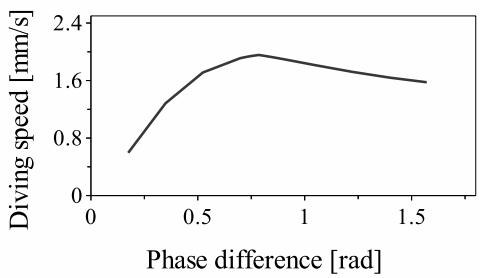

(c) Diving speed vs. phase difference between fin-rays

Fig. 5. Diving speed

6 CONCLUSION

In this paper, we have proposed a diving method for the rajiform type fish robot. The diving speed obtained by the proposed diving method is calculated from the propulsive force obtained from a pectoral fin, and the resistance force that the fish robot receives from water. Furthermore, the effectiveness of the calculated propulsive force is examined by numeric simulation results. In the future, the effectiveness of the proposed technique will be confirmed by experiments using an actual rajiform type fish robot.

REFERENCES

[1] Yuh J (2000), Design and control of autonomous underwater robots: a survey. Autonomous Robots 8(1): 7–24

[2] Watanabe K and Izumi K (2008), Skilful control for underactuated robot systems: from the ground to the air and underwater. Proc. of the 2nd International Conference on Underwater System Technology: Theory and Applications 2008 (USYS '08), pp. 4–5

[3] Ynag S, Qiu J, Han X (2009), Kinematics modeling and experiments of pectoral oscillation propulsion robotic fish. Journal of Bionic Engineering 6: 174–179

[4] Zhou C, Low KH (2012), Design and locomotion control of a biomimetic underwater vehicle with fin propulsion, IEEE/ASME Transactions on Mechatronics 17(1): 25–35

© ISAROB 2013

The Eighteenth International Symposium on Artificial Life and Robotics 2013 (AROB 18th '13),
Daejeon Convention Center, Daejeon, Korea, January 30-February 1, 2013

Underactuated Control for a Blimp with Four-Propellers by a Logical Switching Method

Yoshikazu Nakamura[1], Keigo Watanabe[1], and Isaku Nagai[1]

[1]Department of Intelligent Mechanical Systems, Division of Industrial Innovation Sciences,
Graduate School of Natural Science and Technology,
Okayama University,
3-1-1 Tsushima-naka, Kita-ku, Okayama 700-8530, Japan
E-mail: nakamura-y@usm.sys.okayama-u.ac.jp; {watanabe, in}@sys.okayama-u.ac.jp
Tel&Fax: +81-86-251-8064

Abstract: Although most of existing airships employ control methods by combining propellers and rudders, such a control approach has the problem that the maneuverability is deteriorated if their traveling speed is slow. In this research, "X4-Blimp" controlled by only four propellers is proposed. Since the X4-Blimp can control its position and attitude by regulating the output of four propellers, it can realize high maneuverability, irrespective of its traveling speed. However, it is not easy to control the X4-Blimp, because it is an underactuated system. This paper proposes a method for controlling the X4-Blimp by switching two controllers, one of which is constructed by combining models that include nonlinear terms and models that only include linear terms, where those are separated from the derived dynamic model. The effectiveness of the proposed method is verified by some simulations.

Keywords: X4-Blimp, Underactuated control, Switching control

1 INTRODUCTION

In recent years, unmanned aerial vehicles are being expected to be used for the vegetational observation and the information collection of disaster sites [1]. Especially, airships that can float by its own buoyancy are attractive, because they are effective in energy consumption. Small airships called "blimp" have been developing to make the management easy. Although most of existing airships employ control methods by combining propellers and rudders, such a control approach has the problem that the maneuverability is deteriorated if their traveling speed is slow because the airflow received by rudders is weakened. In this research, "X4-Blimp" is propsed as a blimp controlled by only four propellers without any rudders, and the objective aims at controlling it.

This paper is organized as folllows: the proposed X4-Blimp is explained in section 2. A dynamic model is derived in section 3 and partial underactuated controllers are designed in section 4. Logical switching rules are created in section 5, simulaton results are shown in section 6 and the conclusion is drawn in secton 7.

2 OVERVIEW OF THE X4-BLIMP

2.1 Structure of the X4-Blimp

The X4-Blimp proposed in this research is composed of an envelope, a gondola and propellers as shown in Fig. 1. The envelope is filled with helium gas to balance airframe mass with the buoyancy. The envelope form is a spheroid to decrease air resistance for traveling direction. The gondola includes batteries and controllers, and it is suspended from the envelope. The gondola form is a rectangular solid to maintain the space for the controllers etc. and simplify a calculation of the moment of inertia. The four propellers are attached on up, down, left and right sides of the gondola with the same distance from the center of the gondola.

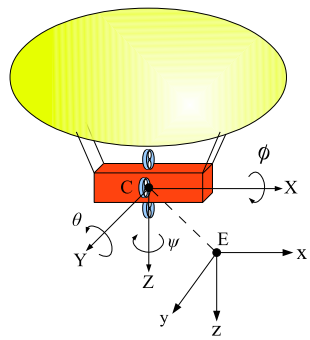

Fig. 1. Definition of the coordinates

2.2 Definition of the coordinates

In general, when rigid body motion is considered, the center of gravity of the rigid body is discussed as the representative point. However, the X4-Blimp motion is considered with the center of the gondola as a representative point in this paper. A definition of coordinates is shown in Fig. 1, and the robot coordinate C is defined such that the origin is the center of the gondola, positive X-axis is set as the forward direction of the airframe, positive Y-axis is set as the right direction of the airframe, and positive Z-axis is set to be downward perpendicular to the airframe. Similarly, the world coordinate E is a right-handed coordinate where positive z-axis is set to be vertically downward. The center position of the gondola is represented by $\boldsymbol{\xi} = [x, y, z]^T$ in the world coordinate, and the rotational angles for roll, pitch, and yaw in the robot coordinate system are represented as ϕ, θ and ψ respectively, then the attitude of the gondola is represented by $\boldsymbol{\eta} = [\phi, \theta, \psi]^T$. A rotation matrix $\boldsymbol{R}$ to transform the robot coordinate to the world coordinate is derived as follows:

$$\boldsymbol{R} = \begin{bmatrix} c\theta c\psi & s\phi s\theta c\psi - c\phi s\psi & c\phi s\theta c\psi + s\phi s\psi \\ c\theta s\psi & s\phi s\theta s\psi + c\phi c\psi & c\phi s\theta s\psi - s\phi c\psi \\ -s\theta & s\phi c\theta & c\phi c\theta \end{bmatrix} \quad (1)$$

© ISAROB 2013

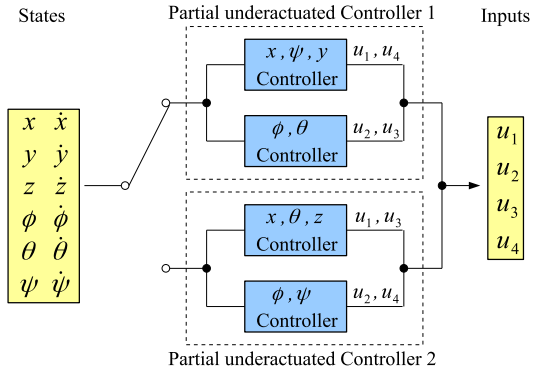

Fig. 2. Concept of the proposed controller

where cA is $\cos A$ and sA is $\sin A$.

3 DERIVATION OF DYNAMIC MODEL

A dynamic model of the X4-Blimp is derived by refering to X4-AUV studied in Watanabe et al. [2], the dynamic model of the X4-Blimp is derived as

$$\begin{cases} \ddot{x} &= (\cos\theta\cos\psi u_1)/m \\ \ddot{y} &= (\cos\theta\sin\psi u_1)/m \\ \ddot{z} &= (-\sin\theta u_1)/m \\ \ddot{\phi} &= (\dot{\theta}\dot{\psi}(I_Y - I_Z) + u_2)/I_X \\ \ddot{\theta} &= (\dot{\phi}\dot{\psi}(I_Z - I_X) - J_p\dot{\psi}\Omega + lu_3)/I_Y \\ \ddot{\psi} &= (\dot{\phi}\dot{\theta}(I_X - I_Y) + J_p\dot{\theta}\Omega + lu_4)/I_Z \end{cases} \tag{2}$$

where the mass of the airframe is m, the moment of inertia for each axis is represented by I_X, I_Y and I_Z respectively, the moment of inertia of the propeller is J_p and $\Omega = \omega_2 + \omega_4 - \omega_1 - \omega_3$. When four propellers are numbered from 1 to 4 in the clockwise from the upper propeller and the direction of rotatinal velocity of each propeller is positive if it is defined as clockwise. And the input u_1 of translational motion, the input u_2 of roll motion, the input u_3 of pitch motion and the input u_4 of yaw motion are represented by

$$u_1 = b(\omega_1^2 + \omega_2^2 + \omega_3^2 + \omega_4^2) \tag{3}$$
$$u_2 = d(-\omega_2^2 - \omega_4^2 + \omega_1^2 + \omega_3^2) \tag{4}$$
$$u_3 = b(\omega_1^2 - \omega_3^2) \tag{5}$$
$$u_4 = b(\omega_2^2 - \omega_4^2) \tag{6}$$

4 DESIGN OF PARTIAL UNDERACTUATED CONTROLLERS

Since the system of the X4-Blimp represented by the dynamic model of Eq. (2) is an underactuated system with four inputs and 12 states, it is different to realize underactuated control. As shown in Fig. 2, two partial underactuated controllers for a model with 4 inputs 10 states are designed by combining a controller for a 2-input/4-state partial model with a controller for a 2-input/6-state partial model. The whole system is controlled by switching these two partial underactuated contollers. To perform a chaind from transformation, the dynamic model is partially linearized such that

$$\begin{aligned} \ddot{x} &= w_1 \\ \ddot{y} &= \tan\psi w_1 \\ \ddot{z} &= -\tan\theta\sec\psi w_1 \\ \ddot{\phi} &= w_2 \\ \ddot{\theta} &= w_3 \\ \ddot{\psi} &= w_4 \end{aligned} \tag{7}$$

Then, the inputs are transformed as follows

$$w_1 = \cos\theta\cos\psi u_1/m \tag{8}$$
$$w_2 = (\dot{\theta}\dot{\psi}(I_Y - I_Z) + u_2)/I_X \tag{9}$$
$$w_3 = (\dot{\phi}\dot{\psi}(I_Z - I_X) - J_p\dot{\psi}\Omega + lu_3)/I_Y \tag{10}$$
$$w_4 = (\dot{\phi}\dot{\theta}(I_X - I_Y) + J_p\dot{\theta}\Omega + lu_4)/I_Z \tag{11}$$

The partial underactuated controller 1 is designed from a 2-input/6-state partial model for x, ψ and y, and from a 2-input/4-state partial model for ϕ and θ. The partial underactuated controller 2 is designed from a 2-input/6-state partial model for x, θ and z, and from a 2-input/4-state partial model for ϕ and ψ. When a chained form transformation in [4] is applied, the 2-input/6-state partial model for x, ψ and y is denoted by

$$z_{11} = h_1 = x \tag{12}$$
$$z_{12} = L_f h_1 = \dot{x} \tag{13}$$
$$z_{21} = L_{g_1} L_f h_2 = \tan\psi \tag{14}$$
$$z_{22} = L_f L_{g_1} L_f h_2 = \frac{\dot{\psi}}{\cos^2\psi} \tag{15}$$
$$z_{31} = h_2 = y \tag{16}$$
$$z_{32} = L_f h_2 = \dot{y} \tag{17}$$

Then, the inputs are transformed as follows

$$v_1 = w_1 \tag{18}$$
$$v_2 = \frac{1}{\cos^2\psi} w_4 + \frac{2\tan\psi}{\cos^2\psi}\dot{\psi}^2 \tag{19}$$

From the above results, a chained from is derived by

$$\begin{aligned} \ddot{z}_{11} &= v_1 \\ \ddot{z}_{21} &= v_2 \\ \ddot{z}_{31} &= z_{21} v_1 \end{aligned} \tag{20}$$

To apply a method in Xu and Ma [3] to Eq. (20), it is rewritten for state variables such as

$$\begin{aligned} \dot{x}_1 &= x_2, & \dot{x}_2 &= v_1 \\ \dot{x}_3 &= x_4, & \dot{x}_4 &= v_2 \\ \dot{x}_5 &= x_6, & \dot{x}_6 &= x_3 v_1 \end{aligned}$$

Then the control input v_1 is denoted by

$$v_1 = -(s_1 + s_2)x_2 - s_1 s_2 x_1 \tag{21}$$

where $s_2 > s_1 > 0$. To control the underactuated system, a coordinate transformation is performed to design a controller based on a discontinuous model:

$$z_i = x_i \ (i = 1, 2, 3, 4), \quad z_i = \frac{x_i}{x_1} \ (i = 5, 6) \tag{22}$$

© ISAROB 2013

The Eq. (22) is rewritten as follows

$$\dot{z_1} = z_2 \quad (23)$$
$$\dot{z_2} = -(s_1+s_2)z_2 - s_1 s_2 z_1 \quad (24)$$
$$\dot{Z}_{3-6} = (A_1 + A_2(t))Z_{3-6} + Bv_2 \quad (25)$$

where $Z_{3-6} = [z_3, z_4, z_5, z_6]^T$. Here, A_1, $A_2(t)$ and B are denoted by

$$A_1 = \begin{bmatrix} 0 & 1 & 0 & 0 \\ 0 & 0 & 0 & 0 \\ 0 & 0 & s_1 & 1 \\ s_1^2 & 0 & 0 & s_1 \end{bmatrix}, \quad B = \begin{bmatrix} 0 \\ 1 \\ 0 \\ 0 \end{bmatrix}$$

$$A_2(t) = C \begin{bmatrix} 0 & 0 & 0 & 0 \\ 0 & 0 & 0 & 0 \\ 0 & 0 & -1 & 0 \\ -(s_1+s_2) & 0 & 0 & -1 \end{bmatrix}$$

where $C = \frac{z_2}{z_1} + s_1$. The controllability of $[A_1, B]$ is confirmed. A controllable matrix is represented as $[B\ A_1B\ A_1^2B\ A_1^3B]$. It is regular because $s_1>0$. Since A_1+BL is controllable, the feedback gain $L = [l_1, l_2, l_3, l_4]$ is calculated to make matrix A_1+BL as the Hurwitz matrix by the pole placement method. The control input v_2 is denoted by

$$v_2 = LZ_{3-6} = l_1 z_3 + l_2 z_4 + l_3 z_5 + l_4 z_6 \quad (26)$$

Thus, since it can be stabilized to the origin, the control inputs for the chained form are derived as follows

$$v_1 = -(s_1+s_2)\dot{x} - s_1 s_2 x \quad (27)$$
$$v_2 = l_1 \tan\psi + l_2 \frac{\dot{\psi}}{\cos^2\psi} + l_3 \frac{y}{x} + l_4 \frac{\dot{y}}{x} \quad (28)$$

In this way, the controller for the 2-input/6-state partial model for x, ψ and y is designed. Next, the controller for the 2-input/6-state partial model for ϕ and θ is designed by a linear feedback such as

$$w_2 = -k_1\phi - k_2\dot{\phi} \quad (k_1, k_2 > 0) \quad (29)$$
$$w_3 = -k_3\theta - k_4\dot{\theta} \quad (k_3, k_4 > 0) \quad (30)$$

The partial underactuated controller 1 for a model with 4 inputs and 10 states is designed by combining the controllers for x, ψ and y with the controller for ϕ and θ.

Similarly, the partial underactuated controller 2 is designed by combining the controller for the 2-input/6-state partial model for x, θ and z with the controller for the 2-input/4-state partial model for ϕ and ψ. When the partial model for x, θ and z is transformed to a chained form, the input transformation is denoted by

$$v_1 = -(s_1+s_2)\dot{x} - s_1 s_2 x$$
$$v_2 = l_1\left(-\frac{\tan\theta}{\cos\psi}\right) + l_2\left(-\frac{\dot{\theta}}{\cos\psi\cos^2\theta}\right) + l_3\frac{z}{x} + l_4\frac{\dot{z}}{x}$$

The control inputs based on the chained form transformation is denoted by

$$w_1 = v_1 \quad (31)$$
$$w_3 = -\cos\psi\cos^2\theta \cdot v_2 - 2\tan\theta \cdot \dot{\theta}^2 \quad (32)$$

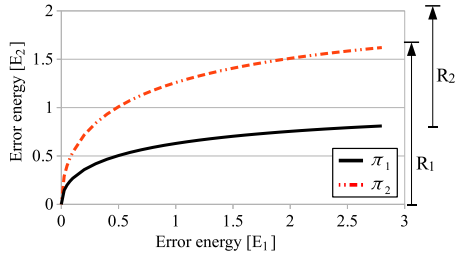

Fig. 3. Structure of energy regions

The 2-input/4-state partial model for ϕ and ψ is derived by a linear feedback such as

$$w_2 = -k_1\phi - k_2\dot{\phi} \quad (k_1, k_2 > 0) \quad (33)$$
$$w_4 = -k_3\psi - k_4\dot{\psi} \quad (k_3, k_4 > 0) \quad (34)$$

The partial underactuated controller 2 for the model with 4 inputs and 10 states is designed by combining the controller for x, θ and z with the controller for ϕ and ψ.

5 ENERGY REGION BASED SWITCHING METHOD

Switching the two partial underactuated controllers for 4 inputs 10 states is considered to control an underactuated system with 4 inputs 12 states. However, if input chattering phenomena occur when controllers are switched, an excessive burden is placed on motors. Therefore, a switching method[5] that has multiple boundary regions is used to prevent the chattering phenomena.

The energy is defined from the errors of generalized coordinates. Since the state x is doubly generated from the set of (x, ψ, y) and (x, θ, z), and similarly the corresponding attitude angle ϕ is also doubly generated from the set of (ϕ, θ) and (ϕ, ψ), the errors for the stabilization to the origin are directly represented by ψ, y, θ and z because both partial underactuated controllers always stabilize the state x and the angle ϕ to the origin. Then, the energy based on the errors is defined as follows:

$$E_1 = \psi^2 + y^2 \quad (35)$$
$$E_2 = \theta^2 + z^2 \quad (36)$$

In Fig. 3, a two-dimensional plane is represented by E_1 and E_2, and hysteresis like boundary lines π_1 and π_2 to separate the energy plane are represented respectively by

$$\pi_1(E_1) = 1 - e^{-\sqrt{E_1}} \quad (37)$$
$$\pi_2(E_1) = 2\pi_1 \quad (38)$$

In Fig. 3, the partial underactuated controller 1 is used on the region R_1, whereas the partial underactuated controller 2 is used on the regionR_2. Considering an overlapped region, switching rules are decided as follows:

Rule 1 :
If $0 < E_2 \le \pi_1(E_1)$ then $s_t = y$
Rule 2 :
If $\pi_1(E_1) < E_2 < \pi_2(E_1)$ and $s_{t-1} = y$ then $s_t = y$
Rule 3 :

© ISAROB 2013

Table 1. Parameters for the X4–Blimp

Parameter	Description	Value	Unit
m	Mass	0.464	kg
l	Distance	0.1	m
I_X	Roll Inertia	0.0377	$\mathrm{kg \cdot m^2}$
I_Y	Pitch Inertia	0.0624	$\mathrm{kg \cdot m^2}$
I_Z	Yaw Inertia	0.0309	$\mathrm{kg \cdot m^2}$

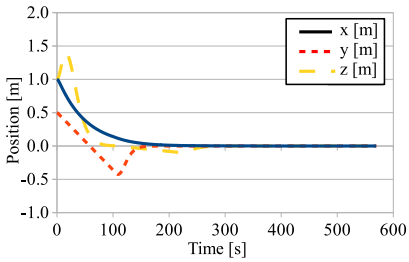

Fig. 4. Controlled positions

If $\pi_1(E_1) < E_2 < \pi_2(E_1)$ and $s_{t-1} = z$ then $s_t = z$

Rule 4 :

If $\pi_2(E_1) < E_2$ then $s_t = z$

where s_t represents the controller used for each rule. When s_t=y, the partial underactuated controller 1 is used, whereas when s_t=z, the partial underactuated controller 2 is used. s_{t-1} represents the controller used before one-sampling time. According to this switching rule, the partial underactuated controller 2 is used to control the state z, if the error energy on z becomes large when using the partial underactuated controller 1 to control states except the state z. Similarly, the partial underactuated controller 1 is used to control the state y, if the error energy on y becomes large when using the partial underactuated controller 2 to control states except the state y. It should be noted that, in this switching rule, the chattering phenomena are unlikely to occur because an overlapped region between the boundary lines π_1 and π_2 exists to switch the controllers.

6 SIMULATION

This simulation is intended to verify that the state variables related to the position and attitude of the airframe converge to the origin by switching the two partial underactuated controllers using the switching rules created in previous section. The initial state of X4-Blimp is $\boldsymbol{q_0} = [1, 0.5, 1, \pi/18, \pi/4, \pi/4]^T$, and the goal state is $\boldsymbol{q_r} = [0, 0, 0, 0, 0, 0]^T$. The physical parameters used for simulation are shown in Table 1. The feedback gains k_1=0.8, k_2=1.2, k_3=0.6, k_4=0.7, s_1=1/40, s_2=0.45, l_1=−0.18, l_2=−0.68, l_3=−1.74 and l_4=−38.7 are for the partial underactuated controller 1, whereas the feedback gains k_1=0.8, k_2=1.6, k_3=1/30, k_4=0.7, s_1=1/50, s_2=0.45, l_1=−0.09, l_2=−0.48, l_3=−0.68 and l_4=−21.3 are for the partial underactuated controller 2.

It is found from Fig. 4 that the positions, i.e., the states x, y and z converge from the initial positions to the goal positions. Similarly, it is seen from Fig. 5 that all the attitudes ϕ, θ and ψ converge to the desired angles. Fig. 6 shows the energy trajectory, where it starts from the point S. It is found that the controller 2 was switched to the controller 1 at the point P and the energy finally converges to the origin at the point G. Switching of controllers occurs at the point P and the state variables are changed suddenly, if the energy trajectory exceeds the boundary line π_1. Thus, it is confirmed that the positions and attitudes of the X4-Blimp can be stabilized by switching the two partial underactuated controllers.

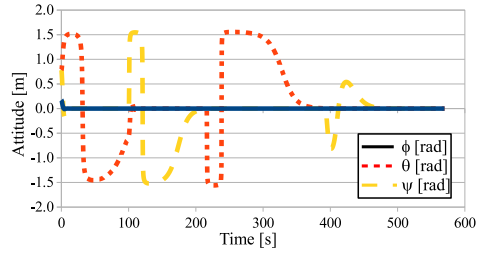

Fig. 5. Controlled attitudes

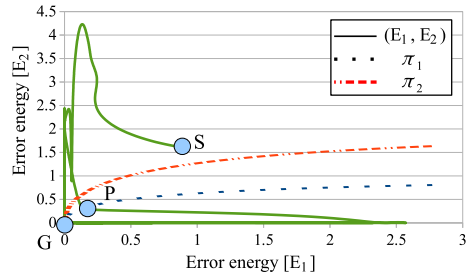

Fig. 6. Energy trajectory

7 CONCLUSION

In this paper, an underactuated controller has been proposed for stabilizing an X4-Blimp, where two partial underactuated controllers were designed from the derived dynamic model, and switching rules for switching two such controllers were constructed by applying the conventional logical rules based on hysteresis-like switching boundaries. The effectiveness of the proposed method was verified by the simulation. For future work, it needs to confirm the effectiveness of this approach on real robot experiments.

REFERENCES

[1] Kawabata K, Hada Y, Asama H (2006), Robotics research related to lighter than air aircraft. Journal of Robotics Society of Japan 24(8): 901–905

[2] Watanabe K, Izumi K, Okamura K, Rafiuddin S (2008), Discontinuous underactuated control for lateral X4 autonomous underwater vehicles. Proc. of the 2nd International Conference on Underwater System Technology: Theory and Applications 2008 (USYS '08) Paper ID 14

[3] Xu WL and Ma BL (2001), Stabilization of second-order nonholomic systems in canonical chained form. Robotics and Autonomous Systems 34: 223–233

[4] Laiou MC, Astolfi A (2004), Local transfomations to generalized chained forms. Proc. of the 16th International Symposium on Mathematical Theory of Networks and Systems

[5] Hespanha JP, Morse AS (1999), Stabilization of nonholonomic intergrators via logic-based switching. Automatica 35: 385–393

© ISAROB 2013

The Eighteenth International Symposium on Artificial Life and Robotics 2013 (AROB 18th '13),
Daejeon Convention Center, Daejeon, Korea, January 30-February 1, 2013

Continuous shape-grinding experiment based on model-independent force / position hybrid control method with spline approximation

Akira Yanou[1], Mamoru Minami[1] and Hiro Tanimoto[1]

[1]Graduate School of Natural Science and Technology, Okayama University, Japan
(Tel: +81-86-251-8924; E-mail: yanou@suri.sys.okayama-u.ac.jp)

Abstract: Based on the analysis of interaction between manipulator's hand and working object, a model representing the constrained dynamics of robot is first discussed. The constraint forces are expressed by an algebraic function of states, input generalized forces, and constraint condition, and then a decoupling control method of force and position of manipulator's hand tip is proposed. In order to give the grinding system the ability to adapt to any object shape being changed by the grinding, we added estimating function of the constraint condition in real time for the adaptive force / position control, which is indispensable for our method instead of not using force sensor. This paper explores whether the performance of the proposed controller is independent of alloy work-piece models or not. The experimental result is shown in order to verify the feature of the decoupling control of force and position of the tip.

Keywords: Continuous shape-grinding, Force / position hybrid control, Spline approximation

1. INTRODUCTION

Many researches have discussed on the force control of robots for contacting tasks. Most force control strategies are to use force sensors [1],[2] to obtain force information, where the reliability and accuracy are limited since the work-sites of the robot are filled with noise and thermal disturbances, reducing the sensor's reliability. On top of this, force sensors could lead to the falling of the structure stiffness of manipulators, which is one of the most essential defects for manipulators executing grinding tasks. To solve these problems, some approaches using no force sensor have been presented [3]. To ensure the stabilities of the constrained motion, those force and position control methods have utilized Lyapunov's stability analysis under the inverse dynamic compensation[4],[5]. Their force control strategies have been explained intelligibly in books[6] and recently interaction control for six-degree-of-freedom tasks has been compiled in a book [7]. The problem to be solved in our approach is that the mathematical expression of algebraic constraint condition should be defined in the controller instead of the merit of not using force sensor. In order to make the performance of proposed controller be independent of target work-piece model, grinding task requires on-line estimation of changing constraint condition since the grinding is the action to change the constraint condition in nature. In this paper, we estimate the object's surface using the grinder as touch sensor. In order to give the system the ability to grind any working object into any shape, we focus on how to update the constraint condition in real time, obtaining the result that spline function is best for on-line shape estimation. Based on the above preparation we explored a continuous shape-grinding experiment to evaluate the proposed shape-grinding system, which aims for grinding to desired shape without force sensor.

2. MODELING

2.1 Constrained Dynamic Systems

Hemami and Wyman have addressed the issue of control of a moving robot according to constraint condition

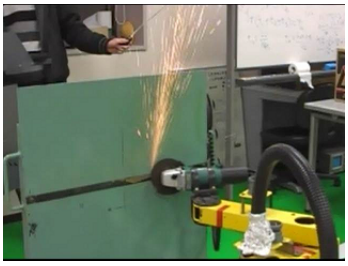

Fig. 1 Grinding robot system

and examined the problem of the control of the biped locomotion constrained in the frontal plane. Their purpose was to control the position coordinates of the biped locomotion rather than generalized forces of constrained dynamic equation involved the item of generalized forces of constraints. And the constrained force is used as a determining condition to change the dynamic model from constrained motion to free motion of the legs. In this paper, the grinding manipulator shown in Fig. 1, whose endpoint is in contact with the constrained surface, is modeled according (1) with Lagrangian equations of motion in term of the constraint forces, referring to what Hemami and Arimoto have done:

$$\frac{d}{dt}(\frac{\partial L}{\partial \dot{\boldsymbol{q}}}) - (\frac{\partial L}{\partial \boldsymbol{q}}) = \boldsymbol{\tau} + \boldsymbol{J_c}^T(\boldsymbol{q})F_n - \boldsymbol{J_r}^T(\boldsymbol{q})F_t, \quad (1)$$

where, F_n is the constrained force associated with constraint C, F_t is the tangential grinding force, $\boldsymbol{J_c}$ and $\boldsymbol{J_r}$ satisfy;

$$\boldsymbol{J_c} = \frac{\partial C}{\partial \boldsymbol{q}} / \parallel \frac{\partial C}{\partial \boldsymbol{r}} \parallel = \frac{\partial C}{\partial \boldsymbol{r}} \tilde{\boldsymbol{J}}_r / \parallel \frac{\partial C}{\partial \boldsymbol{r}} \parallel,$$

$$\tilde{\boldsymbol{J}}_r = \frac{\partial \boldsymbol{r}}{\partial \boldsymbol{q}}, \qquad \boldsymbol{J}_r^T = \tilde{\boldsymbol{J}}_r^T \dot{\boldsymbol{r}} / \parallel \dot{\boldsymbol{r}} \parallel,$$

$\boldsymbol{r}$ is the l position vector of the hand and can be expressed as a kinematic equation

$$\boldsymbol{r} = \boldsymbol{r}(\boldsymbol{q}). \quad (2)$$

L is the Lagrangian function, $\boldsymbol{q}$ is $l(\geq 2)$ generalized coordinates, $\boldsymbol{\tau}$ is l inputs. The discussing robot system does

© ISAROB 2013

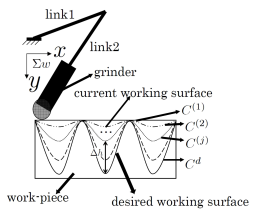

Fig. 2 Model of shape-grinding

not have kinematical redundancy. C is a scalar function of the constraint, and is expressed as an equation of constraints

$$C(\boldsymbol{r}(\boldsymbol{q})) = 0, \tag{3}$$

(1) can be derived to be

$$\boldsymbol{M}(\boldsymbol{q})\ddot{\boldsymbol{q}}+\boldsymbol{H}(\boldsymbol{q},\dot{\boldsymbol{q}})+\boldsymbol{G}(\boldsymbol{q})=\boldsymbol{\tau}+\boldsymbol{J}_c^T(\boldsymbol{q})F_n-\boldsymbol{J}_r^T(\boldsymbol{q})F_t, \tag{4}$$

where $\boldsymbol{M}$ is an $l \times l$ matrix, $\boldsymbol{H}$ and $\boldsymbol{G}$ are l vectors. The state variable $\boldsymbol{x}$ is constructed by adjoining $\boldsymbol{q}$ and $\dot{\boldsymbol{q}}$: $\boldsymbol{x} = (\boldsymbol{x}_1^T, \boldsymbol{x}_2^T)^T$=$(\boldsymbol{q}^T, \dot{\boldsymbol{q}}^T)^T$. The state-space equation of the system are

$$\begin{aligned}\dot{\boldsymbol{x}}_1 &= \boldsymbol{x}_2,\\ \dot{\boldsymbol{x}}_2 &= -\boldsymbol{M}^{-1}(\boldsymbol{H}(\boldsymbol{x}_1,\boldsymbol{x}_2)+\boldsymbol{G}(\boldsymbol{x}_1))\\ &\quad +\boldsymbol{M}^{-1}(\boldsymbol{\tau}+\boldsymbol{J}_c^T(\boldsymbol{x}_1)F_n-\boldsymbol{J}_r^T\boldsymbol{x}_1)F_t),\end{aligned} \tag{5}$$

or the compact form is given as $\dot{\boldsymbol{x}} = \boldsymbol{F}(\boldsymbol{x}, \boldsymbol{\tau}, F_n, F_t)$. Using the inverted form of combination from (3) and $\dot{\boldsymbol{x}} = \boldsymbol{F}(\boldsymbol{x}, \boldsymbol{\tau}, F_n, F_t)$, F_n can be expressed as (this part had been detailedly introduced in [10] by us)

$$F_n = F_n(\boldsymbol{x}, \boldsymbol{\tau}, F_t), \tag{6}$$

$$\triangleq a(\boldsymbol{x}_1, \boldsymbol{x}_2) + \boldsymbol{A}(\boldsymbol{x}_1)\boldsymbol{J}_r^T F_t - \boldsymbol{A}(\boldsymbol{x}_1)\boldsymbol{\tau}, \tag{7}$$

where, $a(\boldsymbol{x}_1, \boldsymbol{x}_2)$ is a scalar representing the first term in the expression of F_n, and $\boldsymbol{A}(\boldsymbol{x}_1)$ is an l vector to represent the coefficient vector of $\boldsymbol{\tau}$ in the same expression. $\dot{\boldsymbol{x}} = \boldsymbol{F}(\boldsymbol{x}, \boldsymbol{\tau}, F_n, F_t)$ and (6) compose a constrained system that can be controlled, if $F_n = 0$, describing the unconstrained motion of the system. Substituting (7) into (5), the state equation of the system including the constrained force (as $F_n > 0$) can be rewritten as

$$\begin{aligned}\dot{\boldsymbol{x}}_1 &= \boldsymbol{x}_2,\\ \dot{\boldsymbol{x}}_2 &= -\boldsymbol{M}^{-1}[\boldsymbol{H}(\boldsymbol{x}_1,\boldsymbol{x}_2)+\boldsymbol{G}(\boldsymbol{x}_1)-\boldsymbol{J}_c^T(\boldsymbol{x}_1)a(\boldsymbol{x}_1,\boldsymbol{x}_2)]\\ &\quad +\boldsymbol{M}^{-1}[(\boldsymbol{I}-\boldsymbol{J}_c^T\boldsymbol{A})\boldsymbol{\tau}+(\boldsymbol{J}_c^T\boldsymbol{A}-\boldsymbol{I})\boldsymbol{J}_r^T F_t],\end{aligned} \tag{8}$$

Solutions of these dynamic equations always satisfy the constrained condition (3).

2.2 Shape-grinding

In the past, we did the continuous shape grinding simulations[10] to try to extend the grinding ability of our grinding robot[9]. Now in this paper, the continuous shape grinding experiment which has been done by the proposed force sensorless force/position control method will be introduced.

To make the grinding task to be different from the former flat grinding experiment[9], we want to grind the work-piece into the one with different kinds of shapes, for example, grinding the flat surface into a curved one, just like Fig. 2. In Fig. 2, we can find that the desired working surface is prescribed (it can be decided by us.), which means the desired constrained condition C^d is known, so

$$C^d = y - f^d(x) = 0 \tag{9}$$

But the constrained condition $C^{(j)}$ ($j = 1, 2, \cdots, d-1$) changed by the previous grinding is hard to define as an initial condition. So we define

$$C^{(j)} = y - f^{(j)}(x) = 0 \tag{10}$$

where, y is the y position of manipulator's end-effector in the coordinates Σw depicted in Fig. 2 and we assume $C^{(1)}$ is known, that is to say, $f^{(1)}(x)$ is initially defined. $f^{(j)}(x)$ is the working surface remained by i-th grinding. And $f^{(j)}(x)$ is a function passing through all points, $(x_1,\ f^{(j)}(x_1))$, $(x_2,\ f^{(j)}(x_2))$, $\cdots$, $(x_p,\ f^{(j)}(x_p))$, these observed points representing the (j)-th constraint condition obtained from the grinding tip position since we proposed previously the grinding tip used for the touching sensor of ground new surface. Here we assume $f^{(j)}(x)$ could be represented by a polynomial of $(p-1)$-th order of x. Given the above p points, we can easily decide the parameters of polynomial function $y = f^{(j)}(x)$. If the current constrained condition can be got successfully, which means the current working surface $f^{(j)}(x)$ can be detected correctly, the distance from the current working surface to the desired working surface which is expressed as $\Delta h^{(j)}$ shown in Fig. 2 can be obtained easily.

$$\Delta h^{(j)}(x_i) = f^d(x)\big|_{x=x_i} - f^{(j)}(x)\big|_{x=x_i} \tag{11}$$

In this case, we can obviously find that the desired constrained force should not be a constant. It should be changed while $\Delta h^{(j)}$ changes. So we redefine the desired constrained force $F_{nd}^{(j)}$ as a function of $\Delta h^{(j)}$ with constant k', shown as follows:

$$F_{nd}^{(j)}(x_i) = k'\Delta h^{(j)}(x_i) \tag{12}$$

3. FORCE / POSITION CONTROLLER

3.1 Controller using Estimated Constraint Condition

Reviewing the dynamic equation (1) and constraint condition (3), it can be found that as $l > 1$, the number of input generalized forces is more than that of the constrained forces. From this point and (7) we can claim that there is some redundancy of constrained force between the input torque $\boldsymbol{\tau}$, and the constrained force F_n. This condition is much similar to the kinematical redundancy of redundant manipulator. Based on the above argument and assuming that, the parameters of the (7) are known and its state variables could be measured, and $a(\boldsymbol{x}_1, \boldsymbol{x}_2)$ and $\boldsymbol{A}(\boldsymbol{x}_1)$ could be calculated correctly, which means that the constraint condition $C = 0$ is prescribed. As a result, a control law is derived and can be expressed as

$$\begin{aligned}\boldsymbol{\tau} &= -\boldsymbol{A}^+(\boldsymbol{x}_1)\left\{F_{nd}-a(\boldsymbol{x}_1,\boldsymbol{x}_2)-\boldsymbol{A}(\boldsymbol{x}_1)\boldsymbol{J}_r^T K_t F_{nd}\right\}\\ &\quad +(\mathbf{I}-\boldsymbol{A}^+(\boldsymbol{x}_1)\boldsymbol{A}(\boldsymbol{x}_1))\boldsymbol{k},\end{aligned} \tag{13}$$

where it is assumed that $F_t = K_t F_n \approx K_t F_{nd}$. K_t is an empirical coefficient, $\mathbf{I}$ is a $l \times l$ identity matrix, F_{nd} is the desired constrained forces, $\boldsymbol{A}(\boldsymbol{x}_1)$ is defined in (7) and $\boldsymbol{A}^+(\boldsymbol{x}_1)$ is the pseudoinverse matrix of it, $a(\boldsymbol{x}_1, \boldsymbol{x}_2)$ is also defined in (7) and $\boldsymbol{k}$ is an arbitrary vector which is defined as

© ISAROB 2013

$$\boldsymbol{k} = \widetilde{\boldsymbol{J}}_r^T(\boldsymbol{q})\Big\{\boldsymbol{K}_p(\boldsymbol{r}_d - \boldsymbol{r}) + \boldsymbol{K}_d(\dot{\boldsymbol{r}}_d - \dot{\boldsymbol{r}})\Big\}, \qquad (14)$$

where $\boldsymbol{K}_p$ and $\boldsymbol{K}_d$ are gain matrices for position and the velocity control by the redundant degree of freedom of $\boldsymbol{A}(\boldsymbol{x}_1)$, $\boldsymbol{r}_d(\boldsymbol{q})$ is the desired position vector of the end-effector along the constrained surface and $\boldsymbol{r}(\boldsymbol{q})$ is the real position vector of it. (14) describes the 2-link rigid manipulator's arm compliance, we have to set $\boldsymbol{K}_p$ and $\boldsymbol{K}_d$ with a reasonable value, otherwise high-frequency response of position error will appear. The controller presented by (13) and (14) assumes that the constraint condition $C = 0$ be known precisely even though the grinding operation is a task to change the constraint condition. This looks like to be a contradiction, so we need to observe time-varying constraint conditions in real time by using grinding tip as a touch sensor. The time-varying condition is estimated as an approximate constrained function by position of the manipulator hand, which is based on the estimated constrained surface location. The estimated condition is denoted by $\hat{C} = 0$(in this paper, "$\hat{}$" means the situation of unknown constraint condition). Hence, $a(\boldsymbol{x}_1, \boldsymbol{x}_2)$ and $\boldsymbol{A}(\boldsymbol{x}_1)$ including $\partial\hat{C}/\partial\boldsymbol{q}$ and $\partial/\partial\boldsymbol{q}(\partial\hat{C}/\partial\boldsymbol{q})$ are changed to $\hat{a}(\boldsymbol{x}_1, \boldsymbol{x}_2)$ and $\hat{\boldsymbol{A}}(\boldsymbol{x}_1)$ as shown in (16) and (17). They were used in the later experiments of the unknown constrained condition. As a result, a controller based on the estimated constrained condition is given as

$$\begin{aligned}\hat{\boldsymbol{\tau}} &= -\hat{\boldsymbol{A}}^{+}(\boldsymbol{x}_1)\Big\{F_{nd} - \hat{a}(\boldsymbol{x}_1, \boldsymbol{x}_2) - \hat{\boldsymbol{A}}(\boldsymbol{x}_1)\boldsymbol{J}_R^T F_t\Big\} \\ &\quad + (\mathbf{I} - \hat{\boldsymbol{A}}^{+}(\boldsymbol{x}_1)\hat{\boldsymbol{A}}(\boldsymbol{x}_1))\boldsymbol{k}, \qquad (15)\end{aligned}$$

$$m_c{}^{-1}\| \frac{\partial\hat{C}}{\partial\boldsymbol{r}} \|\{-[\frac{\partial}{\partial\boldsymbol{q}}(\frac{\partial\hat{C}}{\partial\boldsymbol{q}})\dot{\boldsymbol{q}}]\dot{\boldsymbol{q}} + (\frac{\partial\hat{C}}{\partial\boldsymbol{q}})\boldsymbol{M}^{-1}(\boldsymbol{h} + \boldsymbol{g})\} \triangleq \hat{a}(\boldsymbol{x}_1, \boldsymbol{x}_2) \qquad (16)$$

$$m_c{}^{-1}\| \frac{\partial\hat{C}}{\partial\boldsymbol{r}} \|\{(\frac{\partial\hat{C}}{\partial\boldsymbol{q}})\boldsymbol{M}^{-1}\} \triangleq \hat{\boldsymbol{A}}(\boldsymbol{x}_1) \qquad (17)$$

It can be found from (7) and (15) that the constrained force always equals to the desired one explicitly if the estimated constraint condition equals to the real one, i.e., $C = \hat{C}$ and $F_t = 0$. This is based on the fact that force transmission is an instant process. In the next section, we will introduce an estimation method which is used to get $\hat{C}$ in current time.

3.2 On-line Estimation Method of Constraint

Now shape-grinding method is given to be solved in our research. But how to estimate the unknown constraint surface is the nodus and key point. Here, an unknown constrained condition is assumed as following,

Assumptions:

1. The end point position of the manipulator during performing the grinding task can be surely measured and updated.
2. The grinding task is defined in $x - y$ plane.

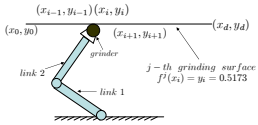

Fig. 3 Situation of known constraint surface model

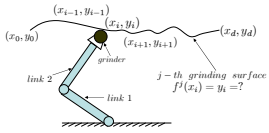

Fig. 4 On-line estimation model

3. When beginning to work, the initial condition of the end-effector is known and it has touched the work object.
4. The chipped and changed constraint condition can be approximated by connections of minute sections.

Some relations between position value and time value are written here, in this section, you'd better remember these relations because it will help you understand the concept of "on-line estimation method".

$$x_{i-1} = x(t_{i-1}) = x(t_0 + (i-1)\Delta t), \qquad (18)$$
$$x_i = x(t_i) = x(t_0 + i\Delta t), \qquad (19)$$
$$x_{i+1} = x(t_{i+1}) = x(t_0 + (i+1)\Delta t). \qquad (20)$$

Before on-line estimation method is introduced, let's take a look at the situation of known flat constraint surface. For example, just like the grinding surface shown in Fig. 3, the expression of this surface is straight linear equation

$$f^j(x_i) = y_i = 0.5173(i = 0, 1, 2, 3...n), \qquad (21)$$

and point (x_i, y_i) is the current position of grinding robot's end-effector. As a result, points before (x_i, y_i) have been already ground by grinder when $t <= t_0 + i\Delta t$. In the next moment, when time $t_{i+1} = t_0 + (i+1)\Delta t$, constraint condition

$$C_{i+1}^j = y - f^j(x_i) = 0 \qquad (22)$$

can be used for calculation of deriving torque $\boldsymbol{\tau}$. And also, grinder will move to next point (x_{i+1}, y_{i+1}) with no hesitation driven by the input torque $\boldsymbol{\tau}$. By "no hesitation", it means on this known surface, grinder has nowhere to go but point (x_{i+1}, y_{i+1}), since this whole grinding surface $f^j(x_i) = y_i = 0.5173(i = 0, 1, 2, 3...n)$ is determined obviously. However, we all know that the grinding surface on work-piece after ground will turn into some kind of irregular shape that no mathematic equation can express. What should we do to obtain the future constraint condition C_{i+1}^j if the grinding surface is unknown? Like the situation shown in Fig. 4, the grinding surface is not a simple straight line or some curve line which can be defined and expressed by some certain curve equation, after current time $t_i = t_0 + i\Delta t$, where should the grinder go? Grinding robot has no idea since input torque $\boldsymbol{\tau}$ cannot be derived without constraint condition C_{i+1}^j. To solve this problem, we consider that some kind of on-line estimation function should be utilized to imitate the unknown grinding surface, in order to

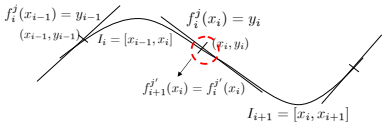

Fig. 5 Fitting by quadratic spline curve

obtain an unknown constraint condition $\hat{C}_{i+1}^j$, which can be used to calculate the input torque $\hat{\boldsymbol{\tau}}$.

Therefore, now let's take a look at Fig. 4, in current time $t_i = t_0 + i\Delta t$, end-effector of grinding robot is at position (x_i, y_i), so far, point (x_{i-1}, y_{i-1}) and point (x_i, y_i) have become known because they were just ground by the grinder in the moment $t_{i-1} = t_0 + (i-1)\Delta t$ and $t_i = t_0 + (i)\Delta t$ and the information of point (x_{i-1}, y_{i-1}) and (x_i, y_i) can be derived through the position of robot's end-effector. Now building an estimation function going through these two points, for example, a quadratic spline function

$$\begin{aligned} f_i^j(x_i) &= f_{spline}(x_i) = y_i \\ &= \alpha_i(x - x_{i-1})^2 + \beta_i(x - x_{i-1}) + \gamma_i \\ & \quad x \in [x_{i-1}, x_i](i = 0, 1, 2, 3...n), \end{aligned} \tag{23}$$

we can figure out the coefficients α_i, β_i and γ_i uniquely according to the information of points (x_{i-1}, y_{i-1}), (x_i, y_i) and derivation at point (x_i, y_i) as follows.

Firstly, let $f_i^j(x_i)$ satisfy the following conditions shown in Fig. 5.

(A) Go through two ends of the interval

$$y_{i-1} = f_i^j(x_{i-1}) \tag{24}$$

$$y_i = f_i^j(x_i) \tag{25}$$

(B) First-order differential of the spline polynomials are equal at the end-point of adjoined function.

$$f_{i+1}^{j'}(x_i) = f_i^{j'}(x_i) \tag{26}$$

From the relation among (23), (24), (25) and (26), we can obtain:

$$\gamma_i = y_{i-1}, (i = 1, 2, \cdots, n) \tag{27}$$

$$\beta_{i+1} = 2u_i - \beta_i, (i = 1, 2, \cdots, n-1) \tag{28}$$

$$\alpha_i = \frac{\beta_{i+1} - \beta_i}{2h_i}, (i = 1, 2, \cdots, n-1) \tag{29}$$

Where, $h_i = x_i - x_{i-1}$, $u_i = \frac{y_i - y_{i-1}}{h_i}$. The above-mentioned result can update the constrained conditional expression $\hat{C}_{i+1}^j$ step by step.

Making an expansion of the interval between point (x_{i-1}, y_{i-1}) and point (x_{i+1}, y_{i+1}) on the grinding surface which is shown in Fig. 6, we can see the first half of grinding surface before the current position - point (x_i, y_i) is shown by black line, which means this part has been already ground, and second half after point (x_i, y_i) is shown by break point line, which means this part has not been ground yet. Now let's pay our attention on the interval between point (x_i, y_i) and point (x_{i+1}, y_{i+1}), which means this part has been estimated by quadratic

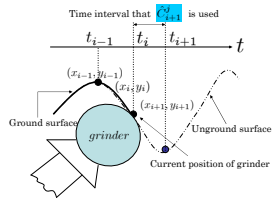

Fig. 6 Expansion of interval between point (x_{i-1}, y_{i-1}) and point (x_{i+1}, y_{i+1}) on the on-line estimation model

spline function. With the estimation function the next point (x_{i+1}, y_{i+1}) can easily be found to be known, and then this point can be the position where grinder should go in the next moment when $t_{i+1} = t_0 + (i+1)\Delta t$, At the same time, this imitative function can be used as the on-line estimation function to obtain the unknown constraint condition

$$\begin{aligned} \hat{C}_{i+1}^j &= y - f_i^j(x) \\ &= y - [\alpha_i(x - x_{i-1})^2 + \beta_i(x - x_{i-1}) + \gamma_i] = 0, \\ &(x_i \le x \le x_{i+1}) \end{aligned} \tag{30}$$

during the period when grinder goes from point (x_i, y_i) to point (x_{i+1}, y_{i+1}), which means in this unknown interval on the grinding surface, the future unground part (x_i, y_i) to (x_{i+1}, y_{i+1}) can be ground by this on-line estimation method based on the information obtained from already ground part (x_{i-1}, y_{i-1}) to (x_i, y_i). So, in the situation of unknown constraint surface, using this on-line estimation method point to point, the problem for grinding robot that it doesn't know where it should go in future time can be solved theoretically.

4. EXPERIMENT

In this section, we verify the feature of the proposed controller (13). In the previous papers[11],[12] we have already confirmed the ability in on-line shape measurement based on spline approximation (on-line estimation of the constraint condition $\hat{C}_{i+1}^j$) and continuous shape-grinding. Whereas alloy model of work-piece to be ground has been just one type, and the performance of proposed force / position controller has not been confirmed for various types of alloy models with different hardness. In other words, it is necessary to confirm whether its performance is independent of alloy model or not. Therefore this section shows the experimental results of model-independent force / position hybrid control by using three types of alloy models with different hardness. Fig. 2 shows the experiment's grinding task. In Fig. 2, we can find that the desired surface is known (it can be determined by us, here we use (31) as this desired surface)

$$\begin{aligned} f^d(x_i) &= 0.5173 + \left|0.015\cos(3 \times 5\pi x_i - \frac{\pi}{2})\right| \text{ [m]} \\ & (0.0[\text{m}] \le x_i \le 0.2[\text{m}]) \end{aligned} \tag{31}$$

and also the initial flat surface is known as $f^1(x_i) = 0.5173[\text{m}]$. Here we notice that although the initial constraint surface $f^1(x_i)$ and desired constraint surface $f^d(x_i)$ are known already, those functions $f^j(x_i)$ who

© ISAROB 2013

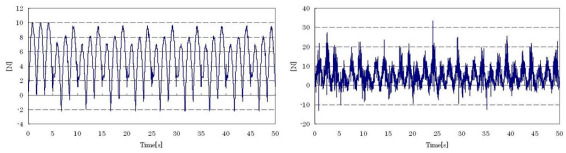

Fig. 7 Desired constraint force F_{nd} (left) and real constraint force F_n measured by force sensor (right) (Alloy type: S45C)

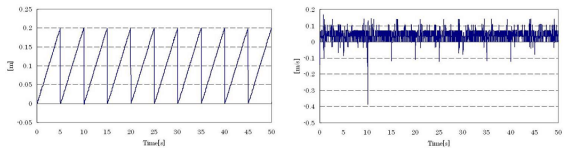

Fig. 8 Grinding position x_i (left) and its velocity $\dot{x}_i$ (right) (Alloy

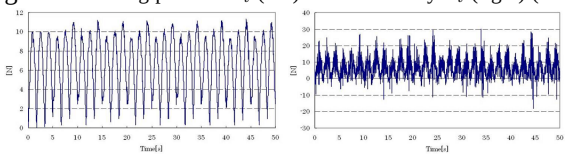

Fig. 9 Desired constraint force F_{nd} (left) and real constraint force F_n measured by force sensor (right) (Alloy type: A2017P)

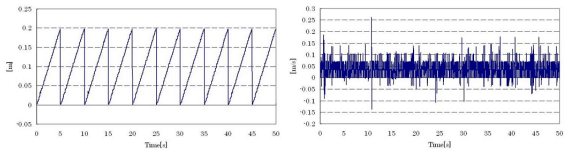

Fig. 10 Grinding position x_i (left) and its velocity $\dot{x}_i$ (right) (Alloy type: A2017P)

can express the constraint working surfaces between $f^1(x_i)$ and $f^d(x_i)$ are unknown. Therefore, we utilize the quadratic spline function to estimate them by means of $f^j(x_i) = f_{spline}(x_i)$. The initial constraint surface to be ground is defined as $(x, y) = (0.0, 0.5173) \sim (0.2, 0.5173)$[m] in time 5.0[s], and the desired velocity along the surface is 0.04[m/s]. The desired force F_{nd} is set as $F^j_{nd}(x_i) = k'\Delta h^j(x_i)$. k' is set to be 666 and $\Delta h^j(x_i) = f^d(x_i) - f^j(x_i)$ indicates the distance between the current surface and desired surface as shown in Fig. 2. Fig. 7 and Fig. 8 give the experimental result for alloy type S45C with Vickers hardness 170-195 [HV]. The result of Fig. 9 and Fig. 10 is for alloy type A2017P with Vickers hardness 125-130 [HV]. And the result of Fig. 11 and Fig. 12 is for alloy type A5083P with Vickers hardness 80-90 [HV]. One trial takes 5 [s] and the number of trials is 10 in these experimental results. So the experiment of each alloy type takes 50 [s]. Fig. 7, Fig. 9 and Fig. 11 show desired constraint force F_{nd} and real constraint force F_n measured by force sensor. Fig. 8, Fig. 10 and Fig. 12 show grinding position x_i and the velocity $\dot{x}_i$. From these figures, it can finds that the proposed controller (13) can decouple position and force control independent of alloy models although the results of real constraint force and grinding velocity are affected by grinding.

5. CONCLUSIONS

In order to verify the feature of the proposed force-sensorless force/position hybrid control, the experiments of the proposed force/position hybrid control method

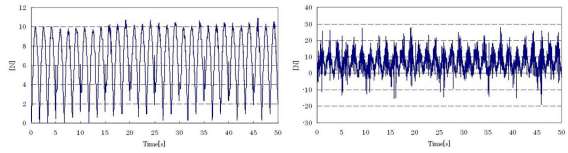

Fig. 11 Desired constraint force F_{nd} (left) and real constraint force F_n measured by force sensor (right) (Alloy type: A5083P)

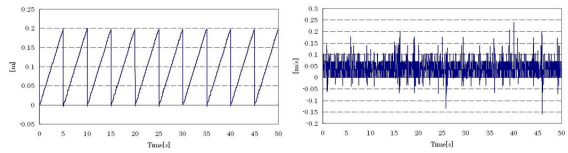

Fig. 12 Grinding position x_i (left) and its velocity $\dot{x}_i$ (right) (Alloy type: A5083P)

were executed for three types of alloy models with different hardness. From the experimental results, it is found that the proposed controller can decouple force and position control for continuous shape-grinding independent of alloy models. As future work, the relation between hardness of alloy model and shape to be ground will be explored in order to utilize in many robotic control fields.

REFERENCES

[1] M.H.Raibert and J.J.Craig: Hybrid Position/Force Control of Manipulators, Trans. of the ASME, J. of Dynamic Systems, Measurement and Control, Vol.102, pp.126-133, June, 1981.

[2] T. Yoshikawa: Dynamic Hybrid Position/Force control of Robot Manipulators — Description of Hand Constraints and Calculation of Joint Driving Force, IEEE J. on Robotics and Automation, Vol.RA-3, No.5, pp.386-392, 1987.

[3] L. Whitcomb, S. Arimoto, T. Naniwa and F. Osaki, Experiments in Adaptive Model-Based Force Control, IEEE Control Systems Society, Vol.16, No.1, pp.49-57, 1996.

[4] D.Wang and N.H. McClamroch: Position and Force Control for Constrained Manipulator Motion: Lyapunov's Direct Approach, IEEE Trans. Robotics and Automation, Vol.9, pp.308-313, 1993.

[5] Jaydeep. Roy and Louis L. Whitcomb: Adaptive Force Control of Position/Velocity Controlled Robots: Theory and Experiment, IEEE Transactions on Robotics and Automation, Vol.18, No.2, April, 2002.

[6] B. Siciliano, L. Villani, Robot Force Control, Kluwer Academic Publishers, U.K., 1999.

[7] C. Natale, Interaction Control of Robot Manipulators, Springer Tracts in Advanced Robotics, Germany, 2003.

[8] Hooshang Hemami and Bostwick F. Wyman: Modeling and Control of Constrained Dynamic Systems with Application to Biped Locomotion in the Frontal Plane, IEEE Trans. on Automatic Control, Vol.AC-24, No.4, pp.526-535, 1979.

[9] Takeshi Ikeda, Mamoru Minami, Position/Force Control of a Manipulator by Using an Algebraic Relation and Evaluations by Experiments, The 2003 IEEE/ASME Int. Conf. on Advanced Intelligent Mechatronics (AIM2003), Proceeding CD-ROM paper No.159, 503-508, 2003

[10] Mamoru Minami, Weiwei Xu, Shape-grinding by Direct Position / Force Control with On-line Constraint Estimation, 2008 IEEE/RSJ International Conference on Intelligent Robots and Systems, Acropolis Convention Center, Nice, France, Sept, 22-26, 2008. pp. 943-948

[11] Hiro Tanimoto, Mamoru Minami, Akira Yanou and Masaki Takebayashi, Continuous Shape-Grinding Experiment based on Constraint-combined Force / Position Hybrid Control Method, Proceedings of 2012 IEEE/SICE International Symposium on System Integration (SII2012), 2012.

[12] Hiro Tanimoto, Mamoru Minami, Akira Yanou and Masaki Takebayashi, Constraint-combined Force / Position Decoupling Control Experiment for Shape-Grinding, The 2013 IEEE International Conference on Robotics and Automation (ICRA 2013) (to be submitted)

© ISAROB 2013

The Eighteenth International Symposium on Artificial Life and Robotics 2013 (AROB 18th '13),
Daejeon Convention Center, Daejeon, Korea, January 30-February 1, 2013

Catastrophic chaos theory: predicting the edge between health and death

Ken Naitoh[1] and Hirofumi Inoue[1]

[1]Waseda University, 3-4-1 Ookubo, Shinjuku, Tokyo 169-8555, Japan
(Tel: 81-3-5286-3265)
[1]k-naito@waseda.jp

Abstract: Recently, we proposed a macroscopic model for explaining the reason why organs such as a blast cyst, ectodermal endoderm, mesoderm, heart, and hand generate at about sevenfold cell divisions during the morphogenetic process and the bio-chemical standard clock such as circadian one. (Naitoh, AROBJ 2008, 2012, JJAIM 2011) The present standard clock model derived logically with experimental observations is described by a nonlinear differential equation predicting time-evolutions of six macroscopic molecular groups: three gene groups and three enzyme groups, which include acceleration and depression factors. In our previous reports (Naitoh, Proc. JSST, 2011, J. of Physics, 2012), we also find that the fundamental network pattern of neurons, which has been a mystery for a long time, will be dominated by the equation. Here, the macroscopic model extended for describing also aging processes shows various types of cycles and reveals the physical condition for determining whether or not living beings such as the human beings can survive after getting ill. It is stressed that, after getting ill, living systems with too fast generation of information molecules such as various genes result in the death, whereas too fast production of enzymes leads to regeneration. This may also explain an essential feature underlying cancerous process.

Keywords: Health, Death, Catastrophe, chaos.

1. INTRODUCTION

Our previous reports [1,2] clarified the minimum excitatory network of chemical reactions necessary for biological self-replication, which is the origin of life such as primitive bacteria and archaea. The minimum system as a closed loop has four types of macroscopic molecular groups: two information groups x11 and x12 and two functional molecular groups x21 and x22. (Fig. 1) It should be stressed that only three molecular groups are necessary for realizing the self-organizing replication, i.e., x11, x12, and x22, because x21 can be automatically generated by these three groups. As collision of two molecules generally occurs with a high probability in nonliving molecular pool, simultaneous collision of three molecules or impact of third molecules on two connecting molecules are possible with a certain probability, although simultaneous collision of four molecules is relatively difficult. Only three molecules of x11, x12, and x22 led to the emergence of living beings.

We can topologically see the symmetric and asymmetric circles of reaction networks in Fig. 1. [1,2] Fusion of asymmetric and symmetric size ratios of molecules (bipolarity of sizes of 1:1 and about 2:3) [1,4,5,7] will naturally result in the fusion of asymmetrical and symmetrical network patterns (bipolarity of topology).

Complementary pairs of RNA such as double-strand RNA (dsRNA), i.e., only one molecular group, may form the simplest excitatory cycle. However, information and a catalytic function are undetached in this type of system, because each strand of dsRNA has both of them. This leads to the fact that the dsRNA and DNA suitable for stabilizing information is not conducive to the production of various functions for inducing multi-cellar systems having complex geometries. Thus, living beings select the detachment of information and function. [13]

2.MORPHOGENETIC PROCESS

The main temporal mystery is the standard clock, i.e., the basic molecular instrument regulating the biological rhythm common to the cell cycle, proliferation and differentiation induced by the stem cell cycle, neural pulse, neural network, and circadian clock. In order to generate the standard clock, at least two more inhibitory molecules (molecular groups) of information and function should be added to depress a monotonous increase in DNA. [2-5, 10,11,12,13].

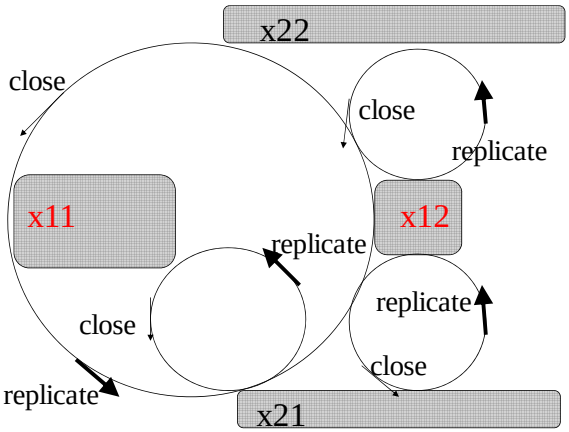

Fig. 1 Four-stroke molecular engine for living systems as minimum biological cycle

Here, we define x13 and x23 as the other molecular groups for inhibitory factors repressing reactions. These two groups are incorporated in the four groups of x11, x12, x21, and x22, because today's cells, the morphogenetic processes of multi-cellar systems, and neural systems use negative controllers such as Oct-4 and SOX2 for producing tissues and organs [6]. This leads to a macroscopic model having six types of molecular groups, or in other words, a six-stroke engine (Fig. 2). We can describe the densities of the six molecular groups x_{ij} at generation N after the mother cell generation in the morphogenetic process, by the following equations.

© ISAROB 2013

$$x_{1i}^{N+1} - x_{1i}^{N} = \alpha_{i1} x_{1i}^{N} \otimes x_{21}^{N} \quad ,(i = 1,2,3)$$
$$x_{2i}^{N+1} - x_{2i}^{N} = \alpha_{i2} \delta(x_{1i}^{N} - \xi_i x_{23}^{N}) \otimes x_{22}^{N} \quad ,(i = 1,2,3) \tag{1}$$

where $x_{ij} \otimes x_{km}$ denotes the smaller value among x_{ij} and x_{km} and also where $\delta(x)$ and α_{ij} denote the larger value of x or 0, i.e., max (x, 0) and constant of reaction probability, respectively.[2-5] Statistical mechanics inevitably leads to the mathematical form on the right-hand side in Eq. 1, because of collision probability.

Numerical solutions for Eq. 1 show about a sevenfold beat cycle of densities for molecular groups on average, while varying the parameters in Eq. 1 results in four- to ten- fold beat cycles.

An important point is that the actual morphogenetic processes show about seven-beat cycles of molecular densities [2-5].

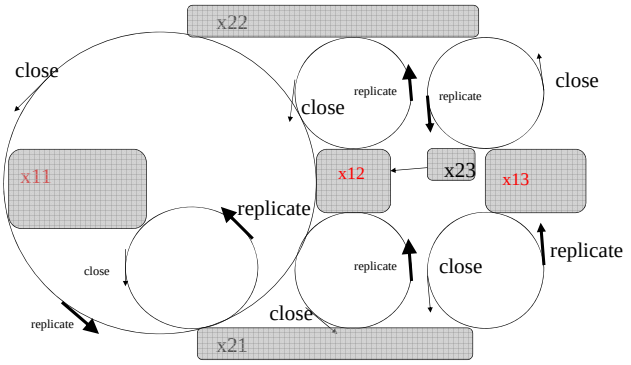

Fig. 2 Six-stroke molecular engine including depression effect

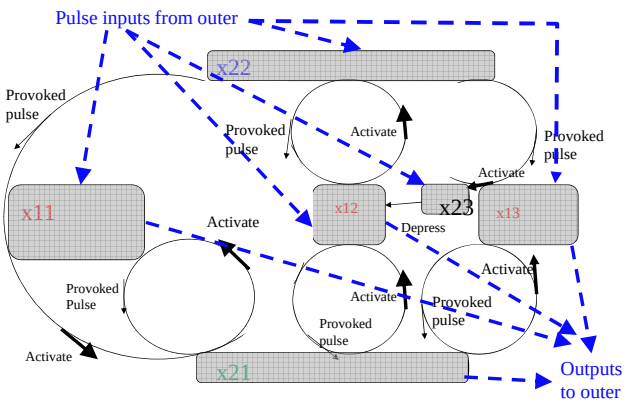

Fig. 3 Six cellar network for the brain system

3. NEURAL TOTWORK

Equation 1 will also reveal the standard topology of the cortical neural circuit (network), the integration mechanism of brain functions, the neural system for muscle control, and the chemical reaction network inside a neuron [3,5,7].

Figure 3 shows the standard pattern for neural networks, which includes inputs and outputs. For the network, six variables of x_{ij} (i=1-2, j=1-3) are redefined as the activation level of neurons, related to the density of molecules and amount of total energy inside the neurons.

There are two sides in Fig. 3, one for inputs and the other for outputs, which correspond to information and functional molecules in Eq. 1 and Fig. 3. The upside-down topology of inputs and outputs in Fig. 3 will also be possible.

The most important point is that the present equation (Eq. 1) and Fig. 3 describe the essential physics underlying the network of neural cells and the molecular network inside a neuron, whereas the Hodgkin-Huxley (H-H) model [8] describes only the outer electrical quantities such as electron flow and voltage for a single neuron. [It should be added that some variations modified from the network pattern in Fig. 3 and Eq. 1 are also possible, by varying the arbitrary constants and also by adding more molecular types except for x13 and x23.]

It should be stressed that the circadian clock of about 24-25 hours are also seven times the fundamental temperature oscillation of about 3.5 hours. [9]

Equation 1 is an ordinary differential one that eliminates spatial variations of quantities, because the spatial diffusion of molecules and cells is relatively fast in comparison with temporal oscillations and also because a lot of molecules move between cells.

Moreover, emphasis is placed on the fact that the cycles of boom and bust appearing in economic and social systems are also the seven-beat on average, because economic systems are produced by human brains. Flux and reflux of companies and capital can also be clarified by the present analysis. [2]

4 MODEL EXTENDED WITH TOTAL ENERGY LIMIT

The model (Eq. 1) in the previous sections was derived under the assumption of an infinite energy supply. However, energy supplied for molecular networks, cell colonies, organs, neural networks, or economic systems will be limited, because the surface-to-volume ratio of each system decreases according to an increase in the number of molecules, cells, neurons, or populations, leading to a condition of insufficient energy. Thus, a new energy restriction term should be added to Eq. 1, which results in Eq. 2 [3, 7].

$$x_{ij}^{N+1} - x_{ij}^{N} = \alpha_{ij}(x_{1j}^{N} - \beta_{ij} x_{23}^{N}) \otimes x_{2i}^{N} - \varepsilon_{ij} [x_{ij}^{N}]^{q},$$
$$x_{ij} \geq 0, \quad x_{1j}^{N} - \beta_{ij} x_{23}^{N} \geq 0. \ (i = 1-2, j = 1,-3) \tag{2}$$

where $q > 2$ is set in case that the symbol $\otimes$ is defined as product, whereas $q > 1$ if the symbol $\otimes$ means smaller value among two.

Let us solve the time-dependent process including morphogenesis and aging processes by using Eq. 2. Numerical solutions for the equation extended with total energy limit show a transition to sick situation such as cancer in the aging process of the human beings including the brain, i.e., a mysterious transition from chaotic oscillation at 2nd stage (from 80 to 200 generation) to periodic one at 3rd stage (after about 250), while the

© ISAROB 2013

vibration amplitude keeps a constant level. (Fig. 4)

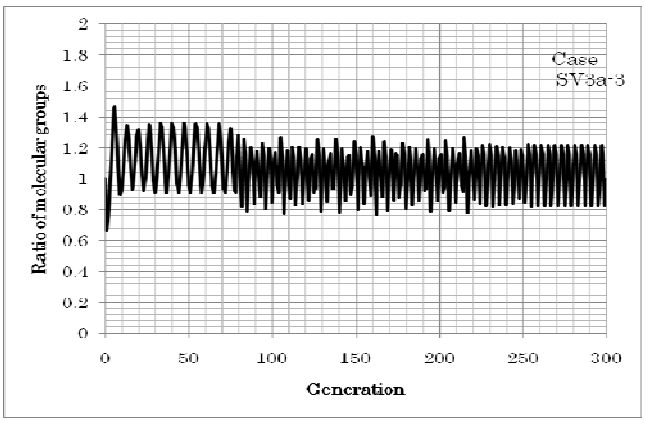

Fig. 4.Transition to sick condition as the 3rd stage in the aging process of the human being including the brain.

5. DEATH OR REGENERATION

Here, we further examine the mysterious equation (Eq. 2) by varying the parameters in detail. Increasing values of α_{11} and α_{21} result in very rapid decreases of densities for some molecular groups: biological catastrophe. An important point is that there are two essential patterns of the catastrophic processes: death and regeneration from asphyxia. (See Figs. 5 and 6) Figure 5 demonstrates the regeneration from asphyxia, whereas Fig. 6 shows the death, because densities of molecular groups cannot increase again. The critical condition for determining whether or not the living system comes back is related to the densities D1, D2, and D3 of information groups x11, x12, and x13 just after the crash occurred. If the densities of D1, D2, and D3 are zero, the death comes.

6. CONCLUSION

The present model clarifies the edge between the death and regeneration after becoming ill. Excessive replication of information molecules leads to the death of information system, which results in the death of the whole system.

References

[1] Naitoh K Stochastic Determinism. Artificial Life and Robotics, 13, pp10-17. 2008. (also in K. Naitoh. Onto-biology: Inevitability of Five Bases and Twenty Amino-acids. Proc. of 13th Int. Conf. on BioMedial Engineering, (ICBME), Singapore. Springer-Verlag (2008)).
[2] Naitoh K Morphogenic economics. Japan J. of Industrial and Applied Mathematics, Vol. 28, No.1, 2011.
[3] Naitoh K Onto-neurology. Proc. of JSST2011, Int. Conf. Modeling and Simulation Technology, Tokyo, pp.322-327, 2011.
[4] Naitoh K (2011) Proc. of 15th Nordic and Baltic Conf. on Biomedical Engineering and Biophysics, Denmark.
[5] Naitoh K Spatiotemporal structure: common to subatomic systems, biological processes, and economic cycles. J. of Physics, Conf. Ser. 344, 2012.
[6] Takahashi K, Yamanaka Cell 126, pp663-676., 2006.
[7] Naitoh K. Hyper-gourd theory. Artificial Life and Robotics, 2012.
[8] Hodgkin A L and Huxley A F, A quantitative descr iption of membrane current and its application to cond uction and excitation in nerve. J. of Physiology. 117, 5 00-544, 1952.
[9] Bear M F, Connors B W, and Paradiso M A,Neuro science, Lippincott Williams & Wiklins Inc., USA, 2 007.
[10] K. Naitoh. The universal bio-circuit: underlying normal and abnormal reaction networks including cancer, Proc. of European IFMBE Conference, IFMBE Proceedings 37, pp.247-250, Budapest, 2011.
[11] K. Naitoh. Onto-oncology: a mathematical physics underlying the proliferation, differentiation, apoptosis, and homeostasis in normal and abnormal morphogenesis and neural system. Proc. of 15th Nordic and Baltic Conf. on Biomedical Engineering and Biophysics, IFMBE proceedings 34, Denmark. Pp.29-32, 2011.
[12] K. Naitoh. Onto-biology: clarifying also the standard clock for pre-biotic process, stem-cell, organs, brain, and societies, Proc. of CBEE, Singapore. 2009.
[13] K. Naitoh, Onto-biology, Aritificial Life and Robo tics, 2010.

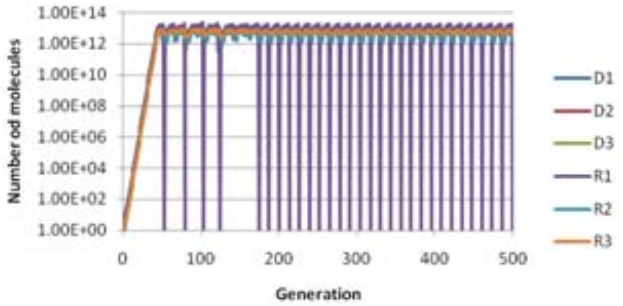

Fig. 5 Recoverable catastrophes appearing in the solution for Eq. 2.
$\alpha_{11}=1.0, \alpha_{12}=1.0, \alpha_{13}=1.0, \alpha_{21}=3.2, \alpha_{22}=1.0, \alpha_{23}=1.0, q=2.0, \varepsilon_{ij}=1.0\times10^{-13}$

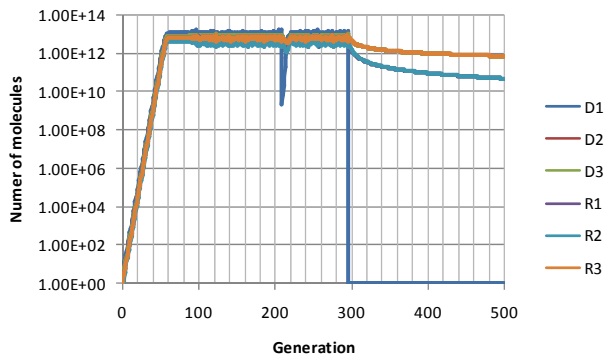

Fig. 6 Unrecoverable catastrophe seeing in the solution of Eq. 2 in case of very high increase of information proteins.
$\alpha_{11}=2.0, \alpha_{12}=1.0, \alpha_{13}=1.0, \alpha_{21}=1.0, \alpha_{22}=1.0, \alpha_{23}=1.0, q=2.0, \varepsilon_{ij}=1.0\times10^{-13}$

© ISAROB 2013

The Eighteenth International Symposium on Artificial Life and Robotics 2013 (AROB 18th '13),
Daejeon Convention Center, Daejeon, Korea, January 30-February 1, 2013

Supercomputing of transition to turbulence in pipe with adit flow

Tsuyoshi Nogami[1], Takahiro Tobe[1], and Ken Naitoh[1]

[1]Waseda University, 3-4-1 Ookubo, Shinjuku, Tokyo 169-8555, Japan
(Tel: 81-3-5286-3265)
[1]k-naito@waseda.jp

Abstract: Transition from laminar flow to turbulence often occurs in closed pipes such as pathologic blood vessels and artificial systems such as micro-tubes. While varying disturbances entering at pipe inlet or at heart pump, the transition points in space from laminar flow to turbulence in closed pipe are solved by using the weakly-stochastic Navier-Stokes equation and a finite difference method proposed previously by us (Naitoh and Shimiya, 2011), although the previous numerical simulations and instability theories based on the deterministic Navier-Stokes equation could never indicate the transition point in closed tunnel. The most important point of our approach is a philosophical method proposed for determining the stochasticity level, which is deeply related to boundary condition. Here, we qualitatively clarify the relation between the transition point and amount of adit on solid wall, because living systems exchange water and molecules through the wall of blood vessel. A mysterious feature obtained is that a larger amount of additional adit at the inlet may result in laminalization of the boundary layer.
.

Keywords: Transition, Turbulence, Drag, Adit.

1. INTRODUCTION

Reynolds experimentally showed the transition to turbulence in pipe flow 100 years ago.[1] However, traditional stability theories based on deterministic continuum mechanics [2, 3, 4, 5] cannot indicate the critical Reynolds number, i.e., the transition points in closed pipe flow for various inlet disturbances, although a great deal of effort has been exerted over the years to reveal the transition points in pipe flow using experimental, theoretical, and computational approaches.

Experimental researches related to puffs and slugs [6, 7, 8, 9] have yielded important information for clarifying the early stage of the transition process around the critical Reynolds number. However, these previous studies could not clarify clearly whether or not the stochasticity coming from molecular fluctuations influence the transition point in pipes, because the spatial resolution was not sufficient.

Recent mathematical and physical theories [10, 11] have revealed important aspects about the early stage of the transition in pipes. Numerical computations of pipe flow have also been tried using the deterministic Navier-Stokes equations [12, 13, 14, 15]. However, the influence of inlet disturbances on the transition point in space and the critical Reynolds number in pipe flow cannot be analyzed by these approaches.

There are also some theoretical researches for the mesoscopic regime lying between molecular dynamics and continuum mechanics. [16, 17, 18] However, the role of stochasticity for the nonlinear unsteady phenomena in multi-dimensional space such as those described by the Navier-Stokes equation are still mysterious.

This has led to the possibility that averaging the phenomenon in a relatively large window for the continuum assumption eliminates the instability driven by small physical fluctuations in the mesoscopic regime. This may be true because our previous computations in a straight and closed pipe using numerical disturbances close to the random number generator have qualitatively showed the transition in space for various Reynolds numbers and inlet disturbances, which suggests the possibility of a stochastic Navier-Stokes equation. [19]

Our previous reports [19-22] showed that weakly stochastic field equations averaged in a mesoscopic window (MW) smaller than that for continuum mechanics will lead to solutions to various transient and critical problems still unsolved even numerically. An important study [19-22] is that we could solve the transition point in space in the transition to turbulence in pipes while varying velocity fluctuations at the inlet. Thus, in this report, we apply the new numerical model based on the weakly-stochastic Navier-Stokes equation to the pipe flow including adit on wall. This is important, because adit on wall appear in various flows such as artifact test inside wind tunnel, blood flow, and fuel cell.

2.METHODOLOGY

It is stressed that actual pipe flow shows a transition to turbulence, although traditional linear instability analysis based on a deterministic governing equation such as the potential equation and Navier-Stokes equation with the divergence of velocity of

$$\hat{D} = \frac{\partial \overline{u}_i}{\partial x_i} = 0$$

shows no transition in closed pipes, even if large disturbances are input.

The early laminar boundary layer in pipes is thinner than the Kolmogorov scale [25]. Then, there are no actual flows without inlet disturbances. Thus, they lead to an inhomogeneous and wavy velocity distribution at the starting point of instability inside the very early laminar boundary layer that is thinner than the Kormogolov scale.

Let us consider the smallest size of vortex in fully-turbulent flow, i.e., the Kolmogorov scale. This is on the order of 1000 times as large as the mean free path of molecules in high Reynolds number flows. [25] Thus, the molecular discontinuity produces stochastic fluctuations of 0.1% in density and velocity in the Kolmogorov-scale vortex. Even if the deterministic Navier-Stokes equation is

© ISAROB 2013

numerically solved using a fine grid system on the Kolmogorov scale, this stochasticity is not evaluated. This stochastic level is also close to the ratio between the inlet disturbance and main flow in wind tunnels. It is also emphasized that stronger inlet disturbances produce shorter transition points, which apparently come from the smaller minimum scale of the fluctuation in the thin boundary layer.

For these reasons, deterministic models such as the deterministic Navier-Stokes equations based on the continuum assumption are essentially defective for solving the transition. Thus, the mesoscopic window size (Dmw) should be identical to this minimum scale of the weak fluctuation in the thin boundary layer.

To say more, an asymmetric distribution of numerical errors in space similar to a random force induced vertical asymmetric flows in many previous computational studies, which include the Karman vortex streets. [4, 12, 13, 29] This fact also supports the inevitability of stochastic terms. It was also confirmed previously that the mean velocity profiles after the transition point computed by the stochastic Navier-Stokes equation [19-22, 26] agreed well with the experimental data in Refs. 27 and 28. The early stage of the transition for a low Reynolds number of 6,000 in our computations also shows a two-dimensional path of particles (corresponding to the well-known Squire theorem), although relatively high Reynolds numbers suddenly generate three-dimensional flow.

In this section, we first show the concrete formulation for the stochastic Navier-Stokes equation related to boundary condition and the computational results performed with a fine grid system having high resolution and accurate random force, while there is no adit on wall.

The definition of physical quantities such as fluid velocity $\vec{u}(=u_1, u_2, u_3)$ and density ρ in molecular velocity $\vec{c}(=c_1, c_2, c_3)$ and physical space $\vec{x}(=x_1, x_2, x_3)$ in Eqs. (3) and (4) leads to the deterministic Navier-Stokes equation, when the window size for averaging is large on the basis of continuum assumption. [2]

$$\rho = m\int f(\vec{c},\vec{x},t)d\vec{c}, \tag{3}$$

$$\vec{u} = \frac{m\int \vec{c} f(\vec{c},\vec{x},t)d\vec{c}}{\rho} \tag{4}$$

where $m, f(\vec{c},\vec{x},t), \text{and } t$ denote molecular weight, probability density function, and time, respectively, while $\vec{c}$ denotes the molecular speed.

Here, we redefine physical quantities such as fluid velocity and density in the mesoscopic window size (D_{mw}) smaller than that for deriving continuum mechanics.

Averaging should be done in the D_{mw}, which is the minimum scale dominating the flow phenomenon, L_{ms}. As a result, we obtain

$$\bar{\rho} = m\int \int f(\vec{c},\vec{x},t)d\vec{c}\, d\vec{x}_{mw} / V_{mw} = \rho - \rho' \text{ and}$$

$$\bar{\vec{u}} = \frac{m\int \int \vec{c} f(\vec{c},\vec{x},t)d\vec{c}\, d\vec{x}_{mw} / V_{mw}}{\bar{\rho}} = \vec{u} - \vec{u}'$$

where dx_{mw} and V_{mw} denote the length scale for integration and control volume with the diameter D_{mw}, respectively, while $\bar{\rho}$ and $\bar{\vec{u}}$ imply the corresponding values averaged in D_{mw} and ρ' and u' are stochastic fluctuations indeterminate. [19,21,22]

A mesoscopic averaging window size, smaller than that for the continuum assumption, yields a stochastic compressible Navier-Stokes equation in a non-conservative form in the case where specific heat and viscosity coefficient have constant values, written as the governing equation below,

$$F \equiv \begin{bmatrix} f_1 \\ f_2 \\ f_3 \end{bmatrix} = \begin{bmatrix} \dfrac{\partial \bar{u}_i}{\partial x_i} + \dfrac{1}{\bar{\rho}}\dfrac{D}{Dt}\bar{\rho} \\ \dfrac{D\bar{u}_i}{Dt} + \dfrac{\partial \bar{p}}{\partial x_i} - \dfrac{1}{\mathrm{Re}}\dfrac{\partial^2 \bar{u}_i}{\partial x_j^{\,2}} \\ \dfrac{D\bar{T}}{Dt} - \dfrac{D\bar{p}}{Dt} - \dfrac{1}{Pe}\dfrac{\partial^2 \bar{T}}{\partial x_i^{\,2}} \end{bmatrix} = \begin{bmatrix} \varepsilon_1 \\ \varepsilon_2 \\ \varepsilon_3 \end{bmatrix} \tag{6a}$$

where u_i, p, ε_i $(i = 1-3)$, t, Re, and Pe denote the dimensionless quantities of velocity components in the i-direction, pressure, random forces, time, Reynolds number, and Peclet number, respectively.

Equation (6a) is transformed to Eq. (6b), which is a multi-level formulation. [29]

$$F \equiv \begin{bmatrix} f_1 \\ f_2 \\ f_3 \\ f_4 \end{bmatrix} = \begin{bmatrix} \hat{D} + \dfrac{1}{\bar{\rho}}\dfrac{D}{Dt}\bar{\rho} \\ \dfrac{D\bar{u}_i}{Dt} + \dfrac{\partial \bar{p}}{\partial x_i} - \dfrac{1}{\mathrm{Re}}\dfrac{\partial^2 \bar{u}_i}{\partial x_j^{\,2}} \\ \dfrac{\partial^2 \bar{p}}{\partial x_i^{\,2}} + \bar{\rho}\dfrac{\partial}{\partial t}\hat{D} + \Phi \\ \dfrac{D\bar{T}}{Dt} - \dfrac{D\bar{p}}{Dt} - \dfrac{1}{Pe}\dfrac{\partial^2 \bar{T}}{\partial x_i^{\,2}} \end{bmatrix} = \begin{bmatrix} \varepsilon_1 \\ \varepsilon_2 \\ \varepsilon_3 \\ \varepsilon_4 \end{bmatrix} \tag{6b}$$

where $\hat{D}(=\dfrac{\partial \bar{u}_i}{\partial x_i})$ denotes the divergence of velocity and also the equation for f_3 is the spatial derivative of that of f_2, while the third term on the left-hand side

$$\Phi = \frac{\partial}{\partial x_i}[\bar{u}_j \frac{\partial \bar{u}_i}{\partial x_j} - \frac{1}{\mathrm{Re}}\frac{\partial^2 \bar{u}_i}{\partial x_j^{\,2}}]$$

denotes the spatial derivative of the convection and viscosity terms in f_2. Four variables of $\hat{D}, \bar{u}_i, \bar{p}$, and $\bar{T}$ can be solved by the four equations in Eq. (6b).

The second term on the left-hand side of the energy conservation law in Eq. (6b) can approximately be eliminated for low Mach number conditions.

In this study, the initial velocity distribution is set to be that of the potential flow, i.e.,

$$\overline{u}_1(t=0) = Uo = 1$$

$$\overline{u}_2(t=0) = \overline{u}_3(t=0) = 0 \quad (7)$$

at each point, while the initial pressure and temperature are constants.

The inlet boundary condition is given as

$$\overline{u}_1 = Uo + \delta = 1 + \delta,\ \overline{u}_2 = \overline{u}_3 = 0 \quad (8a)$$

and the outlet boundary condition as

$$\frac{\partial}{\partial n}\overline{u}_i = 0 \quad (8b)$$

where Uo, δ, and n denote the dimensionless inlet velocity, dimensionless inlet disturbance, and the direction normal to the outlet, respectively.

A no-slip boundary condition

$$\overline{u}_i = o \quad (8c)$$

is imposed at the solid walls of the pipe.

Next, let us consider ε_1 in Eq. (6b). Stronger inlet disturbances result in a smaller characteristic scale, because they lead to more inhomogeneous velocity distributions at the starting point of instability inside the laminar boundary layer.

Two types of indeterminacies, in the boundaries and inner regions, should be set to the same level. [19, 20, 21, 22, 26]

Thus, the relation

$$\sum_{n=1}^{N} \varepsilon_1 / N = Ce\ \delta \quad (9)$$

is used with an arbitrary constant Ce and the number of grid points *N*. In this report, C_e is set to be of the order of 1.0. [Comparisons with computations and experiments on the transition point in space and the theoretical considerations based on statistical mechanics including the Liouville equation brings that C_x should be about 1.0.]

Stochastic terms $\varepsilon_2, \varepsilon_3$, and ε_4 in Eq. (6b) should also be added to the momentum conservation law, the Poisson equation, and the energy conservation law averaged in the mesoscopic averaging window (MW). However, in this study, $\varepsilon_2, \varepsilon_3$, and ε_4 are set to be 0.0, because their role is similar to small variations of Reynolds and Peclet numbers in space and time, resulting in less influence on the transition point than in the case of the mass conservation law. This is clear from the fact that even the turbulence viscosity model based on the RNG theory [23] has less influence on the transition point, when the model is used in numerical computations. The stochastic terms $\varepsilon_2, \varepsilon_3$, and ε_4 have relatively weak influence on the transition phenomenon, because those in momentum and energy conservation laws can also be dissipative, while mass with ε_1 cannot essentially be dissipative.

There are two ways to calculate the random force term of ε_1: One involves the use of a random number generator and the other a special numerical disturbance close to the actual random number.

The second approach uses numerical errors coming from the iteration method for the matrix calculation, because the rounding error due to the iteration method such as the SOR method [30] is close to the random number generator, although truncation errors distorting the phenomenon should be eliminated.

One reason why previous attempts to compute the transition point in space have not succeeded [12, 13] is that the criterion of ε_1 in Eq. (6b) was set to zero based on mathematics [30], not on fluid physics taking into account indeterminacy and molecular discontinuity. Evaluations of ε in previous reports [30] were too small. Most of the previous studies on computational fluid dynamics have controlled only truncation errors, whereas the approach proposed here also provides physical control of rounding error.

The numerical algorithm used here is based on a multi-level formulation [29] that can simulate both incompressible and compressible flows. The momentum conservation law and the second derivative of the pressure equation in the formulation clarify the mathematical structure that the governing equation varies from an elliptic type to a hyperbolic type as the Mach number increases. Thus, the numerical algorithm is extended from the Marker and Cell (MAC) [31], SIMPLE [32], ICE [33], and CUP methods [34]. Details of the numerical discretizations and numerical algorithms are described in Refs. 29 and 34.

Computational results computed on mean velocity, turbulence intensity, and transition point agree well with the experimental data reported by Laufer, while the present approach also reveals the critical Reynolds number around 1,500 - 2,500. [19-22, 26]

4. TRANSITION TO TURBULENCE IN A ST RATGHT PIPE WITH ADIT

Here, we examine the relation between the transition point in space and flow amount injected from solid wall into a straight pipe. Figure 1 qualitatively shows that larger amount of adit from the wall results in later transition point in space. This may be used for reducing the drag force.

9. CONCLUSION

The present result obtained by computation should be checked by comparing with experiments.

REFERENCES

1. Reynolds O, An experimental investigation of the circumstances which determine whether the motion of water in parallel channels shall be direct or sinuous and of the law of resistance in parallel channels. Proceedings of the Royal Society of London, 35, (1883), 84-99.
2. Hirschfelder J.O., Curtiss C.F., and Bird R.B., Molecular Theory of Gases and Liquids, (John Willey & Sons, Inc. New York 1964).
3. Aris R., Vectors, tensors, and the basic equations of fluid mechanics (Dover, New York 1989).

4. Tatsumi T., Fluid dynamics, (Baifukan, Tokyo 1982).
5. Landau, E.D. and Lifshitz, E.M., Fluid Mechanics. 2nd Edition, (Butterworth-Heinemann Elsevier, Oxford 2004).
6. Wygnanski I.J. and Champagne F.H. On transition in a pipe. Part 1. The origin of puffs and slugs and the flow in a turbulent slug. J. of Fluid Mechanics, 59-2. 281. (1973).
7. Hof B., Westerweel J., Schneider T.M. & Eckhardt B. Finite lifetime of turbulence in shear flows. Nature 443, 59. (2006).
8. Nishi M., Ünsal B., Durst F. and Biswas G. Laminar-to-turbulent transition of pipe flow through slugs and puffs, Journal of Fluid Mechanics. 614. 425. (2008).
9. Kanda H. and Yanagiya T. Hysteresis Curve in Reproduction of Reynolds' Color-Band Experiments, J. of Fluid Engineering. Transaction of ASME, 130. 051202. (2008).
10. Faisst H. and Eckhardt B., J. Fluid Mechanics, 504, 343. (2004).
11. Eckhardt B., Schneider T.M., Hof B., and Westerweel J. Annual Review of Fluid Mechanics. 39, 447. (2007).
12. Moin P. and Kim J., J. Fluid Mech. 118, 341. (1982).
13. Kawamura T. and Kuwahara K., K. Direct simulation of a turbulent inner flow by finite-difference method. AIAA paper 85-0376 (1985).
14. Kanda H. and Shimomukai K.. Numerical study of pressure distribution in entrance pipe flow, J. of Complexity. (2009).
15. Orlandi P. Time evolving simulations as a tentative reproduction of the Reynolds experiments on flow transition in circular pipes. Physics of fluids. 20, 101516. (2008).
16. Haken H. Synergetics, an Introduction: Nonequilibrium Phase Transitions and Self-Organization in Physics, Chemistry, and Biology, 3rd rev. enl. ed. New York: Springer-Verlag, 1983.
17. Kitahara K., Nonequilibrium statistical physics, Iwanami, 1997.
18. Funaki T. and Otobe T. Scaling limits for weakly pinned random walks with two large deviation minimizers. J. Math. Soc. Japan, 62 (2010), 1005—1041.
19. Naitoh K. and Shimiya H. Stochastic determinism. Japan Journal of Industrial and Applied Mathematics, Vol.28, No.1, pp.3-14. (2011). [(also in Proceedings of 5th International Conference on Computational Fluid Dynamics, (ICCFD5), 2008].
20. Naitoh K., Maeguchi H., Ryu K., Matsushita S.. Stochastic Determinism. The 60th Nat. Cong. of Theoretical and Applied Mechanics. (2011)
21. Naitoh K. Stochastic determinism: revealing the critical Reynolds number in pipes and fast phase transitions. Proceeedings of ISAIF, Brussels, 2011.
22. Naitoh K, Ryu k, Matsushita S, Tanaka S, Kurihara M, Marui M, Weakly-stochastic Navier-Stokes equation and shocktube experimenys: revealing the Reynolds' mystery in pipe flows. AIAApaper 2012-2689, 2012.
23.Yakhot V. and Orszag S., Renormalization Group Analysis of Turbulence. I. Basic Theory. J. of Scientific Computing, 1, 3. (1986).
24. Drelaand M. and Giles M.B., Viscous-inviscid analysis of transonic and low Reynolds number airfoils. AIAA J, 25, 10, 1347 (1987).
25. Pope S.B., Turbulent Premixed Flames. Ann. Rev. Fluid Mechanics, 19, 237 (1987).
26. Naitoh K., Noda A., Kimura S., Shimiya H., and Maeguchi H. Transition to Turbulence and Laminarization clarified by Stochastic Determinism. Proceedings of 8th International Symposium on Engineering Turbulence Modeling and Measurements (ETMM8). Marseille, 775 (2010).
27.Laufer J., Investigation of turbulent flow in a two-dimensional channel, NACA Technical Note 2123, 68 (1950).
28.Kuan C.L. and Wang T., Experimental Thermal and Fluid Science, 3, 157 (1996). Also in Zhou D. and T. Wang T. Experimental Thermal and Fluid Science, 12, 338. (1996).
29.Naitoh K. and Kuwahara K., Large eddy simulation and direct simulation of compressible turbulence and combusting flows in engines based on the BI-SCALES method. Fluid Dynamics Research, 10, 299 (1992).
30.Roache P.J., Fundamentals of Computational Fluid Dynamics, (Hermosa Publishers, New Mexico1972).
31.Harlow F.H. and Welch J.E., Physics of Fluid, 8, 12 (1965).
32.Harlow F.H. and Amsden A.A., J. of Computational Physics, 8, 197 (1971).
33.S.V. Patanker and D.B. Spalding, International J. of Heat and Mass Transfer, 15, 1787 (1972).
34.Yabe T. and Wang P.Y., J. of Phys. Soc. Japan, 60, 2105, (1991).

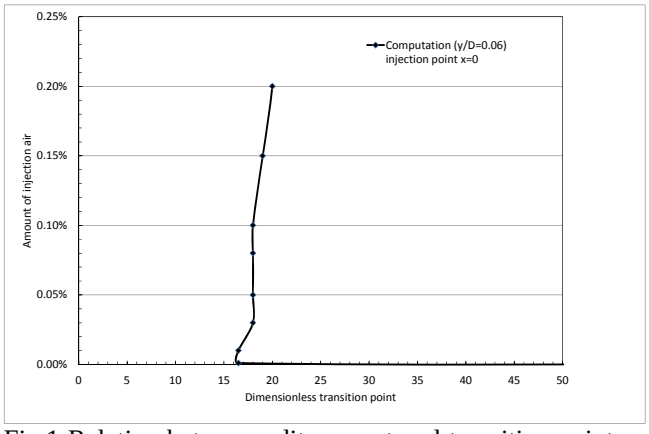

Fig.1 Relation between adit amount and transition point, which is computed by the present approach.

The Eighteenth International Symposium on Artificial Life and Robotics 2013 (AROB 18th '13),
Daejeon Convention Center, Daejeon, Korea, January 30-February 1, 2013

Stock market dynamics derived from a cognitive bias

Moto Kamiura[1]* and Yu Murata[1]

[1]Tokyo Denki University, Japan

*kamiura@mail.dendai.ac.jp

Abstract: Econophysics and behavioral economics give two new directions to economics. In econophysics, Non-Gaussianity of a distribution on stock market returns and generating mechanisms of that have been researched. Behavioral economics gives some approaches to human economic behaviors derived from cognitive biases. In these two approaches, we can find contrastive views on markets: i.e. "collective and individual". Connecting the two approaches, we can see a new aspect on market dynamics. In this study, we present a cognitive experiment which simulates human prediction of stock market returns, which follow an intermediate distribution between a Gaussian and a Cauchy's. Stock market dynamics may be based on not only self-organization of collective traders but also cognitive processes of individuals. Each of individuals can generate non-Gaussian distributions on the predicted prices. As the result of a cognitive experiment, we obtained distributions which are similar to the ones of stock market returns.

Keywords: Abducive reasoning, Overgeneralization, Distribution feature.

1 INTRODUCTION

Econophysics and behavioral economics give two new directions to economics. Non-Gaussianity of a distribution on stock market returns and generating mechanisms of that have been researched in econophysics, which had been presented by Mantegna and Stanley [1]. Some important ideas in econophysics are inspired by statistical mechanics and complex systems science: i.e. phase transitions of a market system and self-organization of market traders [2-4]. On the other hand, behavioral economics, which evolved from prospect theory presented by Kahneman and Tversky [5], gives some approaches to human economic behaviors derived from cognitive biases.

In these two approaches, we can find contrastive views on markets: i.e. "macroscopic and microscopic" or "collective and individual". Econophysics describes market dynamics as collective phenomena. It focuses on interaction structures of traders and on statistical features such as a sort of distributions of stock market returns. Behavioral economics researches human reactions to some stock trading situation: i.e. its research object is an individual and one's behaviors. Connecting the two approaches, we can see a new aspect on market dynamics.

In our previous researches [6-7], we studied relations between abduction (or abductive reasoning, which is a sort of heuristic reasoning) and parameter estimation with overgeneralization. The estimates based on the "simulated abduction" follow non-Gaussian distributions, which have features as intermediate distributions between a Gaussian and a Cauchy's. The intermediate feature is also in a distribution of stock market returns.

The above facts suggest that non-Gaussianity of stock market returns is derived from overgeneralization on time series of stock dynamics. A cognitive bias generating the overgeneralization is a subject of behavioral economics, and non-Gaussianity of stock market returns is a subject of econophysics. The two subjects have to be discussed in the view to connect them.

In this study, we present a cognitive experiment which simulates human prediction of stock market returns, which follow an intermediate distribution between a Gaussian and a Cauchy's. Stock market dynamics may be based on not only self-organization of collective traders but also cognitive processes of individuals. This study focuses on the latter: i.e. the ability of individuals generating non-Gaussian distributions. The experiments were done by 142 volunteers, using Windows PCs and application programs for the cognitive experiments. Each subject watches one's monitor displayed a graph of random walk time series, operates one's mouse and input a predicting value on the graph. In the result, we obtained distributions which are similar to the ones of stock market returns.

2 ABDUCTIVE REASONING AND ITS MATHEMATICAL MODEL

Conventional formal logic, which is equal to deduction, is based on transitivity of entailment. The simplest model is a syllogism: i.e. A→B and B→C imply A→C. On the other hand, whole of human reasoning includes not only deduction which is secure reasoning but also abduction which is insecure and creative reasoning [8-10]. Abduction

© ISAROB 2013

is a type of reasoning which has the following form: i.e. A →C and B→C imply A→B. Three types of reasoning, deduction, induction and abduction, are coordinated by C.S.Peirce [8]. The three types can be represented by Sawa-Gunji diagrams [6,7,10].

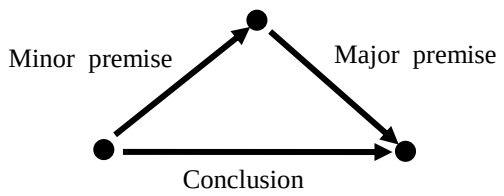

Fig. 1. Sawa-Gunji diagram

A Sawa-Gunji diagram (Fig.1) is a triangle with three arrows which correspond to a minor premise, a major premise and conclusion. Each of the three types of reasoning is represented by an operation in which one arrow induced from the other two arrows.

In our previous works [6-7], we show a correspondence between abduction based on a Sawa-Gunji diagram and generalized parameter estimation on a numerical function: i.e. when transitivity of a syllogism is equated with that of a system $y = f(x; a)$, abduction in which a minor premise is induced from a major premise and a conclusion is translated into estimation of a parameter a. It is not constrained by some conditions for conventional parameter estimation. The generalized parameter estimation, which has multi-aspect according to constraints, can be "simulated abduction" on a numerical system.

An example of simulated abduction is incomplete AR(p) parameter estimation based on the small number of data N. Under $N \to \infty$, the incomplete estimation results in conventional estimation, and the estimated parameters follow a Gaussian distribution. The Gaussianity disappears under $N \to p+1$, and the distribution approaches asymptotically to Cauchy distribution. Under $p+1 < N << \infty$, we obtain intermediate distribution between a Cauchy's and a Gaussian.

Conventional parameter estimation on a system $y=f(x;a)$ is a kind of mathematically appropriate generalization for given data x and y. On the other hand, incomplete parameter estimation like the above can be summed up as a kind of overgeneralization for given data. Avoiding overgeneralization and pursuing "appropriate" generalization are based on mathematical and technological requirements. Human beings would have ability of overgeneralization, although some apparent irrationality is in it as well as in abduction.

In the present study, we have a conjecture: i.e. non-Gaussianity of stock market returns would be induced from overgeneralization for market data series. In the following sections, we check non-Gaussianity of real market data (Nikkei 225), and we present a cognitive experiment to study causes of the non-Gaissanity.

3 NON-GAUSSIANITY ON STOCK DYNAMICS

A blue line of Fig.1 is a histogram of returns $\Delta x_t := x_t - x_{t-1}$ of Nikkei225 closing price x_t. The histogram consists of 7006 daily data from 4/January/1984 until 3/July/2012.

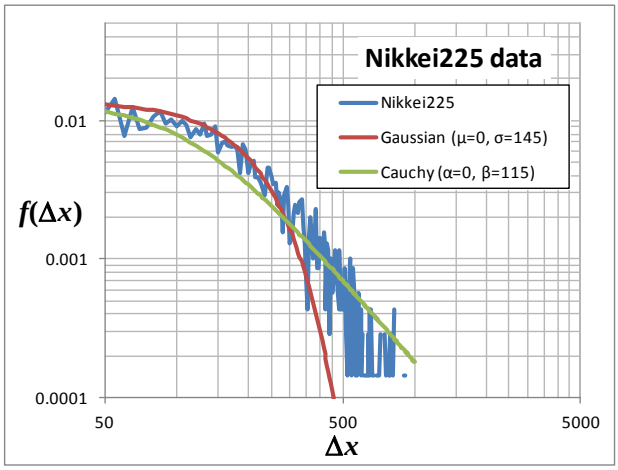

Fig. 2. Distributions of returns of Nikkei225 closing price, a Gaussian and a Cauchy's.

Note that Fig.2 is double logarithmic. A red line and a green line of Fig.1 are a Gaussian distribution (μ=0, σ=145) and a Cauchy distribution (α=0, β=155). The peaks of that are fitted to the peak of the Nikkei225 histogram, which is characterized as intermediate distributions between a Gaussian and a Cauchy's. This fact induces motivation of a cognitive experiment described in the next section: i.e. does prediction of an individual generate the intermediate distribution?

4 COGNITIVE EXPERIMENT

Patzelt, et al. [11] show that distances between a moving target and a mouse-driven cursor on a PC monitor follow a power law distribution by a cognitive experiment. In the present study, we propose a cognitive experiment, which is inspired by the Patzelt's experiment, simulates a process of pseudo stock price predicting. In the experiment, each

© ISAROB 2013

subject uses application software with the following GUI on a PC (Fig.3).

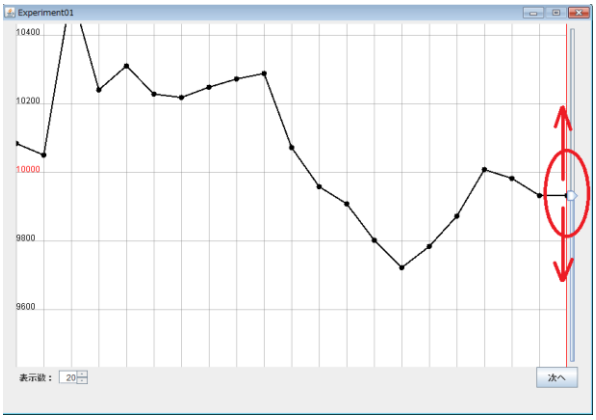

Fig. 3. The GUI of application software for the experiment on stock price predicting

The application indicates just random work time series $p_{t+1} = p_t + \varepsilon_t$ where ε_t follows a Gaussian distribution with the S.D. =145 and the initial price is p_{-25} = 9839. For the subject, we explain the time series as a daily chart on an artificial stock market, and we instruct them to input a predicting price of the next day via the slider of the application. A subject can see 20 days data of the time series on the application window. (S)He iterates through 100 times (i.e. 100 days) to move the slider, to decide the prediction price and to push a "next" button to go to the next day. The predicted prices $\{ x_t \mid 0 \leqq t \leqq 100 \}$ do not influence the indicated time series.

5 EXPERIMENTAL RESULT

A total of 142 men and women in their twenties participated in the cognitive experiment. Each person iterated 100 predictions in the experiment therefore we obtained 14200 data on the predicted prices x_t and the difference $\Delta x_t := x_t - p_{t-1}$, where $1 \leqq t \leqq 100$ and p_{t-1} is an indicated price as a value on the random walk time series. A blue line in Fig.4 shows a histogram of the difference $\Delta x_t := x_t - p_{t-1}$. A red line and a green line are a Gaussian distribution and a Cauchy distribution which are the same in Fig.2. The histogram of the difference in Fig.4 is also characterized as an intermediate distribution between them.

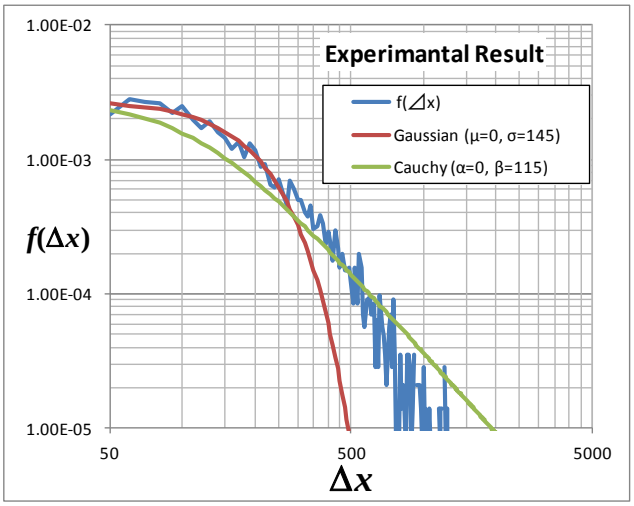

Fig. 4. The distribution of the differences between the predicted prices and the indicated prices.

6 CONCLUSION

Econophysics and behavioral economics give two new directions to economics. In these two approaches, we can find contrastive views on markets: i.e. "macroscopic and microscopic" or "collective and individual". Connecting the two approaches, we can see a new aspect on market dynamics. In this study, we presented a cognitive experiment which simulates human prediction of stock market returns, which followed an intermediate distribution between a Gaussian and a Cauchy's. Stock market dynamics may be based on not only self-organization of collective traders but also cognitive processes of individuals. This study focuses on the latter: i.e. each of individuals can generate non-Gaussian distributions on the predicted prices. As the result of a cognitive experiment, we obtained distributions which are similar to the ones of stock market returns.

REFERENCES

[1]R.N.Mantegna & H.E.Stanley (1999) Introduction to Econophysics: Correlations and Complexity in Finance Cambridge Univ. Press.

[2]V.M.Eguíluz & M.G.Zimmermann (2000) Transmission of Information and Herd Behavior: An Application to Financial Markets, Vol.85, No.26, pp.5659-5662.

[3]D.Sornette (2002) Why Stock Markets Crash: Critical Events in Complex Financial Systems, Princeton Univ. Press.

© ISAROB 2013

[4]M.Bartolozzi, D.B.Leinweber & A.W.Thomas (2005) Self-organized criticality and stock market dynamics: an empirical study, PhysicaA, Vol.350, pp.451–465.

[5]D.Kahneman & A.Tversky (1979) Prospect Theory: An Analysis of Decision under Risk, Econometrica, Vol.47, No.2, pp. 263-291.

[6]M.Kamiura (2010) Implication of Abductiton: Complexity Without Organized Interaction. Computing Anticipatory Systems, AIP Conf. Proc., Vol.1303, pp.60-67.

[7]M.Kamiura (2012) Abduction as Incomplete Parameter Estimation, Triple C, Vol.9, No.2, pp.494-501.

[8]C.S.Peirce (1955) Chap.11, Philosophical Writings of Peirce, Dover Publications.

[9]J.Finlay & A.Dix (1996) An Introduction to Artificial Intelligence. UCL press, London.

[10]K.Sawa & Y-P.Gunji (2010) Dynamical Logic Driven by Classified Inferences Including Abduction, AIP Conf. Proc., Vol.1303, pp. 52-59.

[11]F.Patzelt, M.Riegel, U.Ernst & K.Pawelzik (2007) Self-organized critical noise amplification in human closed loop control, Frontiers in Computational Neuroscience, Vol.1, Article 4.

© ISAROB 2013

The Eighteenth International Symposium on Artificial Life and Robotics 2013 (AROB 18th '13),
Daejeon Convention Center, Daejeon, Korea, January 30-February 1, 2013

Fusion visualization of surface and volume on AVS/Express

Hideo Miyachi[1], Koji Koyamada[2], and Naohisa Sakamoto[2]

[1]CYBERNET SYSTEMS CO., LTD., Japan
[2]Kyoto University, Japan
(Tel: 81-3-5297-3799, Fax: 81-3-5297-3637)

[1]miyachi@cybernet.co.jp

Abstract: Due to the innovation of super computer technology, the output of simulation by using such high performance computers has complexity and the data size is going to be too large. That makes difficulty to visualize the output for the evaluation and the analysis. To solve the issue, we have started a project sponsored by Japan Science and Technology Agency (JST) in which we develop a new visualization system named "Fusion Visualization" on a commercial software package AVS/Express. It will provide the volume rendering visualization with the surface rendering for conventional visualization methods. In this paper, we will present the plan and some preliminary visualization outputs by using the prototype system.

Keywords: visualization, super computing, volume rendering

1 INTRODUCTION

A volume rendering has an advantage that is smaller memory cost than a surface rendering. However, most of volume rendering methods requires the sorting of objects when the scene includes semi-transparency cells. It makes a difficulty of the parallel processing. To avoid the drawback, we have developed a sort free volume rendering method called Particle Base Volume Rendering (PBVR).[1] It solved the parallel issue, but it brought about a new problem. That was a difficulty of combining with surface rendering.

Then, we have started a project to develop new visualization software which can apply a volume rendering and a surface rendering to a scene. In this paper, we introduce the project plan and some outputs by the prototype version.

2 Particle Base Volume Rendering

A volume rendering is an image generation method that can be applied to scalar value defined at volume cells. In a typical method: ray casting method, a ray is extended from a pixel on a screen and sampling points are generated on the ray. Then, color and opacity values at each sampling point are calculated from the scalar value by a transfer function. Finally the color and opacity values on the pixel are calculated by integrating values along the ray (Fig.1).

Within this method, the integration has to be accumulated from the back to the front if one or more semi-transparency volume cell exist. It brings about the performance down especially to unstructured grid data.

To overcome the drawback, we have proposed a new model to volume rendering shown in Fig.2. In our model, it assumed that the inside of a cell is full of the light emission particles. The density of the particles is defined by the cell's transparency value. High transparency cell has a probability of small number of particles and low transparency cell has a probability of large number of particles.

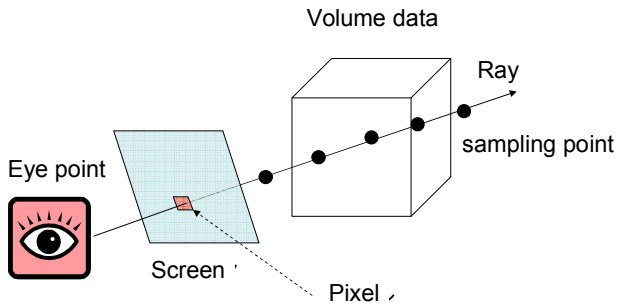

Fig.1 Ray casting volume rendering

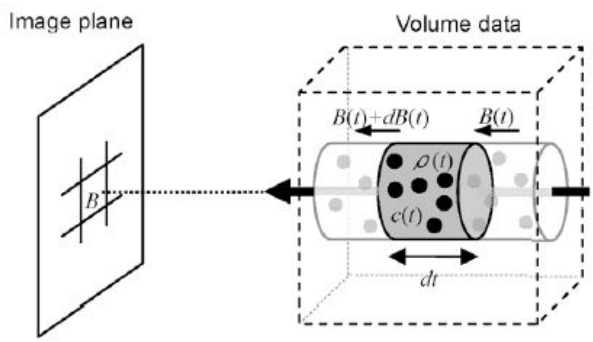

Fig.2 Light emission particles model

Particles generation and volume rendering are performed repeatedly. It is known that the ensemble

© ISAROB 2013

average of all images is approaching to the correct image. We called this method PBVR. This method does not require the sorting of cells, but requires much computer cost in proportion to the number of rendering. However, the number is controllable. Users can select the number of repeat according to the image quality needed.

3 Integrating PBVR to conventional surface ren dering

There are two ways to integrate volume rendering to surface rendering. The first is a method of carrying out a volume rendering after a surface rendering. The color and Z value which the surface rendering generated are used as an initial value of volume rendering. The second is voxelization. A volume rendering is carried out after converting surfaces to volume. Most of cases are using the first way.

Figure 3 shows an integration result of surface and volume rendering by a commercial software package: AVS/Express[2].

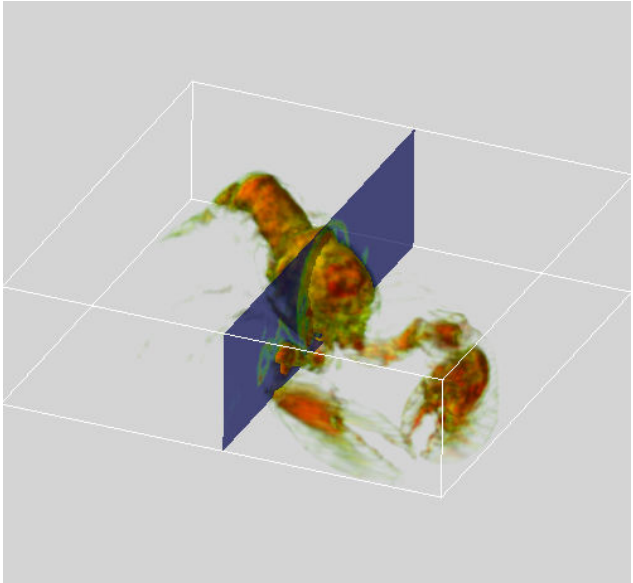

Fig.3 Integration of surface and volume rendering

The volume data in Fig.3 includes a lobster CT-scan image. A volume rendering visualizes the shape of the lobster and a surface rendering visualizes the density profile on a cross section and the external edges of the volume data. It may seem perfect, but it is not guaranteed the correct rendering when the visualization includes semi-transparency surface and volume.

Figure 4 is a case that the conventional method makes an ambiguous visualization about depth judging. This figure includes a teapot and a hydrogen molecule. The teapot is shown by a surface rendering and the hydrogen is shown by a volume rendering.

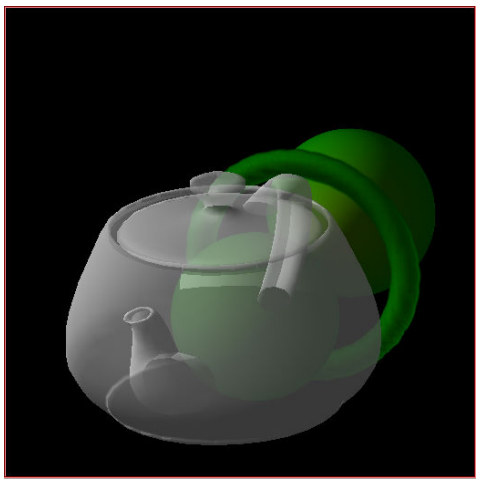

Fig.4 Ambiguous depth judging

As far as seeing this picture, it seems that the teapot is located in front of the molecule. It is misunderstanding which comes from the ambiguity of a depth judging.

4 Our goal and the implementation plan

We are going to implement a fusion visualization in which PBVR is integrated to conventional surface rendering. The goal of our project is to make a base of a sustainable product. Therefore, we are planning to implement the new visualization method on AVS/Express which has been maintained by CYBERNET SYSTEMS CO., LTD.(Tokyo, Japan) and .Advanced Visual Systems Inc.(MA, USA). The user interface is shown in Fig.5.

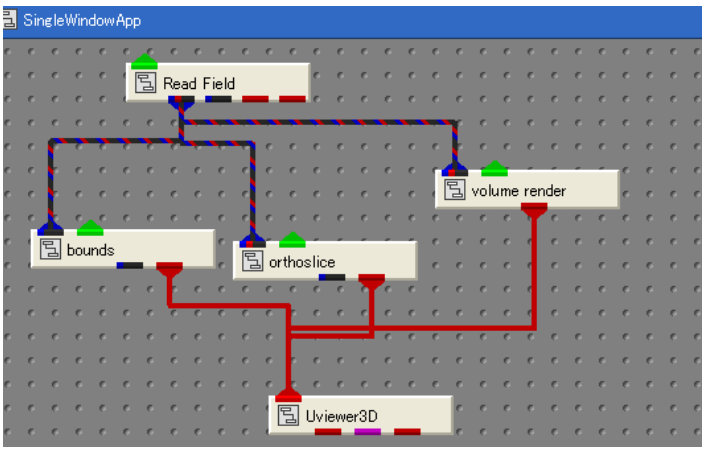

Fig. 5 User interface of AVS/Express

AVS/Express is designed by object orientation. Rectangle icons in Fig.5 represent modules. Lines between icons represent data flow. A set of the modules and the lines is called network that means a visualization program. For example, figure 5 illustrates the program to visualize Fig.3. Read Field loads the lobster volume data from a disk. And bounds, orthoslice and volume render visualize the external edge, the cross section profile and the lobster volume rendering respectively. Uviewer3D gives us mouse interaction to rotate, scale or translate the object. We plan to implement our fusion visualization as modules in it.

Within the first year (Oct 1st 2012 - Mar 31st 2013), we will develop the prototype version. It works on AVS/Express and visualize surface and volume data by OpenGL surface rendering and PBVR respectively. In the second year (Apr 1st 2013 – Mar 31st 2014), we will evaluate the prototype. We are looking for the evaluation partners who need large scale visualization or complex visual data mining. The points of the evaluation are as follows.

(1) Ease of use of a user interface
(2) Performance and efficient memory use
(3) Image quality of fusion visualization

In the final year (Apr 1st 2014 – Mar 31st 2015), we will enhance the software to respond the comments from evaluators.

5 Preliminary results by early prototype

5.1 Correct depth judging

Figure 6 shows the visualization result by our early prototype.

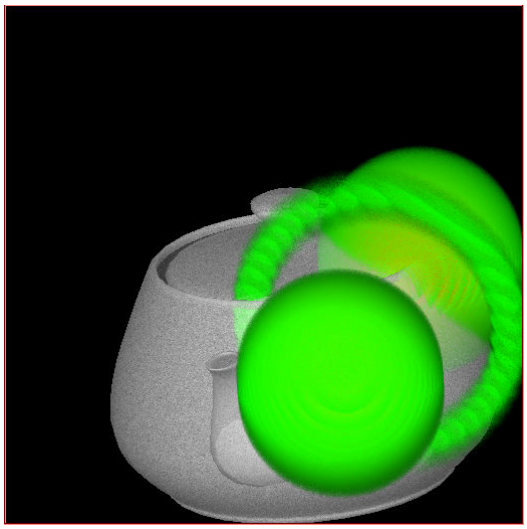

Fig. 6 Correct dept judging by our early prototype

The visualized data is the same as Fig.4. The conventional method could not visualize it with the correct depth judging. On the other hand, PBVR can visualize it correctly. The teapot and hydrogen are located in the same area.

5.2 Visualization of ocean data

Another trial result is shown in Fig.7. It shows a oceanographic data set simulated by the MRI Multivariate Ocean Variational Estimation (MOVE) System developed by Japan Meteorological Agency (JMA) and Meteorological Research Institute (MRI).

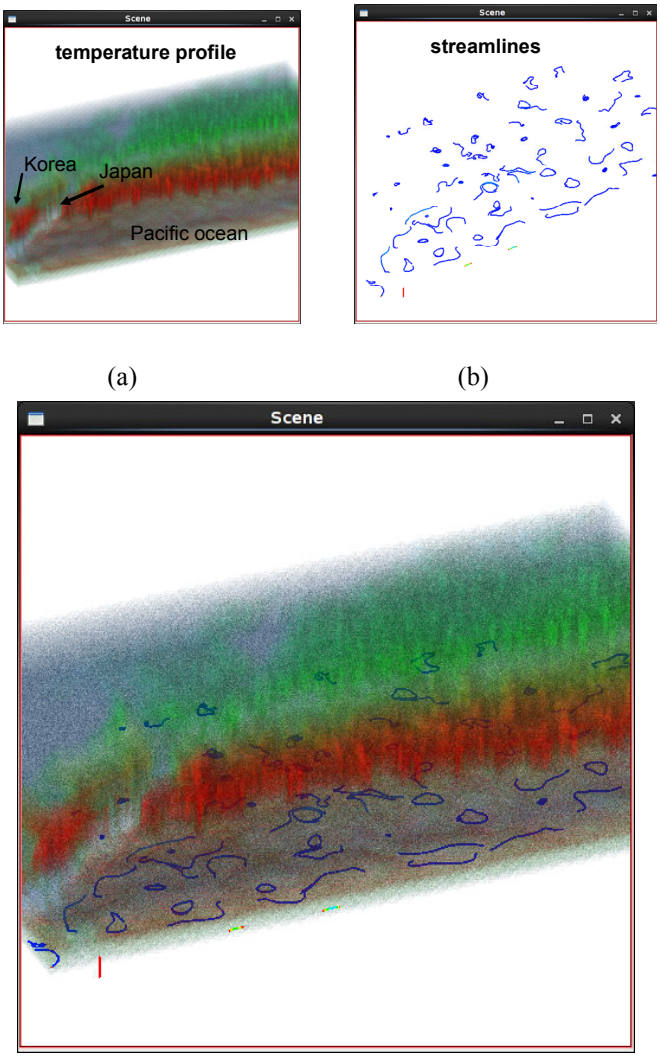

Fig.7 A fusion visualization trial result
(a) Volume rendering (b) Streamlines
(c) Fusion visualization

This picture Fig.7 (c) includes both surface rendering and volume rendering. The streamlines representing the

© ISAROB 2013

velocity profile (Fig.7 (b)) are shown by surface rendering and the temperature profile (Fig.7 (a)) is shown by volume rendering. The transfer function should be more optimized for the picture, but the early prototype does not have interactive interface to adjust it. That point will be one of our future works.

4 CONCLUSION

We have proposed a fusion visualization of surface and volume rendering for large scale visualization. We have developed an early prototype and showed some trial results by it. We will finish the first version for evaluation until the end of March 2013 and evaluate it in 2014 with voluntary evaluators. In the spring of 2015, the fusion visualization system will work with commercial software: AVS/Express with easy-to-use interface.

Acknowledgment

This work was partially supported by a project A-STEP<AS2415031H>: "The research and development of Fusion Visualization technology", of Japan Science and Technology Agency (JST). We would like to thank Dr. Hiromichi Igarashi from Japan Agency for Marine-Earth Science and Technology (JAMSTEC) for giving us the oceanographic datasets and Mr. Takashi Uenaka for supporting to our visualization.

REFERENCES

[1] Naohisa Sakamoto, Takuma Kawamura, Koji Koyamada,, " Improvement of particle-based volume rendering for visualizing irregular volume data sets", Computers & Graphics, Vol.34, No.1,2010, pp.34-42, 2010

[2] C. Upson, T. Faulhaber, D. Kammins, D. Laidlaw, D. Schlegert, J. Vroom, R. Gurwitz and A. Van Dam. : The Application Visualization System: a computational environment for scientific visualization, IEEE Computer Graphics and Applictaions, Vol. 9, No. 7, July. pp. 30-42., 1989

The Eighteenth International Symposium on Artificial Life and Robotics 2013 (AROB 18th '13),
Daejeon Convention Center, Daejeon, Korea, January 30-February 1, 2013

Autonomous polymer actuators

Yusuke Hara[1]

[1] Nanosystem Research Institute, NRI, National Institute of Advanced Science and Technology, AIST,
Central 5-2, 1-1-1 Higashi, Tsukuba 305-8565, Japan[1]
(Tel.: +81-29-861-9318; Fax: +81-29-81-6236)
[1]y-hara@aist.go.jp

Abstract: In this paper, in order to design the autonomous polymer actuators for soft robots and microfluidic devices, the effect of the molecular structure of the polymer chain on the self-oscillating behavior and the oscillation period was investigated by utilizing two-types of polymer chains; one is consist of N-isopropyl acrylamid (NIPAAm) and Ru catalyst of the BZ reaction, the other has NIPAAm and Ru catalyst, Acrylamide-2-methylpropanesulfonic acid (AMPS) with anionic charge as a solubility control site. As a result of the measuring the transmittance self-oscillation, it is clarified that the self-oscillating behavior is much affected by the molecular structure of the polymer chain. Moreover, this paper demonstrated the effect of the initial concentration of the three substrates of the Belousov-Zhabotinsky (BZ) reaction on the period of the aggregation-disaggregation self-oscillation.

Keywords: BZ reaction, molecular robot, soft actuator, oscillation period, self-oscillating polymer chain

1 INTRODUCTION

The self-oscillating polymer system can cause the aggregation-disaggregation self-oscillation synchronized with the periodically solubility change of the metal catalyst moiety in the polymer. [1-3] The cyclic solubility change of the metal catalyst is induced by the Belousov-Zhabotinsky (BZ) reaction. The BZ reaction is well known as an oscillating reaction accompanying spontaneous redox oscillations. [4-6] The overall process is the oxidization of an organic substrate by an oxidizing agent in the presence of the catalyst under acidic conditions. The solubility of the Ru catalyst changes with the oxidant state. In order to convert the cyclic solubility change of the Ru catalyst into the aggregation-disaggregation self-oscillation, the poly(Nisopropylacrylamide) (poly(NIPAAm)) covalently bonded to the Ru catalys was synthesized. As a result, the polymer chain caused the aggregation-disaggregation self-oscillation under the constant temperature conditions with the coexistence of the BZ substrates other than the metal catalyst. Therefore, the driving environment of the polymer chain was strongly restricted in the BZ reaction field. In my previous studies, in order to modify the driving environment, the molecular structure of the self-oscillating polymer chain was modified. As a result, the novel self-oscillating polymer chain can cause the aggregation-disaggregation self-oscillation only in the presence of malonic acid. [7] That is because the novel self-oscillating polymer chain has both a pH control and an oxidant supply sites in the self-oscillating polymer chain. In the process of this study, the self-oscillating polymer system with a negatively charged acrylamide-2-methylpropanesulfonic acid (AMPS) has a lot of potentials to control the self-oscillating behavior. [8-12] By utilizing this potential, the self-oscillating polymer system can cause an on-off switching of the self-oscillation by controlling the external temperature and a viscosity self-oscillation under acid-free condition.

In this paper, in order to design the autonomous polymer actuators for soft robots and microfluidic devices, the effect of the molecular structure of the polymer chains on the self-oscillating behavior and the oscillation period was investigated by utilizing two-types of polymer chains; one is consist of N-isopropyl acrylamid (NIPAAm) and Ru catalyst of the BZ reaction, the other has NIPAAm and Ru catalyst, Acrylamide-2-methylpropanesulfonic acid (AMPS) with anionic charge as a solubility control site. As a result of the measuring the transmittance self-oscillation, it is clarified that the self-oscillating behavior is much affected by the molecular structure of the polymer chain. Moreover, it is demonstrated the effect of the initial concentration of the three substrates of the BZ reaction on the period of the aggregation-disaggregation self-oscillation.

2 EXPERIMENTAL SECTION

Polymerization of poly(NIPAAm-*co*-Ru(bpy)$_3$)

poly(NIPAAm-*co*-Ru(bpy)$_3$) (Figure 1) was synthesized by utilizing N-isopropyl acrylamid (NIPAAm) and Ru(bpy)$_3$ monomer (ruthenium (4-vinyl-4'-methyl-2,2-bipyridine)bis(2,2' bipyridine)bis(hexafluorophosphate)) and 2,2'-azobisisobutyronitrile (AIBN) as an initiator by radical polymerization in an ethanol solution under a total monomer concentration of 20 wt% at 60°C. The feed composition (wt%) was as follows; NIPAAm : Ru(bpy)$_3$ = 10 : 90. The resulting reaction mixture was dialyzed against water for 4 days followed by ethanol for 3 days, and then freeze-dried.

Polymerization of poly(NIPAAm-*co*-Ru(bpy)$_3$-*co*-AMPS)

Using NIPAAm, Acrylamide-2-methylpropanesulfonic acid (AMPS), Ru(bpy)$_3$ monomer and AIBN, poly(NIPAAm-*co*-Ru(bpy)$_3$-*co*-AMPS) (Figure 2) was synthesized by radical polymerization in a mixture of ethanol and water (1:1 wt/wt%) under a total monomer

© ISAROB 2013

concentration of 20 wt% at 60 °C. The feed composition (wt%) was as follows; NIPAAm : $Ru(bpy)_3$: AMPS = 40 :10 : 50. The resulting reaction mixture was dialyzed against water for 4 days followed by ethanol for 3 days, and then freeze-dried.

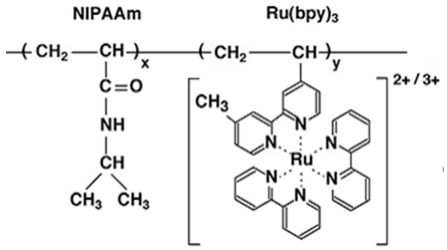

Figure 1. Chemical structure of poly(NIPAAm-*co*-$Ru(bpy)_3$)

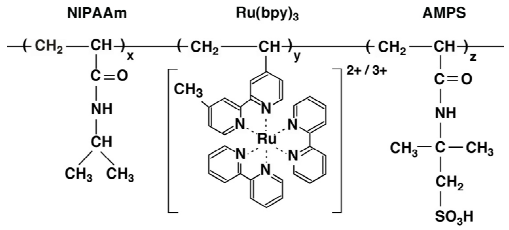

Figure 2. Chemical structure of poly(NIPAAm-*co*-$Ru(bpy)_3$-*co*-AMPS).

Measurement of transmittance self-oscillations.

The self-oscillating polymer solutions were prepared by dissolving the polymer (0.5 wt%) into an aqueous solution containing the three BZ substrates (nitric acid (HNO_3), sodium bromate ($NaBrO_3$) and malonic acid (MA)). The transmittance self-oscillations of the polymer solutions were measured under constant temperature (18 °C) and stirring condition. In order to detect the transmittance change which is based on the autonomous aggregation-disaggregation change, 570-nm wavelength was used. This is because 570-nm wavelength is the isosbestic point of the reduced and oxidized states of $Ru(bpy)_3$. [3, 7-9] The time course of the transmittance at 570 nm was monitored by a spectrophotometer.

3 RESULT AND DISCUSSION

Figure 3 shows self-oscillating behaviors of the poly (NIPAAm-*co*-$Ru(bpy)_3$-*co*-AMPS) (Figure 3(A) and 3 (B)) and the poly(NIPAAm-*co*-$Ru(bpy)_3$) (Figure 3(C) a nd 3(D)) solutions in the different concentrations of so dium bromate ([$NaBrO_3$] = 0.4 and 0.5 M) at 18 °C u nder the fixed concentration of malonic acid ([MA] = 0.1M) and nitric acid ([HNO_3] = 0.3 M). As sho wn in Figure 3(A) and 3(B), the amplitude of the tran smittance self-oscillation for the AMPS-containing poly mer solution is significantly stable. In contrast, the a mplitude of the self-oscillation for the poly(NIPAAm-*co* -$Ru(bpy)_3$) is not constant.

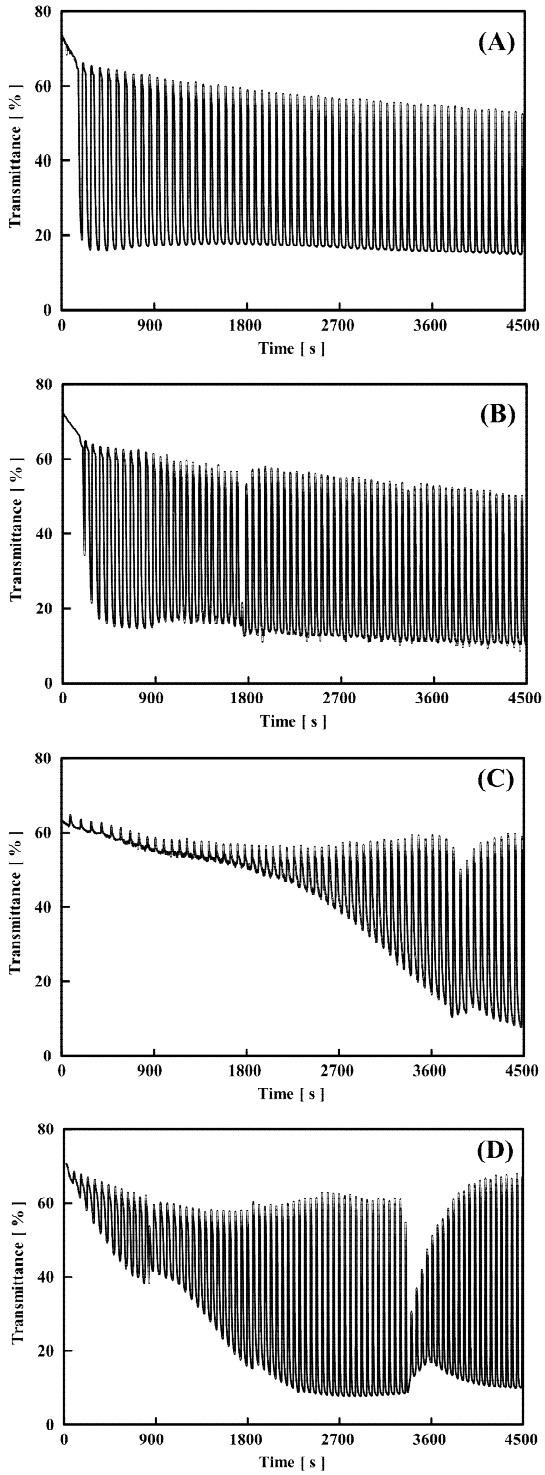

Figure 3. Oscillating profiles of transmittance at 18 °C for 0.5 wt% poly(NIPAAm-*co*-$Ru(bpy)_3$-*co*-AMPS) ((A) and (B)) and poly(NIPAAm-*co*-$Ru(bpy)_3$) ((C) and (D)) solutions in the fixed nitric acid and malonic acid conditions ([HNO_3] = 0.3 M and [MA] = 0.1 M): (A) [$NaBrO_3$] = 0.4 M, (B) [$NaBrO_3$] = 0.5 M, (C) [$NaBrO_3$] = 0.4 M, (D) [$NaBrO_3$] = 0.5 M.

© ISAROB 2013

That is because the self-oscillating polymer chain wit hout the AMPS moiety is easy to aggregate in the pol ymer solution because the solution containing three BZ substrates has the high ionic strength. On the other hand, the AMPS-containing polymer solution with the l ow polymer concentration is hard to aggregate due to the repulsive force of the AMPS moiety in the polyme r chain. In my previous studies, in the polymer concen tration above 1 wt%, the poly(NIPAAm-*co*-Ru(bpy)$_3$-*co*-AMPS) chain is easy to aggregate due to the electrost atic attractive force among the polymer chains. [12-13]

This is because the polymer chain has the cationic Ru(bpy)$_3$ and the anionic AMPS moieties in the polym er chain. As shown in Figure 3(C) and 3(D), the am plitude of the self-oscillation gradually increased with t ime.

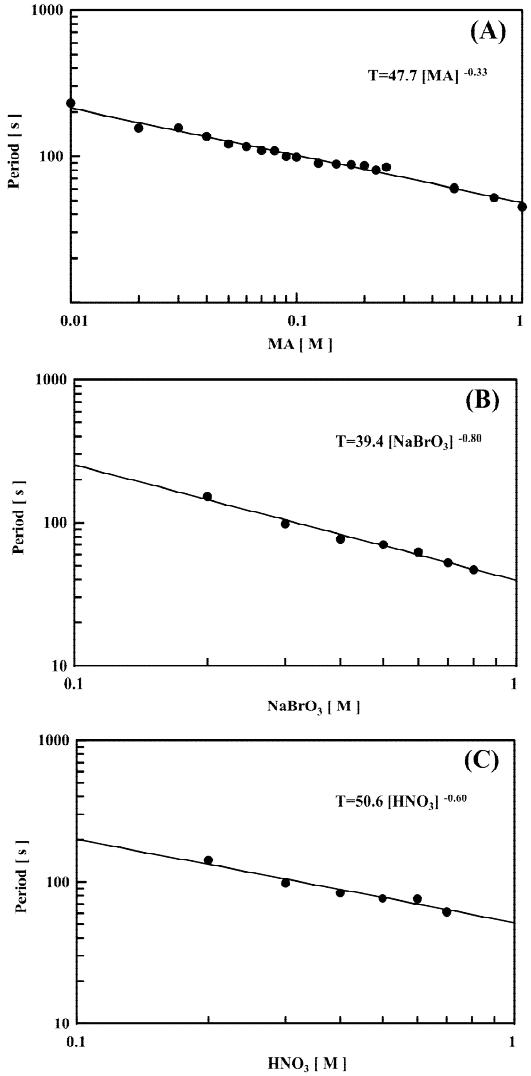

Figure 4. Logarithmic plots of period ***T*** (in s) for 0.5 wt% poly(NIPAAm-*co*-Ru(bpy)$_3$-*co*-AMPS) solution vs i nitial molar concentration of one BZ substrate at a con stant temperature (T = 18 °C) under fixed concentratio ns of the other two BZ substrates: (A) [NaBrO$_3$] = 0.3 M and [HNO$_3$] = 0.3 M; (B) [MA] = 0.1 M and [H NO$_3$] = 0.3 M; (C) [MA] = 0.1 M and [NaBrO$_3$] = 0. 3 M.

This behavior indicates that the aggregated polymer ch ains gradually disaggregated in the self-oscillating beha vior.

Figure 4 and 5 showed the logarithmic plots of the period against the initial concentration of one substrate under fixed the other two BZ substrates at the consta nt temperature (T = 18 °C). As shown in Figure 4 a nd 5, all the logarithmic plots had a good linear relati onship. Therefore, the period [T(s)] of the transmittan ce self-oscillation can be expressed as a[substrate]^b wh ere a and b are the experimental constants and bracket s assign the initial concentration. As shown in Figure 4 and 5, there are no saturation points in this experi mental condition. In the case of the nonthermorespons ive polymer chain, the period of the self-oscillation ha ve the saturation point at the [HNO$_3$] = 0.3 M. [14]

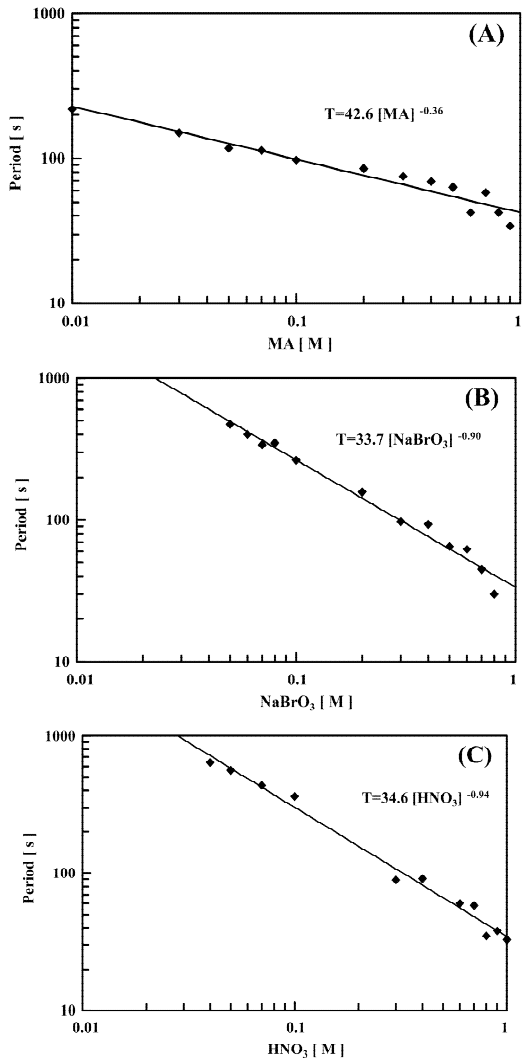

Figure 5. Logarithmic plots of period ***T*** (in s) of 0.5 wt% poly(NIPAAm-*co*-Ru(bpy)$_3$) solution vs initial mol ar concentration of one BZ substrate at a constant tem perature (T = 18 °C) under fixed concentrations of the other two BZ substrates: (A) [NaBrO$_3$] = 0.3 M and [HNO$_3$] = 0.3 M; (B) [MA] = 0.1 M and [HNO$_3$] = 0.3 M; (C) [MA] = 0.1 M and [NaBrO$_3$] = 0.3 M.

© ISAROB 2013

As shown in Figure 4(C) and 5(C), the, the *b* value of the poly(NIPAAm-*co*-Ru(bpy)$_3$) is much larger than that of poly(NIPAAm-*co*-Ru(bpy)$_3$-*co*-AMPS). In the case of the poly(NIPAAm-*co*-Ru(bpy)$_3$-*co*-AMPS) solution (Figure 4(C)), the aggregation-disaggregation self-oscillation do not occur in the condition under the [HNO_3] = 0.1 M. Moreover, in the case of the poly(NIPAAm-*co*-Ru(bpy)$_3$-*co*-AMPS) solution (Figure 4(B)), there are no aggregation-disaggregation self-oscillation in the condition under the [$NaBrO_3$] = 0.1 M. These results indicate that the concentration range of the three BZ substrates for the AMPS-containing polymer solution where the self-oscillation occur is much narrower than that for the poly(NIPAAm-*co*-Ru(bpy)$_3$) solution. In addition, as shown in Figure 4(C) and 5(C), the period has the different aspect as compared to the conventional-type poly(NIPAAm-co-Ru(bpy)$_3$) gel [15]. In the case of the poly(NIPAAm-co-Ru(bpy)$_3$) gel, when increasing in the concentration of nitric acid, the period increased. However, in general, the period of the self-oscillation decreased with increasing the initial concentration of the BZ substrates because of the increase in the collision frequency among the BZ substrates. Therefore, I consider that the tendency of the Figure 4(C) and 5(C) is more natural tendency

4 CONCLUSION

In this study, in order to design the autonomous polymer actuators for soft robots and microfluidic devices, the effect of the molecular structure of the self-oscillating polymer chain on the self-oscillating behavior and the oscillation period was investigated by utilizing the poly(NIPAAm-*co*-Ru(bpy)$_3$-*co*-AMPS) and the poly(NIPAAm-*co*-Ru(bpy)$_3$) solutions. As a result, the amplitude of the poly(NIPAAm-*co*-Ru(bpy)$_3$) is not stable due to the aggregation property of the polymer chains. On the other hand, the amplitude of the poly(NIPAAm-*co*-Ru(bpy)$_3$-*co*-AMPS) is significantly stable. This result indicates that the AMPS-containing polymer chain is hard to aggregate originating in the repulsive force of the AMPS moiety in the polymer chain in the low polymer concentration. In addition, this paper demonstrated the period of the two-types of self-oscillating polymer solutions. The concentration range of three BZ substrates for the poly(NIPAAm-*co*-Ru(bpy)$_3$) solution where the self-oscillation occur is much wider than that for the poly(NIPAAm-*co*-Ru(bpy)$_3$-*co*-AMPS) solution.

5 ACKNOWLEDGMENT

This work is supported also by Grants-in-Aid (KAKENHI) (No. 24656178) for Challenging Exploratory Research. In addition, this work was carried out under the auspices of the New Energy and Industrial Technology Development Organization (NEDO) of Japan under the Industrial Technology Research Grant Program in 2011. Moreover, this work was supported by a Grant-in-Aid for Scientific Research on Innovative Areas "Molecular Robotics" (No. 24104003) of The Ministry of Education, Culture, Sports, Science, and Technology, Japan.

REFERENCES

[1] Ishiwatari T, Kawaguchi M, Mitsuishi, M (1984), Oscillatry reactions in polymer systems, *J. Polym. Sci. Part. A: Polm. Chem*, 22, pp. 2699-2704.

[2] Yoshida R, Takahashi T, Yamaguchi T, Ichijo H (1996), Self-oscillating gel, *J. Am. Chem. Soc.* **1996**, 118, pp. 5134-5135.

[3] Yoshida R, Sakai T, Ito S, Yamaguchi T (1996), Self-oscillation of polymer chains with rhythmical soluble-insoluble changes, *J. Am. Chem. Sci.* 124, pp. 8095-8098.

[4] Zaikin A.N, Zhabotinsky A.M (1970), Concentration Wave propagation in two-dimensional liquid-phase self-oscillating system, *Nature*, 225, pp.535–537.

[5] Field, R.J, Burger M (1985),Oscillations and Traveling Waves in Chemical Systems; John Wiley & Sons: New York, NY, USA, 1985.

[6] Field, R.J, Noyes R.M (1974), Oscillations in chemical systems. IV. Limit cycle behavior in a model of a real chemical reaction. J. Chem. Phys., 60, pp.1877–1884.

[7] Hara Y, Yoshida R (2008), Self-oscillating polymer fueled by organic acid. *J. Phys. Chem. B*, 112, pp.8427–8429.

[8] Hara Y, Yoshida R (2005), Self-oscillation of polymer chains induced by the Belousov-Zhabotinsky reaction under acid-free conditions. *J. Phys. Chem. B*, *109*, pp. 9451–9454.

[9] Hara Y, Yoshida R (2009), Damping behavior of aggregation-disaggregation self-oscillation for a polymer chain, *Marcomol. Rapid Commun. 30*, pp.1656–1662.

[10] Hara Y, Yoshida R (2005), Control of oscillating behavior for the self-oscillating polymer with pH-control site. *Langmuir*, *21*, pp. 9773–9776.

[11] Hara Y, Yoshida R (2008), A viscosity self-oscillation of polymer solution induced by the BZ reaction under acid-free condition. *J. Chem. Phys. 128*, 224904.

[12] Hara Y, Jahan R.A (2011), Influence of temperature and the BZ substrate on aggregation-disaggregation self-oscillation of a polymer chain, *Key Engineering Materials*, 467-469, pp.1472-1477.

[13] Hara Y, Jahan R.A (2011), Self-oscillating behaviors of negatively charged polymer chain induced by the Belousov-Zhabotinsky reaction, *Advanced Materials Research*, 181-182, pp.206-211.

[14] Hara Y, Jahan R.A (2011), Influence of initial substrate concentration of the Belouzov-Zhabotinsky reaction on transmittance self-oscillation for a nonthermoresponsive polymer chain, *Polymers*, 3, pp.330–339.

[15] Yoshida R, Onodera S, Yamaguchi T, Kokufuta E (1999), Aspects of the Belousov-Zhabotinsky reaction in polymer gels, *J. Phys. Chem. A*, 103, pp.8573-8578.

© ISAROB 2013

The Eighteenth International Symposium on Artificial Life and Robotics 2013 (AROB 18th '13),
Daejeon Convention Center, Daejeon, Korea, January 30-February 1, 2013

Cyanobacterial circadian clock is nullified under low temperature via Hopf bifurcation

Yoriko Murayama[1], Hiroshi Kori[2], Takao Kondo[1], Hideo Iwasaki[1], Hiroshi Ito[4]

[1]Graduate School of Sciences and Engineering, Waseda University, Japan
[2]Division of Advanced Sciences, Ochanomizu University, Japan
[3]Division of Biological Science, Graduate School of Science, Nagoya University, Japan
[4]Department of Design, Kyushu University, Japan
(Tel: 81-92-553-4535)

[4]hito@design.kyushu-u.ac.jp

Abstract: One of the key characteristics of all circadian rhythms is that the free-running period remains stable under a relatively broad range of ambient temperatures, referred to as "temperature compensation" of the period. Outside of the range of temperature compensation, circadian clocks stop running and are arrested at a certain phase. Based on bifurcation theory, Hopf bifurcation and saddle-node bifurcation are plausible scenarios of circadian arrhythmia at low temperature. We focused on a biochemical circadian oscillation, KaiC phosphorylation rhythms, which can be reconstituted in a test tube by mixing the three protines , KaiA, KaiB, and KaiC in the presence of ATP. The KaiC phosphorylation rhythm in vitro is the simplest circadian oscillation to observe directly and precisely dynamics of circadian oscillator. We found that the phenomena of nullification of KaiC phosphorylation rhythm by low temperature was explained by theory of Hopf bifurcation.

Keywords: circadian rhythms, cyanobacteria, Hopf bifurcation

1 INTRODUCTION

Biological rhythms are the physiological oscillation in living things. The oscillation with a 24 hours period is called circadian rhythms in biology and extensively studied. Awake-sleep cycle, nyctinasty movement of leaves, and periodical gene expressions are well examined in this research area.

One of the shared characteristics among all circadian rhythms is that the free-running period remains stable for a relatively broad range of ambient temperatures, referred to as "temperature compensation" of the period. Temperature at which temperature compensation is effective typically lies well within the physiological range, that is, the range permissive for growth. Interestingly, outside of the range of temperature compensation, circadian clocks stop running and are arrested at a certain phase [1, 2]. Although essentially identical results have been found in various organisms, it remains unclear if temperature stimuli affect the circadian clock directly or indirectly through such as metabolic changes.

In this presentation, we will focus on why circadian rhythms cannot be observed at low temperature conditions. Cyanobacterium, *Synechococcus elongatus* PCC 7942 is the simplest organism that exhibit circadian rhythms. The cyanobacterial circadian timing requires neither de novo transcription nor translation [3], and the post-translational oscillation can be reconstituted in a test tube using only three clock proteins, KaiA, KaiB, and KaiC [4]. The KaiC phosphorylation rhythm in vitro (hereafter referred to as "in vitro clock") satisfies the criteria of circadian rhythms [4,5] and disappears below a certain critical temperature (around 20 ºC: [6]).

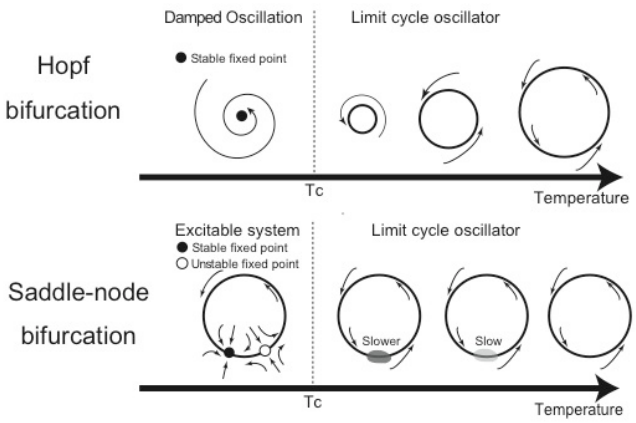

Fig.1 Two types of bifurcation for arrhythmia

2 BIFURCATION FOR ARRHYTHMIA

There are two typical scenarios for nullification of rhythmic phenomena according to bifurcation theory [7] (Fig.1, 2). One is called Hopf bifurcation and the other is called Saddle-node bifurcation on circle. The behavior of self-sustained oscillators (limit-cycle oscillators) depends on the

© ISAROB 2013

type of bifurcations. In the case of Hopf bifurcation, the amplitude of the oscillations can be altered and then the amplitude monotonically approach to 0 around bifurcation point. Below bifurcation point, self-sustained oscillator can not sustain its amplitude and is changed into a damping oscillator.

On the other hand, the amplitude does not change significantly in the case of Saddle-node bifurcation on circle. When a control parameter is altered, the period can be lengthened because the phase progress at a certain phase become s lower. The period of the oscillation approaches to infinity around the bifurcation point. Below critical point, stable and unstable fixed points are created on the circle.

Cell cycle is known as the famous example of the scenario of Saddle-node bifurcation on circle[8]. By inducing gene expressions involved in cell cycle (e.g. Cyclin), cell cycle can be arrested at a certain stable fixed point on circle. The fixed point is called "check point" in the research area of cell biology.

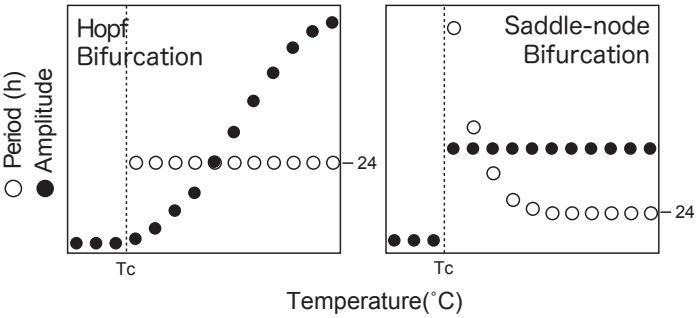

Fig.2 Amplitude and Period for Hopf and Saddle-node bifurcations

To distinguish the type of bifurcations of arrhythmia of in vitro clock, we prepared 15 samples mixing the three Kai proteins with ATP and incubated at various ambient temperatures. From 30 ºC to the critical temperature (ca. 19ºC), the amplitude of in vitro clock declined monotonically but its period remained relatively constant (Fig.3). This result indicates the rhythms can be nullified at low temperature conditions via Hopf bifurcation.

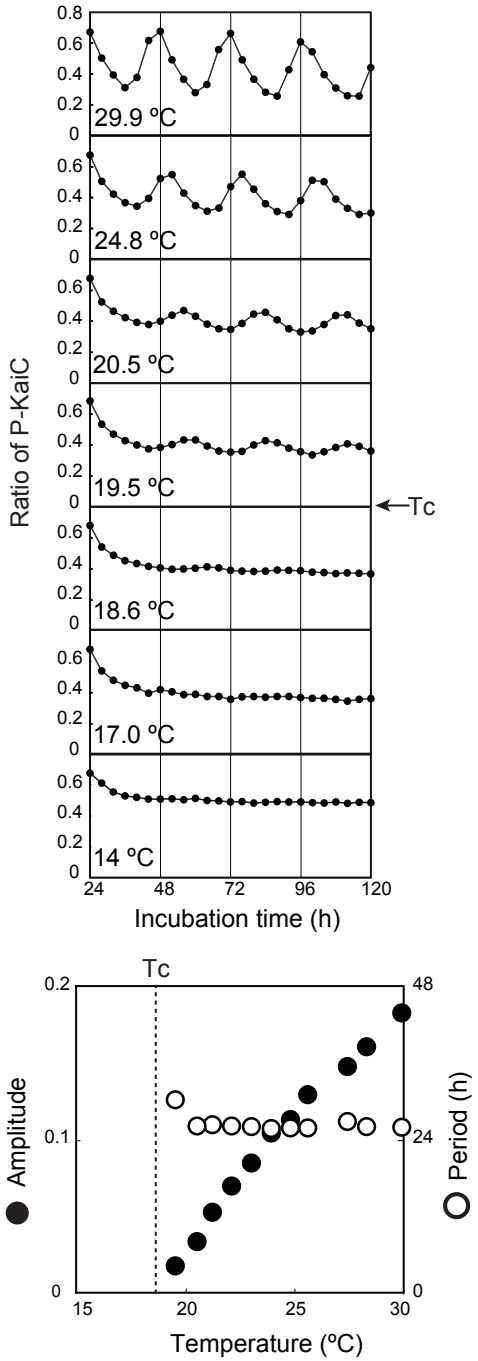

Fig3. Rhythms of in vitro clock at low temperature

3 DAMPING OSCILLATIONS BELOW CRITICAL TEMPERATURE

As stated at the previous section, the damping oscillation should be observed below critical point. We chilled samples at 4 ºC and exposed 30ºC pulse to them for 12 hours. Then we transferred the samples to below critical temperatures (10ºC – 19 ºC). The damping oscillator was kicked by high temperature pulse and the rapid damping rhythms were successively observed (Fig.3). Especially in

the case of the lowest conditions, we can not observe damping oscillation. Instead, no overshooting relaxation (over-damping) was observed. This result also suggests that circadian rhythms are abolished by low temperature through Hopf bifurcation.

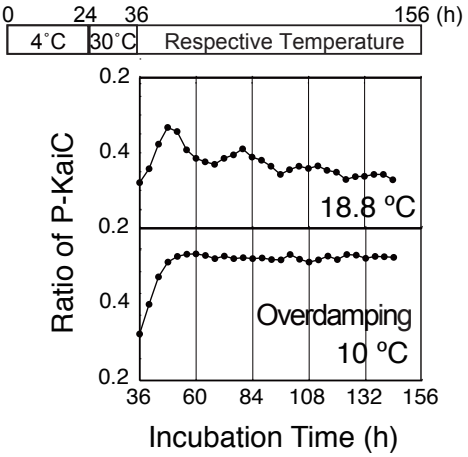

Fig.4 Damping oscillation of in vitro clock

4 RESONANCE BELOW CRITICAL TEMPERATURE

Under the critical point of Hopf bifurcation, the limit cycle oscillator can be changed into damping oscillator. Linear oscillator or damping oscillator under the external periodic environment can show resonance phenomena. When the damping oscillators is exposed to oscillatory external forces with the period of the natural frequency of the oscillator, the amplitude of the oscillator can grow significantly. In that sense, there is optimal frequency in external force, which can grow the amplitude of the oscillators.

We tested if there is optimal frequency of external force for the damping oscillation of in vitro clock below critical temperature. We observed in vitro clock under ambient temperature cycles of 16.7ºC / 18.7 ºC with a various period (6 hours – 36 hours). Both 16.7ºC and 18.7 ºC are below critical temperature.

We observed the forced oscillation with large amplitude when the period of external forces was 26 hours (Fig. 5). The observed resonant behavior might have a physiological meaning. Cyanobacteria populate most sea or lakes even near the north pole. The water temperature of cold area should be kept below critical temperature (19 ºC) for all day. However, diurnal change of water temperature might act as a periodical external force and grow the amplitude of KaiC phosphorylation rhythms in a cell. Thus, even under critical temperature, KaiC phosphorylation rhythms might function as a biological clock.

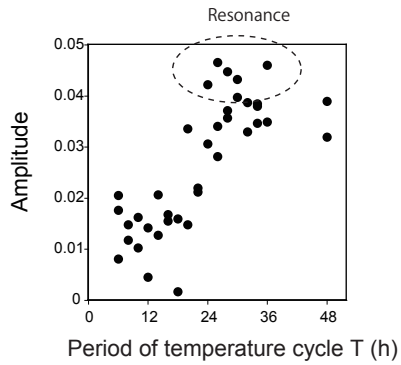

Fig. 5 Resonance of in vitro clock

5 A SIMPLE MODEAL FOR RESONANCE

To mathematically interpret the resonance phenomena, we performed a simple simulation. Consider Stuart-Landau oscillator,

$$\dot{z} = (a + i\omega - z^2)z$$

which is the generalized model near Hopf bifurcation point. a is a parameter specifying the distance from Hopf bifurcation and ω is the natural frequency (here, ω was fixed to 3). This model exhibits self- sustained oscillations if $a > 0$ and settles down at fixed point if $a \leq 0$. We chose parameter sets which can reproduce in vitro oscillation at 16 ºC and 18 ºC.

Under 16 ºC and 18ºC, in vitro clock exhibits damping oscillations. We hypothesized that the position of equilibrium points depends on the ambient temperature. Then, changing the ambient temperature corresponds to shifting the equilibrium point.

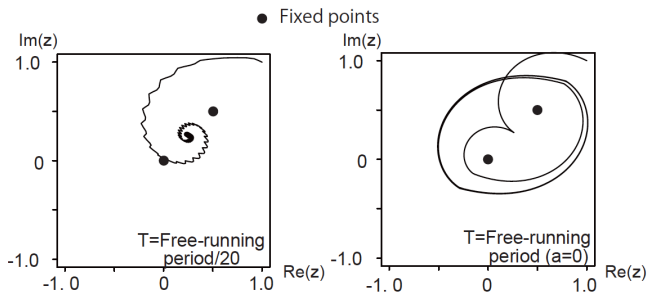

Fig. 6 Resonance of SL oscillator

The simulation can successively reproduce the resonance when the period of switching the equilibrium point (denoted as T) equals to the free-running period of the oscillator (Fig. 6). The periodic orbit on the phase plane surrounded the both equilibrium points. When much smaller T was chosen, the system settled down to a mid point between the two equilibrium points.

© ISAROB 2013

6 CONCLUSIONS

We have showed KaiC phosphorylation circadian rhythms in a test tube can be nullified via Hopf bifurcation. As bifurcation theory predicted, we succeeded in observing damping oscillation of the in vitro clock. We also succeeded in observing resonance of KaiC phosphorylation rhythms under low temperature cycles.

REFERENCES

[1] Pittendrigh CS (1975), Circadian Clocks: What are They? In: Hastings JW, Schweiger H-G, editors. The Molecular Basis of Circadian Rhythms. Berlin: Abakon Verlagsgesellschaft. pp. 11–48.

[2] Kondo T (1980), Phase progress under low temperature treatment of the potassium uptake rhythm in a duckweed, Lemna gibba G3. Plant and Cell Physiology. 21 95-103.

[3] Tomita J, Nakajima M, Kondo T, Iwasaki H (2005), No transcription-translation feedback in circadian rhythm of KaiC phosphorylation. Science 307, 251–254.

[4] Nakajima M, Imai K, Ito H, Nishiwaki T, Murayama Y, Iwasaki H, Oyama T, Kondo T (2005), Reconstitution of circadian oscillation of cyanobacterial KaiC phosphorylation in vitro. Science 308, 414-5.

[5] Yoshida T, Murayama Y, Ito H, Kageyama H, Kondo T (2009), Nonparametric entrainment of the in vitro circadian phosphorylation rhythm of cyanobacterial KaiC by temperature cycle. Proceedings of the National Academy of Sciences USA. 106, 1648-53.

[6] Kitayama Y, Nishiwaki T, Terauchi K, Kondo T (2008), Dual KaiC-based oscillations constitute the circadian system of cyanobacteria. Genes Development 22, 1513-21.

[7] SH Strogatz (1994), Nonlinear Dynamics and Chaos, Addison-Wesley, New York

[8] Borisuk M & Tyson J (1998), Bifurcation analysis of a model of mitotic control in frog eggs. Journal of Theoretical Biology 195, 69–85.

© ISAROB 2013

The Eighteenth International Symposium on Artificial Life and Robotics 2013 (AROB 18th '13),
Daejeon Convention Center, Daejeon, Korea, January 30-February 1, 2013

Development of Entertainment Based Learning Features in Programming Learning support System

Eiji Nunohiro, Masanori Ohshiro, and Takashi Yamaguchi

Tokyo University of Information Sciences, 4-1 Onaridai, Wakaba-ku, Chiba 265-8501, Japan
(Tel: 81-43-236-1292; Fax : 81-43-236-1292)
nunohiro@rsch.tuis.ac.jp

Abstract: In this research, we developed a self learning programming support system called CAPTAIN (Computer Aided Programming Training And Instruction) that stimulates students' interest and motivation of their study continuously. When students use CAPTAIN, they feel that they are just like playing their computer games. In order to identify advantage and disadvantage or to investigate how to improve CAPTAIN, we are now using CAPTAIN for the tutorials of a Java programming course. We developed an improved version of CAPTAIN, a learning programming support system which has the feature of entertainment. In this paper, we describe the overview of the proposed learning programming support system CAPTAIN3.4 which contains entertainment features, such as interactively showing animation and inciting the students to compete like their games. The proposed system has been applied to an actual university programming course and we evaluate the effect of this system by comparison between the students' progress with this system and that without using this system. We then discuss possible future works based on the evaluation.

Keywords: E-learning, Programming, Entertainment Based learning.

1 Introduction

It is said that the interests of students taking computer or information sciences courses in educational institution are expanding various directions. Their interests do not only include computer science but also Web design, game, multi-media and so on. In order to teach those students effectively in a same class, those students in the tutorial classes of programming are classified into small groups depending upon their initial skill, experience and ability and teach those tutorial groups separately. However the restriction of staff resource, it is often happened that the size of those tutorial groups is between 40 and 50 which is not ideal to give a high quality support to every one of the member of the students. In conclusion, slow learning students could not achieve their targets, whereas advanced students finish quicker, so get bored. In either case, the motivation of those students will be lost. It is therefore required a learning support system that stimulates every students' interest and the motivation of their studies.

For past research on learning programming systems, one of the methods, suggested, provides spaces in a source program then students fill program code in the spaces by instructions provided [1]. For the research on motivational learning methods, there is a method based on ARCS model [2] [3]. However, we could not find a teaching system, applied by ARCS model in the literature, which continuously stimulates students' interest and motivation.

In this research, we developed a self learning programming support system called CAPTAIN (Computer Aided Programming Training And Instruction) that stimulates students' interest and motivation of their study continuously. When students use CAPTAIN, they feel that they are just like playing their computer games. In order to identify advantage and disadvantage or to investigate how to improve CAPTAIN, we are now using CAPTAIN for the tutorials of a Java programming course.

In this paper, we describe the overview of the proposed learning programming support system CAPTAIN ver.3.4 (CAPTAIN3.4) which contains entertainment features, such as interactively showing animation and inciting the students to compete like their games.

The proposed CAPTAIN3.4 has been applied to an actual university programming course and we evaluate the effect of this system, especially the function of competitive learning function using nickname which is a new function of CAPTAIN3.4 by comparison between the students' progress with this system and that without using this system. We then discuss possible future works based on the evaluation.

2 Purpose of the programming learning support system

From past experience, the low motivation of learners who have difficulty in programming is strongly related to stumbling in the early stages of programming training. We considered that a game-based programming learning

© ISAROB 2013

environment that focuses on program structure recognition and training would stimulate and sustain the learning motivation as well as improve programming skill. From this, we proposed a programming training system with game based learning features to stimulate and sustain motivation for beginners and slow learners in programming. We aimed at developing a learning environment that can expect the following learning effects.

(a) To introduce programming training through a gaming experience in order to stimulate interest in programming.
(b) To improve understanding of programming structures and control flow through a gaming experience, instead of focusing on the language syntax or particular algorithms.

3 Feature of the programming learning support system

We have already reported [4]-[9] about CAPTAIN, a puzzle-based programming training system with motivational learning methods, in which learners create programs similarly to solving a puzzle game. In this research, we developed learning programming support system which contains entertainment features and implemented these functions in CAPTAIN3.4, based on the previous version of CAPTAIN. The main features of this system are shown in Table 1 and the content of each function is described below.

3.1 Competitive learning function using nickname (Nickname function)

This function provides a competitive learning environment using nicknames which is new function of CAPTAIN3.4. This function aims to introduce the game nature between students, and improved a concentration skill such as raising the number of programming exercise which is solved in a definite period of time. The function assigns different nicknames to each learner individually in the beginning of an exercise at each time and displays ranking using nicknames to all learners and teachers. Each leaner can know own relative rank compared to other learners in the same group. Figure 1 shows a screenshot of the ranking display using nicknames.

3.2 Puzzle style program exercise function

This function implements puzzle-based interface in order to introduce programming training through a gaming experience. Programming training from the viewpoint of program structure comprehension and program flow comprehension can be compared to solving a 2-dimensional puzzle by logically laying out the puzzle pieces. From this standpoint, this function breaks up a program into puzzle pieces, and the user must reconstruct the program by selecting the correct program puzzle pieces in the correct order. Figure 2 shows a screenshot of the puzzle interface during programming exercise.

Table 1 main function of CAPTAIN3.4

No	main function	contents
1	Nickname function	This function monitors the statuses of all students' progresses and evaluates their degrees of achievement and ranks them using nickname in real time and continuously.
2	Puzzle style program exercise function	This function automatically creates puzzle pieces from the problem source code according to the progress and comprehension level of the learner, and offers the puzzle based interface for program exercise.
3	Animation display function	This function provides user interface in order to give effective breaks and to keep the motivation in program exercise.
4	Learning history display function	This function displays individual learning history with the progress report and the accuracy rate to give the sense of accomplishment.
5	Learning progress monitoring function	This function provides real-time progress monitor to display every learner's progress status.

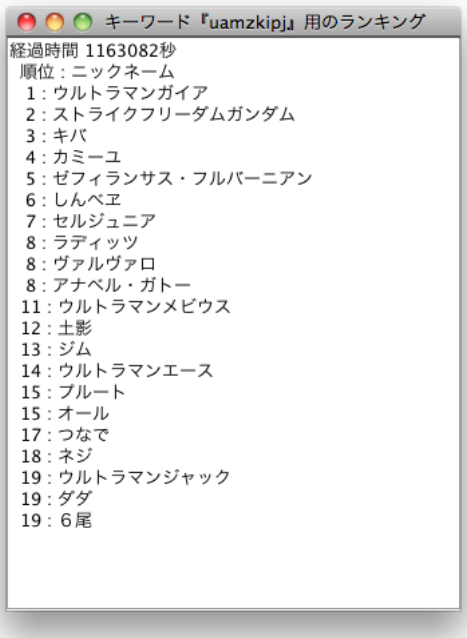

Figure 1 Example of ranking list using nicknames.

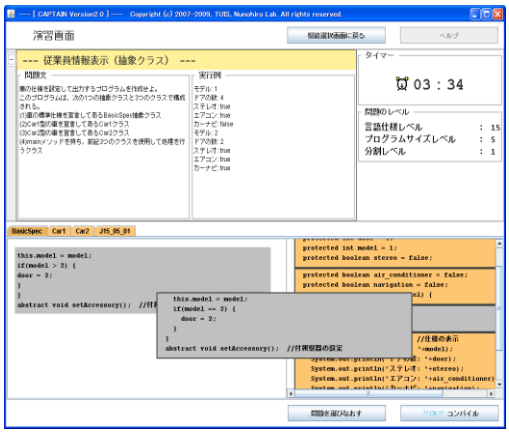

Figure 2 Programming training screenshot

3.3 Animation display function

This function aims to give effective breaks and to keep the motivation by using the visual stimulus such as display of the animation depending on the learner's exercise result and progress report in the programming training. Figure 3 is an example screenshot of an animation for a correct answer.

Figure 3 Animation for correct answer

3.4 Learning history display function

This function aims to give sense of accomplishment can be given to the learner by displaying the study history and the acquired training contents. The learner can confirm the exercise which were answered correctly and correct answer rate on the progress monitoring screen. Figure 4 shows an example screenshot of a learner's progress monitoring screen.

Figure 4 Progress monitoring screenshot

3.5 Learning progress monitoring function

This function aims to improve the satisfaction of learners by providing progress situation of learners to teachers in real time, and allowing teachers to quickly support the learners who fall behind or repeatedly error on particular problems. Figure 5 shows the instructor's monitoring screen displayed as a Web application. The monitoring program retrieves updated progress status of all learners from the database on a short time interval, and displays the progress visually on a Web browser. On the monitoring screen, the seating layout of the learners using CAPTAIN3.4 is shown and user ID and the degree of achievement are expressed as numerical value and color in each seat.

Figure 5 Progress monitoring Web application

4 Application and evaluation of Captain system

4.1 Application

CAPTAIN3.4 was applied in a Java programming course for 2nd year students in the Department of Information Systems, Tokyo University of Information Sciences. In this course, the students were divided into 3 classes (advanced, intermediate, introductory) according to the results of a preliminary test. CAPTAIN3.4 was applied in the introductory class. The applied programming course is a half year course consisting of 90 minutes lecture and 90 minutes lab per week. The students recognize grammar at the lecture and recognize the program structure and the flow of processing by solving programming exercise. Here, the experience about programming education of the teachers is also similar.

4.2 Evaluation

We executed the same progress evaluation test (2 mid-term exams and 1 final exam) for 3 classes (advanced, intermediate, introductory) in order to evaluate the learning

effect by using CAPTAIN3.4. Moreover, the introductory class was divided into the class using the nickname feature and the class which is not used in order to evaluate the efficient of nickname feature which is main function supported in CAPTAIN3.4, and an anonymous questionnaire was taken in the classes. The evaluation period is from April in 2012 to July in 2012 and the evaluation was applied to student data (21 students in the advanced, 31 students in the intermediate and 39 students in the introductory classes) who had attended all mid-term and final exams. The flow of programming course and evaluation is shown in Figure 6. The number in ( ) is the number of lectures between evaluation.

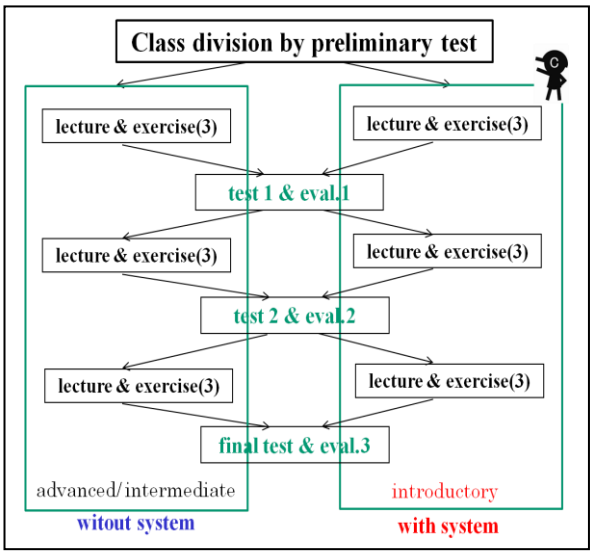

Figure 6 Flow of programming course and evaluation

4.2.1 Comprehension evaluation test

The Comprehension evaluation test were classified into the following five skill groups, and the maximum total points for each test were 35 points.

(a) Basic knowledge for Java programming
(b) Program creation (fill in the blanks without answer group)
(c) Program analysis (execution results analysis without answer group)
(d) Program creation (fill in the blanks with answer group)
(e) Program reconstruction (program reconstruction using program pieces with answer group)

Figure 7 shows the transition of average score for the mid-term and the final exam of the advanced/intermediate (CAPTAIN3.4 not used) and introductory (CAPTAIN3.4 used) classes. Figure 7 shows that there was not enough improvement in programming skill immediately since the difference of average score for the tests between the advanced, intermediate and introductory classes was almost no change.

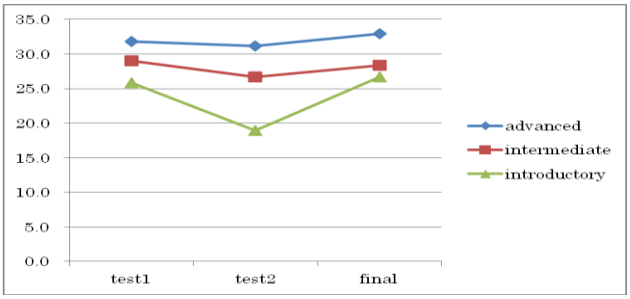

Figure 7 Transition of average

4.2.2 Questionnaire

An anonymous questionnaire was taken in the introductory level classes. The questions were chosen to evaluate CAPTAIN system, and student selected from 1 to 5 for each question where 5 was the highest positive reply. The questionnaire results of the class which uses the nickname function and the class which did not use the nickname function are shown in Table 4.

The results of questionnaire show that the evaluation result of the class using a nickname function is higher than the class which did not use a nickname function in all questionnaire item. It seems that the student showed interested in programming by using nickname function.

Table 4 Results of the questionnaire

questionnaire item	class	Results(%)				
		5	4	3	2	1
(a) Did you feel the game like programming training?	with nickname	27.5	50.0	5.0	7.5	10.0
	without nickname	22.2	27.8	11.1	11.1	27.8
(b) Did you feel the sense of accomplishment by the display of your study history?	with nickname	15.0	50.0	17.5	10.0	7.5
	without nickname	16.7	33.3	5.6	16.7	27.8
(c) Did you feel that greediness for learning improved by the display of your ranking?	with nickname	17.5	35.0	25.0	12.5	10.0
	without nickname	22.2	27.8	11.1	0.0	38.9

The questionnaire also accepted free comments, in order to collect other opinions that were not covered in the fixed questions. From among the free comments, there were many positive comments as follows.

© ISAROB 2013

Q1: Did you feel the game like programming training?

A1: Although I was poor at programming, I was able to enjoy like the game.

Q2: Did you feel the sense of accomplishment by the display of your study history?

A2: Since this function displayed the mistaken part intelligibly, it was able to do the given exercise comfortably.

Q3: Did you feel that greediness for learning improved by the display of your ranking?

A3: I was able to keep the motivation in order to get 1st rank.

5 Conclusion and future works

In this paper, we developed game based learning features in a programming learning support system, to offer a learning environment that stimulates and sustains the motivation of the learner during programming training. The proposed system was applied to an actual college programming course to verify the effectiveness of the proposed system.

From the result of questionnaire, we concluded that the developed CAPTAIN system was effective in the viewpoint that the student showed interested in programming. However, from the result of the transition of average score of the mid-term and the final exam for the advanced/intermediate (CAPTAIN3.4 not used) and introductory (CAPTAIN3.4 used) classes, it could not be established that the proposed method had a positive effect in improvement of the programming skill, and improvement of the learning features and revision on method for applying the proposed system is necessary. There was also another education effect considered that some students who were using CAPTAIN got interested in development of an education system. For future works, we plan to improve learning functions which support improvement in the capability to constitute the flow of processing or programming creation capability with entertainment features.

Acknowledgments

This research was supported by The Ministry of Education, Culture, Sports, Science and Technology (MEXT), Grant-in-Aid for Scientific Research(C) (24501207).

References

[1] Sugumura Akira, Mine Tsunenori, Shoudai Takayoshi "Automatic Exercise Generating System That Dynamically Evaluates both Students' and Questions' Levels(Learning Support)", IPSJ Journal, Vol.46,No.7, pp.1810-1818 (2005)

[2] Principles of Instructional Design (2005), Robert M. Gagne, Walter W. Wager, Katharine C. Golas, John M. Keller, Wadsworth Pub Co.

[3] Wenyong WANG, Mitsuru IKEDA, Fengrong LI (2007), Proposal and Evaluation of the "Motivation-Oriented" Teaching Method in Programming Education, Japan Society for Educational Technology, Vol.31, No.3, pp.349-357 (in Japanese)

[4] E.Nunohiro, K.J.Mackin, M.Ohshiro, K.Matsushita, K.Yamasaki (2007), Implementation of a GA driven programming training support system, The 12th International symposium artificial life and robotics, pp.517-522

[5] E.Nunohiro, K.Matsushita, K.J.Mackin, M.Ohshiro, K.Yamasaki (2008), Design and development of a puzzle based programming learning support system with genetic algorithm, Transactions of Japanese society for information and system in education, vol.25, No.2, pp.207-213 (in Japanese)

[6] Yuji Yoneyama, Kotaro Matsushita, Kenneth J. Mackin, Masanori Ohshiro, Kazuko Yamasaki, Eiji Nunohiro (2008), Puzzle Based Programming Learning Support System with Learning History Management, The 16th International Conference on Computers in Education (ICCE2008), pp. 623-627

[7] Yuuko Yamakawa, Masanori Ohshiro, Kotaro Matsushita, Kenneth J.Mackin, Eiji Nunohiro: "Programming Learning Support System 'CAPTAIN' with Motivational Study Model", The 18th International Conference on Computers in Education (ICCE2010), pp.171-175

[8] Eiji Nunohiro, Kotaro Matsushita, Kenneth J.Mackin, Masanori Ohshiro:"Development of Game Based Learning features in Programming Learning Support System", The Seventeenth International Symposium on Artificial Life and Robotics (AROB 17th '12), February, 2012, ISBN 978-4-9902880-6-8, Proceeding,230-233

[9] Masanori Ohshiro, Kotaro Matsushita, Kenneth J. Mackin, Eiji Nunohiro:"Programming Learning Support System with Competitive Gaming Using Monitoring and Nicknames", The Seventeenth International Symposium on Artificial Life and Robotics (AROB 17th '12), February, 2012, ISBN 978-4-9902880-6-8, Proceeding,238-241

© ISAROB 2013

The Eighteenth International Symposium on Artificial Life and Robotics 2013 (AROB 18th '13),
Daejeon Convention Center, Daejeon, Korea, January 30-February 1, 2013

Programming Learning Support Systems Focused on Structures of Programming Language and Code

Masanori Ohshiro[1], Takashi Yamaguchi1, and Eiji Nunohiro[1]

[1]Tokyo University of Information Sciences, 4-1 Onaridai, Wakaba-ku, Chiba, Chiba, 265-8501, Japan
(Tel: +81-43-236-4667, Fax: +81-43-236-4667)
ohshiro@rsch.tuis.ac.jp

Abstract: The authors have developed a programming training system CAPTAIN (Computer Aided Programming Training And INstruction). In this training system, each complete program is fragmented randomly into a few lines by the system. Students sort the lines as an original program similarly to solving a puzzle game. In this paper, we propose an advanced feature for the system. In order to write correct programs, students must know important structures of language 's syntax. For example, block syntax is used for significant structures in Java. Therefore, in the new system, a program is divided into block syntax elements. First, contents of theses elements are empty except for their frame. Students are instructed to place them into correct position and to fill contents of the block syntax elements. It is expected that students will understand the structures of the programs in such process and their ability of writing programs will be improved.

Keywords: programming, learning, game, java

1 INTRODUCTION

The authors have developed a programming training system CAPTAIN (Computer Aided Programming Training And INstruction) and have applied the system in an actual programming course. Fig.1 is a login window of CAPTAIN[1, 2, 3, 4, 5, 6]. In this training system, learners create programs similarly to solving a puzzle game as follows. Each complete runnable program is fragmented randomly into a few lines by the system. Users must sort the lines as an original source program (fig.2). The system compiles the source program sorted by the user and checks the correctness of it.

In our previous version of the system, exercises are executed in style of a puzzle, sorting lines into correct source programs as mentioned above. It seems that such a puzzle method improves students ' ability of reading source programs and understanding algorithms in the codes. However, it will not improve learners ' ability for creating and writing programs. A typical and simple learning method for program writing is typing programs in a programming editor. But, such a typing method brings many unexpected troubles and needs sufficient time. On the other hand the puzzle method is advantageous for lessons with a time limit, for example class in school. Accordingly, we designed a new method for lesson of writing and creating programs in the puzzle-style method.

Fig. 1. CAPTAIN

2 SYNTAX-ORIENTED FRAGMENTATION

In order to write correct source programs, students must know important structures of language's syntax. For some popular programming languages (Java, C, C++, etc.), block syntax is used as significant structures. Fig.3 shows the typical applications of block syntax in Java. These structures based on the block syntax are important part of programs. Such block syntax element is a span of tokens enclosed by a pair of parentheses, brackets, and braces. Almost part of a source program written in these languages consists of block structures. Therefore, in the new system, a program source is divided in block syntax elements. At the first, contents of theses elements are empty except their block frame. Students are instructed to place them into correct position. In succession, students must fill contents of the block syntax elements. It is expected that students will understand the structures of the programs in such process and their ability of writing programs will be improved.

© ISAROB 2013

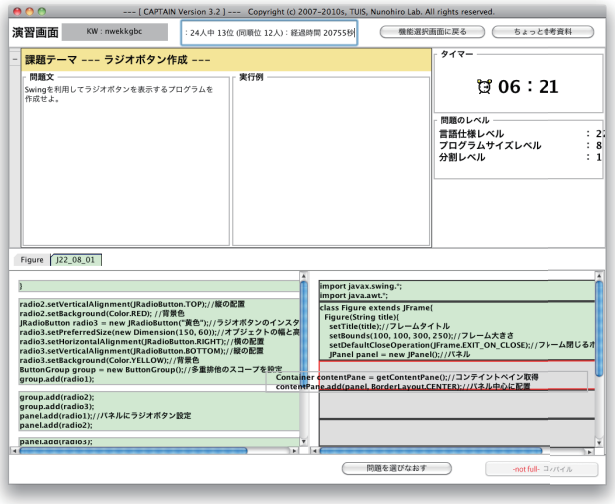

Fig. 2. Each learner must sort fragmented and randomly listed parts of a program at the lower left panel into the correct order at right lower panel using drag and drop.

3 METHOD OF THE FRAGMENTATION

The method of syntax-oriented fragmentation besed on block syntax is displayed in fig.4. Lines of a source code are symbolized and analyzed using simple syntax parsing. Blank lines in the source program are regard as equivalent to each other. These blank lines are defined as follows:

```
blankline = B3 = B6 = B9;
```

These blanklines are ignored in symbolic expressions mentioned below. All lines that contains the same contents are regard as equivalent to each other and defined as follows:

```
C3 = D4 = C6 = C9 = C12 = C15 = A3;
```

A Class 'Person' is analyzed and described as follows:

```
"class Person"
  = A1, A2 { B1, B2, B4, B5,
             B7, B8, B10 }, A3;
```

The above symbolic expression describes that a class 'Person' is defined as sequence of A1, A2, A3. Moreover, the expression shows A2 is set of B1, B2, B4, B5, B7, B8, B10 (the blank lines are ignored). In brief, contents of a pair of braces may appear in random order in these symbolic expressions. If some part of contents of such a pair of braces must be in particular order for some context, we may use a pair of brackets as follows:

```
{ B1, [ B2, B3 ] }
```

In this case, two instances shown below are permitted.

```
B1, B2, B3
B2, B3, B1
```

In many cases, such necessity of particular order is caused by semantic context, therefore [ ] may be specified manually. The expression below describes method 'setAge' is defined as B5 or a sequence of C4, C5, C6.

```
class A {
  // members
}

int max ( int a, int b ) {
  // statements
}

if( x > 0 ) {
  // statements
}

for ( i = 0; i < n; i++ ) {
  // statements
}

else {
  // statements
}

try {
  // statements
}

while ( i < n ) {
  // statements
}

catch ( Exception e ) {
  // statements
}
```

Fig. 3. Typical applications of the block syntax in Java.

A1					class Person {	1
A2	B1				private int age;	2
	B2				private String name;	3
	B3					4
	B4	C1			public int getAge() {	5
		C2	D1		return age;	6
		C3			}	7
	B5	C4			public void setAge(int age) {	8
		C5	D2		if(age >= 0) {	9
			D3	E1	this.age = age;	10
			D4		}	11
		C6			}	12
	B6					13
	B7	C7			public String getName() {	14
		C8	D5		return name;	15
		C9			}	16
	B8	C10			public void setName(String name) {	17
		C11	D6		this.name = name;	18
		C12			}	19
	B9					20
	B10	C13			public Person(int age, String name) {	21
		C14	D7		setAge(age);	22
			D8		setName(name);	23
		C15			}	24
A3					}	25

```
blankline = B3 = B6 = B9;
C3 = D4 = C6 = C9 = C12 = C15 = A3;
"class Person"
   = A1, A2 { B1, B2, B4, B5, B7, B8, B10 }, A3;
"method setAge" = B5 = C4, C5{D2, D3{ E1 }, D4}, C6;
```

Fig. 4. An example of syntax-oriented fragmentation besed on block syntax.

© ISAROB 2013

```
"method setAge" = B5
  = C4, C5 { D2, D3 { E1 }, D4 }, C6;
```

This expression can be written in two expressions as follows:

```
 D3 = { E1 };
"method setAge" = B5
  = C4, C5 { D2, D3, D4 }, C6;
```

class Person {	A1	"class Person"
}	A3	
private int age;	B1	
public Person(int age, String name) {	C13	"ctor Person" (B10)
}	C15	
setAge(age);	D7	
this.age = age;	E1	
return name;	D5	
public void setName(String name) {	C10	"method setName" (B8)
}	C12	
	B9	
	B3	
setName(name);	D8	
public String getName() {	C7	"method getName" (B7)
}	C9	
private String name;	B2	
if(age >= 0) {	D2	C5
}	D4	
	B6	
this.name = name;	D6	
public int getAge() {	C1	"method getAge" (B4)
}	C3	
return age;	D1	
public void setAge(int age) {	C4	"method setAge" (B5)
}	C6	

Fig. 5. An example of fragments in random order.

The source program is analyzed in the manner mentioned above. At the next, the fragments are sorted in random order. It is important that lines of every block syntax are integrated into one fragment without its contents in this process (fig.5). By the way, white spaces for indent is omitted in the display because such indents are unexpected hints.

4 USER OPERATION

Fig.6 shows typical user operation. At the first, fragments are displayed. A user is instructed to place them into correct position. User can select and move the fragments to construction panel using drag and drop (fig.6-(1)). Especially, contents of every block syntax fragment can be inserted (fig.6-(2)). A user can fill and sort fragments in construction panel any number of times. At the last, a user check the correctness of the sorted fragments.

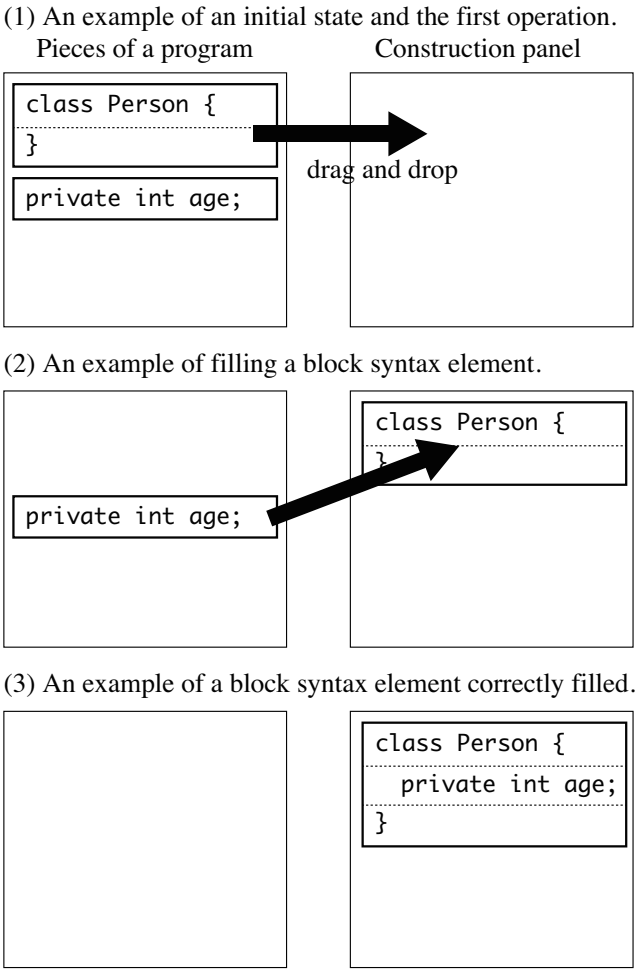

Fig. 6. An example of typical user operation.

5 CHECKING CORRECTNESS OF RESULTS

Fig.7 is a example of an answer. In order to check the correctness of the answer, the system matching the symbolic expressions extracted from original source code with the symbolic expressions extracted from user's answer according to the rules as follows:

(1) Blank lines are ignored.

(2) Symbols in `{ }` may appear in random order.

(3) Inside `{ }`, symbols in `[ ]` must appear in specified order.

For example of fig.4 and fig.7, the first different point is detected as follows:

```
Original:
  "method setAge" = B5
    = C4, C5 { D2, D3 { E1 }, D4 }, C6;
Answer:
  "method setAge" = B5
    = C4, C5 { D2, D3 { D1 }, D4 }, C6;
```

The different part of these symbolic expressions is underlined. Therefore, the answer is incorrect.

A1					class Person {	1
A2	B3					4
	B2				private String name;	3
	B1				private int age;	2
	B5	C4			public void setAge(int age) {	8
		C5	D2		if(age >= 0) {	9
			D3	D1	return age;	6
			D4		}	11
		C6			}	12
	B4	C1			public int getAge() {	5
		C2	E1		this.age = age;	10
		C3			}	7
	B9					20
	B7	C7			public String getName() {	14
		C8	D5		return name;	15
		C9			}	16
	B8	C10			public void setName(String name) {	17
		C11	D6		this.name = name;	18
		C12			}	19
	B10	C13			public Person(int age, String name) {	21
		C14	D8		setName(name);	23
			D7		setAge(age);	22
		C15			}	24
	B6					13
A3					}	25

```
"class Person"
   = A1, A2 { B2, B1, B5, B4, B7, B8, B10 }, A3;
"method setAge" = B5 = C4, C5{D2, D3{ D1 }, D4}, C6;
```

Fig. 7. An example of an answer.

6 CONCLUSION

We proposed a new feature, syntax-oriented fragmentation for CAPTAIN. It is expected that students may pay much more attention to structures of source code and syntax of Java using this new feature. It seems that the feature is useful to know weak points of students' because it is easy to detect where the students made mistakes. We will implement the feature in CAPTAIN and examine the effect of the feature.

ACKNOWLEDGMENTS

This research was supported by The Ministry of Education, Culture, Sports, Science and Technology (MEXT), Grant-in-Aid for Scientific Research(C) (24501207).

REFERENCES

[1] Nunohiro E, Mackin K, Ohshiro M, Matsushita K, Yamasaki K (2007), Implementation of a GA driven programming training support system, The 12th International symposium artificial life and robotics, pp.517-522.

[2] Nunohiro E, Matsushita K, Mackin K, Ohshiro M, Yamasaki K (2008), Design and development of a puzzle based programming learning support system with genetic algorithm (in Japanese), Transactions of Japanese society for information and system in education, vol.25, No.2, pp.207-213.

[3] Yoneyama Y, Matsushita K, Mackin K, Ohshiro M, Yamasaki K, Nunohiro E (2008), Puzzle Based Programming Learning Support System with Learning History Management, The 16th International Conference on Computers in Education (ICCE2008), pp. 623-627

[4] Yamakawa Y, Ohshiro M, Matsushita K, Mackin K, Nunohiro E (2010), Programming Learning Support System 'CAPTAIN' with Motivational Study Model, The 18th International Conference on Computers in Education (ICCE2010), pp. 171-175

[5] Ohshiro M, Mackin K, Matsushita K, Nunohiro E, Yamakawa Y (2010), Programming Learning Support System with Learning Progress Monitoring Feature, Joint 5rd International Conference on Soft Computing and Intelligent Systems and 11th International Symposium on Advanced Intelligent Systems (SCISISIS 2010), pp.1465-1468

[6] Ohshiro M, Matsushita K, Mackin K, Yamaguchi T, Nunohiro E (2012), Programming Learning Support System with Competitive Gaming Using Monitoring and Nicknames, The 17th International symposium artificial life and robotics, pp.238-241.

© ISAROB 2013

The Eighteenth International Symposium on Artificial Life and Robotics 2013 (AROB 18th '13),
Daejeon Convention Center, Daejeon, Korea, January 30-February 1, 2013

Individual Student Support System for Teacher and TAs using Mobile Devices in Exercise Classes

Masaki Hanada[1], Takashi Yamaguchi, and Yasuo Nagai

Tokyo University of Information Sciences, Japan
(Tel/Fax: 81-43-236-1224)
[1]mhanada@rsch.tuis.ac.jp

Abstract: The paper describes a student support system for a teacher and Teaching Assistants (TAs) in order to support individual students effectively and satisfactorily in computer exercise classes. In general, a teacher teaches some classes in universities and several TAs engage in the activities to support students under guidance from a teacher in charge. Introduction of a student support system for a teacher and TAs is essential in order to support all the students effectively and satisfactorily by fewer teaching staff. In this research, we develop a system which visualizes the seat location of the questioner and shares the responses of questions, in order to answer students' questions during the class effectively and satisfactorily. In this paper, we report the proposed student support system and the results of the system evaluation.

Keywords: Computer exercise classes, Mobile devices, Teacher, Student support system, Teaching assistants

1 Introduction

The paper describes a student support system for a teacher and Teaching Assistants (TAs) in order to support individual students effectively and satisfactorily in computer exercise classes. In general, a teacher teaches some classes in universities and several TAs engage in the activities to support students under guidance from teacher in charge.

Introduction of a student support system for a teacher and TAs is essential in order to support all the students effectively and satisfactorily by fewer teaching staff.

In this research, we develop a system which visualizes the seat location of the questioner and shares the responses of questions, in order to answer students' questions during the class effectively and satisfactorily. By using this system, it is expected that a teacher and TAs are able to support individual students effectively and satisfactorily.

Moreover, we develop an user-interface in which students easily ask questions for the exercise. By using this user-interface, it is expected that students are able to ask questions without hesitation.

In this paper, we report the proposed student support system and the results of the system evaluation.

In Section 2, we present some related work about education support systems. In Section 3, we describe main jobs of a teacher and TAs. In Section 4, we describe the proposed individual student support system. In Section 5, we describe the operation and the evaluation of the proposed system. Finally, Section 6 gives concluding remarks and the directions of our future work.

2 Related Work

In [1], the authors developed a system which shares the responses of questions between a teacher and TAs. In [2], the authors developed a system which visualizes the students' progresses of an exercise on tablet PCs.

By using these systems, these authors reported that students who do not have a clear understanding were founded early, and the overall level of understanding in the class was improved. Based on the result of these early researches, we develop a new system for a teacher and TAs in order to support individual students effectively and satisfactorily.

3 Main Jobs of a Teacher and TAs in Exercise Classes

In computer exercise classes (e.g., the programming and the operating system), the main jobs of teachers are as follows:

(1) Make and prepare educational materials for the class.
(2) Take students attendance in the class.
(3) Check students' exercise answers.
(4) Answer students' questions during the class.
(5) Support individual students that have insufficient understanding and have a problem about an exe rcise during the class.
(6) Give a grade to each student.

TAs mainly do the jobs from (2) to (5) under guidance from a teacher in charge. In particular, the above jobs from (4) to (5) are important for computer exercise classes because each student has different problems and the

© ISAROB 2013

feedback about mistakes must be given at the time the mistakes for exercise are made.

In this research, we focus on the jobs of (4) and (5).

The job of (4) means that when a teacher and TAs are asked a question from a student during the class, they answer the question of the student. In this job, a teacher and TAs may be not able to do this job smoothly. This is because there is the potential for an increase of students' questions. The students' questions increase when the instruction for the exercise is unclear or the understanding of students is insufficiency.

The job of (5) means that a teacher and TAs visit each student during the class and if a student has insufficient understanding and has a problem about a exercise, they support the student. In this job, a teacher and TAs are overloaded and may be not able to do this job smoothly.

In this research, we develop a student support system in order to do these above jobs smoothly.

4 Proposed Individual Student Support System

4.1 Functional Requirements

In order to do the jobs of (4) and (5) smoothly, a teacher and TAs need to understand the entire status of questions from questioners (e.g., the content of the questions and the seat location of questioners). If a teacher and TAs are able to gather the entire status of questions from questioners quickly, they visit the questioners quickly and support the questioners smoothly.

Moreover, if a teacher and TAs share the responses of questions from questioners, they can support the questioner smoothly when the asked question is similar to the past question.

From these functional requirements, we develop a student support system which visualizes the seat location of the questioner and shares the responses of questions from questioners.

4.2 Student Support Model

In this section, we show a system function which visualizes the seat location of the questioner and shares the responses of questions from questioners.

The student support model using the proposed individual student support system is shown in Fig.1. A student asks a question through the user-interface for question. Then, the entire status of questions from questioners (e.g., the content of question, the seat location of questioners, the number of questions and the number of TAs which is supporting a student) is visualized on tablet PC of a teacher and TAs.

By using the user-interface (Fig.1 ①), students are able to ask a question without hesitation, compared with asking a question by a show of hands. As a result, a teacher and TAs can support all the students which have insufficient understanding and have a problem about the exercise smoothly.

By providing the entire status to a teacher and TAs using the tablet PC (Fig.1 ②), if the individual support is needed (e.g., the question is endemic question), a teacher or TAs visit and support individual questioners (Fig.1 ③). If the entire support is needed (e.g., the number of similar question is large), teacher gives guidance to all the student (Fig.1 ④). As a result, a teacher and TAs support all the students effectively and satisfactorily by fewer teaching staff.

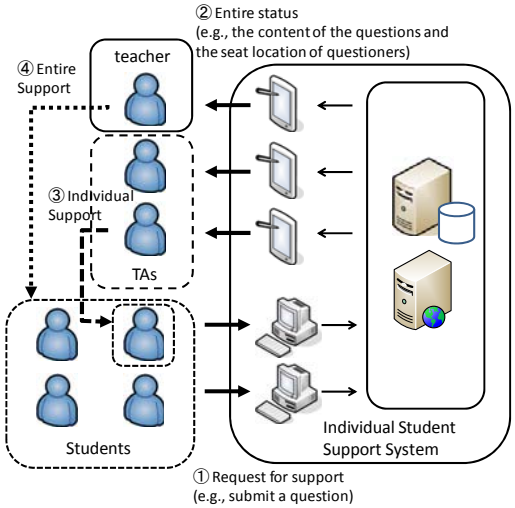

Figure 1 Individual Student Support System

4.3 Processing Flow

The proposed individual student support system is composed of a Web client application for students, a client application for a teacher and TAs and two servers (i.e., Web server and Database (DB) server).

Fig 2 shows a process flow of the proposed system. A student selects a question from the question list and then pushes the submit button (Fig.2 ①). If the question which the student wants to ask is not registered in advance, the student selects other questions (i.e., "etc" on the screen) and pushes the submit button.

The submitted question is sent to the Web and DB servers and is stored in the DB (Fig.2 ②). Then, the question and the seat location of the questioner are sent to the tablet PC of a teacher and TAs. The client application on the tablet PC visualizes the seat location of the questioner with the question (Fig.2 ③).

After the teacher or TA supports the questioner, the responder inputs a response of the question on the tablet PC

© ISAROB 2013

(Fig.2 ④). The response of the question is sent to the server and is stored in the DB.

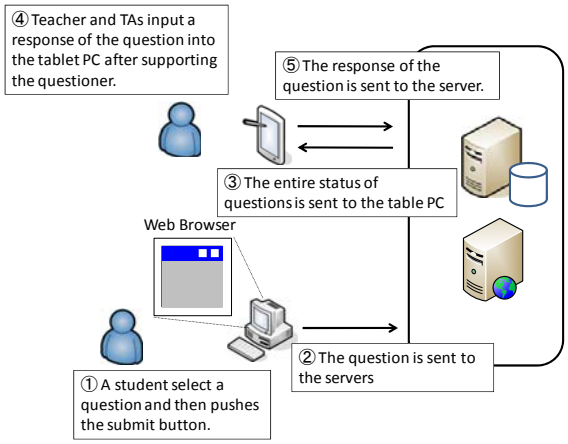

Figure 2 Process Flow

4.4 Client Application for Students

In the proposed system, Web browser is used as a client application to accept a question from a student, because the Web browser is already installed in many computer environments and the educational materials are often constructed as Web contents.

Example of the Web browser user-interface (UI) for students is shown in Fig.3.

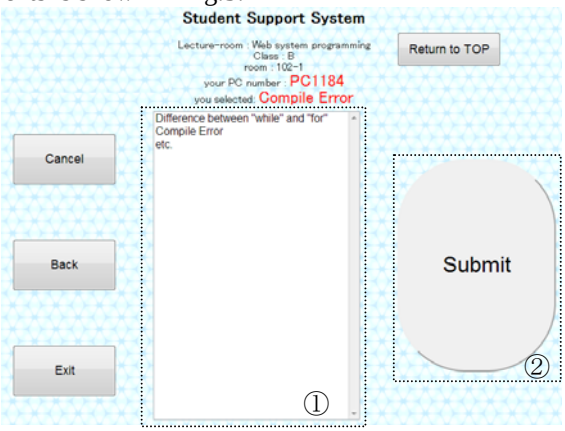

Figure 3 Web browser UI for students

When a student has a question, the student selects the question which the student wants to ask from the question list (Fig3. ①) and pushes the submit button (Fig3. ②). If the question which the student wants to ask is not registered in advance, the student select "etc" and pushes the submit button. The reasons that the question is listed on the Web browser user-interface are as follows:

(1) The students make their incomprehensible point clear by selecting the question from the question list.

(2) If the number of similar question is large, the teacher can give guidance about the question to all the students.

4.5 Client Application for a Teacher and TAs

In the computer exercise class, we assume that a teacher and TAs have a tablet PC respectively because a teacher and TAs should support a student individually with circulating during classes. By using the tablet PC, a teacher and TAs can view the entire status and input the response of the question after supporting the questioner.

In the proposed system, client application for a teacher and TAs is developed as application for Android tablet PC.

Examples of the user-interface (UI) for a teacher and TAs are shown in Fig.4 and Fig.5.

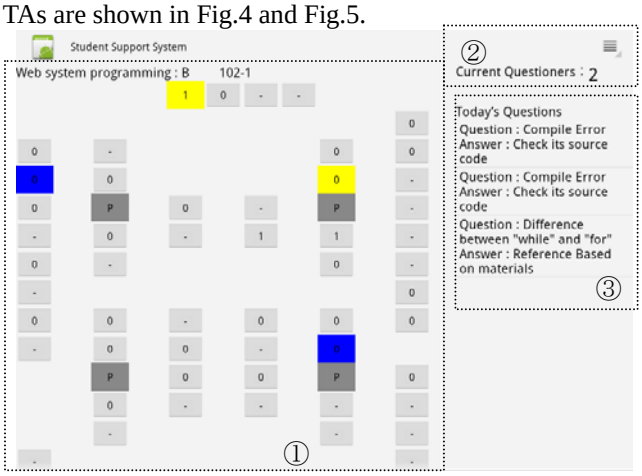

Figure 4 UI for a Teacher and TAs (1)

In the left of Fig.4 (Fig.4 ①), the seating map of the classroom is shown. The seats are displayed as boxes and the boxes of the current questioners are colored in yellow. The boxes of the questioners who is currently being supported are colored in blue. The number shown in the boxes is the number of questions of the questioner. The number of the current questioners is shown in the upper right of Fig.4 (Fig.4 ②).

In the lower right of Fig.4 (Fig.4 ③), the list of the questions and the response is shown. The teacher always checks the list during the class, and if the number of similar question is large within the list, the teacher can give guidance about the question to all the students.

If a teacher or TAs click the seat box in the left of Fig.4 (Fig.4 ①), the screen as shown in Fig.5 is displayed.

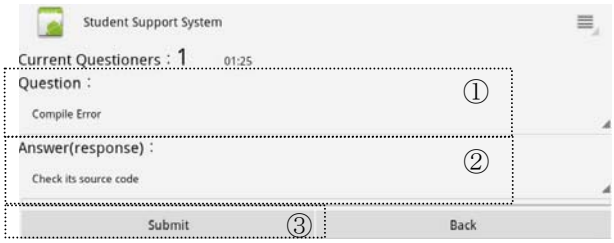

Figure 5 UI for a Teacher and TAs (2)

© ISAROB 2013

The question and the response are shown in the upper and lower of Fig.5 (Fig.5 ①, ②) respectively. The responder submits the response of the question after supporting the questioner (Fig.5 ③).

5 Operation and Evaluation

The proposed individual student support system is operated in the three kinds of computer exercise classes held at 2012 first semester in Tokyo University of Information Sciences.

One objective of the proposed system is to prevent the leakage of question and to support as much question as possible. Therefore, we evaluate the number of the supported questions using the proposed system, compared with no using the proposed system.

The average number of supported questions for one class is shown in Table.1.

In the computer exercise class for the first grade, the class is separated into three sub-classes (i.e., Class A, Class B and Class C). the different three teachers use the same educational materials. In one of three sub-classes (i.e., Class A), the proposed system is operated. In the other two sub-classes (i.e., Class B and Class C), the proposed system is not operated.

In the above classes, the influence by the different teachers is not avoided. Therefore, one teacher teaches in the following two classes.

In the computer exercise class for the second grade (i.e., Class A), one teacher uses the original educational materials. In the computer exercise class for the third grade, two teachers use the same educational materials. The class is separated into two sub-classes (i.e., Class A and Class B). To reduce the influence by the difference of teachers, the proposed system is operated every other week in the computer exercise classes for the second and third grade.

From the results of the average number of supported questions for a lesson of one class (Table.1), the average number of supported questions using the proposed system is small except the exercise class for the second grade, compared with no using the proposed system.

The two reasons are considered.

The first reason is that the teacher gives guidance about the question to all the students because the number of similar question is large.

The second reason is that a teacher or TAs forget to input the responses of questions to the tablet PC because a teacher and TAs are overloaded.

Moreover, from the questionnaire, we confirm that there are two types of students. First one is the students who are willing to ask a question by a show of hands. Second one is the students who are willing to ask a question using the proposed system. Therefore, we need to re-establish the manner of the operation of the proposed system according to requirements of students.

Table 1 The average number of supported questions

Exercise class for the first grade		
Use of the proposed system	yes	no
Class A	15.50	
Class B and C		39.06
Exercise class for the second grade		
Use of the proposed system	yes	no
Class A	6.40	5.80
Exercise class for the third grade		
Use of the proposed system	yes	no
Class A	2	8.33
Class B	3.33	7

6 Conclusion

In this research, we developed a student support system in order to support individual students effectively and satisfactorily. In this paper, we reported the operation and evaluation of the proposed system.

From the results of the evaluation, we confirmed an effect of the proposed system. However, the proposed system needs further modification.

Our future work are as follows :

(1) The improvement of the user-interface (UI) for students, the improvement of the application for a teacher and TAs, and the improvement of the manner of the operation are needed.

(2) Re-examination of the evaluation method including the score of exam is needed.

(3) Combining the proposed system with educational materials is needed in next version to support students more effectively and satisfactorily.

References

[1] Masafumi Takeda and Osamu Akizuki,``A lecture support system with using network environment,`` IEICE ET, vol.111, no.213, pp.59-63, 2011. (in Japanese)

[2] Seigo Yasutome and Takuya Ito,``Web application for TA activity with Tablet PC,`` JSiSE General Conference, vol.36, pp.34-35, 2011. (in Japanese)

© ISAROB 2013

The Eighteenth International Symposium on Artificial Life and Robotics 2013 (AROB 18th '13),
Daejeon Convention Center, Daejeon, Korea, January 30-February 1, 2013

Research on XP approach using The Personal Software Process Practice

Daisuke Yamaguchi[1]

1:Toin University of Yokohama, 1614 Kurogane-cho, Aoba-ku, Yokohama, JAPAN
yamaguti@intlab.toin.ac.jp

***Abstract*: In this paper, we propose the PSP Practice Support System that we realize record-keeping support of flame work performing data acquisition of process flow offered in PSP in other Android carrying e nd with a software development environment using based on the Multiagent technologies. It is thought that we can tie that we come true with an Android mobile terminal when we perform the convenienc e that we don't affect to a software development environment and reference of a document if dated c onsciousness of flow. So, We can be conscious of process flow in every environment with development by this system can transmit programming to specific human among many software processes using Ag ent's technology. Applying the proposed method to a personal process remove task, a flexible program ming for quality of software.**

Keywords: Personal Software Process, Software Engineering, Agile Development, eXtreme Programming

I. INTRODUCTION

Software architecture has emerged as an important sub discipline of software engineering [1]. PSP support system is built using this. Moreover, We think that the data inputted can acquire software development process by sorting out using a user action record table [2].

In this paper, the Personal Software Process (PSP) practice support system that we realize record-keeping support of flame work performing data acquisition of process flow offered in PSP in other Android carrying end with a software development environment using based on the Multiagent technologies [3]. It is thought that we can tie that we come true with an Android mobile terminal when we perform the convenience that we don't affect to a software development environment and reference of a document if dated consciousness of flow. So, We can be conscious of process flow in every environment with development by this system can transmit programming to specific human among many software processes using Agent's technology. Intelligent agents and multiagent systems are one of the most important emerging technologies in computer science today [4]. Multiagent systems deal with coordinating intelligent behavior among a collection of autonomous agents. Emphasis is placed on how the agents coordinate their knowledge, goals, skills, and plans jointly to take action or to solve problems. Constructing the multiagent systems is difficult [5,6].

Since interruption time is essentially random, ignoring these times would add a large random error into the time data and reduce estimating accuracy. In this we propose that the PSP Practice who realize record-keeping support an flame-work performing data acquisition of the process flow offered in other Android end user with a software development environment. It is thought that reference of a document if dated coscious-ness of flow when perform the convenience don't affect to a software development environment with an Adroid mobile terminal. Because, we can be conscious of process flow in every environment with development by this system can transmit programming to specific human among many software processes using Agent's technology. The system is also synthesized to do parallel and cooperative proposing internally. Applying the proposed method to a personal process remove task, a flexible programming for quality of software.

II. Android Personal Digital Assistant

The PSP data has record on the framework prescribed by the aforementioned individual specific exercise in support system. Therefore, Record time has been take many form to conducts based on the PSP base-line framework. Support System should be record processes by different development, quality control and large forms. So, it will be not very worried about an activity recording a process form that dealt in an experienced developer of the PSP and working-out of software for a long time. However, it increases that kept record of a form about becomes vague of that still pressed by eve-

© ISAROB 2013

ryday various works. In order to perform accurate record, their needs for support system automate and reduce the work measurement process.

It content is missing records, which it does not exactly the plan. Therefore, support systems is to record all the work, record and share information, and record information with other differences between them, what do you consider that characterize the individual.

This will be an important resource to support the ability to provide the information necessary to improve the process. However, to be commissioned to present the contents of any process improvement is not help from the Android devices. The recorded information itself, are working will consider process to improvement. An important aspect of this device, by allowing all times and there is early detection of leaks of personal records.

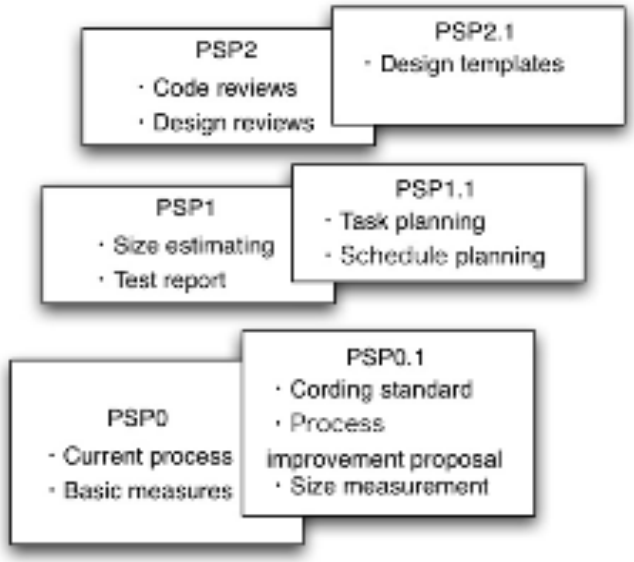

Fig.1. PSP Process Evolution

III. Personal Software Process and XP

The PSP is a self-improvement process that helps you to control, manage, and improve the way you work. It is a structured framework of forms, guidelines, and procedures for developing software [2]. Properly used, the PSP provides the data you need to make and meet commitments, and it makes the routine elements of your job more predictable and efficient.

The PSP's sole purpose is to help you improve your software engineering skills. It is a powerful tool that you can use in many ways. Rather than using one approach for every job, you need an array of tools and methods and the practiced skills to use them properly. The PSP provides the data and analysis techniques you need to determine which technologies and methods work best for you. PSP write several program using the evolving process shown Figure 1.

The PSP is not a magical answer to all of your software engineering problems, but it can help you identify where and how you can improve. However, you must make the improvements yourself. PSP0 and PSP0.1 hierarchy include introduces process discipline and measurement. PSP1 and PSP1.1 hierarchy include introduces estimating and planning. PSP2 and PSP2.1 hierarchy include Introduces quality management and design. Team Software Process exists over the PSP hierarchies.

So, This any measure record to support agent consider with using this Agent Learner expanded of PSP support. A person engaging in a person who experienced PSP and software development for many years is not very worried about a form record-keeping work.

Record keeping is vague, and what is performed of a person pressed by a work still increases. Necessity to perform automatically is important in a soldier, remission of an activity and process assay to record an activity precisely.

The first Extreme Programming project was started March 6, 1996[7]. Extreme Programming is one of several popular Agile Processes. It has already been proven to be very successful at many companies of all different sizes and industries worldwide.

Extreme Programming is successful because it stresses customer satisfaction. Instead of delivering everything you could possibly want on some date far in the future this process delivers the software you need as you need it. Extreme Programming empowers your developers to confidently respond to changing customer requirements, even late in the life cycle.

Extreme Programming emphasizes teamwork. Managers, customers, and developers are all equal partners in a collaborative team. eXtreme Programming implements a simple, yet effective environment enabling teams to become highly productive. The team self-organizes around the problem to solve it as efficiently as possible. This case study used to Pair Programming only. Because, This XP Method improvement of Software Process Time for The PSP0.

IV. Research tool Digital Assistant for Android mobile tools at Software Estimate Efficiency

In this section, explain assistant of Software Estimate used to the Android Digital Assistant based on inter-

nal Agent Learner for Intelligent Agent. Intelligent Agent techniques give connects in other Intelligent Agent record data on PSP. Hence, that Intelligent Agent put the Agent Learner on necessary thoughts in Multiagent [8].

In the PSP, engineers use the time recording log to measure the time spent in each process phase. In this log, they note the time they started working on a task, the time when they stopped the task, and any interruption time. For example, an interruption would be a phone call, a brief break, or someone interrupting to ask a question. By tracking time precisely, engineers track the effort actually spent on the project tasks. Since interruption time is essentially random, ignoring these times would add a large random error into the time data and reduce estimating accuracy.

Since the time it takes to develop a product is largely determined by the size of that product, when using the PSP, engineers first estimate the sizes of the products they plan to develop. Then, when they are done, they measure the sizes of the products they produced. This provides the engineers with the size data they need to make accurate size estimates. However, for these data to be useful, the size measure must correlate with the development time for the product. While a line of code (LOC) is the principal PSP size measure, any size measure can be used that provides a reasonable correlation between development time and product size. It should also permit automated measurement of actual product size.

As for the Android terminal unit, it process take possible for archiving to convey the information that it is necessary in the PSP activity through a screen to an internal intelligent agent. Information to convey has memorized the time that activity content in form archiving was really performed.

When "Record" button be push the Android terminal unit Screen, in order of Figure 2, Figure 3, Figure 4, and activity changes screen design. Because a screen design changes, button of a new context format appears. Agent express current activity contents sequentially whether it has been work-in-process hereby whether it is activity record keeping. An optional category have take the problems number, work-in-process practicing now. This work-in-process consists of all seven items that the Agent put activity break in as well as six items established in PSP. About activity cutoff, I step over a day and can record an activity.

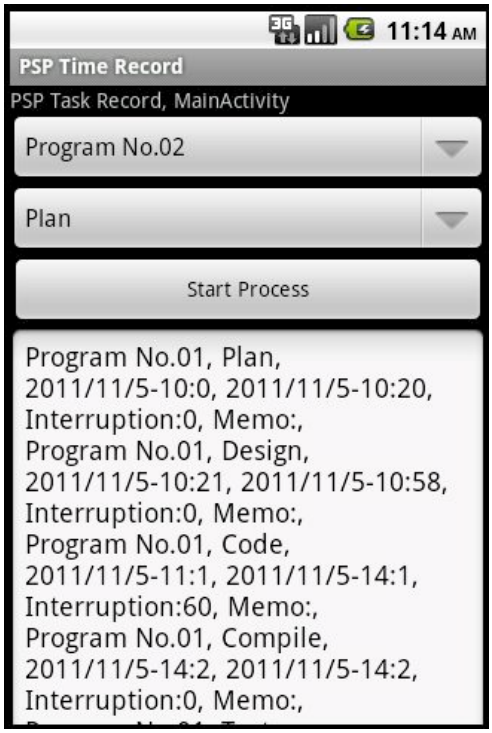

Fig.2. The Android Terminal Unit for first phase on the Agent Interface

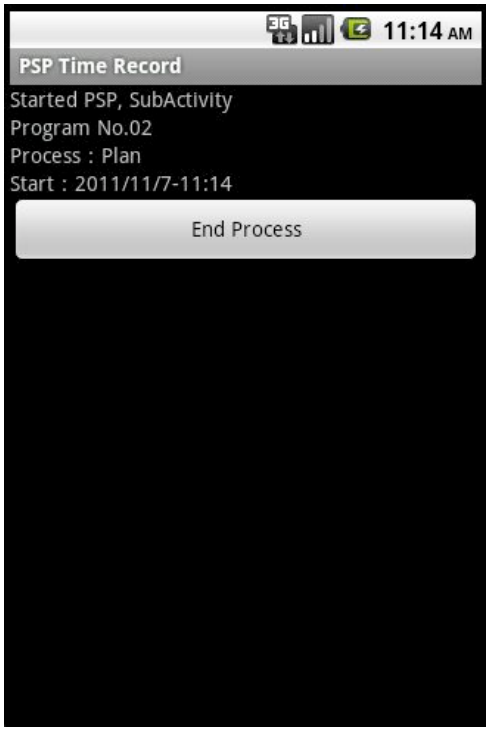

Fig.3. The Android Terminal Unit for second phase on the Agent Interface

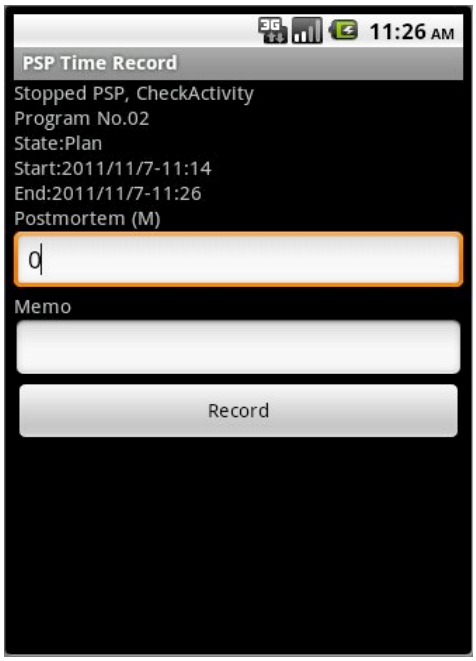

Fig.4. The Android Terminal Unit for third phase on the Agent Interface

Actually, I am recordable like Figure 3 when the Agent stepped over a day. A work to perform in this interface, work-in-process is recorded by the operation that it is easy only pushing it in button sequentially.

VI. CONCLUSION

In this research we were analyses PSP Practice Support System used to of flame work performing data acquisition of process flow offered in PSP by the Android terminal unit Interface. We were able to evidence user software working process data. We create agent learner data in real time work data beside with agent running and wrote PSP Practice process type and problem number.

For future works, we will consider methods used on record time data for agent learner in machine learning and user experience. It is necessary for us to consider only a clock through this system about the cause that a description error to be generated by human error.

Future versions of PSP Practice Support System based on Android Terminal Unit record of error type code or fact process from error message of compiler and executer to test pattern data. But, This model will show at the system in a more natural, unscripted scenario, involving multiple parts in addition to other forms of process and error type phenomenon. Now, This system Interface cannot edit by the record data that evidence and work in a process task on Agent Learning data. We consider to support system by what cannot edit record data activity archiving be able to offer the usability as evidence to test pattern data. But, This model will show at the system in a more natural, unscripted scenario, involving multiple parts in addition to other forms of process and error type phenomenon. XP Method aim to role-playing Navigators into the time record and work process think support. But, This control working Interface support Navigator only to be Android Digital Assistant device processing space. Next approach product in to this dual work support system used on the navigation techniques.

REFERENCES

[1] Paul Clements, Felix Bachmann, Len Bass, David Garlan, James Ivers, Reed Little, Paulo Merson, Robert Nord, Judith Stafford (2010), Documenting Software Architectures SECOUND WDITION, Addison-Wesley
[2] Watts S. Humphrey (2005), PSP - A Self Improvement Process for Software Engineers, Addison-Wesley
[3] Daisuke Yamaguchi, Ayahiko Niimi and Muneo Takahashi (2010), Improvement of a Software Estimate Efficiency Centered PSP Practice Support System Using Multiagent Techniques, The Fifteenth International Symposium on Artificial Life and Robotics 2010, pp.857-860
[4] Weiss, G. (1999), Multiagent Systems, A Modern Approach to Distributed Artificial Intelligence, the MIT Press
[5] Abul, O., Polat, F., and Alhajj, R. (2000), Multiagent Reinforcement Learning Using Function Approximation, IEEE Transaction on systems, man, and cybernetics-part c: application and reviews, Vol. 30, No. 4, pp. 485-497.
[6] Khosla, R., and Dillon, T. (1997), Engineering Intelligent Hybrid Multi-Agent Systems, Kluwer Academic Publishers
[7] Kent Beck's (1996), Extreme Programming, http://www.cs.usfca.edu/~parrt/course/601/lectures/xp.html
[8] Carles Sierra, JohnThangarajah, Lin Padgham and Michael Winikoff (2007), Designing Institutional Multi-Agent Systems, AOSE 2006, LNCS 4405, PP.84-103

The Eighteenth International Symposium on Artificial Life and Robotics 2013 (AROB 18th '13),
Daejeon Convention Center, Daejeon, Korea, January 30-February 1, 2013

Non-Event Driven Graphics API for Programming Education

Kenneth J. Mackin

Tokyo University of Information Sciences, Chiba 265-8501, Japan
(Tel: 81-43-236-1329, Fax: 81-43-236-1329)

mackin@rsch.tuis.ac.jp

Abstract: Current multitasking window-based operating systems have adopted an event-driven model to support graphics and user interface control in application programs. But for beginner programmers, the idea of threads and event handling can be difficult to grasp, thus preventing beginner programmers for creating graphics applications, leaving programmers in the early stages to create simple text based console applications. In this research, a non-event driven graphics API for programming education is proposed. By applying the proposed graphics API, programmers can create graphics and real-time user interface applications by simple state-request method calls not requiring any event handling or event call-back methods. The proposed graphics API also supports text based console I/O such as print line and line input, so beginner programmers can shift from console based applications to graphics applications without any paradigm changes.

Keywords: BASIC graphics, Graphics programming, programming education

1 INTRODUCTION

After the introduction of Graphical User Interface (GUI) by Xerox PARC in 1973, computer operating systems have moved from Character User Interface (CUI) centric designs to GUI-centric designs. As GUI-centric application development became popular, GUI widget toolkits were introduced, in which 'GUI widgets', or GUI components such as buttons and text fields, are controlled through an event-driven programming model.

Current multitasking window-based operating systems, including UNIX X Windows and Microsoft Windows, have adopted this event-driven model to support graphics and user interface control in application programs. Naturally, most of current programming languages, such as C and Java, which support graphical user interfaces, use the event-driven API model.

In an event-driven programming model, an 'event' is an action that triggers some program code, such as a mouse click or a key stroke. A program registers which event triggers which program code, called event-callback or event-handler. The event-driven model allows the programmer to concentrate on only the related event for a particular code, and facilitates independent GUI design and reusable GUI widget programming. In recent programming languages such as Java, the event dispatching routine, which receives the event signal from the underlying operating system, manages the list of event handlers, and calls the appropriate event-handler for the appropriate event, is hidden altogether from the user, and GUI programmer simply programs the event-handler and waits for the event-handler to be called.

But for beginner programmers, the idea of threads and event dispatching can be difficult to grasp, leading the beginner to program something that he/she does understand what is happening. This initial barrier prevents beginner programmers from creating graphics applications, leaving programmers in the early stages of education to create simple text based console applications which are not event driven.

Text based console applications have limited value in current GUI-centric operating systems, so there is a natural need for an intermediate step between text-based programming and event-based GUI programming to ease the jump between the two paradigms. Also, a GUI program can be much more useful than a text-based program and closer to 'real' applications in a GUI operating system environment, which can greatly improve the motivation and satisfaction of the beginner programmer during programming education.

In order to overcome this problem, a non-event driven graphics application programming interface (API) for programming education is proposed in this research. By applying the proposed graphics API, programmers can create graphics and real-time user interface applications by simple state request method calls not requiring any event handling or event call-back methods. The proposed graphics API also supports text based console I/O such as print line and line input, so beginner programmers can shift from console based applications to graphics applications without any paradigm changes and minimal code changes.

© ISAROB 2013

2 NON-EVENT DRIVEN GRAPHICS API

The proposed non-event driven graphics API, named Basic Graphics, is implemented as a Java language class. Basic Graphics receives its design hints from 1980's BASIC language graphics approach. In particular, many of the graphics commands are based on F-BASIC by Fujitsu Limited.

Basic Graphics consists of only 1 public class, jp.ac.tuis.basic.BasicGraphics class. Basic Graphics class consists of methods to draw text, graphics and images, retrieve line input from the keyboard, and retrieve keyboard and mouse states. Additionally Basic Graphics includes features to play music and beep, as well as create network connections with other Basic Graphics applications and send and receive network data. Basic Graphics applications can be run as a stand-alone Java application or a Java Applet.

Example 1 below is an example of a hello world program written in Basic Graphics.

```
//Example 1
import jp.ac.tuis.basic.*;
public class HelloWorld{
  public static void main(String[] args){
    BasicGraphics g = new BasicGraphics();
    g.println("Hello, world!");
  }
}
```

Example 1 will create a window and print "Hello, world!" on the top of the created window.

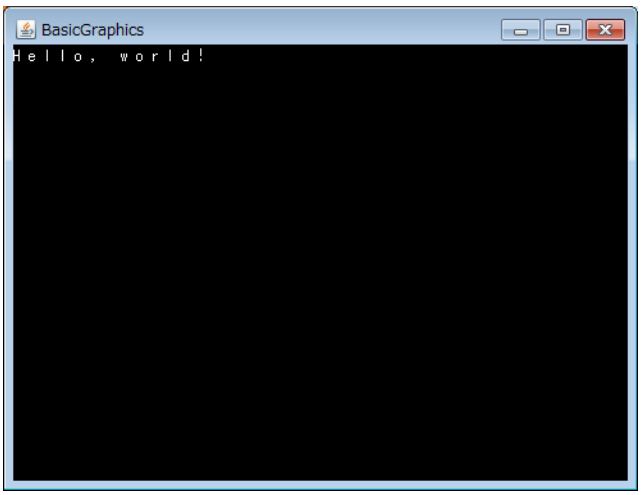

Fig. 1. Hello world program using Basic Graphics

Example 2 below is an example of a simple animation program.

```
//Example 2
import jp.ac.tuis.basic.*;
public class Animation{
  public static void main(String[] args){
    BasicGraphics g = new BasicGraphics();
    for(int i=0; i<40; i++){
      g.locate(i,10);
      g.print('X');
      g.sleep(200);
      g.locate(i,10);
      g.print(' ');
    }
  }
}
```

The locate(x,y) method in Example 2 defines the x,y coordinates of the location of the following print() method. The program will wait further execution in the sleep() method for the given milliseconds. In this example, an 'X' will move from the left of the screen to the right.

Example 3 below is an example of a program to retrieve keyboard input.

```
//Example 3
import jp.ac.tuis.basic.*;
public class Type{
  public static void main(String[] args){
    BasicGraphics g = new BasicGraphics();
    while(true){
      char key = g.inkey();
      if(key != 0){
        g.print(key);
      }
    }
  }
}
```

The inkey() method returns the key of the pressed keyboard key. If no key is pressed, then inkey() returns 0 (zero).

By using the proposed Basic Graphics API, the programmer can draw graphics and retrieve key input events (and similarly mouse events) without using the event-driven model. The proposed model relies only on the simple main method architecture of console based

© ISAROB 2013

application programming which the programmer is familiar with. Example 3 is also a simplified model of a event dispatcher, and can be built upon to describe the implementation of a event dispatching loop later in the programming education.

3 EXPERIMENTAL USE IN PROGRAMMING EDUCATION

The proposed Basic Graphics API was introduced to 10 2rd year college students who have had 1 year prior Java programming education, but could not understand event handling and were not able to create GUI applications yet. After a 30 minutes lecture on how to use the Basic Graphics API, the students were given a graphical programming assignment (Fig.2) to complete. All participating students were able to complete the assignments within 60 minutes. Some of the students were able to create individual graphical applications on their own (Fig.3,4). The participating students are gave positive feedback on the usefulness of the Basic Graphics API, it was clear that the motivation and satisfaction of the students had been improved.

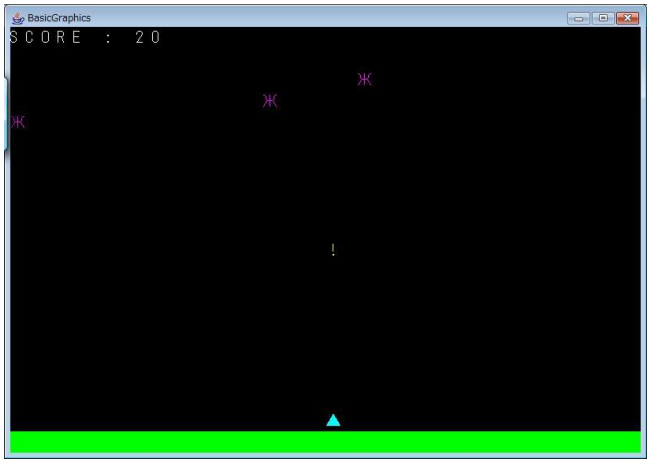

Fig. 2. Graphical programming assignment

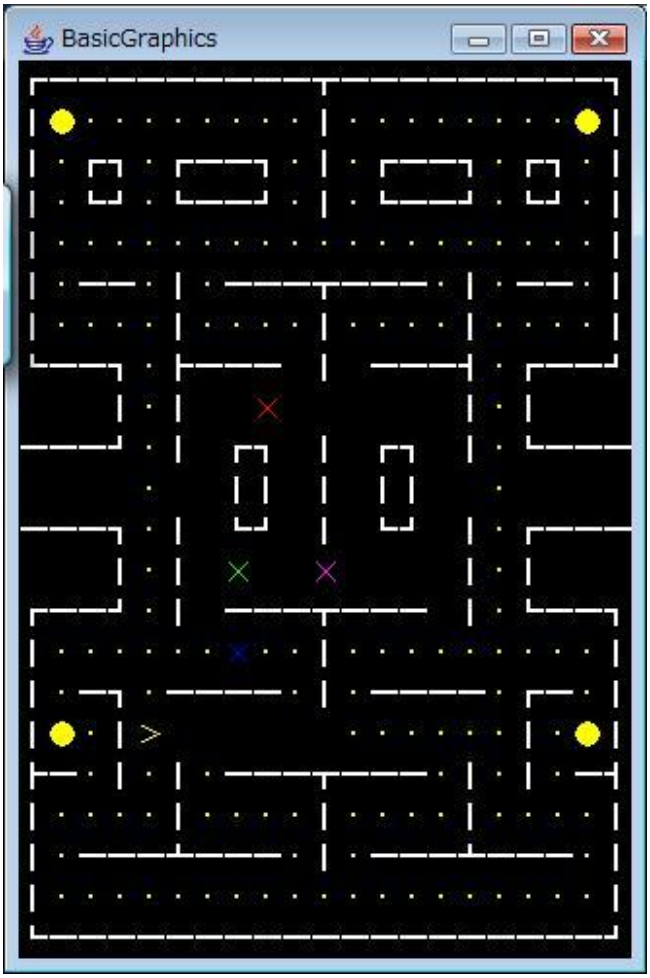

Fig. 3. Example graphical application of students

Fig. 4. Example graphical application by student

© ISAROB 2013

4 CONCLUSION

In this research, a non-event driven graphics API for programming education is proposed. By applying the proposed graphics API, programmers can create graphics and real-time user interface applications by simple state request method calls not requiring any event handling or event call-back methods. The proposed graphics API also supports text based console I/O such as print line and line input, so beginner programmers can shift from console based applications to graphics applications without any paradigm changes.

The proposed API was introduced to 2nd year college students with text-based console programming experience to verify the effectiveness of the proposed method. All participating students were able to complete the graphical application assignment in the total 90 minutes period, and the motivation and satisfaction of the students had been improved.

For future works, a complete self-learning tutorial for using the Basic Graphics API will be developed, to allow students to use the training material at their own learning pace.

REFERENCES

[1] Ephraim P. Glinert (ed) (1990), Visual Programming Environments: Paradigms and Systems. IEEE Computer Society Press

The Eighteenth International Symposium on Artificial Life and Robotics 2013 (AROB 18th '13),
Daejeon Convention Center, Daejeon, Korea, January 30-February 1, 2013

An Education of Social Media Literacy to High School Students in Social Media Times

Yoshihiro Kawano[1], Takuya Miya[1], Naoki Furuya[1], and Yuka Obu[2]

[1]Tokyo University of Information Sciences, Chiba 265-8501, Japan
[2]Unicast, Inc., Hitachi 316-0033, Japan
(Tel: 81-43-236-1149, Fax: 81-43-236-1149)

[1]{ykawano@rsch.tuis.ac.jp, s10155tm@edu.tuis.ac.jp, s10140nf@edu.tuis.ac.jp}, [2]yuka.obu@gmail.com

Abstract: Social media, such as Twitter and Facebook, has been popularized to our society. In the social media times, many people become more active between online and offline. Today, personal branding is very important to harness an individual strong point. We are studying about the personal branding for high school and university students by practical use of social media. This research aims at a career design of the students by personal branding. Concretely, we gave lectures to high school students and teachers (junior high school, high school) about social media and personal branding. We conduct surveys about individual strong points and personal branding for high school students. As the result, we confirmed that they had improved literacy and understanding of social media. From this survey, we propose a personal branding support service named "Mentors". In the near future, Mentors may be launched.

Keywords: career design, personal branding, social media literacy

1 INTRODUCTION

Today, the employment rate of students in Japan is very low level by the economic conditions caused by global depression, and major company intention of many students. The increase in the early unemployment rate for less than three years is a serious problem by the mismatch of adoption between students and companies [1]. People are required to harness individual strong point for survival in the society.

Recently, social media, such as Twitter [2] and Facebook [3], has been popularized to our society. In the social media times, many people become more active between online and offline. Then, personal branding (the activity which asserts own specialty and builds own brand) [4] is very important to harness an individual strong point [5]. In this case, social media literacy is important to use real name for personal branding.

There are several companies which uses social media for a recruitment activity as a communication tool with students in such circumstances. The purpose of these companies is to employ students with high information sensitivity who masters these tools, and the student excellent in communications skills. This new stream is called "social recruiting" or "so-katsu (the meaning of the job hunting activities using social media)".

We are studying about the personal branding for high school and university students by practical use of social media. This research aims at a career design of the students by personal branding. Here, career is "lifetime products". Personal branding brings opportunities to get good human network and information. This may be good supports to construct own career and business. However, personal branding takes much time until effect appears. Therefore, the practice of personal branding and social media literacy in information education at high school class are important for their career design. However, many high school teachers cannot teach to students about advantage or risk of social media effectively, because they are not using social media. In addition, there is no true answer in how to use social media, because social media is dependent on discretion of each person.

Therefore, when people use social media, people need to have the purpose, and creatively uses of social media are required. There are few reports of case study about personal branding of students [6]. In this report, course inclusion experience about personal branding with social media was carried out to students who major in internet marketing. However, the case study which specialized in the social circumstances in Japan has not been reported. This research aims at the contribution to "students", "university", and "society", paying attention to the possibility of personal branding with social media.

© ISAROB 2013

2 SOCIAL MEDIA LECTURE

2.1 Purpose

We gave lectures to high school students and teachers (junior high school, high school) about social media and personal branding. Purposes of the lectures are as follows.

(1) Basic use of social media and practical use as a tool of information gathering.

(2) Social media literacy and suitable information disclosure and information transmission.

(3) Students have relation with society positively (participation of events, make human connections).

(4) Discovery of an effective use of social media for the personal branding of students by active discussions among professors and students.

2.2 Lecture to high school students

In our university, there is cooperation lecture between neighbor high schools and our university for high school students. We gave a lecture to students about practice of social media and personal branding [7][8]. Overview of this lecture is as follows.

- Date time: August 1, 2012, 10:00-17:00
- Number of students: 21
- Contents:
  - Own strong points
  - Social media literacy
  - Personal branding
  - Discussions about above theme

In this lecture, 21 students were divided into four groups. Each group consists of 4-5 students, and discussed about various theme.

2.3 Lecture to teachers

Our university also provides a lecture place for renewal of teaching credential. We gave a lecture to teachers about almost same as the students. Overview of this lecture is as follows.

- Date time: August 9, 2012, 9:15-16:20
- Number of teachers: 29
- Contents:
  - Own strong points
  - Social media literacy
  - Information education in the school
  - Personal branding for high school students
  - Discussions about above theme

In this lecture, 29 teachers were divided into six groups. Each group consists of 4-6 teachers, and discussed about various theme.

2.4 Discussions

2.4.1 Discussions of lecture to students

In the lecture of students, their strong points were surveyed. We classified according to consciousness level of strong points. Level 0 is without recognition. Level 1 is only liking. Level 2 is abstract strong point. Level 3 is concrete strong point. Level 4 is connected with actual activity. Fig.1 shows the consciousness level of strong points of students. About 70 % of students have own strong points. However, 0 students connected with actual activity. Our mission is to promote consciousness level of the students. Concretely, many students answered as strong points that continuity (5 answers), creativity (5 answers), volition (4 answers), imaginary skill (3 answers), curiosity (3 answers), and communication skill (3 answers). And, there are language, human network, sense of commitment and leadership as a minor reply.

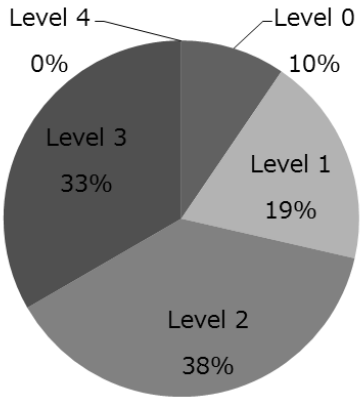

Fig. 1. The consciousness level of strong points

Next, we investigated whether high school students could practice personal branding. It answered that the students of 1/3 could practice personal branding, and the students of 2/3 answered that they could do conditionally. The merit of being the high school student whom the students answered is as follows.

- Easy to be observed from the society
- Easy to gather opinions from young people
- Can know about society from the young age
- Easy to construct human network
- Useful for information gathering

Personal branding from a young age is very important in respect of human networking, because it takes long time.

2.4.2 Discussions of lecture to teachers

In the lecture of teachers, their strong points as an educator to support the students were surveyed. Table 1 shows strong points as a teacher whom the teachers answered.

Table 1. Strong point as a teacher

Strong points as a teacher	Answers
Specialty about own subject	21
Human network	10
Student guidance, career guidance	8
Social credibility	7
Sense of commitment	7
Keep youth	6
Communication skill	5
Experience in industries	1

From Table 1, it is confirmed that the teachers harness the strong point to education of students. Next, we investigated how the teachers could support the students to practice personal branding. The support to personal branding of the students that the teachers answered is as follows.

- Actual use of Twitter, Facebook
- Case introduction
- Observation of the students, interposition
- Training of sociality
- Improvement of writing skill
- Management instruction of personal information
- Responsibility to the information
- Installation of an opportunity to face oneself
- Information moral, literacy education
- Instruction corresponding to a trouble

There are many teachers with the volition to student guidance. The necessity of lecture about social media literacy and personal branding for the high school students were confirmed.

3 PROPOSED SERVICE

3.1 Purpose

From the above discussions, a support service for personal branding is required all over the world. In personal branding, it is very important to harness individual strong point. And, existence of mentors which advises to find own strong point is necessary. Then, we propose a personal branding support service named "Mentors".

3.2. Overview of Mentors

Mentors is a service which connects mentor and mentee. Fig. 2 shows overview of Mentors. In Fig. 2, mentee asks for advice to Mentors, mentor registers own strong points. Then, Mentors matches mentor and mentee.

The concept of Mentors is "Everyone has face of both mentor and mentee". An actual human had better judge an individual strong point rather than a system judges. The mind of Mentors are "actually met", "talking various theme", and "communication after meeting". Then, the functions of Mentors are as follows.

- Registration of searching mentor type
- Registration of own strong points
- Matching of mentor and mentee

Mentors is similar to Forkwell [9] and Wantedly [10]. Forkwell is skill based networking site for engineers and creators, and seems to be engineer version LinkedIn. The engineers can make a personal brand with Forkwell, and there is mechanism which has own skills evaluated from other people. Wantedly is matching service to meet others who has same purpose (project member, party friends etc.).

Mentors specializes in finding the mentor who mentee wants to meet. Mentors will be developed by Facebook based Web application, because social graph of Facebook is based on actual human network. Mentors aims at promotion of human life by understanding their strong points and using social media effectively.

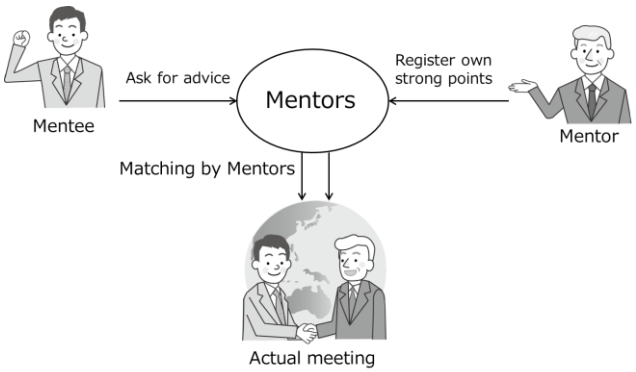

Fig. 2. Overview of Mentros

4 CONCLUSION

This research aims at a career design of the students by personal branding with social media, and we gave a lecture about social media to the students. The contents of the lecture are mechanism about social media, social media literacy, and personal branding with social media. We conduct surveys about individual strong points and personal branding for high school students.

As the result, we confirmed that they had improved literacy and understanding of social media. For practical use of social media, not only an understanding of social media literacy, but also actual use by each person is necessity. From this survey, we propose a personal branding support service named "Mentors". In the near future, Mentors may be launched.

Future works are more long time observation about behavior of students, modeling to find suitable social media for each person, and evaluation method for teaching portfolio.

REFERENCES

[1] Japan Center for Economic Research (2011), "The shock of 30 percent of the early unemployment rate for less than three years (in Japanese)," http://www.jcer.or.jp/report/econ100/pdf/econ100bangai20110715.pdf.

[2] Twitter, http://twitter.com/.

[3] Facebook, https://facebook.com/.

[4] Tom Peters (1997), "The Brand Called You," August 1997, http://www.fastcompany.com/magazine/10/brandyou.html.

[5] Takashi Ohmoto (2011), Social Media Jissen No Syo (in Japanese). Ric Telecom, June 2011.

[6] Lyle Wetsch (2011), "Personal Branding with Social Media; An Essential Application of Direct Marketing Skills for Today's Students," Memorial University of Newfoundland, May 2011.

[7] Y. Kawano (2012), "Social Media Lecture 1st", http://www.slideshare.net/YoshihiroKawano/social-media-personalbranding201208011.

[8] Yoshihiro Kawano (2012), "Social Media Lecture 2nd", http://www.slideshare.net/YoshihiroKawano/social-media-personalbranding201208012.

[9] Forlwell, https://forkwell.com/.

[10] Wantedly, https://www.wantedly.com/.

[11] LinkedIn, http://www.linkedin.com/.

© ISAROB 2013

The Eighteenth International Symposium on Artificial Life and Robotics 2013 (AROB 18th '13),
Daejeon Convention Center, Daejeon, Korea, January 30-February 1, 2013

Syntax Structure Based Typing Tool for Source Code Writing

Takashi Yamaguchi[1], Shinya Iwasaki[1], Kazuma Mori[1], Kenneth J. Mackin[1], Masaki Hanada[1], Eiji Nunohiro[1]

[1]Tokyo University of Information Sciences, Japan
(Tel: 81-43-236-1232, Fax: 81-43-236-1232)

[1]tyamagu@rsch.tuis.ac.jp

Abstract: Typing is a fundamental skill for the computer works that has the tasks of text inputting by keyboard. For improving computer work efficiency, the training of fast typing is very important. In this paper, we proposed a typing tool that presents a source code for the subject word. Proposed application has following three aims: the learning of touch typing, the learning of the syntax structure of programming language, the learning of source code writing process, and the improvement of continuity in programming language practice. Our typing tool presents a part of source code for the subject words. The parts of source code are derived by blocks of syntax structure on programming language. These parts are presented by the sequences from super to sub nested blocks. From this source code presentation, the learner can feel the syntax structure and the writing process of expert programmers.

Keywords: e-learning, programming, typing tool, game

1 INTRODUCTION

Typing is a fundamental skill for the computer works that has the tasks of text inputting by keyboard. For improving computer work efficiency, the training of fast typing is very important. Therefore, in an elementary information technology education, students are often trained the touch typing that faster typing technique without using the sense of sight to find the keys. However, the long iterative practices are necessity because the finger placement of touch typing must be learned and unconsciously used.

For the training of touch typing, the typing tools are commonly used. The typical typing tool is software product that presents the subject words to make a learner types this subject words, and shows the result of typing errors for help the training of typing. Because the learning of touch typing is based on the iterative practice, the typical typing tools are designed like the computer games to improve the continuity of practice by make the attention and competitive spirit of learner [1].

The improvement of learning continuity is very important characteristics for self-learning using e-learning systems because typical e-learning systems are used for self-learning. For improvement of learning continuity, John M. Keller proposed ARCS model that is an instructional design model by focusing on Attention, Relevance, Confidence, and Satisfaction [2]. These 4 ARCS model features are considered to be fundamental features to develop the design of products and package soft wares that include the typing tool or game.

In our past research, we develop an e-learning system for JAVA programming [3-8] that focus on the improvement continuity by ARCS model. Our e-learning system focuses on the programming learning with entertainment. In this paper, we investigate an application of typing tool for the elementary training of the programming language as another approach of entertainment e-learning system for programming.

2 PROGRAMMING LEARNING SYSTEM

2.1 puzzle-based programming learning system

In our past research, we develop CAPTAIN (Computer Aided Programming Training And INstruction) that is an e-learning system for JAVA programming. Fig.1 is screenshot of CAPTAIN client.

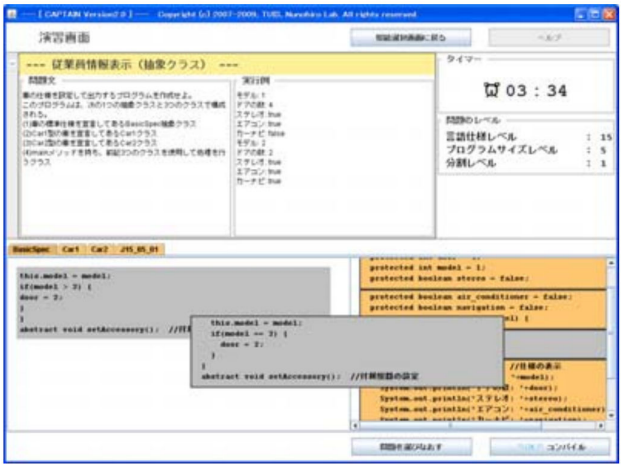

Fig.1. Screenshot of CAPTAIN client

© ISAROB 2013

CAPTAIN focuses on the feature of entertainment for e-learning system. CAPTAIN has following three major functions; the puzzle-based programming, the score ranking, score visualization. CAPTAIN trains the ability to read the source code by puzzle-based programming function and improve the motivation by score ranking function. Moreover, the teachers can confirm the learner's understanding and individually support their understanding led by teacher.

The puzzle-based programming is a main function of CAPTAIN client for training JAVA programming language. The source code is separated into the multiple source code parts like the orange colored area in Figure 1. These parts are presented to the learner with randomly ordering. The learner drag and drop the source code parts to restore to original source code. From this system, the learner is trained the ability of source code reading. On the other hand, the ability of source code writing is not improve since the learner has nothing to write in programming training on CAPTAIN system. Therefore, we proposed a typing tool based programming training system in order to improve the ability of source code writing.

2.2 Typing tool based programming learning system

In this paper, we proposed a typing tool based programming training system that presents a source code as the subject word for each syntax structure. Proposed application has following four aims: the learning of touch typing, the learning of the syntax structure of programming language, the learning of source code writing process, and the improvement of continuity in programming language practice. In the scene of programming lecture, the teachers have a problem that the slowness of programming task disturbs the learner's understanding and the progress of lecture. The proposed training system is expected to resolve this problem by the training of touch typing and source code writing with continuous self-learning.

Figure 2 is a prototype of source code typing tool. The subject words are shown in the text pain of left side and the learner writes the words to match the subject words. The subject words are incompletely shown in initial state. The subject words are updated when the learner correctly write the subject words. Moreover, the input error check method of our typing tool is different from the typical typing tools. The typical typing tool requires the keyboard input and check the input errors for each word. Our typing tool check the input errors for each time that line feed is input in order to check syntax error in the future. Additionally, the number of times that learner hit the back space and delete key is counted for the typing error summary.

Our typing tool presents a part of source code for the subject words. The parts of source code is derived by blocks of syntax structure on programming language such as class definition, method definition, if statement, for statement, and etc. Typically, this syntax structure can be seen as the indention of source code in general programming languages. Our typing tool presents the parts of source code for each the indention level.

In this research, we defined the source code partition rules for JAVA language. The details of source code presentation method are described in next section.

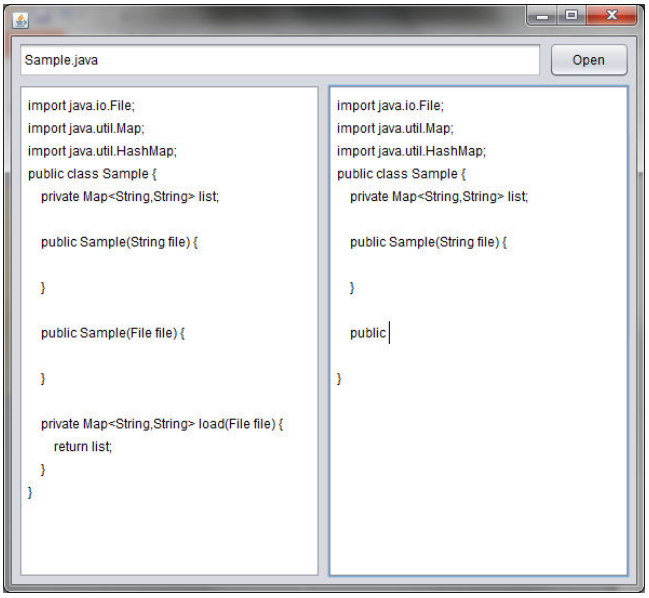

Fig.2. Prototype of source code typing tool

3 IMPLEMENTATION ON JAVA

In JAVA language, source code can be grouped by nested structure of class and interface definition, field definition, method definition, if statement, for statement, while and do statement, switch statement. The JAVA source code is partitioned into these nested syntax structures and these parts are presented by the sequences from super to sub nested blocks similar to the common writing sequence of expert JAVA programmer. Therefore, proposed source code presentation method is expected to effective for elementally programming training that requires the learning of the source code writing procedure and the fundamental syntax structure.

© ISAROB 2013

```
/* SAMPLE PROGRAM */
import java.io.BufferedReader;
import java.io.File;
import java.io.FileInputStream;
import java.io.IOException;
import java.io.InputStreamReader;
import java.util.HashMap;
import java.util.Map;

public class Sample {

   public static String DELIMITER = ",";
   private Map<String, String> values;

   public Sample(String file) {
      this(new File(file));
   }

   public Sample(File file) {
      values = load(file);
   }

   private Map<String, String> load(File file) {
      <… code …>
      return list;
   }
}
```

Fig.3. Sample source code

For example, the source code presentation process is explained using an original source code of sample program shown in Figure 3. Only class definitions and package definitions are presented for initial subject words like as a Figure 4. The learner should write to match the bolded words.

When the learner input the line feed or move cursor to another line, the typing error was checked and the words include the error are highlighted in input text pain. In this time, the number of typographic error is counted for the result summary. The number of times that learner hit the back space and delete key is separately counted as keyboard input error in order to separate the result to typographic error and keyboard input error. The typographic error is considered to be occurred by the lack of understanding of programming language syntax. From this function, the learner can easily discover the error words in real time, and understands that the week point is syntax of programming language or keyboard input.

When the learner completes the initial words writing, the field, constructer and method definitions are newly presented as 2nd subject words shown as bold words in Figure 5. After the completion of 2nd subject words, the complete source code is presented as 3rd subject words.

```
/* SAMPLE PROGRAM */
import java.io.BufferedReader;
import java.io.File;
import java.io.FileInputStream;
import java.io.IOException;
import java.io.InputStreamReader;
import java.util.HashMap;
import java.util.Map;

public class Sample {

}
```

Fig.4. Initial subject words

```
/* SAMPLE PROGRAM */
import java.io.BufferedReader;
import java.io.File;
import java.io.FileInputStream;
import java.io.IOException;
import java.io.InputStreamReader;
import java.util.HashMap;
import java.util.Map;

public class Sample {

   public static String DELIMITER = ",";
   private Map<String, String> values;

   public Sample(String file) {

   }

   public Sample(File file) {

   }

   private Map<String, String> load(File file) {

   }
}
```

Fig.5. 2nd subject words

© ISAROB 2013

After the training, the error summary is presented to the learner. Currently, the summary consists of the number of typographic error, the number of keyboard input error, and average times of key board input. We plan to enhance the summary based on the syntax check to be able to suggest the lack of understanding on syntax of programming language in the future.

4 CONCLUSION

In this paper, we proposed a typing tool based programming training system that presents a source code as the subject word for each syntax structure in order to train the touch typing and the source code writing in continuous self-learning. Moreover, we develop a prototype of proposed typing tool based programming training system for JAVA programming language. This system expected to effective for training touch typing, understanding syntax structure, and continuous self-learning.

For future works, we plan to evaluate the effectiveness of our system on the practical use in the self-learning the programming lectures because it is necessary to separately evaluate on the effectiveness of touch typing training, effectiveness of programming training, and the continuity of self-learning.

ACKNOWLEDGMENTS

This research was supported by The Ministry of Education, Culture, Sports, Science and Technology (MEXT), Grant-in-Aid for Scientific Research (C) (24501207).

REFERENCES

[1] M Prensky (2005), Computer games and learning: Digital game-based learning, New York: McGraw Hill

[2] JM Keller (1987), Development and use of the ARCS model of instructional design, Journal of instructional development,Springer

[3] Nunohiro E, Mackin K, Ohshiro M, Matsushita K, Yamasaki K (2007), Implementation of a GA driven programming training support system, The 12th International symposium artificial life and robotics, pp.517-522.

[4] Nunohiro E, Matsushita K, Mackin K, Ohshiro M, Yamasaki K (2008), Design and development of a puzzle based programming learning support system with genetic algorithm (in Japanese), Transactions of Japanese society for information and system in education, vol.25, No.2, pp.207-213.

[5] Yoneyama Y, Matsushita K, Mackin K, Ohshiro M, Yamasaki K, Nunohiro E (2008), Puzzle Based Programming Learning Support System with Learning History Management, The 16th International Conference on Computers in Education (ICCE2008), pp. 623-627

[6] Yamakawa Y, Ohshiro M, Matsushita K, Mackin K, Nunohiro E (2010), Programming Learning Support System 'CAPTAIN' with Motivational Study Model, The 18th International Conference on Computers in Education (ICCE2010), pp. 171-175

[7] Ohshiro M, Mackin K, Matsushita K, Nunohiro E,Yamakawa Y (2010), Programming Learning Support System with Learning Progress Monitoring Feature, Joint 5rd International Conference on Soft Computing and Intelligent Systems and 11th International Symposium on Advanced Intelligent Systems (SCIS-ISIS 2010), pp.1465-1468

[8] Ohshiro M, Matsushita K, Mackin K, Yamaguchi T,N unohiro E (2012), Programming Learning Support System with Competitive Gaming Using Monitoring and Nickname s, The 17th International symposium artificial life and robot ics, pp.238-241.

© ISAROB 2013

The Eighteenth International Symposium on Artificial Life and Robotics 2013 (AROB 18th '13),
Daejeon Convention Center, Daejeon, Korea, January 30-February 1, 2013

Robust digital control for interleave PFC boost converter

Yuto Adachi[1], Kohji Higuchi[1], Tatsuyoshi Kajikawa[1], Tomoaki Sato[2], and Kosin Chamnongthai[3]

[1] The University of Electro-Communications 1-5-1, Chofu-ga-oka,Chofu-shi, Tokyo 182-8585, Japan
[2] C&C SYSTEMS CENTER Hirosaki University, Bunkyo-Cho 3, Hirosaki-shi, Aomori 036-8561, Japan
[3] King Mongkut's University of Technology Thonburi, 126 Pracha-uthit Rd., Bangmond, Tungkru, Bangkok 10140, Thailand
(Tel: 81-42-443-5182, Fax: 81-42-443-5183)

[1]arobsecr@isarob.org

Abstract: In recent years, improving of power factor and reducing harmonic distortion in electrical instruments are needed. In general, a current conduction mode boost converter is used for active PFC (Power Factor Correction). Especially, an interleave PFC boost converter is used in order to make a size compact, make an efficiency high and make noise low. In this paper, a robust digital controller for suppressing the change of step response characteristics and variation of output voltage at a load sudden change with high power factor and low harmonic is proposed. Experimental studies using a micro-processor for controller demonstrate that this type of digital controller is effective to improve power factor and to suppress output voltage variation.

Keywords: interleave PFC, boost converter, digital robust control, micro-processor

1 INTRODUCTION

In recent years, improving of power factor and reducing harmonic of power supply using nonlinear electrical instruments are needed. A passive filter and an active filter in AC lines are used for improving of the power factor and reducing the harmonic. Generally a current conduction mode boost converter is used for an active PFC (Power Factor Correction) in electrical instruments. Especially, an interleave PFC boost converter is used in order to make a size compact, make an efficiency high and make noise low. In the PFC boost converter, if a duty ratio, a load resistance and an input voltage are changed, the dynamic characteristics are varied greatly, that is, the PFC converter has non-linear characteristics. In many applications of the interleave PFC converters, loads cannot be specified in advance, i.e., their amplitudes are suddenly changed from the zero to the maximum rating. This is the prime reason of difficulty of controlling the PFC boost converter.

Usually, a conventional PI or analog IC controller designed to the approximated linear controlled object at one operating point is used for the PFC converter. In the nonlinear PFC boost converter system, those controllers are not enough for attaining good performance. In this paper, the robust controller for suppressing the change of step response characteristics and variation of output voltage at a load sudden change with high power factor and low harmonic is proposed. An approximate 2-degree-of-freedom (A2DOF) method [1] is applied to the interleave PFC boost converter with the load. The PFC converter is a nonlinear system and the models are changed at each operation point. The design and combining methods of two controllers which can cope with nonlinear system or changing of the models with one controller is proposed. One is an approximate 2-Dgree-of-freedom (A2DOF) controller for a current control system and another is a PI controller. These controller are actually implemented on a micro processor and is connected to the PFC converter. Experimental studies demonstrate that the digital controllers designed by proposed method satisfy the desired performances and are useful.

2 INERLEAVE PFC BOOST CONVERTER

2.1 State-space model of interleave boost converter

The interleave boost converter shown in Fig. 1 is manufactured.

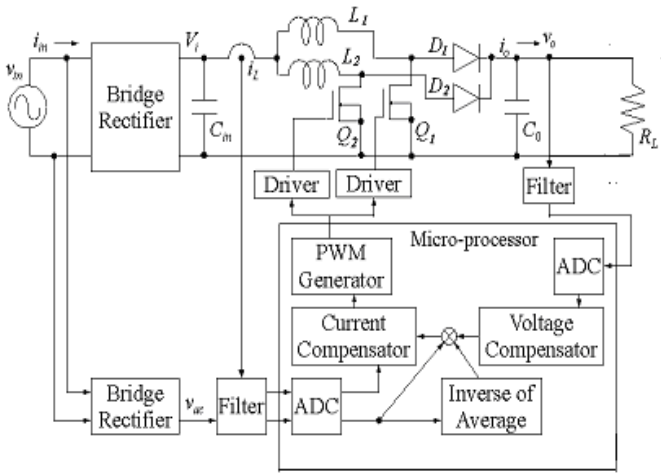

Fig.1 Interleave PFC boost converter

© ISAROB 2013

Fig.1, v_{in} is an input AC voltage, i_{in} is an input AC current, C_{in} is a smoothing capacitor, V_i is a rectifying and smoothing input voltage, Q_1 and Q_2 are MOSFETs or IGBTs, L_1 and L_2 are interleave boost inductances, D_1 and D_2 are interleave boost diodes, C_0 is an output capacitor, R_L is an output load resistance, i_L is the sum of inductor current, v_{ac} is an absolute value of the input AC voltage and v_o is an output voltage. The inductor currents i_L is controlled to follow the rectified input voltage v_{ac} for improved power factor, reduced harmonics and stable the output voltage.

At some operating point, let v_o, i_L and μ, be V_s, I_s and μ_s, respectively. Then the linear approximate state equation of the boost converter using small perturbations $\Delta i_L = i_L - I_s$, $\Delta v_o = v_o - V_s$ and $\Delta\mu = \mu - \mu_s$ is as follows:

$$\begin{aligned} \dot{x}(t) &= A_c x(t) + B_c u(t) \\ y(t) &= C_c x(t) \end{aligned} \tag{3}$$

where

$$A_c = \begin{bmatrix} -\dfrac{R_0}{L_0} & -\dfrac{1-\mu_s}{L_0} \\ \dfrac{1-\mu_s}{C_0} & -\dfrac{1}{R_L C_0} \end{bmatrix}, B_c = \begin{bmatrix} \dfrac{V_s}{L_0} \\ -\dfrac{I_s}{C_0} \end{bmatrix}$$

$$x(t) = \begin{bmatrix} \Delta i_L(t) \\ \Delta v_o(t) \end{bmatrix}, u(t) = \Delta\mu(t), y = \begin{bmatrix} y_i \\ y_v \end{bmatrix}, C_c = \begin{bmatrix} 1 & 0 \\ 0 & 1 \end{bmatrix}$$

Here μ is duty ratio. When controlling the current i_L of the sum of each phase, R_0 (equivalent resistance of inductor) is $R_1R_2/(R_1+R_2)$ and L_0 is $L_1L_2/(L_1+L_2)$. And Δi_L, Δv_o, $\Delta\mu$ are small-signal variables. And $y_i = \Delta i_L$ is a small signal inductor current and $y_v = \Delta v_o$ is a small signal output voltage.

From this equation, matrix A and B of the interleave boost converter depends on duty ratio μ_s. Therefore, the converter response will be changed depending on the operating point and other parameter variations. The changes of the load R_L, the duty ratio μ_s, the output voltage V_s and the inductor current I_s in the controlled object are considered as parameter changes in eq. (1). Such parameter changes can be replaced with the equivalent disturbances inputted to the input and the output of the controlled object. Therefore, what is necessary is just to constitute the control systems whose pulse transfer functions from equivalent disturbances to the output y become as small as possible in their amplitudes, in order to robustize or suppress the influence of these parameter changes.

3 DIGITAL ROBUST CONTROLLERS

3.1 Discretization of controlled object

The continuous system of eq. (1) is transformed into the discrete system as follows:

$$\begin{aligned} x_d(k+1) &= A_d x_d(k) + B_d u(k) \\ y(k) &= C_d x_d(k) \end{aligned} \tag{4}$$

3

where

$$A_d = \left[e^{A_c T}\right], B_d = \left[\int_0^T e^{A_c \tau} B_c d\tau\right], C_d = C_c$$

Here, in order to compensate the delay time by A/D conversion time and micro-processor operation time etc., one delay (state ξ_1) is introduced to input of the controlled object. Then the state-space equation is described as follows:

$$\begin{aligned} x_{dt}(k+1) &= A_{dt} x_{dt}(k) + B_{dt} v(k) \\ y(k) &= C_{dt} x_{dt}(k) \end{aligned} \tag{3}$$

where

$$A_{dt} = \begin{bmatrix} e^{A_c T_s} & e^{A_c (T_s - L_d)} \int_0^{L_d} e^{A_c \tau} B_c d\tau \\ 0 & 0 \end{bmatrix} = \begin{bmatrix} a_{11} & a_{12} & a_{13} \\ a_{21} & a_{22} & a_{23} \\ 0 & 0 & 0 \end{bmatrix}$$

$$B_{dt} = \begin{bmatrix} \int_0^{T_s - L_d} e^{A_c \tau} B_c d\tau \\ 1 \end{bmatrix} = \begin{bmatrix} b_{11} \\ b_{21} \\ 1 \end{bmatrix} \qquad x_{dt}(k) = \begin{bmatrix} x(k) \\ \xi_1(k) \end{bmatrix}$$

$$C_{dt} = \begin{bmatrix} C_c & 0 \end{bmatrix} = \begin{bmatrix} 1 & 0 & 0 \end{bmatrix}$$

3.2 A2DOF digital current controller

The transfer function from the reference input r_i' to the output y_i is specified as follows:

$$W_{r_i' yi}(z) = \frac{(1+H_1)}{(z+H_1)} \frac{(1+H_2)}{(z+H_2)} \frac{(1+H_3)}{(z+H_3)} \times \frac{(z-n_{1i})}{(1-n_{1i})} \frac{(z-n_{2i})}{(1-n_{2i})} \tag{4}$$

Here H_i, i=1,…,3 are the specified arbitrary parameters, n_{1i} and n_{2i} are the zeros of the discrete-time controlled object. This target characteristic W_{ryi} is realizable by constituting the model matching system shown in Fig.5 using the following state feedback to the controlled object (5).

$$v = -F x_{dt} - G_i r_i' \tag{5}$$

Here $F = [f_1 \;\; f_2 \;\; f_3]$ and G_i are selected suitably. In Fig. 5, q_v and q_{yi} are the equivalent disturbances with which the parameter changes of the controlled object are replaced.

© ISAROB 2013

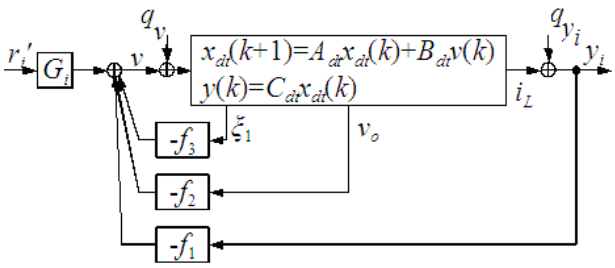

Fig.2 Model matching system using state feedback

It shall be specified that the relation of H_1 and H_3 become $|H_1| >> |H_3|$ and $n_{1i} \approx H_2$. Then $W_{ri'yi}$ can be approximated to the following first-order discrete-time model:

$$W_{r_i'y_i}(z) \approx W_{mi}(z) = \frac{1+H_1}{z+H_1} \qquad (5)$$

The transfer function $W_{Qyi}(z)$ between the equivalent disturbance $Q_i = [q_v \ q_{yi}]^T$ to y_i of the system in Fig.2 is defined as

$$W_{Qyi}(z) = \left[W_{qvyi}(z) \quad W_{qyyi}(z)\right] \quad (10) \qquad (6)$$

The system added the inverse system and the filter to the system of Fig.2 is constituted as shown in Fig.3.

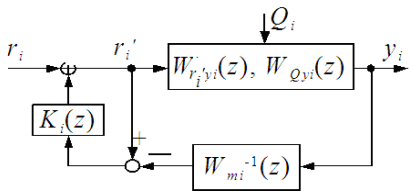

Fig. 3 System Reconstituted with Inverse System and F ilter

In Fig. 3, the transfer function $K_i(z)$ is as follows:

$$K_i(z) = \frac{k_{zi}}{z-1+k_{zi}} \qquad (7)$$

The transfer functions between r_i -y_i, q_{ui} -y_i and q_{yi} -y_i of the system in Fig.6 are given by

$$y_i = \frac{1+H_1}{z+H_1}\frac{z-1+k_{zi}}{z-1+k_{zi}W_{si}(z)}W_{si}(z)r_i \qquad (8)$$

$$y_i = \frac{z-1+k_{zi}}{z-1+k_{zi}}\frac{z-1+k_{zi}}{z-1+k_{zi}W_{si}(z)}W_{Qyi}(z)Q_i \qquad (9)$$

where

$$W_{si}(z) = \frac{(1+H_3)}{(z+H_3)}\frac{(z-n_{1i})}{(1-n_{1i})}$$

Here, if $W_{si}(z) \approx 1$, then eq. (8) and eq. (9) are approximated, respectively as follows:

$$y_i = \frac{1+H_1}{z+H_1}r_i \qquad (10)$$

$$y_i = \frac{z-1}{z-1+k_{zi}}W_{Qyi}(z)Q_i \qquad (11)$$

From eq. (10), (11), it turns out that the characteristics from r to y can be specified with H_1 and the characteristics from Q_i to y_i can be independently specified with k_{zi}. That is, the system in Fig. 3 is an A2DOF system, and its sensitivity against disturbances becomes lower with the increase of k_{zi}. If equivalent conversion of the controller in Fig.3, we obtain Fig. 4. Then, substituting a system of Fig. 2 to Fig. 4, A2DOF digital integral type control system will be obtained as shown in Fig. 5. In Fig. 5, the parameters of the controller are as follows:

$$k_1 = -f_1 - \frac{Gk_{zi}}{1+H_1}, \quad k_2 = -f_2 \qquad (12)$$

$$k_3 = -f_3, \quad k_{ii} = G_i k_{zi}, \quad k_{ri} = G_i$$

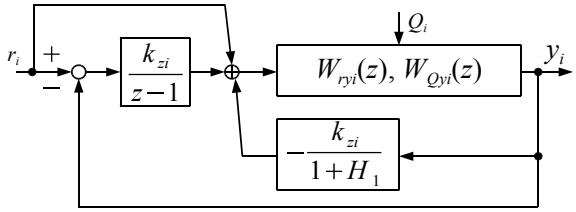

Fig. 4 Equivalent Conversion of the Robust Digital

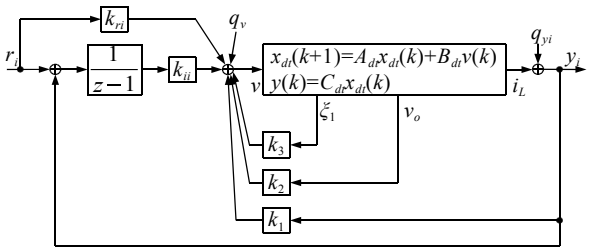

Fig. 5 Approximate 2DOF Digital Integral Type Curren t Control System

4 DIGITAL VOLTAGE CONTROLLER

4.1 Addition of u_v and v_{ac} to r_i

Add the multiplier in front of the reference input r_i of the current control system. Let the inputs of the multiplier be v_{ac} and u_v as shown in Fig. 6. v_{ac} is the absolute value of the input voltage v_{in} and u_v is a new input. This addition is for making the inductor current i_L follow the AC voltage v_{ac}.

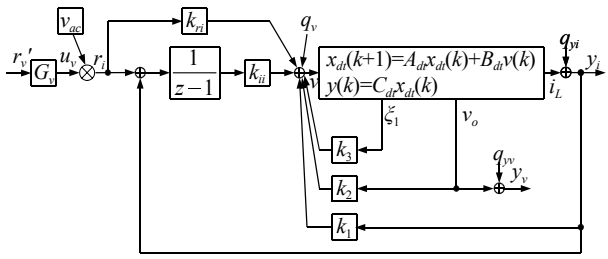

Fig. 6 Current Control System Added Multiplier

© ISAROB 2013

Next, the digital PI voltage controller is added to the input of Fig. 6. Then the digital robust control system including the A2DOF current controller and the PI voltage controller is obtained as shown in Fig, 7.

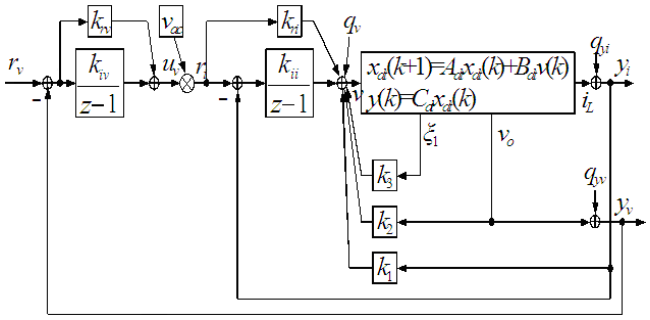

Fig. 7 Digital Robust Control System Including the A2DOF Current Controller and the PI Voltage Controller

4 Expermental Studies

All experimental setup system is manufactured. A micro-controller (RX) from Renesas Electronics is used for the digital controller. The digital PI current, and voltage controllers were implemented on 1 micro-processor.

The design parameters of the A2DOF current control system have been determined as

$$H_1=-0.999866 \quad H_2=-0.6 \quad H_3=0.1 \quad k_{zi}=0.5$$

And the parameters of the PI voltage controller have been determined as

$$k_{rv}=8 \qquad k_{iv}=0.01_$$

The experiment results are shown in Fig. 8, 9, 10. The experiment result of the steady state at load RL=500Ω by proposed method are shown in Fig. 8. The input current waveform and the phase are the almost same as the input voltage at each load and PFC of the converter at load RL=500Ω are 0.991 and 0.985, respectively. The experiment result of the steady state at load RL=500Ω by usual phase lead-lag method are shown in Fig. 10. PFC of the converter at load RL=500Ω are 0.985. The experiment result of load sudden change from 1kΩ to 500Ω is shown in Fig. 6. In Fig. 6, the output voltage variation in sudden load change is less than 3V (0.78%). It turns out that the digital robust controller proposed is effective practically.

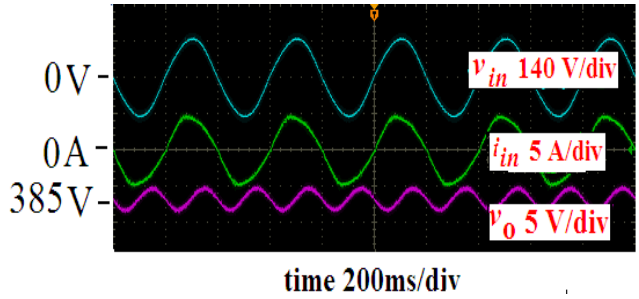

Fig.8 Experimental Results of Steady State Waveform, at load RL=500Ω by proposed method

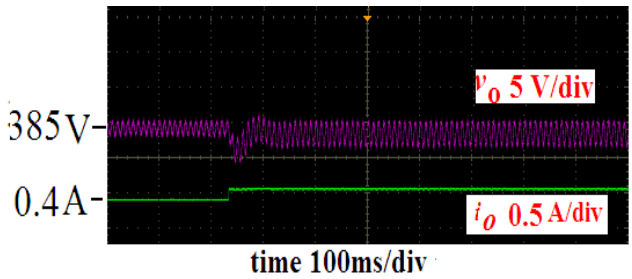

Fig.9 Experimental Results of Sudden Load Change from 1kΩ to 500Ω controlling the current for every phase

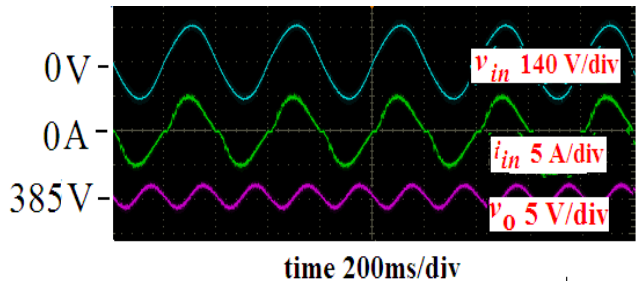

Fig.10 Experimental Results of Steady State Wavefor ms at load RL=500Ω by usual phase lead-lag method

4 CONCLUSION

. In this paper, the concept of controller of non-linear interleave PFC boost converter to attain good robustness was given. It was shown from experiments that the proposed A2DOF digital current controller can attain better performance.

REFERENCES

[1] K. Higuchi, K. Nakano, T. Kajikawa, E. Takegami, S. Tomioka, K. Watanabe, "A New Design of Robust Digital Controller for DC-DC Converters", IFAC 16th Triennial World Congress, (CD-ROM), 2005

© ISAROB 2013

The Eighteenth International Symposium on Artificial Life and Robotics 2013 (AROB 18th '13),
Daejeon Convention Center, Daejeon, Korea, January 30-February 1, 2013

Synthesis of continuous-time dynamic quantizers for LFT type quantized feedback systems

Kenji Sawada[1] and Seiichi Shin[1]

[1]The University of Electro-Communications, Tokyo, Japan
(Tel: +81-42-443-5253; E-mail: {knj.sawada,seiichi.shin}@uec.ac.jp)

Abstract: This paper focuses on analysis and synthesis methods of continuous-time dynamic quantizers for LFT type quantized feedback systems. Our aim is to find multiple (decentralized) quantizers such that a given linear system is optimally approximated by the given linear system with the quantizer in terms of invariant set analysis. In the case of minimum phase systems, this paper clarifies that optimal dynamic quantizers and its performance are parameterized by a design parameter. Also, an analytical relation between the static and dynamic quantizers will be presented.

Keywords: Quantizer, Continuous-time, LFT

1. INTRODUCTION

The cyber-physical system connects the physical systems with the information systems. In the research field of control theory, the control problem of such the system is one of the most active topics since the system covers various systems including discrete-valued-signals such as networked systems, hybrid systems, embed devices with D/A-A/D converters [1]. For the above challenging problem, it is important to focus on optimality of systems controlled by the discrete-valued signals. There clearly exits a difference between control performances of the systems controlled by the continuous-valued signal and the discrete-valued signal. Motivated by this, this paper focuses on the quantized feedback systems including the discrete-valued signals.

Considering optimality of quantized feedback systems, some existing results have provided optimal dynamic quantizers for the following problem formulation: When a plant and a controller are given in the usual feedback system, the framework synthesizes a dynamic quantizer that minimizes the maximum output difference between before and after the quantizer insert. In this case, the quantized feedback system with such the quantizer optimally approximates the original feedback system in the sense of the input-output relation. The two main types of dynamic quantizer are discrete-time and continuous-time settings. A number of the dynamic quantizer studies have been done in the discrete-time setting [2-5]. On the other hand, continuous-time dynamic quantizer is a key device for recent broadband wireless communication and mobile systems because of lower power and longer battery life compared with discrete-time ones [6]. Also, it is natural to consider the continuous-time setting in the sense that model uncertainty expressed in continuous-time domain is suitable for robust control of physical model.

Motivated by the above, this paper considers a continuous-time dynamic quantizer design for quantized feedback systems. In particular, we consider the LFT (linear fractional transformation) type quantizer feedback system. Our early work has provides an optimal dynamic quantizer which is applicable for the centralized control system. Since the sensors and actuators are distributed in the networked control system, it is natural to implement multiple (decentralized) quantizers rather than a centralized quantizer for the I/O quantized feedback system. Focusing on the LFT type system that covers various quantized feedback systems, we will provide extension results of our early work [7]. As space is limited, this paper concentrates on the minimum phase case. We will clarify the effectiveness and the limitation of our proposed quantizers. In the case of minimum phase systems, it is clarified that optimal dynamic quantizers and its performance are parameterized by a design parameter.

Notation: The set of $n \times m$ (positive) real matrices is denoted by $\mathbb{R}^{n\times m}$ ($\mathbb{R}_+^{n\times m}$). The set of $n\times$ (positive) integer matrices is denoted by $\mathbb{N}^{n\times m}$ ($\mathbb{N}_+^{n\times m}$). $0_{n\times m}$ and I_m (or for simplicity of notation, 0 and I) denote the $n\times m$ zero matrix and the $m\times m$ identity matrix, respectively. For a matrix M, M^{T}, $\lambda(M)$, $\lambda_i(M)$ and $\lambda_{\max}(M)$ denote its transpose, its eigenvalue set, the ith element of the set $\lambda(M)$ and its maximum eigenvalue, respectively. For a number $n \in \mathbb{N}_+$, $n!$ denotes its factorial. For a complex number c, $\mathbf{Re}(c)$ is its real part. For a vector x, x_i is the ith entry of x. For a symmetric matrix X, $X > 0$ ($X \geq 0$) means that X is positive (semi) definite. For a full row rank matrix M, $M^\dagger$ denotes its pseudo inverse matrix which is given by $M^\dagger = M^{\mathrm{T}}(MM^{\mathrm{T}})^{-1}$. For a matrix X, $\|X\|_2$ denotes its 2-norms. Finally, we use the "packed" notation: $\left(\begin{array}{c|c} A & B \\ \hline C & D \end{array}\right) := C(sI-A)^{-1}B+D$.

2. PROBLEM FORMULATION

Consider the quantized feedback system which consists of the LTI continuous-time plant $P(s)$ with the state $x_p \in \mathbb{R}^{n_p}$, the LTI continuous-time controller $C(s)$ with the state $x_c \in \mathbb{R}^{n_c}$, and the dynamic quantizers $v_1 = Q_{d_1}(u_1)$, $v_2 = Q_{d_2}(u_2)$. The systems $P(s)$ and $C(s)$ are given by

$$\begin{bmatrix} z_p \\ u_2 \end{bmatrix} = \left(\begin{array}{c|c} A_p & B_p \\ \hline C_{p1} & 0 \\ C_{p2} & 0 \end{array}\right) v_1, \quad u_1 = \left(\begin{array}{c|cc} A_c & B_{c1} & B_{c2} \\ \hline C_c & D_{c1} & D_{c2} \end{array}\right) \begin{bmatrix} v_2 \\ r \end{bmatrix}$$

© ISAROB 2013

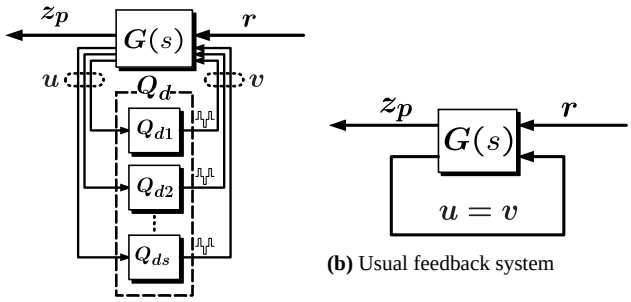

(a) LFT type quantized feedback system with multiple quantizers

(b) Usual feedback system

Fig. 1. Generalized quantized and unquantized systems

where $z_p \in \mathbb{R}^q$, $r \in \mathbb{R}^p$, $u_1 \in \mathbb{R}^{m_1}$, $u_2 \in \mathbb{R}^{m_2}$, $v_1 \in \mathbb{R}^{m_1}$, and $v_2 \in \mathbb{R}^{m_2}$ denote the measured output, the exogenous input, the controller output, the plant measured output, the plant input, and the controller input, respectively. The continuous-valued signals u_1 and u_2 are quantized into the discrete-valued signals v_1 and v_2 because of $v_1 = Q_{d_1}(u_1)$ and $v_2 = Q_{d_2}(u_2)$. For the above systems, define the following vectors: $x_g := [\ x_p^{\mathrm{T}}\ \ x_c^{\mathrm{T}}\ ]^{\mathrm{T}} \in \mathbb{R}^{n_g}(n_g := n_p + n_c)$, $u := [\ u_1^{\mathrm{T}}\ \ u_2^{\mathrm{T}}\ ]^{\mathrm{T}}$, $v := [\ v_1^{\mathrm{T}}\ \ v_2^{\mathrm{T}}\ ]^{\mathrm{T}}$, and matrices:

$$A := \begin{bmatrix} A_p & 0 \\ 0 & A_c \end{bmatrix},\ B_1 := \begin{bmatrix} 0 \\ B_{c2} \end{bmatrix},\ B_2 := \begin{bmatrix} B_p & 0 \\ 0 & B_{c1} \end{bmatrix},$$

$$C_1 := [\ C_{p1}\ \ 0\ ],\ D_{11} := 0,\ C_2 := \begin{bmatrix} 0 & C_c \\ C_{p2} & 0 \end{bmatrix},$$

$$D_{21} := \begin{bmatrix} D_{c2} \\ 0 \end{bmatrix},\ D_{22} := \begin{bmatrix} 0 & D_{c1} \\ 0 & 0 \end{bmatrix},$$

and the quantizer $Q_d = \mathsf{diag}(Q_{d_1}, Q_{d_2})$. In this case, one gets the linear fractional transformation (LFT) type quantized feedback system in **Fig. 1 (a)** where the LTI continuous-time generalized plant $G(s)$ with the state $x_g \in \mathbb{R}^{n_g}$ is represented by

$$\begin{bmatrix} \dot{x}_g \\ z_p \\ y \end{bmatrix} = \begin{bmatrix} A & B_1 & B_2 \\ C_1 & D_{11} & 0 \\ C_2 & D_{21} & D_{22} \end{bmatrix} \begin{bmatrix} x_g \\ r \\ v \end{bmatrix}. \tag{1}$$

As shown above, the LFT formulation in (1) covers the various systems. Then this paper considers the LFT type quantized feedback systems. Also, we assume that the matrix $A + B_2(I - D_{22})^{-1}C_2$ is Hurwitz, that is, the usual feedback system in **Fig. 1 (b)** is stable in the continuous-time domain.

For the system $G(s)$, we define the discrete-valued vector $v := [\ v_1^{\mathrm{T}}, ..., v_s^{\mathrm{T}}\ ]^{\mathrm{T}} \in \mathbb{R}^m$ and the continuous-valued vector $u := [\ u_1^{\mathrm{T}}, ..., u_s^{\mathrm{T}}\ ]^{\mathrm{T}} \in \mathbb{R}^m$, respectively, and consider the dynamic quantizer $v = Q_d(u)$ which consists of the multiple dynamic quantizers $v_i = Q_{di}(u_i)$ $(i = 1, ..., s)$ with the state vector $x_{qi} \in \mathbb{R}^{n_{qi}}$. The case $s > 1$ implies that the multiple dynamic quantizers Q_{di} are distributedly implemented. The sub-quantizer Q_{di} consists of the static quantizer $q_{st} : \mathbb{R}^{m_i} \to d\mathbb{N}^{m_i}$ with the quantization interval $d \in \mathbb{R}_+$,

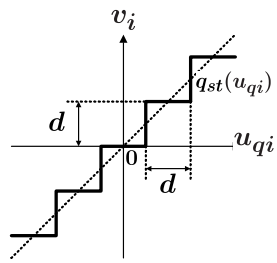

Fig. 2. Midtread type quantization

i.e.,

$$v_i = q_{st}(u_{qi}), \quad u_{qi} := v_{qi} + u_i$$

and the dynamic compensator $Q_i(s)$ given by

$$\begin{bmatrix} \dot{x}_{qi} \\ v_{qi} \end{bmatrix} = \begin{bmatrix} A_{qi} & B_{qi} \\ C_{qi} & 0 \end{bmatrix} \begin{bmatrix} x_{qi} \\ e_{qi} \end{bmatrix}, \quad e_{qi} := v_i - u_i$$

where $v_i \in \mathbb{R}^{m_i}$, $u_i \in \mathbb{R}^{m_i}$, and $v_{qi} \in \mathbb{R}^{m_i}$. For $s = 2$, one gets the i/o type dynamic quantizers. Then the quantizer $Q_d := \mathsf{diag}(Q_{d1}, ..., Q_{ds})$ is realized by the static quantizer $Q_{st} := [q_{st}^{\mathrm{T}}, .., q_{st}^{\mathrm{T}}]^{\mathrm{T}} : \mathbb{R}^m \to d\mathbb{N}^m$, i.e.,

$$v = Q_{st}(u_q), \quad u_q := v_q + u \tag{2}$$

and the compensator $Q(s) := \mathsf{diag}(Q_1(s), ..., Q_s(s))$, i.e.,

$$\begin{bmatrix} \dot{x}_q \\ v_q \end{bmatrix} = \begin{bmatrix} A_q & B_q \\ C_q & 0 \end{bmatrix} \begin{bmatrix} x_q \\ e_q \end{bmatrix}, \tag{3}$$
$$A_q := \mathsf{diag}(A_{q1}, ..., A_{qs}),\ B_q := \mathsf{diag}(B_{q1}, ..., B_{qs}),$$
$$C_q := \mathsf{diag}(C_{q1}, ..., C_{qs})$$

where $x_q := [\ x_{q1}^{\mathrm{T}}, ..., x_{qs}^{\mathrm{T}}\ ]^{\mathrm{T}} \in \mathbb{R}^{n_q}$, $v_q := [\ v_{q1}^{\mathrm{T}}, ..., v_{qs}^{\mathrm{T}}\ ]^{\mathrm{T}} \in \mathbb{R}^m$, $u_q := [\ u_{q1}^{\mathrm{T}}, ..., u_{qs}^{\mathrm{T}}\ ]^{\mathrm{T}} \in \mathbb{R}^m$ and $e_q := [\ e_{q1}^{\mathrm{T}}, ..., e_{qs}^{\mathrm{T}}\ ]^{\mathrm{T}} \in \mathbb{R}^m$. Note that q_{st} is of the nearest-neighbor type toward $-\infty$ with the quantization interval $d \in \mathbb{R}_+$ and the initial state is given by $x_q(0) = 0$ for the drift-free of Q_d[2, 3] such as the midtread type quantizer in **Fig. 2**.

For the LFT system with $G(s)$ and Q_d in **Fig. 1 (a)** with the initial state $x_0 = x_g(0)$ and the exogenous signal $r \in \mathcal{L}_\infty^p$, $z_p(t, x_0, r)$ denotes the output of z_p at the time t. Also, for the system in **Fig. 1 (b)** without Q_d, $z_p^*(t, x_0, r)$ denotes its output at the time t. This paper considers the following cost function:

$$J(Q_d) := \sup_{(x_0, r) \in \mathbb{R}^{n_g} \times \mathcal{L}_\infty^p} z(x_0, r)$$

where

$$z(x_0, r) := \max_i \sup_t |z_{pi}(t, x_0, r) - z_{pi}^*(t, x_0, r)|$$

and z_{pi}, z_{pi}^* denote the ith entry of z_p and z_p^*, respectively.

If the quantizer Q_d minimizes $J(Q_d)$, the system in **Fig. 1 (a)** optimally approximates the usual system in **Fig. 1 (b)** in the sense of the input-output relation. In this case, we can use the existing continuous-time controller design methods for the system in **Fig. 1 (b)**.

Motivated by the above, our objective is to solve the following continuous-time dynamic quantizer synthesis

© ISAROB 2013

problem **(E)**: *For the LFT system composed of (1), (2) and (3) with the initial state $x_0 \in \mathbb{R}^{n_g}$ and the exogenous signal $r \in \mathcal{L}_\infty^p$, suppose that the quantization interval $d \in \mathbb{R}_+$ and the performance level $\gamma \in \mathbb{R}_+$ are given. Characterize a stable continuous-time dynamic quantizer Q_d (i.e., find parameters $(n_{qi}, A_{qi}, B_{qi}, C_{qi})$) achieving $J(Q_d) \le \gamma$.*

3. MAIN RESULT

Define the following matrices:

$$\mathsf{D} := (I - D_{22})^{-1}, \quad \mathsf{C} := \mathsf{D}C_2, \quad \mathsf{A} := A + B_2\mathsf{C},$$
$$\mathsf{B} := B_2\mathsf{D}, \quad \mathcal{A} := \begin{bmatrix} \mathsf{A} & \mathsf{B}C_q \\ 0 & A_q + B_qC_q \end{bmatrix}, \quad \mathcal{B} := \begin{bmatrix} \mathsf{B} \\ B_q \end{bmatrix},$$
$$\mathcal{C} := \begin{bmatrix} C_1 & 0 \end{bmatrix}.$$

For the matrix $\mathsf{B} \in \mathbb{R}^{n_g \times m}$ and $i = 1, ..., s$, $\mathsf{B}_i \in \mathbb{R}^{n_g \times m_i}$ denotes the ith block column of B, i.e., $\mathsf{B} := [\, \mathsf{B}_1, ..., \mathsf{B}_s \,]$.

Assumption 1: For every $i = 1, ..., s$, the matrix $C_1\mathsf{A}^{\tau_i}\mathsf{B}_i$ is full row rank where $\tau_i \in \{0\} \cup \mathbb{N}_+$ is the smallest integer satisfying $C_1\mathsf{A}^{\tau_i}\mathsf{B}_i \neq 0$.

In quantizer analysis, by using our early result [7], we obtain the the optimization problem **(Aop)**:

$$\min_{\mathcal{P}>0, \min_i\{|\mathbf{Re}(2\lambda_i(\mathcal{A}))|\}>\alpha>0, \gamma>0} \gamma \quad \text{s.t.}$$
$$\begin{bmatrix} \mathcal{A}^{\mathrm{T}}\mathcal{P} + \mathcal{P}\mathcal{A} + \alpha\mathcal{P} & \mathcal{P}\mathcal{B} \\ \mathcal{B}^{\mathrm{T}}\mathcal{P} & -\frac{4\alpha}{md^2}I_m \end{bmatrix} \le 0, \tag{4}$$
$$\begin{bmatrix} \mathcal{P} & \mathcal{C}^{\mathrm{T}} \\ \mathcal{C} & \gamma^2 I_q \end{bmatrix} \ge 0. \tag{5}$$

That is, the performance level γ in (5) evaluates the upperbound of the difference between $z_p^*(t, x_0, r)$ and $z_p(t, x_0, r)$ within in invariant set framework, and

$$J(Q_d) \le \gamma$$

holds. Also, the infimum of γ can be expressed by the following lemma [7].

Lemma 1: *Suppose that the quantization interval $d \in \mathbb{R}_+$ is given. Consider the problem* **(Aop)**. *The infimum of γ is given by*

$$\inf \gamma = \inf_\alpha \frac{d\sqrt{m}}{2\sqrt{\alpha}} \sqrt{\lambda_{\max}\mathcal{D}(\alpha)}, \tag{6}$$
$$\mathcal{D}(\alpha) := \int_0^\infty \mathcal{C}e^{(\mathcal{A}+\alpha/2I)t}\mathcal{B}\mathcal{B}^{\mathrm{T}}e^{(\mathcal{A}+\alpha/2I)^{\mathrm{T}}t}\mathcal{C}^{\mathrm{T}}dt,$$
$$\alpha \in (0, \min_i\{|\mathbf{Re}(2\lambda_i(\mathcal{A}))|\}).$$

The problem **(Aop)** suggests that the quantizer synthesis problem **(E)** reduces to the following non-convex optimization problem **(OP)**:

$$\min_{\mathcal{P}>0, A_q, B_q, C_q, \bar{\alpha}>\alpha>0, \gamma>0} \gamma \quad \text{s.t. (4) and (5)}$$

where $\bar{\alpha} := \min_i\{|\mathbf{Re}(2\lambda_i(\mathcal{A}))|\}$. That is, if **(OP)** is feasible, **(E)** is feasible and the obtained quantizer is stable. Under some circumstances, we obtain an closed form solution from (6) as follow.

Theorem 1: *Consider the non-convex optimization problem* **(OP)**. *Suppose that $s > 1$ and Assumption 1 holds. For a given scalar $f \in \mathbb{R}_+$, an optimal solution of $(n_{qi}, A_{qi}, B_{qi}, C_{qi})$ $(i = 1, 2, ..., s)$ and its infimum of $\gamma \in \mathbb{R}_+$ to the problem* **(OP)** *are given by*

$$\begin{cases} n_{qi} = n_g, \quad A_q = \mathsf{A}, \quad B_{qi} = \mathsf{B}_i \\ C_{qi} = -(C_1\mathsf{A}^{\tau_i}\mathsf{B}_i)^\dagger C_1(\mathsf{A} + fI)^{\tau_i+1} \end{cases} \tag{7}$$

for every $i = 1, 2, ..., s$ and

$$\inf \gamma = \frac{d\sqrt{m}}{2\sqrt{\rho}} \| [\, \sigma_{\rho 1} \ \ldots \ \sigma_{\rho i} \ \ldots \ \sigma_{\rho s} \,] \|_2, \tag{8}$$
$$\sigma_{\rho i} := \sqrt{\frac{(2\tau_i)!}{(\tau_i!)^2(2f-\rho)^{2\tau_i+1}}}\, C_1\mathsf{A}^{\tau_i}\mathsf{B}_i,$$
$$\rho = \min_i\{|\mathbf{Re}(2\lambda_i(\mathsf{A}))|, |\mathbf{Re}(2\lambda_i(A_q + B_qC_q))|\}$$

if the matrix $A_{qi} + B_{qi}C_{qi}$ defined in (7) is Hurwitz for every $i = 1, 2, ..., s$.

In this paper, we call the quantizer in (7) the decentralized optimal dynamic quantizer Q_d^{op}. Theorem 1 indicates that Q_d^{op} and its achievable performance are parameterized by the scalar f. Next, this paper considers the relation between the scalar f and the stability of Q_d^{op} for the simple case $q = m$, in addition, presents a tractable adjustable range of f similar to [7]. For the simplicity, we consider the centralized quantizer case $s = 1$ and $\tau_i = \tau$.

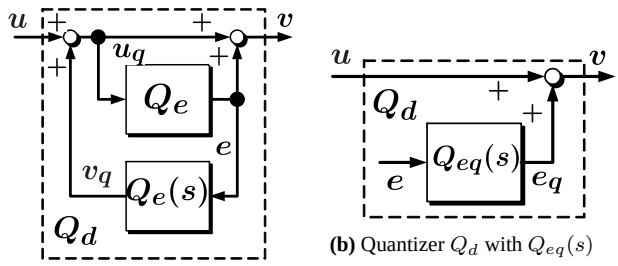

(a) Quantizer Q_d with $Q_e(s)$ **(b)** Quantizer Q_d with $Q_{eq}(s)$

Fig. 3. Equivalent expression of dynamic quantizer Q_d

As shown in **Fig. 3 (a)**, an equivalent expression of the quantizer Q_d is given by the quantization error Q_e and $Q_e(s) := C_q(sI - (A_q + B_qC_q))^{-1}B_q$. The quantizer structure in **Fig. 3 (a)** can be recast as the system with $Q_{eq}(s) := Q_e(s) + I$ in **Fig. 3 (b)** where the signal e is the difference $e := v - u_q$ and $e_q = v_q + e$. For the quantizer Q_d^{op}, then one gets

$$Q_{eq}^{op}(s) := \left(\begin{array}{c|c} \mathsf{A} - \mathsf{B}(C_1\mathsf{A}^\tau\mathsf{B})^{-1}C_1(\mathsf{A} + fI)^{\tau+1} & \mathsf{B} \\ \hline -(C_1\mathsf{A}^\tau\mathsf{B})^{-1}C_1(\mathsf{A} + fI)^{\tau+1} & I \end{array} \right)$$

which is corresponding to the compensator $Q_{eq}(s)$ in **Fig. 3 (b)**. The inverse system of $Q_{eq}^{op}(s)$ is given by

$$\tilde{Q}_{ep}^{op}(s) = \sum_{k=0}^{\infty} \left(\frac{(C_1\mathsf{A}^\tau\mathsf{B})^{-1}C_1(\mathsf{A} + fI)^{\tau+1}\mathsf{A}^k\mathsf{B}}{s^{k+1}} \right) + I$$
$$= (C_1\mathsf{A}^\tau\mathsf{B})^{-1}(s + f)^\tau\mathsf{G}_e(s)$$

where $\mathsf{G}_e(s) := C_1(sI - \mathsf{A})^{-1}\mathsf{B}$. Then we obtain the stability condition of Q_d^{op}.

Theorem 2: *The following statements hold. (i) The transmission poles of $Q_{eq}^{op}(s)$ consist of both "$-f$" and the transmission zeros of $\mathsf{G}_e(s)$. (ii) The optimal dynamic quantizer Q_d^{op} in (7) is stable if and only if the all transmission zeros of $\mathsf{G}_e(s)$ are stable (i.e., the system $G(s)$ is minimum phase).*

© ISAROB 2013

Denote by $\beta_{\max}(\delta_{\max})$ the maximum real part of the stable transmission poles (zeros) for the system $\mathsf{G}_e(s)$. From the statement (i) of Theorem 2, one gets the range of f as follows:

$$f > \min\{|\beta_{\max}|, |\delta_{\max}|\}.$$

Also, the following theorem derived from (6) in Lemma 1 and (8) in Theorem 1 provides an analytical relation between the quantizers Q_d and Q_{st} in the continuous-time domain.

Theorem 3: *Consider the problem* **(OP)** *and denote by γ_{st} and γ_d upper bounds of $J(Q_{st})$ and $J(Q_d)$, respectively. In the case of $n_g = 1$,*

$$\inf \frac{\gamma_d}{\gamma_{st}} = \frac{\sqrt{|\mathsf{A}|}}{\sqrt{f}}, \quad f > |\mathsf{A}| \tag{9}$$

holds.

Since the matrix A is stable, $\mathsf{A} < 0$ holds in (9). Theorem 3 guarantees that the scalar f of the quantizer Q_d improves $J(Q_d)$ compared with the quantizer Q_{st} in terms of the infimum of the upper bound ratio of the cost functions. Then the larger value the scalar f is set to be, the better approximation the quantizer Q_d^{op} achieves between the minimum phase systems in **Figs. 1 (a)** and **(b)**.

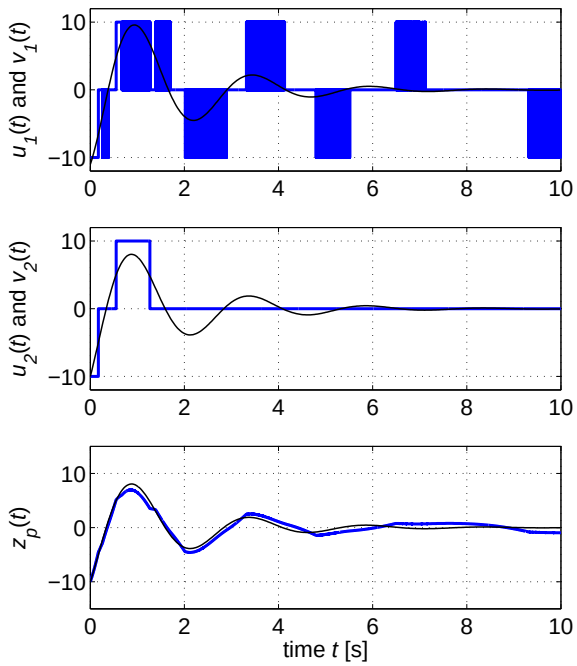

Fig. 4. Time responses with Q_d

Consider the decentralized I/O quantizer system. The plant $P(s)$ is the unstable minimum phase LTI system:

$$\begin{bmatrix} \dot{x}_p \\ u_2 \end{bmatrix} = \left[\begin{array}{cc:c} 0 & 1 & 0 \\ -2 & 1 & -2 \\ \hdashline 4 & 1 & 0 \end{array}\right] \begin{bmatrix} x_p \\ v_1 \end{bmatrix}, \quad z_p = u_2.$$

Its eigenvalues are $0.5 \pm 0.866i$ and its zero is $\{-2\}$. The stabilizing controller $C(s)$ is given by

$$\begin{bmatrix} \dot{x}_c \\ u_1 \end{bmatrix} = \left[\begin{array}{c:c} -3 & 1 \\ \hdashline -1 & 1 \end{array}\right] \begin{bmatrix} x_c \\ v_2 \end{bmatrix}.$$

The resultant zeros of $\mathsf{G}_e(s)$ are -3 and -4. For the quantizer Q_d^{op} in (7), we set $d = 10$ and $f = 10$. The performance $\inf \gamma = 4.23$. **Fig. 4** shows the time responses of $u_1(t)$, $u_2(t)$, $v_1(t)$, $v_2(t)$ and $z_p(t)$ for the dynamic quantizer in Theorem 1 with the initial state $x_g(0) = [\,-4\ 0\ -1\,]^{\mathrm{T}}$. The thin lines and the thick lines illustrate the time responses of the usual feedback system in **Fig. 1 (b)** and the quantized feedback system in **Fig. 1 (a)**, respectively. The controlled output z_p of the dynamic quantizer does not go to zero. However, we see that the controlled output of **Fig. 1 (a)** approximates that of **Fig. 1 (b)** even if the discrete-valued signals $v_1 \in \{-10, 0, 10\}$ and $v_2 \in \{-10, 0, 10\}$ are applied. Not that the larger value of f not only provides the better approximation performance, but also switches the outputs v_1 and v_2, more quickly.

4. CONCLUSION

Focusing on continuous-time LFT type quantized feedback systems, we have proposed the continuous-time dynamic quantizer analysis and synthesis conditions. This paper has concentrated on the case of minimum phase systems, clarified that optimal dynamic quantizers and their performance are parameterized by the design parameter. Also, an analytical relation between the static and dynamic quantizers has been presented. Finally, it has been pointed out that the proposed method is helpful through the numerical example.

REFERENCES

[1] P. J. Antsaklis and J. Baillieul, Guest Editors (2007), Special Issue on the Technology of Networked Control Systems, Proc. IEEE, Vol. 95, No. 1.

[2] S. Azuma and T. Sugie (2008), Optimal dynamic quantizer for discrete-valued input control, Automatica, Vol. 44, No. 12, pp. 396–406.

[3] S. Azuma and T. Sugie (2008), Synthesis of optimal dynamic quantizers for discrete-valued input control, IEEE Trans. Auto. Contr., Vol. 53, No. 9, pp. 2064–2075.

[4] K. Sawada and S. Shin (2011), Synthesis of dynamic quantizers for quantized feedback systems within invariant set analysis framework, Proc. of ACC, pp. 1662–1667.

[5] H. Okajima, K. Sawada, N. Matsunaga, and Y. Minami (2011), Dynamic quantizer design for MIMO systems based on communication rate constraint, Proc. of IECON, pp. 2497–2502.

[6] K. Matsukawa, Y. Mitani, M. Takayama, K. Obata, S. Dosho, and A. Matsuzawa (2010), A Fifth-Order Continuous-Time Delta-Sigma Modulator With Single-Opamp Resonator, IEEE J. Solid-State Circuits, Vol. 45, No. 4, pp. 697-706.

[7] K. Sawada and S. Shin (2012), Synthesis of continuous-time dynamic quantizers for quantized feedback systems, Proc. of 4th IFAC Conference on Analysis and Design of Hybrid Systems (ADHS 12), pp. 248–253.

© ISAROB 2013

The Eighteenth International Symposium on Artificial Life and Robotics 2013 (AROB 18th '13),
Daejeon Convention Center, Daejeon, Korea, January 30-February 1, 2013

Optimal scheduling of automatic guided vehicle transportation system based on MLD system modeling

Kenji Sawada[1] and Seiichi Shin[1]

[1]The University of Electro-Communications, Japan
(Tel: 81-42-443-5253, Fax: 81-42-443-5253)

[1]{knj.sawada, seiich.shin}@uec.ac.jp

Abstract: This paper proposes an optimal scheduling method of transportation systems in semiconductor manufacturing within MLD (mixed logical dynamical) modeling framework. We consider an optimal scheduling problem of AGV (automatic guided vehicle) system transfer problem, which is to control the AGV congestion around the meeting points and the dividing points of the transportation road in this paper. The problem is recast as an ILP (Integer Linear Programming) problem within model predictive control framework.

Keywords: automatic guided vehicle, MLD modeling, scheduling

1 INTRODUCTION

Recently, there is a growing need to increase productivity in semiconductor manufacturing with the improvement of the producing technology. In semiconductor fabrication (FAB) in **Fig. 1**, a few hundred of Automatic Guided Vehicles (AGVs) transpose Front Open Unified Pods (FOUPs) that store semiconductor wafers [1].

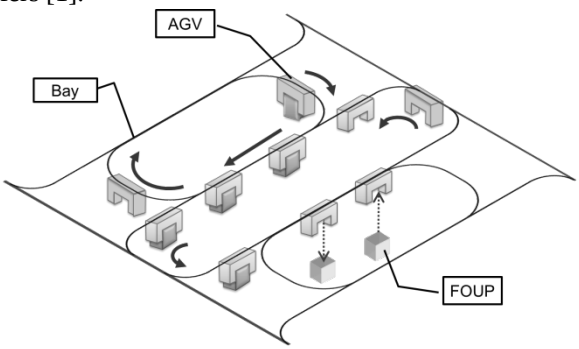

Fig. 1. Semiconductor fabrication

Nowadays, the size of the wafers will be getting lager (from 300mm to 450mm) and the number of the vehicles in a factory will be increasing. This implies that each of the AGVs must follow the vehicle in front of one closely and transpose heavy wafers within a set time. In particular, it is important to consider the AGV congestion on the transportation roads which consist of inter-bays and intra-bays since the congestion results in the production delay. The congestion tends to occur around the junctions between the bays and/or the transfer equipment of the FOUPs. In particular, this paper focuses on an optimal scheduling problem of the meeting points and the dividing points of the FAB junctions, while the existing results [2-4] tend to consider scheduling problems that focus on all areas of FAB.

The typical scheduling process on the junctions is as follows: (i) The prioritized AGV which goes through the meeting point without stopping is automatically determined by the distance from the meeting point. (ii) When some of the other AGVs around the meeting point come close to colliding with the prioritized one, they continuously slow down or stop according to their collision avoidance systems. Such a scheduling procedure does not previously consider both the positional relation and the number of the vehicles which may collide, and/or the influence of the AGVs' stopping and slowing down on other AGVs except the meeting point area. These factors can lead to the AGV congestion as shown in **Fig. 2**. Also, it is important to consider the behaviors of the AGVs around the dividing point area in front of the meeting point area. If we know in advance that some AGVs go to the parking area through the dividing point, such the information makes it easier to maximize the number of the AGVs come out from the meeting point area.

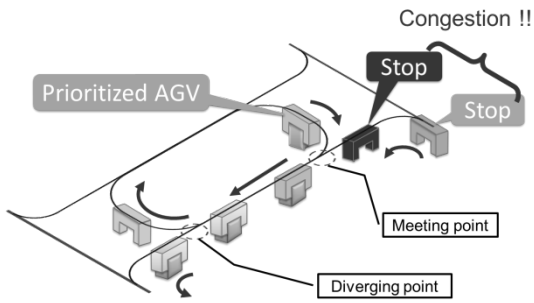

Fig. 2. Congestion on junction

Motivated by the above, our early work considers the AGV congestion problem of the meeting point based on the

© ISAROB 2013

state space realization modeling [5] and the model predictive control framework. As an extension of our existing result [5], this paper proposes a mixed logical dynamical (MLD) modeling [6-8] of the meeting and the dividing points considering the positional relation (the area of the bay model), the number of the vehicles, and the time of the AGV congestion. By using the model, in addition, this paper considers the optimal scheduling problem considering the AGV congestion within model predictive control framework. In this case, the problem is recast as an Integer Programming.

Notation: The set of $n \times m$ real (integer) matrices is denoted by $\mathbf{R}^{n\times m}$ ($\mathbf{N}^{n\times m}$). The set of $n \times n$ diagonal matrices with the diagonals being 1 or 0 is denoted by $\mathbf{D}^n$. $O_{n\times m}$, I_n, $\mathbf{0}_m$ and $\mathbf{1}_m$ (or for simplicity of notation, O, I, $\mathbf{0}$ and $\mathbf{1}$) denote the $n \times m$ zero matrix, the $n \times n$ identity matrix, the $n \times 1$ vector whose all elements are zero and the $n \times 1$ vector whose all elements are one, respectively. For a matrix M, M^{T} denotes its transpose. For a vector x, x_i is the i-th entry of x. $\mathrm{diag}(D_1, \dots, D_n)$ denotes the block diagonal matrix of matrices $D_1, \dots, D_n$. $\{0,1\}^n$ denotes the set of n-dimensional vectors, which consists of elements 0 and 1.

2 PROBLEM FORMUILATION

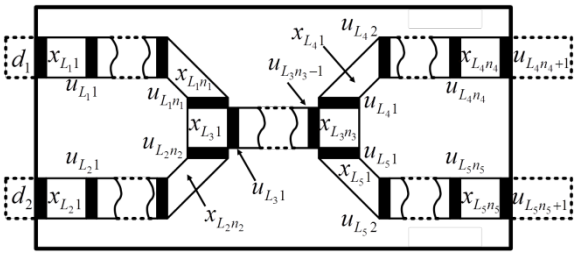

Fig. 3. Bay model of meeting and dividing points

Fig. 3 shows a bay model of the meeting and dividing points. The area surround by the black border is the area of the bay model that we focus on. The bay is divided into several parts $x_{L_i j}$ by the gates $u_{L_i j}$ and d_i similar to our earlier work. Each AGV behavior is expressed by the gate opening/closing. In particular, the gate d_i implies the behavior of the AGVs that come in from the outside.

We define the notations. The bay model consists of 5 links L_i $(i = 1, \dots, 5)$ as shown in **Fig. 3**. $x_{L_i j}(t)$ indicates the number of the AGVs on the corresponding j-th area of the link L_i at the t-th time. For example, if one AGV moves on the 4-th area of the link L_2 at the 2-nd time, $x_{L_2 4}(2) = 1$ holds. $u_{L_i j}(t) = 1$ or 0 indicates the corresponding j-th gate opening or closing of the link L_i at the t-th time, respectively. For the exogenous gate $d_i(t) \in \{0,1\}$, $d_i(t) = 1$ indicates that one AGV comes in through the corresponding i-th exogenous gate at the t-th time. Denote by $x_{L_i}(t) \in \mathbf{R}^{n_i}$, $u_{L_i}(t) \in \mathbf{R}^{m_i}$ and $d(t) \in \mathbf{R}^2$ the vectors of which the i-th entries are $x_{L_i j}(t)$, $u_{L_i j}(t)$ and $d_i(t)$, respectively.

According to the above notations, the bay model of the meeting and dividing points can be expressed by the state space realization. First, the link L_1 and L_2 are given by

$$x_{L_i}(t+1) = A_{L_i} x_{L_i}(t) + B_{1L_i} u_{L_i}(t) + B_{2L_i}\, d_i(t)$$

where $i = 1,2$ and the matrices are given by

$$A_{L_i} := I_{n_i},\ B_{1L_i} := \begin{bmatrix} -1 & 0 & 0 & \cdots & 0 \\ 1 & -1 & 0 & \ddots & \vdots \\ 0 & 1 & -1 & \dots & \vdots \\ \vdots & \ddots & \ddots & \ddots & 0 \\ 0 & \cdots & 0 & 1 & -1 \end{bmatrix} \in \mathbf{R}^{n_i \times n_i},$$

$$B_{2L_i} := [1 \quad 0 \quad \cdots \quad 0]^{\mathrm{T}} \in \mathbf{R}^{n_i}.$$

Second, the link L_3 is given by

$$x_{L_3}(t+1) = A_{L_3} x_{L_3}(t) + \sum_{i=1}^{2} B_{13L_i} u_{L_i}(t) + B_{1L_3} u_{L_3}(t) + \sum_{i=4}^{5} B_{13L_i} u_{L_i}(t)$$

where the matrices are given by

$$A_{L_3} := I_{n_3},\ B_{1L_3} := \begin{bmatrix} -1 & 0 & \cdots & 0 \\ 1 & -1 & \ddots & \vdots \\ 0 & 1 & \ddots & \vdots \\ \vdots & \ddots & \ddots & -1 \\ 0 & \cdots & 0 & 1 \end{bmatrix} \in \mathbf{R}^{n_3 \times (n_3 - 1)},$$

$$B_{13L_i} := \begin{cases} \begin{bmatrix} 0 & \cdots & 0 & 1 \\ 0 & 0 & \cdots & 0 \\ \vdots & \ddots & \ddots & \vdots \\ 0 & \ddots & 0 & 1 \end{bmatrix} \in \mathbf{R}^{n_3 \times n_i}, & i = 1,2, \\ \begin{bmatrix} 0 & \cdots & 0 & 0 \\ \vdots & 0 & \cdots & 0 \\ 0 & \ddots & \ddots & \vdots \\ -1 & 0 & \cdots & 0 \end{bmatrix} \in \mathbf{R}^{n_3 \times (n_i + 1)}, & i = 4,5. \end{cases}$$

Finally, the link L_4 and L_5 are given by

$$x_{L_i}(t+1) = A_{L_i} x_{L_i}(t) + B_{1L_i} u_{L_i}(t)$$

where $i = 4,5$ and the matrices are given by

$$A_{L_i} := I_{n_i},\ B_{1L_i} := \begin{bmatrix} 1 & -1 & 0 & \cdots & 0 \\ 0 & 1 & -1 & \ddots & \vdots \\ \vdots & \ddots & \ddots & \ddots & 0 \\ 0 & \cdots & 0 & 1 & -1 \end{bmatrix} \in \mathbf{R}^{n_i \times (n_i + 1)}.$$

By defining the vectors as follows:

$$x(t) := \left[x_{L_1}(t)^{\mathrm{T}}\, x_{L_2}(t)^{\mathrm{T}}\, x_{L_3}(t)^{\mathrm{T}}\, x_{L_4}(t)^{\mathrm{T}}\, x_{L_5}(t)^{\mathrm{T}}\right]^{\mathrm{T}},$$

$$u(t) := \left[u_{L_1}(t)^{\mathrm{T}}\, u_{L_2}(t)^{\mathrm{T}}\, u_{L_3}(t)^{\mathrm{T}}\, u_4(t)^{\mathrm{T}}\, u_{L_5}(t)^{\mathrm{T}}\right]^{\mathrm{T}},$$

we obtain the state space realization of the bay model:

$$x(t+1) = Ax(t) + B_1 u(t) + B_2 d(t) \tag{1}$$

where the matrices are given by $n \equiv \sum_{i=1}^{5} n_i,\ A \coloneqq I_n$,

$$B_1 \coloneqq \begin{bmatrix} B_{1L_1} & O & O & O & O \\ O & B_{1L_2} & O & O & O \\ B_{13L_1} & B_{13L_2} & B_{1L_3} & B_{13L_4} & B_{13L_5} \\ O & O & O & B_{1L_4} & O \\ O & O & O & O & B_{1L_5} \end{bmatrix} \in \mathbf{R}^{n\times(n+1)},$$

$$B_2 \coloneqq \begin{bmatrix} B_{2L_1}^{\mathrm{T}} & O & O \\ O & B_{2L_2}^{\mathrm{T}} & O \end{bmatrix}^{\mathrm{T}} \in \mathbf{R}^{n\times 2}.$$

3 SCHEDULING ALGORITHM

3.1 Modeling of AGV scheduling

By using the bay model (4), this paper considers the scheduling problem **(I)**: *Suppose that the area of the bay model, the number of the vehicles, and the time of the AGV congestion are given. Formulate a scheduling algorithm (i) maximizing the number of the AGVs come out from the area and (ii) avoiding the AGV collision.*

Denote by M the time of the AGV congestion (the horizon length). To achieve the property (i), first, we consider the following cost function:

$$\max_{u(0),\dots,u(M-1)} J \ \text{ s.t. } J := q_M^{\mathrm{T}} x(M) + \sum_{t=0}^{M-1} \left(q^{\mathrm{T}} x(t) + r^{\mathrm{T}} u(t)\right),$$

$$q_{\mathrm{M}} \in \mathbf{R}^n,\ q \in \mathbf{R}^n \ \text{ and } \ r \in \mathbf{R}^{n+1}. \quad (2)$$

We consider the "throughput maximization" of the links 4 and 5. In this case, the throughputs of the links 4 and 5 are the opening and closing times of $u_{L_4 n_4+1}(t)$ and $u_{L_5 n_5+1}(t)$, the weight vector r is given by

$$r \coloneqq \left[0 \cdots 0\ \ q_{L_4}^{\mathrm{T}}\ \ q_{L_5}^{\mathrm{T}}\right]^{\mathrm{T}},\quad q_{L_i} \coloneqq [0 \cdots 0\ \ 1]^{\mathrm{T}} \in \mathbf{R}^{n_i+1}.$$

We denote by $\lambda_i^{d_4} \in \mathbf{R}$ or $\lambda_i^{d_5} \in \mathbf{R}$ the distance between x_i $(i \in \{1, n\})$ and $x_{L_4 n_4}$ or $x_{L_5 n_5}$, respectively. In this case, the sum of the distances from $x_{L_4 n_4}$ or $x_{L_5 n_5}$ to any vehicles in the bay model at the *t*-th time (we denote it $d_s(t)$) is expressed by

$$d_s(t) = \sum_{j}^{2} \Lambda_j^{\mathrm{T}} x(t),\quad \Lambda_j \coloneqq \left[\lambda_1^{d_j} \cdots \lambda_n^{d_j}\right]^{\mathrm{T}} \in \mathbf{R}^n.$$

If $\sum_{t=0}^{M} d_s(t)$ is minimized, the throughput within the time $t \in [0, M]$ of the bay also may increase. Then, we set

$$q = q_M = -(\Lambda_1 + \Lambda_2).$$

Also, we consider the throughput difference $\theta \in \mathbf{R}$ between the links 4 and 5, which is expressed by

$$-\theta \le g_\theta^{\mathrm{T}} u(t) \le \theta, \quad (3)$$

$$g_\theta \coloneqq \left[\mathbf{0}^{\mathrm{T}}\quad q_{L_4}^{\mathrm{T}}\quad -q_{L_5}^{\mathrm{T}}\right]^{\mathrm{T}} \in \mathbf{R}^{n+1}.$$

To achieve the property (ii), next we consider the following rules.

(a) Capacity of each area: For the areas $x_{L_i j}(t)$ $(i = 1, \dots, 5, j = n_1, \dots, n_5)$, each capacity is set to be up to one AGV. This rule is expressed by the constraint:

$$\mathbf{0} \le x(t) \le \mathbf{1}. \quad (4)$$

(b) Meeting and dividing points: To avoid the collision at the meeting of two gates $u_{L_1 n_1}(t)$ and $u_{L_2 n_2}(t)$, we consider the rule that does not allow the two gates to open at the same time. Also, we consider the rule that does not allow the two gates $u_{L_4 1}(t)$and $u_{L_5 1}(t)$ of the dividing point to open at the same time. These rules are given by the constraint:

$$\mathbf{0} \le G_b u(t) \le \mathbf{1}, \quad (5)$$

$$G_b \coloneqq \begin{bmatrix} g_{bL_1}^{\mathrm{T}} & g_{bL_2}^{\mathrm{T}} & O & O & O \\ O & O & O & g_{bL_4}^{\mathrm{T}} & g_{bL_5}^{\mathrm{T}} \end{bmatrix} \in \mathbf{R}^{2\times(n+1)},$$

$$g_{bL_i} \coloneqq [0\ \ \cdots\ \ 0\ \ 1]^{\mathrm{T}} \in \mathbf{R}^{n_i},\ \ i = 1,2,$$

$$g_{bL_i} \coloneqq [1\ \ 0\ \ \cdots\ \ 0]^{\mathrm{T}} \in \mathbf{R}^{n_i+1},\ \ i = 4,5.$$

(c) Speed condition: The acceleration of AGV around the meeting point can lead to the collision. Then we consider the logic:

$$u_i(t) = 1 \to x_i(t) = 1,\ \ i \in \left\{1, \dots, \sum_{i=1}^{3} n_i - 1\right\},$$

$$u_{L_4 1}(t) + u_{L_5 1}(t) = 1 \to x_{L_3 n_3}(t) = 1,$$

$$u_{L_i j+1}(t) = 1 \to x_{L_i j}(t) = 1, i \in \{1, \dots, n_i\}, j \in \{4,5\}.$$

This logic indicates that an AGV does not go through more than two gates on the corresponding areas at a time. By using the lemma in [6-8], the above logic can be expressed by the inequality:

$$G_{cu} u(t) \le\ G_{cx} x(t), \quad (6)$$

$$G_{cu} \coloneqq \begin{bmatrix} G_{cL} & \mathbf{0} & O & \mathbf{0} & O \\ O & 1 & O & 1 & O \\ O & \mathbf{0} & G_{cL_4} & \mathbf{0} & O \\ O & \mathbf{0} & O & \mathbf{0} & G_{2cL_5} \end{bmatrix},$$

$$G_{cL} \coloneqq \mathrm{diag}\left(G_{cL_1}, G_{cL_2}, G_{cuL_3}\right),\ \ G_{cuL_3} \in \mathbf{D}^{n_3-1},$$

$$G_{cx} \coloneqq \mathrm{diag}\left(G_{cL_1}, G_{cL_2}, G_{cxL_3}, G_{cL_4}, G_{cL_5}\right),$$

$$G_{cL_i} \in \mathbf{D}^{n_i},\ \ i \in \{1,2,4,5\},\ \ G_{cxL_3} \in \mathbf{D}^{n_3}.$$

If G_{cL_i}, G_{cuL_3}, G_{cxL_3} are set to be the identity matrix, the all areas does not allow the AGVs to speed up.

Therefore, the bay model with the control rules **(a)-(c)** can be expressed by the pair of the linear state space system (1) and the linear inequalities (3)-(6). We consider the

initial time t=0. In this case, the problem (I) is recast as the following problem **(II)**: *Suppose that the initial position* $x(0) := x_0$ *and the sequence* $d(0), d(1), \dots, d(M-1)$ *of the AGVs which come in are given. Find* $u(0), u(1), \dots, u(M-1)$ *maximizing the cost function (2) for the bay model with the control rules realized by*

$$\begin{cases} x(t+1) = Ax(t) + B_1 u(t) + B_2 d(t) \\ \quad Cx(t) + Du(t) \le E \end{cases}, \tag{7}$$

$$C := \begin{bmatrix} 0 \\ 0 \\ I \\ -I \\ \mathbf{0} \\ \mathbf{0} \\ -G_{cx} \end{bmatrix}, \quad D := \begin{bmatrix} g_\theta^{\mathrm{T}} \\ -g_\theta^{\mathrm{T}} \\ O \\ O \\ G_b \\ -G_b \\ G_{cu} \end{bmatrix}, \quad F := \begin{bmatrix} \theta \\ \theta \\ \mathbf{1} \\ \mathbf{0} \\ \mathbf{1} \\ \mathbf{0} \\ O \end{bmatrix}.$$

3.2 ILP based scheduling

In this subsection, we reduce the problem (II) to an ILP problem by using the model predictive control technique in [6] similar to our early work [5]. For the time M, we define vectors as follows:

$$x_M(t) := [x(t)^{\mathrm{T}}\ x(t+1)^{\mathrm{T}} \cdots\ x(t+M)^{\mathrm{T}}]^{\mathrm{T}},$$

$$u_M(t) := [u(t)^{\mathrm{T}}\ u(t+1)^{\mathrm{T}} \cdots\ u(t+M-1)^{\mathrm{T}}]^{\mathrm{T}},$$

$$d_M(t) := [d(t)^{\mathrm{T}}\ d(t+1)^{\mathrm{T}} \cdots\ d(t+M-1)^{\mathrm{T}}]^{\mathrm{T}}.$$

In this case, the cost function can be recast as

$$J = Q_M x_M(t) + R_M u_M(t) \tag{8}$$

and $x_M(t)$ is given by

$$x_M(t) = A_M x(t) + B_{M_1} u_M(t) + B_{M_2} d_M(t)$$

where the matrices are defined by

$$A_M := \begin{bmatrix} I \\ A \\ A^2 \\ \vdots \\ A^M \end{bmatrix}, \quad B_{M_i} := \begin{bmatrix} O & O & \cdots & O \\ B_i & O & \cdots & O \\ AB_i & B_i & \ddots & \vdots \\ \vdots & \ddots & \ddots & O \\ A^{M-1}B_i & \cdots & AB_i & B_i \end{bmatrix},$$

$$Q_M := [q^{\mathrm{T}} \quad \cdots \quad q^{\mathrm{T}} \quad q_M^{\mathrm{T}}], \quad R_M := [r^{\mathrm{T}} \quad \cdots \quad r^{\mathrm{T}}].$$

Also, the inequality of (7) can be also rewritten as

$$C_M x_M(t) + D_M u_M(t) \le E_M \tag{9}$$

where the matrices are defined by

$$C_M := [\mathrm{diag}(C, \dots, C) \quad O], \quad D_M := \mathrm{diag}(D, \dots, D),$$

$$E_M := [E^{\mathrm{T}} \quad \cdots \quad E^{\mathrm{T}}]^{\mathrm{T}}.$$

By using (8) and (9), we see that the following theorem holds of the problem **(II).**

Theorem 1: *The problem* **(II)** *is equivalent to the following optimization problem* **(III)***:*

given x_0 and $d_{M_{0_M}}$

find $u_{M_0} \in \{0,1\}^{nM}$

$$\max \quad Q_M B_{M_1} u_{M_0} + Q_M (A_M x_0 + B_{M_2} d_{M_0})$$

$$\text{subject to} \quad (C_M B_{M_1} + D_M) u_{M_0} \le E_M - C_M (A_M x_0 + B_{M_2} d_M_0)$$

where the vectors are defined by

$$u_{M_0} := [u(0)^{\mathrm{T}}\ u(1)^{\mathrm{T}} \cdots\ u(M-1)^{\mathrm{T}}]^{\mathrm{T}},$$

$$d_{M_0} := [d(0)^{\mathrm{T}}\ d(1)^{\mathrm{T}} \cdots\ d(M-1)^{\mathrm{T}}]^{\mathrm{T}}.$$

This problem can be solved by the appropriate solvers such as Optimization toolbox of MATLAB in [9] and/or ILOG CPLEX in [10] because of ILP framework. Numerical examples will be shown in the conference room.

4 CONCLUSION

This paper has proposed a dynamic modeling of transportation systems in semiconductor manufacturing. Utilizing our modeling method, we have considered an optimal scheduling problem focusing on the AGV congestion at the meeting point of the transportation road junctions. As a result, the problem can be recast as an ILP problem within model predictive control framework.

REFERENCES

[1] K. Gartland (1999), Automated Material handling system (AMHS) framework use requirements documen t version 1.0, International SEMATECH, Technol. Trans fer #99073793A-TR

[2] G. K. Agrawal and S. Heragu (2006), A survey of automated material handling systems in 300-mm se miconductor fabs, IEEE trans. Semiconductor Manufac turing, 19(1), pp.112-119

[3] F. Kato and S. Shin (2010), Multistep optimal sc heduling of automated guided vehicles in a semiconduc tor fabrication, Proc. of SICE Annual Conference in Ta iwan, pp.985-989

[4] T. Nishi and R. Maeno (2010), Petri Net Decom position Approach to Optimization of Route Planning P roblems for AGV Systems, IEEE Trans. Aut. Sci. Eng., 7(3), pp.523-537

[5] K. Sawada, S. Shin, K. Kumagai and H. Yoneda (2011), Dynamic modeling for optimal scheduling of automatic guided vehicle system, Proc. of SICE Annua l Conference, pp.580-583

[6] A. Bemporad and M. Morari (1999), Control of systems integrating logic, dynamics, and constraints, Au tomatica, 35(3), pp.407-427

[7] T. M. Cavalier, P. M. Pardalos, and A. L. Soyst er (1990), Modeling and integer programming techniqu es applied to propositional calculus, Computer & Opera tions Research, 17(2), pp.561-570

[8] H. P. Williams (1999), Model building in mathe matical programming, 4th ed., John Willey&Sons. Ltd

[9] http://www.mathworks.com/

[10] http://www-01.ibm.com/software/integration/optimi zation/cplex-optimizer/

The Eighteenth International Symposium on Artificial Life and Robotics 2013 (AROB 18th '13),
Daejeon Convention Center, Daejeon, Korea, January 30-February 1, 2013

Direct Multivariable PI Controller Tuning from Closed-Loop Response Data

Yoshihiro Matsui[1], Hideki Ayano[1], and Kazushi Nakano[2]

[1]Tokyo National College of Technology, Japan
[2]The University of Electro-Communications, Japan
(Tel/Fax: +81-42-668-5173)

[1]matsui@tokyo-ct.ac.jp

Abstract: This paper proposes a PI controller tuning method for multivariable plants. The method requires only one set of the input-output transient data of the plant under closed-loop operation to tune the controller. The data is used to obtain an appropriate controller parameter by solving a model matching problem of FRIT (Fictitious Reference Iterative Tuning) in time domain, and the data is also used in frequency domain to confirm if the parameter tuned by FRIT is stable and if the model matching is achieved. The method is applied to a non-interacting control of a gas turbine engine and its effectiveness is shown through simulations.

Keywords: CMA-ES, data driven controller tuning, FRIT, non-interacting control

1 INTRODUCTION

In recent years, in order to save the time and the cost to tune controller parameters for industrial systems, some direct controller parameter tuning methods from the transient data of the plant under closed-loop operation without modeling the plant have been proposed. The FRIT (Fictitious Reference Iterative Tuning) proposed by Souma et al [1] is one of those methods and is expected to be applied to some practical applications. However the FRIT does not show how to specify the reference model for the model matching to tune controller, and the stability of the parameter tuned by the FRIT is no clear. This paper shows how to resolve the problems using the information of the data in frequency domain. The method is applied to a controller tuning for a multivariable plant.

2 Controller tuning for multivariable plant

2.1 Problem setting

This paper deals with the closed-loop system for multivariable plant shown by **Fig.1**. The system consists of a plant given by a $n \times n$ transfer function matrix $\boldsymbol{P}(s)$ and a controller given by a $n \times n$ controller matrix $\boldsymbol{K}(\boldsymbol{\rho}, s)$ with the controller parameter $\boldsymbol{\rho}$. And $\boldsymbol{r}$, $\boldsymbol{e}$, $\boldsymbol{n}$, $\boldsymbol{u}$ and $\boldsymbol{y}$ are the reference vector, the error vector, the observation noise vector, the input and the output vectors of the plant, respectively. In order to make the explanation easier, the closed-loop system for a 2-input 2-output plant shown by **Fig. 2** is used in the following.

The controllers of the system are assumed to be PI

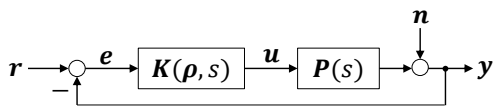

Fig. 1. Closed-loop system for multivariable plant

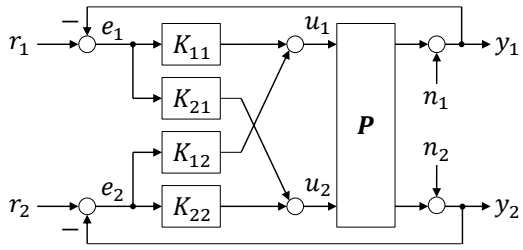

Fig. 2. Closed-loop system for 2-input 2-output plant

controllers given by (1)~(4).

$$K_{11}(s) = k_{11}\frac{\tau_{11}s + 1}{\tau_{11}s} \tag{1}$$

$$K_{12}(s) = k_{12}\frac{\tau_{12}s + 1}{\tau_{12}s} \tag{2}$$

$$K_{21}(s) = k_{21}\frac{\tau_{21}s + 1}{\tau_{21}s} \tag{3}$$

$$K_{22}(s) = k_{22}\frac{\tau_{22}s + 1}{\tau_{22}s} \tag{4}$$

The controller matrix consists of (1)~(4) is given by

$$\boldsymbol{K}(\boldsymbol{\rho}, s) = \begin{pmatrix} K_{11}(s) & K_{12}(s) \\ K_{21}(s) & K_{22}(s) \end{pmatrix}. \tag{5}$$

© ISAROB 2013

The proportional gains and the integral time constants of the PI controllers are defined as the controller parameter $\boldsymbol{\rho}$ given by

$$\boldsymbol{\rho} = (k_{11}, k_{21}, k_{12}, k_{22}, \tau_{11}, \tau_{21}, \tau_{12}, \tau_{22}). \quad (6)$$

The goal of this problem is to find the controller parameter such that a non-interacting control with stability is achieved. To achieve this, the loop transfer function matrix $\boldsymbol{P}(s)\boldsymbol{K}(\boldsymbol{\rho}, s)$ must be a diagonal matrix for non-interacting control and its diagonal elements must have appropriate gain crossover frequencies to satisfy the Nyquist stable criterion. Let us assume $\boldsymbol{L}^*(s)$ given by (7) to be one of such the loop transfer function matrix.

$$\boldsymbol{L}^*(s) = \mathrm{diag}[L_{11}^*(s), L_{22}^*(s)] \quad (7)$$

If $\boldsymbol{P}(s)\boldsymbol{K}(\boldsymbol{\rho}, s)$ becomes $\boldsymbol{L}^*(s)$ by $\boldsymbol{\rho} = \boldsymbol{\rho}^*$, the transfer function matrix from $\boldsymbol{r}$ to $\boldsymbol{y}$ of the closed-loop system is

$$\boldsymbol{T}^*(s) = \mathrm{diag}[T_{11}^*(s), T_{22}^*(s)]\,, \quad (8)$$

where

$$T_{11}^*(s) = \frac{L_{11}^*(s)}{1 + L_{11}^*(s)} \quad (9)$$

and

$$T_{22}^*(s) = \frac{L_{22}^*(s)}{1 + L_{22}^*(s)}. \quad (10)$$

Therefore, the solution of this problem is to find $\boldsymbol{\rho}^*$ such that $\boldsymbol{P}(s)\boldsymbol{K}(\boldsymbol{\rho}^*, s)$ is as similar to $\boldsymbol{L}^*(s)$ as possible.

2.2 Controller tuning by FRIT

In order to find $\boldsymbol{\rho}^*$, the FRIT is employed. The FRIT requires only one set of input-output transient data of the plant under closed-loop operation. The fictitious reference $\tilde{\boldsymbol{r}}(t) = (\tilde{r}_1(t), \tilde{r}_2(t))^T$ given by (11) is used to find $\boldsymbol{\rho}^*$ without additional experiments.

$$\tilde{\boldsymbol{r}}(t) = \tilde{\boldsymbol{e}}(t) + \boldsymbol{y}_0(t), \quad (11)$$

where $\tilde{\boldsymbol{e}}(t) = (\tilde{e}_1(t), \tilde{e}_2(t))^T$ is the fictitious error and given by

$$\tilde{\boldsymbol{e}}(t) = \boldsymbol{K}^{-1}(\boldsymbol{\rho}, t) * \boldsymbol{u}_0(t)\,. \quad (12)$$

$\boldsymbol{K}^{-1}(\boldsymbol{\rho}, t)$ shows the impulse response of the inverse matrix of the controller transfer function matrix $\boldsymbol{K}(\boldsymbol{\rho}, s)$. As (11) and (12) show, the fictitious reference $\tilde{\boldsymbol{r}}(t)$ and the fictitious error $\tilde{\boldsymbol{e}}(t)$ can be obtained only from the input data $\boldsymbol{u}_0(t) = (u_{10}(t), u_{20}(t))^T$ and the output data $\boldsymbol{y}_0(t) = (y_{10}(t), y_{20}(t))^T$ of the plant in the closed-loop system with the initial controller parameter $\boldsymbol{\rho}_0$.

The parameter $\boldsymbol{\rho}^*$ which makes the transfer function matrix from $\boldsymbol{r}$ to $\boldsymbol{y}$ of the closed-loop system be similar to $\boldsymbol{T}^*(s)$ can be obtained by (13) and (14) using some non-linear optimization methods.

$$\boldsymbol{\rho}^* = \arg\min_{\boldsymbol{\rho}} \sum_{t}^{N-1} \boldsymbol{\varepsilon}^T(\boldsymbol{\rho}, t)\, \boldsymbol{\varepsilon}(\boldsymbol{\rho}, t) \quad (13)$$

$$\boldsymbol{\varepsilon}(\boldsymbol{\rho}, t) = \boldsymbol{W}(t)\{\boldsymbol{y}_0(t) - \boldsymbol{T}^*(t) * \tilde{\boldsymbol{r}}(t)\} \quad (14)$$

Here, N is the data length of the input-output data, $\boldsymbol{W}(s)$ is a weighting function diagonal matrix which specifies the frequency band to emphasis the error vector of the model matching $\boldsymbol{y}_0(t) - \boldsymbol{T}^*(t) * \tilde{\boldsymbol{r}}(t)$ for searching $\boldsymbol{\rho}^*$, and $\boldsymbol{W}(t)$ and $\boldsymbol{T}^*(t)$ are the impulse responses of $\boldsymbol{W}(s)$ and $\boldsymbol{T}^*(s)$, respectively.

2.3 Confirmation in frequency domain

It is difficult to specify $\boldsymbol{T}^*(s)$ or $\boldsymbol{L}^*(s)$ for unknown $\boldsymbol{P}(s)$. Therefore the information in frequency domain of $\boldsymbol{u}_0(t)$ and $\boldsymbol{y}_0(t)$ is also used.

When $\boldsymbol{u}(t) = \boldsymbol{u}_0(t)$ and $\boldsymbol{y}(t) = \boldsymbol{y}_0(t)$ and $\boldsymbol{n}$=**0** in **Fig.1**, (15) holds in frequency domain.

$$\begin{aligned} \boldsymbol{y}_0(j\omega) &= \boldsymbol{P}(j\omega)\boldsymbol{u}_0(j\omega) \\ &= \boldsymbol{L}(\boldsymbol{\rho}, j\omega)\tilde{\boldsymbol{e}}(j\omega), \end{aligned} \quad (15)$$

where

$$\begin{aligned} \boldsymbol{L}(\boldsymbol{\rho}, j\omega) &= \boldsymbol{P}(s)\boldsymbol{K}(\boldsymbol{\rho}, j\omega) \\ &= \begin{pmatrix} L_{11}(\boldsymbol{\rho}, j\omega) & L_{12}(\boldsymbol{\rho}, j\omega) \\ L_{21}(\boldsymbol{\rho}, j\omega) & L_{22}(\boldsymbol{\rho}, j\omega) \end{pmatrix}. \end{aligned} \quad (16)$$

From (15) and (16), (17) and (18) are derived.

$$\frac{y_{10}(j\omega)}{\tilde{e}_1(j\omega)} = L_{11}(\boldsymbol{\rho}, j\omega) + L_{12}(\boldsymbol{\rho}, j\omega)\frac{\tilde{e}_2(j\omega)}{\tilde{e}_1(j\omega)} \quad (17)$$

$$\frac{y_{20}(j\omega)}{\tilde{e}_2(j\omega)} = L_{22}(\boldsymbol{\rho}, j\omega) + L_{21}(\boldsymbol{\rho}, j\omega)\frac{\tilde{e}_1(j\omega)}{\tilde{e}_2(j\omega)} \quad (18)$$

Therefore if we can estimate $y_{10}(j\omega)/\tilde{e}_1(j\omega)$ and $y_{20}(j\omega)/\tilde{e}_2(j\omega)$ with $\boldsymbol{\rho} = \boldsymbol{\rho}^*$, and compare them to $L_{11}^*(j\omega)$ and $L_{22}^*(j\omega)$, respectively, we can investigate to see if $L_{11}(\boldsymbol{\rho}^*, j\omega) \simeq L_{11}^*(j\omega)$, $L_{12}(\boldsymbol{\rho}^*, j\omega) \simeq 0$, $L_{22}(\boldsymbol{\rho}^*, j\omega) \simeq L_{22}^*(j\omega)$ and $L_{21}(\boldsymbol{\rho}^*, j\omega) \simeq 0$. However $y_{01}(j\omega)/\tilde{e}_1(j\omega)$ and $y_{02}(j\omega)/\tilde{e}_2(j\omega)$ cannot be estimated from $y_{10}(j\omega)$, $\tilde{e}_1(j\omega)$, $y_{20}(j\omega)$ and $\tilde{e}_2(j\omega)$ directly since $y_{10}(t)$, $\tilde{e}_1(t)$, $y_{20}(t)$ and $\tilde{e}_2(t)$ are not

© ISAROB 2013

absolute integrable and the Fourier transform cannot be applied to them. To resolve the problem, a band pass filter proposed by Matsui et al [2] is introduced. The filter is given by

$$F(s) = \frac{100T_s s}{(100T_s s + 1)(10T_s s + 1)}\ , \tag{19}$$

where T_s is the sampling period for $\boldsymbol{u}_0(t)$ and $\boldsymbol{y}_0(t)$. The filter and a correlation method are used for the estimation. The estimated frequency responses of $y_{10}(j\omega)/\tilde{e}_1(j\omega)$ and $y_{20}(j\omega)/\tilde{e}_2(j\omega)$ are defined as $\hat{L}_{11}(\boldsymbol{\rho}, j\omega)$ and $\hat{L}_{22}(\boldsymbol{\rho}, j\omega)$, and are estimated by (20) and (21), respectively.

$$\hat{L}_{11}(\boldsymbol{\rho}, j\omega) = \frac{F[R_{ye1}(t)]}{F[R_{ee1}(t)]} \tag{20}$$

$$\hat{L}_{22}(\boldsymbol{\rho}, j\omega) = \frac{F[R_{ye2}(t)]}{F[R_{ee2}(t)]} \tag{21}$$

Here, $F[\cdot]$ denotes the Fourier transform, $R_{ye1}(t)$ and $R_{ye2}(t)$ are the cross-correlations, and $R_{ee1}(t)$ and $R_{ee2}(t)$ are the autocorrelations. The correlations are calculated as shown in (22)~(25) using $y_{10f}(t), y_{20f}(t)$, $\tilde{e}_{1f}(t)$ and $\tilde{e}_{2f}(t)$ which are all filtered $y_{10}(t), y_{20}(t)$, $\tilde{e}_1(t)$ and $\tilde{e}_2(t)$ by $F(s)$, respectively.

$$R_{ye1}(t) = \sum_{\tau=0}^{N-1} y_{10f}(\tau)\tilde{e}_{1f}(\tau + N - 1 - t) \tag{22}$$

$$R_{ye2}(t) = \sum_{\tau=0}^{N-1} y_{20f}(\tau)\tilde{e}_{2f}(\tau + N - 1 - t) \tag{23}$$

$$R_{ee1}(t) = \sum_{\tau=0}^{N-1} \tilde{e}_{1f}(\tau)\tilde{e}_{1f}(\tau + N - 1 - t) \tag{24}$$

$$R_{ee2}(t) = \sum_{\tau=0}^{N-1} \tilde{e}_{2f}(\tau)\tilde{e}_{2f}(\tau + N - 1 - t) \tag{25}$$

3 Numerical example

The LV100, which is taken from Hjalmarsson [3], is a gas turbine engine modeled as a continuous-time linear system with five state variables, two inputs and two outputs. The state variables are the gas generator spool speed, the power output, the temperature, the fuel flow and the variable area turbine nozzle. The inputs are the forth and the fifth state variables. The outputs are the first and the third state variables. The state matrix $\boldsymbol{A}_p$, the input matrix $\boldsymbol{B}_p$ and the output matrix $\boldsymbol{C}_p$ are given by (26), (27) and (28), respectively.

$$\boldsymbol{A}_p = \begin{pmatrix} -1.4122 & -0.0552 & 0 & 42.9536 & 6.3087 \\ 0.0927 & -0.1133 & 0 & 4.2204 & -0.7581 \\ -7.8467 & -0.2555 & -3.333 & 300.4167 & -4.4894 \\ 0 & 0 & 0 & -25.00 & 0 \\ 0 & 0 & 0 & 0 & -33.3333 \end{pmatrix} \tag{26}$$

$$\boldsymbol{B}_p = \begin{pmatrix} 0 & 0 & 0 & 1 & 0 \\ 0 & 0 & 0 & 0 & 1 \end{pmatrix}^T \tag{27}$$

$$\boldsymbol{C}_p = \begin{pmatrix} 1 & 0 & 0 & 0 & 0 \\ 0 & 0 & 1 & 0 & 0 \end{pmatrix} \tag{28}$$

The input-output transient data sets of the plant to find $\boldsymbol{\rho}^*$ were obtained in the simulation for the step reference response of the closed-loop system with $\boldsymbol{\rho_0}$ given by (29), and the data sets were saved as $\boldsymbol{u}_0(t)$ and $\boldsymbol{y}_0(t)$, respectively. The observation noises n_1 and n_2 which were white and independent each other were added in the simulation, and their means and variances were 0 and 0.0025, respectively. **Fig. 3** shows $\boldsymbol{y}_0(t)$.

$$\boldsymbol{\rho_0} = (1, 0.1, -1, 1, 10, 10, 10, 10) \tag{29}$$

The reference model for the FRIT was given by

$$T_{11}^*(s) = T_{22}^*(s) = \frac{1}{T_d^2 s^2 + 2\zeta_d T_d s + 1}, \tag{30}$$

where $T_d = 0.1$ and $\zeta_d = 0.7$. Then

$$L_{11}^*(s) = L_{22}^*(s) = \frac{1}{T_d^2 s^2 + 2\zeta_d T_d s}. \tag{31}$$

The diagonal elements of $\boldsymbol{W}(s)$ were given by

$$W_{11}(s) = W_{22}(s) = \frac{1}{T_w^2 s^2 + 2\zeta_w T_w s + 1}, \tag{32}$$

where $T_w = 0.05$ and $\zeta_w = 0.7$.

The parameter to achieve the model matching of (13) was obtained by the CMA-ES proposed by Hansen N [4] as given by

$$\boldsymbol{\rho}^* = (0.434, 0.449, 33.3, -4.59, 0.0935, 0.254, 3.70, 0.295)\ . \tag{33}$$

© ISAROB 2013

Figs. 4 and **5** show that although the estimated frequency responses of $\hat{L}_{11}(\boldsymbol{\rho}^*, j\omega)$ and $\hat{L}_{22}(\boldsymbol{\rho}^*, j\omega)$ are contaminated by the noises at the high frequencies, they are very close to the true loop transfer functions $L_{11}^*(s)$ and $L_{22}(\boldsymbol{\rho}^*, s)$, they are similar to the specified reference

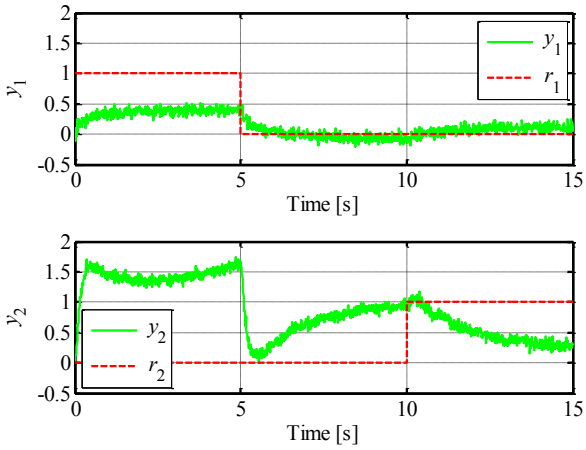

Fig. 3. Step reference responses with $\boldsymbol{\rho_0}$

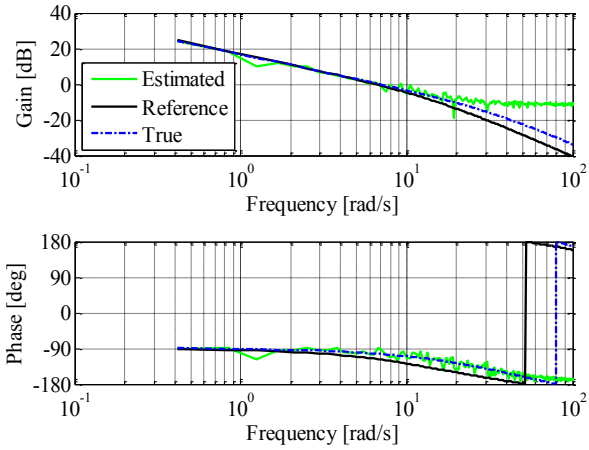

Fig. 4. Bode plots of $\hat{L}_{11}(\boldsymbol{\rho}^*, j\omega)$, $L_{11}^*(s)$ and $L_{11}(\boldsymbol{\rho}^*, s)$

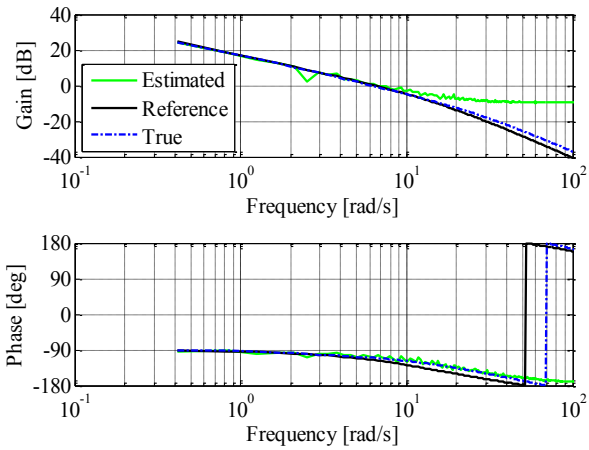

Fig. 5. Bode plots of $\hat{L}_{22}(\boldsymbol{\rho}^*, j\omega)$, $L_{22}^*(s)$ and $L_{22}(\boldsymbol{\rho}^*, s)$

transfer functions $L_{11}^*(s)$ and $L_{22}^*(s)$ at the frequencies less than the gain crossover frequencies, respectively, and they have enough phase margins. Therefore the reference models for the model matching and $\boldsymbol{\rho}^*$ were considered to be chosen and tuned appropriately, respectively. **Fig.6** shows that the step reference responses were improved significantly and a non-interacting control of $y_1(t)$ and $y_2(t)$ was achieved by $\boldsymbol{\rho}^*$.

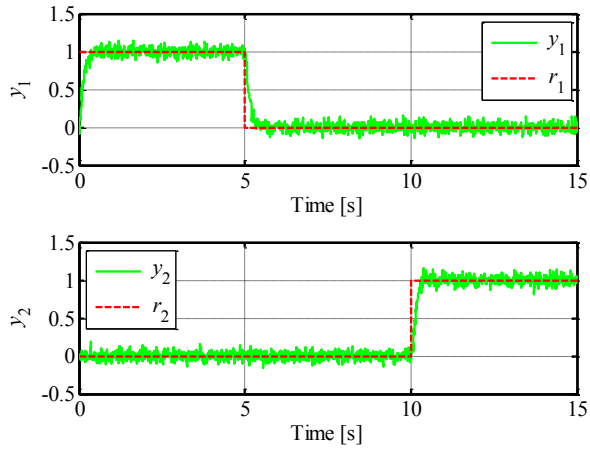

Fig. 6. Step reference responses with $\boldsymbol{\rho}^*$

4 CONCLUSION

A method to improve the weakness of the FRIT using the information of the experimental data in frequency domain was proposed. The method is able to show that the adequacy of the reference model for the model matching of the FRIT and the stability of the controller tuned by the FRIT. The effectiveness of the method was shown by a numerical example of a controller tuning for a multivariable system.

REFERENCES

[1] Souma S, Kaneko O, Fujii T (2004), A new method of controller parameter tuning based on input-output data – fictitious reference iterative tuning (frit) –, Proc. of IFAC Workshop on Adaptation and Learning in Control and Signal Processing 2004, pp.788-794

[2] Matsui Y, Kimura T, Nakano K (2010), Plant model analysis based on closed loop step response data, IEEE Conf. on Control Applications 2010, pp.677-682

[3] Hjalmarsson H (1999), Efficient tuning of multivariable controllers using iterative feedback tuning. Int. J. of Adaptive Control and Signal Processing, pp.553-572

[4] Hansen N (2006), The CMA evolution strategy: a comparing review, Towards a new evolutionary computation, Springer, pp.75-102

© ISAROB 2013

The Eighteenth International Symposium on Artificial Life and Robotics 2013 (AROB 18th '13),
Daejeon Convention Center, Daejeon, Korea, January 30-February 1, 2013

On inhibition of premature convergence in Genetic Algorithms for mobile robot control

Satoshi Shintaku[1], and Kazushi Nakano[1,2]

[1]Dept. of Mechanical Eng. and Intelligent Systems, The University of Electro-Communications, Japan
[2]Dept. of Electronic Eng. , The University of Electro-Communications, Japan
(Tel: 81-42-443-5190, Fax: 81-42-443-5183)
(shintaku@francis.ee.uec.ac.jp)

Abstract: Methods of Evolutionary Robotics using the evolutionary computation has been applied to design of mobile robot controllers. Genetic algorithms (GAs), ones of the typical methods in the evolutionary computation, have advantages that hardly fall into local minima compared to the other optimization algorithms. However the GAs have a big problem of premature convergence that the variety of the population is reduced, so the searching ability is degraded. In this study, through analysis of a new individual generation in GAs, we propose two methods of Probabilistic Crossover and Fluctuant Mutation to inhibit the premature convergence. We apply our proposal methods to benchmark problems in optimization and to controller design of the peg pushing robot, and demonstrate the effectiveness of our proposed methods.

Keywords: Genetic Algorithms, Premature Convergence, Optimization Problem, Evolutionary Robotics

1 INTRODUCTION

Many researchers have recently focused on methods of Evolutionary Robotics (ER) using the evolutionary computation to design controllers for mobile robots [1]. In the ER, teacher signal consisting of a hypothetical input and a desired response is not required. So, the ER learns only evaluation of robot's behavior. A robot controller can be built to achieve the desired operation adapting to a variety of environments by the ER. However, the control performance depends highly on the performance of evolutionary computation itself.

Genetic algorithms (GAs), ones of the typical methods in the evolutionary computation, used for optimization have been made to mimic the process of natural evolution [2]. In the GAs, the population is built from some solutions called individuals, which are encoded binary like a genome. The GAs search the optimal solution by alternating between the evaluation of individuals and genetic operations such as crossover and mutation.

The GAs have a highly global search ability, which have a big problem of "premature convergence" . If an individual exists which has much higher fitness than others, genetic information of this individual rapidly spreads throughout the population, and the variety of the population is reduced. Because the searching ability of the GAs depends on the variety of the population, the searching ability is degraded by the occurrence of premature convergence, and the population has a possibility of converging to local solutions.

Although there are the methods to increase the number of individuals so as to maintain the variety of the population, an increase in the number of individuals causes to an increase in the computational effort, so there is a risk that a robot controller cannot be implemented in real time. In robot controller design using the ER, the premature convergence tends to occur because of the difficulties in the fitness function design and hardware restrictions such as robot sensors. Therefore GAs approaches that enable to inhibit the premature convergence are required.

In this study, we discuss about the changes in the variety of population by crossover and mutation in GAs using uniform crossover. We divide the convergence of individuals into two parts; one is "learning convergence" that comes from the difference between the fitness of individuals, and the other is "nature convergence" that occurs independently of the fitness of individuals. Next we propose two methods of Probabilistic Crossover (PC) and Fluctuant Mutation (FM). The PC is a crossover method for determining the probability distribution of the allele, and to generate individuals of new generation according to the probability distribution, so the PC is a crossover method for putting forward learning convergence. The FM is a method for tetermining the mutation rate so as to complement the decrease of variance based on the natural convergence from the variances of the individuals after crossover.

We apply our proposal methods to benchmark problems in optimization and to controller design of the peg pushing robot, and demonstrate the effectiveness of the methods in terms of the quality and robustness of solution and the convergence speed of learning.

2 RELATED WORKS

The GAs introduced by J. H. Holland in the 1970s are optimization algorithms that mimic the evolution of life. The

© ISAROB 2013

GAs have the following features: first, the GAs are iterative calculation methods, which update concurrently multiple solution candidates, secondly, the GAs use unique operations called "crossover" that encode candidate solutions to binary data called "genotype" and generate new candidate solutions by combining genotype, finally the GAs are flexible algorithms that can be applied to a wide variety of problems.

There are two methods for analysis of the GAs, one is Schema theory and the other is for analysis using Markov chain. The Schema theory determines the change of a subset of genes (Schema) that are components of each individual in Simple Genetic Algorithms (SGAs) using one-point crossover and mutation [3]. The Schema theory shows that the SGAs can increase exponentially the schema which has partially favorable information and get globally favorable solutions. However the Schema theory cannot give the convergence to the optimal solution.

The analysis of the Markov chain calculates the probability of discovery of the optimal solution and shows the convergence to the optimal solution in the GAs [4]. From the Markov chain analysis, the probability of discovery of the globally optimal solution converges to "1" after calculating in an infinite time if keeping the storage of the best individual that has been found so far and having the positive mutation rate. However the assumption is independent of the main algorithms of the GAs such as crossover and selection. It is synonymous with that the probability of discovery of the optimal solution converges to 1 in random search.

The Schema theory and the Markov chain analysis show that the GAs get the globally optimal solution after calculating in an infinite time, on the contrary, these cannot show the quality of the solution obtained in a realistic time. So we do not get exactly how to design many parameters used in the GAs from the Schema theory and the Markov chain analysis.

Meanwhile, the GAs have improved its searching ability of the optimal solution by absorbing the advantage of the other optimization algorithms and creating a new method.

Thermodynamical Genetic Algorithms (TDGAs) select the individual of the next generation based on Free Energy Minimization at Simulated Annealing [5]. The TDGAs can control explicitly the variety of individual by setting temperature schedule and avoid the premature convergence. On the other hand, the TDGAs have the following problems: the TDGAs require more computational time than the SGAs, and the TDGAs causes the TDGAs convergence that loses the variety of the individual due to approximate calculation of the entropy.

Distributed Genetic Algorithms (DGAs) are ones of the GAs methods that make some islands that the population is divided into, and the crossover and evaluation are performed [6]. The DGAs provide the immigration that lets individuals move between the islands once in several generations. Emigrated individuals are the candidates of the optimal solution in other islands, so they have a higher fitness compared to mutated individuals and are hardly lost by selection. Emigrated individuals are candidates of the solution optimized the different situation, so they can contribute to the maintenance of variety compared to mutated individuals changed only a small part of the genome. As a result, the DGAs can obtain a higher fitness than GAs that learn in a single population. But at the same time, because the number of individuals per island is reduced, the environment of each island makes it easy to converge the local minimum. Therefore, the improvement of the searching ability in DGAs has never been theoretically proven yet.

Diploid Genetic Algorithms (Diploid GAs) have two genotypes and represent a phenotype through a new type called "agency-type" [7]. Because the Diploid GAs have the locus that does not appear in the phenotype, does not affect the fitness and carry over low fitness genome to the next generation, it is possible to maintain the variety of individuals.

These methods are said to get a higher searching ability than the GAs. However the parameters that should be set up are increased, for example, temperature scheduling in the TDGAs, the number of islands and the timing of immigration in the DGAs, and the methods for converting genotype to phenotype in the Diploid GAs. In order to search the optimal solution efficiently, it is necessary to determine these parameters appropriately.

3 PROBABILISTIC CROSSOVER AND FLUCTUANT MUTATION

3.1 Analyses of Genetic Algorithms

In this section, we discuss about the crossover and the mutation of the GAs from the viewpoint of probability theory. First, we derive an expression for the probability distribution of the allele of a new individual generated by the crossover. The analyzed GAs consist of the roulette selection and the uniform crossover.

Selecting an individual $\boldsymbol{s_i}$ as the parent, the probability $p(\boldsymbol{s_i})$ that the i-th individual becomes a factor for determining a new individual's locus is described as

$$p(\boldsymbol{s_i}) = \frac{f(\boldsymbol{s_i})}{\sum_{i=1}^{N} f(\boldsymbol{s_i}).} \tag{1}$$

where N is the number of individuals, and $f(\boldsymbol{s_i})$ is the fitness for a given $\boldsymbol{s_i}$.

The probability $p(x'_j = 1)$ that the j-th locus of the generated individual is equal to 1 is described as

$$
\begin{aligned}
p(x'_j = 1) &= \sum_{i=0}^{N-1} p(\boldsymbol{s_i}|x_{ij} = 1) \\
&= \frac{\sum_{i=0}^{N-1} f(\boldsymbol{s_i}) x_{ij}}{\sum_{i=0}^{N-1} f(\boldsymbol{s_i})} \\
&= \frac{p(x_{ij} = 1)F}{1 + p(x_{ij} = 1)(F - 1),} \qquad (2) \\
F &= \frac{ave(f(\boldsymbol{s_i})|_{x_{ij}=1})}{ave(f(\boldsymbol{s_i})|_{x_{ij}=0}).} \qquad (3)
\end{aligned}
$$

where x_{ij} is the j-th locus of the i-th individual of parent generation, and $ave(f(\boldsymbol{s_i})|_{x_{ij}=1})$ is the average value of $f(\boldsymbol{s_i})$ if x_{ij} is equal to 1.

Figure 1 shows some examples of the above equation.

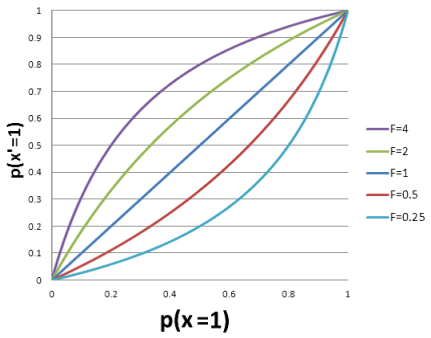

Fig. 1. Change of $p(x)$ from crossover in GAs

Next, we discuss about a new population named S to generate the N-th individual from the probability distribution $p(x')$. Here, $R[S|x' = 1]$ is the rate that the locus is equal to 1 in S, and $E[\mathrm{var}[S]]$ represents the expectation of the variance of S. These are represented as

$$
\begin{aligned}
R[S|x' = 1] &= p(x' = 1), \qquad (4) \\
E[\mathrm{var}[S]] &= \frac{N-1}{N} p(x' = 1)p(x' = 0). \qquad (5)
\end{aligned}
$$

As shown by the above equation, $E[\mathrm{var}[S]]$ is smaller than the variance of $p(x')$ because of sample variance.

Finally, when the population S is mutated with the probability P_m, we show $E[\mathrm{var}[\mathrm{S}']]$ as follows: the probability that locus x^* representing mutated locus x of S is equal to 1 is calculated by

$$
p\left(x^* = 1\right) = p\left(x = 1\right) + P_m \left(p\left(x = 0\right) - p\left(x = 1\right)\right). \qquad (6)
$$

Therefore, $E[\mathrm{var}[\mathrm{S}']]$ is described by

$$
\begin{aligned}
E[\mathrm{var}[S']] &= \left(P_m - P_m^2\right)\left(\frac{N-1}{N} - 4\mathrm{var}[x]\right) \\
&+ E[\mathrm{var}[S]]. \qquad (7)
\end{aligned}
$$

From the above equation, we find that the mutation acts in a direction to increase the variance, and that this action works strongly in the proportion to the variance in prior mutation.

3.2 Consideration from analyses of GAs

Figure 1 shows that the crossover changes the probability of the locus in the direction of increasing the fitness. As a result, the individuals converge to the genome having a higher fitness as the generation repeated. This is defined as "learning convergence".

Furthermore, Eq. (5) shows that the generation of the individuals reduces the variance independently of the fitness. It means that the individuals converge independent of the fitness with the generation. This is defined as "natural convergence".

Figure 1 shows that the difference is small between the probability distribution of the allele of generated individuals and the rate of the genome in the parent generation. In other words, $p(x' = 1) - p(x = 1)$ is very small. Thereby, in the case of converging in a wrong direction, even if F in Eq. (3) is determined to correct the wrong convergence, there is a risk that the natural convergence cancels a modification of learning by the learning convergence. This causes the premature convergence of the GAs.

In our study, we propose a probabilistic crossover method for determining the probability distribution of the allele of generated individuals in crossover, and also do a fluctuant mutation for changing the mutation rate according to the variance of the locus. We intend to solve this premature convergence problem.

3.3 Probabilistic Crossover and Fluctuant Mutation

The probabilistic crossover of our first proposing method is one of the crossover methods for calculating the probability distribution of the allele of generated individuals:

$$
p(x' = 1) = \begin{cases} F * p(x = 1)\,(F < 1) \\ 1 - \frac{(1-p(x=1))}{F}\,(F \geq 1)\,, \end{cases} \qquad (8)
$$

and generate individuals according to this probability distribution instead of selecting parent individuals and crossing over the genome.

Equation (8) is designed so as to be a tangent line to the point $p(x = 1) = 0$ or $p(x = 1) = 1$ in (2). Figure 2 shows some examples of (8).

In $F > 1$ we design $p(x)$ to increase an increment of $p(x)$ at around $p(x = 1) = 0$, the learning convergence is likely to occur even in the neighborhood of $p(x = 1) = 1$ or 0 while the premature convergence is less likely to occur.

The fluctuant mutation is our second method for estimating the reduction of the variance by the natural convergence and for determining the mutation rate to complement the lost variance.

Since the effects of the natural convergence are different in each locus, the mutation rate uses different values in each locus. Moreover, the mutation handles only the individuals

© ISAROB 2013

generated by the crossover and does not effect the individuals selected by the elite selection.

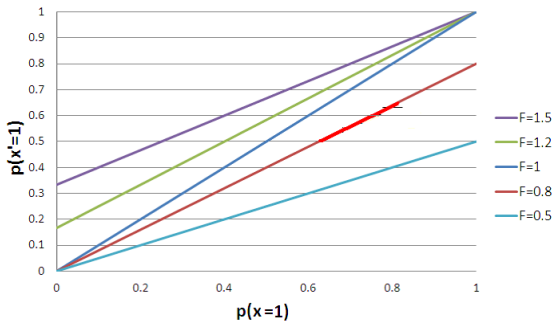

Fig. 2. Change of $p(x)$ from probabilistic crossover

Thus, the fluctuant mutation must complement the natural convergence that occurs in the entire population with the mutation only for the individuals generated by the crossover. So, the mutation rate $p_m(\mathrm{var}[x'])$ in the fluctuant mutation is determined by

$$p_m(\mathrm{var}[x']) = \frac{1}{P_c}\left(\frac{1}{2} - \sqrt{\frac{1}{4} - \frac{1}{N-1}\frac{\mathrm{var}[x']}{\frac{N-1}{N} - 4\mathrm{var}[x']}}\right). \quad (9)$$

In the above equation, if $\mathrm{var}[x']$ equals to 0, $p_m(\mathrm{var}[x'])$ will be 0. This does not fulfill the condition that the mutation rate is a positive value in the Markov chain analysis, and the convergence to the optimal solution is not guaranteed. Hence, by extending Eq. (9) to Eq. (10), the fluctuant mutation avoids this problem.

$$p_m(\mathrm{var}[x']) = \begin{cases} \frac{1}{P_c}\left(\frac{1}{2} - \sqrt{\frac{1}{4} - \frac{1}{N-1}\frac{\mathrm{var}[x']}{\frac{N-1}{N} - 4\mathrm{var}[x']}}\right) & (\mathrm{var}[x'] \geq \epsilon) \\ P_m & (\mathrm{var}[x'] < \epsilon) \end{cases} \quad (10)$$

The use of the fluctuant mutation inhibits the convergence of the variance of the allele by the natural convergence as well as the premature convergence.

4 SIMULATION RESULTS

4.1 Application to optimization problem

To investigate the performance of the proposed methods, each optimization algorithm is evaluated through the typical benchmark problems in optimization. The optimization algorithms to be compared are the GAs using the uniform crossover and the constant mutation rate as the conventional method. The GAs using the probabilistic crossover (PCGAs), the GAs using the fluctuant mutation (FMGAs), and the GAs using both the probabilistic crossover and the fluctuant mutation as the proposed methods. We examine the learning processes for the cases that the number of elite individuals is given as 30, and the number of original individuals is given as 50, 100 and 200.

4.1.1 Rastrigin function

The aim of each optimization algorithm is to find the minimum value of Rastrigin function:

$$F(x) = 10N + \sum_{i=0}^{N}\left(x_i^2 - 10\cos(2\pi x_i)\right) \quad (11)$$

$$-5 \leq x_i < 5. \quad (12)$$

The Rastrigin function has a global minimum at $x = 0$ where $F(x) = 0$, and it has the suboptimal solutions in a reticular pattern near the global minimum. The fitness function is defined by

$$fitness = 1 - \frac{F(x)}{(20 + 5^2)N}. \quad (13)$$

Table 1 summarizes the maximum fitness values for the 100-dimensional Rastrigin function at the 1000-th generation in each learning method. These values show the average of 100 trials, and within the parenthesis shows their standard deviation.

Table 1. Fitness for Rastrigin function

Individuals	50	100	200
GAs	0.919(0.006)	0.941(0.005)	0.945(0.006)
PCGAs	0.957(0.004)	0.962(0.004)	0.963(0.004)
FMGAs	0.939(0.008)	0.951(0.005)	0.952(0.004)
PCFMGAs	0.778(0.063)	0.964(0.004)	0.968(0.003)

Figures 3 and 4 show the transitions of the maximum fitness values and their variances in 100 individuals.

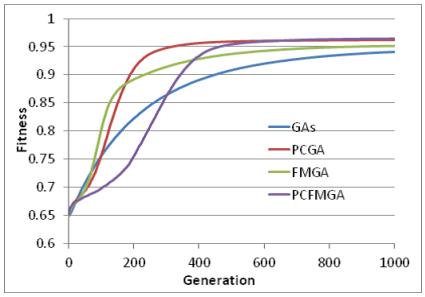

Fig. 3. Transition of fitness for Rastrigin function

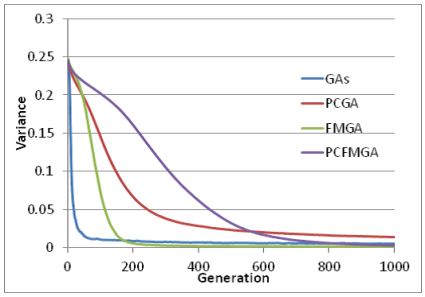

Fig. 4. Transition of variance of fitness for Rastrigin function

© ISAROB 2013

4.1.2 Schwefel function

The aim of each optimization algorithm is to find the minimum value of the Schwefel function:

$$F(x) = -\sum_{i=0}^{N}\left(x_i \sin(\sqrt{|x_i|})\right) \quad (14)$$

$$-500 \leq x_i < 500. \quad (15)$$

The Schwefel function has a global minimum at $x = 420$ where $F(x) = -418.98N$, and it does not have the suboptimal solutions near the global minimum. The fitness function is defined by

$$fitness = 1 - (F(x) + 418.98N)/840N. \quad (16)$$

Table 2 summarizes the maximum fitness values for the 100-dimensional Schwefel function at the 1000-th generation in each learning method. These values show the average of 100 trials, and within the parenthesis shows their standard deviation.

Table 2. Fitness for Schwefel function

Individual	50	100	200
GAs	0.83(0.011)	0.88(0.012)	0.89(0.011)
PCGAs	0.95(0.006)	0.93(0.005)	0.95(0.006)
FMGAs	0.91(0.009)	0.92(0.008)	0.92(0.008)
PCFMGAs	0.95(0.006)	0.96(0.006)	0.97(0.005)

4.1.3 Rosenbrock function

The aim of each optimization algorithm is to find the minimum value of the Rosenbrock function:

$$F(x) = -\sum_{i=0}^{N-1}\left(100(x_i^2 - x_{i+1})^2 + (1 - x_i)^2\right) \quad (17)$$

$$-2 \leq x_i < 2. \quad (18)$$

The Rosenbrock function has a global minimum at $x = 1$ where $F(x) = 0$, and it has a high dependence between the variables. The fitness function is defined by

$$fitness = 1 - \sqrt{F(x)/3609/(N-1)}. \quad (19)$$

Table 3 summarizes the maximum fitness values for the 100-dimensional Rosenbrock function at the 1000-th generation in each learning method. These values show the average of 100 trials, and within the parenthesis show their standard deviation.

4.2 Controller design for peg pushing robot

We simulate the problem of peg pushing robot control as an application task. The control task is to push the peg toward the goal by a two-wheel robot. The feedforward neural network (NN) having three layers is used as the robot controller. The inputs of robot controller are the relative coordinates of the goal and peg, and the outputs are the rotational speed of the wheel. The number of the hidden layer of the NN is 10.

Table 3. Fitness for Rosenbrock function

Individual	50	100	200
GAs	0.941(0.005)	0.956(0.005)	0.961(0.005)
PCGAs	0.959(0.005)	0.963(0.005)	0.964(0.004)
FMGAs	0.943(0.005)	0.954(0.005)	0.956(0.005)
PCFMGAs	0.946(0.014)	0.961(0.004)	0.965(0.004)

In this simulation, each optimization algorithm optimizes the synapse of the NN. The fitness function is defined by

$$fitness = \exp\left(-\frac{dist(\mathrm{goal}, \mathrm{peg_{end}})}{dist(\mathrm{goal}, \mathrm{peg_{start}})}\right) \quad (20)$$

where, $dist(\mathrm{goal}, \mathrm{peg_{start}})$ is the initial distance between the peg and goal, and $dist(\mathrm{goal}, \mathrm{peg_{end}})$ is the final distance between the peg and goal.

We evaluate the fitness values of controllers obtained from 10 different initial positions of the peg.

The optimization algorithms used in this simulation are the GAs, TDGAs, DGAs and Diploid GAs as the conventional methods and the PCFMGAs as proposed method. The number of individuals is 100 in each optimization algorithms, and the number of elite selection is 30 other than the TDGAs, and the mutation rate is 0.1% in the conventional methods, and P_m is 0.01% in the FMGAs. In the DGAs, the number of the island is 5, and the migration interval is 20. The temperature schedule of TDGAs is defined by

$$T(t) = \exp\left(-\frac{t}{25}\right). \quad (21)$$

Table 4 summarizes the maximum fitness values and success rate that the maximum fitness value is greater than 0.95 at the 1000-th generation in each learning method. The maximum fitness value shows the average of 100 trials, and within the parenthesis shows their standard deviation.

Table 4. Maximum fitness and success rate for robot controller

Alghrithm	Maximum Fitness	Success Rate
GAs	0.912(0.102)	0.48
TDGAs	0.675(0.160)	0.04
DGAs	0.889(0.079)	0.20
Diploid GAs	0.758(0.186)	0.30
PCFMGAs	0.952(0.076)	0.72

Figure 5 shows the transition of the maximum fitness values.

© ISAROB 2013

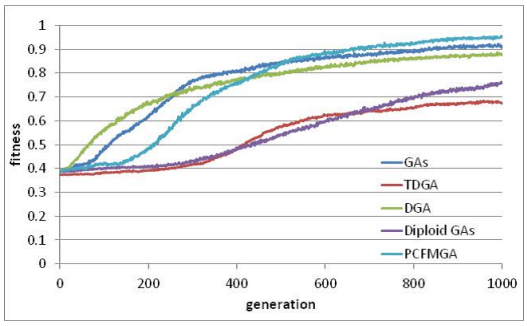

Fig. 5. Transition of fitness of peg pushing robot

5 CONSIDERATION OF PROPOSED METHODS

5.1 Learning method for benchmark problems

Tables 1 - 3 show that the PCGAs gain higher fitness values than the GAs in all benchmark problems. In contrast, the FMGAs cannot gain higher fitness values than the GAs in the Rosenbrock function, and the fitness of the FMGAs tends to be lower than that of the PCGAs in all the benchmark problem. While the PCFMGAs gain the highest fitness values among the other algorithms in the case of many individuals, the fitness values of the PCFMGAs are lower than the other algorithms in the case of a few individuals.

Figure 4 proves the convergence of the individuals of the GAs at around 100-th generation. For this reason, the learning convergence does not work well in the GAs, and only the mutation. Exponentially increasing of the fitness value in Fig. 3 shows that searching the optimal solution become heuristic by the mutation.

Figures 3 and 4 show that the PCGAs and FMGAs slowly reduce the variances of the individuals, and the learning processes according to the convergence of the individuals. The PCGAs maintain the variances to some extent even if the learning progresses at the long generations. On the contrary, the FMGAs lose the variances after the generation. Therefore, the PCGAs gain a higher fitness than the FMGAs in the final result of learning. Thus, a proper setting of P_m in the FMGAs can gain a higher fitness.

The PCFMGAs make the convergence of the individuals very slow, and aquire the high global search ability. As a result, the PCFMGAs gain the highest fitness values among all the algorithms after the long generation. However the PCFMGAs are not suitable in the case of a limited number of generations because of slow convergence.

5.2 Learning method for robot controller design

Figure 5 shows that the TDGAs, DGAs and Diploid GAs do not gain higher fitnesses than the GAs in design of the mobile robot controller. Table 5 shows that the success rate is low while the DGAs gain a high fitness. The fact demonstrates that the DGAs do not have the local search ability while it has the global search ability.

Moreover Fig. 5 shows the potential that the Diploid GAs gain s higher fitness at more advanced generation. However, it requires longer computational time than the other algorithms. Hence, each algorithm is not suitable for optimization of the robot controller design.

On the other hand, the PCFMGAs of the proposed methods gain the highest fitness and success rate among all the optimization algorithms. The number of generations required in the PCFMGAs nearly equals to that required in the GAs and DGAs. Hence, the PCFMGAs are not suitable for optimization of the robot controllerdesign.

6 CONCLUSION

To inhibit the premature convergence which is a problem in the mobile robot controller design, we proposed the new crossover method and the method for determining the mutation rate, through the analysis of a new individual generation in GAs. We applied our proposal methods to the benchmark problems in optimization and to the controller design for the peg pushing robot, and demonstrated the effectiveness of our proposed methods.

REFERENCES

[1] Toshiyuki Kondo: Evolutionary design and behavior analysis of neuromodulatoryneural networks for mobile robots control: Applied Soft Computing, Volume 7, Issue 1, pp.189-202,2007

[2] J. H. Holland: Adaptation in Natural and Artificial Systems: University of Michigan Press, 1975

[3] David E. Goldberg: A Practical Schema Theorem for Genetic Algorithms Design and Tuning: IlliGAL Report, No. 2001017, January, 2001

[4] A. E. Eiben,E. H. L. Aarts and K. M. Van Hee: Global convergence of genetic algorithms: A markov chain analysis: Lecture Notes in Computer Science Volume 496, pp.3-12, 1991

[5] Naoki Mori, Junji Yoshida, Hisashi Tamaki, Hajime Kita and Yoshikazu Nishikawa: A thermodynamical selection rule for the genetic algorithm : Evolutionary Computation, 1995, IEEE International Conference on

[6] Xiong Shengwu: A distributed genetic algorithm to TSP: Intelligent Control and Automation, 2002. Proceedings of the 4th World Congress on, pp.1827-1830, volume 3, 2002

[7] Shengxiang Yang: On the Design of Diploid Genetic Algorithms for Problem Optimization in Dynamic Environments: Evolutionary Computation, 2006. CEC 2006. IEEE Congress on, pp.1362-1369 , 2006

The Eighteenth International Symposium on Artificial Life and Robotics 2013 (AROB 18th '13),
Daejeon Convention Center, Daejeon, Korea, January 30-February 1, 2013

Digital PI control for interleave PFC boost converter

Yuto Adachi[1], Kohji Higuchi[1], Tatsuyoshi Kajikawa[1], Tomoaki Sato[2], and Kosin Chamnongthai[3]

[1] The University of Electro-Communications 1-5-1, Chofu-ga-oka,Chofu-shi, Tokyo 182-8585, Japan
[2] C&C SYSTEMS CENTER Hirosaki University, Bunkyo-Cho 3, Hirosaki-shi, Aomori 036-8561, Japan
[3] King Mongkut's University of Technology Thonburi, 126 Pracha-uthit Rd., Bangmond, Tungkru, Bangkok 10140, Thailand
(Tel: 81-42-443-5182, Fax: 81-42-443-5183)

Abstract: In recent years, improving of power factor and reducing harmonic distortion in electrical instruments are needed. In general, a current conduction mode boost converter is used for active PFC (Power Factor Correction). Especially, an interleave PFC boost converter is used in order to make a size compact, make an efficiency high and make noise low. In this paper, a PI digital controller for suppressing the change of step response characteristics and variation of output voltage at a load sudden change with high power factor and low harmonic is proposed. Experimental studies using a micro-processor for controller demonstrate that the PI digital controller is effective to improve power factor and to suppress output voltage variation and is more advantageous to control the current of the sum of each phase in hardware.

Keywords: interleave PFC, boost converter, digital PI control, micro-processor

1 INTRODUCTION

In recent years, improving of power factor and reducing harmonic of power supply using nonlinear electrical instruments are needed. A passive filter and an active filter in AC lines are used for improving of the power factor and reducing the harmonic. Generally a current conduction mode boost converter is used for an active PFC (Power Factor Correction) in electrical instruments. Especially, an interleave PFC boost converter is used in order to make a size compact, make an efficiency high and make noise low. In the interleave PFC boost converter, if a duty ratio, a load resistance and an input voltage are changed, the dynamic characteristics are varied greatly, that is, the interleave PFC converter has non-linear characteristics. In many applications of the interleave PFC converters, loads cannot be specified in advance, i.e., their amplitudes are suddenly changed from the zero to the maximum rating. This is the prime reason of difficulty of controlling the interleave PFC boost converter.

Usually, a conventional analog phase lead-lag compensation controller or an analog IC controller designed to the approximated linear controlled object at one operating point is used for the PFC converter. The interleave PFC converter is difficult to control because of the nonlinearity and the complicated configuration. In the nonlinear interleave PFC boost converter system, those conventional controllers are not enough for attaining good performance. So the gain scheduling control using many controllers for many operating points is applied to PFC boost converter. This control method is very complicated and not easy to implement because of many switching of controllers. In this paper, a PI digital controller for suppressing the change of step response characteristics and variation of output voltage at a load sudden change with high power factor and low harmonic is proposed. The PFC converter is a nonlinear system and the models are changed at each operation point. When controlling the current for every phase, the interleave PFC boost converter needs three controllers, two for interleave current control and one for voltage control, When controlling the current of the sum of each phase, it needs two controller, one for interleave current control and one for voltage control. The digital PI controllers are used for these controllers. The design and combining methods of these PI digital controllers which can cope with nonlinear system or changing of the models are proposed. These controller are actually implemented on a micro processor and is connected to the PFC converter. That is, three or two digital PI controllers are equipped with one micro processor. Simulations and experimental studies demonstrate that the PI digital controllers designed suitably satisfy the desired performances and is more advantageous practically to control the current of the sum of each phase.

2 INERLEAVE PFC BOOST CONVERTER

2.1 State-space model of interleave boost converter

The interleave boost converter shown in Fig. 1 is manufactured. When controlling the current for every phase, i_{s1} and i_{s2} are measured and used. And when controlling the current of the sum of each phase, i_l is measured and used. When controlling the current for every phase, two current

© ISAROB 2013

controllers are required. But when controlling the current of the sum of each phase, what is necessary is to shift a phase for the output of one controller 180 degrees, and just to build two outputs

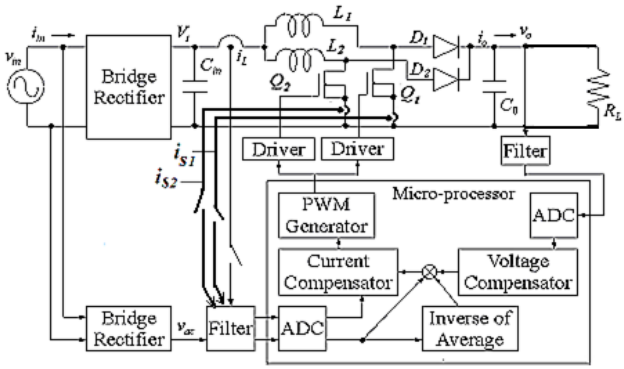

Fig.1 Interleave PFC boost converter

Fig.1, v_{in} is an input AC voltage, i_{in} is an input AC current, C_{in} is a smoothing capacitor, V_i is a rectifying and smoothing input voltage, Q_1 and Q_2 are MOSFETs or IGBTs, L_1 and L_2 are interleave boost inductances, D_1 and D_2 are interleave boost diodes, C_0 is an output capacitor, R_L is an output load resistance, i_{s1} and i_{s2} are inductor currents of inductance L_1 and L_2, respectively, i_L is the sum of inductor current, v_{ac} is an absolute value of the input AC voltage and v_o is an output voltage. The inductor currents i_{s1} and i_{s2} or i_L is controlled to follow the rectified input voltage v_{ac} for improved power factor, reduced harmonics and stable the output voltage. Using the state-space averaging method, the state equation of the inter leave boost converter becomes as follows [11]:

$$\frac{d}{dt}\begin{bmatrix} i_L \\ v_o \end{bmatrix} = \begin{bmatrix} -\frac{R_0}{L_0} & -\frac{1}{L_0} \\ \frac{1}{C_0} & -\frac{1}{R_L C_0} \end{bmatrix}\begin{bmatrix} i_o \\ v_o \end{bmatrix} + \begin{bmatrix} \frac{V_i}{L_0} \\ 0 \end{bmatrix} + \left\{ v_o \begin{bmatrix} \frac{1}{L_0} \\ 0 \end{bmatrix} + i_o \begin{bmatrix} 0 \\ -\frac{1}{C_0} \end{bmatrix} \right\}\mu \tag{1}$$

Here μ is duty ratio. When controlling the current for every phase, i_o is i_{s1} or i_{s2}, R_0 (equivalent resistance of inductor) is R_1 or R_2 and L_0 is L_1 or L_2. When controlling the current of the sum of each phase, i_o is i_L R_0 is $R_1R_2/(R_1+R_2)$ and L_0 is $L_1L_2/(L_1+L_2)$. The boost converter has non-linear characteristics because this equation has the product of state variable v_o, i_o and duty ratio μ.

2.2 Static characteristics of boost converter

At some operating point of eq. (1), let v_o, i_o and μ, be V_s, I_s and μ_s, respectively. Then average of output voltage V_s and inductor current I_s at the operating points becomes as follows:

$$V_s = \frac{1}{1+\frac{1}{(1-\mu_s)^2}\frac{R_0}{R_L}}\frac{1}{1-\mu_s}V_i$$
$$I_s = \frac{1}{R_L}\frac{V_s}{1-\mu_s} \tag{2}$$

The actual measurement results of the static characteristics of μ_s to V_s are shown in Fig.2. In Fig.2, it turns out that the boost converter is a non-linear system.

The static characteristic of the boost converter is changed greatly with load resistances, and it influences the dynamic characteristics of converter. In addition, the static characteristics will be changed with input voltage variation Sasaki [1].

2.3 Dynamic characteristics of boost converter

The linear approximate state equation of the interleave boost converter using small perturbations $\Delta i_o = i_o - I_s$, $\Delta v_o = v_o - V_s$ and $\Delta\mu = \mu - \mu_s$ is as follows:

$$\dot{x}(t) = A_c x(t) + B_c u(t)$$
$$y(t) = C_c x(t) \tag{3}$$

where

$$A_c = \begin{bmatrix} -\frac{R_0}{L_0} & -\frac{1-\mu_s}{L_0} \\ \frac{1-\mu_s}{C_0} & -\frac{1}{R_{LDC}C_0} \end{bmatrix}, B_c = \begin{bmatrix} \frac{V_s}{L_0} \\ -\frac{I_s}{C_0} \end{bmatrix}$$

$$x(t) = \begin{bmatrix} \Delta i_o(t) \\ \Delta v_o(t) \end{bmatrix}, u(t) = \Delta\mu(t), y = \begin{bmatrix} y_i \\ y_v \end{bmatrix}, C_c = \begin{bmatrix} 1 & 0 \\ 0 & 1 \end{bmatrix}$$

Here, Δi_o, Δv_o, $\Delta\mu$ are small-signal variables. And $y_i = \Delta i_o$ is a small signal inductor current and $y_v = \Delta v_o$ is a small signal output voltage.

From this equation, matrix A and B of the interleave boost converter depends on duty ratio μ_s. Therefore, the converter response will be changed depending on the operating point and other parameter variations. The changes of the load R_L, the duty ratio μ_s, the output voltage V_s and the inductor current I_s in the controlled object are considered as parameter changes in eq. (1). Such parameter changes can be replaced with the equivalent disturbances inputted to the input and the output of the controlled object. Therefore, what is necessary is just to constitute the control

© ISAROB 2013

systems whose pulse transfer functions from equivalent disturbances to the output y become as small as possible in their amplitudes, in order to robustize or suppress the influence of these parameter changes.

3 DESIGN OF DIGITAL CONTROLLERS

3.1 Discretization of controlled object

The continuous system of eq. (1) is transformed into the discrete system as follows:

$$x_d(k+1) = A_d x_d(k) + B_d u(k) \qquad (4)$$
$$y(k) = C_d x_d(k)$$

3

where

$$A_d = \left[e^{A_c T}\right], B_d = \left[\int_0^T e^{A_c \tau} B_c d\tau\right], C_d = C_c$$

This dicrete-time controlled object is shown in Fig. 2. In Fig. 2, q_v, q_{yi} and q_{yv} are the equivalent disturbances with which the parameter changes of the controlled object are replaced.

3.2 Digital PI current and voltage control system

First, in order to make the input i_{in} follow the input voltage v_{ac}, the current control system is constituted by making current i_{s1} and i_{s2} or i_L into the controlled output y_i as shown in Fig. 2. The transfer function of the digital PI controller is as follows:

$$G_i(z) = k_{ri} + \frac{k_{ii}}{z-1} \qquad (5)$$

Next, a voltage control system is constituted by making output voltage vo of the current control system into the controlled output yv as shown in Fig. 2. The transfer function of the digital PI controller is as follows:

$$G_v(z) = k_{rv} + \frac{k_{jv}}{z-1} \qquad (6)$$

The parameters k_{ri} and k_{ii} of eq. (5) are appropriately decided from the Bode diagram of the transfer function from r_i to y_i and from q_v, q_{yi} and q_{yv} to y_i of the system of Fig. 2.

The parameters k_{rv} and k_{iv} of eq. (6) are appropriately decided from the Bode diagram of the transfer function between r_v and y_v yv and from q_v, q_{yi} and q_{yv} to y_v of the system of Fig. 2.

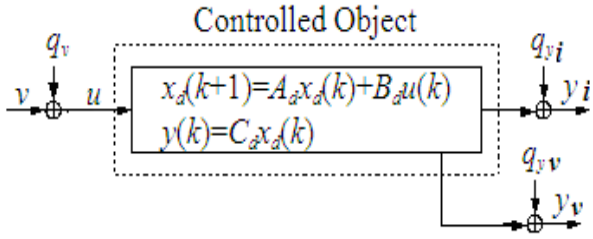

Fig.2 Discrete-time Controlled Object

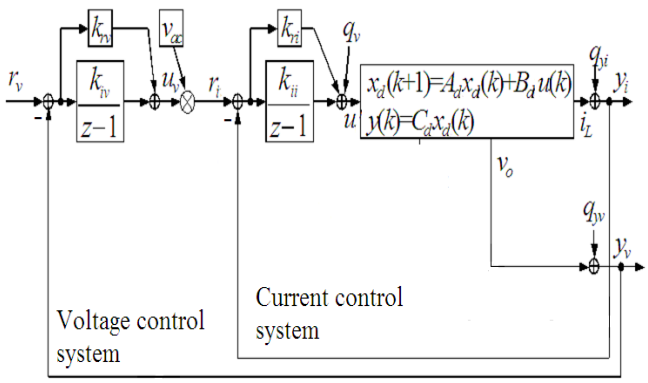

Fig.3 Interleave control system with digital PI current controller and digital PI voltage controller

4 Expermental Studies

All experimental setup system is manufactured. A micro-controller (RX) from Renesas Electronics is used for the digital controller. The digital PI current, and voltage controllers were implemented on 1 Micro Controller.

When controlling the current for every phase, two $G_i(z)$ and $G_v(z)$ are needed. Then each PI controller parameters for each phase are determined as follow:

$$k_{ri} = 0.8 \qquad k_{ii} = 0.2$$
$$k_{ri} = 0.5 \qquad k_{iv} = 0.001$$

The experiment results of this case are shown in Fig. 4, 5, 6. The experiment result of the steady state at load RL=1kΩ and 500Ω are shown in Fig. 4 and 5. The input current waveform and the phase are the almost same as the input voltage at each load and the power factor (PFC) of converter at load RL=500Ωand 1kΩ are 0.9780 and 0.975, respectively. The experiment result of load sudden change from 1kΩ to 500Ω is shown in Fig. 6. In Fig. 6, the output voltage variation in sudden load change is less than 5V (1.30%). and.994 and 0.972

© ISAROB 2013

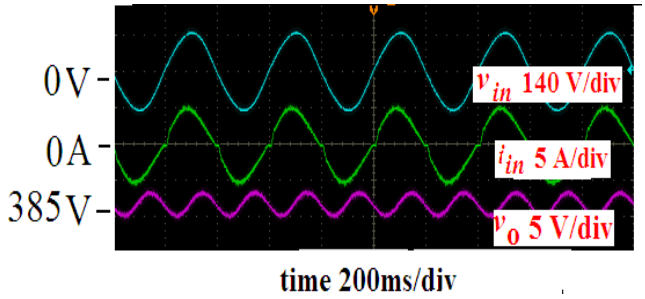

Fig, 4 Experimental Results of Steady State Waveform, at load RL=500Ω controlling the current for every phase

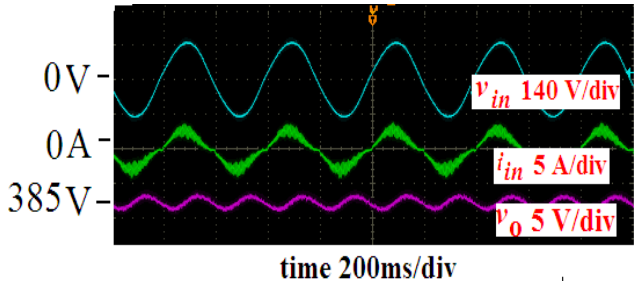

Fig.5 Experimental Results of Steady State Waveform, at load RL=1kΩ controlling the current for every phase

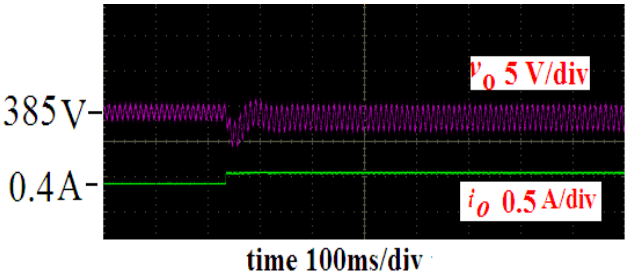

Fig.6 Experimental Results of Sudden Load Change from 1kΩ to 500Ω controlling the current for every phase

When controlling the current of the sum of each phase, one $G_i(z)$ and $G_v(z)$ are needed. Then the PI controller parameters are as follows:

$$k_{ri} = 1.0 \qquad k_{ii} = 0.2$$
$$k_{ri} = 0.28 \qquad k_{iv} = 0.001$$

The experiment results of this case are shown in Fig. 7, 8, 9. From Fig.8, at the light load the harmonic is reduced. PFC of converter at load RL=500Ωand 1kΩ are 0.994 and 0.972, respectively. So it turns out that and the PI digital controllers are more advantageous to control the current of the sum of each phase in performance and hardware.

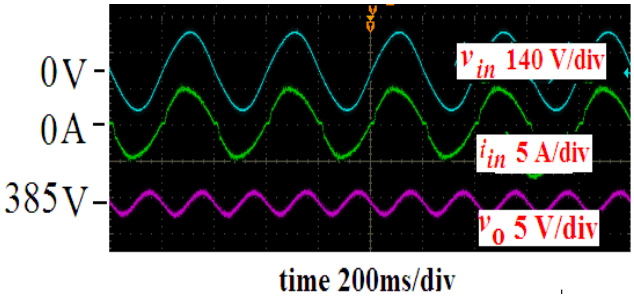

Fig.7 Experimental Results of Steady State Waveform, at load RL=500Ωcontrolling the current of the sum of each phase

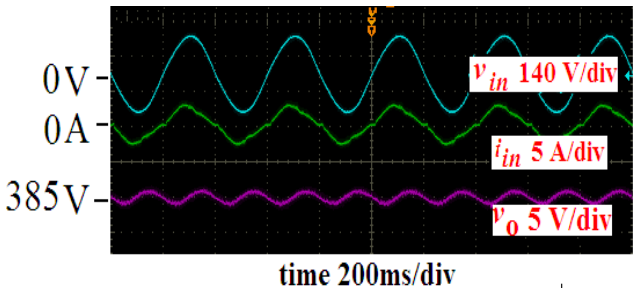

Fig.8 Experimental Results of Steady State Waveform, at load RL=1kΩ controlling the current of the sum of each phase

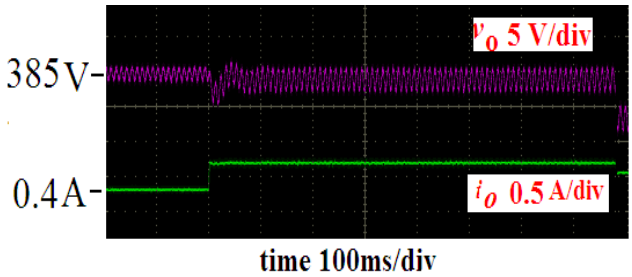

Fig.9 Experimental Results of Sudden Load Change from 1 kΩ to 500Ωcontrolling the current of the sum of each phase

4 CONCLUSION

. In this paper, the concept of controller of non-linear PFC boost converter with DC-DC converter load to attain good robustness was given. It was shown from experiments that the proposed A2DOF digital controller can attain better performance.

REFERENCES

[1] S. Sasaki, and H. Watanabe (2005), Analysis of Multiple Operating Points for Dynamical Control of Switching Power Converters (in Japanese). IEIC Technical Report, pp.33-38

© ISAROB 2013

The Eighteenth International Symposium on Artificial Life and Robotics 2013 (AROB 18th '13),
Daejeon Convention Center, Daejeon, Korea, January 30-February 1, 2013

Adaptive Steering Controller for Vehicles with Driving/Braking Force Distribution

Bo Zhou, Masahiro Oya, Jinxin Zhuo, Panfeng Shu

Department of Mechanical and Control Engineering, Kyushu Institute of Technology
1-1 Sensui-cho, Tobata-ku, Kitakyushu-City, Fukuoka, Japan
(Tel: +81-93-884-3186; Fax: +81-93-861-1159)

k344232s@tobata.isc.kyutech.ac.jp

Abstract: In this paper, we propose an adaptive steering controller with driving/braking force distribution of direct yaw-moment. To achieve good steering performance, a design scheme for ideal vehicle model is proposed. To consider the effects of the driver dynamics, in the scheme, numerical simulations including a driver model are carried out and an ideal vehicle model having good steering performance is designed by using a trial and error method. To realize the good steering performance also in the actual vehicles, an adaptive tracking controller is developed so that the behavior of the actual vehicle can track that of the designed ideal vehicle model.

Key word: steering control of vehicle, adaptive tracking control, ideal vehicle model

1 INTRODUCTION

When a vehicle is running on the low-μ road surface, it is very difficult to achieve good steering performance. In recent years, in order to overcome the problem, active Four-Wheel Steering(4WS) schemes have been proposed [1]-[4]. In the methods, it is assumed that tire lateral forces are linear with respect to steering angles and saturations are not occurred. If the saturations of tire lateral forces are ignored and a steering controller is designed, good steering performance cannot be expected. To address the problem, the control schemes[5]-[6] using Direct Yaw-moment Control(DYC) have been developed. However, in these schemes, the saturations of the tire driving/braking force have not been taken into account. Caused by the influence of the driving/braking force and the lateral forces, the saturations of tire forces may occur. Recently, a scheme[7] has been proposed that can prevent steering instability caused by the saturations of tire forces. To achieve the objective, in the scheme, an optimal distribution of driving/braking force was used and a sliding mode controller was employed to guarantee good robust performance. However, chattering of control input will occur. Furthermore, there is the problem that the influence of the driver characteristics has not been considered.

In order to improve the steering stability on the low-μ road surface, we propose a new adaptive steering control scheme with driving/braking force distribution. By employing an adaptive control scheme, chattering of control input does not occur and good robust performance can be achieved. In the control scheme, the variation of the driver characteristics is taken into consideration. Carried out numerical simulations including the driver characteristics, the effectiveness of the proposed controller is shown.

2 VEHICLE MODEL

In this paper, we use the two degrees of freedom Four-Wheel Steering vehicle model shown in Fig.1. The explanations of parameters are shown in Table 1. The motion equation of the vehicle is given as follows. The state variable $\boldsymbol{z}(t)=\begin{bmatrix} v_y & \gamma \end{bmatrix}^T$ expresses lateral velocity $v_y(t)$ and yaw rate $\gamma(t)$ of vehicle, and $\boldsymbol{u}(t)=\begin{bmatrix} u_f & u_r & M \end{bmatrix}^T$ is input that includes steering angle of front and rear wheels and yaw-moment.

$$
\begin{aligned}
&M_c\dot{\boldsymbol{z}}(t)=\left(-v_x^{-1}HKH^T-M_cD\right)\boldsymbol{z}(t)+HK\boldsymbol{u}(t)\\
&K=\begin{bmatrix} 2K_f & 0 & 0\\ 0 & 2K_r & \dfrac{1}{I_z}\end{bmatrix},H=\begin{bmatrix} 1 & 1\\ l_f & -l_r\end{bmatrix}\\
&D=\begin{bmatrix} 0 & v_x\\ 0 & 0\end{bmatrix},M_c=\begin{bmatrix} m & 0\\ 0 & I_z\end{bmatrix}
\end{aligned}
\tag{1}
$$

3 CONVENTIONAL METHOD[7]

In this section, we explain a distribution method and problems of conventional control system method.

3.1 Necessity of driving/braking force distribution

If the resultant force vector of driving/braking force X and lateral force Y remains in the circle of radius μZ where Z is the vertical load of the tire and μ road surface friction coefficient, the vehicle can be driven stably. The circle of radius μZ is called friction circle(see Fig.2) and represented by the following equation.

$$\sqrt{X^2+Y^2}\le \mu Z \tag{2}$$

We defined the new signal μ_i as the estimated load

$$\sqrt{\frac{X_i^2+Y_i^2}{Z_i^2}}=\mu_i. \tag{3}$$

If one of the estimated load μ_i is greater than the road surface friction coefficient μ, the saturation of the tire forces occur. Then, the behavior of vehicle will become unstable. Therefore, in order to prevent saturation of the tire force, it is necessary to redistribute the forces of tires.

© ISAROB 2013

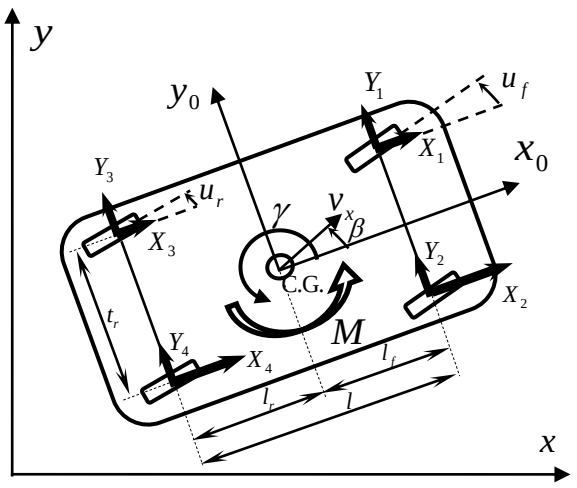

Fig.1. Vehicle model

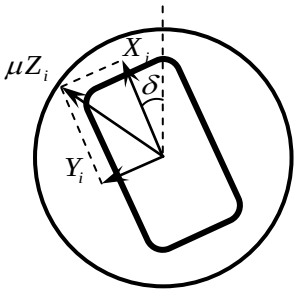

Fig.2. Friction circle

3.2 Optimum minimax distribution

As mentioned in the previous subsection, no saturation of the tire force occurs as long as the following equation holds.

$$\max \mu_i \le \mu \tag{4}$$

To hold the equation, tire forces are redistributed so that the estimated load of the tires may become same as follows.

$$\mu_1 = \mu_3, \mu_2 = \mu_4 \tag{5}$$

3.3 Problems of the conventional method

In the paper[7], a sliding mode controller is proposed to achieve good robust tracking performance for the parameter uncertainty of the vehicle(Fig.3). However, in order to prevent chattering in the control input, the controller was approximated as

$$\mathrm{sgn}(\sigma_i) = \frac{\sigma_i}{|\sigma_i|} \approx \frac{\sigma_i}{|\sigma_i| + \tau_i}, \tau_i > 0 (i = 1, 2). \tag{6}$$

Reducing the value of τ_i, control performance can be improved. However, chattering will occur in the control input. In addition, the driver characteristics have not considered in the control system shown in Fig.3.

4 DESIGN OF IDEAL VEHICLE MODEL

4.1 Driver model

In this paper, in order to design the ideal vehicle model that takes into account the variation of the driver steering characteristics, we used a predicted driver model[8]. Steering dynamics is given as

$$T_s \ddot{\delta}_c(t) + \dot{\delta}_c(t) = -g_p \dot{\tilde{y}}(t) - g_i \tilde{y}(t) \tag{7}$$

where T_s is a steering constant including the delay of muscular system and mechanical systems, T_p is predicted time and g_p, g_i are the gain steering. The predicted deviation $\tilde{y}(t)$ at the predicted position P_p is given by

$$\tilde{y}(t) = y_r(t) + T_p \dot{y}_r(t) \tag{8}$$

where $y_r(t)$ is relative deviation between target lane and vehicle.

Table 1. Notation of vehicle

C.G.	center of gravity of vehicle
m	mass of vehicle
m_s	sprung mass
m_{fs}, m_{rs}	unsprung mass of front and rear wheels
X_i, Y_i	driving/braking force and lateral force of the tire i
Z_i	vertical load of the tire
M	yaw moment
β_i, β	side slip angle of tire and vehicle body center
γ	yaw rate
u_f, u_r	steering angle of front and rear wheels
I_z	yaw moment of inertia of vehicle
v	longitudinal velocity
a_y	lateral acceleration of vehicle center of gravity
a_x	longitudinal acceleration of vehicle center of gravity
l_f, l_r	distance from C.G to front and rear wheels
l	wheelbase
t_r	tread
K_f, K_r	cornering stiffness of front and rear wheels
h_s	height of the center of gravity of the sprung weight

4.2 Ideal vehicle model

Based on the design scheme of ideal model proposed in [8], we use the ideal vehicle model given by

$$v_{yd}(t) = L^{-1}\left[\frac{g_v \omega^2 s}{s^2 + 2\xi\omega s + \omega^2} L\left[v_x \delta_c(t)\right]\right] \tag{9}$$

$$\gamma_d(t) = L^{-1}\left[\frac{g_\gamma \omega^2 (s\eta + 1)}{s^2 + 2\xi\omega s + \omega^2} L\left[v_x \delta_c(t)\right]\right] \tag{10}$$

where s is Laplace operator, L, L^{-1} represent Laplace transform and Inverse Laplace transform, $\omega, \xi, \eta, g_v, g_\gamma$ are positive design parameters.

In the case that commanded steering angle $\delta_c(t)$ is constant(steady-state circular), ideal lateral velocity $v_{yd}(t)$ is asymptotic to zero, and ideal yaw rate $\gamma_d(t)$ is converged to a constant value as $\lim_{t\to\infty} \gamma_d(t) = \bar{\gamma}_d$. Then, the vehicle will be driven in contact with a circle of radius $v_x / \bar{\gamma}_d$. This is one of the advantages of the ideal vehicles model given by (9) and (10).

In below, we show a design method of parameters in the ideal vehicle model mentioned above.

(1) To prevent vibration in the ideal vehicle model, ξ sets as 1.

(2) In the passive vehicle, when the speed v_x is constant, the steady gain from the front wheel steering angle to the

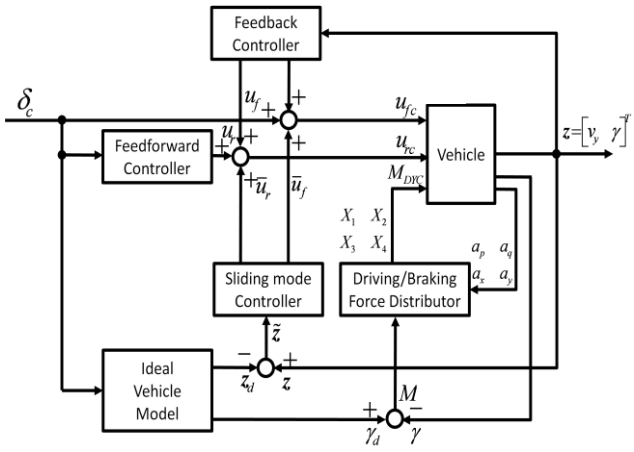

Fig.3. Block diagram of the conventional scheme

Table 2. Nominal values of vehicle parameter

m	1070Kg	l_f	1.033m
m_s	860Kg	l_r	1.657m
m_{fs}	120 Kg	t_r	1.540m
m_{rs}	80 Kg	h_s	0.542m
K_f	29770N/rad	K_r	41460N/rad
I_z	1507[kgm^2]		

yaw rate is give by

$$g_{p\gamma} = \frac{2.10\times10^2}{5.25\times10^2 + 1.8v_x(t)^2} \quad . \tag{11}$$

We set the parameter g_γ as $g_\gamma = g_{p\gamma}$ so that the steady yaw rate gain of the ideal vehicle model becomes the same as that of the passive vehicle.

(3) Carrying out numerical simulations with the driver model and using a trial and error technology, we set the design parameters ω, g_v, η so that good steering performance can be achieved for any driver's characteristics $0.05\text{s} \le T_s \le 0.4\text{s}, 1.5\text{s} \le T_p \le 4.5\text{s}, 0 \le g_p \le 1,$ $0 \le g_i \le 1$.

$$\omega = 5.4, g_v = 0.25, \eta = 0.39 \tag{12}$$

5 ADAPTIVE TRACKING CONTROLLER

In order to design the adaptive steering controller which makes behavior of actual vehicle track that of ideal vehicle model, we define the following tracking error $\tilde{\boldsymbol{z}}(t)$.

$$\tilde{\boldsymbol{z}}(t) = \boldsymbol{z}(t) - \boldsymbol{z_d}(t) \tag{13}$$

Where $\boldsymbol{z_d}(t) = \begin{bmatrix} v_{yd} & \gamma_d \end{bmatrix}^T$ represents the state of the ideal vehicle model. If we can realize $\lim_{t\to\infty} \tilde{\boldsymbol{z}}(t) = \begin{bmatrix} 0 & 0 \end{bmatrix}^T$, the behavior of actual vehicle can track that of designed ideal vehicle model.

Error equation of the tracking error $\tilde{\boldsymbol{z}}(t)$ is given by

$$M_c\dot{\tilde{\boldsymbol{z}}}(t) = -v_x^{-1}HKH^T\tilde{\boldsymbol{z}}(t) + HK\left[\boldsymbol{u}(t) - v_x^{-1}H^T\boldsymbol{z_d}(t) - \Theta(t)\boldsymbol{\omega}(t)\right], \tag{14}$$

$$\Theta(t) = \left(M_c^{-1}HK\right)^{-1}, \tag{15}$$

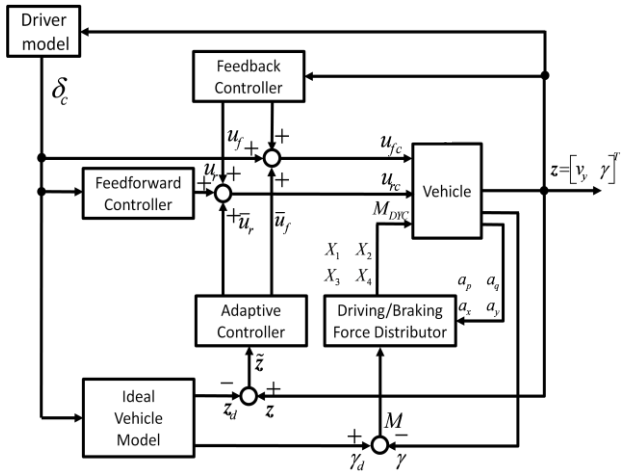

Fig.4. Block diagram of the proposed scheme

$$\boldsymbol{\omega}(t) = D\boldsymbol{z}(t) + M_c\dot{\boldsymbol{z}}_{\boldsymbol{d}}(t). \tag{16}$$

The adaptive tracking controller is designed as

$$\boldsymbol{u}(t) = -\beta H^T\tilde{\boldsymbol{z}}(t) + v_x^{-1}H^T\boldsymbol{z_d}(t) + \hat{\Theta}(t)\boldsymbol{\omega}(t) \tag{17}$$

$$\dot{\hat{\Theta}}(t) = -\tilde{\boldsymbol{z}}(t)^T H\bar{K}\boldsymbol{\omega}(t)^T\Gamma, \tilde{\Theta}(t) = \Theta(t) - \hat{\Theta}(t) \tag{18}$$

where β is positive design parameter, Γ is positive definite matrix, $\bar{K}$ is the nominal value of conering stiffness K and $\hat{\Theta}(t)$ is the estimated matrix of unknown matrix $\Theta(t)$. Fig.4 shows the configuration of the proposed control system.

6 NUMERICAL SIMULATION

The numerical simulations were carried out in order to show the effectiveness of the proposed controller. In the simulations, the values of parameters of the vehicle are shown in Table 2. The driver parameters are set as T_s=0.1s, T_p=1.5s, g_p=g_i=0.05, and the target lane is a circular lane of radius 400m.

Fig.5(a), (b) show the responses of acceleration and longitudinal velocity of the vehicle. The responses of the controlled vehicle, the passive vehicle and the ideal vehicle model are shown in Fig.5(c)-(f). Fig.5 (c) shows the trajectory of vehicles, Fig.5(d) shows the responses of driver's steering angle, Fig.5(e) shows the responses of yaw rate of vehicles, and Fig.5(f) show responses of the relative deviation between target lane and the vehicle.

As shown in Fig.5(d), in the case of deceleration, vibration occurs in the responses of the steering angle and the yaw rate of the passive vehicle. However, in the controlled vehicle, the steering angle and the yaw rate become smooth. From this, it can be expected that driver's burdens is improved in the controlled vehicle. Moreover, as shown in Fig.5(f), the relative deviation between the passive vehicle and target lane is larger than that of the controlled vehicle. From this, it can be seen that the controlled vehicle is more stable than the passive vehicle.

7 CONCLUSION

© ISAROB 2013

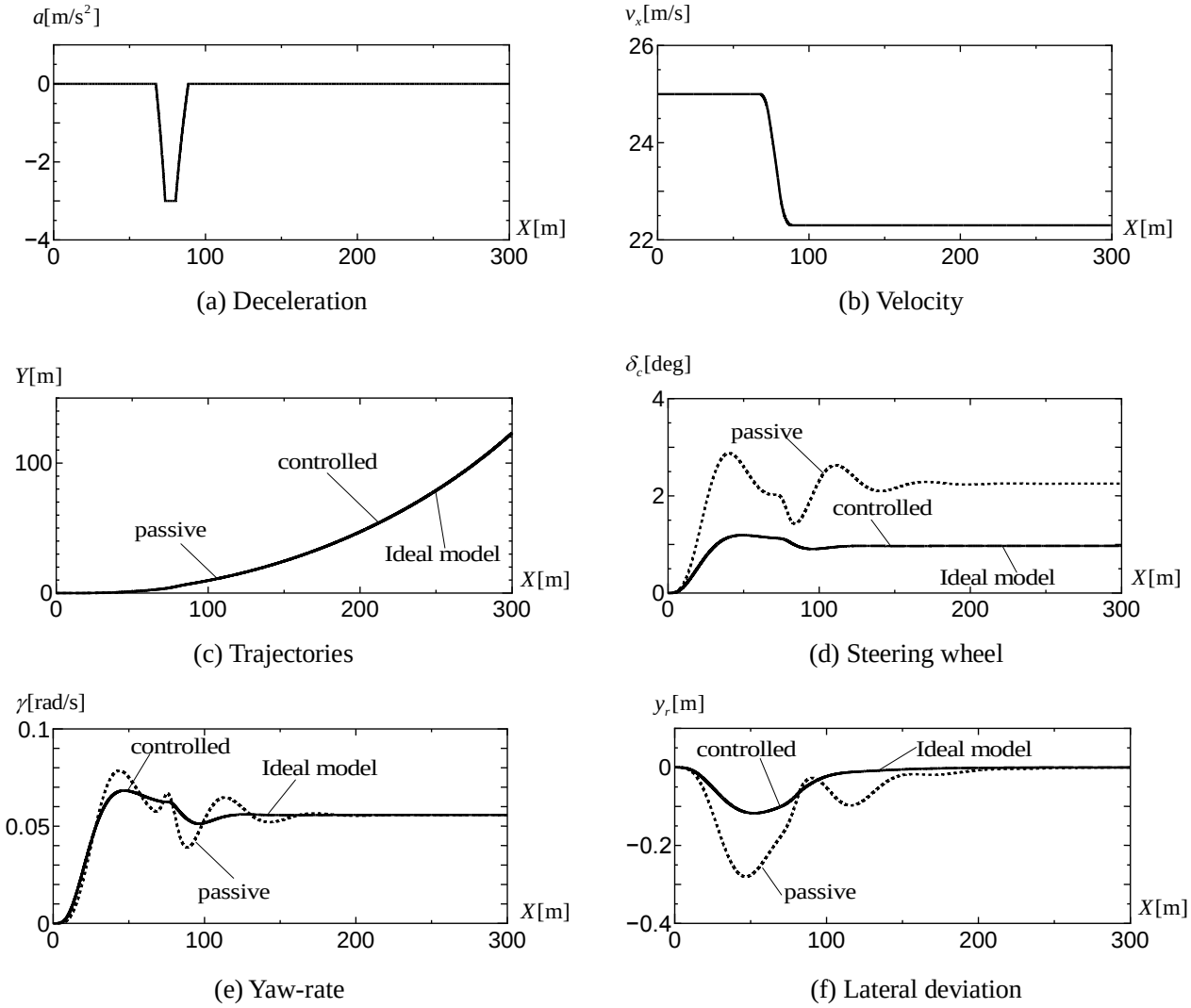

Fig. 5 Simulation results

In this paper, we propose an adaptive steering controller with driving/braking force distribution to improve the steering stability in low-μ road surface. Carrying out numerical simulations, it has been shown that the control objective was achieved.

REFERENCES

[1] J.Ackermann , T.B ünte , and D.Odentha , Advantages of active steering vehicle dynamic contr. 99ME013,1999.

[2] Willy Klier, Gerd Reimann and Wolfgang Reinelt, Concept and Functionality of the Active Front Steering System 2003 SAE International 2004-21-0073.

[3] Toshihiro Hiraoka, Osamu Nishihara, Hiromitsu Kumamoto, Model Following Sliding Mode Control for Active Four-Wheel Steering Vehicle , JSAE Spring Convention No. 77-03(2003-9), 5-10.

[4] Toshihiro Hiraoka, Osamu Nishihara and Hiromitsu Kumamoto, Automatic path-tracking controller of a four-wheel steering vehicle. Vehicle System Dynamics Vol. 47, No. 10, October 2009, 1205–1227.

[5] NAGAI Masao, YAMANAKA Sachiko, HIRANO Yutaka, Integrated Control of Active Rear Wheel Steering and Yaw Moment Control Using Braking Forces, Trans. Jpn. Soc. Mech. Eng, 64－622C(1998), 2132－2193.

[6] Sagai shin-ichiro, Sado Hideo, Hori Yoichi, Dynamic Driving/Braking Force Distribution in Electric Vehicle with Independently Driven Four Wheels, IEEJ Transactions D, 120－D－6(2000) , 761－768.

[7] Toshihiro Hiraoka, Osamu Nishihara and Hiromitsu Kumamoto, Driving/Braking Force Distribution by Minimax Optimization of Tire workload(Case of Active Four-Wheel Steering for Zero-sideslip Control), Trans. Jpn. Soc. Mech. Eng. Vol. 71, No. 704, 2005-4.

[8] Masahiro OYA Yoshiaki ARAKI Trans. Jpn. Soc. Mech. Eng(C), 75-715(2006-3) No.05-0591.

© ISAROB 2013

The Eighteenth International Symposium on Artificial Life and Robotics 2013 (AROB 18th '13),
Daejeon Convention Center, Daejeon, Korea, January 30-February 1, 2013

Oscillation Control of a Contact Scanning Scanners System

Hideki Wada[1], Hiroyuki Koga[2], Katsuhiro Okumura[3] and Masahiro Oya[2]
[1]Shin-Nippon Nondestructive Inspection Co.,4-10-13 Ibori, Kokurakita-ku, Kitakyusyu-shi, Fukuoka, 803-8517 Japan
(Tel: 81-93-581-1256, Fax: 81-93-581-2232, E-mail: h-wada@shk-k.co.jp)
[2]Kyushu Institute of Technology, 1-1 Sensui-cho, Tobata-ku, Kitakyusyu-shi, Fukuoka, 804-8550 Japan
[3]Fukuoka Industrial Technology Center, Norimatu, Yahatanisi-ku, Kitakyusyu-shi, Fukuoka 807-0831 Japan

Abstract: In the inspection of the deterioration state of the structures such as plants, contact scanning type sensors are useful devices. Using the sensors, we can check deterioration of structure and matter inside pipes during the production process. However, in case of the high-speed scanning, oscillation occurs in the sensor part due to unevenness and friction on the measured surface. In this paper, to overcome the problem, we propose an oscillation controller for scanning sensor systems. At last, to show the effectiveness of the proposed controller, numerical simulations are carried out.

Keywords: The scanning system of a sensor, Contact type sensor, Oscillation control, Accelerometers, Ultrasonic sensor

1 INTRODUCTION

In the inspection of the deterioration state of the structures such as plants, the manufacturing inspection of metals, inspection of the welded junction part and so on, usually, contact type scanning sensor systems [1-5] with ultrasonic are used. In case of the high-speed scanning, oscillation occurs in the sensor part due to unevenness and friction on the measured surface. If oscillation occurs in the sensor part, measurement accuracy may worsen remarkably caused by the fluctuation of the ultrasonic incident angle to inspection surface. In addition, the durability of the mechanism of inspection systems is also reduced. For the reasons, in the real inspection, a slow scanning speed is used to achieve the measurement accuracy. Moreover, since the amplitude of oscillation varies according to surface conditions of materials, the operators need to determine the scanning speed by using a trial and error technology so that the occurred oscillation in the sensor part can be reduced in the permissible level. To address the problem, there are the following two methods. One is to increase the number of sensors. Another one is to control oscillation of the sensor part with accurate measurements of the oscillation. However, both methods require expensive measuring instruments and sensors.

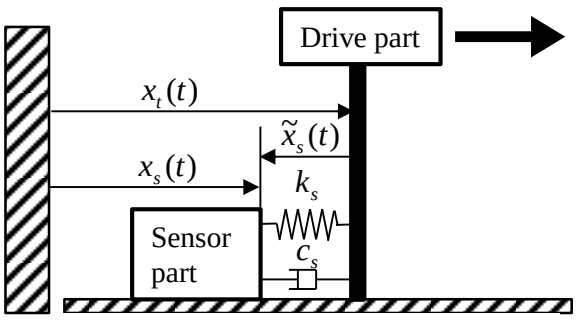

Fig.1 Simplified Model

In this research, in order to overcome the problem mentioned above, we propose a new oscillation controller. One of the main features of the controller is that cheap accelerometers are only used for measurements of the sensor part.

2 CONTROL OBJECT AND CONTOROL PURPOSE

Fig. 1 shows the simplified model of a scanning type sensor system. The dynamic equation of this model is expressed by the following equation. The symbol $f(t)$ denotes the dead zone and shows friction occurring in the sensor part. In addition, explanations of the symbols used in the following equations are shown in Table.1, and the nominal values of parameters are shown in Table.2.

$$\ddot{x}_t(t) = -\frac{c_t}{m_t}\dot{x}_t(t) + \frac{b_t}{m_t}u(t) \tag{1}$$

$$\ddot{\tilde{x}}_s(t) = f(t) - \ddot{x}_t(t) \tag{2}$$

$$f(t) = \begin{cases} -\frac{c_s}{m_s}\dot{\tilde{x}}_s(t) - \frac{k_s}{m_s}\tilde{x}_s(t) - d & -\frac{c_s}{m_s}\dot{\tilde{x}}_s(t) - \frac{k_s}{m_s}\tilde{x}_s(t) > d \\ 0 & \left|-\frac{c_s}{m_s}\dot{\tilde{x}}_s(t) - \frac{k_s}{m_s}\tilde{x}_s(t)\right| \le d \\ -\frac{c_s}{m_s}\dot{\tilde{x}}_s(t) - \frac{k_s}{m_s}\tilde{x}_s(t) + d & -\frac{c_s}{m_s}\dot{\tilde{x}}_s(t) - \frac{k_s}{m_s}\tilde{x}_s(t) < -d \end{cases} \tag{3}$$

The control objective is to reduce the oscillation of $|\tilde{x}_s(t)|$. To achieve the objective, we make the following assumptions for the controlled object.

A1: The position $x_t(t)$ and speed $\dot{x}_t(t)$ of the drive part are measurable.

© ISAROB 2013

A2: The position $x_s(t)$ and speed $\dot{x}_s(t)$ of the sensor part can not be measured.

A3: The acceleration $\ddot{x}_t(t)$ and the relative acceleration $\ddot{\tilde{x}}_s(t)$ are measurable.

3 OSCILLATION CONTROL SCHEMES

In order to simplify development of an oscillation controller, consider the linearized model of the inspection system given as

$$\ddot{x}_t(t) = -\frac{c_t}{m_t}\dot{x}_t(t) + \frac{b_t}{m_t}u(t) \tag{4}$$

$$\ddot{\tilde{x}}_s(t) = -\frac{c_s}{m_s}\dot{\tilde{x}}_s(t) - \frac{k_s}{m_s}\tilde{x}_s(t) - \ddot{x}_t(t) \tag{5}$$

where c_s is a small damping constant and k_s is a spring constant.

In the equation (5), if it is assumed that the signal $\ddot{x}_t(t)$ can be used as a control input, we may use the controller given by

$$\ddot{x}_t(t) = \alpha\dot{\tilde{x}}_s(t) \tag{6}$$

where α is a design parameter. By using this control input, the oscillation can be reduced in a relative position $\tilde{x}_s(t)$. However, according to the assumption A2, the relative speed $\dot{\tilde{x}}_s(t)$ is unavailable. Moreover, in fact, $\ddot{x}_t(t)$ cannot be used as an input signal.

In order to overcome the problem, the following new signal is defined.

$$\ddot{\tilde{x}}_t(t) = \ddot{x}_t(t) - \alpha L^{-1}\left[\frac{Ts}{Ts+1}\frac{T}{Ts+1}\ddot{\tilde{X}}_s(s)\right] - \dot{v}_{td}(t) \tag{7}$$

Here, T is the design parameter, and $v_{td}(t)$ is the ideal speed of the drive part given by

$$V_{td}(s) = \frac{\omega_n^2}{s^2 + 2\xi\,\omega_n\, s + \omega_n^2}V_d(s) \tag{8}$$

where ω_n, ς are design parameters and v_d is the final constant speed.

$$\frac{Ts}{Ts+1}\frac{T}{Ts+1}\ddot{X}_s(s) = \left(\frac{Ts}{Ts+1}\right)^2\dot{X}_s(s) \tag{9}$$

The right hand side denotes the high frequency signals of $\ddot{\tilde{x}}_s(t)$. Using the new signal (7) in (5) and rewriting, we have

Table.1 Notation of Board Thickness Scanners

x_t	position of drive division
$\tilde{x}_s$	relative position of sensor division to drive system
m_t, m_s	mass of drive part and sensor part
b_t, c_t	gain of input and viscosity resistance of motor
k_s, c_s	spring constant and damper constant
u	control input

Table.2 Simulation parameter

$\frac{b_t}{m_t}$	0.55	$\frac{k_s}{m_s}$	2518	d	0.9
$\frac{c_t}{m_t}$	5.05	$\frac{c_s}{m_s}$	1.88		

$$\tilde{X}_s(s) = G_s(s)\left(\ddot{\tilde{X}}_t(s) + \dot{V}_{td}(s)\right) \tag{10}$$

$$\left.\begin{aligned} A_{z41} &= \frac{k_s}{m_s}\frac{1}{T^2}\ ,\ A_{z42} = 2\frac{k_s}{m_s}\frac{1}{T} + \frac{c_s}{m_s}\frac{1}{T^2} \\ A_{z43} &= \frac{k_s}{m_s} + 2\frac{c_s}{m_s}\frac{1}{T} + \frac{1}{T^2} \\ A_{z44} &= \frac{c_s}{m_s} + \alpha + \frac{2}{T} \end{aligned}\right\} \tag{11}$$

where the design parameter α and T are set so that the transfer function $G_s(s)$ can become asymptotically stable. Since the ideal acceleration $\dot{v}_{td}(t)$ of the drive pert converges to zero, if $\ddot{\tilde{x}}_t(t)$ can be designed so as to converge to zero, then, $\tilde{x}_s(t)$ becomes also asymptotically stable. In order to realize this, a new state

$$\boldsymbol{x}(t) = \left[\dot{\tilde{x}}_t(t) \quad \ddot{\tilde{x}}_t(t)\right]^T \tag{12}$$

is defined. Using the state, we have

$$\dot{\boldsymbol{x}}(t) = A\,\boldsymbol{x}(t) + B\,\boldsymbol{z}(t) + D\boldsymbol{v}_d(t) + \boldsymbol{b}\left(\dot{u}(t) + u(t)\right) \tag{13}$$

$$\left.\begin{aligned} &\mathbf{z}(t) = \left[z_1 \quad z_2 \quad z_3 \quad z_4\right]^T \\ &z_i = L^{-1}\left[\frac{s^{i-1}}{(Ts+1)^2}\tilde{X}_s(s)\right]\ (i = 1,2,3,4) \\ &\mathbf{v}_d(t) = \left[v_{td}(t) \quad \dot{v}_{td}(t) \quad \ddot{v}_{td}(t)\right]^T \\ &A = \begin{bmatrix} 0 & 1 \\ -\frac{c_t}{m_t} & -\left(\frac{c_t}{m_t} + 2\right) \end{bmatrix},\ \mathbf{b} = \begin{bmatrix} 0 \\ \frac{b_t}{m_t} \end{bmatrix} \\ &B = \begin{bmatrix} 0 & 0 & 0 & 0 \\ B_{21} & B_{22} & B_{23} & B_{24} \end{bmatrix} \\ &D = \begin{bmatrix} 0 & 0 & 0 \\ -\frac{c_t}{m_t} & -\left(\frac{c_t}{m_t} + 2\right) & -1 \end{bmatrix} \\ &B_{21} = -\left(\frac{c_s}{m_s} + \frac{c_t}{m_t} + 1\right)T^2 + 2T \\ &B_{22} = -\left(\frac{c_t}{m_t} + \frac{k_s}{m_s}\right)T^2 - 2\frac{c_s}{m_s}T + 1 \\ &B_{23} = -\alpha T^2 + 2\frac{k_s}{m_s}T + \frac{c_s}{m_s}\ ,\ B_{24} = \frac{k_s}{m_s} \end{aligned}\right\} \tag{14}$$

$$\dot{\boldsymbol{z}}(t) = A_z\boldsymbol{z}(t) + B_z\boldsymbol{x}(t) + D_z\boldsymbol{v}_d(t) \tag{15}$$

© ISAROB 2013

$$\left.\begin{aligned} A_z &= \begin{bmatrix} 0 & 1 & 0 & 0 \\ 0 & 0 & 1 & 0 \\ 0 & 0 & 0 & 1 \\ A_{z41} & A_{z42} & A_{z43} & A_{z44} \end{bmatrix} \\ B_z &= \begin{bmatrix} 0 & 0 \\ 0 & 0 \\ 0 & 0 \\ 0 & -\dfrac{1}{T^2} \end{bmatrix}, \quad D_z = \begin{bmatrix} 0 & 0 & 0 & 0 \\ 0 & 0 & 0 & -\dfrac{1}{T^2} \\ 0 & 0 & 0 & 0 \end{bmatrix} \end{aligned}\right\} \quad (16)$$

where A_z is an asymptotically stable matrix. Based on the system, we developed the following controller.

$$\dot{u}(t) = -u(t) - \boldsymbol{k}^T \boldsymbol{x}(t) \ , \boldsymbol{k}^T = \begin{bmatrix} \beta^2 \dfrac{m_t}{b_t} & 2\beta \dfrac{m_t}{b_t} \end{bmatrix} \quad (17)$$

Where β is the design parameter. Using the new state

$$\mathbf{x}_\beta(t) = \mathrm{diag}[1 \quad \beta^{-1}]\mathbf{x}(t) \quad (18)$$

we have

$$\begin{aligned} \dot{\mathbf{x}}_\beta(t) &= \beta A_\beta \mathbf{x}_\beta(t) + \left(A_{\beta 1} + \beta^{-1} A_{\beta 2}\right)\mathbf{x}_\beta(t) \\ &\quad + \beta^{-1} B\, \mathbf{z}(t) + \beta^{-1} D\, \mathbf{v}_d(t) \end{aligned} \quad (19)$$

$$\dot{\mathbf{z}}(t) = A_z \mathbf{z}(t) + \beta B_z \mathbf{x}_\beta(t) + D_z \mathbf{v}_d(t) \quad (20)$$

$$\left.\begin{aligned} A_\beta &= \begin{bmatrix} 0 & 1 \\ -1 & -2 \end{bmatrix}, \ A_{\beta 1} = \begin{bmatrix} 0 & 0 \\ 0 & -\left(\dfrac{c_t}{m_t} + 2\right) \end{bmatrix} \\ A_{\beta 2} &= \begin{bmatrix} 0 & 0 \\ -\dfrac{c_t}{m_t} & 0 \end{bmatrix} \end{aligned}\right\} \quad (21)$$

The stability of the control system (19)-(21) using the controller (17) is shown below.

Theorem: In the control system (19)-(21), the design parameter β is set such that the following inequalities are satisfied.

$$\rho_{x1} = \frac{1}{2}\rho_1 - \beta^{-1}\left(\rho_2 + \rho_3 + \rho_4\right) > 0 \quad (22)$$

$$\rho_{z1} = \frac{1}{4}\rho_{vz}\rho_5 - \beta^{-1}\rho_3 > 0 \quad (23)$$

$$\left.\begin{aligned} &\rho_1 = \lambda_{\min}\left[Q_\beta\right], \rho_2 = 2\left(\left\|P_\beta A_{\beta 1}\right\| + \left\|P_\beta A_{\beta 2}\right\|\right), \\ &\rho_3 = \left\|P_\beta B\right\|, \rho_4 = \left\|P_\beta D\right\|, \rho_5 = \lambda_{\min}\left[Q_z\right] \\ &\rho_{vz} = \frac{\rho_1 \rho_5}{\left\|P_z B_z\right\|^2} \end{aligned}\right\} \quad (24)$$

Where matrixes P_β and P_z are the positive definite matrix solutions of the Liapounov equations as

$$\begin{aligned} A_\beta{}^T P_\beta + P_\beta A_\beta &= -Q_\beta, \quad Q_\beta > 0 \\ A_z{}^T P_z + P_z A_z &= -Q_z, \quad Q_z > 0 \end{aligned} \quad (25)$$

If the initial states are $\boldsymbol{x}_\beta(0) = 0$ and $\mathbf{z}(0) = 0$, there exists a positive constant ρ_6 independent of the design parameter β such that

$$\left\|\boldsymbol{x}_\beta(t)\right\|^2 \le \beta^{-4}\rho_6 \quad (26)$$

Proof: Consider the positive definite function $V_1(t)$.

$$V_1(t) = \mathbf{x}_\beta^T(t) P_\beta \mathbf{x}_\beta(t) + \beta^{-1}\rho_{vz}\mathbf{z}^T(t) P_z \mathbf{z}(t) \quad (27)$$

The time derivative of $V_1(t)$ satisfies the following relation.

$$\dot{V}_1 \le -\beta\rho_{x1}\left\|\boldsymbol{x}_\beta(t)\right\|^2 - \beta^{-1}\rho_{z1}\left\|\mathbf{z}(t)\right\|^2 + \beta^{-1}\rho_7 \quad (28)$$

The parameter ρ_7 is a positive constant independent of the design parameter β. Consider the inequalities

$$\left.\begin{aligned} &2\beta^{-1}\rho_3\left\|\mathbf{x}_\beta(t)\right\|\left\|\mathbf{z}(t)\right\| \le \rho_3\left(\left\|\mathbf{x}_\beta(t)\right\|^2 + \beta^{-2}\left\|\mathbf{z}(t)\right\|^2\right) \\ &2\beta^{-1}\rho_4\left\|\mathbf{x}_\beta(t)\right\|\left\|\mathbf{v}_d(t)\right\| \le \rho_4\left\|\mathbf{x}_\beta(t)\right\|^2 + \beta^{-2}\rho_8 \\ &2\rho_{vz}\left\|P_z B_z\right\|\left\|\mathbf{z}(t)\right\|\left\|\mathbf{x}_\beta(t)\right\| \le \frac{1}{2}\beta^{-1}\rho_{vz}\rho_5\left\|\mathbf{z}(t)\right\|^2 \\ &\qquad\qquad + \frac{1}{2}\beta\rho_1\left\|\mathbf{x}_\beta(t)\right\|^2 \\ &2\beta^{-1}\rho_{vz}\left\|P_z D_z\right\|\left\|\mathbf{z}(t)\right\|\left\|\mathbf{v}_d(t)\right\| \le \frac{1}{4}\beta^{-1}\rho_5\left\|\mathbf{z}(t)\right\|^2 + \beta^{-1}\rho_9 \end{aligned}\right\} \quad (29)$$

where ρ_8 and ρ_9 are positive constants independent of the design parameter β. Using (29), (23) and (24), we have

$$\dot{V}_1(t) \le -\rho_v V_1(t) + \beta^{-1}\rho_{10} \quad (30)$$

where ρ_{10} is a positive constant independent of the design parameter β. From (30), it can be seen that the control system becomes stable. Moreover, it can be obtain that there exists a positive constant ρ_z independent of the design parameter β such that $\left\|\mathbf{z}(t)\right\| \le \rho_z$.

In order to analyze the detail control performance of the control system, consider the following positive definite function $V_2(t) = \boldsymbol{x}_\beta^T(t) P_\beta \boldsymbol{x}_\beta(t)$. Using the relations

$$\begin{aligned} &2\beta^{-1}\rho_3\left\|\mathbf{x}_\beta(t)\right\|\left\|\mathbf{z}(t)\right\| \le \frac{1}{4}\beta\rho_1\left\|\mathbf{x}_\beta(t)\right\|^2 + \beta^{-3}\rho_{11}\left\|\mathbf{z}(t)\right\|^2 \\ &2\beta^{-1}\rho_4\left\|\mathbf{x}_\beta(t)\right\|\left\|\mathbf{v}_d(t)\right\| \le \frac{1}{4}\beta\rho_1\left\|\mathbf{x}_\beta(t)\right\|^2 + \beta^{-3}\rho_{12} \end{aligned} \quad (31)$$

we obtain

$$\dot{V}_2(t) \le -\beta\rho_{x2}\left\|\mathbf{x}_\beta(t)\right\|^2 + \beta^{-3}\rho_{13} \quad (32)$$

$$\rho_{x2} = \frac{1}{2}\rho_1 - \beta^{-1}\rho_2 \quad (33)$$

where ρ_{11}, ρ_{12} and ρ_{13} are positive constants independent of the design parameter β. According to (22), ρ_{x2} is a positive value. Therefore, from (32), we can derive the inequality (26).

© ISAROB 2013

From the theorem, it can be concluded that the absolute values of $\dot{\tilde{x}}_t(t)$ and $\ddot{\tilde{x}}_t(t)$ can be reduced by setting the value of the design parameter β.

4NUMERIC SIMULATIONS

Carrying out numerical simulations, the effectiveness of the developed controller is shown. The system (1) and (2) are used as the dynamic equation of the controlled object. The values of system parameters are shown in Table 2. The design parameters except β are set as $\omega_n = 11$, $\xi = 1$, $T = 0.1$ and $\alpha = 60$. The final ideal speed of the drive part is set as $v_d = 5$. Fig. 2 shows responses for the design parameter $\beta = 5, 10, 300$. Fig.2 (a) and (b) show the responses of the signals $\dot{\tilde{x}}_t(t)$ and $\ddot{\tilde{x}}_t(t)$. Fig.2 (c) shows the responses of the ideal speed $v_{td}(t)$ of the drive part and the speed of the drive part $\dot{x}_t(t)$.

As shown in Fig. 2 (a) and (b), by increasing the value of β, the maximum values of the absolute values of $\dot{\tilde{x}}_t(t)$ and $\ddot{\tilde{x}}_t(t)$ become smaller. As shown in Fig.2 (a) and (c), when β is set as 300, the absolute value of $\dot{\tilde{x}}_t(t)$ become almost zero, and $\dot{x}_t(t)$ follows $v_{td}(t)$.

Fig.3 shows the responses of the controlled system with $\beta = 300$ and the passive system with a constant input （$u = 45.9$）. As shown in Fig.3, compared with the passive system, the speed of drive part of the control system converges to the ideal value 5 m/s quickly. Moreover, as shown in Fig.3 (b), it can be seen that oscillation occurs in the passive system but the oscillation can be controlled in the control system.

5CONCLUSION

In this paper, based on the linearlized dynamic equation, we proposed the oscillation control technique for the contact type scanning sensor systems using the accelerometer. Carrying out numerical simulations for the nonlinear controlled object, effectiveness of the developed controller was confirmed. As a result, it has been shown that the oscillation of the sensor part can be prevented in high-speed scanning.

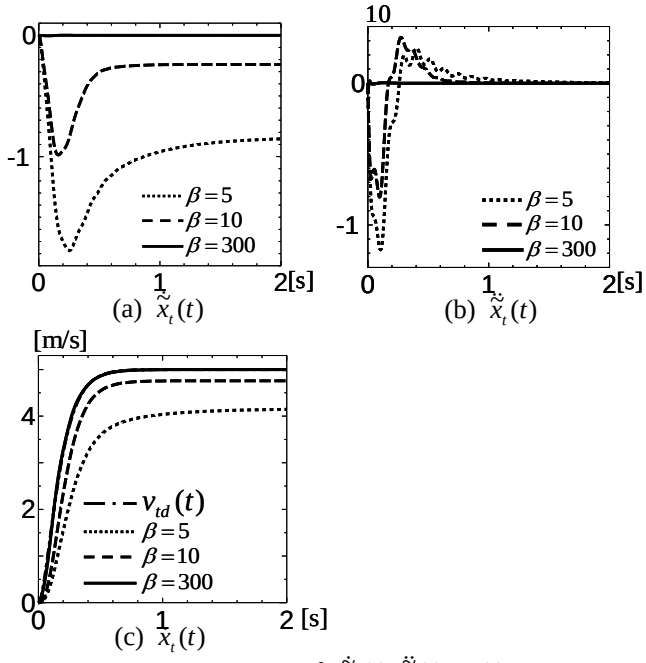

Fig.2 Response of $\dot{\tilde{x}}_t(t), \ddot{\tilde{x}}(t)_t, \ddot{x}(t)_t$

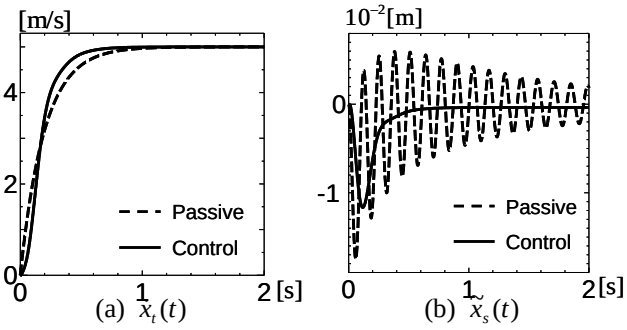

Fig.3 Respnse of $\dot{x}_t(t), \tilde{x}_s(t)$

REFERENCES

[1] Hideyuki Chikuri, Morihiro Fukushima, Noriyuki Nagahama, Yuko Nishiaki, Tadashi Ishigaki "Industrial Applied Techniques of Ultrasonic Time of Flight Diffraction (TOFD) for Various Field Targets", KOBE STEEL ENGINEERING REPORTS, Vol. 57, No. 3, pp38-42, (2007)

[2]Shigeki Watanabe, Hideaki Tanaka, Shuichiro Fukuzawa, Kazuya Fujii "Development of an Inspection Machine Boiler Tubes of Power Station", proceedings of JSNDI Fall Conference 2007 October18-19, Hokkaido Japan, pp217-218, (2007)

[3] Hiroyuki Haga, Yuji Matsuo, Minehiro Nakagawa, Tateyuki Tomitaka, Yuji Nisimura, Koichi Tamura and Masanori Hanaguchi "Development of Ultrasonic Continuous Thickness Measurement Equipment for Piping", Journal JSNDI, No4, pp189-193, (2010)

[4]Hiroyuki Fukutomi, Shan Lin, Takashi Ogata "Ultrasonic Testing to Type IV Damage in Welded Joints of Boiler Piping Part1 Compact Automatic Inspection System", proceedings of JSNDI Fall Conference 2010, Okinawa, Japan, pp159-160, (2010)

[5]Hideki Wada , Masahiro Oya , Katsuhiro Okumura "Development of a position control scheme for rotating sensor unit attached to in-pipe robot", Artificial Life Robotics(2012) Vol.17, No.2, pp317-321

The Eighteenth International Symposium on Artificial Life and Robotics 2013 (AROB 18th '13),
Daejeon Convention Center, Daejeon, Korea, January 30-February 1, 2013

Rollover Prevention Control of Driver-Heavy Vehicle Systems

Yusuke Suetake [1], Masahiro Oya [1], Panfeng Shu[1], Jinxin Zhuo[1]

[1]Kyushu Institute of Technology, Japan
(Phone: +81-93-884-3186, Fax: +81-93-861-1159)
E-mail: k344212y@tobata.isc.kyutech.ac.jp

In this paper, we propose an adaptive rollover prevention controller. At first, using a evaluation function, we propose a design method for an ideal vehicle model achieving good rollover control performance even if driver's steering characteristics vary. Next, an adaptive tracking controller is developed so that the behavior of the actual heavy vehicle can track that of the ideal vehicle model.

Keywords: Intelligent Truck & Heavy Duty Vehicle Control

1. INTRODUCTION

Recently, to present rollover of heavy vehicles, a lot of rollover prevention control schemes were developed[1]-[8]. The papers [1]-[7] provided the schemes using the yaw moment force due to the torque difference between left and right. In the paper[8], the rollover prevention controller was proposed using the active steering of the front wheel. In the control schemes proposed in [1]-[8], only one control input is used. To prevent the rollover and achieve good steering performance, we have to control four states of the lateral velocity, the yaw rate, roll angle and the roll rate. Therefore, using the control inputs more than one, it is expected that better control performance can be achieve. To address the problem , the papers[9]-[10] provided the control schemes using the lateral force of the front active steering and the yaw moment force, and the scheme using the active steering force of front and rear was proposed in [11]. However, there exist problems in the papers [9]-[11] that the uncertainties of the vehicle system parameters were not considered. In addition, the variation of the driver characteristics was also ignored. For example, there exist large differences in handle operation characteristics between young drivers and elder drivers. Even for the same driver, if the driver becomes tired, the handle operation characteristics may vary. Using the rollover prevention controller ignoring the facts, the designed control performance may not be achieved.

In the paper, to overcome the problems, we propose an adaptive rollover prevention controller. At first, we develop a design method of an ideal vehicle model achieving good rollover control performance even if the handle operation characteristics vary. Next, an adaptive tracking controller is developed so that the behavior of the actual vehicle can track of the ideal vehicle model.

2. DYNAMIC EQUATION OF VEHICLE

Consider the vehicle model shown in Fig.1. It is assumed that the pitch dynamics can be ignored. In addition, it is also assumed that the front steering angle, the rear steering angle and the roll angle are small. The dynamic equation using the new state can be

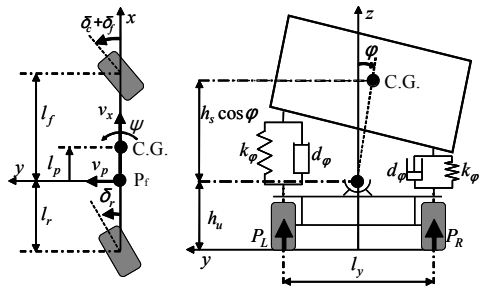

Fig.1 vehicle model

described as

$$\left.\begin{array}{l}
\dot{\boldsymbol{x}}(t) = A\boldsymbol{x}(t) + B\left(\boldsymbol{b}_u\delta_c^*(t) + \boldsymbol{u}^*(t)\right) \\
\delta_c^* = \delta_c(t) + \dot{\delta}_c(t),\ \boldsymbol{u}^*(t) = \boldsymbol{u}(t) + \dot{\boldsymbol{u}}(t) \\
\boldsymbol{x}(t) = [\ \boldsymbol{q}_p^T(t), \boldsymbol{q}_s^T(t), \boldsymbol{\mu}^T(t)\ ]^T, \boldsymbol{\mu} = T^{-1}\boldsymbol{\mu}_1(t) \\
\boldsymbol{\mu}_1(t) = M_\mu^{-1}H_T^T K_u\left\{-v_x H_T \boldsymbol{q}_v(t) + \boldsymbol{b}_u\delta_c(t) + \boldsymbol{u}(t)\right\} \\
\qquad -\dfrac{m_s h_s}{m(I_x + m_s h_s^2) - m_s^2 h_s^2}\boldsymbol{b}_u\boldsymbol{g}_s^T\boldsymbol{q}_s(t) \\
M_\mu = \mathrm{diag}\left[\dfrac{I_x + m_s h^2}{m(I_x + m_s^2 h_s^2)}, I_z\right],\ H = \begin{bmatrix} 1 & l_f \\ 1 & -l_r \end{bmatrix} \\
H_T = HT^{-1} \\
\boldsymbol{q}_s(t) = [\phi(t)\ ,\ \dot{\phi}(t)]^T\ ,\ \boldsymbol{q}_p(t) = [v_p(t)\ ,\ \psi(t)]^T
\end{array}\right\}, \quad (1)$$

$$\left.\begin{array}{l}
A = \begin{bmatrix} A_1 & 0 & I \\ 0 & A_2 & A_3 \\ A_4 & A_5 & A_6 \end{bmatrix} B = \begin{bmatrix} 0 \\ 0 \\ M_p^{-1}H^T K_u \end{bmatrix} \\
A_1 = -v_x D\ ,\ A_2 = D - \dfrac{1}{I_x + m_s h_s^2}\boldsymbol{b}_s\boldsymbol{g}_s^T \\
A_3 = \dfrac{1}{I_x + m_s h_s^2}\boldsymbol{b}_s\boldsymbol{b}_u^T T \\
A_4 = -v_x^{-1}M_p^{-1}H^T K_u H(I + A_1) \\
A_5 = -m_m T^{-1}\boldsymbol{b}_u\boldsymbol{g}_s^T(I + A_2) \\
A_6 = -v_x^{-1}M_p^{-1}H^T K_u H - m_m T^{-1}\boldsymbol{b}_u\boldsymbol{g}_s^T A_3 - I \\
M_p = T^T M_\mu T\ ,\ K_u = \mathrm{diag}\left[k_f, k_r\right] \\
D = \begin{bmatrix} 0 & 1 \\ 0 & 0 \end{bmatrix},\ \boldsymbol{b}_u = \begin{bmatrix} 1 \\ 0 \end{bmatrix},\ \boldsymbol{b}_s = \begin{bmatrix} 0 \\ 1 \end{bmatrix} \\
\boldsymbol{g}_s^T = \left[k_\phi l_y^2 - m_s g h_s, d_\phi l_y^2\right],\ T = I + l_p D
\end{array}\right\}. \quad (2)$$

In the dynamic equation, $\delta_c(t)$ is the driver's steering angle input

© ISAROB 2013

Table 1 Meaning of Symbols

v_x	Longitudinal velocity	h_u	Height of roll axis over ground
v_p	Lateral velocity	h_s	Height of C.G. over roll axis
ψ	Yaw rate	l_p	Distance C.G. to P_f
ϕ	Roll angle	l_f	Distance front axle to P_f
$\dot{\phi}$	Roll rate	l_r	Distance rear axle to P_f
g	acceleration of gravity	l_y	Track width
m	Vehicle mass	k_f	Front cornering stiffness
m_s	Sprung mass	k_r	Rear cornering stiffness
k_ϕ	Spring constant	δ_c	Driver's steering input
d_ϕ	Damper constant	δ_f	Control input for front wheel
I_x	Roll moment of inertia	δ_r	Control input for rear wheel
I_z	Yaw moment of inertia	P_L	Vertical load for left wheel
C.G.	Center of gravity	P_R	Vertical load for right wheel
$\mathrm{P_f}$	Reference point		

Table 2 Nominal value

m	14300	[kg]	k_ϕ	132100	[N/m]
m_s	12487	[kg]	d_ϕ	28905	[N·s/m]
h_u	0.68	[m]	I_x	24201	[kg·m^2]
h_s	1.15	[m]	I_z	34917	[kg·m^2]
l_f	3.95	[m]	k_f	582	[kN/rad]
l_r	4.54	[m]	k_r	783	[kN/rad]
l_y	1.86	[m]	g	9.81	[m/s^2]
l_p	0	[m]			

and $\boldsymbol{u}(t) = [\delta_f(t), \delta_r(t)]^T$ is the control steering input for the front wheel and the rear wheel. Definitions for the parameters of heavy vehicles are shown in Table 1.

The rollover index $R(t)$ for the roll dynamics is defined as follows.

$$\left.\begin{aligned}
&R(t) = \frac{P_L - P_R}{P_L + P_R} = \frac{2m_s\left(ha_{ys}(t) + gh_s\phi(t)\right)}{mgl_y} \\
&\quad = \boldsymbol{c}_{\dot{v}p}^T\boldsymbol{x}(t) + \boldsymbol{c}_o^T\boldsymbol{x}(t) \\
&a_{ys}(t) = \dot{v}_p(t) + v_x\psi(t) + l_p\dot{\psi}(t) - h_s\ddot{\phi}(t) \\
&h = h_u + h_s \\
&\boldsymbol{c}_{\dot{v}p}^T\boldsymbol{x}(t) = \frac{2I_x m_s h}{mgl_y(I_x + m_s h_s^2)}([1\ \ 0]\boldsymbol{\mu} - v_x\psi(t)) \\
&\boldsymbol{c}_o^T\boldsymbol{x}(t) = \frac{2m_s}{mgl_y(I_x + m_s h_s^2)}(I_x h v_x\psi(t) \\
&\qquad +(m_s g h_s^2(h_s - h) + h_s(hk_\phi l_y^2 + gI_x))\phi(t) \\
&\qquad +h_s h d_\phi l_y^2\dot{\phi}(t) + [0\ \ hl_p(I_x + m_s h_s^2)]\boldsymbol{\mu}(t))
\end{aligned}\right\} \quad (3)$$

To represent the rollover index by using the state $\boldsymbol{x}(t)$, we introduce the state including the signal $\boldsymbol{\mu}(t)$. The range of $R(t)$ is $0 \leq |R(t)| < 1$. If $|R(t)| = 1$, the total vertical loads is loaded on right wheel or left wheel. Then, we can see that vehicles were rollover.

When the values of system parameters are nominal values, the vehicle is called the nominal vehicle. Especially, in case of $\boldsymbol{u}(t) = 0$, the vehicle is called the passive vehicle. Nominal values are shown in Table 2.

For the heavy vehicle (1), we make the following assumptions.

A1 The lateral velocity $v_p(t)$ of vehicle, the yaw rate $\psi(t)$, the roll angle $\phi(t)$ and the roll rate $\dot{\phi}(t)$ are measured.

A2 The distances l_f, l_r from the reference point P_f to the front axle and the rear axle are known.

A3 The vehicle parameters except l_f, l_r include uncertainties.

A4 The longitudinal velocity v_x is a bounded constant and measured.

A5 The matrix A_2 is asymptotically stable.

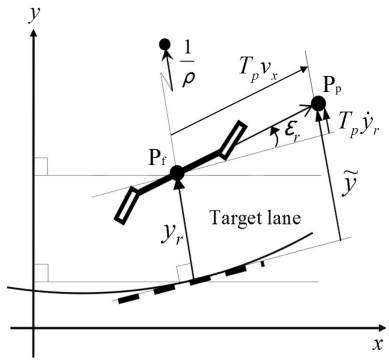

Fig.2 Predictive driver model

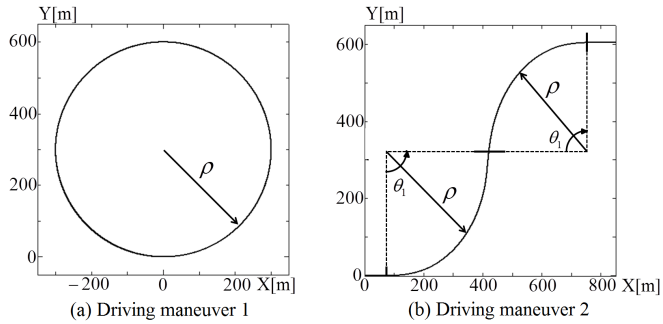

Fig.3 Target lane

3. IDEAL VEHICLE MODEL

In order to design an ideal vehicle model in which the variations of the driver's characteristics is considered, we employ the predictive driver model given by

$$T_s\ddot{\delta}_c(t) + \dot{\delta}_c(t) = -g_p\dot{\tilde{y}}(t) - g_i\tilde{y}(t) \quad (4)$$

where g_p,g_i are the steering gains, T_s is the steering time constant and denotes the reaction delay of drivers and mechanical systems. To explain the predicted distance $\tilde{y}(t)$, the predictive driver model is shown in Fig.2. The solid line represents a state of the vehicle and the dashed line represents the ideal state where the vehicle tracks a target lane. $y_r(t)$ is the lateral distance between $\mathrm{P_f}$ and the target lane, $\varepsilon_r(t) = \varepsilon(t) - \varepsilon_d$ is the relative yaw angle between the vehicle and the target lane, ε_d is the yaw angle of the target lane and ρ is the curvature of target lane. The predicted distance $\tilde{y}(t)$ is the lateral distance at the preview point $\mathrm{P_p}$ and given by

$$\tilde{y}(t) = y_r(t) + T_p\dot{y}_r(t) \quad (5)$$

where T_p is the preview time constant. Drivers steer so that the predicted distance $\tilde{y}(t)$ can converge to zero.

Using the driver model, and carrying out numerical simulations, we propose the following design scheme for an ideal vehicle.

① We determine the values of weighting coefficients of the following evaluation function.

$$\begin{aligned}
J(t) = \int \left(q_1 y_r^2(t) + q_2\ddot{y}_r^2(t) + q_3\varepsilon_r^2(t)\right)dt + \\
q_4 \max|y_r^2(t)| + q_5 \max|\ddot{y}_r^2(t)| + q_6 \max|R^2(t)|
\end{aligned} \quad (6)$$

② We design the ideal vehicle model with the control input $\boldsymbol{u}_M^*(t)$ given by

© ISAROB 2013

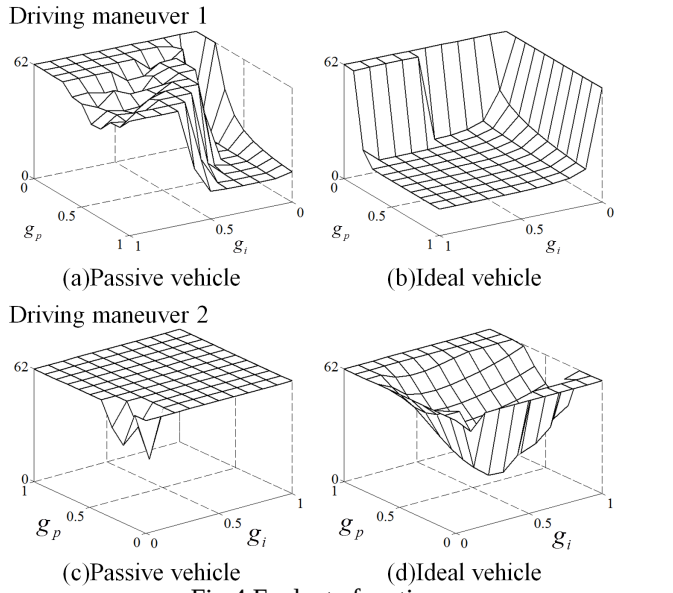

Fig.4 Evaluate function

$$\left.\begin{array}{l}\dot{\boldsymbol{x}}_M(t) = \overline{A}\boldsymbol{x}_M(t) + \overline{B}\left(\boldsymbol{b}_u\delta^*_{cM}(t) + \boldsymbol{u}^*_M(t)\right)\\ R_M(t) = \overline{\boldsymbol{c}}^T_{\dot{v}p}\boldsymbol{x}_M + \overline{\boldsymbol{c}}^T_o\boldsymbol{x}_M\\ \boldsymbol{x}_M(t) = [\ \boldsymbol{q}^T_{pM}(t)\ ,\ \boldsymbol{q}^T_{sM}(t)\ ,\ \boldsymbol{\mu}^T_M(t)\ ]^T\end{array}\right\} \tag{7}$$

where $\overline{\bullet}$ denotes matrixes and vectors in which the values of elements of $\bullet$ are nominal values and $\delta^*_{cM}(t)$ is the steering input $\delta^*_{cM}(t) = \delta_{cM}(t) + \dot{\delta}_{cM}(t)$ generated by $T_s\ddot{\delta}_{cM}(t) + \dot{\delta}_{cM} = -g_p\dot{\tilde{y}}_M - g_i\tilde{y}_M$. The controller $\boldsymbol{u}^*_M(t)$ is designed so that the values of the evaluation function (7) become less than that of the passive vehicle.

③ We check the region of driver's parameters in which the following conditions are satisfied. In the following equations, $y_{rM}(t), \varepsilon_{rM}(t)$ denote the lateral distance and the relative yaw angle in the case when the driver is driving the ideal vehicle model.

$$\left.\begin{array}{l}|y_{rM}(t)| < 0.6[\mathrm{m}], |\ddot{y}_{rM}(t)| < 3[\mathrm{m/s^2}]\\ R_M(t)| < 0.85, \varepsilon_{\mathrm{rM}} < 0.2[\mathrm{rad}]\end{array}\right\} \tag{8}$$

When $|y_{rM}(t)| < 0.6[\mathrm{m}]$, the heavy vehicle doesn't stray from a driving lane. Moreover, when $|\ddot{y}_{rM}(t)| < 3[\mathrm{m/s^2}]$, we consider that burdens hardly move.

④ If the obtained region in ③ is large enough compared with that in the passive vehicle, the design of the ideal vehicle model is completed. Otherwise, we return to step ①〜③.

Using a concrete example and carrying out numerical simulations, we show detail explanations of the design steps stated above. Fig.3 shows the target lane used in the example. Fig.3 (a) shows the target lane with the curvature ρ (driving maneuver 1). Fig.3 (b) shows the target lane with the curvature ρ and the angle θ_1 (driving maneuver 2). In the driving maneuver 1, the ideal model is checked for $\rho = 1/300[\mathrm{m}]$〜$1/500[\mathrm{m}]$. In the driving maneuver 2, the ideal vehicle model is checked for $\rho = 1/300[\mathrm{m}]$〜$1/500[\mathrm{m}]$ and $\theta_1 = 0[\mathrm{rad}]$〜$\pi/2[\mathrm{rad}]$. For the driver parameters, we check the ideal vehicle model in the region of $T_s = 0.1[\mathrm{s}]$〜$0.4[\mathrm{s}], \mathrm{T_p} = 1.5[\mathrm{s}]$〜$4.5[\mathrm{s}], \mathrm{g_p} = 0$〜$1, \mathrm{g_i} = 0$〜$1$ and the vehicle speed $v_x = 120[\mathrm{Km/h}]$.

① Determination of the weighting coefficients

Weighting coefficients are set as $q_1 = 26, q_2 = 10, q_3 = 40, q_4 = 10, q_5 = 5, q_6 = 20$ by the trial-and-error approach.

② Design of an ideal vehicle model

The controller for the ideal vehicle model (7) is developed as

$$\boldsymbol{u}^*_M(t) = -\frac{1}{2\varepsilon_1}\overline{B}^T P\boldsymbol{x}_M(t) \tag{9}$$

$$\left.\begin{array}{l}\overline{A}^T P + P\overline{A} - \dfrac{1}{\varepsilon_1}P\overline{B}\,\overline{B}^T P + \varepsilon_2\overline{\boldsymbol{c}}_{\dot{v}p}\overline{\boldsymbol{c}}^T_{\dot{v}p} + \varepsilon_3 I = 0\\ \varepsilon_1 = 0.1, \varepsilon_2 = 0.2, \varepsilon_3 = 0.01\end{array}\right\}. \tag{10}$$

Fig.4 shows the values of the evaluation function J of the ideal vehicle model and the passive vehicle model. The vertical axis is the values of J, x axis and y axis are steering gains g_i, g_p. In the case where J exceed 62, the values of J are fixed as 62.In Fig.4, v_x, T_s, T_p are set as $v_x = 120[\mathrm{Km/h}]$, $T_s = 0.4[\mathrm{s}]$ and $T_p = 1.5[\mathrm{s}]$, and the values of the evaluation function J are shown for the driving maneuver 1 with $\rho = 1/300[\mathrm{m}]$ and the driving maneuver 2 with $\rho = 1/300[\mathrm{m}]$ and $\theta_1 = \pi/2[\mathrm{rad}]$. It can be seen that the region of the ideal vehicle model where the values of J become less than 62 is larger than that of the passive vehicle. For lack of space, the simulation results for the other values of ρ, θ_1, v_x, T_s and T_p are not shown. However, it was ascertained that similar results to Fig.4 could be obtained.

③ Evaluation of conditions

The conditions (8) are checked. As a result of the check, in the case where the values of J are less than 62, the conditions (8) are satisfied in the designed ideal vehicle.

④ Dicision to end of the iteration

As shown in Fig.4(a) and (b), the obtained region where the conditions (8) are satisfied is large enough compared with that in the passive vehicle. Then the design of the ideal model is completed.

4. ADAPTIVE TRACKING CONTROLLER

In order to develop an adaptive tracking controller so that the behavior of the actual vehicle tracks that of the ideal vehicle model, the tracking errors are defined as

$$\left.\begin{array}{l}\widetilde{\boldsymbol{q}}_p(t) = \boldsymbol{q}_p(t) - \boldsymbol{q}_{pM}(t), \widetilde{\boldsymbol{q}}_s(t) = \boldsymbol{q}_s(t) - \boldsymbol{q}_{sM}(t)\\ \widetilde{\boldsymbol{\mu}}(t) = \boldsymbol{\mu}(t) - \boldsymbol{\mu}_M(t)\end{array}\right\}. \tag{11}$$

Moreover, the new tracking error signal $\boldsymbol{z}(t) = \widetilde{\boldsymbol{q}}_p(t) + \widetilde{\boldsymbol{\mu}}(t)$ is also defined. Then, we have

$$\begin{aligned}\dot{\boldsymbol{z}}(t) = -d\boldsymbol{z}(t) + M_p^{-1}H^T K_u H\Big(&H^{-1}\boldsymbol{u}^*(t)\\ &-v_x^{-1}(A_1 + I)\boldsymbol{q}_p(t) + \Theta\boldsymbol{\omega}(t)\Big),\end{aligned} \tag{12}$$

$$\left.\begin{array}{l}\Theta = \left(M_p^{-1}H^T K_u H\right)^{-1}[\ A_5\ ,\ A_6\ ,\ I\ ]\\ \boldsymbol{\omega}(t) = [\ \boldsymbol{q}^T_s(t)\ ,\ \boldsymbol{\mu}^T(t)\ ,\ \boldsymbol{\xi}^T(t)\ ]^T\\ \boldsymbol{\xi}(t) = (dI + A_1)\widetilde{\boldsymbol{q}}_p(t) + (d+1)I\widetilde{\boldsymbol{\mu}}(t) - \dot{\boldsymbol{\mu}}_M(t)\end{array}\right\}, \tag{13}$$

$$\left.\begin{array}{l}\dot{\widetilde{\boldsymbol{q}}}_s(t) = A_2\widetilde{\boldsymbol{q}}_s(t) + A_3\widetilde{\boldsymbol{\mu}}(t) + \widetilde{A}_2\boldsymbol{q}_{sM}(t) + \widetilde{A}_3\boldsymbol{\mu}_M(t)\\ \widetilde{A}_2 = A_2 - \overline{A}_2\ ,\ \widetilde{A}_3 = A_3 - \overline{A}_3\end{array}\right\}, \tag{14}$$

where d is a positive design parameter, Θ is the unknown constant

© ISAROB 2013

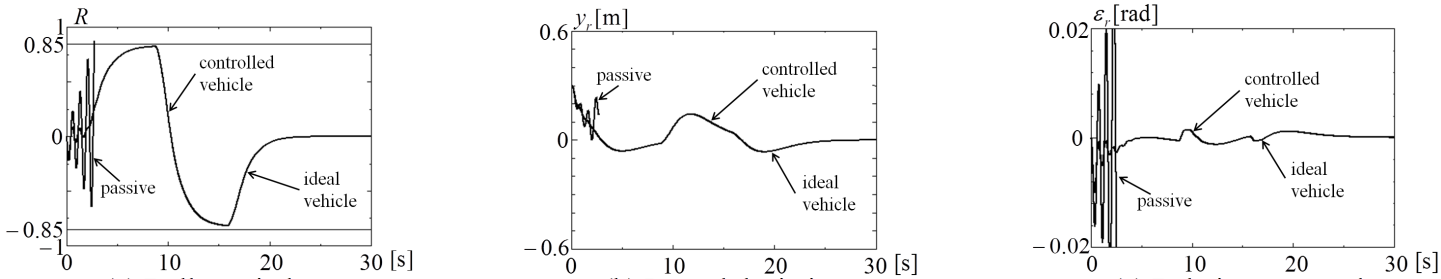

(a) Rollover index (b) Lateral deviation (c) Relative yaw angle

Fig.5 Response of the controlled heavy vehicle with nominal parameters.

matrix and $\boldsymbol{\omega}(t)$ is the known signal vector.

If the tracking error $\boldsymbol{z}(t)$ becomes asymptotically stable, it can be seen that the tracking errors $\widetilde{\boldsymbol{q}}_p(t)$ and $\widetilde{\boldsymbol{\mu}}(t)$ become asymptotically stable. Then, from (14) and the assumption, it can be also seen that the tracking error $\widetilde{\boldsymbol{q}}_s(t)$ also becomes stable. Especially, in the case where $\widetilde{A}_2$ and $\widetilde{A}_3$ are zero matrixes, the tracking error $\widetilde{\boldsymbol{q}}_s(t)$ becomes asymptotically stable.

Using the adaptive tracking controller given by

$$\left.\begin{aligned} \dot{\boldsymbol{u}}(t) &= -\boldsymbol{u}(t) - \beta H\boldsymbol{z}(t) + v_x^{-1}H(A_1+I)\boldsymbol{q}_p(t) \\ &\quad - H\hat{\Theta}(t)\boldsymbol{\omega}(t) \qquad , \ \beta > 0 \\ \dot{\hat{\Theta}}(t) &= \gamma\boldsymbol{z}(t)\boldsymbol{\omega}^T(t) \qquad , \ \gamma > 0 \end{aligned}\right\}, \tag{15}$$

the tracking errors become stable and the tracking error $\boldsymbol{z}(t)$ converges to zero. For lack of space, the proof is omitted.

5. NUMERICAL SIMULATION RESULTS

The numerical simulation results are shown to demonstrate the effectiveness of the proposed adaptive tracking controller. The driver parameters T_s, T_p, g_p, g_i are set as $T_s = 0.4$[s], $\mathrm{T_p} = 1.5$[s], $g_p = 0.3$, $g_i = 0.5$. The target trajectory shown in Fig.3(b) is used. The parameters ρ and θ, are set as $\rho = 1/300[\mathrm{m}], \theta_1 = \pi/2[\mathrm{rad}]$ and the longitudinal velocity is $v_x = 120[\mathrm{Km/h}]$. In the passive vehicle, if the driver parameters stated above are used, the rollover occurs and it very difficult to stabilize the vehicle.

Fig.5 shows the responses of the ideal vehicle, the controlled vehicle and the passive vehicle. Fig.5 (a) shows the responses of the rollover index, Fig.5 (b) shows the responses of the lateral deviation and Fig.5 (c) shows the responses of the relative yaw angle.

From Fig.5, it can be seen that the rollover occurs in the passive vehicle. On the other hand, the rollover didn't occur in the controlled vehicle. For lack of space, we couldn't show responses for the variations of the driver parameters and the vehicle system parameters. However, it was ascertained that the good control performance could be achieved. It can be concluded that for the variations of system parameters, the proposed rollover prevention controller has good robust performance.

6. CONCLUSIONS

In this paper, a new design method for an ideal vehicle model was proposed. It has been shown by carrying out numerical simulation that in the ideal vehicle, the good rollover control performance can be achieved. Moreover, we proposed an adaptive tracking controller so that the behavior of the actual heavy vehicle can track that of the ideal vehicle model even if the actual vehicle system parameters vary. Carrying out numerical simulations, the effectiveness of proposed rollover prevention controller was shown.

REFERENCES

[1] B. Schofield and T. Hagglund, Optimal Control Allocation in Vehicle Dynamics Control for Rollover Mitigation, Proceedings of American Control Conference, pp3231-3236

[2] L-k Chen, C-f Cheng and M-f Luo, Rollover Prevention through Model Predictive Direct Yaw Moment Control, Proceedings of Advanced Vehicle Control, pp.721-726

[3] S. Solmaz, M. Corless and R. Shorten, A methodology for the design of robust rollover prevention controllers for automotive vehicles : Part 1-Differential braking, Proceedings of IEEE Conference on Decision and Control

[4] B. Johansson and M. Gafvert, Untripped SUV Rollover Detection and Prevention, IEEE Conference on Decision and Control, pp.5461-5466

[5] B. Schofield, T. Hagglund and A. Rantzer, Vehicle Dynamics Control and Controller Allocation for Rollover Prevention, IEEE International Conference on Control Application

[6] S. Solmaz, M. Akar and R. Shorten, Adaptive Rollover Prevention for Automotive Vehicles with Differential Braking, Proceedings of the 17th IFAC, world Congress

[7] J. YOON, D. KIM and K. YI, Design of a rollover index-based vehicle stability control scheme, Vehicle System Dynamics, Vol. 45, No. 5, 459-475

[8] S. Solmaz, M. Corless and R. Shorten, A Methodology for the Design of Robust Rollover Prevention Controllers for Automotive Vehicles Part 2-Active steering, Proceedings of American control Conference

[9] K. Feng, H.Tan, M. Tomizuka, Automatic Steering Control of Vehicle Lateral Motion with the Effect of Roll Dynamics, Proceedings of American Control Conference, pp.2248-2252

[10] D. Odenthal, T. Bunte and J. Ackermann, Nonlinear Steering and Braking Control for Vehicle Rollover Avoidance, European Control Conference

[11] C. Cheng and D. Cebon, Improving roll stability of articulated heavy vehicles using active semi-trailer steering, Vehicle System Dynamics, Vol. 46, pp.373-388

The Eighteenth International Symposium on Artificial Life and Robotics 2013 (AROB 18th '13),
Daejeon Convention Center, Daejeon, Korea, January 30-February 1, 2013

Development of a dual-shaft propeller thruster equipped with rotational speed sensor for UVMS control

Radzi Bin Ambar Shinichi Sagara Takuya Yamaguchi

Department of Mechanical and Control Engineering, Kyushu Institute of Technology
Tobata, Kitakyushu 804-8550, Japan
Email: m584204b@tobata.isc.kyutech.ac.jp

Abstract: Majority of underwater robots utilize single propeller thrusters for navigation. A disadvantage on using a single propeller thruster is the thrust force generated from a single propeller for reverse and forward thrust is asymmetric due to the disturbed flow caused by the thruster's body which may reduce thruster efficiency. Measurement procedures to precisely calculate propeller's rotation speed were also not available. To address these problems, this paper proposes a dual-shaft magnetic coupling driven propeller thruster for underwater vehicle-manipulator system (UVMS) equipped with sensors for measuring propeller's rotational speed. Numerical studies and experimental results on the position and orientation control of the proposed thruster are presented. Detail comparison of the rotational speed, thrust force and duty-ratio between numerical calculation and actual experimental measurement results shows the effectiveness of the proposed thruster. The ability to determine propeller rotation directions is also a major advantage.

Keywords: dual-shaft, thruster, rotational speed, UVMS, control

1 INTRODUCTION

The main purpose of this research is to design a new underwater thruster for an underwater vehicle-manipulator system (UVMS) equipped with a 2-link manipulator which the authors have been actively carried out [1-3].

To date, a large number of underwater robots utilize single propeller thrusters for navigation [3-6]. A disadvantage on using a single propeller thruster is the thrust force generated from a single propeller for reverse and forward thrust is asymmetric due to the disturbed flow caused by the thruster's body which may reduce thruster efficiency. A magnetic coupling driven propeller thruster transmits torque through an air gap between motor driven shaft and load shaft (propeller). However, due to magnetic coupling mechanism, it is difficult to measure precisely the actual rotational speed of the propeller and the thrust generated from it. Although there are researchers demonstrating the relation between propeller's torque rotational speed and the generated thrust, they utilized unknown parameters and only focusing on motor driven propeller thruster without magnetic coupling. Measurement procedures to specifically calculate propeller's rotation speed were also not available.

To address these problems, this paper proposes a dual-shaft magnetic coupling driven propeller thruster for UVMS equipped with sensors for measuring rotational speed of the propellers. The developed thruster is consists of two magnetic coupling driven propellers which rotate in directions opposite one another. Magnetic coupling mechanism has been selected, due to the several advantages such as cushioned start, low power usage and low maintenance cost. The paper also proposes a method on calculating the propeller thruster's thrust force through measuring rotational speed and thrust forces generated from the propellers and compared it with commercially available thruster for performance comparison.

2 DESIGN METHODOLOGY

2.1 Thruster design

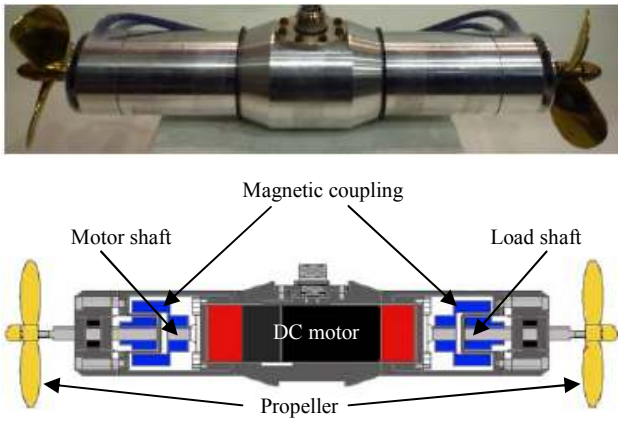

Fig. 1. Dual-shaft magnetic coupling propeller thruster

In this section, the developed dual-shaft propeller thruster driven by co-axial magnetic coupling is described. Fig.1 shows the developed thruster. Basically, one of the magnets is driven by a motor through a motor shaft. This mechanism is designed inside a waterproof container. The other magnets is connected to the propeller via a load shaft. Two Raboesch 3-blade brass propellers are being used. A dual-shaft Faulhaber 3863A024C DC motor with planetary gearheads is being used to drive two sets of MTL-03 co-axial magnetic coupling from Magnetic Technologies. The motor is controlled by a PIC30F3010 microcontroller. Table 1 shows the physical parameters of the developed thruster.

© ISAROB 2013

Table 1. Physical parameters of thruster

Length	383 [mm]
Outer diameter	57 [mm]
Weight	3130 [g]
Propeller pitch	102.5 [mm]
Propeller diameter	100 [mm]
Propeller weight	84 [g]

(a) (b)

Fig. 2. Reflective photosensors and metal disk position

2.2 Reflective photosensor

The rotation speed of the propellers can be measured by using two units of RPR-220 (ROHM Co. Ltd.) reflective photosensors embedded in both of the motor shaft housings facing towards the propeller as shown in Fig.2 (a). The reflective photosensors consists of an infrared emitted diode and a phototransistor which can detect the reflected infrared light. The infrared light is reflected by a metal disc which is attached on the propeller's shaft, located between the propeller shaft housing and propeller as shown in Fig.2 (b). The metal disc will rotate along with the propeller. It is carved with 8 holes and layered with thin black colored rubber attached on the back of the discs which is to prevent infrared reflection. The metal reflective surface and black colored rubber surface makes a perfect reflecting and non-reflecting surfaces.

2.3 Rotational speed measurement

As described in the previous section, propeller's rotational speed can be measured using two units of reflective photosensors embedded side by side. The sensors are embedded in such a way that provides two voltage outputs with the phase differences of 90°. When the propeller and metal disc rotated, the rotational speed can be calculated by the embedded sensors. Moreover, the voltage outputs phase differences of 90° provide the ability to determine the directions of rotation for both propellers. The metal discs have 8 holes, where 1 rotation of the propeller produces 32 pulse (11.25°/pulse). The relationship between number of pulse and rotational speed is expressed with

$$R = \frac{60 \times P}{32 \times T} \tag{1}$$

where R is propeller's rotational speed (unit: rpm), T is sampling period (unit: s), P is number of pulse between a sampling period.

To control thruster's force, the desired rotational speed which corresponded to the desired thrust force need to be calculated. The desired rotational speed can be calculated by the following equation:

$$R_{d_i} = 0.1576\ f_{d_i}{}^3 - 6.075\ f_{d_i}{}^2 + 112.2 f_{d_i} + 136.7 \tag{2}$$

Here, d_i is desired thruster number i (i=1, 2), R_{d_i} is the desired rotational speed (unit: rpm), f_{d_i} is the desired thrust force (unit: N). While the desired input signal which correspond to the desired rotational speed can be calculated by the following equation:

$$u_{d_i} = 0.913 \times 10^{-7} R_{d_i}{}^3 - 5.292 \times 10^{-5} R_{d_i} \times 10^{-5} R_{d_i}{}^2 + 4.298 \times 10^{-2} R_d - 2.786 \tag{3}$$

Where u_{d_i} is the desired input signal (duty ratio, unit: %).

Based on these desired thrust, rotational speed and input signal calculated in equation (2) and (3), and also rotational speed measured through reflective photosensors, R_i in equation (1), the actual input signal u_i for the thruster can be calculated as below:

$$u_i = u_{d_i} + k_P (R_{d_i} - R_i) + k_I \int (R_{d_i} - R_i) dt \tag{4}$$

Here, k_P is proportional gain and k_I is integral gain.

3 EXPERIMENTAL SETUP

3.1 Thruster control system experiment

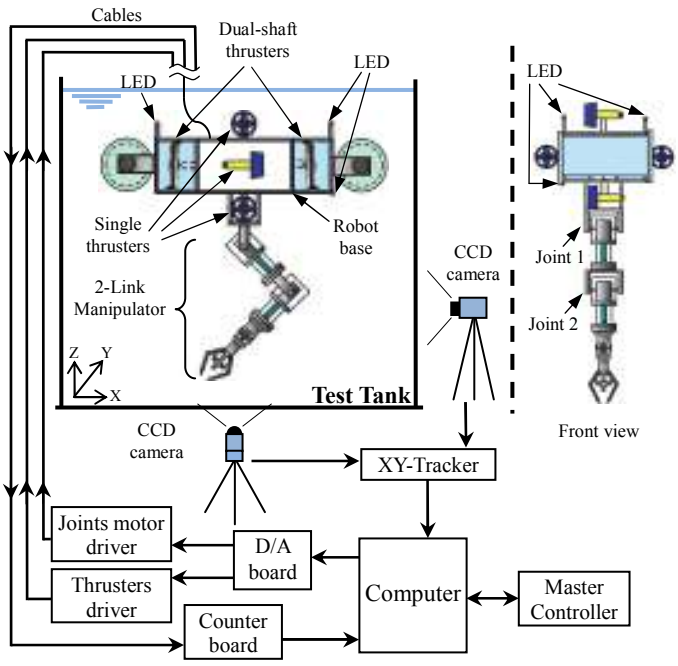

Fig. 3. Experimental setup for the developed thruster

© ISAROB 2013

Fig.3 shows an illustration of the experimental setup for the developed thruster on an UVMS to measure the robot position and orientation. Two of the proposed thrusters were attached on the robot as shown in Fig.3, and then compared with two commercially available single propeller thrusters. Three LEDs are attached to the robot base, and their motion is monitored by CCD cameras. Video signals from the LEDs are converted into position data by X-Y tracker and transmitted to PC for calculation of the positions and orientation of robot base. Robot control is achieved using resolved acceleration control (RAC) method with sampling period of T=1/60sec [1-3]. For experiments using the developed thrusters, the gain for rotational speed control are set as $k_P = 0.031$, $k_I = 0.0017$.

4 RESULTS

Experiments have been carried out on two newly developed propeller thrusters. Firstly, based on the calculations of desired thrust, rotational speed and input signal described in section 2.3, performances comparison with actual measurements using reflective photosensors on two proposed thrusters has been implemented. Fig.4(a) and Fig.4(b) shows the relation between rotational speed, duty ratio and generated thrust force. Fig.4(a) shows that measurement results of the increased in duty ratio on propeller's rotational speed from both thrusters have similar performances with calculated results. Fig.4(b) shows that an increase of rotational speed resulting in increase of thrust force. The measurement results also gave similar performance with calculation results which demonstrated the usefulness of the proposed thrusters equipped with reflective photosensors for rotational speed measurements.

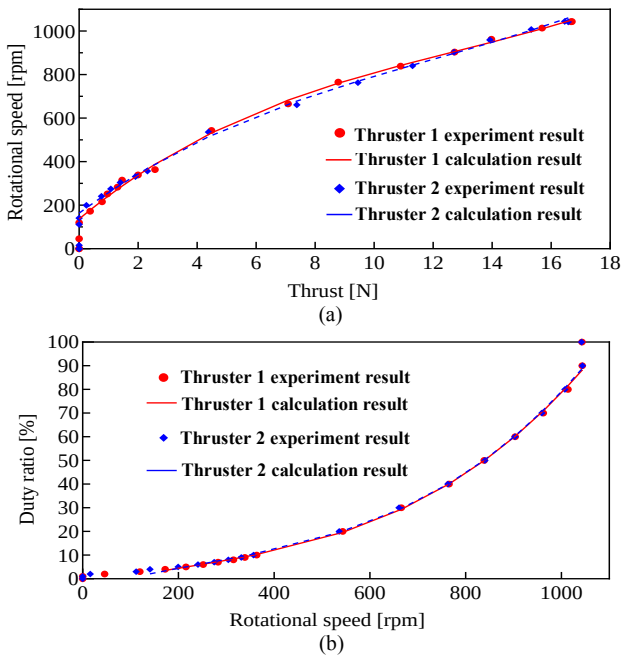

Fig. 4. (a) Relation between thrust and rotational speed, (b) relation between speed and duty ratio

Next, Fig.5 and Fig.6 shows experiment results for position and orientation of UVMS. Based on the experimental setup in Fig.3, the robot base was controlled to move 0.15m downward. The results of position and orientation (x, y, z, roll, pitch and yaw axes) from the robot base using the traditional single propeller thrusters and the proposed dual-shaft propeller thrusters are shown in Fig.5 and Fig.6 respectively. Fig.5 shows that the commercially available single propeller thrusters produced large vibration on x axis during the first 20sec from the start of movement. Large vibrations also recorded in y and z axes, during the first 20sec and 40sec respectively. Orientation of the base also demonstrated large vibration for the first 40sec. However, Fig.6 shows that by using the proposed thrusters, UVMS demonstrated no large vibration occurrence on position and orientation axes. The above results proved that the proposed thrusters design demonstrated good performance compared to the commercially available thrusters.

5 CONCLUSION

A dual-shaft magnetic coupling driven propeller thruster for underwater vehicle-manipulator system (UVMS) equipped with sensors for measuring propeller's rotational speed have been proposed. Numerical studies and experimental results on the position and orientation control of the dual shaft propeller thruster shows the effectiveness of the developed thruster. The ability to determine propeller rotation directions is also a major advantage.

REFERENCES

[1] S. Sagara et al. (2006), Digital RAC for Underwater Vehicle-Manipulator Systems Considering Singular Configuration, J. Artificial Life and Robotics, Vol. 10, No.2, pp.106-111.

[2] S. Sagara et al. (2010), Digital RAC with a Disturbance Observer for Underwater Vehicle-Manipulator Systems, J. Artificial Life Robotics, Vol. 15, No.3, pp. 270-274.

[3] S.Sagara et al. (2012), A master-slave control system for a semi-autonomous underwater vehicle-manipulator system. J. Artificial Life Robotics, Vol.16, No.4, pp. 465-468.

[4] Yoerger D.R. et al. (1990), The influence of thruster dynamics on underwater vehicle behavior and their incorporation into control system design, IEEE J. Oceanic Eng., vol.15, no.3, pp.167-178.

[5] Allen, B. et al. (1997), REMUS: a small low cost AUV; system description, field trials and performance results, Proceedings of the IEEE Oceans 97, New Orleans, USA, pp. 994–1000.

© ISAROB 2013

[6] Zhang Ming-jun et al. (2009), Development and experiment of an underwater vehicle test-bed controlled by rudders and thrusters, Proceedings of the IEEE International Conference on Robotics and Biomimetics (ROBIO), pp.1633-1638.

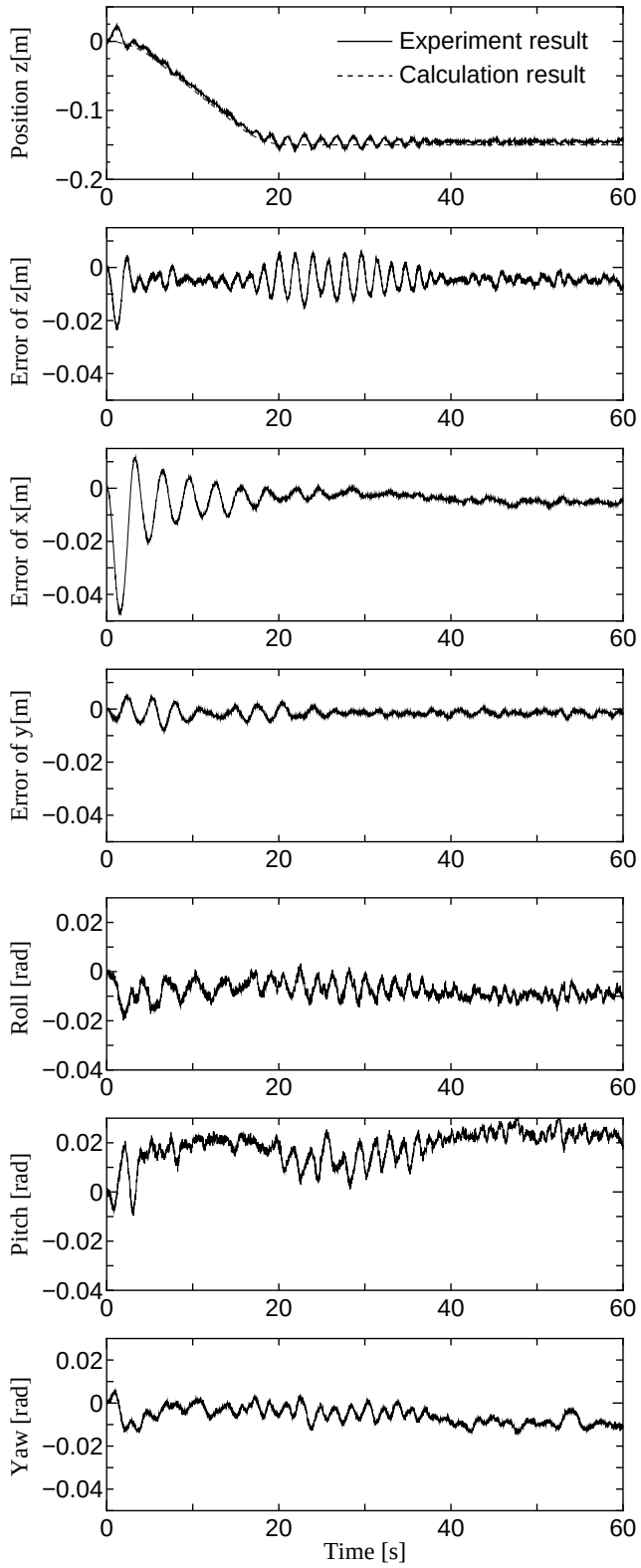

Fig. 5. Experimental results using commercial thrusters

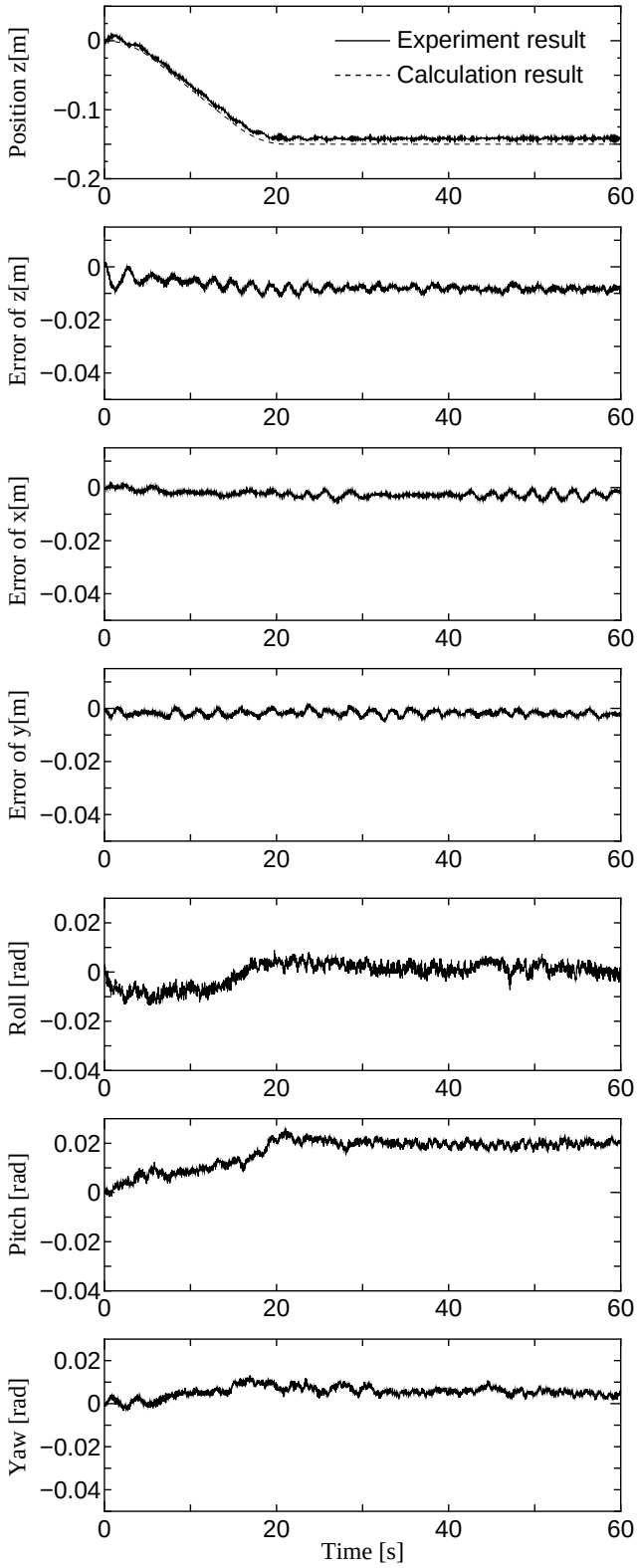

Fig. 6. Experimental results using proposed thrusters

© ISAROB 2013

The Eighteenth International Symposium on Artificial Life and Robotics 2013 (AROB 18th '13),
Daejeon Convention Center, Daejeon, Korea, January 30-February 1, 2013

Control of a dual arm underwater robot

Shinichi Sagara Radzi Bin Ambar Kenichi Imaike
Department of Mechanical and Control Engineering, Kyushu Institute of Technology
Tobata, Kitakyushu 804-8550, Japan
E-mail: sagara@cntl.kyutech.ac.jp

Abstract: Since Underwater Vehicle-Manipulator Systems (UVMS) are expected to make important roles in ocean exploration, many studies about control of single arm UVMSs have been reported. We have also been proposed a resolved acceleration control (RAC) method for a single arm UVMS. In this paper, we propose a RAC method for a dual arm UVMS. Simulation results show the effectiveness of the proposed control method.

Keywords: Underwater Robot, Manipulator, Control

1 Introduction

Underwater robots are expected to be actively involved in various activities such as researches, environment and ecological investigation at locations mainly in the ocean, river and lakes. Many studies on Underwater Vehicle-Manipulator Systems (UVMS) are performed in recent years [1–7]. However there are only a few experimental studies. We have proposed digital Resolved Acceleration Control (RAC) methods for UVMS [8, 9] and the effectiveness of the RAC methods has been demonstrated by experiments using a floating underwater robot with vertical planar 2-link manipulator.

The main objective of this paper is to design a control system for dual arm UVMS. Many of research studies have been focusing on the development of single arm UVMSs. Sakagami et al. have been proposed a simultaneous operation of dual arm underwater robot [10]. However, there is no study on control of dual arm UVMS. In this paper, we propose a RAC method for dual arm UVMS based on Reference [8]. Simulation results show the effectiveness of the proposed control method.

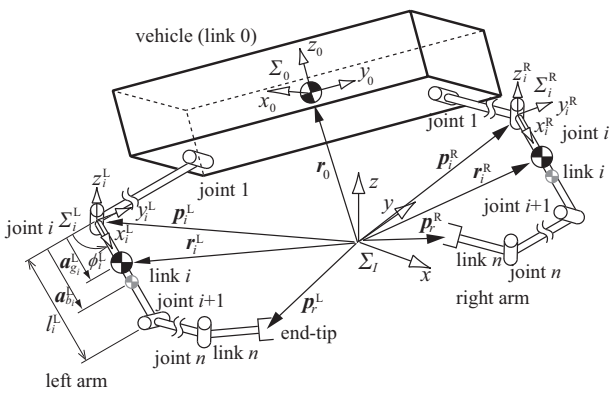

Fig. 1 Model of a dual arm underwater robot

2 Modeling

2.1 UVMS

The underwater robot model used in this paper is shown in Fig. 1. It has a robot base (vehicle) and dual n-DOF manipulators. Thrusters are mounted on the base to provide propulsion for position and attitude control of the base. Symbols used in this paper are defined as follows:

- n^* : number of joint of arm $*$ ($*$=R: Right arm, $*$=L: Left arm)
- Σ_I : inertial coordinate frame
- Σ_0 : base coordinate frame
- Σ_i^* : link i coordinate frame of arm $*$ ($*$=R: Right arm, $*$=L: Left arm)
- ${}^i\boldsymbol{R}_j^*$: coordinate transformation matrix from Σ_j^* to Σ_i^*
- $\boldsymbol{p}_e^*$: position vector of manipulator end-tip with respect to Σ_I
- $\boldsymbol{p}_i^*$: position vector of origin of Σ_i^* with respect to Σ_I
- $\boldsymbol{r}_i^*$: position vector of gravity center of link i^* with respect to Σ_I
- $\boldsymbol{v}_0$: linear velocity vector of origin of Σ_0 with respect to Σ_I
- $\boldsymbol{v}_e^*$: linear velocity vector of manipulator end-tip with respect to Σ_I
- $\boldsymbol{\psi}_0$: roll-pitch-yaw attitude vector of Σ_0 with respect to Σ_I
- $\boldsymbol{\psi}_e^*$: roll-pitch-yaw attitude vector of end-tip of manipulator with respect to Σ_I
- $\boldsymbol{\omega}_i^*$: angular velocity vector of Σ_i^* with respect to Σ_I
- $\boldsymbol{\omega}_e^*$: angular velocity vector of manipulator end-tip with respect to Σ_I
- ϕ_i^* : relative angle of joint i^*
- $\boldsymbol{\phi}$: relative joint angle vector ($= [(\boldsymbol{\phi}^{\mathrm{R}})^T, (\boldsymbol{\phi}^{\mathrm{L}})^T]^T$, and ($\boldsymbol{\phi}^* = [\boldsymbol{\phi}_1^*, \boldsymbol{\phi}_2^*, \cdots, \boldsymbol{\phi}_n^*]^T$)

© ISAROB 2013

$\boldsymbol{k}_i^*$: unit vector indicating a rotational axis of joint i^*
m_i^* : mass of link i^*
$\boldsymbol{M}_{a_i}^*$: added mass matrix of link i^* with respect to Σ_i^*
$\boldsymbol{I}_i^*$: inertia tensor of link i^* with respect to Σ_i^*
$\boldsymbol{I}_{a_i}^*$: added inertia tensor of link i^* with respect to Σ_i^*
$\boldsymbol{x}_0$: position and attitude vector of Σ_0 with respect to Σ_I $(= [\boldsymbol{r}_0^T,\ \boldsymbol{\psi}_0^T]^T)$
$\boldsymbol{x}_e^*$: position and attitude vector of $*$ manipulator end-tip with respect to Σ_I $(= [(\boldsymbol{p}_e^*)^T,\ (\boldsymbol{\psi}_e^*)^T]^T)$
$\dot{\boldsymbol{\chi}}_0$: linear and angular vector of Σ_0 with respect to Σ_I $(= [\boldsymbol{v}_0^T,\ \boldsymbol{\omega}_0^T]^T)$
$\dot{\boldsymbol{\chi}}_e^*$: linear and angular vector of $*$ manipulator end-tip with respect to Σ_I $(= [(\boldsymbol{v}_e^*)^T,\ (\boldsymbol{\omega}_e^*)^T]^T)$
$\boldsymbol{a}_{g_i}$: position vector from joint i^* to gravity center of link i^* with respect to Σ_I
$\boldsymbol{a}_{b_i}^*$: position vector from joint i^* to buoyancy center of link i^* with respect to Σ_I
l_i^* : length of link i^*
D_i^* : width of link i^*
V_i^* : volume of link i^*
ρ : fluid density
$C_{d_i}^*$: drag coefficient of link i^*
$\boldsymbol{g}$: gravitational acceleration vector
$\boldsymbol{E}_j$: $j \times j$ unit matrix
$\tilde{\boldsymbol{r}}$: skew-symmetric matrix defined as

$$\tilde{\boldsymbol{r}} = \begin{bmatrix} 0 & -z & y \\ z & 0 & -x \\ -y & x & 0 \end{bmatrix},\ \boldsymbol{r} = \begin{bmatrix} x \\ y \\ z \end{bmatrix}$$

2.2 kinematics

In this subsection, based on the reference [8] kinematic and momentum equations are derived.

First, from Fig. 1 a time derivative of the end-tip position vector $\boldsymbol{p}_e^*$ ($*$ =R: Right arm, L: Left arm) is

$$\boldsymbol{v}_e^* = \boldsymbol{v}_0 + \tilde{\boldsymbol{\omega}}(\boldsymbol{p}_e^* - \boldsymbol{r}_0) + \sum_{i=1}^{n} \{\tilde{\boldsymbol{k}}_i^*(\boldsymbol{p}_e^* - \boldsymbol{p}_i^*)\}\dot{\phi}_i^*. \quad (1)$$

On the other hand, relationship between end-tip angular velocity and joint velocity is expressed with

$$\boldsymbol{\omega}_e^* = \boldsymbol{\omega}_0 + \sum_{i=1}^{n} \boldsymbol{k}_i^* \dot{\phi}_i^*. \quad (2)$$

From Eqs. (1) and (2) the following equation is obtained:

$$\dot{\boldsymbol{\chi}}_e^* = \boldsymbol{A}^* \dot{\boldsymbol{\chi}}_0 + \boldsymbol{B}^* \dot{\boldsymbol{\phi}}^* \quad (3)$$

where

$$\boldsymbol{A}^* = \begin{bmatrix} \boldsymbol{E}_3 & -(\tilde{\boldsymbol{p}}_r^* - \tilde{\boldsymbol{p}}_0) \\ \boldsymbol{0}^* & \boldsymbol{E}_3 \end{bmatrix}, \quad \boldsymbol{B}^* = \begin{bmatrix} \boldsymbol{b}_1^* & \boldsymbol{b}_2^* & \cdots & \boldsymbol{b}_n^* \end{bmatrix}$$

and $\boldsymbol{b}_i^* = [\{\tilde{\boldsymbol{k}}_i^*(\boldsymbol{p}_r^* - \boldsymbol{p}_i^*)\}^T,\ (\boldsymbol{k}_i^*)^T]^T$.

Next, let $\boldsymbol{\eta}$ and $\boldsymbol{\mu}$ be a linear and an angular momentum of the robot including hydrodynamic added mass tensor $\boldsymbol{M}_{a_i}^*$ and added inertia tensor $\boldsymbol{I}_{a_i}^*$ of link i^*. Then

$$\boldsymbol{\eta} = \boldsymbol{M}_{T_0}\dot{\boldsymbol{r}}_0 + \boldsymbol{\eta}^{\mathrm{R}} + \boldsymbol{\eta}^{\mathrm{L}}, \quad (4)$$

$$\boldsymbol{\mu} = \boldsymbol{I}_{T_0}\boldsymbol{\omega}_0 + \tilde{\boldsymbol{r}}_0\boldsymbol{M}_{T_0}\dot{\boldsymbol{r}}_0 + +\boldsymbol{\mu}^{\mathrm{R}} + \boldsymbol{\mu}^{\mathrm{L}} \quad (5)$$

where

$$\boldsymbol{\eta}^* = \sum_{i=1}^{n^*} \boldsymbol{M}_{T_i}^*\dot{\boldsymbol{r}}_i^*, \quad \boldsymbol{\mu}^* = \sum_{i=1}^{n^*} \boldsymbol{I}_{T_i}^*\boldsymbol{\omega}_i^* + \tilde{\boldsymbol{r}}_i^*\boldsymbol{M}_{T_i}^*\dot{\boldsymbol{r}}_i^*$$

and $\boldsymbol{M}_{T_i}^* = m_i^*\boldsymbol{E}_3 + {}^I\boldsymbol{R}_i^*\boldsymbol{M}_{a_i}^*{}^i\boldsymbol{R}_I^*$ and $\boldsymbol{I}_{T_i}^* = {}^I\boldsymbol{R}_i^*(\boldsymbol{I}_i^* + \boldsymbol{I}_{a_i}^*)^i\boldsymbol{R}_I^*$. Here, linear and angular velocities of gravity center of link i^* are described as

$$\dot{\boldsymbol{r}}_i^* = \boldsymbol{v}_0 + \tilde{\boldsymbol{\omega}}_0(\boldsymbol{r}_i^* - \boldsymbol{r}_0) + \boldsymbol{J}_{v_i}^*\dot{\boldsymbol{\phi}}^*, \quad (6)$$

$$\boldsymbol{\omega}_i^* = \boldsymbol{\omega}_0 + \boldsymbol{J}_{\omega_i}^*\dot{\boldsymbol{\phi}}^*, \quad (7)$$

$$\boldsymbol{J}_{v_i}^* = \begin{bmatrix} \boldsymbol{j}_{i_1}^* & \boldsymbol{j}_{i_2}^* & \cdots & \boldsymbol{j}_{i_i}^* & \boldsymbol{0} & \cdots & \boldsymbol{0} \end{bmatrix},$$

$$\boldsymbol{J}_{\omega_i}^* = \begin{bmatrix} \boldsymbol{k}_1^* & \boldsymbol{k}_2^* & \cdots & \boldsymbol{k}_i^* & \boldsymbol{0} & \cdots & \boldsymbol{0} \end{bmatrix}$$

where $\boldsymbol{j}_{i_j}^* = \boldsymbol{k}_j^* \times (\boldsymbol{r}_i^* - \boldsymbol{p}_j^*)$. Therefore, the following equation is obtained from Eqs. (4)-(7):

$$\boldsymbol{s} = [\boldsymbol{\eta}^T,\ \boldsymbol{\mu}^T]^T = \boldsymbol{C}\dot{\boldsymbol{\chi}}_0 + \boldsymbol{D}\dot{\boldsymbol{\phi}} \quad (8)$$

where

$$\boldsymbol{C} = \begin{bmatrix} \boldsymbol{c}_{11} & \boldsymbol{c}_{12} \\ \boldsymbol{c}_{21} & \boldsymbol{c}_{22} \end{bmatrix},$$

$$\boldsymbol{D} = \begin{bmatrix} \boldsymbol{d}_{11}^{\mathrm{R}} & \boldsymbol{d}_{12}^{\mathrm{R}} & \cdots & \boldsymbol{d}_{1n^{\mathrm{R}}}^{\mathrm{R}} & \boldsymbol{d}_{11}^{\mathrm{L}} & \boldsymbol{d}_{12}^{\mathrm{L}} & \cdots & \boldsymbol{d}_{1n^{\mathrm{L}}}^{\mathrm{L}} \\ \boldsymbol{d}_{21}^{\mathrm{R}} & \boldsymbol{d}_{22}^{\mathrm{R}} & \cdots & \boldsymbol{d}_{2n^{\mathrm{R}}}^{\mathrm{R}} & \boldsymbol{d}_{21}^{\mathrm{L}} & \boldsymbol{d}_{22}^{\mathrm{L}} & \cdots & \boldsymbol{d}_{2n^{\mathrm{L}}}^{\mathrm{L}} \end{bmatrix},$$

$$\boldsymbol{c}_{11} = \boldsymbol{M}_{T_0} + \sum_{i=1}^{n^{\mathrm{R}}} \boldsymbol{M}_{T_i}^{\mathrm{R}} + \sum_{i=1}^{n^{\mathrm{L}}} \boldsymbol{M}_{T_i}^{\mathrm{L}},$$

$$\boldsymbol{c}_{12} = -\sum_{i=1}^{n^{\mathrm{R}}} \boldsymbol{M}_{T_i}^{\mathrm{R}}(\tilde{\boldsymbol{r}}_i^{\mathrm{R}} - \tilde{\boldsymbol{r}}_0) - \sum_{i=1}^{n^{\mathrm{L}}} \boldsymbol{M}_{T_i}^{\mathrm{L}}(\tilde{\boldsymbol{r}}_i^{\mathrm{L}} - \tilde{\boldsymbol{r}}_0),$$

$$\boldsymbol{c}_{21} = \tilde{\boldsymbol{r}}_0\boldsymbol{M}_{T_0} + \sum_{i=1}^{n^{\mathrm{R}}} \tilde{\boldsymbol{r}}_i^{\mathrm{R}}\boldsymbol{M}_{T_i}^{\mathrm{R}} + \sum_{i=1}^{n^{\mathrm{L}}} \tilde{\boldsymbol{r}}_i^{\mathrm{L}}\boldsymbol{M}_{T_i}^{\mathrm{L}},$$

$$\boldsymbol{c}_{22} = \boldsymbol{I}_{T_0} + \sum_{i=1}^{n^{\mathrm{R}}} \boldsymbol{I}_{T_i}^{\mathrm{R}} - \sum_{i=1}^{n^{\mathrm{R}}} \tilde{\boldsymbol{r}}_i^{\mathrm{R}}\boldsymbol{M}_{T_i}^{\mathrm{R}}(\tilde{\boldsymbol{r}}_i^{\mathrm{R}} - \tilde{\boldsymbol{r}}_0)$$

$$+ \sum_{i=1}^{n^{\mathrm{L}}} \boldsymbol{I}_{T_i}^{\mathrm{L}} - \sum_{i=1}^{n^{\mathrm{L}}} \tilde{\boldsymbol{r}}_i^{\mathrm{L}}\boldsymbol{M}_{T_i}^{\mathrm{L}}(\tilde{\boldsymbol{r}}_i^{\mathrm{L}} - \tilde{\boldsymbol{r}}_0),$$

$$\boldsymbol{d}_{1i}^* = \sum_{j=i}^{n^*} \boldsymbol{M}_{T_i}^*\tilde{\boldsymbol{k}}_i^*(\boldsymbol{r}_j^* - \boldsymbol{p}_i^*),$$

$$\boldsymbol{d}_{2i}^* = \sum_{j=i}^{n^*} \boldsymbol{I}_{T_j}^*\boldsymbol{k}_i^* + \tilde{\boldsymbol{r}}_j^*\boldsymbol{M}_{T_j}^*\tilde{\boldsymbol{k}}_i^*(\boldsymbol{r}_j^* - \boldsymbol{p}_i^*).$$

Here, we assume that the added mass and added inertia are constant. In reality, the added mass and inertia are variable but the influence of the variation is compensated by a control method in section 3.

© ISAROB 2013

2.3 Equation of motion

Considering the hydrodynamic forces described above and using the Newton-Euler formulation, the following equation of motion can be obtained:

$$\boldsymbol{M}(\boldsymbol{q}_1)\ddot{\boldsymbol{q}}_2 + \boldsymbol{b}_C(\boldsymbol{q}_1,\ \dot{\boldsymbol{q}}_2) + \boldsymbol{f}_D = \boldsymbol{u} \tag{9}$$

where $\boldsymbol{q}_1 = [\boldsymbol{x}_0^T,\ \boldsymbol{\phi}^T]^T$ and $\dot{\boldsymbol{q}}_2 = [\dot{\boldsymbol{\chi}}_0^T,\ \dot{\boldsymbol{\phi}}^T]^T$, $\boldsymbol{M}$ is the inertia matrix including the added mass $\boldsymbol{M}_{a_i}^*$ and inertia $\boldsymbol{I}_{a_i}^*$, $\boldsymbol{b}_C$ is the vector of Coliolis and centrifugal forces, $\boldsymbol{f}_D$ is the vector consisting of the drag, gravitational and buoyant forces and moments, $\boldsymbol{u} = [\boldsymbol{f}_0^T,\ \boldsymbol{\tau}_0^T, \boldsymbol{\tau}_m^T]^T$, $\boldsymbol{f}_0$ and $\boldsymbol{\tau}_0$ are the force and torque vectors of vehicle, $\boldsymbol{\tau}_m$ is the joint torque vector of manipulator. Furthermore, the relationship between $\boldsymbol{\omega}_*$ and $\dot{\boldsymbol{\psi}}_\dagger = [\psi_{r_\dagger},\ \psi_{p_\dagger},\ \psi_{y_\dagger}]^T$ ($\dagger = 0,\ e_{\mathrm{R}},\ e_{\mathrm{L}}$) is described as

$$\boldsymbol{\omega}_\dagger = \boldsymbol{S}_{\boldsymbol{\psi}_\dagger}\dot{\boldsymbol{\psi}}_\dagger \tag{10}$$

where

$$\boldsymbol{S}_{\boldsymbol{\psi}_\dagger} = \begin{bmatrix} \cos\psi_{p_\dagger}\cos\psi_{y_\dagger} & -\sin\psi_{y_\dagger} & 0 \\ \cos\psi_{p_\dagger}\sin\psi_{y_\dagger} & \cos\psi_{y_\dagger} & 0 \\ \sin\psi_{p_\dagger} & 0 & 1 \end{bmatrix}.$$

Thus the relationship between $\dot{\boldsymbol{q}}_1$ and $\dot{\boldsymbol{q}}_2$ is described as

$$\dot{\boldsymbol{q}}_2 = \boldsymbol{S}\dot{\boldsymbol{q}}_1 \tag{11}$$

where $\boldsymbol{S} = \mathrm{bolckdiag}\left\{\boldsymbol{E}_3, \boldsymbol{S}_{\boldsymbol{\psi}_0}, \boldsymbol{E}_{(n^{\mathrm{R}}+n^{\mathrm{R}})}\right\}$.

3 Digital RAC [8]

Differentiating Eqs. (3) and (8) with respect to time, the following equation can be obtained:

$$\boldsymbol{W}(t)\boldsymbol{\alpha}(t) = \boldsymbol{\beta}(t) + \boldsymbol{f}(t) - \dot{\boldsymbol{W}}(t)\boldsymbol{v}(t) \tag{12}$$

where

$$\boldsymbol{W} = \begin{bmatrix} \boldsymbol{C} + \boldsymbol{E_6} & \boldsymbol{D} \\ \boldsymbol{A} & \boldsymbol{B} \end{bmatrix},\ \boldsymbol{\alpha} = \begin{bmatrix} \ddot{\boldsymbol{\chi}}_0 \\ \ddot{\boldsymbol{\phi}} \end{bmatrix}, \boldsymbol{\beta} = \begin{bmatrix} \ddot{\boldsymbol{\chi}}_0 \\ \ddot{\boldsymbol{\chi}}_e \end{bmatrix},$$

$$\boldsymbol{f} = \begin{bmatrix} \dot{\boldsymbol{s}} \\ \boldsymbol{0} \end{bmatrix},\ \boldsymbol{v} = \begin{bmatrix} \dot{\boldsymbol{\chi}}_0 \\ \dot{\boldsymbol{\phi}} \end{bmatrix},\ \ddot{\boldsymbol{\chi}}_e = \begin{bmatrix} \ddot{\boldsymbol{\chi}}_e^{\mathrm{R}} \\ \ddot{\boldsymbol{\chi}}_e^{\mathrm{L}} \end{bmatrix},$$

$$\boldsymbol{A} = \mathrm{blockdiag}\{\boldsymbol{A}^{\mathrm{R}}, \boldsymbol{A}^{\mathrm{L}}\},\ \boldsymbol{B} = \mathrm{blockdiag}\{\boldsymbol{B}^{\mathrm{R}}, \boldsymbol{B}^{\mathrm{L}}\}$$

and $\dot{\boldsymbol{s}}$ is the external force including hydrodynamic force and thrust of the thruster which act on the base.

Discretizing Eq. (12) by a sampling period T, and applying $\boldsymbol{\beta}(k)$ and $\dot{\boldsymbol{W}}(k)$ to the backward Euler approximation, the following equation can be obtained:

$$\begin{aligned} T\boldsymbol{W}(k)\boldsymbol{\alpha}(k-1) &= \boldsymbol{\nu}(k) - \boldsymbol{\nu}(k-1) + T\boldsymbol{f}(k) \\ &\quad - \{\boldsymbol{W}(k) - \boldsymbol{W}(k-1)\}\boldsymbol{v}(k) \end{aligned} \tag{13}$$

where $\boldsymbol{\nu} = \left[\dot{\boldsymbol{\chi}}_0^T,\ \dot{\boldsymbol{\chi}}_e^T\right]^T$. Note that computational time delay is introduced to Eq. (13), and the discrete time kT is abbreviated to k.

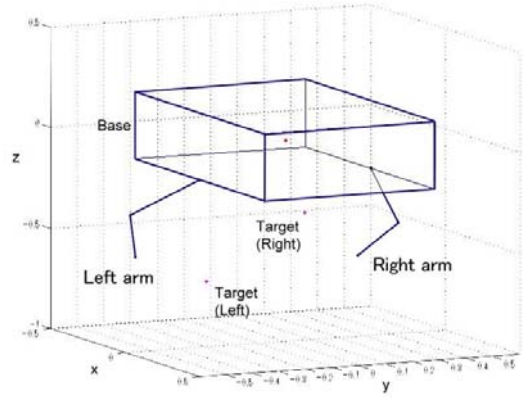

Fig. 2 Simulation model

Table 1 Physical parameters

	Base	Link 1	Link 2
Mass [kg]	23.25	4.65	3.1
Moment of inertia [kgm^2]	2.40	0.075	0.075
Link length [m]	0.5	0.3	0.3
Drag coefficient	1.2	1.0	1.0

For Eq. (13) the desired acceleration is defined as follows:

$$\begin{aligned} \boldsymbol{\alpha}_d(k) &= \frac{1}{T}\boldsymbol{W}^\sharp(k)\left[\boldsymbol{\nu}_d(k+1) - \boldsymbol{\nu}_d(k)\right. \\ &\quad \left. + \boldsymbol{\Lambda}\boldsymbol{e}_\nu(k) + T\boldsymbol{f}(k)\right] \end{aligned} \tag{14}$$

$$\boldsymbol{\nu}_d(k) = \frac{\boldsymbol{S}_{0e}}{T}\left\{\boldsymbol{x}_d(k) - \boldsymbol{x}_d(k-1) + \boldsymbol{\Gamma}\boldsymbol{e}_x(k-1)\right\} \tag{15}$$

where $\boldsymbol{e}_\nu(k) = \boldsymbol{\nu}_d(k) - \boldsymbol{\nu}(k)$, $\boldsymbol{e}_x(k) = \boldsymbol{x}_d(k) - bmx(k)$, $\boldsymbol{S}_{0e} = \mathrm{blockdiag}\{\boldsymbol{E}_3, \boldsymbol{S}_{\psi 0}, \boldsymbol{E}_3, \boldsymbol{S}_{\psi e_{\mathrm{R}}}, \boldsymbol{E}_3, \boldsymbol{S}_{\psi e_{\mathrm{L}}}\}$, and $W^\sharp$ is the pseudoinverse of W, $\boldsymbol{x}_d$ is the desired value of $\boldsymbol{x} = [\boldsymbol{x}_0^T, \left(\boldsymbol{x}_0^{\mathrm{R}}\right)^T, \left(\boldsymbol{x}_0^{\mathrm{L}}\right)^T]^T$, $\boldsymbol{\Lambda} = \mathrm{diag}\{\lambda_i\}$ and $\boldsymbol{\Gamma} = \mathrm{diag}\{\gamma_i\}$ ($i = 1, \cdots, (6 + n^{\mathrm{R}} + n^{\mathrm{L}})$) are the velocity and the position feedback gain matrices.

From Eqs. (13), (14) and (15), if λ_i and γ_i are selected to satisfy $0 < \lambda_i < 1$ and $0 < \gamma_i < 1$, respectively, and the convergence of the acceleration error, $\boldsymbol{e}_\alpha(k) = \boldsymbol{\alpha}_d(k) - \boldsymbol{\alpha}(k)$, tends to zero as k tends to infinity, then the convergence of $\boldsymbol{e}_\nu(k)$ and $\boldsymbol{e}_x(k)$ to zero as k tends to infinity can be ensured.

4 Simulation

In this section, simulations using a robot shown in Fig. 2 are done. Physical parameters of the robot are shown in Table 1. These parameters are based on the Reference [8].

The simulation was carried out under the following condition.

© ISAROB 2013

The initial relative angles of the robot were $\phi_1^{\mathrm{R}} = -\pi/9$[rad], $\phi_2^{\mathrm{R}} = \pi/9$[rad], $\phi_1^{\mathrm{L}} = \pi/3$[rad] and $\phi_2^{\mathrm{L}} = -\pi/9$[rad]. The desired end-tip positions were set up along a straight path from the initial positions to the targets in $y - z$ plane. calculated from trapezoidal velocity pattern. On the other hand, the basic desired position and attitude of vehicle were set up the initial values. The sampling period was T=1/60[s] and the feedback gains were $\boldsymbol{\Lambda} = \boldsymbol{\Gamma} = \mathrm{diag}\ \{$ 0.01, 0.01, 0.01, 0.01, 0.01, 0.01, 0, 0.2, 0.2, 0, 0, 0, 0, 0.2, 0.2, 0, 0, 0 $\}$.

The simulation result is shown in Fig. 3. In this figure, (a) is the motion of the robot, (b) is the time history. From Fig. 3 it can be seen that the end-tips of two armsr and base follow the reference trajectories in spite of the influence of the hydrodynamic forces and the tracking errors are very small. The experimental result shows that the control performance can be improved by using the proposed method.

5 Conclusion

In this paper, we propose a RAC method for dual arm UVMS based on Reference [8]. Simulation results showed the effectiveness of the proposed control method.

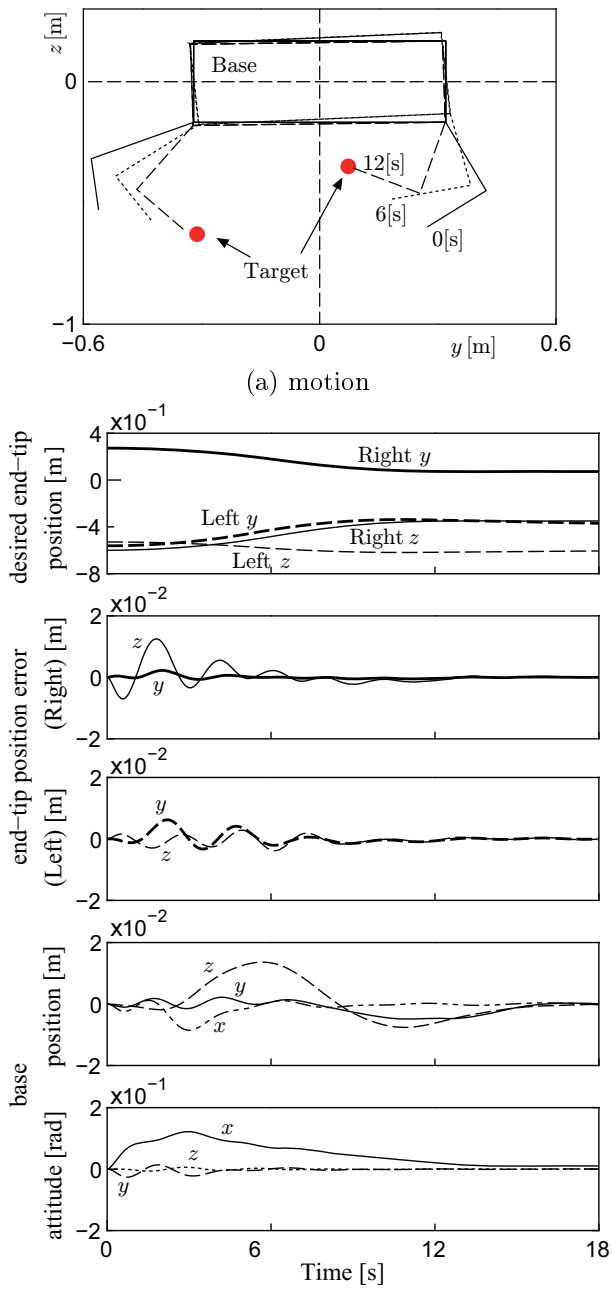

(a) motion

(b) time history

Fig. 3 Simulation result

References

[1] H. Maheshi *et al.*, "A Coordinated Control of an Underwater Vehicle and Robotic Manipulator", *J. Robotic Systems*, Vol. 8, No. 3, pp. 339 – 370, 1991.

[2] T. W. McLain *et al.*, "Experiments in the Coordinated Control of an Underwater Arm/Vehicle System", *Autonomous Robots 3*, Kluwer Academic Publishers, pp. 213 – 232, 1996.

[3] G. Antonelli *et al.*, "Tracking Control for Underwater Vehicle-Manipulator Systems with Velocity Estimation", *IEEE J. Oceanic Eng.*, Vol. 25, No. 3, pp. 399 – 413, 2000.

[4] N. Sarkar and T. K. Podder, "Coordinated Motion Planning and Control of Autonomous Underwater Vehicle-Manipulator Systems Subject to Drag Optimization", *IEEE J. Oceanic Eng.*, Vol. 26, No. 2, pp. 228 – 239, 2001.

[5] G. Antonelli, *Underwater Robotics*, Springer, pp. 1194–1206, 2003.

[6] B. Xu, S. R. Pandian, N. Sakagami and F. Petry, "Neuro-Fuzzy Control of Underwater Vehicle-Manipulator Systems", *J. Franklin Institute*, 349, pp. 1125–1138, 2012.

[7] S. Mohan and J. Kim, "Indirect Adaptive Control of an Autonomous Underwater Vehicle-Manipulator System for Underwater Manipulation Tasks", Ocean Engineering, Vol. 54, pp. 233–243, 2012.

[8] S. Sagara *et al.*,"Digital RAC for Underwater Vehicle-Manipulator Systems Considering Singular Configuration", *J. Artificial Life and Robotics*, Vol. 10, No. 2, pp. 106 – 111, 2006.

[9] S. Sagara *et al.*,"Digital RAC with a Disturbance Observer for Underwater Vehicle-Manipulator Systems", *J. Artificial Life and Robotics*, Vol. 15, No. 3, pp. 270 – 274, 2010.

[10] N. Sakagami *et al.*, "Development of a Human-Sized ROV with Dual-Arm", Proc. MTS/IEEE OCEANS 2010, 2010.

© ISAROB 2013

The Eighteenth International Symposium on Artificial Life and Robotics 2013 (AROB 18th '13),
Daejeon Convention Center, Daejeon, Korea, January 30-February 1, 2013

Speech synthesis of emotions using vowel features of a speaker

K. Boku, T. Asada, Y. Yoshitomi, and M. Tabuse

Graduate School of Life and Environmental Sciences, Kyoto Prefectural University,

1-5 Nakaragi-cho, Shimogamo, Sakyo-ku, Kyoto 606-8522, Japan

E-mail: {boku, t_asada}@mei.kpu.ac.jp, {yoshitomi, tabuse}@kpu.ac.jp

Abstract: Recently, methods for adding emotion to synthetic speech have received considerable attention in the field of speech synthesis research. We previously proposed a case-based method for generating emotional synthetic speech by exploiting the characteristics of the maximum amplitude and the utterance time of vowels, and the fundamental frequency of emotional speech. In the present study, we propose a method in which our reported method is further improved by controlling the fundamental frequency of emotional synthetic speech. As an initial investigation, we adopted the utterance of a Japanese name that is semantically neutral. By using the proposed method, emotional synthetic speech made from the emotional speech of one male subject was discriminable with a mean accuracy of 90.0% when 18 subjects listened to the emotional synthetic utterances of "angry," "happy," "neutral," "sad," or "surprised" when the utterance was the Japanese name "Taro."

Keywords: Emotional speech, Feature parameter, Synthetic speech, Emotional synthetic speech, Vowel

1 INTRODUCTION

Recently, methods for adding emotions to synthetic speech have received considerable attention in the field of speech synthesis research [1]-[8]. To generate emotional synthetic speech, it is necessary to control the prosodic features of the utterances. Natural language is mainly composed of vowels and consonants. The Japanese language has five vowels. A vowel has a more dominant impact on the listener's impression than does a consonant, primarily because a vowel has a longer utterance time and a larger amplitude in comparison with a consonant. We previously proposed a case-based method for generating emotional synthetic speech by exploiting the characteristics of the maximum amplitude and the utterance time of the vowels, as obtained by using a speech recognition system, and the fundamental frequency of emotional speech [9].

In the present study, we propose a method in which the method reported in [9] is further improved by controlling the fundamental frequency of emotional synthetic speech. The advantage of our study over reported research [1]-[8] is usage of the vowel feature in emotional speech to generate emotional synthetic speech.

2 PROPOSED METHOD

In the first stage, we obtain audio data of emotional speech as a WAV file when a subject speaks with each of the intentional emotions of "angry," "happy," "neutral," "sad," and "surprised." Then, for each kind of emotional speech, we measure the time of each vowel utterance and the value of the maximum amplitude of the waveform while speaking the vowel, and the fundamental frequency of emotional speech.

In the second stage, we synthesize the phoneme sequence uttered by the subject. This stage consists of the following five steps.

Step 1: For a vowel with a consonant appearing just before it in synthetic speech with neutral emotion, the total phonation duration time of the vowel and the consonant is transformed into the time for speech with neutral emotion by the human subject. The synthetic speech obtained by this processing is hereinafter called "neutral synthetic speech."

Step 2: For a vowel with a consonant appearing just before it in synthetic speech with one of the intentional emotions of "angry," "happy," "sad," and "surprised," the total phonation duration time of the vowel and consonant is set as the value whose ratio to that in neutral synthetic speech is equal to the ratio of the phonation duration time of the vowel in emotional speech to the phonation duration time of the vowel in neutral speech.

Step 3: The fundamental frequency of synthetic speech, obtained by the processing up to Step 2, is initially adjusted based on the fundamental frequency of the emotional speech.

Step 4: For a vowel with a consonant appearing just before it in synthetic speech obtained by the processing up to Step 3, the amplitudes are transformed into final values by twice multiplying the ratio (Max_{em}/Max_{ne}), where Max_{em} and Max_{ne} denote the maximum amplitude of the vowel in emotional speech and that in neutral speech, respectively. The synthetic speech obtained by the processing of Steps 1 to 4 is hereinafter called "emotional synthetic speech."

© ISAROB 2013

Step 5: The fundamental frequency of emotional synthetic speech, obtained by the processing up to Step 4, is further adjusted based on the fundamental frequency of the emotional speech.

If no consonant appears, the process described in Steps 1 to 5 applies to just the vowel. In the present study, the processing described in Step 5 is added to the method reported in [9].

3 EXPERIMENTS

3.1 Condition

We used a speech recognition system named Julius [10] to save the timing positions of the start of speech, and the first and last vowels. A male subject (Subject A) in his 50s spoke the semantically neutral utterance of the Japanese first name "Taro" with each of the intentional emotions of "angry," "happy," "neutral," "sad," and "surprised." His audio data were recorded as WAV files. We measured the utterance time of the first vowel and the maximum absolute value of the amplitude of the waveform while speaking the first vowel. For the last vowel, we also measured the utterance time and the maximum absolute value of the amplitude of the waveform. Tables 1 and 2 show the phonation time and the maximum amplitude, respectively, of each vowel in each emotion category as spoken by the subject.

Table 1. Phonation time of vowels as spoken by the subject [9]

Emotion category	Phonation time (s)		Normalized phonation time (Ratio to the value of "Neutral")	
	/a/	/o/	/a/	/o/
Angry	0.030	0.090	1.000	0.310
Happy	0.100	0.240	3.333	0.828
Neutral	0.030	0.290	1.000	1.000
Sad	0.100	0.140	3.333	0.483
Surprised	0.050	0.200	1.667	0.690

Table 2. Maximum amplitude of vowels as spoken by the subject [9]

Emotion category	Maximum amplitude		Normalized maximum amplitude (Ratio to the value of "Neutral")	
	/a/	/o/	/a/	/o/
Angry	1216	459	1.332	0.630
Happy	1904	1055	2.085	1.447
Neutral	913	729	1.000	1.000
Sad	587	295	0.643	0.405
Surprised	1408	1256	1.542	1.723

We performed a principal component analysis (PCA) to reveal the prosodic characteristics of "angry," "happy," "neutral," "sad," and "surprised" in emotional speech by using the normalized utterance time and the normalized maximum amplitude of the first and last vowels as the feature parameters. Here, normalization of the utterance time and the maximum amplitude was performed by setting the mean value for the five emotions to zero and setting the standard deviation for each of the five emotions to one. Fig. 1 shows the feature vector space expressed by the first and second components obtained by PCA for the five kinds of emotional speech for /taro/.

Then, the fundamental frequency of emotional speech with each of the intentional emotions of "angry," "happy," "neutral," "sad," and "surprised" was measured for the Japanese first name "Taro." The fundamental frequency was selected because it is one of the best-known feature parameters for speech. As shown in Fig. 2, each emotion had the characteristic time-dependence of the fundamental frequency.

Voice Sommelier Neo (premium version; Hitachi Business Solution Co., Ltd., Yokohama, Japan) [11] was

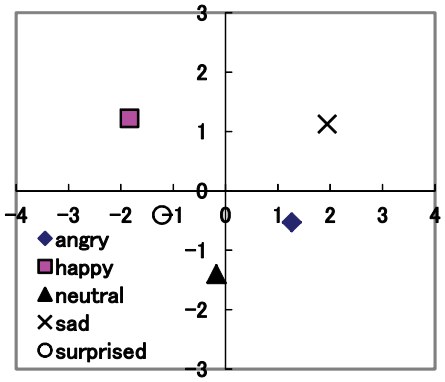

Fig. 1. Feature space of the first (horizontal) and second (vertical) components for /taro/ [9]

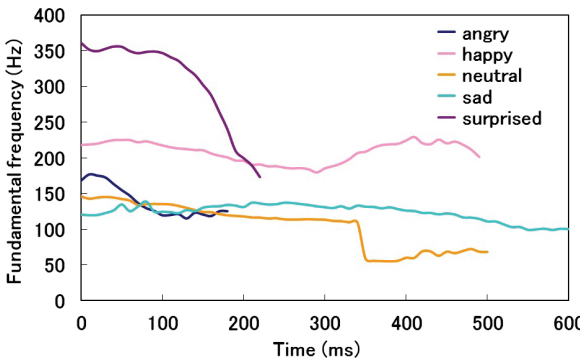

Fig. 2. Fundamental frequencies of waveforms of Subject A while speaking "Taro"

© ISAROB 2013

used as the speech synthesizer for Steps 1 to 3 in Section 2. For conversion of the amplitude of each vowel and consonant described in Step 4 in Section 2, a digital audio editor was used. Then, the method [12] using resampling and a correlation function were used for Step 5 in Section 2.

When we applied the method described in Section 2 to the above case, the mode of Male 1 (bright voice) in Voice Sommelier Neo was used. In this case, each vowel was /a/ and /o/, and then the vowel and the consonant just before the vowel was /ta/ and /ro/.

The emotional synthetic speech without adding the processing described in Step 5 of Section 2 is hereinafter called "emotional synthetic speech No. 1," whereas the emotional synthetic speech with adding the processing described in Step 5 of Section 2 is hereinafter called "emotional synthetic speech No. 2." The emotional synthetic speech No. 1 was made only by the method reported in [9] and used for the evaluation of Step 5 of Section 2, which is the new processing in the proposed method.

The 18 subjects participating in the experiments consisted of the following: Subjects A and B, two males in their 50s; Subject C, one male in his 30s; Subjects D, E, F, G, H, I, J, K, L, M and N, 11 males in their 20s; Subjects O, P, Q and R, four females in their 20s. The subjects made a judgment of the emotional category after listening to five utterances one by one in the following order: emotional speech by Subject A, emotional synthetic speech No. 1, emotional speech by Subject A, and emotional synthetic speech No. 2.

3.2 Results and discussion

Figs. 3 and 4 show the fundamental frequencies of emotional synthetic speech Nos. 1 and 2, respectively. The characteristics of each type of emotional speech shown in Fig. 2 are more precisely reflected in Fig. 4, which was obtained by the proposed method, than they were in Fig. 3, which was obtained by the method reported in [9]. As illustrated in Fig. 5, differences among the emotional speech waveforms were observed. To some extent, the differences of the waveforms were also reflected in each emotional synthetic speech. Voice Sommelier Neo used in Step 3 in Section 2 has some restrictions in controlling the frequency of synthetic speech, so it was difficult to adjust the fundamental frequency adequately. The differences between the waveforms of the emotional speech waveform of "neutral" and the synthetic speech waveform of "neutral" are shown in Fig. 5. As expected, the emotional synthetic speech inevitably had some waveform differences in comparison with the corresponding emotional speech.

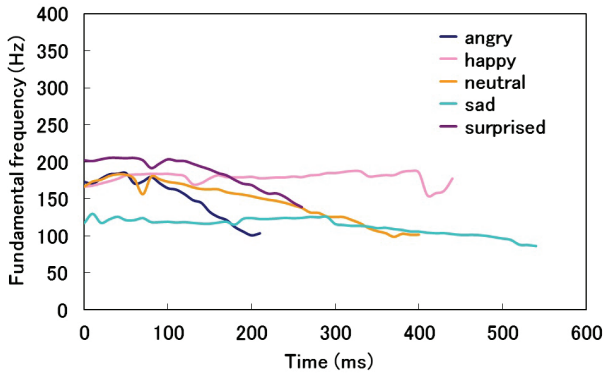

Fig. 3. Fundamental frequencies of waveforms of emotional synthetic speech No. 1 of "Taro"

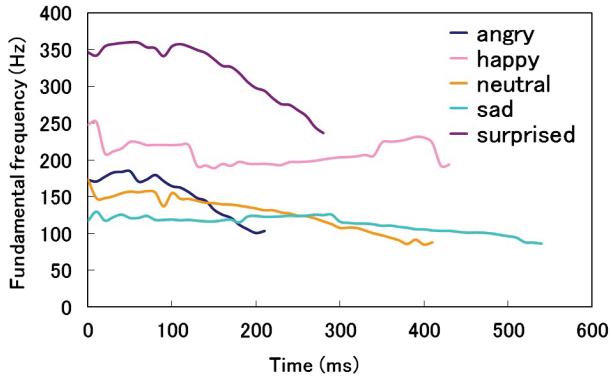

Fig. 4. Fundamental frequencies of waveforms of emotional synthetic speech No. 2 of "Taro"

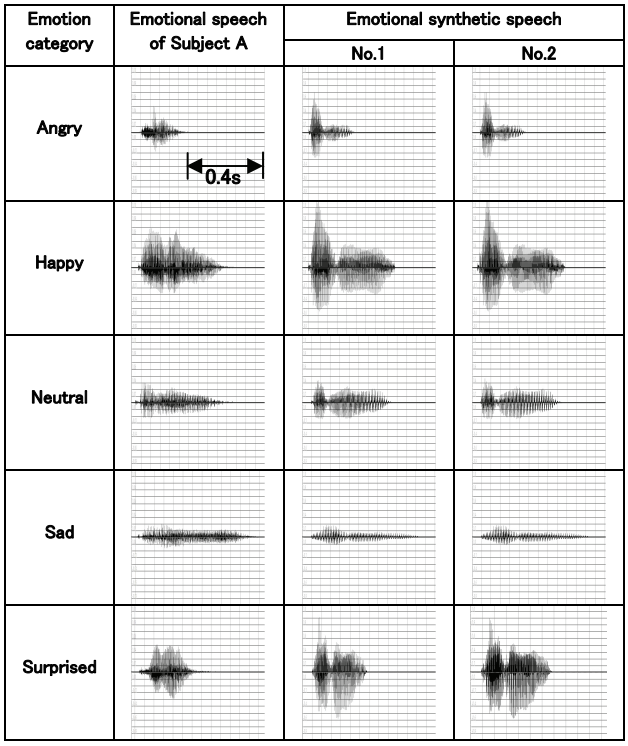

Fig. 5. Waveforms of emotional speech of Subject A and emotional synthetic speech Nos. 1 and 2

© ISAROB 2013

Table 3 shows the results of the subjective evaluations. In Table 3, the results for emotional speech were calculated as an average of the values obtained in two sets of listening by all 18 subjects. As illustrated in Table 3, the mean accuracy of emotional speech, emotional synthetic speech No. 1, and emotional synthetic speech No. 2 was 95.0%, 70.0%, and 90.0%, respectively. The advantage of emotional synthetic speech No. 2 over No. 1 suggests that further adjustment of fundamental frequency in the proposed method made a much clearer impression on the subjects for emotional synthetic speech.

Table 3. Results of the subjective evaluation

(1) Emotional speech

		Input				
		Angry	Happy	Neutral	Sad	Surprised
Recognition	Angry	97.2	0	0	2.8	0
	Happy	0	94.4	0	0	5.6
	Neutral	0	2.8	94.4	2.8	0
	Sad	0	0	5.6	94.4	0
	Surprised	2.8	2.8	0	0	94.4

(%)

(2) Emotional synthetic speech No.1

		Input				
		Angry	Happy	Neutral	Sad	Surprised
Recognition	Angry	83.3	0	0	0	22.2
	Happy	0	50.0	38.8	0	5.6
	Neutral	0	44.4	55.6	11.1	0
	Sad	0	0	5.6	88.9	0
	Surprised	16.7	5.6	0	0	72.2

(%)

(3) Emotional synthetic speech No.2

		Input				
		Angry	Happy	Neutral	Sad	Surprised
Recognition	Angry	88.8	5.6	0	0	11.1
	Happy	5.6	88.8	0	0	0
	Neutral	0	5.6	94.4	11.1	0
	Sad	0	0	5.6	88.9	0
	Surprised	5.6	0	0	0	88.9

(%)

4 CONCLUSION

We previously proposed a case-based method for generating emotional synthetic speech by exploiting the characteristics of the maximum amplitude and the utterance time of the vowels, as obtained by using a speech recognition system, and the fundamental frequency of emotional speech. In the present study, we propose a method in which our reported method is further improved by controlling the fundamental frequency of emotional synthetic speech. By using the proposed method, emotional synthetic speech made from the emotional utterances of one male subject was discriminable with a mean accuracy of 90.0% when 18 subjects listened to one of the emotional synthetic speech utterances of "angry," "happy," "neutral," "sad," or "surprised" for the Japanese name "Taro."

Acknowledgments

We would like to thank all the participants who cooperated with us in the experiments.

REFERENCES

[1] Donna E (2005), Expressive speech: Production, perception and application to speech synthesis. Acoustical Science and Technology, 26(4):317–325

[2] Iida A, Iga S, Higuchi F, et al (2000), A prototype of a speech synthesis system with emotion for assisting communication (in Japanese). Transaction of Human Interface Society, 2(2): 63-70

[3] Katae N, Kimura S (2000), An effect of voice quality and control in emotional speech synthesis (in Japanese). Proceedings of the autumn meeting the Acoustical Society of Japan: Vol. 2. pp.187-188

[4] Moriyama T, Mori S, Ozawa S (2009), A synthesis method of emotional speech using subspace constraints in prosody (in Japanese). Transaction of Information Processing Society of Japan, 50(3): 1181-1191

[5] Murray IR, Arnott JL (1993), Toward the simulation of emotion in synthetic speech: A review of the literature on human vocal emotion. Journal of the Acoustical Society of America, 93(2):1097–1108

[6] Murray IR, Edgington MD, Campion D, et al (2000), Rule-based emotion synthesis using concatenated speech. Proceedings of Speech and Emotion, ISCA Tutorial and Research Workshop, Newcastle, Northern Ireland, UK pp.173–177

[7] Ogata S, Yotsukura T, Morishima S (2000), Voice conversion to append emotional impression by controlling articulation information (in Japanese). IEICE technical report, human information processing, 99(582):53-58

[8] Schröder M (2001), Emotional speech synthesis – A review. In: Dalsgaard P, Lindberg B, Benner H (eds), Proceedings of 7th European Conference on Speech Communication and Technology, Aalborg, Kommunik Grafiske Losninger A/S, Vol.1, pp.561–564

[9] Boku K, Asada T, Yoshitomi Y et al (2012), In: Roger L (ed), Software engineering, artificial intelligence, networking, and parallel/distributed computing 2012, Springer, Berlin, Germany, pp.129-141

[10]Julius development team (2011), Open-source large vocabulary CSR engine Julius. Retrieved June 23, 2012, from http://julius.sourceforge.jp/en_index.php?q=index-en.html

[11]Hitachi Business Solution Co. Ltd. (2012), Voice Sommelier Neo. Retrieved June 23, 2012, from http://hitachi-business.com/products/package/sound /voice/index.html

[12]Aoki N (2008), Sound programming in C (in Japanese). Ohmsha, Tokyo, Japan, pp.141-160

© ISAROB 2013

The Eighteenth International Symposium on Artificial Life and Robotics 2013 (AROB 18th '13),
Daejeon Convention Center, Daejeon, Korea, January 30-February 1, 2013

A system for facial expression recognition of a speaker using thermal image processing and feature vector space characteristics

T. Asada, Y. Yoshitomi, Y. Nakanishi, and M. Tabuse

Graduate School of Life and Environmental Sciences Kyoto Prefectural University,
1-5 Nakaragi-cho, Shimogamo, Sakyo-ku, Kyoto 606-8522, Japan
E-mail: t_asada@mei.kpu.ac.jp, yoshitomi@kpu.ac.jp, y_nakanishi@mei.kpu.ac.jp, tabuse@kpu.ac.jp

Abstract: We developed an on-line system for the facial expression recognition of a speaker. In the feature vector space in image processing, the positions of feature vectors generated with imperfection, which caused misrecognition of facial expression, tended to be far from the center of gravity of the class to which the feature vectors belonged. In the present study, to omit the feature vectors generated with imperfection in image processing, a module using reject criteria in the feature vector space was added to the system for facial expression recognition. We adopted the utterance of the Japanese name "Taro," which is semantically neutral, to investigate the improved system. The facial expressions of one subject were analyzed when he exhibited one of the intentional facial expressions of "angry," "happy," "neutral," "sad," and "surprised." By using the facial expression strength, the position of the test feature vector in the feature vector space is shown.

Keywords: Facial expression recognition, Feature vector space, Reject criteria, Speech recognition, Thermal image processing.

1 INTRODUCTION

Although the mechanism for recognizing facial expressions has received considerable attention in the field of computer vision research, it still falls far short of human capability, especially from the viewpoint of robustness under widely varying lighting conditions. One of the reasons for this lack of robustness is that nuances of shade, reflection, and local darkness influence the accuracy of facial expression recognition through the inevitable change of gray levels. To avoid this problem and to develop a method for facial expression recognition applicable under widely varied lighting conditions, we do not use visible ray images. Instead, we use images produced by infrared rays (IR), which show the thermal distribution of the face [1]-[17]. We previously developed an on-line system for the facial expression recognition of a speaker by image processing [13]. In the feature vector space, the positions of feature vectors generated with imperfection, which caused misrecognition of facial expression, tended to be far from the center of gravity of the class to which the feature vectors belonged.

In the present study, to omit the feature vectors generated with imperfection in image processing, a module using reject criteria in the feature vector space was added to the system [13] for facial expression recognition. As an initial investigation, we adopted the utterance of the Japanese name "Taro," which is semantically neutral.

2 IMAGE ACQUISITION

The principle behind thermal image generation is the Stefan–Boltzmann law, expressed as $W = \varepsilon\sigma T^4$, where ε is emissivity, σ is the Stefan–Boltzmann constant (=5.6705×10^{-12} W/cm^{2}K^4), and T is the temperature (K). For human skin, ε is estimated as 0.98 to 0.99 [18], [19]. In the present study, the approximate value of 1 was used as ε for human skin because the value of ε for almost all substances is lower than that of human skin [14]. Consequently, the human face region is easily extracted from an image by using the value of 1 for ε [1]–[17]. In principle, the temperature measurements by IR do not depend on skin color [19], darkness, or lighting condition, and so the face region and its characteristics are easily extracted from a thermal image.

3 PROPOSED SYSTEM

Fig. 1 illustrates the flowchart of our method [17]. We have two modules in our system. The first is a module for speech recognition and dynamic image analysis, and the second is a module for learning and recognition. In the module for learning and recognition, we embedded the module for front-view face judgment [10]. Some details of our method are explained in our book [14].

3.1 Speech recognition and dynamic image analysis

We use a speech recognition system named Julius [20] to obtain the timing positions of the start of speech and the first and last vowels in a WAV file [8]–[10]. Fig. 2 shows an example of the waveform of the Japanese name "Taro"; the

© ISAROB 2013

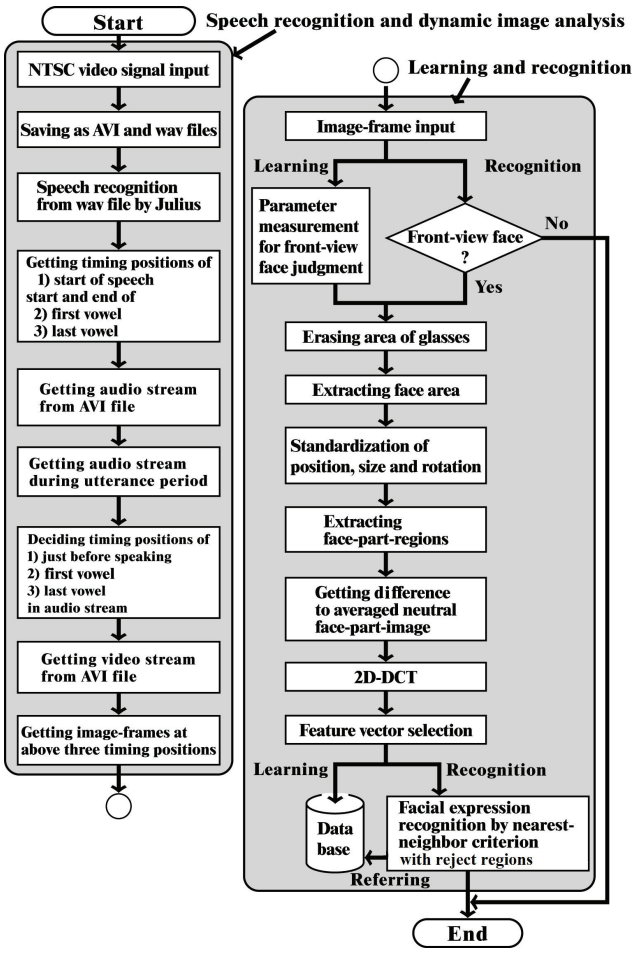

Fig. 1. Flowchart of our method [17]

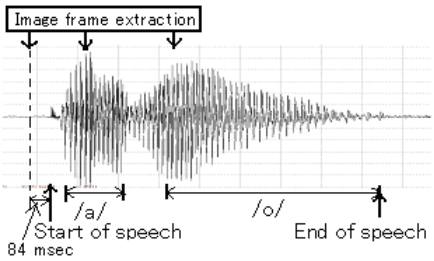

Fig. 2. Speech waveform of "Taro" and timing positions for image frame extraction [8]

timing position of the start of speech and the timing ranges of the first vowel (/a/) and the last vowel (/o/) are decided by Julius. By using the timing position of the start of speech and the timing ranges of the first and last vowels obtained from the WAV file, three image frames are extracted from an AVI file at the three timing positions. For the timing position just before speaking, we use the timing position of 84 ms before the start of speech, as determined in our previously reported study [7]. For the timing position of the first vowel, we use the position where the absolute value of the amplitude of the waveform is the maximum while speaking the vowel. For the timing position of the last vowel, we apply the same procedure used for the first vowel.

3.2 Learning and recognition

For the static images obtained from extracted image frames, the process of erasing the area of the glasses, extracting the face area, and standardizing the position, size, and rotation of the face are performed according to the method described in our previously reported study [7]. Fig. 3 shows the blocks for extracting the face areas in a thermal image having 720×480 pixels. In the next step, we generate difference images between the averaged neutral face image and the target face image in the extracted face areas to perform a 2D discrete cosine transform (2D-DCT). The feature vector is generated from the 2D-DCT coefficients according to a heuristic rule [6], [7]. We call the method used in our previously reported research [8]-[16] the "conventional" method, in which the facial expression was recognized by the nearest-neighbor criterion in the feature vector space by using the training data just before speaking and when speaking the phonemes of the first and last vowels.

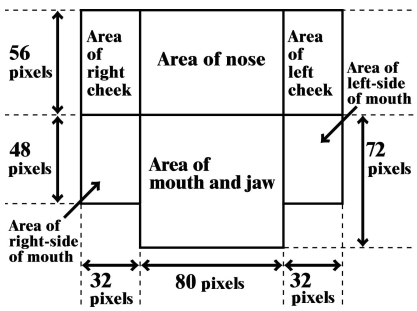

Fig. 3. Blocks for extracting face areas in the thermal image [13]

3.3 Proposed method for facial expression recognition

Imperfection in image processing with our method for facial expression recognition inevitably occurs, and results in the misrecognition of facial expression. To overcome this difficulty, a method is proposed that uses reject criteria in the feature vector space by using the training data just before speaking and when speaking the phonemes of the first and last vowels.

The new algorithm of pattern recognition in the feature vector space of facial expression recognition is as follows:

Step 1: For all classes in the initial condition, the following procedure is performed. Vector $\boldsymbol{g}_i$ of the center of gravity of the class $i\,(i = 1,2,\cdots,n)$, where n is the number of classes, is obtained. Then, go to Step 2.

***Step 2*:** For each class i, the following procedure is performed. The elements of class i are narrowed using the way that the feature vector having the largest distance from vector $\boldsymbol{g}_i$ among those in class i is omitted from the elements in class i. Then, if the number of feature vectors of class i at that moment is bigger than half the number N_i of feature vectors in the class defined in Step 1, go to Step 3. Otherwise, go to Step 4.

***Step 3*:** For class i, vector $\boldsymbol{g}_i$ is updated. Then, return to Step 2.

***Step 4*:** Except the class of neutral facial expression, the threshold T_j of class j is decided as (a) the value of the maximum distance between vector $\boldsymbol{g}_j$ and the feature vector of class j in the initial condition, under the constraint that vector $\boldsymbol{g}_j$ among all vectors $\boldsymbol{g}_i$ $(i = 1,2,\cdots,n)$ is the nearest to the feature vector. Similarly, for the class of neutral facial expression, the threshold T_j of class j is decided as the mean value of (a) and (b), where (b) is the minimum value among the values of the distance between vector $\boldsymbol{g}_j$ and the feature vector of class j in the initial condition, under the constraint that vector $\boldsymbol{g}_j$ among all vectors $\boldsymbol{g}_i$ $(i = 1,2,\cdots,n)$ is not the nearest to the feature vector. Go to Step 5.

***Step 5*:** The elements of each class i are narrowed using the constraint that the distance between the feature vectors and vector $\boldsymbol{g}_i$ should not be bigger than threshold T_i. Go to Step 6.

***Step 6*:** The facial expression is recognized by the nearest-neighbor criterion in the feature vector space using (1) the feature vectors selected by the procedure up to Step 5, (2) the vector $\boldsymbol{g}_i$. Then, the recognized result showing class i is rejected if the distance between the test feature vector and the selected vector by the vector nearest-neighbor criterion is bigger than the threshold T_i. Otherwise the recognized result showing class i is accepted. Then, go to Step 7.

***Step 7*:** The element $\boldsymbol{v}_i$ having the shortest distance d_i to the test feature vector is found among (1) those selected by the procedure up to Step 5 for each class i and (2) the vector $\boldsymbol{g}_i$. The facial expression strength FES_i for each class i is defined as (d_s/d_i), where $d_s = \min_{i \in I} d_i$ under the condition that set I consists of all classes.

In the present study, the Euclidean distance is used as the distance in the feature vector space. Special treatment for the class of neutral facial expression is used because in many cases the value of (a) tends to be too small to accept the recognized result showing class j. Steps 1 to 6 are the same as those in [17]. The facial expression strength FES_i described in Step 7 is used for expressing the position of the test feature vector in the feature vector space.

3.4 Proposed system

Fig. 4 shows the structure of the proposed system. Figs. 5 and 6 show flow charts of the system during facial expression learning and recognition, respectively. Figs. 5 and 6 demonstrate the processing shared by three computers (PC1, PC2, and PC3) connected by cables to form a local area network for performing the flow chart shown in Fig. 1. In Figs. 5 and 6, a line with an arrow attached denotes a process order, while a dotted line with an arrow attached denotes a communication from a PC to another PC in the local area network. The only difference between Figs. 5 and 6 is the processing in PC3. An NTSC video signal from a thermal video system is successively inputted to either PC1 or PC2 to obtain image frames: (i) just before speaking, and speaking (ii) the first vowel and (iii) the last vowel in an utterance. We use the proposed system with our previously reported method [10] for front-view face judgment.

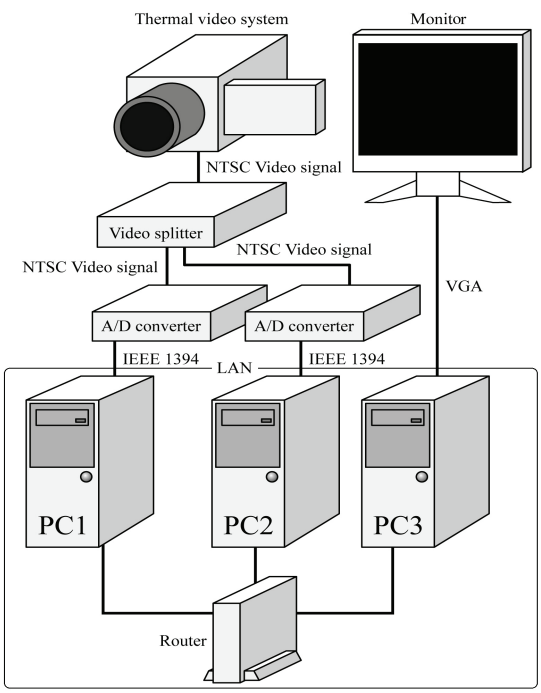

Fig. 4. Structure of the proposed system [13]

© ISAROB 2013

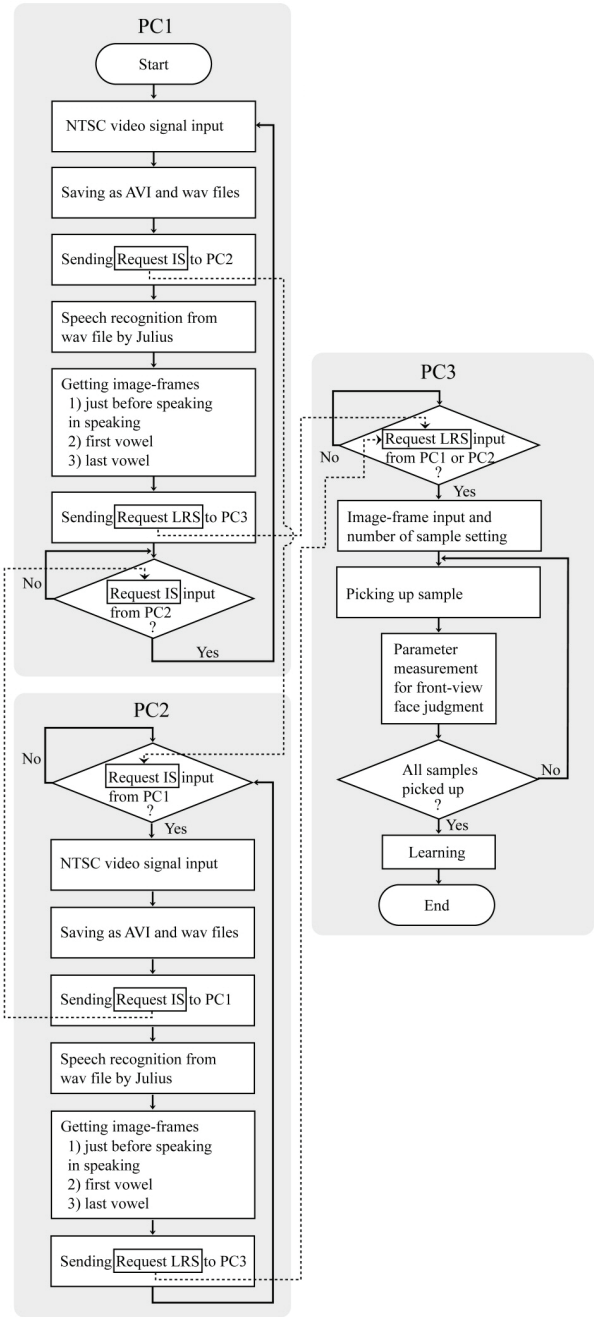

Fig. 5. Flow chart of the proposed system in learning for facial expression recognition [13]

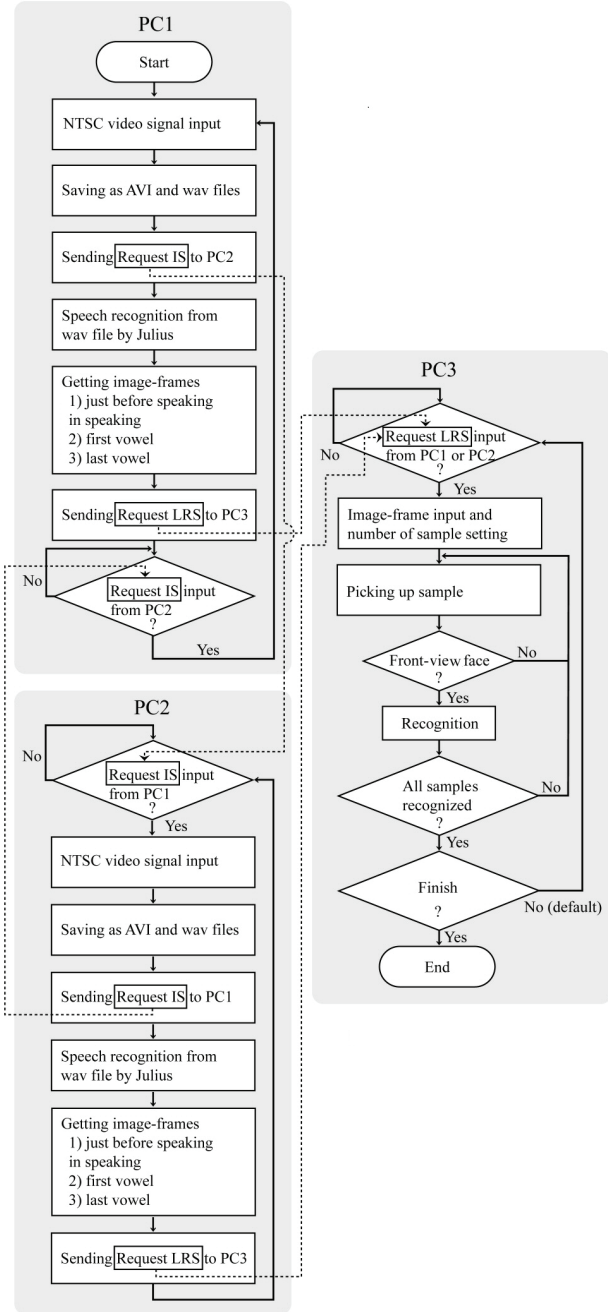

Fig. 6. Flow chart of the proposed system during facial expression recognition [13]

4 EXPERIMENTS

4.1 Condition

The thermal image produced by the thermal video system (Nippon Avionics TVS-700) and the sound captured from an Electret condenser microphone (Sony ECM-23F5), as amplified by a mixer (Audio-Technica AT-PMX5P), were transformed through an audio and video distribution amplifier (Maspro Denkoh VSP4) into a digital signal by two A/D converters (Thomson Canopus ADVC-100 for PC1 in Fig. 4 and Thomson Canopus ADVC-300 for PC2 in Fig. 4) and input into two computers (PC1 and PC2 in Fig. 4) with the same specification (Dell Optiplex 780, CPU: Intel Core 2 Duo E8400 3.00 GHz, main memory: 4.00 GB, OS: Windows 7 Professional (Microsoft) with an IEEE1394 interface board (I·O data device 1394-PCI3/DV6)). As PC3 in Fig. 4, we used a computer (Dell Precision T1600, CPU: Intel Xeon CPU E31225 3.10 GHz, main memory: 8.00 GB, OS: Windows 7 Professional (Microsoft)). The three computers (PC1, PC2, and PC3) were connected through a router (Buffalo WZR-HP-AG300H) with cables. We used

© ISAROB 2013

Visual C++ 6.0 (Microsoft) as the programming language. To generate a thermal image, we set the condition that the thermal image had 256 gray levels for the detected temperature of 304 to 309 K. Therefore, one gray level corresponded to 1.95 10^{-2} K. The temperature range for generating a thermal image was decided to easily extract the face area on the image. We saved the visual and audio information in the computer as a Type 2 DV-AVI file, in which the video frame had a spatial resolution of 720×480 pixels and 8-bit gray levels, and the sound was saved in a stereo PCM format, 48 kHz and 16-bit levels.

Subject A, a male wearing glasses, exhibited in alphabetic order each of the intentional facial expressions of "angry," "happy," "neutral," "sad," and "surprised," while speaking the semantically neutral utterance "Taro." Fig. 7 shows examples of the thermal images of subject A.

In the experiment, subject A intentionally kept front-view faces in the AVI files saved as both the training and test data. From one sample, we obtained three images at the timing positions of just before speaking and just speaking the phonemes of the first and the last vowels.

We assembled twenty samples as training data and ten samples as test data for each facial expression in each case, in which all facial expressions of test data for all subjects were judged as front-view faces by the method mentioned in our previously reported paper [10]. For each sample, we obtained three images at the timing positions of just before speaking and while speaking the phonemes of the first and the last vowels.

4.2 Results and discussion

Table 1 shows the facial expression recognition accuracy and rejection ratio for each facial expression. The mean recognition accuracy was 77.2%. The facial expressions of "others" were more difficult to recognize than those of "happy," and "neutral," which were perfectly recognized with 100% accuracy (Table 1).

Table 2 shows examples of the results of facial expression recognition. By using the facial expression strength described in Step 7, the position of the test feature vector in the feature vector space is quantitatively shown.

In the present experiment, a subject spoke one word that was the semantically neutral utterance "Taro." The system recognized the facial expression in speaking each word. When we are ready to apply the proposed system for recognizing facial expressions in daily conversation, we should be able to recognize the facial expression during speaking for a certain interval, such as sentence by sentence. This is because we focus on human feeling through facial expression and it is difficult for humans to change their feeling on a word-by-word basis. When we use the training data for all combinations of the first and the last vowels [11], we can apply the proposed system to a speaker for any utterance. Though several studies on facial expression recognition using thermal image processing have been reported (see references [5]–[17], [21]), only our research [5]–[17] has focused on a speaker. In this paper, we propose an on-line system for recognizing the facial expression of a speaker by adding a module using reject criteria in the feature vector space to our previously reported system [13], which is

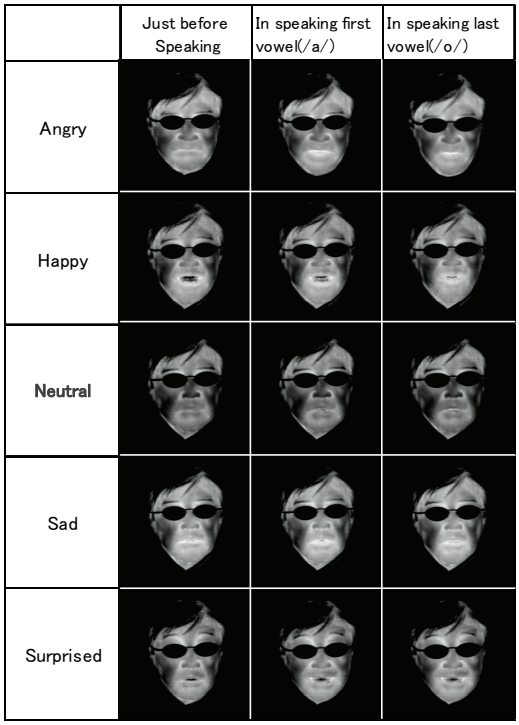

Fig. 7. Examples of thermal images of subject A having each facial expression in speaking [13]

Table 1. Recognition accuracy and rejection ratio

		Input facial expression		
		Happy	Neutral	Others
Output	Happy	**100**		10.5
	Neutral		**100**	57.9
	Others			**31.6**
Rejected		76.0	0.0	59.2

(%)

Table 2. Results of facial expression recognition

Input facial expression	Facial expression strength					Nearest	Second nearest
	A	H	N	Sa	Su		
Angry	**0.98**	0.57	0.30	0.51	1.0	Su	A
Happy	0.21	**1.0**	0.26	0.61	0.19	H	Sa
Neutral	0.13	0.23	**1.0**	0.27	0.12	N	Sa
Sad	0.24	0.56	1.0	**0.71**	0.22	N	Sa
Surprised	0.68	0.45	0.24	0.38	**1.0**	Su	A

A=Angry, H=Happy, N=Neutral, Sa=Sad, Su=Surprised

© ISAROB 2013

based on our previously reported method [10], [11], which is superior to our earlier reported method [5]–[8]. Compared with the conventional method, the effect of adding reject criteria in the feature vector space is shown in detail in [17].

5 CONCLUSION

We propose an on-line system for recognizing the facial expression of a speaker by adding a module using reject criteria in the feature vector space to our previously reported system [13]. Using the proposed system, the facial expressions of a subject were discriminable with 77.2% accuracy for the facial expressions of "happy," "neutral," and "others" when the subject exhibited one of the intentional facial expressions of "angry," "happy," "neutral," "sad," and "surprised." By using the facial expression strength, the position of the test feature vector in the feature vector space is quantitatively shown. We expect the proposed system to be applicable for recognizing facial expressions in daily conversation.

Acknowledgment

This work was supported by KAKENHI (22300077).

REFERENCES

[1] Yoshitomi Y, Kimura S, Hira E, et al (1996), Facial expression recognition using infrared rays image processing. Proceedings of the Annual Convention IPS Japan, Osaka, Japan, Sep 4-6, 1996, 2:339-340

[2] Yoshitomi Y, Kimura S, Hira E, et al (1997), Facial expression recognition using thermal image processing. IPSJ SIG Notes, CVIM103-3, Kyoto, Japan, Jan 23-24, 1997, pp. 17-24

[3] Yoshitomi Y, Miyawaki N, Tomita S, et al (1997), Facial expression recognition using thermal image processing and neural network. Proceedings of 6th IEEE International Workshop on Robot and Human Communication, Sendai, Japan, Sep 29-Oct 1, 1997, pp. 380-385

[4] Sugimoto Y, Yoshitomi Y, Tomita S (2000), A method for detecting transitions of emotional states using a thermal face image based on a synthesis of facial expressions. J. Robotics and Autonomous Systems 31:147-160

[5] Yoshitomi Y, Kim SIll, Kawano T, et al (2000), Effect of sensor fusion for recognition of emotional states using voice, face image and thermal image of face. Proceedings of 6th IEEE International Workshop on Robot and Human Interactive Communication, Osaka, Japan, Sep 27-29, 2000, pp. 178-183

[6] Ikezoe F, Ko R, Tanijiri T, et al (2004), Facial expression recognition for speaker using thermal image processing (in Japanese). Trans. Human Interface Society 6(1):19-27

[7] Nakano M, Ikezoe F, Tabuse M, et al (2009), A study on the efficient facial expression using thermal face image in speaking and the influence of individual variations on its performance (in Japanese). J. IEEJ 38(2):156-163

[8] Koda Y, Yoshitomi Y, Nakano M, et al (2009), Facial expression recognition for a speaker of a phoneme of vowel using thermal image processing and a speech recognition system. Proceedings of 18th IEEE International Symposium on Robot and Human Interactive Communication, Toyama, Japan, Sep 29-Oct 1, 2009, pp. 955-960

[9] Yoshitomi Y (2010), Facial expression recognition for speaker using thermal image processing and speech recognition system. Proceedings of 10th WSEAS International Conference on Applied Computer Science, Appi Kogen, Iwate, Japan, Oct 4-6, 2010, pp. 182-186

[10]Fujimura T, Yoshitomi Y, Asada T, et al (2011), Facial expression recognition of a speaker using front-view face judgment, vowel judgment, and thermal image processing. J. Artificial Life and Robotics 16(3):411-417

[11]Yoshitomi Y, Asada T, Shimada K, et al (2011), Facial expression recognition of a speaker using vowel judgment and thermal image processing. J. Artificial Life and Robotics 16(3):318–323

[12]Yoshitomi Y, Tabuse M, Asada T (2011), Speech Technologies. InTech, pp.405-424

[13]Asada T, Yoshitomi Y, Tabuse M (2012), A system for facial expression recognition of a speaker using front‐view face judgment, vowel judgment and thermal image processing. J. Artificial Life and Robotics, 17(2):263-269

[14]Yoshitomi Y, Tabuse M, Asada T (2012), Image processing: methods, applications and challenges. Nova Science Publisher, pp.57-85

[15]Yoshitomi Y (2012), Facial expression recognition of speaker using vowel judgment and features of thermal face image", Proceedings of 1st WSEAS International Conference on Information Technology and Computer Networks, Vienna, Austria, Nov 10-12, 2012, pp.139-145

[16]Nakanishi Y, Yoshitomi Y, Asada T, et al (2012), Robust facial expression recognition of a speaker using thermal image processing and updating of fundamental training-data. J. Artificial Life and Robotics 17, in press

[17]Nakanishi Y, Yoshitomi Y, Asada T, et al (2013), Facial expression recognition of a speaker using thermal image processing and reject criteria in feature vector space, In:Sugisaka M (ed), Proceedings of the International Symposium on Artificial Life and Robotics (AROB 18th), Daejeon, Korea, Jan 30 - Feb 1, 2013, in press

[18]Kuno H (1994), Infrared rays engineering (in Japanese). Tokyo, IEICE, pp.22

[19]Kuno H (1994), Infrared rays engineering (in Japanese). Tokyo, IEICE, pp.45

[20]http://julius.sourceforge.jp/

[21]Hernández B, Olague G, Hammoud R, et al (2007), Visual learning of texture descriptors for facial expression recognition in thermal imagery. Computer Vision and Image Understanding 16 (2-3): 258–269

© ISAROB 2013

The Eighteenth International Symposium on Artificial Life and Robotics 2013 (AROB 18th '13),
Daejeon Convention Center, Daejeon, Korea, January 30-February 1, 2013

Facial expression recognition of a speaker using thermal image processing and reject criteria in feature vector space

Y. Nakanishi, Y. Yoshitomi, T. Asada, and M. Tabuse

Graduate School of Life and Environmental Sciences Kyoto Prefectural University,
1-5 Nakaragi-cho, Shimogamo, Sakyo-ku, Kyoto 606-8522, Japan
E-mail: y_nakanishi@mei.kpu.ac.jp, yoshitomi@kpu.ac.jp, t_asada@mei.kpu.ac.jp, tabuse@kpu.ac.jp

Abstract: In our previously developed method for the facial expression recognition of a speaker, the positions of feature vectors in the feature vector space in image processing were generated with imperfections. The imperfections, which caused misrecognition of the facial expression, tended to be far from the center of gravity of the class to which the feature vectors belonged. In the present study, to omit the feature vectors generated with imperfections, a method using reject criteria in the feature vector space was applied to facial expression recognition. By using the proposed method, the facial expressions of two subjects were discriminable with 90.0% accuracy for the three facial expressions of "happy," "neutral," and "others" when they exhibited one of the five intentional facial expressions of "angry," "happy," "neutral," "sad," and "surprised," whereas these expressions were discriminable with 78.0% accuracy by the conventional method.

Keywords: Facial expression recognition, Feature vector space, Reject criteria, Speech recognition, Thermal image processing.

1 INTRODUCTION

Although the mechanism for recognizing facial expressions has received considerable attention in the field of computer vision research, it still falls far short of human capability, especially from the viewpoint of robustness under widely varying lighting conditions. For example, nuances of shade, reflection, and local darkness influence the accuracy of facial expression recognition through the inevitable change of gray levels. To develop a method for facial expression recognition applicable under widely varied lighting conditions, we used images produced by infrared rays (IR), which show the thermal distribution of the face [1]-[13].

In experiments, imperfections in image processing in our method for facial expression recognition inevitably occurred and resulted in misrecognition of facial expressions. To overcome this difficulty, in the present study, a method using reject criteria in the feature vector space is applied to the recognition of facial expression of two male subjects when exhibiting the intentional facial expressions of "angry," "happy," "neutral," "sad," and "surprised."

2 IMAGE ACQUISITION

The principle behind thermal image generation is the Stefan–Boltzmann law, expressed as $W = \varepsilon\sigma T^4$, where ε is emissivity, σ is the Stefan–Boltzmann constant (=5.6705×10^{-12} W/cm^{2}K^4), and T is the temperature (K). For human skin, ε is estimated as 0.98 to 0.99 [14], [15]. In the present study, the approximate value of 1 was used as ε for human skin because the value of ε for almost all substances is lower than that of human skin [14]. Consequently, the human face region is easily extracted from an image by using the value of 1 for ε [1]-[13]. In principle, temperature measurements by IR also do not depend on skin color [15], darkness, or lighting condition, and so the face region and its characteristics are easily extracted from a thermal image.

3 PROPOSED METHOD

Fig. 1 illustrates the flowchart of our method. We have two modules in our system. The first is a module for speech recognition and dynamic image analysis, and the second is a module for learning and recognition. In the module for learning and recognition, we embedded the module for front-view face judgment [10]. Some details of our method are explained in our book [16].

3.1 Speech recognition and dynamic image analysis

We use a speech recognition system named Julius [17] to obtain the timing positions of the start of speech and the first and last vowels in a WAV file [8]-[10]. Fig. 2 shows an example of the waveform of the Japanese name "Taro"; the timing position of the start of speech and the timing ranges of the first vowel (/a/) and the last vowel (/o/) are decided by Julius. By using the timing position of the start of speech and the timing ranges of the first and last vowels obtained from the WAV file, three image frames are extracted from an AVI file at the three timing positions. For the timing position just before speaking, we use the timing position of

© ISAROB 2013

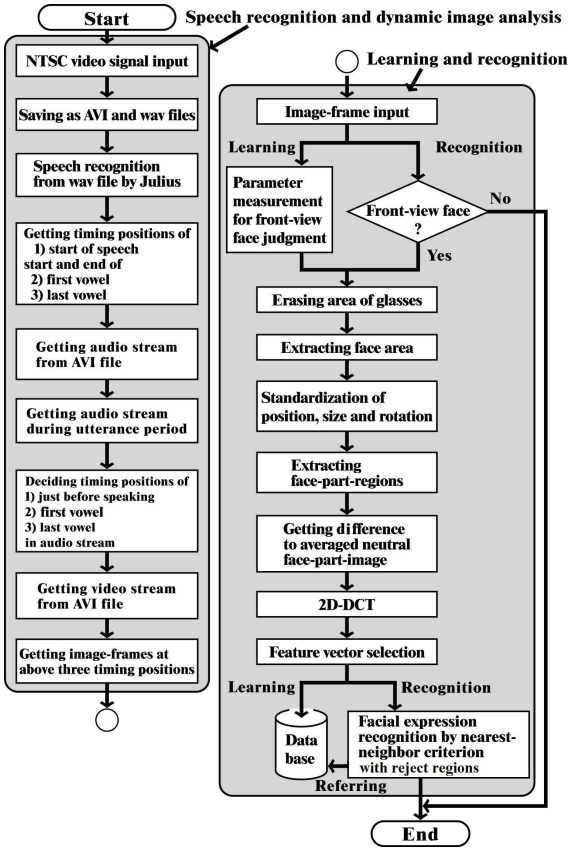

Fig. 1. Flowchart of our method

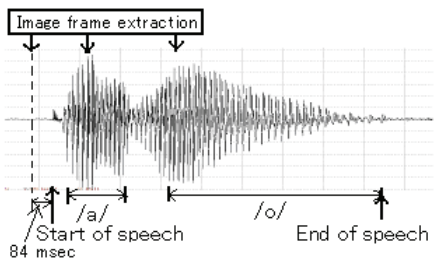

Fig. 2. Speech waveform of "Taro" and timing positions for image frame extraction [8]

84 ms before the start of speech, as determined in our previously reported study [7]. For the timing position of the first vowel, we use the position where the absolute value of the amplitude of the waveform is the maximum while speaking the vowel. For the timing position of the last vowel, we apply the same procedure used for the first vowel.

3.2 Learning and recognition

For static images obtained from the extracted image frames, the process of erasing the area of the glasses, extracting the face area, and standardizing the position, size, and rotation of the face are performed according to the method described in our previously reported study [7], [16]. Fig. 3 shows the blocks for extracting the face areas in a thermal image having 720×480 pixels. In the next step, we

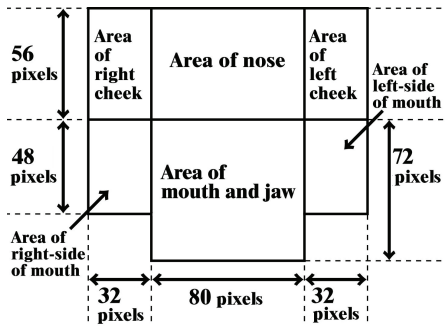

Fig. 3. Blocks for extracting face areas in the thermal image [18]

generate difference images between the averaged neutral face image and the target face image in the extracted face areas to perform a 2D discrete cosine transform (2D-DCT). The feature vector is generated from the 2D-DCT coefficients according to a heuristic rule [6], [7]. We refer to the method used in our previously reported research [8]-[13], [16], [18], [19] as the conventional method, where the facial expression is recognized by the nearest-neighbor criterion in the feature vector space by using the training data just before speaking and when speaking the phonemes of the first and last vowels.

3.3 Proposed method for facial expression recognition

Imperfections in image processing in our method for facial expression recognition inevitably occurred and resulted in misrecognition of facial expressions. To overcome this difficulty, in the present study, a method using reject criteria in the feature vector space of the training data just before speaking and when speaking the phonemes of the first and last vowels is proposed.

The new algorithm of pattern recognition in the feature vector space of facial expression recognition is as follows:

***Step 1*:** For all classes in the initial condition, the following procedure is performed. Vector $\boldsymbol{g}_i$ of the center of gravity of the class $i\,(i = 1,2,\cdots,n)$, where n is the number of classes, is obtained. Then, go to Step 2.

***Step 2*:** For each class i, the following procedure is performed. The elements of class i are narrowed using the way that the feature vector having the largest distance from vector $\boldsymbol{g}_i$ among those in class i is omitted from the elements in class i. Then, if the number of feature vectors of class i at that moment is bigger than half the number N_i of feature vectors in the class defined in Step 1, go to Step 3. Otherwise, go to Step 4.

***Step 3*:** For class i, vector $\boldsymbol{g}_i$ is updated. Then, return to Step 2.

***Step 4*:** Except the class of neutral facial expression, the threshold T_j of class j is decided as (a) the value of the

maximum distance between vector $\boldsymbol{g}_j$ and the feature vector of class j in the initial condition, under the constraint that vector $\boldsymbol{g}_j$ among all vectors $\boldsymbol{g}_i$ $(i = 1,2,\cdots,n)$ is the nearest to the feature vector. Similarly, for the class of neutral facial expression, the threshold T_j of class j is decided as the mean value of (a) and (b), where (b) is the minimum value among the values of the distance between vector $\boldsymbol{g}_j$ and the feature vector of class j in the initial condition, under the constraint that vector $\boldsymbol{g}_j$ among all vectors $\boldsymbol{g}_i$ $(i = 1,2,\cdots,n)$ is not the nearest to the feature vector. Go to Step 5.

***Step 5*:** The elements of each class i are narrowed using the constraint that the distance between the feature vectors and vector $\boldsymbol{g}_i$ should not be bigger than threshold T_i. Go to Step 6.

***Step 6*:** The facial expression is recognized by the nearest-neighbor criterion in the feature vector space using (1) the feature vectors selected by the procedure up to Step 5, (2) the vector $\boldsymbol{g}_i$. Then, the recognized result showing class i is rejected if the distance between the test feature vector and the selected vector by the vector nearest-neighbor criterion is bigger than the threshold T_i. Otherwise the recognized result showing class i is accepted.

In the present study, the Euclidean distance is used as the distance in the feature vector space. The class of neutral facial expression receives special treatment because in many cases the value of (a) tends to be too small to accept the recognized result showing class j.

4 EXPERIMENTS

4.1 Condition

The thermal image produced by the thermal video system (Nippon Avionics TVS-700) and the sound captured from an Electret condenser microphone (Sony ECM-23F5), as amplified by a mixer (Audio-Technica AT-PMX5P), were transformed into a digital signal by an A/D converter (Thomson Canopus ADVC-300) and input into a computer (DELL Optiplex 780, CPU: Intel Core 2 Duo E8400 3.00 GHz, main memory: 3.21 GB, and OS: Windows 7 Professional (Microsoft) with an IEEE1394 interface board (I·O Data Device 1394-PCI3/DV6)). We used Visual C++ 6.0 (Microsoft) as the programming language. To generate a thermal image, we set the condition that the thermal image had 256 gray levels for the detected temperature range. As a result, one gray level corresponded to 1.95×10^{-2} to 5.04×10^{-2} K. The temperature range for generating a thermal image was decided for each subject to easily extract the face area on the image. We saved the visual and audio information in the computer as a Type 2 DV-AVI file, in which the video frame had a spatial resolution of 720×480 pixels and 8-bit gray levels, and the sound was saved in a stereo PCM format, 48 kHz and 16-bit levels.

Two subjects exhibited in alphabetic order each of the five intentional facial expressions of "angry," "happy," "neutral," "sad," and "surprised," while speaking the semantically neutral utterance "Taro." In the present study, we categorized all of the "angry," "sad," and "surprise" expressions as "others" in making the recognition results. Subjects A and B were males with glasses. Figs. 4 and 5 show examples of thermal images of the neutral expression captured in each period for Subjects A and B, respectively. We captured the thermal images for subject A on June 20, 2006 (hereinafter referred to as First_period_A) (Fig. 6); at approximately 3:00 pm on January 22, 2010 (hereinafter referred to as Second_period_A); and at approximately 5:00 pm on January 22, 2010 (hereinafter referred to as Third_period_A). For subject B, we captured the same thermal images on June 20, 2006 (hereinafter referred to as First_period_B) (Fig. 7); and January 25, 2010 (hereinafter referred to as Second_period_B). In the present study, we investigated several combinations of training and test data for each subject, as listed in Tables 1, 2, and 3 in Section 4.2. Case-A-1-2 for subject A consisted of the following cases: (1) thermal images for both training and test data captured on First_period_A, (2) thermal images for both

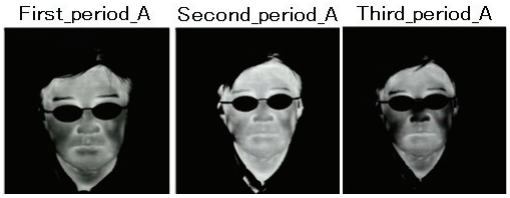

Fig. 4. Examples of thermal images of subject A having a neutral facial expression captured just before speaking at each period

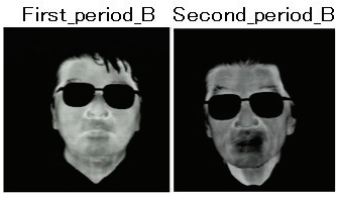

Fig. 5. Examples of thermal images of subject B having a neutral facial expression captured just before speaking at each period

© ISAROB 2013

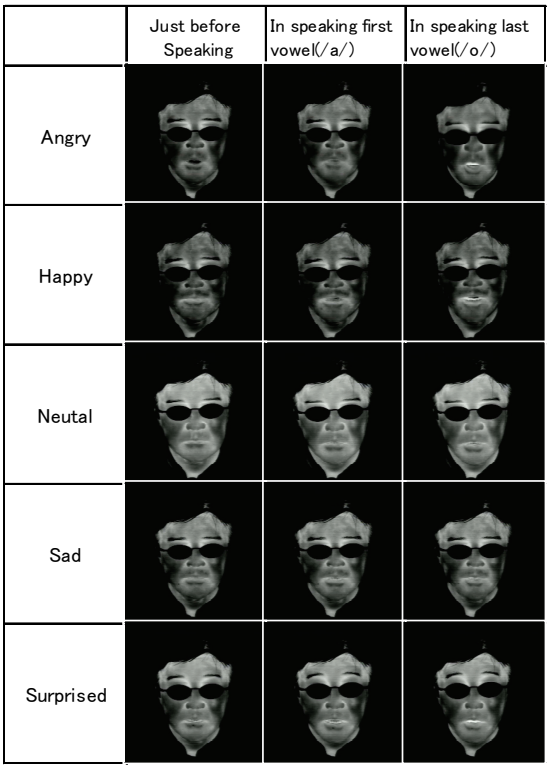

Fig. 6. Examples of thermal images of subject A captured on First_period_A and having each facial expression [12]

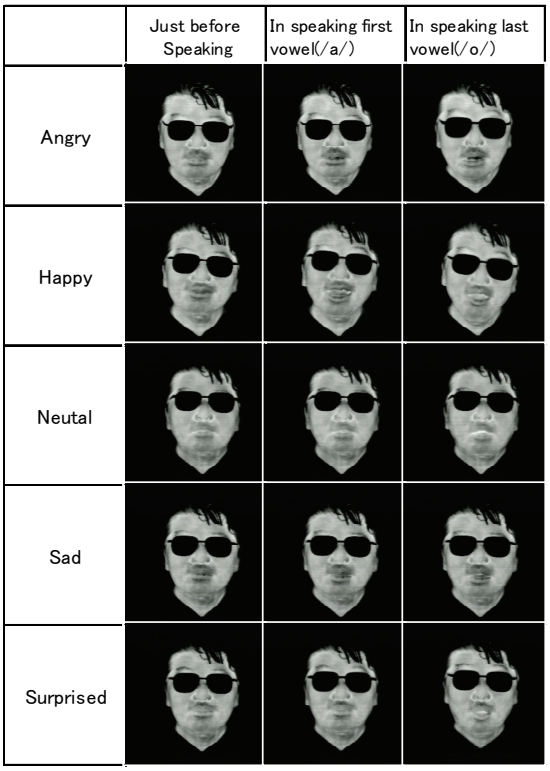

Fig. 7. Examples of thermal images of subject B captured on First_period_B and having each facial expression [12]

training and test data captured on Second_period_A, (3) thermal images for training and test data captured on First_period_A and Second_period_A, respectively, and (4) thermal images of training data of the facial expressions of "happy" and "neutral" captured on Second_period_A, thermal images of training data of the facial expressions of "others" captured on First_period_A, and the test data were captured on Second_period_A. In addition, Case-A-2-3 for subject A consisted of four cases decided by changing the data of First_period_A and Second_period_A in Case-A-1-2 to those of Second_period_A and Third_period_A, respectively. Case-B-1-2 for subject B consisted of the four cases defined in the same manner described above as Case-A-1-2 for subject A.

For Case-A-1-2, Case-A-2-3, and Case-B-1-2, we compared (3) and (4) for investigating the effects of updating the training data of the facial expressions of "happy" and "neutral", whereas (1) and (2) were added for reference of thermal images for the training and the test data captured without intentional intervals.

Subjects A and B freely changed their face direction during the capturing of thermal images for the test data on Second_period_A and Second_period_B, respectively. We assembled twenty samples as training data and ten samples as test data for all five facial expressions in all cases of Case-A-1-2, Case-A-2-3, and Case-B-1-2. All facial expressions of the test data for both subjects were judged as front-view faces by the method mentioned in our previously reported paper [10]. As one sample, we obtained one image each at the timing positions of just before speaking and while speaking the phonemes of the first and last vowels. If Julius misrecognized the vowel of the test sample, the corresponding image was not used for facial expression recognition. We had four cases of misrecognition for the vowel(s): (i) no misrecognition for the first and last vowels, (ii) misrecognition only for the first vowel, (iii) misrecognition only for the last vowel, and (iv) misrecognition for both the first and last vowels. We prepared feature vectors of the training data in each of the four cases.

4.2 Results and discussion

Tables 1, 2, and 3 show the facial expression recognition accuracy for the case of Case-A-1-2, Case-A-2-3, and Case-B-1-2, respectively. The total facial recognition accuracy by the conventional method was (429/550=78.0%), whereas that by the proposed method was (376/418=90.0%). Because the time period_ subject of Table 1 (2) is the same as that of Table 2 (1), the data in Table 2 (1) are not taken

© ISAROB 2013

Table 1. Recognition accuracy of Case-A-1-2

(1) Training and test data: First_period_A

		Input facial expression					
		Conventional			Proposed method		
		Happy	Neutral	Others	Happy	Neutral	Others
Output	Happy	**10/10**		7/30	**10/10**		7/29
	Neutral		**8/10**			**8/10**	
	Others		2/10	**23/30**		2/10	**22/29**
Rejected					0/10	0/10	1/30
Accuracy		**41/50**			**40/49**		

(2) Training and test data: Second_period_A

		Input facial expression					
		Conventional			Proposed method		
		Happy	Neutral	Others	Happy	Neutral	Others
Output	Happy	**9/10**			**7/8**		
	Neutral		**9/10**			**9/10**	
	Others	1/10	1/10	**30/30**	1/8	1/10	**28/28**
Rejected					2/10	0/10	2/30
Accuracy		**48/50**			**44/46**		

(3) Training data: First_period_A,
Test data: Second_period_A

		Input facial expression					
		Conventional			Proposed method		
		Happy	Neutral	Others	Happy	Neutral	Others
Output	Happy	**4/10**	1/10	19/30	**4/10**	1/7	18/29
	Neutral		**9/10**			**6/7**	
	Others	6/10		**11/30**	6/10		**11/29**
Rejected					0/10	3/10	1/30
Accuracy		**24/50**			**21/46**		

(4) Training data: "happy" and "neutral"; Second_period_A, "others"; First_period_A,
Test data: Second_period_A

		Input facial expression					
		Conventional			Proposed method		
		Happy	Neutral	Others	Happy	Neutral	Others
Output	Happy	**10/10**		2/30	**7/7**		3/25
	Neutral		**10/10**			**10/10**	
	Others			**28/30**			**22/25**
Rejected					3/10	0/10	5/30
Accuracy		**48/50**			**39/42**		

into account in calculating the total recognition accuracy. The proposed method improved the total facial recognition accuracy by 12.0%. The reject criteria explained in Section 3.3 were effective for improving facial recognition accuracy, as shown in Table 3 (3) in particular. The proposed method effectively judged whether the training data were acceptable for facial expression recognition at the moment; as shown in Table 3 (3), the training data should be updated.

The total facial recognition accuracy by the proposed method under condition (3) in Tables 1 and 2 was (43/71=60.6%), whereas that under condition (4) in Tables 1 and 2 was (81/84=96.4%), which was better than (134/145=92.4%), obtained under the conditions of Table 1 (1) and (2) and Table 2 (2). The total facial recognition accuracy by the conventional method under condition (3) in Tables 1, 2, and 3 was (76/150=50.7%), whereas that under condition (4) in Tables 1, 2, and 3 was (119/150=79.3%), which was lower than (234/250=93.6%), obtained under the conditions of Table 1 (1) and (2), Table 2 (2), and Table 3 (1) and (2). In both the proposed method and the conventional method, updating the training data for the facial expressions of "happy" and "neutral" remarkably improved the accuracy of facial expression recognition, as demonstrated in our previously reported paper [12].

Table 2. Recognition accuracy of Case-A-2-3

(1) Training and test data: Second_period_A
The same as Table 1 (2)

(2) Training and test data: Third_period_A

		Input facial expression					
		Conventional			Proposed method		
		Happy	Neutral	Others	Happy	Neutral	Others
Output	Happy	**10/10**			**10/10**		
	Neutral		**10/10**			**10/10**	
	Others			**30/30**			**30/30**
Rejected					0/10	0/10	0/10
Accuracy		**50/50**			**50/50**		

(3) Training data: Second_period_A,
Test data: Third_period_A

		Input facial expression					
		Conventional			Proposed method		
		Happy	Neutral	Others	Happy	Neutral	Others
Output	Happy	**0/10**			**0/3**		
	Neutral		**10/10**			**10/10**	
	Others	10/10		**30/30**	3/3		**12/12**
Rejected					7/10	0/10	18/30
Accuracy		**40/50**			**22/25**		

(4) Training data: "happy" and "neutral"; Third_period_A, "others"; Second_period_A,
Test data: Third_period_A

		Input facial expression					
		Conventional			Proposed method		
		Happy	Neutral	Others	Happy	Neutral	Others
Output	Happy	**10/10**			**7/7**		
	Neutral		**10/10**			**10/10**	
	Others			**30/30**			**25/25**
Rejected					3/10		5/30
Accuracy		**50/50**			**42/42**		

Table 3. Recognition accuracy of Case-B-1-2

(1) Training and test data: First_period_B

		Input facial expression					
		Conventional			Proposed method		
		Happy	Neutral	Others	Happy	Neutral	Others
Output	Happy	**10/10**			**10/10**		
	Neutral		**10/10**			**10/10**	
	Others			**30/30**			**30/30**
Rejected					0/10	0/10	0/30
Accuracy		**50/50**			**50/50**		

(2) Training and test data: Second_period_B

		Input facial expression					
		Conventional			Proposed method		
		Happy	Neutral	Others	Happy	Neutral	Others
Output	Happy	**10/10**		5/30	**1/1**		
	Neutral		**10/10**			**10/10**	
	Others			**25/30**			**24/24**
Rejected					9/10	0/10	6/30
Accuracy		**45/50**			**35/35**		

(3) Training data: First_period_B,
Test data: Second_period_B

		Input facial expression					
		Conventional			Proposed method		
		Happy	Neutral	Others	Happy	Neutral	Others
Output	Happy	**10/10**	8/10	30/30			
	Neutral		**2/10**				
	Others			**0/30**			
Rejected					10/10	10/10	30/30
Accuracy		**12/50**			**(All were rejected.)**		

(4) Training data: "happy" and "neutral"; Second_period_B, "others"; First_period_B,
Test data: Second_period_B

		Input facial expression					
		Conventional			Proposed method		
		Happy	Neutral	Others	Happy	Neutral	Others
Output	Happy	**10/10**		15/30	**8/8**		13/15
	Neutral		**10/10**	14/30		**10/10**	
	Others			**1/30**			**2/15**
Rejected					2/10	0/10	15/30
Accuracy		**21/50**			**33/33**		

Though several studies on facial expression recognition using thermal image processing have been reported (see references [1]-[13], [16], [18]-[20]), only our research [5]-[13], [16], [18], [19] has focused on a speaker. In this paper,

© ISAROB 2013

we propose a method for using reject criteria in the feature vector space. The advantage of our method over the conventional method is demonstrated in Tables 1 to 3.

After preparing the training data for all combinations of the first and last vowels, we could apply our method to a speaker for any utterance [11], [16].

5 CONCLUSION

We previously developed a method for the facial expression recognition of a speaker. In the present study, a method using reject criteria in the feature vector space was applied. With the proposed method, the facial expressions of two male subjects were discriminable with 90.0% accuracy for the facial expressions of "happy," "neutral," and "others" when they exhibited one of the intentional facial expressions of "angry," "happy," "neutral," "sad," and "surprised." The proposed method effectively judged whether the training data were acceptable for the facial expression recognition at that moment.

Acknowledgment

This work was supported by KAKENHI (22300077).

REFERENCES

[1] Yoshitomi Y, Kimura S, Hira E, et al (1996), Facial expression recognition using infrared rays image processing. Proceedings of the Annual Convention IPS Japan, Osaka, Japan, Sep 4-6, 1996, 2:339-340

[2] Yoshitomi Y, Kimura S, Hira E, et al (1997), Facial expression recognition using thermal image processing. IPSJ SIG Notes, CVIM103-3, Kyoto, Japan, Jan 23-24, 1997, pp. 17-24

[3] Yoshitomi Y, Miyawaki N, Tomita S, et al (1997), Facial expression recognition using thermal image processing and neural network. Proceedings of 6th IEEE International Workshop on Robot and Human Communication, Sendai, Japan, Sep 29-Oct 1, 1997, pp. 380-385

[4] Sugimoto Y, Yoshitomi Y, Tomita S (2000), A method for detecting transitions of emotional states using a thermal face image based on a synthesis of facial expressions. J. Robotics and Autonomous Systems 31:147-160

[5] Yoshitomi Y, Kim SIll, Kawano T, et al (2000), Effect of sensor fusion for recognition of emotional states using voice, face image and thermal image of face. Proceedings of 6th IEEE International Workshop on Robot and Human Interactive Communication, Osaka, Japan, Sep 27-29, 2000, pp. 178-183

[6] Ikezoe F, Ko R, Tanijiri T, et al (2004), Facial expression recognition for speaker using thermal image processing (in Japanese). Trans. Human Interface Society 6(1):19-27

[7] Nakano M, Ikezoe F, Tabuse M, et al (2009), A study on the efficient facial expression using thermal face image in speaking and the influence of individual variations on its performance (in Japanese). J. IEEJ 38(2):156-163

[8] Koda Y, Yoshitomi Y, Nakano M, et al (2009), Facial expression recognition for a speaker of a phoneme of vowel using thermal image processing and a speech recognition system. Proceedings of 18th IEEE International Symposium on Robot and Human Interactive Communication, Toyama, Japan, Sep 29-Oct 1, 2009, pp. 955-960

[9] Yoshitomi Y (2010), Facial expression recognition for speaker using thermal image processing and speech recognition system. Proceedings of 10th WSEAS International Conference on Applied Computer Science, Appi Kogen, Iwate, Japan, Oct 4-6, 2010, pp. 182-186

[10]Fujimura T, Yoshitomi Y, Asada T, et al (2011), Facial expression recognition of a speaker using front-view face judgment, vowel judgment, and thermal image processing. J. Artificial Life and Robotics 16(3):411-417

[11]Yoshitomi Y, Asada T, Shimada K, et al (2011), Facial expression recognition of a speaker using vowel judgment and thermal image processing. J. Artificial Life and Robotics 16(3):318–323

[12]Nakanishi Y, Yoshitomi Y, Asada T, et al (2012), Robust facial expression recognition of a speaker using thermal image processing and updating of fundamental training-data. J. Artificial Life and Robotics, 17(2):263-269

[13]Yoshitomi Y (2012), Facial expression recognition of speaker using vowel judgment and features of thermal face image", Proceedings of 1st WSEAS International Conference on Information Technology and Computer Networks, Vienna, Austria, Nov 10-12, 2012, pp.139-145

[14]Kuno H (1994), Infrared rays engineering (in Japanese). Tokyo, IEICE, pp.22

[15]Kuno H (1994), Infrared rays engineering (in Japanese). Tokyo, IEICE, pp.45

[16]Yoshitomi Y, Tabuse M, Asada T (2012), Image processing: methods, applications and challenges. Nova Science Publisher, pp.57-85

[17]http://julius.sourceforge.jp/

[18]Asada T, Yoshitomi Y, Tabuse M (2012), A system for facial expression recognition of a speaker using front‐view face judgment, vowel judgment and thermal image processing. J. Artificial Life and Robotics, 17, in press.

[19]Yoshitomi Y, Tabuse M, Asada T (2011), Speech Technologies. InTech, pp.405-424

[20]Hernández B, Olague G, Hammoud R, et al (2007), Visual learning of texture descriptors for facial expression recognition in thermal imagery. Computer Vision and Image Understanding 16 (2-3): 258–269

© ISAROB 2013

The Eighteenth International Symposium on Artificial Life and Robotics 2013 (AROB 18th '13),
Daejeon Convention Center, Daejeon, Korea, January 30-February 1, 2013

Music recommendation hybrid system for improving recognition ability using collaborative filtering and impression words

S. Yoshizaki[1], Y. Yoshitomi[2], C. Koro[3], and T. Asada[2]

[1]Works Applications Co., Ltd., 1-12-32 Akasaka, Minato-ku, Tokyo, Japan
[2]Graduate School of Life and Environmental Sciences Kyoto Prefectural University,
1-5 Nakaragi-cho, Shimogamo, Sakyo-ku, Kyoto 606-8522, Japan
E-mail: yoshitomi@kpu.ac.jp, t_asada@mei.kpu.ac.jp
[3]ISI Software Corp., 4-6-17 Honmachi, Chuo-ku, Osaka 541-0053, Japan

Abstract: Music therapy for improving recognition ability may be more effective when the favorite music of each person is adopted. In the proposed system, first, the recommendation process using collaborative filtering is terminated when no users in the reference list have the same preference of recommended music as that of a new user. Then, the second recommendation process finds the most similar music, from the scores for impression words, to those successfully recommended among music not recommended up to the moment. The average number of recommended songs for each user by the proposed system was 12.1, whereas that of collaborative filtering was 4.3. The recommendation accuracy of the proposed system was 70.2%, whereas that of collaborative filtering was 62.1%. The ratings of songs can be added on a user-by-user basis in the recommendation process, and this increased number of cases improves the recommendation accuracy and increases the number of recommended songs.

Keywords: Collaborative filtering, Music recommendation, Music therapy, Impression word, and Recognition ability.

1 INTRODUCTION

In Japan, the average age of the population has been increasing, and this trend is expected to continue. Recently, music therapy has been used for improving the recognition ability of people, particularly older people. Music therapy may be more effective when the favorite music of each person is adopted. We have been developing music recommendation methods aimed at improving recognition ability [1]. However, it is not easy to recommend much music to a user using the initially developed method. To overcome this difficulty, we proposed a music recommendation method that combines collaborative filtering and our initial music recommendation process based on impression words [2].

For this study, we further improved the method reported in [2] by adding a function that adds the ratings of songs on a user-by-user basis in the recommendation process to increase both the recommendation accuracy and the number of recommended songs by increasing the number of cases. We implemented the updated method on a personal computer and evaluated the proposed system by using children's songs, which tend to be familiar to older people.

2 MUSIC RECOMMENDATION METHOD USING IMPRESSION WORDS

We use ten pairs of impression words (Table 1) [3]. As an example, we show the user scores for one pair of impression words (quiet - busy). A user scores the word pairs according to seven levels, which are then transformed to three levels, as shown in Table 2 [2]. In a music database, 52 songs were assigned scores $i\,(-3 \le i \le 3)$ for each pair of impression words evaluated by the participants. Fig. 1 shows a flowchart of the music recommendation based on impression words. When music not recommended to a user has the same values except "0" as that for at least one recommended music having a high evaluation by the user on the three-level score for at least five impression words, the music is treated as having a positive evaluation by the user. In contrast, when music not recommended to the user has the same scores except "0" as that for another music just recommended to the user and having a negative evaluation by the user on the

Table 1. Pairs of impression words [3]

quiet - busy
bracing - heavy
easy - uneasy
cheerful - gloomy
refreshing - depressing
happy - sad
comforting - harmful
calm - elevating
clean - dirty
magnificent - superficial

© ISAROB 2013

Table 2. Scores for pairs of impression words quiet – busy [2]

Score	Three-level score	impression
3	-1	very busy
2		busy
1	0	slightly busy
0		neutral
-1		slightly quiet
-2	1	quiet
-3		very quiet

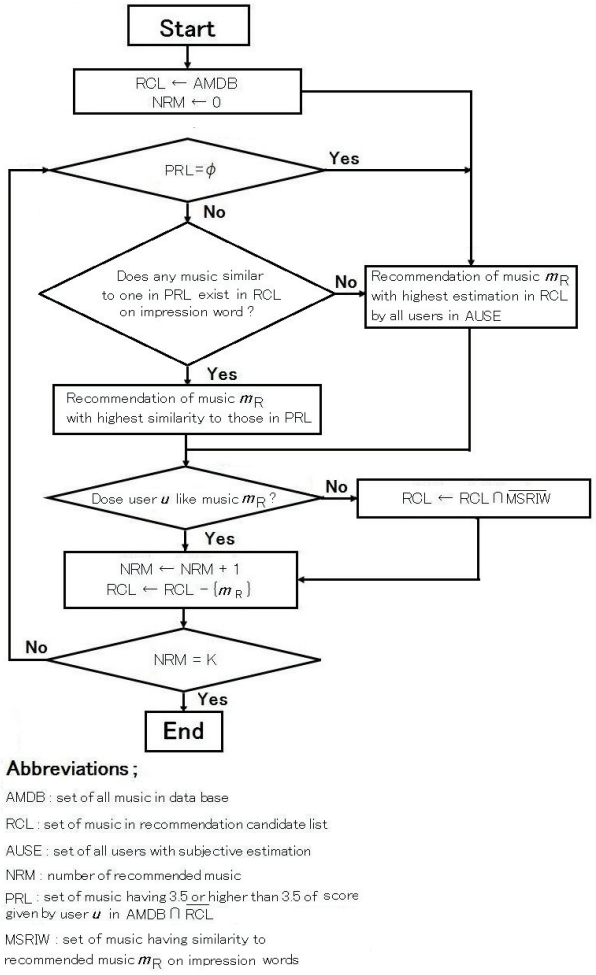

Fig. 1. Flowchart of music recommendation by using impression words [2]

three-level score for at least seven impression words, the music is treated as having a negative evaluation by the user. In Fig. 1, when none of the not recommended music receives a positive evaluation by the user, another recommendation is performed by using the subjective estimations of all users whose subjective estimations are stored in the database. It is expressed by "with highest similarity" in Fig. 1 that the music has the highest proportion of the same three-level scores except "0" as that of other music recommended to the user and given a positive evaluation by the user among the music not yet recommended to the user. In Fig. 1, the "set of music with a similarity to the recommended music based on impression words" (MSRIW) is decided by using at least seven pairs of impression words in the case of a negative evaluation.

3 PROPOSED SYSTEM

Figs. 2 and 3 show two music recommendation methods. Method 1 (Fig. 2) is collaborative filtering only, and Method 2 (Fig. 3) is the proposed system, which combines collaborative filtering and our music recommendation process based on impression words. In the proposed system, the recommendation process using collaborative filtering is terminated when the number of users is zero in the reference list of users showing exactly the same evaluation for the recommended music as that of the user up to that moment. Then, the recommendation process performs by finding out the most similar music, from the viewpoints of three-level scores except "0" on impression words, to that successfully recommended among music not yet recommended. The proposed system recommends music stored in the database to user u, as shown in Fig. 3. Both

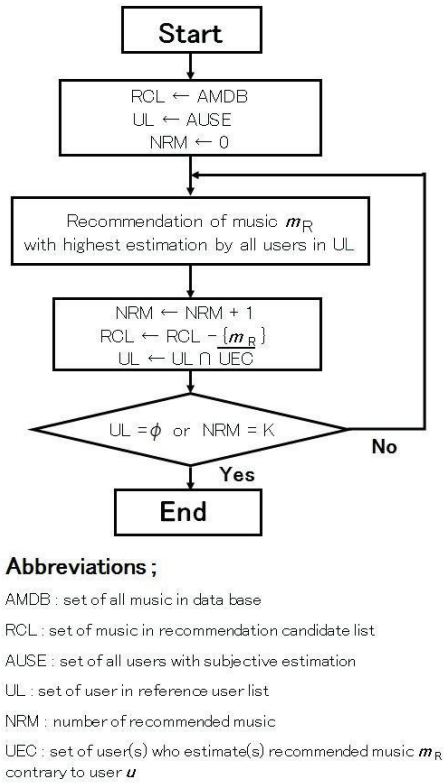

Fig. 2. Flowchart of music recommendation by collaborative filtering [2]

© ISAROB 2013

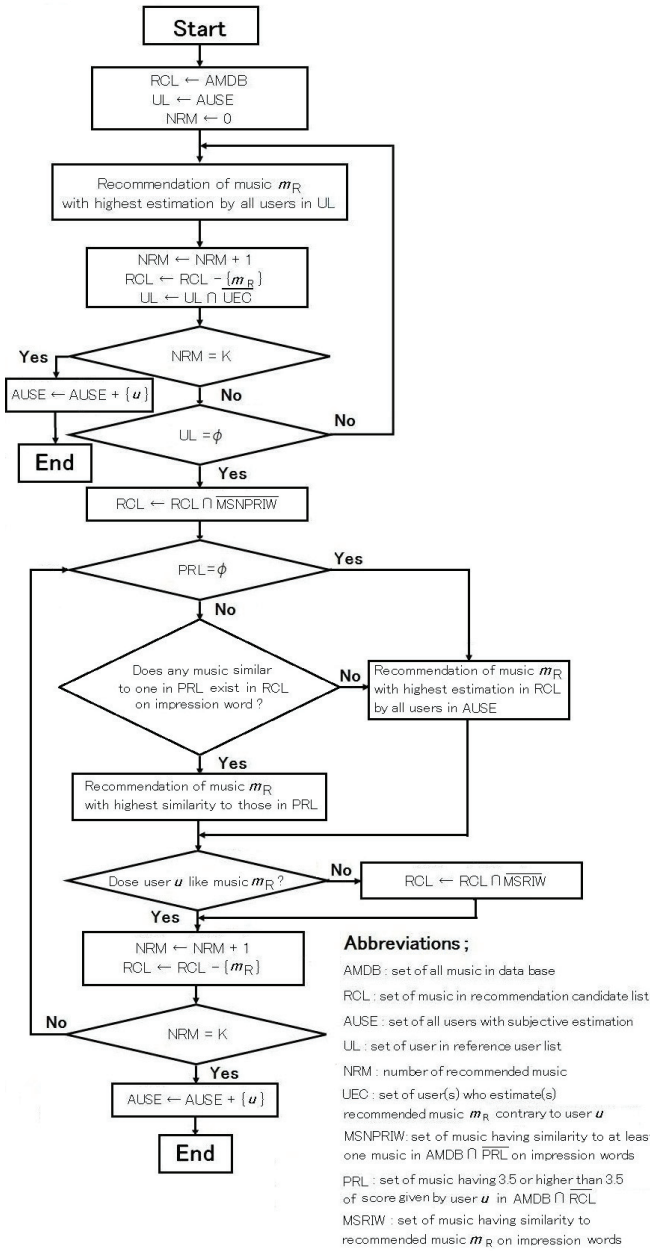

Fig. 3. Flowchart of music recommendation used in the proposed system

the recommendation process using collaborative filtering and that using the proposed system are terminated when the number of recommended songs reaches the upper limit K, decided previously. Just before finishing the recommendation process, the database of users with subjective estimations of the music is updated by adding the subjective estimations of the user for whom the proposed system recommends music.

In the flowcharts of Method 1 and Method 2 shown in Figs. 2 and 3, respectively, the estimation of user u for song m_R is set as 1 when the score of user u for song m_R is 4 or 5 ("slightly favorite" or "favorite"), and it is set as 0 when the score is 1 to 3 ("dislike," "slightly dislike," or "neutral").

For programming, we used Visual C++ 6.0 (Microsoft) on a PC (Dell Latitude E6599, CPU: Intel Core 2 Duo P8700 2.54 GHz, main memory: 4.00 GB, and OS: Windows 7, Microsoft) for the experiment.

4 PERFORMANCE EVALUATION

4.1 Conditions

Because older people tend to prefer children's songs [4], we selected a CD described as an anthology of older songs enjoyed by older people with dementia [5], and then we selected 52 songs on the CD that were also included in a music textbook database for elementary schools [6]. To evaluate the music recommendation methods, all 52 of the selected songs in the database were assigned scores s $(1 \le s \le 5)$ by 12 users of different ages (teens: 1, twenties: 6, fifties: 5). For evaluating the proposed system, we chose each of the 12 users as user u and put the remaining users in the reference user list UL described in Fig. 3. Thus, each user was user u one time and in the reference list 11 times. We used 15 as the value of K in the evaluations of both Method 1 and Method 2. In addition, all 52 of the selected songs in the database were assigned scores i $(-3 \le i \le 3)$ for each pair of impression words by five subjects of different ages (twenties: 3, forties: 1, fifties: 1). Of the five subjects, the one who was in his fifties was also one of the users who assigned scores s. The average of scores i obtained from the five subjects for each pair of impression words was used as scores i for the performance evaluation. The 15 songs having the values except "0" as the three-level score for one impression word at most were not recommended in the process of recommendation based on impression words because they did not have distinct characteristics from the viewpoints of impression words.

Then, we obtained the result of the music recommendation for each new user for each method described in Section 3. To evaluate the two music recommendation methods described in Section 3, 10 new users (user Nos. 1 to 10) participated in the experiment without the updating of the AUSE, which is the set of all users with subjective estimations in Fig. 3, just before finishing the recommendation process, and then one user who had the worst accuracy of recommendation among the new 10 users was selected for additional recommendations with the updating of the AUSE. Moreover, 14 older users,

© ISAROB 2013

Nos. 11 to 24 of different ages (seventies: 2, eighties: 8, nineties: 4) participated in the experiment with the user-by-user updating for the AUSE.

4.2 Results and discussions

The number of recommended songs for users previously registered in the AUSE by the proposed system was 15 per user. In this case, the recommendation process by collaborative filtering was not terminated because the number of users staying in the UL did not become zero. Therefore, the proposed system recommended the most songs under the condition that the upper limit K of recommended songs was 15. The mean value of the recommendation accuracy of the proposed system was 93.9%, whereas that of the random recommendation (i.e., not using Method 1 and/or Method 2) was 47.9%.

As an example, Table 3 shows the process of the music recommendation for user No. 8. As shown in Table 3, Method 2 tended to recommend more music than did Method 1.

Table 3. Music recommendation process for user No. 8

[Method 1]

Order	Recommended music No.	Acceptance	User No. in UL
1	52	○	1,2,3,4,5,7,8,9,10,11,12
2	41	○	1,2,3,4,5,7,8,9,10,11,12
3	50	○	1,2,3,4,5,7,8,9,10, 12
4	21	○	1,2,3,4,5,7,8,9,10, 12
5	26	×	12
6	23	×	none

[Method 2]

Order	Recommended music No.	Acceptance	User No. in UL
1～6	Same as Method 1		
7	5	○	
8	17	○	
9	36	○	
10	43	×	
11	18	○	
12	13	○	
13	6	○	

Fig. 4 shows the performance of the two methods in the experiment, where updating of the AUSE was not performed in the proposed system. The mean value of the number of recommended songs by Method 2 in the proposed system was 12.1 per user, whereas that of only collaborative filtering (Method 1) was 4.3 per user. The mean value of the recommendation accuracy of the proposed system was 70.2%, whereas that of only collaborative filtering was 62.1%. In the collaborative filtering (Method 1), the recommendation process was terminated because the number of users staying in the UL became zero. In contrast, in Method 2, the recommendation process was performed while the recommendation using the impression words was possible under the condition shown in Fig.3. As compared with only using the collaborative filtering (Method 1), we could increase the number of recommended songs while achieving a better accuracy of the recommendation than with Method 1 by combining the recommendation based on the impression words with the collaborative filtering.

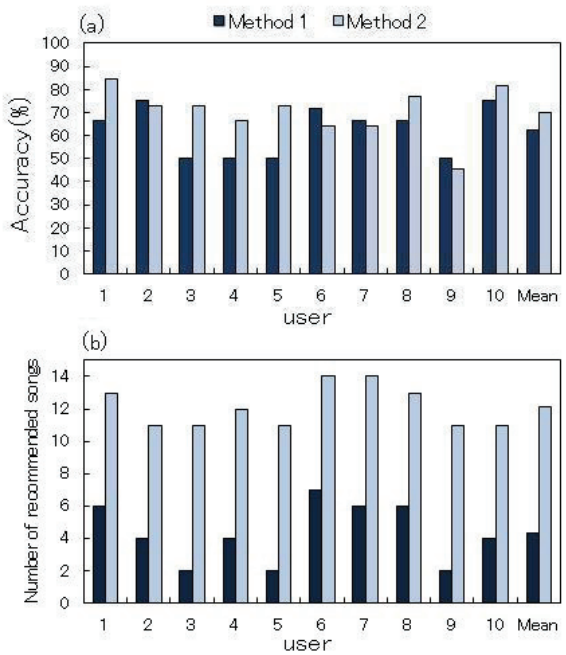

Fig. 4. Performance of music recommendation methods:
(a) recommendation accuracy,
(b) number of recommended songs

Fig. 5 shows the effect of updating the AUSE for user No. 9. By updating the AUSE, the accuracy of the recommendation improved (Fig. 5(a)) and the number of recommended songs also increased (Fig. 5(b)).

Fig. 6 shows the performance of the proposed system, with the updating of the AUSE for users Nos. 11 to 24. User No. 19 stated that he disliked all children's songs. As a result, the accuracy of the recommendation was 0% for user No. 19. The mean value of the number of recommended songs for users Nos. 11 to 24 was 11.4 per user. The mean

© ISAROB 2013

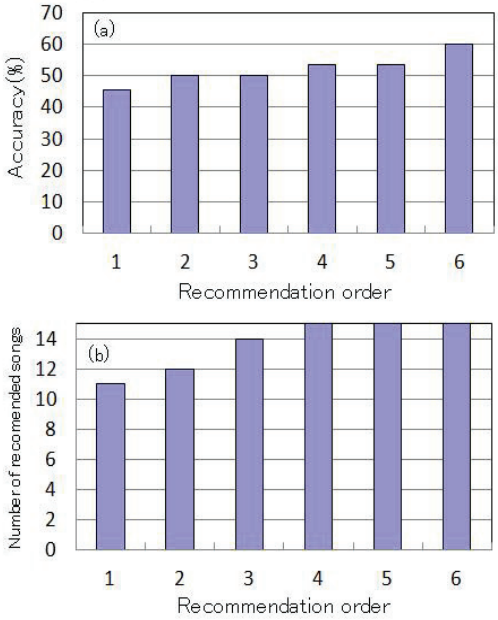

Fig. 5. Effect of updating the AUSE using user No. 9:
(a) recommendation accuracy,
(b) number of recommended songs

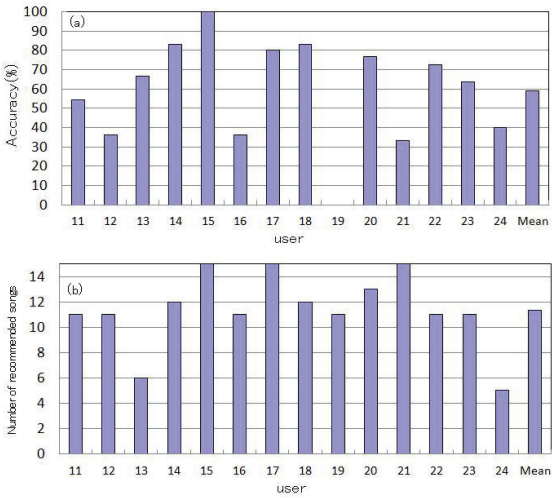

Fig. 6. Performance of the proposed system:
(a) recommendation accuracy,
(b) number of recommended songs

value of the recommendation accuracy for users Nos. 11 to 24 was 59.1%, whereas that without user No. 19 was 63.6%.

The mean value of the recommendation accuracy of the proposed system was 93.9% for users previously registered in the AUSE. Moreover, updating of the AUSE was effective for both the improved accuracy of the recommendation and the increase in the number of recommended songs. Therefore, to improve the performance of the proposed system, we should use the proposed system with updating of the AUSE for more people, particularly those who are older and/or have a cognitive impairment.

5 CONCLUSION

We propose a music recommendation system that combines collaborative filtering and music recommendation based on impression words. We showed that the proposed system was more effective for music recommendation than the system of only collaborative filtering when used on a music database composed of children's songs. The function by which the ratings of songs can be added on a user-by-user basis in the recommendation process was effective for both improving the accuracy of the recommendation and increasing the number of recommended songs.

Acknowledgments

We would like to thank Associate Professor M. Tabuse of Kyoto Prefectural University for his valuable advice and support. We would also like to thank all the participants who cooperated with us in the experiments.

REFERENCES

[1] Konishi H, Yoshitomi Y (2011), Music recommendation system aimed at improving recognition ability. In:Sugisaka M (ed), Proceedings of 16th International Symposium on Artificial Life and Robotics (AROB16th), Beppu, Oita Japan, Jan 27-29, 2011, pp.241-244

[2] Koro C, Yoshitomi Y, Asada T, Yoshizaki S (2012), Music recommendation aimed at improving recognition ability using collaborative filtering and impression words. In:Sugisaka M (ed), Proceedings of 17th International Symposium on Artificial Life and Robotics (AROB17th), Beppu, Oita Japan, Jan 19-21, 2012, pp.222-225

[3] Ohta K, Kumamoto T (2002), A design of music adjective pairs based on linguistic knowledge (in Japanese) IPSJ SIG Notes 40:97-102

[4] Takahashi T (1997), Research report on songs familiar to people advanced in years (in Japanese) Journal of Japanese music therapy associate 15(1):68-75

[5] Akahoshi T (2009), Good old anthology enjoyable for people advanced in years and troubled with dementia. Kirara shobo (in Japanese)

[6] Music textbook database for elementary school by Kanagawa prefectural education center (in Japanese); http://kjd.edu-ctr.pref.kanagawa.jp/daizai_music/

© ISAROB 2013

The Eighteenth International Symposium on Artificial Life and Robotics 2013 (AROB 18th '13),
Daejeon Convention Center, Daejeon, Korea, January 30-February 1, 2013

Study on the Efficient Use of Satellite Image Data Analysis System

Hayao Mori[1], Seiji Tsukamoto[1],
Takashi Yamaguchi[2], Masaki Hanada[2], Jong Geol Park[2], Eiji Nunohiro[2],

[1] Graduate School of Tokyo University of Information Sciences, Japan
[2] Tokyo University of Information Sciences, Japan
(Tel: 81-43-236-1292, Fax: 81-43-236-1292)

[1]{g10022hm, g12008st}@edu.tuis.ac.jp, [2]{tyamagu, mhanada, amon, nunohiro}@rsch.tuis.ac.jp

Abstract: Tokyo University of Information Sciences receives MODIS (Moderate Resolution Imaging Spectroradiometer) data, one of the sensors equipped by NASA's Terra and Aqua satellites, and researches of the analysis on change of environment as part of the academic frontier project. For the information infrastructure of this frontier research, we are developing a satellite image data analysis system to support of web system, a parallel distributed system configuration using multiple PC clusters, database for MODIS data to open the research results and MODIS data for public use. This paper presents the overview of satellite data analysis system and new feature which are the composite of multiple satellite data, and LSM with virtualization of storage system for satellite data, scheduling for multiple cluster nodes and performance evaluation.

Keywords: Scheduling, Virtualization, MODIS

1 INTRODUCTION

Tokyo University of Information Sciences (TUIS) receives MODIS (Moderate Resolution Imaging Spectroradiometer) data from one of the sensors equipped by NASA's Terra and Aqua satellites, and provides processed data to universities and research institutes as a part of academic frontier project organized by TUIS. The main research theme of this project is on "the sustainable development of economic and social structure dependent on the environment in Eastern Asia". One of the major fields of the research using MODIS data is to analyze environmental change. In the frontier project, we are developing satellite image data analysis system (SIDAS) to support the frontier research such as to forecast weather change and environmental changes as well as processing and maintaining the satellite data.

2 SATELLITE IMAGE DATA ANALYSIS SYS TEM (SIDAS)

2.1. Overview

This system works as the main platform of the total satellite image data analysis service, maintains the satellite image data, and implements satellite image data analysis applications. The user can access the system over the network via Web browser or other web applications. Users can request for data analysis, check the results and download satellite image data through the system.

The satellite image data is extremely large, and direct manipulation of the large data leads to a high load on both the processor and network. In order to improve the throughput and turnaround time of data processing, in the proposed system the computer nodes are configured from high performance servers and multiple PC clusters, implemented as a parallel distributed system. The various analysis applications and the preprocessing of satellite image data are run on this distributed computer nodes.

2.2. System configuration

SIDAS consists of a web server, an application server consisting of multiple PC clusters, and a database server. Figure 1 shows the overview of SIDAS. The application server schedules the execution of applications, manages the satellite data, and controls PC clusters which execute applications. The user can access the system, request data analysis and check the results over the network via a Web browser or other web applications, and the user can also download satellite image data through the system.

The Web server accepts request of the user and submits processing of the request to the application server. The application server transmits the MODIS data used by the processing from the MODIS database to the local disk in the application server. The application server executes application for the request and returns the results to Web server.

© ISAROB 2013

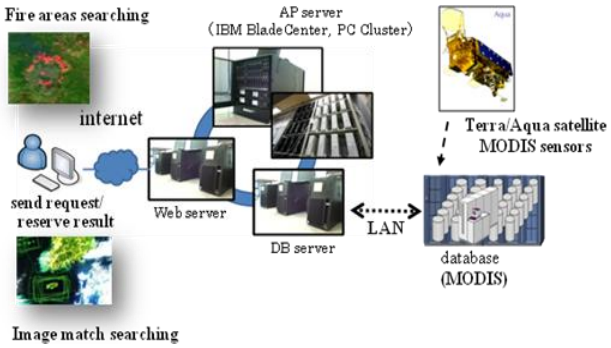

Fig. 1. Overview of SIDAS

3 SATELLITE IMAGE DATA ANALYSIS SYS TEM (SIDAS)

3.1. MODIS data using

MODIS is a multiple band radiometric sensor instrument aboard Terra and Aqua satellites to monitor the environment of a large region of the earth covering a width of 2,330 km. It measures 36 spectral bands between 0.405 and 14.385 µm with three spatial resolutions (250m, 500m, 1,000m). Table 1 shows the band information of MODIS data.

Tokyo University of Information Sciences (TUIS) is receiving MODIS data from three places in Hokkaido, Tokyo and Okinawa, and received the data 3 or 4 times in the daytime and 3 or 4 times in the nighttime from each place. The observing areas from the three places are from 80 degrees to 180 degrees of east longitude and from 0 degrees to 80 degrees of north latitude.

- MOD02 (spatial resolution: 500m) is used to create visualized data from satellite data and to calculate NDVI, and we use 7 spectral bands between visible range and short wave infrared range. BAND1 (red in visible region), BAND4 (green in visible region) and BAND3 (blue in visible region) are used to create the visual information from the satellite data.BAND2 (near-infrared region) are mainly used to measure the vegetation index (The correlation is high in the photosynthesis activity).BAND5, 6, 7 (short wave infrared) has the feature of temperature and reflection factors.
- MOD03 (spatial resolution: 1KM) has geological information containing geodetic latitude, longitude, surface height above sea level, solar zenith, solar azimuth angles, satellite zenith, satellite azimuth angles, and a land/sea mask. Mod03 is used to make a map information from satellite data (MOD02, MOD09, MOD11, MOD28 and MOD35) according to map projection.
- MOD11 (spatial resolution: 1KM) is used to estimate the land surface temperature by using reflectance of land cover. MOD11 is effective data for the heat island phenomenon analysis of urban areas, soil moisture conditions analysis and the heat flux analysis.
- MOD13 (spatial resolution: 500m) is vegetation index data after atmospheric correction.
- MOD14 (spatial resolution: 1KM) is thermal Anomalies data includes fire occurrence (day/night).
- MOD28 (spatial resolution: 1KM) is Sea Surface Temperature data. This data is mainly used to analyse the change of sea surface temperature and the flow of sea.

Table 1. Band information

BAND	WAVELENGTH (nm)	SPATIAL RESOLUTIONS	KEY USE
1	620 ~ 670	250m	Absolute Land Cover change, Vegetation Chlorophyll
2	841 ~ 876	250m	Cloud Amount, Vegetation Land Cover change
3	459 ~ 479	500m	Soil/ Vegetation Differences
4	545 ~ 565	500m	Green Vegetation
5	1230 ~ 1250	500m	Leaf/Canopy Differences
6	1628 ~ 1652	500m	Snow/Cloud Differences
7	2105 ~ 2155	500m	Cloud Properties, Land Properties

3.2. Data format

MODIS data is converted into Raw data for every band by the database creation processing, so that it may be easy to use public and processing of the various analysis.

Raw data is a data format near a general graphics format. In the data part of Raw data, photography data at equal intervals are stored continuously.

Additional information such as position information and time of MODIS data are stored in another file (header file).

© ISAROB 2013

3.3. Preprocessing of satellite image data

3.3.1 Mosaic processing

Figure 2 shows the example of mosaic processing. The mosaic process aggregates the converted Raw data sets into one data set per one orbit. The aggregated data set is generated from three data sets respectively received from the three stations and is maintained consistency because the three received data sets are the same data at the same point.

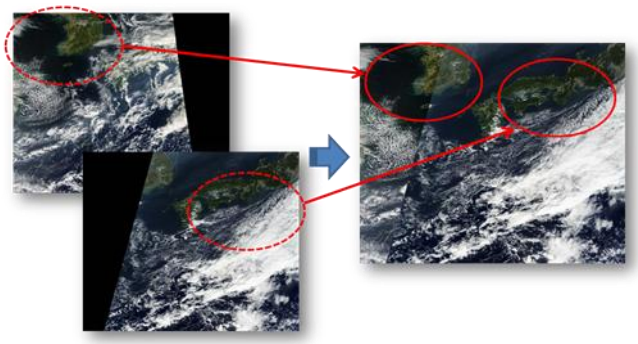

Fig. 2. Example of mosaic processing

3.3.2 Composite processing

When analyzing large area satellite data, one common problem is noise caused by cloud interference. In order to remove the interference of clouds, the standard solution is to create a composite data of the same regions during a selected time span, and to patch together data not covered by clouds to create a clear image.

3.4. Example of the use of MODIS data

One of the purposes of SIDAS is to support researches which use the MODIS data such as environmental perturbation analysis and earth surface temperature analysis.

Main researches under development are as follows.

1) To search for fire regions in forests and fields.

2) To search for a set of data, from the satellite data in TUIS, which is similar image data analyzed by the system.

3) To provide the spatiotemporal analysis of land cover changes of East Asia.

4) To create the disaster map of East Asian.

5) To forecast NDVI by using auto-regression analysis.

6) To provide statistical and soft computing analysis for land cover estimation.

4 EXECUTION CONTROL OF APPLICATION

The analysis processing which uses MODIS data uses large-scale satellite data.

In order to process at the high speed of analysis processing, efficient employment of a system resource is required.

For this reason, we developed LSM (Logical Storage Manager) which manages the execution status of PC cluster and satellite data stored in each cluster.

LSM includes the scheduling function of PC cluster, and the reuse function of satellite imagery data, and determines the PC cluster configuration dynamically which AP (application program) uses.

4.1. Scheduling function of PC cluster

The purpose of the scheduling function of PC cluster is to reduce the execution time of APs by effective use of resources such as CPU and local disk of each PC cluster node. Figure 3 shows an example of the scheduling function. LSM manages the system status such as the operation status of all PC cluster nodes and status of the data stored on the local disk of each PC cluster node. LSM dynamically determines the configuration of the PC cluster nodes (i.e., the number and location of PC cluster nodes) to execute the AP by considering both the operation status and the data which the AP uses. Dynamic resource allocation can be performed with dynamically combining the AP and the data which the AP uses. The procedure of the scheduling function is shown as follows.

① The AP requires the number of PC cluster nodes and the data which the AP uses.

② From ①, the assigned number of PC cluster nodes is determined.

③ LSM determines the configuration of the PC cluster nodes to execute the AP with comparing the data stored on the local disk of each PC cluster node to the data which the AP uses.

④ The AP and the data which the AP uses are combined.

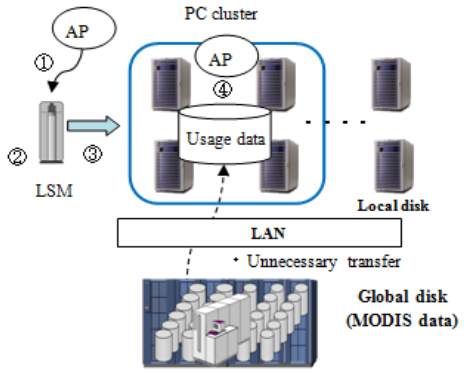

Fig. 3. PC cluster scheduling

4.2 Data reuse function

The purpose of the data reuse function is to reduce an amount of transferred data between PC cluster node and the global disk by reuse of the data stored on the local disk. Figure 4 shows an example of data reuse. The procedure of the data reuse function is shown as follows.

① LSM assigns the AP to the PC cluster node in which the data which it uses is stored.
② When the data which the AP uses is stored on the local disk of a running PC cluster node, the data is transferred from the running PC cluster node to a PC cluster node to execute the AP.
③ When the data which the AP uses is not stored on the local disk of any PC cluster nodes, the data is transferred from the global disk to a PC cluster node to execute the AP.

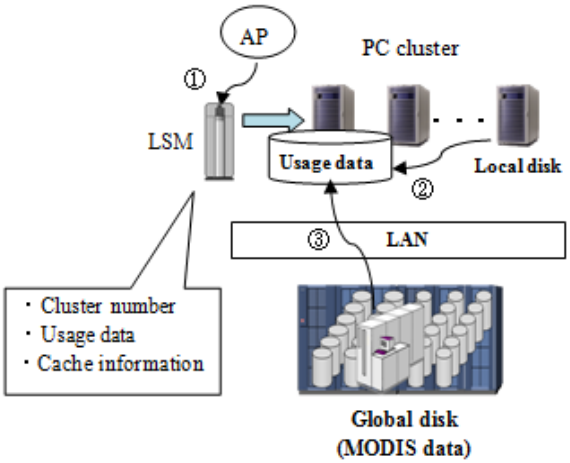

Fig. 4. Data reuse

5 PERFORMANCE EVALUATION

5.1 Evaluation method

The following conditions was used for evaluation of the data reuse function.

- Assess changes reusability of satellite image data (hit rate)
- Multiple tasks are register to the queue of LSM, and are performed in order.
- Number of clusters and the data used for a single task is determined by the random number
  - The following types random number was used
    - Uniform random number
    - Normal random number
- Evaluation condition
  - Number of PC cluster : 32 units
  - local data retention limit of PC cluster : 4
  - Number of data in the database : 128 RAW data
  - the number of tasks to be performed on PC cluster : 200

5.2 Evaluation result

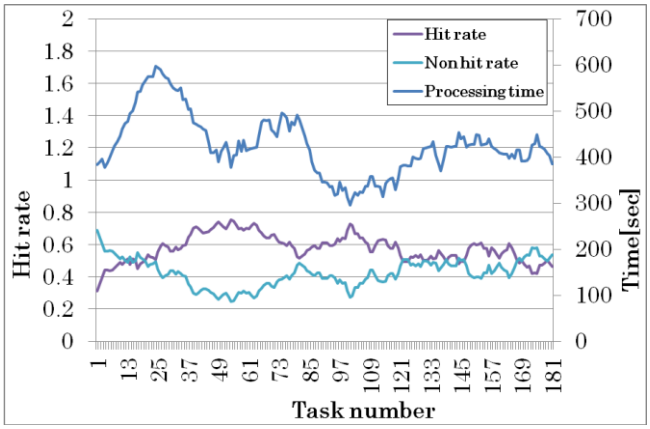

Fig. 5. Hit rate versus time

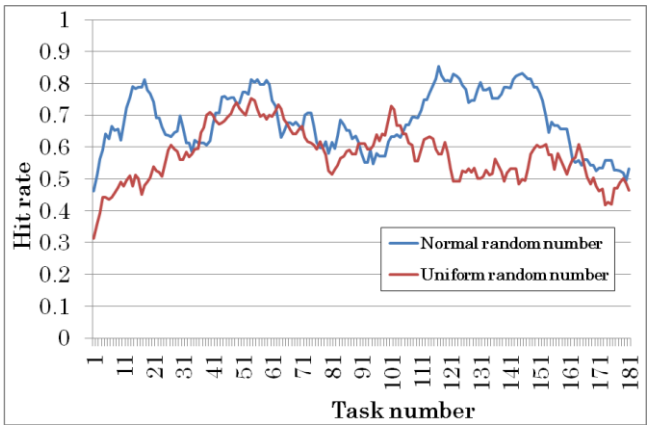

Fig. 6. Comparison of hit rate

Figure 5 and 6 show the results of the evaluation of the proposed functions. In the evaluation, 200 tasks are generated and the proposed functions are evaluated in terms of hit rate. Here hit rate is a rate of the number of data found on the local disk to the number of the generated tasks. The processing time is reduced as the hit rate increases. Figure 5 shows the hit rate and task processing time. The hit rate under normal distribution is higher than uniform distribution. Figure 6 shows the hit rate under normal distribution and uniform distribution.

5.3 CONCLUSIONS

In the satellite image data analysis system, we have proposed and implemented LSM to improve the processing performance and the data reusability. We measured the hit rate of the data that is stored on the local disk of PC clusters to evaluate the scheduling function and the data reuse function of LSM. From the evaluation results, we confirmed that the processing time was reduced as the hit rate increases.

© ISAROB 2013

In the future, we aim the efficient use of the system resources by more improving the scheduling function and the data reuse function.

Acknowledgments

This research was supported by the Research project of Tokyo University of Information Sciences for the sustainable development of economic and social structure dependent on the environment in eastern Asia.

REFERENCES

[1] Akihiro Nakamura, Jong Geol Park, Kenneth J. Mackin, Eiji Nunohiro, et al, Development and Evaluation of Satellite Image Data Analysis Infrastructure, The Sixteenth International Symposium on Artificial Life and Robotics, Proceeding Index OS18-3, (AROB 16th' 2011)

[2] Eiji Nunohiro, Jong Geol Park, Kenneth J. Mackin, et al, Development of satellite data analysis system, Proceedings of the 5th International Conference on Information (2009), pp.143-146

[3] Eiji Nunohiro, Kei Katayama, Kenneth J. Mackin, Jong Geol Park, Forest and Field Fire Search System using MODIS Data, Journal of Advanced Computational Intelligence and Intelligent Informatics (JAC 3, 2007), vol.11 No.8, pp.1043-1048

[4] Kenneth J. Mackin, Eiji Nunohiro, Development of Satellite Image Searching using Distributed Genetic Algorithm with Normalized Correlation, The twelfth International Symposium on Artificial Life and Robotics, Proceeding Index GS12-7, (AROB 12th' 2007)

[5] National Aeronautics and Space Administration (NASA), MODIS Web, http://modis.gsfc.nasa.gov/

© ISAROB 2013

The Eighteenth International Symposium on Artificial Life and Robotics 2013 (AROB 18th '13),
Daejeon Convention Center, Daejeon, Korea, January 30-February 1, 2013

Administrative division based data segmentation for autonomous paddy field classifier modeling

Takashi Yamaguchi[1], Shinya Iwasaki[1], Kazuma Mori[1], Kenneth J. Mackin[1], Masaki Hanada[1], Eiji Nunohiro[1]

[1]Tokyo University of Information Sciences, Japan
(Tel: 81-43-236-1232, Fax: 81-43-236-1232)

[1]tyamagu@rsch.tuis.ac.jp

Abstract: Monitoring changes in paddy area is important since rice is staple food, and paddy agriculture is a major cropping system in Asia. The decision trees or stochastic analysis based methods using spatiotemporal satellite sensor data is effective to monitor paddy area by the remote sensing. On the other hand, it is difficult to apply the same models for different countries and regions. Therefore we applied artificial neural network to classify paddy area in order to automatically generate the classifier. From the computer simulation, the proposed paddy classifier yielded high classification rate in the data subset of north region of Chiba. However, the accuracy was corrupted by the difference of annual cycle pattern. Thus, in this paper, we investigate an administrative division based data segmentation method in order to divide the data set into different groups so that the different patterns of paddy annual cycle is divided to different groups.

Keywords: artificial neural network, classification, remote sensing

1 INTRODUCTION

Monitoring changes in paddy area is important since rice is staple food, and paddy agriculture is a major cropping system in Asia. For monitoring change in land surface, many satellites were launched and its applications were researched in the field of remote sensing. However monitoring paddy area with remote sensing is difficult due to the temporal change in land surface, and difference of spatiotemporal characteristics in countries and regions.

In our past research, we applied artificial neural network to classify paddy areas using moderate resolution sensor data that includes spatiotemporal information. Our aim is to automatically generate a paddy classifier in order to create localized classifiers for each countries and region. From the experiments, proposed paddy field classifier yielded a good result in the classification accuracy. However, the classification accuracy is depends on the set geographical area for the training data sampling. In this paper, we investigate an administrative division based data segmentation method in order to divide the data set into different groups so that the different patterns of paddy annual cycle is divided to different groups.

This classified paddy field data is visualized on a web system that called Satellite Image Data Analysis System (SIDAS). Tokyo University of Information Sciences receives Moderate Resolution Imaging Spectroradiometer (MODIS) data, one of the sensors equipped by NASA's Terra and Aqua satellites, and researches of the analysis on change of environment as part of the academic frontier project. For the information infrastructure of this frontier research, we are developing a SIDAS to support of web system, a parallel distributed system configuration using multiple PC clusters, database for MODIS data to publish the research results and MODIS data for public use. In this research, we develop the sub-systems of satellite image preprocessing, the analysis using satellite image and the map visualization in order to publish the research results.

2 PADDY FIELD CLASSIFIER

2.1 Paddy Field Classifications on Remote Sensing

Monitoring paddy area with remote sensing is difficult because a paddy has an annual cycle that can be classified into three main periods: (1) the flooding and rice transplanting period, when the land surface is observed as water; (2) the growing period, when vegetation index is increased by the vegetative growth; (3) the fallow period, when land surface is observed as soil. For monitoring change in land cover, moderate resolution remote sensing is effective because of the high frequency of these satellites to scan the same area.

In the past research for paddy areas estimation using remote sensing, decision trees or stochastic analysis based methods using spatiotemporal information were proposed. On the other hand, it is difficult to apply the same models for different countries and regions. In this paper we applied artificial neural network to classify paddy area using moderate resolution remote sensing data in order to automatically generate the classifier.

© ISAROB 2013

2.2 Multi-Layered Perceptron Classifier

In this paper, Multi-layered perceptron (MLP) was used. MLP is a type of artificial neural network that can approximate complex function by machine learning. MLP is trained by data set that consists of a feature vector and a teaching signal.

Multi-layered perceptron (MLP) is a type of artificial neural network (ANN) that can approximate complex function by machine learning. In this research, we used MLP shown as Fig. 1 in order to learn a classification function of paddy field area from the MODIS data set.

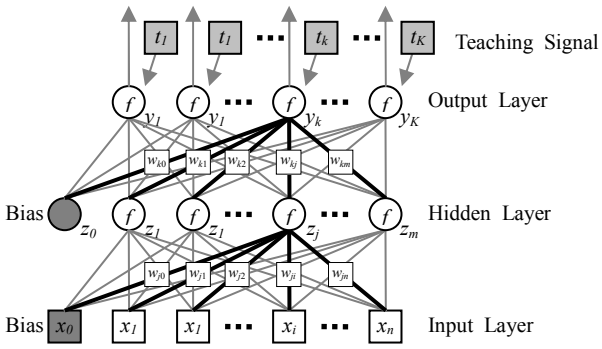

Fig.1. MLP Network Structure

MLP consists of 3 layers: input layer with n neurons and a bias neuron, hidden layer with m neurons and a bias neuron, and output layer with K neurons. Each neuron is connected with every neuron in the next layer, and each connection has a weight value. When an input signal $\mathbf{x} = \{x_1, x_2, \ldots x_n\}$ is given, jth output signal z_j of hidden layer's neuron and kth output signal y_k of output layer's neuron are calculated by following expressions:

$$z_j = f\left(\sum_{i=0}^{n} w_{ji} x_i\right), \tag{1}$$

$$y_k = f\left(\sum_{j=0}^{m} w_{kj} z_j\right), \tag{2}$$

where $i = 0, 1, 2 \ldots, n$; $j = 0, 1, 2 \ldots, m$; $k = 0, 1, 2 \ldots, K$; f is the activation function, and z_0 and x_0 are bias neurons. Bias neuron always output 1.0 to next layer's neurons. For activation function, sigmoid function was used.

MLP modifies each weight value using back propagation (BP) training [3]. Let be $x^p = \{x_1^p, x_2^p, \ldots x_n^p\}$, $p = 1, 2, \ldots, N$ is pth input signal, and $t^p = \{t_1^p, t_2^p, \ldots t_K^p\}$ is pth teaching signal. The teaching signal is true output signal that correspond to pth input signal x^p where projection function can be defined as follow

$$t_p = g(x_p). \tag{3}$$

When pth training pattern $\{x^p, t^p\}$ is given, BP training modifies weights for minimizing mean square error E defined as following expression

$$E = \frac{1}{N}\sum_{p=1}^{N}\left\| t^p - y^p \right\|^2 . \tag{4}$$

At the training step in BP training, the weight modification $\Delta w_{ji}(s)$ and $\Delta w_{kj}(s)$ are defined as follows:

$$\Delta w_{ji}(s) = -\lambda \cdot \frac{\partial E}{\partial w_{ji}} + \mu \cdot \Delta w_{ji}(s-1), \quad (5),$$

$$\Delta w_{kj}(s) = -\lambda \frac{\partial E}{\partial w_{kj}} + \mu \cdot \Delta w_{kj}(s-1), \quad (6)$$

where λ is a learning rate, and μ is a momentum rate. Each weight is commonly initialized by random value. As a result of training, MLP learns a function $g(x)$ by modifying weight values.

In this research, MLP was used as 2 class classifier such that classifies positive or negative (1 or 0) for paddy field class. However MLP output is continuous value, so that it is necessary to decide positive or negative from the continuous output value. In this experiment, pth final output was defined by following function.

$$Output^p = \begin{cases} positive & if \quad y^p > \theta \\ negative & otherwize \end{cases}. \tag{7}$$

where θ is predefined threshold value.

MLP learning result is unstable from the initialization problem that MLP learning falls into different local minima by the initial weight values. For resolving unstableness, combination with ensemble learning and MLP is commonly used. Ensemble Learning is a method for improving the stability of machine learning algorithms by using multiple learners. For ensemble method, bagging method was used [4]. Bagging is a typical ensemble method that aggregates multiple training results. For aggregating, voting was used, as this is commonly used in bagging for classifier. Let $L(x)$ be an aggregated learner, $L_s(x)$ be a multiple weak learner where $s = 1, 2, \ldots, r$; and $c = 1, 2, \ldots, C$ be class label. A robust learner $L(x)$ is defined by following expression.

$$L(x) = \arg\max_c \left| \{s; L_s(x) = c\} \right| . \tag{8}$$

Each learner is trained by using bootstrap samples [5]. Let T be training data set, training data subset $T_s \in T$ for sth learner is constructed by using random sample.

2.3 MLP Paddy Classifier

For the input signals of samples, 1-month composite MODIS sensor data on 1 pixel was used. The input signals consist of red, infra-red and short wave infra-red of January to September per 1-month (36 inputs) in order to learn temporal pattern of paddy area. The band data of each month was derived from 1-month composite MODIS sensor data of 500m resolution. 1-month composite data is the technique that composites multiple satellite image between 1 month into a single satellite image in order to reduce the noise and distortion such as the cloud and the sensor angle. 1-month composite data is a commonly used for the analysis on the remote sensing.

For teaching signal, 1km meshed land use map provided by the Japanese Ministry of Land, Infrastructure, Transport and Tourism (JMLIT) were used. The land use map is converted into the raster image of same pixel size by the liner interpolation because the meshes of land use map are not matched to the pixels of satellite image.

2.4 Training Data Segmentation

From the experiments of our previous research, proposed paddy field classifier yielded a good result in the classification accuracy. However, the classification accuracy is depends on the set geographical area for the training data samples. The paddy annual cycle patterns is diversified when the training data area is increased in size, therefore the large number of hidden layer neurons and the long training iterations are necessity to learn the annual cycle patterns.

Considering that the difference of paddy annual cycle is occurred by the culture, the political decision and the geographical feature, we investigated an administrative division based data segmentation method that the data set is divided by the administrative division. From the viewpoint of the geomorphology, it is expected that the administrative division based segmentation is effective to separate the pattern of paddy annual cycle because the boarder of administrative division is generally decided on the geographical feature such as the river and the mountain.

The samples that consist of the input signal values and a teaching signal value are divided into the groups by the administrative division. For the data of administrative division, the administrative division map provided by JMLIT was used. The maps provided by JMLIT was converted into the raster image because the maps constructed by vector image. The MLP classifier is separately trained for each divided data sets. Therefore the MLP learned the patterns of paddy annual cycle for the target prefecture that derived by the administrative division.

2.5 Visualization System of Paddy Classification

In this research we develop a paddy map visualization system as an application framework of SIDAS in order to publish the latest paddy map by the latest satellite images. Figure 2 shows an overview of paddy map visualization system.

The data set provider has a data divider that divides the samples of MODIS sensor data and land use data for the MLP paddy classifier regard to the administrative division. The divided data is used to train the MLP paddy classifiers and classify the samples by corresponding learned paddy classifiers. The MLP paddy classifier is separately trained by the given data for an area of administrative division. After the training, the samples can be classified into paddy or non-paddy by the learned MLP paddy classifier for each administrative division. Finally, the classification result is visualized as RGB image by the map visualizer for web publishing.

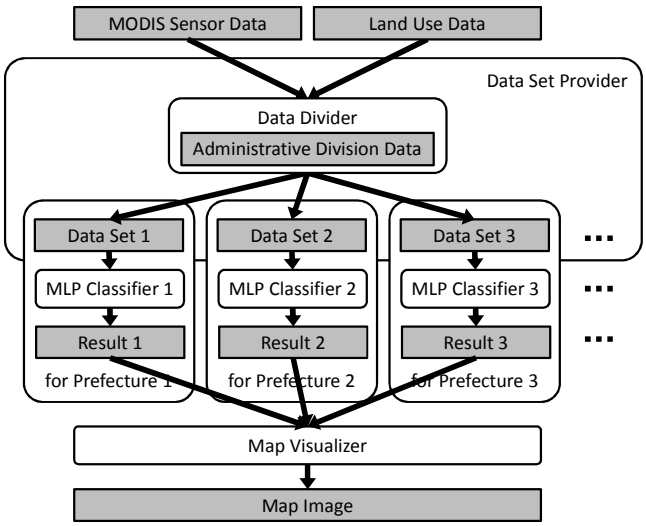

Fig.2. Overview of paddy map visualization system

SIDAS has a database of MODIS sensor data as the raster image format. The land use data and administrative division data also stored in SIDAS database as raster image. The data divider is implemented by using the composite function in SIDAS middleware. SIDAS has a middleware for satellite image analysis such as the image I/O, image composition, image masking, image visualization, and etc. The data division function was implemented as the image masking of MODIS sensor data by the administrative division data. Because the mask image should be consisted by {0, 1} value in SIDAS middleware, the administrative

© ISAROB 2013

division data was converted into the raster image with {0, 1} value.

The divided data set is provided as the multi-channel RAW image format similar to MODIS sensor data. In this system, MLP classifier is implemented to handle the multi-channel RAW image for input signals. The input channels consist of red, infra-red, short wave infra-red, and land use of January to September per 1-month. The result of classification is also provided as the multi-channel RAW image. The output channel consists of the label of classification.

For the visualization of paddy map, the multi-channel RAW image to RGB image convert functions on SIDAS was used. The SIDAS image convert functions is developed to visualize the maps of visual light, vegetation index and sea surface temperature, and land surface temperature. This convert functions can convert the multi and single channel RAW image into the RGB color image. The RGB color image is used for the web publishing of satellite image.

3 EXPERIMENT

In this experiment, we evaluated classification accuracy by using proposed paddy classifier. For evaluating classification accuracy, MODIS data was divided into 2 disjoint sub set, training data set and test data set, by using random sampling. The number of test data set was 10% of the number of training data set.

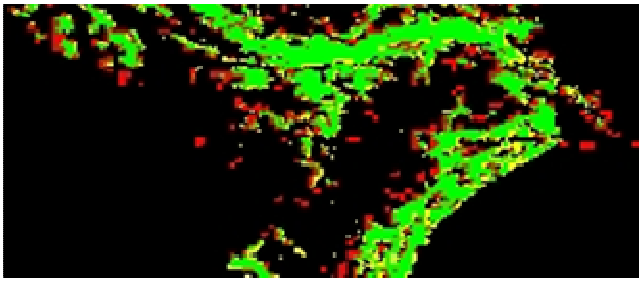

Fig.3. Result of Paddy Map Visualization

From the computer simulation, the proposed paddy classifier yielded 0.851 classification rate in the data subset of Chiba prefecture. Figure 3 is a result of paddy map visualization. Green colored area is correctly classified area as paddy field. Red colored area is incorrectly classified as non-paddy for paddy field and Yellow colored area is incorrectly classified as non-paddy for paddy field. This result shows that the larger area of paddy field can be correctly classified. On the other hand, the small paddy field area and the neighbor of the boarder of paddy area are difficult to classify due to the mixture of different land use in pixel.

4 CONCLUSION

In this paper, we proposed an administrative division based data segmentation method in order to divide the data set into different groups to separate the different pattern of paddy annual cycle by administrative division. Moreover, we develop the SIDAS application framework and implement the proposed method on this framework.

From the result of paddy map visualization, the paddy map generated by proposed paddy classifier is yielded good result in the classification accuracy. On the other hand, it was clarified a problem of the mixture of different land use in pixel for improving accuracy.

For future works, we plan to generate the maps for whole prefecture in Japan. Moreover, we evaluate the accuracy and investigate the effectiveness for the practical use of paddy field monitoring.

ACKNOWLEDGEMENT

This research was supported by the Research project of Tokyo University of Information Sciences for the sustainable development of economic and social structure dependent on the environment in eastern Asia

REFERENCES

[1] T. Le Toan, F. Ribbes, L. Wang, et al (1997), Rice crop mapping and monitoring using ERS-1 data based on experiment and modeling results. IEEE Transactions on Geoscience and Remote Sensing, 1, 41-56

[2] X. Xiao, S. Boles, S. Frolking, C. Li, et al (2006), Mapping paddy rice agriculture in south and southeast Asia using multi-temporal MODIS images. Remote Sensing of Environment, 100, 95-113

[3] D. E. Rumelhart, G. E. Hinton, R. J. Williams (1986) Learning representations by back-propagating Errors. Nature, vol. 323, pp. 533-536

[4] L. Breiman, (1996) Bagging Predictors. Machine Learning, 24(2), 123-140

[5] B. Efron, R. Tibshirani (1993), "An Introduction to the Bootstrap". Chapman and Hall.

[6] Takashi Yamaguchi, Eiji Nunohiro, Jong Geol Park (2009) Application of Artificial Neural Network for Land Cover Classification using Spatiotemporal Information, 5th International Conference on Information,

[7] W.Takeuchi, Y. Yasuoka (2004), Development of normalized vegetation, soil and water indices derived from satellite remote sensing data, Journal of the Japan Society of Photogrammetry and Remote Sensing, Vol. 43, No. 6, pp. 7-19 (in Japanese).

© ISAROB 2013

The Eighteenth International Symposium on Artificial Life and Robotics 2013 (AROB 18th '13),
Daejeon Convention Center, Daejeon, Korea, January 30-February 1, 2013

Analysis of seasonal variability of methane over global land area

Jonggeol Park[1], Sooyoung Park[1], Youngjoo Kwak[2], Eiji Nunohiro [1], and Takashi Yamaguchi [1]

[1]Tokyo University of Information Sciences, Japan
[2]International Centre for Water Hazard and Risk Management (ICHARM) under the auspices of UNESCO, Japan
(Tel: 81-43-236-4644, Fax: 81-43-236-4644)

[1]amon@rsch.tuis.ac.jp

Abstract: In this study, we determine the global emission concentration of methane using SCIAMACHY data. We analyzed land and sea area to investigate the nine-year changes in methane concentrations from 2003 to 2011. Moreover, by subtracting the concentration of methane from land and sea, we can found the methane emission concentration of land. As a result, it is cleared that a big amount of CH4 emission concentration was found not only in the Northern Hemisphere paddy fields but also in the Southern Hemisphere broadleaf evergreen areas (Central Africa and South America). And we also found that the global land CH4 growth rate is 3-5ppb/year during 9 years.

Keywords: CH4, emission concentration, Greenhouse gases, SCIMACHY, Sources, NDVI.

1 INTRODUCTION

A greenhouse gas is a gas in atmosphere that absorbs and emits radiation within the thermal infrared range. This process is the original cause of the greenhouse effect. The primary greenhouse gases in the Earth's atmosphere are water vapor, carbon dioxide (CO2), methane (CH4), nitrous oxide (N2O), and ozone (O3). Which from four of the principal greenhouses gases are human activities results (CO2, CH4, N2O, and the halocarbons). These gases increase concentrations of the long-lived greenhouse gases (LLGHGs). Greenhouse gases affect the temperature of the Earth. Since the beginning of the Industrial Revolution, the burning of fossil fuels have contributed to the increase in carbon dioxide in the atmosphere from 280ppm to 390ppm, despite the uptake of a large portion of the emissions through various natural "sinks" involved in the carbon cycle. In the past few years, many workers have noted that the combined effect on climate of the increase in the concentrations of a large number of trace gases could rival or even exceed the increasing concentration of carbon dioxide. Atmospheric CH4 is the second most important anthropogenic greenhouse gas after CO2. CH4's mixing ratio has increased by a factor of 2.5 compared to preindustrial levels and reached almost 1,800 ppb today. The direct radiative forcing of anthropogenic CH4 is 0.48W/m2 that is almost one third that of anthropogenic CO2 (1.66W/m2) [1][2]. CH4 emissions are separated into anthropogenic and natural sources. According to Lelieveld et al. (1998) and IPCC (2001), natural sources amount is only one-third of the total CH4 emission budget, which the most important natural source is wetland. Anthropogenic sources account for the other two-thirds of the total CH4 emission budget, with the most important being energy consumption (coal mining and combustion, oil- and gas-related emissions), domestic ruminants and waste treatment, rice paddies, biomass burning, landfills and waste water. A study from Nisbet et al. (2009) suggests that the emission of methane from plants under normal conditions is due to the transport of water containing dissolved methane from the soil to the atmosphere through transpiration. Transpiration could help to explain the satellite-observed methane enhancement over the tropical regions of South America and some of the published ground-based measurements (Carmo 2005, Miller 2007). Recent studies have proposed that there is an additional significant CH4 source that could radically impact the current CH4 budget estimates. Keppler et al. (2006) suggested that living plants with CH4 emissions (aerobic) 10–40% of the total annual source, may be a major CH4 source on a global scale. Wang et al (2008) have confirmed that some plant species emit methane under aerobic condition in the Inner Mongolia steppe. After a decade of near stable concentrations, the growth rate of atmospheric methane has started to increase again.

Recently SCIAMACHY (launch 2002) and GOSAT (launch 2009) enabled precise measurements of atmospheric CH4 from space. Unfortunately the global source strength of CH4 remains uncertain. In this study, we will focus on CH4 sources of global area using these satellite data, vegetation map and MODIS NDVI to investigate the characteristics of this CH4 sources

© ISAROB 2013

2 DATA

The World Data Centre for Greenhouse Gases (WDCGG) is one of the WDCs under the Global Atmosphere Watch (GAW) program. It serves to gather, archive and provide data on greenhouse gases (CO2, CH4, CFCs, N2O, surface ozone, etc.) and related gases (CO, NOx, SO2, VOC, etc.) in the atmosphere and ocean, as observed under GAW and other programs. Vegetation Index (VI) have trended to estimate a large number of vegetation properties such as LAI, biomass, chlorophyll concentration in leaves. The enhanced vegetation index(EVI) is an `optimized` index designed to enhance the vegetation signal with improved sensitivity in high biomass region and improved vegetation monitoring and reduction in atmosphere influences. Global Land Cover by National Mapping Organization (GLCNMO) has twenty land cover classes using 16-day composite MODIS data of 2003.The SCanning Imaging Absorption spectroMeter for Atmospheric CHartographY (SCIAMACHY) instrument (Burrows 1995) is a part of the atmospheric chemistry payload of the European Space Agencies (ESA) environmental satellite ENVISAT, launched in March 2002. SCIAMACHY is the first satellite instrument that measures near-infrared spectra in the 1–2.4μm spectral range from space at high spectral resolution. The SCIAMACHY near-infrared spectra contain atmospherically interesting molecules such as CH4, CO2, CO, and H2O, of which the bulk resides in the troposphere. Retrieval algorithms applied to this wavelength range include the Iterative Maximum A Posteriori-DOAS (IMAP-DOAS) algorithm (Frankerberg 2005). The Greenhouse Gases Observing Satellite (GOSAT) instrument was launched in January 2009 with the aim of measuring the column amounts of CO2 and CH4. GOSAT has a CO2 target to achieve 4 ppm accuracy for a three month regional average using a combination of short-wavelength infrared (SWIR), and infrared (IR) channels (Kuze 2009).

3 ANALYSIS AND RESULT

3.1 Data Process

Frankenberg's method was used to reduce cloud effect from SCIAMACHY data. By using a cloud free pixel data, a 15-day composite data was made to understand the CH4 source and its circulation. In addition, this data was spatially and temporally interpolated. As a result, the data was made up in 24 scenes per year during a period from 2003 to 2011. After removing the clouds, GOSAT data was distributed as a monthly data. Cloud free GOSAT data is valid because of the use of Thermal And Near infrared Sensor for carbon Observation-Cloud and Aerosol Imager (TANSO-CAI). GOSAT can only provide us four years of data, which is not sufficient, so we use it as SCIAMACHY data supplement (Fig. 1).

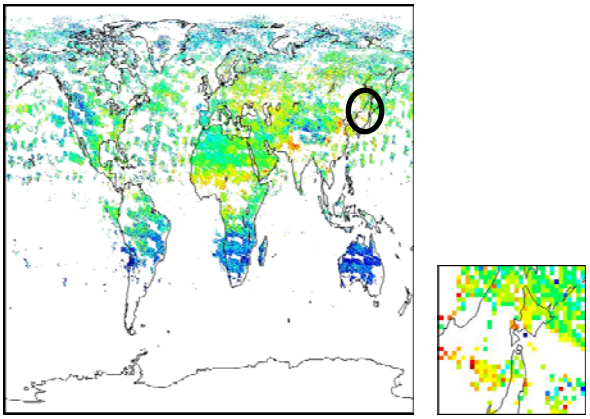

a) Cloud free image

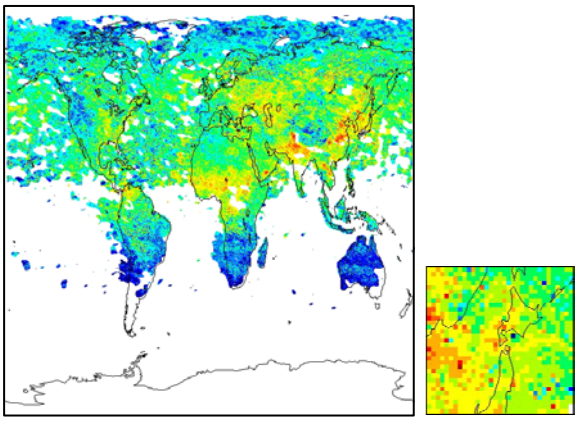

b) Interpolated image

Fig. 1. Cloud Free and Interpolation CH_4 concentration SCIMACHY

3.2 Change in methane concentration on land

Figure 2 shows the concentration of CH_4 by terrestrial latitude band for nine years. CH_4 concentration in the Northern Hemisphere mid-latitude regions is higher than other regions. It increased approximately by 20ppb from 2003 (1750ppb) until 2011(1780ppb).Mainly in September, the high concentration areas are distributed on the paddy fields of Asia. It shows that in the rice harvest period, CH_4 concentration raised up to 1780ppb max. CH_4 concentration in the high latitudes of the north hemisphere is 1680ppb, near the equator is 1740ppb and in the south hemisphere is lower than 1670ppb. After 2007 every year, from January to February, it becomes clear that the CH_4 concentration was

© ISAROB 2013

increasing near the equator. There were no concentration changes of CH_4 from 2003 to 2006 but from 2007 to 2011 we understand that it was increasing.

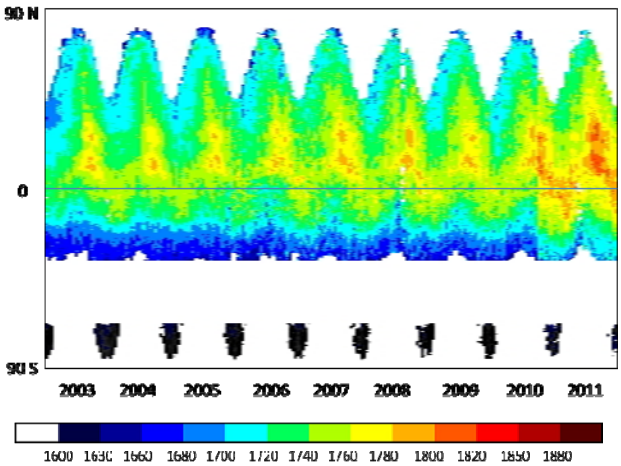

Fig. 2. Land methane concentration in time series from 2003 to 2011

3.3 CH4 emission concentration

CH4 emission concentration is defined as the emission of land CH4 concentration. Time series changes in the CH4 concentration of land can be relatively compared. it is difficult to compare the CH4 emission concentration because of the different background concentration of CH4. Therefore, we can assume that a very small amount of CH4 is emitted from the sea surface, that CH4 concentration of the sea is used as a same latitude background. The difference of CH4 concentration between land and sea is equal to the CH4 emission concentration of land at the same latitude (Fig. 3). As a result, it is cleared that a big emission concentration of CH4 was found not only in the Northern Hemisphere paddy fields but also in the Southern Hemisphere broadleaf evergreen areas (Central Africa and South America)(Fig. 4).

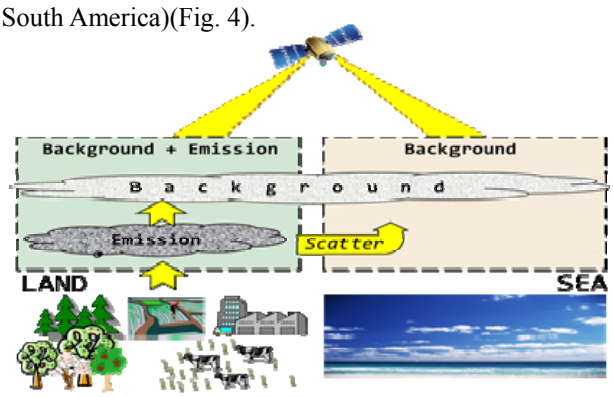

Fig. 3. CH_4 emission concentration

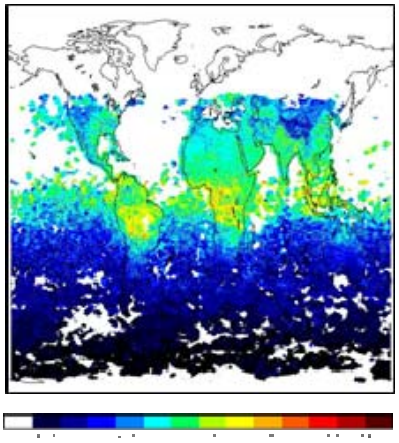

a) CH4 concentration

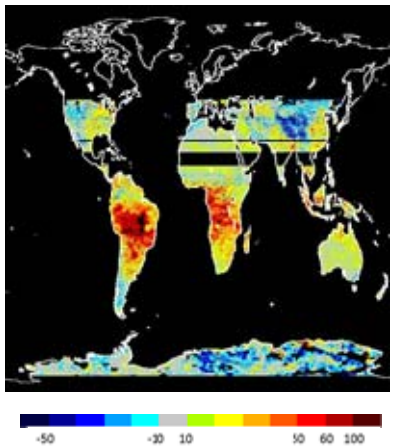

b) CH4 emission concentration

Fig. 4. CH4 concentration (a) and CH_4 emission concentration (b) in January 2004

3.4 Relation between CH4 emission concentration ar ea and Landcover type

We understood that CH4 emission concentration increased in the Southern Hemisphere from 2007. Figure 6 shows CH4 average emission in 2009 and the vegetation map that was used to determine the geographical features of the CH4 emission concentration areas. From that we understood that there are a lot of broadleaf evergreen areas near the equator of the southern hemisphere, which emits 50-80ppb/year of methane (b). CH4 emission concentration areas of the northern hemisphere are consistent with the distribution of paddy fields which emits 80ppb/year (c). And because of the clouds in Northern hemisphere high latitude areas, we don't dispose of enough data to extract information about CH4 emission concentration on wetland areas.

© ISAROB 2013

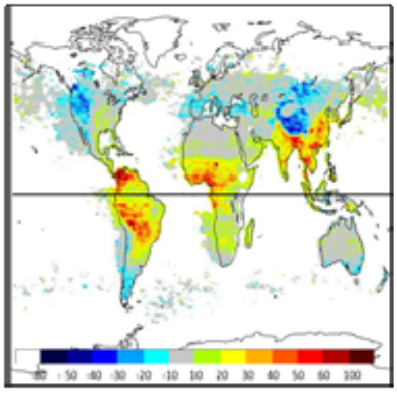

a) CH_4 average emission concentration

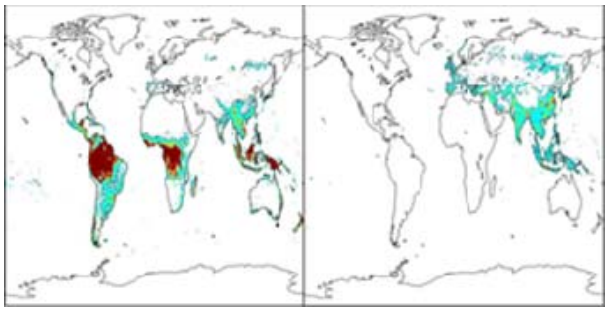

b) Broadleaf Evergreen c) Paddy field

Fig. 5. The comparison of the CH_4 emission concentration and Land Cover Type by MODIS

3.5 The growth rate of CH4 concentration

We investigated the CH4 concentration's growth rate during 9 years of its data that reduces a seasonal change effect. As a result, in almost of land, there was a trend of 3-5 ppb/year, but especially, in Brazil, China and Indonesia we noticed that it increased to more than 6ppb/year (Figure 7). According to the WMO-GAW, the average growth rate is 2.2ppb/year during 10 years until 2009. From 2003 to 2006 there was no CH4 growth, but announced that from 2006 it has been increasing by about 6ppb/year. This means that there is no big difference from our results.

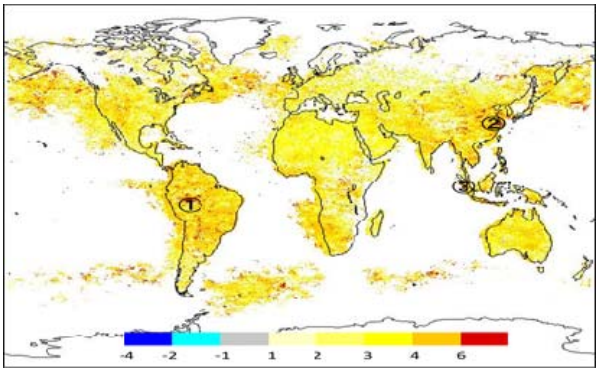

Fig. 6. CH_4 growth rate during 9years

4 CONCLUSION

In this study, we examined separately the changes in methane concentration in land and sea areas using a time series SCIMACHY. Paddy field in Southeast Asia showed the highest among the CH4 concentration areas by 1780ppb. According to the MODIS NDVI comparison, the CH4 concentration increases by the paddy growth. And in the harvest time, the CH4 concentration raises its maximum. Methane concentration in the sea becomes higher gradually during 9 years. It reaches its maximum at the mid-latitude of the northern hemisphere, but becomes lower as it goes to the polar regions. Assuming that CH4 does not emit in the sea, the increase in CH4 concentration of sea areas is caused by the flowing CH4 emitted in land. The difference of land and sea methane concentration is the emission of land CH4 concentration. According to the land CH4 emission concentration, the high CH4 emission concentration areas are not only in paddy fields (80ppb/year) but also broadleaf evergreen areas in South America and Central Africa(50- 80ppb/year).

Finally, we removed the seasonal variation of CH_4 concentration from land during 9 years to investigate the CH_4 growth rate. As a result, in most of land areas, the growth rate of CH_4 concentration is 3-5ppb/year, but in some areas in Brazil, Indonesia and China is more than 6ppb/year. Next, it is necessary to search the cause of this growth rate increasing in these 3 areas.

ACKNOWLEDGEMENT

This research was supported by JSPS KAKENHI Grant-in-Aid for Scientific Research (C) and the Research project of Tokyo University of Information Sciences for the sustainable development of economic and social structure dependent on the environment in eastern Asia.

REFERENCES

[1] IPCC, 2007, Climate Change 2007: The Physical Science Basis. Contribution of Working Group I to the Fourth Assessment Report of the Intergovernmental Panel on Climate Change,S. Solomon, D. Qin, M. Manning, Z. Chen, M. Marquis, K.B. Averyt, M. Tignor and H.L. Miller (Eds) (Cambridge, UK: Cambridge University Press)

[2] IPCC, 2001, Climate Change 2001: The Scientific Basis. Contribution of Working Group I to the Third Assessment Report of the Intergovernmental Panel on Climate Change, J.T.Houghton, Y. Ding, D.J. Griggs, M. Noguer, P.J. van der Linden, X. Dai, K. Maskell and C.A. Johnson (Eds) (Cambridge, UK: Cambridge University Press)

© ISAROB 2013

The Eighteenth International Symposium on Artificial Life and Robotics 2013 (AROB 18th '13),
Daejeon Convention Center, Daejeon, Korea, January 30-February 1, 2013

Estimating a floodwater from MODIS time series and SRTM DEM data

Youngjoo Kwak[1], Jonggeol Park[2], and Kazuhiko Fukami[1]

[1]International Center for Water Hazard and Risk Management, Tsukuba 305-8516, Japan
[2] Tokyo University of Information Sciences, Chiba 265-8501, Japan
(Tel: 81-29-879-6779, Fax: 81-29-879-6709)

[1]kwak55@pwri.go.jp

Abstract: Extreme climate event, such as heavy rainfall and Typhoon, is anticipated to escalate extreme floods. In fact, many flood plains in the Asian-Pacific region have already experienced a rising number of flood disasters. In this circumstance, real-time flood mapping with automatic detection technique is increasingly important in emergency response efforts. However, current mapping technology is still limited in accurately expressing information in flood areas such as inundation depth and extent. For this reason, the authors attempt to improve a floodwater detection method with a simple algorithm for a better discrimination capacity to discern flood areas from turbid floodwater, mixed vegetation areas, snow, and cloud. In this research, pixel classification was performed on the Moderate Resolution Imaging Spectroradiometer (MODIS) time series images (8-day composites, MOD09A1, 500-m resolution) for floodwater detection. The purpose of this image classification was to estimate a flood area based on the spatial distribution of a nation-wide flood from near real-time MODIS images coupled with a digital elevation model (DEM). Moreover, the authors improved the accuracy of the water extent boundary using a 8-direction tracking algorithm to find the same level between flood-prone area and non-flood area. The results showed the superiority of the developed method in providing instant and accurate flood mapping by using three algorithms, which indicates decision tree, modified land surface water index (MLSWI) and 8-direction tracking based on DEM data.

Keywords: Flood mapping, floodwater, MODIS, DEM.

1 INTRODUCTION

Over the last decades, the number of fatalities and the scale of economic damage caused by river floods have considerably increased worldwide. Moreover, extreme rainfall and typhoon are projected to increase the frequency and magnitude of river floods in the future, which are likely to cause a further increase in flood risk leading to more human and economic damage given the current population growth and the ongoing accumulation of value assets in river deltas. The Asia-Pacific region is particularly vulnerable to the impacts of natural disasters [13]. Satellite remote sensing is a useful tool for interpretation and analyses of water bodies, including floodwater with cost-effective, accurate monitoring at frequent time steps over large areas. Various remote sensing methods have been introduced to detect surface water or estimate floodwater during flooding while considering floodplain topography [4, 7, 9, 12]. Flood detection is one of the classical themes of satellite-based remote sensing. Despite its usefulness, satellite-based remote sensing has also limitations, particularly, in spatial coverage and detection of mixed floodwater. Gao [3] developed the Normalized Difference Water Index (NDWI), a satellite-derived index from near-infrared (NIR, band 2) and short wave infrared (SWIR, band 6) bands: $NDWI=(\rho_{0.85}-\rho_{1.24})/(\rho_{0.85}+\rho_{1.24})$, where ρ represents the radiance in reflectance units. Both $\rho_{0.85}$ and $\rho_{1.24}$ are the reflectance at 0.85 μm and 1.24 μm wavelength, respectively. NDWI is used to derive water fraction and a flood map from MODIS data. Xiao et al. [14, 15] used the multi-temporal MODIS images (8-day composites, MOD09A1, 500-m resolution) to extend the approach to larger regions, south China, South and Southeast Asia. They used a relaxed set of criteria, LSWI+0.05 > EVI or LSWI+0.05 > NDVI, to identify flooded paddy rice fields. The land surface water index (LSWI) is calculated using the spectral signals in shortwave infrared (SWIR) and in NIR ranges to detect water at the soil surface [4].

The purpose of this study was to detect flood areas in near real-time accurately and rapidly, based on the spatial distribution of nationwide flooding by using an improved version of MODIS indices so that mapping the spatial and temporal dynamics of flooding is possible. To determine the water extent boundary more accurately, the authors improve an extraction method of surface water with a simplified decision tree method using reflectance of MODIS bands 6 (CH6) and 7 (CH7) acquired from a regional flooding. The improved method was then applied to the Indus River basin in Pakistan, which was selected as the prime research focus area. The selected area suffered from a huge, severe flood caused by abnormally heavy rainfall from late July to early August 2010.

© ISAROB 2013

2 DATA

2.1 MODIS MYD09A1

The Moderated Resolution Imaging Spectroradiometer (MODIS) is an Earth Observing System (EOS) instrument onboard the Terra and Aqua platforms, launched in December 1999 and May 2002, respectively. The sensor scans ±55° from nadir in 36 spectral bands. During each scan, 10 along-track detectors per spectral band simultaneously sample the earth. From its polar orbit, MODIS provides day-time and night-time global coverage every 1 to 2 days [8]. MODIS Surface Reflectance products are the estimates of surface spectral reflectance as if they were measured at the ground level in the absence of atmospheric scattering or absorption. The MODIS L3 8-day composite surface reflectance product (MYD09A1) provides reflectance values for bands 1-7 from the MODIS Level 1B land bands, which are centered at 0.648 μm, 0.858 μm, 0.470 μm, 0.555 μm, 1.24 μm, 1.64 μm, and 2.13 μm at 500-meter resolution in a gridded level-3 product in the sinusoidal projection [10].

2.2 SRTM DEM

The Shuttle Radar Topography Mission (SRTM) obtained elevation data on a near-global scale to generate the most complete high-resolution digital topographic database model of the Earth. SRTM consisted of a specially modified radar system that flew onboard the Space Shuttle Endeavour during an 11-day mission in February of 2000. It used dual radar antennas to acquire interferometric radar data, processed to digital topographic data at 1 arc-sec resolution. SRTM is an international project spearheaded by the National Geospatial-Intelligence Agency (NGA) and the National Aeronautics and Space Administration (NASA) [2]. The elevation layers, DEM, are based on a combination of the original SRTM-3 and DTED-1 elevation models of SRTM. The DEM is provided in geographic projection (latitude/longitude) referenced to the WGS84 horizontal datum and EGM96 vertical datum. The DEM were acquired from Hydrological data and maps based on the SHuttle Elevation Derivatives at multiple Scale (HydroSHEDS) [6, 11]. In this study, DEM is used to calculate potential flood areas at 15 arc-second resolution (approximately 500 meters at the equator).

3 METHODOLOGY

The proposed three-step process reduces errors in the direct extraction of water bodies including floodwater. First step is a decision tree method. Second step is the new flood index, Modified LSWI (MLSWI). Third step is a 8-direction tracking algorithm based on DEM, which uses the flow direction of the same elevation pixels resulting from the previous two steps.

3.1 Decision tree method

Illustrations Decision tree classification is employed on 500 m MODIS reflectance images, in which regions of interest as samples are collected from each flood case for trial, to generate the map by using a post-classification water detection process while comparing with SRTM Water Body Data (SWBD) product. Decision tree classification can be divided into two categories: water surface and dry land surface. Water surface areas are considered to be permanent water bodies such as rivers, lakes, and ponds while dry land areas are considered to be non-water areas that are never flooded. A water surface needs to satisfy the following three conditions to be extracted as water areas: band 7 (CH7) < 10%, band 1 (CH1) +10% > band 2 (CH2) and band 3 (CH3) < 20% (e.g., forest = 0.14, clean water = 0.1, Fig. 1.A). The reflectance of bands 6 and 7 are lower than the other bands in the case of surface water such as clean water, muddy water, and floodwater, which reflect the temporal-spatial pattern of water content (Fig. 1.B).

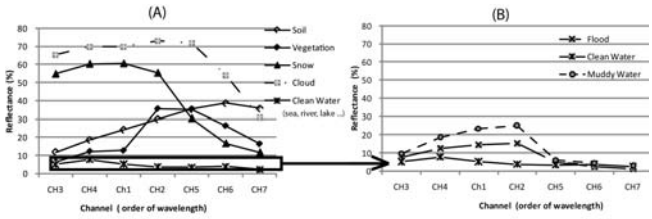

Fig. 1. Spectral reflectance of the land cover classification (A) and the characteristic of the turbid water in flooding (B)

3.2. Modified LSWI

After examining the water and land pixels using the decision tree classification, the flood map is produced based on the modified LSWI (MLSWI) by comparing it with NDVI, NDWI and LSWI, which are the most frequently used and has been proved effective in detecting soil moisture, vegetation and water-related objects, though their detecting ability is somewhat different depending on their characteristics [1, 5]. These indices are calculated as follows:

$$\mathrm{NDVI} = \frac{R_{RED} - R_{NIR}}{R_{RED} + R_{NIR}} \quad (1)$$

$$\mathrm{NDWI} = \frac{R_{RED} - R_{SWIR}}{R_{RED} + R_{SWIR}} \quad (2)$$

© ISAROB 2013

$$\mathrm{LSWI} = \frac{R_{NIR} - R_{SWIR}}{R_{NIR} + R_{SWIR}} \quad (3)$$

where, R_{RED}, R_{NIR}, and R_{SWIRD} are reflectance values of MODIS bands 1, 2 and 7.

Compared with the extraction of the floodwater, MLSWI was modified and proposed as a new algorithm for identifying flood areas by using the combination of NIR (841-875 nm, band 2) with SWIR (1 628-1 652 nm, band 7). Equation (4) for MLSWI used in this study is as follows:

$$\mathrm{MLSWI}_{Flood} = \frac{1 - R_{NIR} - R_{SWIR}}{1 - R_{NIR} + R_{SWIR}} \quad (4)$$

3.3. Tracking algorithm

After determining floodwater from MLSWI, tracking algorithm for calculating the floodwater boundary is applied to each pixel as the height difference between floodwater area and non-flood area. The floodwater flows into the next pixel with the lower DEM among 8-direction pixels (Fig. 2.). The relative height of floodwater pixel ($\mathrm{Floodwater}_{_DEM}$) indicates the potential flood inundation depth of a given target pixel with the accuracy of 1 m. In the case of $\mathrm{Floodwater}_{_DEM} \geqq \mathrm{Non\text{-}flood}_{_DEM}$, Fig. 2 shows that floodwater area is calculated because it means that flooding is expected to occur over such pixels.

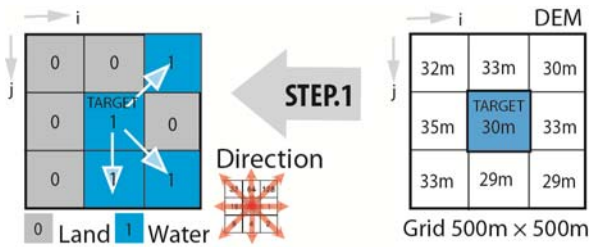

Fig. 2. Flood map from the MLSWI and DEM algorithm in the Indus river flood case

4 RESULT

This study focused on the characterization of flood index for the flood mapping by using a comprehensive approach within a whole basin, solely based on remotely sensed data sources via open internet. The pixel-based water detection for flood identification using training data, and the application in flood area was obtained according to the simple index model process with spectral influences between land cover types water and land. As a result, the MLSWI threshold, the critical value of the reflectance ratio was found at 0.5 for detecting water bodies, such as clean water, muddy water, and turbid floodwater. On the other hand, NDVI, NDWI and LSWI, which usually detect water bodies at a critical reflectance ratio of over 0.5, fail to distinguish water from dry land in some cases, especially when the area contains snow or cloud cover. The process of integrated floodwater detection was made possible to estimate the water extent boundary using a 8-direction tracking algorithm to find the same level between floodwater area and non-flood area, because we found particularly an underestimation of floodwater pixels obtained from MLSWI. Fig. 3 showed the superiority of the developed method in providing instant and accurate mapping of not only water extent but also indirect flood detection for a 2010 extreme event. Flood map was generated with 500 m resolution product in Fig. 3.b. On the other hand, the permanent water body was marked in Fig. 3.d. Moreover, the satellite-derived product uncertainties in the Indus river basin were verified through ground gauge stations by examining actual high water marks and ALOS PALSAR images.

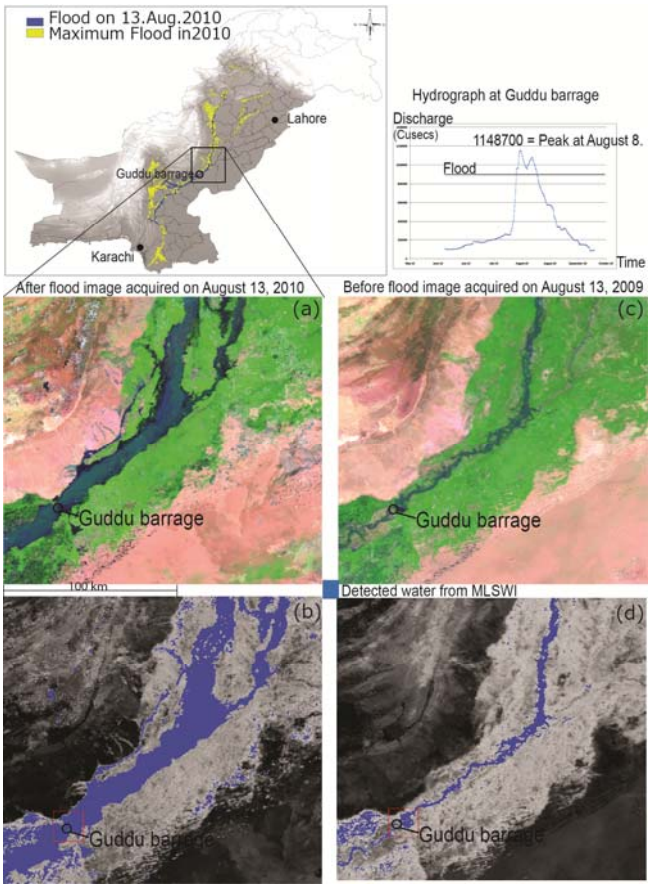

Fig. 3. Flood map from the MLSWI and DEM algorithm in the Indus river flood case

5 CONCLUSION

To conclude, the authors suggested to consider the spatial resolution in horizontal and vertical directions for detecting floodwater. We improved the accuracy of detecting flood areas in the Indus River basin from near-real-time MODIS images of 500 m resolution by using a MLSWI and DEM tracking algorithm. Particularly MODIS images have a higher practicability to detect water body because of moderate-resolution optical sensor (250-500 m) and high temporal resolution (daily). It is clear that MLSWI is detecting directly floodwater during the period of flooding to reduce the ambiguity of floodwater. And DEM surface has the effect of the buffer zone at the boundary of the flood extent which is typically 1 meter vertical resolution in turbid floodwater and mixed vegetation areas. Ultimately, this new approach for nationwide flood map in this study is expected to play an important role to support emergency relief efforts in high-risk flood areas not only in a national level but also Asia-Pacific region.

However, this approach has a limited evaluation of a real flood differed from a hydrological inundation simulation. In addition, MODIS image is easily affected by weather conditions, especially by cloud cover. Also a pixel of 500 meter is too coarse to estimate the temporal dynamics of flooding at different pixels, the authors are planning to improve the spatial resolution in horizontal and vertical directions by using the integrated high resolution images and self-organizing map (SOM) neural network for detection of floodwater area on the land surface. Moreover, the combination of SAR and ASTER image should be further considered to improve the accuracy of flood detection.

ACKNOWLEDGEMENTS

This research was supported by the Ministry of Education, Culture, Sports, Science, and Technology (MEXT)/Japan Society for the Promotion of Science (JSPS) KAKENHI Grant-in-Aid for Young Scientists (B: 24710211).

REFERENCES

[1] Ceccato, P., Flasse, S., Tarantola, S., Jacquemond, S., and Gregoire, J.M. (2001), Detecting vegetation water content using reflectance in the optical domain. Remote Sensing of Environment 77:22–33

[2] Farr T., P. Rosen, E. Caro, R. Crippen, R. Duren, S. Hensley, M. Kobrick, M. Paller, E. Rodriguez, L. Roth, D. Seal, S. Shaffer, J. Shimada, J. Umland, M. Werner, M. Oskin, D. Burbank, Alsdorf D. (2007), The Shuttle Radar Topography Mission, Review of Geophysics 45

[3] Gao, bo-cai (1996), NDWI a normalized difference water index for remote Sensing of Vegetation Liquid water from space, Remote Sensing of Environment 58:257-266

[4] Islam A.S., Bala. S.K. and Haque. M.A. (2010), Flood inundation map of Bangladesh using MODIS time-series image, J. Flood Risk Management 99(4):333–339

[5] Kwak Y, J. Park, A. Yorozuya, K. Fukami, (2012), Estimation of flood volume in Chao Phraya river basin, Thailand from MODIS images coupled with flood Inundation level", IEEE-IGARSS2012, pp887-890

[6] Lehner B., K, Verdin, Jarvis A. (2006), HydroSHEDS Technical Documentation, Version 1.0, World Wildlife Fund US, Washington DC, pp. 1-27

[7] Ordoyne C., Friedl M.A. (2008), Using MODIS data to characterize seasonal inundation patterns in the Florida Everglades, Remote Sensing of Environment 112:4107-4119

[8] Pinheiro A.C.T., Descloitres J., Privette J.L., Susskind J., Iredell L., Schmaltz J. (2007), Near-real time retrievals of land surface temperature within the MODIS Rapid Response System, Remote Sensing of Environment 106:326–336

[9] Sakamoto T., Nguyen V., Kotera A., Ohno H., Ishitsuka N., Yokozawa M. (2007), Detecting temporal changes in the extent of annual flooding within the Cambodia and the Vietnamese Mekong Delta from MODIS time-series imagery, Remote Sensing of Environment 109 (3):295–313

[10] USGS, The United States Geological Survey, last access: Jan.2011,https://lpdaac.usgs.gov/lpdaac/products/modis_products_table/surface_reflectance/8_day_l3_global_500m/myd09a1

[11] USGS, HydroSHEDS, Technical Documentation Version 1.0 1-27, 2006, http://hydrosheds.cr.usgs.gov/

[12] Weng Q., Hu X., Liu H. (2009), Estimating impervious surfaces using linear spectral mixture analysis with multi-temporal ASTER images, International Journal of Remote Sensing 30:4807–4830

[13] World Bank (2005), Natural Disaster Hotspots: Case Studies, Disaster Risk Management Series, ISBN 0-8213-6332-8 pp.1-184

[14] Xiao X., Boles S., Frolking S., Li C., Bau J.Y. Salas W. (2006), Mapping paddy rice agriculture in South and Southeast Asia using multitemporal MODIS images. Remote Sens Environ 100:95–113

[15] Xiao X., Boles S., Liu J., Zuang D., Frolking S. Li C. (2005), Mapping paddy rice agriculture in southern China using multitemporal MODIS images. Remote Sensing of Environment 95:480–492

© ISAROB 2013

The Eighteenth International Symposium on Artificial Life and Robotics 2013 (AROB 18th '13),
Daejeon Convention Center, Daejeon, Korea, January 30-February 1, 2013

Adaptive learning neural networks for system identification of a magneto-rheological damper

Chia-Nan Ko[1], Guan-Yu Liu[2], Yu-Yi Fu[3], and Pi-Yun Chen[4]

[1,2,3]Nan-Kai University of Technology, Taiwan
[4]National Chin-Yi University of Technology, Taiwan

[1]t105@nkut.edu.tw

Abstract: In this article, adaptive learning neural networks (ALNNs) are proposed to identify nonlinear systems. In the proposed NNs, integrating support vector regression (SVR) and adaptive learning algorithm is adopted to optimize the structure of neural networks. In the evolutionary procedure, first, SVR is adopted to determine the number of hidden layer nodes and the initial structure of the NNs. After initialization, adaptive learning algorithm (ALA) with nonlinear time-varying learning rate is then applied to train NNs. In ALA, a computationally efficient optimization method, particle swarm optimization (PSO) method, is adopted to simultaneously find optimal learning rates. Due to the advantages of SVR and adaptive learning algorithm, the proposed NNs (SVR-ALNNs) have good performance for identifying a magneto-rheological (MR) damper system. Simulation results are illustrated the feasibility and superiority of the proposed SVR-ALNNs.

Keywords: adaptive learning neural networks, support vector regression, magneto-rheological damper system.

1 INTRODUCTION

Due to the characteristic of structure simplicity, low power requirement, large force capacity, and high dynamic range, a magneto-rheological (MR) damper attracts attentions as developed semi-active control devices for structural control applications recently. In order to describe the performance of an MR damper, Spencer et al. in 1997 proposed a phenomenological model based on a Bouc-Wen model [1], Chang and Chang and Zhou [2] developed a neural network model, Zhou and Chang [3] proposed an adaptive fuzzy control, and Du et al. designed a model of an MR damper by evolving radial basis function networks [4]. A nonlinear black-box model was proposed to identify an MR damper system to design a force-sensorless control method [5].

In this article, adaptive learning neural networks (ALNNs) are proposed to identify an MR damper system. In the proposed NNs, integrating support vector regression (SVR) and adaptive learning algorithm is adopted to optimize the structure of neural networks. In the evolutionary procedure, first, SVR [6, 7] is adopted to determine the number of hidden layer nodes and the initial structure of NNs. After initialization, ALA with nonlinear time-varying learning rate is then applied to train NNs. In the adaptive learning algorithm, a computationally efficient optimization method, particle swarm optimization (PSO) method, is adopted to simultaneously find optimal learning rates. Due to the advantages of SVR and adaptive learning algorithm, the proposed NNs (SVR-ALNNs) have good performance for identifying the MR damper system. Simulation results are illustrated the feasibility and superiority of the proposed SVR-ALNNs.

2 SVR-BASED INITIAL NNs

Neural networks can be used to estimate the input–output relation of a nonlinear system. In this paper, radial basis function neural networks (RBFNNs) are adopted because they have a simple structure. When the Gaussian function is chosen as the radial basis function, RBFNNs can be expressed in the form

$$\hat{y}_j(t+1) = \sum_{i=1}^{L} w_{ij} \exp\left(-\frac{\|\hat{\mathbf{x}} - \mathbf{m}_i\|^2}{2\sigma_i^2}\right) \quad \text{for} \quad j = 1, 2, \cdots, p \quad (1)$$

where $\hat{\mathbf{x}}(t) = \left[\hat{x}_1(t) \quad \cdots \quad \hat{x}_m(t)\right]^{\mathrm{T}}$ is the input vector; $\hat{\mathbf{y}}(t) = \left[\hat{y}_1(t) \quad \cdots \quad \hat{y}_p(t)\right]^{\mathrm{T}}$ is the output vector; w_{ij} is the synaptic weight; $\mathbf{m}_i$ and σ_i are the center and width of Gaussian functions respectively; and L is the number of Gaussian functions, which is also equal to the number of hidden layer nodes.

It is very difficult, if not impossible, to solve the above problem directly. Usually, the initial values of L, w_{ij}, $\mathbf{m}_i$, and σ_i are chosen first. Then a training algorithm is applied to the NNs to search for the optimal combination of these values in an iterative manner.

In support vector machine (SVM), an SVR method can approximate an unknown function. An output of the RBFNNs and its corresponding training pairs will be used for simulations. Meanwhile, assume that a set of basis functions, $g_l(\mathbf{x})$, $l = 1, 2, \cdots, M$, is given. Then the problem of function approximation is transformed into one of finding the parameters of the basis linear expansion.

$$f(\mathbf{x}, \boldsymbol{\theta}) = \sum_{l=1}^{M} \theta_l g_l(\mathbf{x}) + b \quad (2)$$

© ISAROB 2013

where $\boldsymbol{\theta}$ is a parameter vector to be identified and b is a constant to be determined.

From [8], one sees that the solution is to find $f(\mathbf{x}, \boldsymbol{\theta})$ that minimizes

$$R(\boldsymbol{\theta}) = \frac{1}{N}\sum_{i=1}^{N} L_\varepsilon(y_i - f(\mathbf{x}_i, \boldsymbol{\theta})) \tag{3}$$

subject to the constraint

$$\|\boldsymbol{\theta}\|^2 < C \tag{4}$$

where $L_\varepsilon(\cdot)$ is the ε-insensitive loss function defined as

$$L_\varepsilon(e) = \begin{cases} 0 & \text{for } |e| \le \varepsilon \\ |e| - \varepsilon & \text{otherwise} \end{cases} \tag{5}$$

for some non-negative numbers ε.

By using the Lagrange multiplier method, it has been shown in [6] that the minimization of (3) leads to a dual optimization problem. A set of basis functions $g_l(\mathbf{x}_r)$ is replaced via the kernel function.

$$K(\mathbf{x}_r, \mathbf{x}_s) = \sum_{l=1}^{M} g_l(\mathbf{x}_r) g_l(\mathbf{x}_s) \tag{6}$$

Then the dual optimization problem can be expressed as follows:
Minimize

$$\begin{aligned} Q(\alpha, \alpha^*) &= \varepsilon\sum_{r=1}^{N}(\alpha_r + \alpha_r^*) - \sum_{r=1}^{N} y_r(\alpha_r - \alpha_r^*) \\ &+ \frac{1}{2}\sum_{r,s=1}^{N}(\alpha_r^* - \alpha_r)(\alpha_s^* - \alpha_s)K(\mathbf{x}_r, \mathbf{x}_s) \end{aligned} \tag{7}$$

subject to the constraint

$$\sum_{r=1}^{N}\alpha_r^* = \sum_{r=1}^{N}\alpha_r \quad 0 < \alpha_r^*, \alpha_r < C \tag{8}$$

and the solution is in the form of the following linear expansion of kernel functions [6]

$$f(\mathbf{x}, \alpha, \alpha^*) = \sum_{l=1}^{M}(\alpha_l^* - \alpha_l)K(\mathbf{x}, \mathbf{x}_l) + b \tag{9}$$

Note that some of the $(\alpha_l^* - \alpha_l)$ values are not zeros and the corresponding vectors $\mathbf{x}_l$ are called support vectors (SVs).

In this study, since the Gaussian function is used as the kernel function, (9) can be rewritten as

$$f(\mathbf{x}, \lambda) = \sum_{l=1}^{\#SV} \lambda_l \exp\left(-\frac{\|\mathbf{x} - \mathbf{x}_l\|^2}{2\sigma_l^2}\right) + b \tag{10}$$

where l is the number of SVs, $\lambda_l = (\alpha_l^* - \alpha_l) \neq 0$, and $\mathbf{x}_l$ denotes SVs. Comparing (10) with (1), $\#SV$ l, λ_l, and $\mathbf{x}_l$ in (10) can be regarded as L, i, w_{ij}, and $\mathbf{m}_i$ in (1), respectively.

3 ADAPTIVE LEARNING NNs

To overcome the existing problems in robust backpropagation learning algorithms, the annealing robust learning algorithm (ARLA) is adopted in the training procedure of the presented NNs by Chung et al. [7]. A cost function for the annealing learning is defined here as

$$J_j(t) = \frac{1}{N}\sum_{k=1}^{N}\rho\left[e_j^{(k)}(t); \beta(t)\right] \text{ for } j = 1, 2, \cdots, p \tag{11}$$

where

$$e_j^{(k)}(t) = y_j^{(k)} - \sum_{i=1}^{L} w_{ij} \exp\left(-\frac{\|x^{(k)} - m_i\|^2}{2\sigma_i^2}\right) \tag{12}$$

t is the epoch number, $e_j^{(k)}(t)$ is the error between the kth desired output $y_j^{(k)}$ of the annealing learning NNs at epoch t for the jth input–output training data in an identification system, $\beta(t)$ is a deterministic annealing schedule acting as the cut-off point, and $\rho(\cdot)$ is a logistic loss function defined as

$$\rho[e_j^{(k)}; \beta] = \frac{\beta}{2}\ln\left[1 + \frac{(e_j^{(k)})^2}{\beta}\right] \text{ for } j = 1, 2, \cdots, p \tag{13}$$

To evaluate the performance of training NNs, the root mean square error (*RMSE*) of the training data is adopted and defined as

$$RMSE = \sqrt{\frac{1}{N}\sum_{k=1}^{N}\left(e_j^{(k)}\right)^2} \text{ for } j = 1, 2, \cdots, p \tag{14}$$

Based on a gradient descent type of learning algorithm, the synaptic weights w_{ij}, the centers $\mathbf{m}_i$, and the widths σ_i of Gaussian functions are updated, respectively, as

$$\Delta w_{ij} = -\eta_w \frac{\partial J_j}{\partial w_{ij}} = -\frac{\eta_w}{N}\sum_{k=1}^{N}\varphi_j(e_j^{(k)}; \beta)\frac{\partial e_j^{(k)}}{\partial w_{ij}} \tag{15}$$

$$\Delta \mathbf{m}_i = -\eta_m \frac{\partial J_j}{\partial \mathbf{m}_i} = -\frac{\eta_m}{N}\sum_{j=1}^{p}\sum_{k=1}^{N}\varphi_j(e_j^{(k)}; \beta)\frac{\partial e_j^{(k)}}{\partial \mathbf{m}_i} \tag{16}$$

$$\Delta \sigma_i = -\eta_\sigma \frac{\partial J_j}{\partial \sigma_i} = -\frac{\eta_\sigma}{N}\sum_{j=1}^{p}\sum_{k=1}^{N}\varphi_j(e_j^{(k)}; \beta)\frac{\partial e_j^{(k)}}{\partial \sigma_i} \tag{17}$$

$$\varphi_j(e_j^{(k)}; \beta) = \frac{\partial \rho(e_j^{(k)}; \beta)}{\partial e_j^{(k)}} = \frac{e_j^{(k)}}{1 + (e_j^{(k)})^2 / \beta(t)} \tag{18}$$

where η_w, η_m, and η_σ are the learning rates for the synaptic weights w_{ij}, the centers $\mathbf{m}_i$, and the widths σ_i, respectively, and $\varphi(\cdot)$ is usually called the influence function. The adaptive annealing schedule has the following properties [7]:

(A) β_{initial}, $\beta(t)$ for the first epoch, has large values.

(B) $\beta(t) \to 0^+$ for $t \to \infty$.

In the ALA, a nonlinear time-varying evolution concept is adopted over iterations, in which the learning rates η_w, η_m, and η_σ with a high value $\eta_{\max}$ and nonlinearly decreases to

$\eta_{\min}$ at the maximal number of epochs, respectively. This means that the mathematical expressions are given as shown as

$$\eta_w = \eta_{\min} + \left(1 - \frac{h}{epoch_{\max}}\right)^{pw} (\eta_{\max} - \eta_{\min}), \tag{19}$$

$$\eta_m = \eta_{\min} + \left(1 - \frac{h}{epoch_{\max}}\right)^{pm} (\eta_{\max} - \eta_{\min}), \tag{20}$$

$$\eta_\sigma = \eta_{\min} + \left(1 - \frac{h}{epoch_{\max}}\right)^{p\sigma} (\eta_{\max} - \eta_{\min}), \tag{21}$$

where $epoch_{\max}$ is the maximal number of epochs and h is the current number of epochs. In the updated procedure, appropriate functions for the learning rate and η_w, η_m, and η_σ can promote the performance of ALNNs. However, simultaneously determining the optimal combination of pw, pm, and $p\sigma$ is a time-consuming work. An efficient evolutionary algorithm, PSO, will be adopted to determine the optimal solution $(pw, pm, p\sigma)$.

4 SIMULATION RESULTS

The identification scheme of a nonlinear system is depicted in Fig. 1, training input-output data are obtained by feeding a signal $\mathbf{x}(k)$ to the system and measure its corresponding output $\mathbf{y}(k+1)$ Then subject to the same input signal, the objective of identification is to construct an SVR-ALNNs using PSO method, which produces an output $\hat{\mathbf{y}}(k+1)$ to approximate $\mathbf{y}(k+1)$ as closely as possible.

In this section, a magneto-rheological (MR) damper system adopted to verify the feasibility of the proposed SVR-ALNNs. When applying the proposed algorithm, the population size, the maximal iteration number, and the maximal epoch number are chosen to be 30, 100, and 1000, respectively. The variables pw, pm, and $p\sigma$ in learning rate functions (19) to (21) are all chosen as real numbers in the range $[0.1, 0.5]$. Meanwhile, the values of $\eta_{\max}$ and $\eta_{\min}$ are set as 4.0 and 1.0, respectively.

***Example*:**

A phenomenological model has been proposed by Spencer [1] to portray the behaviour of a prototype MR damper. This phenomenological model is based on a Bouc–Wen model, the model as shown in Fig. 2, and is governed by the following seven simultaneous equations:

$$F = c_1\dot{y} + k_1(x - x_0), \tag{22}$$

$$\dot{y} = \frac{1}{(c_0 + c_1)}[\alpha z + c_0\dot{x} + k_0(x - y)], \tag{23}$$

$$\dot{z} = -\gamma|\dot{x} - \dot{y}|z|z|^{n-1} - \zeta(\dot{x} - \dot{y})|z|^n + A(\dot{x} - \dot{y}), \tag{24}$$

$$\alpha = \alpha_a + \alpha_b u, \tag{25}$$

$$c_1 = c_1^a + c_1^b u, \tag{26}$$

$$c_0 = c_0^a + c_0^b u, \tag{27}$$

$$\dot{u} = -\lambda(u - v), \tag{28}$$

where F is the force generated by the MR damper; x is the displacement of the damper; y is an internal pseudo displacement of the MR damper; u is the output of a first order filter; v is the command voltage sent to the current driver; k_1 is the accumulator stiffness; c_0 and c_1 are the viscous damping coefficients observed at large and low velocities, respectively; k_0 is the gain to control the stiffness at large velocities; x_0 is the initial displacement of spring k_1 associated with the nominal damper force due to the accumulator; γ, ζ, A are hysteresis parameters for the yield element, and α is the evolutionary coefficient. A set of parameters which is obtained by Spencer to characterize one MR damper using experimental data and a constrained nonlinear optimization algorithm is listed in Table 1.

The data is generated using a sinusoidal displacement function with an amplitude of ± 1 cm and a frequency of 3Hz and a sinusoidal voltage function with mean value of 1.6 V, an amplitude of 0.5V and a frequency of 0.5 Hz. The time duration for this validation data is 4s and the time increment is 0.002s which amounts to a total of 2000 training data sets.

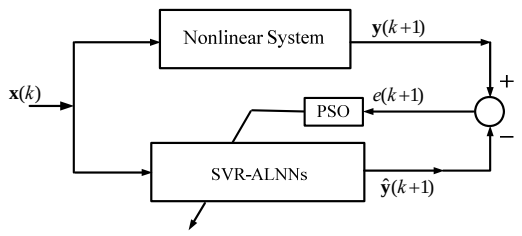

Fig. 1. The proposed PSO-based SVR-ALNNs scheme for identification of a nonlinear system.

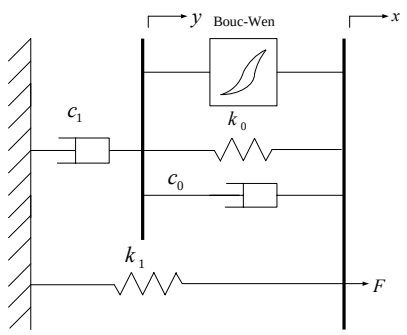

Fig. 2. Phenomenological model of MR damper.

Table 1. Parameters for an MR damper

Parameter	Value	Parameter	Value
c_0^a	$21.0 Ns/cm$	α_a	$140 N/cm$
c_0^b	$3.50 Ns/cm\ V$	α_b	$695\ N/cm\ V$
k_0	$46.9 N/cm$	γ	$363\ cm^{-2}$
c_1^a	$283 Ns/cm$	ζ	$363\ cm^{-2}$
c_1^b	$2.95 Ns/cm\ V$	n	2
k_1	$5.00 N/cm$	λ	$190\ s^{-1}$
x_0	$14.3\ cm$	A	301

***Problem 1*:**
In this investigation, when applying SVR, various parameters of $\varepsilon = 0.2$ and $\varepsilon = 0.1$ in (7) for $C = 100$ in (8) are adopted to determine the initial structure of NNs, respectively. In the ARLA, various learning rates, $1.0 \le \eta \le 4.0$, are used to train the NNs. After 1000 training epochs, the *RMSE* values for various learning rates are obtained, respectively. The details of the simulation results are shown in Table 2.

***Problem 2*:**
With the nonlinear learning rates, the ALA is adopted to train NNs, in which the optimal learning rates are determined by linear time-varying evolution PSO method [9]. The optimal sets are obtained as (pw, pm, $p\sigma$)=(4.3658, 0.01, 1.3637) and (pw, pm, $p\sigma$) =(2.4125, 0.1035, 3.0082) for $\varepsilon = 0.2$ and $\varepsilon = 0.1$ respectively. Meanwhile, the final values of RMSE with ALNNs are found to be 0.0070, and 0.0038 shown in Table 2. To show the superiority of the proposed SVR-ALNNs, the comparison of the proposed NNs with SVR-ARLA-NNs has been shown in Table 2. From Table 2, the proposed SVR-ALNNs have obtained promising results after only 1000 training epochs.

5 CONCLUSIONS

This paper presents the integrating SVR and ALA to train NNs for identification of an MR damper system. With the initial structure of the NNs using SVR method, the nonlinear time varying learning rates are simultaneously determined by PSO method to perform the ALA. Then the optimal NNs are obtained to identify the MR damper system. From the simulation results, one can conclude that the proposed SVR-ALNNs using PSO method have good performance for identification of the MR damper system using only few training epochs. Meanwhile, the superiority of the proposed SVR-ALNNs with nonlinear learning rates over SVR-ARLA-NNs with fixed learning rates for identification has been verified. The proposed SVR-ALNNs can be further extended to identify more complex systems.

Table 2. The values of *RMSE* (14) for an MR damper system after 1000 training epochs, in which ARLA with various learning rates and ALA with time-varying learning rates are applied to train NNs.

ε	ALA	ARLA (learning rate η)						
		4.0	3.5	3.0	2.5	2.0	1.5	1.0
0.2	**0.0070**	0.0092	0.0090	0.0114	0.0083	**0.0081**	0.0101	0.0152
0.1	**0.0038**	0.0056	0.0058	**0.0049**	0.0062	0.0080	0.0083	0.0111

ACKNOWLEDGMENT

This work was supported in part by the National Science Cou ncil, Taiwan, R.O.C., under grants NSC 99-2221-E-252-017.

REFERENCES

[1] Spencer Jr BF, Dyke SJ, Sain MK, Carlson JD (1997), Phenomenological model for magnetorheological dampers. Journal of Engineering Mechanics 123(3):230-238

[2] Chang CC, Zhou L (2002), Neural network emulation of inverse dynamics for a magnetorheological damper. Journal of Structural Engineering 128(2):231-239

[3] Zhou L, Chang CC (2003), Adaptive fuzzy control for nonlinear building-magnetorheological dramper system. Journal of Structural Engineering 129(7):905-913

[4] Du H, Lam J, Zhang N (2006), Modelling of a magneto-rheological damper by evolving radial basis function networks. Engineering Applications of Artificial Intelligence 19:869-881

[5] Truong DQ, Ahn KK (2011), Nonlinear black-box models and force-sensorless damping control for damping systems using magneto-rheological fluid dampers. Sensors & Actuators: A. Physical 167(2):556-573

[6] Vapnik VN (1995), The Nature of Statistical Learning Theory. Springer, New York

[7] Chuang CC, Jeng JT, Lin PT (2004), Annealing robust radial basis function networks for function approximation with outliers. Neurocomputing 56:123-139

[8] Pei L, Liu JB, Guinness R, Chen YW, Kuusniemi H, Chen RZ (2012), Using LS-SVM based motion recognition for smartphone indoor wireless positioning. Sensors 12:. 6155-6175

[9] Ratnaweera A, Halgamuge SK, Watson C (2004), Self-organizing hierarchical particle swarm optimizer with time-varying acceleration coefficients. IEEE Transactions on Evolutionary Computation 8(3):240-255

© ISAROB 2013

Identification of RBFNs with SVR under censored data

Yu-Yi Fu[1], Yu-Fen Fu[2], Kuo-Lan Su[3] , Chia-Nan Ko[4] and Jhih-Cheng Chang[5]

[1,4,5] Department of Automation Engineering, Nan Kai University of Technology
Tsaotun, Nantou 542, Taiwan
[2]Department of Information Management, China University of Technology
Wunshan, Taipei 116, Taiwan
[3]Department of Electrical Engineering,National Yunlin University of Science and Technology
Douliou, Yunlin 640, Taiwan
(email:[1]t098@nkut.edu.tw;[2]yfen@cute.edu.tw;[3]sukl@yuntech.edu.tw;[4]t105@nkut.edu.tw;[5]cjcb@nkut.edu.tw)

Abstract: In this paper, we proposed RBFNs with SVR to identify a distribution under censored data. Radial basis function networks (RBFNs) with one hidden layer and rapid convergence speed used to identify system generally. Support vector regression (SVR) with optimal quadratic programming to determine the number of hidden nodes and the initial parameters of kernel and the initial weights of RBFNs. By annealing robust learning algorithm to tune the parameters of kernel and the weights and to overcome the error measurement due to data censored. The simulation result of bivariate normal distribution identification under censored data shows the feasibility of proposed method.

Keywords: Radial basis function networks, Support vector regression, censored data, bivariate normal distribution.

1. INTRODUCTION

Interval censored data analysis is important in survival analysis and biomedical statistics. It has lower limit and upper limit, the lower limit replaces the data values when the data values are lower or equal to lower limit, the upper limit replaces the data values when the data values are greater or equal to upper limit. Therefore the data we get are not correct data but censored data. Zheng et al [1] proposed Hybrid Monte Carlo Markov chain and Hamiltonian method to estimate parameters of interval censored data. Cheng and Mordeson [2] investigated the fuzzy estimation of the parameter of underlying probability distribution for total failure time of censored data. In this article we proposed RBFNs with SVR to identify a distribution under the censored data.

Radial basis function networks (RBFNs) with one hidden layer and rapid convergence speed used to identify system and predict generally [3-7]. But the number of hidden nodes, the initial parameters of the kernel and the initial weights of the networks not decided mathematically yet. Besides, the data we obtained sometimes contain the error measurement due to data censored.

Vapnik [8] proposed Support vector regression (SVR) approach in 1995, by the ε insensitive loss function can make use of a small subset of the training data, called the support vectors (SVs), to approximate the desired outputs within a tolerance band. That is, the SVR uses the quadratic programming optimization to determine the initial structure of the traditional RBFNs.

In this article, the purpose is to identify a system under censored data in one of the variables. First, an ε SVR is used to determine the number of hidden nodes, the initial parameters of the kernel, and the initial weights of the RBFNs. Then the algorithm is applied to tune the parameters of radial basis functions and the synaptic weights. It is expected that the proposed method has fast convergence speed and the ability coping with censored data can identify perfectly.

2. RBFNs FOR THE IDENTIFICATION OF THE NONLINEAR SYSTEM

Assume that the unknown nonlinear system is expressed by

$$y(t+1) = f(y(t),\cdots,y(t-n),u(t),\cdots,u(t-m)), \qquad (1)$$

where $y(t)$ is the output of the system, $u(t)$ is the input of the system, $f(\cdot)$ is the unknown nonlinear function to be estimated by a neural network, and n and m are the structure orders of the system. Our purpose is to find a identification model

$$\hat{y}(t+1) = \hat{f}(y(t),\cdots,y(t-n),u(t),\cdots,u(t-m)) \qquad (2)$$

to approximate $y(t+1)$ as close as possible.

A structure of the RBFNs consists of an input layer, a hidden layer of radial basis functions and a linear output layer. When the radial basis functions are chosen as Gaussian functions, an RBFNs can be expressed in the form

$$\hat{y}_j(t+1) = \sum_{i=0}^{L} w_{ij} \exp\left(-\frac{\|\boldsymbol{x}-\boldsymbol{m}_i\|^2}{2\sigma_i^2}\right) \qquad (3)$$

where $\hat{y}_j$ is the jth output, $\boldsymbol{x} = (y(t), y(t-1),\cdots,y(t-n),u(t),u(t-1),\cdots,u(t-m))$ is the input to the neural networks, $w_{ij}, 0 \le i \le L, 1 \le j \le p$, are the synaptic weights, $\boldsymbol{m}_i, 0 \le i \le L$, and $\sigma_i, 0 \le i \le L$, are the centers and the widths of Gaussian functions respectively, and L is the number of the Gaussian functions, in which we can find that L also denotes the number of hidden nodes.

3. INITIAL STRUCTURE BY SVR APPROACH

© ISAROB 2013

An SVR approach is used to approximate an unknown function from a set of (input, output) samples $\{(\boldsymbol{x}_i, y_i), i = 1, \cdots, N\}$. Suppose that a set of basis functions $\{g(\boldsymbol{x}_k)\}_{k=1}^{N}$ is given, there exists a family of functions that can be expressed as a linear expansion of the basis functions. The theme is then be changed into finding the parameters of the following basis linear expansion

$$f(\boldsymbol{x}, \boldsymbol{\theta}) = \sum_{k=1}^{N} \theta_k g(\boldsymbol{x}_k) + b, \tag{4}$$

where $\boldsymbol{\theta} = (\theta_1, \theta_2, \cdots, \theta_m)$ is a parameter vector to be identified and b is a constant to be found.

Vapnik [4] firstly proposed the ε-SVR approach. The solution for the theme is to find $f(\boldsymbol{x}, \boldsymbol{\theta})$ that minimizes

$$R(\boldsymbol{\theta}) = \frac{1}{N} \sum_{i=1}^{N} L_\varepsilon (y_i - f(\boldsymbol{x}_i, \boldsymbol{\theta})), \tag{5}$$

subject to the constraint

$$\|\boldsymbol{\theta}\|^2 < C, \tag{6}$$

where $L_\varepsilon(\cdot)$ is the ε-insensitive loss function defined as

$$L_\varepsilon(e) = \begin{cases} 0 & \text{for } |e| \le \varepsilon \\ |e| - \varepsilon & \text{otherwise} \end{cases}, \tag{7}$$

for some previously chosen nonnegative number ε.

By using the Lagrange multiplier method, it was shown in [8] that the minimization of (5) leads to the following dual optimization problem.

Minimize

$$\begin{aligned} Q(\alpha, \alpha^*) = {} & \varepsilon \sum_{r=1}^{N} (\alpha_r + \alpha_r^*) - \sum_{r=1}^{N} y_r (\alpha_r^* - \alpha_r) \\ & + \frac{1}{2} \sum_{r,s=1}^{N} (\alpha_r^* - \alpha_r)(\alpha_s^* - \alpha_s) \langle g(\boldsymbol{x}_r) \cdot g(\boldsymbol{x}_s) \rangle. \end{aligned} \tag{8}$$

subject to the constraint

$$\sum_{r=1}^{N} \alpha_r^* = \sum_{r=1}^{N} \alpha_r, \quad 0 < \alpha_r^*, \alpha_r < C \quad \text{for } r = 1, 2, \cdots, N. \tag{9}$$

It proposed by Vapnik [8] and Smola et al. [9] and the inner product of basis function $\langle g(\boldsymbol{x}_r) \cdot g(\boldsymbol{x}_s) \rangle$ is replaced via the kernel function

$$K(\boldsymbol{x}_r, \boldsymbol{x}_s) = \langle g(\boldsymbol{x}_r) \cdot g(\boldsymbol{x}_s) \rangle, \tag{10}$$

Hence the optimization of (8) is rewritten as

Minimize

$$\begin{aligned} Q(\alpha, \alpha^*) = {} & \varepsilon \sum_{r=1}^{N} (\alpha_r + \alpha_r^*) - \sum_{r=1}^{N} y_r (\alpha_r^* - \alpha_r) \\ & + \frac{1}{2} \sum_{r,s=1}^{N} (\alpha_r^* - \alpha_r)(\alpha_s^* - \alpha_s) K(\boldsymbol{x}_r, \boldsymbol{x}_s). \end{aligned} \tag{11}$$

It was shown in Vapnik [8] that the solution of the SVR approach is in the form of the following linear expansion of kernel function

$$f(\boldsymbol{x}, \alpha, \alpha^*) = \sum_{k=1}^{N} (\alpha_k^* - \alpha_k) K(\boldsymbol{x}, \boldsymbol{x}_k) + b. \tag{12}$$

This means that the parameter θ_k in equation (4) can be represented as $\sum_{k=1}^{m} (\alpha_k^* - \alpha_k) g(\boldsymbol{x}_k)$. Note that only some of $(\alpha_k^* - \alpha_k)$'s are not zeros and the corresponding vectors $\boldsymbol{x}_k$'s are called support vectors (SVs).

In this paper, the Gaussian function is used as the kernel function. And let $f_s(\boldsymbol{x}, \lambda) = f(\boldsymbol{x}, \lambda) - b$, hence, (9) can be rewritten as

$$f_s(\boldsymbol{x}, \boldsymbol{\lambda}) = \sum_{k=1}^{\#SV} \lambda_k \exp\left(-\frac{\|\boldsymbol{x} - \boldsymbol{x}_k\|^2}{2\sigma_k^2}\right), \tag{13}$$

where $\#SV$ is the number of SVs, $\lambda_k = (\alpha_k^* - \alpha_k) \neq 0$ and $\boldsymbol{x}_k$ are SVs.

From equation (13) and (3), $\#SV$, k, λ_k, $\boldsymbol{x}_k$ and σ_k in (13) can be regarded as the $L, i, w_{ij}, \boldsymbol{m}_i$ and σ_i in (3), respectively. From the above derivation, we can find that the number of hidden nodes L, the initial weights w_{ij}, the initial parameters $\boldsymbol{m}_i$ and σ_i, of the RBFNs are determined via the SVR approach.

4. ANNEALING ROBUST LEARNING ALGORITHM FOR UPDATING PARAMETERS

When utilizing the RBFNs for the identification of systems, the goal is to minimize

$$J_N(h) = \frac{1}{N} \sum_{i=1}^{N} \rho[e_k(h); \beta(h)], \tag{14}$$

where

$$e_k(h) = y(k) - \hat{y}_s(\boldsymbol{x}_k), \tag{15}$$

h is the epoch number, $e_k(h)$ is the error between the kth desired output and the kth output of the RBFNs at epoch h and $\rho(\cdot)$ is a logistic loss function and defined as

$$\rho[e_k; \beta] = \frac{\beta}{2} \ln\left[1 + \frac{(e_k)^2}{\beta}\right], \tag{16}$$

where $\beta(h)$ is a deterministic annealing schedule acting like the cut-off points. In this paper, the annealing robust learning algorithm (ARLA) is applied to train the proposed RBFNs. In the ARLA, the properties of the annealing schedule $\beta(h)$ have [10]:

(A) β_{intial}, $\beta(h)$ for the first epoch, has large values;

(B) $\beta(h) \to 0^+$ for $h \to \infty$;

(C) $\beta(h) = c/h$ for any h epoch, where c is a constant.

Based on the gradient-descent kind of learning algorithms, the synaptic weights w_{ij}, the centers $\boldsymbol{m}_i$ and the width σ_i of Gaussian function are updated as

$$\Delta w_{ij} = -\eta \frac{\partial J_N}{\partial w_{ij}} = -\eta \sum_{k=1}^{N} \varphi(e_k; \beta) \frac{\partial e_k}{\partial w_{ij}} \tag{17}$$

© ISAROB 2013

$$\Delta \boldsymbol{m}_i = -\eta \frac{\partial J_N}{\partial \boldsymbol{m}_i} = -\eta \sum_{k=1}^{N} \varphi(e_k;\beta) \frac{\partial e_k}{\partial \boldsymbol{m}_i} \tag{18}$$

$$\Delta \sigma_i = -\eta \frac{\partial J_N}{\partial \sigma_i} = -\eta \sum_{k=1}^{N} \varphi(e_k;\beta) \frac{\partial e_k}{\partial \sigma_i} \tag{19}$$

$$\varphi(e_k;\beta) = \frac{\partial \rho(e_k;\beta)}{\partial e_k} = \frac{e_k}{1+(e_k)^2/\beta(h)}, \tag{20}$$

where η is a learning constant.

5. SIMULATION RESULTS

In this section, the root mean square error (RMSE) of the training data is used to measure the performance of the proposed networks. The RMSE is defined as

$$RMSE = \sqrt{\frac{\sum_{i=1}^{N}(y_i - \hat{y}_i)^2}{N}}, \tag{21}$$

where y_i is the desired output and $\hat{y}_i$ is the output of the proposed method.

Example:

A bivariate normal distribution is defined as

$$f(x,y) = \frac{1}{2\pi\sigma_x\sigma_y\sqrt{1-\rho^2}} \exp\left\{-\frac{1}{2(1-\rho^2)}\left[\left(\frac{x-\mu_x}{\sigma_x}\right)^2 + \left(\frac{y-\mu_y}{\sigma_y}\right)^2 - 2\rho\left(\frac{x-\mu_x}{\sigma_x}\right)\left(\frac{y-\mu_y}{\sigma_y}\right)\right]\right\}, \tag{22}$$

where μ_x and μ_y are the mean of x and y, σ_x^2 and σ_y^2 are the variance of x and y, and ρ is the correlation coefficient of x and y. We suppose that x data have censored, and the upper limit is equal to 3, the lower limit is equal to -3. The diagram of exact data and censored data are shown in Fig. 1 and Fig. 2. The proposed networks are chosen as

$$\hat{y}(t+1) = \hat{f}(y(t), y(t-1), x(t), x(t-1), x(t-2)). \tag{23}$$

50 simulation data points are generated from equation (19). The parameters in ε-SVR are set as C=10, the Gaussian kernel function with $\varepsilon = 0.95$, $\sigma = 2$, with the hidden nodes (i.e. the number of SVs) is obtained as 15. Based on the initial structure and the learning constant is 0.05, after 3000 epochs training, the final training output, the error are shown in Fig. 3 and Fig. 4, and the final RMSE is 0.0242. From the simulation results show that the proposed method can overcome the error measurement due to censored data and attain a good identification.

6. CONCLUSIONS

In this paper, an SVR based the RBFNs with ARLA for the identification of bivariate normal distribution is developed. We firstly utilize the SVR approach to determine the number of hidden nodes, the initial parameters of the kernel and the initial weights of the proposed RBFNs. Then the ARLA is applied to tunes the parameters of the kernel and the weights of the bivariate normal distribution. From the result indicated that the proposed method can be used as a reliable technique for the training of bivariate normal distribution.

ACKNOWLEDGMENTS

This work was supported in part by the National Science Council, Taiwan, R.O.C., under grants NSC101-2221-E-252-009.

REFERENCES

[1] Zheng G, Liu J, Zhang G (2010), A Novel Hybrid MCMC Method for Interval-Censored Data, International Conference on Computer Application and System Modeling, Taiyuan, China, Oct 22-24, 2010, pp. V12-66 - V12-69

[2] Cheng SH, Mordeson JN (2008), Fuzzy Confidence Estimation of the Parameter Involving in the Distribution of the Total Time on Test for Censored Data, Fuzzy Information Processing Society, Annual Meeting of the North American, May 19-22, 2008, pp. 1 - 5

[3] Fu YY, Wu CJ, Ko CN, Jeng JT (2011), Radial basis function networks with hybrid learning for system identification with outliers, Applied Soft Computing, 11: 3083–3092

[4] Fu YY, Wu CJ, Ko CN, Jeng JT, Lai LC (2009), ARRBFNs with SVR for prediction of chaotic time series with outliers, Artif Life Robotics, 14:29–33

[5] Liu J, Ling D, Wang S (2012), Ammunition Storage Reliability Forecasting Based on Radial Basis Function Neural Network, International Conference on Digital Object Identifier, Chengdu, China, June 15-18, 2012, pp. 599 – 602

[6] Venkateswarlu RLK, Kumari RV, Jayasri GV (2011), Speech recognition using Radial Basis Function neural network, International Conference on Electronics Computer Technology, Kanyakumari, India, April 8-10, 2011, pp. 441 – 445

[7] Hao Y, Tiantian X, Paszczynski S, Wilamowski BM (2011), Advantages of Radial Basis Function Networks for Dynamic System Design, IEEE Transactions on Industrial Electronics, 58 (12): 5438 – 5450

[8] Vapnik V (1995), *The Nature of Statistical Learning Theory*, Springer, Berlin

[9] Smola AJ, Schölkopf B (1998), From regularization operators to support vector kernels. *Neural Inf. Process System* 10:343–349

[10] Chuang CC, Su SF, and Hsiao CC (2000), The annealing robust backpropagation (BP) learning algorithm. *IEEE Trans. Neural Networks* 11(5): 1067–1077

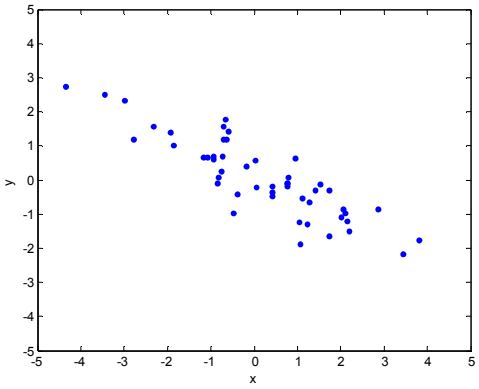

Fig. 1. The diagram of example for exact data.

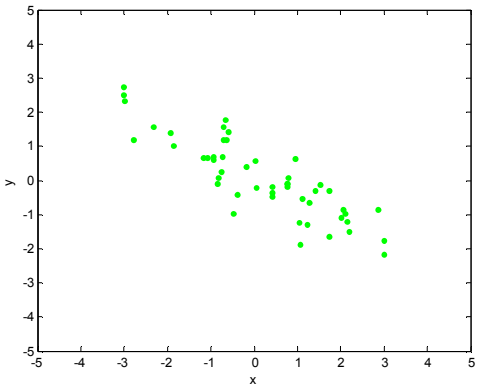

Fig. 2. The diagram of example for censored data.

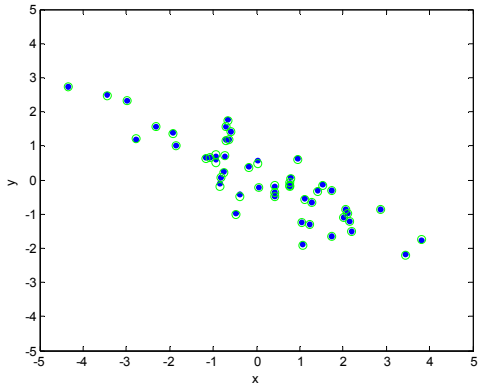

Fig. 3. The diagram of example (dot scatter) and the final result of the identification example (circle scatter) under censored data.

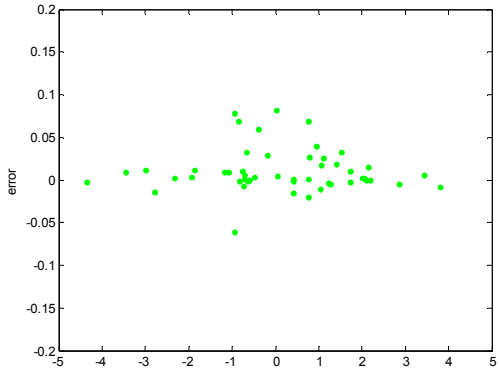

Fig. 4. The error of training under censored data.

© ISAROB 2013

The Eighteenth International Symposium on Artificial Life and Robotics 2013 (AROB 18th '13),
Daejeon Convention Center, Daejeon, Korea, January 30-February 1, 2013

Drift Algorithm Second Order Sliding Mode Control for a Synchronous Reluctance Motor

Wen-Bin Lin[1,2], Huann-Keng Chiang[3], and Yi-Chang Chang[3]
[1] Graduate School of Engineering Science & Technology, National Yunlin University of Science & Technology, Yunlin 64002, Taiwan, R.O.C.
[2] Department of Optoelectronic Engineering, Far East University, Tainan 74448, Taiwan, R.O.C.
[3] Department of Electrical Engineering, National Yunlin University of Science & Technology, Yunlin 64002, Taiwan, R.O.C.
(Tel: 886-5- 5342601 ext: 4247, Fax :+886-5-5312065)

[3]chianghk@yuntech.edu.tw

Abstract: This paper shows the design of a drift algorithm second order sliding mode controller (SOSMC) for a synchronous reluctance motor. The second order sliding mode control is an effective tool for the control of uncertain nonlinear systems since it conquers the main shortcomings of the classical sliding mode control, namely, the large control effort and the chattering effect. Its theory implies simple control laws and assures an improvement of the sliding accuracy with respect to conventional sliding mode control. This paper proposes a novel scheme that based on the technique of drift algorithm second order sliding mode control. First, the SOSMC is obtained by mathematics. Finally, the presentation of the proposed method is verified by simulation. The proposed SOSMC shows the robustness for the motor parameters variation and the elimination of chattering effect.

Keywords: Drift Algorithm, Second Order Sliding Modes, Synchronous Reluctance Motor, Chattering Effect.

1 INTRODUCTION

The motor control system with the high robustness is an important issue in research. Synchronous reluctance motors (SynRMs) have a mechanically simple and robust structure. They can be used in high speed and high temperature environments. The rotor circuit of the SynRM is open circuit such that the flux linkage of SynRM is directly proportional to the stator currents. The torque of SynRM can be controlled by adjusting the stator currents. Therefore, there has been renewed interest in SynRM [1-3].

Sliding mode control (SMC) has attracted increasing attention in recent years because it is an effective and robust technology for parameter variation and external disturbance rejection. It has been applied to robot and motor control [3,4-6]. Sliding mode control (SMC) is a robust control for nonlinear systems. However, sliding mode is a mode of motions on the discontinuity set of a discontinuous dynamic system. Therefore, reducing the chattering is very important for SMC. The second-order sliding mode technique has the same properties of robustness to uncertainties of model and external disturbances. Second-order SMC (SOSMC) [7] improves the chattering phenomenon. Due to few literatures about SOSMC in SynRM control application, therefore, it has valuable on investigation in SynRM control application for SOSMC.

Distinct from the conventional first order SMC, the SOSMC is belonging to the region of higher-order sliding mode (HOSM). Levant [7] had discussed the theory of HOSM. HOSM control has been applied to motor, and automatic docking [8-10].

The rest of this paper is organized as follows. SynRM modeling is discussed in Section 2. In Section 3, integral variable structure sliding mode controller is introduced. In Section 4, drift algorithm second-order sliding mode controller is described. In Section 5, simulation results show that the proposed algorithm controller provides high-performance dynamic characteristics and robustness under parameter variation and external load disturbances. Finally, conclusions are presented in Section 6.

2 MODELING OF THE SYNRM

The d-q equivalent voltage equations of ideal SynRM model with a synchronously rotating rotor reference frame are shown in Fig. 1:

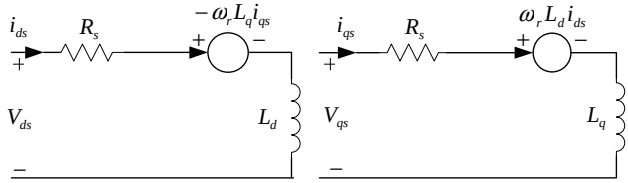

Fig.1. The d-q axis equivalent-circuit of SynRM

$$V_{ds} = R_s i_{ds} + L_d \frac{di_{ds}}{dt} - \omega_r L_q i_{qs} \tag{1}$$

$$V_{qs} = R_s i_{qs} + L_q \frac{di_{qs}}{dt} + \omega_r L_d i_{ds} \tag{2}$$

The corresponding electromagnetic torque T_e is:

$$T_e = \frac{3}{4} P_{ole} \left(L_d - L_q\right) i_{ds} i_{qs} \tag{3}$$

The corresponding motor dynamic equation is:

$$T_e - T_L = J_m \frac{d\omega_r}{dt} + B_m \omega_r \tag{4}$$

where V_{ds} and V_{qs} are direct and quadrature axis

© ISAROB 2013

terminal voltages, respectively; i_{ds} and i_{qs} are, respectively, direct axis and quadrature axis terminal currents or the torque producing current; L_d and L_q are the direct and quadrature axis magnetizing inductances, respectively; R_s is the stator resistance; and ω_r is the speed of the rotor. P_{ole}, T_L, J_m, and B_m are the poles, the torque load, the inertia moment of the rotor, and the viscous friction coefficient, respectively. In this paper, the maximum torque control (MTC) strategy [3,4] is adopted. The torque current commands are shown in equation (5) and (6) [3]:

$$i_{ds}^* = \sqrt{\frac{|T_e|}{\frac{3}{8}P_{ole}(L_d - L_q)}}\cos\left(\frac{\pi}{4}\right) \tag{5}$$

$$i_{qs}^* = \mathrm{sgn}(T_e)\sqrt{\frac{|T_e|}{\frac{3}{8}P_{ole}(L_d - L_q)}}\sin\left(\frac{\pi}{4}\right) \tag{6}$$

3 INTEGRAL VARIABLE STRUCTURE SLIDING MODE CONTROLLER

We can rewrite the equation (4) as

$$\begin{aligned}\frac{d\omega_r}{dt} &= \left(-\frac{B_m}{J_m}\right)\omega_r + \frac{1}{J_m}(T_e - T_L)\\ &= a\omega_r + b(T_e - T_L)\\ &= (a_0 + \Delta a)\omega_r + (b_0 + \Delta b)(T_e - T_L)\\ &= a_0\omega_r + b_0(u(t) + f)\end{aligned} \tag{7}$$

where

$$a \equiv -\frac{B_m}{J_m} = a_0 + \Delta a$$

$$b \equiv \frac{1}{J_m} = b_0 + \Delta b$$

$$u \equiv T_e$$

$$f \equiv \frac{1}{b_0}(\Delta a\omega_r + \Delta b u(t) - bT_L)$$

$$J_m \equiv J_0 + \Delta J$$

$$B_m \equiv B_0 + \Delta B$$

The subscript index "o" indicates the nominal system value; "Δ" represents uncertainty, and f represents the lumped uncertainties.

Define the velocity error as $e(t) = \omega_r^* - \omega_r$, where ω_r^* is the velocity command. The velocity error differential equation of SynRM can be expressed as equation (8):

$$\frac{de(t)}{dt} = \dot{\omega}_r^* - a_0\omega_r - b_0[u(t) + f] \tag{8}$$

Let

$$S = e(t) + c\int_{-\infty}^{t} e(t)d\tau, \quad c > 0 \tag{9}$$

The input control $u(t)$ (the electromagnetic torque T_e) of (8) can be defined as equation (10):

$$u(t) = u_{eq}(t) + u_n(t) \tag{10}$$

where $u_{eq}(t)$ is used to control the overall behavior of the system and $u_n(t)$ is used to suppress parameter uncertainties and to reject disturbances. By making mathematical calculation, we get the overall control $u(t)$ as equation (10) [3]:

$$u(t) = \frac{1}{b_0}\left[\dot{\omega}_r^* - a_0\omega_r + ce(t)\right] + (K + \frac{\eta}{b_o})\mathrm{sgn}(S) \tag{11}$$

where $|f| \le K$ and $\eta > 0$.

4 DRIFT ALGORITHM SECOND-ORDER S LIDING MODE CONTROLLER

In conventional sliding mode control design, the control target is let the system states move into sliding surfaces $S = 0$. But a second-order sliding mode controller aims for $S = \dot{S} = 0$. The system states converge to zero intersection of S and $\dot{S}$ in state space. Drift algorithm mainly develops relative one order system for reducing chattering phenomenon [7]. The state trajectory of S and $\dot{S}$ phase plane is shown in Fig.2. The drift algorithm in the phase trajectories on the 2-sliding plane are characterized by loops with constant sign of the sliding variable y_1, furthermore it is characterized by the use of sampled values of the available signal y_1 with sampling period δ.

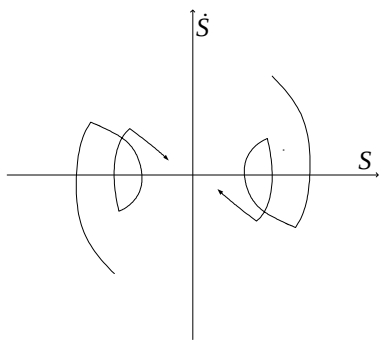

Fig.2. The phase plane trajectory of drift algorithm

Now consider the following uncertain second order system:

$$\begin{cases}\dot{y}_1(t) = y_2(t))\\ \dot{y}_2(t) = \varphi(\mathbf{x}(t), \mathbf{y}(t), t) + \gamma(\mathbf{x}(t), \mathbf{y}(t), t)\nu(t)\end{cases} \tag{12}$$

in which $\varphi(\cdots)$ and $\gamma(\cdots)$ are uncertain functions with the upper and lower bounds of equation (13).

$$\begin{cases}|\varphi(\mathbf{x}(t), \mathbf{y}(t), t)| \le \Phi\\ 0 < \Gamma_m \le \gamma(\mathbf{x}(t), \mathbf{y}(t), t) \le \Gamma_M\end{cases} \tag{13}$$

By the control rule of equation (14), we can define this control method [8,9]：

$$v(t)=\begin{cases}-u, & if \quad |u|>U \\ -V_m \operatorname{sgn}(\Delta y_{1_i}), & if \quad y_1\Delta y_{1_i}\le 0;\ |u|\le U \\ -V_M \operatorname{sgn}(\Delta y_{1_i}), & if \quad y_1\Delta y_{1_i}>0;\ |u|\le U\end{cases} \quad (14)$$

where V_m and V_M are suitable positive constants such that $V_m < V_M$ and $\frac{V_M}{V_m}$ sufficiently large, and $\Delta y_{1_i} = y_1(t_i) - y_1(t_i-\delta)$, $t\in[t_i, t_{i+1})$. The corresponding sufficient conditions for the convergence to the sliding manifold are rather cumbersome [8] and are omitted here for the sake of simplicity. After substituting y_2 for Δy_{1_i} a first order sliding mode on $y_2 = 0$ would be achieved. This implies y_1 = *const.*, but, since an artificial switching time delay appears, we ensure a real sliding on y_2 with most of time spent in the set $y_1 y_2 < 0$, and therefore, $y_1 \to 0$. The accuracy of the real sliding on $y_2 = 0$ is proportional to the sampling time interval δ; hence the duration of the transient process is proportional to δ^{-1}.This algorithm has no overshoot if parameters are chosen properly [8].

Equation (4) can be rewritten as equation (15):

$$\frac{d\omega_r}{dt}=\frac{1}{J_m}(T_e - T_L - B_m\omega_r) \quad (15)$$

We define state variable as shown in equation (16):

$$\begin{cases} x_1(t)=\int_{-\infty}^{t} x_2(\tau)d\tau \\ x_2(t)=e(t)=\omega_r^* - \omega_r \end{cases} \quad (16)$$

We define sliding function y_1, and y_2 as

$$\begin{cases} y_1 = x_2 + cx_1 \\ y_2 = \dot{y}_1 \end{cases} \quad (17)$$

Then, the system equation can be expressed as

$$\begin{cases} \dot{y}_1(t)=y_2(t) \\ \dot{y}_2(t)=\ddot{\omega}_r^* + \frac{B_m}{J_m}\dot{\omega}_r^* + \left(-\frac{B_m}{J_m}+c\right)\dot{x}_2 + \frac{1}{J_m}\dot{T}_L + v(t) \end{cases} \quad (18)$$

where

$$\begin{cases} \varphi(\cdot)=\ddot{\omega}_r^* + \frac{B_m}{J_m}\dot{\omega}_r^* + \left(-\frac{B_m}{J_m}+c\right)\dot{x}_2 + \frac{1}{J_m}\dot{T}_L \\ \gamma(\cdot)=1 \\ v(t)=-\frac{1}{J_m}\dot{T}_e \end{cases} \quad (19)$$

According to (19) T_e is calculated from the integration of *v*(t) which is a switching signal defined in (14), so improving the chattering problem in SOSMC control of SynRM.

5 SIMULATION RESULTS

A block diagram of the experimental SynRM drive and the drift algorithm second-order sliding mode controller speed control block diagram of the SynRM servo drive are shown in Fig. 3.

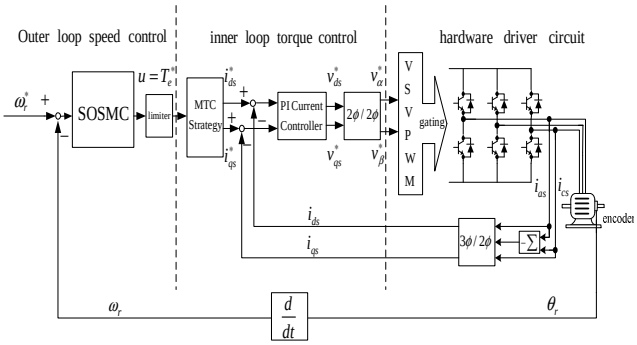

Fig.3. Drift algorithm SOSMC speed control block diagram of SynRM servo drive

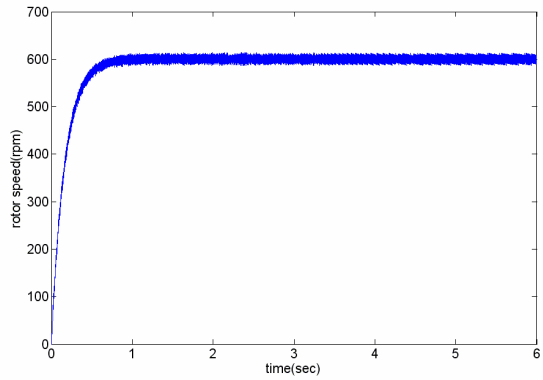

Fig.4. Simulation velocity response of the SMC due to $\omega_r^* = 600$ rev/min without machine load in the nominal motor inertia and friction coefficient condition

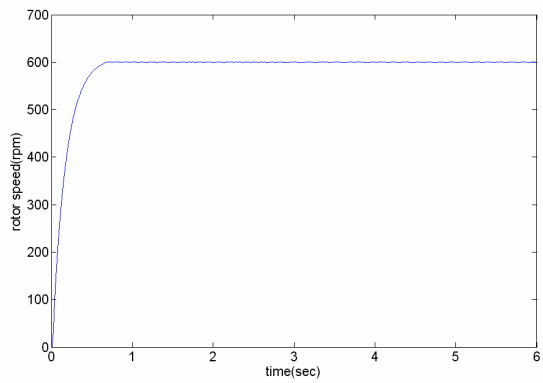

Fig.5. Simulation velocity response of the drift algorithm SOSMC due to $\omega_r^* = 600$ rev/min without machine load in the nominal motor inertia and friction coefficient condition

The proposed controller was applied to a 0.37 kw three-phase SynRM whose nominal parameters and proposed controller parameters are shown in Table 1. In Fig.4, the simulation velocity response of the SMC due

to $\omega_r^* = 600$ rev/min without machine load in the nominal motor inertia and friction coefficient condition is depicted. In Fig.5, the simulation velocity response of the proposed SOSMC due to $\omega_r^* = 600$ rev/min without machine load in the nominal motor inertia and friction coefficient condition is depicted. The velocity response of SOSMC is smoother than the convention SMC.

In Fig.6, the simulation velocity response of the SOSMC due to $\omega_r^* = 600$ rev/min under an 0.3 Nt-m machine load at the beginning and an 0.9 Nt-m machine load at 3seconds is added for the 2 times nominal case of the motor inertia and friction coefficient condition is presented. Hence, the SOSMC is a robust controller and improve the chattering phenomenon when the system has external disturbances and parameter variations.

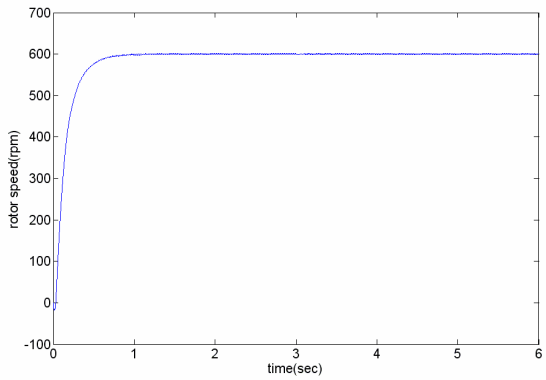

Fig.6. Simulation velocity response of the drift algorithm SOSMC due to $\omega_r^* = 600$ rev/min under an 0.3 Nt-m machine load at the beginning and an 0.9Nt-m machine load at 3 seconds in the 2 times nominal case of the motor inertia and friction coefficient condition

Table 1. Parameters of SynRM (0.37kW)

$R_s = 4.2\,\Omega$	$P_{ole} = 2$
$L_{ds} = 0.328$ H	$L_{qs} = 0.181$ H
$J_m = 0.00076$ Kg-m^2	$B_m = 0.00012$ Nt-m/rad/sec

6 CONCLUSION

In this paper, a drift algorithm second-order sliding mode speed control design for robust stabilization and disturbance rejection of SynRM is presented. The simulation results show good performance of SOSMC under uncertain load subject to variaitons in inertia and system frcition. Also with SOSMC, there is no need for acceleration feedback. The proposed SOSMC law shows the advantage of continuous control signal which eliminates the chattering effect apparently and is more acceptable in application.

ACKNOWLEDGMENT

This work is supported by the National Science Council in Taiwan, Republic of China, through grant NSC100-2221-E-224-002.

REFERENCES

[1] Bianchi N., Bolognani S., Bon D., and Pre M. D. (2009), Rotor flux-barrier design for torque ripple reduction in synchronous reluctance and PM-assisted synchronous reluctance motors. IEEE Transactions on Industry Applications 45(3):921-928

[2] Kim W. H., Kim K. S., Kim S. J., Kang D. W., Go S. C., Chun Y. D., and Lee J. (2009), Optimal PM design of PMA-SynRM for wide constant-power operation and torque ripple reduction. IEEE Transactions on Magnetics 45(10):4660-4663

[3] Lin W. B., Chen C. A., and Chiang H. K. (2011), Design and implementation of a sliding mode controller using a Gaussian radial basis function neural network estimator for a synchronous reluctance motor speed drive. Electric Power Components and Systems 39(6): 548- 562.

[4] Shyu K. K., and Lai C. K. (2002), Incremental motion control of synchronous reluctance motor via multisegment sliding mode control method. IEEE Transactions on Control Systems Technology 10(2): 169-176

[5] Huang Y. S., and Sung C. C. (2010), Implementation of sliding mode controller for linear synchronous motors based on direct thrust control theory. IET Proceedings on Control Theory & Applications 4(3):326-338

[6] Bartolini G., Ferrara A., Levant F., and Usai E. (1999), Variable Structure Systems, Sliding Mode and Nonlinear Control. Springer-Verlag

[7] Levant A. (1993), Sliding order and sliding accuracy in sliding mode control. International Journal of Control 58(6):1247-1263

[8] Bartolini G., Ferrara A., Levant F., and Usai E. (1999), On second order sliding mode controllers, in Variable Structure Systems, Sliding Mode and Nonlinear Control, Lecture Notes in Control and Information Sciences K. D. Young and U. Ozguner, Eds., Springer-Verlag, London Ltd: 329-350

[9] Tournes C., and Shtessel Y. (2007), Automatic docking using second order sliding mode control. 2007 American Control Conference, New York City, USA, July 11-13, 2007 , pp.3455-3460

[10] Mohamadian M., Pedram M. M., and Ashrafzadeh F. (2004), Digital second order sliding mode control for a synchronous reluctance motor. Proceeding of 2004 IEEE Industry Applications Conference, Seattle, U.S., Oct 3-7, 2004, pp.1899-1902

© ISAROB 2013

The Eighteenth International Symposium on Artificial Life and Robotics 2013 (AROB 18th '13),
Daejeon Convention Center, Daejeon, Korea, January 30-February 1, 2013

Development of the Multi-detection system using Multi-sensor Fusion Algorithms

Ying-Yao Ting[1,3] and Huan-Sheng Wang[2]
[1]Institute of Engineering Science and Technology, National Kaohsiung First University of Science of Technology, Taiwan
[2]Department of Computer and Communication Engineering, National Kaohsiung First University of Science of Technology, Taiwan
[3]Department of Information Management, WuFeng Universityof Science of Technology, Taiwan
E-mail: u9615903@ccms.nkfust.edu.tw

Abstract: The paper develops the multi-detection system using multi-level surveillance structure. The system contains active detection modules, passive detection modules, a supervised computer, an image system and an intelligent home. The passive detection modules contain wire/wireless detection modules and appliance control modules, and decide the event to be true or not using fusion algorithms, and transmit detection signals to the supervised computer. Mobile robots are active detection modules and carry various sensors to search dangerous events. Each mobile robot transmits the real-time event signal to the supervised computer and the other mobile robots via wireless RF interface. The image system detects fire source using Otsu algorithm. The system integrates wire/wireless passive detection modules, mobile robots and image system to detect fire source using weighted average method. If the fire event occurrence, the supervised computer calculates the dangerous grade using logical filter method according to the signals of detection modules in the first step, and transmits the position of the fire event to the other mobile robots. The assigned mobile robots move to the event location for double check autonomously, and transmit the detection results to the supervised computer. The supervised computer gives the final decision according to the feedback signals in the second step. Finally, we present some experimental scenarios using active detection modules, passive detection modules and image recognition for the fire detection in the intelligent home.

Keywords: mobile robots, wireless RF interface, Otsu algorithm, weighted average method, logical filter method

I. INTRODUCTION

Intelligent building and home can provides safety, convenience and welfare for human living in the 21st century. The most important issue of the intelligent building is fire detection. The fire disaster hurts many people's life and brings great losses to the society in every year. Fire detection becomes more and more importance in surveillance system [1]. In generally, the measured values of the security system is redundant and complementally information, and uses fusion algorithms to enhance system reliability and certainty, and constructs the safety detection network using multiple processing protections. The multi-detection security system solves the negligence of the users. The paper proposes the multi-detection system that contains various detection modules and image system, and develops the intelligent home to implement the functions of the proposed security system.

In the past literatures, many experts research the security system of the intelligent home. Azegami [2] described a systematic approach to intelligent building design. Chung and Fu expected to set up the standard of appliances and communication protocols, and proposed a complete system architecture with integrate control kernel to construct an intelligent building [3]. Su designed multi0level security system using active detection modules and passive detection modules to detect gas leakage in the chamber [4].

In the fire detection, Ding proposed a hierarchical framework for a more efficient fire detection using modified Hidden Markov Model (HMM) [1]. Ha concentrated on the smoke detection system in video for early fire alarming using block-based smoke detection algorithm consist of three basic steps [5]. Liu used temperature, smoke concentration and CO concentration to detect fire source using multi-sensor fusion algorithm [6]. Yang used the trained (Support Vector Machine) SVM with RBF kernel and SMO algorithm to recognize image of the fire source [7].

II. SYSTEM ARCHITECTURE

The system architecture has four levels to be shown in Fig. 1. There is passive detection level, active detection level, system supervised level and remote supervised level [8]. The active detection modules are mobile robots. The robot carries various sensors to detect the environment moving in various floor of the intelligent home. The passive detection modules contain detection modules, position system and elevator system. The detection modules include wire/wireless detection modules and image system. Position system locates the position of each mobile robot moving in the intelligent home. The elevator carries mobile robots to search dangerous event in various floors. The system supervised

© ISAROB 2013

level receives detection signals from active detection modules and passive detection modules via wire/wireless interface, and decides the event to be true or not. The remote supervised computer communicates with the supervised computer via Internet.

In the intelligent home system, there are many detection modules and appliance control modules. These modules are independent and autonomous, and work cooperation. Each detection module of intelligent home system can transmits the measurement values, parameter values and decision results to the supervised computer, and uses multi-level processing to enhance the accuracy of the event detection, and speaks Chinese language using the voice module for real-time event status.

In the active detection modules, there are more merits to use multi-robot cooperation capabilities to such a large fleet of robots. In general, the control structure of the large fleet mobile robots is classified centralized control and decentralized control. A centralized control requires robust and permanent communication capabilities between all mobile robots and the supervised system. A decentralized control only requires local communication between robots and the supervised system. Each mobile robot of the multiple robots' system will communicates with the other robots [9]. We combine the centralized control and the decentralized control in the intelligent home system.

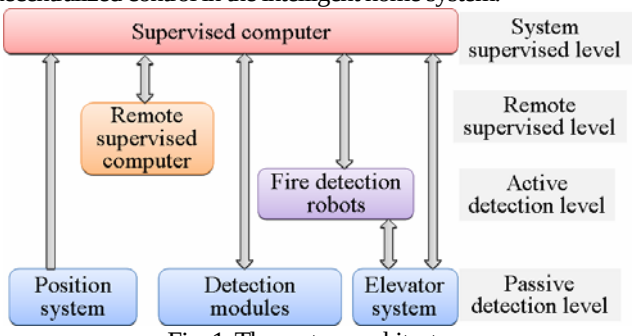

Fig. 1. The system architecture

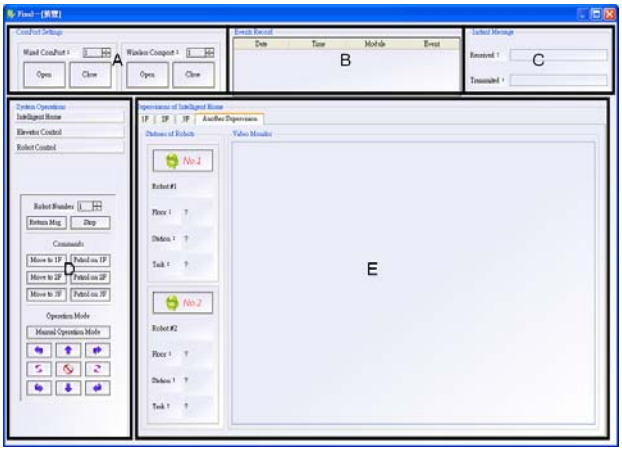

Fig. 2. User interface

The user interface of the multi-robot system is shown in Fig. 2, and contains five parts. The label "A" can programs the communication protocol between the supervised computer and the mobile robots, and sets the communication port between the supervised computer and the wire detection modules. The label "B" displays relation information from mobile robots and the wire/wireless detection modules, and records the time and location of the dangerous event. The label "C" displays the information between the supervised computer and detection modules. The label "D" can sets the threshold of the passive detection modules, control command of the elevator and mobile robots. The label "E" displays the real-time status of the intelligent home, detection signals, image signals and mobile robots, and displays the alarm position of the home.

III. DETECTION MODULES

The detection processing of intelligent home system is shown in Fig. 3, and contains active detection modules and passive detection modules. We use dash line to represent the wireless interface. The detection processing of the system has two steps. We explain the detection processing as following. In the first step, the system uses wire detection modules, wireless detection modules and image system as the passive detection modules to detect dangerous event, and uses mobile robots as the active detection modules to detect the same event simultaneously. These detection modules transmit the decision signals to the supervised computer using fusion algorithms, respectively. The supervised computer decides the event to be true or not using weighted average method. In the weighted average method, we set the same weight value for the detection signals of these modules. The decision rule is according to equation (1) and (2). Then we set a threshold value for the detection module. The average value $\bar{x}$ is over than threshold, and we can say the event to be true. Otherwise we can say no event condition. The *ith* measurements value of n sensors is presented x_i, and the weight must be satisfied $0 \le \omega_i \le 1$ is

$$\bar{x} = \sum_{i=1}^{n} \omega_i x_i \tag{1}$$

$$\sum_{i=1}^{n} \omega_i = 1 \tag{2}$$

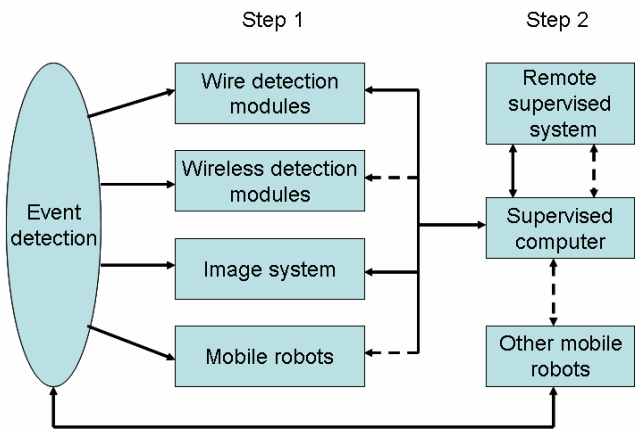

Fig 3. The detection processing

The supervised computer decides the dangerous event to be true, and controls other mobile robot moving to the event position for the second step, and transmits the event signal to the remote supervised computer, too. The main role of the active detection modules is mobile robots. The mobile robot is equipped with a microchip (HT46RU25) as controller, and calculates the

movement distance from the pulse numbers of the encoder, and uses the compass module and the IR distance module to compute the orientation and the relation distance from the elevator and the wall.

The mobile robot has the shape of cylinder, and uses IR receiver to locate the position of the elevator. The position system uses IR sensors to decide the location of each mobile robot, and communicates with the mobile robot through the supervised computer. the mobile robot knows the real-time location via wireless RF interface. The mobile robot can communicate with the others robot and the supervised computer via wireless RF interface, and knows the location of each mobile robot, too.

We use flame sensor (R2686) in the passive fire detection module. Flame sensors look for characteristic emissions of either infra-red or ultra-violet light from the flames. Its peak wavelength is 220 *um* and sensing wavelength is 185~260 *um*. The R2868 has wide angular sensitivity (directivity) and can reliably and quickly detect weak ultraviolet radiations emitted from flame due to use of the metal plate cathode. It can detect the flame of a cigarette lighter at a distance of more than 5 m. The R2868 is well suited for use in flame detectors and fire alarms, and also in detection of invisible discharge phenomena such as corona discharge of high-voltage transmission lines. We use three flame sensors to detect fire source, and use the same reliability value to decide event. The block diagram of the fire detection module is shown in Fig. 4. We use logical filter method to compute the reliability of the fire detection module. The AND filter has been applied could then be expected to correspond to significant aspects of the environment. In a similar manner, an OR filter could be used to reliably segment an image because all of the sensory information would be available for use in the segmentation process. In the logical filter method, we can use AND or OR filter on the fire detection module. Then we can calculate the system reliability of AND filter (R_S) and OR filter (R_P)

$$R_S = \prod_{i=1}^{n} R_i(t) \tag{3}$$

$$R_P = 1 - \prod_{i=1}^{n} [1 - R_i(t)] \tag{4}$$

$R_i(t)$ is the reliability of each flame sensor of the fire detection module. We can use the modules to integrate the fusion results of passive detection modules and active detection modules, and get the high accuracy of the security detection.

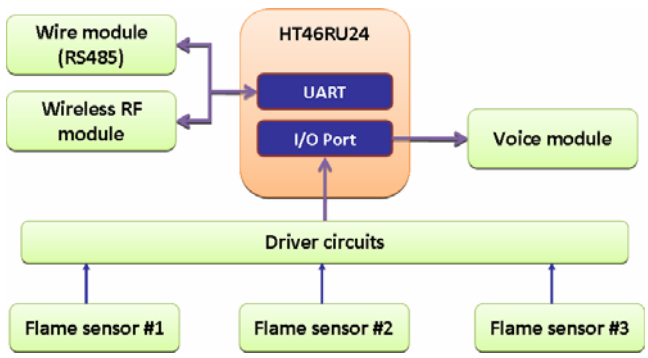

Fig 4. Block diagram of the fire detection module

IV. EXPERIMENTAL RESULTS

We use the fire detection processing to implement the security system of the intelligent home. We use passive fire module, image system and fire based mobile robots to detect fire sources in the intelligent home. We use the candle to represent the fire source. The intelligent home contains some passive detection modules, image system (outside), a supervised computer and two mobile robots. One is moving in the first floor (No. 1); the other is moving in the second floor (No. 2).

(a)

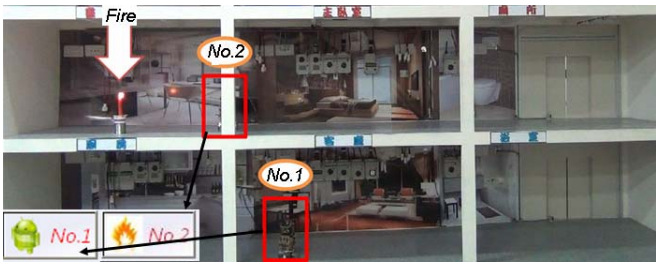

(b)

(c)

Fig. 5. The experimental result of fire detection for step one

Fig. 6. The robot moves into and leaves the elevator

The passive fire module detects the fire source in the second floor, and displays the fire symbol in the right side of Fig. 5(a). The image system recognizes the fire source using the Otsu method, and decides the fire event to be true, and transmits the fire signal to

© ISAROB 2013

the supervised computer. The user interface displays the fire symbol, too. The mobile robot detects the fire source in the second floor. The supervised computer decides the fire event to be true using weighted average method according to the signals of the passive fire module, the image system and the mobile robot, and orders command to the other mobile robot that is moving in the first floor. The detection processing is step one. We can see the fire symbol is plotted in the robot (No. 2). The robot (No. 1) moves in the first floor, and has not searched the fire source. The user interface displays no fire symbol to be shown in Fig. 5(b).

(a)

(b)

Fig. 7. The experimental result of fire detection for step two

The mobile robot of the first floor receives the command from the supervised computer, and moves to the front side of the elevator using the IR distance module autonomously. The movement scenarios are shown in Fig. 5(c). The assigned robot controls the elevator via wireless RF interface, and moves into the elevator going up to the second floor. The elevator moves to the assigned floor to stop, and opens the doors to trip the mobile robot leaving the elevator via wireless RF interface. The assigned mobile robot leaves the elevator, and turns right 90^0 moving to the fire source. The movement scenarios are shown in Fig. 6(c).

The assigned mobile robot moves approach to the location of the robot (*No.2*), and detects the fire event using flame sensor, and transmits the event signal to the supervised computer to be shown in Fig. 7(a). The user interface displays fire symbol for the two robots. The supervised computer receives the event signal to give the final decision. The detection result presents the fire event to be true according the logical filter method. The detection processing is step two to be shown in Fig. 7(b). .

V. CONCLUSION

We have presented a multi-level based intelligent security system to be applied in intelligent home. The controller of the detection modules is HOLTEK microchip. We use multiple fusion algorithms to enhance the accuracy for the fire detection. Mobile robots, image system and passive detection modules are integrated in the security system, and can transmit real-time event signals to the supervised computer. The supervised computer decides the fire event to be true using fusion algorithm, and orders command to the other mobile robots. The assigned mobile robots can move to the position of the fire event doing double check. The experimental results are very nice to decide the fire event occurrence. In the future, we want to integrate more and more detection modules, and cooperate with the multi-robot system, and use multi-sensor fusion algorithms to enhance the accuracy. The intelligent security can be applied in many fields, such as hospital, transportation, building and factory. We can extend the results to be applied in gas leakage detection and intruder detection, too.

REFERENCES

[1] Ding J and Ye M (2011), A Novel Way for Fire Detection in the Video Using Hidden Markov Model, IEEE International Conference on Electronic & Mechanical and Information Technology, pp.4413-4416.

[2] Azegami M and Fujixoshi H (1993), A systematic Approach to Intelligent Building Design, IEEE Communications Magazine, pp.46-48.

[3] Chung WL, Fu LC (2001), A Flexible, Hierarchical and Distributed Control Kernel Architecture for Rapid Resource Integration of Intelligent System, IEEE International Conference on Robotics Automation, pp.1981-1987.

[4] Su KL, Liao YL, Chen CH and Yang YC (2012), Multisensor Fusion Algorithm Based Intelligent Home Using Multi-Team Mobile Robots, The Innovative Computing, Information and Control – Express Letters (ICIC-EL),Vol. 6, No. 5, pp.1283-1289

[5] Ha C, Jeon G and Jeong J (2011), Vision-based Smoke Detection Algorithm for Early Fire Recognition in Digital Video Recording System, International Conference on Signal Image Technology & Internet-Based System, pp. 209-212.

[6] Liu W, Wang F, Hu X and Yang Y (2011), Detection of Fire Based on Multi-Sensor Fusion, International Conference on Computer Science and Network Technology, pp.223-227.

[7] Yang X, Wang J and He S (2012), A SVM Approach for Vessel Fire Detection Based on Image Processing, International Conference on Modelling, Identification and Control, June, 24-26, pp.150-153.

[8] Chia SH, Su KL (2010), Multi-level Multi-sensor Based Security System for Intelligent Home, International Symposium on Artificial Life and Robotics (AROB 15th), Beppu, Japan, Feb. 4-6, pp.379-382.

[9] Liu MT and Yu PT (2010), Robust candidate purring approach based on the Dempster-Shafter evidence theory for fast corner detection with noise tolerance in gray-level image, International journal of Innovative Computing, Information and Control, Vol. 6, No. 7, pp.3131-3143.

© ISAROB 2013

Design a Feasible Docking Station for Mobile Robots

Yi-Lin Liao[1], Li-Chun Lai[2], Kuo-Lan Su[3], Jr-Hung Guo[1]
[1]Graduate Electrical Engineering, National Yunlin University of Science & Technology
Douliou, Yunlin, Taiwan,
[2.]Bachelor Program in Robotics, National Pingtung University of Education
Pingtung City, Pingtung County 900, Taiwan
[3.]Department of Electrical Engineering, National Yunlin University of Science & Technology, Taiwan
(Tel: +886-5-5342601, Fax: +886-5-5312065)
E-mail: sukl@yuntech.edu.tw, g9910813@yuntech.edu.tw, g9710801@yuntech.edu.tw

Abstract: The article develops a docking station that has feasible movement and rotation function for mobile robots. The docking station contains a docking structure, a limit switch, a charger, a power detection module and a wireless RF module. The docking structure is designed with one active degree of freedom and two passive degrees of freedom. It rotates in the Z-axis, and uses compression spring to move for various docking condition. The weight of the docking station is almost 6 kg, and its length, and height, and width are 70cm, 50cm and 80cm. The maximum rotational angle and horizontal offset are 30 degree and 2 cm respectively. The power detection module is controlled by HOLTEK microchip. We calculate the power values using redundant management method, and isolate the error values using statistical signal prediction method, and execute the auto-recharging processing for mobile robots. The processing can enhances the successful rate to guide the mobile robot moving to the feasible docking station from various directions. In the experimental results, the power of the mobile robot is under the threshold value. The mobile robot searches the landmark of the docking station using laser range finder (SICK). The laser range finder guides the mobile robot approach to the docking station, and uses the adequate docking angle to be approach to the station.

Keywords: mobile robots, wireless RF module, HOLTEK microchip, redundant management method, statistical signal prediction method, laser range finder

I. INTRODUCTION

Mobile robots have been widely applied in many fields such as factory automation, dangerous environment detection, office automation, hospital, entertainment, space exploration, farm automation, military, education and security system and so on. The power of the mobile robot is under the threshold value for working in long time. The mobile robot executes auto-recharging processing; otherwise users can not control the mobile robot, and some dangerous event may be happened.

We have designed a power detection and diagnosis module applying in the mobile robot using HOLTEK microchip [1,2]. The module can detect multiple powers simultaneously, and extend the interface function to transmit the data to the main controller of the mobile robot via series interface, and reduce detection error using redundant management method and statistically method, and predicts the residual power to work [3].

In the past literature, many researches have been proposed power detection methods. Malaiy and Su use I_{DD} testing and estimating the effects of increased integration on measurement resolution [4]. Frenzel proposed the likelihood ration test method applying on power-supply current diagnosis of VLSI circuits [5]. Song presented the development and characterization of a surveillance robot with automatic docking and recharging capabilities using mobile wireless sensor network gateway for home security [6]. Oliveira proposed a method based on the Extended Kalman Filter (EKF) to estimate the batteries state of charger [7]. Keshmiri proposed an opportunistic control approach to address the multi-robot, multi-rendezvous recharging problem. The control strategy adapted attempts to take advantages of both centralized and distributed methodologies [8]. How to design a general charging structure is an important problem for mobile robots. The paper develops the feasible docking station that has widely docking angle.

II. SYSTEM ARCHITECTURE

The auto-recharging system is shown in Fig. 1 to be classified two parts: one is designed to supply and detect power for target device. The other receives the power to be a mobile robot. In the docking station, there are a connection structure, a limit switch, a landmark, a power detection module, a wireless RF module and a charger. The landmark can guides the mobile robot to find out the docking station using laser range finder. The power detection module can detects and controls the current output, and decides the status of the charging current, such as over loading (short), no current (shutoff) or normal current. The limit switch detects the mobile robot to touch the docking station or not. The wireless RF

© ISAROB 2013

module can communicates with the mobile robot, and transmits and receives the real-time signals of the auto-recharging processing. In the mobile robot, there are a charging connection structure, a laser range finder, a wireless RF module, an auto-switch, a power detection module and power system.

The mobile robot has the shape of cylinder and its diameter, height, and weight are 40 cm, 60 cm, and 30 kg, respectively. The robot is equipped with an IPC (Industry Personal Computer) as the main controller. The power detection module is embedded in the docking station and the mobile robot. The controller of the module is HOLTEK microchip, and computes the exact power using redundant management method. In the mobile robot, the module measures the exact power using four current sensors, and isolates the faulty measurement values, and predicts the residual power of the power system.

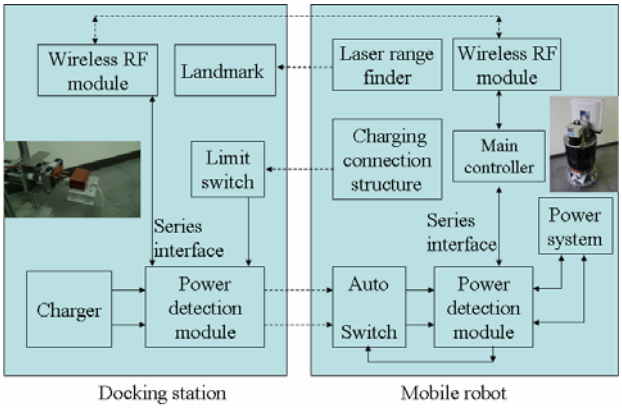

Fig. 1 The auto-recharging system

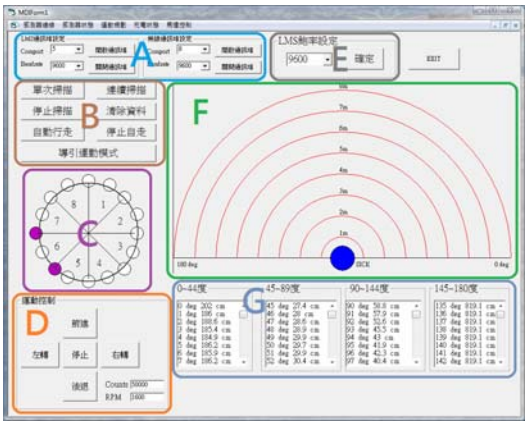

Fig. 2 The user interface of motion planning

The user interface is the motion planning of the mobile robot to be shown in Fig. 2, and contains eight parts. The label "A" can programs the communication protocol of the laser range finder and wireless RF interface, and sets the communication port is 3 for wireless RF interface. The label "B" is control command for the mobile robot, and sets the motion mode of the mobile robot. The label "C" displays the information of the IR sensors and the compass. Users control the mobile robot moving forward, backward, turn right, turn left and stop to be shown in the label "D". The label "E" sets the baud-rate of the laser range finder. The label "F" displays the direction of the docking station. The outlook of the detected environment is plotted in the label "G" by the laser range finder. The relation information of the LRF is shown in the label "H".

The user interface of the auto-recharging system contains five parts to be shown in Fig. 3. The label "A" displays the measured values of current and voltage, and computes the estimation value and average value of the power system. The label "B" displays the charging processing of the auto-recharging system, and contains alarm, start charging and finished. The label "C" displays the real-time information in the processing. Users want to stop and restart the charging processing to shown in the label "D". The label "E" plots the current curve and the voltage curve of the charging processing.

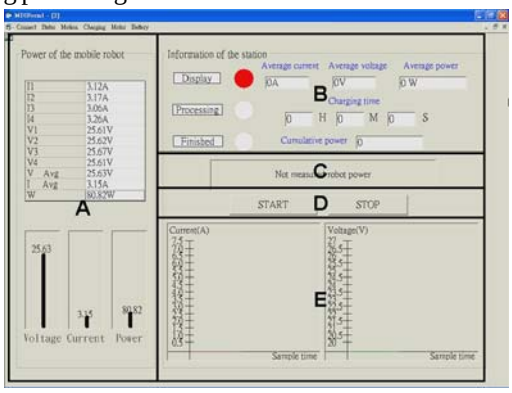

Fig. 3 The user interface of auto-recharging system

III. DOCKING STATION

The overview of the docking station is shown in Fig. 4. The docking station provides two contact points to connect the charging connection structure of the mobile robot. The docking station is designed with two passive DOF (Degree Of Freedom) and one active DOF. In the two passive DOF, it rotates on the Z-axis, and uses compression spring to move on the x axis for various docking condition. The active DOF rotates on z axis, and controls the connection pins moving forward to touch the connection structure of the mobile robot. The connection structure of the mobile robot is mounted on the back side of the mobile robot, and places on the same side of the laser range finder. The prototype of the docking station is shown in Fig. 4.

The recharging adapters of the mobile robot are at the inside of the holes. Each hole is shaped as a cone in order to help the docking smoothly. Since both the connection pins and adapters are rigid, the docking station is designed for providing compliance for reasonable robot docking angle and offset. When the mobile robot is approach to the docking station with offset and docking angle, the guiding stick mounted on the docking station functions to

© ISAROB 2013

guide the recharging pins for inserting into the adapters. The maximum rotational angle and horizontal offset are 30^0 and 2 cm respectively.

In the fig. 5, the mobile robot moves to the docking station with offset angle. The guiding stick can't touch the center of the connection structure, and rotates on the z axis to guide the connection pins to insert into the adapters. In the other condition, extension sprints are used to bring the recharging pins backing to the center after the robot disengages. A little entry offset and angle are allowed when the robot is in the docking process. The experimental result is shown in Fig. 6.

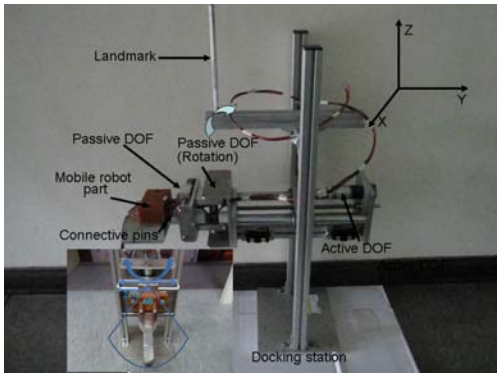

Fig. 4 The docking station

Fig. 5 The docking processing with offset angle

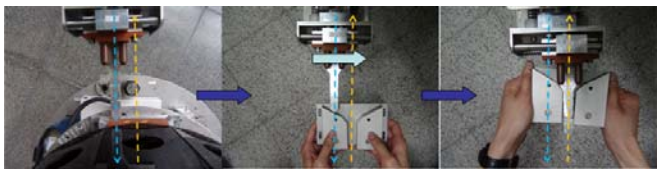

Fig. 6 The docking processing with offset distance

IV. EXPERIMENTAL RESULTS

The mobile robot moves autonomously in the free space, and uses the power detection module to detect power variety, and calculates the residual power. Then it computes the residual time to be under the threshold time. The user interface of the mobile robot displays to execute the auto-recharging processing. The mobile robot searches the docking station using laser range finder according to the landmark. The landmark is fixed on the top of the station to be shown in the right side of Fig. 7. In general, the docking station is fixed on the front side of the wall. The landmark is more near to the mobile robot than the wall. The mobile robot decides the position of the station according to the information of the laser range finder to be shown in Fig. 7.

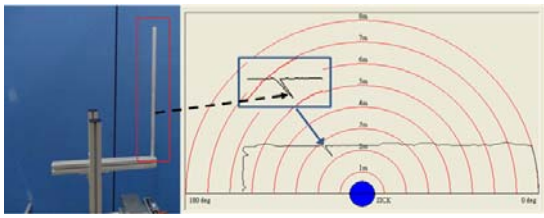

Fig. 7 The landmine detection

We explain the docking processing for two cases. The first case, the mobile robot locates on the right side of the station, and detects the landmine on the left side to be shown in Fig. 8(a). It computes the relation distance using the equation:

$$x = R\cos\theta \tag{1}$$

The parameter R is the distance far from the docking station. The mobile robots turns left θ, and moves the distance x. Then the mobile robot turns right 90^0 moving approach to the station. The experimental scenario is shown in Fig. 8(b). In the other case, the mobile robot locates on the right side of the docking station. The mobile robot executes the similar processing moving to the station. The docking station is detected by the mobile robot, and locates on the right side. The mobile robot turns left θ moving the assigned distance. Then the mobile robot turns left 90^0 moving approach to the station to be shown in Fig. 9.

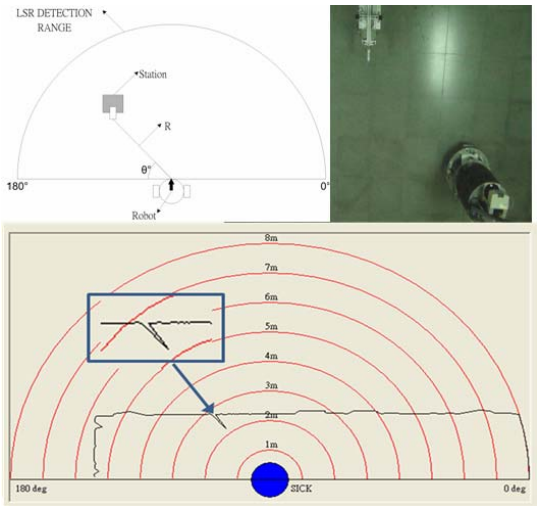

(a)

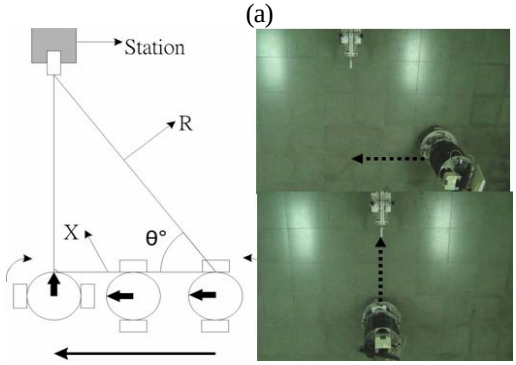

(b)

Fig. 8 The docking processing from right side

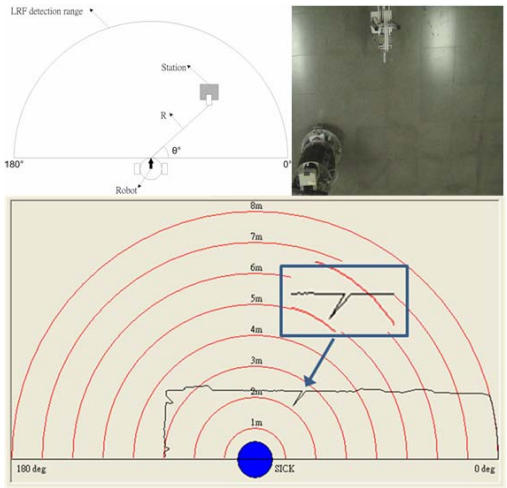

(a)

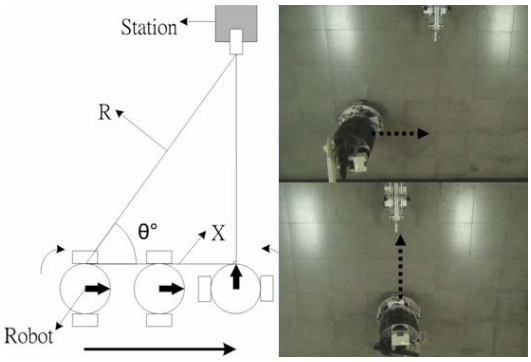

(c)

Fig. 9 The docking processing from left side

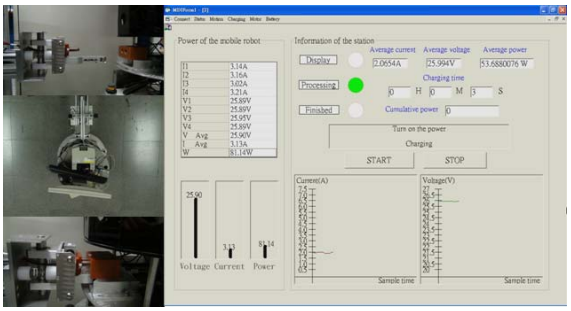

Fig. 10. The charging processing

The mobile robot moves to the docking station, and touch the connect pins and the limit switch to be shown in the left side of Fig, 9. The docking station transmits RF signal to the mobile robot. The mobile robot must stops, and prepares to execute the charging processing. Then the mobile robot turns on the auto-switch to receive the charging current. The docking station supplies the charging current to the mobile robot. The user interface displays green label on "Charging" to present the docking station is successful, and plots the current curve and voltage curve, and computes the charging time for the mobile robot. The charger of the station provides the power to the mobile robot. The experimental result is shown in Fig. 8 (a) and (b). Then the power detection module measures the charging current to be about 2.5A. The user interface of the mobile robot displays the charging processing to be shown in Fig. 10.

V. CONCLUSION

We have developed a feasible docking station of the auto-recharging system for the mobile robot, and finished a series auto-recharging processing. The docking station uses the landmark to guide the mobile robot, and adjusts two passive axis to connect the charging pins of the mobile robot. The mobile robot uses laser range finder to search the docking station, and moves to the docking station according to the landmark. We program a new auto-recharging processing to enhance the successful rate of the docking behavior for the mobile robot. In the docking processing, the system detects the charging current of the docking station and the mobile robot. The docking station communicates with the mobile robot using wireless RF interface.

ACKNOWLEDGMENT

This work was supported by the National Science Council of Taiwan, (NSC 101- 2221- E-224-007)

.

REFERENCES

[1] Su KL (2006), Automatic Fire Detection System Using Adaptive Fusion Algorithm for Fire Fighting Robot, IEEE International Conference on System, Man and Cybernetics, Grand Hotel, Taipei, Taiwan, October, pp966-971.

[2] Chien TL, Guo JH, Su KL and Shiau SV (2007), Develop a Multiple Interface Based Fire Fighting Robot, IEEE International Conference on Mechatronics, Kumamoto, Japan, May 8-10, WA1-B-3.

[3] Su KL, Tzou JH and Liu CC (2007), Development of a Multisensor-Based Residual Power Prediction System for Mobile Robots, IEEE Workshop on Advanced Robotics and its Social Impacts, Hsinchu, Taiwan, December 9-11, pp.114-119.

[4] Malaiya YK (1984), Testing stuck-on faults in CMOS integrated circuits, Proceedings of International Conference on Computer-Aided Design, pp.248-250.

[5] Frenzel JF (1994), Power-Supply Current Diagnosis of VLSI Circuits, IEEE Transaction on reliability Vol. 43, No.1, pp.30-38.

[6] Song G, Wang H, Zhang J and Meng T (2011), Automatic docking system for recharging home surveillance robots, IEEE Trans. on Consumer Eletronics, Vol. 57, No. 2, pp. 428-435.

[7] Oliceira MM, Galdames JPM, Vivaldini KTand Magalhaes DV (2011), Battery state estimation for applications in intelligent warehouses, IEEE International Conference on Robotics and Automation, Shanghai, China, May 9-13, pp.5511-5516.

[8] Keshmiri S (2011), Multi-robot, multi-rendezvous recharging paradigm: an opportunistic control strategy, IEEE International Symposium on robotic and sensors environments, Montreal, Canada, Step. 17-18, pp.31-36.

© ISAROB 2013

The Eighteenth International Symposium on Artificial Life and Robotics 2013 (AROB 18th '13),
Daejeon Convention Center, Daejeon, Korea, January 30-February 1, 2013

A PSO method for time-optimal motion planning of a mobile robot

Li-Chun Lai[1], Kuo-Lan Su [2], Chia-Nan Ko[3], Sheau-Wen Lin[4], and Chia-Hung Shih[1]

[1] Bachelor Program in Robotics, National Pingtung University of Education
Pingtung City, Pingtung County 900, Taiwan
[2]Department of Electrical Engineering, National Yunlin University of Science and Technology
Douliou, Yunlin 640, Taiwan
[3]Department of Automation Engineering, Nan Kai University of Technology
Tasotun, Nantou 542, Taiwan
[4] Graduate Institute of Mathematics and Science Education, National Pingtung University of Education
Pingtung City, Pingtung County 900, Taiwan

(email:[1]lclai@mail.npue.edu.tw; [2]sukl@yuntech.edu.tw; [3]t105@nkut.edu.tw; [4]linshewen @mail.npue.edu.tw;
[5]hiroshi.seki@gmail.com)

Abstract: Based on a particle swarm optimization (PSO) algorithm for time-optimal control problem of a two-wheeled mobile robot is addressed in this paper. The PSO algorithm is that it is easier to implement and there are fewer parameters to be adjusted. Different from usual cases, in which the Pontryagin's Minimum Principle (PMP) is used, an iterative procedure is proposed to transform the time-optimal problem into a nonlinear programming (NLP) one. Motion planning of a mobile robot is a NLP problem. In the NLP problem, the count of control steps is fixed initially and the sampling period is treated as a variable in the optimization process. Because the NLP has a initial feasible solutions problem that is not easier to find. In this paper, The PSO algorithm and fitness function to solve initial feasible solutions problem and optimal problem. To show the feasibility of the proposed method, simulation results are included for illustration.

Keywords: Particle Swarm Optimization (PSO), Mobile Robot, Time-optimal Control.

1. INTRODUCTION

Motion planning is an important issue in mobile robotics. In recent years, many research works have been addressed the control problem associated with mobile robots [1,2]. Among these works, a typical mission for a mobile robot can be described as to move from one configuration (position and orientation) to another. This problem has been thoroughly studied by assuming that the motors control the wheel velocities [3]. On the other hand, one also can use the motor to control the accelerations of the wheels [4]. For mobile robots equipped with two independently driven wheels, the time-optimal motion planning problem is that of finding the time-optimal motion in an unobstructed environment between two configurations. Usually, this kind of time-optimal control problem leads to the utilization of the Pontryagin's Maximum Principle (PMP) [5], in which the dynamical equations of the mobile robot are used and one needs to solve a set of differential equations. Since this set of equations is usually highly nonlinear and coupled, it is very difficult to obtain the closed-form solution for the time-optimal trajectory of any mobile robot. Because of the disadvantage in applying the PMP, a NLP method that does not utilize the PMP was developed by one of the authors of this paper to solve the time-optimal control problem of linear systems [6]. The basic idea of this method is that instead of considering a fixed sampling period, the count of control steps is fixed initially and the sampling period is treated as a variable in the optimization process. Extending the concept in [6] to nonlinear systems, this paper shows the generation of time-optimal motion between two configurations for a mobile robot with two independently driven individual wheels. In the beginning of this study, a mobile robot is introduced and its kinematic equations are derived. Then an iterative procedure is proposed to transform the time-optimal problem into a constrained NLP one. However, since the NLP has a initial feasible solutions problem that is not easier to find and two level time-optimal process is very complex. In this paper, The PSO algorithm and fitness function to solve initial feasible solutions problem and time-optimal problem.

© ISAROB 2013

Particle Swarm Optimization (PSO) algorithm proposed by Kennedy and Eberhart [7] is another kind of evolutionary computation techniques. This method was based on the simulation of simplified animal social behaviors such fish schooling and bird flocking. In PSO searching space, each single solution acts as a flying bird, which we call it a particle. The PSO algorithm works on a social behavior of particles in the swarm. It finds the global best solution by simply adjusting the trajectory of each particle its own best particle and toward the best particle of the entire swarm at each generation. The PSO algorithm has been used in solving many optimization problems successfully. Compared with GA, the advantage of PSO is that it is easier to implement and there are fewer parameters to be adjusted. In this paper, The PSO algorithm is proposed to determine velocities of two wheels. The path of a mobile robot is time-optimal from a given initial configuration to a desired final configuration.

The remaining sections of this paper are organized as follows. Section 2 shows kinematics equations of a mobile robot. Section 3 presents time-optimal control between two configurations. Section 4 presents time-optimal motion planning with PSO algorithm. Simulations are performed in Section 5 to confirm the feasibility of the proposed algorithm. Section 6 concludes the paper.

2. KINEMATICS EQUATIONS OF A MOBILE ROBOT

In the section, the kinematics of a mobile robot with two independent driven wheels will be described. The configuration of the mobile robot will be denoted by (x, y, θ) as shown in Fig. 1. Where x and y are the coordinates of the midpoint of the wheel axis, and θ is the heading angle of the robot. L is the distance between two wheels and r is the radius of the wheel.

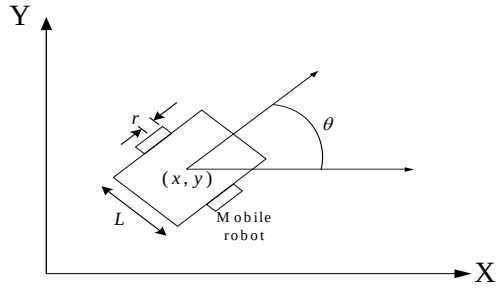

Fig. 1. A diagram of a mobile robot

By assuming that the wheels do not slip, the kinematics of the mobile robot as shown in (1).

$$\begin{bmatrix} \dot{\omega}_r(t) \\ \dot{\omega}_l(t) \\ \dot{\theta}(t) \\ \dot{x}(t) \\ \dot{y}(t) \end{bmatrix} = \begin{bmatrix} u_r(t) \\ u_l(t) \\ \dfrac{r(\omega_r(t)-\omega_l(t))}{L} \\ \dfrac{r\cos\theta(t)(\omega_r(t)+\omega_l(t))}{2} \\ \dfrac{r\sin\theta(t)(\omega_r(t)+\omega_l(t))}{2} \end{bmatrix} \tag{1}$$

where $\omega_r(t)$ and $\omega_l(t)$ represent the angular veloci ties of the right and left wheels, respectively. $u_r(t)$ and $u_l(t)$ are the control inputs.

3. TIME-OPTIMAL MOTION PLANNING PROBLEM BETWEEN TWO CONFIGURATIONS

The time-optimal motion planning problem between two configurations is to find the control inputs that will move the initial configuration (x_0, y_0, θ_0) to the final configuration (x_f, y_f, θ_f) while minimizing the traveling time. The control inputs $u_r(t)$ and $u_l(t)$ are assumed to meet the following constraints in (2) and (3).

$$u_{\min} \le u_r(t) \le u_{\max} \tag{2}$$

$$u_{\min} \le u_l(t) \le u_{\max} \tag{3}$$

The mobile robot moves time $[0, t_f]$ is to divide into N equal time intervals as shown in (4).

$$\Delta t = \frac{t_f}{N} \tag{4}$$

With (1) through (3), it is turned into (5) through (7).

$$\begin{bmatrix} \omega_r(i\cdot\Delta t) \\ \omega_l(i\cdot\Delta t) \\ \theta(i\cdot\Delta t) \\ x(i\cdot\Delta t) \\ y(i\cdot\Delta t) \end{bmatrix} = \begin{bmatrix} \omega_r((i-1)\cdot\Delta t) + u_r(i\cdot\Delta t)\cdot\Delta t \\ \omega_l((i-1)\cdot\Delta t) + u_l(i\cdot\Delta t)\cdot\Delta t \\ \theta((i-1)\cdot\Delta t) + \dfrac{r(\omega_r(i\cdot\Delta t)-\omega_l(i\cdot\Delta t))}{L}\cdot\Delta t \\ x((i-1)\cdot\Delta t) + \dfrac{r\cos\theta(i\cdot\Delta t)(\omega_r(i\cdot\Delta t)+\omega_l(i\cdot\Delta t))}{2}\cdot\Delta t \\ y((i-1)\cdot\Delta t) + \dfrac{r\sin\theta(i\cdot\Delta t)(\omega_r(i\cdot\Delta t)+\omega_l(i\cdot\Delta t))}{2}\cdot\Delta t \end{bmatrix}$$

$$\text{for } i = 1, 2, \ldots, N \tag{5}$$

$$u_{\min} \le u_r(i\cdot\Delta t) \le u_{\max} \qquad \text{for } i = 1, 2, \cdots, N \tag{6}$$

$$u_{\min} \le u_l(i\cdot\Delta t) \le u_{\max} \qquad \text{for } i = 1, 2, \cdots, N \tag{7}$$

With (5) through (7), the time-optimal motion planning can be formulated. Assume the following conditions are given:

$$(x(0), y(0), \theta(0)) = (x_0, y_0, \theta_0) \tag{8}$$

$$\omega_r(0) = 0 \tag{9}$$

$$\omega_l(0) = 0 \tag{10}$$

© ISAROB 2013

Determine the control inputs $u_r(t)$ and $u_l(t)$ for $[0, t_f]$ to minimize as shown in (11).

$$J = N \cdot \Delta t \tag{11}$$

Subject to

$$(x(t_f), y(t_f), \theta(t_f)) = (x_f, y_f, \theta_f) \tag{12}$$

$$\omega_r(t_f) = 0 \tag{13}$$

$$\omega_l(t_f) = 0 \tag{14}$$

and the constraints in (6) and (7).

4. TIME-OPTIMAL MOTION PLANNING PROBLEM WITH PSO ALGORITHM

The mathematic description of PSO is as the follow:

Suppose the dimension of the searching space is D, the number of particle is n. Vector $\vec{x}_j = (x_{j1}, x_{j2}, \ldots, x_{jD})$ represents the position of the i-th particle and $P_j = (p_{j1}, p_{j2}, \ldots, p_{jD})$ is the best position searched by now, and the whole particle swarm's best position is represented as $P_g = (p_{g1}, p_{g2}, \ldots, p_{gD})$ Vector $\vec{v}_j = (v_{j1}, v_{j2}, \ldots, v_{jD})$ is the position change rate of the i-th particle. Each particle updates its position according to the following formulas:

$$\begin{aligned} v_{jd}(k+1) = {} & w \times v_{jd}(k) + c_1 \times rand(\,) \times (p_{jd}(k) - x_{jd}(k)) \\ & + c_2 \times rand(\,) \times (p_{gd}(k) - x_{jd}(k)) \end{aligned} \tag{15}$$

$$x_{jd}(k+1) = x_{jd}(k) + v_{jd}(k) \tag{16}$$

Where c_1 and c_2 are positive constant parameters called acceleration coefficients. The $rand(\,)$ is a random function with the range [0,1]. w is called the inertia weight and is less than 1.

The fitness function of PSO algorithm is defined as shown in

$$fitness = \frac{1}{\lambda e e^T + 1} \tag{17}$$

where e is a error between the final states of the mobile robot and final configuration. The λ is a penalty value that the error e is convergence to zero fastly. In order to reach final configuration in optimal time, the paper is used PSO algorithm repeatedly. The method is used the optimal time of the last to replace the next initial time until the maximum iteration.

The details of the determination of the attractive factor can be summarized as follows:

Algorithm:

Step 1: Define the problem space.

Step 2: Initialize an array of particles with random positions and velocities.

Step 3: Evaluate the desired fitness function of the particles using equation (17).

Step 4: Determine the best personal position visited so far by each particle.

Step 5: Determine the best global position visited so far by all the particles.

Step 6: Update velocities using Eq. (15).

Step 7: Update particles' positions using Eq. (16).

Step 8: Repeat the procedure in Step 3 through Step 7 until all the particles have attained their desired fitness.

5. SIMULATION RESULTS

Example 1:

In this simulation example, the mobile robot will be moved from $(x_0, y_0, \theta_0) = (0,0,0)$ to $(x_f, y_f, \theta_f) = (1\text{m}, 1\text{m}, \frac{\pi}{3})$. The initial time of Δt, the initial value of *N*, the radius of the wheel r, and the distance between two wheels L are chosen to be 5 (sec.), 10, 5 cm, and 30 cm, respectively. Meanwhile, the bounds on the control inputs, $u_{\min}$ and $u_{\max}$ are chosen to be $-0.5\ rad/s^2$ and $0.5\ rad/s^2$. In applying PSO algorithm, the population size and maximal generation number are chosen to be 1000 and 1000, respectively. The value c_1, c_2, the inertia weight, and λ are chosen to be 2, 2, 0.8, and 10000, respectively. The error e will be defined as in (18).

$$e = [\Delta x_f \ \Delta y_f \ \Delta\theta_f \ \Delta\omega_{rf}(t_f) \ \Delta\omega_{lf}(t_f)] \tag{18}$$

$$\Delta x_f = x(t_f) - x_f \tag{19}$$

$$\Delta y_f = y(t_f) - y_f \tag{20}$$

$$\Delta\theta_f = \theta(t_f) - \theta_f \tag{21}$$

$$\Delta\omega_{rf} = \omega_r(t_f) - 0 \tag{22}$$

$$\Delta\omega_{lf} = \omega_l(t_f) - 0 \tag{23}$$

Applying PSO algorithm, the optimal time of Δt is found to be $\Delta t = 1.6073$ (sec.) and the plots of $x(t)$, $y(t)$, $\theta(t)$, $\omega_r(t)$, $\omega_l(t)$, $u_r(t)$, and $u_l(t)$ are shown in Fig. 2 through 8, respectively.

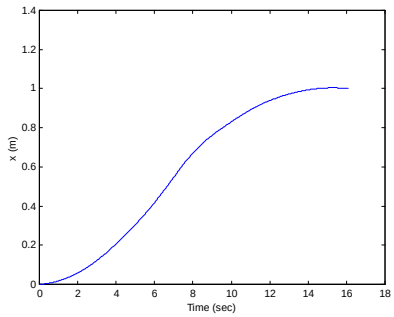

Fig. 2. Plot of $x(t)$

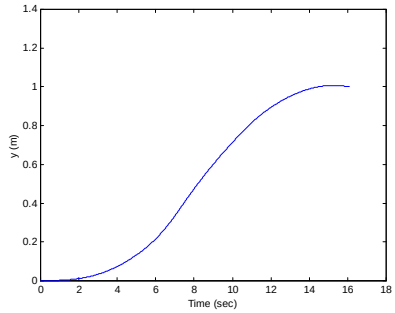

Fig. 3. Plot of $y(t)$

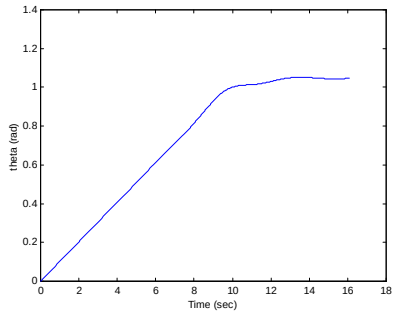

Fig. 4. Plot of $\theta(t)$

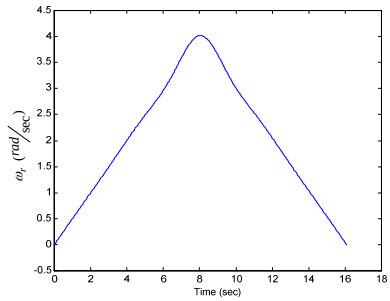

Fig. 5. Plot of $\omega_r(t)$

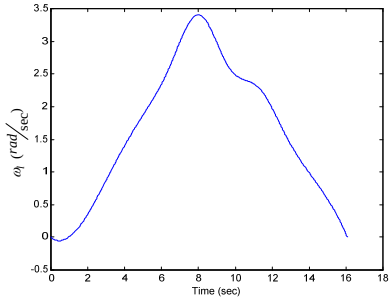

Fig. 6. Plot of $\omega_l(t)$

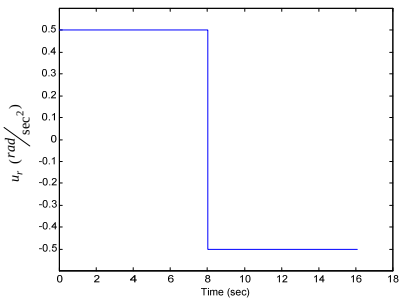

Fig. 7. Plot of $u_r(t)$

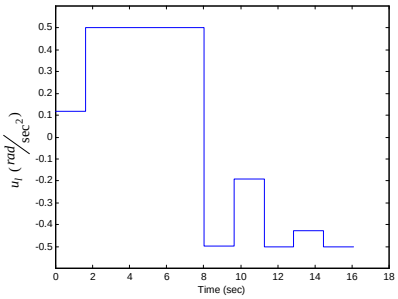

Fig. 8. Plot of $u_l(t)$

6. CONCLUSIONS

The paper uses PSO algorithm to solve time-optimal motion planning problem of a mobile robot with two independently driven wheels. The PSO algorithm and fitness function to solve initial feasible solutions problem and optimal problem. Compared with GA, the advantage of PSO is that it is easier to implement and there are fewer parameters to be adjusted. The simulation results can show the feasibility of the proposed method.

ACKNOWLEDGMENTS

This work was supported in part by the National Pingtung University of Education, Taiwan, R.O.C.

REFERENCES

[1] Wang SM, Lai LC, Wu CJ Shiue YL (2007), Kinematic control of omni-directional robots for time-optimal movement between two configurations. Journal of Intelligent and Robotic Systems 49(4):397-410

[2] Lai LC, Wu CJ, Shiue YL (2007), A potential field method for robot motion planning in unknown environments. Journal of the Chinese Institute of Engineers 30(3):369-377

[3] Soueres P, Laumond JP (1996), Shortest paths synthesis for a car-like robot. IEEE trans. on Automatic Control 41(5):672-688

[4] Reister DB, Pin FG (1994), Time–optimal trajectories for mobile robots with two independently driven wheels. The International Journal of Robotics Research 13(1): 38-54

[5] Pontryagin LS, Boltyanskii VG, Gamkrelidze RV, Mishchenko EF (1986), The Mathematical Theory of Optimal Processes Gordon and Breach Science Publishers. New York

[6] Chung TS, Wu CJ (1992), A computationally efficient numerical algorithm for the minimum-time control problem of continuous systems. Automatica 28:841-847

[7] Kennedy J, Eberhart R (1995), Particle swarm optimization. IEEE International Conference on Neural Network, pp. 1942-1948

© ISAROB 2013

The Eighteenth International Symposium on Artificial Life and Robotics 2013 (AROB 18th '13),
Daejeon Convention Center, Daejeon, Korea, January 30-February 1, 2013

The implementation of driving anti-sleep safety warning system

Yi-Yu Lu, Kuo-Kung Chen, Po-Yu Chen, and Wen-Bin Lin

Far East University, Taiwan
(Tel: 886-6-597-9566, Fax: 886-6-597-7570)

yiyu@cc.feu.edu.tw

Abstract: Sometimes a driver deviates from his natural or normal driving style due to inadequate attention or faces abnormal situation caused by a number of psychological and physical factors. Such abnormalities often lead a driver to a mistake that may cause an accident. This paper presents a novel approach called driver-adaptive assist system to avoid such abnormalities in driving scenario as a preventive measure against occurrence of vehicle collisions, assuming that natural driving style of individual drivers is the safest style. This paper presents a driving anti-sleep safety warning system. To prevent from traffic collision due to the driver fall asleep, the proposed system can supervise the driver by LED and buzzer. The system consists of three-axis accelerometer, LED, buzzer, and control circuit. When the system horizontal angle is bigger than setting ones, the system turns on the buzzer to alarm the driver. Finally, a driving anti-sleep safety warning system for vehicle is implemented and to verify the theoretical analysis.

Keywords: alarm systems, automation, driver warning systems, human factors, safety.

1 INTRODUCTION

Increasing trend in traffic collisions has become a serious social problem all over the world. A number of factors contribute to the risk of collision including; vehicle design, speed of operation, road design, road environment, driver skill and/or impairment and driver behavior. A 1985 study by K. Rumar, using British and American crash reports as data, found that 57% of crashes were due solely to driver factors, 27% to combined roadway and driver factors, 6% to combined vehicle and driver factors, 3% solely to roadway factors, 3% to combined roadway, driver, and vehicle factors, 2% solely to vehicle factors and 1% to combined roadway and vehicle factors [1]. Human factors in vehicle collisions include all factors related to drivers and other road users that may contribute to a collision. Examples include driver behavior, visual and auditory acuity, decision-making ability, and reaction speed. Worldwide motor vehicle collisions lead to death and disability as well as financial costs to both society and the individuals involved. Traffic collisions are often caused by mistakes of human drivers. A large number of mistakes are due to drivers with inadequate attention in driving led by fatigue, tiredness, drowsiness, having drunk, etc. It is obvious that a warning systems could be effective in most rear-end crushes and other accidents.

Researchers have been working to develop collision avoidance and steady following systems to avoid traffic collisions by providing automatic warning to the driver or braking the car in an emerged danger. Most of such systems use a similar algorithm to warn a driver when the inter-vehicle gap reduces to less than a critical distance. The critical distance for warning a driver is often determined heuristically based on the skill of an average driver in each of the systems [2-4]. Thus those warning systems provide the same type and the same level of assistance to all drivers, regardless of their driving behaviors, skills, ages and preferences. But it is believed that in reality the types and the levels of assistance desired by drivers vary widely according to their driving behaviors, because driving behavior of a beginner and an expert person, a young and an old person are completely different. So a typical assist system that assists all drivers in the same way may not be accepted widely due to mismatch with individual preference. This system may seem appropriate to only some drivers whereas it may seem noisy for providing unwanted advice to some other and may seem insufficient assistance to the others.

Since abnormality in driving leads a mistake that may cause an accident, a system of notifying abnormality in driving rather than only notifying at emerging collision probably produces a much more conducive outcome for reducing rear-end collisions. Some researchers have been working on the development of safety systems using different techniques based on physiological measures like brain waves, heart rate, pulse rate, respiration, etc. [5-7]. There are different methods that can be used to detect fatigue, drowsiness and other psychological facts in driving. But these techniques have the drawbacks since they require sensing equipment (electrocardiogram, electromyogram, respiration, skin conductance, wristband etc.) to be attached to the drivers causing annoyance to them [7], [8]. The other

© ISAROB 2013

techniques monitor eyes and gaze movement using complicated image analysis.

A driver's state of attention can also be characterized by comparing current driving behavior with his natural driving behaviors like the lateral position, variation in headway range, braking and acceleration characteristics, speed and range fluctuations, steering wheel movements, and time-to line crossing. To cope with the actual inattentiveness in driving it is necessary to develop a non-intrusive system based on observation of indirect driving behavior of individual driver. Although, these methods seem a bit complicated due to variation in vehicle type, driver experience, road type, weather etc., it may be an efficient and widely accepted system, and contribute in reducing traffic accident due to mistakes greatly [9].

This study develops the design and fabrication for a 3-axis accelerometer and Programmable System-on-Chip Controller (PSoC) devices-based driving anti-sleep safety warning system.

2 ELEMENT CONFIGURATION AND OPERATING PRINCIPLE

2.1 Three-axis accelerometer

A micromachined capacitive accelerometer is used for the motion tracker. There are various types of accelerometers with piezoresistive, capacitive, tunneling, resonant, and thermal properties. Among them, the capacitive type has high sensitivity, good DC response and noise performance, low drift, low temperature sensitivity, lower power dissipation, and simple structure. Shown in Fig. 1 and 2, the ADXL330 [10] is a small, thin, low power, complete 3-axis accelerometer with signal conditioned voltage outputs, all on a single monolithic IC.

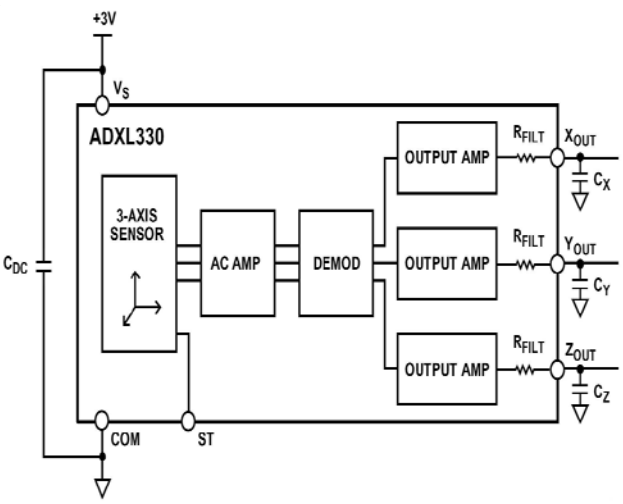

Fig. 1. ADXL330 functional block diagram

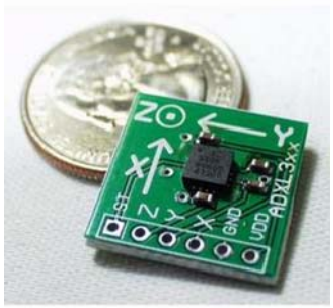

Fig. 2. ADXL330

The product measures acceleration with a minimum full-scale range of ±3 g (g=9.8m/m^2). It can measure the static acceleration of gravity in tilt-sensing applications, as well as dynamic acceleration resulting from motion, shock, or vibration. The user selects the bandwidth of the accelerometer using the C_X, C_Y and C_Z capacitors at the X_{OUT}, Y_{OUT}, and Z_{OUT} pins. Bandwidths can be selected to suit the application, with a range of 0.5 Hz to 1600 Hz for X and Y axes, and a range of 0.5 Hz to 550 Hz for the Z axis.

2.2 Programmable system-on-Chip (PSoC)

The PSoC family consists of many Programmable System-on-Chip Controller devices. These devices are designed to replace multiple traditional MCU-based system components with one, low cost single-chip programmable device. PSoC devices include configurable blocks of analog and digital logic, as well as programmable interconnects. This architecture allows the user to create customized peripheral configurations that match the requirements of each individual application. Additionally, a fast CPU, Flash program memory, SRAM data memory, and configurable I/O are included in a range of convenient pinouts and packages.

Shown in Fig. 3 and 4, the PSoC architecture, as illustrated on the left, is comprised of four main areas: PSoC Core, Digital System, Analog System, and System Resources. Configurable global busing allows all the device resources to be combined into a complete custom system. The PSoC CY8C29x66 family can have up to five I/O ports that connect to the global digital and analog interconnects, providing access to 8 digital blocks and 12 analog blocks [11].

© ISAROB 2013

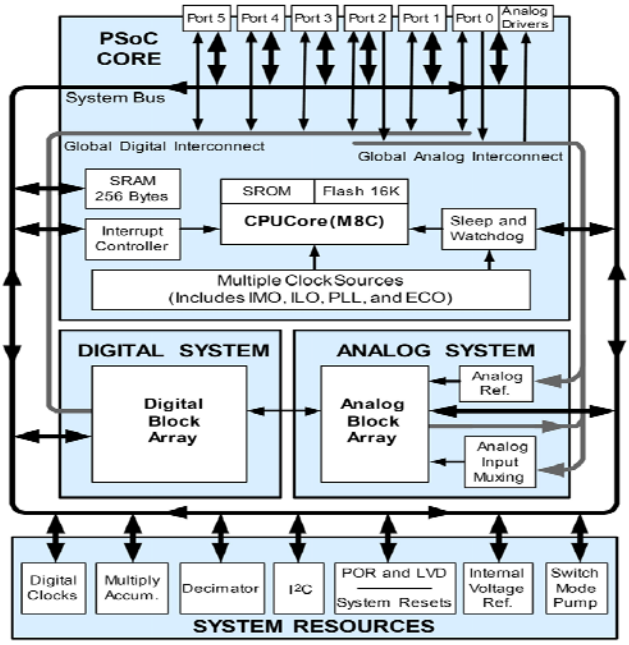

Fig. 3. CY8C29466 functional logic block diagram

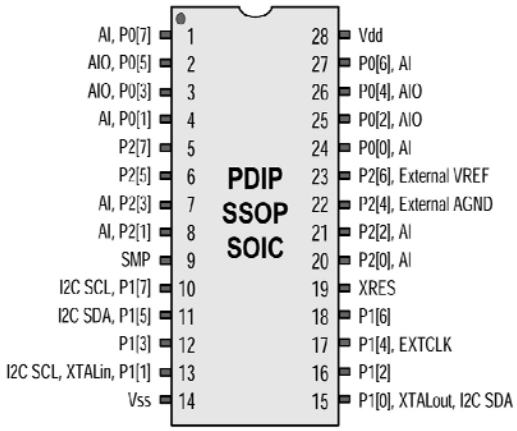

Fig. 4. CY8C29466 connection diagram

3 THE DESIGN STEPS

Fig. 5 is the flow chart diagram of design. From the beginning, we found the related literature reviews and confirmed basic model and material as we need. Secondly, we use PSoC to edit the program to control output element by ADXL330. And then, wiring these elements at solderless breadboard to pre-test. After several trial and errors, we can find the angle sensitivity as we need. Third, we check each function of the combination of pre-test solderless breadboard. Finally, we finish and validity a 3-axis accelerometer and PSoC-based driving anti-sleep safety warning system by the assembly of ADXL330, useful output elements, and power.

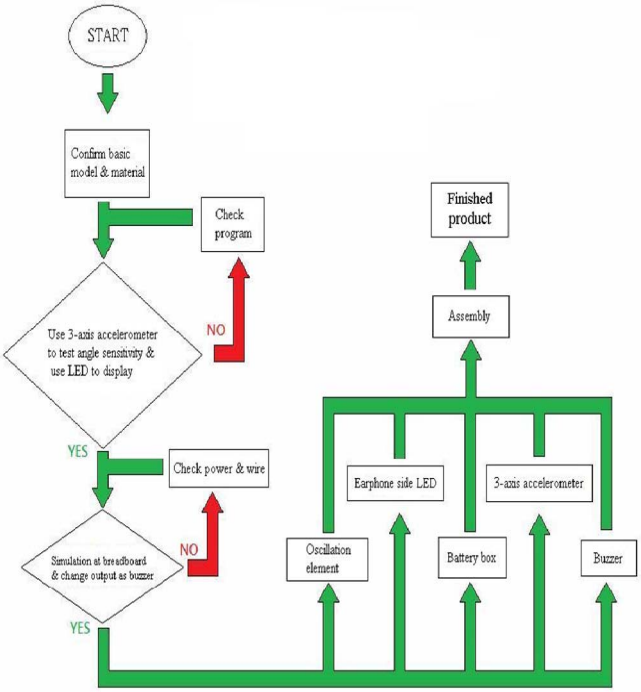

Fig. 5. The flow chart diagram of design

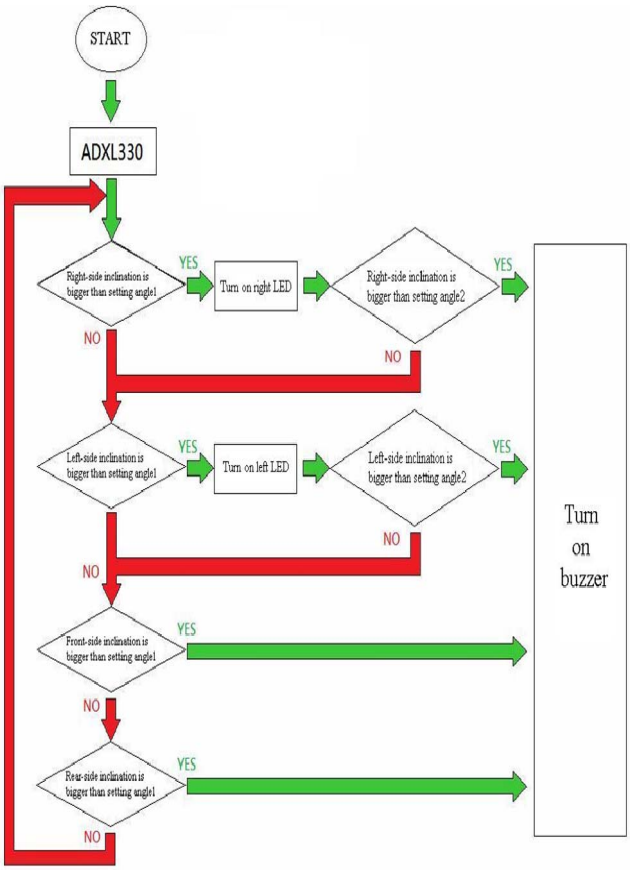

Fig. 6 The flow chart diagram of PSoC system programing

4 PSoC SYSTEM PROGRAMING

In PSoC System program, we declare a variable of ADXL330 inclination angle of human head as a virtual switch in Fig. 6. When the angle is bigger than setting angle 1, it will trigger and turn on the LED. When the angle is bigger than setting angle 2, it will trigger and turn on the buzzer to alarm the driver. Whatever the direction of left, right, front, and rear, they all have the same function. Angle 2 is bigger than angle 1, consequently.

5 HARDWARE F ABRICATION AND CONCLUSION

Shown in Fig.7, we place the ADXL330 at control module region due to sense balancing angle. The power circuit includes 5V circuit and 3.3 V circuit. Using 9V battery box, then converts 5Vpart by IC7805, and 3.3V part by IC LM1804 [12]. Because the voltage supply of ADXL330 and CY8C29466 is different, so it needs two voltage sources. And then, we write the program into CY8C29466 by PSoC Designer 5.0 Service. It cooperates with ADXL330 to control LED and buzzer. We wear the finished product to test four-side inclination angles. Various function testing has been completed to verify the accuracy of the hardware design.

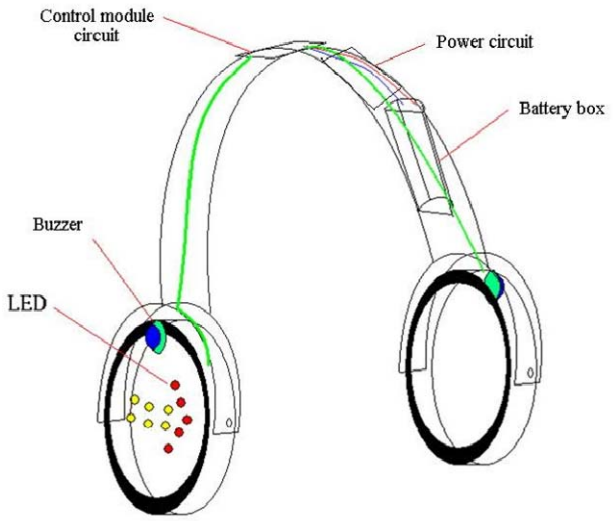

Fig. 7 The hardwere schematincs

ACKNOWLEDGMENT

This work is supported by the National Science Council, TAIWAN, ROC under the Research Grant NSC 97-2622-E-269-013-CC3.

REFERENCES

[1] Lum H and Reagan JA (1995), Interactive highway safety design model: accident predictive module. Public Roads Magazine

[2] Nagiri S, Amano Y, Fukui K and Doi S (2004), A Study of a Personally Adaptive Driving Support System Using a Driving Simulator,Driver Behavior and Active Safety, Special Issue R&D Reviw of Toyota CRDL, 39(2)

[3] Doi A, Butsuen T, Niibe T, Yakagi T, Yamamoto Y and Seni H (1994), Development of a Rear-End Collision Avoidance System with Automatic Braking Control, JSAE Review, 15(4), pp.335-340

[4] Fujita Y, Akuzawa K, and Sato M (1994), Radar Brake System, in 1995 Annual Meeting of ITS America, Washington D.C., vol. 1, pp.95-101

[5] Bergasa LM, Nuevo J, Sotelo MA, Barea R and Lopez ME, Real-Time System for Monitoring Driver Vigilance (2006), IEEE Trans. on Intel. Trans. Syst., 7(1):63-77

[6] Kaneda M, Obara H and Owada M (1999), Study on a Method of Using Image Processing Technology to Detect Inattentive Driving, Proceedings. JSAE Annual Congress, pp. 21-24

[7] Healey J, and Picard R (2000), SmartCar: Detecting driver stress, Proceedings. 15th International Conference on Pattern Recognition, Barcelona, Spain, 2000, vol. 4, pp.218-221

[8] Kircher A, Uddman M and Sandin J (2002), Vehicle control and drowsiness, Tech. Rep. VTI-922A, Swedish National Road and Transport Research Institute, Linkoping, Sweden, 2002

[9] Kamal MAS, Kawabe T, Murata J and Mukai M (2007), Driver-Adaptive Assist System for Avoiding Abnormality in Driving, 16th IEEE International Conference on Control Applications Part of IEEE Multi-conference on Systems and Control Singapore, Oct. 1-3, 2007, pp. 1247-1252

[10]http://www.alldatasheet.com/datasheet-pdf/pdf/150893/AD/ADXL330.html

[11]http://www.alldatasheet.com/view.jsp?Searchword=CY8C29466

[12] http://www.ti.com/lit/ds/symlink/lm1084.pdf

The Eighteenth International Symposium on Artificial Life and Robotics 2013 (AROB 18th '13),
Daejeon Convention Center, Daejeon, Korea, January 30-February 1, 2013

Motion Planning of the Multi-robot Based Chess Game

Yung-Chin Lin[1,3], Yi-Lin Liao[1], Cheng-Yun Chung[1], Kuo-Lan Su[2]
[1]Graduate school Engineering Science and technology, National Yunlin University of Science & Technology
Douliou, Yunlin, Taiwan,
[2]Department of Electrical Engineering, National Yunlin University of Science & Technology, Taiwan
(Tel: +886-5-5342601, Fax: +886-5-5312065)
[3] Department of Electrical Engineering, WuFeng University of Science of Technology, Taiwan
E-mail: yclin@wfu.edu.tw, sukl@yuntech.edu.tw, g9910801@yuntech.edu.tw

Abstract: The article uses mobile robots to present movement scenario of each chess for Chinese chess game, and programs the shortest motion path using enhance A* searching algorithm. We play the Chinese chess game using the mouse according to the evaluation algorithm on the user interface of the supervised computer. The supervised computer controls mobile robots according to the programmed motion paths of the designed chesses moving on the platform via wireless RF interface. We develop the user interface using Borland C++ Builder language. The user interface displays the positions of the mobile robot based chesses, and plots the motion paths of the assigned chesses. The proposed algorithm can programs the shortest motion trajectories of the chesses that move to target positions from start positions, and avoids the collision points of the motion trajectories for the assigned chesses simultaneously, and can re-programs the new motion path to avoid collision. Finally, we implement the movement scenario on the chessboard platform using mobile robots. Mobile robots move on the platform according to the programmed motion paths, and uses IR sensor modules to avoid the obstacles (mobile robots) and detect the cross points of the platform, and calculate numbers of the cross point to decide the final locations.

Keywords: mobile robots, Chinese chess game, enhance A* searching algorithm, wireless RF module, Borland C++ Builder

I. INTRODUCTION

Chinese chess [1] game is one of the most popular games. A two-player game with a complexity level is similar to Western chess. The Chinese chess game has gradually attracted many researchers' attention, and many evolutionary algorithms to be proposed in the recent. In the paper, we use thirty-two mobile robots to present the movement scenario of each chess, and uses enhance A* searching algorithm to program the shortest paths for mobile robots moving to the target positions. In general, users move chess (robot) to the target position according to the game rules. In some conditions, user moves the chess to take the chess of the other side. There are two chesses (robots) moving in the platform simultaneously. The assigned two robots may collide on the programmed motion paths. We want to solve the collision condition to improve the shortest motion paths of the two robots using enhance A* searching algorithm.

There are many algorithms to be proposed in Chinese chess game. Darwen and Yao proposed the co-evolutionary algorithm to solve problems where an object measure to guide the search process is extremely difficult to device [2]. Wang used adaptive genetic algorithm (AGA) to solve the problems of computer Chinese chess [3]. Su developed smart mobile robot using voice module, and programmed the motion trajectories for multiple mobile robots based Chinese chess game [4]. Fu used the position evaluation function to play an important role for building an intelligent Chinese chess computer game [5]. Zhou constructed the computer Chinese chess game platform that created favorable conditions for the development of discrete event dynamic system theory and provided a good research platform for solving dynamic counter measure problems [6].

We use multiple mobile robots to present the movement scenario of the chesses. In some condition, mobile robots must program the shortest path and avoid the obstacles moving to the next positions. The obstacles may be static or dynamic obstacles. We used A* searching algorithm to program the shortest path on the Chinese chess game. A^* heuristic function is introduced to improve local searching ability and to estimate the forgotten value. Kong used adaptive harmony search algorithm to solve optimization problems [7]. Flavio presented a multi-robot exploration algorithm that aims at reducing the exploration time and to minimize the overall traverse distance of the robots by coordinating the movement of the robots performing the exploration [8].

II. SYSTEM ARCHITECTURE

The system architecture of the multiple robots based Chinese chess game system is shown in Fig. 1. The system contains a supervised computer, a chessboard platform, some wireless RF modules and thirty-two mobile robots. The players of the chess game are classified red side and black side. Each side includes sixteen chesses. Each player only moves chess on one step, and waits to play the next step until the other side moving chess on the

© ISAROB 2013

user interface. These chesses stay at fixed positions to start the chess game. The movement rules of the chess game have two cases. Player moves chess to free position of the chessboard platform in the case one. The user interface programs the shortest path for the assigned robot. In the case two, player moves the chess to take the chess of the other side. The user interface programs two motion paths for the assigned chesses, and avoids collision points on the programmed motion paths. The two mobile robots move in the chessboard platform using the programmed motion paths.

Players move chesses using the mouse on the user interface of the supervised computer to be shown in upper side of Fig. 1. The supervised computer transmits the ID code and motion command to the assigned mobile robots, and receives the ID code and position from the mobile robots via wireless RF interface. Users can set game time until one player wins the game, and programs the using time for player moving chess on one step. The mobile robot has the shape of cylinder, and it's equipped with a microchip (MCS-51) as the main controller [9].

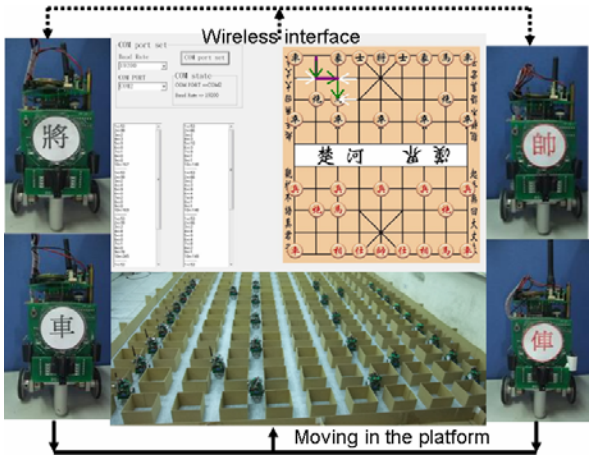

Fig. 1. System architecture

We implement the Chinese chess game using mobile robots on the grid based chessboard platform to be shown in the bottom of Fig. 1. The arrangement of the chessboard is 11 grids on the horizontal direction (X axis), and is 12 grids on the vertical direction (Y axis). The game only uses 9×10 grids based platform to arrange all chesses. The taken chesses move to the assigned positions around the chessboard. The distance is 30cm between the center of aisle on the X direction and Y direction of the chess board, and the width of the corridor is 12cm. The mobile robot uses the IR sensor modules to detect static and dynamic obstacles, and stays at the cross points of the chessboard platform.

The communication protocol of the system is 10 bytes. There are start byte (1 byte), data byte (8 bytes) and check byte (1 byte). We set the communicate protocol from the supervised computer to the mobile robot to be listed in Table 1. The start byte trigs the wireless RF module to receive the signals from the transmitter. The data bytes contain ID code (one byte), robot number (one byte), and movement direction and distance of the mobile robot. The definition of the movement direction is listed in right side of Fig. 2 for mobile robots. There are four various directions to match the grid based platform. The communication protocol is listed in Table 2 from the mobile robot to the supervised computer. The data bytes contain ID code, robot number, and position and orientation of robots and obstacles and finished command feedback data.

Table 1. Control command

Byte	0	1	2	3	4
Definition	Start	ID	R_CH	Work[1]	Work[2]
5	6	7		8	9
Work[3]	Work[4]	R_D		GO_flag	Check

Table 2. Feedback command

Byte	0	1	2	3	4
Definition	Start	ID	R_CH	Work[1]	Work[2]
5	6	7		8	9
Work[3]	Work[4]	No use		Text	Check

III. Motion Planning

We use A* searching algorithm to solve the shortest path problem of multiple nodes travel system. The formula of A* searching algorithm is following

$$f(n)=g(n)+h(n) \tag{1}$$

The core part of an intelligent searching algorithm is the definition of a proper heuristic function $f(n)$. $g(n)$ is the exact cost at sample time n from start point to the target point. $h(n)$ is the minimum cost. In this study, n is reschedules as n' to generate an approximate minimum cost schedule for the next point. The equation (1) can be rewritten as follows:

$$f(n)=g(n)+h(n') \tag{2}$$

The programmed motion path only computes the movement distance, and can't considers the total displacement using A* searching algorithm. We use pulse numbers of the encoder to define the total movement cost $f(n)$. The pulse numbers are 355 to move one grid on the platform, and the pulse numbers are 92 to rotate 90^0 for the mobile robot. The total displacement contains movement distance and turning numbers. The paper uses enhance A* searching algorithm to programs the shortest motion path, and considers the turning numbers. We can program seven steps to compute the shortest motion path using the proposed algorithm to be following:

Step 1: We construct two labels to be Open list and Close list.

Step 2: The "Close list" fills the start point and evaluation points, and the neighbour points of the start point fill in the "Open list".

Step 3: We construct label on the first searching result, and calculate the values of $f(n), g(n)$ and $h(n)$ function, and compares the values of the function. Then we select the minimum value of the function $f(n)$ to be stored in "Close list".

Step 4: Repeat the processing from step 2 to step 4.

Step 5: We can find the target point on the final searching.

Step 6: We compare the motion paths on the neighbour points of

each turning points, and we can decide a shortest path to control the mobile robot moving to the target point.

Step 7: The "Open list" can't include the target point. We decide the path does not exist.

We make an example to explain the motion planning using enhance A* searching algorithm. Player moves the chess "red cannon" to take the chess "black horse". The user interface programs the motion path using A* searching algorithm to be shown in Fig. 2, and avoid the obstacles (chesses). The programmed motion path turns right four times and turns left four times. We can find out the four points to make the landmarks "B" "C" "D" and "4", and select the new motion path from the landmarks "4" "C" and "B" to reduce two turning numbers. The experimental results are shown in Fig. 3(a) and (b).

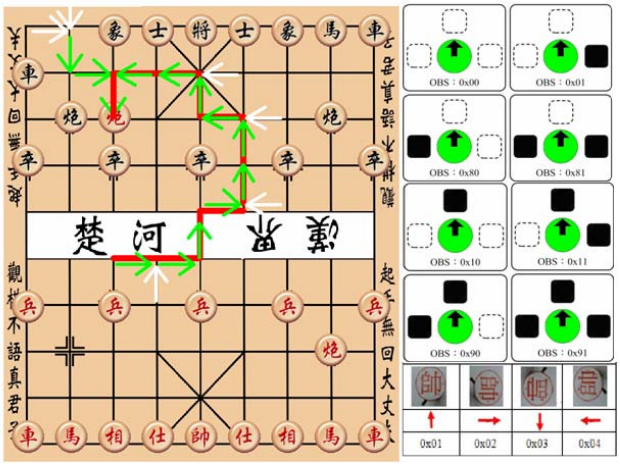

Fig. 2. Path planning

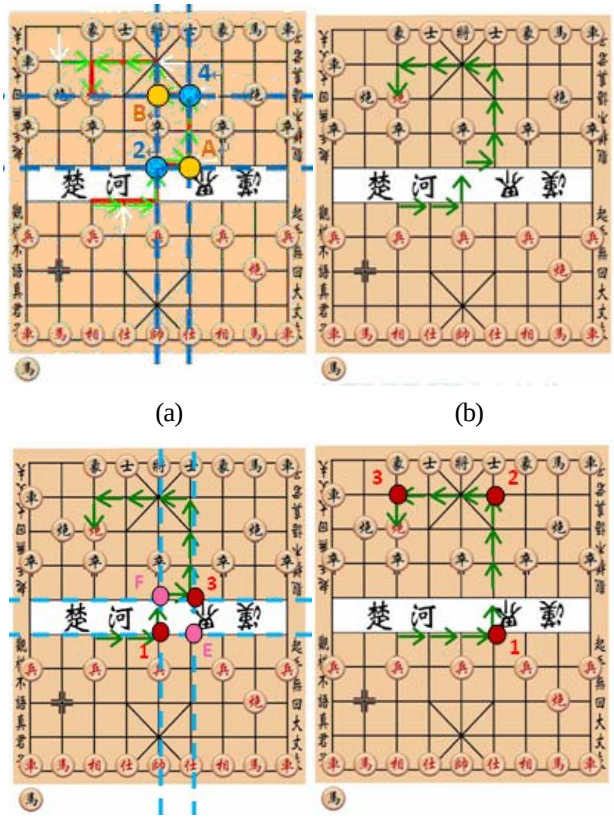

(a) (b)

(c) (d)

Fig. 3. Re-programmed motion path

Then we can find out new programming motion path to make four landmarks "1" "E" "3" and "F". We can select the new motion path through three points "1" "E" and "3" to instead of the old motion path through three points "1" :F" and "3". The new path can reduces two turning numbers to be shown in Fig. 3(c). Finally, we can search the shortest motion path to be shown in Fig. 3(d). The motion path turns left two times and turns right two times.

We compare the pulse numbers of the two motion paths. The total pulse numbers of the old shortest path $f(n)$ can be calculated as

$$f(n) = 11 \times 355 + 8 \times 92 = 4694 \tag{3}$$

In the other condition, we rebuild enhance A* searching algorithm on the step 6. We can calculate the pulse numbers of the new motion path moving to the target position. The total pulse numbers $f(n)$ as

$$f(n) = 11 \times 355 + 4 \times 92 = 4218 \tag{4}$$

IV. EXPERIMENTAL RESULTS

Users move the chess to play Chinese chess game, and present movement scenario of mobile robots using enhance A* searching algorithm. The experimental scenario is the chess "red cannon" moving to take the chess "black horse" on the user interface. The user interface programs two motion paths using A* searching algorithm for the assigned two robots. The first motion path is the chess "black horse" moving to the back side of the red side. The programmed motion path is shown in Fig. 4(a). The motion paths have eight times to turn right or left, and must spend more time moving to the target position for the mobile robot. The user interface programs the new motion path using enhance A* searching algorithm. The new motion path reduces turning right one time and turning left one time. The supervised computer orders the command to the mobile robot "black horse" via wireless RF interface. The mobile robot moves one grid, and turns right 90^0 moving six grids. Then it turns right 90^0 moving four grids. The chess moves to the final position to be shown in Fig. 4(b).

Then the user interface programs the motion path for the chess "red cannon" that moves to the position of the chess "black horse". The assigned motion path has the collision points with the pre-programmed motion path of the chess "black horse". The user interface displays the alarm signal to re-program the new motion path. The experimental result is shown in Fig. 4(c). The programming processing is shown in Fig. 3. We can find out the final motion path of the chess "red cannon" to be shown in Fig. 4(d).

The user interface has been programmed the two motion paths for two chesses "red cannon" and "black horse". Then the supervised computer orders command to the two mobile robots (red cannon and black horse) moving on the chessboard platform according to the programmed motion paths. The two mobile robots move on the platform simultaneously, and speak the

movement status using Chinese language. The movement scenario is shown in Fig. 5(a). We plot the motion trajectories of the two mobile robots in Fig. 5. Finally, we can see the chess "black horse" moving to the back side of the chess "red rook", and see the robot "red cannon" moving to the target position.

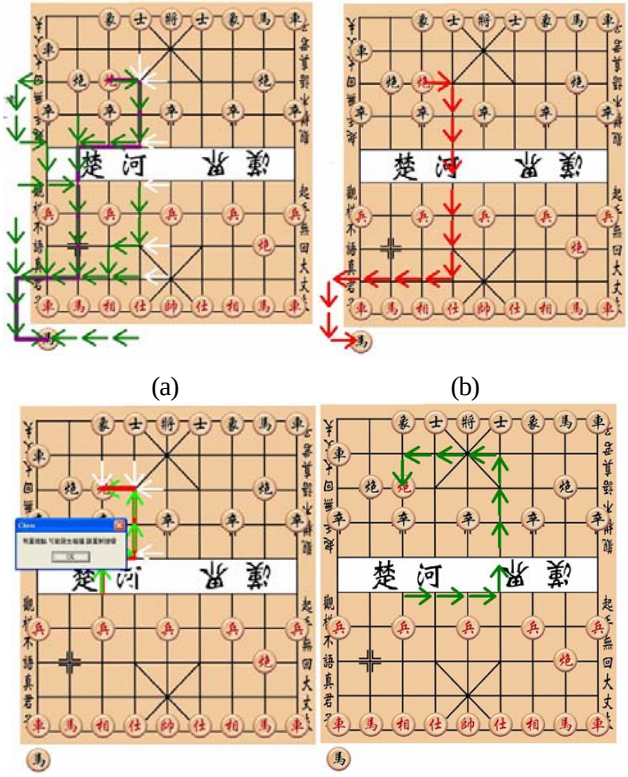

(a) (b)

(c) (d)

Fig. 4. Motion paths of two chesses

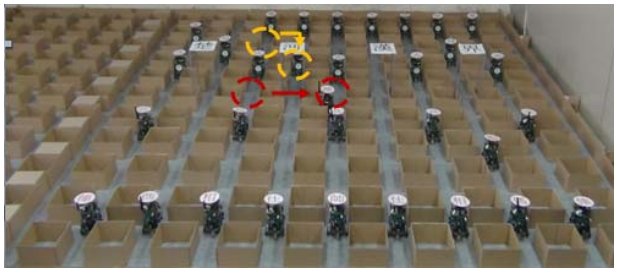

(a)

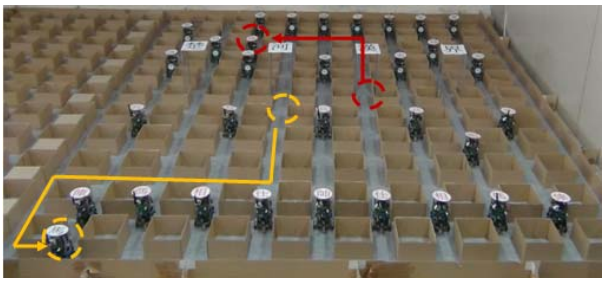

(b)

Fig. 5. Movement scenario of two robots

V. CONCLUSION

We have presented a Chinese chess game system using multiple mobile robots. Mobile robots execute the chess attribute using two interfaces. One is wireless RF interface, and the other is voice interface. The user interface displays the total time to play the game, and computes using time to move chess by player on one step, and receive the status of mobile robots via wireless RF interface. The user interface programs the shortest path using evaluation algorithm and A* searching algorithm. Then the user interface improves the motion paths to reduce the turning numbers, and avoid static and dynamic obstacles (chesses) using enhance A* searching algorithm. Users can move the chess using the mouse on the supervised computer, and moves the chess in the assigned time.

ACKNOWLEDGMENT

This work was supported by the National Science Council of Taiwan, (NSC 101- 2221- E-224-007)

.

REFERENCES

[1] Yen SJ, Chen JC, Yang TN and Hsu SC (2004), Computer Chinese Chess, ICGA Journal, Vol.27, No. 1, pp.3-18.

[2] Darwen P and Yao X (2002), Coevolution in Iterated Prisoner's Dilemma with Intermediate Levels of Cooperation: Application to Missile Defense, International Journal of Computational Intelligence Applications, Vol. 2, No. 1, pp.83-107.

[3] Wang J, Luo YH, Qiu DN and Xu XH (2005), Adaptive Genetic Algorithm's Implement on Evaluation Function in Computer Chinese Chess, Proceeding of ISCIT, pp.1206-1209.

[4] Su KL, Shiau SV, Guo JH and Shiau CW (2009), Mobile Robot Based Onlin Chinese Chess Game, The Fourth International Conference on Innovative Computing, Information and Control, pp.63.

[5] Fu T and Yin H (2012), Designing a hybrid position evaluation function for Chinese-chess computer game, International Conference on Software Engineering and Service Science, Beijing, China, pp.75-78.

[6] Zhou W, Liu JC and Zhao YH (2011), The construction of Chinese chess computer game platform, International Conference on Computer Science & Education, SuperStar Virgo, Singapore, pp.126-128,.

[7] Kong Z, Gao LQ, Wang LF and Ge YF, Onan adaptive harmony search algorithm, International journal of Innovative Computing, Information and Control, Vol. 5, No. 9, pp.2551-2560.

[8] Flavio CM and Xiao JH (2012), Aflood algorithm for multirobot exploration, IEEE Transactions on Systems, Man, and Cybernetics—Part B: Cybernetics, Vol. 42, No. 3, pp.850-863.

[9] Su KL, Chung CY, Liao YL and Guo JH (2011), A^* Searching Algorithm Based Path Planning of Mobile Robots, The Innovative Computing, Information and Control – Express Letters, Part B: Applications (ICIC-ELB),Vol. 2, No. 1, pp.273-278.

© ISAROB 2013

The Eighteenth International Symposium on Artificial Life and Robotics 2013 (AROB 18th '13),
Daejeon Convention Center, Daejeon, Korea, January 30-February 1, 2013

An Indoor Autonomous Surveillance Robot via Humanoid Vision System

Kuo-Hsien Hsia[1], Shao-Fan Lien[2], Juhng-Perng Su[3] and Wei-Yi Ciou[4]

[1]Department of Computer Science and Information Engineering, Far East University, Tainan, Taiwan, R.O.C.
[2]Graduate School of Engineering Science & Technology, National Yunlin University of Science & Technology, Yunlin, Taiwan, R.O.C.
[3, 4]Department of Electrical Engineering, National Yunlin University of Science & Technology, Yunlin, Taiwan, R.O.C.
([1]Tel: 886-6-597-9566#7599; [1]Fax: 886-6-597-7595)

[1]khhsia@cc.feu.edu.tw, [2]g9510801@hotmail.com.tw, [3]sujp@yuntech.edu.tw, [4]g9912712@yuntech.edu.tw

Abstract: This paper is devoted to develop a positioning and tracking scheme for a surveillance robot aiming at suspicious target and measuring the distance to the target. The vision of a general camera is too narrow for tracking fast moving targets. In addition, the flexibility of tracking is limited by robot's dynamics. We design a particular humanoid vision system with two pan-tilt servo systems which can be operated collaboratively or independently. The humanoid vision system is fast and flexible for tracking a moving target and measuring the distance. An embedded system is exploited for the humanoid vision system and robot servo control. An image recognition and tracking algorithm has been developed using LabVIEW for the system. Camshift tracking algorithm can recognize and track suspicious targets efficiently. Different from the previous systems, this system is cheap and easy to control.

Keywords: Surveillance robot, Humanoid vision system, Image process, Image tracking.

1 INTRODUCTION

The efficient image positioning and tracking method for an indoor autonomous surveillance robot for security technology has been a very important issue. An excellent surveillance robot must have the ability to recognize and to track suspicious targets. Furthermore, the relative distance between the target and robot is the significant information for the remote observers.

Luo [1] and Chien [2] et al proposed the system architecture of security robot with multiple sensors. Hsia [3] proposed the mobile robot autonomous obstacle avoidance in unknown indoor environment with a scanning laser rangefinder. However, a scanning laser rangefinder cannot identify the suspicious targets. Therefore, this paper is devoted to develop a positioning and tracking scheme for a surveillance robot aiming at a suspicious target and measuring the distance to the target. From many references, we know that the vision system is a good sensor for robots to achieve the surveillance missions in complex indoor environments. However, the vision of a general camera is too narrow for tracking fast moving targets. In addition, the vision systems are usually fixed on robots. Thus the flexibility of tracking is limited by robot's dynamics.

In this paper, we have accomplished three major objectives. Firstly, in order to track and to measure the distance between the robot and the moving target, we designed a particular humanoid vision system with two pan-tilt servo systems. Different from [4] and [5], our system is very cheap and easy to control. These two pan-tilt servo systems can be operated collaboratively or independently. The humanoid vision system is fast and flexible for tracking the moving target and measuring the distance to an intruder or a suspicious person. The robot system is shown in Fig. 1.

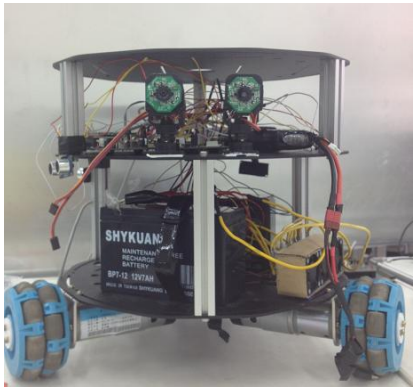

Fig. 1. The surveillance robot system

An embedded system, called PSoC (Programmable System-on-Chip), is exploited for the humanoid vision system and robot servo control. PSoCs integrate memory, analog and digital peripheral functions, and a microcontroller on a single chip. It has good performance for servo control. An image recognition and tracking algorithm has been developed using LabVIEW software for

© ISAROB 2013

the humanoid vision system. Camshift tracking algorithm can recognize and track suspicious targets efficiently. Based on the triangulation method, the position of the target in a 3D space can be measured by the humanoid vision system. In addition, we have succeeded in designing human-computer interface which makes the operation, data logging and real-time image observation of the robot system possible.

To investigate the performance of the proposed humanoid vision system from a practical point of view, a red target is used for demonstrating the image recognition and tracking algorithm. The Camshift tracking algorithm can not only recognize but also track the suspicious target quickly. Moreover, it shows that the humanoid vision system computes the distance to the target successfully in the experiments. The robot with a humanoid vision system is able to track and recognize the target, and it also can measure the distance to the target in the indoor environment. The practicality of the humanoid vision system has been verified in this paper.

2 TARGET POSITION ESTIMATION VIA HUMANOID VISION SYSTEM

The humanoid vision system is composed by two pan-tilt servo systems. Therefore the two pan-tilt servo systems can drive the cameras to align the target at the same time. The target image will be located in both cameras. The geometric relationship of the humanoid system is shown as **Fig. 2.** Based on the special architecture of the humanoid vision system, the complex pair image matching problem and 3D coordinate computing problem [6] can be simplified significantly. For a real-time robot system, this is a good solution for fast distance measuring.

By analyzing the relationship shown in **Fig. 2,** we can obtain the depth, Z, and the height, H, of the object. From **Fig. 3**, we have

$$\tan\theta_1 = \frac{p}{Z}, \tan\theta_2 = \frac{D-p}{Z}. \tag{1}$$

From (1), we have

$$\tan\theta_1 Z = p. \tag{2}$$

Substituting (2) into (1), we have

$$\tan\theta_2 = \frac{D-(\tan\theta_1 Z)}{Z}. \tag{3}$$

The Z and H can be obtained as

$$Z = \frac{D}{(\tan\theta_1 + \tan\theta_2)}, \tag{4}$$

$$H = \tan\theta_3 S, \tag{5}$$

where $S = \left[(D-p)^2 + Z^2\right]^{1/2}$. The θ_1, θ_2 and θ_3 are provided by the encoders of the pan-tilt servo systems.

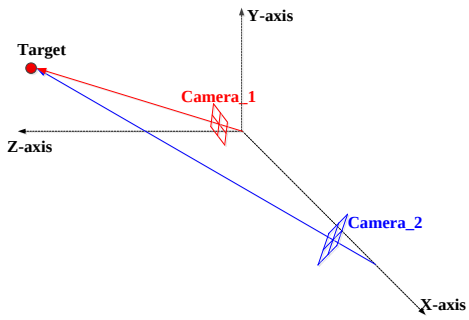

Fig. 2. The geometric relationship of the humanoid visi on system

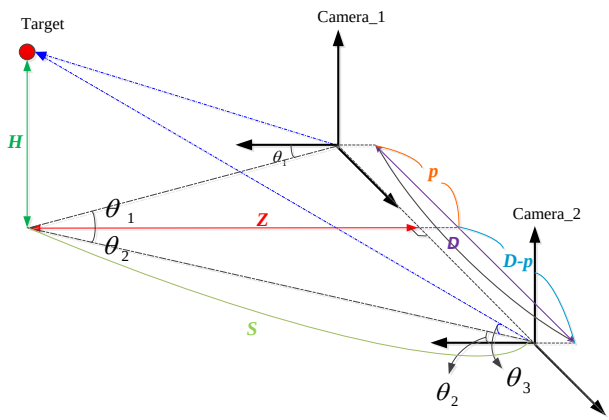

Fig. 3. The target position estimation

3 IMAGE TRACKING METHOD

3.1 HSV Color Model

Color model transformation aims to simplify the image and to segment the object preliminary. In here, HSV (Hue-Saturation-Value) color model is utilized in the image tracking applications [7]. The transformation from RGB to HSV is:

$$V = \max(R,G,B),\ S = \frac{(V - \min(R,G,B))}{V},$$
$$H = \begin{cases} (G-B)*60/S, if\ V = R \\ 180 + (B-R)*60/S, if\ V = G. \\ 240 + (R-G)*60/S, if\ V = B \end{cases} \tag{6}$$

3.2 CamShift tracking algorithm

The CamShift [8] (Continuously Adaptive Mean Shift) tracking algorithm is a very effective way to track the target.

The steps of CamShift tracking algorithm are:

Step 1 Calculate the HSV color histogram of target and set it to be the template.

Step 2 Calculate the target's color histogram of next image and start to search.

Step 3 Calculate the moving vector *V*. (If *V* is divergent, back to Step 1.)

Step 4 Calculate the Bhattacharyya coefficient for finding the best matching block.

Step 5 Record the coordinate of the best matching block from Step 4 as the initial searching position for the next image.

CamShift algorithm has good results for moving target tracking problem. For our application, CamShift algorithm is very quickly and efficiently for tracking and locking the target.

3.3 Moving Vector of the Target

The moving vector of the target is computed by the Camshift tracking algorithm. **Fig. 4** shows the moving vector analysis.

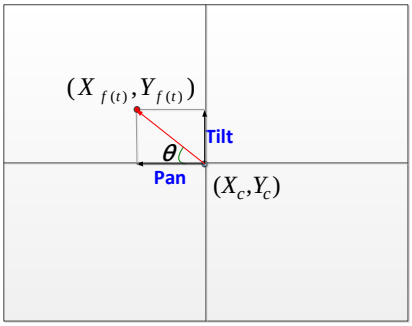

Fig. 4. The moving vector of target

From **Fig. 4**, we have

$$\theta = \tan^{-1}\left(\frac{V_y}{V_x}\right) \tag{7}$$

where $V_x = X_{f(t)} - X_c$, $V_y = Y_{f(t)} - Y_c$. Define

$$|V|^2 = V_x^{\,2} + V_y^{\,2}. \tag{8}$$

Therefore, the moving vectors along the pan and tilt directions are

$$\begin{cases} Pan = |V| * \cos\theta \\ Tilt = |V| * \sin\theta \end{cases}. \tag{9}$$

4 EXPERIMENTAL RESULTS

4.1 Hardware and Image Display Interface

The humanoid vision system is composed by two pan-tilt servo systems. The pan-tilt camera system is shown as **Fig. 5.** This system is very small and agile. More preferably, this design can be used in pairs or individually. In our application, the distance between the two pan-tilt servo systems is 10cm.

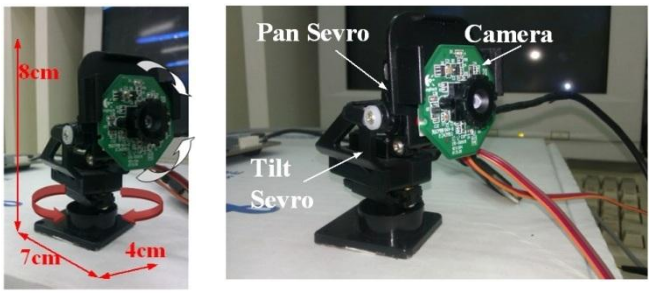

(a) (b)

Fig. 5. Pan-tilt camera system

The controller of the pan-tilt servo systems is a PSoC 5, as shown in **Fig. 6.** The PSoC 5 provides PWM control signals to the servo system and captures the signals of encoders. Moreover, the position of the target is computed by the PSoC 5. The human-computer interface is shown in **Fig. 7.** The real-time image, image processing results and the signals of encoders are displayed on it. In addition, the threshold values of HSV can be adjusted by this interface.

Fig. 6. PSoC 5

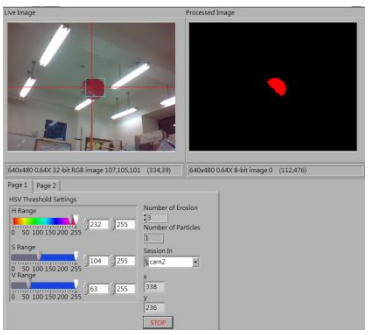

Fig. 7. Image display interface

The tracking results are illustrated as **Fig. 8**. **Figs. 8 (a-L) - (d-L)** and **Figs. 8 (a-R) - (d-R)** are the images captured by the left and the right camera, respectively. The images of target are all located at the centers of captured images.

© ISAROB 2013

For further investigating the measurement ranges of the humanoid vision system, we measure the target positions 10 times in each interval. The measurement range is from 0.5m to 6m and the interval is 0.5m. **Fig. 9** shows the average absolute errors of *Z* (depth) and *H* (height), where *Z* and *H* have been described in **Fig. 3**. The acceptable measurement error for our robot is less than 0.2m. In other words, the effective measurement range of the humanoid vision system is 3.5m. This measurement range for indoor surveillance robot is adequate.

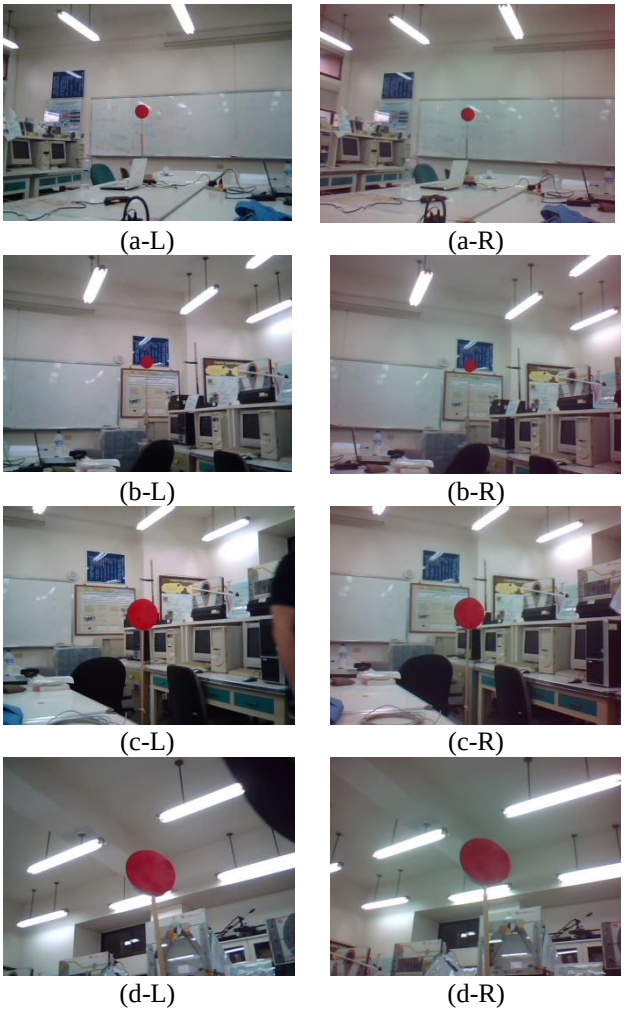

Fig. 8. The image tracking results

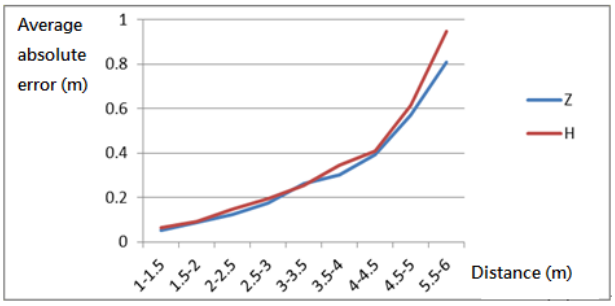

Fig. 9. The target position estimation results

5 CONCLUSION

In this paper, we proposed a particular humanoid vision system for indoor autonomous surveillance robot. The humanoid vision system is composed by two pan-tilt servo systems. Different from other humanoid vision system, our system is very cheap and easy to control.

In experimental results, the Camshift tracking algorithm can not only recognize but also track the suspicious target quickly. The images of target are all located at the center of the captured images. Moreover, it shows that the humanoid vision system computes the distance to the target successfully. The human-computer interface displays the real-time image, image processing results and the signals of encoders.

The robot with humanoid vision system is able to measure the distance of the target. It also can track and recognize the target in the indoor environment. The practicality of humanoid vision system has been verified in this paper.

REFERENCES

[1] Luo RC, Hsu TY and Su KL (2005), The development of a multisensor based intelligent security robot: Chung Cheng #1. Proceedings of IEEE International Conference on Mechatronics, Taipei, Taiwan, Jul 10-12, 2005, pp.970-975

[2] Chien TL, Su KL and Guo JH (2005), The multiple interface security robot – WFSR-II. Proceedings of IEEE International Workshop on Safety, Security and Rescue Robotics, Kobe, Japan, Jun 6-9, 2005, pp.47-52

[3] Hsia KH, Su JP, Lien SF and Lin WC (2011), The mobile robot autonomous obstacle avoidance in unknown indoor environment. Proceedings of International Conference on Automation Technology, Douliou, Yunlin, Taiwan, Nov 18-20, 2011, Paper No. R052

[4] Dankers A, Barnes N, Bischof WF (2009), Humanoid vision resembles primate archetype. Experimental Robotics, 54: 495-504

[5] Rougeaux S, Kuniyoshi Y (1998), Robust tracking by a humanoid vision system. Proceedings of IAPR the First International Workshop on Humanoid and Friendly Robotics, Tsukuba, Japan, Oct 26-27, 1998

[6] Hsia KH, Lien SF, Su JP (2011), Camera position estimation and feature extraction from an incomplete image of a landmark. Artificial Life Robotics, 16:152–156

[7] Gonzalez RC, Woods RE (2002), Digital image processing, second edition. Prentice-Hall

[8] Ju MY, Ouyang CS, Chang HS (2010) Mean shift tracking using fuzzy color histogram. International Conference on Machine Learning and Cybernetics (ICMLC), Jul 11-14, 2010, 6:2904-2908

© ISAROB 2013

The Eighteenth International Symposium on Artificial Life and Robotics 2013 (AROB 18th '13),
Daejeon Convention Center, Daejeon, Korea, January 30-February 1, 2013

An ultra-high speed motor driver with hybrid modulations

Chung-Wen Hung

Department of Electrical Engineering
National Yunlin University of Science and Technology, Yunlin, R.O.C. Taiwan
(Tel: 886-5-534-2601)

wenhung@yuntech.edu.tw

Abstract: An ultra-high speed motor driver with hybrid modulations is proposed in this paper. The speed range of a spindle motor is more wider and trends to ultra-high, but the traditional driver which provides either sinusoidal pulse width modulation or six-step modulation could not support so wide speed range. Normally, the variable voltage variable frequency control is used to support different type motors, then, SPWM is chosen in low speed range drivers and six-step is picked in high speed application. In this paper, the hybrid modulation driver with adjustable DC bus voltage is proposed, and the modulation could be selected for different motor and speed by users. For lower switching power loss, the six-step modulation is better when ultra-high speed application. For low speed range, the trapezoidal PWM is used to replace the SPWM for the reduction of switching power loss. The experimental results show the performance of proposed driver.

Keywords: Ultra-high Speed, Trapezoidal modulation, Hybrid Modulation

1 INTRODUCTION

In most applications, an inverter is the popular solution to driver motors, such as electric vehicles, appliances, machine tool and so on. As the applications increasing, there are many researches studied the control method to enhance the performance of system, and got good improvement [1-3]. But they didn't discuss the ultra-high speed case. As the speed variation is wider, the range of the fundamental frequency supported by inverter is more extensive. These years, it is extended to 300,000 rpm, even to 500,000 rpm. The traditional modulation method, sinusoidal pulse width modulation (SPWM), is considered to implement ultra-speed inverter [4-6], but the switching frequency of power switches are requested to support 20-times higher than the frequency of the sinusoidal, then the material cost will rise and the switching power loss will also up. Another solution is six-step modulation with variable DC bus voltage [7], nevertheless, the current includes big harmonic distortion, and which will cause torque ripple. The other modulation strategies are also discussed: Third harmonic injection modulation could improve the modulation ratio, and it could get the same line to line voltage of motor driven by the lower DC bus voltage[8], but the switching power loss is still the same like SPWM. With variable DC bus voltage, the trapezoidal modulation is used to perform similar modulation ratio effect, but to reduce about 66% of switching power loss [9-11]. A series of the current harmonic distortion are analysis for different kinds of trapezoidal modulation in [11]. Author proposed the hybrid modulation strategy for such kind of wide speed rage [12], with the variable DC bus voltage, the trapezoidal modulation is applied for the low speed range to reduce torque ripple, but the six-step modulation is used to lower the switching power loss when running in high speed range. The simulation results of every modulation method in different speed show the strategy is workable. A hybrid modulation driver for ultra-high speed spindle motors is proposed in this paper, the hybrid modulation strategy will detail, and the driver hardware structure will be described. Finally, the THD of motor current in the experimental results will show the hardware and the modulation method of the proposed driver feasible and valuable.

2 THE MODULATION STRATEGY

2.1 SPWM, third harmonic injection modulation, and Trapezoidal modulation

The SPWM is a standard and popular modulation method, and the power switch turn-on/-off intervals of three phases are proportional to the voltage of a three phase sinusoidal waveform. If the switching frequency is fast enough, the line current of motor will be also sinusoidal, and the motor rotates smoothly. However, the switching power is proportional to switching frequency. On the other hand, due to property of a power switch, the dead-time is necessary when switching, and it will induce torque ripple. The THD is increasing when the fundamental frequency of sinusoidal waveform is getting higher. So, the fundamental frequency supported by SPWM is limited.

To get higher phase voltage in the same DC bus voltage, the third harmonic injection modulation is proposed [8]. It means the same performance of motor could be driven lower DC bus voltage, and the cost of power switch device is also lower. In other words, the third harmonic injection modulation could improve the modulation ratio. If the original phase voltage is V_{bus}•sin(2πf), the third harmonic with 1/6 amplitude is injected. Then the phase voltage is shown in (1), and VXN3 (X is U, V and W) denotes the phase voltage with third harmonic injection. The phase to phase voltage with third harmonic injection (ex: VUN) is as same as original sinusoidal waveform. As shown in Fig.1, the dash line is the original sinusoid and the dot line is

© ISAROB 2013

sinusoid with third harmonic, the amplitude of the latter is about 86.5% of the former, but it could perform the same line to line voltage effect in three phase power source.

$$
\begin{aligned}
V_{UN3} &= V_{bus}\cdot\sin(2\pi f)+\frac{V_{bus}}{6}\sin(3\cdot 2\pi f)\\
V_{VN3} &= V_{bus}\cdot\sin(2\pi f+2\pi/3)+\frac{V_{bus}}{6}\sin(3\cdot(2\pi f+2\pi/3))\\
&= V_{bus}\cdot\sin(2\pi f+2\pi/3)+\frac{V_{bus}}{6}\sin(3\cdot 2\pi f)\\
V_{WN3} &= V_{bus}\cdot\sin(2\pi f-2\pi/3)+\frac{V_{bus}}{6}\sin(3\cdot(2\pi f-2\pi/3))\\
&= V_{bus}\cdot\sin(2\pi f-2\pi/3)+\frac{V_{bus}}{6}\sin(3\cdot 2\pi f)
\end{aligned}
\tag{1}
$$

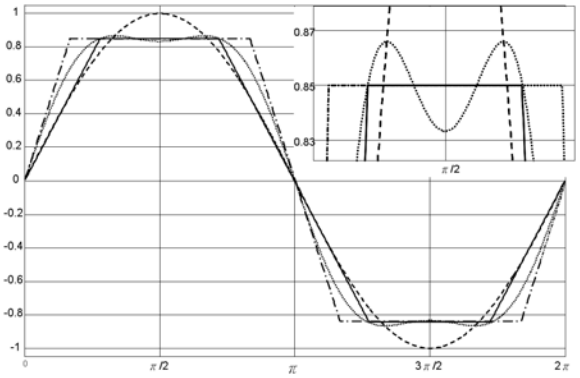

Fig. 1. The comparison of the sinusoid (60Hz), sinusoid with third harmonic and two trapezoids, and the partial zoon-in

From the Fig. 1, the sinusoid with third harmonic approximates to the trapezoids, specifically around the peak portion. Obviously, if the system hardware could provide a variable DC bus voltage and keep the output in a same voltage, the trapezoid is a good choice to approach the sinusoid with third harmonic. The reason is that there is not switching power loss when the output keeps in high or low base voltage. Two trapezoids are shown in Fig. 1, the slops of trapezoids are different. The fig. 2 shows the FFT analysis results of the sinusoid with third harmonic and trapezoids, 'x' denotes the frequency components of the former, then 'o' and '*' indicate the latter's'. The frequency analyses of three waves look similar.

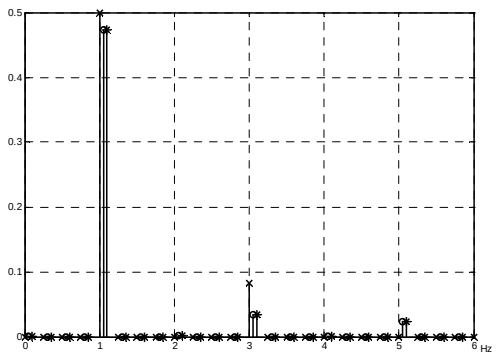

Fig. 2. The FFT analysis results of the sinusoid with th ird harmonic and trapezoids (Note: To identify, the 'o' and '*' are right shifted)

To get high modulation ratio, the sinusoid could be replaced with the sinusoid with third harmonic. And, to reduce the power switching loss, the sinusoid with third harmonic could be replaced by trapezoid with variable DC bus. However, due to the dead-time request of a power switch, a trapezoid is not suitable for ultra high speed.

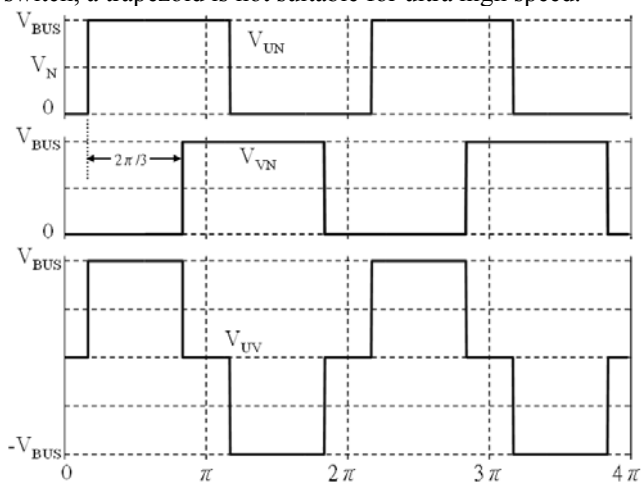

Fig. 3. The six-step modulation and the line-to-line voltage

2.2 Six-step modulation

The Six-step modulation is applied to driver motor in ultra high speed. For three phase driver, every phase is connected to DC bus or ground for a half of a cycle, and the time interval is 1/3 cycle, 2π/3. The phase voltage is shown in Fig. 3. If the fundamental frequency is very high, the phase current will be quasi-sinusoid due to the low pass filter effect of the resister and Inductor (RL) in static coil. This method will introduce bigger harmonic distortion in low speed, but switching power loss is lower than above modulations due to less switching.

2.3 The modulation strategy

To design an ultra-high speed motor driver and lower switching power loss, a hybrid modulation driver is proposed in [12]. The effect is verified by simulation, from THD comparison of the different speed with variable modulation methods. The driver is designed to supply the adjustable voltage of DC Bus, and then a motor is driven by the six-step modulation in high speed range and handled by trapezoidal modulation in lower speed.

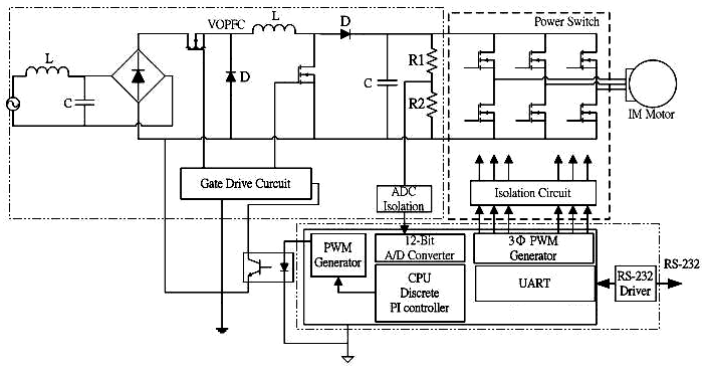

Fig. 4. The system block diagram of the experimental hardware

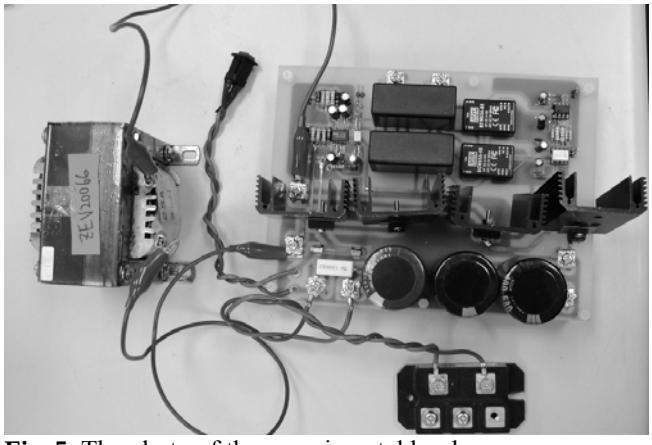

Fig. 5. The photo of the experimental hardware

3 EXPERIMENT

3.1 The hardware system

The block diagram and photo of the hardware system are shown respectively in Fig. 4 and Fig. 5, it includes three blocks: the variable output DC bus voltage control block, the power switch block, and control block. To provide a variable voltage, a variable output power factor correction structure is considered, however, only the buck function is used in the experiment. The power switch block is used to perform modulation, and the six switches belong to three legs to supply three phase power. The other block is the control system block, and the controller could be the TI TMS320F28x35 DSP or Renesas RX600 MCU. Note, only the VOPFC block and power switch block are shown in Fig. 5. To prevent shoot through current, the dead time is necessary when switching, both of controllers support the automatic dead time generation function in the build-in PWM peripheral block. However, the dead time will cause the distortion for motor voltage and current, this distortion is worse when the switching frequency is getting higher.

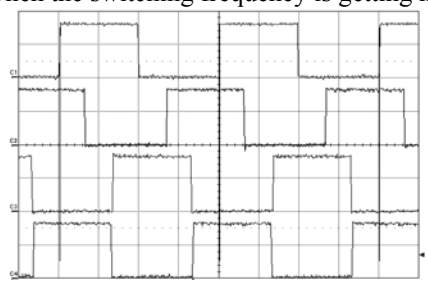

(a)

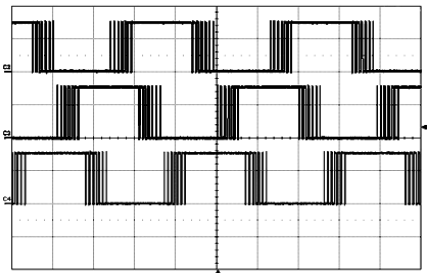

(b)

Fig. 6. The phase voltage of three phases for (a) the six-step modulation and (b) the trapezoidal modulation

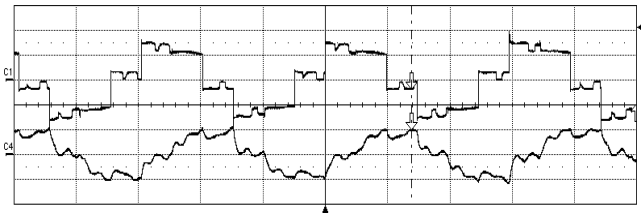

(a)

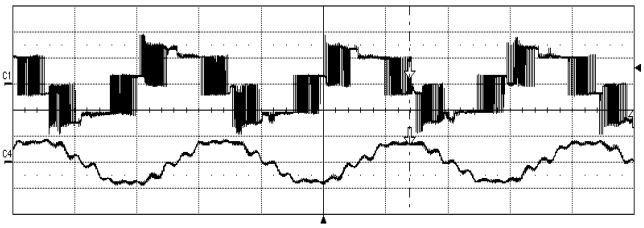

(b)

Fig. 7. The line-to-line voltage and phase current run in 10k rpm for (a) the six-step modulation and (b) the trapezoidal modulation

3.2. Experimental results

In low speed, the phase voltage of three phases for the six-step modulation and trapezoidal modulation are shown in Fig. 6 (a) and Fig. 6 (b) respectively. Every phase voltage of the six-step modulation is constructed from a 50% duty square-wave, what changes between variable DC bus voltage and ground. To simplify program, the original trapezoid is the dash dot line shown in the Fig. 1, waveform is formed with two straight line segments of 120 degree, one segment is connected to the variable DC bus voltage, and the other is turned to ground. The phase voltage between two segments is the PWM base and the duty is proportional to the slope. However, when motors run in ultra-high speed, due to the dead-time limitation, only the six-step modulation could be performed.

Next, the low speed (10k rpm) experimental results of the line to line voltage and line current for the six-step modulation and trapezoidal modulation are shown in Fig. 7 (a) and Fig. 7 (b) respectively. The current waveform of latter is more similar to sinusoid than formers. Then, the experimental results in middle speed (130k rpm) are shown in Fig. 8, and the two current waveforms are not different. And, for high speed (here is the 300k rpm), the experimental current of the six-step modulation is shown in Fig. 9, the current looks more like sinusoid than the current in low speed. Although only the six-step modulation could be applied in ultra-high speed range, it is more suitable for higher speed.

To compare the effect of two modulation method, the THDs of the motor current are measured and shown in Fig. 10. In low speed, the THD of the trapezoidal modulation is lower than the six-step modulation's, and it means former is more suitable to implement. As the speed is increasing, the THD is getting higher. However, the THD of the six-step modulation will reduce when over 130k rpm, it shows that the six-step could be used to driver in ultra-high speed. Note, due to instrument issue, the vertical-axle scale of Fig. 10 is skipped.

© ISAROB 2013

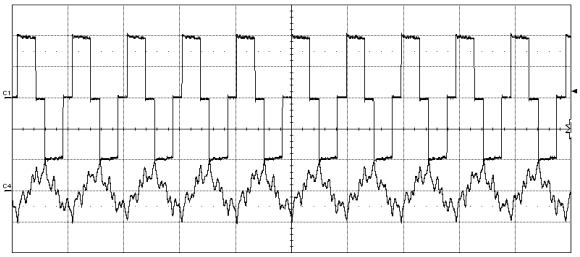

(a)

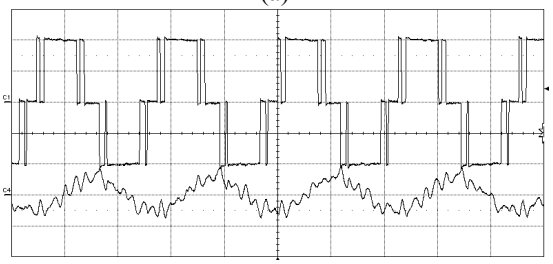

(b)

Fig. 8. The line-to-line voltage and phase current run in 130k rpm driven by (a) the six-step modulation and (b) the trapezoidal modulation

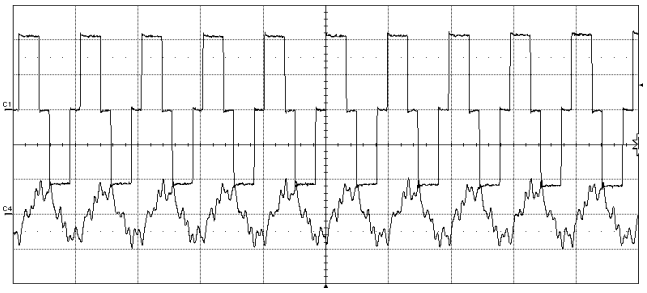

Fig. 9. The line-to-line voltage and phase current run in 300k rpm driven by the six-step modulation

4 CONCLUSION

An ultra-high speed motor driver with hybrid modulations is proposed in this paper. Due to dead-time limitation and reduction of switching power loss, the six-step modulation is considered to driver motor in ultra-high speed range. But in low speed range, the trapezoidal modulation is implemented into the driver, for the similar THD but lower DC bus voltage. Depended on the property of a motor, for different speed, the modulation method could be selected to provide better driver current and lower torque ripper.

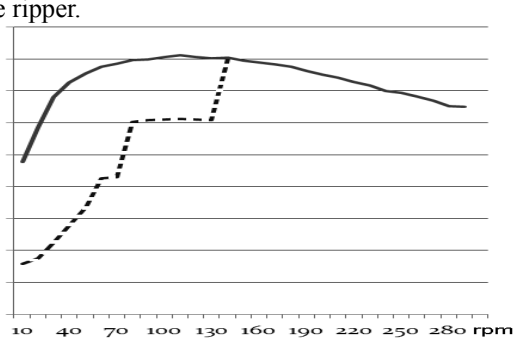

Fig. 10. The THD comparison between the six-step modulation (solid) and the trapezoidal modulation

REFERENCES

[1] Jianru Wan, Yingpei Liu, Hailiang Zhou and Runqing Bai," Direct Torque Controlled Permanent Magnet Synchronous Motor Based on Active Disturbance Rejection Controller", Advanced Science Letters. Vol. 4, pp. 2087-2091, 2011

[2] Guohai Liu and Yi Zhang, "LSSVM Inverse Control of Two-Motor Variable Frequency Speed-Regulating System", Advanced Science Letters. Vol. 4, pp. 1208-1213, 2011

[3] Chung-Wen Hung, Cheng-Tsung Lin, Chih-Wen Liu, and Jia-Yush Yen," A Variable-Sampling Controller for Brushless DC Motor Drives With Low-Resolution Position Sensors", IEEE Transactions on Industrial Electronics, Vol. 54, pp. 2846- 2852, 2007

[4] Christof Zwyssig, Simon D. Round, and Johann W. Kolar, "An Ultrahigh-Speed, Low Power Electrical Drive System", IEEE Transaction on industrial electronics. Vol. 55, No. 2, pp. 577-585, 2008

[5] Christof Zwyssig, Simon D. Round, and Johann W. Kolar, "An Ultra-High-Speed, 500000 rpm, 1 kW Electrical Drive System", Power Conversion Conference , Nagoya, Japan, April 2-5, 2007, PP.1577-1583

[6] J. Oyama, T. Higuchi, T. Abe, K. Shigematm, X. Yang, and E. Matsuo, " A trial production of small size ultra-high speed drive system", Proceedings of the IEMDC 2003, Madison, Wisconsin, USA, June 1-4, 2003, PP. 31-36

[7] A. Mishra, O. Ojo, "Analysis of an induction motor fed from a six step voltage source inverter", IEEE Proceedings of Southeastcon, Williamsburg, Virginia , USA, April 7-10, 1991, pp. 1001 – 1004

[8] John A. Houldsworth and Duncan A. Grant," The Use of Harmonic Distortion to Increase the Output Voltage of a Three-Phase PWM Inverter", IEEE Transactions on Industry Applications, Vol. IA-20, pp. 1224-1228, 1984

[9] Katsunori Taniguchi, Masakazu Inoue, Yoji Takeda, and Shigeo Morimoto, " A PWM strategy for reducing torque-ripple in inverter-fed induction motor", IEEE Transactions on Industry Applications, Vol. 30, pp. 71-77, 1994

[10] Katsunori taniguchi and Hisaichi Irie, "Trapezoidal Modulating Signal for Three-Phase PWM Inverter", IEEE Transactions on Industry Electronics, Vol. IE-33, pp. 193-200 , 1986

[11] Francisco Vargas-Merino, Mario J. Meco-Gutiérrez, Juan R. Heredia-Larrubia, and Antonio Ruiz-Gonzalez, "Low Switching PWM Strategy Using a Carrier Wave Regulated by the Slope of a Trapezoidal Modulator Wave", IEEE Transactions on Industry Electronics, Vol. 56, pp. 2270-2274, 2009

[12] Chung-Wen Hung, Tsun-Hsi Chang and Wen-Yu Chu, "A Modulation Strategy for a Super Wide Speed Range Inverter", ICIC Express Letter-An international Journal of Research and Surveys, Vol. 6, No. 3, pp.825-831, 2012

The Eighteenth International Symposium on Artificial Life and Robotics 2013 (AROB 18th '13),
Daejeon Convention Center, Daejeon, Korea, January 30-February 1, 2013

A current balance strategy for multi channel interleaved power converters

Jhih-Han Chen[1], Chung-Wen Hung[2]

Graduate School of Engineering Science and Technology[1]
Department of Electrical Engineering[2]
National Yunlin University of Science and Technology, Yunlin, R.O.C. Taiwan
(Tel: 886-5-534-2601)

wenhung@yuntech.edu.tw

Abstract: The multi-channel scheme is a more and more popular solution in high power electronic system, due to the current limitation of an inductor, the power switch in every channel, and the reduction of output voltage or current ripple. However, the current unbalance is an issue for the multiphase scheme, because the current control is independent in high number channel scheme. To solve this issue, a novel current balance control method is introduced in this paper. Compared with the traditional method which needs a current sensor in each cannel, the bill of material cost in the proposed method is much lower, because there are only three sensors in the structure: one is used to sense the total current to control the totally current, and the other two sensors are built in the first phase and the last phase for the current balance. The simulation results will be illustrated in this paper to prove this method is workable.

Keywords: multi-channel scheme, current balance, sequential trigger

1 INTRODUCTION

In high power system, the multi-phase scheme is more and more popular. This scheme could be used to solve the limitation of the components issue, and reduce the output voltage and current ripple. But, based on this multi-channel scheme, the current unbalance will be the problem. There are several papers[1] to [6] discussed how to solve the unbalance. [1] introduced a multiphase voltage-mode hysteretic controlled point-of-load (POL) dc–dc converter. This paper used a current sharing technique to implement the voltage-mode hysteretic-controlled without current reference, current compensation and loop compensation. [2] introduced a buck converter in the multiphase scheme. It is based on the mismatch-error shaping technology to implement it. And, the proposed technology is used the concept of 1-bit Delta-Sigma DAC to implement it. [3] discussed an Automatic multi-phase digital pulse width modulator Automatic multi-phase digital pulse width modulator, it implemented in the Field- Programmable Gate Arrays (FPGA). And, it used a duty cycle distribution algorithm to divide the duty cycle in each phase, and it based on this algorithm to perform the current balance. [4] discussed an active multiphase converter with mixed-signal current programmed mode controller. This research used a capacitor charge balance algorithm to implement the current balance. [5] introduced a multiphase buck converter with single controller. This circuit only used one controller with the output voltage to be the feedback. To sense the current of each phase with a current sensor, and based on it to change the ramp of carrier to modify the duty cycle of PWM. [6] introduced a multiphase DC-DC converter, it used a average current method to balance the current in each phase. And, it used the PWM of build-in peripheral in digital control processor to control each phase.

In this paper, a current balance method is presented by different beginning time and two current sensors. The sequential triggers performed the different phase delay. By the trigger sequence, the first and last phase which build the current sensor could be assigned. Next, based on that information from the first and last phase, the current balance method can be performed. The simulation results will be discussed in the section 4 and demonstrate the efficiency of the proposed method.

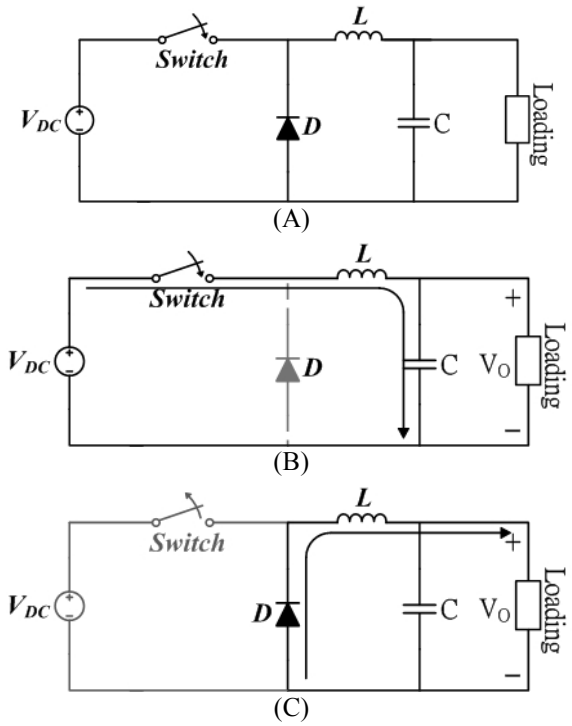

Figure 1. Buck Circuit

© ISAROB 2013

2 THE BASIC CONCEPT OF BUCK CIRCUIT AND MULTIPHASE SCHEME

2.1 Buck Scheme

The single phase buck circuit will be discussed in this subsection, then the operating concept of the multiphase scheme will be more clear. The buck circuit is illustrated in Fig. 1, (A). Depending on the switch state, this circuit could be divided into two modes, and shown in Fig. 1 (B), and Fig. 1, (C). And, the charged and discharged inductor current in these two modes could be described as (1) and (2). The inductor current, inductance, output voltage, and input voltage, duty and time are i_L, L, V_O, V_{DC}, D, and T, respectively. The (3) and (4) could be obtain from the (1) and (2). The (3) is a charged equation, in which, the relationship between the inductor current and charged time could be clearly identified. And, the (4) is obviously describing the discharged state for the inductor current.

$$\frac{di_L}{dt} = \frac{\Delta i_L}{\Delta t} = \frac{\Delta i_L}{Dt} = \frac{V_{DC} - V_O}{L} \tag{1}$$

$$\frac{\Delta i_L}{\Delta t} = \frac{\Delta i_L}{(1-D)T} = -\frac{V_O}{L} \tag{2}$$

$$\Delta i_{L(on)} = \left(\frac{V_{DC} - V_O}{L}\right)DT \tag{3}$$

$$\Delta i_{L(off)} = -\left(\frac{V_O}{L}\right)(1-D)T \tag{4}$$

Based on the (1) to (4), the operating concept of inductor current of buck circuit can be understood.

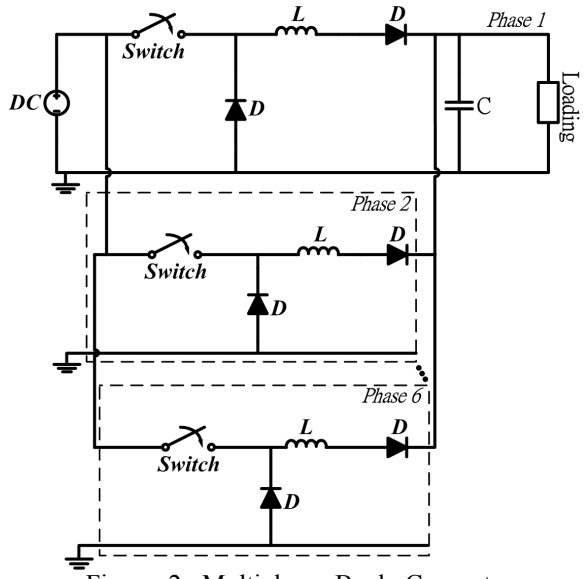

Figure 2. Multiphase Buck Converter

2.2 Multiphase Scheme of Buck circuit

The multiphase scheme is shown in fig. 2. This scheme is a parallel structure consists with more than two buck circuits. However, the output capacitor useds the same component, and input power is the same source. The Fig. 2 shows a 6 phases parallel scheme. The control method of this multi-channel scheme is called an interleave technique, which is used to turned on power switch of each phase in the same duty, but the turn-on timing of each switch are different. To perform the operation of the interleave structure above, a single controller is to used to handle all phase circuit.

Based on this structure, there are some obviously questions should be considered, like the current balance issue. The traditional method would sense each phase inductor current. For example, if this is a 6 phases scheme, it will need 6 current sensors. For approaching the current balance and reducing the cost, a low cost current balance strategy which is proposed to overcome the balance problem is proposed in this paper.

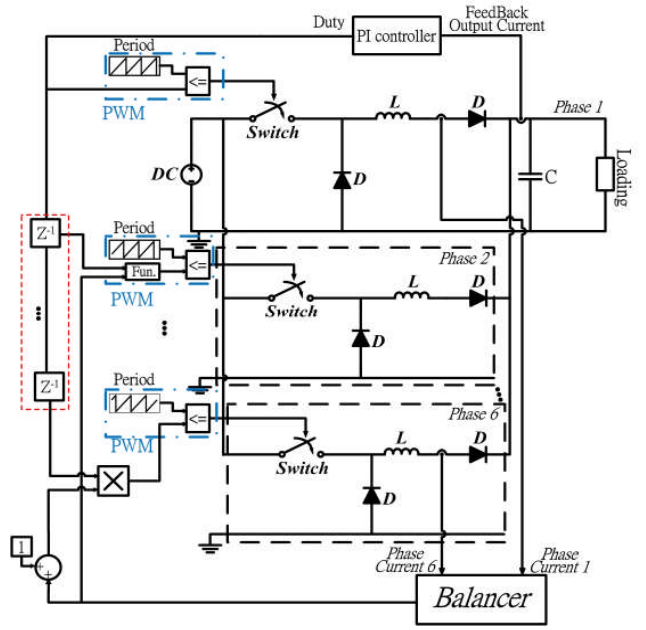

Figure 3. Diagram of System Block

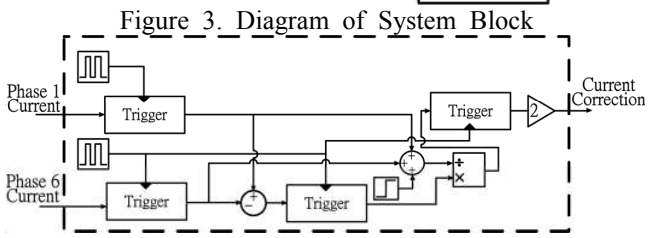

Figure 4. The block diagram of Balancer

3 CURRENT BALANCE METHOD FOR LOW COST SOLUTION

3.1 Current Balance Method

The proposed method for the current balance is a low cost strategy. Compared with traditional method, this current balance method only costs three sensors for sensing inductor current. This current balance method could be divided into two parts: sequential trigger technique and a balancer.

The Sequential trigger technique. The purpose of sequential trigger is used to perform the sequentially start timing of current phases. And, this technique is used to avoid the forward trigger issue of last phases. When the beginning of the system, the duty cycle obtains from the PI

controller will be very large even close to 80% or much more. Because, the feedback signal of inductor current is very small. This situation could cause the conduction of first and last phases in the high number phase system. This forward trigger problem will cause unexpected situation of phase current which situation will be shown in sec. 4. The sequential trigger is performed by adding phase delay to the duty cycle. The phase delay time is depended on the number of the phase.

The balancer. Due to the start timing of conduction of every phase is different. The current is also non-uniform when steady state. The inductor current of every phase is should be the arithmetic progression, and the balancer uses the average of the first and last phase to calculate the adjusted proportions of the duty cycle for every phase. Then, the duty cycle is multiplied by the adjusted proportion to get a compensational duty cycle for every phase. The balance of phase current will be approached.

3.2 Simulation structure

The simulation scheme is illustrated in Fig. 3. This schematic consists of main circuit, proportional integration (PI) controller, PWM, balancer block and the function block that is used to generate adjusted duty cycle of PWM. The main circuit is a multiphase buck converter that has already discussed in section II. There is only single controller to regulate each phase circuit in this study, and the feedback signal is the total current. The PWM modulation which duty cycle is from the PI controller is used to perform the conduction time of the switches. However, the duty cycle in each phase will be delivered at different timing with the sequential trigger. And, the sequential trigger is implemented by delay block Z^{-1}, as shown in the box of dash line in the Fig. 3. Next, the balancer block is the most important part in this research. This block is used to generate the duty compensation by the first and last phase current. The balancer block diagram is shown in the Fig, 4. This block produces a total compensation ratio which will be used to adjust the duty of every phase in function block. Last, the function block is used to generate the adjusted duty cycle of PWM is shown in the dot-dash line box of the second PWM in the Fig. 3. And, this function block could be described as (5). The D_{PI} is the duty cycle from the PI controller. The $R_{compensation}$ is the total compensation ratio from the balancer. The $D_{NewDuty}$ is a calculation result that is used to be a new adjusted duty cycle of PWM. The P_i is a proportion that is depends on the ordinal number of phase circuit.

$$D_{NewDuty}=D_{PI}*(R_{compensation}*P_i+1) \quad (5)$$

4 SIMULATION RESULTS

Simulation results are discussed in this section. The environment of the simulation is Matlab/Simulink. The specification of the system is described as below:

Input voltage = 48V
Output voltage = 15V
Output current = 60A.

This simulation could clearly illustrate the circuit function, as shown in the Fig. 5 to 10. The Fig. 5 and Fig. 6 show the inductor current of the multi-channel scheme without the sequential trigger technique, as discussed in the section 3.1. The Fig. 7 to Fig. 10 are the inductor current of each channel with the proposed current balanced method, the two enlarge figures and the balanced result, respectively. To compare with the Fig. 5 to Fig. 8, the proposed method could be demonstrated the correction impression is very well. And, the inductor current of each phase can be asthmatic progress by the sequential trigger technique. The effect of the current balanced method is very good, and it only cost 0.8ms for balanced current. The balanced processing and result are shown in the Fig. 9 and Fig. 10.

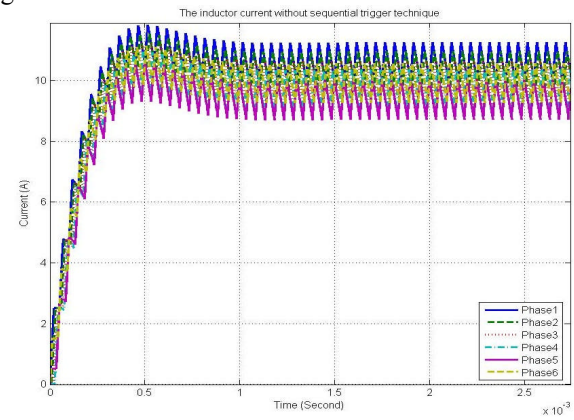

Figure 5. The inductor current of each phase without the sequential trigger

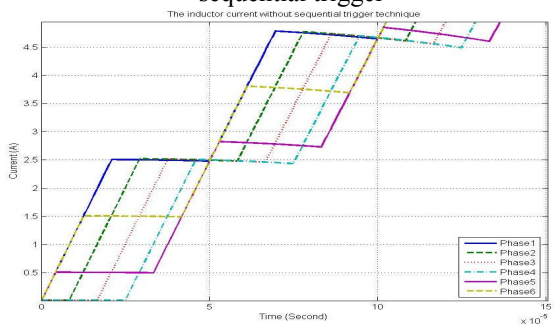

Figure 6. The enlarge figure of inductor current without the sequential trigger

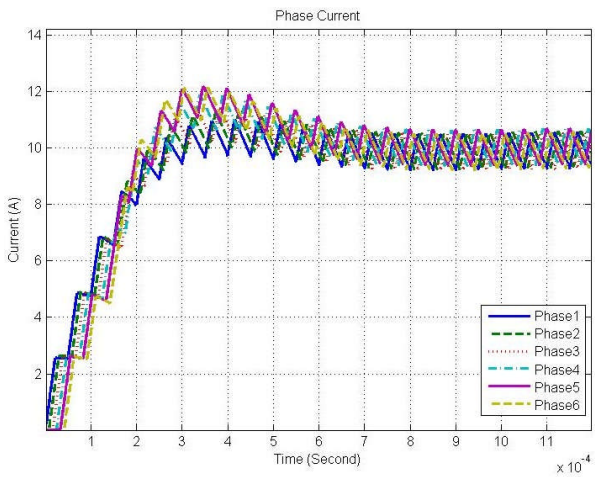

Figure 7. Phase current of each phase by the proposed current method

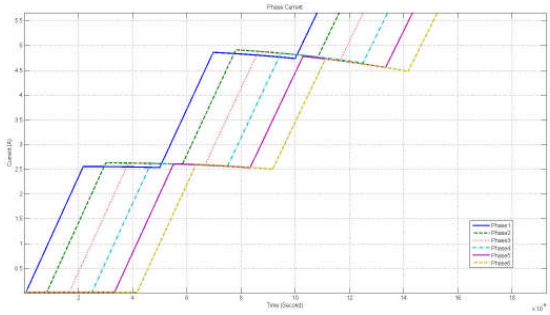

Figure 8. Enlarge figure of the beginning timing of the inductor current.

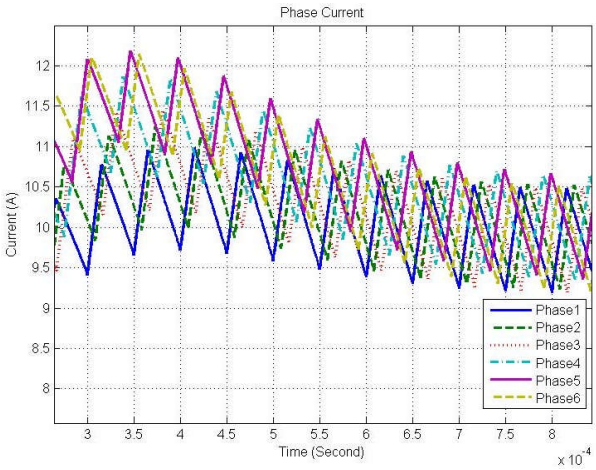

Figure 9. Enlarge figure of current balanced processing.

According to these simulation results, this multiphase buck converter with the current balance method is proved workable, and these methods are also demonstrated that could be implemented in physical circuit and the performance is well.

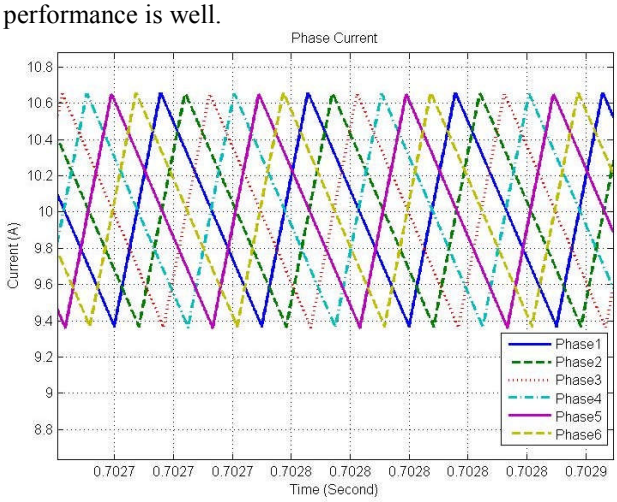

Figure 10. The result of the balanced current

5 CONCLUSION

A current balance method is proposed in this paper for the multiphase buck converter. This proposed balance method is consisting with a sequential trigger technique and a balancer. The sequential trigger technique successfully avoids the forward trigger issue of last phases and reduces the unexpected situation of the multiphase scheme. The balancer accomplishes the current balance goal by the average of the first and last phase. And, this current balance method also effectively reduces the current sensor numbers. It only costs three current sensors for implementing the current balanced. One is utilized to be the current feedback sensor for sensing the total current. And, the other two sensors are placed for sampling the first and the last phase circuit for performing the current balance. Next, the simulation results can show and demonstrate the current balance method and this simulation scheme is workable.

REFERENCES

[1] J. Abu-Qahouq, Hong Mao, I. Batarseh, "Multiphase Voltage-Mode Hysteretic Controlled DC–DC Converter With Novel Current Sharing", IEEE Transactions on Power Electronics Vol. 19, Nov. 2004, PP. 1397 – 1407.

[2] M. Rodriguez, P.F. Miaja,J. Sebastián, D. Maksimovic, "Mismatch-Error Shaping-Based Digital Multiphase Modulator", IEEE Transactions on Power Electronics, Vol. 27, April 2012, pp. 2055 – 2066 .

[3] S. Effler, M. Halton and K. Rinne, "Automatic multi-phase digital pulse width modulator", 2010 Twenty-Fifth Annual IEEE Applied Power Electronics Conference and Exposition (APEC), 21-25 Feb. 2010, pp. 1087 – 1092.

[4] J. Alico, A. Prodic, "Multiphase Optimal Response Mixed-Signal Current- Programmed Mode Controller" Annual IEEE Applied Power Electronics Conference and Exposition (APEC), Palm Springs, CA, Feb. 2010, pp. 1113 - 1118 .

[5] Yu-Ping Huang, Yi-Ping Su, Yu-Huei Lee, Kuan-Yu Chu, Chun-Jen Shih, Ke-Horng Chen, Ming-Jhe Du, Shih-Hsien Cheng "Single Controller Current Balance (SCCB) Technique for Voltage-Mode Multi-Phase Buck Converter", IEEE International Symposium on Circuits and Systems (ISCAS), Rio de Janeiro, May 2011, pp. 761 - 764 .

[6] Guo Guoyong, Shi Bingxue, "Design of multi-phase DC-DC converter with averaged current sharing control", 5th International Conference on ASIC, Vol. 1, Oct. 2003, pp. 522 - 525.

© ISAROB 2013

The Eighteenth International Symposium on Artificial Life and Robotics 2013 (AROB 18th '13),
Daejeon Convention Center, Daejeon, Korea, January 30-February 1, 2013

Automatic identification of 3-D shape of head for wig manufacture

Yonghu Zhu[1], Yoshiaki Adaniya, Tsujino Kazuhiro, and Cunwei Lu[2]

Fukuoka Institute of Technology, Japan
(Tel: +81-92-606-3578, Fax: +81-92-606-0726)

[1] mam12004@bene.fit.ac.jp
[2] lu@fit.ac.jp

Abstract: When making an order-made wig, in order to reduce cost, production of wig is performed in overseas factory where personnel expenses are usually cheap. In order to send the information of customer's head to the overseas factory, a wrap-model is often used. There are two problems in this method, one is that the production cycle time is too long, and another is that when the wig is damaged it is inconvenient for re-production. The aim of our research is to propose a wig manufacture system whose production cycle is short and re-production of the wrap-model is convenient. The key point is using three-dimensional (3-D) information instead of the customer's wrap-model. We use the 3-D image measurement method based on Optimal Intensity-Modulation Pattern (OIMP) projection technique to obtain each side of the wrap-model, and then synthesize it to represent the entire wrap-model. Then we send the 3-D information of the wrap-model to overseas factory by using the internet. In the overseas factory, according to the 3-D information of the wrap-model, we select one mold which is the fittest to produce the wig. Now, we are developing the application of the proposed method.

Keywords: Three-dimension measurement, Optimal Intensity-Modulation Pattern, wig manufacture, wrap-model, mold.

1 INTRODUCTION

For young ladies and famous actors who always need to change their fashion style in different places, the wear of wig is high, which will make them more confident and beautiful. When people get older, the hair will become less and less. In addition, the cancer patients who are undergoing the chemical treatment will cause a certain degree of hair loss. In these conditions, a wig is also necessary. The wig which is commercially available in a supermarket is cheap, but it is difficult to accord with the shape of the head accurately. The order-made can make a wig according to the shape of the user's head, but it is expensive and the production cycle is long.

When making a wig, besides the information of the size, we also need to know the property of the hair, the position of the whorl, the flow direction of the hair and the hair shades. In order to make the wig cost cheaper, almost all the production makers usually use the overseas factory instead of the factory in Japan. In order to send the information of customer's head to the overseas factory, a wrap-model is often used. In the overseas factory according to the sent wrap-model to select the fittest mold to make the wig, and send the completed wig back to Japan and reach the customer.

This method has two deficiencies. First of all, this production method will have to spend 30 days to finish the cycle, so the time needs to be shortened. It will take a long time for the consumers to decide whether to put on a wig for the first time. However, they hope to obtain the wig as soon as possible when decide the purchase once and ask it for production. So, shortening the time is necessary during the period of the production process. Secondly, when the wig is damaged the re-production of the wrap-model is inconvenient. As for the use of the wig, the customers do not want to be noticed by neighboring acquaintances or a friend. Therefore a lot of customers think that when the damage of the wig occurs they cannot go to the company or the school. Furthermore, the wig is used every day, so it should be re-purchased every 2 or 3 years. It is better to use the wrap-model which is the same as is produced several years ago. However, the material of the wrap-model is plastic film, and it's easy to become shrinkage and transformation by a secular variation. The re-production of the wrap-model is necessary and the customers have to come to the store again.

The target of our research is to solve the two problems. That is to shorten the time and to make the re-production more convenient. And in this way, the satisfaction of the customer could be improved.

The key point is using three-dimensional (3-D) information instead of the customer's wrap-model. There are many methods in 3-D measurement field. Such as the stereo vision method, it uses two cameras, just as the eyes of human. With the triangulation principle, the 3-D information was calculated. The system of stereo vision

© ISAROB 2013

measurement method contains the camera and computer, and it has a wide range of measurement. However, when do the measurement, because it is difficult to obtain the character information, the reliability is very low. And it is also very hard to be automated. The Kinect developed by Microsoft could also get the color image and depth of the objects. The core of it is regardless of ambient lighting conditions, you can let Kinect COMS IR sensor of the sensible world. This sensor to sense the environment through the black and white spectrum: pure black on behalf of infinity, white represents infinity. Grey area between the black and white object that corresponds to the physical distance sensors. It collects every point within the vision, and form the environment around a picture that represents the depth of field images. Sensor to generate depth of field image flows at a rate of 30 frames per second, real-time 3-D rendering environment. However, the error of Kinect is larger than 1mm, it is cheap and well used in moving object. But what we are measuring is the Wrap-model, which record the human head's size and form, needs higher precision.

In this paper, we use the 3-D image measurement method based on Optimal Intensity-Modulation Pattern (OIMP) projection technique to obtain each side of the wrap-model, and then synthesize it to represent the entire wrap-model. Then we send the 3-D information of the wrap-model to overseas factory by using the internet. In the overseas factory, according to the 3-D information of the wrap-model, we select one mold which is the fittest to produce the wig.

2 CONFIGURATION OF MANUFACTURE SYSTEM

There are three parts of the configuration of the manufacture system. First we use the 3-D measurement to get the 3-D image of the wrap-model. Then take photos from multiple aspects to synthesis the images, so that we get the whole image of the wrap-model. Finally according to the 3-D image of the wrap-model, we will choose the fittest mold by using the software.

2.1 Improvement of the production process

Now, the production of the wig is like this, which can be clear seen in **Fig. 1**. First we record the size of the wig and other information of the hair by using the wrap-model which is made of plastic film (Step 1). Then we transport the wrap-model to the Indonesian manufacturing facility to make the wig (Step 2). According to the wrap-model, we select one mold which is the fittest (Step 3). After that we will make the wig by using the mold (Step 4). Finally we send the completed wig back to the customer in Japan (Step 5).

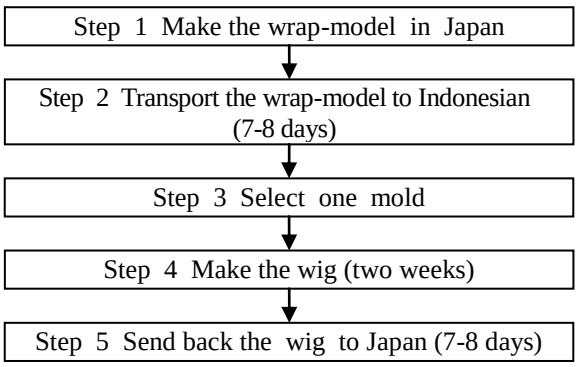

Fig. 1. The production flow of the wig

There are two problems in this method, one is that the production cycle time is too long, and another is that when the wig is damaged it is inconvenient for re-production. The aim of our research is to propose a wig manufacture system whose production cycle is short and re-production of the wrap-model is convenient. In order to achieve the goal of our study, we propose our method that is shown in **Fig. 2**. Instead of transport the wrap-model to overseas, we just take several minutes to measure the 3-D information of the wrap-model in Japan, and then take several seconds to send the 3-D information to Indonesian. Then we use the sent 3-D information to select the mold. In this way, the time of 7-8 days lost in transportation of the wrap-model can be saved. Therefore, the production cycle is shortened by 25%. In addition, we can make a database of the wig production information so that the re-production is convenient. This also

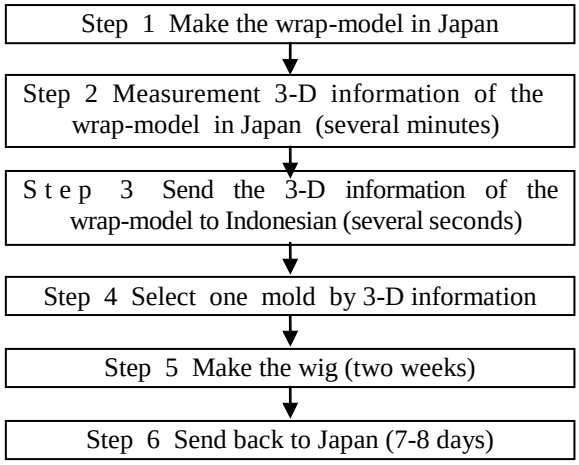

Fig. 2. The production flow of our method

© ISAROB 2013

solves the second problem. As we can see from this method, how to measure the 3-D information of the wrap-model is become quite important.

In this study, by using the 3-D image measurement, we could find out the fittest mold to produce the wig for the elderly people and the cancer patients who are undergoing the chemical treatment and the necessity for wear of wig is high. We measure 3-D information of shapes of user's head in Japan and send the result to the overseas factory using the Internet. At the overseas factory, according to the 3-D information, we choose one mold which resembles the form of a user's head most, from the inside of tens of thousands of mold, to produce the suitable wig.

2.2 3-D measurement system

When we say 3-D measurement, it means that we measure the shape or the position of the target object. Now, in a lot of field the 3-D measurement is widely used, from topographic survey, building surveying to products, the human body and semiconductor industry and so on. 3-D is very practical. In addition, as the rapid development of information process and image process, in the research of machine vision, the 3-D measurement method which has high-speed, high precision and adaptability was needed.

In order to obtain the 3-D information of wrap-model, we use the 3-D image measurement technique based on pattern projection method. The composition graph of measurement system is shown in **Fig. 3**. We send the pattern by using the projector, according to the projection pattern, we can make a recognition of the stripes, and correspond the pattern between the original and the photo taken by the camera, after that we can get the 3-D image of the wrap-model [3].

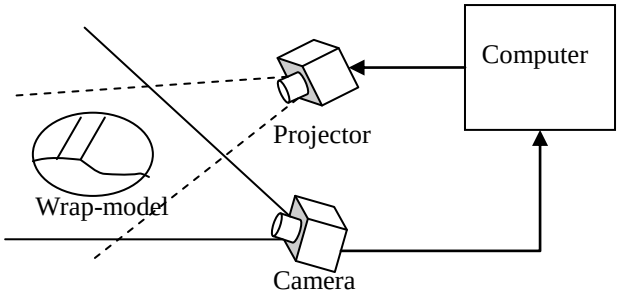

Fig. 3. Measurement system

The optimal intensity-modulation pattern projection method is a technique for improving the accuracy of the stripes address detection by optimizing the combination of stripes intensity of the projected pattern, and maximizing the intensity differences between adjacent stripes. The function is defined in cases like that when the projection light intensity difference of the stripes strength distribution combination $(I_1, I_2, \ldots I_N)$ is at the maximum, evaluation function $d(I_1, I_2, \ldots I_N)$ is also at the maximum.

$$d(I_1, I_2, ..., I_N) = \sum_{i=M+1}^{N} \sum_{j=1}^{M} k_j \left| I_i - I_{i-j} \right| \tag{1}$$

Here, *kj* is a weight factor. *M* is width of the filter on which evaluation function has been set. **Fig. 4.** shows the example of the projected pattern generated with formula 1[6].

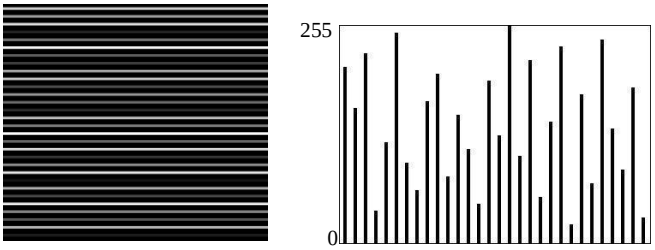

Fig. 4. Optimized pattern

As we can see from **Fig. 5, Fig. 5.(a)** shows the original image of the wrap-model taken by the camera. **Fig. 5. (b)** is the optimized pattern projected by the projector. And **Fig. 5. (c)** is the initial image of observation pattern image. After doing the image processing, we get the extracted pattern shown in **Fig. 5. (d)**. As we compare the stripes of the optimized pattern and the extracted pattern calculated by the software by using the triangulation principle, we could get the 3-D image of the wrap-model [2].

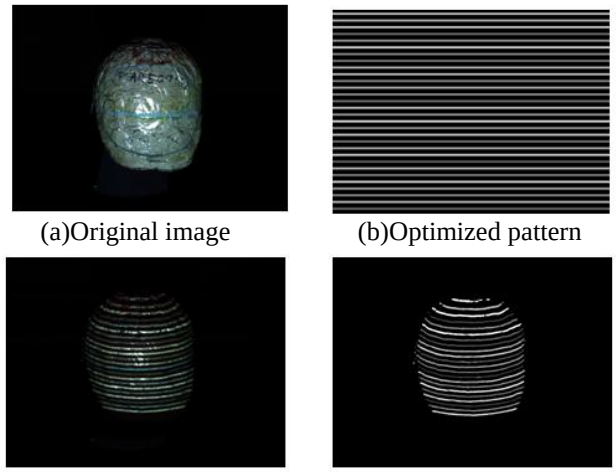

(a)Original image (b)Optimized pattern

(c)Observation pattern image (d)Extracted pattern

Fig. 5. Measurement principle

If we find out the corresponding relationship, we can use it to do the 3-D measurement with the triangulation principle, as is shown in **Fig. 6**.

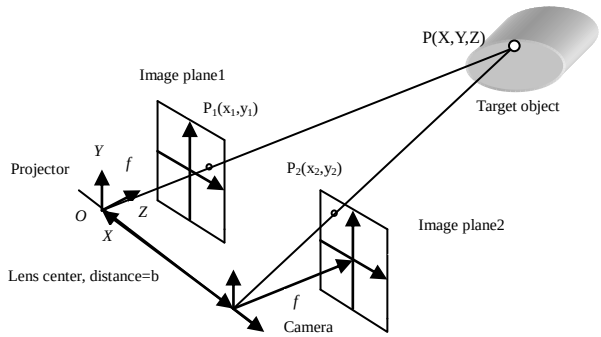

Fig. 6. Principle of calculation

$$\beta_1 = tan^{-1}(\boldsymbol{x}_1 / \boldsymbol{f}) \tag{2}$$

$$\beta_2 = tan^{-1}(\boldsymbol{x}_2 / \boldsymbol{f}) \tag{3}$$

While we find out viewing angle and observation plane coordinate, the coordinate of point P can be calculated out through triangulation principle.

$$\boldsymbol{X} = \frac{\boldsymbol{b}\boldsymbol{x}_1}{\boldsymbol{x}_1 + \boldsymbol{x}_2} \tag{4}$$

$$\boldsymbol{Y} = \frac{\boldsymbol{b}\boldsymbol{y}_1}{\boldsymbol{x}_1 + \boldsymbol{x}_2} \tag{5}$$

$$\boldsymbol{Z} = \frac{\boldsymbol{b}}{tan\,\beta_1 + tan\,\beta_2} \tag{6}$$

Because the relation of all stripes can be correctly detected by calculating the intensity value of noteworthy stripes in the observation image and adjacent stripes based on intensity change rule, this measurement method can be measured by only one projection and capturing two pictures. Therefore, it can be declared that it is a technique to achieve a high-speed measurement, and to expect the application of the measurement for the moving object possibly.

2.3 Synthesis of 3-D images

When performing 3-D measurement, since the measurement of the area can only fit into the camera in one measurement, it is not easy to get the entire circumference shape information of the object. So we need to synthesize the obtained measurement results from multiple directions. Therefore we can represent 3-D shape of the entire wrap-model.

Because 3D image of each aspect obtained is recorded in the independent coordinate system that depends on the camera respectively, it is necessary to convert coordinates into a common coordinate system. As can be seen from

Fig. 7. The relation of coordinates *Xi* in an independent coordinate system and coordinates *X'i* in a common coordinate system is like the following formula [4].

$$X'_i = RX_i + t \tag{7}$$

Here, *R* is a rotation matrix, and *t* is a translation vector. The synthesis becomes possible by calculating *R* and *t*, and doing the geometric transformation. Feature points between two 3D images are necessary to calculate *R* and *t* by at least three points. Among *R* and *t*, *t* can be easily calculated by taking the differences of coordinates of the common feature points. In this research, we have calculated each coordinate of the center of gravity from the specified common feature

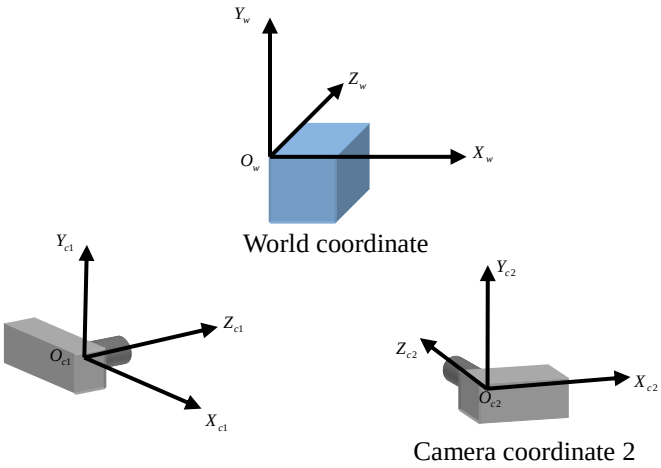

Fig. 7. World coordinate

points, and have matched them.

Consideration of measurement error, *R* is calculated as follows:

$$\sum_{i=1}^{n} \left\| X'_i - RX_i \right\|^2 \rightarrow \min \tag{8}$$

According to formula 8, we can get the following which is the same meaning, as can be calculated:

$$\begin{aligned}
&\sum_{i=1}^{n}\left(\left\|X'_i\right\|^2 - 2(X'_i, RX_i) + \left\|RX_i\right\|^2\right) \\
&= \sum_{i=1}^{n}\left\|X'_i\right\|^2 - 2\sum_{i=1}^{n}(R^T X'_i, X_i) + \sum_{i=1}^{n}\left\|RX_i\right\|^2 \\
&= \sum_{i=1}^{n}\left\|X'_i\right\|^2 - 2Tr[R^T \sum_{i=1}^{n} X'_i X_i^T] + \sum_{i=1}^{n}\left\|X_i\right\|^2 \\
&= \sum_{i=1}^{n}\left\|X'_i\right\|^2 - 2Tr[R^T N] + \sum_{i=1}^{n}\left\|X_i\right\|^2
\end{aligned} \tag{9}$$

Here, *n* is the number of common feature points, when the correlation matrix is as follows:

$$N = \sum_{i=1}^{n} X'_i X_i^T \tag{10}$$

© ISAROB 2013

The formula 8 is the same as solving the following formula:

$$Tr[R^T N] \rightarrow \max \tag{11}$$

We have solved this by using method of the quaternion [1].

The quaternion can represent rotation with four components, as a composite of a scalar and an ordinary vector, or as a complex number with three different imaginary parts.

$$q = (q_0, q_1, q_2, q_3) = q_0 + q_1 i + q_2 j + q_3 k \tag{12}$$

The rotation matrix is represented by the quaternion as follows:

$$R = \begin{bmatrix} q_0^2 + q_1^2 - q_2^2 - q_3^2 & 2(q_1 q_2 - q_0 q_3) & 2(q_1 q_3 + q_0 q_2) \\ 2(q_1 q_2 + q_0 q_3) & q_0^2 - q_1^2 + q_2^2 - q_3^2 & 2(q_2 q_3 - q_0 q_1) \\ 2(q_1 q_3 - q_0 q_2) & 2(q_2 q_3 + q_0 q_1) & q_0^2 - q_1^2 - q_2^2 + q_3^2 \end{bmatrix} \tag{13}$$

The rotation matrix R is obtained by the unit eigenvector to the maximum eigenvalue of four-dimensional matrix when $Tr[R^T N]$ is maximized [5].

$$\tilde{N} = \begin{bmatrix} N_{11} + N_{22} + N_{33} & N_{32} - N_{23} & N_{13} - N_{31} & N_{21} - N_{12} \\ N_{32} - N_{23} & N_{11} - N_{22} - N_{33} & N_{12} + N_{21} & N_{31} + N_{13} \\ N_{13} - N_{31} & N_{12} + N_{21} & -N_{11} + N_{22} - N_{33} & N_{23} + N_{32} \\ N_{21} - N_{12} & N_{31} + N_{13} & N_{23} + N_{32} & -N_{11} - N_{22} + N_{33} \end{bmatrix} \tag{14}$$

Thus, due to calculating rotation matrix, it is possible to synthesize 3D image.

2.3 Choice of mold

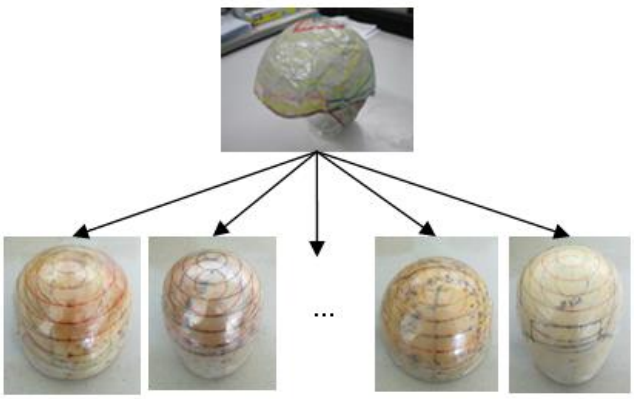

Fig. 8. Choose the mold

When producing the wig in overseas factory, we choose one mold which resembles the form of the user's head most, from the inside of tens of thousands of mold, to produce the suitable wig. As can be seen from **Fig. 8**.

First of all, we find out the highest point of the mold, then according to this point, draw 6 curves on the surface of the mold whose distance to the highest point are respectively 2cm, 4cm, 6cm, 8cm, 10cm, 12cm. In the same way, by using the 3-D image information on computer, we find out the 6 curves on the surface of the wrap-model. By comparing the length of the curves, we find out which mold have the smallest error from the wrap-model. We will use this mold as the fittest to produce the wig.

3 EXPERIMENTS

In this study, the purpose of the experiment is to find out the fittest mold by using the measured 3-D information of the wrap-model. First of all, we use the 3-D shape measurement system to obtain the image of the wrap-model, then synthesis the images to get the entire shape information. According to the 3-D information of the wrap-model we could select the fittest mold to make the wig.

3.1 synthesis of the wrap-model

In this experiment, we measured from the direction of the front, rear, right and left and right above to obtain the three-dimensional information of the entire wrap-model.

It can be seen from the results shown in **Fig. 9** that the wrap-model could be synthesized correctly and 3-D information of the entire wrap-model could be obtained.

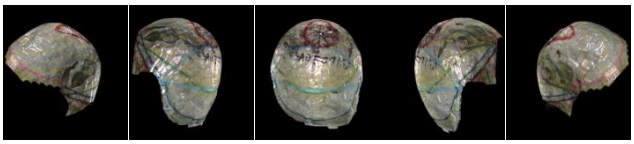

Fig. 9. Synthesis wrap-model

3.2 Choose the mold

Now we get the 3-D image of the wrap-model, then we will use the software to calculate the data of the image to find out the fittest mold. The method is that we find out the highest point of the wrap-model, and according to this point, draw 6 curves on the surface of the wrap-model whose distance to the highest point are respectively 2cm, 4cm, 6cm, 8cm, 10cm, 12cm. After that we compare the form and size between the 3-D image of the wrap-model and the mold, to find out the fittest mold. We will use this mold as the fittest to produce the wig. As can be seen from **Fig. 10**, **Fig. 10(a)** is the flat figure and **Fig. 10(b)** shows the space curve length, the sixth curve is broken so it can't be used.

© ISAROB 2013

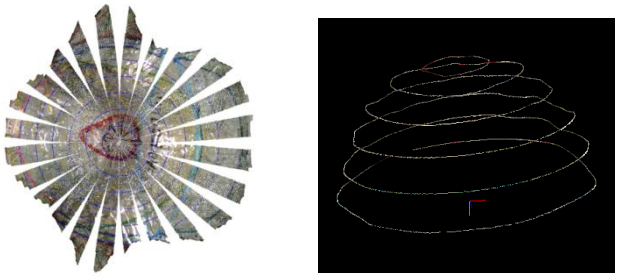

(a) Flat figure (b) Space curve length

Fig. 10. Curves on the surface of the wrap-model

After that we compare the data between the wrap-model detected by the software and the mold detected by hand, to find out the fittest 3 mold from 100 mold models. The result can be seen from **Table 1**.

Table 1. Wrap-model and the fittest three molds

Lap	Wrap-model (mm)	The first fittest(mm)	The second fittest(mm)	The third fittest(mm)
1	118.9	123	123	122
2	240.7	239	241	239
3	339.5	338	339	340
4	417.4	418	420	419
5	473.5	473	472	471
6	/	502	509	501
error	/	0.53%	0.56%	0.59%

As we can see from the result, the error is very small, but actually we could not always find out the fittest mold, sometimes the mold and the wrap-model don't fit quite well. As we can see from **Fig. 11**, this mold fit quite good except the back side of the mold.

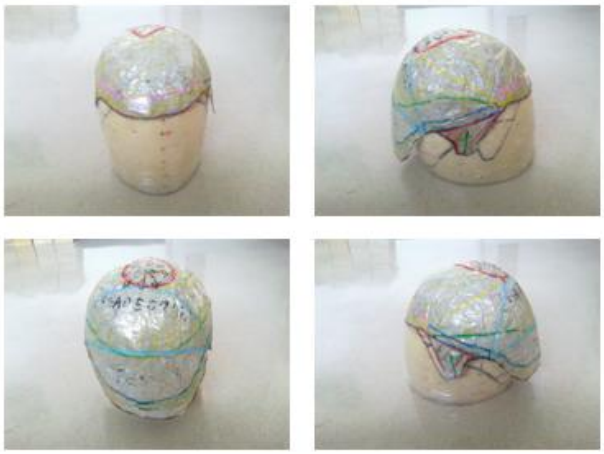

Fig. 11. The result

4 CONCLUSION

In this study, we propose a new manufacture system whose production cycle is short and re-production of the wrap-model is convenient. The key point is using 3-D information data instead of the customer's wrap-model. In order to obtain the 3-D information of wrap-model, we use the 3-D image measurement method based on Optimal Intensity-Modulation Pattern (OIMP) projection technique. When performing 3-D measurement, since the measurement of the area can only fit into the camera in one measurement, it is not easy to get the entire circumference shape information of the object. So we need to synthesize the obtained measurement results from multiple directions. Therefore we can represent 3-D shape of the entire wrap-model. Then we send the 3-D information data of the wrap-model to overseas factory by using the internet. In the overseas factory, according to the 3-D information of the wrap-model, we select one mold which is the fittest to make the final wig.

But there are also problems that the mold and the wrap-model don't fit quite well actually. Maybe we should change the curves we select in the further study.

REFERENCES

[1] B. K. P. Horn: "Closed-Form Solution of Absolute Orientation Using Unit Quaternion," JOSA A, Vol. 4, No. 4, 1987.

[2] C. Lu and L. Xiang: "Optimal Intensity-Modulation Projection Technique for Three-Dimensional Shape Measurement," Applied Optics-IP, Vol. 42, No. 23, pp. 4649-4657, 2003.

[3] C. Lu and G. Cho: "Projection pattern intensity control technique for 3-D optical measurement," Optics Express, Vol. 13, No. 1, pp. 106-114, 2005.

[4] K. Kanatani: "Unbiased Estimation and Statistical Analysis of 3-D Rigid Motion from Two Views," IEEE Trans. Patt. Anal. Machine Intell., vol. 15, No. 1, pp. 37-50, 1993.

[5] I. Shimizu and K. Deguchi: "A method to register multiple range images from unknown viewing directions," Proc. MVA'96, pp. 106-114, 1996.

[6]C. Lu, G. Cho and J. Zhao, "Practical 3-D Image Measurement System using Monochrome-Projection Color-Analysis Technique," Proc. of the 7th IASTED International Conference on computer grapics and imaging (CGIM 2004), pp.254-259, Kauai, Hawaii, USA, August, 2004.

© ISAROB 2013

The Eighteenth International Symposium on Artificial Life and Robotics 2013 (AROB 18th '13),
Daejeon Convention Center, Daejeon, Korea, January 30-February 1, 2013

Retrieval method for augmented reality objects based on color impression

Kazunori Nakamura, Kaoru Sugita, and Masao Yokota

Fukuoka Institute of Technology, Japan
(Tel: 81-92-606-4965, Fax: 81-92-606-4965)

mgm11010@bene.fit.ac.jp, sugita@fit.ac.jp, yokota@fit.ac.jp

Abstract: In this paper, we propose a retrieval method for Augmented Reality (AR) objects based on color impression. In this method, AR objects can be retrieved by *Kansei* words and superposed on a live video at the positions specified dynamically by users in use of special markers. The retrieval method employs color information such as RGB value and ratio of the color in the texture. We are implementing a virtual clothes fitting software as a smart-phone application.

Keywords: augmented reality, *Kansei* retrieval method, color impression

1 INTRODUCTION

Nowadays, Augmented Reality (AR) has become a popular technology with many applications on PCs, tablets and smart phones. Also, there have been many studies conducted on AR technologies to augment live videos with artificial objects [1-3]. However, these studies are to treat objects registered in advance only and therefore they are not dynamically replaceable to user's order.

On the other hand, several methods have been proposed to intuitively retrieve images from the viewpoint of *Kansei* engineering [4-7]. Most of them are so-called *Kansei* retrieval methods where images are retrieved by affective words representing characteristics of objects such as shape and color.

Considering these facts, we have developed a *Kansei* retrieval method based on color impression. In this paper, such human intuitive and subjective emotion is statistically quantized via affective adjective phrases such as elegant and pretty [8]. The remaining sections are as follows. Firstly, Section 2 digests our extension of AR technology and Section 3 details the proposed method for dynamic AR object retrieval based color impression. In Section4, the *Kansei* retrieval method is designed for computer implementation. The development environment and the applications are presented in Section 5. Lastly, Section 6 discusses and concludes this paper.

2 The Expansion of AR Technology

In the traditional AR technologies, neither content providers nor users could exchange any desired object after release of AR contents. The AR can be categorized as 4 types as shown in Table 1.

(1) **Static AR (SAR)** is the traditional AR only supporting one object at one mark.

(2) **Provider Oriented AR (POAR)** allows only providers to exchange objects. Users can only specify the places of AR objects.

(3) **User Oriented AR (UOAR)** allows users to exchange objects at markers. Providers cannot any operation.

(4) **Dynamic AR (DAR)** allows both users and providers to exchange objects using retrieval function at markers.

3 AR Object Retrieval Method based on Color Impression

In this method, an AR content is composed of a retrieved object and a live video on AR space. The user puts a marker on a certain real object to specify the display position and selects one of *Kansei* words concerning color only here as shown in Fig.1. The system retrieves its corresponding objects from the database, consisting of the following modules. Figure 2 shows their organization.

(M1) *Kansei* **Retrieval Engine** retrieves several objects with textures matching with the *Kansei* word.

(M2) Database stores markers, objects and relations between *Kansei* word and color information in RGB.

(M3) AR Space Compositor synthesizes the retrieved objects and the live video according to the pairs of marker and *Kansei* word.

Table 1. Expansion of AR technologies

	Non-exchangable by Provider	Exchangable by Provider
Non-exchangable by User	Static Augmented Reality (Traditional Technology)	Provider Oriented Augmented Reality
Exchangable by User	User Oriented Augmented Reality	Dynamic Augmented Reality

© ISAROB 2013

4 *Kansei* Retrieval Method

Conventionally, it is difficult for users to obtain desired objects or data from databases by using keywords or indices because these are prepared by the system designers and influenced by their subjectivities. Considering this fact, we have employed the *Kansei* retrieval method based on color impression. This method evaluates an object *O* by a *Kansei* word *Key* formalized as Equation (1).

$$F_{uo}(Key, O)=U(Key) \circ F_o(Key, O) \quad (1)$$

where

$F_{uo}(Key, O)$: Calculated value for the pair of *Kansei* word *Key* and object *O*,

$U(Key)$: Calculated value of subjectivity for *Kansei* word *Key*,

$F_o(Key, O)$: Statistic value for the pair of *Kansei* word *Key* and object *O*.

The color impression is quantized in terms of adjective phrases associated with a certain statistics [8]. In this study, for *Key*, 16 adjective phrases were employed considering their independency in color impression as shown in Fig.1. On the other hand, *O* is an element belonging to the set of objects same in shape and different in texture color as shown in Fig.3. Each *O* is translated into a vector representing area ratios of all the colors involved in advance to compute the correlation value with the *Key* as shown in Fig.4.

The value $U(Key)$ is calculated based on statistics of users' *Knasei* evaluation of retrieved objects. The value $F_o(Key, O)$ is given by (2).

$$F_o(Key, O)=F_{ilt}(F_c(Key),F_s(O),k_o) \quad (2)$$

where

$F_c(Key)$: Set of objects retrieved by *Key*,

$F_s(O)$: Set of objects retrieved by *O*.

$F_{ilt}(F_c(Key),F_s(O),k_o)$: Set of objects with area ratios over k_0 included in both $F_c(Key)$ and $F_s(O)$.

Avant-garde	**Fresh**
Clear	**Romantic**
Sexy	**Ethnic**
Noble	**Chic**
Casual	**Wild**
Elegant	**Dandy**
Pretty	**Gorgeous**
Formal	**Sporty**

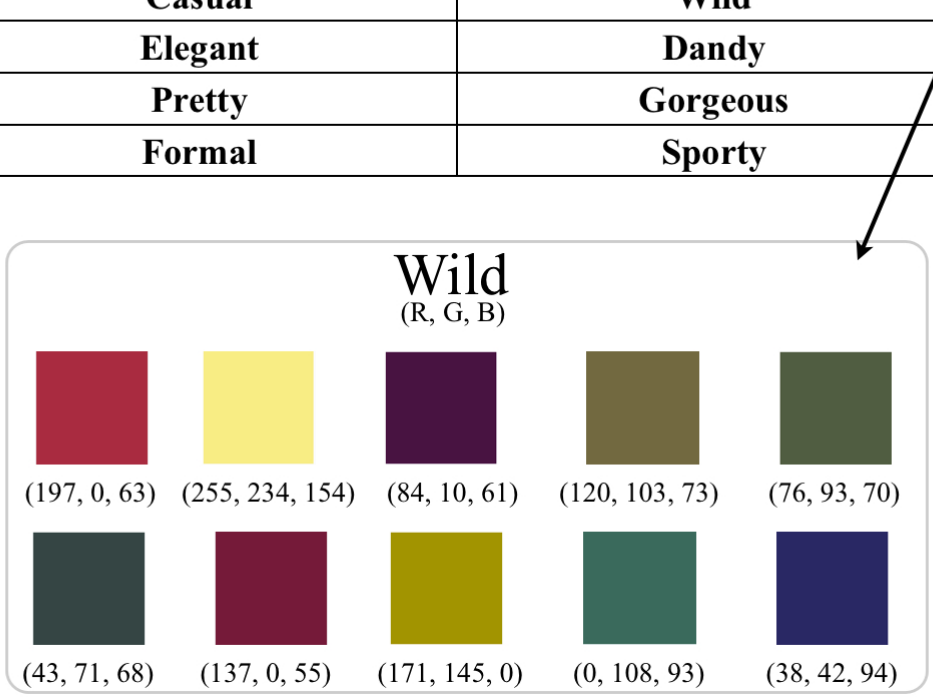

Fig. 1. Conversion of *Kansei* words based on color impression

© ISAROB 2013

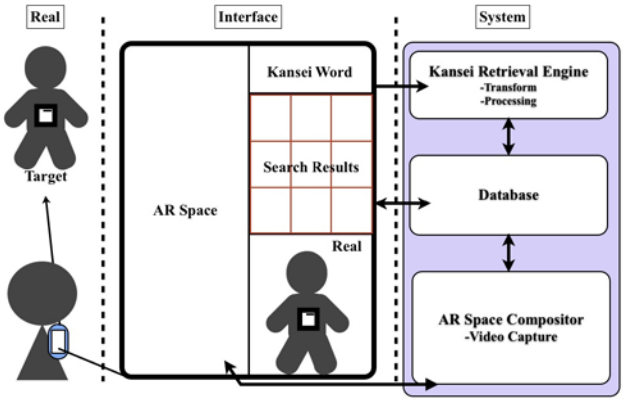

Fig. 2. AR Object Retrieval Method based on Color Impression

Fig. 3. Objects in the Database

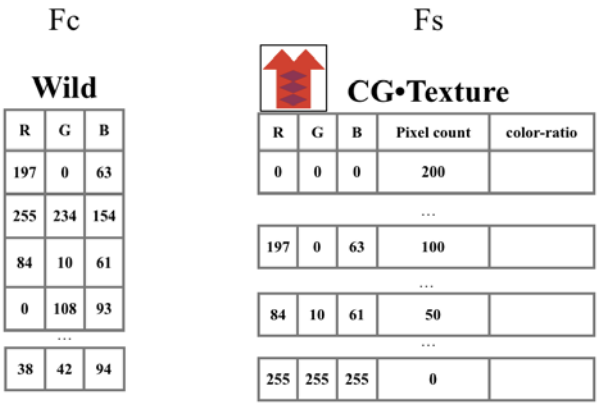

Fig. 4. Comparison in RGB between *Kansei* words and objects

5 Implementation

Our method has been implemented as a virtual clothes fitting system running on smart phones as shown in Fig.5. This system enables a user to try clothes on virtually by putting a marker on him/her and to select one among those retrieved by his/her *Kansei* word.

The software supports video capturing, AR space composition and *Kansei* retrieval configured by such modules as shown in Fig.6. The video capturing function and AR space composition are available on smart phone clients while *Kansei* retrieval works on the PC server.

The system was developed in C++ using STL, open frameworks and Magic++ as shown in Fig.7.

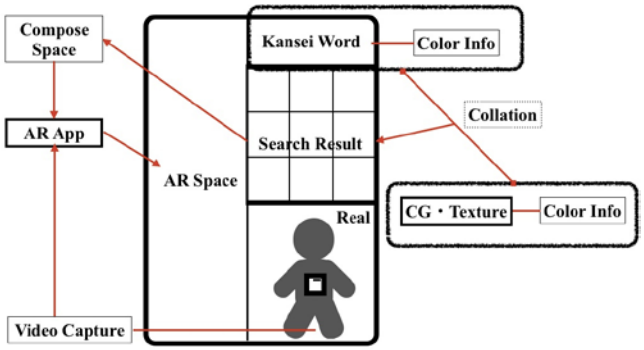

Fig. 5. The user interface of the software

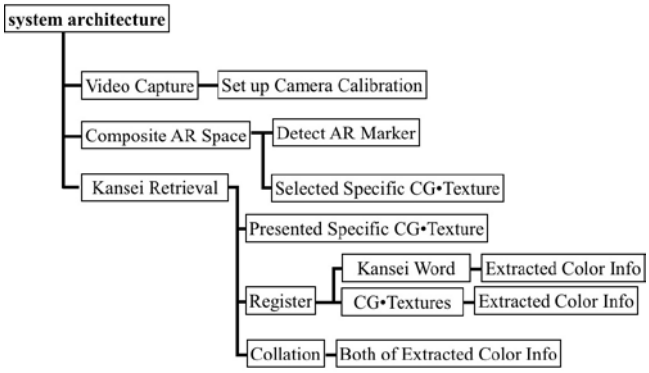

Fig. 6. Module configuration

Xcode			Database Management System
C++	Standard Template Liblary (STL)	Open frame works	Magic++
MacOS X			

Fig. 7. Software development environment

6 CONCLUSION

In this paper, we proposed a *Kansei* retrieval method for AR technology expanding from the static AR to the dynamic AR and its application. Currently, we are implementing a virtual clothes fitting software in order to adapt our method appropriate to the statistic color impression and to much more objects both in quantity and kind. In future, we will evaluate and improve our *Kansei* retrieval method enforced with user models.

REFERENCES

[1] Mark B, Hirokazu K, Ivan P (2001); The MagicBook: a transitional AR interface. Computers & Graphics 25 (2001): 745-753

[2] Hirokazu K (2002); ARToolkit: Library for Vision-based Augmented Reality (in Japanese). Technical report of IEICE PRMU 101(652): 79-86

[3] Hirokazu K, Mark B, Koichi A and Keihachiro T (1999); An Augmented Reality System and its Calibration based on Marker Tracking (in Japanese). Journal of the virtual reality society of Japan 4(4): 607-616

[4] Manabu F and Yoshitaka S (1996); *Kansei* Retrieval Method Reflecting Shape Pattern of Design Images (in Japanese). IPSJ DPSWS 96(1): 267-274

[5] Takio K, Toshikazu K, Ikumi F and Ayumi S (1992); Sense Retrieve on a Image Database of Full Color Paintings (in Japanese). IPSJ 33(11): 1373-1383

[6] Shoji H, Yukihiro I and Hiromasa N (1999); On Constructing Shape Feature Space for Interpreting Subjective Expressions (in Japanese). IPSJ 40(5): 2356-2366

[7] Kaoru S, Akihiro M and Yoshitaka S (2003); Relation Between *Kansei* Words and the Room Space in Digital Traditional Japanese Crafting System. Proc. of the International Conference on Advanced Information Networking and Applications (AINA): 159-162

[8] Shigenobu K (1990); Color Image Scale. Nippon Color & Design Research Institute Inc., ISBN-4-7700-1564-x.

© ISAROB 2013

The Eighteenth International Symposium on Artificial Life and Robotics 2013 (AROB 18th '13),
Daejeon Convention Center, Daejeon, Korea, January 30-February 1, 2013

Preparatory data analysis for customer servicing interface of Buddhism statue ordering system

Tzu-Hsuan Huang Kaoru Sugita Masao Yokota

Fukuoka Institute of Technology
(Tel: 81-92-606-5897, Fax: 81-92-606-8923)

yokota@fit.ac.jp

Abstract: The authors have proposed a human mind model consisting of Stimulus, Knowledge, Emotion and Response Processing Agents and simulated human-robot communication based on it. This paper describes artificial *Kansei*, namely, *Kansei* for a robot as tight collaboration of Knowledge and Emotion Processing Agents of our mind model, and verbalization of affective information so called *Kansei* expression by Response Processing Agent, focusing on basic analysis of *Kansei* words for the customer servicing interface of a Buddhism statue ordering system under development.

Keywords: artificial *Kansei*, customer servicing interface, image retrieval

1 INTRODUCTION

In not so far a future, there will come true a symbiotic world of people and robots where they interact as naturally as people do without robots. For such a symbiosis, robots will be required to understand, as exactly as possible, what people do. Recently, there have been developed various types of real or virtual robots as artificial partners. However, they are to play their roles according to programmed reactions to stimuli and have not yet come to perform human higher-order mental functions such as *Kansei*. The multi-agent model of human mind was proposed by Minsky, M. [1]. This mind model, however, was too theoretical and complicated to computerize. The authors have proposed a human mind model consisting of Stimulus, Knowledge, Emotion and Response Processing Agents, much simpler and practical than the Minsky's model, and defined *Kansei*, more exactly, artificial *Kansei* as tight collaboration of Knowledge and Emotion Processing Agents [2].

Recently, they have been considering its application to the customer servicing interface of a Buddhism statue ordering system. This system is intended to help the customers specify their favorite Buddhism statues intuitively by *Kansei* expression.

The remaining sections of this paper are as follows. Firstly, the Buddhism statue ordering system is overviewed in Section 2 and a brief sketch of the multi-agent mind model and artificial *Kansei* is given in Section 3. Section 4 analyses several kinds of preparatory data of the system from the viewpoint of *Kansei* (or affective) engineering. Lastly, Section 5 discusses and concludes this paper.

2 SYSTEM OVERVIEW

Figure 1 shows the configuration of the Buddhism statue ordering system intended here. The customers are expected to input keywords and *Kansei* words and specify their intended statues well enough. At the present stage, such specifications are limited to statue categories (e.g., *Dainichi-nyorai*, *Fudomyoo*), materials (e.g., ebony, sandalwood), and facial expressions (e.g., fearful, peaceful).

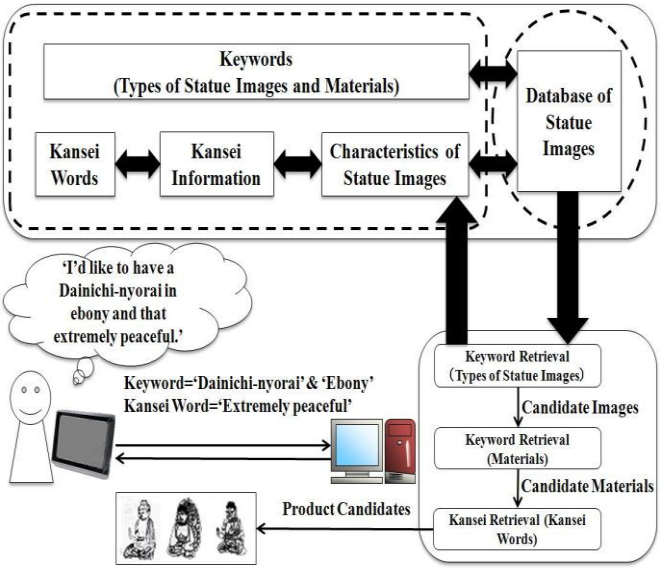

Fig.1. Buddhism statue ordering system

3 MIND MODEL AND ARTIFICIAL KANSEI

Figure 2 shows the multi-agent mind model proposed by the authors [2]. This is a functional model of human central nervous system consisting of the brain and the spine. The basic performances of its agents are as follows.

© ISAROB 2013

(1) **Stimulus Processing Agent** (**St**) receives stimuli from the world (**W**) and encodes them into mental images (i.e. encoded sensations) such as *"I sensed something cold."* (if verbalized in English.)
(2) **Knowledge Processing Agent** (**Kn**) evaluates mental images received from the other agents based on its memory (e.g. knowledge), producing other mental images such as *"It is false that the sun goes around the earth."*
(3) **Emotion Processing Agent** (**Em**) evaluates mental images received from the other agents based on its memory (e.g. instincts), producing other mental images such as *"I dislike the food."*
(4) **Response Processing Agent** (**Re**) converts mental images (i.e. encoded physical actions such as *"I'll run fast."*) received from the other agents into real physical actions against **W**.

A *performance* ***P*** for a *stimulus X* with a *result Y* at each agent can be formalized as a function by the expression (1).

$$Y=\boldsymbol{P}(X) \qquad (1)$$

where

P: a combination of ***atomic performances*** described later

X: a spatio-temporal distribution of stimuli from **W** to **St** or a mental image for another agent

Y: a series of signals to drive an actuator for **Re** or a mental image for another agent

A performance ***P*** is assumed as a function formed either consciously or unconsciously. In a conscious case, a set of atomic performances are to be chosen and combined according to *X* by a meta-function, so called, '***Performance Selector*** (PS)' assumed as '***Conscience***'. On the contrary, in an unconscious case, such a performance as associated most strongly with *X* is to be applied automatically.

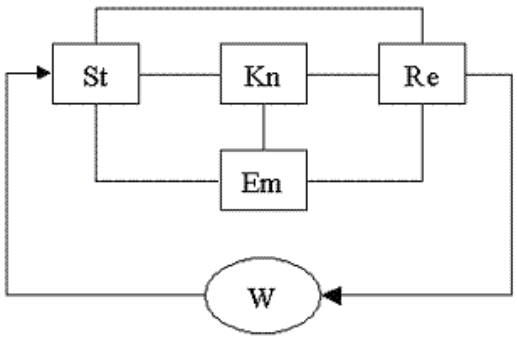

St: Stimulus Processing Agent.
Kn: Knowledge Processing Agent.
Em: Emotion Processing Agent.
Re: Response Processing Agent.
W: World surrounding human mind, including his/her body.

Fig.2. Multi-agent model of human mind

It is well known that emotion in a human can be affected by his/her world, namely, ***W*** in Fig.2. For example, a person's evaluation of live image of an object (i.e. image output from **St**) expressed by such words as 'favorite', 'beautiful', 'tasty', etc. can vary depending on his/her emotional bias such as 'hunger', 'depression', etc.

Kansei is one of mental functions with emotion involved but has a more complicated phase than pure emotion originated from instincts or imprinting. For example, sweet jam may be nice on toast but not on pizza for certain people knowledgeable about these foods. For another example, people can be affected on their evaluation of an art by its creator's name, for example, 'Picasso'. These are good examples of *Kansei* processing as emotional performance affected by knowledge in humans.

Therefore, *Kansei* can be defined as human emotion toward an object affected by its information, so called, 'concept', including his/her intellectual pursuits, traditions, cultures, religions, etc. concerning it. In this sense, *Kansei* is assumed to be reasonable among the people sharing such concepts unlike pure emotion. These hypothetic considerations are formalized as (2) and (3).

$$I_P(\mathrm{x})= \boldsymbol{P_E}(\mathrm{S(x)}) \qquad (2)$$

$$I_K(\mathrm{x}) =\boldsymbol{P_E}(\mathrm{S(x)}\wedge\mathrm{O(x)}) = \boldsymbol{P_E}(\mathrm{S'(x)}) \qquad (3)$$

where

$\boldsymbol{P_E}$(X): Performance of **Em** for mental image 'X',
I_P(x): Mental image as pure emotion for object 'x',
I_K(x): Mental image as *Kansei* value for object 'x',
S(x): Live image of object 'x' from **St**,
O(x): Concept of object 'x' from **Kn**,
S'(x): Unified image of live image and concept.

4 AFFECTIVE ANALYSIS OF STATUES

Many psychologists have claimed that certain emotions are more basic than others [3]. We have assumed that human emotion consists of 5 primitives representing the degrees of 1) Anger, 2) Disgust, 3) Anxiety, 4) Happiness, and 5) Superiority. For example, the degree of Anger is intuitively measured by using such a word set as {terror, fear, scare, annoyance, upset, irritation, displeasure, anger, furry}, whose each element is possibly arranged on a coordinate axis and fuzzified with a certain characteristic function. Therefore, we have assumed *Kansei* as a certain function to evaluate totally the loci in the attribute spaces of these primitives [4]. Figure 3 shows our tentative arrangement of the word meanings on the scales of the primitive emotions (i.e., -9 through +9), where each wedge points the representative value of the corresponding word without characterization such as fuzzification.

Based on the 5 primitive emotional parameters, we have analyzed 18 Buddhism statues of 11 categories as shown in Fig.4 in order to plot them in the attribute space of *Kansei*

© ISAROB 2013

[4]. At the present stage of our study, semantic characterization of the involved words has not been completed yet and therefore we have used a rough scale with three ordered ranges such as 'Anti-emotion degree range (A)', 'Neutral degree range (N)' and 'High degree range (H)', whose intervals on each axis are [-9, -3], (-3, 3), and [3, 9], respectively. Table 1 and Fig.5 show an example of such analysis using this scale, where the values represent the averaged subjective scores of the authors (3 persons) and, as a matter of course, the averaged image (AI) was put at the origin (0,0,0,0,0) of the *Kansei* space [2, 4] (See Fig.6 in APPENDIX).

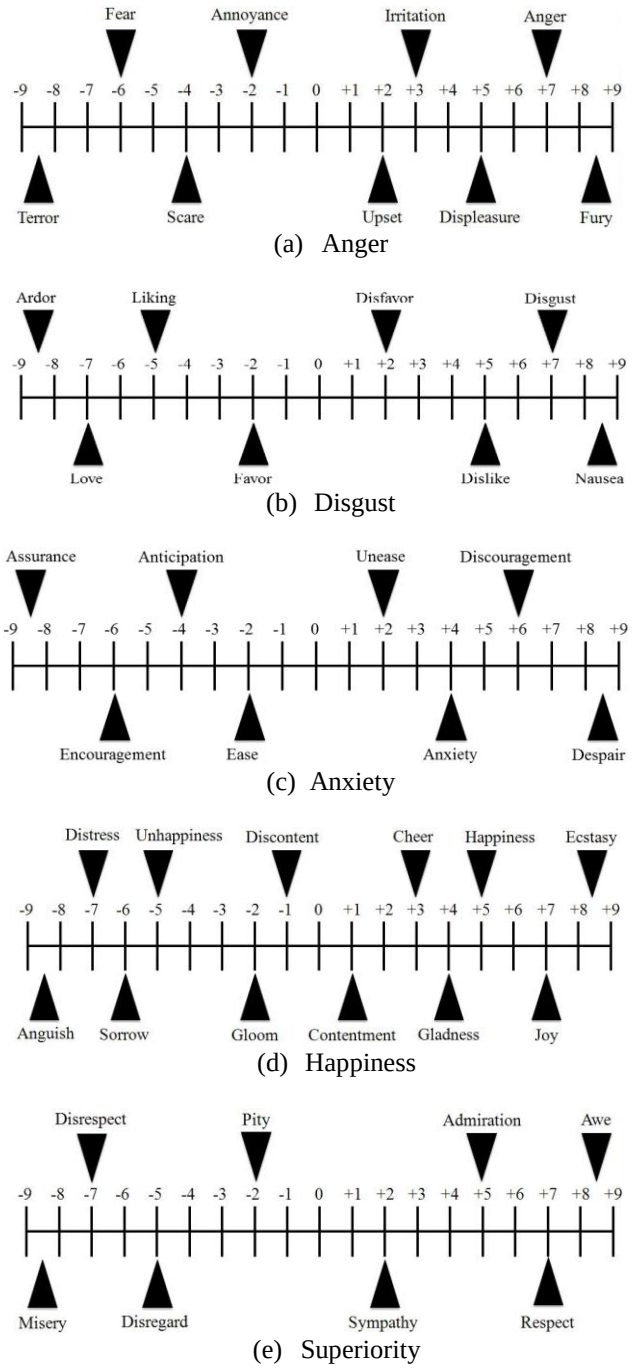

Fig.3. Scales of the primitive emotions

Fig.4. Samples of Buddhism statue images

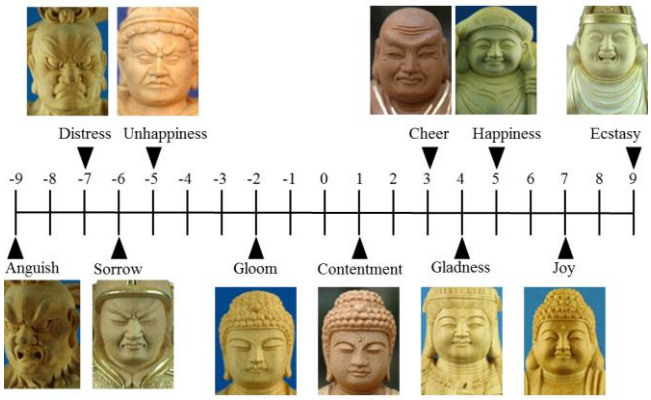

Fig.5. Tentative arrangement of images on Happiness-axis

Table 1 Affective analysis of Buddhism statues

Sample	anger	disgust	anxiety	happiness	superiority
AI	0	0	0	0	0
DN	N	N	N	N	N
FM	H	H	H	A	N
DT	N	N	N	H	N
AS	H	N	H	A	N
DS	N	N	N	N	H
SK	N	N	N	H	H
MT	H	N	H	A	H
NO	H	H	H	A	H

© ISAROB 2013

5 DISCUSSION AND CONCLUSION

The affective analysis of Buddhism statue images and the semantic analysis of *Kansei* words were described. Quite distinguished from others [e.g., 5], the images and the words are associated with each other indirectly via their semantic expressions, namely, vectors in the 5-dimensional space of *Kansei* and therefore their semantic analyses were conducted independently each other.

These results are to be associated with more sophisticated *Kansei* words for Buddhism statues such as peaceful, divine, gentle, reverential, noble, valiant, etc. and finally to be applied to the customer servicing interface of a Buddhism statue ordering system. The meanings of such words are to be represented as certain complicated vectors in the *Kansei* space as well as the images while each of primitive words such as happy, angry, etc. is represented simply in terms of the unit vector for each corresponding primitive emotion. The customers of the system are expected to use these words together with primitive ones for describing their own favorite statues at ordering and the system is bound to propose the users several candidates of high correlation values.

The averaged image was generated through the processes shown in Fig.6 in APPENDIX. Firstly, the image data were arranged for the noses to come to the center of the frame. Secondly, the faces were resized for their contours to touch the rectangular border of the frame and finally, they were averaged at each pixel. The computed cross-correlation values show, for example, that the average image is near to *Dainichi-nyorai* and far from *Fudomyoo*. This fact corresponds well with our intuition shown in Table 1. By the way, the variance image is not considered for any use at present.

As defined by Equation (3), *Kansei* can be affected by the knowledge of the person involved as well as his/her pure emotion. For example, the legend of Acala (*Fudomyo*) says that he is to be a powerful deity who protects 'All the Living (*Shujo*)' by burning away all impediments and defilements, thus aiding them towards enlightenment [6]. The knowledge of this fact can affect persons in their emotions so as to weaken the degrees of 'Disgust' and 'Anxiety' in comparison with their pure emotions evoked by its appearance. However, our qualitative and quantitative study of this point is still shallow and therefore its further elaboration will be also included in our future work.

Our mind model is much simpler than Minsky's but its realization based on the attribute spaces can work for representing and computing mental phenomena fairly well [2, 4]. The attribute space of *Kansei* is to play an important role in a certain robotic individuality of general use. For realizing a plausible *Kansei*, it is most essential to find out functional features of **Em** and to deduce from them such laws that rule $\boldsymbol{P_E}$. The most important problems to be solved are how to realize the attribute space of *Kansei* and how to build its corresponding atomic performance. In order to solve these problems, focusing on Buddhism statues, we will consider the application of soft computing theories such as neural network, genetic algorithm, fuzzy logic, etc. in near future.

REFERENCES

[1] Minsky, M: The society of mind, Simon and Schuster, New York, 1986.
[2] Yokota,M., Shiraishi,M. and Capi,G.: "Human-robot communication through a mind model based on the Mental Image Directed Semantic Theory," Proc. of the 10th International Symposium on Artificial Life and Robotics (AROB '05), pp.695-698, 2005.
[3] Ortony,A. and Turner,T.J.: "What's basic about basic emotions?", Psychological Review, Vol.97, pp.315-331,1990.
[4] Huang, T., Sugita, K. and Yokota, M.: "Toward artificial *Kansei* based on Mental Image Directed Semantic Theory", Artificial Life and Robotics: Vol.17-2, pp. 186-190, 2012.
[5] Sugita, K., Ishida, T., Miyakawa, A. and Shibata, Y.: "*Kansei* Retrieval Method using the Quantitative Feature of Traditional Japanese Crafting Object," Proc. of The 6th International Workshop on Multimedia Network Systems and Applications (MNSA'2004), 112-117, 2004.
[6] 'Acala', Wikipedia.

APPENDIX

The 18 image data were averaged through the processes shown in Fig.6 below. Additionally, the variance and the cross-correlation values among them were computed.

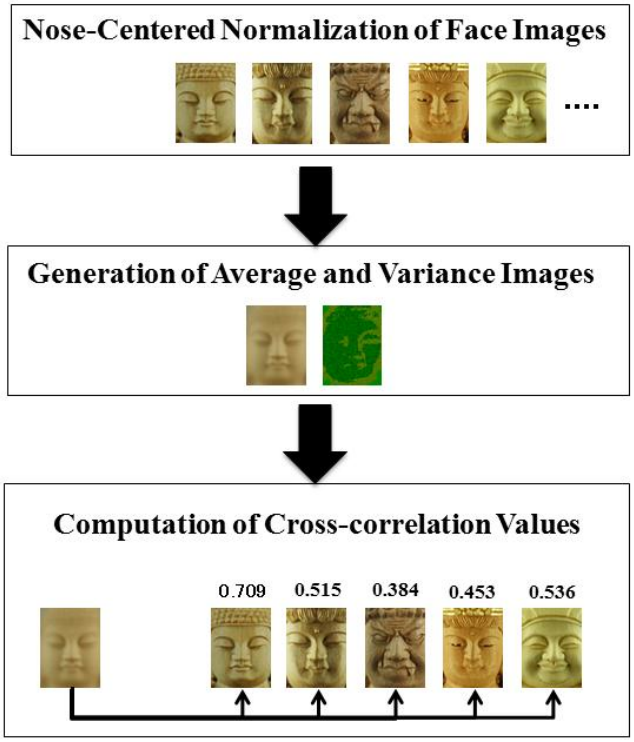

Fig.6. Process flow for image averaging

The Eighteenth International Symposium on Artificial Life and Robotics 2013 (AROB 18th '13),
Daejeon Convention Center, Daejeon, Korea, January 30-February 1, 2013

Toward multimodal user interface for intuitive interaction with Buddhism statue ordering system

Tzu-Hsuan Huang Kaoru Sugita Masao Yokota

Fukuoka Institute of Technology
(Tel: 81-92-606-5897, Fax: 81-92-606-8923)

yokota@fit.ac.jp

Abstract: The authors have been developing a Buddhism statue ordering system which enables customers to use affective words such as peaceful and divine, intending to specify the facial expressions of their favorite statues. Such affective words, however, are bound to vague and ambiguous specification of their demands. This paper proposes an innovative two-staged specification method allowing customers to elaborate their demands by graphical inputs following *Kansei* words.

Keywords: artificial *Kansei*, multimodal interface, product customization

1 INTRODUCTION

For ordinary people, natural language is the most important among the various communication media because it can convey the exact intention of the sender to the receiver due to its syntax and semantics common to its users [1]. This is not necessarily the case for another medium such as gesture and therefore natural language can as well play the most crucial role in intuitive human-robot interaction [1]. Natural language, without any doubt, is an extremely powerful means for people to express their ideas of various kinds in abstract, i.e., conceptual level. However, for example, it is not so powerful to describe natural scenery in concrete as picture. This is also the case for certain customer servicing systems allowing users to specify their demands for the favorite products in natural language. Recently, the authors have been developing a Buddhism statue ordering system which enables customers to use affective words such as *peaceful* and *divine*, intending to specify the facial expressions of their favorite statues. Such affective words, however, are bound to vague and ambiguous specification of their demands. This paper proposes an innovative two-staged specification method allowing customers to elaborate their demands by graphical inputs following affective words, so-called *Kansei* words.

The remaining sections of this paper are as follows. Firstly, the multimodal interface of the Buddhism statue ordering system is overviewed in Section 2. Secondly, Section 3 describes the methodology of semantic definition of *Kansei* words as membership functions. Thirdly, Section 4 and 5 present linguistic and graphical expression processing, and lastly, Section 6 concludes this paper.

2 MULTIMODAL DEMAND SPECIFICATION

The Buddhism statue ordering system under development is expected to customize prototypes according to the user's demands specified both linguistically and graphically as shown in Fig.1. The interactions between the user and the system are largely such as follows.

(Step 1) User asks the system for the favorite statue in natural language such as 'Extremely peaceful'.
(Step 2) System retrieves candidate prototypes such as Fig.2 (a)-(c) from Raw Image Database to display.
(Step 3) System retrieves line-drawn faces of the candidates such as Fig.3 (a)-(c), respectively, from Sketch Database to display through a certain line-drawing tool.
(Step 4) User retouches the sketches through the drawing interface.
(Step 5) System reedits and customizes the prototype image data according to the graphical demand specification.
(Step 6) User continues the interaction by returning to Step 1 or Step 4. Otherwise, User terminates the interaction.

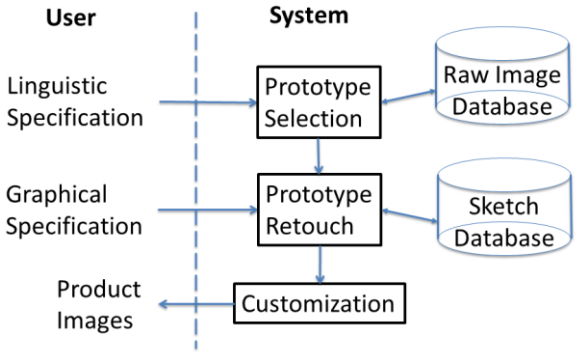

Fig.1. Multimodal intuitive interaction in Buddhism statue ordering system

© ISAROB 2013

(a) DN1R (b) DN2R (c) DN3R

Fig.2. Examples of raw images of statues

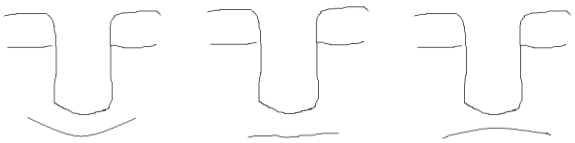

(a) DN1S (b) DN2S (c) DN3S

Fig.3. Face sketches of the statues in Fig.2

3 SEMANTIC DEFINITION OF KANSEI WORDS AS MEMBERSHIP FUNCTIONS

The meaning of a *Kansei* word is characterized by a set of membership functions defined respectively at 5 dimensions of the Attribute space of *Kansei*, each of which corresponds with the 5 primitive emotions, namely, 1) Anger, 2) Disgust, 3) Anxiety, 4) Happiness, and 5) Superiority [2]. In this study, each of the membership functions for a *Kansei* word W is given in such a way that it is characterized by a trapezoid, symmetric at the vertical line passing (C, 0) on a primitive emotion axis, with the height 1, the top length T, and the bottom length B as shown in Fig.4. Therefore, the membership function $f_{ki}(x)$ for *i-th* dimension of a word W_k is defined uniformly as (1), where x denotes some degree of a certain primitive emotion. Hereafter, for the sake of simplicity, each trapezoid is normalized as $T=1$ and $B=4$, which necessarily implies that the meaning of each *Kansei* word is representable simply by the coordinate consisting of Cs for all the primitive emotions. Each C ranges over [-9, +9] on its corresponding axis [2] and is called MFI (Membership Function Identifier) here.

$$
\begin{aligned}
f_{ki}(x) &= 0 && (x<C_{ki}-B_{ki}/2),\\
&= \frac{2}{(B_{ki}-T_{ki})}(x-C_{ki}+B_{ki}/2)+1 && (C_{ki}-B_{ki}/2\le x< C_{ki}-T_{ki}/2),\\
&= 1 && (C_{ki}-T_{ki}/2\le x<C_{ki}+T_{ki}/2),\\
&= \frac{-2}{(B_{ki}-T_{ki})}(x-C_{ki}-T_{ki}/2)+1 && (C_{ki}+T_{ki}/2\le x< C_{ki}+B_{ki}/2),\\
&= 0 && (C_{ki}+B_{ki}/2\le x). \qquad (1)
\end{aligned}
$$

According to this definition and its normalization, such primitive *Kansei* word concepts as *fury*, *favor*, and *joy* can be defined as Table 1 (tentative) because they are represented simply in terms of the unit vector for each corresponding primitive emotion. On the other hand, the meanings of such complex *Kansei* words as *divine* and *peaceful* are defined as certain complicated vectors in the *Kansei* space as shown in Table 2 (tentative). Figure 5 shows the membership functions assigned to several *Kansei* words of 'Happiness', namely, the 4th dimension of the Attribute space of *Kansei*.

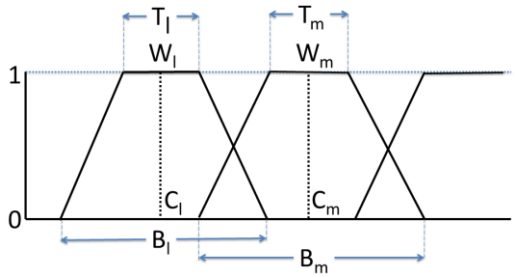

Fig.4. Fuzzification of *Kansei* word meanings

Table 1 Primitive *Kansei* words and MFIs†

Word	1) Ag	2) Dg	3) Ax	4) Hp	5) Sp
Fury	+8.5				
Anger	+7				
Displeasure	+5				
Irritation	+3				
Upset	+2	0	0	0	0
Annoyance	-2				
Scare	-4				
Fear	-6				
Terror	-8.5				
Nausea		+8.5			
Disgust		+7			
Dislike		+5			
Disfavor		+2			
Favor	0	-2	0	0	0
Liking		-5			
Love		-7			
Ardor		-8.5			
Despair			+8.5		
Discouragement			+6		
Anxiety			+4		
Unease			+2		
Ease	0	0	-2	0	0
Anticipation			-4		
Encouragement			-6		
Assurance			-8.5		
Ecstasy				+8.5	
Joy				+7	
Happiness				+5	
Gladness				+4	
Cheer				+3	
Contentment				+1	
Discontent	0	0	0	-1	0
Gloom				-2	
Unhappiness				-5	
Sorrow				-6	
Distress				-7	
Anguish				-8.5	
Awe					+8.5
Respect					+7
Admiration					+5
Sympathy					+2
Pity	0	0	0	0	-2
Disregard					-5
Disrespect					-7
Misery					-8.5

†Ag=Anger, Dg=Disgust, Ax=Anxiety, Hp=Happiness, Sp=Superiority

© ISAROB 2013

Table 2 Complex *Kansei* words and MFIs

Word	1) Ag	2) Dg	3) Ax	4) Hp	5) Sp
Peaceful	0	0	0	+1	+1
Divine	-5	0	0	+1	+8
Reverential	-1	-1	+1	-1	+7
Noble	0	0	0	+1	+5
Valiant	+7	+5	+4	-7	-7
Jingoistic	+5	+5	+2	-5	-6

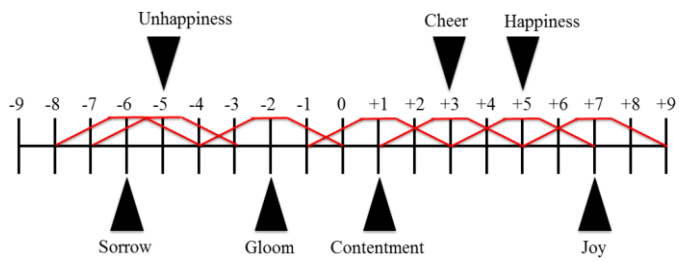

Fig.5 Membership functions of 'Happiness'

4 LINGUISTIC EXPRESSION PROCESSING

The syntax of *Kansei* expression K is defined by (2) as a set of production rules of a context-free grammar. According to this definition, for example, such a considerably complex *Kansei* expression as (4) can be generated as well as rather simple ones such as (3). Moreover, such an extreme expressions as (5) can be as well generated as one of the terminal expressions for D^nW (n≥0), the generalized form of the structure A.

$$\{K \rightarrow A \mid (K) \mid \text{not } K \mid K \text{ and } K \mid K \text{ or } K,\ A \rightarrow W \mid DA,\ W \rightarrow \text{peaceful} \mid \text{noble} \mid \ldots,\ D \rightarrow \text{extremely} \mid \text{very} \mid \text{much} \mid \text{more} \mid \text{less} \mid \text{slightly} \mid \text{a little} \mid \text{scarcely} \mid \ldots\} \quad (2)$$

peaceful, more noble, a little fearful (3)

not very valiant and (peaceful or awful) (4)

very very very extremely peaceful (5)

Simultaneously, the semantics of *Kansei* expression is given in terms of membership functions although, as easily imagined, most of the expressions generated from the above rules are semantically anomalous or of no significance.

Firstly, the semantic interpretation $Sem(W_k)$ of *Kansei* word W_k is formally represented as (6) while it is conventionally given as an ordered set of membership functions as shown in Table X and Y. This formalization reads that the value of the *i-th* primitive emotion at W_k, V_i is equal to $f_{ki}(x)$ *with* C_{ki} and that all the 5 equations are combined with the logical AND denoted by $\wedge$.

$$Sem(W_k) \equiv (V_1=\mu(x,C_{k1}) \wedge V_2=\mu(x,C_{k2}) \wedge \ldots \wedge V_5=\mu(x,C_{k5})),\ \text{where } \mu(x,C_{ki}) \text{ is } f_{ki}(x) \text{ with } C_{ki}. \quad (6)$$

Secondly, such a structure as $D_1D_2\ldots D_nW_k$ (n≥1) is semantically interpreted so that the combination of adverbials $D_1D_2\ldots D_n$ modify (6) by replacing each C_{ki} with (7). Here, *deg(D)* is a function to assign a certain degree to the adverbial D as shown in Table 3 (tentative) in order to magnify or deduce each primitive emotion identified by C_{ki}.

$$C_{ki} \cdot (deg(D_1) \cdot deg(D_2) \cdot \ldots \cdot deg(D_n)) \quad (7)$$

Table 3 Adverbials and degrees

D	*deg(D)*	*D*	*deg(D)*
Extremely	10	Scarcely	1/20
Very	3/2	Slightly	1/10
Much	3/2	A little	1/5
More	11/10	Less	10/11

That is, the modifiers $D_1D_2\ldots D_n$ work only to translate the membership functions of *Kansei* word W_k on each corresponding axis. According to this formalization, for example, the meaning of such a *Kansei* expression as '*more noble*' is given as (8) by consulting Table 2 as well.

$$V_1=V_2=V_3=\mu(x,0) \wedge V_4=\mu(x,1.1) \wedge V_5=\mu(x,5.5) \quad (8)$$

Thirdly, the logical expressions '*not K*', 'K_1 *and* K_2', and 'K_1 *or* K_2' are translated into (9), (10), and (11), respectively, '~' and '$\vee$' are the logical NOT and OR, respectively.

$$\sim Sem(K) \quad (9)$$

$$Sem(K_1) \wedge Sem(K_2) \quad (10)$$

$$Sem(K_1) \vee Sem(K_2) \quad (11)$$

Meanwhile, semantic synthesis of membership functions in the logical structures of K is in principle all the same as in the conventional multivalued logic. That is, the equivalences listed in (12) hold for any single or paired membership functions, where *Min* and *Max* are such functions that they take the minimum and the maximum value, respectively, of the two functions at each x.

$$\{\sim(V_i=g(x)) \equiv (V_i=1-g(x)),\ (V_i=g(x) \wedge V_i=h(x)) \equiv (V_i=Min(g(x),h(x))),\ (V_i=g(x) \vee V_i=h(x)) \equiv (V_i=Max(g(x),h(x)))\} \quad (12)$$

For example of negation, '*not* W_k', one of the simplest structures, is interpreted as (13) so that '*not*' modifies (6) by replacing each $\mu(x,C_{ki})$ with $1-\mu(x,C_{ki})$, and $\wedge$ with $\vee$.

$$V_1=1-\mu(x,C_{k1}) \vee V_2=1-\mu(x,C_{k2}) \vee \ldots \vee V_5=1-\mu(x,C_{k5}) \quad (13)$$

For stereotypical example of conjunction, the meaning of 'W_k *and* W_j' is synthesized as (14).

$$V_1=Min(f_{k1}(x), f_{j1}(x)) \wedge \ldots \wedge V_5=Min(f_{k5}(x), f_{j5}(x)) \quad (14)$$

For disjunction, exclusively in the case that the two words in 'W_k *or* W_j' are both primitive for the same emotional category like the pair of *happy* and *joyful*, such a semantic synthesis as (15) is possible, where the very same

category is denoted by the suffix *d* and the 4 remainders, by *a*, *b*, *c*, and *d*, respectively.

$$V_s=Max(f_{ks}(x),f_{js}(x))\wedge V_a=V_b=V_c=V_d=\mu(x,0) \quad (15)$$

As easily understood, semantic synthesis in more complicated structures has only to employ the corresponding membership functions synthesized from a certain set of primitive ones, namely, $\{f_{ki}(x)\}$ involved. At conclusion, any *Kansei* expression can be translated into such a disjunctive normal form as (16), where each $g(x)$ denotes a membership function resulted from some conjunctions or negations for each dimension.

$$\vee_{j=1,n}\ (\wedge_{k=1,5}V_k=g_{jk}(x)) \quad (16)$$

Lastly, the candidateship of a statue *S* for a demand *D* is evaluated by the function F_c (Candidateship Function) defined by (17), employing a special function *Hst* to detect the highest peak (i.e., maximum value) of the synthesized function $h(x)$. Each statue image is characterized by a pair of $f(x)$ and MFI as well as a *Kansei* word, and therefore $0\leq F_c(S|D)\leq 1$. Table 4 (tentative) shows the MFIs of the statues shown in Fig.6.

$$F_c(S|D)=Max(M_1,M_2,\ldots,M_n),$$
$$\text{where}$$
$$M_j=Min(Hst(h_{j1}(x)), Hst(h_{j2}(x)), \ldots, Hst(h_{j5}(x)))$$
$$h_{jk}(x)= Min(f_k(x),g_{jk}(x)),$$
$$Sem(S)\equiv (V_1=f_1(x)\wedge V_2=f_2(x)\wedge\ldots\wedge V_5=f_5(x)),$$
$$Sem(D)\equiv \vee_{j=1,n}\ (\wedge_{k=1,5}V_k=g_{jk}(x)). \quad (17)$$

Table 4 Statue images in Fig.6 and their MFIs

Statue	1) Ag	2) Dg	3) Ax	4) Hp	5) Sp
DT	0	0	0	8	1
DN	0	0	0	-2	2
AS	6	2	5	-3	-1
FM	8	4	6	-5	2

(a) DT (b) DN (c) AS (d) FM

Fig.6. Examples of images of statues

5 GRAPHICAL EXPRESSION PROCESSING

The graphical expressions to be processed in the system here are limited to sketches of the faces of statues. A sketch here is to show only how the main parts (i.e., mouth, nose, eyes, and eyebrows, here) of the face lie, for example, lying gradient, direction, curvature, extent, etc. [3] each of which is called 'Attribute' (of a matter such as face part) in general [1]. The syntax of face sketch *F* is defined by the set of production rules (18).

$$\{F\rightarrow HDCDG,\ H\rightarrow B_lRB_r,\ C\rightarrow E_lPNPE_r,\ G\rightarrow M,$$
$$B_l\rightarrow b_{l1}|b_{l2}|\ldots,\ B_r\rightarrow b_{r1}|b_{r2}|\ldots,\ E_l\rightarrow e_{l1}|e_{l2}|\ldots,$$
$$E_r\rightarrow e_{r1}|e_{r2}|\ldots,\ N\rightarrow n_1|n_2|\ldots,\ M\rightarrow m_1|m_2|\ldots,$$
$$D\rightarrow d_1|d_2|\ldots,\ P\rightarrow p_1|p_2|\ldots\} \quad (18)$$

This definition consists of non-terminal symbols such as follows, respectively representing a set of real sketches of face parts or their placements denoted by terminal symbols (i.e., *b, e, n, m, d,* and *p*).

H, C, G: The upper, middle and lower part of the face, respectively,

B_l, B_r: The eyebrow left and right from viewers, respectively,

E_l, E_r: The eye left and right from viewers, respectively,

N, M: The nose and the mouth, respectively,

D, P: Downward and rightward placement of the following part, respectively.

The users of the system are allowed to rearrange what are represented by the terminal symbols through a certain graphical interface as shown in Fig.1. Figure 7 shows several examples of such rearrangements.

On the other hand, the semantics of face expression can be defined in terms of $f(x)$ and MFI as well as *Kansei* expression while, in general, nonlinguistic expression such as picture cannot bear definite meaning comprehensible for every one [1].

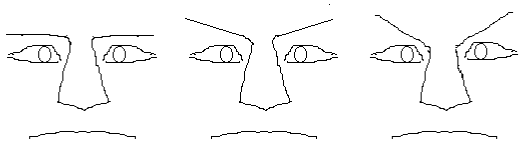

Fig.7. Faces with different eyebrows ($\in B_l$ or B_r)

6 CONCLUSION

Here was presented an innovative specification method based on semantic processing of both linguistic and graphical demands in the Buddhism statue ordering system. Our proposed method interactively allows Users to gradually approximate System's proposals to their real intentions unlike others [e.g., 4] while it is still on the way to practical implementation.

REFERENCES

[1] Yokota, M.: "Subjective Knowledge Representation for Intuitive Human-Robot Interaction Based on Mental Image Directed Semantic Theory", in (Ed. Thomas S. Clary) Knowledge representation, Nova Publishers, 2012.

[2] Huang, T., Sugita, K. and Yokota, M.: "Toward artificial *Kansei* based on Mental Image Directed Semantic Theory", Artificial Life and Robotics: Vol.17-2, pp. 186-190, 2012.

[3] Ekman, P. & Friesen, W.: The facial action coding system: A technique for the measurement of facial movement, Consulting Psychologists Press. 1978.

[4] Sugita, K., Ishida, T., Miyakawa, A. and Shibata, Y.: "*Kansei* Retrieval Method using the Quantitative Feature of Traditional Japanese Crafting Object," Proc. of The 6th International Workshop on Multimedia Network Systems and Applications (MNSA'2004), 112-117, 2004.

© ISAROB 2013

The Eighteenth International Symposium on Artificial Life and Robotics 2013 (AROB 18th '13),
Daejeon Convention Center, Daejeon, Korea, January 30-February 1, 2013

On a relation between feeling Impression and 3PACF of sound signal

Yusuke Kawakami[1], Tetsuo Hattori[1], Hiromichi Kawano[2] and Tetsuya Izumi[3]

[1]Graduate School of Engineering, Kagawa University
2217-20 Hayashi, Takamatsu City, Kagawa 761-0396, Japan
(Tel: 81-87-864-2292, Fax: 81-87-864-2302)
[2]NTT Advanced Technology
19-18 Nakamachi, Musashino-shi, Tokyo 180-0006, Japan
[3]Micro Technica Co., Ltd.
3-12-2 Higashi-ikebukuro, Toshima-ku, Tokyo 170-0013, Japan

[1]s11d621@stmail.eng.kagawa-u.ac.jp, hattori@eng.kagawa-u.ac.jp

Abstract: This paper presents an experimental investigation correlation between human feeling impression and some physical feature quantity in sound signal. We focus on three kinds of values, that is, fluctuation value, intercept, and sum of squared errors that are obtained when making a regression analysis of sound signal in Fourier domain, as for the feature quantity. In our investigation using a questionnaire survey over 34 persons, we apply multiple regression model to the relation between the feature quantity of signal and human evaluation about Kansei impression for each person. And, after making the construction of the regression equation for each person, we show the strength between the quantity and impression. Moreover, we classify the set of coefficients of the equation into three groups and discuss some tendency of human impression resulting from the quantity.

Keywords: feeling impression, fluctuation value, intercept, signal processing, sum of squared errors

1 INTRODUCTION

Recently, 1/*f* fluctuation in various fields of signal has been actively researched, and it brings about an effect of such healing as a human being psychologically feels at ease, if there is a 1/*f* relation between the power spectrum of the signal and the frequency *f* ([1]-[7]).

However, in the past research about 1/*f* fluctuation focused attention on the value of fluctuation. And it has not yet led to analyze when signals have the same 1/*f* fluctuations those power spectrum distributions. Therefore, we wonder that feeling impression strongly affects not only value of fluctuation but also other factors.

In this paper, we introduce three kinds of parameters such as fluctuation value, intercept, and sum of squared errors (or residual) as feature quantity in sound signal obtained from the calculation of the signals' fluctuation degree, and we investigate the relation between feeling impression and those parameters. We investigate sensitivity of the feeling impression by those parameters, especially fluctuation value and residual.

2 QUANTITIES ACCOMPANYING CALCULATION OF FLUCTUATION

2.1 3PACF

Fig. 1 shows an example of the regression line. Its horizontal axis shows the logarithm of the frequency and vertical axis shows the logarithm of the PS. Where, this regression line has an absolute-slope of a. In this paper, we call the absolute-degree of the slope "Fluctuation value".

Accompanying when the regression line is computed as shown in Fig. 1, three kinds of parameters are defined, i.e., (1) Fluctuation value as the absolute value of slope a, (2) Intercept b, and (3) Residual of the line. We call the set of these parameters "3PACF" that stands for Three Parameters Accompanying Calculation of Fluctuation [8].

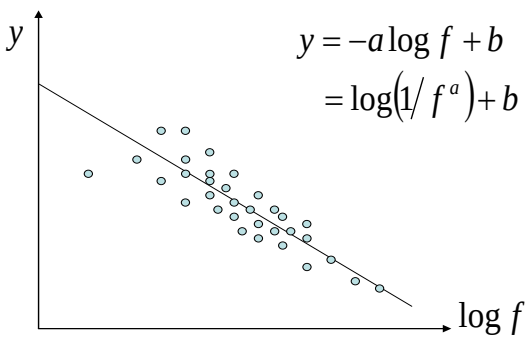

Fig. 1. Example of regression line

The residual of the regression line is defined by Eq. (1) as in the form of a sum of the squared error, where *y* and *Y* show a target variable and an estimated regression value respectively.

$$s = \sum_i e_i^2 = \sum_i (y_i - Y_i)^2 \quad (1)$$

© ISAROB 2013

2.2 Correlation between 3PACF

We have investigated as to whether or not there exists correlation between 3PACFs of music. Table 1 shows using music list of wave file. Their sampling rate and quantization bit rate are 44.1 kHz and 16 bit. Fig. 2 (a)-(c) shows the plotted graph between two parameters of 3PACF of music.

Table 1. Music list of wave file

No	Title (.wav)	Genre
1	Another_Sky	Easy Listening
2	Londonderry_Air	Classic
3	Blieve_you	Easy Listening
4	Drafting	Easy Listening
5	Down_by_the_Riverside	Jazz
6	Space_Odessey3_Revelation	Easy Listening
7	TOMORROW	Pops
8	Old_French_Song	Classic
9	Freedom	Pops
10	Red_River_Valley (brass)	Jazz

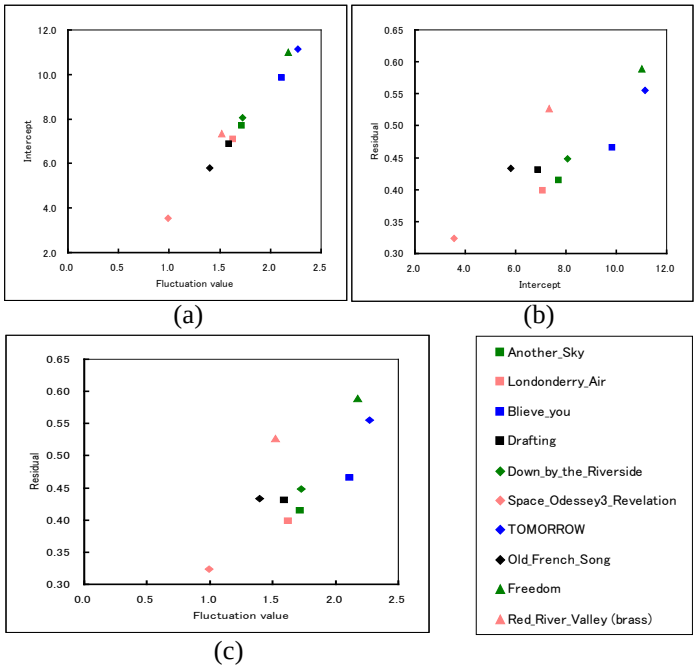

(a) (b) (c)

Fig. 2. Correlation of 3PACF (a) Fluctuation value and Intercept (b) Intercept and Residual (c) Fluctuation va lue and Residual

The correlation coefficient in Fig. 2: (a) 0.99061 between Fluctuation value and Intercept. (b) 0.85238 between Intercept and Residual. (c) 0.78630 between Fluctuation value and Residual. We consider that there exist high correlation between Fluctuation value and Intercept, between Intercept and Residual, or between Fluctuation value and Residual.

3 INVESTIGATION

3.1 Outline

We have used questionnaire survey in order to investigate the relation between 3PACF and feeling impression of music. The examinees are 34 university students in the age of early twenties. We have given some questions about their feeling impressions for 10 pieces of music. The list of music used in this survey is the same as shown in Table 1. For every piece of the music, we have taken 20 seconds to play it. After that, we have asked the students to evaluate the 4 items as shown in Table 2, by scoring from one to four. Also the students have judged the total evaluation for each music by scoring from 1 to 10.

Table 2. Questions in the survey

Item 1	Slow	1 ⇔ 4	Quick
Item 2	Heavy	1 ⇔ 4	Light
Item 3	Natural	1 ⇔ 4	Artificial
Item 4	Negative	1 ⇔ 4	Positive

3.2. Multiple regression analysis

We have conducted multiple regression analysis of the results as shown in Eq. (2) in the four-item score (item1, item2, item3, and item4) and the total evaluation score, where, y is the score of the each examinee, x_1 and x_2 are explanatory variables of "Fluctuation" and "Residual", respectively. And, error ε is independence variable and follows the normal distribution N(0, σ^2). We eliminate the third variable for "Intercept", because this quantity (or parameter) is substantially equal to the volume of sound [8].

$$y = \alpha_0 + \alpha_1 x_1 + \alpha_2 x_2 + \varepsilon, \quad \varepsilon \sim N\left(0, \sigma^2\right) \quad (2)$$

Also, we have noticed that the influence of four kinds of frequency domains, i.e. (i) All-frequency domain (AF; 0~22050Hz), (ii) Low-frequency domain (LF; 0~300Hz), (iii) Middle-frequency domain (MF; 300~1000Hz), (iv) High-frequency domain (HF; 1000~22050Hz). So, we have analyzed the results of questionnaire for each person using Eq. (2), for each item, and for each frequency domain.

Then we will obtain the concrete the coefficients and regression equation for Item1 in AF using the Least Squares Method. However we have set the coefficient α_0 = 0, because the multiple correlation coefficient tends to be higher as a result of analysis at this time, as a whole. In this way, the regression equation for each item of {Item1, Item2, Item3, Item4, Total Evaluation} and for each person will be available. So we will obtain five regression equations from

© ISAROB 2013

feeling impression data of each examinee, and we carry out this analysis for 34 examinees.

After that, we make a clustering analysis for them, using Ward Method [9]. As the result, those equations are generally classified into three groups. We will get regression coefficient of Fluctuation (α_1) and regression coefficient Residual (α_2). However we have to calculate Normalized Fluctuation Coefficient (NFC) α_1^* and Normalized Residual coefficient (NRC) α_2^* using Eq. (3) and Eq. (4), in order to compare α_1 and α_2.

$$x_n^* = \frac{x_n - \overline{x_n}}{\sigma_n}, \quad \therefore\ x_n = x_n^* \sigma_n + \overline{x_n}, \quad (n = 1, 2) \tag{3}$$

$$\begin{aligned} y &= \alpha_1 x_1 + \alpha_2 x_2 = \alpha_1\left(x_1^* \sigma_1 + \overline{x_1}\right) + \alpha_2\left(x_2^* \sigma_2 + \overline{x_2}\right) \\ &= \left(\alpha_1 \sigma_1\right) x_1^* + \left(\alpha_2 \sigma_2\right) x_2^* + \left(\alpha_1 \overline{x_1} + \alpha_2 \overline{x_2}\right) \\ &= \alpha_1^* x_1^* + \alpha_2^* x_2^* + \alpha_3^* \end{aligned} \tag{4}$$

Where $\overline{x_n}$ is average of explanatory variables of Fluctuation or Residual, and x_n^* is normalized explanatory variables of Fluctuation or Residual. And σ_n is standard deviation.

3.3. Results

3.3.1 AF (All-frequency domain)

Table 3 shows correlation coefficient and average of normalized regression coefficient of AF. The average of normalized regression coefficient is between Normalized Fluctuation Coefficient (NFC) and Normalized Regression Coefficient (NRC).

As shown in Table 3, in Group1, NRC α_2^* is higher than NFC α_1^*. So we consider that the Residual has more affected feeling impression than the Fluctuation. This situation is same in Group2 or Group3. Further more, we have used the Wilks-Lambda Test for statistical tests to the grouping in each evaluation item. Those groupings hold within 1% of significance whole frequency domains, i.e. AF, LF, MF and HF. Fig. 3(a) shows the clustering result for Total Evaluation in AF, as an example of classification.

3.3.2 LF (Low-frequency domain)

Table 4 shows correlation coefficient and average of normalized regression coefficient of LF.

Where, we have to pay attention to Evaluation Item in Table 4. NRC α_2^* is higher than the NFC α_1^* same as AF in Item1 through Item4. Then, Item3 and Total evaluation have weak correlations, and NFC α_1^* is higher than NRC α_2^* in Total Evaluation of Group2 and Group3.

From these results, Item1, Item2 and Item4 have slightly strong correlations, but Item3 and Total Evaluation have very poor correlations. Though Residual is the stronger factor than Fluctuation in this feeling impression evaluation. Fig. 3(b) shows the clustering result for Total Evaluation in LF, as an example of classification.

Table 3. Correlation coefficient and regression coefficient (a)AF, (b)LF, (c)MF, (d)HF

(a)

Evaluation Item	Multiple correlation coefficient	Significance level of regression	Average of Regression Coefficient					
			Group 1		Group 2		Group 3	
			α_1^*	α_2^*	α_1^*	α_2^*	α_1^*	α_2^*
Item 1	0.991	1%	-0.949	1.082	-0.295	0.625	0.132	0.252
Item 2	0.980	1%	-0.941	1.154	-0.404	0.772	0.024	0.408
Item 3	0.980	1%	-0.657	0.968	-0.097	0.528	0.395	0.112
Item 4	0.990	1%	-0.812	1.103	0.199	0.317	0.620	0.014
Total Evaluation	0.949	1%	-0.939	1.925	1.478	-0.186	0.150	0.831

(b)

Evaluation Item	Multiple correlation coefficient	Significance level of regression	Average of Regression Coefficient					
			Group 1		Group 2		Group 3	
			α_1^*	α_2^*	α_1^*	α_2^*	α_1^*	α_2^*
Item 1	0.763	1%	-0.182	0.662	0.403	0.448	-	-
Item 2	0.669	1%	0.099	0.757	0.563	0.520	-	-
Item 3	0.316	1%	0.085	0.788	0.258	0.634	-	-
Item 4	0.829	1%	-0.143	0.862	0.449	0.629	-	-
Total Evaluation	0.021	1%	0.904	1.684	1.177	1.228	0.830	0.317

(c)

Evaluation Item	Multiple correlation coefficient	Significance level of regression	Average of Regression Coefficient					
			Group 1		Group 2		Group 3	
			α_1^*	α_2^*	α_1^*	α_2^*	α_1^*	α_2^*
Item 1	0.831	1%	-0.671	0.887	-0.174	0.670	-	-
Item 2	0.816	1%	-0.293	0.880	0.112	0.629	0.699	0.349
Item 3	0.879	1%	-0.444	0.983	-0.050	0.778	0.303	0.422
Item 4	0.911	1%	-0.556	1.048	-0.218	0.842	0.289	0.583
Total Evaluation	0.613	1%	-0.173	2.070	0.397	1.365	0.841	0.620

(d)

Evaluation Item	Multiple correlation coefficient	Significance level of regression	Average of Regression Coefficient					
			Group 1		Group 2		Group 3	
			α_1^*	α_2^*	α_1^*	α_2^*	α_1^*	α_2^*
Item 1	0.984	1%	-0.361	0.502	0.359	0.143	0.649	-0.031
Item 2	0.973	1%	-0.846	0.840	-0.293	0.503	0.280	0.240
Item 3	0.947	1%	-0.423	0.585	0.046	0.398	0.367	0.178
Item 4	0.984	1%	-0.859	0.841	0.365	0.227	0.709	0.061
Total Evaluation	0.880	1%	-0.620	1.299	0.260	0.661	1.053	0.193

3.3.3 MF (Middle-frequency domain)

Table 5 shows correlation coefficient and average of normalized regression coefficient of MF.

As shown in Table 5, NRC α_2^* is higher than NFC α_1^* in Group1 and Group2. So we thought that the feeling impression of them has much more related NRC. Generally speaking, Residual is the stronger factor than Fluctuation in MF-feeling impression evaluation, too. Fig. 3(c) shows the clustering result for Total Evaluation in MF, as an example of classification.

3.3.4 HF (High-frequency domain)

Table 6 shows correlation coefficient and average of normalized regression coefficient of HF.

© ISAROB 2013

As shown in Table 6, in Group2 and Group3, NFC α_1^* is higher than NRC α_2^* in Item1 and Item4. In the rest of them, NRC α_2^* is higher than NFC α_1^*. As for the feeling impression of Group2 and Group3 in Item1 and Item4, Fluctuation is stronger factor than Residual. And rest of them, Residual is stronger factor than Fluctuation.Fig. 3(d) shows the clustering result for Total Evaluation in AF, as an example of classification.

3.4. Discussion

In section 3.3, we have found that each item of feeling impressions can be expressed as Eq. (2), and the average of regression coefficient as shown as Table 3 (AF), Table 4 (LF), Table 5 (MF), and Table 6 (HF).

As shown in Table 3 trough Table 6, we can see the tendency that Normalized Residual Coefficient (NRC) α_2^* is higher than Normalized Fluctuation Coefficient (NFC) α_1^* as investigation results, generally. And Group1 has a feature that the NFC is negative value for all items in whole frequency domain. From these results, NRC α_2^* is much higher than NFC α_1^*, so normalized explanatory variable of Residual x_2^* has more affective to feeling impression score y than normalized explanatory variable of Fluctuation x_1^*.

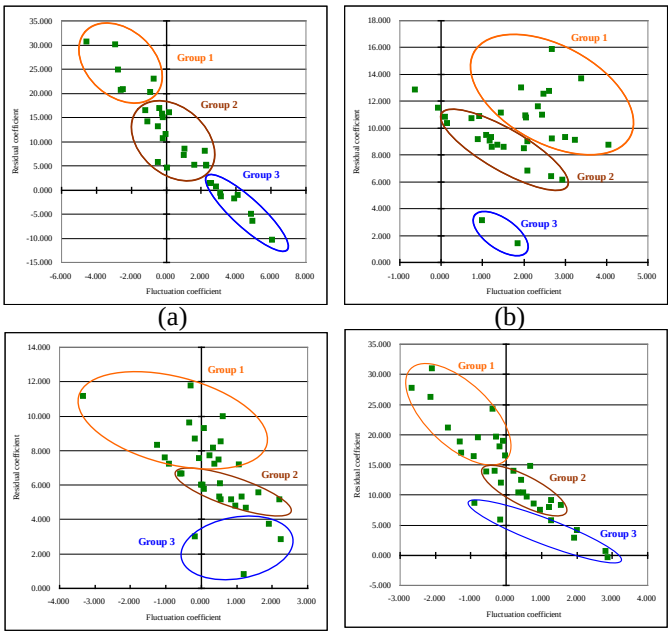

(a) (b) (c) (d)

Fig. 3. Example of Regression analysis of feeling impression (a)AF, (b)LF, (c)MF, (d)HF

4 CONCLUSION

In this paper, we have researched the relationship between 3PACF of frequency domains and feeling impression in sound signal. As a way of research, we have used a questionnaire survey concerning how the relation between 3PACF and the feeling impression of music is. Based on the constructed multiple linear regression equations, we can also consider the statistical tendency as to how the human impression will change if the explanatory variable of Fluctuation (x_1) or Residual (x_2) change. Briefly speaking, the effect of the Residual seems to be stronger than that of Fluctuation. For further study, we need some sensitivity analysis for those parameters.

The questionnaire survey was acquired by limited number of persons or age, music as investigation objects was also limited, though we have understood the feeling impression of music can be some classified using 3PACF of the frequency domains.

For further study, we need some sensitivity analysis for 3PACF or we need to use principal component analysis. Moreover, we have to investigate if we modify 3PACF of the each frequency domains independence, how affect feeling impressions change.

REFERENCES

[1] T. Musha (1999), Reason why person feels pleasantness and unpleasantness--- sound, image, and sense of touch--- that approaches to the mystery of "pleasantness" (in Japanese), Kawade Shobo Shinsya (KAWADE dream new book).
[2] T. Musha (1980), The world of fluctuation – Mystery of 1/f fluctuations of the world – (in Japanese), Kodansha Bluebacks, Kodansha.
[3] H. Akaike and T. Wada (1997), Fluctuation and rhythm of living body (in Japanese), Kodansha Scientific.
[4] S. Horiuchi (1997), Mystery of fluctuation (in Japanese), Shinano Mainichi Newspapers Co.
[5] E. Teramoto, R. Hirota, T. Musha, and M. Yamaguchi (1985), Infinity, chaos, and fluctuation (in Japanese), Bifukan.
[6] T. Musha(1998), Conception of fluctuation that approaches to the mystery of 1/f fluctuation (in Japanese), NHK Books.
[7] T. Musha (1991-1999), Science of fluctuation, <1> through <10> (in Japanese), Morikita Publication.
[8] Y. Kawakami, T. Hattori, T. Yamamatsu, T. Izumi, H. Kawano (2011), Experimental Investigation of the Relation between Feeling Impression and Quantities Accompanying Fluctuation Calculation in Sound Signal (in Japanese), Transactions of Japan Society of Kansei Engineering, Vol.10, No.3, pp.365-374, 2011.
[9] B. S. Everitt (2002), The Cambridge Dictionary of Statistics, Cambridge University Press 2nd edition

© ISAROB 2013

The Eighteenth International Symposium on Artificial Life and Robotics 2013 (AROB 18th '13),
Daejeon Convention Center, Daejeon, Korea, January 30-February 1, 2013

Color image arrangement by elastic transform based on histogram matching

Daisuke Kutsuna[1], Tetsuo Hattori[1], Yusuke Kawakami[1], Haruna Matsushita[1],
Yoshiro Imai[1], Tetsuya Izumi[2]

[1]Kagawa University, Japan
[2]Micro Technica Co., Ltd., Japan
Corespondence:hattori@eng.kagawa-u.ac.jp

Abstract: Aiming at automated affective color image arrangement, this paper proposes a new method using histogram based Elastic Transform (ET) on some kinds of axis including Lightness axis. If we represent a pixel of input image as a vector in the three-dimensional RGB color space, the input image corresponds to a set of the three-dimensional pixel vectors. As for axis other than the Lightness axis, there are PC axes that can be obtained by Principal Component Analysis (PCA) from the set of three-dimensional vectors. In this paper, we present a principle of the ET on the Lightness axis and PC one. We also illustrate that HMGD (Histogram Matching based on Gaussian distribution) is regarded as one of the ET method. In addition, for the investigation of the performance, we show the experimental results by applying the transform (especially HMGD) to some images.

Keywords: Color arrangement, elastic transform, histogram equalization, histogram matching.

1 INTRODUCTION

Recently, automated image processing for enhancement and/or arrangement is becoming more familiar to us according to the spreading of Digital Camera, Smart Phone, DVD, etc. ([1]-[3]). However, we consider that the research on the automated image arrangement method with sensibility effect is still on the way to practical use.

In this paper, we propose a method for image arrangement by elastic transform utilizing histogram (e.g. Histogram Equalization (HE), Histogram Matching (HM)) on some kinds of axis ([4]-[6]). As for the axis, there are Lightness axis and principal component axis that can be obtained by Principal Component Analysis (PCA). Also in this paper, we show the principle of the method and some application results.

2 ELASTIC TRANSFORM (ET)

2.1 Principle

We describe the principle of histogram based elastic transform in the following. Let $f(x)$ and $g(y)$ be two probabilistic density functions on real variables x and y, respectively. The probabilistic density function (pdf) is corresponding to histogram of gray level image. However, the histogram is defined on discrete variable. In addition, let $y=\phi(x)$ be a continuous and monotonous increase function between variables x and y as shown in Fig. 1. In addition, let value of x be the range from 0 to L. Accordingly, variable y ranges from 0 to $\phi(L)$. Let P mean the probability. From the above definitions and Fig.1, we have Eq.(1)-Eq.(3). From Eq.(3), we obtain Eq.(4)and Eq.(5).

Thus, if we know the $y=\phi(x)$ and $g(y)$, then we have the $f(x)$.

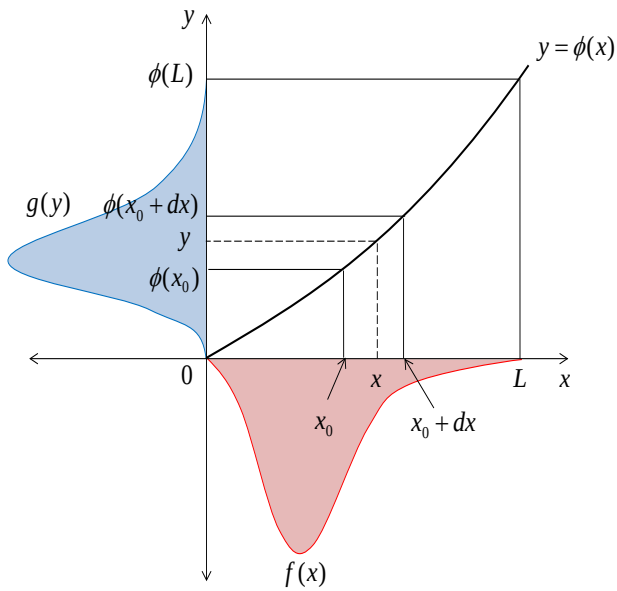

Fig.1. Continuous and monotonous increase function $y=\phi(x)$ and probabilistic density functions $f(x)$ and $g(y)$.

$$P(0 \le x \le L) = \int_{x=0}^{x=L} f(x)dx = 1 \tag{1}$$

$$P(0 \le y \le \phi(L)) = \int_{y=0}^{y=\phi(L)} g(y)dy = 1 \tag{2}$$

© ISAROB 2013

$$\begin{aligned} f(x)dx &= P(x_0 \le x \le x_0 + dx) \\ &= P(\phi(x_0) \le y \le \phi(x_0 + dx)) \\ &= P(y_0 \le y \le y_0 + dy) \\ &= g(y)dy \end{aligned} \tag{3}$$

where $y_0 = \phi(x_0)$, $y_0 + dx = \phi(x_0 + dx)$.

$$f(x)dx = g(y)dy = g(y)\phi'(x)dx \tag{4}$$

$$f(x) = g(y)\phi'(x) \tag{5}$$

Using the above equations, we derive the principle of Histogram Equalization (HE). Let $\phi(x)$ be defined by the following Eq.(6).

$$\phi(x) = L\int_0^x f(x)dx \tag{6}$$

Since $\phi'(x) = Lf(x)$, according to Eq.(5),

$$f(x) = g(y)Lf(x) \tag{7}$$

Then we have

$$g(y)L = 1 \text{ and } g(y) = 1/L. \tag{8}$$

Using the above equations, we derive the principle of Histogram Equalization (HE). Let $\phi(x)$ be defined by the following Eq.(6).

Therefore, we understand that, if we take the transform function as Eq.(6), $g(y)$ becomes uniform distribution as shown in Fig.2. It corresponds to the Histogram Equalization (HE) processing, which means that function defined by cumulative histogram transforms the original histogram into the uniform one.

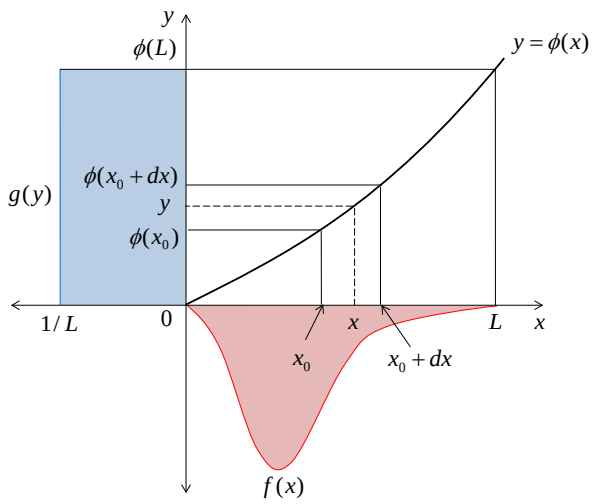

Fig.2. Conceptual image of the relation between uniform distribution and original distribution.

Inversely, if we define the transform function $\phi(x)$ as an integral of desired pdf $f(x)$ for example, Gaussian distribution, we can obtain the desired pdf using the $\phi(x)$ and the uniform distribution such as Eq.(8) (Fig.3).

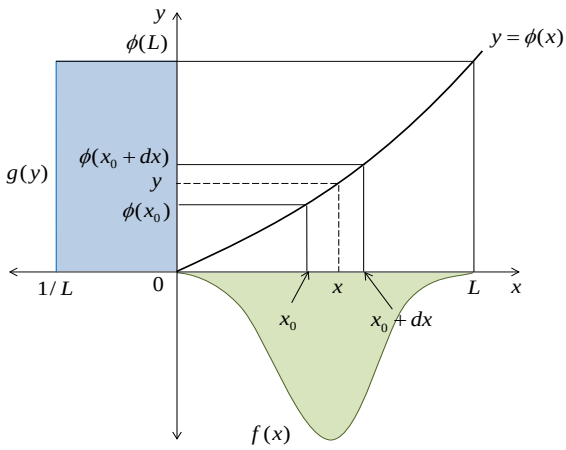

Fig.3. Conceptual image of the transform from uniform distribution (pdf) to the desired one (pdf).

The abovementioned theory means that, if we combine the both transform, we can obtain the transformation from an original distribution (pdf) to a desired one. This means that an image with original histogram can be transformed into another image with desired histogram. We consider that it is the principle of the Histogram Matching (HM) [4] (Fig.4).

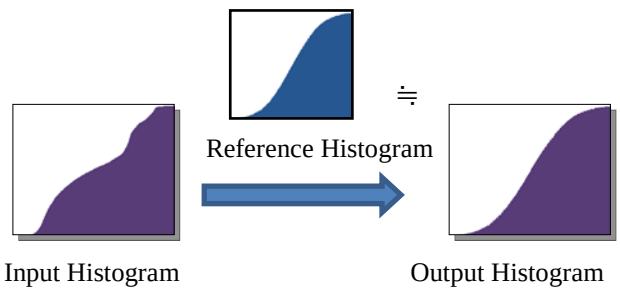

Fig.4. Histogram Matching (HM) [4].

2.2 Transform on axis

We can choose the abovementioned transform such as HE and HM on arbitrary axis (for example, principal component axis) in the color attribute space (RGB space) as shown in Fig.5.

For example, if we choose HE processing on the light axis, it can bring about image enhancement by contrast stretching. In addition, if we choose the HE on a principal component axis in RGB space, we guess that the contrast stretching will be done along to a certain tone of color. Fig.6 shows examples of the HE on Lightness axis and PC (Principal Component) axis.

For example, if we choose HE (Histogram Equalization) processing on the light axis, it can bring about image enhancement by contrast stretching. And if we choose the HE on a principal component axis in RGB space, we guess that the contrast stretching will be done along to a certain tone of color as shown in Fig.6 that shows examples

© ISAROB 2013

of the HE on Lightness axis and PC (Principal Component) axis.

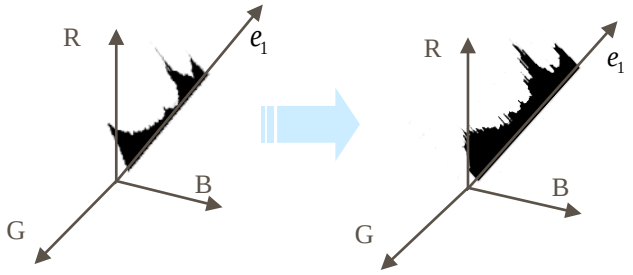

Fig.5. Conceptual image of histogram based elastic transform on arbitrary axis in the RGB space.

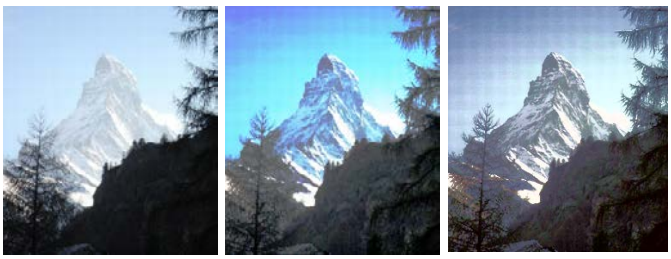

(a)Original image. (b)Lightness axis. (c)PC axis.
Fig.6. Examples of the HE on Lightness and PC axis.

3 HISTOGRAM MATCHING BASED ET

The abovementioned Histogram Matching (HM) can be regarded as one of the Elastic Transform (ET) method. Since there are many kinds of reference histogram and axis, we will find various ET methods as much.

As one of those ETs, we focus on a histogram based ET method in which the reference histogram is Gaussian distribution (Fig.6) on Lightness axis. We call it "Histogram Matching based on Gaussian Distribution (HMGD)".

Fig.7 shows the results by two histogram based ET methods such as HE and HMGD on Lightness axis. From this, we find that HMGD results in moderate transformation from the original image, comparing with HE.

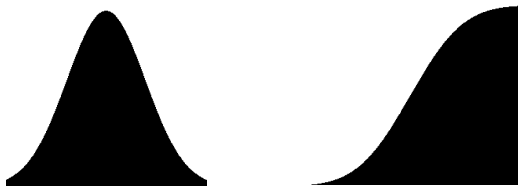

(a) Gaussian distribution (b)Cumulative histogram
Fig.6. Gaussian distribution histogram.

4 INVESTIGATION OF HMGD

In this paper, we investigate the effects by the HMGD. Fig.8 shows examples that HMGD works well from feeling impression. From Fig.9, we can find out that the cumulative histogram of the resultant image clearly approaches to the cumulative Gaussian distribution.

(a)Original image. (b)HE. (c)HMGD.
Fig.7. Example of the results by HE and HMGD.

(a)Input image A (b) Output image A

(c)Input image B (d) Output image B
Fig.8. Examples of the resultant HMGD.

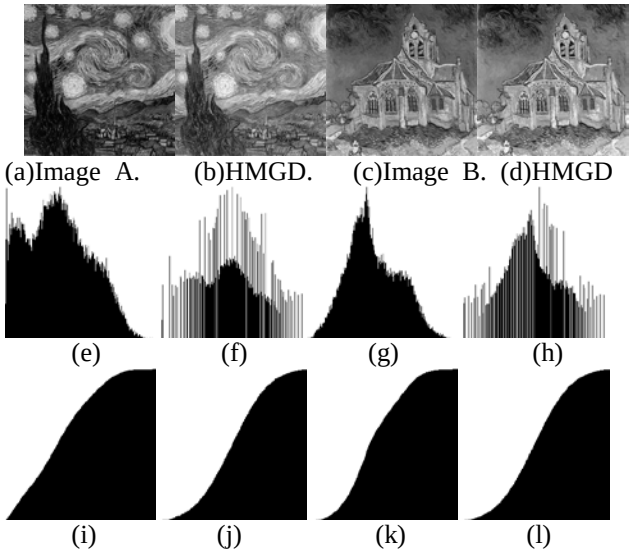

Fig.9. Results of HMGD and the corresponding histogram ((e)-(h): histogram of the above image, (i)-(l):cumulative histogram of the above histogram).

© ISAROB 2013

On the contrary, Fig.10 shows examples that it does not so work well, judging from our feeling impression. From, Fig.11 shows that the corresponding histograms. If we compare with Fig.9, we can find out that there are double peaks in the histogram of Image C and D (Fig.12), while there is single peak in that of the Image A and B.

(a)Input image C

(b) Output image C

(c)Input image D

(d) Output image D

Fig.10. Examples of the resultant HMGD in the case where it does not work well.

(a) Image C. (b)HMGD. (c)Image D. (d)HMGD.

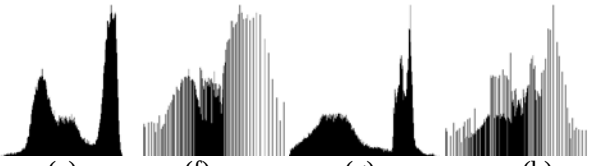

(e) (f) (g) (h)

(i) (j) (k) (l)

Fig.11. Results of HMGD and the corresponding histogram ((e)-(h): histogram of the above image, (i)-(l):cumulative histogram of the above histogram).

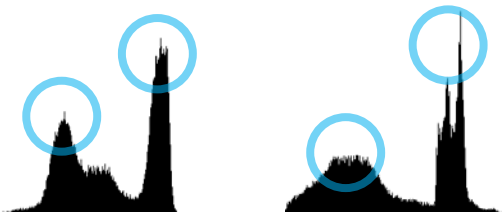

(a)Histogram of Image C. (b)Histogram of Image D.

Fig.12. Bimodality histogram on Lightness of Image C and D. ((a) and (b): the same as (e)and (g) in Fig.11,respectively. There are double peaks in each histogram.)

5 CONCLUSION

Aiming at automated affective color image arrangement, we have proposed a concept of Elastic Transformation (ET) method based on histogram, that varies on some kinds of axis such as Lightness axis and Principal Component one in RGB space. We also have described the principle in the details. And we have explained that HMGD (Histogram Matching based on Gaussian Distribution) is regarded as one of the ET method. Moreover, for the investigation of the performance, we have shown the experimental results. From the experimentation, we have found that HMGD works well for images if the histogram has single peak. Then we consider that automated detection of the single peak is promising for our aim.

REFERENCES

[1] Rafael C. Gonzalez, Richard E. Woods (1993), Digital Image Processing, Addison-Wesley Publishing Company.

[2] Bernd Jahne (1995), Digital Image Processing -- Concepts, Algorithms, and Scientific Applications --, 4th Edition, Springer.

[3] Scott E Umbaugh (1998), Computer Vision and Image Processing: A Practical Approach Using CVIPtools, Prentice Hall PTR.

[4] Wilhelm Burger, Mark J. Burge (2009), Principles of Digital Image Processing: Fundamental Techniques, Springer, 2009.

[5] Tetsuya IZUMI, Tetsuo HATTORI, Shunichi SUGIMOTO, Toru TAKASHIMA (2009), "Color Image Arrangement Using Elastic Transform on Principal Component Axis", Journal of Japan Society of Kansei Engineering, Vol.8, No.3, pp.667-674, Feb. 2009 (in Japanese).

[6] Tetsuya IZUMI, Tetsuo HATTORI, Emiko FUJITA, Shunichi SUGIMOTO, Hiromichi KAWANO (2010), "Feeling Impression and Quantities Accompanying Calculation of Fluctuation in Color Image", Journal of Japan Society of Kansei Engineering, ISSN 1882-8930, Vol.9, No.2, pp.243-250, Feb. 2010 (in Japanese).

© ISAROB 2013

The Eighteenth International Symposium on Artificial Life and Robotics 2013 (AROB 18th '13),
Daejeon Convention Center, Daejeon, Korea, January 30-February 1, 2013

Face identification insensitive to facial expression in the crowded people scene

Qingyu Shu[1], Tetsuo Hattori[1], Saki Masunari[1], Tetsuya Izumi[2],
Hiromichi Kawano[3], Bahram Javidi[4]
[1]Kagawa University, Japan
[2]Micro Technica Co., Ltd., Japan
[3]NTT Advanced Technology, Japan
[4]University of Connecticut, USA
Corespondence:hattori@eng.kagawa-u.ac.jp

Abstract: Face identification in the crowded people with various facial expressions is one of the most difficult themes in the pattern recognition field. In addition, the recognition of facial expression after the identification is very important as an advanced pattern recognition problem in Kansei Engineering field. Currently, there have been developed some methods at the level of practical use such as personal authentication. However, neither the theory nor the method has been established yet for the partial recognition problem that means the identification of a specific person's face from the crowd people scene. In this paper, we propose a novel face identification method insensitive to facial expressions using the notion of weighted vector field and weighted similarity. Also, we show the effectiveness by showing the experimental results.

Keywords: face identification, KL Expansion, region weighted vector field, spatial correlation, weighted similarity

1 INTRODUCTION

Although research on identification of person by face has being widely done ([1]-[6]), the recognition for arbitrary plural people image under genaral background is still difficult problem.

For such a problem, we have proposed a recognition method using a vector field ([7]-[12],[15]), that judges whether the face of acquaintance exists or not in the crowded people image, and also detects and extracts the face region from the image. In the method, there is an assumption that the pattern to be recognized is perturbed by some variation which is roughly equals to be an Affine transform (rotated, enlarged/reduced, and translated) from a registered original face pattern.

However, since the recognition method using the vector field method is sensitive to the facial expression, when the expression is big, there occurs a case where the method does not work well.

Then in this paper, we propose a region weighted vector field (RWVF) method insensitive to the facial expression. The RWVF itself is obtained by emphasizing some characteristic parts in the vector field that is constructed by making a normalized gradient vector field (NGVF) of grey level image ([13],[14]). This method is also aimed for the recognition of the kansei (feeling) information from the facial expression. That is, the method is proposed not only for the identification but also for the recognition of feeling after the identification processing.

This paper also describes the effectiveness of this method, by showing the experimental results for people images that are naturally acquired indoor and outdoor.

2 RECOGNITION METHOD

This method is composed of 2 stages, one is Learning and Analysis stage as a preprocessing one and another is Recognition stage. The input images are monochrome grayscale (or gray level) images with a size of 256x256 pixels. Color images are converted into grayscale images before input to recognition processing.

Here, we use the following terminology.

(a)Original registered pattern: the original face image to be recognized, also called original pattern.

(b)Registered pattern: the variation of original pattern obtained by Affine transform.

(c)Reference pattern: the eigenvector obtained from a set of several registered patterns by Karhunen-Loeve (KL) expansion. It will be used for similarity computation with input image.

This method automatically generates reference patterns at the learning and analysis stage, and after that, it executes the recognition process as recognition stage.

© ISAROB 2013

2.1. Learning and analysis stage as preprocessing

The flow of this processing is as follows.

STEP1 : Make plural registered patterns from an original face pattern by Affine transform (enlarged or reduced, rotated).

STEP2 : Divide registered patterns into some groups, and construct the Normalized Gradient Vector Field (NGVF) expression. Then, apply the KL (Karhunen- Loeve) expansion to every group, and make the reference pattern that has common component.

2.2. Generation of registered patterns

Applying Affine transform to given original registered pattern, our method automatically makes some registered patterns by enlargement/reduction and rotation (Fig.1).

As an experiment, this method totally generates 240 registered patterns, changing original registered pattern by every 3% enlargement/reduction from 50% to 150%, and by every 3 degrees rotation from -10 degrees to +10 degrees. Then it can be divided them into 20 groups, where each group contains 12 registered patterns.

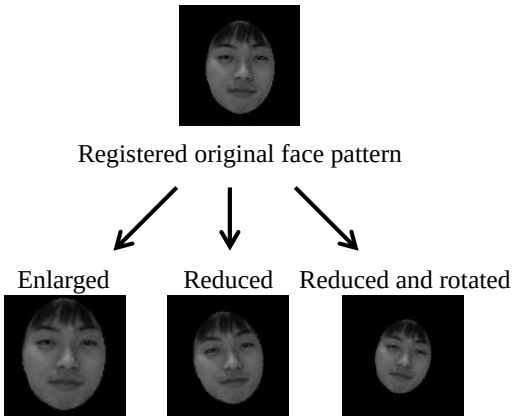

Fig.1. Example of registered patterns ([12],[15]).

2.3. Normalized Vector Field（NGVF）

Gradient vector is obtained at each point $(x,\ y)$ by partial differentiation of the gray level image as Eq.(1). To obtain the NGVF, normalize the size (norm) of the gradient vector to 1.0 if the norm is greater than a threshold, else to 0.

$$\mathbf{grad}\ f(x,y)=\left(\frac{\partial f}{\partial x},\frac{\partial f}{\partial y}\right)=\|\mathbf{grad}\ f(x,y)\|\cdot(\cos\theta,\ \sin\theta) \quad (1)$$

where θ is the phase of the vector.

2.4. Making reference patterns

By using Karhunen-Loeve(KL) expansion for each group of registered patterns represented as NGVF, we can obtain the reference patterns (eigenvectors in KL expansion) which has the common feature among patterns in each group. These reference patterns are used in the subsequent spatial correlation and similarity computation.

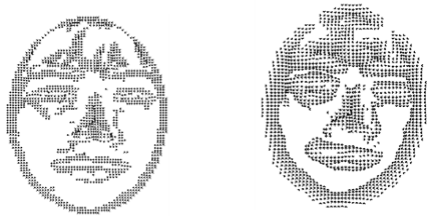

Fig.2. (a) Example of NGVF. (b) Example of reference pattern ([12],[15]).

2.5. Recognition stage

The flow of this recognition processing is as follows.

STEP1: Calculate the similarity which are based on spatial correlation between input image and the reference pattern (pattern matching), and find similarity distribution with the reference pattern in each point in an input image.

STEP2: Based on similarity distribution, detect a candidate locations where the face pattern of interest may exist in the input image, and roughly estimate the scaling and rotation parameters.

STEP3: Repeatedly calculating the similarity, perform the adjustment (fine estimation) of parameter values by means of correction formulas based on Taylor expansion of the affine transforms.

STEP4: Recognize the biggest similarity using the corrected parameters, and extract the face patterns exhibiting the maximum similarity.

2.6. Similarity computation

In order to detect the existence of a target face pattern, our method computes the similarity between input image and reference pattern both of which are represented as NGVF, based on the spatial correlation as shown in Eq.(2). The input image g ($g(x,y)$) and the reference pattern ev ($ev(x,y)$) are defined as complex valued functions.

The similarity between reference pattern ev and input g is given by Eq.(2).

$$Similarity=\frac{|\mathbf{Re}\{\langle g|ev\rangle\}|}{\|ev\|\cdot\|g_s\|} \quad (2)$$

where $\langle g|ev\rangle$ is the inner product between input image and reference pattern, and the inner product is defined as $\langle g|ev\rangle=\iint g(x,y)\cdot\overline{ev(x,y)}dxdy$. The notations **Re** and | | stand for real number of complex number and absolute value, respectively. || || denotes norm of pattern, and it is defined as $\|ev\|=\sqrt{\langle ev|ev\rangle}$. $\|g_s\|$ represents the norm of the subpattern g_s in input image g, which is defined on the

overlapped region between g and ev. The spatial correlation can be considered as inner product $\langle g|ev\rangle$ at every pixel when the reference pattern ev is shifted.

(a) Original face. (b) Input image.(c) Recognition and extraction result.

Fig.3. Recognition processing using NGVF ([12],[15]).

2.7. Region Weighted Vector Field (RWVF)

In RWVF, the absolute of the vector is normalized using some weights (e.g., 1.5, 2.0), depending on face regions. At the pixel other than the weighted region, the norm becomes 1.0 (i.e. the same as the usual NGVF). The purpose of using this **RWVF** is to emphasize the characteristic part of the face (i.e. eyes, nose) and to reduce the lighting influence.

In the similarity calculation, we use a spatial weight function $w(x, y)$ (real variable function). And so, the inner product between input image and reference pattern is shown as Eq.(3). Then, the similarity is defined as Eq.(4).

$$\iint w(x,\ y)\cdot g(x,\ y)\cdot \overline{ev(x,\ y)}dxdy = \iint g(x,\ y)\cdot \overline{w(x,\ y)ev(x,\ y)}dxdy = \langle g|w\cdot ev\rangle \tag{3}$$

$$Similarity = \frac{\left|\mathbf{Re}\{\langle g|w\cdot ev\rangle\}\right|}{\|w\cdot ev\|\cdot\|g_s\|} \tag{4}$$

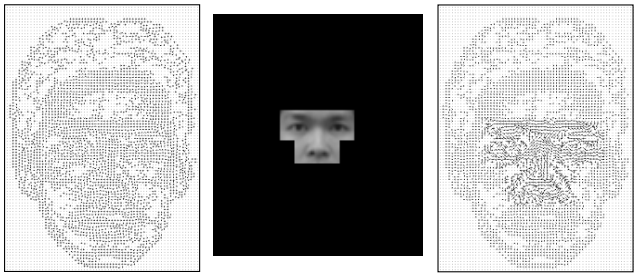

(a) (b) (c)

Fig.4. (a)NGVF, (b)Weighted region, (c)RWVF.

3 EXPERIMENTATION

3.1. Environment

Using the RWVF method, we perform some experiments. The experimental environment is in the following.

OS: Microsoft Windows XP Professional. CPU: Intel(R) Core(TM)2. Drive frequency: 2.40GHz. Memory storage: 1.85GB. Programming Language: Borland C++ 5.02J.

3.2. Experimentation of comparison between the NGVF method and RWVF one

(i) Outline of the experiment

We compare the recognition rate and recognition time by the two methods, NGVF method and RWVF one by experimenting for 100 pieces of input images that are taken indoors and outdoors. There are 2-5 people in the images. The weight in RWVF is 2.0, that is, the vector norm on the weighted region is 2.0, otherwise the same as NGVF.

(ii) Experimental results

In this time experimentation, recognition rate has been almost same level. But the failed images are different (Fig. 5 and 6). In Fig.5 and Fig.6, the persons in the red circle and blue circle are the target to be recognized and misrecognized person, respectively. From this result, the recognition failure by the usual NGVF method can be improved by RWVF method. The results are shown as in the following.

[NGVF]

Accurate recognition rate: 99/100 (99%).

Average recognition time: 3.6 sec.

(Rough estimation: 2.6 sec. Fine estimation: 1 sec.)

[RWVF (weight:2.0)]

Accurate recognition rate: 98/100 (98%).

Average recognition time: 3.8 sec.

(Rough estimation: 2.5 sec. Fine estimation: 1.3 sec.)

Fig.5. Recognition failed image by NGVF.

Fig.6. Recognition failed images by RWVF method in the case where the weight is 2.0.

3.3. Relation between weight and recognition rate by RWVF method

Based on the result of the comparative experiment, we

change the weight of the RWVF method and investigate the relation between the weight and the recognition rate for the same 100 pieces of images. We have changed the weight from 1.0 to 2.0. Fig.7 shows that the recognition rate becomes 100% when the weight lies in the range from 1.09 to 1.46. Then we consider that RWVF with suitable weight is effective to the facial expression variations.

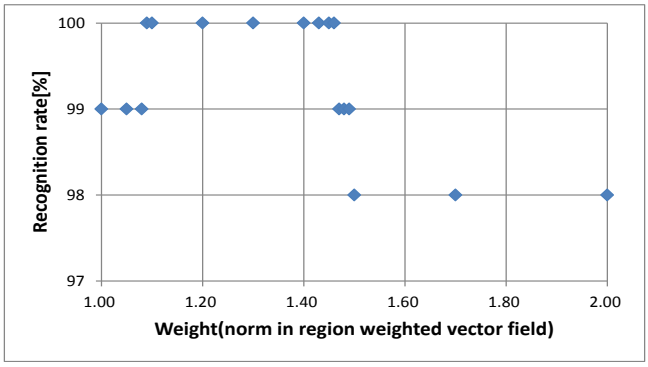

Fig.7. Relationship between weight and recognition rate.

4 CONCLUSION

The aim of our study is not only the identification of the person by face but also to read the Kansei (or feeling) information from the facial expressions. However, because our previous method is sensitive to the facial expression, it does not work so well if the expression is big. This paper has proposed RWVF method insensitive to the facial expression. The experimental results for 100 images have shown that, if the weight value is in the range from 1.09 to 1.46, the face identification is very successful (100% recognition rate).

REFERENCES

[1] M.A.Turk and A.P.Pentland, "Face recognition using eigenfaces," Proc. of IEEE conference on Computer Vision and Pattern Recognition, pp.586-591, June, 1991.

[2] Murase and S.K.Nayar, "Learning object models from appearance," Proc. of AAAI-93, American Association for Artificial Intelligence, pp.836-843, July, 1993.

[3] A.Pentland, B.Moghaddam, T.Starner, "View based and modular eigenspace for face recognition," Proc. of IEEE conference on Computer Vision and Pattern Recognition, pp.84-91, 1994.

[4] Hiroshi Murase and Shree K.Nayar, "Illumination Planning for object recognition using parametric eigenspace," IEEE Trans. on Pattern Analysis and Machine Intelligence, Vol.16, No.12, pp.1219-1227, 1994.

[5] H.Wechsler, P. Jonathon Phillips, V. Bruce, F.F. Soulie, T.S. Huang, ed., Face Recognition --From Theory to Applications--, Springer-Verlag, 1998.

[6] M. Weber, W. Einhauser, M. Welling, P. Perona, "Viewpoint-Invariant Learning and Detection of Human Heads," Proc. of the International Conference on Automatic Face and Gesture Recognition 4TH, pp.20-27, 2000.

[7] T. Hattori, W. Fukuda, K. Takeda, and T. Yamasaki, "Face Recognition among Others as an Affine Transformed Subpattern," Intelligent Autonomous Systems, Y. Kakazu et al.(Eds.), IOS Press, pp.791-796, ISBN:9051993986, June, 1998.

[8] Tetsuo Hattori, Seiu Shu, Waka Fukuda, Toshinori Yamasaki, "New Face Recognition Method among Others in Complex background," Proc. of 2000 NOLTA2000, IEICE, pp.201-204, ISBN: 3933592844, Sept., 2000.

[9] Tetsuo Hattori, Seiu Shu, Toshinori Yamasaki,Waka Fukuda,"Face Pattern Recognition under Complex Background", CD ROM Proceedings of IEEE International Conference on SMC, pp.3890-3895, ISBN:0-7803-6586-0, Oct. 2000.

[10] Tetsuo Hattori, Hiroyuki Kitajima, Toshinori Yamasaki, "Face Recognition in the Crowded People under General Background," Proc. of IEEE IECON2002, vol.2/4, pp.1428-1433, ISBN: 0780374754, Nov., 2002.

[11]Tetsuya Izumi, Tetsuo Hattori, Shu Qing Yu, Hiroyuki Kitajima, Toshinori Yamasaki, "Face Identification for People Image with General Background," Proc. of ISHS'06, pp.140-145, Busan, Korea, Oct., 2006.

[12]Tetsuya Izumi, Tetsuo Hattori, Shu Qing Yu, Hiroyuki Kitajima, Toshinori Yamasaki, "Face Recognition for Image of People under General Background Using Approximate Parameter Estimation of Affine Transform", IEEJ Trans. EIS, Vol.127, No.4, pp.623-629, April 2007 (in Japanese).

[13] Shu Qing Yu, Tetsuo Hattori, Tetsuya Izumi, Hiroyuki Kitajima, and Toshinori Yamasaki: "Face Recognition Method for People Image Using Vector Phase Field and Region-weighted Similarity", Proc. of The 3rd International Symposium on Humanized Systems (ISHS'07), Japan Society of Kansei Engineering, Chinese Association for Artificial Intelligence, The Institute of Control, Automation, and System Engineers (Korea), pp.115-118, Muroran Japan, Sept.13-15, 2007.

[14] Qingyu Shu, Tetsuo Hattori, Tetsuya Izumi, Hiroyuki Kitajima, Toshinori Yamasaki: "Face Identification for People Image with General Background Using Vector Phase Field," CD Proc. of IEEE ICIT2008, WP1-D5, pp.1-5, IEEE Catalog Number: CFP08CIT-CDR, ISBN:978-1-4244-1706-3, Chengdu, China, 2008.

[15]Tetsuya Izumi, Tetsuo Hattori, Shu Qing yu, Hiroyuki Kitajima, Toshinori Yamasaki: "Face recognition for images of persons against a general background using approximate parameter estimation of affine transform", Journal of Electronics and Communications in Japan, John Wiley & Sons, ISSN 1942-9541, Vol.92, No.11, pp.1-8, Nov. 2009.

© ISAROB 2013

The Eighteenth International Symposium on Artificial Life and Robotics 2013 (AROB 18th '13),
Daejeon Convention Center, Daejeon, Korea, January 30-February 1, 2013

Kansei Engineering based Evaluation for Distance Learning on Distributed Multiple Servers

Yoshio Moritoh[1], Yoshiro Imai[2], Tetsuo Hattori[2]

[1]Department of Management Information, Kagawa Junior College, 1-10 Utazu-cho, Ayautagun 769-0201 Japan
[2]Graduate School of Engineering, Kagawa University, 2217-20 Hayashi-cho, Takamatsu 761-0396 Japan
(Tel : +81-87-864-2244)
E-mail: [1]moritoh@kjc.ac.jp, [2]{imai, hattori}@eng.kagawa-u.ac.jp

Abstract: A distributed multiple server system is designed and implemented with Web-DB based services for Distance Learning as well as Emergency Communication. The system has employed multiple servers located in a distributed campus network environment. Each server of the system has multi-core processors. With virtualized CPUs by server virtualization, some programs are executed in parallel (on the virtual servers) so that our system can efficiently perform several functions. Based on our related works, two major applications are realized as a Cloud services on the system. It can provide Distance Learning environment for educational tool as well as Web-based surveillance functions with Emergency Contact. With Kansei Engineering approach, trial evaluation of system has been performed in some classrooms of distributed campus.

Keywords: Visual Computer Simulator, Distance Learning, Distributed Multiple Server System

1. INTRODUCTION

Computer Architecture education is very much useful in the domain of Information Science education because it provides total image computer structure and behaviour and then explains how a computer works correctly. Serval educational tools[1]have been developed and utilized in the practical education fields

Cloud approach is effective and efficient for realization of some e-Learning environment, especially, for development of Distance Learning and/or Collaborative Learning. Some powerful LSI technologies can provide multi-Core CPUs and virtualized servers with such CPUs. These are relatively useful to realize multiple server system for Cloud services.

This paper presents a visual computer simulation for Computer Architecture education and its conventional evaluation in the next (second) section, realization of cloud service with distributed multiple server system for Distance Learning environment and detail of cloud service with virtualized CPUs in the third section, approach of Kansei Engineering-based evaluation to relevant cloud service in the fourth section, and finally summarized conclusion in the last (fifth) section.

2. VISUAL COMPUTER SIMULATOR

2.1 Summaries of a visual computer simulator

First of all, a simulator called *VisuSim* has been implemented as pure Java program to provide two kinds of entries for both Java applet code and Java application one[2]. Each can be selected automatically to invoke the suitable mode of Java program. Namely, for example, *VisuSim* recognizes its invoking environment and decide to execute as a Java applet in the environment of browser or to work as a Java application in the environment where the Java VM executes in the DOS prompt of Windows or in the command interpreter of Linux.

A necessary condition is to equip the Java VM prepared to execute the simulator. So it is very useful because any executable environment will do, just like Windows, Linux and/or Macintosh. There are both sides of views for our visual simulator as are summarized below. The first one is a tool to visualize an internal structure and behavior of computer. It is useful for teacher to show students how a computer works graphically and to explain step-by-step actions of internal register and memory with *VisuSim* which is shown in Figure1. The second is an e-Learning tool to provide an Assembly Programming environment. Such a case is suitable enough to support Assembly Programming Exercise during lecture.

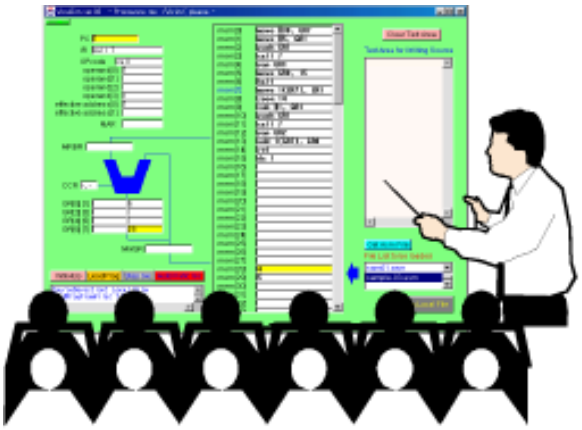

Fig. 1 Using *VisuSim* in Classroom Lecture of Computer Architecture.

- Visualization tool:

VisuSim has 8 sets of general-purpose registers, including Stack Pointer, and 256/512 words of main memory. It can

© ISAROB 2013

simulate computer internal behavior in a register-transfer level. For example, a teacher of Computer Architecture can utilize it to demonstrate graphical view about von Neumann computer architecture by means of wall-hanging screen and PC projector just like Figure1.

- e-Learning tool for Exercise environment:

VisuSim is utilized for writing essays and answering problems of Assembly Programming exercise. Users(Students) of *VisuSim* can understand computer behavior, program processing and well-defined algorithm through verification of assembly program execution. So it is very applicable for users to write correct programs and recognize how a computer processes their programs at the register-transfer level.

2.2 Relation between Scores of Essay and Examination of Computer Architecture

Secondly, it is investigated whether there is any relation of Scores between "Essay using *VisuSim* " and semester-end Examination or not. It has been not yet a perfect investigation and confirmation to analyze any relation between Essay and Examination yet. We should not exactly mention about a kind of relation between Essay and Examination. So we would like to demonstrate some kind of good correlation of Scores between Essay and Examination in 2009. Such a relation is shown in Figure 2.

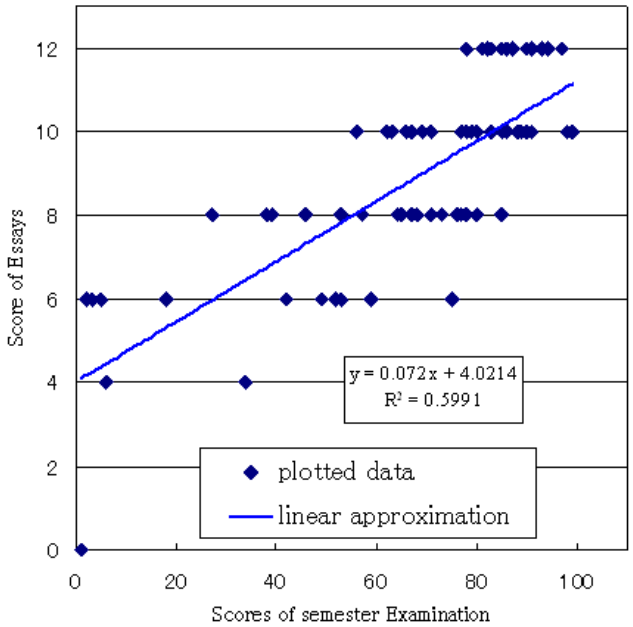

Fig. 2 Relation of Scores between Essay and semester Examination.

This result of comparison is the same aptitude of previous ones, for example, in 2007 and 2008. So it can be confirmed that the simulator *VisuSim* helps students learn "Computer Architecture" in some way according to the above comparison and/or correlation between Scores of Essay and semester-end Examination. Of course, it is necessary to explain that contents of semester-end Examination are not only about basic vonNeumann computer architecture but also include Logic Circuits, Microprogramming, Pipeline Processing and its expansive Architecture, memory architecture,and System Architecture.

Students who know only vonNeumann computer architecture cannot perfectly understand the above themes of "Computer Architecture" and cannot always make excellent scores of semester-end Examination. So we would like to confirm that understanding several themes of "Computer Architecture" is significantly affected by understanding vonNeumann computer and such a case is also significantly affected by using our simulator, *VisuSim* .

3. CLOUD SERVICES ON VIRTUALIZED CPUS OF MULTIPLE SERVER SYSTEM

3.1 Cloud Services on Virtualized CPUs

It is very efficient to realize parallel programs execution and smart management of concurrent services. If some applications need more powerful CPU services, with virtualized CPUs by server virtualization, some programs are executed in parallel (on the virtual servers) so that such a specific system can efficiently perform several functions. In the above case, each information server and its hypervisor (mentined below) can adjust its facilities to migrate (assign) virtualized server and related resources to relevant applications according to dynamic demand changing and/or modification.

One of multi-core CPUs is assigned to execute most useful Linux-based Web-DB software fundamentals. This is a basic layer (i.e. platform) for usual and classical applications. Another is sometimes assigned to multimedia information processing modules, such as image understanding, video transmission, voice generation and so on. Some of them are potentially adjusted to carry out asynchronous information sharing functions and support for emergency contact and/or urgent situation changing.

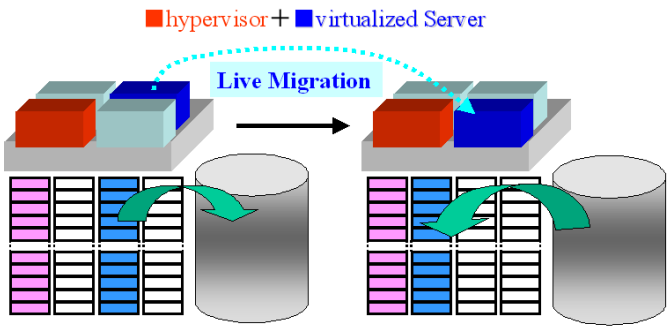

Fig. 3 Live Migration in multi-core CPU architecture.

In figure 3, special-purpose controlling monitor called "hypervisor" can switch one task on some virtualized server from one to another through "Live Migration" context-switching mechanism.

© ISAROB 2013

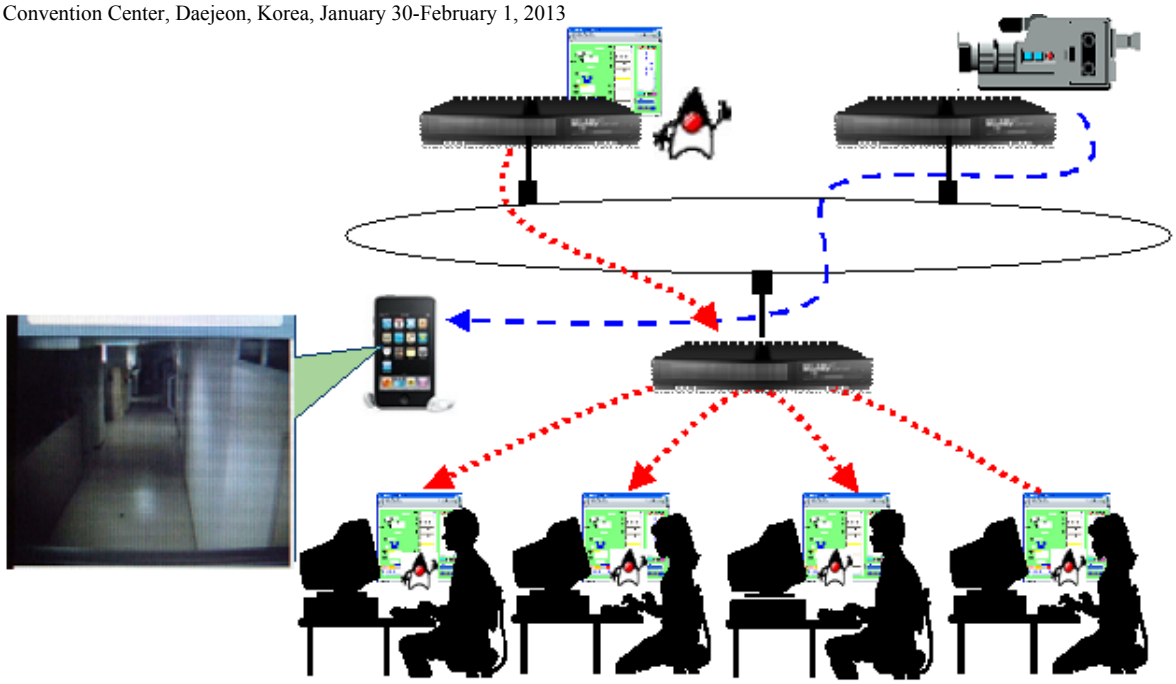

Fig. 4 Overview of Distributed Multiple Server System with *VisuSim* for Distance Learning Environment

3.2 Distributed Multiple Server System for Distance Learning Environment

Figure 4 shows an overview of system configuration for a distributed multiple server system. The system has been implemented in a distributed campus network environment. And each sub-system includes rack-mounted server, UPS and some kinds of clients, such as usual PC, PDA/mobile phone and multimedia input/output devices. Sub-systems are linked and interconnected with campus network by means of Giga high speed and/or Wi-Fi wireless LAN.

Each information server also employs multi-core CPU architecture and virtualized server technology, namely Virtual Machine Scheme, provided by Citrix Xen Server Virtualization[1]. With such a powerful technology, the same system configuration can support stationary normal routines as well as emergent special routines without extra scheme nor irreglar provision.

Key idea for distributed multiple sever system is to utilize the above "Virtual Machine Scheme" in order to construct not only Distance Learning environment with *VisuSim* as one of stationary routines but also Web-based surveillance functions with Emergency Contact as one of other routines. Merits of the system shown in Figure 4 are as follows;

- The system has been utilized for daily business routine of Distance Learning environment. With *VisuSim* , Assembly Programming exercises can be carried out through "Computer Architecture" education as one of Distance Learning practices.
- The system can provide Web-based surveillance service and could be useful with Emergency Contact in the case of extraordinary condition like fire, earthquake, and so on.

For the sake of suitable evaluation about our distributed multiple server system, we would like to take an opportunity to employ Kansei Engineering approach and perform trial evaluation in some classrooms of distributed campus. And the relevant results are demonstrated in the next section.

[1] http://www.xen.org/

4. EVALUATION WITH KAISEI ENGINEERING

4.1 Qualitative Evaluation of Simulator on Cloud

There are some comments and recommendation described in Essays from the students, who learned "Computer Architecture" education. They includes relatively subjective expressions, but, at the same time, they can be also qualitative evaluation about *VisuSim* and the relevant distributed multiple server system from the students who were real users of them. Some of positive comments are as follows:

- It is easy to verify and point out mistakes through step-by-step excution and display the result by *VisuSim* .
- I can check change for contents of registers and memory provided by *VisuSim* .
- As I use sample programs through *VisuSim* , it is good enough for me to write new similar ones.

At the same time, some of negative comments are as follows:

- It is difficult for me to operate *VisuSim* , so I must help my friends teach me to operate it. Finally I do write my essay only just until deadline.
- When I modify my program, I have found mistake at the point where program jump from another routine. So I must adjust and shift the according routine.

These are not convenient so that it will be necessary to be improved. These comments must be considered to be precious recommendations for improvement of *VisuSim* and teaching methods. We should have a plan to modify our visual simulator from these feedbacks.

© ISAROB 2013

4.2 Using Condition under Distance Learning

It has been introduced in the previous papers that *VisuSim* is applied to Distance Learning. And it is also reported that using effect of *VisuSim* has been evaluated quantitatively through statistics analysis. In our case, it is confirmed that effectiveness of *VisuSim* is well evaluated in a domain for small users' space only.

Our assertion can be expansible to the following assumption; If some e-Learning tools have original communication facilities and/or information sharing ones, they can provide some kind of effect for Distance Learning under using condition of small member's space.

Based on our experience, we will introduce and discuss a category of member's size for Distance Learning. The category seems to be three scale of member's size, namely, a small scale for no more than 10 members, a medium one for no more than 30 members, and finally a large one for more than 30 members.

Table1 gives a category for Distance Learning environment. Methods for achievement are e-mail as uni-cast communication and bulletin board as broadcast one in Table1. These services are easily available in our distributed multiple server system for Distance Learning environment.

Table 1 Effect of Usage for Distance Learning Environment by means of Communication Facilities

	Unicast	Broadcast
small scale	Confirmation of Effect	Not Confirmed (But expectable)
medium scale	It is necessary to be confirmed	Same as in the left
large scale	Only unicast method would be difficult from our experience	It is considered to be useful

4.3 Evaluation based on Comments with Kansei Engineering approach

In the above case, multi-cast communication includes broadcasting one so that we will denote explicitly "multi-(broad)cast" in the later explanation. In uni-cast communication, e-mail needs knowledge about the participants in a small scale of cooperative education environment. There is a trend that a user who want to ask his/her question do communicate to others who seems to reply such a question. Probability and expectation are very important in order to achieve communication for information sharing in Distance Learning environment. Some comments in student's essay may include useful information and knowledge[3].

These comments has been analyzed and categorized in the six criteria, namely, "operate easily", "communicate efficiently", "response quickly", "virtualize smoothly", "reproduct(= repeat) flexibly" and "understand effectively". Evaluation has been performed in some classrooms of distributed campus through their students' essay. And analyzed results are averaged and expressed in Radar Chart shown in Figure5. Especially, it is confirmed that Communicabiliy, Virtuality, Reproductability and Understanding are good for students through real experience.

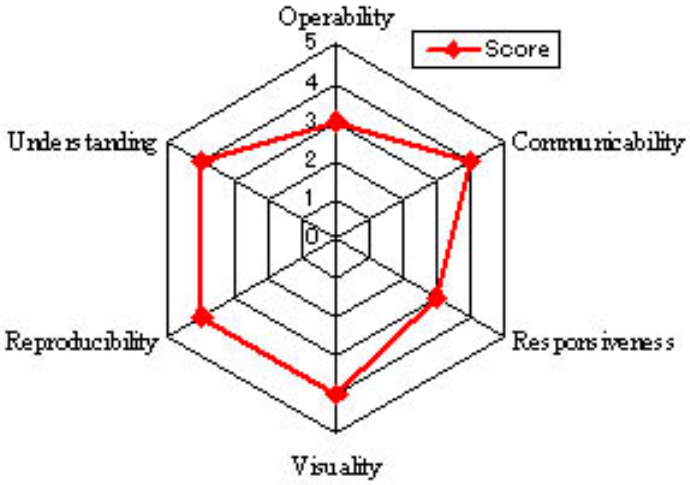

Fig. 5 Radar Chart of Evaluation for System by Kansei Engineering Approach.

5. CONCLUSION

This paper reports summaries of Distance Learning tool for Computer Architecture (visual computer simulator *VisuSim*), construction of distributed multiple server system with virtualized CPUs by server virtualization, and some evaluation for such server system from the aspect of users by means of Kansei Engineering approach.

It is concluded as follows;

- *VisuSim* is effective for students to learn "Computer Architecture" through a practical education.
- Distributed multiple sever system with "Virtual Machine Scheme" can construct Distance Learning environment with *VisuSim* as one of stationary routines as well as Web-based surveillance functions with Emergency Contact as one of other routines.
- Some kinds of evaluations have been performed through qualitative analysis and Kansei Engineering approach.

REFERENCES

[1] Null, L. and Lobur, J.: MarieSim: The MARIE Computer Simulator. ACM Journal of Educational Resources in Computing. Vol. 3, No. 2, Article #1, 29 pages (June 2003)

[2] Imai,Y. and Tomita,S.: A Web-based Education Tool for Collaborative Learning of Assembly Programming. In: 2nd IADIS International Conference on WWW /Internet 2003(Algarve), Vol.1, pp. 703–711.

[3] Scott, K., Benlamri, R. : Context-Aware Services for Smart Learning Spaces. IEEE Transactions on Learning Technologies, Vol.3, No.3, pp.214–227, July-September 2010.

© ISAROB 2013

The Eighteenth International Symposium on Artificial Life and Robotics 2013 (AROB 18th '13),
Daejeon Convention Center, Daejeon, Korea, January 30-February 1, 2013

An Application of Kansei Engineering to Community-base Collaboration

Masatoshi Imai[1], Yoshiro Imai[2], Tetsuo Hattori[2]

[1]Department of Management Information, Kagawa Junior College, 1-10 Utazu-cho, Ayautagun 769-0201 Japan
[2]Graduate School of Engineering, Kagawa University, 2217-20 Hayashi-cho, Takamatsu 761-0396 Japan
(Tel : +81-87-864-2244)
E-mail: [1]imai@kjc.ac.jp, [2]{imai, hattori}@eng.kagawa-u.ac.jp

Abstract: This paper presents a proposal to reconstruct some specific towns which were attacked and destroyed by Huge Tsunami, for example, in Tohoku region of Japan on the 11th of March, 2011. A collaborative approach have been employed to provide some trial proposal to reconstruct such damaged towns by means of Internet Community as follows. (1) Providing a proposal and pictures to reconstruct, especially offering visual design concept of living space for slope topography through Social Network System as an example of Internet Community, (2) Consulting and discussing the above proposal and pictures among specific Internet Community with analysis by Kansei Engineering, and (3) Improving an original proposal into more efficient and suitable one. The paper also explains detail of the senario to brush up the proposal by means of the above collaborative approach and some problems to be resolved in order to make it more fruitful.

Keywords: Collaborative Design, Information Sharing through Social Network, Evaluation by Kansei Engineering Approach

1. INTRODUCTION

Collaborative Design is one of the suitable and reasonable approaches to reach the temporal goal with help from related members and/or community in the relatively short period. Our research focuses on procedure for arranging or improving of residence through collaborative design methodology. One of key ideas is to utilize Social Network in order to achieve collaborative design. And other is to apply Kansei Engineering methodology to evaluation of procedure and decision making of results such a design has produced.

This paper includes concept for collaborative design in the next section, prototyping and improving of collaboration in the third section, evaluation and improvement by Kansei engineering in the fourth section, and summarized conclusion in the final section.

2. COLLABORATIVE DESIGN CONCEPT

It is difficult to decide the most efficient and/or effective element(s) for the relevant users in a short period. Especially, only one or very few persons cannot resolve several problems which one positively evaluate but at the same time another negatively does. Certain size of group can provide a lot of valuable ideas which can determine and adjust such problems into more acceptable solutions for wider range of human requests. Community-based approach will realize such valuable ideas and good design methodology.

Some people say Internet looks like one of huge communities. Of course, Internet itself provides loosely coupled human connectivity so that Internet users always want to have seamless access to LAN, WAN and/or global network in order to obtain several kinds of information, benefits, hints, idea and so on. But unfortunately Internet also includes a lot of evil-mind and ill-intention for a third party.

Whenever connected with Internet, its users have to confirm that information and/or ideas obtained from it are suitable and constructive for them at the glance. Therefore the users want to have not only access to Internet but also specific connectivity of Internet with trust and reliability. Social Network Systems in Internet, which is abbreviated as only SNS, can provide a suitable environment for the members to be safe and confortable in order to perform suitable collaboration for work, evaluation and discussion[1].

One user of SNS can work together with his/her other members in order to communicate one another, exchange each information, and discuss about common problems asynchronously (i.e. not in realtime) but directly (almost without misreading). With connectivity of SNS, users can show their concept/solution, obtain efficient criticism about them from others, evaluate them among their community, and rebuild/modify original concept/solution into improved ones.

3. PROTOTYPING OF COLLABORATION

3.1 A Draft Senario of Collaboration

First of all, we illustrates a draft senario of collaboration and implementation with SNS and then demonstrates an example of Collaborative Design[2] of living space for slope topography through "Facebook" as an example of SNS. Our attempt has been carried out with utilization of Facebook as a efficient SNS of Internet Community.

Reasons to employ Facebook connectivity as SNS are as follows;

- In Japan, there are some famous SNS's for several kinds of users as Internet Community. But almost all are not so famous for foreign countries and also not so convenient for foreign users of Internet Community. Currently, Facebook has a huge numbers of members who belong to several countries and it seems to bes one of most powerful and influential SNS's of the world.

© ISAROB 2013

• Even in the case of our personal experiences, Facebook is more affective and available for us to communicate with our friends and colleagues and exchange several kinds of information and ideas by means of multimedia than others. Users of Facebook must enjoy easy handling of Information, multimedia and computer programming.

Figure1 shows a scheme for data distribution by means of Facebook. It shows that it is convenient for users to distribute original design and idea into their friends and colleagues through a function of Facebook asynchronously and directly. This user wants to proposes his idea and detail of design, transfer the relevant set of idea/design to his colleagues and realize information exchange with utilization of engineering drawing and photos of prototype.

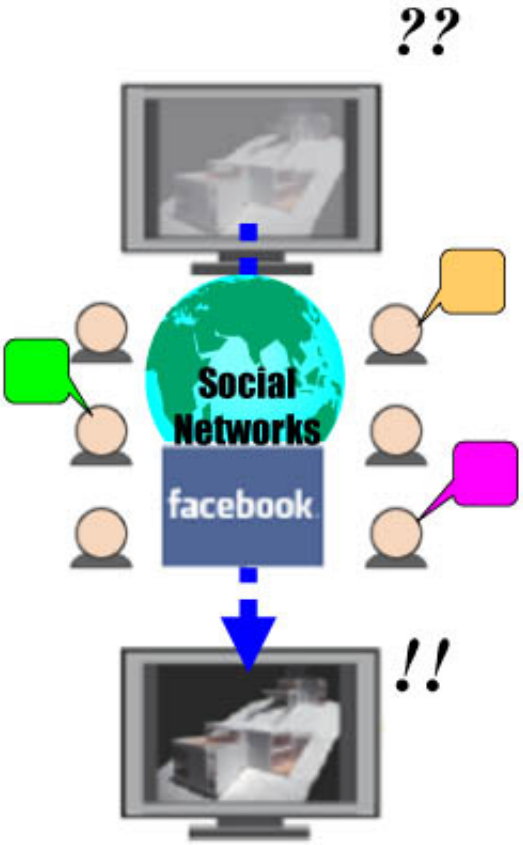

Fig. 1 Collaborated Degin among distributed Colleagues with utilization of benefit by Social Networks

With utilization of SNS, we will be able to expect some effects of Collaborative Design which realize a typical story as follows in Figure1;

1. One of the relevant user's colleagues obtained an original idea through Facebook as Internet Community.
2. He/She thought about such idea and had some different idea and relevant comments for it.
3. He/She sent such different idea and his/her comments to the relevant user for convenience and improvement.
4. The user obtained such useful idea and comments for the sake of his convenient and improvement directly and on-line.
5. Finally, the user can rebuild his original idea and reconstruct design based on the more useful concept and recognition.

With some benefits of Internet Community, we can prepare collaborative environment for efficient design methodology and discussion. We can expect direct communication with foreign colleagues although they are away from us and living in other countries. As the results of communication and discussion, we can obtain professional idea and criticism about our current problems asynchronously but smoothly. In the next subsection, we will demonstrate practical example of Collaborative Design for living space for slope topography through human connectivity of Facebook.

3.2 Example of Collaborative Design

We have been wanting to propose some specific idea to reconstruct living space and/or home for slope topography especially near the seashore for the sake of avoidance of Tsunami's damage. One of authors, namely Masatoshi Imai, has a lot of idea, design concept, and images of prototyping about living space and/or building for slope topography. He is in domain of design field and not so familiar with practical architecture for building and construction.

So he has been expecting that colleagues discuss his design concept, check and evaluate it and finally improve it into more fruitful new one together with himself. Because it is very nice for not only him but also people, who want to live in such a living space for slope topography without a fear about Tsunami, to propose more suitable design concept of living space/building for slope topography, he want to discuss his idea and perform collaborative design through Facebook as a creative environment of Collaborative Design.

We will introduce a practical design concept to build living space for slope topography on window of Facebook shown in Figure2. The relevant design concept displayed in Figure2 can be realized and explained by means of several multimedia information such as engineering drawing, some views of prototyping and physical images for beginners and experts(professional engineers).

Fig. 2 Design Concept to Build Living Space for Slope Topography on Facebook.

© ISAROB 2013

If someone has a glance at such URL, he/she can look at each information as precisely as he/she wants. In order to watch in detail, he/she can focus specific information, namely engineering drawing and/or three dimensional view of relevant building/living space. Figure3 is an example of three dimensional image which demonstrates other view as design concept.

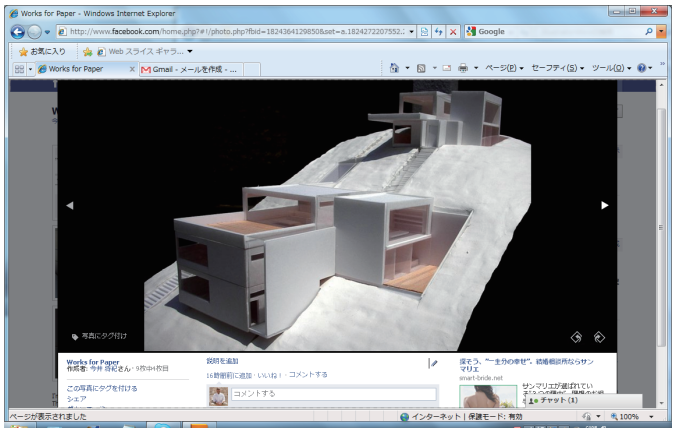

Fig. 3 Sample Three-Dimensional View as a Design Concept on FaceBook.

As described before, we are not professional engineers for architecture, so a chart of engineering drawing is not perfectly suitable to discuss our idea among professional engineers, but three dimensional image will be able to provide certain viewpoints even for nonprofessional persons. We want to obtain some comments and criticism for our draft proposal of design concept of living space for slope topography.

We think that beginners of architecture/landscape need some practical images in order to understand whether living space for slope topography is suitable or not even they want to avoid potential damage of disaster from Tsunami. So we have provide some three dimensional views of living space for slope topography and let the relevant people imagine as if they were living there more closely. Of course, we think that virtual reality and other visualization techniques are necessary for people who want to have more information about our idea. That must be another problem to be resolved by ourselves in future.

4. EVALUATION AND IMPROVEMENT

4.1 Evaluation procedure by Kansei Engineering

As is known, Kansei Engineering[3] is one of efficient approaches to "translate users' psychological (emotional) feeling about a product/image into perceptual (machine-understandable) design element/methodology" for the sake of efficient realization[4]. Our key idea to utilize Kansei Engineering for Collaborative Design are summarized as follows;

- One proposal may obtain a few comments and criticism which differ from one another. In such a case, we need smart strategy to accommodate the above comments and criticism for more suitable and allowable design, product, image and so on. Sometimes, comments and criticism are expressed in not quantitative but qualitative notation, so that we need some efficient mechanism to translate qualitative expression into qualitative one smoothly and suitably. Kansei Engineering is one of the most excellent methodologies to obtain quantitative (i.e. numerical and computer-oriented) parameters from psychological (emotional) expression or feeling.
- Kansei Engineering is one of the well-established methodologies founded in Japan and one of the most applicable procedures to analyze and classify multiple-parameterized input data, which sometimes differ each other for the unified targets. In the world, Kansei Engineering is utilized from car manufacturing to fashion design and available in many kinds of domains which include not only engineering but also several decision making.

For example, in the case of discussion about window size of living space for slope topography, we want to decide whether height and width of window size is suitable for relevant height and width of according wall or not and to obtain information about parameter to enlarge or reduce the height and width of window against the fixed size of wall. For the sake of realization of Collaborative Design, the problem is how to get and find such parameterized request in comments and criticism from colleagues of Internet Community.

4.2 Improvement procedure by Kansei Engineering

We have employed Kansei Engineering approach and its powerful procedure of attribute rating. In order to determine whether size of window should be remained, enlarged or reduced and obtain scale of parameterization for enlargement or reduction of window size, we will apply the following steps;

1. preparing some questionary investigation with 5 stepwise graduations, namely, "enlarge more", "enlarge a little", "remain (or keep this size)", "reduce a little", and "reduce more".
2. defining the maximal amplitude for enlargement and reduction.
3. comparing the result rating from the answer against questionary investigation with 5 stepwise graduations statistically.
4. calculating quantitative result with compared rating into the value from "enlarge more" to "reduce more".
5. mapping the above value into parameterized scale and get scaled amplitude to enlarge or reduce.

For example, we can define mapping function to translate emotional expression into rating of Kansei Engineering shown in "param."-column of Table1. Parameter 'f' in this table means a factor to specify how to enlarge windows or reduce ones for the adjustment according to request from colleagues from Internet Community. Therefore, when the value of 'f' is plus, we decide to choose an operation for enlarging of window. In contrast, when it is minus, we do for reducing

© ISAROB 2013

of window. And absolute value of 'f' specifies amplitude of factor for level of enlarging/reducing.

Table 1 Calculation of Parameterized Attribute with Emotional Expression from Internet Community

emotional ex.	param.	P_1	P_2	P_3	P_4	P_5	
enlarge more	$1.0f$	√	-	-	-	-	$1.0f$
enlarge a little	$0.5f$	-	√	√	-	-	$1.0f$
remain	0.0	-	-	-	√	-	0.0
reduce a little	$-0.5f$	-	-	-	-	√	$-0.5f$
reduce more	$-1.0f$	-	-	-	-	-	$0.0f$

If there are 5 numbers of emotional expressions as comments or criticism from Internet Community,namely from P_1 to P_5, we can try to calculate a parameterized attribute based on some criteria with such expression, which are demonstrated in the right side of Table1 and below numeral expression. And then we can obtain the precise factor to enlarge the relevant window by below calculation.

$$(1.0f + 2 * 0.5f + 0.0f + (-0.5f) + 0.0f)/5 = 0.3f$$

For example, assuming that default value of scaling factor is 10%, we can draw from the above result into enlargement by only 30% $\times f$ in this example. Of course, 'f' can play a role for characteristic constant for original designers to adjust their final decision to operate. If they want to keep their original idea, they should specify 'f' as small as possible.

Just like the above procedure, we can obtain other parameterized requests for Window's size as well as Window's position (namely, XY-position means Width and Height) and some suitable information for Collaborative Design among Internet Community. With Kansei Engineering methodology, we can determine which sensory attributes express particular subjective requests and draw conclusion about which perceptual elements are responsible to enhance emotional decision, for example in Figure4. It is convenient for us to realize Collaborative Design based on Internet Community precisely and sufficiently.

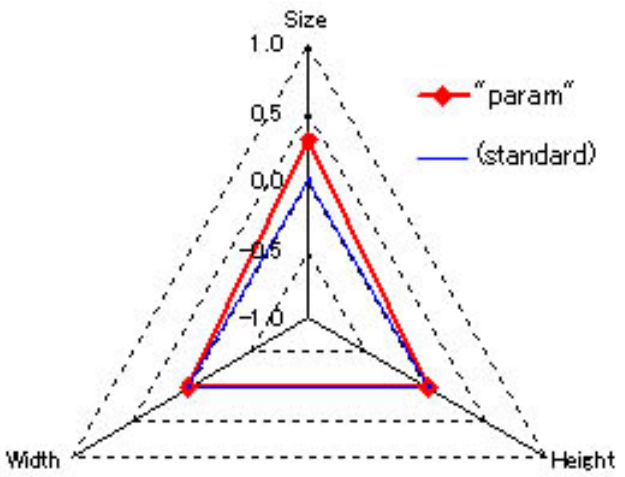

Fig. 4 Radar Chart of Parameters' Value for Improvement.

5. CONCLUSION

This paper describes an example approach of Collaborative Design through Internet Community, which is implemented to provide an idea to reconstruct some living space and environment for people who had been attacked by disaster such as Earthquake and especially Huge Tsunami. We want to provide a visual design concept of living space for slope topography, which is normally seemed not to be suitable for ordinary living but to be of advantage for avoidance of disaster near from sea shore especially.

With our approach, we can conclude as follows;

1. It is necessary to discuss more suitable design concept and/or idea for people who want to have temporary or permanent living environment because they have been damaged by disaster. We decide to employ efficient and effective approach which can be faster and more flexible than usual.
2. It is suitable and convenient for people to provide their idea for some domain by means of Internet Community such as Social Network System. Utilization of "Facebook" as SNS is to obtain several comments and/or messages from Community.
3. Kansei Engineering is good enough to evaluate proposals and analyze their comments, notices and criticism from Community, because of being qualitative ways and data.

As one of our future works, we will develop new information server system to provide an efficient environment for Collaborative Design and analyze in-bound comments and criticism for specific idea and design concept by means of Kansei engineering methodology. We want to communicate with people who consider to live where they are really afraid of potential damage of Tsunami and discuss about our original plan/design concept of living space for slope topography through SNS and/or Internet Community in near future.

REFERENCES

[1] Wang, Y., Yang, J.: Relation Based Service Networks for Reliable Service Selection. In: Proc. of IEEE Conference on Commerce and Enterprise Computing (CEC 2009). pp.209–214, 2009.

[2] Steimle, J.,Brdiczka, O., Mühlhäuser, M. : CoScribe: Integrating Paper and Digital Documents for Collaborative Knowledge Work. IEEE Transactions on Learning Technologies, Vol.2, No.3, pp.174–188, July-September 2009.

[3] Nagamachi, M.: Kansei Engineering: A new ergonomic consumer-oriented technology for product development. International Journal of Industrial Ergonomics, Vol.15, No.1, pp.3–11, January 1995.

[4] Bouchard, C., Lim, D., Aoussat, A.: Development of a KANSEI ENGINEERING SYSTEM for Industrial design: Identification of input data for KES. http://citeseerx.ist.psu.edu/viewdoc/versions?doi=10.1.1.100.7761

© ISAROB 2013

The Eighteenth International Symposium on Artificial Life and Robotics 2013 (AROB 18th '13),
Daejeon Convention Center, Daejeon, Korea, January 30-February 1, 2013

Bottom-Up Pyramid Cellular Acceptors with n-dimensional Layers

Makoto SAKAMOTO[1], Tatsuma KUROGI[1], Makoto NAGATOMO[1], Takao ITO[2], Yasuo UCHIDA[2], Tsunehiro YOSHINAGA[3], Satoshi IKEDA[1],Masahiro YOKOMICHI[1],and Hiroshi FURUTANI[1]

[1] University of Miyazaki, Miyazaki, Miyazaki 889-2192, Japan
[2] Ube National College of Technology, Ube, Yamaguchi 755-8555, Japan
[3] Tokuyama College of Technology, Shunan, Yamaguchi 745-8585,Japan

Abstract

In theoretical computer science,the Turing machine was introduced as a simple mathematical model of computers in 1936, and has played a number of important roles in understanding and exploiting basic concepts and mechanisms in computing and information processing. After that, the development of the processing of pictorial information by computer was rapid in those days.Therefore, the problem of computational complexity was also arisen in the two-dimensional information processing. M.Blum and C.Hewitt first proposed two-dimensional automata as a computaional model of two-dimensional pattern processing in 1967[1]. Since then, many researchers in this field have been investigating many properties of two- or three-dimensional automata. In 1997, C.R.Dyer and A.Rosenfeld introduced an acceptor on a two-dimensional pattern (or tape), called the *pyramid cellular acceptor*, and demonstrated that many useful recognition tasks are executed by pyramid cellular acceptors in time proportional to the logarithm of the diameter of the input. They also introduced a *bottom-up pyramid cellular acceptor* which is a restricted version of the pyramid cellular acceptor, and proposed some interesting open problems about bottom-up pyramid cellular acceptors. On the other hand, we think that the study of n-dimensional automata has been meaningful as the computational model of n-dimensional infomation processing[9]. In this paper,we investigate about bottom-up pyramid cellular accptors with n-dimensional layers, and show their some accepting powers.

Key Words **:** cellular automaton, diameter, finite automaton, n-dimension, pattern recognition.

1 Introduction

In 1967, M.Blum and C.Hewitt first proposed two-dimensional automata as a computational model of two-dimensional pattern processing, and investigated their pattern recognition abilities [1]. Since then, many researchers in this field have been investigating a lot of properties about automata on a two- or three-dimensional tape. In [2], C.R.Dyer and A.Rosenfeld introduced an acceptor on a two-dimensional pattern (or tape), called the *pyramid cellular acceptor*, and demonstrated that many useful recognition tasks are executed by the pyramid cellular acceptors in time proportional to logarithm of the diameter of the input. They also introduced a *bottom-up pyramid cellular acceptor*, which is a restricted version of the pyramid cellular acceptor, and proposed some interesting open problems about it. On the other hand, the question of whether processing n-dimensional digital patterns is much difficult than (n-1)-dimensional ones is of great interest from the theoretical and practical standpoints. Thus, the study of n-dimensional automata as the computasional model of n-dimensional pattern processing has been meaningful. From this point of view, we are interested in n-dimensional automata.

In this paper, we study about bottom-up pyramid cellular acceptors with n-dimensional layers, and deal with the following problems (which is one of the open problems) : Does the class of sets accepted by deterministic bottom-up pyramid cellular acceptors with n-dimensional layers include the class of sets accepted by deterministic *n-dimensional finite automata* [3-7]? This paper shows that the class of sets accepted by n-dimensional finite automata is incomparable with the class of sets accepted by deterministic bottom-up pyramid cellular acceptors which operate in time of order lower than the *diameter* of the input.

2 Definition

Let Σ be a finite set of symbols. An *n-dimensional tape* over Σ is an n-dimensional array of elements of Σ. The set of all the n-dimensional tapes over Σ is denoted by $\Sigma^{(n)}$. Given a tape $x \in \Sigma^{(n)}$, for each j ($1 \leq j \leq n$), we let $l_j(x)$ be the length of x along the jth axis. The set of all $x \in \Sigma^{(n)}$ with $l_1(x) = n_1$, $l_2(x) = n_2, \ldots, l_n(x) = n_n$ is denoted by $\Sigma^{(n_1,n_2,\ldots,n_n)}$. When $1 \leq i_j \leq l_j(x)$ for each j ($1 \leq j \leq n$), let x (i_1, i_2, $\ldots$, i_n), denote the symbol in x with coordinates (i_1, i_2, $\ldots$, i_n). Furthermore, we define x [(i_1, i_2, $\ldots$, i_n), (i_1', i_2', $\ldots$, i_n')], when $i \leq i_j \leq i_j' \leq l_j(x)$ for each integer j ($1 \leq j \leq n$), as the n-dimensional input tape

© ISAROB 2013

y satisfying the following (i) and (ii) : (i) for each j ($1 \leq j \leq n$), $l_j(y) = i_j$' - i_j + 1; (ii) for each r_1, r_2, ... ,r_n($1 \leq r_1 \leq l_1(y)$, $1 \leq r_2 \leq l_2(y)$, ..., $1 \leq r_n \leq l_n(y)$), y (r_1, r_2, ..., r_n) = x ($r_1 + i_1$ - 1, $r_2 + i_2$ - 1, ..., $r_n + i_n$ - 1).

We next give some basic concepts about bottom-up pyramid cellular acceptors with n-dimensional layers [7]. A *bottom-up pyramid cellular acceptor with n-dimensional layers* (n-$UPCA$) is a pyramidal stack of n-dimensional arrays of cells in which the bottom n-dimensional layer has size $2^t \times 2^t \times \cdots \times 2^t$ ($t \geq 0$), the next lowest $2^{t-1} \times 2^{t-1} \times \cdots \times 2^{t-1}$, and so forth, the (t + 1)st n-dimensional layer consisting of a single cell, called the *root*. Each cell is defined as an identical finite-state machine, $M = (Q_N, Q_T, \delta, A)$, where Q_N is a nonempty, finite set of states, $Q_T \subseteq Q_N$ is a finite set of *input states*, $A \subseteq Q_N$ is the set of *accepting states*, and $\delta : Q_N^{2^n+1} \rightarrow Q_N$ is the *state transition function*, mapping the current states of M and its 2^n son cells in a $2 \times 2 \times \cdots \times 2$ block on the n-dimensional layer below into M's next state. For example, the definition in the case of four-dimensional case as follows. Let c be some cell on the (i + 1)st n-dimensional layer, and let c ($UNWP$), c ($UNWF$), c ($USWP$), c ($USWF$), c ($USEP$), c ($USEF$), c ($UNEP$), c ($UNEF$), c ($DNWP$), c ($DNWF$), c ($DSWP$), c ($DSWF$), c ($DSEP$), c ($DSEF$), c ($DNEP$), and c ($DNEF$) be sixteen son cells (on the ith n-dimensional layer) of c, where c($UNWF$) is c's upper northwest son in the most future direction, c ($DNWP$) is c's lower northwest son in the most past direction, etc. For example, if the coordinates of c on the (i + 1)st layer is (1, 1, 1, 1) ((2^t, 2^t, 2^t, 2^t)), the coordinates of sixteen son cells of c on the ith layer c ($UNWP$), c ($UNWF$) ,c ($USWP$), c ($USWF$), c ($USEP$), c ($USEF$), c ($UNEP$), c ($UNEF$), c ($DNWP$), c ($DNWF$), c ($DSWP$), c ($DSWF$), c ($DSEP$), c ($DSEF$), c ($DNEP$), and c ($DNEF$) are (1, 1, 1, 1), (1, 1, 1, 2), (1, 2, 1, 1), (1, 2, 1, 2), (1, 2, 2, 1), (1, 2, 2, 2), (1, 1, 2, 1), (1, 1, 2, 2), (2, 1, 1, 1), (2, 1, 1, 2), (2, 2, 1, 1), (2, 2, 1, 2), (2, 2, 2, 1), (2, 2, 2, 2), (2, 1, 2, 1), (2, 1, 2, 2), (($2^t - 1$, $2^t - 1$, $2^t - 1$, $2^t - 1$), ($2^t - 1$, $2^t - 1$, $2^t - 1$, 2^t), ($2^t - 1$, 2^t, $2^t - 1$, $2^t - 1$), ($2^t - 1$, 2^t, $2^t - 1$, 2^t), ($2^t - 1$, 2^t, 2^t, $2^t - 1$), ($2^t - 1$, 2^t, 2^t, 2^t), ($2^t - 1$, $2^t - 1$, 2^t, $2^t - 1$), ($2^t - 1$, $2^t - 1$, 2^t, 2^t), (2^t, $2^t - 1$, $2^t - 1$, $2^t - 1$), (2^t, $2^t - 1$, $2^t - 1$, 2^t), (2^t, 2^t, $2^t - 1$, $2^t - 1$), (2^t, 2^t, $2^t - 1$, 2^t), (2^t, 2^t, 2^t, $2^t - 1$), (2^t, 2^t, 2^t, 2^t), (2^t, $2^t - 1$, 2^t, $2^t - 1$), (2^t, $2^t - 1$, 2^t, 2^t)),respectively. Then q_c ($t+1$) = δ ($q_c(t)$, $q_{c(UNWP)}$ (t), $q_{c(UNWF)}$ (t), $q_{c(USWP)}$ (t), $q_{c(USWF)}$ (t), $q_{c(USEP)}$ (t), $q_{c(USEF)}$ (t), $q_{c(UNEP)}$ (t), $q_{c(UNEF)}$ (t), $q_{c(DNWP)}$ (t), $q_{c(DNWF)}$ (t), $q_{c(DSWP)}$ (t), $q_{c(DSWF)}$ (t), $q_{c(DSEP)}$ (t), $q_{c(DSEF)}$ (t), $q_{c(DNEP)}$ (t)), $q_{c(DNEF)}$ (t)), where for example $q_c(t)$ means the state of c at time t. At time $t = 0$, the input tape $x \in Q_T^{(4)}$ [$l_1(x) = l_2(x) = l_3(x) = l_4(x) = 2^t$, $t \geq 0$] is stored as the initial states of the bottom n-dimensional layer, henceforth called the *base*, in such a way that x (i_1, i_2, i_3, i_4) is stored at the cell of the i_1th row and the i_2th column on the i_3th plane of the i_4th n-dimensional rectangular array, and the other cells are initialized to a *quiescent state* q_s ($\in Q_N - Q_T - A$). As usual, we let δ (q_s, q_s, q_s, q_s, q_s, q_s, q_s, q_s, q_s, q_s, q_s, q_s, q_s, q_s, q_s, q_s, q_s) = q_s. The input is *accepted* if and only if the root cell ever enters an accepting state. This 4-$UPCA$ is called *deterministic*. A *nondeterministic bottom-up pyramid cellular acceptor* is defined as a 4-$UPCA$ using $\delta : Q_N^{17} \rightarrow 2^{Q_N}$ instead of the state transition function of the deterministic 4-$UPCA$. Below, we denote a deterministic n-$UPCA$ by n-$DUPCA$, and a nondeterministic n-$UPCA$ by n-$NUPCA$. An n-$DUPCA$ (or n-$NUPCA$) operates in time $T(n)$ if for every n-dimensional tape of size $2^t \times 2^t \times 2^t \times 2^t$ ($t \geq 0$) it accepts the n-dimensional tape, then there is an accepting computation which uses no more than time $T(t)$. By n-$DUPCA$ ($T(t)$) [n-$NUPCA(T(t))$] we denote a $T(t)$ time-bounded n-$DUPCA$ [n-$NUPCA$] which operates in time $T(t)$.

We next introduce an n-dimensional finite automaton [8]. An *n-dimensional finite automaton* (n-FA) is an n-dimensional Turing machine with no workspace. An n-FA M has a read-only n-dimensional tape with boundary symbols #'s, finite control, and an input head. For example, we explain the definition in the case of four-dimensional case as follows. The input head can move in eight direction − east, west, south, north, up, down, future, or past − unless it falls off the input tape. Formally, M is defined by the 5-tuple $M = (K, \Sigma \cup \{\#\}, \delta, q_0, F)$, where K is a finite set of *states*, Σ is a finite set of *input symbols*, # is the *boundary symbol* (not in Σ), $\delta : K \times (\Sigma \cup \{\#\}) \rightarrow 2^{K \times \{E,W,S,N,U,D,F,P,H\}}$ is the *state transition function*, where E, W, S, N, U, D, F, P, and H represent the move directions of the input head − east, west, south, north, up, down, future, past, and no move, respectively, $q_0 \in K$ is the *intial state*, and $F \subseteq K$ is the set of *accepting states*. The action of M is similar to that of the one-dimensional (or two-dimensional) finite automaton [4], except that the input head of M can move in eight directions. That is, when an input tape $x \in \Sigma^{(4)}$ with boundary symbols is presented to M, M starts in its initial state q_0 with the input head on x (1, 1, 1, 1), and determines the next state of the finite control and the move direction of the input head, depending on the present state of the finite control and the symbol read by the input head. We say that M *accepts* the tape x if it eventually enters an accepting state. We denote a deterministic n-FA [nondeterministic n-FA] by n-DFA [n-NFA].

We let each sidelength of each input tape of n-dimensional automata, throughout this paper, be equivalent. We denote the set of all n-dimensional tapes accepted by M by $T(M)$. Define $\pounds$ [n-$DUPCA$] = $\{T \mid T(M)$ is accepted by some n-$DUPCA$ $M\}$.

$\pounds[n\text{-}NUPCA]$, $\pounds[n\text{-}DFA]$, etc. are defined similarly.

Finally, we give definition of *diameter*. For example, we explain the definition in the case of four-dimension. Given a subset S of a tape $x \in \Sigma^{(4)}$, we can define its *extent* in a given direction θ as the length of its projection on a plane in that direction. Here the length of a projection is the distance between its farthest apart nonzero values. Thus the extent of S is the distance between a pair of parallel planes perpendicular to θ that just bracket S. The *diameter* of S is defined as its extent in any direction.

3 Results

In this section, we show that the class of sets accepted by *n-DFA's* is imcomparable with the class of sets accepted by *n-DUPCA's* which operate in time of order lower than the diameter of the input. It has often been noticed that we can easily get several properties of n-dimensional automata by directly applying the results of (n-1)-dimensional case, if each sidelength of each n-dimensional input tape of these automata is not equivalent. So we let each sidelength of each input tape, throughout this paper, be equivalent in order to increase the theoretical interest.

Lemma 3.1. *Let* $T_1 = \{\ x \in \{\ 0,1\ \}^{(n)} \mid \exists\ t\ (\ t \geq 1)$ $[\ell_1(x) = \ell_2(x) = \cdots = \ell_n(x) = 2^t]$ *and* $x\ (2^{t-1},\ 2^{t-1},\ \ldots,\ 2^{t-1}) = 1\ \}$. *Then,*
(1) $T_1(x) \notin \pounds[n\text{-}DFA]$, *and*
(2) $T_1(x) \in \pounds[n\text{-}DUPCA(t)]$.

Proof : The Proof of (1) is similar to that of Theorem 3 in [7]. On the other hand, by using the same technique as in the proof of Lemma 1 in [6], we can get Part (2) of the lemma. □

Lemma 3.2. *Let* $T_2 = \{x \in \{0,1\}^{(n)} \mid \exists t\ (t \geq 1)$ $[\ell_1(x) = \ell_2(x) = \cdots = \ell_n(x) = 2^t]$ *and* $x\ [(1,1,\ldots,1),$ $(2^t, 2^t, \ldots, 1)] = x\ [(1,1,\ldots,2^t),\ (2^t, 2^t, \ldots, 2^t)]\ \}$. *Let* $T(t)$ *be a time function such that* $\lim_{t\to\infty}\ [T(t)/2^{2^t}] = 0$. *Then,*
(1) $T_2 \in \pounds\ [n\text{-}DFA]$,*and*
(2) $T_2 \notin \pounds\ [n\text{-}DUPCA(T(t))]$.

Proof : It is obvious that there is an *n-DFA* accepting T_2, and so (1) of the lemma holds. Below, we prove (2). Suppose that there is an *n-DUPCA* B which accepts T_2 and operates in time $T(t)$, and that each cell of B has k states. For each $t \geq 2$, let

$$W(t) = \{x \in \{0,1\}^{(n)} | \ell_1(x) = \ell_2(x) = \cdots = \ell_n(x) = 2^t\},$$ and

$$\begin{aligned} W'(n) = \{x \in \{0,1\}^{(n)} | \ell_1(x) = \ell_2(x) = \cdots = \ell_n(x) \\ = 2^{t-1} \\ \&\ x[(1,1,\ldots,1),(2^{t-1},2^{t-1},\ldots,1)] \in \{0,1\}^{(n)} \\ \&\ x[(1,1,\ldots,2),(2^{t-1},2^{t-1},\ldots,2^{t-1})] \in \{0\}^{(n)}\}. \end{aligned}$$

We consider the cases when the tapes in $W(t)$ are presented to B. Let c be the cell which is situated at the first row, the first column, the first plane, ..., and the first (n-1)-dimensional array in the tth layer (i.e., the layer just below the root cell). (Note that there are 2n−1 cells in the tth layer.) For each x in $W(t)$ such that $x[(1,1,\ldots,1),(2^{t-1},2^{t-1},\ldots,2^{t-1})] \in W'(t)$, and for each $r \geq 1$, let $q_r(x)$ be the state of c at time r when x is presented to B. Then the following proposition must hold.

Proposition 3.1. *Let* x, y *be two different tapes in* $W(t)$ *such that both*
$x[(1,1,\ldots,1),(2^{t-1},2^{t-1},\ldots,2^{t-1})]$*and*
$y[(1,1,\ldots,1),(2^{t-1},2^{t-1},\ldots,2^{t-1})]$*are in* $W'(t)$ *and*
$x[(1,1,\ldots,1),\ (2^{t-1},2^{t-1},\ldots,2^{t-1})]$
$\neq y[(1,1,\ldots,1),\ (2^{t-1},2^{t-1},\ldots,2^{t-1})]$.
Then, $(q_1(x), q_2(x), \ldots, q_{T(t)}(x))$
$= (q_1(y), q_2(y), \ldots, q_{T(t)}(y))$.

[**Proof :** For suppose that $(q_1(x), q_2(x), \ldots, q_{T(t)}(x))$ $= (q_1(y), q_2(y), \ldots, q_{T(t)}(y))$. We consider two tapes z, z' in $W(t)$ such that

(i) $z\ [(1,1,\ldots,1),\ (2^{t-1},2^{t-1},\ldots,2^{t-1})]$
$= x\ [(1,1,\ldots,1),\ (2^{t-1},2^{t-1},\ldots,2^{t-1})]$
and
$z'\ [(1,1,\ldots,1),\ (2^{t-1},2^{t-1},\ldots,2^{t-1})]$
$= y\ [(1,1,\ldots,1),\ (2^{t-1},2^{t-1},\ldots,2^{t-1})]$,

(ii) the part of z except for $z\ [(1,1,\ldots,1),\ (2^{t-1},\ 2^{t-1},\ \ldots,\ 2^{t-1})]$ is identical with the part z' except for $z'[(1,1,\ldots,1),(2^{t-1},2^{t-1},\ldots,2^{t-1})]$,

and

(iii) $z[(1,1,\ldots,1),(2^t,2^t,\ldots,1)]$
$= z[(1,1,\ldots,2^t),(2^t,2^t,\ldots,2^t)]$.

By assumption, the root cell of B enters the same states until time $T(t)$, for the tapes z and z'. Since B operate in time $T(t)$ and z is in T_2, it follows that z' is also accepted by B. This contradicts the fact that z' is not in T_2. □]

Let $s(t)$ be the number of different sequences of states which c enters until time $T(t)$. Clearly, $s(t) \leq k^{T(t)}$. On the other hand (for any set S, let $|S|$ denote the number of elements of S.), $|W'(t)| = 2^{2^{(t-1)^2}}$. Since $\lim_{n\to\infty} T(t)/2^{2^t} = 0$ (by assumption of the

lemma), it follows that $|W'(t)| > s(t)$ for lange t. Therefore, it follows that for large t there must exist two different tapes x, y in $W(t)$ such that

(i) both $x[(1,1,\ldots,1),(2^{t-1},2^{t-1},\ldots,2^{t-1})]$ and $y[(1,1,\ldots,1),(2^{t-1},2^{t-1},\ldots,2^{t-1})]$ and in $W'(t)$,

(ii) $x[(1,1,\ldots,1),(2^{t-1},2^{t-1},\ldots,2^{t-1})]$ $\neq y[(1,1,\ldots,1),(2^{t-1},2^{t-1},\ldots,2^{t-1})]$, and

(iii) $(q_1(x),q_2(x),\ldots,q_{T(t)}(x))$ $= (q_1(y),q_2(y),\ldots,q_{T(t)}(y))$.

This contradicts the above Proposition 3.1, and thus the Part (2) of the lemma holds. □

From Lemmas 3.1 and 3.2, we can get the following theorem.

Theorem 3.1. *Let $T(t)$ be a time function such that $\lim_{n\to\infty}[T(t)/2^{2^t}] = 0$ and $T(t) \geq t (t \geq 1)$. Then £ [n-DFA] is imcomparable with £ [n-DUPCA($T(t)$)].*

Corollary 3.1. *£[n-DFA] is incomparable with £ [n-DUPCA(t)], which is the class of sets accepted by n-DUPCA's operating in real time.*

Corollary 3.2. *£ [n-DFA] is incomparable with £[n-NUPCA(t)].*

4 Conclusion

In this paper, we dealt with the accepting powers of bottom-up pyramid cellular acceptors with n-dimensional layers, and showed that the class of sets accepted by *n-DFA*'s is incomparable with the class of sets accepted by *n-DUPCA*'s which operate in time of order lower than the diameter of the input. It is still inknown whether the class of sets accepted by *n-DUPCA*'s includes the class of sets accepted by *n-DFA*'s.

References

[1] M.Blum and C.Hewitt, Automata on a two-dimensional tape, *in IEEE Symposium on Switching and Automata Theory*, pp.155-160, 1967.

[2] C.R.Dyer and A.Rosenfeld, Cellular pyramids for image analysis, *Technical Report TR*-544, *Computer Science Center*, *University of Maryland*, 1977.

[3] K.Inoue, and A.Nakamura, Some properties of two-dimensional o*n*-line tessellation acceptors, *Information Sciences*, Vol.13, pp.95-121, 1977.

[4] K.Inoue, I.Takanami, and A.Nakamura, A note on two-dimensional finite automata, *Information Processing Letters*, Vol.7, No.1, p.49, 1978.

[5] K.Inoue and I.Takanami, Remaks on two-dimensional finite automata with multiplication and bottom-up pyramid acceptors, *Technical Report IECE of Japan*, No.AL77-61, 1978.

[6] K.Inoue and I.Takanami, A note on bottom-up pyramid acceptors, *Information Processing Letters* Vol.8, No.1, pp.34-37, 1979.

[7] M.Sakamoto, S.Nogami, K.Inoue, and M.Kono, A relationships between the accepting powers of three-dimensional finite automata and time-bounded bottom-up pyramid cellular acceptors with three-dimensional layers, *Trans. of SCI*(Japan), Vol.17, No.10, pp.451-458, 2004.

[8] H.Taniguchi, K.Inoue, and I.Takanami, A note on three-dimensional finite automata, *Information Siences*, Vol.26, pp.65-85, 1982.

[9] Y.Uchida, T.Ito, H.Okabe, M.Sakamoto, H.Furutani, and M.Kono, four-dimensional multi-inkdot finite automata, *WSEAS Trans. on Computers*, Issue 9, Vol.7, pp.1437 - 1446, 2008.

© ISAROB 2013

The Eighteenth International Symposium on Artificial Life and Robotics 2013 (AROB 18th '13),
Daejeon Convention Center, Daejeon, Korea, January 30-February 1, 2013

Homogeneous Systolic Pyramid Automata with n-Dimensional Layers

Makoto SAKAMOTO[1], Takao ITO[2], Tatsuma KUROGI[1],
Makoto NAGATOMO[1],Yasuo UCHIDA[2],Tsunehiro YOSHINAGA[3],
Satoshi IKEDA[1],Masahiro YOKOMICHI[1],and Hiroshi FURUTANI[1]

[1] Dept. of Computer Science and Systems Engineering, University of Miyazaki, Miyazaki 889-2192, JAPAN
[2] Dept. of Business Administration, Ube National College of Technology, Ube 755-8555, JAPAN
[3] Dept. of Computer Science & Electronic Engineering, Tokuyama College of Technology, Shuman 745-8585, JAPAN

Abstract

Cellular automata were investigated not only in the viewpoint of formal language theory, but also in the viewpoint of pattern recognition. Cellular automata can be classified into some types. A systolic pyramid automata is also one parallel model of various cellular automata. A homogeneous systolic pyramid automaton with n-dimensional layers (n-$HSPA$) is a pyramid stack of n-dimensional arrays of cells in which the bottom n-dimensional layer (level 0) has size a^n ($a \geq 1$), the next lowest $(a-1)^n$, and so forth, the (a-1)st n-dimensional layer (level (a-1)) consisting of a single cell, called the root. Each cell means an identical finite-state machine. The input is accepted if and only if the root cell ever enters an accepting state. An n-$HSPA$ is said to be a real-time n-$HSPA$ if for every n-dimensional tape of size an ($a \geq 1$) it accepts the n-dimensional tape in time a-1. Moreover, a 1-way n-dimensional cellular automaton (1-nCA) can be considered as a natural extension of the 1-way two-dimensional cellular automaton to n-dimension. The initial configuration is accepted if the last special cell reaches a final state. A 1-nCA is said to be a real-time 1-nCA if when started with n-dimensional array of cells in nonquiescent state, the special cell reaches a final state. In this paper, we propose a homogeneous systolic automaton with n-dimensional layers (n-$HSPA$), and investigate some properties of real-time n-$HSPA$. Specifically, we first investigate a relationship between the accepting powers of real-time n-$HSPA$'s and real-time 1-nCA's. We next show the recognizability of n-dimensional connected tapes by real-time n-$HSPA$'s.

Key Words **:** cellular automaton, diameter, finite automaton, n-dimension, parallelism, pattern recognition, real time.

1 Introduction and Preliminaries

The question of whether processing n-dimentional digital patterns is much more difficult than (n-1) dimentional ones is of great in terest from the theoretical and practical standpoints. Thus, the study of n-dimensional automata as a computational model of n-dimensional pattern processing has been meaningful[4-23]. Cellular automata were investigated not only in the viewpoint of formal language theory, but also in the viewpoint of pattern recognition. Cellular automata can be classified into some types [2]. A systolic pyramid automaton is also one parallel model of various cellular automata. In this paper, we propose a homogeneous systolic automaton with n-dimensional layers (n-*HSPA*), and investigate some properties of real-time n-*HSPA*.

Let Σ be a finite set of symbols. An *n-dimensional tape* over Σ is an $(n-1)$-dimensional array of elements of Σ. The set of all n-dimensional tapes over Σ is denoted by $\Sigma^{(n)}$. Given a tape $x \in \Sigma^{(n)}$, for each $j (1 \leq j \leq n)$, we let $l_j(x)$ be the length of x along the jth axis. When $1 \leq i_j \leq l_j(x)$ for each $j (1 \leq j \leq n)$, let $x(i_1, i_2, \ldots, i_n)$ denote the symbol in x with coordinates $(i_1, i_2, \ldots, i_n)$. We concentrate on the input tape x with $l_1(x) = l_2(x) = l_3(x) = \cdots = l_n(x)$.

A *homogeneous systolic pyramid automaton with n-dimensional layers* (n-*HSPA*) is a pyramidal stack of n-dimensional arrays of cells in which the bottom n-dimensional layer (level 0) has size a^n ($a \geq 1$), the next lowest $(a-1)^n$, and so forth, the $(a-1)$st n-dimensional layer (level $(a-1)$) consisting of a single cell, called the *root*. Each cell means an identical finite-state machine, $M = (Q, \Sigma, \delta, \#, F)$, where Q is a finite set of *states*, $\Sigma \subseteq Q$ is a finite set of *input states*, $\# \in Q - \Sigma$ is the *quiescent state*, $F \subseteq Q$ is the set of *accepting states*, and $\delta : Q^{2^n+1} \to Q$ is the *state transition function*, mapping the current states of M and its 2^n son cells in a $2 \times 2 \times \cdots \times 2$ block on the n-dimensional layer below into M's next state. The input is *accepted* if and only if the root cell ever enters an accepting state. An n-*HSPA* is said to be a *real-time* n-*HSPA* if for every n-dimensional tape of size a^n ($a \geq 1$) it accepts the n-dimensional tape in time $a-1$. By $\pounds^R[n\text{-}HSPA]$ we denote the class of the sets of all the n-dimensional tapes accepted by a real-time n-*HSPA*[1].

A 1-*way* n-*dimensional cellular automaton* (1-nCA) can be considered as a natural extension of the

© ISAROB 2013

1-way two-dimensional cellular automaton to n dimensions [3]. The initial configuration of the cellular automaton is taken to be an $l_1(x) \times l_2(x) \times \cdots \times l_n(x)$ array of cells in the nonquiescent state. The initial configuration is *accepted* if the last special cell reaches a final state. A 1-nCA is said to be a *real-time* 1-nCA if when started with an $l_1(x) \times l_2(x) \times \cdots \times l_n(x)$ array of cells in the nonquiescent state, the special cell reaches a final state in time $l_1(x)+l_2(x)+\cdots+l_n(x)-1$. By $\pounds^R$[1-nCA] we denote the class of the sets of all the n-dimensional tapes accepted by a real-time 1-nCA [3].

2 Main Results

We mainly investigate a relationship between the accepting powers of real-time n-$HSPA$'s and real-time 1-nCA's. The following theorem implies that real-time n-$HSPA$'s are less powerful than real-time 1-nCA's.

Theorem 2.1. $\pounds^R[n\text{-}HSPA] \subsetneq \pounds^R[1\text{-}nCA]$.

Proof : Let V=$\{x \in \{0,1\}^{(n)} | l_1(x) = l_2(x) = \cdots = l_n(x) \& [\forall_{i_1}, \forall_{i_2}, \ldots, \forall_{i_{n-1}}\ (1 \le i_1 \le l_1(x), 1 \le i_2 \le l_2(x), \ldots, 1 \le i_{n-1} \le l_{n-1}(x))[x(i_1, i_2, \ldots, i_{n-1}, 1) = x(i_1, i_2, \ldots, i_{n-1}, l_n(x))]]\}$.

It is easily shown that $V_1 \in \pounds^R[1\text{-}nCA]$. Below, we show that $V \notin \pounds^R[n\text{-}HSPA]$. Suppose that there exists a real-time n-$HSPA(n = 3)$ accepting V. For each $t \ge 4$, let

$W(n) = \{x \in \{0,1\}^{(3)} | l_1(x) = l_2(x) = \cdots = l_n(x)$ & $[x\ (1,2,1),(t,t-1,t)] \in 0^{(3)}\}$.

Eight sons of the root cell $A_{(t-1,1,1,1)}$ of M $A_{(t-2,1,1,2)}$, $A_{(t-2,1,2,2)}$, $A_{(t-2,2,1,2)}$, $A_{(t-2,2,2,2)}$, $A_{(t-2,1,1,3)}$, $A_{(t-2,1,2,3)}$, $A_{(t-2,2,1,3)}$, $A_{(t-2,2,2,3)}$ are denoted by C_{UNW}, C_{USW}, C_{USE},C_{UNE}, C_{DNW}, C_{DSW}, C_{DSE}, C_{DNE}, respectively. For each x in $W(n)$, $x(UNW)$, $x(USW)$, $x(USE)$, $x(UNE)$, $x(DNW)$, $x(USW)$, $x(USE)$, $x(UNE)$ are the states of C_{UNW}, C_{USW}, C_{USE}, C_{UNE}, C_{DNW}, C_{DSW}, C_{DSE}, C_{DNE}, at time t-2, respectively. Let $\sigma\ (x) = (x(UNW), x(USW), x(DNW), x(DSW))$, $\gamma\ (x) = (x(USE), x(UNE), x(DSE), x(DNE))$. and $\rho(x) = (x(UNW), x(USW), x(DNW), x(DSW), x(USE), x(UNE), x(DSE), x(DNE))$. Then, the following two propositions must hold:

Proposition 2.1. (i) *For any two tapes $x, y \in W(n)$ whose $1st(1-3)$ planes are same, $\sigma\ (x) = \sigma\ (y)$.* (ii) *For any two tapes $x, y \in W(n)$ whose $n-th(1-3)$ planes are same, $\gamma\ (x) = \gamma\ (y)$.*

[**Proof :** From the mechanism of each cell, it is easily seen that the states of C_{UNW}, C_{USW}, C_{DNW}, C_{DSW} are not influenced by the information of $x(1-3)_t$'s. From this fact, we have (i). The proof of (ii) is the same as that of (i). Q.E.D.]

Propositon 2.2. *For any two tapes $x, y \in W(t)$ whose 1st (1-3) planes are different, $\sigma(x) \neq \sigma(y)$.*

[**Proof :** Suppose to the contrary that $\sigma(x) = \sigma(y)$. We consider two tapes x',$y' \in W(t)$ satisfying the follwing :
(i) $x(1-3)_1$ and $x(1-3)_t$, are equal to $x(1-3)_1$ of x, respectively
(ii) $y'(1-3)_1$ is equal to $y(1-3)_1$, and $y'(1-3)_t$ is equal to $x(1-3)_1$.

As is easily seen, $x' \in V$ and so x' is accepted by M. On the other hand, from Proposition 2.1(ii), $\gamma(x') = \gamma(y')$. From Proposition 2.1(i), $\sigma(x) = \sigma(x')$, $\sigma(y) = \sigma(y')$. It follows that y' must be also accepted by M. This contradicts the fact that y' is not in V. *Q.E.D*]

Proof of Theorem 2.1 (*continued*) **:** Let $p(t)$ be the number of tapes in $W(t)$ whose 1st (1-3) planes are different, and let $Q(t) = \{\sigma(x) | x \in W(t)\}$, where k is the number of states of each cell of M. Then, $p(t) = 2^{t^2}$, and $Q(t) \le k^4$. It follows that $p(n) > Q(t)$ for large t. Therefore, it follows that for large t, there must be two tapes x,y in $W(t)$ such that their 1st (1-3) planes are different and $\sigma(x) = \sigma(y)$. This contradicts Proposition 2.2, so we can conclude that $V \notin \pounds^R[3\text{-}HSPA]$. In the case of n-dimention, we can show that $V \notin \pounds^R[n\text{-}HSPA]$ by using the same technique. This completes the proof of Theorem 2.1. *Q.E.D.*

We next show the recognizability of n-dimensional connected tapes by real-time n-$HSPA$'s by using the name technique of Ref.[3]. Let x in $\{0,1\}^{(n)}$. A maximal subset P of $\boldsymbol{N}^n$ satisfying the following conditons is called a 1-*component* of x.
(i) For any $(i_1,i_2,\ldots,i_n \in P$, we have $1 \le i_1 \le l_1(x)$, $1 \le i_2 \le l_2(x)$,...,$1 \le i_n \le l_n(x)$, and $x(i_1, i_2, \ldots, i_n) = 1$.
(ii) For any $(i_1,i_2,\ldots,i_n)$, $(i'_1,i'_2,\ldots,i'_n) \in P$, there exists a sequence $(i_{1,0},i_{2,0},\ldots,i_{n,0})$,$(i_{1,1},i_{2,1},\ldots,i_{n,1})$,..., $(i_{1,n},i_{2,n},\ldots,i_{n,n})$ of elements in P such that $(i_{1,0},i_{2,0},\ldots,i_{n,0}) = (i_1,i_2,\ldots,i_n)$, $(i_{1,n},i_{2,n},\ldots,i_{n,n}) = (i'_1,i'_2,\ldots,i'_n)$, and $|i_{1,j}\text{-}i_{1,j-1}| + |i_{2,j}\text{-}i_{2,j-1}| + \ldots + |i_{n,j}\text{-}i_{n,j-1}| \le 1 (1 \le j \le n)$. A tape $x \in \{0,1\}^{(n)}$ is called *connected* if there exists exactly one 1-component of x.

Let T_c be the set of all the n-dimensional connected tapes. Then, we have

Theorem 2.2. $T_c \notin \pounds^R[n\text{-}HSPA]$.

3 Conclusion

We investigated a relationship between the accepting powers of homogeneous systolic pyramid automaton with n-dimensional layers(n-$HSPA$) and one-way

© ISAROB 2013

n-dimensional cellular automata (1-nCA) in real time, and showed that real-time n-$HSPA$'s are less powerful than real time 1-nCA's.

References

[1] K.Culik II, J.Gruska and A Salomaa, Systolic trellis automata, Part I, *International Journal of Computer Mathmatics*, 15:145-212,1984.

[2] K.Inoue and I.Takanami, A survey of two-dimensional automata theory, *Information Sciences*, 55:pp.99-121, 1991.

[3] C. Iwamoto, K. Inoue, and I. Takanami, Some Properties of Homogeneous Pyramid Automata, *The IEICE Transactions on Information and Systems* (*Japanese Edition*), J73-D-I(9) : 778-780, 1990.

[4] K. Krithivasan and M. Mahajan, Systolic pyramid automata, cellular automata and array languages, *International Journal of Pattern Recognition and Artificial Intelligence*, 3(3 4):405-433, 1989.

[5] M.Sakamoto, Three-Dimensional Alternating Turing Machines, *Ph.D. Thesis*, *Yamaguchi University*, 1999.

[6] M.Sakamoto, H.Okabe, and K.Inoue, Some properties of four-dimansional finite automata, *in* 2002 *Chugoku – Section Joint Convention Record of Insistes of Electrical and Information Engineerings*, *Japan*, p.351,2002.

[7] M.Sakamoto, S.Nagami, K.Kono, A relationship between the accepting powers of three-dimentional layers, *Trans. of SCI*(*Japan*), Vol.17, No.10, pp.451-458,2004.

[8] M.Sakamoto, H.Okabe, S.Nagami, S.Taniguchi, T.Maki, Y.Nakama, M.Saito, M.Kono, and K.Inoue, A note on four-dimensional finite automata, *WSEAS Transactions on Computers*, Issue 5,Vol.3, pp.1651-1656,2004.

[9] M.Sakamoto, T.Ito, N.Tomozoe, and H.Furutani, Asurvey of three-dimensional automata, *The papers of Technical Meeting on Information Systems*, *IEE*, *Japan*, IS-07-12, pp.11-17,2007.

[10] M.Sakamoto, T.Ito, H.Furutani, and M.Kono, Some accepting powers of three-dimensional parallel Turning machines, *in* 1*st European Workshop on Artificial Life and Robotics*, *Vienna*, *Austria*, pp.73-79,2007.

[11] M.Sakamoto, N.Tomozoe, H.Furutani, M.Kono, T.Ito, Y.Uchida, and H.Okabe, A survey of automata on three-dimensional input tapes, *WSEAST Transactions on Computers*,Issue 10,Vol.7, pp.1638-1647,2008.

[12] M.Sakamoto, T.Ito, H.Furutani, and M.Kono, Some accepting powers of three-dimensional parallel Turning machines, *International Journal of Artificial Life and Robotics*,Vol.13,No.1, pp.27-30,2008.

[13] M.Sakamoto, M.Fukuda, S.Okatani, T.Ito, H.Furutani, and M.Kono, Path-bouded Three-dimensional finite automata, *International Journal of Artificial life and Robotica*, *Springer*,Vol.13,No.1,pp.54-57,2008.

[14] M.Sakamoto, S.Okatani, M.Fukuda, T.Ito, and H.Furutani, and M.Kono, A relationship between Turning machines and finite automata on four-dimensional input tapes, *International Journal of Artificial life and Robotica*, *Springer*, Vol.13,No.1, pp.58-60,2008.

[15] M.Sakamoto, S.Okatani, K.Kajisa, M.Fukuda, T.Matsuawa, A.Taniue, T.Ito, H.Furutani, and M.Kono, Hierarchies based on the number of cooperating systems of three-dimensional finite automata,International Journal of Artificial Life and Robotics,Vo.4,No.3, pp.425-428.2009.

[16] M.Sakamoto, T.Matsukawa, R.Katamune, H.Furutani, M.Kono, S.Ikeda, T.Ito, Y.Uchida, and T.Yoshinaga, Four-dimensional synchronized alternating Turning machines,*Proceedings of the* 10*th American Conference on Applied Mathmatics*, *Harvard University*, *Cambridge*, *USA*, pp.195-200,2010(CD-ROM).

[17] M.Sakamoto, R.Katamune, T.Matsukawa, H.Furutani, M.Kono, S.Ikeda, T.Ito, Y.Uchida, and T.Yoshinaga, Some result about hierarchy and recognizability of four-dimensional sychronized alternating Turning machines, *Proceedings of the* 10*th American Conference on Applied Mathmatics*, *Harvard University*, *Cambridge*, *USA*, pp.201-205, 2010(CD-ROM).

[18] M.Sakamoto, T.Matsukawa, R.Katamune, H.Furutani, M.Kono, S.Ikeda, T.Ito, Y.Uchida, and T.Yoshinaga, Synchronized Alternating Turning Machines on Four-Dimensional Input Tapes, *WSES TRANSACTIONS on COMPUTERS*,Issue 4,Vol.9, pp.319-328,2010.

[19] M.Sakamoto, R.Katamune, T.Matsukawa, H.Furutani, M.Kono, S.Ikeda, T.Ito, Y.Uchida, and T.Yoshinaga, Hardware Hierarchies and Recognizabilities of Four-Dimensional Synchronized Alternating Turning Machines, *WSES*

© ISAROB 2013

TRANSACTIONS on COMPUTERS,Issue 4. pp.329-338,2010.

[20] M.Sakamoto, T.Ito, X.Qingquan, Y.Uchida, T.Yochinaga, M.Yokomichi, S.Ikeda, and H.Furutani, A Note on Three-dimensional Probabilistic Finite Automata, *The Seventeenth International Symposium on Artificial Life and Robotics* 2012, Oita, Japan, pp.492-495,2012(CD-ROM).

[21] M.Sakamoto, Y.Uchida, T.Hamada, T.Ito, T.Yoshinaga, M.Yokomichi, S.Ikeda, and H.Furutani, A Relationship between the Accepting Powers of Nondeterministic Finite Automata and Probabilistic Finite Automata on Three-Dimensional Input Tapes, *in the* 2012 *IEICE General Conference*, *Okayama University*, p.4,2012(CD-ROM).

[22] T. Toffoli and N. Margolus, *Cellullar automaton machines − new environment for modeling*, MIT Press, 1987.

[23] J. Wiedermann, Parallel Turing machines, *Technical Report* RUU-CS-84-11, *Department of Computer Science*, *University of Utrecht*, *the Netherlands*, 1984.

© ISAROB 2013

The Eighteenth International Symposium on Artificial Life and Robotics 2013 (AROB 18th '13),
Daejeon Convention Center, Daejeon, Korea, January 30-February 1, 2013

A proposition of addition and integration of q-values in Q-Learning

Kathy Thi Aung[1], Takayasu Fuchida[2]

[1,2]Kagoshima University, Kagoshima 890-0065, Kohrimoto 1-21-40, Japan
[1,2]Graduate School of Science and Engineering, Department of System Information Science
(Tel: 81-99-285-3408, Fax: 81-99-285-8464)

[1]kathythiaung@gmail.com , [2]fuchida@ibe.kagoshima-u.ac.jp

Abstract: This article presents a method of addition and integration of q-values to reduce the number of states and memory usage based on Q-learning algorithm in continuous state space using the concept of Voronoi space division. It also aims to show the improvement of learning efficiency when it is compared to the existing method, such as lattice. We constructed an experimental model to examine these scenarios. This model is based on continuous state and discrete action of feeder mouse. The results indicate that the proposed method greatly improve than normal Q-learning. As a method of space division, we used Voronoi diagram that is a general space division method. However, Voronoi diagram has a lot of flexibility therefore it becomes a problem to decide the position of q-values. Therefore, we presented the addition method in order to realize the position of q-values using LBG algorithm though there are many methods for adaptive vector grouping. In addition, we integrate the q-values which have the same action selections using Delaunay tessellation technique to find the nearest q-values.

Keywords: Q-Learning, Voronoi Diagram, LBG algorithm, Delaunay Tessellation technique

1 Introduction

There are several kinds of learning methods but reinforcement learning (RL) is the most suitable method in machine learning that deals with the decision to take an action using an agent at discrete time steps and expected that would be useful anywhere in the future [1]. RL methods attempt to improve the agent's decision-making policy over the time. The agent's goal is to get as much reward as it can over the long run.

In this paper, we present an experimental study in continuous state space based on Q-learning algorithm with addition and integration of q-values method using Delaunay tessellation technique, addition method of q-values using LBG algorithm, and normal lattice arrangement. It also aims to show the improvement of learning efficiency using the proposed method when it is compared to the existing method, such as lattice.

We constructed a computational model to examine these scenarios. In the model, an agent aims to get as much reward as possible during a specific period, and observes the angle (θ) and the distance (d) to reward-area. If the agent reaches to the reward-area, the agent gets a reward of +1 and the position of agent is randomly changed.

2 Methods and procedures

2.1 Q-Learning algorithm

There are several ways to implement the learning process. However, Q-learning algorithm due to Watkins [2] is a policy for estimating the optimal state-action value, and one of the most fundamental in RL. Q-learning can also apply in many practical applications based on the idea of expected future reinforcements, and can be estimated by the function of each action in each state. However, it works only for discrete state space, and difficult to handle in continuous state space because of curse of dimensionality problem therefore it needs to discretize the state space into a lot of smaller discrete regions when we treat such continuous cases.

Curse of dimensionality means if the number of state and action variables increase, the size of the Q-Table used to store Q-values grows exponentially and the learning speed decrease suddenly.

In general Q-learning, every action and state pair have their own Q-value denoted by $Q(s_t, a_t)$, and it stores in a table called Q-Table. It looks like a square lattice in 2-dimesions. These Q-values are initialized to small random numbers and gradually change toward the optimal values through learning. The Q-value is updated in taking the maximum Q-value of next state using this following equation.

$$Q(s_t, a_t) = Q(s_t, a_t) + \alpha(r + \gamma \max_a Q(s_{t+1}, a) - Q(s_t, a_t))$$

In this equation, a state in time t is s_t , Q-value of action a_t in the state s_t is $Q(s_t, a_t)$, α is the learning rate, γ is the discount rate, and r is a reward. Furthermore, $max\ Q(s_{t+1},a)$ shows the maximum Q-value of next state in time t+1.

© ISAROB 2013

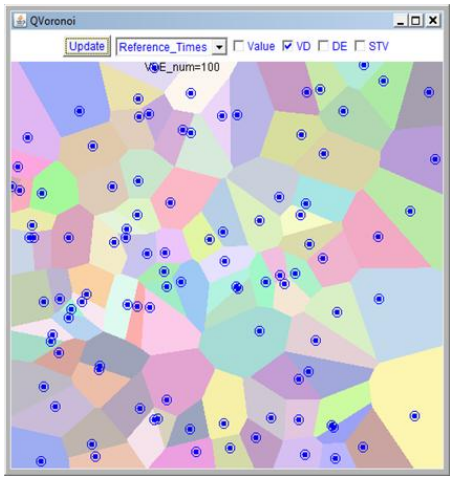

Fig.1. Voronoi diagram in a random set of point

2.2 Voronoi diagram

Voronoi diagram is used in our approach to partitions space into cells or a number of regions, where each region consists of all points that are closer to one site than to any other. It can also be used to perform nearest-neighbor searches. As a simple illustration, show in figure 1. Voronoi regions are bounded by line segments and Voronoi edge is a bisector of two sites whose regions are adjacent.

2.3 Addition of q-values

In the first stage of addition process, we put the temporary points into lattice structure on state space firstly. When the learning process is started, we save the state transition vector (STV) that enters from the position of the agent to the reward area on action space. If we get 1000 STV or more, we quantize or group those STV by continuously taking the same action using LBG algorithm (section 2.3.1). Furthermore, we seek representative vectors and describe STV groups as representative vectors.

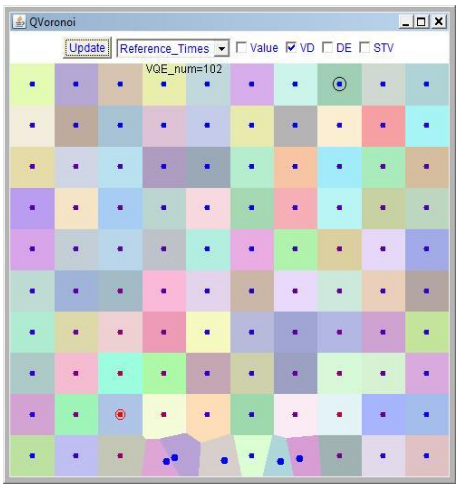

Fig.2. First-stage of q-values addition

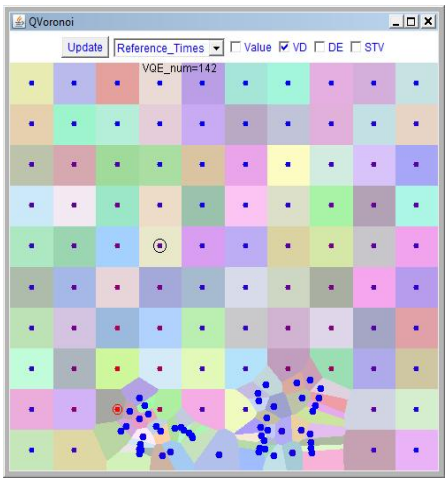

Fig.3. An image of q-values addition

Additionally, generate the new point at the place of each representative vectors. Moreover, delete the temporary points in which new points are added. A first-stage formation of addition is illustrated in figure 2.

In the second stage of addition, we save STV again that come from temporary points to new points of the first stage output. Nevertheless, we do not take STV that come from new points to new points. In addition, generate the new points at the position of the representative vectors and repeat the above process. In algorithm, a new point is put on the position of a suitable multiple at the direction of representative state transition vectors but we do not judge yet whether that position is really appropriate location or not. Figure 3 shows the image of addition of q-values.

2.3.1 LBG algorithm

We used LBG (Linde-Buzo-Gray) algorithm for vector quantization. It is like a clustering algorithm which takes a set of input vectors as input and generates a representative subset of vectors with a quantum vector. The modification of adaptive vector quantization method was introduced

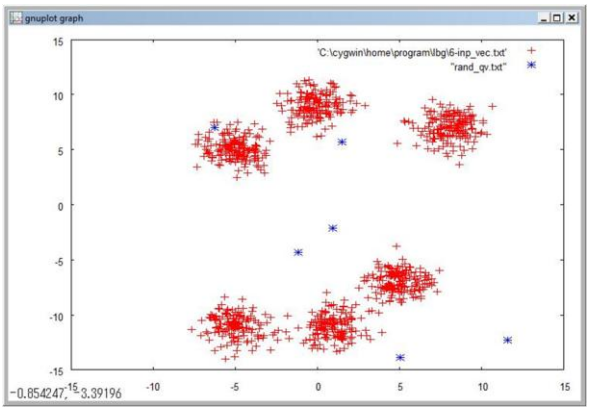

Fig.4. Initial state of vector quantization

© ISAROB 2013

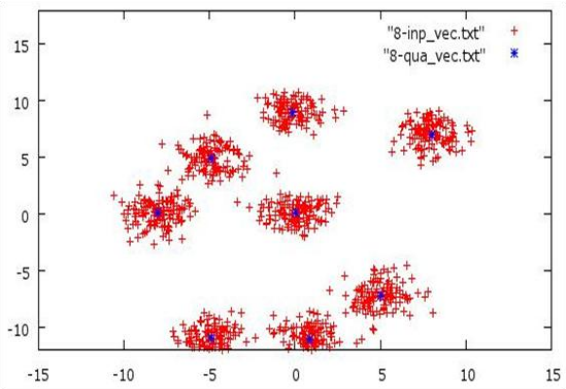

Fig.5. Illustration of the LBG vector quantization

enhanced LBG (Patane & Russo, 2001) [3], and adaptive incremental LBG (Shen & Hasegawa, 2006) [4]. LBG algorithm is as

1. Collect input vectors.
2. Initiate quantum vector at random.
3. Make group that input vectors belongs to the cluster of nearest quantum vector that yields minimum distance.
4. Shift quantum vector to the gravity center of the group dividing the own coordinates by the number of input vectors.
5. Move quantum vector in random direction and repeat the process in several times until the amount of quantum vector is less than a threshold value of 0.1.

The convergence of LBG algorithm depends on the initial quantum vector and the threshold in implementation. Figure 4 describes an initial state of vector quantization algorithm. The input vectors are marked with red and quantum vector are marked with blue. Figure 5 obtained by using the above mentioned algorithm.

2.4 Integration of q-values

There are five conditions to integrate q-values.

(1) both two points must be new added points.
(2) Those two adjoining points must take the same optimal action (Figure 6).
(3) Both two optimal actions have not changed over the number of 10,000 action times in 500,000 integrated timing of new points.
(4) Both two new points are not already used for integration.
(5) Start the integration process after the number of q-values is added to 300 as a restriction of integration theory and reduces to 169.

A new point is added to the center of adjoining point, and those two adjoining points are deleted. The key point of our integration method is to integrate same actions.

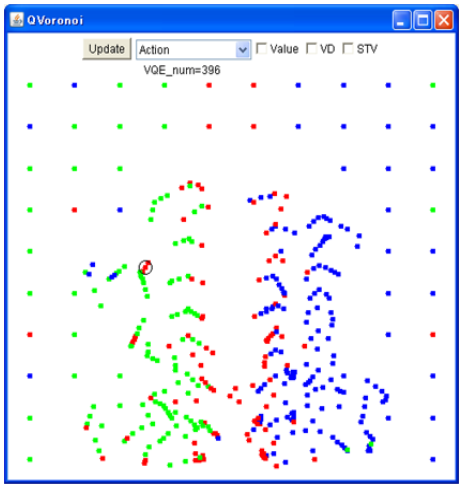

Fig.6. Type of actions on state space for integration

2.4.1 Delaunay tessellation algorithm

We applied a Delaunay tessellation (DT) technique to integrate the closest q-values. Delaunay tessellation is another fundamental computational geometry structure and dual tessellation of Voronoi diagram. DT is the straight-line dual of the Voronoi diagram obtained by joining all pairs of points belongs to the set. In our algorithm, we assume that the number of points are three or more but finite.

All triangles of the Delaunay triangulation are obtained by connecting the adjoining points. Then, we draw a hypercube rectangle containing all points that adjacent to nearest point and generate a random point inside of inclusive rectangle. After that, it finds the connection of nearest point and second-nearest point by measuring the distance from that random point. Finally, two nearest points with high mark are connected. An example of java applet animation of Delaunay tessellation is shown in figure 7.

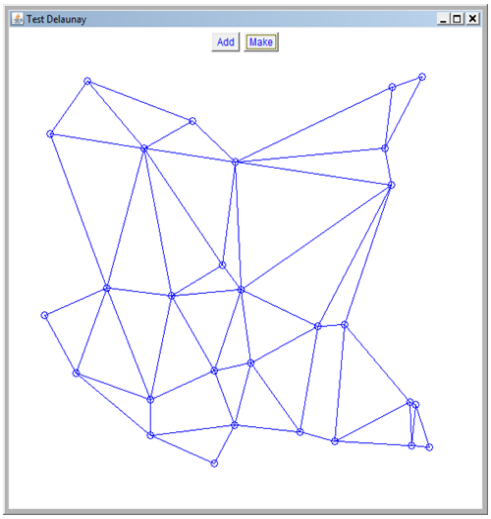

Fig.7. Java applet animation of Delaunay tessellation

Fig.8. Bait View World experimental model

3 Experiments

In the simulation, an agent is supposed to head toward the reward-are. We call this model "bait view world", also called "non-coincidence of state space and action space model", shown in figure 8. An agent gets a reward when it enters the reward-area and the agent's position change randomly on this bait view world. The objective of agent is to get as much reward as possible during a specific period. This model is based on continuous state and discrete action of feeder mouse.

The agent observes the angle and distance to reward-area as shown in figure 9 and these 2 input values construct the 2-dimensional state space. The agent has 3-types of control actions selection; 1) go straight ahead, left rotation and right rotation. Each action is displayed by color "red", "green" and "blue" (Fig 6). The agent normally selects the next action which has a maximum Q-value but sometimes selects the next action at random.

We conducted the experiments with 100,000 continuous learning times make one "episode" and executed 160 episodes in one "experiment". We did 10 trials for each episode by changing the random initial seed and took an average. The learning rate **α** was set to 0.1 and discount rate γ was set to 0.9.

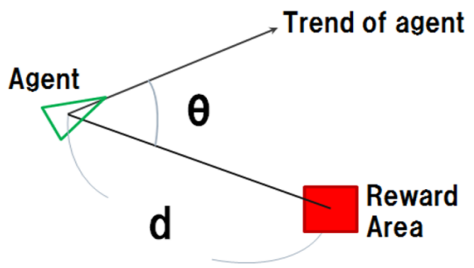

Fig.9. 2-input values for experimental model

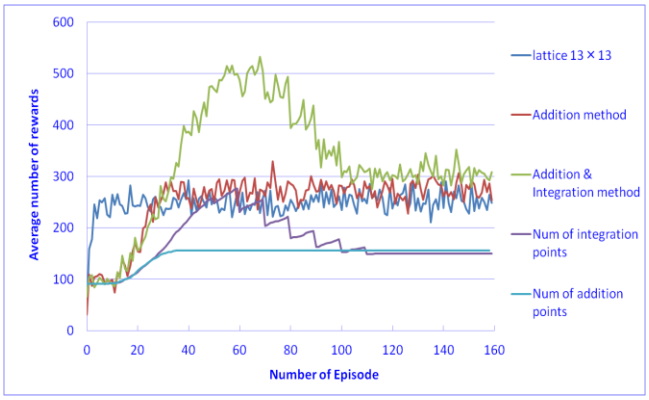

Fig.10. Experimental results of 3-methods

3.1 Experimental results

We examined the performance of the following several different methods in a stationary situation of reward-area through the computer simulations. These are 1) lattice arrangement of normal Q-learning on discrete state space, 2) implementation of addition method using LBG algorithm, and 3) implementation of integration method using Delaunay tessellation technique on continuous state space. Figure 10 shows the result of these three experiments.

4 Conclusions

We presented the addition and integration method of q-values on continuous state space in order to realize the position of Voronoi points and to reduce the number of states and to speed up the learning efficiency. Moreover, we investigated the performance and efficiency of our proposed methods using Bait View World experimental model. As a result of experiments, the number of state decreases greatly and our proposed methods give good results in simulation. However, we occurs the over-integration problem though the number of states has decreased and the learning speed is suddenly decreased at the halfway. Therefore, we need to consider about this problem and it is need to able to change the integrated timing adaptively. Furthermore, we applied Voronoi diagram, LBG algorithm and Delaunay Tessellation technique in this study.

References

[1] Sutton RS, Barto AG (1998), Reinforcement learning an introduction, MIT Press, Cambridge.
[2] Watkins CJCH, Dayan P. Technical notes: Q-learning. Machine Learning 1992;8:279-292.
[3] G.Patane and M.Russo, The enhanced LBG algorithm, In proceedings of Neural Networks, 2001, pp.1219-1237.
[4] F.Shen, O.Hasegawa, An adaptive incremental LBG for vector quantization, Neural Networks 19 (2006) 694-704.

© ISAROB 2013

The Eighteenth International Symposium on Artificial Life and Robotics 2013 (AROB 18th '13),
Daejeon Convention Center, Daejeon, Korea, January 30-February 1, 2013

Recipe search engine inspired by ant colony's foraging

Jinwook KIM[1], Kazuyuki ITO[1], and Katsunori TACHIBANA[2]

[1]Hosei University, Tokyo 184-8584, Japan
[2]NEC Communication Systems, Ltd., Tokyo, Japan
(Tel: 81-42-387-6093, Fax: 81-42-387-6381)

[1] jinwook.kim.d5@stu.hosei.ac.jp, [1] ito@hosei.ac.jp

Abstract: These days, concern with link between consumer electrical appliances and information devices has been growing such as the refrigerator which has a managing function of food ingredients. This environment is called 'Ubiquitous computing', 'Smart home appliance' which has possibility of further development. In this environment, we consider the system which suggests users some well-balanced recipes that can be cooked by the available ingredients. Especially, we focus on recipe search engine for limited state such as using only existing foods ingredients in the refrigerator. However, conventional keyword search does not suit this system. In this paper, we focus on the ant colony's foraging in order to make a new recipe search engine. We confirm the effectiveness of the proposed search engine by conducting simulations.

Keywords: ant colony's foraging, ubiquitous computing, smart home appliance, recipe search

1 Introduction

With progress of information network technology, our life style becomes remarkably convenient. Furthermore, according to link with mobile phone, consumer electrical appliances and many other information devices recently, we can get a lot of high quality services more and more. This environment is called 'Ubiquitous computing', 'Smart home appliance' which has possibility of further development [1].

Especially, the concern with link between consumer electrical appliances and information devices has been growing for these days. The refrigerator which has a managing function of food ingredients and a recipe search engine, also a built-in kitchen linked this are expected leading example of application.

Now, we propose the system which suggests users some well-balanced recipes that can be cooked by the available food ingredients in the refrigerator. However, conventional keyword search does not suit this system.

In this paper, we focus on the ant colony's foraging in order to make a new recipe search engine. Ant repeats simple actions – 'Lifting up', 'Carrying', 'Lifting down' and ant colony make food clusters. Ant colony makes food clusters at random, so it is different size and placed position. We consider ant's food as food ingredients in refrigerator, and food clusters as recipes. Then we can make a recipe search engine by represent ant colony's foraging on simulation. We confirm the effectiveness of the proposed search engine by conducting simulations.

2 Goal of the proposal system

We propose the system which suggests users some well-balanced recipes that can be cooked by the available food ingredients in the refrigerator. Therefore, new recipe search engine have to find various desirable combinations as recipes from existing foods ingredients in refrigerator.

Furthermore, In order to improve usefulness, the system makes general Japanese menu plans per serving.

3 Problem with conventional keyword recipe search engine

In conventional keyword search, users input some keywords such as name of dish or food ingredient to search engine, then it give them information about relative to keywords. Because of keyword search engine provide us information that only based on input keyword, and food ingredients are not unlimited, many search results containing a keyword are obtained.

On the other hand, we keep food ingredients in the refrigerator, and we consider using these every day. There are many kinds of combinations from existing food ingredients in the refrigerator. So we can make use of those combinations as recipes. In this case, conventional system can not make useful combinations from limited state such as only existing foods ingredients in refrigerator, because it depend on only keyword and does not consider foods ingredients in refrigerator.

Therefore, we need new concept for new recipe search engine and we focus on the ant colony's foraging. Using this ant's simple repeat action, the recipe search engine

© ISAROB 2013

gives information to users even if user does not input keywords.

4 Ant colony's foraging

Ant colony does not have central controller, however ants can collect foods on the basis of local information. Using following Fig. 1, we explain this mechanism.

An ant moves at random on the environment where objects are scattered such as Fig. 1 a). When it finds an object, ant lifts up the object by a certain probability. An ant which has the object moves to other place. When it finds other objects, ant lifts down the object by a certain probability, and then a small cluster is made by these objects.

The probability is determined by the size of that cluster which placed somewhere. In certain place where are many objects, ant tends to lift down the object. Conversely, in certain place where are few objects, ant tends to lift up the object. Ant colony repeat simple actions – 'Lifting up', 'Carrying', 'Lifting down' and they make many small clusters. Smaller size cluster move to larger one by repeat of ant colony simple actions. As a result, clusters grow up and it becomes a few larger clusters [2].

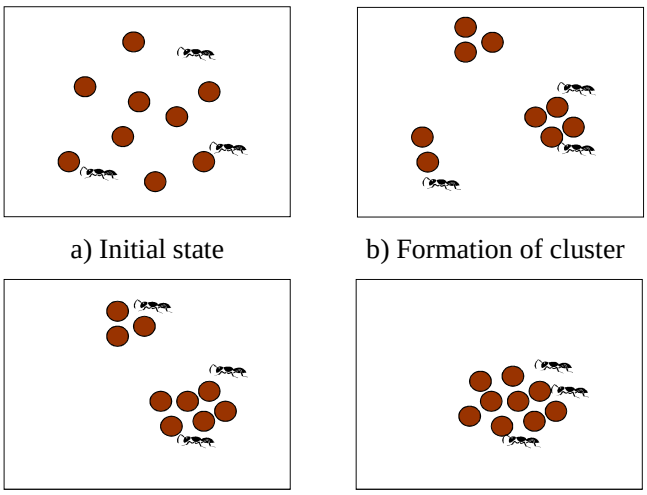

a) Initial state b) Formation of cluster

c) Growth of cluster d) End state

Fig. 1. Ant colony's foraging

We apply this ant colony's foraging algorithm to recipe search engine, we consider ant's object as food ingredients in refrigerator, and clusters as recipes on simulation.

5 Proposal method

Ant colony's foraging is reproduced on virtual environment, and it uses for recipe search engine. Food ingredients in refrigerator correspond to ant's food and collected by ant colony's foraging algorithm to make recipe. When all required food ingredients are collected to make recipe, it shows as a recipe which can cook.

5.1 Environment of recipe search engine

As shown in Fig. 2, environment of recipe search engine is one-dimensional space with several cells in the shape of a straight line.

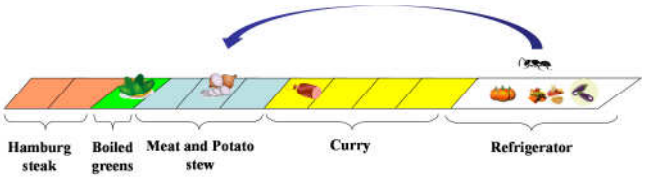

Fig. 2. Environment of recipe search engine

Recipes are assigned on a several cells. To make Recipe which is required a large number of food ingredients, takes more times for carry food ingredients and it is hard to be made up. Therefore, several recipe cells are proportional to the number of food ingredients and we consider that agent visits the recipe cell which is more required number of food ingredients. Food ingredients are arranged in the refrigerator cell at first and carry on the recipe cell by the agent which is reproduced ant colony's foraging. Agent moves at random such as jumping each cell. The recipe which all the required food ingredients are collected on an own cell is recognized as a recipe which can be cooked.

5.2. Recipe search engine inspired by ant colony's fo raging

The flowchart of recipe search engine inspired by ant colony's foraging is shown in Fig.3.

First, agent moves at random on the each cell. When it enters the cell which is existing food ingredient, agent lifts up the food ingredient by a certain probability. The probability of lifting up the food ingredient is shown in equation (1).

・Lifting up probability

$$P_i = 1 - \left\{ 0.999 \cdot \left(\frac{a_i}{n_i} \right) + 0.001 \right\} \quad (1)$$

i : Identification number of a recipe

n_i : Total number of food ingredients required for the i-th recipe

a_i : Number of food ingredients which placed current recipe cell

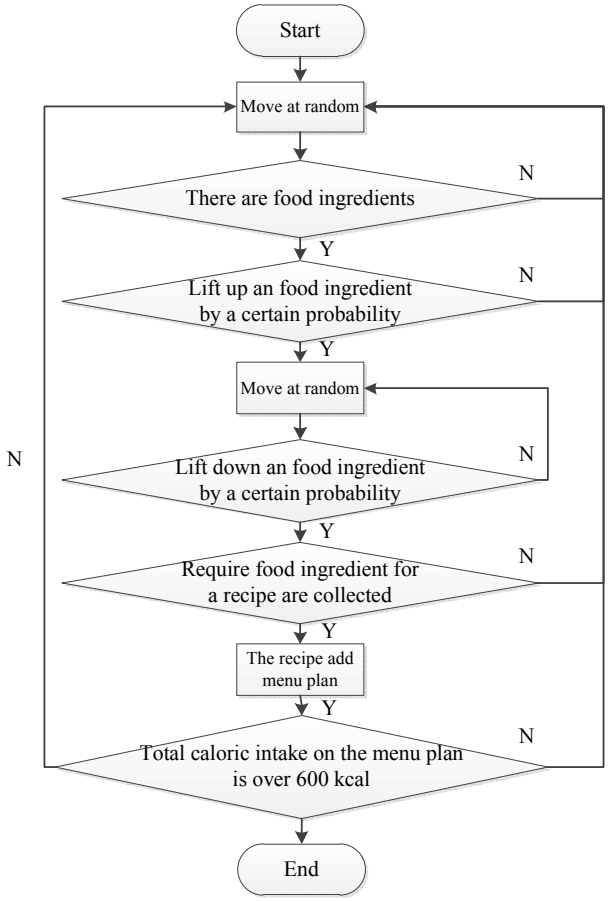

Fig. 3. Flowchart of ant colony's foraging

The agent which has the food ingredients moves at random on the each cell again. When it enters the cell which is existing food ingredient, agent lifts down the food ingredient by a certain probability. The probability that agent lifts down the food ingredient is shown in equation (2).

·Lifting Down probability

$$Q_i = 0.999 \cdot \left(\frac{a_i}{n_i} \right) + 0.001 \qquad (2)$$

When all required food ingredient for certain recipe are collected, it is recognized as a recipe which can be cooked, and the recipe adds menu plan. We consider that caloric intake set 600 kcal for serving, and when the total caloric intake on menu plan is over that value, recipe search is end.

6 Simulation

We simulate recipe search engine inspired by ant colony's foraging. The recipes used for the simulation are selected 80 kinds of recipes as shown in the following Table. 1[3].

Table 1. Recipes used for the simulation

Recipe No.	Name of Recipe
1	Beef curry
2	Chicken cream stew
3	Japanese-style pancake
4	Hashed beef with rice
5	Omelet rice
6	Spaghetti with meatballs
. . .	. . .
79	Hamburg steak
80	Pork cutlet

6.1 Simulation condition

To confirm the effectiveness of the proposed method, we conduct simulations with 3 different conditions written below.

a) General search: In order to verify the usefulness of the recipe search engine, we simulate it with the co ndition that a lot of food ingredients which is enough to search various recipes are in the refrigerator.
b) Search with condition that a lot of meat: We simulate recipe search engine with the condition that a lot of meat are in the refrigerator.
c) Search with condition that a lot of vegetables: We s imulate recipe search engine with the condition that a lot of vegetables are in the refrigerator.

6.2 Simulation results

Each simulation results are shown below.

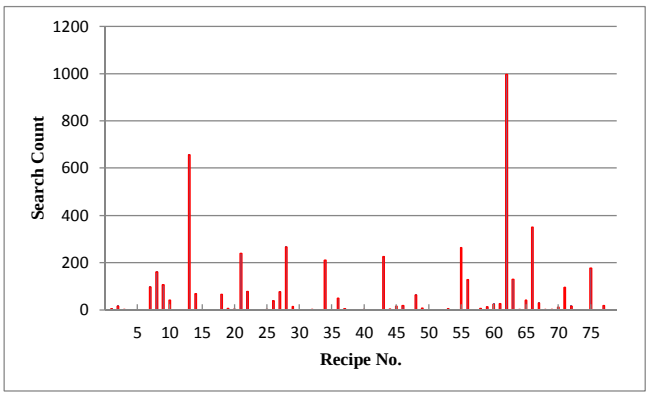

Fig. 4. The result of general search

© ISAROB 2013

The vertical axis of Fig. 4 shows each recipe search count and the horizontal axis show recipe number in Table. 1. As a result, various recipes were searched by search engine. Most searched 2 recipes are as below.

Table 2. Most searched 2 recipes

Recipe No.	Recipe Name	Food ingredient
13	Boiled spinach	Spinach
62	Salmon meuniere	Salmon

Least searched 2 recipes are as below.

Table 3. Most searched 2 recipes

Recipe No.	Recipe Name	Food ingredient
25	Sukiyaki	Beef, Mushroom Egg, Welsh onion
53	Green pepper steak	Beef, Green pepper Ginger, Welsh onion

Compare Table 3 with Table 4, we can figure out that recipes which is required lower number of food ingredients are well-searched than others. If users would like to get other recipes, they can get useful recipe information by re-search.

Table 4 - Table 6 show the examples of the searched menu plans for each condition.

Table 4. The result of condition a) – various food ingredients

Menu 1	Menu 2
Mackerel simmered in miso sauce	Potato gratin
Rice with bamboo shoot	Japanese hotchpotch
Boiled spinach	Boiled spinach
Chop suey	Scallop cream croquette

Table 5. The result of condition b) – A lot of meat

Menu 1	Menu 2
Hamburg steak	Chinese dumpling
Potato croquette	Cabbage roll
Fishcake soup	Fishcake soup
Omelet rice	Omelet rice

Table 6. The result of condition c) – A lot of vegetables

Menu 1	Menu 2
Rice with bamboo shoot	Rice with bamboo shoot
Boiled spinach	Spaghetti with tomato sauce
Scallop cream croquette	Japanese-style pancake (Okonomiyaki)
Potato gratin	Boiled spinach

Each table shows that recipes were searched according to food ingredients in the refrigerator. If users would like to get other menu plans, they can get useful menu plan information by re-search.

7 Conclusion

In this paper, we consider the recipe search engine inspired by ant colony's foraging for the refrigerator which has a managing function of food ingredients. In order to verify the usefulness of the proposed system, the proposed system was mounted on the personal computer and we have conducted several simulations by each condition.

As a result, various recipes were searched by new search engine, proposal system was realized.

Our future work is to take the nutritional information into consideration and to add learning mechanism to the search engine for adapting user's taste.

REFERENCES

[1] R. Kango, P.R. Moore, J. Pu (2002), Networked smart home appliances - enabling real ubiquitous. Proceedings 5th IEEE international workshop on networked appliances, pp.76-80

[2] J. L. Deneubourg (1991), The dynamics of collective sorting robot-like ants and ant-like robots. Proceedings of the First International Conference on Simulation of Adaptive Behavior, pp.356-363

[3] Tanaka O (2008), The useful standard recipe for ever y day. (Mainichi yakudatu teiban okazu, in Japanese), Shog akukan Inc.

© ISAROB 2013

The Eighteenth International Symposium on Artificial Life and Robotics 2013 (AROB 18th '13),
Daejeon Convention Center, Daejeon, Korea, January 30-February 1, 2013

Constructing Obstacle-Based Triangularized Roadmap

JeongHyeon Wang[1] and JuJang Lee[2], *Fellow, IEEE*

[1]Korea Advanced Institute of Science and Technology, Daejeon, Korea
[2]Korea Advanced Institute of Science and Technology, Daejeon, Korea

[1]jh_wang@kaist.ac.kr
[2]jjlee@ee.kaist.ac.kr

Abstract: This paper proposes an algorithm which makes roadmap quite fast using obstacle information. The proposed algorithm purposes to expand graphs which consist of edge and vertex based on obstacles. After the algorithm detects corner information, using Harris corner detection, keep all data and use it. The proposed algorithm consists of two parts, one is arranging initial nodes using space decomposition, and the other is constructing a graph from initial nodes. In this case, we assume that all the obstacles are polygon. And then we can detect corners of obstacles. Using this, connecting each node to visible corners, we can expand our graph. The proposed algorithm is quite simple and straightforward to understand and it has advantage of constructing fully-covered roadmap. This property has been verified through several experiments.

Keywords: Central Voronoi Tessellation, PRM, Roadmap, Triangularize;

1 INTRODUCTION

Path planning is becoming an important one in the many of the fields such as indoor and outdoor mobile robot planning, underwater path planning, motion planning and so on. Also it increases needs for searching optimal path in any environments.

Different from grid-based approach, the probabilistic roadmap method (PRM) is one of the typical sampling based approaches [1]. Contrary to Rapidly-exploring Random Trees (RRT), it deals with constructing multiple queries [2]. The PRM based planner searches for free spaces using two phases, a learning phase and a query phase. But efficiency of PRM is not good because it produces lots of redundant samples to maintain total connectivity and it also needs lots of sample points to reach whole connectivity. In order to solve this problem many of the sampling-based roadmap constructing method is proposed. In [3], [4] to increase connectivity of PRM, various sampling strategies such as narrow passage sampling, bridge test and so on are introduced. In [5], [6] creating useful cycles, It increases total connectivity and also controls the essential number of vertices. In [7], adopting new node sampling method, efficiency of probabilistic roadmap planner's performance increases. From these papers, we can think about that how to construct simple and straightforward roadmap without including complex and burden tasks. That is the starting points of our idea.

In this paper, we propose a new algorithm to construct the roadmap. The proposed method has two phases. First, in initializing phase, the algorithm randomly selects several points in the free space. But when we select this randomly, we cannot guarantee about well-distribution of this points. It is important to our proposed algorithm because after finishing initializing phase, we will use these points as start points and expand to free configuration space in the map. The more evenly distributed initial points, the better results in next step. The position of these initial points will be selected by the construction of Central Voronoi Tessellation (CVT) [8] in order to spread randomly chosen samples evenly. After evaluating well-distributed initial nodes, we use the Harris Corner Detector [9] to get information about geometric configuration of the environment. All the obstacles are approximated by polygon. So using Harris Corner Detector, we can find lots of corners and with these corners, we will explore uncovered region in the map.

This paper is organized as follows. Section 2 describes the node distribution method using CVT. and using this result, Section 3 describes the proposed node expansion algorithm. An implementation and simulation results are presented in Section 4, and the discussion follows

2 Node Initialization

The proposed algorithm distributes initial nodes considering geometric information, using CVT construction process. Before explaining CVT, we introduce a voronoi tessellation first. Figure 1 shows an example of the voronoi tessellation. In this figure, there are two generators z_1 and z_2. In this case, we can divide two regions V_1 and V_2. These two regions are divided by opposite sides of perpendicular bisector. This is voronoi tessellation. If there are more than two generators in constrained region, voronoi tessellation constructs regions for a number of generators in entire region. Furthermore we can define the center of mass. For example, given a region V in $\mathbb{R}^n$ and a density function $\rho(w)$ defined as $w \in V$, the center of mass $Z^*$of V is given as follows.

$$z^* = \frac{\int_V w\rho(w)dw}{\int_V \rho(w)dw} \tag{1}$$

CVT is the special cases for the generators of voronoi sets and centers of mass in voronoi region do actually coincide. Figure 2 shows an example of the comparison about general voronoi tessellation and CVT. Left figure is general voronoi tessellation and right is CVT. Contrary to general voronoi

© ISAROB 2013

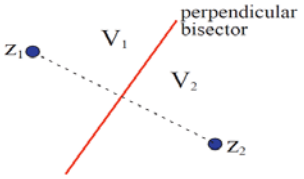

Figure 1 example of voronoi tessellation

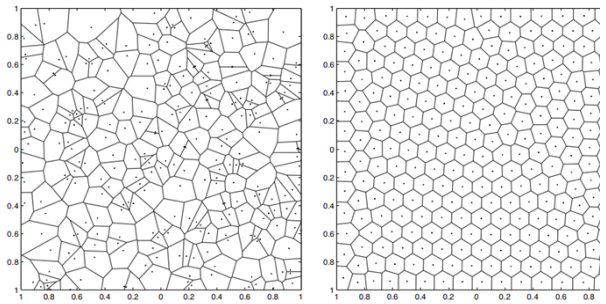

Figure 2 Comparison between random sampling and CVT

tessellation, CVT has almost well-distributed sample nodes. That's why CVT needs to distribute generators regularly in our proposed algorithm.

In the real construction process of the CVT, positions of nodes are updated iteratively until each position of the nodes is equivalent to each centroid of voronoi cells. The McQueen's algorithm [10] and Lloyd's algorithm [11] are well known process of constructing CVT. Algorithm 1 describes McQueen's Algorithm in detail. The McQueen's algorithm doesn't require the construction of voronoi sets or centers of mass. Despite this, the points produced by McQueen's method converge to the generators of a CVT. However the problem with McQueen's method is that it samples only one point before it averages. So at worst, it takes more than millions of steps to obtain a CVT set of points from an initial set of points. The Lloyd's algorithm is also called K-Means algorithm in computer science. It may have better result than McQueen's algorithm under same constraints. Algorithm 2 describes Lloyd's Algorithm in detail. Compared to McQueen's algorithm, it also has a heavy computational burden because the samples in the voronoi region should be calculated with generators in every iterations. But in my algorithm, it doesn't matter how many times to iterate this algorithm to approximate exact center of voronoi regions. Just we spread out our initial generators appropriately. There is no need to step out many times.

When the iteration of Lloyd's algorithm ends, there is a probability that center of voronoi region is on the obstacle regions. In this case, we cannot use this initial position to expand nodes and edges from this point. Because it doesn't

Algorithm 1 McQueen's Method
(Random sampling and Averaging).

1. Start with some initial set of K points $\{Z_i\}_{i=1}^{K}$
2. Sample another point w
3. Determine which of the z_i's is closest to the w
4. Find the average of w and the z_i closest to it.
5. Replace the z_i used in the averaging by the average point.

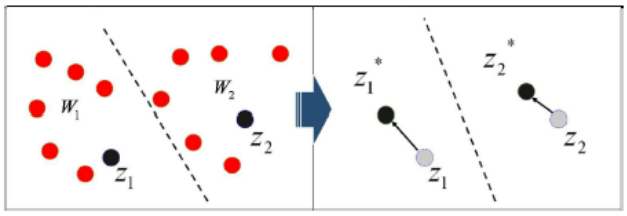

Figure 3 positions of center of mass are updated using Lloyd's algorithm

Algorithm 2 Lloyd's Method

1. Start with some initial set of K points $\{Z_i\}_{i=1}^{K}$
2. Construct the voronoi tessellation $\{V_i\}_{i=1}^{K}$ of omega associated with the points $\{Z_i\}_{i=1}^{K}$
3. Construct the centers of mass of the voronoi regions $\{Z_i\}_{i=1}^{K}$ found in Step 1; these centroids are the new set of points $\{Z_i\}_{i=1}^{K}$
4. If under some convergence criterion, quit otherwise go base to step 2.

satisfy the properties that all the expansions are in the free configuration spaces. So we use the Lloyd's algorithm once again only in that region. Choose any two generators in that region and iterate Lloyd's algorithm again. This step will be end when all generators are on the free configuration space.

3 Node Expansion

The purpose of proposed algorithm is to construct roadmap covering entire map so that wherever the start and goal position is, total feasibility of expected path will be guaranteed. Before we start next step, we deal with some useful and needed properties to construct roadmap

- Assume all the obstacles are estimated by polygon.
- Entire free space will be surrounded by triangles.
- Expansion algorithm will construct triangles iteratively keeping triangularity.

The reason why we estimate obstacle to polygon is to divide entire free space with triangles. The advantage of triangular-based approach is as follows.

- It represents detailed areas better and it doesn't complicate open areas.
- Triangulation has much fewer cells and is more accurate than grid-based approach.
- It can deal with non-point objects quite easier than grid-based approach.

Under these advantages, we can construct triangular-based roadmap satisfying properties. Algorithm 3 describes main algorithm of construction step. Key idea of algorithm is as follows. First find visible corners using Harris Corner Detectors and find convex-hull of corners. Convex-hull is the smallest convex set that contains corners. If edge of convex-hull is on the free space, not on the obstacle, add new vertex in the middle of two points. If possible, connect to other vertex which has already made before. The proposed construction step will be classified by three cases. One is just add vertex and edge, another is first case plus connects toward other vertex made before and the other is

© ISAROB 2013

Algorithm 3 Construct Roadmap(E, V, Xset, initialCentroids)

```
Begin
  if firstIteration  and  ∃ Visibility(initialCentroids) then
    removeVisibleNodes(initialCentroids)
    V ← V ∪ {initialCentroids}
  Endif
  Xset ← {initialCentroids}
  do
    [CornerSet, numOfVisitingTime]
    ← connectVisibleCorners (Xset(i), numOfVisitingTime)
    makeConvexHull(CornerSet)
    if numOfVisitingTime >= 2 then
      if findAlreadyMadeVertex(CornerSet,
                               V, numOfVisitingTime) == TRUE then
        addEdge(E, V, Xset, CornerSet)
      Else
        addVertexAndEdge(E, V, Xset, CornerSet)
      Endif
    Else
      addVertexAndEdge(E, V, Xset, CornerSet)
    Endif
  While isEmpty(Xset) == TRUE
End
```

first case plus check possibility of existing vertex before.

Add vertex and edge.

Figure 4 shows how to add vertex and edge in the first case. Before start construction roadmap, check geographical condition of initial nodes. Although we spread initial nodes regularly, there will be a problem when a couple of initial vertices are visible each other. It will break up whole triangularity when we expand from these nodes. So we must ensure that each initial node is not visible. In the first step, pre-expanded initial node will invade the area where other initial node has to be covered. First, detect visible corners from frontier vertex using Harris Corner and update the number of visiting times for each node. In this case, there are no corners that the number of visiting time is more than two. That is, it is the first time to visit whole corners. And check if adding new vertex in the middle of the corners on the convex-hull is possible. In figure 4, green stars are on the line of obstacle, so discard them. But brown star is on the free space. So add new edge from frontier vertex and add new edge.

Add edge to the vertex made before.

Figure 5 shows how to add edge to the vertex made before. Other step is same as the first case. But in this figure, when checking the number of visiting time in all visible corners, there are two corners that the number of visiting time is more than two. That is, other vertices had already visited before. So there can be a probability of existing vertex in the middle of two points. If find them, add edge to that vertex made before and other step is the same as first case. If there is more than three corners which satisfies this cases, we make a temporary vertex set with that corners and check any vertex is exists in that set. Other step is same.

Possibility that vertex exists.

Figure 6 shows how to consider when there is a possibility of existing vertex. When detecting visible corners from frontier vertex, there exist two corners, left top

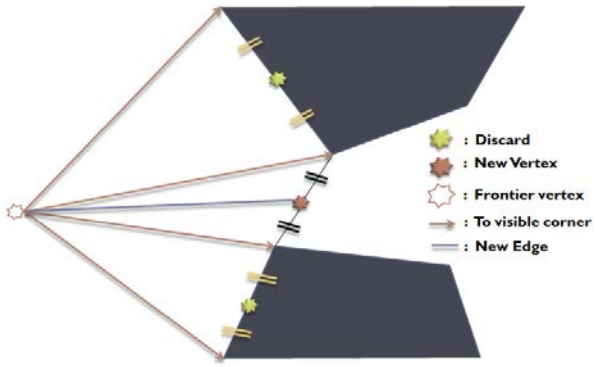

Figure 4 Roadmap construction case: Add vertex and edge

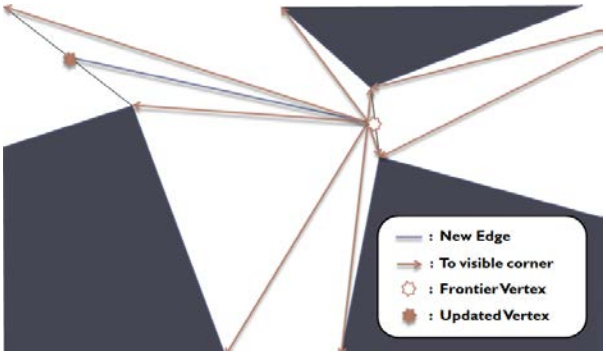

Figure 5 Roadmap construction case: Add edge to the vertex made before

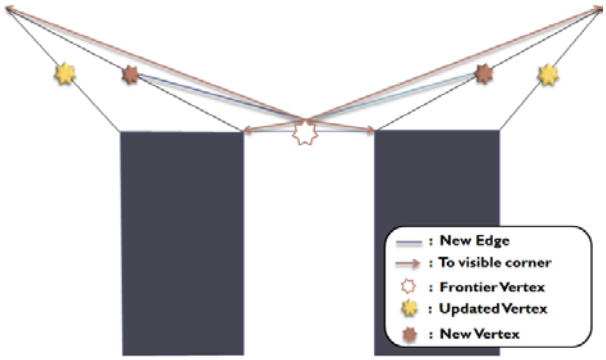

Figure 6 Roadmap construction case : Possibility of existing vertex

and right top, that the number of visiting time is more than two in this figure. So there can be a probability of existing vertex in the middle of two points. Same as second case, check if edge exists in the middle of two points. But in this case, there is no vertex between two corners. So there is no need to add new edge toward that. Other step is the same as first case.

4 Simulation Results and Discussion

All our experiments were run with MATLAB in Windows 7 Service Pack1 on an Intel(R) Core(TM) i5 2.67GHz 2.66GHz with 4.00GB of internal memory. The results are as follows.

Simulation Results

Figure 7 describes several results. In this figure, result (a) and (b) are the results based on the same obstacle. Blue lines are edges and blue points are vertices. Red line is convex hull and in each iteration, we plotted to see whether

it finds convex hull of corners or not. And small dot in the background tells about a result of Lloyd's algorithm. In this figure there are two colors so clustered in two parts. It also represents that even though the same environment is given, it is possible to construct different roadmap. Additionally constructing roadmap relies on the position of initial nodes. That's why the result (a) and (b) have different figure. Result (c) and (d) are the examples of different number of initial nodes.

Figure 8 also describes several results in more complicated environment. It shows that whether the complexity of environment increases, we construct well-covered roadmap.

Evaluation

But in these results, quite inefficient connections are founded. In figure 7-(c), right top two vertices are not connected. Because two vertices have same parents node. If we use this algorithm to real path planning, for example, we can always find a feasible path but not the shortest path in this roadmap. That's why we need to extra refinement step to construct more realistic roadmap. For example, using many search algorithms, we can find shorter path to evaluate each vertex whether extra connection will be needed or not.

Furthermore, there is no appropriate definition of number of initial nodes. For my experiment, the less complexity is, the fewer initial nodes will be needed. In other words, in the complex geometric environments, arranging more initial nodes is better than arranging only one or two nodes. But it is the conclusion about our several simulation results. It seems to be needed to certain rule to control the number of initial nodes.

REFERENCES

[1] L. E. Kavraki, P. Svestka, J. Latombe and M. H. Overmars, "Probabilistic Roadmaps for Path Planning in high-dimensional configuration spaces," in *IEEE Transactions on Robotics and Automation*, vol. 12, no. 4, pp. 566-580, 1996

[2] S. LaValle, "Rapidly-exploring random trees: A new tool for path planning," CS. Dept., Iowa State Univ., Ames, IA, Tech. Rep. TR 98-11, 1998

[3] Z. Sun, D. Hsu, T. Jiang, H. Kurniawati and John H. Reif, "Narrow passage Sampling for Probabilistic Roadmap Planning," in *IEEE Transactions on Robotics*. Vol. 21, No. 6, pp. 1105-1115, 2005

[4] M. Morales, S. Rodriguez, Nancy M. Amato, "Improving the Connectivity of PRM Roadmaps," in *International Conference on Robotics and Automation*, pp 4427-4432, 2003.

[5] D. Nieuwenhuisen and M. Overmars, "Useful cycles in probabilistic roadmap graphs," in *IEEE International Conference on Robotics and Automation*, pp. 446-452, 2004

[6] R. Geraerts and Mark H. Overmars, "Creating High-quality Roadmaps for Motion Planning in Virtual Environments," in *IEEE/RSJ International Conference on Intelligence Robots and Systems*, 2006.

[7] B. Park, W.K. Chung, "Adaptive Node Sampling Method for Probabilistic Roadmap Planners," in Proc. of *IEEE/RSJ International Conference on Intelligent Robots and Systems*, pp. 4399-4405, 2009

[8] Q. Du, V. Faber and M. Gunzburger, "Central Voronoi Tessellations: Applications and Algorithms," in *SIAM Review*, vol. 41, no. 4, pp.637-676, 1999

[9] C. Harris and M. Stephens, "A Conbined Corner and Edge Detector," in *proc. of The Fourth Alvey Vision Conference*, pp. 147-151, 1988

[10] J. McQueen, "Some methods for classification and analysis of multivariate observations," in Proceedings, *Fifth Berkeley Symposium on Mathematical Statistics and Probability*, Vol. 1, pp. 281-297, 1967.

[11] S. Lloyd, "Least square quantization in PCM," in *IEEE Transactions on Information theory*, Vol. 28, pp. 129-137, 1982

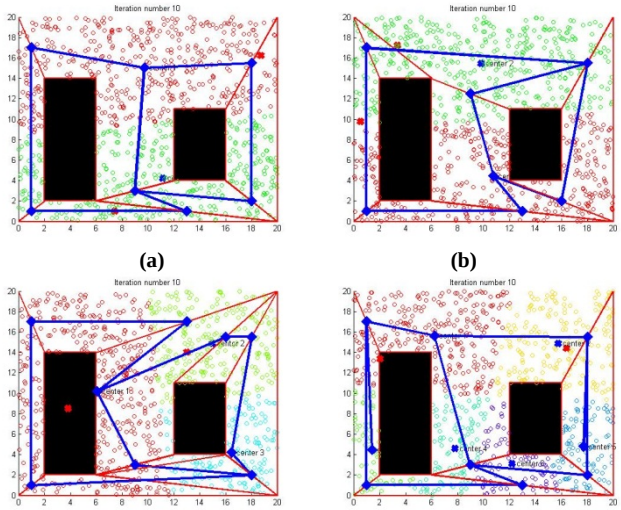

Figure 7 Four results of constructing roadmap under same environment and different number of initial nodes

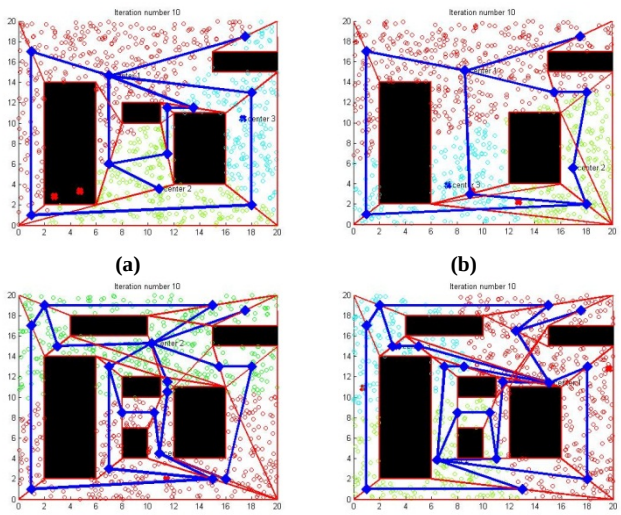

Figure 8 Four results of constructing roadmap more complicated environment and different number of initial nodes

The Eighteenth International Symposium on Artificial Life and Robotics 2013 (AROB 18th '13),
Daejeon Convention Center, Daejeon, Korea, January 30-February 1, 2013

Non-uniform Cellular Automata based on Open-ended Rule Evolution

Noritsugu Sughimura, Reiji Suzuki and Takaya Arita

Graduate School of Information Science, Nagoya University
Furo-cho, Chikusa-ku, Nagoya 464-8601, Japan
E-mail: nxsughi@alife.cs.is.nagoya-u.ac.jp, {reiji, arita}@nagoya-u.jp

Abstract: Cellular automata (CAs) are mathematical models of spatially and temporally discrete mathematical systems. Non-uniform CAs are the cellular automata in which each cell may contain a different transition rule and change it with time, while all cells share the same transition rule in regular CAs. Little is still known about the dynamics of open-ended evolution of rules in non-uniform CAs. The purpose of our study is to construct and investigate a model of non-uniform CAs capable of open-ended rule evolution exhibiting a wide variety of behavior across all Wolfram's classes. For this purpose, we construct 1-dimensional 2-state 3-neighborhood non-uniform CAs with evolving transition rules. In the model, we found an interesting dynamics that Class II (periodical behavior) and III (chaotic behavior) patterns emerged alternately, between which Class IV patterns sometimes emerged.

Keywords: Complexity, Elementary cellular automata, Non-uniform cellular automata, Open-ended, Rule evolution

1 INTRODUCTION

Cellular automata (CAs) are mathematical models of spatially and temporally discrete mathematical systems. They consist of a large number of relatively simple units ("cells"). Each cell is a simple finite automaton that repeatedly updates its own state depending on the cell's current state and those of its immediate neighbors. They have been commonly used to describe and explore complex systems. One of the pioneering work is the classification of the CA behavior into four classes (Class I, II, III and IV) by Wolfram [1]. In a typical Class IV CA, initial patterns evolve into structures that interact in complex ways based on a mixture of order and randomness ("edge of chaos"). The connection between such a complexity and the (origin of) life have been frequently discussed in the artificial life community. Additionally, Langton [2] has been successful in assessing Wolfram's each classes quantitatively. He indicated that Class III show the highest entropy and Class IV show the highest mutual information. Moreover, Mori et al. [3] have proposed a rule-changing CA model based on internal dynamics. They indicated that this CA model may show higher mutual information than normal CA.

Non-uniform CAs are the cellular automata in which each cell may contain a different transition rule and change it with time, while all cells share the same transition rule in regular CAs. In the previous studies, non-uniform CAs often have been evolved to perform computational tasks including density classification and synchronization. Before then, Packard [4] and Mitchell [5] used a genetic algorithm to evolve CA rules to perform a specific task. Sipper [6] demonstrated that non-uniform CAs is partially superior to uniform CAs. However, little is still known about the dynamics of open-ended evolution of rules in non-uniform CAs.

The purpose of our study is to construct and investigate a model of non-uniform CAs capable of open-ended rule evolution exhibiting a wide variety of behavior across all Wolfram's classes. We also aim at applying it to visual artwork based on a never-ending autonomous flow of information. For this purpose, we construct 1-dimensional 2-state 3-neighborhood non-uniform CAs with evolving transition rules. Each cell has not only its state but also its transition rules. The transition rules of cells with high fitness that is calculated using entropy tend to propagate to neighboring cells. Specifically, we use the fitness of each transition rule defined as Shannon entropy for the state distribution of the 3-step history of 5-neighborhood cells. In addition, mutation may change the transition rule of each cell into another rule, which brings a novelty into the system.

2 MODEL

2.1 Algorithm

We use 1-dimensional 2-state 3-neighborhood cellular automata (CAs) and their states of the cells. Each cell also has a transition rule, represented as a binary sequence $(x_7x_6x_5x_4x_3x_2x_1x_0)$. This rule maps 3-neigborhood states to a decimal number $x_i \in (0, 1)$: [000] to x_0, [001] to x_1, $\cdots$, and [111] to x_7.

Each cell is updated by the the procdures as follows: (i) N cells are arranged on a 1-dimensional array. Each cell has a state that is set 0 or 1 arbitrarily, and a rule that is chosen arbitrarily from 1-dimensional 2-state 3-neighborhood CAs (elementary CA, ECA) rules. (ii) Each cell determines its next state on the basis of its rule and the states of 3-neighborhood cells including itself. (iii) Each cell calculates its own fitness

© ISAROB 2013

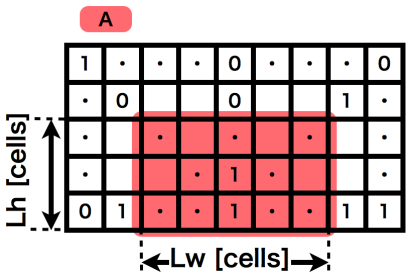

Fig. 1. The state distribution A.

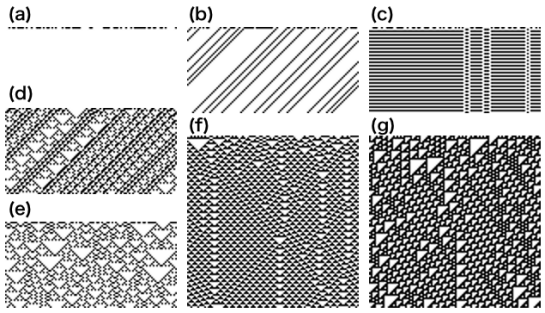

Fig. 2. The typical state patterns of the 7 classes in ECA.

Fig. 3. The artwork.

(Section 2.2). (iv) Each cell replaces its own rule by the rule of the cell with the highest fitness in 3-neighborhood. (v) Each bit x_i in the rule representation $(x_7x_6x_5x_4x_3x_2x_1x_0)$ is flipped with a mutation rate μ as mutation. (vi) Update each cell's state and time step. (vii) Return to (ii) ((ii) - (vi) are repeated G times with (iii) and (iv) being skipped during the first Lh repetitions).

2.2 Fitness

The fitness of each cell is defined as Shannon entropy as follows. Here, K is set to 2 as the number of possible states (0 or 1), and p_i is the appearance ratio of each state in the spatial (Lw-neighborhood cells) and temporal (Lh-step history) domains (A in Fig. 1). Therefore, when the numbers of 0 and 1 in the domain are the same, it will be the highest and, in contrast, when the number of 0 or 1 is 0, it will be the lowest.

$$Fitness = H(A) = -\sum_{i=1}^{K} p_i \log p_i$$

3 EXPERIMENT

We investigate the rule evolution over the long time steps in Section 3.1 and focus on two characteristic patterns of rule evolution in Section 3.2. To do so, we classify the 256 ECA rules into seven groups (Class I, Class II-F, Class II-P, Class III-LC, Class III-C, Class IV-54 and Class IV-110). It covers four classifications by Wolfram [1] and five classifications by Li and Packard [7] as shown in Table 1.

We used the following parameter values: $N = 200$ (number of cells), $G = 2.0 \times 10^6$ (number of steps), $Lw = 5, Lh = 3$ (parameters for the fitness), $\mu = 1.0 \times 10^{-4}$ (mutation rate). All cells began with the state 0 and the rule 0.

3.1 Rule evolution over the long time steps

Fig. 4 shows the distribution of classes to which the existing rules belong (upper), and the number of the different existing rules and the average fitness (lower), across 2 million time steps. We see a general tendency that Class II-F (fixed point) and Class III-C (chaotic) dominate the population alternatively (Phase II and Phase III). There is also a tendency

Table 1. Classifications of ECA rules. Our classification is as follows (The rules inside the parenthesis are equivalent to the representative rule). Class I: 0 (255), 8 (64, 239, 253), 32, (251), 40 (96, 235, 249), 128 (254), 136 (192, 238, 252), 160 (250), 168 (224, 234, 248), Class II-F: The rest of ECA rules, Class II-P: 1 (127), 3, 5 (95), 6 (20, 159,215), 7 (21, 31, 87), 9 (65, 111, 125), 11 (47, 81, 117), 14 (84, 143, 213), 15 (85), 19 (55), 23, 25 (61, 67, 103), 27 (39, 53, 83), 28 (70, 157, 199), 29 (71), 33 (123), 35 (49, 59, 115), 37 (91), 38 (52, 155, 211), 41 (97, 107, 121), 43 (113), 50 (179), 51, 74 (88, 173, 229), 108 (201), 131 (62, 145, 118), 133 (94), 134 (148, 158, 214), 142 (212), 156 (198), 178, Class III-LC: 26 (82, 167, 181), 73 (109), 154 (166, 180, 210), Class III-C: 18 (183), 22 (151), 30 (86, 135, 149), 45 (75, 89, 101), 60 (102, 153, 195), 90 (165), 105, 106 (120, 169, 225), 129 (126), 146 (182), 150, 161 (122), Class IV-54: 54 (147), Class IV-110: 137 (110, 124, 193)

Fig. 2	Wolfram	Li&Packard	This study
(a)	Class I	null	Class I
(b)	Class II	fixed-point	Class II-F
(c)	Class II	periodic	Class II-P
(d)	Class III	locally chaotic	Class III-LC
(e)	Class III	chaotic	Class III-C
(f)	Class IV	chaotic	Class IV-54
(g)	Class IV	chaotic	Class IV-110

that in Phase II, the average fitness is stable and high, and the number of the different rules is high (10-30), and in contrast, in Phase III, the average fitness is rather unstable and lower, and the number of the different rules is lower (-10). Especially, typically in Phase III, the average fitness sometimes has a sudden decrease to around 0.8, that is accompanied by a sudden increase to around 40 in the number of the different rules.

Concerning the Class IV, which is the most interesting class, Class IV-54 sometimes dominates the population mainly in Phase II and Class IV-110 occasionally emerges a little (0-10 cells) almost instantaneously typically in Phase III. This tendency might due to the resemblance of the patterns generated by Class IV-54 to Phase II patterns or the resemblance of the patterns generated by Class IV-110 to Phase III patterns.

Next, we focus on the process which realize the transition from Phase II to Phase III, or vice versa.

© ISAROB 2013

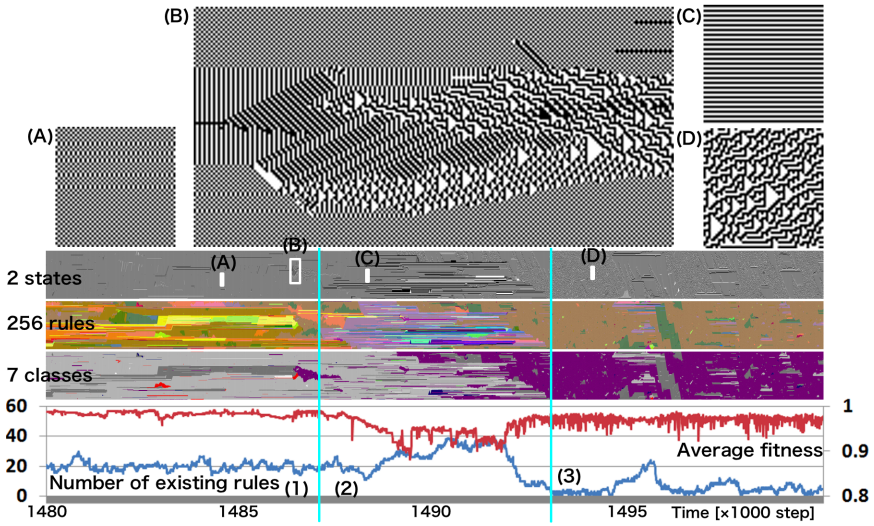

Fig. 5. The number of the existing rules and the average fitness (lower); the distribution of that the 7 classes, the 256 rules and the 2 states (middle); the images of the distinctive patterns (upper) from Phase II to Phase III.

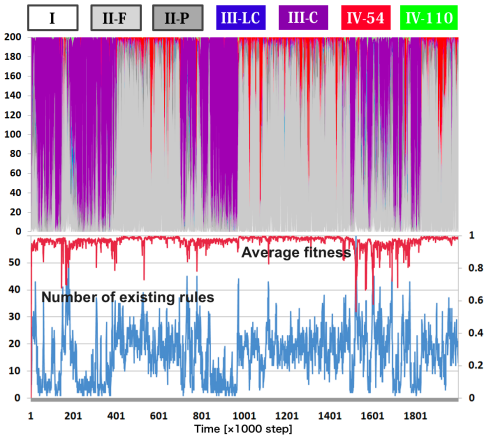

Fig. 4. The number of the existing rules and the average fitness (lower); the distribution of the 7 classes (upper) over 2 million time steps.

3.2 Rule evolution from Phase II (III) to Phase III (II)

Fig. 5 and Fig. 6 show the transitions of the number of the different existing rules, and the average fitness (lower), the state transition between 2 states, rule transition among 256 rules, and class transition among 7 classes (middle), and the enlarged parts of the distinctive patterns in the rule evolution (upper), across 20 thousand time steps, from Phase II to III, and Phase III to II, respectively.

We see from Fig. 5 that a transition from Phase II to III takes place through the three stages: Stage (1) as trigger creation, Stage (2) as rule diversification, and Stage (3) as strategy stabilization. The trigger in Stage (1) shifts the state distribution from Stage (1) to (2) introducing many various transition rules. In Stage (2), the average fitness of the cells is relatively low, and the number of existing transition rules is high. After that, Class III emerges and spreads gradually.

It is also shown from Fig. 6 that a transition from Phase III to II takes place through the three stages similar to the transition from Phase II to III: Stage (1) as trigger creation, Stage (2) as rule diversification, and Stage (3) as strategy stabilization. The trigger in Stage (1) shifts the state distribution from Stage (1) to (2) introducing many various transition rules. Specifically, (D) consists of Class II-F, III-C and IV-54, and (E) consists of Class II-F, II-P and IV-110. In Stage (2), the average fitness is also relatively low, and the number of existing transition rules is high. After that, Class II emerges and spreads gradually.

A closer observation of Fig. 5 reveals that there is a difference in dominant rules and state distribution between Stages (1) and (2), while Class II-F rules dominate the population throughout Stages (1) and (2). We see actually a clear difference between the enlarged patterns (A) and (C) that are the distinct patterns in Stage (1) and (2), respectively. The distinct pattern in Stage (3) is (D), which is a typical pattern of Class III-C behavior.

On the other hand, we see from Fig. 6 that while Class II-F dominates the population throughout Stages (2) and (3), there is also a difference in dominant rules and state distribution between Stages (2) and (3). Similarly, we see from the enlarged patterns that the distinct patterns in Stage (2) and (3) are (C) and (F), respectively, and that in Stage (1) is (A) which is a typical pattern of Class III-C behavior.

It is noticeable fact that the transitions from Phase II to III and from Phase III to II share some common dynamics. Accumulation of mutations suddenly but, in a sense, inevitably induces a state distribution in which several rules work together as a trigger to invoke Stage (2) in both transitions. In

© ISAROB 2013

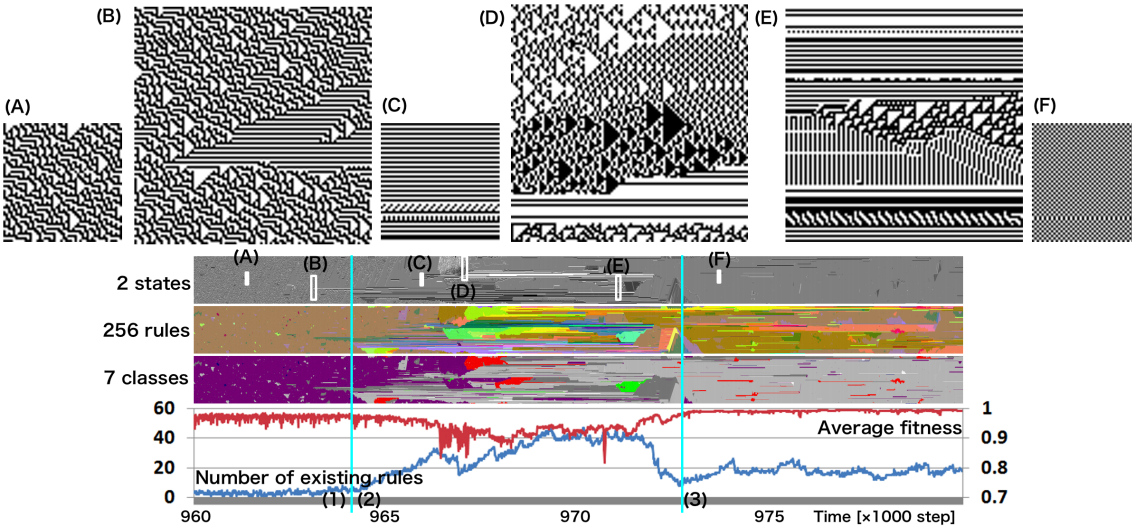

Fig. 6. The number of the existing rules and the average fitness (lower); the distribution of that the 7 classes, the 256 rules and the 2 states (middle); the images of the distinctive patterns (upper) from Phase III to Phase II.

this sense, (B) in both figures can be seen as a part of the triggers.

4 CONCLUSION

We examined the space-time patterns generated by the proposed non-uniform CAs. We found an interesting dynamics that Class II (periodical behavior) and III (chaotic behavior) patterns emerged alternately, between which Class IV patterns sometimes emerged. It was observed continuously over 2 million time steps and therefore, we regard this dynamics as underlying and inherent in the model.

More detailed analysis showed that during the alternation, the average fitness of the cells was relatively low and at the same time, the number of existing transition rules was high. Our interpretation of this is that some decrease in average fitness could start the alternation and this decrease induced various transition rules to emerge. We thus believe that decrease in average fitness and the resulting emergence of various transition rules are the key to the complex dynamics observed in the model.

The art exhibition "ALart_2012" was held at the Nagoya University Project Gallery "clas" in February 2012 featuring the artwork "One-Dimensional Cells". It was based on a never-ending autonomous flow of information created by the proposed model (Fig. 3). The artwork was also used to create the posters of the exhibition [8], which were put up in or around the campus including on the wall in the nearby subway station.

Future work includes investigating analyzing the level of open-ended rule evolution and the complexity of the global state distribution quantitatively.

REFERENCES

[1] S. Wolfram. *A new kind of science*. Wolfram Media Inc, 2002.

[2] C. G. Langton. Computation at the edge of chaos: Phase transitions and emergent computation. *Physica D: Nonlinear Phenomena*, 42(1):12–37, 1990.

[3] T. Mori, K. Kudo, Y. Namagawa, R. Nakamura, O. Yamakawa, H. Suzuki, and T. Uesugi. Edge of chaos in rule-changing cellular automata. *Physica D: Nonlinear Phenomena*, 116(3):275–282, 1998.

[4] N. H. Packard. Adaptation toward the edge of chaos. In A. J. Mandell J. A. S. Kelso and M. F. Schlesinger, editors, *Dynamic Patterns in Complex Systems*, pages 293–301. World Scientific, 1988.

[5] M. Mitchell, P. T. Hraber, and J. P. Crutchfield. Revisiting the edge of chaos: Evolving cellular automata to perform computations. *Complex Systems*, 7:89–130, 1993.

[6] M. Sipper. Co-evolving non-uniform cellular automata to perform computations. *Physica D: Nonlinear Phenomena*, 92(3):193–208, 1996.

[7] W. Li and N. Packard. The structure of the elementary cellular automata rule space. *Complex Systems*, 4(3):281–297, 1990.

[8] Artificial Life Laboratory at Nagoya University. The poster of "Alart_2012". http://www.vision.ss.is.nagoya-u.ac.jp/clas/programs/docs/2012_alart2012.pdf, (in Japanese), 2012.

© ISAROB 2013

The Eighteenth International Symposium on Artificial Life and Robotics 2013 (AROB 18th '13),
Daejeon Convention Center, Daejeon, Korea, January 30-February 1, 2013

A Procedure for Constructing Social Network Using Web Search Engines: The Case for Japanese Automotive Industry

Yuichi Kubota[1], Reiji Suzuki[1] and Takaya Arita[1]

[1] Graduate School of Information Science, Nagoya University, Japan
kubota@alife.cs.is.nagoya-u.ac.jp, {reiji, arita}@nagoya-u.jp

Abstract: Recently, search engines have enabled us to access immense quantities of useful information in an instant. In this paper, we propose a procedure for analyzing the social relationship and structure using Web search engines, which includes novel ways to create a search query and to use the number of hits. This allows us to construct various networks that reflect directed and undirected relationships among actors under arbitrary contexts. As a case study for evaluations of the proposed procedure, we focus on 50 companies belonging to automotive industry in Japan. We constructed several directed and undirected networks under different temporal and geographical contexts. We show that we can obtain more general knowledge about this industrial community from the analyses of these created networks and their centrality measures.

Keywords: Social Network, Web Mining, Visualization

1 INTRODUCTION

Characteristics of social networks are a valuable piece of information for understanding social activities and communications. However, it had been very costly, or even impossible for non-specialists, to obtain large-scale data for measuring the strength of the relationship among many actors (e.g., persons, companies) to create their social network, which had made such an approach only applicable to limited and well-organized data.

On the other hand, the progress in the field of Web technologies have enabled us to access immense quantities of useful information for creating social networks in an instant. Especially, various methodologies for extracting social networks using search engines have been proposed [1].

Lee et al. proposed a method for social network analyses based on the statistical physics using the number of Google search hits in order to estimate the relatedness between two actors [2]. They introduced a general framework for measuring the disparity or heterogeneity of weights a node bears. They constructed a social network of the 109th US Senate members, and successfully showed the division or community structure, reasonably consistent with the senators' political parties, and so on. Recently, Akaishi et al. proposed a method to analyze the temporal change in a social network every year by adding the enumeration of years to a query [3]. They observed the temporal dynamics of the social network composed of the 93 people who have played major roles in the US economy, showing its relational changes surrounding the economic crisis in 2008. They also analyzed the interdisciplinarity of researchers and research topics by constructing a bipartite graph using queries composed of topics and researchers, using a new quantity named *visibility boost* for the calculation of relatedness [4]. These studies clearly show that we can observe various aspects of a social relationship by constructing networks using different ways to use search queries and the search results, although each previous study mainly focused on a specific topic in detail. We believe that such a multifaceted approach gives us valuable insights into understanding of essential properties of social networks.

From this viewpoint, in this paper, we propose a simple procedure for analyzing social relationships and structures using Web search engines, which includes novel ways to create a search query and to use the number of hits. This allows us to construct various networks that reflect directed and undirected relationships among actors under arbitrary contexts. As a case study for evaluations of this procedure, we focus on 50 companies belonging to automotive industry in Japan. We constructed and analyzed several networks using indices for measuring directed and undirected relatedness under different temporal and geographical contexts.

2 METHOD

Generally, the number of hits obtained by a search query consisting two keywords reflects the co-occurrence frequency of these words in the Web. We can approximate the strength of the relationship between actors (e.g. companies, researchers) by using this property of search engines.

If X and Y are the sets of the web pages obtained by search queries for "x y", respectively, we can regard statistical metrics for the relationship between these two sets as the strength of the relatedness between the actors x and y. As for undirected relationships between actors, we use a standard Jaccard coefficient: $\frac{h(X \cap Y)}{h(X \cup Y)}$, where $h(X \cap Y)$ and $h(X \cup Y)$ are the number of hits obtained by the search query for "x y" and "x OR y" (using the Google search engine), respectively. In order to measure the asymmetric relationship between two

© ISAROB 2013

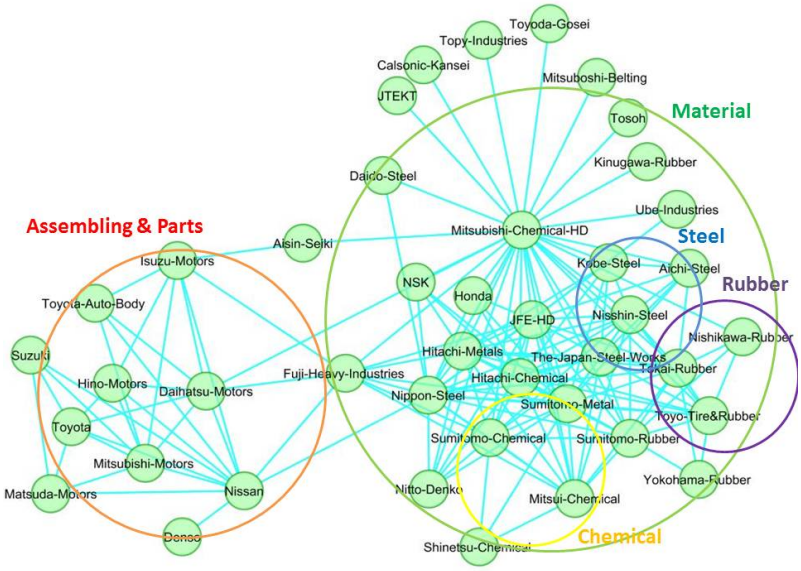

(a) The undirected network based on the Jaccard coefficient.

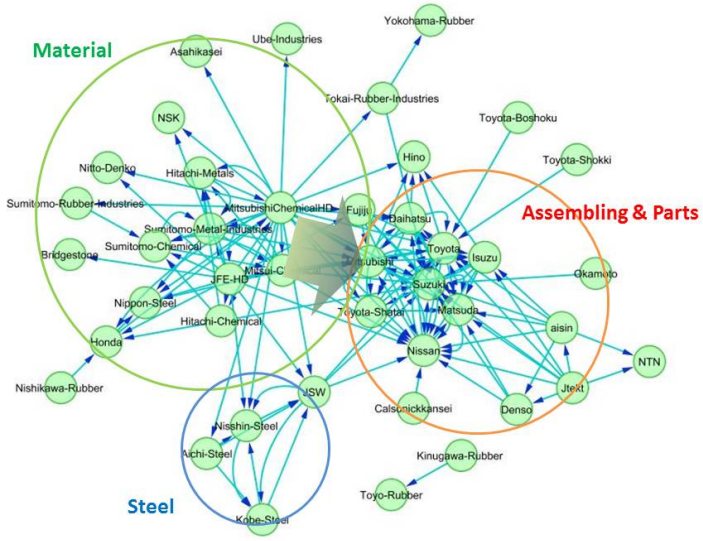

(b) The directed network based on the directed Simpson coefficient.

Fig. 1. The social networks of automotive industry in Japan, constructed by using (a) the Jaccard coefficient and (b) the Simpson coefficient.

Table 1. The 50 companies of automotive industry in Japan.

Toyota, Honda, Nissan, Matsuda Motors, Suzuki Motor Corporation, Daihatsu Motors, Mitsubishi Motors, Fuji Heavy Industries, Isuzu Motors, Hino Motors, Denso, Aisin Seiki, Toyota Auto Body, Toyota Industries, Toyota Boshoku, JTEKT, Calsonic Kansei, NSK Ltd., Toyoda Gosei, NTN Corporation, Bridgestone, Sumitomo Rubber, Yokohama Rubber, Toyo Tire and Rubber, Tokai Rubber, Bando Chemical, Okamoto, Kinugawa Rubber, Nishikawa Rubber, Mitsuboshi Belting, Nippon Steel, JFE Holdings, Kobe Steel, Sumitomo Metal, Nisshin Steel, Hitachi Metals, Daido Steel, The Japan Steel Works, Topy Industries, Aichi Steel, Mitsubishi Chemical HD, Sumitomo Chemical, Mitsui Chemical, Shinetsu Chemical, DIC Corporation, Tosoh, Asahikasei, Nitto Denko, Ube Industries, Hitachi Chemical

© ISAROB 2013

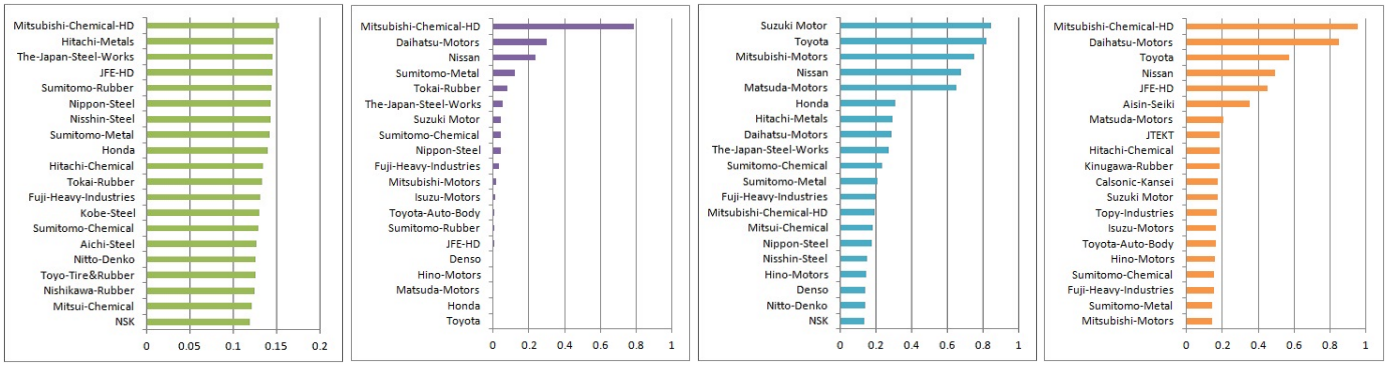

(a) Closeness (b) Betweenness (c) In-degree (d) Out-degree

Fig. 2. Network centralities of the top 20 companies. (a) and (b) are the closeness and betweenness in the undirected network. (c) and (d) are in-degree and out-degree in the directed network.

actors, we introduce a new index named *directed Simpson coefficient*: $\frac{h(X \cap Y)}{h(X)}$, where h(X) is the number of hits obtained by the search query for "x", which reflects the relatedness of the actor y for the actor x. Thus, this coefficient allows us to measure the asymmetric relationship between two actors. As far as we know, the directed Simpson coefficient has not been used in the previous research despite of its simplicity.

In addition, we can calculate the relatedness under an arbitrary context if we measure these indices by adding a specific word related to the context to the all queries for the calculation of relatedness. For example, we use the query "x y z" instead of "x y" in order to obtain $h(X \cap Y)$ under the context of "z". In this paper, we use the name of places in order to analyze the geographical variation of the networks as well as the years to analyze the temporal variation, which has also not been used in the previous research for this purpose, as far as we know.

We construct a network that reflects their social relationship using these indices. Each actor is represented as a node, and the strength of relationship between two actors is represented as the width of the link between their corresponding nodes. Note that two nodes are connected only when the strength between them is equal to or higher than a threshold T. We visualized a network using Cytoscape[1] and adopted a spring model in which the higher relatedness between nodes pull them together, in order to arrange the nodes in a two-dimensional plane. We can examine the topological properties of the network by measuring various metrics used in complex network studies such as the closeness (the average path length from the focal node to the other nodes), the betweenness (the proportion of shortest paths from all nodes to all others that pass through the focal node), and the degree (the number of edges which a node has).

[1]Cytoscape: http://www.cytoscape.org/

3 MULTIFACETED ANALYSES

As a case study for evaluations of the proposed procedure, we constructed social networks of 50 companies, whose names are listed in Table 1, belonging to automotive industry (assembling, material and part makers) in Japan. We used Google Search API for web searches. We also used the setting T = 0.1(Jaccard) and 0.4(directed Simpson).

Fig. 1 (a) and (b) show the constructed networks using the Jaccard coefficient and the directed Simpson coefficient, respectively. In the undirected network (Fig. 1 (a)), we see the two major clusters composed of material companies (including steel, chemical and rubber companies) and parts & assembling companies, respectively. The Jaccard coefficient tends to become large when h(X) and h(Y) are close if h(X OR Y) is large. Because the number of hits obtained by a search query for a company is expected to reflect the scale of the company's business, we can expect that mutually related companies with the more similar scale of business tended to be clustered in the network in Fig. (a). When we used the directed Simpson coefficient (Fig. 2 (b)), we observed the "flows" of the relationships from the former cluster to the latter, implying the significance of the latter companies. We also see that the assembling makers (e.g. Toyota, Nissan) have more input links than output links. This implies that it is likely that the assembling maker is socially depended on by other suppliers in automotive industry.

We calculated the several centrality measures of each node in these networks, and listed the top nodes, as shown in Fig. 2. In this paper, we focused on the closeness and the betweenness in the undirected network (Fig. 2 (a) and (b)). It should be noticed that both centrality measures of a major chemical company (Mitsubishi chemical holdings) tended to be higher than others'. This seems to reflect that this company has wide relationship with other companies in this field. As for the directed network, we focused on the in-degree and

© ISAROB 2013

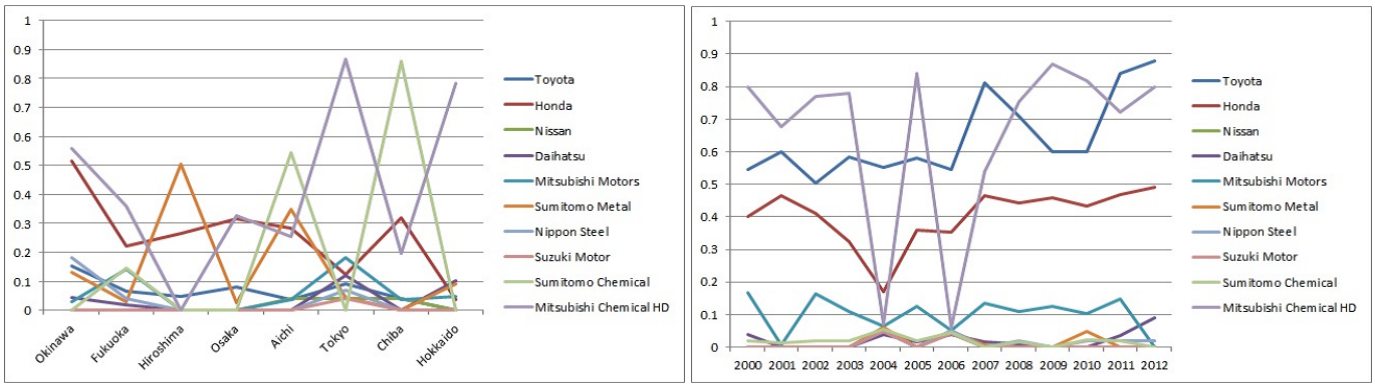

(a) The geographical variation (b) The temporal variation

Fig. 3. The betweenness of each node in the directed networks under the different (a) geographical contexts and (b) temporal contexts.

out-degree (Fig. 2 (c) and (d)). We found that major car manufacturers (e.g. Toyota, Nissan) tended to have both high in-degree and high out-degree, which is expected to be due to their high importance in this industry.

We also constructed different directed networks using the different temporal (from 2000 to 2012) and geographical (from Okinawa to Hokkaido) contexts. Note that these years and names of places themselves were used for additional keywords for a query. The keywords except the focal context are also used to limit search results to a particular context (e.g., "Toyota Nissan Tokyo -Osaka -Aichi, -· · ·" for calculating the relatedness between Toyota and Nissan under the geographical context of Tokyo). Then, we calculated the betweenness of each node in the all networks as shown in Fig. 3. We have chosen some major companies in order to observe the general tendency of the relational variation under these contexts.

We see from Fig 3 (a) that there were significant differences in the betweenness of each company among the networks in different geographical regions. This might to be due to the large difference in the industrial structure or the size of the market in these regions. Fig 3 (b) also shows the temporal changes in the betweenness of each company through the years, implying that some major companies played important roles in turns through this period.

4 CONCLUSION

We have proposed a simple procedure for analyzing social relationships and structures using Web search engines, which includes novel ways to create a search query and to use the number of hits, in order to understand them from a multifaceted view. As a case study, we constructed several networks of companies in automotive industry in Japan, using different indices for measuring directed and undirected relatedness under different temporal and geographical contexts. The analyses clarified not only the overall topological properties of the social network, but also the existence of its geographical and temporal variations. We believe that the proposed procedure enables many people including non-specialists to understand social relationships and structure between individuals, companies or countries through constructing and analyzing the networks by making use of search engines.

ACKNOWLEDGEMENTS

The authors thank Dr. Jin Akaishi for technical advices for web searches using the Google search engine.

REFERENCES

[1] Matsuo, Y., Mori, J., Hamasaki, M., Nishimura, T., Takeda H., Hashida, K. and Ishizuka, M.: POLYPHONET: An advanced social network extraction system from the Web, *Web Semantics*, 5: 262-278 (2007).

[2] Lee, S. H., Kim P. J., Ahn Y. Y. and Jeong, H., Googling social interactions: Web search engine based social network construction, *PLoS ONE*, 5(7): e11233.

[3] Akaishi, J., Sayama, H., Dionne, S. D., Chen, X., Gupta, A., Hao, C., Serban, A., Bush, B. J., Head, H. J. and Yammarino, F. J.: Reconstructing history of social network evolution using web search engines, *Proceedings of BIONETICS 2010*, 155-162 (2010).

[4] Sayama, H. and Akaishi, J.: Characterizing interdisciplinarity of researchers and research topics using web search engines, *PLoS ONE*, 7(6): e38747 (2012).

© ISAROB 2013

Statistical Analysis for Price Changes of Carbon European Union Allowances

zeyu zheng[1], Kazuko yamasaki[2], Jun Yang[3]

[1]Tokyo University of information sciences, Japan

[2]Tokyo University of information sciences, Japan

[3]Economics and Business Administration, Chongqing University, China

(Tel: 81-43-236-4652, Fax: 81-43-236-4652)

[1]zeyuzheng8@gmail.com

Abstract: Recent years, several national and regional emission markets have been established, the carbon emission related assets already become an main investment goods. We analyzed the price changes time series of European Union allowances (EUA) futures in European Climate Exchange (ECX) market, which is the world's largest single market for CO2 emission allowances. We showed probability density function of price changes time series. We find that there are long-range correlations in the absolute of price changes (volatility). Further, detrended fluctuation analysis (DFA) approach is assessed with focus on long-range correlations and Hurst exponent. We find long-range power-law auto-correlations in the absolute of price changes (volatility) that quantify the size of risk, and find that they decay much more slowly than the auto-correlation of return time series. We also investigate the multi-fractal status of volatility of EUA time series. All results show that the EUA price change time series have very similar statistic properties as stocks price changes.

© ISAROB 2013

The Eighteenth International Symposium on Artificial Life and Robotics 2013 (AROB 18th '13),
Daejeon Convention Center, Daejeon, Korea, January 30-February 1, 2013

A Real-Coded Genetic Algorithm Taking Account of the Weighted Mean of the Population

Naotoshi Nakashima[1], Yuichi Nagata[1], and Isao Ono[1]

[1]Tokyo Institute of Technology, Japan
(Tel: +81-45-924-5545, Fax: +81-45-924-5442)

[1]naoto@ic.dis.titech.ac.jp

Abstract: Continuous function optimization is an important problem in science and engineering. The real-coded genetic algorithm (RCGA) has shown good performance in continuous function optimization. AREX/JGG is one of the most promising RCGAs. However, we believe that AREX/JGG has two problems in terms of search efficiency. In this paper, we propose a new RCGA that overcomes the problems of AREX/JGG. In order to examine the effectiveness of the proposed RCGA, we compared the performance of the proposed RCGA with that of AREX/JGG on several benchmark problems in which initial populations do not cover the optimal points. As the result, we confirmed that the proposed RCGA succeeded in finding the optimal points faster than AREX/JGG.

Keywords: function optimization, genetic algorithms, real-coded GAs, AREX/JGG

1 Introduction

Continuous function optimization is an important problem that we often face in various domains such as science and engineering. In recent years, several real-coded Genetic Algorithms (RCGAs) for function optimization have been studied actively [1-4]. It has been reported that RCGAs are effective in optimizing high-dimensional functions with multimodality, epistasis and ill-scaleness. However, most conventional RCGAs have a serious problem that the performance deteriorates when the population does not cover the optimal point.

In order to remedy the above problem of the conventional RCGAs in the case where the population does not cover the optimum, Akimoto *et al*. has proposed AREX/JGG and reported that AREX/JGG shows better performance than the conventional RCGAs in benchmark problems in which initial regions do not cover the optimal points [3, 4]. However, we believe that AREX/JGG has the following two problems in terms of search efficiency: 1) If the population distribution does not cover the optimal point, AREX/JGG does not always generate offspring and eliminate individuals in the population so that the population distribution efficiently moves towards the optimal point. 2) If the population distribution covers the optimal point, AREX/JGG does not always generate offspring and eliminate individuals in the population so that the population efficiently converges towards the optimal point.

In this paper, we propose a new RCGA that overcomes the above two problems of AREX/JGG. In order to examine the effectiveness of the proposed method, we compare the performance of the proposed RCGA with that of AREX/JGG on several benchmark problems with multimodality, strong epistasis and ill-scaleness in which initial regions do not cover the optimal points.

2 AREX/JGG and Its Problems

2.1 Just Generation Gap (JGG)

JGG has been designed as a generation alternation model for multi-parent crossover operators [3, 4]. The algorithm of JGG is as follow.

(1) Initialization:
Randomly generate an initial population $\{p_k \mid k=1,\ldots,\tau\}$ within a specified region. Evaluate the object function values of all the individuals in the population. Initialize the generation number $\boldsymbol{g}$ with 1.

(2) Mating Selection: Randomly choose parents $\{\boldsymbol{y}_j|j=1,\ldots,n+1\}$ from the population $\{p_k|k=1,\ldots,\tau\}$, where n is the dimension of the problem.

(3) Generation of offspring: Generate offspring $\{\boldsymbol{x}_i|i=1,\ldots,\tau\}$ by applying AREX to parents $\{\boldsymbol{y}_j|j=1,\ldots,n+1\}$. Evaluate the object function values of the offspring $\{\boldsymbol{x}_i|i=1,\ldots,\tau\}$.

(4) Survival Selection: Select the best n+1 offspring among the offspring $\{\boldsymbol{x}_i|i=1,\ldots,\tau\}$ and remove the parents $\{\boldsymbol{y}_j|j=1,\ldots,n+1\}$ form the population $\{p_k|k=1,\ldots,\tau\}$.

(5) If termination conditions are satisfied, terminate the algorithm. Otherwise, $\boldsymbol{g} \leftarrow \boldsymbol{g}+1$ and go to step2.

2.2 AREX (Adaptive Real-coded Ensemble Crossover)

AREX has been proposed to remedy a serious problem of conventional real-coded GAs that premature convergence often occurs when the population does not cover the optimal point [3, 4].

AREX generates offspring by

© ISAROB 2013

$$\boldsymbol{x}_i = \boldsymbol{m} + \alpha \sum_{j=1}^{\mu} \epsilon_{i,j} \left(\boldsymbol{y}_j - \langle \boldsymbol{y} \rangle \right) \quad \cdots (1)$$

where $\boldsymbol{m}$ is the center of crossover and α is the expansion rate to be adapted.

The center of crossover $\boldsymbol{m}$ is calculated by

$$\boldsymbol{m} = \sum_{k=1}^{\mu} w_k \boldsymbol{y}_{k;\mu} \quad \cdots (2)$$

where $k;\mu$ denotes the best k individual out of μ parents. w_k (k=1,…,μ) denote weights where $\sum_{k=1}^{\mu} w_k = 1$ and are calculated by Eq.(3).

$$w_k = 2\left(\mu + 1 - k\right) / \left(\mu\left(\mu + 1\right)\right) \quad \cdots (3)$$

Using Eq.(2) as the center of crossover, AREX aims at prompting the center of mass of the population to move towards the promising region.

The expansion rate α is adapted so that offspring are generated wider than their parents in order to keep the diversity of the population when the population moves. The expansion rate α is adapted as follows:

$$\alpha^{(g+1)} := \max\left(\alpha^{(g)} \sqrt{(1 - c_\alpha) + c_\alpha \frac{L_{\mathrm{cdp}}}{L_{\mathrm{avg}}}}, 1 \right) \quad \cdots (4)$$

where the g and c_α are the generation number and the learning rate, respectively. L_{cdp} is the Mahalanobis distance between the center of crossover $\boldsymbol{m}$ and the mean of the best μ offspring $\langle x \rangle_\mu$. L_{cdp} is defined by Eq.(5) and is calculated by Eq.(6).

$$L_{\mathrm{cdp}} = (\langle \boldsymbol{x} \rangle_\mu - \boldsymbol{m})^{\boldsymbol{T}} \boldsymbol{C}^{+} (\langle \boldsymbol{x} \rangle_\mu - \boldsymbol{m}) \quad \cdots (5)$$

$$= \alpha^2 (\mu - 1) \left(\sum_{j=1}^{\mu} \langle \epsilon_j \rangle_\mu^2 - \frac{1}{\mu} \left(\sum_{j=1}^{\mu} \langle \epsilon_j \rangle_\mu \right)^2 \right) \quad \cdots (6)$$

C is the covariance matrix of the offspring distribution and C^{+} is the Moore-Penrose inverse matrix of C. The $i{:}\lambda$ denotes the index of the best i-th individual among the λ offspring. L_{avg} denotes the expected value of the squared distance under random selection and is calculated by Eq.(7).

$$L_{\mathrm{avg}} = \alpha^2 \sigma^2 (\mu - 1)^2 / \mu \quad \cdots (7)$$

2.3 Problems of AREX/JGG

AREX/JGG generates an offspring distribution near around n+1 parents randomly chosen from the population and replaces the n+1 parent with the n+1 best offspring. Therefore, assuming big-valley functions, we believe that AREX/JGG has two problems in terms of search efficiency.

[Problem 1] As shown Fig.1, if the population distribution does not cover the optimal point in the search space, AREX/JGG does not always generate offspring in the outer area of the population distribution near the optimal point, eliminate individuals in the outer area of the population distribution far from the optimal point and extend the population distribution. Therefore, we believe that AREX/JGG cannot effectively move the population distribution toward the optimal point.

[Problem 2] As shown Fig.2, if the population distribution covers the optimal point, AREX/JGG does not always generate offspring near around the optimal point and eliminate individuals in the outer area of the population distribution. Furthermore, if the offspring distribution is not generated so as to cover the optimal point, the expansion rate in Eq.(4) increases, which means that the search becomes inefficient. Therefore, we believe that AREX/JGG cannot efficiently shrink the population distribution to the optimal point.

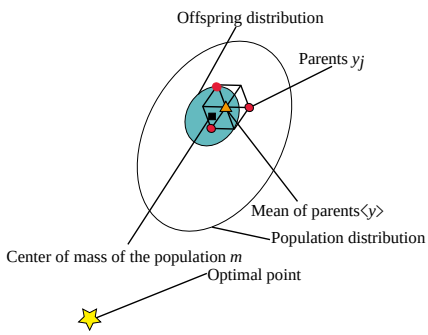

Fig.1. Offspring distribution generated by AREX/JGG when the population does not cover the optimal point.

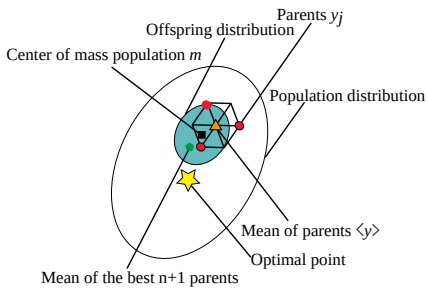

Fig.2. Offspring distribution generated by AREX/JGG when the population covers the optimal point.

3 The Proposed RCGA

3.1 Basic ideas

In this section, we describe our basic ideas to overcome the problems of AREX/JGG pointed out in section 2.3. If the population does not cover the optimal point, we generate offspring in the outer area of the population near the optimal point and eliminate individuals far from the optimal point from the population. This is expected to result in the population quickly moving towards the optimal point. On the other hand, if the population distribution covers the optimal point, we generate offspring near around the optimal point and eliminate individuals in the outer area of the population. By doing this, we expect that the population distribution converges to the optimal point quickly.

Based on the above basic ideas, we propose a new RCGA that consists of the following mating selection method, crossover operator and survival selection method.

Mating selection: The proposed RCGA chooses the n+1 worst individuals in the population as parents. As the result, as shown in Fig.3, if the population distribution does not

cover the optimal point, the proposed mating selection method is expected to choose individuals in the outer area of the population distribution far from the optimal point. On the other hand, if the population distribution covers the optimal point, as shown in Fig.4, the proposed mating selection method is expected to choose individuals in the outer area of the population distribution.

Crossover: As shown in Fig.3 and Fig.4, the proposed RCGA generates an offspring distribution by crossover whose center is a weighted mean of the all individuals in the population. As the result, as shown in Fig. 3, if the population distribution does not cover the optimal point, the proposed RCGA is expected to generate offspring also in the outer area of the population near the optimal point. On the other hands, if the population distribution covers the optimal point, as shown in Fig.4, the proposed RCGA is expected to generate many offspring near around the optimal point. Furthermore, the proposed RCGA also adapts the expansion rate according to the Mahalanobis distance between the center of crossover and the mean of the best n+1 offspring as AREX does. While the expansion rate in AREX/JGG is only for expanding the population distribution in order to avoid the premature convergence, the expansion rate in the proposed RCGA is for not only expanding the population distribution but also shrinking it. As the result, if the population distribution covers the optimal point, the proposed RCGA is expected to be able to shrink the population distribution in the optimal point quickly.

Survival selection: The proposed RCGA replaces the n+1 worst parents in the population with the n+1 best offspring. As the result, if the population distribution does not cover the optimal point, as shown in the Fig.3, the proposed RCGA is expected to eliminate individuals far from the optimal point in the population distribution. On the other hand, if the population distribution covers the optimal point, as shown in the Fig.4, the proposed RCGA is expected to remove the individuals in the outer area of the population distribution.

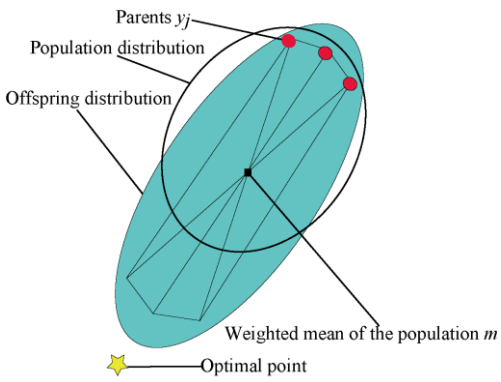

Fig.3. Offspring distribution generated by the proposed RCGA when the population does not cover the optimal point.

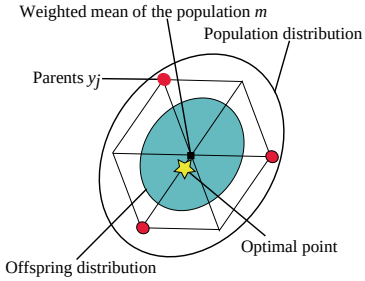

Fig.4. Offspring distribution generated by the proposed RCGA when the population covers the optimal point.

3.2 Algorithm

The algorithm of the proposed RCGA is as follows.

(1) Initialization: Generate an initial population $\{p_k|k=1,\ldots,\tau\}$ randomly within a specified region. Evaluate the objective function values of all the individuals in the population. Initialize the generation number $\boldsymbol{g}$ with 1.

(2) Mating Selection: Choose the n+1 worst individuals in the population $\{p_k|k=1,\ldots,\tau\}$ as parents $\{\boldsymbol{y}_j|j=1,\ldots,n+1\}$, where n is the dimension of the problem.

(3) Generation of offspring: Generate offspring $\{\boldsymbol{x}_i|i=1,\ldots,\tau\}$ with the parents $\{\boldsymbol{y}_j|j=1,\ldots,n+1\}$ according to Eq.(8) and evaluate the objective function values of the offspring $\{\boldsymbol{x}_i|i=1,\ldots,\tau\}$.

$$\boldsymbol{x}_i = \boldsymbol{m}' + \alpha \sum_{j=1}^{\mu} \epsilon_{i,j} \left(\boldsymbol{y}_j - \boldsymbol{m}'\right) \quad \cdots (8)$$

$\boldsymbol{m}'$ is a weighted mean vector calculated by Eq.(9).

$$\boldsymbol{m}' = \sum_{k=1}^{\tau_\alpha} w_k \boldsymbol{p}_{k;\tau} \quad \cdots (9)$$

$k;\tau$ denotes the index of the best k individual in the population whose size is τ. $\boldsymbol{w}_k$ is a linear weight where $\sum_{k=1}^{\mu} w_k = 1$. $\boldsymbol{w}_k$ is calculated by using the best τ_α individuals in the population $\{p_k|k=1,\ldots,\tau\}$ according to Eq.(10).

$$w_k = 2\left(\tau_\alpha + 1 - k\right) / \left(\tau_\alpha\left(\tau_\alpha + 1\right)\right) \quad \cdots (10)$$

α in Eq.(8) is the expansion rate and is given by Eq.(11).

$$\alpha^{(g+1)} = \alpha^{(g)} \sqrt{(1 - c_\alpha) + c_\alpha \frac{L_{\mathrm{cdp}}}{L_{\mathrm{avg}}}} \quad \cdots (11)$$

$$L_{\mathrm{cdp}} = \alpha^2(\mu - 1)\left(\sum_{j=1}^{\mu} \langle \epsilon_j \rangle_\mu^2 - \frac{1}{\mu}\left(\sum_{j=1}^{\mu} \langle \epsilon_j \rangle_\mu\right)^2\right) \quad \cdots (12)$$

$$L_{\mathrm{avg}} = \alpha^2 \sigma^2 (\mu - 1)^2 / \mu \quad \cdots (13)$$

where $\langle \varepsilon_j \rangle_\mu = \sum_{i=1}^{\mu} \varepsilon_{i:\lambda,j} / \mu$ and $\varepsilon \sim \boldsymbol{N}(0, \ \sigma^2)$. $i{:}\lambda$ is the index of the best i individual of the λ offspring. Note that the proposed RCGA allows the expansion rate to become smaller than 1.0 while that in AREX/JGG is always larger than or equal to 1.0.

(4) Survival Selection: Sort the offspring $\{\boldsymbol{x}_i|i=1,\ldots,\tau\}$ by the objective function values. Replace the parents

$\{\boldsymbol{y}_j | j=1,\ldots,n+1\}$ in the population with the n+1 best offspring.

(5) Termination Condition: If termination conditions are satisfied, terminate the algorithm. Otherwise, $\boldsymbol{g} \leftarrow \boldsymbol{g}+1$ and go to step 2.

3 Experiments

In order to examine the effectiveness of the proposed RCGA, we compared the performance of the proposed RCGA with that of AREX/JGG. The system parameters of AREX/JGG are set to the recommended values in the literature [4].

We use the 20-dimensional unimodal benchmark functions (Sphere, Rosenbrock-Star, Rosenbrock-Chain, Ellipsoid, k-Tablet) and the 20-dimensional multimodel benchmark functions (Ackley, Bohachevsky, Schaffer, Rastrigin) as shown in Table 1. The optimal points of the Rosenbrock-Star function and the Rosenbrock-Chain function are $\boldsymbol{x}_{\mathrm{opt}}=[1,\ldots,1]^T$ and the optimal points of the other functions are $\boldsymbol{x}_{\mathrm{opt}}=[0,\ldots,0]^T$. The function value of the optimal point of each function $f(x_{opt})$ is zero. The initial regions are set to $[1,5]^{20}$ for the Sphere, Ellipsoid, k-tablet and Rastrigin functions, $[-2,2]^{20}$ for the Rosenbrock-Star and Rosenbrock-Chain functions, $[1,30]^{20}$ for the Ackley function, $[1,15]^{20}$ for the Bohachevsky function and $[1,100]^{20}$ for the Schaffer function.

We made preliminary experiments to determine the population size and the number of offspring per crossover for the combination of each algorithm and each benchmark problem. They were determined so that the average number of evaluations becomes the smallest under the constraint that the algorithm succeeded in finding the optimum on the benchmark problem in all the ten trials. We use the average number of evaluations as a performance index.

Table 2 shows the experimental result. The proposed RCGA succeeded in finding the optimal points faster than AREX/JGG in all the benchmark functions. This result suggests that the proposed RCGA is more effective than AREX/JGG.

Table 1. : Benchmark functions.

Function	Definition
f_1 : Sphere	$f_1 = \sum_{i=1}^{n} x_i^2$
f_2 : Elliposoid	$f_2 = \sum_{i=1}^{n} (1000^{i-1/n-1} x_i)^2$
f_3 : K_tablet	$f_3 = \sum_{i=1}^{n} x_i^2 + \sum_{i=k+1}^{n} (100x_i)^2$
f_4 : Rosenbrock_Star	$f_4 = \sum_{i=1}^{n} 100(x_i^2 - x_1)^2 + (x_i - 1)^2$
f_5 : Rosenbrock_Chain	$f_5 = \sum_{i=1}^{n} 100(x_i^2 - x_{i+1})^2 + (x_i - 1)^2$
f_6 : Ackley	$f_6 = 20 - 20exp(-0.2\sqrt{1/n \sum_{i=1}^{n} x_i^2})$ $+e - exp(1/n \sum_{i=1}^{n} \cos(2\pi x_i))$
f_7 : Bohachevsky	$f_7 = \sum_{i=1}^{n-1} (x_i^2 + 2x_{i+1}^2$ $-0.3\cos(3\pi x_i) - 0.4\cos(4\pi x_{i+1}) + 0.7)$
f_8 : Schaffer	$f_8 = \sum_{i=1}^{n-1} (x_i^2 + x_{i+1}^2)^{0.25}$ $\times(\sin^2(50(x_i^2 + x_{i+1}^2)^{0.1}) + 1.0)]$
f_9 : Rastrigin	$f_9 = 10n + \sum_{i=1}^{n} x_i^2 - 10\cos(2\pi x_i)$

Table 2. : The average numbers of evaluations of AREX/JGG and the proposed RCGA. The numbers in the parentheses are the population size and the number of offspring per crossover, respectively, where n (=20) is the dimension of the problem. Ratio is the number of evaluations of the proposed RCGA divided by that of AREX/JGG multiplied by 100. If the ratio is smaller than 100%, the proposed RCGA succeeded in finding the optimum with fewer evaluations than AREX/JGG.

f	AREX/JGG	Proposed RCGA	Ratio
f_1	2.25e4 ($5n$, $4n$)	**1.34e4 ($5n$, $3n$)**	60%
f_2	3.39e4 ($6n$, $3n$)	**1.68e4 ($6n$, $3n$)**	50%
f_3	5.12e4 ($6n$, $3n$)	**2.72e4 ($6n$, $4n$)**	53%
f_4	5.96e4 ($9n$, $3n$)	**3.21e4 ($6n$, $3n$)**	54%
f_5	1.06e5 ($5n$, $4n$)	**6.71e4 ($6n$, $4n$)**	63%
f_6	4.21e4 ($6n$, $3n$)	**2.48e4 ($6n$, $4n$)**	59%
f_7	4.32e4 ($10n$, $4n$)	**1.76e4 ($8n$, $3n$)**	41%
f_8	2.08e5 ($16n$, $3n$)	**9.42e4 ($14n$, $6n$)**	45%
f_9	1.83e5 ($25n$, $4n$)	**1.49e5 ($50n$, $8n$)**	81%

4. Conclusions

In this paper, we proposed a new RCGA in order to overcome the problems of AREX/JGG. The proposed RCGA consists of the mating selection that chooses the n+1 worst individuals in the population as parents, the crossover that employs a weighted mean of the population as the center of the crossover and the survival selection that replaces the n+1 worst parents in the population with the n+1 best offspring. We confirmed that the proposed RCGA outperformed AREX/JGG on various benchmark functions through numerical experiments.

We have a plan to evaluate the performance of the proposed RCGA in higher-dimensional problems and, if necessary, we have to improve the proposed RCGA. We also will apply the proposed RCGA to difficult real-world applications such as the lens design problem in order to investigate the effectiveness of the proposed RCGA.

References

[1] Herrera, F., Lozano, M. and Sanchez, A.M. : A taxonomy for the crossover operator for real-coded genetic algorithms: An experimental study, International Journal of Intelligent Systems, 18:309–338 (2003).

[2] Sinha, A., Srinivasan, A. and Deb, K. : A population-based, parent centric procedure for constrained real-parameter optimization. Proc. 2006 IEEE Congress on Evolutionary Computation (CEC2006), pp. 239–245 (2006).

[3] Akimoto, Y., Sakuma, J., Ono, I. and Kobayashi, S.: Adaptation of expansion rate for real-coded crossovers, Proc. Genetic and Evolutionary Computation Conference 2009 (GECCO2009), pp.739-746 (2009).

[4] Akimoto, Y., Nagata, Y., Sakuma, J., Ono, I. and Kobayashi, S. : Proposal and evaluation of adaptive real-coded crossover AREX, Transactions of the Japanese Society for Artificial Intelligence, Vol. 24, No. 6, pp. 446-458 (2009) (in Japanese).

© ISAROB 2013

The Eighteenth International Symposium on Artificial Life and Robotics 2013 (AROB 18th '13),
Daejeon Convention Center, Daejeon, Korea, January 30-February 1, 2013

Diesel Engine Fuel Injection Control with DDVC Hydraulic System

Xing Jin[1], Feifei Zhang[1], Masanori Ito[1],Kyoko Narukawa[1]

[1]Tokyo University of Marine Science and Technology Japan
(Tel: 81-03-5463-0400, Fax: 81-97-594-0181)

[1]salanghieyou@yahoo.co.jp

Abstract: Internal-combustion engine has been used on ship, automobile and so on. However increase of internal-co mbustion engine caused to the environmental and energy problem in those days. Then we must improve the perform ance of it from the level of combustion. From this point of view, we put the target on a diesel engine which is us ually used on ship as the main propulsion engine. Its performance is depending on a fuel injection system and it is well known that controlling injection optimally reduce the fuel consumption and amount of toxic substance. In this study, we proposed a new fuel injection system using Direct Drive Volume Control (DDVC) hydraulic system, and d eveloped basic control method for fuel injection. The new fuel injection system is constructed with conventional inje ction valve and new fuel pump using DDVC hydraulic system. We have already established the method to control f uel injection timing, duration, pressure, rate and pattern.

Keywords: Environmental and energy problem, Fuel injection system, DDVC hydraulic system.

1 INTRODUCTION

In these days, electric fuel injection system is used to improve the combustion efficiency and reduce amount of toxic substance for diesel engine. Common rail type electric fuel injection system is one of the most popular for it. It is keeping high-pressure oil in common duct and inject it into the cylinder with the on-off of electro-magnetic valve equipped on the fuel injection valve. However, it is expensive because it should use high cost material for high pressure common duct and specialized injection valve.

Another electric fuel injection system is also expensive with use of complex pressurizing system and specialized injection valve. Taking into account those situations, we proposed new electric fuel injection system which is constructed with DDVC hydraulic System and using conventional (mechanical) fuel injection valve.

In the conventional electric fuel injection system, effective fuel injection method for improving combustion efficiency and reduction of toxic substance is established.

Here we confirmed that the new injection system is available to realize effective fuel injection with control of DDVC hydraulic system.

2 DDVC TYPE FUEL INJECTION SYSTEM

DDVC type fuel injection system is including DDVC actuator, booster unit and fuel injection valve. System configuration is shown in **Fig. 1.**

DDVC actuator is constructed with AC servo-motor driven reversible gear pump and hydraulic cylinder called low-pressure cylinder. The motion of cylinder piston is controlled with revolution of servo-motor and we can get the high pressure which is proportional to the ratio of cross-section of both cylinders when it pushes the piston of spring back type booster cylinder.

This high pressure fuel is send to injection valve and injection will start when the pressure overcome than spring force in the valve. The fuel injection valve is cheaper and low failure rate because it is not special type.

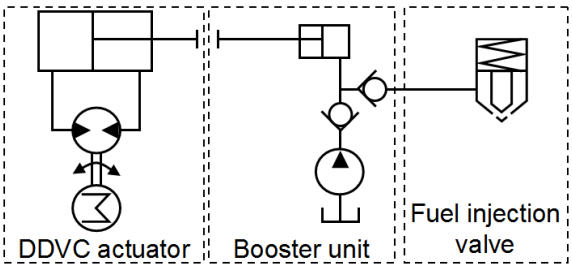

Fig. 1. DDVC type fuel injection system

3 MATHEMATICAL MODEL OF DDVC FUE L INJECTION SYSTEM

3.1 Mathematical model of the DDVC actuator

As shown in **Fig.1 .**, discharged oil from gear pump is supplied to cylinder and pushes piston, and the oil in another side of cylinder is lead to pump suction.

When the piston can move freely, the motion of piston is written with following equation.

$$m_1\ddot{x}_1 + c\dot{x}_1 + kx_1 = p_1 A_1 \tag{1}$$

© ISAROB 2013

Here, m_1 is the mass of piston, c is friction coefficient, k is spring constant, p_1 is the pressure of head piston A_1 is cross sectional space cylinder, and x_1 is displacement of piston.

When the piston is attached to the booster, both piston moves together and kinematic equation become as follows.

$$(m_1 + m_3)\ddot{x}_1 + c\dot{x}_1 + kx_1 = p_1 A_1 - p_2 A_2 - p_3 A_3 \quad (2)$$

Here, m_3 is the mass of booster piston, p_2 is the pressure of booster piston, p_3 is the pressure of booster, A_2 is cross sectional of booster piston, A_3 is cross sectional of booster.

3.2 Mathematical model of booster

If the fuel injection does not start, change rate of high-pressure pipe oil pressure shown in the Eq.(3)

$$\dot{p}_3 = (k/(V_4 - A_3 x_3))A_3 \dot{x}_3 \quad (3)$$

Here, V_4 is the volume of booster unit, x_3 is displacement of booster piston.

$$V_4 - A_3 x_3 \approx V_3 \quad (4)$$

After two pistons are contacting,

$$x_3 = x_1 \quad (5)$$

Therefore, change rate of oil pressure in booster is Eq.(6)

$$\dot{p}_3 = (k/V_3)A_3 \dot{x}_1 \quad (6)$$

With integrating Eq.(6), we can get oil pressure in the booster

$$p_3 = (k/V_3)A_3 x_1 + p_{31} \quad (7)$$

After injection started, oil pressure in the booster is written with following equation.

$$\dot{p}_3 = (k/V_3)\left(A_3 \dot{x}_1 - a\sqrt{2p_3/\rho}\right) \quad (8)$$

And oil pressure in the booster becomes as follows.

$$p_3 = k/V_3 \left(A_3 x_1 - \int Q_i dt\right) + p_{32} \quad (9)$$

When fuel injection is continuing, the change rate of oil pressure will become as Eq.(10)

$$\dot{p}_3 = (k/V_3)\left(-a\sqrt{2p_3/\rho}\right) \quad (10)$$

Then, the oil pressure in the booster is Eq.(11)

$$p_3 = -k/V_3 \int a\sqrt{2p_3/\rho}\, dt + p_{33} \quad (11)$$

3.3 Mathematical model of a fuel injection valve

Fuel injection valve is very important part in fuel injection system. When fuel pressure overcome to spring force, the needle is lifted up and injection starts. Here we make a mathematical model for injection valve as the relation between fuel pressure, motion of needle and flow rate of injection. Unfortunately the flow rate should be estimate because it is difficult to measure. The model of fuel injection valve are illustrated in **Fig. 2.**

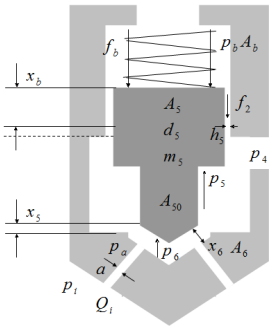

Fig. 2. Fuel injection valve

Kinematic equation of needle valve is shown in Eq.(12)

$$m_5 \ddot{x}_5 = p_6(A_5 - A_{50}) + p_6 A_{50} - p_b A_b + f_b + f_2 \quad (12)$$

Here, f_b , f_2 shows spring force, damping force respectively. Those are shown as following equations.

$$f_b = -k_b x_5 \quad (13)$$
$$f_2 = -\mu\pi d_5 (x_b + x_5)\dot{x}_5 / h_5 \quad (14)$$

We assume there exist no time delay on a pressure of fuel. Then,the injection valve has four (4) injection nozzles.

$$p_3 + \frac{\rho}{2}\left(\frac{Q}{A_6}\right)^2 = 4\left(p_a + \frac{\rho}{2}\left(\frac{Q}{a}\right)^2\right) \quad (15)$$

In accordance with it,

$$Q = \frac{a}{4}\frac{1}{\sqrt{1-(a/4A_6)^2}}\sqrt{\frac{2(p_3 - 4p_a)}{\rho}} \quad (16)$$

When the fuel is injected to air, the flow rate will be Eq.(18)

$$Q_i = \frac{a}{4}\frac{1}{\sqrt{1-(a/4A_4)^2}}\sqrt{\frac{2p_3}{\rho}} \tag{17}$$

As

$$a/4A_4 \approx 0 \ , \tag{18}$$

The flow rate becomes as follows finally.

$$Q_i = \frac{a}{2}\sqrt{\frac{p_3}{\rho}} \tag{19}$$

4. INJECTION CONTROL

4.1 Fuel pressure at booster

Oil pressure at the outlet of booster is determined with displacement and speed of piston, and injection flow rate at fuel injection valve. Since fuel injection valve is mechanical self balance type, we control fuel pressure not at injection valve but booster with displacement and speed of high-pressure cylinder piston.

In DDVC hydraulic actuator, input voltage to the driver of servo-motor has proportional characteristics to the piston speed of low-pressure cylinder. Then we use input voltage for basic estimation of piston speed and add the difference of actual position and estimated position to correct the value. The result of estimation is shown in **Fig. 3.**

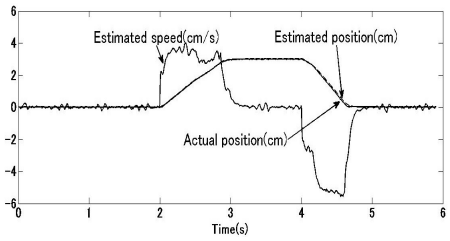

Fig. 3. Piston speed of low-pressure cylinder

In booster unit, volume change of high pressure line with the displacement of high-pressure cylinder is much smaller to total volume of high-pressure pipe.

With this reason, we ignored the influence of high-pressure cylinder piston displacement to the pressure in our experiment and to examine the relationship of low-pressure cylinder piston speed and oil pressure of high-pressure pipe, .we checked the fuel pressure when the input voltage is-2v,-4v,-8v.

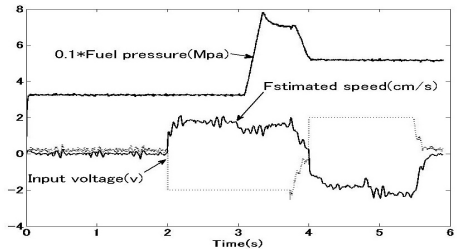

Fig. 4. Results at -2V of input voltage

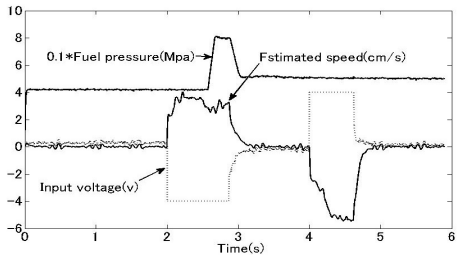

Fig. 5. Results at -4V of input voltage

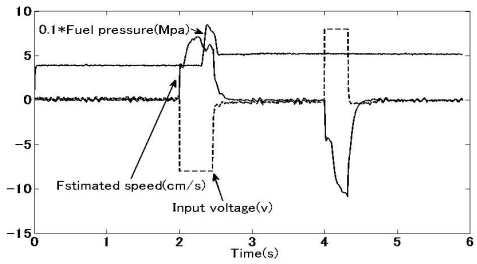

Fig. 6. Results at -8V of input voltage

Those results show that the fuel pressure is rising with the piston speed from contact of both pistons to start of injection. After fuel injection start, the fuel pressure decrease because initial flow rate of injection is so large that piston speed cannot follow to it. However piston speed is rising and it can follow to injection and fuel pressure increase again.

This shows that fuel pressure can be controlled with the speed of low-pressure cylinder.

Control method and control results of fuel-pressure is shown in **Fig. 7.** and **Fig. 8.**

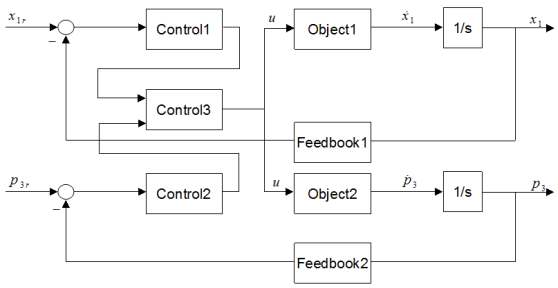

Fig. 7. Control method of fuel pressure

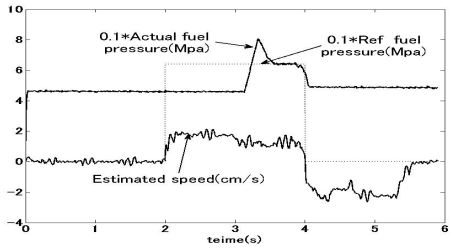

Fig. 8. Control results of fuel pressure

4.2 Fuel injection flow and rate

If initial fuel pressure is same as the pressure of after injection, we can think that the quantity of injected fuel is equal to compressed volume. Considering this, we examined the relationship between injected quantity, piston displacement of low-pressure cylinder and fuel pressure. It is shown in **Fig. 9.**

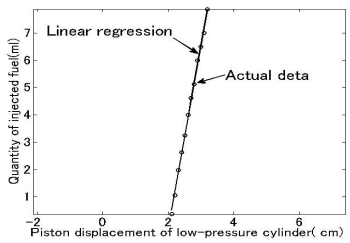

Fig. 9. Relationship between quantity of injected fuel and piston displacement of low-pressure cylinder

Actual flow of fuel injection and estimated flow, estimated rate are shown in **Fig. 10.**

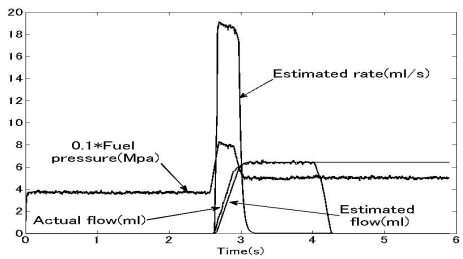

Fig. 10. Actual flow and estimated flow, rate of fuel injection

This result shows that for precise control of fuel injection, piston displacement of low-pressure cylinder should be controlled more precisely.

When conventional P-control is applied for the piston displacement control, offset will remain and when we add I-control for it, it becomes cause to overshoot .Here, we propose a new method to protect offset and overshoot effectively. This method is shown in **Fig. 11.**Control result for piston displacement of Low-pressure cylinder and fuel injection flow with this method is shown in **Fig. 12.** & **Fig. 13.**

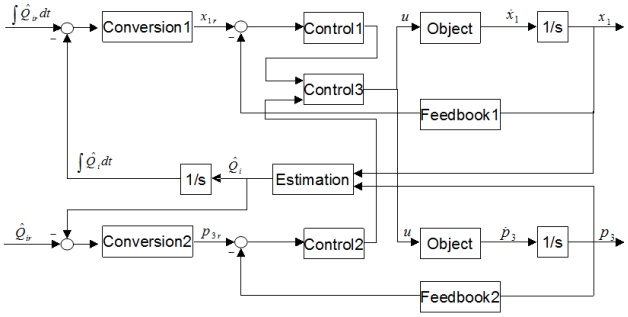

Fig. 11. Control method of injection flow and rate

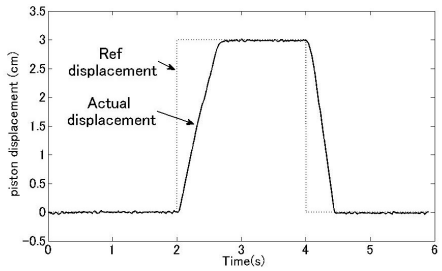

Fig. 12. Control result of piston displacement

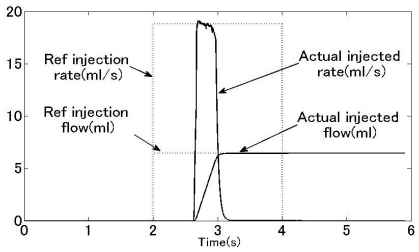

Fig. 13. Control result of injection flow and rate

5 CONCLUSION

In this research, we have constructed the control method of diesel engine fuel injection with DDVC hydraulic system. We can control fuel pressure with the motion of piston in low pressure cylinder, and injected fuel quantity, injection timing or injection rate with using simulation.

Now we are expanding it to total system including the combustion in cylinder and confirming the reduction of fuel consumption, particle emission, and toxic substance such as oxide frugal gas with control to the new fuel injection system.

REFERENCES

[1] Feifei Zhang et. al, New Concept of Diesel Engine Fuel Injection System with DDVC Hydraulic Actuator, Journal of JIME Vol.44,No.1,2009,(pp.127-132)

[2] Naohiro Yamaguchi et. al, A Study on application of DDVC to an electronic fuel injection device for marine engine, of Proc. of 11th MOVIC of JASME(2009),(pp.456-460)

© ISAROB 2013

The Eighteenth International Symposium on Artificial Life and Robotics 2013 (AROB 18th '13),
Daejeon Convention Center, Daejeon, Korea, January 30-February 1, 2013

The Complex Network Study of Money and CO2 Emission Flows between Industrial Sectors in Asian Countries using Input-Output Table

X. Gao[2]; T. Fujiwara[2]; K. Yoshizawa[3]; S. Miyake[3]; Z. Zheng[2]; N. Sakurai[2]; K. Yamasaki[1];

1. (Tokyo University of Information Sciences): department of environmental information, faculty of informatics, Chiba, Japan
2. (Tokyo University of Information Sciences): department of environmental information, faculty of informatics, Chiba, Japan
3. (Tokyo University of Information Sciences): department of business information, faculty of informatics, Chiba, Japan
(Tel/Fax: 81-43-236-4653)

[1] yamasaki@rsch.tuis.ac.jp

Abstract: In 2011, earthquakes in Japan and flood in Thailand revealed the serious risks that local break downs of Motor vehicle sector and Electronic computing sector cause the cascade breakdown of world economy. To estimate such risks, it seems that the connections between international industrial sectors are important and recently developed complex networks method is suitable for this study. We use the data of the Input-Output table of Asian countries and USA made by JETRO in 2000[1]. We regard the table as network matrix and make various directed weighted networks. In these networks, the nodes correspond to each industry sector in a country and the weight of the link corresponds to the amount of the money which uses the product of an industry sector as material to produce the product of another industry sector. We think cascade failure of the industry sector has deep connection with not only quantitative weights of the links but also network structure. So we calculate betweenness centrality of nodes using Dijkstra algorithm [2,3,4], which describes basically the number of paths through the node. We found the betweenness centrality is high in Motor vehicle sector, Electronic computing sector and Semiconductors and integrated circuits sector. Next we use CO2 emission data made by IEA [5] and make environmental extension of Input-Output table. Our results warn that CO2 emission of developing countries is also important problem..

Keywords: Complex Networks, CO2 Emission, Asian Countries, Input-Output Table.

1 INTRODUCTION

The connections among various economic factors or economic units have become complicated more and more according to developing economy and society in each country. We have to pay attention to the risk that a small negative effect is amplified by these complicated connections. In other words, economic factors or economic units with various connections make complex networks and the risk of big economic failure lies behind the structure of these networks. In wide variety of research fields including economy, the complex networks[6,7,8] have been studied earnestly in these 10 years. A lot of analytical methods have been developed and applied to various data. They have contributed to solve the various problems in real world.

Industry-industry connections are described by Input-Output table[9], which has been widely applied in the economic analysis for the past 50 years. In many countries, governments and local states or prefectures make Input-Output tables for analysis of domestic economy in every year. And the environmental extension of the Input-Output table has been used energetically in various environmental problems in these 20 years[10]. This analytic method is one of the most systematic and practical tool for environmental problems. Though Input-Output table includes lots of information, it does not seem that traditional analysis is enough to extract such information and show us understandable way. Connections between nodes are main interest in complex networks study, but only a few complex networks studies have been done using Input-Output table[12-19]. Because Input-Output table corresponds to the complete network with directed weighted links including self loops, the analysis of such networks is not so simple as networks which mainly have been studied in the past. We think the recent development of the various analytical methods enables us to extract new results from different point of view.

2 DATA

We use "Input-Output table for East Asia" in 2000. They are made by JETRO (Japan External Trade Organization) by combining 10 countries tables, 9 Asian countries (China, Taiwan, Indonesia, Japan, Korea, Malaysia, Philippines, Singapore, Thailand) and USA, and include 76 industrial sectors per a country. One of the aims of this paper is to track CO2 emission from the production of an industry sector in a country until the final consumption of the products of other industry sector in other country. IEA(International Energy Agency) issues the data about CO2 emission of each industry sector in each country except Taiwan, so we remove Taiwan's data from the table and analyze 9 countries data. So the inter-industry sectors part of the table is a square matrix of the size of 684(2000). The classification of industry sectors is different between "Input-Output table for East Asia" and "IEA CO2 emission data". So we redistributed CO2

© ISAROB 2013

emission data to sectors in Input-Output table after referring to these papers[].

3 METHOD

3.1 Network Matrix

In this paper, we study the connections between the production in an industry sector in a country and the final consumption of the products in an industry sector in a country. To get network matrix for this study, we start from the traditional induced analysis. In case of Non-Competitive Import Type Input-Output table, induced production vector Y is described by

$$Y = [\mathbf{I} - \mathbf{A}]^{-1} C \qquad (1)$$

Here, $[\mathbf{I} - \mathbf{A}]^{-1}$ is the Leontief inverse and C is final consumption vector. Induced CO2 emission EI is described by,

$$EI = \boldsymbol{\lambda}[\mathbf{I} - \mathbf{A}]^{-1} C \qquad (2)$$

Here, $\boldsymbol{\lambda}$ is the diagonal matrix whose diagonal elements are direct CO2 emission in each industry sector.

To get the information about which sector's final consumption induces which sector's production, we use diagonal final consumption matrix $\mathbf{C}$ whose diagonal elements are the elements of final consumption vector C.

$$\mathbf{Y} = [\mathbf{I} - \mathbf{A}]^{-1} \mathbf{C} \qquad (3)$$

$$\mathbf{EI} = \boldsymbol{\lambda}[\mathbf{I} - \mathbf{A}]^{-1} \mathbf{C} \qquad (4)$$

The induced production matrix $\mathbf{Y}$ represents which sector's final consumption induces which sector's production and the induced CO2 emission matrix $\mathbf{EI}$ represents which sector's final consumption induces which sector's CO2 emission. We consider the matrix $\mathbf{Y}$ and $\mathbf{EI}$ as network matrixes. So the network created by network matrix $\mathbf{Y}$ is constructed by nodes which represent each industry section and constructed by links which represent product flows from productions to consumptions. And the network created by network matrix $\mathbf{EI}$ is constructed by nodes which represent each industry section and constructed by links which represent CO2 emission flows with products. In previous paper[20], we analyzed networks corresponding to these network matrixes $\mathbf{Y}$ and $\mathbf{EI}$. These results are strongly dominated by big countries (Japan, USA and China) and big industry sections, so we can not see the structure well. Sometimes small industry becomes a key of the economic failure.

In this paper, we analyze production ratio not production. That is, we analyze matrix $\mathbf{L}$ and $\mathbf{EL}$ which are described by

$$\mathbf{L} = [\mathbf{I} - \mathbf{A}]^{-1} \qquad (5)$$

$$\mathbf{EL} = \boldsymbol{\lambda}[\mathbf{I} - \mathbf{A}]^{-1} \qquad (6)$$

3.2. Betweenness centrality

Considering a cascade failure of the economy resulting from a breakdown of small industry, we think the neck of the paths in the network relates to the cascade. Betweenness centrality describes the importance of the node under the meaning of path going through it. The definition of Betweenness centrality of node v in simple (undirected unweighted) network is,

$$c_{\mathrm{B}}(v) = \sum_{s \neq v, t \neq v} \frac{\sigma_{s,t}(v)}{\sigma_{s,t}} \qquad (7)$$

Here, $\sigma_{s,t}(v)$ is the number of shortest paths from node s to node t going through node v and $\sigma_{s,t}$ is the number of shortest paths from node s to node t. The extended definition of Betweenness centrality for directed weighted network is counting shortest cost paths with link direction instead of shortest paths. In our network, the costs are the inverses of the network matrix elements. This centrality can be calculated using Dijkstra algorithm for shortest cost paths.

4 RESULT

Table 1 shows top ten sectors (nodes) of total production (total weight of links) in production ratio base network $\mathbf{L}$ In total outward weight, USA and Japan "Other services sector" and "Wholesale and retail trade sector" have heavy weight. In total inward weight, industry sectors do not have so much different weights. They have the same weight on the average.

Table 2 shows top ten sectors (nodes) of betweenness centrality in production ratio base network $\mathbf{L}$. Motor vehicles sector in Japan has high betweenness centrality. This means if breakdown of this sector happens, a lot of paths of the products are destroyed and affects world economy. And it is not proportion to its amount of money. This is really the fact that happened after earthquake in local area of Japan in 2011. Electronic computing equipment sector in Singapore, Semiconductors sector in Malaysia and Philippines have high betweenness centrality either. They are not Thailand but we can guess the situations are similar in Thailand.

Table 1. top ten sectors (nodes) of total production ratio (total weight of links)

	Inward Weight (production ratio base network **L**)		
	Total weight	Industry section	
1	3.18	Japan	Cement and cement products
2	2.67	Korea	Cement and cement products
3	2.10	Japan	Non-metallic ore and quarrying
4	2.09	Japan	Motor cycles
5	2.04	China	Electronic products
6	1.97	Korea	Slaughtering, meat products
7	1.91	USA	Slaughtering, meat products
8	1.90	China	Lighting fixtures
9	1.89	China	Wooden furniture
10	1.87	China	Metal products

	Outward Weight (production ratio base network **L**)		
	Total weight	Industry section	
1	15.23	USA	Other services
2	12.75	Japan	Wholesale and retail trade
3	11.80	Japan	Other services
4	9.58	USA	Wholesale and retail trade
5	9.56	Japan	Iron and steel
6	8.71	Japan	Basic industrial chemicals
7	8.59	Singapore	Wholesale and retail trade
8	8.25	China	Electricity and gas
9	7.44	China	Wholesale and retail trade
10	7.39	Thailand	Wholesale and retail trade

Table 1 shows top ten sectors (nodes) of total production (total weight of links) in production ratio base network **L** In total outward weight, USA and Japan "Other services sector" and "Wholesale and retail trade sector" have heavy weight.

Table 2. top ten sectors (nodes) of betweenness centrality

	Betweenness (Money base network **L**)		
	betweenness	*Industry section*	
1	48945	**Japan**	**Motor vehicles**
2	38390	Singapore	Wholesale and retail trade
3	37084	USA	Transportation
4	36047	**Singapore**	**Electronic computing equi.**
5	36036	**Malaysia**	**Semiconductors**
6	35318	China	Wholesale and retail trade
7	33162	Japan	Electricity and gas
8	31357	**Philippines**	**Semiconductor**
9	31312	Thailand	Wholesale and retail trade
10	29815	China	Other services

Table 2 shows top ten sectors (nodes) of betweenness centrality in production ratio base network **L** .motor vehicles sector in japan has high betweenness centrality.

Table 3. top ten sectors (nodes) of total production (total weight of links)

	Inward Weight (CO2 emission base network **EL**)		
	Total weight	Industry section	
1	1.21	China	Water supply
2	1.14	China	Unclassified
3	1.05	China	Metal products
4	1.04	China	Iron ore
5	1.04	China	Cement and cement products
6	0.93	China	Chemical fertilizers and pesticides
7	0.93	China	Basic industrial chemicals
8	0.93	China	Non-ferrous metal
9	0.92	China	Other metallic ore
10	0.84	China	Other transport equipment

	Outward Weight (CO2 emission base network **EL**)		
	Total weight	Industry section	
1	25.66	China	Electricity and gas
2	8.29	Malaysia	Electricity and gas
3	7.91	Thailand	Electricity and gas
4	7.03	Indonesia	Electricity and gas
5	6.91	Korea	Electricity and gas
6	6.10	Philippines	Electricity and gas
7	5.86	USA	Electricity and gas
8	5.24	China	Iron and steel
9	4.70	Singapore	Electricity and gas
10	4.24	Japan	Electricity and gas

Table 3 shows top ten sectors (nodes) of total production (total weight of links) in CO2 emission base network **EL** . In total outward weight, "Electricity and gas sector" in rather developing countries are dominant.In total inward weight, all top ten sectors are China.

Table 4. top ten sectors (nodes) of betweenness centrality

	Betweenness (**CO2** emission base network **EL**)		
	betweenness	*Industry section*	
1	85563	China	Iron and steel
2	84824	China	Electricity and gas
3	82406	Malaysia	Crude petroleum & natural gas
4	69520	Malaysia	Electricity and gas
5	59840	Singapore	Refined petroleum
6	51189	Japan	Electricity and gas
7	50831	Malaysia	Precision machines
8	49816	Korea	Iron and steel
9	44718	Malaysia	Transportation
10	41394	Japan	Iron and steel

Table 4 shows top ten sectors (nodes) of betweenness centrality in CO2 emission base network **EL** "Iron and steel" and "Refined petroleum" appears. They can be imported and exported between countries, and consequently carry heavy CO2 emission.

© ISAROB 2013

Table 3 shows top ten sectors (nodes) of total production (total weight of links) in CO2 emission base network **EL**. In total outward weight, "Electricity and gas sector" in rather developing countries are dominant.In total inward weight, all top ten sectors are China. It can be thought that the results are caused from the inefficient industrial machines or system in the case of ratio.

Table 4 shows top ten sectors (nodes) of betweenness centrality in CO2 emission base network **EL** "Iron and steel" and "Refined petroleum" appears. They can be imported and exported between countries, and consequently carry heavy CO2 emission.

Figure 1 show the networks constructed by network matrix **L**. To visualize, only 1000 links are left, after cutting small links whose weights are under minimum weight. The directions of links show product flow (counter direction of money flow). "Motor vehicles sector" and "Electronic computing equipment sector" are in the middle part between countries. Coincide These results coincide with the results of betweenness centrality. The nodes connecting different country's industry sectors are neck of the paths and have hight betweenness centralities.These are considered also necks of the world economy.

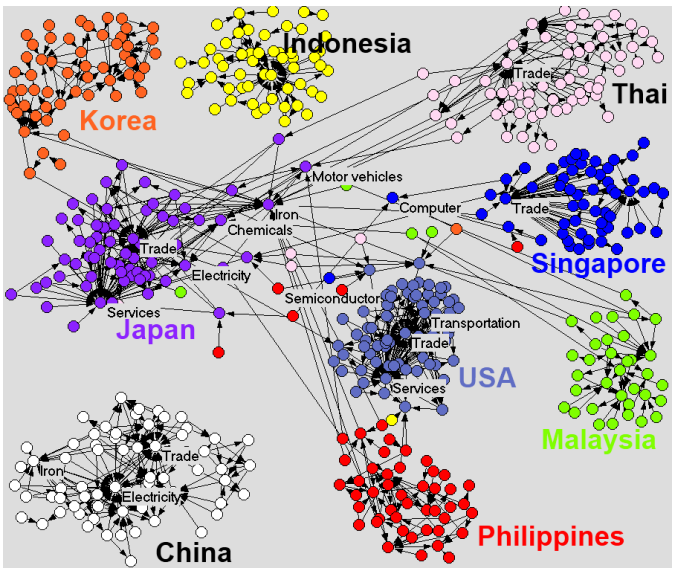

Figure 1 Production ratio base network **L**

5 CONCLUSION

We show the possibility of the cascade failure of the world economy caused by the breakdown of some local industry sectors. The complex networks analysis of the data is consistent with the facts in local breakdowns of Motor vehicle sector in Japan and of Electronic computing sector in Thailand. We have to find the risks of the cascade failure of the world economy from various directions. And also our results warn that CO2 emission of developing countries is also important problem..

We think the complex networks analysis gives us the really useful tools and this paper will be a hint of the research from this direction.

ACKNOWLEDGEMENTS

We thank the Research project for a sustainable development of economic and social structure dependent on the environment of the eastern coast of Asia and Grants-in-Aid for Scientific Research (KAK-ENHI) for financial support. We also thank members of these research projects for various discussions.

REFERENCES

[1] JETRO (Japan External Trade Organization) http://www.ide.go.jp/Japanese/Publish/Books/Tokei/material.html

[2] A. Barrat, M. Barthélemy, R. Pastor-Satorras, and A. Vespignani, "The architecture of complex weighted networks", *Proc. Natl. Acad. Sci.*, Vol. 101, No. 11,2004, pp.3747-3752

[3] U. Brandes, "A faster algorithm for betweenness centrality", *The Journal of Mathematical Sociology*, Vol.25, No.2, 2001, pp.163-177

[4] E. W. Dijkstra, "A note on two problems in connexion with graphs", *Numerische Mathematik* , Vol.1, 1959, pp.269-271

[5] IEA (International Energy Agency) http://data.iea.org/ieastore/statslisting.asp

[6] D. J.Watts, and S. H. Strogatz, "Collective dynamics of 'small world' networks", *Nature*, Vol. 393, 1998, pp.440-442

[7] A.-L.Barab´asi and R. Albert, "Emergence of scaling in random networks", *Science*, Vol. 286, 1999, pp.509-512

[8] S. H. Strogatz, "Exploring complex networks", *Nature*, Vol. 410, 2001, pp.268-276

[9] W.Leontief, "Input-Output Economics", *Oxford University Press*, 1966

[10] S. Joshi, "Product Environmental Life-Cycle Assessment Using Input-Output Techniques", *Journal of Industrial Ecology*, Vol.3, No.2-3,1999, pp. 95-120

[11] P. Changa,b, H. Shiha," Comparing patterns of intersectoral innovation diffusion in Taiwan and China: A network analysis", *Technovation*, Vol. 25, 2005, pp.155-169

[12] A. M. Prieto, J. L. Zofi´o, "Network DEA efficiency in input–output models:With an application to OECD countries", *European Journal of Operational Research* , Vol.178, 2007,pp. 292-304

[13] B. Meng, S.Inomata, "Production Networks and Spatial Economic Interdependence: An International Input-Output Analysis of the Asia-Pacific Region", *IDE Discussion Paper Series*, No.185, 2009

© ISAROB 2013

[14] F. Ai-li, G. Qi-sheng, Z. Si-ying," Clustering and Correlation Analysis of the Industry Networks", S*ystems Engineering* , Vol.29, No.6,2009, pp. 178–183

[15] Wang H. et al, Multi-Weighted Monetary Transaction Network, Advances in Complex Systems, Vol. 14, No. 5, 2011, pp.691–710

[16] K.Yoshizawa, T. Fujiwara, Z. Zheng , R. Shiba, N. Sakurai, K. Yamasaki, "Network Analysis of Japanese Ecological Footprint based on Input-Output Table for the 47 Prefectures in Japan", *Proceedings of FOOT PRINT FORUN 2010*

[17] T.Fujiwara , K. Yoshizawa, N. Sakurai, K. Yamasaki , "The Analysis of Ecological Footprint using Multi-regional Input Output Table for 47 Prefectures in Japan", *Proceedings of 38th Annual Meeting of Environmental Systems Research*, 2010, pp.239-243. (in Japanese)

[18] K.Yamasaki, T. Fujiwara, N. Sakurai, K. Yoshizawa, Z. Zheng , "Effect of Hot Summer against Environment which was induced by Extra Economical Demand via Japanese Ecological Footprint", *Proceedings of 16th International Symposium on Artificial Life and Robotics*,2011

[19] X.Gao, T. Fujiwara, N. Sakurai, K. Yoshizawa, S. Miyake, Z. Zheng, K. Yamasaki ,"Network Analysis of Ecologocal Footprint & CO2 Emission based on Input-Output Table for East Asia", *Proceedings of 17th International Symposium on Artificial Life and Robotics*,2012

[20] K.Yamasaki, T.Fujiwara, K.Yoshizawa, S.Miyake, Zeyu Zheng, Xiang Gao, N.Sakurai, "The Complex Network Study of Money and CO2 Emission Flows between Industrial Sectors in Asian Countries using Input-Output Table", *Proceedings of International Conference on Business Management & Information System*, 2012, pp.213-219

© ISAROB 2013

The Eighteenth International Symposium on Artificial Life and Robotics 2013 (AROB 18th '13),
Daejeon Convention Center, Daejeon, Korea, January 30-February 1, 2013

On a serendipity oriented recommender system based on folksonomy

Hisaki Yamaba[1], Michihito Tanoue[1], Kayoko Takatuka[1], Naonobu Okazaki[1] and Sigeyuki Tomita[1]

[1] University of Miyazaki, Miyazaki, Miyazaki 889-2192, Japan
(Tel: 81-985-58-7425, Fax: 81-985-58-7425)
(yamaba@cs.miyazaki-u.ac.jp)

Abstract: This paper proposes a recommendation method that focuses on not only predictive accuracy but also serendipity. On many of the conventional recommendation methods, each item is categorized according to their attributes (a genre, an authors, etc.) by the recommender in advance, and recommendation is performed using the categorization. In this study, impressions of user to items are adopted as a feature of the item, and each item is categorized according to the feature. The impressions are prepared by using folksonomy. A recommender system based on the method was developed by java language, and the effectiveness of the proposed method was verified through recommender experiments.

Keywords: recommender system, serendipity, folksonomy

1 INTRODUCTION

In these days, importance of recommender systems which can present useful information to users is increasing because numerous information comes to be broadcasted according to the expansion of the Internet.

A lot of researches have been investigated about recommentation systems; many of them were realized based on the collaborative filtering method or the contents based filtering method [1]. The collaborative filtering method recommends items such that users who have similar tastes with an active user (a user who is given recommendation) like. On the other hand, the content based filtering method recommends items that are similar with items that the active user likes.

Recommender systems based on these conventional approaches focus on the predictive accuracy. However, development of recommender systems that consider measure that go beyond the accuracy of its recommendation is attempted in recent years [1].

This study proposes a method for serendipitous recommendation such that users feel surprised by recommended books. A recommender system was developed by Java language and the validity of the proposed method was confirmed through a series of recommendation experiments.

2 PROPOSED METHOD

2.1 Serendipity oriented recommendation

The purpose of recommender systems is to recommend items that are useful for users. However, items that are suit users' tastes are not useful in case that the users are familiar with the items. This means that recommender systems are required to recommend items that not only suit tastes of users but also are novelty (they are unknown to the users) [1]. In these days, serendipity also comes to be required to recommender systems. The word serendipity is created by Horace Walpole based on the fairy tale titled "Three princes of Sarendip." In general, this word means the ability to find something good or useful while not specifically searching for it. However, in the area of research in recommender systems, this word means that recommended items are unforeseeable, unexpected, or surprising for the user [1] . When a user searches an item that suits to his tastes, the search will be performed around the area that the item is expected. Therefore, it is supposed that the user cannot find such an item that does not locates in the expected area. On the contrary, if the user finds such a book by accident, it will be a serendipitous discovery for the user. In this study, it is assumed that a user feels serendipity when a recommended item suits the taste of the user, and is unknown to him/her, and is not included in the area that the user expected such items locate.

Under many of the conventional recommendation methods, items for recommendation (e.g. books) are categorized according to their attributes (a genre, an authors, etc.) by a recommender in advance. Recommendation is performed using the categorization. For example, books that are classified into mystery novels will be recommended to users who love mystery novels. However, a book that is classified into love stories will not be recommended to such users even if the book has flavor of mystery novels (Fig.1). However, such books might be serendipitous books for the kind of users (Fig.2).

In this study, impressions of users on books are adopted as one of attributes of the books. For example, if users feel a flavor of mystery novels from a book, which is not regarded as a mystery novel but regarded as a love story, the impression will be added to the characteristics of the book. It is expected that such books will be recommended to mystery fans by using impressions of users in the process of recommendation. Serendipity in this study means such ability to

© ISAROB 2013

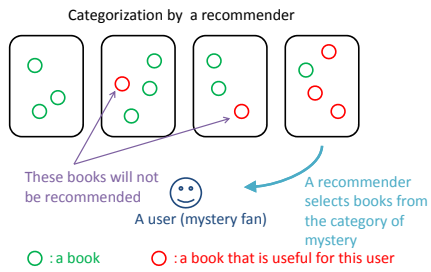

Fig. 1. Conventional recommendation.

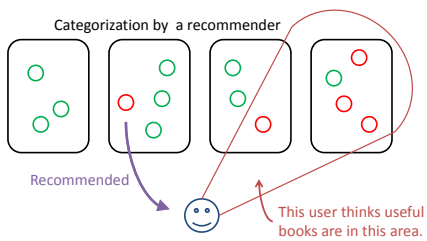

Fig. 2. Serendipity on recommendation.

find out useful books beyond the conventional books classification. In order to realize the books classification mentioned above, folksonomy was adopted.

2.2 Folksonomy

Folksonomy is a bottom up style classification system while conventional classification systems adopt a top down style. Under such conventional systems, items presented to users are classified in advance based on categories defined by service providers. Folksonomy classifies items using tags that are given by users. Tags are keywords that are generated by users following characteristics, impressions and so on of each item. Users are allowed to select any words as tags. And also, users are allowed to give more than two tags to a book. Folksonomy has features shown below:

- The classification reflects impressions or recognition of users.
- It is easy for users to give tags to items because what users have to do is only to input keywords; some special knowledge is not required.
- Classification results are flat, not stratified.

2.3 Introduction of the idea called "concepts"

In cases that classification is performed using tags that are attached to items, problems caused by synonym or polysemy have to be resolved. For example, suppose a tag "blog" is given to an item and a tag "weblog" is attached to another item. Though they have tags that indicate same meanings, the two items are not recognized to have same feature.

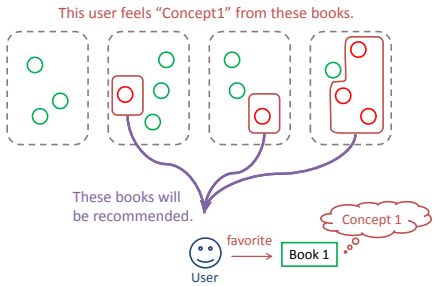

Fig. 3. Basic idea of the proposed method.

In this study, impressions of users themselves are used to classify items. Since an impression that each user feels on a book is not known explicitly, a method to infer such impressions from tags data was developed based on an assumption that tags are selected according to impressions users feel on books. An inferred impression is called a "concept" in this study (Fig.3).

2.4 Proposed method

In this section, books recommendation is used to explain the proposed method (recommendation of books is also used in the experiments mentioned in the next section).

In the proposed method, a concept is expressed in the form of a vector of degrees of relevance from the concept to tags (see 2.4.3). At first, in a case that two tags are given to same books many times, it is assumed that the impression of the users who gave the one of the two tags is same with the impression of users who gave the other tag. Under this assumption, concepts are generated according to the steps as follows. First, "degrees of similarity" between two tags were calculated (see 2.4.1). Next, similar tags are gathered and clusters are generated (see 2.4.2). Such a cluster corresponds to a concept.

Using concepts obtained above, "degrees of relevance" from each book to concepts and "degrees of relevance" from each user to concepts are calculated (see 2.4.4 and 2.4.5). Then, characteristics of each book or each user are represented by a vector of degrees of relevence. The recommender system recommends books that whose characteristics are similar with the tastes of the user.

2.4.1 Degree of similarity between two tags

It is assumed that two tags a and b are used reflecting a same concept in case that tag a and b are both attached to same item in many cases. In this study, such a and b are regarded to be similar. Books are classified into four types

© ISAROB 2013

listed below with tag a and b:

(I) both a and b are attached to the book,

(II) neither a or b is not attached to the book,

(III) only a is attached to the book and b is not.

(IV) only b is attached to the book and a is not.

In case that a sum of percentages of (I) and (II) is large, the similarity between a and b is assumed to be high. On the other hand, the similarity between a and b is assumed to be low when a sum of percentages of (III) and (IV) is large. In this study, "a degree of similarity" between two tags is represented by AEMI (Augmented Expected Mutual Information) [2].

$$AEMI(\ ,\ ) = \frac{\sum_{(A=\alpha,B=\beta),(A=\bar{\alpha},B=\bar{\beta})} MI(A,B)}{\sum_{(A=\bar{\alpha},B=\beta),(A=\alpha,B=\bar{\beta})} MI(A,B)}$$

where is cases that tag a is attached to books and is cases that tag b is attached to books. $^{-}$ represents cases that tag a is not attached to books. $MI(A,B)$ is mutual information that measures co-occurrence of A and B:

$$MI(A,B) = P(A,B)\log\frac{P(A,B)}{P(A)P(B)}$$

where $P(A)$ is the occurrence frequency of A, and $P(A,B)$ is the concurrence frequency of A and B.

2.4.2 Tag clustering

This section explains the process to generate clusters that are composed of similar tags.

1. An empty set $Cset$ is prepared, which is used as the set of created clusters.
2. All tag pairs (Tag_i,Tag_j) ($i \neq j$) are created and sorted in the order of their similarity. Then tag pairs that have higher similarity than the threshold V_t introduced in advance are selected and stored in a list.
3. Tag pairs in the list are processed as follow in the higher order of their similarities:
   (a) A copy of $Cset$ is created ($CopySet$).
   (b) Clusters that include both Tag_i and Tag_j are removed from $CopySet$.
   (c) For each cluster (Cl_k) in $CopySet$,
      - if Tag_i is not included in Cl_K, do step i,
      - if Tag_j is not included in Cl_K, do step ii0.

      i. A degree of similarity between Cl_k and Tag_i is calculated. Similarity of a tag T and a cluster C is the average of similarities between T and all tags included in C. If the value is greater than V_t, Tag_i is added to Cl_k.
      ii. A degree of similarity between Cl_k and Tag_j is calculated. If the value is greater than V_t, Tag_j is added to Cl_k.
   (d) $Cset$ is updated. Concretely, clusters in $CopySet$ substitute corresponding clusters in $Cset$.
   (e) If $Cset$ does not include a cluster that includes both Tag_i and Tag_j, a new cluster is created that includes two tags (Tag_i and Tag_j) and added to $Cset$.

2.4.3 Creation of concepts

A concept (Co_i) is represented by a vector of degrees of relevance from a cluster (Cl_i) obtained above to all tags. A degree of relevance from a cluster Cl_i to a tag Tag_i is calculated as follows:

$$rel(Tag_i, Co_1) = \frac{t(Tag_i, Cl_1)}{\sum_j t(Tag_i, Cl_j)}$$

where $t(Tag_i, Cl_1)$ is an average of degrees of similarity between Tag_i and all tags in a cluster Cl_i.

2.4.4 Representation of characteristics of books

Characteristics of a book are represented by a vector of degrees of relevance from the book to all concepts obtained above. A degree of relevance from a book $Book_1$ to a concept Co_1 is represented as follows:

$$rel(Book, Co_1) = \sum_i rel(Tag_i, Co_1)$$

2.4.5 Representation of characteristics of users

First, a degree of preference from a user ($User$) to a concept (Co_1) is introduced as follows:

$$pre(User, Co_1) = \sum_i rel(Book_i, Co_1)$$

where $Book_i$ is a book that $User$ likes.

Characteristics of a user is represented by a vector of a $pre(User, Co_1)$ for all concept obtained above.

There are several methods to find books that a user likes: questionnaires, interviews, referring records of web viewing, and so on. In the experiments of this paper, examinees indicate their favorite books in direct.

2.4.6 Selection of books for recommendation

In this study, books whose characteristics vectors are similar with that of a target user are selected for recommendation. Concretely, an inner product of characteristics vectors of a book and a user is adopted here.

© ISAROB 2013

3 EXPERIMENTS

A book recommender system that is based on the proposed method was implemented by java language. A series of experiments was carried out using the system in order to confirm the validity of the proposed method.

3.1 Acquisition of data for experiments

Data used in the experiments are collect from Booklog (http://booklog.jp). Booklog is a web service that provides virtual book shelves. Over 500 thousands users are registered at the site and over 33 million items (books, CDs, and so on) are stored as of Jan. 2012. Web pages have been created for every book. Each of the pages provides information about the corresponding book. Each page also includes the links to the pages of the relating books. Booklog adopt folksonomy and its users can attach tags to books arranged on their book shelves.

Books in the top list for 2011 and books linked from them were selected. And 18,922 tags attached to the 6,717 books were obtained.

3.2 Methods of experiments and evaluation

Concepts were generated and specific vectors were calculated from the obtained data by the proposed method. The concepts and the vectors were embedded into the developed recommender system. The system recommended 10 books to each of 50 examinees.

A characteristics vector of each examinee was calculated from favorite books which he/she listed up. Ten books were selected for each examinee according to his/her characteristics vector. Next, the examinees answered the three inquiries listed below about each of the recommended books:

Q1 Are you interested in the book?
(1) Yes. (2) A little. (3) Little. (4) No.

Q2 Do you know the book well?
(1) Yes, I have read it. (2) Yes, but unread.
(3) Only its title. (4) No.

Q3 Do you think the recommendation validates?
(1) Yes. (2) I don't know. (3) No.

3.3 Results

The 500 answers (10 answers from each of the 50 examinees) for the three inquiries were obtained. The numbers of each of the answer are shown in Table 1. Positive answers ((1) or (2)) were selected for 309 recommended books in Q1 (61.8%). This result is as good as the result of the existing research [3] . 200 books that the examinees did not know well ((3) or (4) for Q2) were involved in the 309 books. 38 books that the examinees evaluated to be surprised ((3) for Q3) were involved in the 200 books. This means that about 12 % books were serendipitous books. Since the situation such that almost all recommended books are surprising is not adequate, it is considered that the obtained results, most books are proper and the rest are serendipitous, was appropriate recommendation.

Table 1. The results of the recommendation experiment.

	(1)	(2)	(3)	(4)	
Q1	156	153	149	42	500
Q2	65	55	77	303	500
Q3	228	147	125	N/A	500

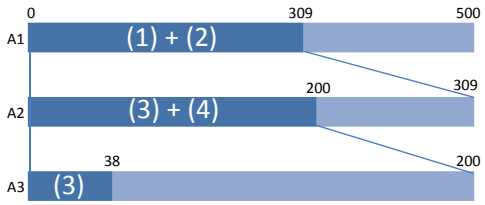

Fig. 4. The ratio of recommended books that were serendipitous.

4 CONCLUSIONS

In this study, the serendipity oriented recommendation method was proposed. Impressions that users felt from a book is extracted as a "concept" using tag data attached to books in the folksonomy style. In the proposed method, the concepts are used for selection of books recommended to users.

The recommender system was implemented and recommendation experiments were carried out using the system. It was confirmed that the recommender system based on the proposed method has enough recommendation accuracy and can recommend serendipituous books to users.

REFERENCES

[1] Kamishima T (2007-2008), Algorithms for Recommender Systems (in Japanese), Journal of JSAI, vol.22,no.6-vol.23,no.2

[2] Philip L. Cahn (1999), A non-invasive learning approach to building web user profiles, KDD.99 Workshop on Web Usage Analysis and User Profiling

[3] Niwa S, Doi T, Honiden S (20066), Web Page Recommender System based on Folksonomy Mining (in Japanese), IPSJ Journal, 47(5), pp.1382-1392

© ISAROB 2013

The Eighteenth International Symposium on Artificial Life and Robotics 2013 (AROB 18th '13),
Daejeon Convention Center, Daejeon, Korea, January 30-February 1, 2013

Self-Triggered Optimal Control Based on Optimization with Prediction Horizon One

Koichi Kobayashi[1] and Kunihiko Hiraishi[1]

[1]Japan Advanced Institute of Science and Technology, Japan
(Tel: +81-761-51-1282; E-mail: k-kobaya@jaist.ac.jp)

Abstract: Self-triggered control is a control method that the control input and the sampling period are computed simultaneously in sampled-data control systems, and is extensively studied in the field of networked control systems. In this paper, a new approach for self-triggered control is proposed based on model predictive control. First, the optimal control problem with horizon one, in which the first sampling period and the control input are found, is formulated. By solving this problem at each sampling interval, self-triggered model predictive control is realized. Next, an iterative solution method is proposed. In this solution method, a quadratic programming problem is repeatedly solved. Finally, the effectiveness of the proposed approach is shown by a numerical example.

Keywords: optimal control, networked control systems, self-triggered control.

1. INTRODUCTION

In recent years, analysis and synthesis of networked control systems (NCSs) have been extensively studied [1, 4]. An NCS is a control system in which plants, sensors, controllers, and actuators are connected through communication networks. In distributed control systems, subsystems are frequently connected via communication networks, and it is important to consider analysis and synthesis of distributed control systems from the viewpoint of NCSs. In design of NCSs, several technical issues such as packet losses and transmission delays are included. However, it is difficult to consider these issues in a unified way, and it is suitable to discuss an individual problem. From this viewpoint, several results have been obtained so far (see, e.g., [6-9]).

In this paper, the periodic paradigm is focused as one of the technical issues in NCSs. The periodic paradigm is that the controller is periodically executed at a given unit of time. The period is chosen based on CPU processing time, communication bandwidth, and so on. However, in NCSs, communication should occur, when there exists important information, which must be transmitted from the controller to the actuator and/or from the sensor to the controller. In this sense, the periodic paradigm is not necessarily suitable, and it is important to consider a new approach for design of NCSs. As one of the methods to overcome this drawback of the periodic paradigm, self-triggered control has been proposed so far (see, e.g., [2, 3, 5, 10, 13]). In self-triggered control, the next sampling time at which the control input is recomputed is computed. That is, both the sampling period and the control input are computed simultaneously. In many existing works, first, the continuous-time controller is obtained, and after that, the sampling period such that stability is preserved is computed. However, few results on optimal control have been obtained so far. From the viewpoint of optimal control, for example, a design method based one-step finite horizon boundary has been recently proposed in [12, 14]. In this method, the first sampling period such that the optimal value of the cost function is improved, is computed under the constraint that other sampling periods are given as a constant. However, a nonlinear equation must be solved. Furthermore, input constraints cannot be considered in this method.

In this paper, a new approach for self-triggered control is proposed based on model predictive control (MPC). First, the optimal control problem with horizon one, in which the first sampling period and the control input are found, is formulated. By solving this problem at each sampling interval, self-triggered model predictive control is realized. Next, an iterative solution method is proposed. In this solution method, quadratic programming (QP) problems are repeatedly solved. Then, we can impose input constraints for the system. Finally, the effectiveness of the proposed approach is shown by a numerical example. The proposed approach provides us a basic result for self-triggered optimal control.

Notation: Let $\mathcal{R}$ denote the set of real numbers. Let I_n, $0_{m\times n}$ denote the $n\times n$ identity matrix, the $m\times n$ zero matrix, respectively. For simplicity, we sometimes use the symbol 0 instead of $0_{m\times n}$, and the symbol I instead of I_n.

2. PROBLEM FORMULATION

Consider the following continuous-time linear system:

$$\dot{x}(t) = Ax(t) + Bu(t) \tag{1}$$

where $x \in \mathcal{R}^n$ is the state, and $u \in [u_{\min}, u_{\max}] \subseteq \mathcal{R}^m$ is the control input. $u_{\min}, u_{\max} \in \mathcal{R}^m$ are given constants, and the interval $[u_{\min}, u_{\max}]$ expresses input constraints. By t_k, $k = 0, 1, \ldots,$ denote the sampling time, and by $h_k := t_{k+1} - t_k$, denote the sampling period. Assume that the control input is piecewise constant, that is, the control input is given as

$$u(t) = u(t_k), \quad t \in [t_k, t_{k+1}).$$

Hereafter, we denote $u(t_k)$ as u_k. In addition, assume that a pair (A, B) is controllable.

© ISAROB 2013

Before the problem studied here is formulated, some preparations are given. Suppose that h_0 is a decision variable, and $h_i = h$, $i \geq 1$ is satisfied, where $h \geq 0$ is a given constant. We also suppose that the input constraint is imposed in the time interval $[t_0, h_0 + h(N-1))$, where $N \geq 1$ is a given integer. Note here that the input constraint is not imposed in the time interval $[h_0 + h(N-1), \infty)$. Then, consider the following cost function

$$J = J_1 + J_2 + J_3, \tag{2}$$

$$J_1 = \int_{t_0}^{h_0} \left\{ x^T(t)Qx(t) + u^T(t)Ru(t) \right\} dt,$$

$$J_2 = \int_{h_0}^{h_0+h(N-1)} \left\{ x^T(t)Qx(t) + u^T(t)Ru(t) \right\} dt,$$

$$J_3 = \int_{h_0+h(N-1)}^{\infty} \left\{ x^T(t)Qx(t) + u^T(t)Ru(t) \right\} dt$$
$$= x^T(h_0 + h(N-1))P(h)x(h_0 + h(N-1)).$$

In the above cost function, $P(h)$ is a symmetric positive definite matrix, which is a solution of the following discrete-time algebraic Riccati equation

$$\tilde{A}^T(h)P(h)\tilde{A}(h) - P(h) - (\tilde{A}^T(h)P(h)\tilde{B}(h) + \tilde{S}(h))$$
$$\times(\tilde{B}^T(h)P(h)\tilde{B}(h) + \tilde{R}(h))^{-1}$$
$$\times(\tilde{B}^T(h)P(h)\tilde{A}(h) + \tilde{S}^T(h)) + \tilde{Q}(h) = 0$$

where

$$\tilde{A}(h) := e^{Ah}, \;\; \tilde{B}(h) := \int_0^h e^{At} dt B$$

and

$$\begin{bmatrix} \tilde{Q}(h) & \tilde{S}(h) \\ \tilde{S}^T(h) & \tilde{R}(h) \end{bmatrix} := \int_0^h e^{F^T t} \begin{bmatrix} Q & 0 \\ 0 & R \end{bmatrix} e^{Ft} dt,$$

$$F := \begin{bmatrix} A & B \\ 0 & 0 \end{bmatrix}.$$

Since the input constraint is not imposed in the time interval $[h_0 + h(N-1), \infty)$, the optimal value of J_3 can be explicitly characterized by $x(h_0 + h(N-1))$.

Under the above preparation, consider the following problem.

Problem 1: Suppose that for the system (1), the initial time t_0, the initial state $x(0) = x_0$, $h_1 = h_2 = \cdots = h$, $N \geq 1$, and $\gamma \geq 1$ are given. Then find a control input sequence $u_0, u_1, \ldots, u_{N-1}$ maximizing a sampling period h_0 under the following constraints

$$h \leq h_0 \leq h_{\max},$$
$$u_{\min} \leq u_k \leq u_{\max}, \;\; k = 0, 1, \ldots, N-1, \tag{3}$$
$$J_{h_0}^* \leq \gamma J_h^* \tag{4}$$

where $h_{\max} \geq 0$ is a given constant, and $J_{h_0}^*$ is the optimal value of the cost function of (2), J_h^* is the optimal value of the cost function of (2) under $h_0 = h$. ■

In Problem 1, control performance can be adjusted by suitably giving γ. We remark that in this problem, h_0 is maximized under some constraints. Furthermore, in this problem, a control input sequence is computed, but on sampling periods, only the first one (h_0) is computed. In this sense, this problem is regarded as a kind of the optimal control problem with prediction horizon one.

3. PROPOSED SOLUTION METHOD

First, for a fixed h_0, consider deriving $J_{h_0}^*$. The value of J_h^* can be derived by a similar method. The value of $J_{h_0}^*$ is given as the optimal value of the following optimal control problem.

Problem 2: Suppose that for the system (1), the initial time t_0, the initial state $x(0) = x_0$, h_0 and $h_1 = h_2 = \cdots = h$, $N \geq 1$ are given. Then find a control input sequence $u_0, u_1, \ldots, u_{N-1}$ minimizing the cost function (2) under the input constraint (3) ■

From the result on sampled-data control theory, Problem 2 can be equivalently rewritten as the following optimal control problem of discrete-time linear systems.

Problem 3: Suppose that the initial time t_0, the initial state $x(0) = x_0$, h_0 and $h_1 = h_2 = \cdots = h$, $N \geq 1$ are given. Consider the following discrete-time linear system

$$x_1 = \tilde{A}(h_0)x_0 + \tilde{B}(h_0)u_0,$$
$$x_{k+1} = \tilde{A}(h)x_k + \tilde{B}(h)u_k, \;\; k \geq 1$$

where $x_k := x(t_k)$. Then find a control input sequence $u_0, u_1, \ldots, u_{N-1}$ minimizing the cost function (2), i.e.,

$$J = \begin{bmatrix} x_0 \\ u_0 \end{bmatrix}^T \begin{bmatrix} \tilde{Q}(h_0) & \tilde{S}(h_0) \\ \tilde{S}^T(h_0) & \tilde{R}(h_0) \end{bmatrix} \begin{bmatrix} x_0 \\ u_0 \end{bmatrix}$$
$$+ \sum_{k=1}^{N-1} \begin{bmatrix} x_k \\ u_k \end{bmatrix}^T \begin{bmatrix} \tilde{Q}(h) & \tilde{S}(h) \\ \tilde{S}^T(h) & \tilde{R}(h) \end{bmatrix} \begin{bmatrix} x_k \\ u_k \end{bmatrix}$$
$$+ x_N^T P(h) x_N \tag{5}$$

under the input constraint (3). ■

Next, consider reducing Problem 3 to a QP problem. Define

$$\bar{x} := \begin{bmatrix} x_0^T & x_1^T & \cdots & x_N^T \end{bmatrix}^T,$$
$$\bar{u} := \begin{bmatrix} u_0^T & u_1^T & \cdots & x_{N-1}^T \end{bmatrix}^T.$$

Then we can obtain $\bar{x} = \bar{A}x_0 + \bar{B}\bar{u}$ where

$$\bar{A} = \begin{bmatrix} I \\ \tilde{A}(h_0) \\ \tilde{A}(h)\tilde{A}(h_0) \\ \tilde{A}^2(h)\tilde{A}(h_0) \\ \vdots \\ \tilde{A}^{N-1}(h)\tilde{A}(h_0) \end{bmatrix}$$

and

$$\bar{B} = \begin{bmatrix} 0 & 0 & \cdots & 0 \\ \tilde{B}(h_0) & 0 & \cdots & \vdots \\ \tilde{A}(h)\tilde{B}(h_0) & \tilde{B}(h) & \cdots & \vdots \\ \tilde{A}^2(h)\tilde{B}(h_0) & \tilde{A}(h)\tilde{B}(h) & \cdots & \vdots \\ \vdots & \vdots & \cdots & 0 \\ \tilde{A}^{N-1}(h)\tilde{B}(h_0) & \tilde{A}^{N-2}(h)\tilde{B}(h) & \cdots & \tilde{B}(h) \end{bmatrix}.$$

In addition, we define

$$\bar{Q} := \text{block-diag}(\tilde{Q}(h_0), \tilde{Q}(h), \ldots, \tilde{Q}(h), P(h)),$$
$$\bar{S} := \begin{bmatrix} \text{block-diag}(\tilde{S}(h_0), \tilde{S}(h), \ldots, \tilde{S}(h)) \\ 0_{n \times (N-1)m} \end{bmatrix},$$
$$\bar{R} := \text{block-diag}(\tilde{R}(h_0), \tilde{R}(h), \ldots, \tilde{R}(h)).$$

© ISAROB 2013

Then the cost function (5) can be rewritten as follows:

$$\begin{aligned} J &= \bar{x}^T \bar{Q} \bar{x} + 2\bar{x}^T \bar{S} \bar{u} + \bar{u}^T \bar{R} \bar{u} \\ &= \bar{u}^T L_2 \bar{u} + L_1 \bar{u} + L_0 \end{aligned}$$

where

$$\begin{aligned} L_2 &= \bar{R} + \bar{B}^T \bar{S} + \bar{S}^T \bar{B} + \bar{B}^T \bar{Q} \bar{B}, \\ L_1 &= 2x_0^T \bar{A}^T (\bar{S} + \bar{Q}\bar{B}), \\ L_0 &= x_0^T \bar{A}^T \bar{Q} \bar{A} x_0. \end{aligned}$$

Finally, $\bar{u}_{\min} := [\ u_{\min}^T\ u_{\min}^T\ \cdots\ u_{\min}^T\ ]^T$ and $\bar{u}_{\max} := [\ u_{\max}^T\ u_{\max}^T\ \cdots\ u_{\max}^T\ ]^T$ are also defined.

Under the above preparation, Problem 3 is equivalent to the following QP problem:

Problem A:

$$\begin{aligned} \text{find} \quad & u_0, u_1, \ldots, u_{N-1}, \\ \min \quad & \bar{u}^T L_2 \bar{u} + L_1 \bar{u} + L_0, \\ \text{subject to} \quad & \bar{u}_{\min} \le \bar{u} \le \bar{u}_{\max}. \end{aligned}$$

A QP problem can be solved by using a suitable solver such as MATLAB and IBM ILOG CPLEX [15].

Finally, by using the obtained QP problem, we propose an algorithm for solving Problem 1.

Algorithm 1:

Step 1: Derive J_h^* by solving Problem A with $h_0 = h$.

Step 2: Set $a = h$ and $b = h_{\max}$, and give a sufficiently small positive real number ε.

Step 3: Set $h_0 = (a + b)/2$.

Step 4: Derive $J_{h_0}^*$ by solving Problem A.

Step 5: If $J_{h_0}^* \le \gamma J_h^*$ in Problem 1 is satisfied, then set $a = h_0$, otherwise set $b = h_0$.

Step 6: If $|a - b| < \varepsilon$ is satisfied, then the optimal h_0 in Problem 1 is derived as a, and the optimal control input sequence is also derived. Otherwise go to Step 3.

In a numerical example (Section 5), we will discuss the computation time of Algorithm 1.

4. SELF-TRIGGERED MODEL PREDICTIVE CONTROL

We show a procedure of MPC based on the proposed solution method for Problem 1.

Procedure of Self-Triggered MPC:

Step 1: Set $t_0 = 0$, and give the initial state $x(0) = x_0$.

Step 2: Solve Problem 1.

Step 3: Apply only $u(t)$, $t \in [t_0, t_0 + h_0)$ to the plant.

Step 4: Compute the predicated state $\hat{x}(t_0 + h_0)$ by using $x(t_0)$, h_0 and u_0.

Step 5: Solve Problem 1 by using $\hat{x}(t_0 + h_0)$ as x_0.

Step 6: Wait until time $t_0 + h_0$.

Step 7: Update $t_0 := t_0 + h_0$, and measure $x(t_0)$. Return to Step 3.

Note here that in this procedure, the timing (i.e., the sampling time) to measure the state and to recompute the control input is computed. In this sense, self-triggered control is realized.

5. NUMERICAL EXAMPLE

Consider the following system:

$$\dot{x}(t) = \begin{bmatrix} 0 & 1 \\ -5 & -8 \end{bmatrix} x(t) + \begin{bmatrix} 0 \\ 1 \end{bmatrix} u(t). \tag{6}$$

The input constraint is given as $u(t) \in [-10, +10]$. Parameters in Problem 1 are given as follows: $h = 0.5$, $\gamma = 1.001$, $h_{\max} = 5$, $Q = 10^3 I_n$, and $R = 1$. In Algorithm 1, we set $\varepsilon = 10^{-4}$. Then $P(h)$ can be derived as

$$P(h) = \begin{bmatrix} 10615 & 593 \\ 593 & 575 \end{bmatrix}.$$

In addition, we consider two cases, i.e., the case of $N = 1$ and the case of $N = 10$.

We show the computation result on self-triggered MPC using Problem 1. The initial state is given as $x_0 = [\ 10\ 10\ ]^T$, and the case of $N = 10$ is considered. Fig. 1 shows the obtained state and input trajectories. From this figure, we see that the sampling period is non-uniform.

Next, compare two cases. In these cases, the obtained state trajectories are almost the same. The difference between two cases is as follows. In Fig. 1, the value of the control input at each time is shown as follows:

$$\begin{aligned} u(t) &= -10.00, \ \ t \in [0, 1.83), \ \ h_0 = 1.83, \\ u(t) &= -1.90, \ \ t \in [1.83, 3.23), \ \ h_0 = 1.41, \\ u(t) &= -0.49, \ \ t \in [3.23, 4.49), \ \ h_0 = 1.25, \\ u(t) &= -0.14, \ \ t \in [4.49, 5.69), \ \ h_0 = 1.21, \\ u(t) &= -0.04, \ \ t \in [5.69, 6.89), \ \ h_0 = 1.20, \\ u(t) &= -0.01, \ \ t \in [6.89, 8.08), \ \ h_0 = 1.19. \end{aligned}$$

On the other hand, in the case of $N = 1$, the value of the control input at each time is derived as follows:

$$\begin{aligned} u(t) &= -10.00, \ \ t \in [0, 0.62), \ \ h_0 = 0.62, \\ u(t) &= -10.00, \ \ t \in [0.62, 1.66), \ \ h_0 = 1.03, \\ u(t) &= -2.62, \ \ t \in [1.66, 2.88), \ \ h_0 = 1.22, \\ u(t) &= -0.75, \ \ t \in [2.88, 4.08), \ \ h_0 = 1.20, \\ u(t) &= -0.22, \ \ t \in [4.08, 5.27), \ \ h_0 = 1.19, \\ u(t) &= -0.06, \ \ t \in [5.27, 6.47), \ \ h_0 = 1.19, \\ u(t) &= -0.02, \ \ t \in [6.47, 7.66), \ \ h_0 = 1.19, \\ u(t) &= -0.01, \ \ t \in [7.66, 8.85), \ \ h_0 = 1.19. \end{aligned}$$

From these results, we can obtain the following observation. In this example, input saturation is needed to improve the transient behavior. However, in the case of $N = 1$, the time interval of input saturation was not computed suitably. As a result, to derive the state trajectory

© ISAROB 2013

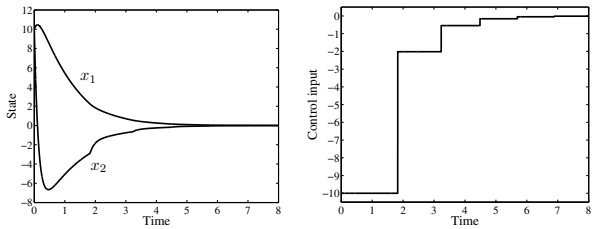

Fig. 1 State and input trajectories ($N = 10$).

at time interval $[0, 8)$, Problem 1 was solved eight times. In the case of $N = 10$, Problem 1 was solved six times, and the above problem is overcome. So it is important to choose a suitable N. We remark that in this example, the computation result in the case of $N = 20$ is the same as that in the case of $N = 10$. In this sense, $N = 10$ is one of the suitable horizons.

In addition, we discuss the effect of changing γ in (4). In the case of $N = 10$, consider the following cases: $\gamma = 1.001, 1.005, 1.010, 1.015, 1.020$. For each case, the first h_0 is obtained as follows:

$$\begin{aligned}
\gamma = 1.001 &: \quad h_0 = 1.83, \\
\gamma = 1.005 &: \quad h_0 = 2.38, \\
\gamma = 1.010 &: \quad h_0 = 2.79, \\
\gamma = 1.015 &: \quad h_0 = 3.12, \\
\gamma = 1.020 &: \quad h_0 = 3.44.
\end{aligned}$$

From these results, we see that h_0 becomes longer by setting a larger γ. Since control performance decreases for a larger γ, it is important to consider the trade-off between γ and h_0.

Finally, we discuss the computation time for solving Problem 1. In the case of $N = 10$, Problem 1 with the different initial state was solved six times. Then the mean computation time for solving Problem 1 was 6.51 [sec], where we used IBM ILOG CPLEX 11.0 [15] as the MIQP solver on the computer with the Intel Core2 Duo 3.0GHz processor and the 2GB memory. In the case of $N = 1$, Problem 1 with the different initial state was solved eight times. Then the mean computation time was 6.22 [sec]. It is one of the future works to consider several approaches for reducing the computation time.

6. CONCLUSION

In this paper, we have proposed a self-triggered optimal control method based on model predictive control. By focusing on only the first sampling period in the optimal control problem, we have proposed an iterative solution method (Algorithm 1). The effectiveness of the proposed method has been shown by a numerical example. The proposed methods are useful as a new method of self-triggered optimal control.

In the future works, it is important to develop a more efficient method for solving Problem 1. Then continuation methods [11] may be useful. It is also significant to analyze stability of the closed-loop system.

This work was partially supported by Grant-in-Aid for Young Scientists (B) 23760387.

REFERENCES

[1] Special section on complex networked control systems, *IEEE Control Systems Magazine*, Vol. 27, No. 4, 2007.

[2] A. Anta and P. Tabuada, Self-triggered stabilization of homogeneous control systems, *Proc. American Control Conf.*, pp. 4129–4134, 2008.

[3] A. Anta and P. Tabuada, To sample or not to sample: Self-triggered control for nonlinear systems, *IEEE Trans. on Automatic Control*, vol. 55, no. 9, pp. 2030–2042, 2009.

[4] P. J. Antsaklis and J. Baillieul (Guest Editors), Special issue on the technology of networked control systems, *Proceedings of the IEEE*, Vol. 95, No. 1, 2007.

[5] A. Camacho, P. Martí, M. Velasco, C. Lozoya, R. Villá, J. M. Fuertes, and E. Griful, Self-triggered networked control systems: an experimental case study, *Proc. IEEE Int'l Conf. on Industrial Technology*, pp. 123–128, 2010.

[6] L.-S. Hu, T. Bai, P. Shi, and Z. Wu, Sampled-data control of networked linear control systems, *Automatica*, Vol. 43, No. 5, pp. 903–911, 2007.

[7] H. Ishii, Stabilization under shared communication with message losses and its limitations, *Proc. 45th IEEE Conf. on Decision and Control*, pp. 4974–4979, 2006.

[8] H. Ishii, H^∞ control with limited communication and message losses, *Systems & Control Letters*, Vol. 57, No. 4, pp. 322–331, 2008.

[9] K. Kobayashi and K. Hiraishi, Optimal control of a class of networked systems based on MLD framework, *Proc. the 18th IFAC World Congress*, pp. 66–71, 2011.

[10] M. Mazo Jr. and P. Tabuada, On event-triggered and self-triggered control over sensor-actuator networks, *Proc. 47th IEEE Conf. on Decision and Control*, pp. 435–440, 2008.

[11] T. Otsuka, A continuation/GMRESmethod for fast computation of nonlinear receding horizon control, *Automatica*, vol. 40, pp. 563–574, 2004.

[12] M. Velasco, P. Martí, J. Yépez, F. J. Ruiz, J. M. Fuertes, and E. Bini, Qualitative analysis of a one-step finite horizon boundary for event-driven controllers, *Proc. 50th IEEE Conf. on Decision and Control and European Control Conf.*, pp. 1662–1667, 2011.

[13] X. Wang and M. D. Lemmon, Self-triggered feedback control systems with finite-gain $\mathcal{L}_2$ stability, *IEEE Trans. on Automatic Control*, vol. 54, no. 3, pp. 452–467, 2009.

[14] J. Yépez, M. Velasco, P. Martí, E. X. Martín, and J. M. Fuertes, One-step finite horizon boundary with varying control gain for event-driven networked control systems, *Proc. 37th Annual Conf. of the IEEE Industrial Electronics Society*, pp. 2531–2536, 2011.

[15] http://www.ilog.com/products/cplex/

© ISAROB 2013

The Eighteenth International Symposium on Artificial Life and Robotics 2013 (AROB 18th '13),
Daejeon Convention Center, Daejeon, Korea, January 30-February 1, 2013

H_∞ controller with graphical LMI region profile for Gantry Crane System

M. Z. Mohd Tumari, M. S. Saealal, M. R. Ghazali and Y. Abdul Wahab[1]

[1]Instrumentation and Control Engineering Research Group (ICE),
Faculty of Electrical and Electronics Engineering, Universiti Malaysia Pahang,
Pekan, Pahang, Malaysia.

[1]zaidimt@ump.edu.my

Abstract: This paper presents investigations into the development of $H\infty$ controller with pole clustering based on LMI techniques to control the payload positioning of INTECO 3D crane system with very minimal swing. The linear model of INTECO 3D crane system is obtained using the system identification process. Using LMI approach, the regional pole placement known as LMI region combined with design objective in $H\infty$ controller guarantee a fast input tracking capability, precise payload positioning and very minimal sway motion. A graphical profile of the transient response of crane system with respect to pole placement is very useful in giving more flexibility to the researcher in choosing a specific LMI region. The results of the response with the controllers are presented in time domains. The performances of control schemes are examined in terms of level of input tracking capability, sway angle reduction and time response specification. Finally, the control techniques is discussed and presented.

Keywords: INTECO 3D crane; sway control; H-infinity; LMI region.

1 INTRODUCTION

The main purpose of controlling an underactuated crane system is transporting the payload in a precise location. However, it is very difficult due to the fact that the payload can exhibit a pendulum-like swinging motion. Various attempts in controlling cranes system based on open loop and closed-loop control system have been proposed. For example, open loop time optimal strategies were applied to the crane by many researchers [1,2]. Poor results were obtained in these studies because open-loop strategy is sensitive to the system parameters and could not compensate for the effect of wind disturbance. In other hand, feedback control which is well known to be less sensitive to disturbances and parameter variations has also been adopted for controlling the crane system. For example, PD controllers has been proposed for both position and anti-swing controls [3]. However, the performance of the controller is not very effective in eliminating the steady state error. In addition, fuzzy logic controller has also been proposed for controlling the crane system by several researchers [4]. However, the fuzzy logic designed still need to struggle in finding the satisfactory rules, membership function, fuzzification and deffuzification parameter heuristically. In addition, since crane system is an underactuated system, sliding mode control also has been proposed by bringing the sliding surface into to the system [5]. Furthermore, the underactuated crane behavior also gives a very challenging problem in achieving good trajectory planning. A few contribution of trajectory planning scheme have been reported in [6]–[12].

In this project, H_∞-synthesis with pole clustering based on LMI techniques is used to control the positioning of payload with very minimal swing. In order to design the controller, the linear model of INTECO 3D crane system as shown in **Fig. 1** is obtained using the system identification process. The reason for choosing H_∞-synthesis is because of its good performance in handling with various types of control objectives such as disturbance cancellation, robust stabilization of uncertain systems, input tracking capability or shaping of the open-loop response. Nevertheless, the weakness of H_∞ controller is in handling with transient response behavior and closed-loop pole location instead of frequency aspects [13]. As we all know, a good time response specifications and closed-loop damping of underactuated crane system can be achieved by forcing the closed-loop poles to the left-half plane. Moreover, many literatures have proved that H_∞ synthesis can be formulated as a convex optimization problem involving linear matrix inequalities (LMI) [14]-[16]. In this case, the normal Riccati equation with inequality condition was used. This behavior will give wide range of flexibility in combining several constraints on the closed loop system. This flexible nature of LMI schemes can be used to handle H_∞ controller with pole placement constraints. In this study, the pole placement constraints will refer directly to regional pole placement [17]. It is slightly difference with point-wise pole placement, where poles are assigned to specific locations in the complex plane based on specific desired time response

© ISAROB 2013

specifications. In this case, the closed-loop poles of crane system are confined in a suitable region of the complex plane. This region consists of wide variety of useful clustering area such as half-planes, disks, sectors, vertical/horizontal strips, and any intersection thereof [17]. Using LMI approach, the regional pole placement known as LMI region combined with design objective in H_∞ controller should guarantee a fast input tracking capability, precise payload positioning and very minimal sway motion. As an extension of previous work, this report presents a graphical profile of the transient response of crane system with respect to pole placement constraint variation. This graphical analysis is very useful in giving more flexibility to the researcher in choosing a specific LMI region.

The rest of this report is structured in the following manner. The next section provides a description of the linear model of underactuated crane system based on system identification procedure. In section 3, the design of H_∞ controller with pole placement constraint is explained. The graphical profile of crane performance with LMI region variation also discussed in this section. Simulation and experimental validation are reported in Section 4. Finally, concluding remarks are offered in the last section.

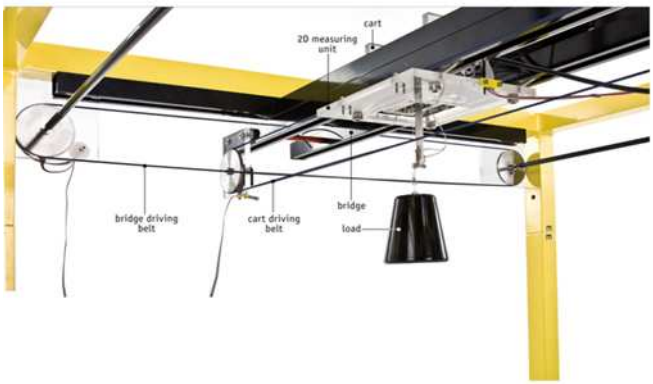

Fig. 1. INTECO 3D Crane.

2 MODELLING OF INTECO 3D CRANE

This section provides a brief description on the modelling of the underactuated crane system, as a basis of a simulation environment for development and assessment of the proposed control scheme. The system identification approach is used to determine the parameter of DC motor for cart position and pendulum behavior for sway motion respectively. In this study, only two-dimensional crane system with payload is considered. In order to have a precise end-point payload motion, the equation of payload position, second order DC motor and pendulum sway motion are described in (1), (2) and (3) respectively

$$x_l = x_c + l\sin\theta \tag{1}$$

$$\ddot{x}_c = -\frac{1}{T}\dot{x}_c + \frac{K}{T}u \tag{2}$$

$$m\ddot{x}_l = -D(\dot{x}_l - \dot{x}_c) - mg\sin\theta \tag{3}$$

where the meaning of different variables is given in **Table 1**.

Table 1: Variable description

Symbols	Meaning
x_l	Payload position
x_c	Cart position
l	Length of the rope
θ	Sway angle
T	Time constant
K	Motor gain
D	Damping constant
m	Mass of the payload
g	Gravity effect
u	Driving voltage

Using the assumption of $\cos\theta \cong 1$ and $\sin\theta \cong \theta$, (1) and (3) can be expressed as follow

$$x_l = x_c + l\theta \tag{4}$$

$$m\ddot{x}_l = -D(\dot{x}_l - \dot{x}_c) - mg\theta \tag{5}$$

Next, by substituting (4) in (5) and (2) respectively, the final equation of motion can be described as

$$\ddot{x}_l = -g\theta - \frac{lD}{m}\dot{\theta} \tag{6}$$

$$\ddot{\theta} = \frac{1}{lT}\dot{x}_l - \frac{g}{l}\theta - \left(\frac{D}{m} + \frac{1}{T}\right)\dot{\theta} - \frac{K}{lT}u \tag{7}$$

Since the design of proposed controller must required the state space representation of the system, equation (6) and (7) are arranged into state space form as shown in (8):

$$\begin{aligned} \dot{x} &= Ax + Bu \\ y &= Cx + Du \end{aligned} \tag{8}$$

© ISAROB 2013

Where

$$A=\begin{bmatrix} 0 & 1 & 0 & 0 \\ 0 & 0 & -g & -\frac{lD}{m} \\ 0 & 0 & 0 & 1 \\ 0 & \frac{1}{lT} & -\frac{g}{l} & -\frac{D}{m}-\frac{1}{T} \end{bmatrix} \quad B=\begin{bmatrix} 0 \\ 0 \\ 0 \\ -\frac{K}{lT} \end{bmatrix}$$

$C=\begin{bmatrix}1 & 0 & 0 & 0\end{bmatrix}$ $D=[0]$

with state variable $x=\begin{bmatrix}x_l & \dot{x}_l & \theta & \dot{\theta}\end{bmatrix}^T$.

Using simple empirical method in system identification process, the parameters value of crane system are defined as m = 0.732 kg, g = 9.8067 m/s^2, T = 0.0999 s, K = 0.3175 m/s^{2}V, D = 0.0168 and l = 0.4335 m.

3 DESIGN OF H$_\infty$ CONTROLLER WITH LMI REGION

In this study, an integral state feedback control is used as a platform to design the proposed controller. The block diagram of integral state feedback control is shown in **Fig. 2.**

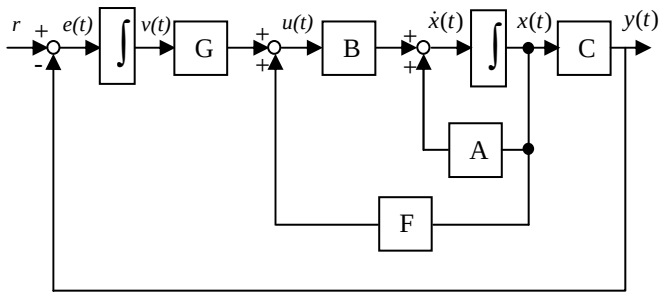

Fig. 2. Block diagram of integral state feedback control.

The main objective of the proposed controller is to find the gain parameter matrix, F and G such that it fulfills the design requirement. From the block diagram of Figure 2, the control input of the system is derived as follow

$$u(t)=Fx(t)+Gv(t) \tag{9}$$

where $v(t)=\int_0^t e(\tau)d\tau$ and $e(t)=r-y(t)$

Using new state variable $x_e=\begin{bmatrix}x^T & v\end{bmatrix}^T$ and equation (9) the representation of state space equation can be rewrite as

$$\begin{bmatrix}\dot{x}(t)\\ \dot{v}(t)\end{bmatrix}=\begin{bmatrix}A & 0\\ -C & 0\end{bmatrix}\begin{bmatrix}x(t)\\ v(t)\end{bmatrix}+\begin{bmatrix}B\\ 0\end{bmatrix}u(t)+\begin{bmatrix}0\\ 1\end{bmatrix}r$$
$$e(t)=r-Cx(t) \tag{10}$$

Next, at the steady state condition as $t\to\infty$, the state space equation can be written in the following form

$$\begin{bmatrix}0\\ 0\end{bmatrix}=\begin{bmatrix}A & 0\\ -C & 0\end{bmatrix}\begin{bmatrix}x(\infty)\\ v(\infty)\end{bmatrix}+\begin{bmatrix}B\\ 0\end{bmatrix}u(\infty)+\begin{bmatrix}0\\ 1\end{bmatrix}r$$
$$0=r-Cx(\infty) \tag{11}$$

By subtracting (10) to (11), the state space form is converted to

$$\dot{\tilde{x}}_e(t)=\tilde{A}\tilde{x}_e(t)+\tilde{B}_2\tilde{u}(t)$$
$$\tilde{e}(t)=\tilde{C}_1\tilde{x}_e(t) \tag{12}$$

where

$$\tilde{A}=\begin{bmatrix}A & 0\\ -C & 0\end{bmatrix},\ \tilde{B}_2=\begin{bmatrix}B\\ 0\end{bmatrix},\ \tilde{x}_e=\begin{bmatrix}\tilde{x}\\ \tilde{v}\end{bmatrix}=\begin{bmatrix}x-x(\infty)\\ v-v(\infty)\end{bmatrix}$$
$$\tilde{C}_1=\begin{bmatrix}-C & 0\end{bmatrix},\ \tilde{e}(t)=e-e(\infty)$$

Then, the new control input function is described as follow

$$\tilde{u}(t)=F\tilde{x}(t)+G\tilde{v}(t)=K\tilde{x}_e(t) \tag{13}$$

Finally, a closed loop state space equation with controller gain, K can be obtained below

$$\dot{\tilde{x}}_e(t)=\tilde{A}_{cl}\tilde{x}_e(t)+\tilde{B}_1 w$$
$$\tilde{y}(t)=\tilde{C}_1\tilde{x}_e(t)+\tilde{D}_{11}w+\tilde{D}_{12}u \tag{14}$$

where

$$\tilde{A}_{cl}=(\tilde{A}+\tilde{B}_2K),\ \tilde{B}_1=\begin{bmatrix}0 & 0 & 0 & 0 & -1\end{bmatrix},\ \tilde{D}_{11}=1,$$
$$\tilde{D}_{12}=0$$

and w is exogenous input disturbance or reference input to the system. Let $G_{yw}(s)$ denote the closed loop transfer function from w to y under state feedback control $u=Kx$. Then, for a prescribed closed loop H$_\infty$ performance $\gamma>0$, our constrained H$_\infty$ problem consists of finding a state feedback gain K that fulfil the following objectives:

(1) The closed loop poles are required to lie in some LMI stability region $\mathcal{D}$ contained in the left-half plane

(2) Guarantees the H$_\infty$ performance $\|G_{yw}\|_\infty<\gamma$

Quote from the definition in [13], a subset $\mathcal{D}$ of the complex plane is called an LMI region if there exist a symmetric matrix $\alpha\in\mathbf{R}^{m\times m}$ and a matrix $\beta\in\mathbf{R}^{m\times m}$ such that

$$\mathcal{D}=\{z\in\mathbf{C}:\ f_{\mathcal{D}}(z)<0\} \tag{15}$$

where

$$f_{\mathcal{D}}(z):=\alpha+z\beta+\bar{z}\beta^T$$

Then, pole location in a given LMI region can be characterized in terms of the $m\times m$ block matrix

$$M_{\mathcal{D}}(\tilde{A}_{cl}, X_{\mathcal{D}}) := \alpha \otimes X_{\mathcal{D}} + \beta \otimes (\tilde{A}_{cl} X_{\mathcal{D}}) + \beta^T \otimes \left(\tilde{A}_{cl} X_{\mathcal{D}}\right)^T \quad (16)$$

Quote from the theorem in [10], the matrix $\tilde{A}_{cl}$ is $\mathcal{D}$-stable if and only if there exists a symmetric matrix X such that

$$M_{\mathcal{D}}(\tilde{A}_{cl}, X_{\mathcal{D}}) < 0, \quad X_{\mathcal{D}} > 0 \quad (17)$$

In this study, the region $S(\lambda, r, \theta)$ of complex numbers $x + jy$ such that

$$x < -\lambda < 0, \quad |x + jy| < r, \quad \tan\theta\, x < -|y| \quad (18)$$

as shown in **Fig. 3** is considered.

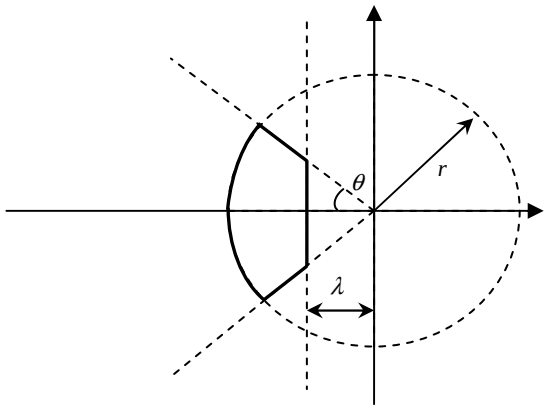

Fig. 3. Region $S(\lambda, r, \theta)$

The advantages of placing the closed loop poles to this region are the cart position response ensures a minimum decay rate λ, a minimum damping ratio $\zeta = \cos\theta$, and a maximum undamped natural frequency $\omega_d = r\sin\theta$ [13]. Equation (19), (20) and (21) show the clustering region used in this study which are λ–stability region, a disk and the conic sector respectively.

$$M_{\mathcal{D}1}(\tilde{A}_{cl}, X_{\mathcal{D}1}) := \tilde{A}_{cl} X_{\mathcal{D}1} + X_{\mathcal{D}1} \tilde{A}_{cl}^T + 2\lambda X_{\mathcal{D}1} < 0 \quad (19)$$

$$M_{\mathcal{D}2}(\tilde{A}_{cl}, X_{\mathcal{D}2}) := \begin{pmatrix} -rX_{\mathcal{D}2} & \tilde{A}_{cl} X_{\mathcal{D}2} \\ X_{\mathcal{D}2} \tilde{A}_{cl}^T & -rX_{\mathcal{D}2} \end{pmatrix} < 0 \quad (20)$$

$$M_{\mathcal{D}3}(\tilde{A}_{cl}, X_{\mathcal{D}3}) := \begin{pmatrix} \sin\theta(\tilde{A}_{cl} X_{\mathcal{D}3} + \tilde{A}_{cl} X_{\mathcal{D}3}^T) & \cos\theta(\tilde{A}_{cl} X_{\mathcal{D}3} - \tilde{A}_{cl} X_{\mathcal{D}3}^T) \\ \cos\theta(X_{\mathcal{D}3} \tilde{A}_{cl}^T - \tilde{A}_{cl} X_{\mathcal{D}3}) & \sin\theta(\tilde{A}_{cl} X_{\mathcal{D}3} + \tilde{A}_{cl} X_{\mathcal{D}3}^T) \end{pmatrix} < 0 \quad (21)$$

where this region is the intersection of three elementary LMI regions ($M_{\mathcal{D}1 \cap \mathcal{D}2 \cap \mathcal{D}3}(\tilde{A}_{cl}, X_{\mathcal{D}})$).

Motivated from the previous work, this study presents an effective way to determine the parameter of region $S(\lambda, r, \theta)$ which in turn bounds the desired maximum overshoot, rise time, settling time, control input and frequency of oscillatory modes. As the transient response profiles varied when the parameter of region is changed, it is suitable to introduce the 3D graphical profiles of LMI region performance. Consider λ is fixed, this investigations only focused on the variation of parameter r and θ. Then, these parameters are chosen based on desired underactuated crane performance from the graphical profile.

Meanwhile, the H_∞ constraint is equivalent to the existence of a solution $X_\infty > 0$ to the LMI

$$\begin{pmatrix} \tilde{A}_{cl} X_\infty + X_\infty \tilde{A}_{cl}^T & X_\infty \tilde{C}_1^T & \tilde{B}_1 \\ \tilde{C}_1 X_\infty & -\gamma I & \tilde{D}_{11} \\ \tilde{B}_1^T & \tilde{D}_{11}^T & -\gamma I \end{pmatrix} < 0 \quad (22)$$

Equation (22) is also known as the Bounded Real Lemma [18]. As mentioned before, the main objective of this study is to minimize the H_∞ norm of $G_{yw}(s)$ over all state feedback gains K that enforce the pole constraints. However, this problem is not jointly convex in the variables $X_{\mathcal{D}1}$, $X_{\mathcal{D}2}$, $X_{\mathcal{D}3}$, X_∞ and K. The convexity can be enforced by seeking a common solution

$$X = X_{\mathcal{D}1} = X_{\mathcal{D}2} = X_{\mathcal{D}3} = X_\infty > 0 \quad (23)$$

to (19)-(22) and rewriting these equations using the auxiliary variable $Y = KX$. These changes of variables lead to the suboptimal LMI approach to H_∞ synthesis with pole assignment in LMI regions. As a result, the new representations of (19)-(22) are shown in the following equation.

$$\mathrm{Herm}[\tilde{A}X + \tilde{B}_2 Y] + 2\lambda X < 0 \quad (24)$$

$$\begin{pmatrix} -rX & \tilde{A}X + \tilde{B}_2 Y \\ * & -rX \end{pmatrix} < 0 \quad (25)$$

$$\begin{pmatrix} \sin\theta(\mathrm{Herm}[\tilde{A}X + \tilde{B}_2 Y]) & \cos\theta(\mathrm{Herm}[\tilde{A}X - \tilde{B}_2 Y]) \\ * & \sin\theta(\mathrm{Herm}[\tilde{A}X + \tilde{B}_2 Y]) \end{pmatrix} < 0 \quad (26)$$

$$\begin{pmatrix} \mathrm{Herm}[\tilde{A}X + \tilde{B}_2 Y] & X\tilde{C}_1^T & \tilde{B}_1 \\ * & -\gamma I & \tilde{D}_{11} \\ * & * & -\gamma I \end{pmatrix} < 0 \quad (27)$$

where $\mathrm{Herm}[\tilde{A}X + \tilde{B}_2 Y] = \tilde{A}X + \tilde{B}_2 Y + X\tilde{A}^T + Y\tilde{B}_2^T$ and $*$ is an ellipsis for terms induced by symmetry [17]. In this study, the entire LMI problem is solved using well known LMI optimization software which is *LMI Control Toolbox*.

Next, to verify the effectiveness of graphical LMI region profile, several specifications have been set up:

- Settling time of 2.5 s with overshoot less than 1% and zero steady state error for the cart movement;

- Sway oscillation is less than ±0.05 rad;
- Control input does not exceed 1 V;

In other words, the designed state feedback gain K also must fulfil the mentioned specifications. Computing (24)-(27) using *LMI Control Toolbox*, the graphical profiles of the underactuated crane system performance are depicted in APPENDIX A. In this case, λ is fixed at -3 while the conic sector and disk are varies.

4 SIMULATION AND EXPERIMENTAL VALIDATION

Applying the LMI conditions in (24)-(27) with the advantage of graphical profiles, the parameter of conic sectors and disk that fulfil the design requirement is at $r = 4$ and $\theta = 28^\circ$. Then, the state feedback gain, K is obtained as followed:

$$K = [-11.2759 \quad -2.9956 \quad 13.6133 \quad 0.9993 \quad 8.42773]$$

with $\gamma = 64.9073$. This state feedback gain also guarantees the H_∞ performance $\|G_{yw}\|_\infty < \gamma$. **Fig. 4** shows that the location of poles has been confined in the selected LMI region. The simulation and experimental validation response of cart position, sway angle and control input are depicted in **Fig. 5**. Close agreement between simulation and experimental results has been successfully achieved. Note that, the cart position response track the desired response of 0.3 m with zero steady state error and settling time of 2.5 s with minimal overshoot. The maximum oscillation of sway angle also has been reduced to ±0.05 rad. Finally, the control input of less than 1 V, has been successfully obtained.

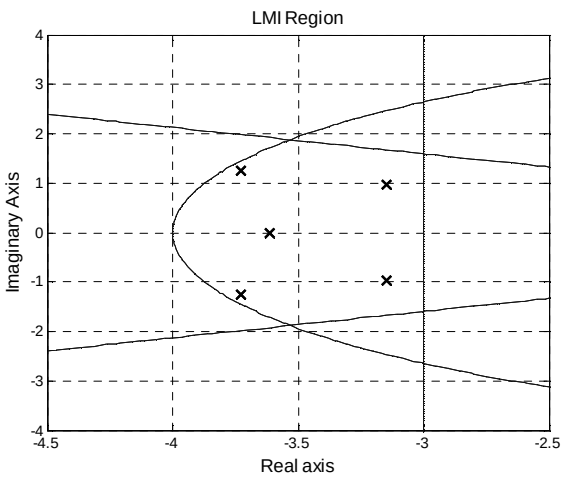

Fig. 4. Location of poles in selected LMI region

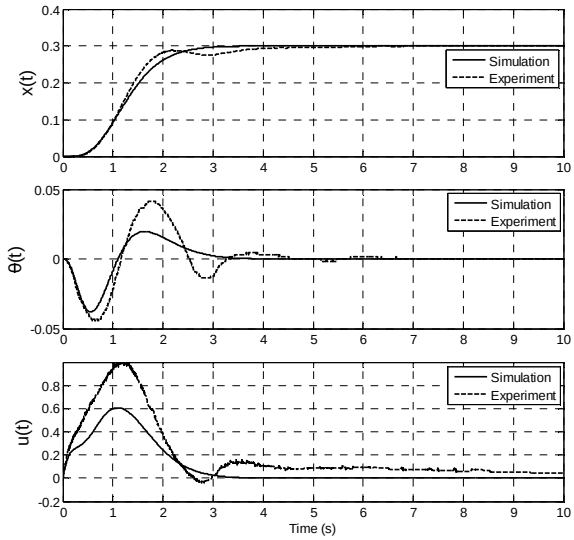

Fig. 5. Response of the underactuated crane system

5 CONCLUSION

This study has introduced new graphical LMI region profile which gives great flexibility in choosing specific parameter of pole placement constraint. The usefulness of this profile has been demonstrated to underactuated crane system using H_∞ synthesis with closed loop pole clustering constraint. This LMI approach has been implemented in the LMI Control Toolbox and validated using INTECO 3D Crane experimental rig with satisfactory results.

REFERENCES

[1] G.A. Manson, "Time-Optimal Control of and Overhead Crane Model," *Optimal Control Applications & Methods*, 3(2), 1992, pp. 115-120.

[2] J. Auernig and H. Troger, "Time Optimal Control of Overhead Cranes with Hoisting of the Load," *Automatica*, 23(4), 1987, pp. 437-447.

[3] H.M. Omar, Control of Gantry and Tower Cranes, M.S. Thesis, Virginia Tech., 2003, Blacksburg, VA.

[4] H.H. Lee and S.K. Cho, "A New fuzzy logic anti-swing control for industrial three-dimensional overhead crane," *Proceedings of the 2001 IEEE International Conference on Robotic and Automation*, 2001, Seoul, pp. 2958-2961.

[5] M. Orbisaglia, G. Orlando, and S. Longhi, "A comparative analysis of sliding mode controllers for overhead cranes," in *Proc. 16th Med. Conf. Control Autom.*, 2008, pp. 670–675.

[6] M.A. Ahmad, A.N.K. Nasir and H. Ishak, "Techniques of anti-sway and input tracking control of a gantry crane system," *IEEE International Conference on Mechatronics and Automation*, pp. 262-267, 2009.

[7] M.A. Ahmad, R.M.T. Raja Ismail, M.S. Ramli, "Hybrid input shaping and non-collocated PID control of a gantry crane system: Comparative Assessment," in *Proc. IEEE/ASME Conf. Adv. Intell. Mechatron.*, 2009, pp. 1792-1797.

[8] M.A. Ahmad, M.S. Ramli, R.M.T. Raja Ismail, A.N.K. Nasir and M.A. Zawawi, "The investigations of PD-type fuzzy logic with different polarities input shaping for anti-sway control of a gantry crane system," in *Proc. of Conference Innovative Technologies in Intelligent Systems and Industrial Applications.*, 2009, pp. 452–457.

[9] M.A. Ahmad, M.S. Saealal, R.M.T. Raja Ismail, M.A. Zawawi, A.N.K. Nasir and M.S. Ramli, "Single input fuzzy controller with command shaping schemes for double-pendulum-type overhead

crane," *AIP conference proceedings*, vol. 1337, no. 1, pp. 113–117, 2011.

[10] M.A. Ahmad, R.M.T. Raja Ismail, M.S. Ramli and N. Hambali, "Comparative assessment of feed-forward schemes with NCTF for sway and trajectory control of a DPTOC," *International Conference on Intelligent and Advanced Systems*, 2010, pp. 1-6.

[11] M.A. Ahmad, R.M.T. Raja Ismail, M.S. Ramli and N. Hambali, "Investigations of NCTF with input shaping for sway control of a double-pendulum-type overhead crane," *Proc. of 2nd IEEE International Conference on Advanced Computer Control*, 2010, pp. 456-461.

[12] M.A. Ahmad, R.M.T. Raja Ismail, M.S. Ramli and N. Hambali, "Analysis of IIR filter with NCTF-PI control for sway and trajectory motion of a DPTOC System," *International Conference on Electronics Devices, Systems and Applications*, 2010, pp. 54-58.

[13] M. Chilali, P. Gahinet, "H_∞ design with pole placement constraints: an LMI approach", *IEEE Transactions on Automatic Control*, Vol. 41(3), pp. 358-367, 1996.

[14] P. Gahinet and P. Apkarian, "A linear matrix inequality approach to H_∞ control," *Int. J. Robust Nonlinear Contr.*, vol. 4, pp. 421-448, 1994; also in *Proc. CDC*, 1993, pp. 656-661.

[15] T. Iwasaki and R. Skelton, "All controllers for the general H_∞ control problem: LMI existence conditions and state-space formulas," *Automatica*, vol. 30, pp. 1307-1317, 1994.

[16] A. Packard, "Gain scheduling via linear fractional transformations," *Syst.Contr. Lett.*, vol. 22, pp. 79-92, 1994.

[17] M. Chilali, P. Gahinet, P. Apkarian, "Robust pole placement in LMI regions", *IEEE Transactions on Automatic Control*, Vol. 44(12), pp. 2257-2270, 1999.

[18] S. Boyd, L. EL Ghaoui, E. Feron and V. Balakrishnan, "Linear Matrix Inequalities in System Control Theory, Vol. 15 of *Studies in Applied Mathematics*, SIAM, Philadelphia, PA, June 1994.

APPENDIX A

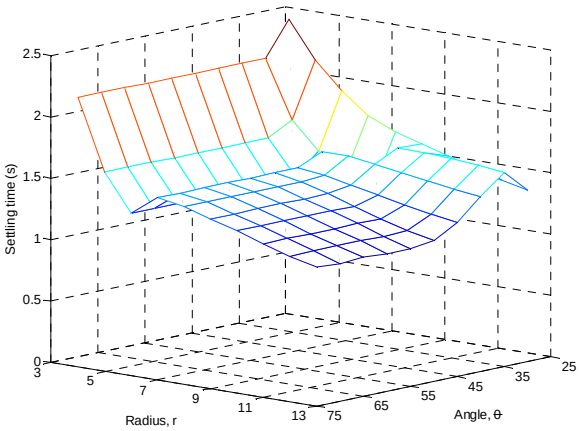

Fig. 6 Settling time profile

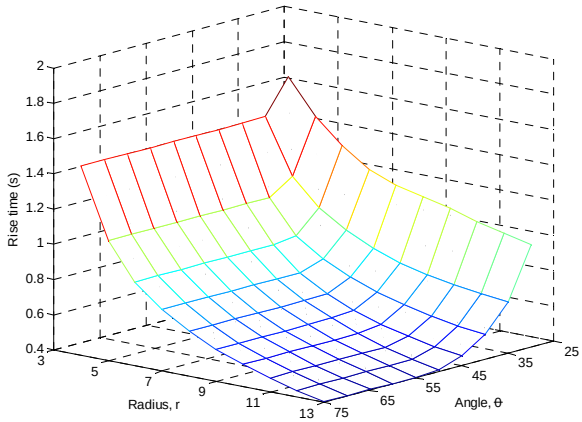

Fig. 7 Rise time profile

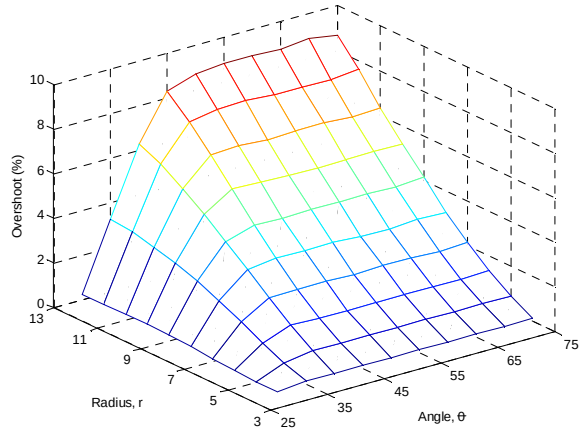

Fig. 8 Overshoot profile

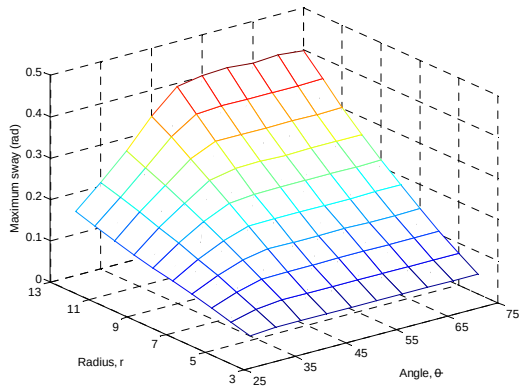

Fig. 9 Maximum sway profile

The Eighteenth International Symposium on Artificial Life and Robotics 2013 (AROB 18th '13),
Daejeon Convention Center, Daejeon, Korea, January 30-February 1, 2013

Optimized Walking Control of a Biped Walking Robot Considering Theory of a Pendulum

Hisashi Koike, Jae Hoon Lee[1], and Shingo Okamoto

Ehime University, Japan
(Tel: 81-089-927-9740, Fax: 81-089-927-9740)

[1]jhlee@ehime-u.ac.jp

Abstract: A motion control based on the theory of passive walking has been investigated in this paper. It has been known that general passive walking robot can walk efficiently on the slope by using potential energy with no actuator. However, it cannot walk on the horizontal ground. In order to utilize the merit of energy efficiency, two motors were installed at the hip joints of the passive-walking-type robot, which generate required torque for walking on the horizontal ground. The proportional control algorithm was applied for successive walking. Computer simulations with its dynamic model were carried out to find out the optimal condition for walking motion. Based on the simulation results, experimental robot was developed. As a result, the capability of walking on the horizontal ground was confirmed through experimental works with the proposed method and the developed robot.

Keywords: Biped walking robot, Passive walking, Walking control.

1 INTRODUCTION

Recent biped robot shows advanced performance in their motion, especially in walking. However, it has been known that the energy efficiency of typical biped robots in walking motion is worse than human [1]. Therefore, walking efficiency has been considered as an important issue for innovation of humanoid robot. Passive walking robot has been investigated as a model to understand and solve the problem [2]. The passive walking robot can walk efficiently on the slope by using their passive legs which rotate like as pendulums. However, it can't walk on the horizontal ground because it has no energy source to move its leg forward.

This research aims to develop the biped walking robot that can walk on the horizontal ground. Besides, to improve walking efficiency, the theory of passive walking is also considered. For that, the minimum number of actuators, i.e. two motors, were installed at the hip joints of the robot, which generate the control torques for walking motion. In the previous researches [3,4], the computer simulations with dynamic model were carried out to investigate the walking capability of the system. In this research, the experimental system with embedded controller has been developed. The system with the proposed method was investigated through experimental works.

2 COMPUTER SIMULATION

The computer simulations with the dynamic model of the biped robot with a torso were performed [4].

2.1 Analysis model

Figure 1 shows the analysis model of the walking robot. The robot consists of a torso, a hip and two legs with feet. By alternating the state of both legs between stance and swing, the robot can walk successively. For generating torque for walking motion, two motors are installed at the hip joints. Where τ_1 and τ_2 denote the control torque between the stance-leg and the torso, and the torque the swing-leg and the torso, respectively.

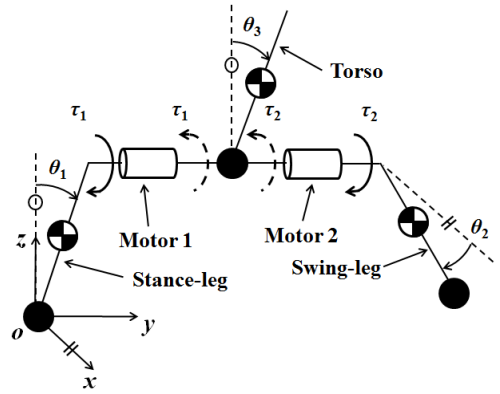

Fig. 1. Analysis model of the walking robot with motors [4]

2.2 Equation of motion

The motion equation of the robot is given by

$$\boldsymbol{M}(\boldsymbol{\theta})\ddot{\boldsymbol{\theta}}+\left[\boldsymbol{C}_c\left(\boldsymbol{\theta},\dot{\boldsymbol{\theta}}\right)+\boldsymbol{C}_d\right]\dot{\boldsymbol{\theta}}+\boldsymbol{g}(\boldsymbol{\theta})=\boldsymbol{B}\boldsymbol{\tau} \tag{1}$$

where, $\boldsymbol{\theta}=\{\theta_1 \quad \theta_2 \quad \theta_3\}^T$, $\boldsymbol{\tau}=\{\tau_1 \quad \tau_2\}$, $\boldsymbol{M}$ is the inertia matrix, $\boldsymbol{C}_c$ is a Coriolis and centrifugal force matrix, $\boldsymbol{C}_d$ is a viscosity damping matrix, $\boldsymbol{B}$ is a coefficient matrix about control torque, and $\boldsymbol{g}$ is the gravity vector, respectively.

2.3 Exchange between stance leg and swing leg

The condition of the touchdown of the swing-leg is given by

$$\theta_1+\theta_2=\pi/2. \tag{2}$$

The contact between the swing-leg and the ground when the swing-leg passes through the stance-leg was ignored.

© ISAROB 2013

Then the impact at the touchdown was assumed to be inelastic. It was also assumed that the stance-leg leaves from the ground at the moment of touchdown.

The angular velocity of the joints after touchdown is computed as follows. The angular momentum is conserved before and after touchdown for the whole robot about the leading contact point, the trailing leg about the hip and the torso about the hip. Equation (3) is given by these conservation laws of angular momentum:

$$\boldsymbol{Q}^{+}\left(\boldsymbol{\theta}^{+}\right)\dot{\boldsymbol{\theta}}^{+}=\boldsymbol{Q}^{-}\left(\boldsymbol{\theta}^{-}\right)\dot{\boldsymbol{\theta}}^{-}. \tag{3}$$

The superscripts "-" and "+" denote the state before and after touchdown, respectively. The relation of the angles before and after touchdown is given by

$$\boldsymbol{\theta}^{+}=\boldsymbol{R}\boldsymbol{\theta}^{-}+\boldsymbol{\theta}_{0}, \tag{4}$$

where

$$\boldsymbol{R}=\begin{bmatrix}0 & 1 & 0\\ 1 & 0 & 0\\ 0 & 0 & 1\end{bmatrix}, \tag{5}$$

$$\boldsymbol{\theta}_{0}=\left\{-\pi/2 \quad \pi/2 \quad 0\right\}^{T}, \tag{6}$$

Resultantly, the angular velocity of all joints after touchdown is calculated by

$$\dot{\boldsymbol{\theta}}^{+}=\boldsymbol{Q}^{+}\left(\boldsymbol{\theta}^{+}\right)^{-1}\boldsymbol{Q}^{-}\left(\boldsymbol{\theta}^{-}\right)\dot{\boldsymbol{\theta}}^{-}. \tag{7}$$

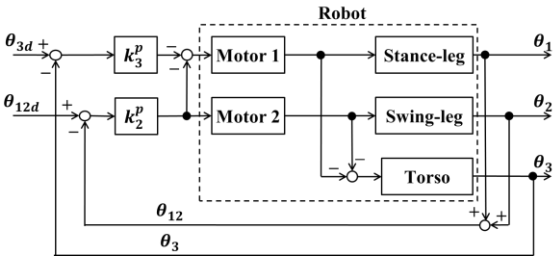

Fig. 2. Block diagram of active control for calculations [4]

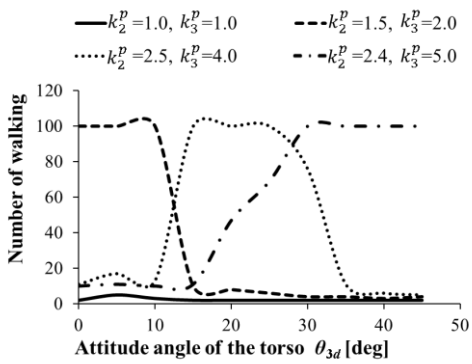

Fig. 3. Relation between control gains and the number of walking [4]

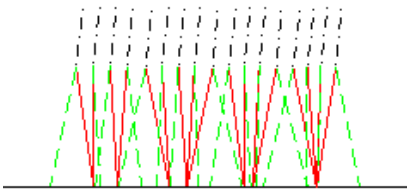

Fig. 4. Walking motion using PD control [4]

2.4 Motion control

The proportional (P) and proportional-differential (PD) control law have been employed. In the case of proportional control, the control torques τ_1 and τ_2 are given by Eq. (8) and (9).

$$-\tau_1-\tau_2=k_3^p\left(\theta_{3d}-\theta_3\right), \tag{8}$$

$$\tau_2=k_2^p\left(\theta_{12d}-\theta_{12}\right), \tag{9}$$

where

$$\theta_{12}=\theta_1+\theta_2, \tag{10}$$

$$\theta_{12d}=\pi/2. \tag{11}$$

The k_2^p and k_3^p denotes the control gains. The control torque τ_1 is given by

$$\tau_1=-k_2^p\left(\theta_{12d}-\theta_{12}\right)-k_3^p\left(\theta_{3d}-\theta_3\right). \tag{12}$$

The block diagram of active control for calculation is shown in Fig. 2, where the proportional control is used.

2.5 Result of computer simulation

The optimal control gains have been found out through simulations with various conditions. Figure 3 shows the relation between θ_{3d} and the number of successive walking motion. An example of the calculated results is given in Fig. 4.

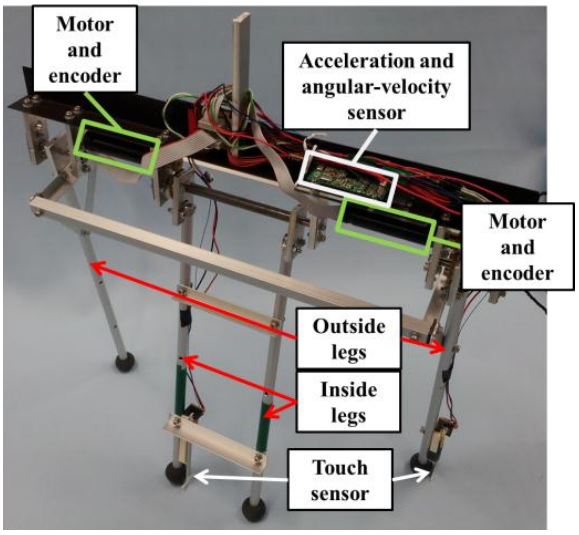

Fig. 5. Experimental robot

3 DEVELOPMENT OF EXPERIMENTAL ROBOT

3.1 Composition of the robot

Figure 5 shows the experimental robot which was developed based on the result of computer simulation. The length of each leg and the torso are 310 [mm] and 140 [mm], respectively. The total mass of whole system is 0.65 [kg]. In order to constrain the walking motion in the vertical planar space, each leg consists of two parallel links. So the inside legs and the outside legs are connected with each other by additional frames, respectively. The control torques are generated by the motors installed at the hip joints. The encoders are installed at the motors to measure the angle of each hip joint. The attitude angle of the torso is

© ISAROB 2013

measured by the attitude sensor (HiBot Co., Japan) attached on the torso. Two micro controllers were employed for motion control and computation of sensor information. Their photographs are given in Fig. 6. Two touch sensors were attached on both, i.e. inside and outside, the feet to detect the contact between the feet and the ground. Figure 7 shows the touch sensor attached on the foot.

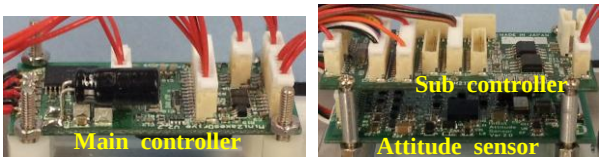

Fig. 6. Controller and attitude sensor

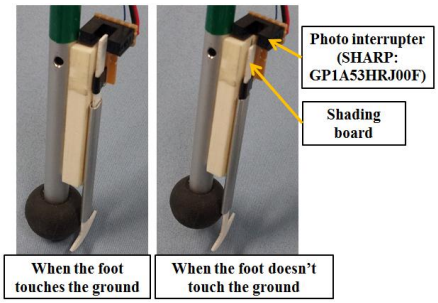

Fig. 7. Touch sensor on the foot

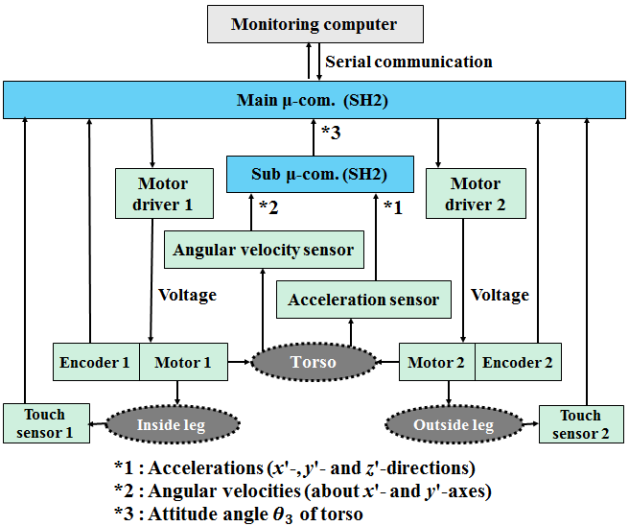

Fig. 8. System configuration of the experimental robot

3.2 System configuration

Figure 6 shows the system configuration of the experimental robot. The robot has two embedded controllers. The main controller is for motor control, and the other, sub controller, is for the attitude sensor. They are connected by CAN communication channel with each other. Besides, the information about motion and sensors is transferred from the main controller to a monitoring computer outside the robot through serial communication channel.

State of the robot is recognized by values of two touch sensors. The angle of the torso, θ_3, is achieved by the sub controller and the attitude sensor that measures the acceleration and angular velocity [5]. This angle is sent to main controller and used for motion control. From the encoders of motors, relative angles between the torso and each leg are measured. The absolute angle of each leg, θ_1 and θ_2, are computed with the attitude angle of the torso and two encoder values, which is used in the feedback control for walking. While the robot moves, all sensor information is sent to monitoring computer in real time. The sampling time of the motor control is set to 1 [ms]. The frequency of communication between main controller and the monitoring computer is set to 100 [Hz].

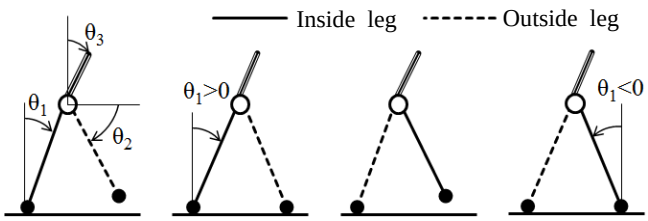

(a)Inside leg is stance leg (b)Both legs are stance leg (θ_1>0) (c)Outside leg is stance leg (d)Both legs are stance leg (θ_1<0)

Fig. 9. The states of the experimental robot

4 WALKING EXPERIMENT

The developed robot system with the proposed method has been confirmed through experiments of walking on the horizontal ground.

4.1 Motion control for walking experiment

In simulation, the stance-leg was assumed to leave from the ground at the moment of the touchdown. However, in the actual walking motion, there exists the period that both legs are in stance state. Therefore, motion control method for the real robot needs to be modified as follows. Walking motion of the real robot is divided into four states according to the values of the touch sensors and the angle of the legs as shown in Fig. 9. The states are as follows.

(a) The inside leg is stance leg.
(b) The outside leg is stance leg.
(c) The both legs are stance legs and θ_1 is positive.
(d) The both legs are stance legs and θ_1 is negative.

Therefore, different control methods are applied according to the states as follows.

In the state (a) or (b), the control torques τ_1 and τ_2 are given as follows

$$\tau_1 = -k_3^p(\theta_{3d} - \theta_3), \tag{13}$$

$$\tau_2 = k_2^p(\theta_{2d} - \theta_2). \tag{14}$$

Where k_2^p and k_3^p denote the control gains. The θ_{2d} and θ_{3d} denote the desired angles.

In the state (c) or (d), the control torques τ_1 and τ_2 are given as follows

$$\tau_1 = k_2^p(\theta_{1d} - \theta_1), \tag{15}$$

$$\tau_2 = -k_3^p(\theta_{3d} - \theta_3). \tag{16}$$

The θ_{1d} denotes the desired angle.

© ISAROB 2013

The control torques are generated at the motors by the PWM (Pulse Width Modulation) signals from the main controller.

4.2 Experimental conditions

The initial posture and velocity is required for the robot when it starts its motion. In order to endow the robot with the same condition through the experiments, a special frame with pushing device was prepared. Besides, the contact between the swing-leg and the ground is occurred when the swing-leg passes through the angle of stance-leg because the length of both legs is same. To solve the problem, the blocks for feet are set on the ground as shown in Fig. 10.

4.3 Experimental result

The appropriate control gains had been found through experiments with the manner of trial and error. Resultantly, it has been observed that the robot can walk on the horizontal ground with the proposed method. The successive scene of the walking motion is shown in Fig. 10. It was captured with a high speed camera (CASIO: EX-FH25). The change of the angles θ_1, θ_2, θ_3 and the values of touch sensors are given in Fig. 11.

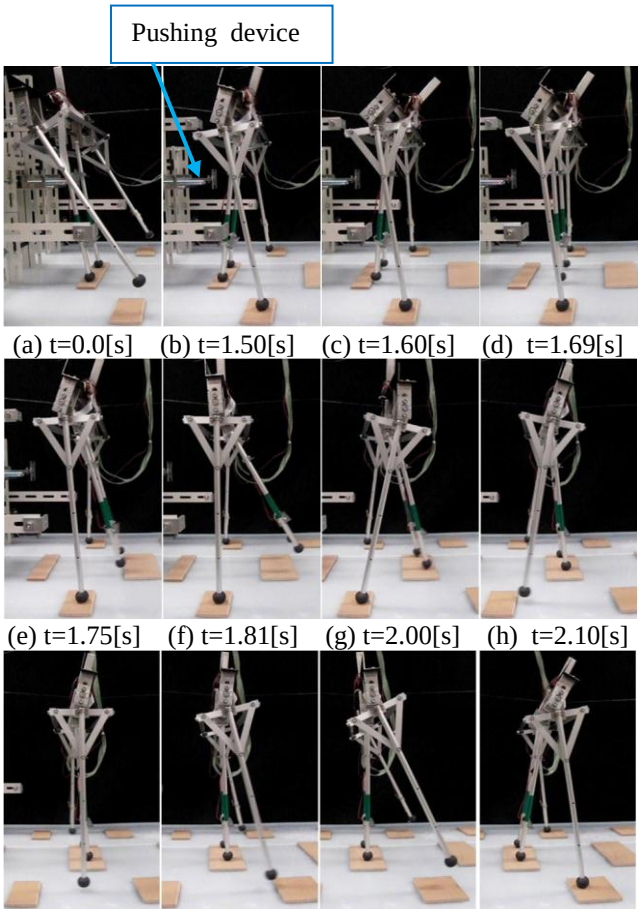

(a) t=0.0[s] (b) t=1.50[s] (c) t=1.60[s] (d) t=1.69[s]
(e) t=1.75[s] (f) t=1.81[s] (g) t=2.00[s] (h) t=2.10[s]
(i) t=2.19[s] (j) t=2.25[s] (k) t=2.31[s] (l) t=2.56[s]

($\theta_{1d} = -12$[deg], $\theta_{2d} = 78$[deg], $\theta_{3d} = 5$[deg], $k_2^p = 0.20\, k_3^p = 0.30$)

Fig. 10. Walking motion of experiment

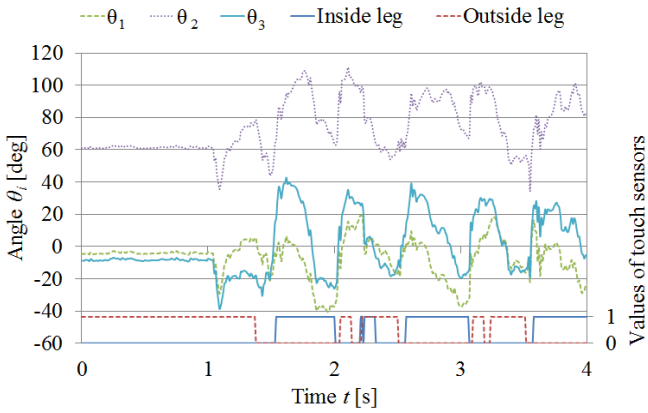

Fig. 11. The change of the joint angles and the values of touch sensors

5 CONCLUSION

The motion control based on passive walking theory had been investigated for biped walking on the horizontal ground. Considering the simulation results, the real robot system was developed. From experiments, it was found that there exists considerable difference between the ideal touchdown and that of real robot. Moreover, it adversely affects proper interchange between legs during touchdown. To cope with the problem, the walking motion was divided into four states. And the appropriate control algorithm for each state was applied in this paper. Resultantly, it was confirmed that the robot can walk on the horizontal ground with the proposed method.

The proposal of control algorithm for more stable walking and that for biped robot with knee joint will be carried out as future works.

REFERENCES

[1] Ono K and Liu R (2002), Optimal Biped Walking Locomotion Solved by Trajectory Planning Method. Journal of Dynamic Systems 124:554–565

[2] McGeer T (1990), Passive Dynamic Walking. The International Journal of Robotics Research 9:2:62-82

[3] Narukawa T, Takahashi M and Yoshida K (2010), Efficient waling with optimization for a planar biped walker with a torso by hip actuators and springs. Robotica 29:641–648

[4] Tani K, Okamoto S, Lee JH and Koike H (2012), Simulations on Motion Control and Development of Biped Walking Robot. Proceeding of the International MultiConference of Engineers and Computer Scientists 2012 2:916-919

[5] Ickowzcy E (2011), Design and Control of a Three-Wheeled Personal Vehicle with Active Suspension for Rough-Terrain Applications.

© ISAROB 2013

The Eighteenth International Symposium on Artificial Life and Robotics 2013 (AROB 18th '13),
Daejeon Convention Center, Daejeon, Korea, January 30-February 1, 2013

Sliding mode control of a quad rotor helicopter using nonlinear sliding surface

Bambang Sumantri[1,2], Naoki Uchiyama[1], Shigenori Sano[1], and Yuma Kawabata[1]

[1]Toyohashi University of Technology, Japan
[2]Electronic Engineering Polytechnic Institute of Surabaya, Indonesia
[1]bambang@eepis-its.edu

Abstract: In this paper, a sliding mode controller (SMC) based on a nonlinear sliding surface (NSS) is designed for controlling a quad rotor helicopter (quadrocopter). It is a well-known that a low overshoot can be achieved with a cost of longer settling time, although a shorter settling time is needed for quick response in a quadrocopter system. In the conventional SMC, the sliding surface is designed as a linear surface that provides a constant damping ratio. The value of damping ratio should be adjusted in order to obtain an optimal performance by making a tradeoff between the two criteria; overshoot and settling time. In this paper, an NSS is designed so that the damping ratio of the control system can be varied from its initial low value to a final high value in a finite time. A low value of damping ratio will cause a quick response, and the later high damping ratio will avoid overshoot, and therefore the control performance can be optimized. First, a dynamics model of a quadrocopter is presented. Next, an SMC with an NSS is designed for tracking control of a quadrocopter. The stability of the proposed control system is proved based on the Lyapunov stability theory. The effectiveness of the proposed design is verified by simulation in which comparative results with the conventional linear sliding surface (LSS) is shown. The NSS is more effective compared to the conventional LSS when the disturbances exist.

Keywords: quad rotor helicopter, sliding mode control, nonlinear sliding surface, tracking control.

1 INTRODUCTION

Quadrocopter is a class of vertical takeoff landing unmanned aerial vehicle that uses two pairs of contra-rotating rotors to provide lift and directional motion. Quadrocopter has some advantages compared to conventional helicopter due to its compactness and simple mechanical structure with high maneuverability. The maneuver is provided by just varying the motors' speed. In order to make the quadrocopter fully autonomous and robustly stable to disturbances are still challenging problems because of its high nonlinearity.

Nonlinear control strategies of a quadrocopter have been concerned by many researchers. Mokhtari *et al.* designed a feedback linearization controller combined with an observer to reduce sensors [1]. They applied feedback linearization to control a partial dynamic system based on rotational motion and an observer to construct translational motion information. Guisser *et al.* proposed an input-output feedback linearization algorithm for stabilizing a quadrocopter and tracking a given trajectory in discrete time [2]. Mian and W. Daobo employed feedback linearization coupled with a PD controller to control translation motion and a backstepping-based PID nonlinear controller for rotational motion [3].

Saturation nonlinearity is also concerned by some researchers. Kendoul *et al.* and Castilo *et al.* proposed a nested saturation strategy for stabilizing a quadrocopter [4][5]. A nested saturation approach was designed based on a priori input bounds of a quadrocopter [6]. This control strategy was designed for stabilizing the attitude of a quadrocopter. Cruz *et al.* used a nested saturation strategy for stabilizing the quadrocopter in a given trajectory [7].

In a real application, a control system of a quadrocopter must be robust to uncertain disturbance such as wind gusting. The SMC is well known as a robust control strategy, and has been applied to a quadrocopter. Yokoyama *et al.* designed a velocity tracking control by using an SMC together with a backstepping method [8]. The robustness of the controller was proved by simulation under a gust of wind. Problems of unmatched disturbance and chattering have been concerned in developing an SMC. Vega *et al.* designed a robust SMC by designing a disturbance estimator [9]. They used a first-order differentiator called a super-twisting algorithm for estimating aerodynamic forces.

As a high speed dynamic system in an uncertain environment, a good control strategy of quadrocopter should be designed to settle its body quickly without any overshoot or oscillation under a disturbance. It is well known that a low overshoot can be achieved with a cost of longer settling time, although a shorter settling time is needed for quick response. Hence, the value of damping ratio should be adjusted in order to obtain an optimal performance by making a tradeoff between the two criteria; overshoot and settling time. In this paper, an NSS is designed so that the damping ratio will be changed from its

© ISAROB 2013

initial low value to a final high value at a finite time. This NSS is designed based on the algorithm presented in [10]. An SMC with an NSS is employed for stable tracking control of a quadrocopter. The performance and robustness of the proposed controller is proved by simulation. A comparison with a conventional SMC is presented.

2 MODELING OF QUADCOPTER

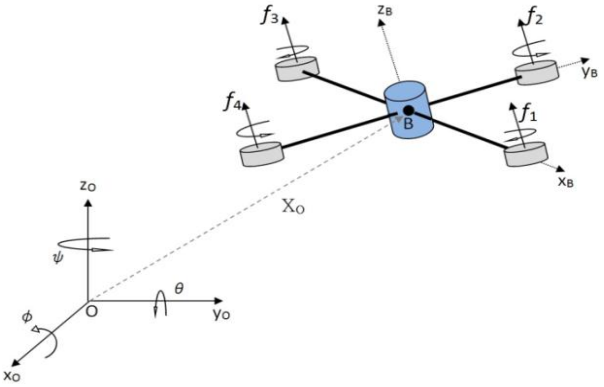

Fig. 1. Coordinate frame of quadrocopter

The position of a quadrocopter, $X_0 = [x, y, z]^T$, is a coordinate position of the centre of gravity of the quadrocopter ("B") with respect to the earth frame ("O") as shown in **Fig. 1**. Its attitude is represented by three angles, $\Theta = [\phi, \theta, \psi]^T$, which are roll, pitch and yaw, respectively. The coordinate position and attitude of the quadrocopter are described in the earth frame, although they are measured in the body frame by using sensors attached to the body of the quadrocopter. Denoting the linear and angular velocities in the earth frame by $\dot{X}_0 \in \mathbb{R}^3$ and $\dot{\Theta} \in \mathbb{R}^3$, respectively, and those in the body frame by $V \in \mathbb{R}^3$ and $\omega \in \mathbb{R}^3$, respectively, we have the following relation:

$$\dot{X}_0 = RV \tag{1}$$
$$T\dot{\Theta} = \omega \tag{2}$$

$$R = \begin{bmatrix} -s\phi s\theta s\psi + c\theta c\psi & -c\phi s\psi & s\phi c\theta s\psi + s\theta c\psi \\ s\phi s\theta c\psi + c\theta s\psi & c\phi c\psi & -s\phi c\theta c\psi + s\theta s\psi \\ -c\phi s\theta & s\phi & c\phi c\theta \end{bmatrix};$$
$$T = \begin{bmatrix} c\theta & 0 & -c\phi s\theta \\ 0 & 1 & s\phi \\ s\theta & 0 & c\phi c\theta \end{bmatrix}$$

where s and c denote sinus and cosines, respectively.

The dynamics of the quadrocopter can be derived by the Newton's second law as follows:

$$\boldsymbol{m}\ddot{X}_0 = \sum F_{ext} \tag{3}$$
$$I\dot{\omega} = -\omega \times I\omega + \sum T_{ext} \tag{4}$$

where $\boldsymbol{m} \in \mathbb{R}^{3x3}$; $I \in \mathbb{R}^{3x3}$; $\sum F_{ext} \in \mathbb{R}^3$ and $\sum T_{ext} \in \mathbb{R}^3$ are the mass matrix, the inertia matrix, the vector of total external forces, and the vector of total external torques, respectively. Eq. (3) can be written as:

$$\begin{bmatrix} m & 0 & 0 \\ 0 & m & 0 \\ 0 & 0 & m \end{bmatrix} \begin{bmatrix} \ddot{x} \\ \ddot{y} \\ \ddot{z} \end{bmatrix} = \begin{bmatrix} s\phi c\theta s\psi + s\theta c\psi \\ -s\phi c\theta c\psi + s\theta s\psi \\ c\phi c\theta \end{bmatrix} u_1 + \begin{bmatrix} 0 \\ 0 \\ -mg \end{bmatrix} \tag{5}$$

where m, g and $u_1 = f_1 + f_2 + f_3 + f_4$ are the total mass of quadrocopter, the gravitational acceleration and the resulting thrust of the four rotors, f_1, f_2, f_3 and f_4, respectively. Eq. (4) is the rotational dynamics of the quadrocopter. Substituting Eq. (2) into Eq. (4), we have

$$I(\dot{T}\dot{\Theta} + T\ddot{\Theta}) = -T\dot{\Theta} \times IT\dot{\Theta} + \sum T_{ext} \tag{6}$$

Eq. (6) leads to

$$J\left[\ddot{\phi}, \ddot{\theta}, \ddot{\psi}\right]^T = [K_1, K_2, K_3]^T + [u_2, u_3, u_4]^T \tag{7}$$

$$J = \begin{bmatrix} I_x c\theta & 0 & -I_x c\phi s\theta \\ 0 & I_y & I_y s\phi \\ I_z s\theta & 0 & I_z c\phi c\theta \end{bmatrix};$$
$$K_1 = (I_x + I_y - I_z)\dot{\phi}\dot{\theta}s\theta + (-I_x + I_y - I_z)\dot{\phi}\dot{\psi}s\phi s\theta + (I_x + I_y - I_z)\dot{\theta}\dot{\psi}c\phi c\theta + (I_y - I_z)\dot{\psi}^2 s\phi c\phi c\theta;$$
$$K_2 = (-I_y + (I_z - I_x)c2\theta)\dot{\phi}\dot{\psi}c\phi + (I_z - I_x)(\dot{\phi}^2 - \dot{\psi}^2 c^2\phi)s\theta c\theta;$$
$$K_3 = (-I_z + I_x - I_y)\dot{\phi}\dot{\theta}c\theta + (I_z + I_x - I_y)\dot{\phi}\dot{\psi}s\phi c\theta + (I_z - I_x + I_y)\dot{\theta}\dot{\psi}c\phi s\theta - (I_x - I_y)\dot{\psi}^2 s\phi c\phi s\theta;$$

where I_x, I_y and I_z are the moment of inertia of the quadrocopter about x, y and z axes, and $u_2 = (f_4 - f_2)L$, $u_3 = (f_1 - f_3)L$ and $u_4 = (-f_1 + f_2 - f_3 + f_4)D$ are torques resulting from the rotors that cause roll, pitch and yaw motion, respectively. L is the distance of rotor to the centre of gravity, D is the anti-torque coefficient. From Eqs. (5) and (7), the dynamics model is written as

$$\begin{bmatrix} \boldsymbol{m} & 0_{3x3} \\ 0_{3x3} & J \end{bmatrix} \begin{bmatrix} \ddot{x} \\ \ddot{y} \\ \ddot{z} \\ \ddot{\phi} \\ \ddot{\theta} \\ \ddot{\psi} \end{bmatrix} + \begin{bmatrix} 0 \\ 0 \\ m\,g \\ -K_1 \\ -K_2 \\ -K_3 \end{bmatrix} = \begin{bmatrix} (s\phi c\theta s\psi + s\theta c\psi)u_1 \\ (-s\phi c\theta c\psi + s\theta s\psi)u_1 \\ c\phi c\theta u_1 \\ u_2 \\ u_3 \\ u_4 \end{bmatrix} \tag{8}$$

For notational simplification, Eq. (8) is written as

$$M\ddot{X} + C = U \tag{9}$$

3 NONLINEAR SLIDING MODE CONTROL

To design an NSS, the original dynamics model in Eq. (9) is transformed into a regular form as follows:

© ISAROB 2013

$$\dot{z}_1(t) = A_{11}z_1(t) + A_{12}z_2(t)$$
$$\dot{z}_2(t) = A_{21}z_1(t) + A_{22}z_2(t) + B_2u(t) + \rho_d \quad (10)$$

where $Z = [z_1, z_2]^T = T_r X$, $z_1 \in \mathbb{R}^{n-l}$, $z_2 \in \mathbb{R}^l$, T_r is a matrix transforming X into Z, $B_2 \in \mathbb{R}^{lxl}$, l is the number of the inputs, and $\rho_d \in \mathbb{R}^l$ is an estimated disturbance vector. By introducing the disturbance term, Eq. (9) leads to

$$z_1 = [x \quad y \quad z \quad \phi \quad \theta \quad \psi]^T$$
$$z_2 = [\dot{x} \quad \dot{y} \quad \dot{z} \quad \dot{\phi} \quad \dot{\theta} \quad \dot{\psi}]^T \quad (11)$$

$$\dot{z}_1 = z_2$$
$$\dot{z}_2 = u(t) + \rho_d \quad (12)$$

where $u(t) = M^{-1}(-C + U)$ as a synthetic input. With regard to the matrices in Eq. (10), $A_{11} = A_{21} = A_{22} \in 0^{6x6}$ are null matrices, and $A_{12} = B_2 = I^{6x6}$ are the identity matrices.

3.1. Nonlinear sliding surface design

The sliding surface is designed as a nonlinear function.

$$s = [F - \Psi P \quad I][e_1 \quad e_2]^T \quad (13)$$

where e_1 and e_2 are tracking error vectors of z_1 and z_2 to desired trajectories z_{1d} and z_{2d}. The matrix $\Psi = \mathrm{diag}(\Psi_i)$, $i = 1,2,..,l$, consists of nonlinear functions as follows:

$$\Psi_i = -\beta_i \frac{\exp(k\|e_i\|)-1}{\exp(\|e_i\|)}, \; e_i \in e_1 \quad (14)$$

where $\beta_i > 0$ and $k > 0$. Next, the control input that considers the system stability will be designed based on the Lyapunov stability theory.

3.2 Stability analysis

Let us define a candidate of the Lyapunov function as

$$V = 0.5s^T s \quad (15)$$

Differentiating Eq. (15) and considering Eq. (13), we have

$$\dot{V} = s^T\left(-\dot{\Psi}Pe_1 + (F - \Psi P)\dot{e}_1 + \dot{e}_2\right) \quad (16)$$

The tracking errors are

$$e_1 = z_1 - z_{1d}$$
$$e_2 = z_2 - z_{2d} \quad (17)$$

By differentiating Eq. (17) and substituting it into Eq. (16) together with dynamics in Eq. (12), the first derivative of the Lyapunov function can be written as

$$\dot{V} = s^T\left(-\dot{\Psi}Pe_1 + (F - \Psi P)\dot{e}_1 + u(t) + \rho_d - \dot{z}_{2d}\right) \quad (18)$$

Designing the control input $u(t)$ as

$$u(t) = -(F - \Psi P)\dot{e}_1 - Ks - Q\mathrm{sign}(s) + \dot{\Psi}Pe_1 + \dot{z}_{2d} \quad (19)$$

where $Q \in \mathbb{R}^{6x6}$ is a positive definite matrix, and substituting Eq. (19) into Eq. (18), we have

$$\dot{V} = s^T(-K\,s - Q\,\mathrm{sign}(s) + \rho_d) \quad (20)$$

If the minimum eigenvalue of Q is greater than the norm of ρ_d and $K \in \mathbb{R}^{6x6}$ is positive definite, then $\dot{V} < 0$, and hence the control input in Eq. (19) will stabilize the system in Eq. (12).

By substituting the control input in Eq. (19) into Eq. (12) and considering ρ_d as the unknown external disturbance, the closed loop dynamics of the system is

$$\ddot{e}_1 + (F - \Psi P)\dot{e}_1 + Ks + Q\mathrm{sign}(s) - \dot{\Psi}Pe_1 + \rho_d = 0 \quad (21)$$

Because $F \in \mathbb{R}^{6x6}$ and $P \in \mathbb{R}^{6x6}$ are positive definite, the damping ratio of the closed loop dynamics will change according to the magnitude of e_1. If the error is relatively large, then the damping ratio will be reduced, and therefore the system will give faster response toward sliding surface. If the system is close to the sliding surface then the error will be reduced, and the damping ratio will be increased, and therefore the response will be slower and overshoot can be reduced. Next, the effectiveness of the SMC using the NSS in Eq. (19) will be verified by simulation and compared with a conventional linear sliding surface.

4 SIMULATION RESULTS

The parameters used in this simulation as follows are those for the experimental system in our laboratory.

$m = 0.2039\mathrm{Kg}$; $I_x = I_y = 5.136 \times 10^{-3}\ \mathrm{Kg.m^2}$;
$I_z = 1.016 \times 10^{-2}\ \mathrm{Kg.m^2}$; $L = 0.212\mathrm{m}$; $g = 9.807\mathrm{m.s^{-2}}$.

The desired trajectories for $[x, y, z, \psi]^T$ are given as $[x_d, y_d, z_d, \psi_d]^T$, and from Eq. (5), desired angles $[\phi_d, \theta_d]^T$ for $[\phi, \theta]^T$ can be calculated as follows:

$$\phi_d = \mathrm{atan}\left(\frac{\ddot{x}_d \sin(\psi_d) - \ddot{y}_d \cos(\psi_d)}{\ddot{z}_d + g}\right)$$

$$\theta_d = \mathrm{atan}\left(\frac{\ddot{x}_d \cos(\psi_d) + \ddot{y}_d \sin(\psi_d)}{\sqrt{\left(\ddot{x}_d \sin(\psi_d) - \ddot{y}_d \cos(\psi_d)\right)^2 + (\ddot{z}_d + g)^2}}\right)$$

The control parameters are as follows:

$F = \mathrm{diag}\{6,6,50,18,18,10\}$; $P = \mathrm{diag}\{10,10,10,10,10,10\}$;

$K = \text{diag}\{1.2,1.2,40,10,10,3\}$; $\beta_i = [20,20,20,30,30,20]^T$;
$Q = \text{diag}\{0.01,0.01,0.01,0.01,0.01,0.01\}$; $k = 4$.

Setting β_i to zero of the control strategy in Eq. (19) leads to a conventional LSS. Both the NSS and the LSS were applied to the tracking control to the same desired trajectory. The result is shown in **Fig. 2**, in which both the NSS and the LSS provides the similar performance.

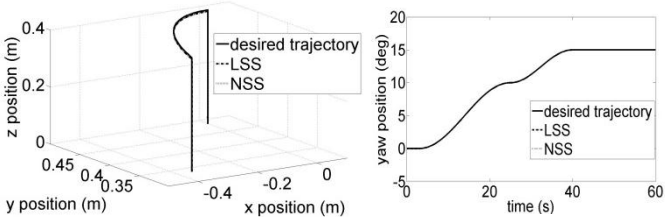

Fig. 2 Helicopter trajectory in NSS and LSS.

The comparison results after applying the step disturbance to the control inputs $[u_1; u_2; u_3; u_4]$ whose values are $[0.5; 0.05; -0.05; 0.005]$, respectively, are shown in **Fig. 3**.

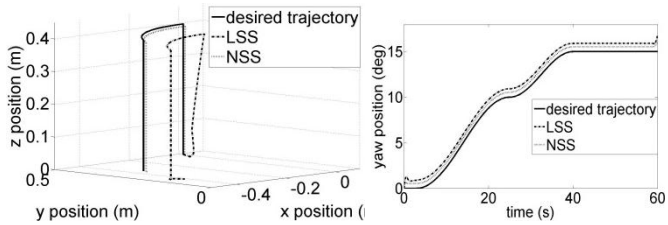

Fig. 3 Helicopter trajectory in NSS and LSS under disturbance

The NSS can track the trajectory with smaller error compared to the LSS. The nonlinear function changes the controller gain according to the error magnitude, and provides the robust performance. The control inputs in **Fig. 3** are shown in **Fig. 4**. The control input magnitudes in the NSS and the LSS show no significant difference.

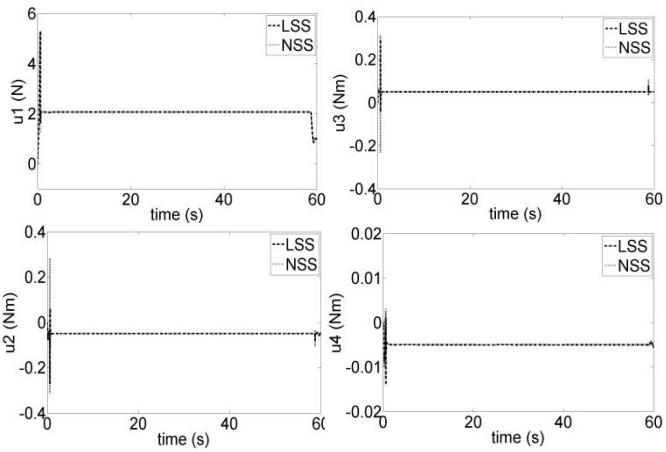

Fig. 4 Control input in NSS and LSS under disturbance.

5 CONCLUSION

A sliding mode controller with a nonlinear sliding surface is designed for robust tracking control of a quadrocopter. The control system stability is proved by the Lyapunov stability theory. The effectiveness of the NSS is proved by simulation. Future work verifies the effectiveness of the NSS by experiment in which the practical disturbance and signal noise exist.

REFERENCES

[1] A. Mokhtari and A. Benallegue (2004), Dynamic Feedback Controller of Euler Angles and Wind parameters estimation for a Quadrotor Unmanned Aerial Vehicle. Proceedings of the 2004 IEEE International Conference on Robotics & Automation, New Orleans, LA, April 2004, pp. 2359-2366.

[2] M. Guisser, H. Medromi, J. Saadi and H. Ifassiouen (2006), Stabilization and Trajectory Tracking in Discrete-Time of an Autonomous Four Rotor Mini-Rotorcraft. Proceedings of Second International Symposium on Communications, Control and Signal Processing, Marrakech, Morocco, 2006.

[3] A. A. Mian and W. Daobo (2008), Modeling and Backstepping-based Nonlinear Control Strategy for a 6 DOF Quadrotor Helicopter. Chinese Journal of Aeronautics, vol. 21, pp. 261-268.

[4] F. Kendoul, D. Lara, I. Fantoni and R. Lozano (2006), Nonlinear control for systems with bounded inputs: Real-time embedded control applied to UAVs. Proceedings of the 45th IEEE Conference on Decision & Control, San Diego, CA, USA, December 13-15 2006, pp. 5888-5893.

[5] P. Castillo, A. Dzul and R. Lozano (2004), Real-Time Stabilization and Tracking of a Four-Rotor Mini Rotorcraft. IEEE Transactions on Control Systems Technology, July 2004, pp. 510 - 516.

[6] J. Guerrero-Castellanos, N.Marchand, A.Hably, S.Lesecq and J.Delamare (2011), Bounded Attitude Control of Rigid Bodies: Real-time Experimentation to a Quadrotor Mini-Helicopter. Journal of Control Engineering Practice, vol. 19, p. 790–797.

[7] S. Salazar-Cruz, A. Palomino and R. Lozano (2005), Trajectory tracking for a four rotor mini-aircraft. Proceedings of the 44th IEEE Conference on Decision and Control, and the European Control Conference, Seville, Spain, December 12-15, 2005, pp. 2505-2510.

[8] M. Yokoyama and K. Fujimoto (2009), Velocity Tracking Control of a Four-Rotor Mini Helicopter. Motion and Vibration Control, Springer, Netherlands, 2009, pp. 335-344.

[9] L. Luque-Vegan, B.Castillo-Toledo and A. G.Loukianov (2012), Robust Block Second Order Sliding Mode Control for a Quadrotor. Journal of The Franklin Istitute, Elsevier, vol. 349, pp. 719-739.

[10] B. Bandyopadhyay, F. Deepak and K.-S. Kim (2009), Sliding Mode Control Using Novel Sliding Surfaces. Springer, Chennai, India.

© ISAROB 2013

The Eighteenth International Symposium on Artificial Life and Robotics 2013 (AROB 18th '13),
Daejeon Convention Center, Daejeon, Korea, January 30-February 1, 2013

Design of a user support system for event addition based on route search using schedule information

Hiroki Imamura[1] and Hiroyuki Nishiyama[1]

[1] Tokyo University of Science, 2641 Yamazaki, Noda-shi, Chiba-ken, Japan
(Tel:+81-47122-1106; Fax:+81-47122-1106)
(j7408022@ed.tus.ac.jp)

Abstract: In recent years, the ability to manage schedules using a mobile device equipped with a touch panel has increased. However, when one wishes to add a new event to the schedule book, taking into account the transit time of an existing event, it is necessary to switch to another application or website. In this paper, we design a support system for additional events to automatically determine whether the new event can be added. If this is impossible, the system proposes a time range that can have events added.

Keywords: mobile device, schedule, context, route search, event addition

1 INTRODUCTION

The recent widespread use of smartphones has encouraged efforts to provide context-aware services (e.g., i concier[1] and Google Now[2]). Here, "context" encompasses various meanings: user context, physical context, computing context, and time context. A context-aware service provides a user with the desired results, depending on the changing context. To achieve this, you must know what, where, and when to understand the current context, but the spread of smartphones is resolving this issue. The smartphone is equipped with various sensor systems (e.g., a GPS sensor, an acceleration sensor, and a touch sensor) and a camera function. In addition, we can easily develop applications that can acquire, collect, and disseminate information obtained from each function.

How to manage time for the individual is another important issue. We have complex schedules, and storing them is difficult. We have to manage events in the calendar and schedule book. With the recent development of an environment using networked computers, we can check and change a schedule anytime and anywhere by using the schedule management system in the smartphone. We believe that this kind of demand is increasing and will continue to increase in the future. In addition, by using the existing scheduling information, we can understand what should be done where and when. When planning an additional appointment, it is necessary to consider the transit time. To determine the transit time, we may use empirical data or use a web route search service. The former approach is less accurate, and the latter is time consuming.

With this as background, the purpose of this study is to design a system that supports the addition of an event while considering existing events and that can quickly add events. To achieve this, our system includes schedule management, which automatically determines whether new events can be added. The system is more accurate than an empirical determination and less troublesome than using a web route search service. In addition, if the event cannot be added, our system searches for times at which it can be added and proposes candidate them.

2 MOTIVATION

Mobile phones are used in many different situations. Therefore, research has focused on gathering information that can be observed using mobile phones with added sensors, and on the use of the collected information to suit the user 's situation. For example, Kamisaka et al. observed actual daily mobile phone user operations with minimal interference for six months[3]. They then demonstrated that machine learning could be used to predict future operations based on the collected information[4]. Additionally, they proposed a system to recommend applications, according to the situation, based on collected information and application usage. In addition, Kozawa et al. proposed a method for extracting prior advice from the web[5]. The method first identifies whether or not a given sentence provides advice. If the sentence is identified as advice, the method then identifies whether or not the sentence constitutes prior advice. Matsuura et al. created a design for a scheduling support system[6]. Their method extracts Web information based on position information and information provided by schedule management. It is possible to provide relevant information after asking the user for information, such as providing a map of the vicinity of a specified destination and the travel route from the user 's current position to that destination. The user can obtain various information related to the schedule without having to search a Web site. In addition, acquiring position information provided by GPS enables providing in-

© ISAROB 2013

formation that reflects the current time and the user's location.

In this paper, we collect the history of a user using the system as a life-log. We have achieved a decision-support system for individuals to use when adding events, which takes into account the transit time for events on the schedule that have already been registered.

3 SYSTEM DESIGN AND IMPLEMENTATION

This section provides an overview of the system's additional support events, the function of each module, and the internal algorithms.

3.1 System Overview

In this study, we design a mobile application system with the function of schedule management, route searching, and support for adding events. For schedule management, we created a calendar that can be synchronized with Google Calendar. For route searching, the system performs a route search based on the event information that the user has registered and displays the information necessary to reach the destination and to assist the action of the user. In addition, it accumulates a life-log search history in a local database stored in the high-performance mobile phone that is designed to speed up the search. To support adding events, the system determines whether a new event can be added. If this is not possible, the system proposes a time when the event can be added.

Figure 1 illustrates using the system.

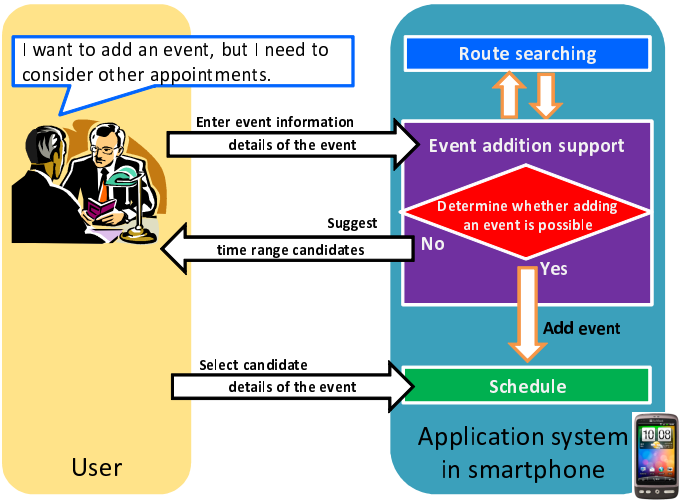

Fig. 1. Use of the system

3.2 Implementation environment

This system is implemented on an HTC Desire SoftBank X06HT equipped with Android 2.2 using Java language. The development environments used Eclipse3.6 (Helios) with Eclipse plug-ins and the Android SDK distributed by Google. For the local database we used SQLite, which is a standard feature on Android devices.

3.3 System configuration

Figure 2 illustrates the overall system configuration.

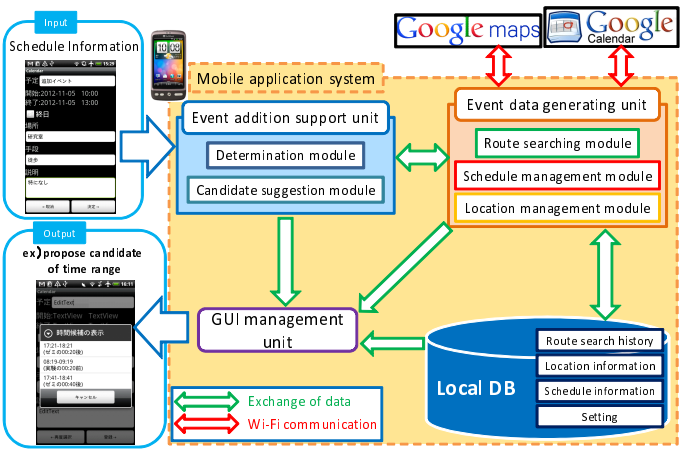

Fig. 2. System configuration

3.4 Schedule management module

The schedule management module manages event information including the title of the event, the location, the start time, the end time, and the means of transportation.

3.5 Location management module

The module is implemented to enable the user to register and manage location information while looking at a map. This module was created in order to reduce the need for typing. Thus, when entering position information into the schedule management module, it is unnecessary to describe the details of the address and buildings. Getting location information uses the location package (android.location) provided with the Android SDK.

3.6 Route searching module

The route searching module displays the daily schedule along with routing information based on the time afforded that takes into account the time margin from the current position, the start time, the end time, the location, and the transportation. Route searching uses the web service provided by Google. Analyzing the html source code of the route search results provides the necessary time, the time required, the departure time, and the arrival time. The time margin has the same meaning as in the Osako et al. study[7], and indicates that there is enough time to prepare the schedule. In addition, the starting point can be selected by the user from the following three.

1. Current position in the GPS information
2. Location that the user has previously registered
3. Position obtained from the schedule information

© ISAROB 2013

The destination point uses position information obtained from the schedule information. Transportation may include car, bicycle, walking, or train. The arrival time is before the scheduled time margin.

3.7 Module to determine whether adding an event is possible

This module checks to determine whether a temporal overlap exists using the route searching module and event information obtained from the schedule management module. If there is no overlap,it is possible to determine additional events from event information stored in the local database. If there is an overlap, the hours of the additional event are calculated using the overlap time and a candidate is proposed.

3.8 Module to propose candidate for time range that can accept an event

When the module determines that it is not possible to add an event, this module proposes a candidate time. Here, a collection of one-day events is referred to as an event group.

Upon calculating the time range in which an event can be added, we perform a two-way case analysis of the location where the new event is to be added.

(a) Pattern to be inserted at the beginning or end of an event group
(b) Pattern to be inserted between events

Case (a) is covered by Eq. (1), which determines the stagger time of the last or first event. We choose the larger of the overlap time or time margin to determine the stagger time. The system proposes the time the user can leave or arrive with a time margin of $T_{Stagger}$.

$$T_{Stagger} = \begin{cases} T_{Overlap} & (T_{Overlap} \geq T_{Margin}) \\ T_{Margin} & (T_{Overlap} < T_{Margin}) \end{cases} \tag{1}$$

Next, we describe Case (b). As an example, assume that you are adding a new event (event z) to existing events (events x and y), as depicted in Fig. 3. The necessary time is defined as the time that you need to consider when you want to add event z. The necessary time is the total of the running time of event z plus the time margin and the travel time between events x and z and the travel time between events z and y. In addition, the time slot between events x and y indicates the time between the start time of event y and the end time of event x.

The system proposes up to three candidate time ranges when the event can be added. Thus, there is a possibility that when the proposals between the same events, the system propose time range biased. To exclude this possibility, it is necessary to consider where new events can be inserted between

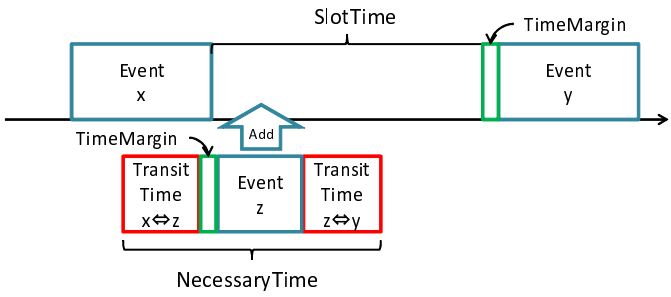

Fig. 3. Adding an event

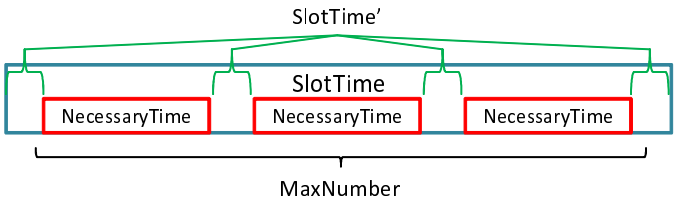

Fig. 4. Maximum number of events that can be added

existing events. Equation 2 gives the maximum number of events that can be added.

$$\begin{aligned} N_{max}(x,y,z) &= \lfloor \frac{T_{Slot}(x,y)}{T_{Necessary}(x,y,z)} \rfloor \\ T_{Necessary}(x,y,z) &= T_{Transit}(x,z) + T_{Transit}(y,z) \\ &\quad + T_{Event}(z) + T_{Margin} \\ T_{Slot}(x,y) &= T_{Start}(y) \quad T_{End}(x) \quad T_{Margin} \end{aligned} \tag{2}$$

To calculate the time range in which an event can be added, we obtain the gap time between the candidates (SlotTime' in Fig. 4). Correcting the value calculated by Eq. (2) so as not to exceed the number of candidates proposed, we obtain the formula for the gap time between the candidates in Eq. (3).

$$\begin{aligned} T'_{Slot}(x,y,z) &= \frac{T_{Slot}(x,y) \quad T_{Necessary}(x,y,z) \times N(x,y,z)}{N(x,y,z)+1} \\ N(x,y,z) &= \begin{cases} N_{Candidate} & (N_{Candidate} < N_{max}(x,y,z)) \\ N_{max}(x,y,z) & (N_{Candidate} \geq N_{max}(x,y,z) > 0) \\ 0 & (otherwise) \end{cases} \end{aligned} \tag{3}$$

Finally, Eq. 4 calculates the start time and end time for

© ISAROB 2013

candidate w-th.

$$\begin{aligned} T'_{Start}(x,y,z,w) &= T_{End}(x) + wT'_{Slot}(x,y,z) \\ &\quad +(w \quad 1)T_{Necessary}(x,y,z) \\ T'_{End}(x,y,z,w) &= T_{Event}(z) + T'_{Start}(x,y,z,w) \end{aligned} \tag{4}$$

4 CONCLUSION

In this paper, we designed a user support system for additional events, taking into account the existing events. It determines the additional events and proposes a time range in which events can be added. This system enables users to schedule new events more smoothly than by conventional decision-making systems. In addition, problems related to determining transit time (such as low precision, or being time-consuming) were addressed in order to facilitate using a life-log. Future work will demonstrate the effectiveness of this system by evaluating the accuracy of the proposed candidates.

REFERENCES

[1] i concier, http://www.nttdocomo.co.jp/service/customize/iconcier/

[2] Google Now, http://www.google.com/landing/now/

[3] Daisuke Kamisaka, Shigeki Muramatsu and Hiroyuki Yokoyama (2008), A Study on Situation-Adaptive Operation-Assisting Method for Mobile Phone. Information Processing Society of Japan SIG Technical Report 2008-UBI-20(110):33-38

[4] Daisuke Kamisaka, Takeshi Iwamoto, Shigeki Muramatsu and Hiroyuki Yokoyama (2009), Long-term Data Analysis and Operation Prediction for Context-Aware UI of Mobile Phones. FIT2009 8(4):23-29

[5] Shunsuke Kozawa, Masayuki Okamoto, Shinichi Nagano, Kenta Cho and Shigeki Matsubara (2011), Advice Extraction from Web for Providing Prior Information Concerning Outdoor Activities. Proceedings of the 4th International Conference on Intelligent Interactive Multimedia Systems and Services (IIMSS 2011):251-260

[6] Hiroshi Matsuura, Tetsuya Tsukamoto and Hiroyuki Nishiyama (2009), Schedule management support system using Web information. IPSJ National Convention 71st

[7] Takashi Osako, Itaru Kuramoto, Yu Shibuya, Yoshihiro Tsujino and Mitsuru Minakuchi (2009), Prior notification technique of tasks/schedules taking account of time margin. Information Processing Society of Japan SIG Technical Report, 1009-HCI-131(4):23-30

The Eighteenth International Symposium on Artificial Life and Robotics 2013 (AROB 18th '13),
Daejeon Convention Center, Daejeon, Korea, January 30-February 1, 2013

The study of walking control with plural cylinder leg robots

Jihao Cao[1] , Feifei Zhang[2] , Masanori Ito[2] and Takumi Yaginuma[3]

[1]Tokyo University of Marine Science and Technology
(Tel: 81-3-5245-7422, Fax:81-3-5245-7422)

[1]M114031@kaiyodai.ac.jp

Abstract: Our goal of this research is to develop a working robot which has a medium level of power and walks with four legs. In our experiment, we used the robot which has two cylinder legs under the concept of multi-cylinder leg. It has very strong structure and it can endure and keep motion under heavy load. Multi-cylinder leg robot can walk any direction and draw any radius circle. In case of two cylinder leg, it can walk forward and backward on a straight or curved course. We are studying the control scheme of walking for this robot, which is put mind especially on smooth and steady movement without rolling, pitching, yawing or heaving motion and keeping the body horizontally. We confirmed the validity of control scheme with experiments.

Keywords: Walking control. Working robot. Cylinder leg.

1 INTRODUCTION

Now, the study of working robot becomes active because there exist very urgent request that robot should be applied, instead of human being to the work at the Fukusima atomic energy generating station where has the high nuclear level and complicated terrain. However, the current technology of crawler-type or wheel-type robots cannot fully work in such condition. Our goal of this research is to develop a working robot which has a medium level of power and walks with four legs. It is thought that the working robot should equip special functions such as for maintenance, management or setting of equipments with using tools. We thought that it was desirable to give robots the function changing their form suitably for work environment and work kinds to get high work performance and suggested the method to environment and the work kinds. In this paper, we refer to the moving mechanism and control of the robot. As well known, robot faces to big reactive force when it is working and it should move stably, carrying heavy goods. We thought a quadruped walking robot which has cylinder for the leg structure is adequate ,and confirmed the basic performances keeping prescribed posture and smooth movement by using the experiment. In the previous paper by Yaginuma[1], He performed a study of geometry and experimental confirmation about the type of the moving cylinder leg for assumed constant speed walking with keeping velocity contour. In this study, based on the results of the previous study we have carried out actual walking with the large scale robot.

2 ROBOT FOR EXPERIMENTS

We constructed each leg with two cylinders. The exper imental apparatus is shown in Fig.1. We equipped this type of leg for front leg of the robot and fixed leg with caster for aft-leg. Although in the previous study, it was a combination of the electric cylinder, we used DDVC hydraulic cylinder for pivoting the main leg and electric cylinder for rocking it. The specifications of the robot are shown in Table.1and Table.2 and Table.3.

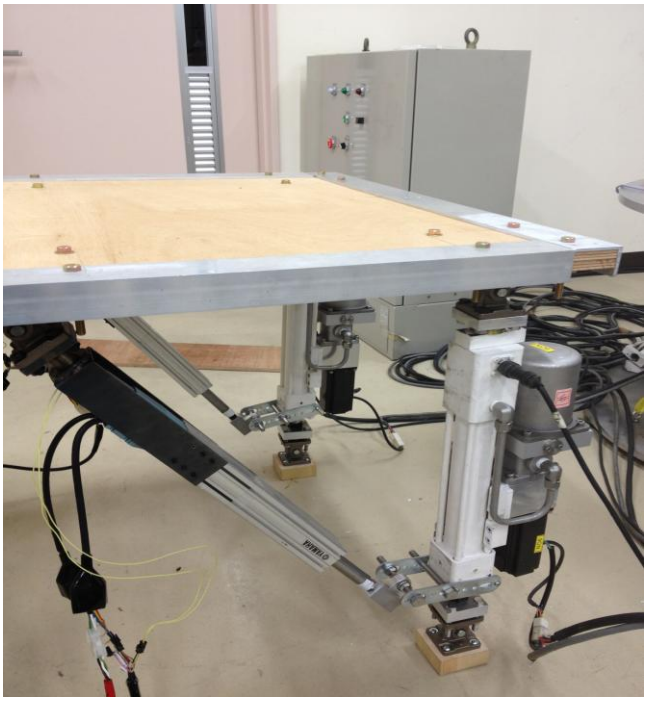

Fig.1 The experimental apparatus

Table1. The main leg cylinder specification

Motor output (kw)		0.4
Speed	Push(mm/sec)	6～75
	Pull(mm/sec)	9～112
Propelling power(N)		1.0
The diameter of a boa		φ40

© ISAROB 2013

Table2. Cylinder specification for rocking

Motor output(W)	30
Speed(mm/sec)	300
Propelling power(N)	64

Table3. The performance of the legs

Height legs(cm)	72
Stride (cm)	12
Cycle(s)	28

2.2 System Configuration

The command signal from a computer is changed into an analog signal through DA board, and is outputted to a driver. Through a driver, Actual speed/position of a cylinder is measured with a sensor and feed-backed to the computer through AD board.

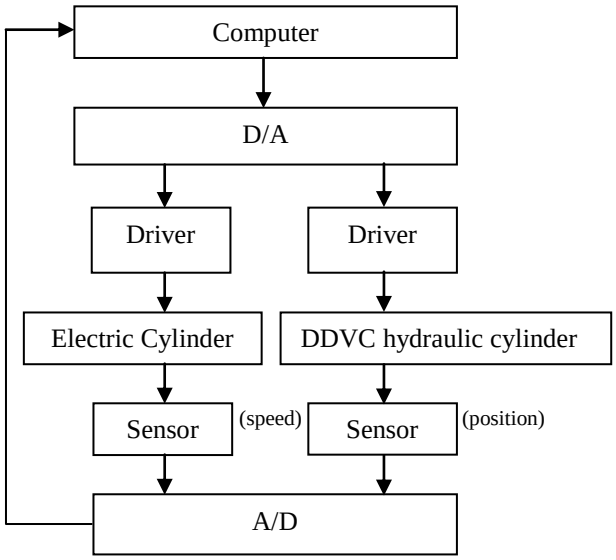

Fig.2 System configuration

3 Walking

3.1walking process

In this study, we assumed constant speed walking with keeping horizontal posture of body plane on a horizontal flat ground as a basic walk.

However we cannot avoid yawing motion caused of the structure.

As shown in previous study, the walking pattern has three mode of walking start, continuous walking and stopping.

3.1.1 Walking start mode

①When it starts walking, lift up the left leg and , move it to the traveling direction with half pitch of walk and lift down on the surface.

②. When left leg land, lift up the right leg and move it to front direction with half pitch of walk. At the same time, move the left leg backward to half pitch of walk.

3.1.2 Continuous walking

After, start motion, the front left leg and a front right leg repeat full pitch motion mutually.

③Stopping

When it stops walking, the landing leg stop the motion at the center of pitch and another leg also moves to center of pitch.

3.2 Walking locus

The human has various walking behavior according to a ground state, when walking on the land. For example, abo ut the motion of leg such as landing-backward moving-floating
forward moving, we set some basic patterns so that a walk of constant speed, horizontal posture and constant height ca n perform smoothly. The pattern is shown in Fig.3.

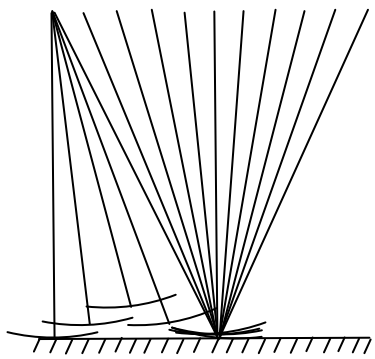

Fig.3 Walking pattern

4 CONTROL

4.1 Walking control

The legs structure of the robot proposed in this study as described above are all the same and same control scheme is applied to both legs. Operation of each leg is determined according to the type of motion of the body.

In this walk control, a speed of operation and locus were patterned from a rising to a start and landing, and the thing which makes a leg expand and contract in the shape of a sine wave was considered. The signal shown in Fig.4 and 5 are the operation of the left leg. With the combination of the signals, the left leg will be lifted in first two(2) seconds, and two cylinders will start motion and reach the peak value in three(3) seconds. Right leg will start motion with the same method at this timing. Continuous walk is performed with this way.

© ISAROB 2013

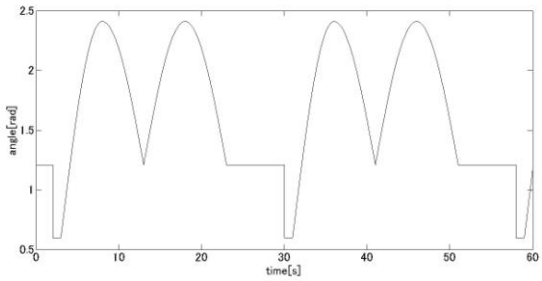

Fig.4 Motion of main cylinder (left leg)

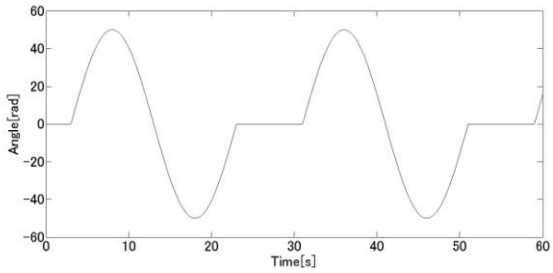

Fig.5 Motion of support cylinder (left leg)

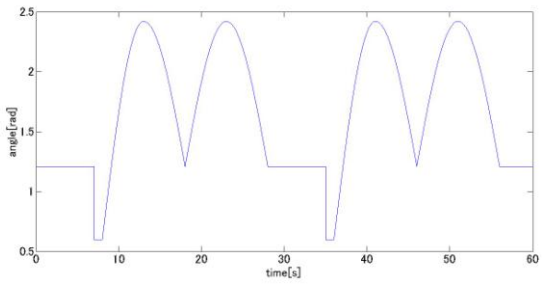

Fig.6 Motion of main cylinder (right leg)

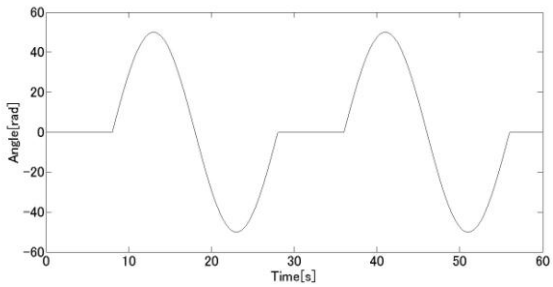

Fig.7 Motion of support cylinder (right leg)

4.2 Control method

When the robot is applied to a constant speed move with a horizontal posture，according to the purpose of the study, the moving pattern of the four (4) legs should be designed in different ways. As a result, the different methods of control are necessary.

In this experiment, PI control was adopted to confirm the walking pattern such as constant velocity contour walk. This control results are shown in Fig.8 and 9.

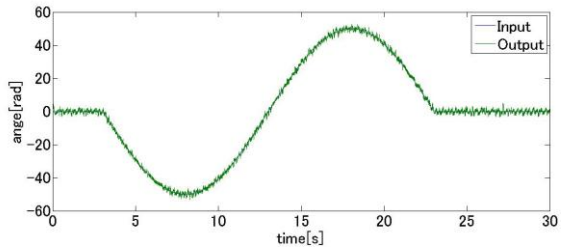

Fig.8 Control result of the left leg

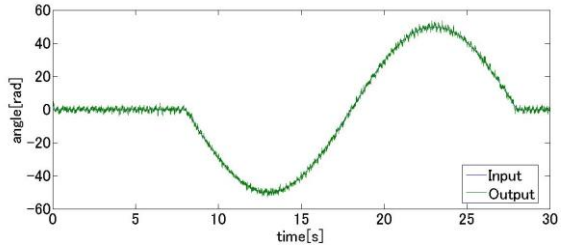

Fig.9 Control result of the right leg

5 CONCLUSION

In this study, we confirmed the results of previous study with actual walking robot. Although there is a little difference on the structure, two cylinder leg worked smoothly and made precise walking following to the pattern. However this is a basic walk and we are thinking to try the walking in actual situation such as not leveled ground, step or place filled with obstacles.

6 REFERENCES

[1] Yaginuma T(2010),Quadruped walking with parallel link legs. Artif Lift Robotics(2010)15:555-559 DOI 10.1007/s10015-010-0868-6

The Eighteenth International Symposium on Artificial Life and Robotics 2013 (AROB 18th '13),
Daejeon Convention Center, Daejeon, Korea, January 30-February 1, 2013

The Ground Reaction Force generation algorithm for tracking the wearer's motion

Sukwoo Lee[1], Jongwon Lee[1], Hyogon Kim[2], Jaeho Jang [2] and Sangdeok Park[2]

[1]University of Science and Technology, Republic of Korea
[2]Korea Institute of Industrial Technology, Republic of Korea
(Tel: 81-31-8040-6348, Fax: 81-31-8040-6310)

[1]sukwoo22@kitech.re.kr

Abstract: This paper explains the desired ground reaction force (GRF) generation algorithm for exoskeleton. Its key point is to generate the desired torque of exoskeleton for tracking the wearer's motion. We can obtain the torque by using the GRF when exoskeleton foot is in contact with the ground. It is not necessary to measure exerted force at contact point. It requires only simple calculation in contrast with inverse dynamics of full body. It can adapt to environment such as flat ground, stairs and uneven surfaces. We present simulation result using our two-leg model, which demonstrates the algorithm is applicable to exoskeleton.

Keywords: Exoskeleton, walking, center of pressure (CoP), zero moment point (ZMP), ground reaction force(GRF).

1 INTRODUCTION

The external forces by the surrounding environment is exerted to the locomotive system During waking. The ground reaction force (GRF) that is one of them has been used for research on control of locomotive system. Satoshi Ito and Haruhisa Kawasaki has been doing research on balance control of the legged system by the method which keeps GRF measured by the force sensor at the foot positive [1]. Since elderly people and persons with hemiplegia may be difficult to maintain balance of their bodies, a wearable lower extremity exoskeleton (LEE) which has been developing at Nanyang Technological University, Republic of Singapore maintain balance instead of wearers by using the zero moment point (ZMP) [2]. The ZMP can be obtained by the GRF measurement of exoskeleton and wearer. The above mentioned control algorithm require force sensor at the ground contact point. Without them, the system cannot adapt to the GRF. But although we install force sensors at all the ground contact point, it is causing complicated calculations because of the number of contact Jacobians. To resolve this issue, Sang-Ho Hyon proposed how to compute the commanded joint torque for a desired contact force without force sensor [3]. As this method is applicable to the exoskeleton, we explain that the method calculate desired ground reaction force for tracking wearer's motion.

2 GAIT OF EXOSKELETON

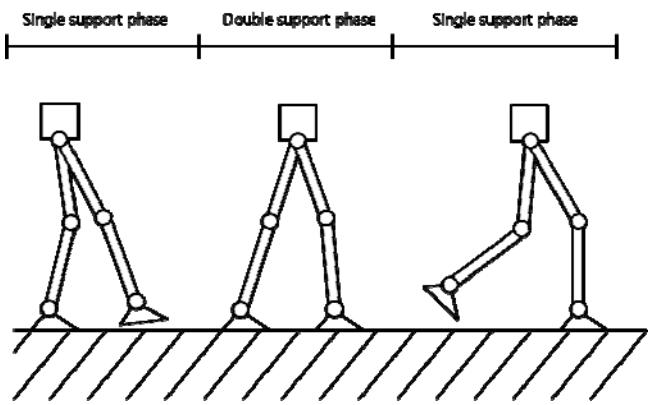

Fig. 1. Gait phases of the exoskeleton. Adapted from [5].

A walking gait of the exoskeleton like figure 1 can be divided into the single support phase and the double support phase [4]. In the single support phase, the only one leg is in contact with the ground. But in the double support phase, both legs are in contact with the ground. The two support phases take place alternately during walking.

Figure 2 shows the connection between ZMP, CoP and GRF in the single support phase. The ZMP introduced in 1968 for the first time is a concept related with dynamics and control of locomotive system [6]. It is the point where the sum of all moments of active forces is equal to zero. If the ZMP trajectory remains within the support area when the locomotive system is walking, gait of the system is stable. The support area is distinguished by the single support phase and the double support phase. In the single

© ISAROB 2013

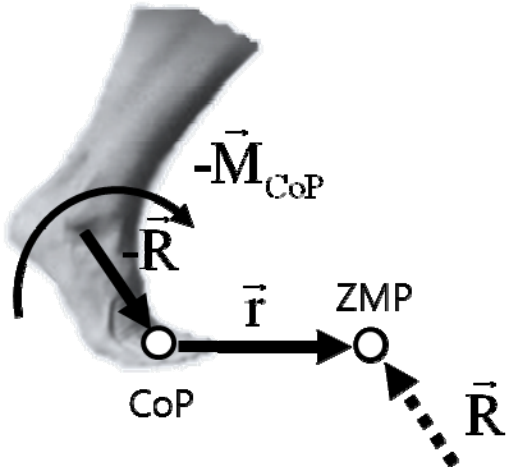

Fig. 2. ZMP, CoP and GRF. Adapted from [6].

support phase, support area is foot surface in contact with ground. In the double support phase, support area is foot surface and the distance between the two feet. And The center of pressure(CoP) is the point on the supporting surface where moment of ground reaction force is zero [7]. If the ZMP is within the support area, the ZMP coincides with CoP. In this paper, we use a concept of ZMP and CoP for calculation of GRF.

3 GRF GENERATION ALGORITHM

The object of our algorithm is to find desired ground reaction force of exoskeleton. Ahead of description of the algorithm, we have to make several assumptions. First, at least one of the feet of the exoskeleton is always in contact with the ground. Second, the acceleration of the exoskeleton seems as that of wearer because the exoskeleton tracks the motion of wearer. Third, ZMP of the exoskeleton always coincides with CoP. Forth, we do not consider swing phase.

3.1 Calculation of GRF

Figure 3 shows Forces exerted to the exoskeleton such as inertia force, gravity force and GRF. Therefore, the sum of the force is as follows:

$$\sum \vec{F} = m\vec{a}$$
$$mg - \vec{R} = m\vec{a} \tag{1}$$

where m is mass of the exoskeleton, $\vec{R}$ is ground reaction force, g is the acceleration of gravity and $\vec{a}$ is the acceleration of the exoskeleton. We can determine the acceleration of exoskeleton provided that we use an accelerometer. In other words, it is possible to calculate desired GRF with accelerometer by using equation (2).

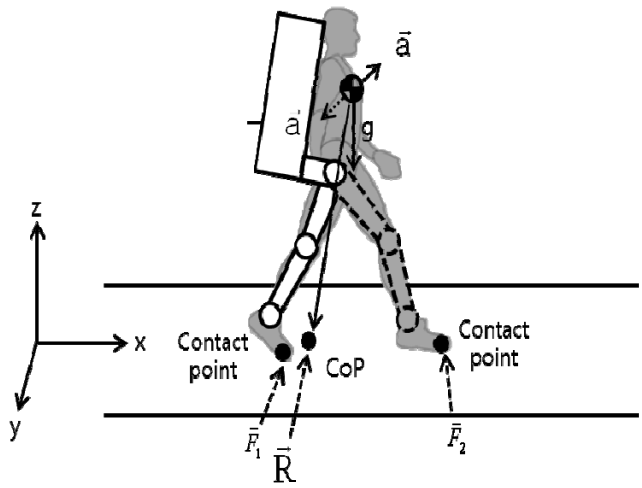

Fig. 3. Forces exerted to the exoskeleton.

$$\vec{R} = m(g - \vec{a}) \tag{2}$$

3.2. Load Distribution in Double Support Phase

In the single support phase and the double support phase, GRF is the same at the CoP of the exoskeleton. But in the double support phase, we have to do load distribution of GRF because both feet are in contact with the ground. Total GRF is sum of GRF at the contact point of feet. If we know GRF and CoP, we can derive (3)

$$\begin{bmatrix} x \\ 1 \end{bmatrix} R_z = \begin{bmatrix} x_1 & x_2 \\ 1 & 1 \end{bmatrix} \begin{bmatrix} \vec{F}_1 \\ \vec{F}_2 \end{bmatrix} \tag{3}$$

where x is distance between CoP and center of mass (CoM), $\vec{R}_z$ is the vertical GRF, x_1 and x_2 are distance between point of application of GRF at the contact point of each foot and CoM. And $\vec{F}_1$ and $\vec{F}_2$ are the vertical GRF at the contact point of feet. CoP can be calculated as

$$x = \frac{\sum_i^n x_i F_i}{\sum_i^n F_i} \tag{4}$$

But as we do not know the distributed force F_i, we could not calculate CoP. Instead, CoP can be replaced by ZMP because ZMP remain within the support area. ZMP can be calculated as

$$x_{ZMP} = \frac{m(g + \ddot{z})x - m\ddot{x}z}{m(g + \ddot{z})} \tag{5}$$

We do not consider the angular momentum around CoM. Finally, we can calculate the desired contact forces by using a GRF and ZMP as (6). Figure 4 shows Distance Between point of application of GRF and CoM.

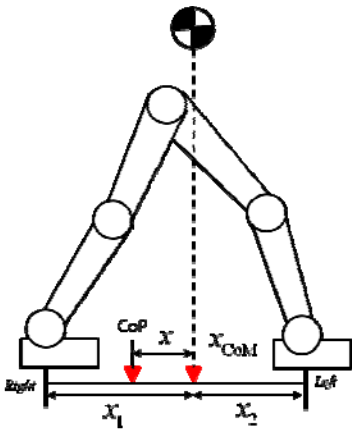

Fig. 4. Distance between point of application of GRF and CoM.

$$\begin{bmatrix} \vec{F}_1 \\ \vec{F}_2 \end{bmatrix} = \begin{bmatrix} x_1 & x_2 \\ 1 & 1 \end{bmatrix}^{-1} \begin{bmatrix} x \\ 1 \end{bmatrix} \vec{R}_z \tag{6}$$

4 SIMULATION

In this section, the exoskeleton walking simulation on flat ground is described. We simulated two cases: the single support phase and the double support phase. Figure 5 shows how to prove the effectiveness of our algorithm. We compare GRF by the algorithm with Actual GRF. In the simulation, we used a 6-DOF model and we gave a specific desired trajectory to controller instead of human.

In the single support phase, we gave the exoskeleton model sine trajectory. Amplitude of sine trajectory was 0.1 m. Figure 6 shows result of calculation of the desired GRF. Errors of GRF by the algorithm and actual GRF was measured within about ±0.2 N. This value represents our algorithm generates desired GRF for tracking wearer's motion.

In the double support phase, we compared GRF by the load distribution with actual GRF at the contact point. Motion trajectory in the double support phase was the same as that in the single support phase. In figure 7, we can

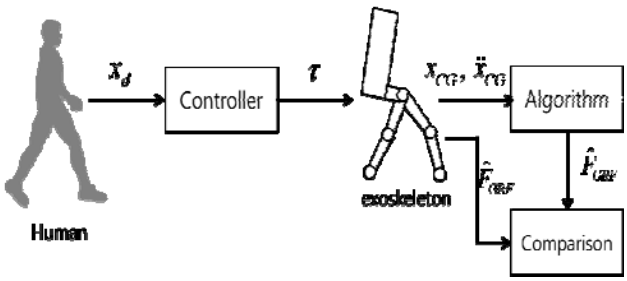

Fig. 5. Block diagram for proof of the algorithm

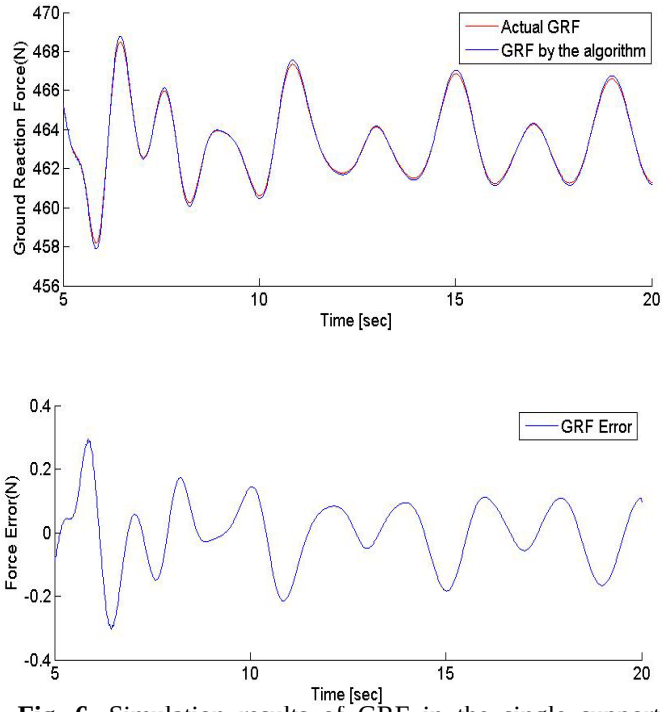

Fig. 6. Simulation results of GRF in the single support phase.

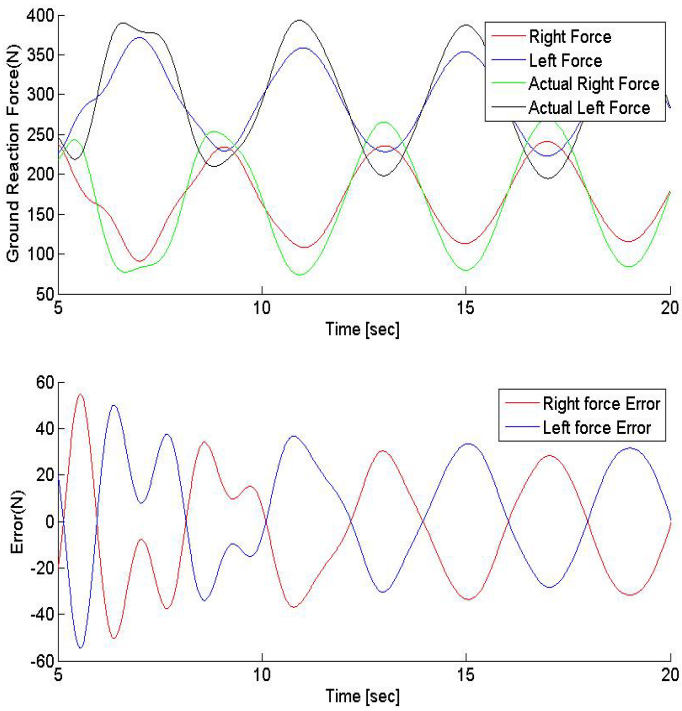

Fig. 7. Simulation results of GRF at the contact point of each foot in the double support phase.

confirm range of errors are ±30 N. As a margin of errors is less than 10 percent, the algorithm for load distribution is applicable to the exoskeleton. Errors tend to be increased when the acceleration of exoskeleton is increased because

ZMP is affected by the acceleration. To raise the accuracy of the load distribution, more accurate ZMP model is needed.

5 CONCLUSION

This paper described the desired GRF generation algorithm for tracking wearer's motion. We demonstrated effectiveness of the algorithm with simulation experiments. The algorithm has the following benefits. First, force sensor is not required at the contact point of the exoskeleton. Second, we can calculate ground contact force regardless of number of contact point. Third, it is not necessary to solve a complicated inverse dynamics of the exoskeleton by using ZMP.

As future research, it is necessary to use accurate ZMP model for more accurate load distribution. Next, we will transform desired contact ground forces into joint torques directly. We will apply the algorithm to the actual exoskeleton.

REFERENCES

[1] Satoshi Ito and Haruhisa Kawasaki (2000), A standing posture control based on ground reaction force, Proceedings of the 2000 IEEE/RSJ International Conference on Intelligent Robots and Systems, Takamatsu, Japan, Oct. 30 – Nov. 5, 2000, pp.1340 -1345 vol.2.

[2] K.H.Low, Xiaopeng Liu, C.H.Goh and Haoyong Yu (2006), Locomotive control of a wearable lower exoskeleton for walking enhancement, Journal of Vibration and Control, Dec 11, 2006, pp.1311-1336 vol.12

[3] Sang-Ho Hyon, Joshua G. Hale, and Gordon Cheng(2007), Full-Body Compliant Human-Humanoid Interaction: Balancing in the Presence of Unknown External Forces, IEEE TRANSACTIONS ON ROBOTICS, Saitama, Japan, Oct, 2007, pp884-898 vol.23

[4] Whittle, M. W. (2007), Gait Analysis: An Introduction, Butterworth-Heinemann, Oxford, UK. pp.54

[5] J. Rose and J.G. Gamble(1994), Human Walking 2nd ed, Boltimore, MD: Williams and Wikins

[6] Vukobratovic, M., Borovac, B. and Surdilovic, D. (2001), Zero-moment point: Proper interpretation and new applications, Proceeding of IEEE-RAS International Conference on Humanoid Robots, Tokyo, Japan, Nov 22-24, 2001, pp.135-144

[7] Phillippe Sardain and Guy Bessonnet (2004), Forces acting on a biped robot. Center of pressure-Zero moment point, IEEE TRANSACTIONS ON SYSTE MS AND HUMANS, Sec, 2004, pp. 630-637 vol.34

© ISAROB 2013

The Eighteenth International Symposium on Artificial Life and Robotics 2013 (AROB 18th '13),
Daejeon Convention Center, Daejeon, Korea, January 30-February 1, 2013

A study on the communication system using Electrooculogram Signals for persons with disabilities

Sou Go[1], Mingmin Yan[2], Hiroki Tamura[1], and Koichi Tanno[1]

[1]Department of Electrical and Electronic Engineering

[2]Interdisciplinary Graduate School of Agriculture and Engineering

University of Miyazaki, Japan

(Tel: 81-985-58-7409, Fax: 81-985-58-7409)

[1]*tc11014@student.miyazaki-u.ac.jp*

Abstract: The aim of this study is to present electrooculogram (abbr. EOG) signals that can be used for human computer interface efficiently. Establishing an efficient alternative channel for communication without overt speech and hand movements is important to increase the quality of life for patients suffering from Amyotrophic Lateral Sclerosis or other illnesses that prevent correct limb and facial muscular responses. Using EOG signals, it is possible to improve the communication abilities of those patients who can move their eyes. Investigating possibility of usage of the EOG for human-computer interface, a relation between sight angle and EOG is determined. In other methodology, most famous approaches involve the use of a camera to visually track of the eye. However, this method has problems that the eyes of user must always be open. In this paper, we introduce the mouse cursor control system for Amyotrophic Lateral Sclerosis patients using EOG and electroencephalograph (abbr. EEG). We proposed the algorithm using alternating current and direct current of EOG corresponding to the drift. Therefore, our proposal EOG system did not have the problem of eye blinking artifacts, the displacement of electrode positions and the drift. In addition, we introduce the EEG that the brainwaves can assist us whether the patient control their eye movements consciously. The EEG is not used to control. We are getting the EEG signals used to determine the control state. In order to test the effectiveness of our proposal, we have tried the experiments of the Questionnaire in NO or YES using our system and electroencephalograph device MYNDPLAY[7]. The three experimental subjects are inexperienced persons about this system. In this experiment, we measured 30 states of EEG signals when EOG was done and analyzed the EEG signals. According to the EEG signals changes and the answers of the questionnaire, 26 of the 30 states of the EEG signals were able to correctly determine the control state of EOG. From these results, the EEG signals can be used to adjust the EOG system according to the condition of EOG signals. In addition, it is expected that can be applied to determine whether patients are the way their want answers that can assist caregivers to know the brain handicapped patient's own thinking.

Keywords: Electrooculogram Signal; Mouse Cursor Control System; Electroencephalograph

1 INTRODUCTION

In the eye movements, a potential across the cornea and retina exists, and it is source of EOG. EOG can be modeled by a dipole [1], and these systems can be used in medical systems. There are several EOG-based Human-Computer Interface studies in literature. The eyes movement signals and sensor signals are combined, and both direction and acceleration are controlled [2]. Using horizontal and vertical eyes movements and two and three blinking signal a movable robot is controlled. Because the EOG signals are slightly different for the each subject, a dynamical threshold algorithm was developed [3].

In this approach, the initial threshold is compared with the dynamic range; the thresh-old value is renewed after each difference. According to this threshold the output signal is made 1 or 0 and afterwards it is processed. Investigating possibility of usage of the EOG for human computer interface, a relation between sight angle and EOG is determined. However, in-depth studies evoked that slow changing baseline drift is difficult to estimate in continuous EOG signals. To overcome this issue, previous system was proposed using alternating current of EOG which reduces baseline drift by segmentation of the signal [4].

In this study, we have developed the mouse cursor control system and new idea of EOG Signal for amyotrophic lateral sclerosis patients using EOG signals. Our proposal EOG device did not have the problem of eye blinking artifacts and the displacement of electrode positions. But, the drift was problem. Then, we proposed the algorithm using alternating current (abbr. AC) and direct current (abbr. DC) of EOG corresponding to the drift. In order to test the effectiveness of our proposal system, we tried the experiments of the questionnaire using our proposal system and EEG device MYNDPLAY. The performance of the proposal system and our proposal are very good, we measured 30states of EEG signals when EOG was done and analyzed the EEG signals. According to the EEG signals changes and the answers of the questionnaire, 26 of the 30 states of the EEG signals were able to correctly determine the control state of EOG.

© ISAROB 2013

2 MOUSE CURSOR SYSTEM USING EOG SIGNALS

2.1 The EOG Device

In this subsection, novel EOG measurement system design has been proposed. Fig. 1 shows the formal scheme for the acquisition and analysis of the EOG signal and how to control organization flow of information through the system.

Horizontal and vertical eye movements are measured with two passive electrodes. Five Ag/AgCl electrodes are used (two for CH1, two for CH2 and one is for ground). Two channels of EOG signals can be used to recognize the eyes movement. EOG signals can be determined as high as 50Hz. However, the signals which are less than 10Hz are safe and enough for our system. Therefore, we used the low pass filter whose cutoff frequency is 10Hz to remove the more than 10Hz power line signals. In our proposal system, channel 3 and 4that apply high pass filter to channel 1 and 2 are used in order to remove the DC level. The cutoff frequency of high pass filter is 0.175Hz. After filtering and the amplification (about 1000 times) stages, the EOG signals are digitized and then transferred to the personal computer. The sampling frequency of the measurement date is 960Hz.

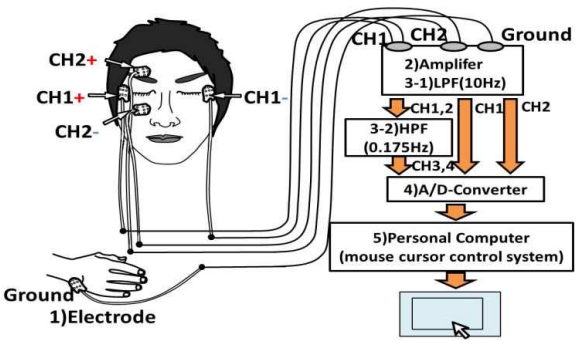

Fig. 1. The mouse cursor control system using EOG

2.2 The EOG signals recording

As seen from the recordings channel 1, 2 and 3 in Fig. 2. (the eyes movements: Right, Left, and intentional Blink), after signal amplitude (about 1000 times) and considering noise reduction measures in designing of the biopotential data acquisition system, the EOG system performance is good. Electronic noise reduction is also successful. Fig. 2 showed that 3 eyes movements are clearly different. Moreover, channel 1 and 2 have the DC level signals, so that the change of the EOG by the eyes movements continues. So, the continuous control for mouse cursor becomes possible. Channel 3 is the AC level signals of the horizontal EOG. Therefore, channel 3 is strongly reacted when eyes moved to right or left. Channel3 and 4signals were removed the DC level by high pass filter. Therefore, channel 3 and 4 signals have the change, only when eyes move. Channel 3 and 4 signals are information that knows the difference between the change by the drift (low frequency) and the change by the eyes movements. When the channel1 or/and channel2 signals change without the channel3 and 4 signal changing, this change is an influence of the drift.

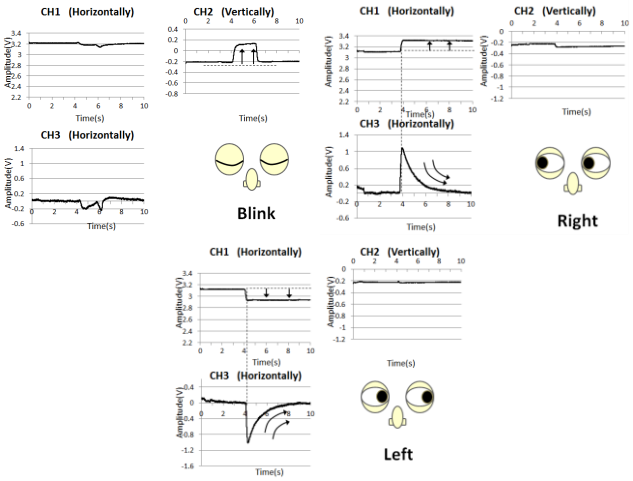

Fig. 2. The EOG signals recording samples in CH 1, 2 and 3 (Blink, Right and Left)

3 PROPOSED METHOD

3.1 Mouse Cursor Control Algorithm

In this section, we introduce our proposal algorithm for the mouse cursor control. The initial thresholds of the eyes movement class (Right, Left, and Voluntary Blink) are set on the user using the initialization screen. 3 eyes movement class (Right, Left, and Blink) are command of the Right movement, Left movement and click processing of the mouse cursor. The values of P_{right}, P_{left}, are defined as the set using the initialization screen. Moreover, the center parameters of the eye (centre) are set. When the experimenter gazes on these points of the initialization screen, the signals change of each channel will be recorded as initial thresholds of the eyes movement class. For example, when the experimenter gazes on the "Centre point", Horizontal centre parameter is set as Cx, and Vertical centre parameter is set as Cy.

At first, in order to remove the more than 60Hz power line noise, we use the moving average method for channel 1 and 2. The moving average method is the unweighted mean of the previous n data points. Because it is the sampling frequency 960Hz, the value of n is 16 (= 960Hz/60Hz). For the reduction of 60Hz power line noise.

Next, the difference between the centre parameter (Cx) and the input of Channel1 is calculated, and it is set to input 1. The input 2 is calculated similarly using difference between the centre parameter (Cy) and the input of Channel2. Our proposal system is judged whether eyes moved by using the input1, 2, channel 3 and channel 4. If eyes do not move, center parameters are updated to correspond to the drift. In this process, Cx and Cy are gradually updated to EOG baseline. I order to keep the security of the system, centre parameters (Cx, Cy) are

© ISAROB 2013

updated every interval by 30% of the drift.

If eyes move, the eyes movement class is identified using each class thresholds using the rules of Table 1. Here, the value of T_{right}, T_{left}, and T_{blink} are defined as the threshold value of the eyes movement class. Since there is individual difference, it is necessary to update the threshold of T_{right}, T_{left} using the other parameters of P_{right} and P_{left}. And, the threshold of the eyes movement class is updated according to the dynamic threshold method. Therefore, our proposal system can respond to online EOG characteristic changes. The code of the dynamic threshold method of the right threshold is as follows:

```
If 0.64 < input 1/(Pright-Cx) and input
1/(Pright-Cx) < 0.8 Then
   Tright = Tright - 0.01* Tright
Else if input 1/(Pright-Cx) > 0.96 Then
   Tright = Tright + 0.01* Tright
End if
```

Other thresholds are similarly processed. In this process, the threshold is updated to low when the value of input is low, and the threshold is updated to higher when the value of input is high. These processes are repeated. The mouse cursor control interval is 0.2 seconds. The continuous control for mouse cursor can be executed while corresponding to the drift by this proposal algorithm and the proposal EOG device.

Table 1. Pattern classification rules

Command	Right	Left	Blink
Input 1	Input 1>T_{right}	Input 1 <T_{left}	
And input 2	|input 2|<0.3	|input 2|<0.3	Input2 < T_{blink}
And channel 3	CH3>$TCH3_{right}$	CH3<$TCH3_{left}$	CH3 > $TCH3_{blink}$
And channel 4			CH4 > $TCH4_{blink}$

3.2 Electroencephalograph

In this study, we also propose using EEG by MYNDPLAY. EEG is the cording of electrical activity along the scalp, measures voltage fluctuations resulting from ionic current flows within the neurons of the brain. Human brain waves can be divided into at least four states. We determine the activity of the brain by using two categories of low-frequency beta waves and alpha waves in the EEG. Alpha is the frequency range from8 Hz to 13 Hz, seen in the posterior regions of the head on both sides, higher in amplitude on the dominant side. Alpha wave increase during wakeful relaxation with closed eyes. Beta is the frequency range from 13 Hz to about 30 Hz. It is seen usually on both sides in symmetrical distribution and is most evident frontally. Low amplitude beta waves with multiple and varying frequencies are often associated with active, busy, or anxious thinking and active concentration. We use EEG changes that can determine whether the patients using our EOG system in their own meaning. Then, in order to test the effectiveness of our proposal, we have tried the experiments of the Questionnaire in NO or YES using our system and EEG device MYNDPLAY.

4 EXPERIMENTS AND RESULTS

Three inexperience subjects have tried the experiments of the Questionnaire what answer is Yes or No using our EOG system and EEG. But, we cannot run the dynamic threshold method and centre parameters updated method to increase the control misses. The size of the monitor is 23 inches and the distance between the eyes of subject and the monitor is 50cm and use Bluetooth to send the EEG signals.

4.1Experiments method

We have tried the experiments using our proposal system and simple brainwave system MYNDPLAY. The EEG signals of three subjects (S.G, KS.NN and KH.NT) are measured and analyzed 30 states. It is defined as:

$$H(t) = \frac{1}{10}\sum_{i=0}^{9}\frac{A(t-i)}{B(t-i)+C} \qquad (1)$$

A(t) is the frequency from 7Hz to 9Hz of alpha wave of t time power spectrum of Fast Fourier Transform(abb. FFT). *B(t)* is the frequency from 14Hz to 16Hz of the Low-frequency beta waves of t time power spectrum of FFT. *C* is constant, the average of *B(t)*. *H(t)* is the 10 pre moving average.

If the average of *H(t)* is less than 0.5 then the EOG system is uncontrollable of the patient's consciousness. If the average of *H(t)* is greater than 0.5, take 50% of it as the threshold and compared to the *H(t)* whether EOG is controllable. In addition, if the 10 pre moving average value greater than threshold, then the patients according to their own consciousness in using EOG system otherwise not.

4.2Experiments results

Table 2 shows the correct rate of each subject. Fig. 3 shows the correct results for 10 pre moving average of EEG power spectrum and Fig. 4 shows the error one. Fig. 5 and Fig. 6 show the statistical significance less than 1% and the average value of subject KS.NN and S.G, error bar is the standard deviation. The average value of *H(t)*-value of each subject when EOG is controlled by the subject's own thinking or cannot in controlling is calculated, then assessing T-test of each trial. Fig. 7 shows the average of subject KH.NT, although it is no statistical significance, but the correct recognition rate of 80% is a good result. By this analytical method, 30 states of data was measured (one subject for 10 states), 26 states of it can be correct analyzed and the offline correct rate is about 87% and the error is not serious than our previous study (using only EOG system with the dynamic threshold method and centre parameters updated method) that the experimental result of using mouse cursor system and camera is 97%. In addition, as future work, we need online experiment.

Table 2 . Correct rate of each subject

Subjects	S.G	KS.NN	KH.NT
Correct rate	90%	90%	80%

© ISAROB 2013

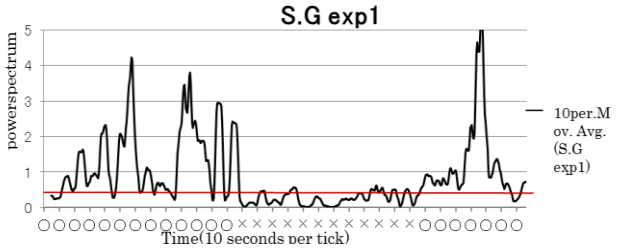

Fig. 3. Correct recognition rate of EEG power spectrum

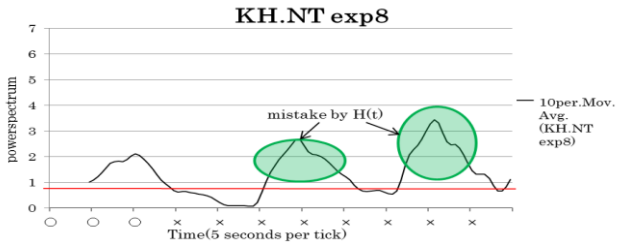

Fig. 4. Error recognition rate of EEG power spectrum

*○ is EOG can be controlled, × is uncontrollable.

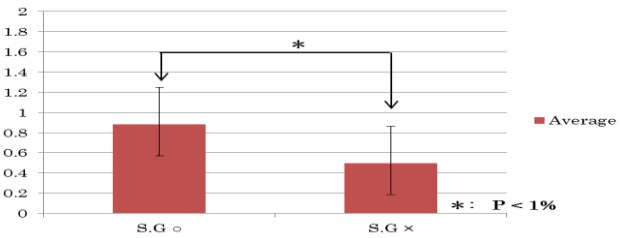

Fig. 5. T-test result of S.G

5 CONCLUSION

In this study, we have developed the mouse cursor control system for amyotrophic lateral sclerosis, by which the amyotrophic lateral sclerosis patients with their own consciousness in control EOG when EOG system was done. The performance of the proposed system was good. According to the EEG signals changes and the answers of the questionnaire, 26 of the 30 states of the EEG signals were able to correctly determine that using Bluetooth to communicate the EOG system and control the EOG. The correct recognition rate of three experimenters is 87%. Two experimenters have the statistical significance less than 1%. From these results, the EEG signals can be used to adjust the EOG system according to the condition of EOG signals. In addition, it is expected that can be applied to determine whether patients are the way their want answers that can assist caregivers to know the brain handicapped patient's own thinking. Our proposed system has one problem that the average time of question increased by wave noise caused by this kind of phenomenon, the whole proposed system should be considered with the properties of electrodes.

ACKNOWLEDGEMENTS

This work was supported by JSPS KAKENHI Grant Number 23700668.

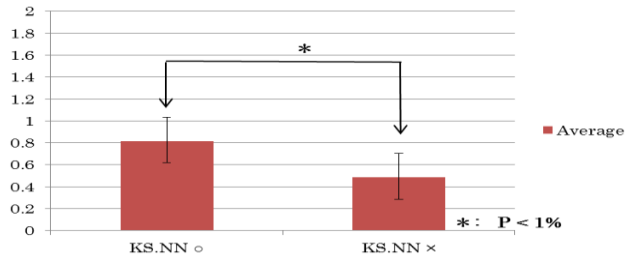

Fig.6. T-test result of KS.NN

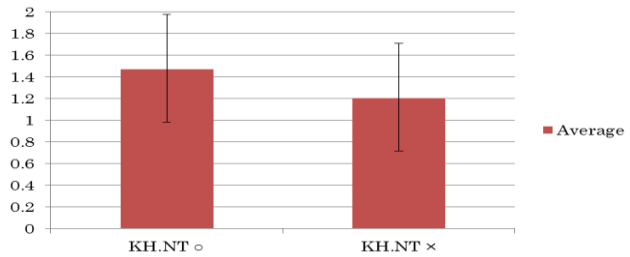

Fig.7. T-test result of KH.NT

REFERENCES

[1] S. Venkataramanan, P. Prabhat, S. R. Choudhury, H. B.Nemade and J. S. Sahambi, Biomedical instrumentation based on electrooculogram (EOG) signal processing and application to a hospital alarm system, Proc. of International Conference on Intelligent Sensing and Information Processing, Chennai, India, pp.535-540, 2005

[2] R. Barae, L. Boquete and M. Mazo, System for assitedmobility using eye movements based on electrooculography, IEEE Transaction on Neural Systems and Rehabilitation Engineering, vol.10, no.4, pp.209-218, 2002

[3] Z. Lv, X. Wu, M. Li and C. Zhang, Implementation of the EOG-based human computer interface system, Proc. of the 2nd International Conference on Bioinformatics and Biomedical Engineering (ICBBE'08), Shanghai, China, pp.2188-2191, 2008

[4] A. B. Usakli, S. Gurkan, F. Aloise, G. Vecchiato and F. Babiloni, on the use of electrooculogram for efficient human computer interfaces, Computational Intelligence and Neuroscience, vol.2010, Article ID 135629, 5 pages, 2010

[5] H.Tamura, M.Miyashita, K.Tanno and Y.Fuse, Mouse cursor control system using electrooculogram signals, Proc. of World Automation Congress 2010, IFMIP 239, CD-ROM, pp.1-6, 2010

[6] M. Yan, H. Tamura and K.Tanno, Development of mouse cursor control system using electrooculogram signals and its applications in revised hasegawa dementia scale task, Proc. of World Automation Congress 2012, CD-ROM, pp.1-6, 2012

[7] http://neuro-bridge.com/entertainment/myndplay.html

© ISAROB 2013

The Eighteenth International Symposium on Artificial Life and Robotics 2013 (AROB 18th '13),
Daejeon Convention Center, Daejeon, Korea, January 30-February 1, 2013

A Study on the Electric Wheelchair Hands-Free Control System using the Laser Range Scanner

Takayuki Murata[1], Hiroki Tamura[1.1], and Koichi Tanno[1]
[1]University of Miyazaki, Miyazaki 889-2192, Japan
(Tel: 81-985-58-7409, Fax: 81-985-58-7409)

htamura@cc.miyazaki-u.ac.jp

Abstract: This paper presents a semi-automatic control system for electric wheelchair using laser range scanner. The user of this system is supposed as severe disabilities paraplegic who cannot move the body under the neck. They can use the surface electromyography (s-EMG) of the facial muscle for controlling the electric wheelchair. When they are controlling the electric wheelchair with the s-EMG signals, to avoid the obstacle is difficult. Therefore, we developed the semi-automatic assist system for avoiding the obstacle. The proposed system is composed by laser range scanner. The electric wheelchair could increase safety by using our proposed assist system. We tried the experiments of driving in the hallway of the building. Our proposed system was confirmed that the electric wheelchair did not clash with the hallway of the building.

Keywords: Surface Electromyogram Signal, Electric Wheelchair, Laser range scanner, Motion Control Command Rule, Semi-Automatic Control

1 INTRODUCTION

An electric wheelchair is indispensable for disabled people. In recent years, the joystick type of electric wheelchair is very popular. However, for persons with severe disabilities who find it difficult to operate the joystick of electric wheelchair, in the other hand, the new types of devices for disabled people have appeared, for example the voice, brain waves and surface electromyogram (abbr. s-EMG) signals etc. Disabled people who have the problem of limbs can use these types of devices, but the well adjustment of the driving route by using these devices is difficult. In addition, the user of electric wheelchair must be safe driving. Disabled people are hard to check the safety around. Thus, it is necessary to check safety using sensors.

This paper presents a semi-automatic control system for the electric wheelchair by using a laser range scanner [1]. The user of the proposed system is supposed as serious disabled people who cannot move the body under the neck. They cannot control the electric wheelchair with hands or legs, but they can use the Bio-signal in their face. For example, the Bio-signal system is the s-EMG system [2][3].

This system can be controlled by using the face s-EMG signals. This system can recognize face motion (a left wink, a right wink and a bite) by using s-EMG sensors. The method of controlling the electric wheelchair in this system is shown in Table 1. This system is attached with a laser range sensor for the safety, and the electric wheelchair could be speed controlled, but this system cannot avoid the obstacle automatically. Thus, the user has to control the electric wheelchair to avoid the obstacle every time. Therefore we developed the automatic control system for avoiding the obstacle.

Table 1. The way of controlling the electric wheelchair.

State of electric wheelchair \ Movement of face	Left wink	Right wink	Bite
During a stop	**Turn left**	**Turn right**	**Foward**
During a forward	**Forward to the left**	**Forward to the right**	**Stop**

2 THE PROPOSED SYSTEM

2.1 Sensor Position

The proposed system is composed by a laser range scanner (HOKUYO AUTOMATIC CO., LTD, sensor model URG-LX04). The specification of this sensor is shown as Figure 1. The measurable range of this sensor is maximum 4 meter in 120 degree left and right, and the sampling interval is 100 msec. The specification of this sensor is shown as Figure 1.

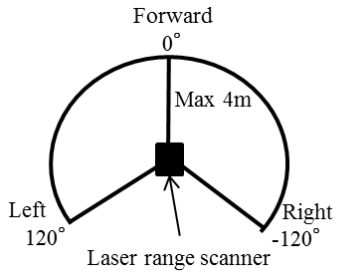

Figure 1. The range of the laser range scanner.

© ISAROB 2013

In the proposed system, the laser range scanner is attached on the brace by the 1.7m high from the ground (Figure 2). This position can measure the side of the electric wheelchair. The laser range scanner can recognize the obstacle even as large as a wall.

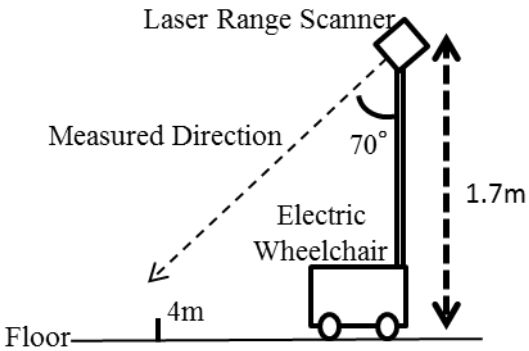

Figure 2. The position of the laser range scanner.

2.2 Pretreatment

First step, get angle values and distance values between the obstacle and the laser range scanner. Second step, convert the angle values and the distance values into Euclidean distance, and plot these values on the picture (width: 160 pixel, height: 160 pixel) with dots. 1 pixel represents 50mm. Thirds step, if the distance between two dots is less than the width of the electric wheelchair, these two dots will be connect with the line. The results of using these steps are shown in Figure 3. Figure 3(a) shows the actual scene. Figure 3(b) shows the measured values of the laser range scanner, and the center on the Figure 3(b) is the laser range scanner position. Figure 3(c) shows reformed values. Figure 3(c) is shown as the confirmation window on the personal computer.

Figure 3(a). Actual scene.

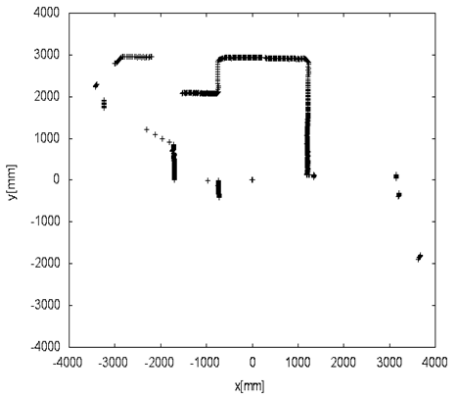

Figure 3(b). Measured values.

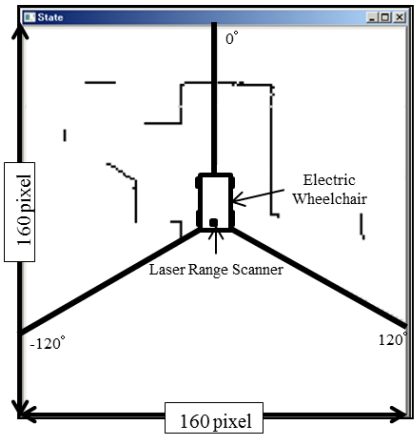

Figure 3(c). The confirmation window.

2.3 Speed Control

The speed of the electric wheelchair could be controlled ac-cording the distance between the obstacle and the laser range scanner. The area of controlling speed is separated into three parts by the distance from the front of the electric wheelchair to the obstacle (Figure 4).

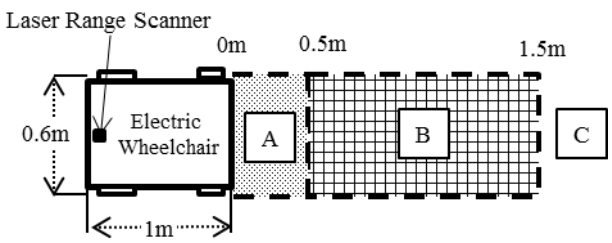

Figure 4. The separated area.

(a) Area A

The area A is less than 0.5 meter. If there is the obstacle, the electric wheelchair will be stopped. The electric wheelchair cannot go forward, but it can also turn on the spot. The electric wheelchair doesn't move until a turn command.

© ISAROB 2013

(b) Area B

The area B is less than 1.5 meter and more than 0.5 meter. If the obstacle exists in the area B, the speed of the electric wheelchair will be slowed down. In addition, for avoiding the obstacle, the area L_B and the area R_B are checked (Figure 5). When both the area L_B and the area R_B does not exist any obstacles, the electric wheelchair will turn to the left. If there is the obstacle in one side, the electric wheelchair will turn to the opposite direction. When both the area L_B and the area R_B exists the obstacles, the electric wheelchair will be slowed down the speed only.

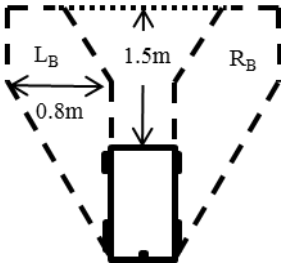

Figure 5. The search area in area B.

(c) Area C

If the obstacle does not exist in the area A and the area B, the proposed system will search the obstacle in the area L_C and the area R_C (Figure 6). The speed of the electric wheelchair is the normal speed. If the obstacle exists in the area L_C or the area R_C, the electric wheelchair will be controlled by the fine adjustment. To check these areas is in order to prevent approaching the wall.

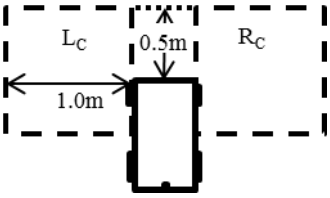

Figure 6. The search area in the area C.

(d) During a stop

When the user commands as the left or the right, the electric wheelchair turns on the spot. By checking the obstacle in the area L_D or the area R_D (Figure 7), the electric wheelchair turns slowly on the spot.

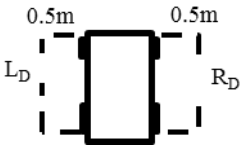

Figure 7. The search area during the stop.

3 EXPERIMENTS

3.1 Structure

The overall structure of the electric wheelchair is shown as Figure 8. The laser range scanner is attached on the electric wheelchair. The subject is attached S-EMG sensors. The data measured by the laser range scanner and s-EMG sensors can be analyzed on the personal computer. The flowchart of the control is shown as Figure 9. The user can command the electric wheelchair by using s-EMG sensors. The laser range scanner is checking the state of the obstacle around the electric wheelchair. The output command is judged on the personal computer by both using s-EMG sensors and the laser range scanner.

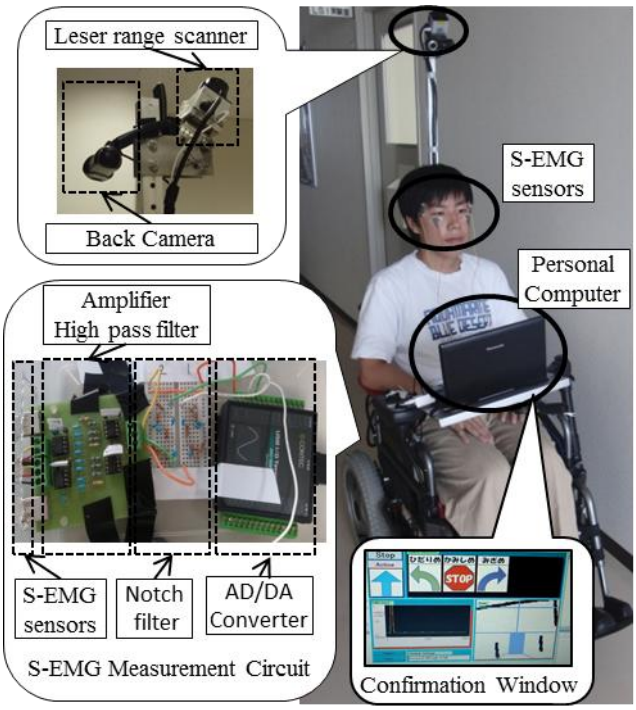

Figure 8. The structure of the proposed system.

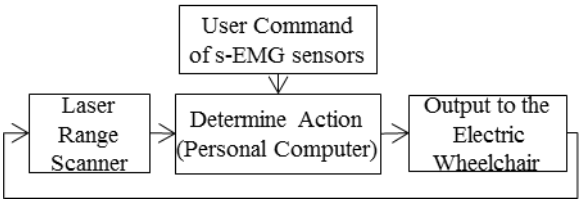

Figure 9. The flowchart of the control.

3.2 Experimental condition

We experimented with proposed system in the building corridor. The width of the building corridor is 1.9 meter. The subject is a healthy twenties male, and he agree to join in the experiments himself. He controlled the electric wheelchair by using s-EMG sensors. To check the proposed

© ISAROB 2013

system, he is supposed as severe disabilities paraplegic who could use bite only.

4 RESULTS

We tried to drive the electric wheelchair with the proposed system. Actual scenes and driven routes are shown as Figure 10. The interval between two points is 2 second. The arrow in the figure shows the direction of driving the electric wheelchair.

The route of starting to the oblique angle against the wall is shown Figure 10(a). In the start position, the user commanded to start the electric wheelchair. When the electric wheelchair turned to the right with the proposed system, the user did not have commanded anything. In the goal, the electric wheelchair was stopped by the user command. In the case of this course, the electric wheelchair did not clash with the wall.

The figure 10(b) is shown as driving routes in the corridor. The area X is the straight corridor. The width of the area Y is larger than the width of the straight corridor. The electric wheelchair did not clash the wall.

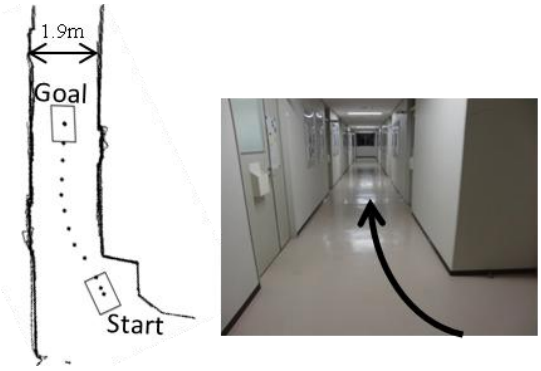

Figure 10(a). Starting to the oblique angle.

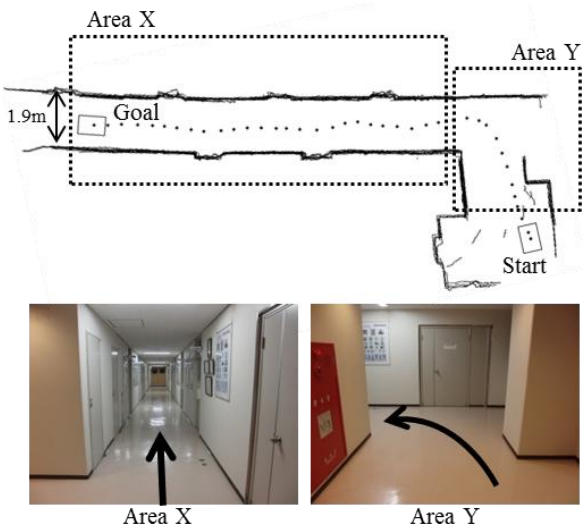

Figure 10(b). Driving routes in the corridor.

5 CONCLUSION

We tried to control the electric wheelchair with the proposed system. The electric wheelchair did not clash the wall. Using the laser range scanner, the user need not command for the fine adjustment. Therefore the electric wheelchair can drive smoothly in the narrow space such as the hallway of the building.

If the laser range scanner cannot measure the obstacle, the user needs to command the stop with s-EMG sensors himself. The proposed system provided the assist to the user. While the obstacle is found of the laser range scanner, the user doesn't need any command, the proposed system avoid the obstacle automatically. Now, we are trying the monitoring test for serious disabled people by using the proposed system.

But the wavelength of the laser range scanner is 785nm, and this wavelength cannot measure such as the glass. So the electric wheelchair needs another sensor such as the ultrasonic wave sensor to deal with the obstacles such as the glass.

REFERENCES

[1] A.Shimada, P.Kiddee, Y.Nishi "Obstacle Avoidance Control on Omnidirectional Vehicle Robots Using Range Sensor", IEEJ Transactions on Industry Applications, Vol.128, Issue 6, pp.849-856, 2008.

[2] H. Tamura, T. Manabe, K. Tanno, Y. Fuse"The electric wheelchair control system using surface-electromygram of facial muscles",Proc. of World Automation Congress 2010, IFMIP 240, CDROM, (pp.1-6), 2010.

[3] H.Tamura, T.Murata, Y.Yamashita, K.Tanno, Y.Fuse "Development of the electric wheelchair hands-free semi-automatic control system using the surface-electromyogram of facial muscles", Artificial Life and Robotics, Vol.17, Issue 2 , pp.300-305, 2012.

© ISAROB 2013

The Eighteenth International Symposium on Artificial Life and Robotics 2013 (AROB 18th '13),
Daejeon Convention Center, Daejeon, Korea, January 30-February 1, 2013

On Driving Assistance using Forearm Vibrotactile Feedback for Wheelchair Drivers

Aydin Tarik ZENGIN, Kazuki NABEKURA, Hiroshi OKAJIMA, and Nobutomo MATSUNAGA

Department of Computer Science and Electrical Engineering, Kumamoto University, Japan
(Tel: 81-96-342-3639)
(matunaga@cs.kumamoto-u.ac.jp)

Abstract: Welfare devices are getting more popular along with the growing population of elder and disable. The significance of an easy to use wheelchair is rising recently. The authors have developed a new wheelchair STAVi which has a unique piggybacking design. Because of the growing importance of environmental safety, new driving assistance systems are required. A superficial vibrotactile feedback mechanism is designed to transmit environmental information to the wheelchair driver unlike the visual or audible signals that distract attention. Our goal is to develop a driving assistance system using vibrotactile feedback to the driver and to guarantee the safety. As a first step we evaluate simple vibrotactile system for the newly designed electric wheelchair. In this paper, we clarify the concept of vibration generation and propose a vibration feedback system. Also, we analyze the cognitive characteristics of vibration in order to show the effectiveness of the obstacle localization using vibrotactile feedback. It is expected that the drivers can easily estimate the location of environmental obstacles just by using the vibrotactile feedback. The effectiveness of the proposed system is confirmed by experiments.

Keywords: Electric wheelchair, vibrotactile feedback, driving assistance, obstacle detection

1 INTRODUCTION

By the increasing demand on the welfare devices, it has been a requirement to focus on the safety of those. Wheelchair drivers need extra information about the environment around them, regardless of their disabilities. These may be the obstacles around, or the road conditions such as the inclination and curves. In the case of electric wheelchairs, the driver needs to spend less effort to move the vehicle than the traditional manual steering methods. Wheelchair can easily be driven on to an obstacle when the driver didn't perceive it especially when he/she has visual deficit or mobility impairment. Also, precise perception of the obstacles such as the stationary bodies or pedestrians is difficult for the disabled. These difficulties make the situation dangerous, because the driver won't run into any physical difficulty to move the vehicle even in an unsuited environment when there is no visual or audible feedback.

Commercially available driving assistance systems use predominantly visual or auditory channels to communicate with the driver. Environmental factors such as the direct exposure to sunlight and background noise makes the driver's distraction increase. Yu et al. discussed and implemented a driving assistant system for automobiles, containing ultrasonic sensors and various indicators including tactile vibrators placed on the steering wheel, a buzzer and an LED display [1]. A similar approach in navigation to provide distance to the destination is presented by Tsukada et al. by changing the pulse interval of the vibration motor [2]. Bial et al. proposed a vibrotactile feedback system for the motorcycle drivers, providing distance and turning direction using vibration motors attached gloves [3]. The connection between the gloves and the control system is not comfortable for the driver.

Previous studies on vibrotactile feedback are generally focused on navigation systems providing basic directions. Audiovisual systems have been studied for driving assistance but vibrotactile feedback systems have not been studied in detail. We have developed a new electric wheelchair "STAVi" [4] and focused on driving assistance using vibrotactile feedback [6] because the obstacle detection for the wheelchair users is an important issue. As the STAVi has a piggybacking design and several body supports such as the chest support and arm rests, it will be effective to construct the vibrotactile feedback system without annoying hard-wiring devices.

We propose a vibrotactile feedback system using arm rests providing environmental information through vibration stimuli. The obstacle distance and direction detected by laser range finder are transferred to the wheelchair user in order to assist him/her. Proposed vibrotactile feedback system is located onto the arm rests in order to provide convenience to the driver. In this paper, we aimed to provide the ability of environmental recognition to the wheelchair driver. Environmental obstacles' location and distance will be attended to the driver just by vibration stimuli. Experiments are conducted to show the accuracy of drivers' obstacle position estimation by using prerecorded data instead of real-time sensor data. The estimation of the obstacle's position and moving trajectory is evaluated by experiments.

© ISAROB 2013

Fig. 1: Appearance of STAVi#2

2 CHARACTERISTICS OF WHEELCHAIR STAVI

In this study, we developed a new electric wheelchair "STAVi", shown in Fig.1 [4]. Users can get into STAVi by piggybacking from a bed or wheelchair. While driving, user weight is supported at three points: seat, chest pad, and arm rests. This serves to distribute user's weight and to reduce the load on any particular point. After the user is safely seated, the seat escalates to the user's standing position so that their eye line is at the same height as it would be in their standing position. The elderly and disabled persons who took a test ride stated that they do not feel inferior because they are at the same height as their care personnel.

In this paper, a stationary experimental setup that has the same frame structure with STAVi such as the seat, chest support and arm rests, was used. Fig.2 shows the experimental system mimicking the STAVi's frame.

3 VIBROTACTILE FEEDBACK SYSTEM

3.1 Concept of vibrotactile feedback

Extra attention is needed by the drivers of STAVi because the target users are the elder and disable. Proposed system provides this extra attention by scanning the environment for the obstacles that may collide with STAVi. In order to warn the driver, our system uses superficial stimuli applied to the driver's arms.

For superficial stimuli, Johansson clarifies the mechanoreceptors' frequency response in his fundamental study that implies a tactile stimulation at frequencies under 100[Hz] improves spatial resolution of vibrations perception [5]. In our previous studies, we analyzed the frequency response of human skin with multiple subjects and confirmed that the vibration frequencies over 100[Hz] are inefficient [6].

We encoded the environmental information in a pattern to

Fig. 2: Experimental system and vibration motors with eccentric mass on the shaft

transmit distance and direction as shown in Fig.3. Johansson et al. gives the maximal cycle response of slowly adapting (SA II) units of skin as 0.5[Hz] even at the low stimulus amplitudes [5]. Therefore, by taking the SA II receptor's sensitivity into consideration, the control period was taken as 1[s] which is the maximal cycle response time, in order to differentiate the pause between vibration stimuli. The maximum vibration frequency was chosen below 100[Hz] in our experiments. Stimulation on-time was varying according to the obstacle's direction detected by the sensor. Maximum on-time interval was chosen as 1[s]. A time delay between vibration signals was used to provide the direction. In light of these information, we created the unique vibration pattern shown in Fig.3.

3.2 Vibration generation method

Environmental information was encoded in two parameters: obstacle distance and direction. We adjust the vibration magnitude in order to indicate the obstacle's distance. Direction indication uses a similar method of interaural time difference (ITD) model to mimic the perception of sound.

The difference on the arrival times of the sound waves

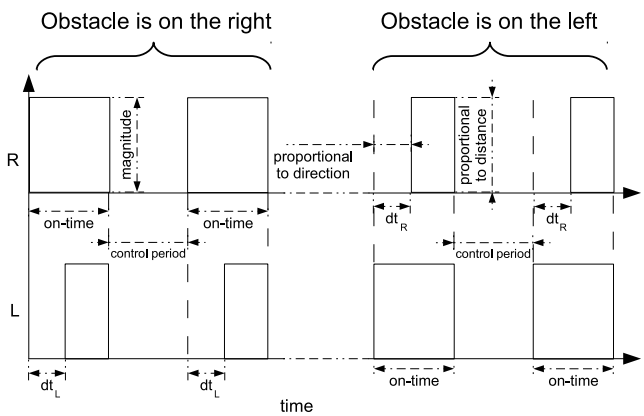

Fig. 3: Vibration pattern

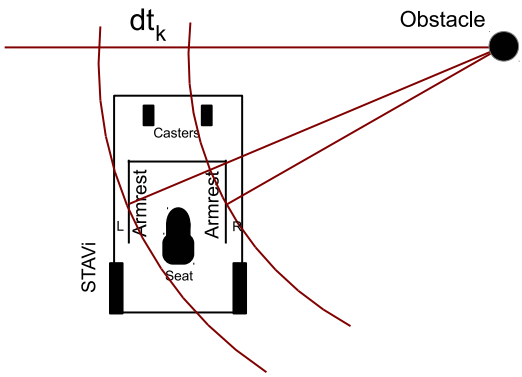

Fig. 4: Vibration time difference model inspired by ITD

is the key feature of the perception. According to this difference, sound source can be localized by the subject. We mimicked this concept in our study and applied a delayed vibration stimuli to one of the arms according to the position of the obstacle as shown in Fig.4. The time difference between the right and left arm vibration signals was adjusted similar to the arrival time of the sound waves to ears. Fig.4 represents the time difference model inspired by ITD. Using this method, subject could get the rough position of the obstacle and protect himself from the collision.

Obstacle distance and direction were given by laser range finder. A decision algorithm decides the position of the obstacle or the approaching object. According to the results of the algorithm, the driver was warned by a unique vibration stimuli that was created considering the obstacle's position. The warning signal is applied using the motors located on the wheelchair's armrests. The driver could have a chance to avoid collision.

3.3 Experimental setup

Experimental setup was conducted with 5 able participants. The average age was 23.16 (SD(Standard Deviation)= 2.48), and the experiments lasted 30 minutes for one participant. Fig.4 shows the schematic diagram of time difference between the right and left arm vibration signals inspired by the ITD. $dt_k : k = \{L, R\}$ was varying according to the obstacle's direction. When the obstacle is in front of the vehicle, dt_k becomes zero. In our experiments, dt_k was varying between 0 and 1[s] as shown in Fig.3.

Each participant was subjected to a training of over 50 random vibration signals and simultaneously was shown the obstacle position on the screen. During the training session, the subject gave response by moving the joystick to the direction of the obstacle and saw the correlation between his response and the actual position on the screen. After the training session, the subject was asked to guess where the obstacle is according to the vibration signal applied to the arms without seeing the actual obstacle position.

Vibration generators are placed on the armrests because the driver continuously contacts to the arms during the motion as shown in Fig.2. We didn't attach the vibration motors directly to the driver's body because of the inconvenience of the permanently attached type stimulators such as arm bands or bracelets which annoy and distract the driver.

Fig.2 shows the experimental system imitating the STAVi's frame. Vibrotactile feedback stimulators made by DC motors ("28L28-416E" from Portescap) with eccentric masses on the shaft are placed inside of the armrests. Vibration motors were driven by TD12770-48W05 servo controllers from Tokushu Denso and provides a maximum power of 6.94[N]. Environmental information was taken by the laser range finder ("UTM-30LX" from Hokuyo Automatic) and processed by the microcontroller (Atmel AVR 328). Vibration pattern was decided according to the obstacles' position and vibration signal was applied to the driver's arms.

4 RESULTS OF PERCEPTION EXPERIMENTS

The effectiveness of the proposed system was measured by experiments. Using the pattern in Fig.3, 5 participants were subjected to a test of 4 moving object trajectories. In this experiment, subjects were asked to guess where the obstacle around STAVi is moving according to the applied vibration signal. A training session was given to the subjects before the actual experiment. Subjects used the same setup as the training session and replied by using the joystick to give their guess. Fig.5 shows the subject response for various trajectories. Solid line represents the actual obstacle trajectory. Colored dashed lines represent the subject responses.

Table 1: Correlation coefficient of the subject response

	Traj. 1	Traj. 2	Traj. 3	Traj. 4
Subj.1	0.987	0.867	0.896	0.968
Subj.2	0.951	0.892	0.869	0.975
Subj.3	0.992	0.911	0.975	0.967
Subj.4	0.988	0.915	0.977	0.971
Subj.5	0.977	0.972	0.965	0.987
Average	0.979	0.911	0.936	0.973

Table 2: Deviation for 2 subjects repating the test

		Traj.1	Traj.2	Traj.3	Traj.4
Subj.1	Trial 1	0.987	0.867	0.896	0.968
	Trial 2	0.983	0.927	0.963	0.983
	Std. Dev.	0.003	0.042	0.047	0.011
Subj.2	Trial 1	0.951	0.892	0.869	0.975
	Trial 2	0.987	0.941	0.952	0.952
	Std. Dev.	0.025	0.035	0.059	0.016

© ISAROB 2013

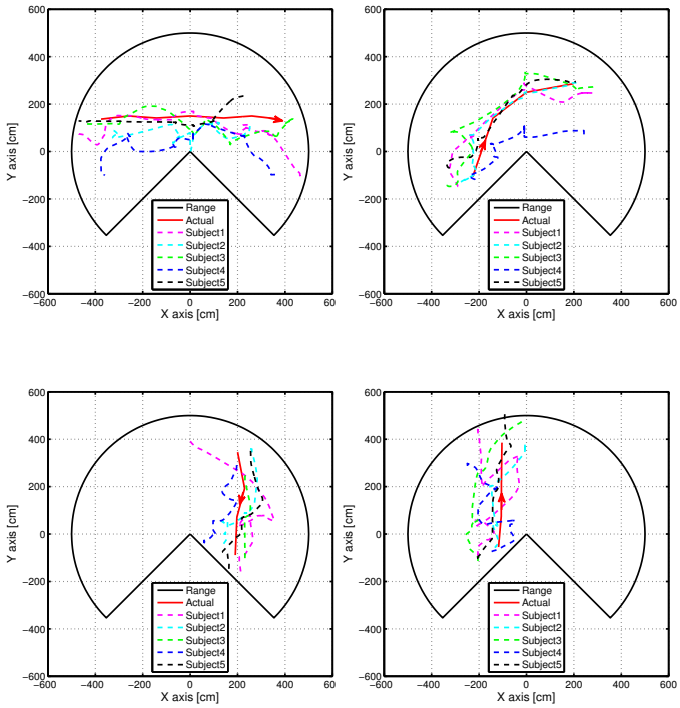

Fig. 5: Multiple user responses for various trajectories

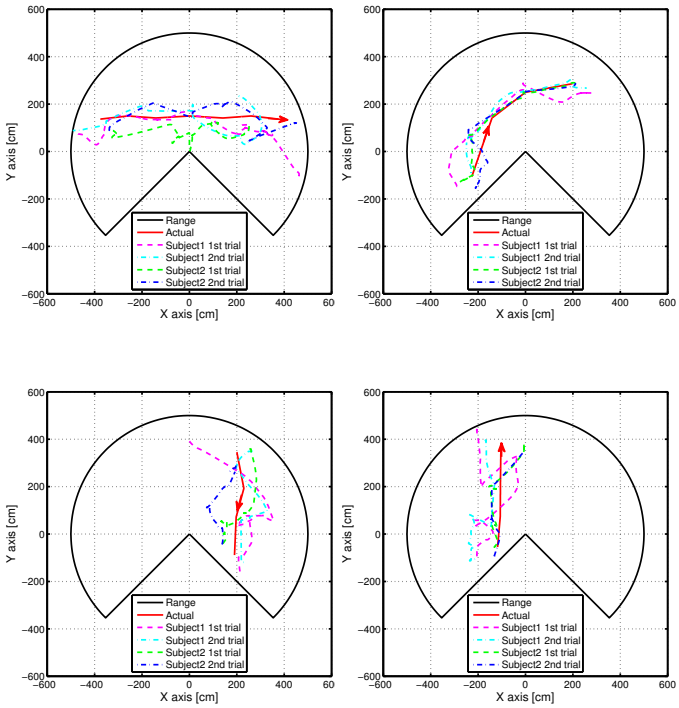

Fig. 6: Repeatability test by 2 subjects

Correlation coefficient for the each subject and average correlation coefficients to show the accuracy of the subject responses are given in Table.1. According to the results, subject's guesses are accurate and the average correlation coefficient for all the different trajectories is 0.949.

Analysis of the repeatability is done by experiments. Two subjects took the same tests at different times and the subject responses are recorded as shown in Fig.6. Table.2 shows the correlation coefficient of the subject response and the standard deviation of the repeated tests to verify the repeatability.

Results show that deviation between each trial is very low and by using the proposed vibrotactile feedback system, wheelchair drivers could estimate the outline of the obstacle location. The estimated accuracy is confirmed by the repeated tests.

5 CONCLUSION

In this study, we proposed a driving assistance system using superficial vibrotactile feedback for wheelchair drivers. Primary goal in this paper is to show the accuracy and repeatability of the proposed system by multiple-subject experiments. Experimental results showed that subjects could estimate the obstacle's position and the moving trajectory sufficiently. Repeated experiments verified the accuracy of the proposed method and showed that the subjects could locate the obstacle just by using the vibrotactile feedback.

In this setup, vibration motors were placed in the armrests. Therefore the accuracy would be low when the subject is not contacting the armrests completely. Support of vibrotactile feedback via the seat and chest support pad is a future work.

REFERENCES

[1] Yu, F. et al.: "A New Driving Assistant for Automobiles", CCECE 2007, pp.1199–1202, 2007

[2] Tsukada, K. and Yasumura, M.: "Activebelt: Belt-type wearable tactile display for directional navigation", UbiComp 2004, pp.384–399, 2004

[3] Bial, D. et al.: "Enhancing outdoor navigation systems through vibrotactile feedback", Proceedings of CHI2011, pp.1273–1278, 2011

[4] Maruno, Y. et al.: "Driving Experiment of Front Drive Type Electric Wheelchair using Yaw-rate Control", SICE Annual Conference 2012, pp.1408–1413, 2012

[5] Johansson, R.S. et al.: "Tactile sensibility in the human hand: receptive field characteristics of mechanoreceptive units in the glabrous skin area", The journal of physiology, vol. 281-1, pp.101–125, 1978

[6] Zengin, A.T. et al.: "On vibration feedback method for pain emulation and its feedback to human", ICCAS 2011, pp.655–658, 2011

© ISAROB 2013

The Eighteenth International Symposium on Artificial Life and Robotics 2013 (AROB 18th '13),
Daejeon Convention Center, Daejeon, Korea, January 30-February 1, 2013

Measurement and analysis of upper-limb essential tremor motion for tremor suppression with an exoskeleton robot

Yosuke Ono[1], Kazuo Kiguchi[1], and Nobuhiro Okada[1]

[1]Kyushu University, Japan
(Tel: 81-92-802-3167)

[1]2TE11304G@s.kyushu-u.ac.jp

Abstract: An essential tremor is one of the most common tremor disorders of the arm and it may occur during a voluntary motion. Power-assist robots are useful for the physically weak persons to perform the daily motion. Although some power-assist robots are controlled based on electromyogram (EMG) signals, EMG signals are also influenced by the essential tremor. Therefore, when the user who suffers from the tremor uses the EMG-based controlled power-assist robot, the robot might magnify the vibration of the tremor. Although the tremor suppression control has been proposed for the EMG-based controlled power-assist robot to suppress the tremor in the hand position, the other part of the upper-limb might still vibrate since actual tremor movement of the upper-limb has not been analyzed precisely. Therefore, an upper-limb tremor sensing system is proposed to measure and analyze the precise tremor motion in this paper.

Keywords: essential tremor, power-assist robot, electromyogram, tremor sensing system

1 INTRODUCTION

A human motion is classified into two groups. One is a voluntary motion and the other is an involuntary motion. In a power-assist robot which is activated based on electromyogram (EMG) signals, the EMG signals are used to estimate the user's motion intention in real-time. Since the amount of EMG signal is related to the muscle activity level, the EMG signal is affected not only a voluntary motion but also an involuntary motion. Therefore, the involuntary motion might be misunderstood as the user's motion intention in the EMG-based controlled power-assist robot.

A tremor is one of the involuntary motions. It is somewhat rhythmic motion that may occur in various body parts such as an arm, a leg and so on. An essential tremor is one of the most common tremor disorders of the arm and it may occur during a voluntary motion. If the essential tremor occurs in the arm, the person may not be able to achieve the target task properly. To suppress a tremor, many methods have been proposed [1,2]. For example, Kiguchi et al. proposed the tremor suppression control method that extract the vibrational component of the estimated motion using band pass filter, and suppress the tremor by adding opposite phase force vector [3]. However, this method focused on only the estimated motion of the hand and the tremor motion of the elbow or the shoulder is not taken into consideration. Therefore, the other part of the upper-limb might still vibrate since actual tremor movement of the upper-limb has not been analyzed precisely yet.

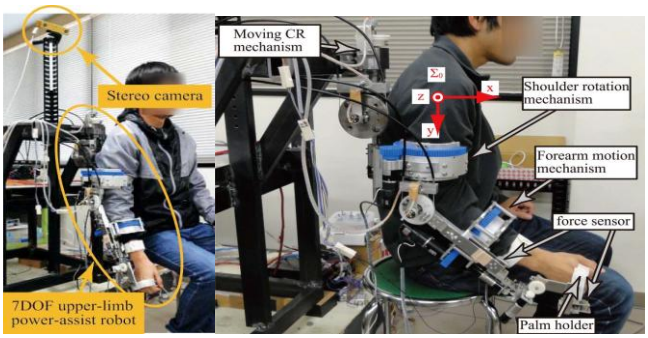

Fig. 1 7DOF upper-limb power-assist exoskeleton robot

Although there are a lot of researches of the essential tremor [4-6], there are no research which investigated about the relationship of the motion of hand, elbow, and shoulder. Therefore, an upper-limb tremor sensing system, which consists of three acceleration sensors, a gyroscope, and an encoder, is proposed to measure and analyze the precise tremor motion in this paper.

2 UPPER-LIMB POWER-ASSIST EXOSKELETON ROBOT

The 7DOF exoskeleton power-assist robot [3] for the upper limb used in this paper is shown in Fig1. The robot consists of seven DC motors. This robot is able to assist the most of each human upper-limb joint motion (shoulder vertical and horizontal flexion/extension motion, shoulder internal/external rotation motion, elbow flexion/extension motion, forearm supination/pronation motion, wrist palm flexion/extension motion and wrist palm radial/ulnar deviation motion).

© ISAROB 2013

3 EMG-BASED CONTROL METHOD

To estimate the user's motion and control the 7DOF upper-limb power-assist exoskeleton robot, sixteen channels of EMG signals are used as main input signals.

Since raw EMG signals are not suitable as input signals to the controller, the feature of the raw signal must be somehow extracted. In order to extract the feature of the raw EMG signal, the root mean square (RMS) of the EMG signal is calculated and used as an input for the controller. The RMS calculation is written as follows:

$$RMS = \sqrt{\frac{1}{N}\sum_{i=1}^{N} v_i^2} \tag{1}$$

where N is the number of the segments ($N=400$) and v_i is the voltage at i^{th} sampling. The sampling frequency is 1.5 kHz. Using sixteen RMS values, the joint torque vector is written as:

$$\tau = \begin{bmatrix} \tau_1 \\ \tau_2 \\ \tau_3 \\ \tau_4 \\ \tau_5 \\ \tau_6 \\ \tau_7 \end{bmatrix} = \begin{bmatrix} w_{11} & w_{12} & \cdots & w_{115} & w_{116} \\ w_{21} & w_{22} & \cdots & w_{215} & w_{216} \\ \vdots & \vdots & \ddots & \vdots & \vdots \\ w_{61} & w_{62} & \cdots & w_{615} & w_{616} \\ w_{71} & w_{72} & \cdots & w_{715} & w_{716} \end{bmatrix} \begin{bmatrix} ch_1 \\ ch_2 \\ \vdots \\ ch_{15} \\ ch_{16} \end{bmatrix} \tag{2}$$

where τ_i are the joint torques for i^{th} joint motor, w_{ij} is the weight value for j^{th} EMG signal to estimate the torque of motor-i, and ch_j represents the RMS value of the EMG signal measured in channel i. The weight matrix (i.e., the muscle-model matrix) in eq.(2) can be defined using the knowledge of human upper-limb anatomy or the results of experiments. Therefore, the joint torque vector generated by muscle force can be calculated if every weight for the EMG signals is properly defined. Furthermore, the posture of the upper-limb affects the relationship between the EMG signals and the generated joint torques because of anatomical reasons such as change of the moment arm. In other words, the role of each muscle for a certain motion varies in accordance with joint angles. Consequently, the effect of the posture difference of the upper-limb must be taken into account to estimate the correct upper-limb motion for the power-assist. Therefore, a neuro-fuzzy muscle-model matrix modifier [3] is applied to take into account the effect of the upper-limb posture change of the user in on-line manner. The neuro-fuzzy modifier is used to adjust the weight matrix in eq. (2) by multiplying the coefficients in accordance with the upper-limb posture of the user, so that the effect of upper-limb posture difference can be compensated effectively.

To estimate user's motion intention, hand force vector is calculated based on the estimated joint torque vector. τ is transferred to the hand force vector of the user as follows:

$$F_{end} = J^{-T}\tau \tag{3}$$

$$F_{avg} = \frac{1}{N_f}\sum_{i=1}^{N_f} F_{end}(i) \tag{4}$$

where F_{end} is the hand forece vector, J is the Jacobian matrix, F_{avg} is average of F_{end} in N_f number of samples. Then, the hand acceleration vector can be calculated based on eq.(4).

$$\ddot{X}_d = M^{-1}F_{avg} \tag{5}$$

where $\ddot{X}_d$ is the desired hand acceleration vector, and M is the weight matrix of the user's upper-limb and the robot. The desired hand velocity and position can be calculated based on eq.(5). In addition, the following impedance control equation is used to calculate the resultant hand force vector F

$$F = M\ddot{X}_d + B(\dot{X}_d - \dot{X}) + K(X_d - X) \tag{6}$$

where B is the viscous coefficient matrix and K is the spring coefficient matrix. The impedance parameters B and K in eq.(6) depend on the upper-limb posture and activity levels of activated upper-limb antagonist muscles. Therefore, the impedance parameters have to be adjusted in real time. So B and K are defined based on the upper-limb posture and activity levels of activated upper-limb antagonist muscles.

Finally, the joint torque command vector τ_{motor} is calculated as follows:

$$\tau_{motor} = \kappa J^T F \tag{7}$$

where κ is the power-assist rate. When the user's muscle activation levels are low, force/torque sensor-based control is used to control the robot.

4 EXPERIMENT.

The tremor is somewhat rhythmic motion that may occur in various body parts. Especially, an essential tremor is one of the most common tremor disorders of the upper-limb and it may occur during a voluntary motion. If the essential tremor occurs in the upper-limb movement, the person may not be able to achieve target task properly. There are various researches in regard to the tremor motion of upper-limb. Although the hand motion of tremor has been analyzed up to the present, the detailed tremor motions such as amplitude of vibration, angular velocity, angular acceleration of the shoulder, the elbow, and the

© ISAROB 2013

wrist joint have not been analyzed. Therefore, in this paper, the upper-limb tremor sensing system which consists of three acceleration sensors, a gyroscope, and an encoder is proposed to measure the tremor motion precisely.

4.1 Experiment equipment

The upper-limb tremor sensing system developed in order to measure tremor is shown as Fig.2. The accelerometer was attached in the elbow, the wrist, and the hand. Moreover, the encoder was attached center of rotation of an elbow. Moreover, the gyroscope was attached in order to measure the angle of 3 DOFs of the shoulder, and the acceleration of an elbow to the upper arm side of an elbow. Since the frequency of the essential tremor 5 to 12 Hz, the band pass filter (5 to 12Hz) is applied to the output of the accelerometers. In order not to restrict a patient's motion, it was made by not using metaled frame as much as possible, and sensors were attached on the human's body directly. However, the encoder which measures angle of rotation of an elbow was attached on the aluminum frame. Moreover, since a wrist had the unstable surface, the accelerometers in the wrist part were attached on the plastic plate. The initial posture of elbow was set to be 90[deg] to avoid a singular configuration when the elbow was extended. The initial postures of the other joints were determined to be 0[deg] in the model of Fig.3. Moreover, I got the subject to take care so that an elbow may not be lengthened. Moreover, in order to avoid a problem of the singular configuration due to the attached position of the singular configuration due to the attached position of an accelerometer, two accelerometers are applied to compensate each other in the proposed system such as Fig.2 right side picture. Since the distal part from the wrist, angular information was calculated by integrating the angular acceleration obtained by the accelerometers of an elbow, a wrist, and a hand.

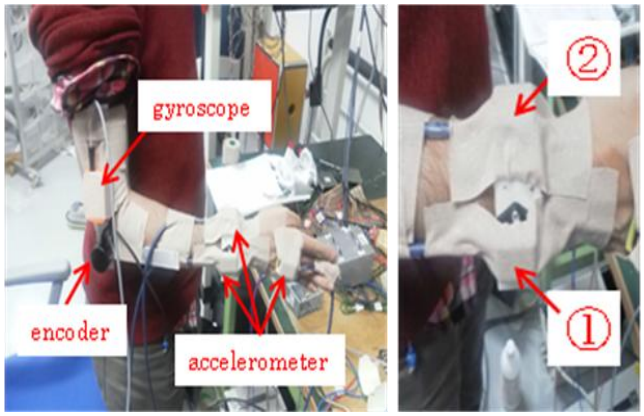

Fig.2 Experiment equipment (left: overall, right: wrist)

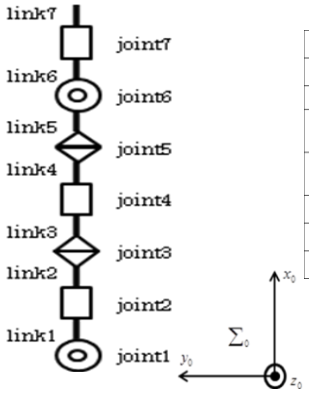

Table.1 D-H parameter

i	a_i	α_i	d_i	θ_i
1	0	0°	0	q_1
2	0	90°	0	90° $+q_2$
3	0	90°	l_u	180° $+q_3$
4	0	90°	0	180° $+q_4$
5	0	90°	l_f	90° $+q_5$
6	0	90°	0	90° $+q_6$
7	0	90°	0	q_7

Fig.3 Model of upper-limb

4.2 The analysis method

The method that calculate the position, the velocity, the accelerometer of an elbow, a wrist, a hand, and angle, angular velocity, angular accelerometer of a shoulder, an elbow, a wrist is explained in this section. The model of upper arm is shown as Fig.3. The coordinate frame Σ_0 in Fig. 3 is a coordinate frame fixed to the shoulder. The coordinate frame fixed to the shoulder is the same as the initial posture of the joint 1. Joint1-7 represent shoulder abduction/adduction, shoulder flexion/extension, shoulder internal/external rotation, elbow flexion/extension, forearm supination/pronation, wrist palm flexion/extension, and wrist palm radial/ulnar deviation, respectively. The D-H parameters were defined as shown in Table.1.

4.2.1 The calculation method of each angular information

The angles of joint1, joint2, joint3, and joint4 can be calculated based on the value acquired from the angle sensor. The angular velocity of joint1, joint2, joint3, joint4 are calculated by differentiating the angle as follows:

$$\dot{q}_{1\sim4}^{i+1} = (q_{1\sim4}^{i+1} - q_{1\sim4}^{i}) / \Delta t \tag{8}$$

where i is the number of times of measurement and Δt is sampling time. Sampling time is 0.01[sec]. Since the angle sensor was not attached for the joint5-7 in order not to restrict the patient's motion, the value of the accelerometer was changed into angular acceleration using the following equation, and the angle and angular velocity are calculated by integrating the angular acceleration using the eq.(10) and a eq.(11).

© ISAROB 2013

$$\begin{bmatrix} \ddot{q}_1 \\ \ddot{q}_2 \\ \ddot{q}_3 \\ \ddot{q}_4 \\ \ddot{q}_5 \\ \ddot{q}_6 \\ \ddot{q}_7 \end{bmatrix}^i = J^{-1}\left(\begin{bmatrix} \ddot{x}_h \\ \ddot{y}_h \\ \ddot{x}_w \\ \ddot{y}_w \\ \ddot{z}_w \\ \ddot{y}_e \\ \ddot{z}_e \end{bmatrix}^i - \dot{J} \begin{bmatrix} \dot{q}_1 \\ \dot{q}_2 \\ \dot{q}_3 \\ \dot{q}_4 \\ \dot{q}_5 \\ \dot{q}_6 \\ \dot{q}_7 \end{bmatrix}^i \right) \tag{9}$$

$$\dot{q}_{5\sim7}^{i+1} = \ddot{q}_{5\sim7}^{i} \times \Delta t + \dot{q}_5^i \tag{10}$$

$$q_{5\sim7}^{i+1} = \frac{1}{2} \times \ddot{q}_{5\sim7}^{i} \times (\Delta t)^2 + q_{5\sim7}^{i} \times \Delta t + q_{5\sim7}^{i} \tag{11}$$

where J^{-1} is the inverse jacobian matrix, which is 7×7 matirix, and $\dot{J}$ is the differentiated jacobian matrix. As shown in eq.(9), it was calculated using the acceleration of 2 axes of a hand's x and y, the acceleration of 3 axes of a wrist, and the acceleration of 2 axes of y of an elbow, and z. In regard to the accelerometers of the wrist, accelerometer1 in Fig.2 becomes singular configuration when $q_5 = 0[\mathrm{deg}]$, and accelerometer2 becomes singular configuration when $q_5 = \pm 90[\mathrm{deg}]$. Therefore when $-80 < q_5 < 80[\mathrm{deg}]$, the accelerometer2 was used, and when $q_5 < -80[\mathrm{deg}]$, $q_5 > 80[\mathrm{deg}]$, the accelerometer1 was used.

4.2.2 The calculation method of other information

All of the position, the velocity, and the acceleration of hand, wrist, and elbow were changed into the value in the fixed coordinate frame of the shoulder. The homogeneous transformation procession and the rotating matrix were calculated with D-H parameters in Table1.

4.3 Experiment results

The effectiveness of the developed upper-limb trem or sensing system was confirmed with a healthy huma n subject as a first step. Healthy person wore an exper iment equipment, and moved arm in the various directi ons at random. The calculated result of elbow position is shown in Fig. 4. The calculated result of wrist pos ition is also shown in Fig.5. As shown in Fig.4, and Fig5, the position of elbow and wrist were calculated precisely from q1-q4 which is taken by attached angle sensor. However, q5-q7's angular information were not calculated precisely. For the reason of this result, the instability of the surface human's skin is considered to be the cause. Because the noise caused by the acceler ometers attached on the unstable surface of the subject skin is accumulated. As a future work, the attachment method of accelerometers must be considered so that the data of acceleration can be acquired correctly.

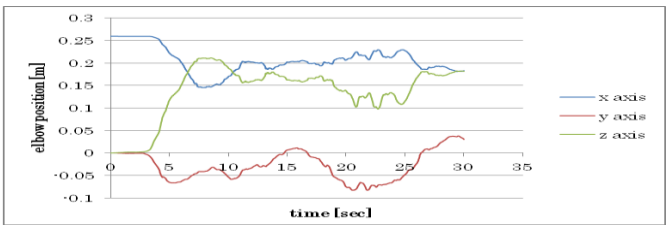

Fig.4 Elbow position

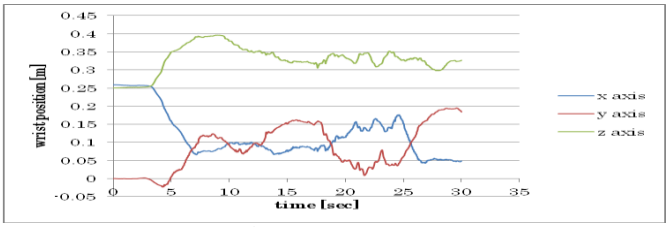

Fig.5 Wrist position

5 CONCLUSION.

In this paper, the upper-limb tremor sensing system which consists of three acceleration sensors, a gyroscope, and an encoder is proposed to measure the tremor motion. The effectiveness of the developed system was evaluated by performing experiments with a healthy human subject. As a result, the position of elbow and wrist is calculated precisely, although q5-q7 could not be calculated precisely since attachment of accelerometers were unstable. As a future work, the attachment method of accelerometers must be considered.

REFERENCES

[1] F.Widjaja, C.Y.Shee, P.Poignet et al, "Filtering Intended Motion for Real-time Tremor Compensation in Human Upper Limb using Surface Electromyography," 31th Annual Inter. Conf. of the IEEEEMBS, pp.2996-2999,2009

[2] K. Yano, E. Ohara, S. Horihata, T.Aoki et al, "Development of Tremor Suppression Control System Using Adaptive Filter and Its Application to Meal-assist Robot," Trans. of the Society of Instrument and Control Engineers, Vol. 45, No. 12, pp. 638-645, 2009.

[3] Kazuo Kiguchi, Yoshiaki Hayashi, Toyoko Asami, "An Upper-Limb Power-Assist Robot with Tremor Su ppression Control," Rehabilitation Robotics (ICORR), 2 011 IEEE International Conference.

[4] S. Pledgie, K. E. Barner, S. K. Agrawal, et al, "Observations on essential (heredofamilial) tremor, " Br ain, Vol. 72, No. 2, pp. 113-139, 1949.

[5] E. D. Louis, B. Ford, and L. F. Barners, "Clinic al subtypes of essential tremor," Arch Neurol, Vol. 57, pp. 1194-1198, 2000.

[6] Juan-Manuel Belda-Lois, Helios de-Rosario, et al, "Can human movement analysis contribute to usability understanding?", Human Movement Science 29(2010)5 29-541

The Eighteenth International Symposium on Artificial Life and Robotics 2013 (AROB 18th '13),
Daejeon Convention Center, Daejeon, Korea, January 30-February 1, 2013

A describing method of latency tolerant hardware for a pure ANSI-C/C++ based high-level synthesis technology

Akira Yamawaki[1] and Seiichi Serikawa[1]

[1]Kyushu Institute of Technology, Japan
(Tel: 81-93-884-3255, Fax: 81-93-884-3214)

[1]yama@ecs.kyutech.ac.jp

Abstract: The image processing is important for the robotics and its hardware implementation is required in order to realize a small and low-power device with the appropriate performance where the high performance computer cannot be used due to the cost, size and power limitation. To reduce the burden of such hardware development, the high-level synthesis (HLS) technologies that automatically convert the algorithmic description to hardware have been proposed and developed. The combination of the memory latency hiding and data process pipelining is very important to extract the hardware performance maximally. However, nobody shows clearly how to describe the hardware behavior to generate such hardware. This paper shows a generic describing method for HLS technology based on ANSI-C/C++ that can realize the combination of the memory latency hiding and data process pipelining. The experimental results show that our method can be applied easily to the intuitive C program. The logic simulation and an FPGA implementation reveal the effects to the performance improvement and the hardware increase induced by our method.

Keywords: high-level synthesis, latency hiding, pipelining, hardware, image processing.

1 INTRODUCTION

The image processing, e.g. the object tracking, the object recognition, and so on, is important for the robotics. Hardware implementation of the image processing is required in order to realize a small and low-power device with the appropriate performance where the high performance computer cannot be used due to the cost, size and power limitation.

However, the hardware is developed by an expert using hardware description language (HDL), spending a significant burden. At last the large development load can realize the image processing hardware optimized to performance and power consumption.

To reduce such burden of hardware development, the high-level synthesis (HLS) technologies that automatically convert the algorithmic description to HDL program have been proposed and developed [1-5]. Most HLS tools employ the C language as the design entry. However, the design entries are C-like language, which is not pure ANSI-C/C++. Also, some HSL tools provide their own grammar suiting to represent the hardware nature. That is, the developers have to learn the dedicated C-like language although they need not to learn HDL.

In contrast, some HLS tools supporting ANSI-C/C++ as a design entry are provided recently [6], [7]. Instead of C-like language that describes parallelism and clock boundary of the hardware explicitly, the HLS tools supporting ANSI-C/C++ automatically extract them from the sequence of statements and loops in a pure C/C++ program.

Actually, the parallelism however cannot be extracted enough. So, the developer must indicate parallelism by pragmas explicitly. Typical and simple examples showing how to insert pragmas are shown by the venders of the HLS tool. But, some describing methods which are expected to generate a sophisticated hardware to improve the hardware performance are not shown mostly. For example, it is to combine the memory latency hiding and data process pipelining. This combination is very important to pull the performance of the hardware maximally.

Using an HLS tool (Vivado HLS of Xilinx [6]) supporting pure ANSI-C/C++, this paper shows a generic describing method of ANSI-C/C++ program that can realize the combination of the memory latency hiding and the data process pipelining. In this method, the memory loading part, the data processing part and the memory storing part are described isolated by FIFO passing the stream data. While the memory loading part and the memory storing part transfer the data to the memory, the data processing part processes the stream data via FIFO simultaneously. Thus, the memory access is overlapped with the data processing efficiently and naturally.

© ISAROB 2013

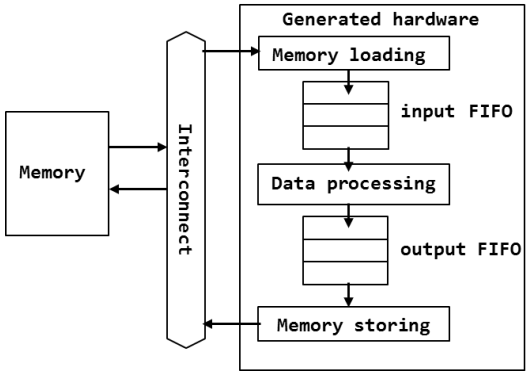

Fig. 1. Hardware model

In a case study to 3x3 image filter, we show that our method can be applied easily to the intuitive C program. In addition, through the logic simulation and implementation to an FPGA, we confirm the effects to the performance improvement and hardware increase induced by our method.

The rest of the paper is organized as follows. Section 2 shows a hardware model to which we map C program. Section 3 intuitively designs the hardware description in C to 3x3 image filter. Section 4 extends the intuitive C program mentioned above to combine the memory latency hiding and data process pipelining by our method. Section 5 evaluates the hardware overhead and the performance improvement induced by our method, compared with the intuitive C program. Finally, Section 6 concludes the paper.

2 HARDWARE MODEL

Fig. 1 shows a hardware model to which we map C program. The organization of this model is commonly used. Thus, any hardware designer can accept to employ this model.

This model is decomposed to the memory loading part, the data processing part and the memory storing part. These parts are separated by FIFOs. They run completely in parallel, communicating via FIFO streamly each other.

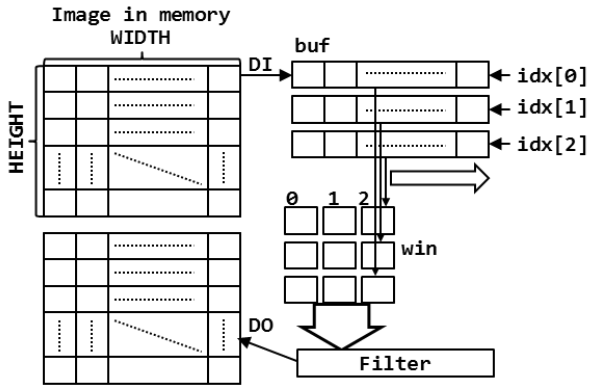

Fig. 2. Image of Data process

```
 1:void Top(uint32_t *DI,uint32_t *DO)
 2:{
 3:  int i, j;
 4:  static uint32_t buf[3][WIDTH];
 5:  static uint32_t win[3][3];
 6:  uint8_t  idx[3];
 7:  uint8_t  tmp;
 8:  uint32_t result;
 9:  idx[0]=0; idx[1]=1; idx[2]=2;
10:  for(i=0;i<HEIGHT;i++){
11:    for(j=0;j<WIDTH;j++)
12:      buf[idx[2]][j]=DI[i*WIDTH+j];
13:    for(j=0;j<WIDTH;j++){
14:      Win_Shift_Right(win);
15:      win[0][2]=buf[idx[0]][j];
16:      win[1][2]=buf[idx[1]][j];
17:      win[2][2]=buf[idx[2]][j];
18:      Filter(win,&result);
19:      DO[i*WIDTH+j]=result;
20:    }
21:    tmp=idx[0];idx[0]=idx[1];
22:    idx[1]=idx[2];idx[2]=tmp;
23:  }
24:}
```

Fig. 3. Intuitive C program

The memory loading part loads the data to be processed in a memory into the input FIFO. The data processing part gets the input data from the input FIFO, processes the input data and pushes the processed data into the output FIFO. The memory storing part pops the processed data from the output FIFO and stores them into the memory.

The data processing part processes the stream data through its own pipelined data path, while the memory loading and storing parts perform the memory accesses. Thus, the memory latency is hidden by the pipelined data processing.

This model is trivial but nobody has explained clearly how to write to generate such hardware. That is, since a generic describing method does not exist, the designer has to write the hardware behavior in C carefully by its own talent so that the hardware model as shown in Fig. 1 is generated.

3 INTUITIVE METHOD

To confirm that our method can be applied easily to the intuitive C program, we describe the case study of 3x3 image filter in this section. Fig. 2 depicts the data processing image of 3x3 image filter and Fig. 3 describes an intuitive C program of the hardware behavior.

For the input image, a column is loaded into the top of the internal ring buffer along the image height as the lines of 11 to 12 in Fig. 3.

To the buffer holding columns, a 3x3 image filter is performed as the lines of 14 to 18 in Fig. 3. 3 pixels in the 3

rows currently indexed in the buffer are pushed into the 3x3 window. Then, an image filter processes this 3x3 window. The result of the image filter is stored into the memory as the line of 19 in Fig. 3.

Once the 3x3 image filter finishes on the buffer, the indexes to banks of the buffer are updated to load a next column to new top entry as the lines of 21 to 22 in Fig. 3.

Inserting pragma, the pipeline structure can be extracted by an HLS tool, Vivado HLS 14.3 [6]. For example, the inner loops of the line 11 and the line 13 are converted to the pipeline hardware. However, the parallel feature among the memory access and data processing cannot be extracted by any pragma. Although we cannot analyze the internal processes of the Vivado HLS in detail, the data dependency over some arrays may be a reason to obstruct the parallelization. That is, the C program must be reconstructed to extract the parallelism between the memory access and data process.

4 PROPOSED METHOD

Our proposed method is very simple and easy way to reconstruct the intuitive C program. Fig. 4 shows the C program of which the intuitive C program shown in Fig. 3 is reconstructed by our method.

The program basically consists of 3 functions which are the memory loading (*mem_load*), the data processing (*data_proc*) and the memory storing (*mem_store*). These functions are connected by the FIFOs. This structure is equal to that of Fig. 1.

Each function runs individually from the top to the bottom of the image. To make them run in parallel, the DATAFLOW pragma [6] is assigned to the function *Top* in order to extract the parallelism among the functions. In addition, the data dependency among the functions has to be cut. Thus, the streaming FIFOs, iFIFO and oFIFO which are bridges among the functions are defined in the function *Top*.

The *mem_load* pushes the pixel in the memory into the iFIFO until the iFIFO becomes full.

Simultaneously, the *data_proc* pops the iFIFO and stores the popped data into the top of the ring buffer while the iFIFO is not empty. Once the top of the ring buffer becomes full, the data_proc performs 3x3 image filter as same as Fig. 3. However, the processed data is pushed into the oFIFO instead of the memory. The pipelining is also performed to the inner loops of the same as Fig. 3 by the PIPELINE pragma [6].

In addition, the *mem_store* pops the oFIFO and stores the popped data into the memory in parallel.

```
 1:void mem_load(uint32_t mem[HEIGHT*WIDTH],
 2:                 stream<32>& iFIFO ){
 3:  int i, j;
 4:  for(i=0;i<HEIGHT;i++)
 5:    for(j=0;j<WIDTH;j++)
 6:      //Push iFIFO
 7:      iFIFO.write(mem[i*WIDTH+j]);
 8:}
 9:void data_proc(stream<32>& iFIFO,
10:                   stream<32>& oFIFO){
11:  int i, j;
12:  static uint32_t buf[3][WIDTH];
13:  static uint32_t win[3][3];
14:  uint8_t  idx[3];
15:  uint8_t  tmp;
16:  uint32_t dat, result;
17:  idx[0]=0; idx[1]=1; idx[2]=2;
18:  for(i=0;i<HEIGHT;i++){
19:    for(j=0;j<WIDTH;j++){
20:      iFIFO.read( dat ); //Pop iFIFO
21:      buf[idx[2]][j]=dat;
22:    }
23:    for(j=0;j<WIDTH;j++){
24:      Win_Shift_Right(win);
25:      win[0][2]=buf[idx[0]][j];
26:      win[1][2]=buf[idx[1]][j];
27:      win[2][2]=buf[idx[2]][j];
28:      Filter(win,&result);
29:      oFIFO.write(result); //Push oFIFO
30:    }
31:    tmp=idx[0];idx[0]=idx[1];
32:    idx[1]=idx[2];idx[2]=tmp;
33:  }
34:}
35:void mem_store(uint32_t mem[HEIGHT*WIDTH],
36:                stream<32>& oFIFO ){
37:  int i, j;
38:  uint32_t tmp;
39:  for(i=0;i<HEIGHT;i++)
40:    for(j=0;j<WIDTH;j++){
41:      oFIFO.read(tmp); // Pop oFIFO
42:      mem[i*WIDTH+j]=tmp;
43:    }
44:}
45:void Top(uint32_t *DI, uint32_t *DO){
46:  int i, j;
47:  static stream<32> iFIFO, oFIFO;
48:  mem_load (DI   , iFIFO);
49:  data_proc(iFIFO, oFIFO);
50:  mem_store(DO   , oFIFO);
51:}
```

Fig. 4. C program reconstructed by our me

Using our method, the memory loading and storing parts are accessing the memory while the data processing part is processing the data fast by the pipelining. That is, our method can naturally express the hardware which hides the memory latency to extract the performance of the pipelined hardware maximally.

5 EXPERIMENT AND DISCUSSION

5.1 Performance evaluation

To evaluate the performance of the hardware to which Vivado HLS 14.3 converts the C program, we have

Table 1. Hardware cost

Resolution	FIFO	LUT	FF	BRAM	Average
QVGA	256	1.47	1.56	1.33	1.45
VGA	512	1.63	1.48	1.33	1.48
720P	1024	1.53	1.51	1.44	1.49
SXGA	1024	1.49	1.48	1.44	1.47
1080P	1024	1.49	1.48	1.44	1.47

performed the logic simulation on the Modelsim 10.1c of Mentor Graphics. We set the clock frequency to 100MHz.

Fig. 5 shows the experimental results. The ORG of the horizontal axis means the intuitive version shown in Fig. 3. Also, the PAR indicates the version that is modified by our method shown in Fig. 4. The values on our method mean the depth of the input and output FIFOs. The vertical axis indicates the normalized execution time to the intuitive version. The data are measured over several resolutions of the input image. The filter was the average filter.

The result shows that our method can improve the performance compared with the intuitive version by the combination of the memory latency hiding and the data process pipelining. The depth of FIFO affects the performance improvement due to our method. The deeper, the better. However, the speedup is saturated by about 1.5 times. That is, the optimum depth exists to improve the performance maximally, suppressing the hardware cost.

5.2 Hardware Overhead

To improve the performance maximally while suppressing the hardware cost, the optimum point of the FIFO depth exists as mentioned above. Thus, we confirm that the hardware cost at the boundary point of the FIFO depth is compensated by the performance improvement compared with the hardware size of the intuitive version. To do this, we have implemented the hardware into an FPGA, Spartan-6 of Xilinx. The used implementation tool is ISE 14.3. Table. 1 shows the result of this evaluation.

FIFO means the depth of the i/o FIFOs. The LUT means the number of lockup tables realizing the combinational logic. The FF means the number of flip-flops. The BRAM means the number of embedded memories in the FPGA.

The result shows that the investment of hardware resources increased by our method is appropriate enough for the performance improvement of 1.5 times.

6 CONCLUSION

We have proposed a generic describing method of a latency tolerant hardware for a pure ANSI-C/C++ based high-level synthesis technology. Through the case study that uses 3x3 image filter, we have shown that our method can be introduced easily into the intuitive C program. Also, it has been confirmed that the performance improvement can be achieved by the moderate hardware investment.

As future work, we will evaluate our method to more application programs and apply it to more HLS tools.

REFERENCES

[1] Mitrionics (2008), Mitrion User's Guide 1.5.0-001, Mitrionics.

[2] Pellerin D and Thibault S (2005), Practical FPGA Programming in C, Prentice Hall.

[3] Lau D, Pritchard O and Molson P (2006) Automated Generation of Hardware Accelerators with Direct Memory Access from ANSI/ISO Standard C Functions, IEEE Symp. on Field Programmable Custom Computing Machines, pp.45-56.

[4] Mentor Graphics (2012), Handel-C Synthesis Methodology, http://www.mentor.com/products/fpga/handel-c/

[5] Yamawaki A and Masahiko I (2011) High-level Synthesis Method Using Semi-programmable Hardware for C program with Memory Access, Engineering Letters, Vol.19, Issue 1, pp.50-56.

[6] Xilinx (2012) Vivado Design Suite User Guide High-Level Synthesis, Xilinx user guide, UG902 (v2012.2).

[7] Calypto (2012) Designing High Performance DSP Hardware Using Catapult C Synthesis and the Altera Accelerated Libraries, Calypto White Paper, WP-0004 05-2012, http://calypto.com.

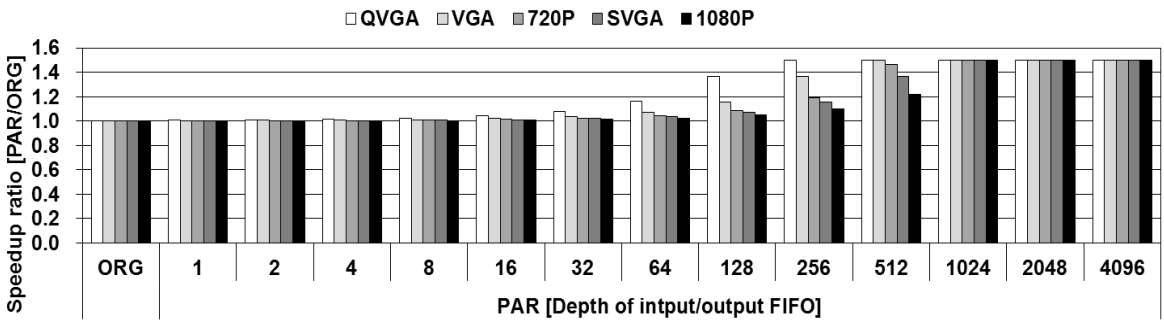

Fig. 5. Performance evaluation

The Eighteenth International Symposium on Artificial Life and Robotics 2013 (AROB 18th '13),
Daejeon Convention Center, Daejeon, Korea, January 30-February 1, 2013

A Research on State Recognition in Wide Area by Aerial Images Analysis

Ganwen Jiang[1], Masayuki KASHIMA[1], Kiminori SATO[1]
and Mutsumi WATANABE[1]

[1]Kagoshima University, Japan
(Tel: 81-80-5264-2806)

[1]kyoukinbun@yahoo.co.jp

Abstract: This paper proposes an autonomous monitoring system to track the subject in real time by using aerial images, novel image processing method, and helicopter control technique. In this study, flying robot named AR.Drone is used for solving the problem of insufficient tracking capability in previous studies. In order to track the subject correctly and control the flying robot in right direction, it is important to understand the information of the subject's moving direction. For calculating the moving direction correctly from aerial images, new method by integrating various kinds of modules is proposed. With experiments, the stability of human tracking capability and the effectiveness of the direction estimation by aerial images analysis is verified.

Keywords: State recognition, Aerial images, Autonomous monitoring system, Moving direction, Automatic human tracking, AR.Drone autonomous control.

1 INTRODUCTION

Recently, the study on state recognition has developed rapidly [1]. For recording the state and behavior of the subject, automatic monitoring system is necessary. In previous studies, multiple fixed cameras are used to analyze the subject state [2]. However, when it is difficult to ensure field of view due to shielding, setting of cameras is restricted. Also, when the subject leaves out of the camera view, the subject would be lost. In other words, insufficient tracking capability and limited field of vision as the main problems exist in conventional technique.

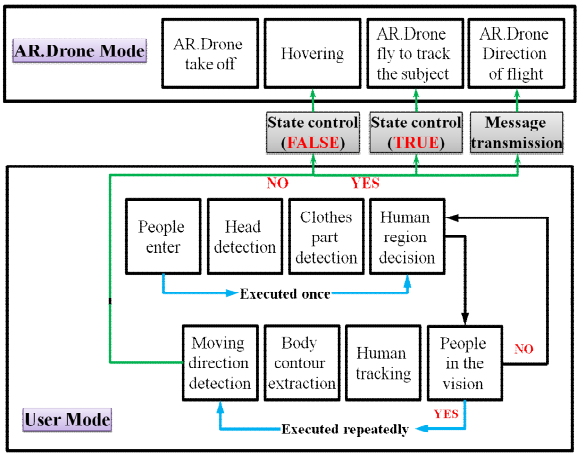

Fig. 1. Functional diagram of study

To ensure effective field of view, and appropriately recognize indoors and outdoors, the aerial images have been our attention in this research. By using flying robot named AR.Drone, the aerial photography system is built. According to aerial photography and motion analysis, the system on state recognition in wide area is developed.

Fig.1 shows the functional diagram of the study. Firstly, flying robot takes off, and hovers in air waiting human entry. When subjects enter, it is to carry out head detection, clothes detection, and human area determination. Then, judges whether human is in the vision. If human is in view, track the subject and calculate the moving direction. If human is out of the viewing range, it will move back to search the subject again by features of head and clothes color learned. If the data of moving direction is received, the flag of state control will become true, and transmit the data to AR.Drone mode to control flying robot tracking the subject. Otherwise, flying robot is hovering continuously. The purpose of this study is to monitor the subject in real time by utilizing flying robot.

The novelties of this study are as follows.

(1) To improve the effective range of vision and tracking capabilities, the aerial images taken by flying robot is utilized.

(2) Comparing to conventional tracking method, new method by integrating various kinds of modules is devised.

(3) Control flying robot accurately with the propeller control and predictive control.

2 PREVIOUS STUDIES

Formerly, there are many studies on human behavior, action, and state recognition. In the present study, it is a

© ISAROB 2013

new idea to monitor human action and behavior by using flying robot and novel image processing method.

In the study of FUKUDA et al. [2], human detection by characteristics of hair color, head shape, clothes color, and position have been done by multiple fixed cameras. When the subject is out of camera view, the subject would be lost. Also, when hair color is not black or clothes color is black, misdetection usually occurs. In the present study, for ensuring effective field of view, flying robot is utilized. From aerial images, the subject can be monitored in any time.

Also, there are many tracking methods such as Mean Shift, Particle Filter, and Active Contour Model (ACM) previously, but there are some problems in each method, so it will affect the tracking result. For example, in studies of YUSUKE et al. [3], NAKAGAWA et al. [4], and AOKI et al. [5], when the number of particle is too much, processing time will increase. On the other hand, if the number of particle is few, accuracy will degrade. On Mean Shift [6], the HSV or BGR information is used to track the subject. However, if the subject is not in the search area at the beginning, the average vector cannot be calculated, so the subject cannot be tracked. About ACM method [7], it is difficult to set the position of initial closed curve exactly. This problem will affect the contour extraction result. In addition, if there are some image noises, it is difficult to extract the subject contour correctly.

From the above, it is necessary to build a novel system to track the subject accurately, and then control flying robot by moving direction of the subject.

3 AERIAL PHOTOGRAPHY SYSTEM

Generally, there are two ways of active flying robot and passive balloon robot.

The advantages of using balloon robot are small power consumption, and high stability, while the disadvantages are poor tracking performance, low degree of freedom, and susceptible to outside influence. On the other hand, the advantages of flying robot are high tracking performance, possible to automatic control, and high stability, but it also has disadvantages of high power consumption.

Depending on the purpose of this research, the high tracking performance is essential, so flying robot is chosen.

In this study, AR.Drone manufactured by the Parrot Company is utilized. About AR.Drone, there are two cameras attached on the front and bottom. Also, there are sensors installed on it, such as the Gyro Sensor, the Ultrasonic Sensor, and the Acceleration Sensor.

4 PROPOSED SYSTEM and METHOD

4.1 Proposed system

Fig.2 shows the proposed system of the study. The proposed system is composed of two threads. One is image processing thread, and another is flying robot control thread. In image processing thread, by carrying out human detection, area determination, and tracking, the human moving direction vector can be obtained by time series analysis. At the same time, flying robot control thread start, and moving direction data is fed back to control thread. After that, flying robot is controlled to track the subject by human direction vector.

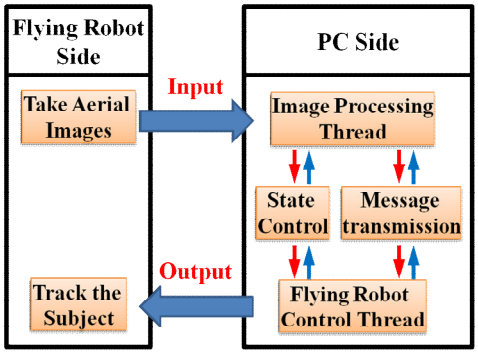

Fig. 2. Proposed system

4.2 Proposed method

In image processing part, this paper proposes the new method by integrating various kinds of modules to detect human moving direction.

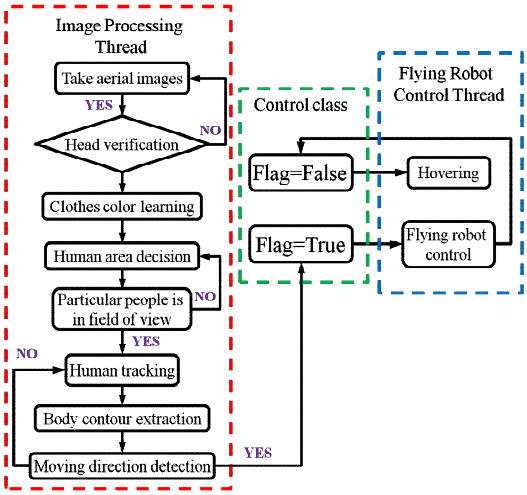

Fig. 3. Flowchart of research

From the top view, characteristics of human are few, such as head shape, head and clothes color, body contour, and moving direction. In order to control flying robot exactly, it is important to detect moving direction accurately. Fig.3 shows the flowchart of our research. From aerial images, head is important feature of people, so head

detection is carried out firstly. To calculate moving direction exactly, precise body contour is essential. Thence, through calculating the human area and human tracking, accurate initial contour can be determined for ACM algorithm. Therefore, accurate body contour can be got by initial contour extracting. It is the different from the conventional ACM method.

In flying robot control part, through controlling the propellers speed and rotation direction, flight direction of AR.Drone can be controlled. In addition, by predictive control, AR.Drone will be controlled to track the subject correctly.

4.2.1 Head detection

Beforehand, the standard HSV histogram (Hist1) is calculated by analyzing standard head image. Then, head candidates are detected from aerial images of each frame by the Hough Transform method. The edge image processed by the Sobel Operator is used for detecting head candidates. In addition, HSV histogram (Hist2) of each head candidate is calculated. Furthermore, head can be determined by comparing Hist1 to Hist2.

4.2.2 Human area decision

From aerial images, clothes part is in the surrounding of head. Therefore, by the algorithm of repeatedly outward diffusing based the head, the rough outline around head can be obtained.

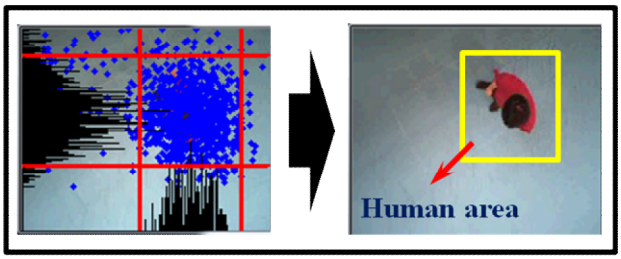

Fig. 4. Human area determination

Within this range, clothes color can be detected. After that, the color of clothes and head are learned. Then, many particles are distributed randomly on the image. Furthermore, the maximum likelihood of particles can be calculated due to BGR or HSV of head and clothes. Then, particles distribution could be calculated shown in Fig .4. In addition, human area will be determined according to particles distribution. Because color of clothes and head are learned, when particular people is out of view, subject can be detected again by Particle Filter algorithm. Otherwise, system must return to head detection again. Therefore, this process not only improves the accuracy of detection, but also reduces the processing time of whole system.

4.2.3 Human tracking

Human area has been determined in previous paragraph. In human area, according to the BGR or HSV histogram of clothes, human motion vector can be decided by Mean Shift algorithm. However, when multiple people are wearing the same color clothes, it is difficult to judge who the particular people is. Therefore, stability of moving direction with time series analysis is used to decide who the particular person is (as shown in Fig.5). It is important to achieve multiple people tracking with aerial images.

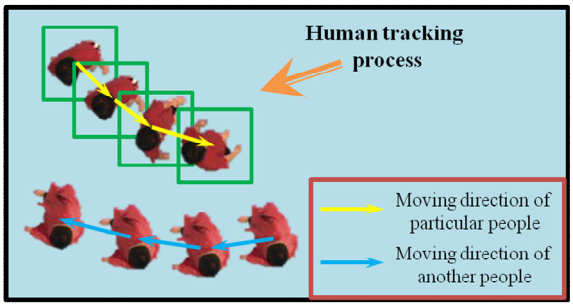

Fig. 5. Human tracking

4.2.4 Body contour extraction

In order to get human body contour, the Active Contour Model (ACM) is utilized [8]. In conventional ACM method, if image background is complex or object contour is irregular, it is difficult to set the initial contour and parameters. In this study, since human area has been determined accurately, the inscribed circle of human area can be as the initial contour. Then, body contour can be extracted exactly by initial converging.

4.2.5 Moving direction detection

From aerial images, moving direction is perpendicular to the shoulder. Therefore, it is necessary to know the direction of shoulder. The connecting line between the farthest points of body contour is as the direction of shoulder in this study. However, wrong results are received sometimes. Therefore, the time series analysis is utilized to except wrong results and predict moving direction next time.

4.2.6 Flying robot control part

The movement of AR.Drone is controlled by controlling speed and turning direction of four propellers. When moving direction is obtained in image processing thread, it is fed back to AR.Drone. At the same time, flying robot control thread starts, and then AR.Drone flies along the moving direction of human. However, when the moving direction of human changes, AR.Drone cannot automatically put on the brake rapidly in air, so predictive control is also important. By using time series analysis, the probability of moving direction in next time can be

© ISAROB 2013

predicted. By chance, if a particular person is out of view, AR.Drone will go up to detect particular people again.

5 EVALUATION EXPERIMENT

5.1 Experiment environment

The experiment is carried out in gymnasium. The third person view image and AR.Drone camera image are shown in Fig.6. This experiment is carried out when AR.Drone is hovering in air.

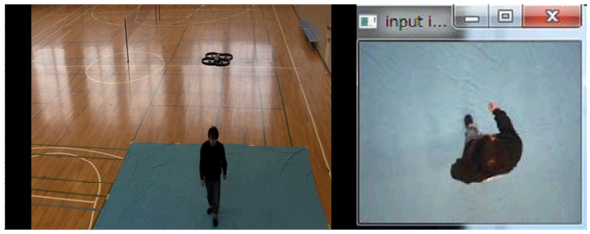

Third person view image Camera image

Fig. 6. Experiment environment

5.2 Experimental result

There are three cases in the evaluation experiment. First case is only one person is in the scene. Second case is there are two persons wearing clothes with different color. Third case is there are two persons wearing clothes with the same color. Sample images of each case are shown in Fig.7.

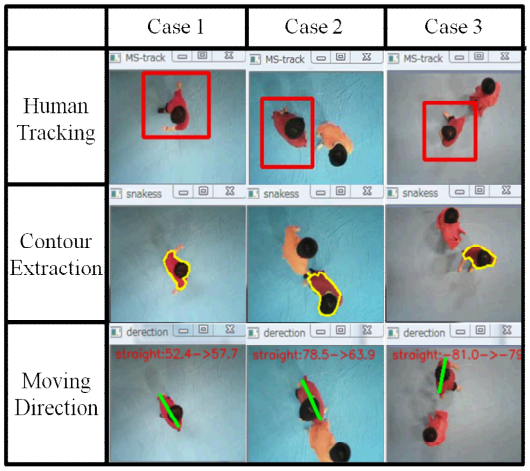

Fig. 7. Sample images of experiment results

With experiment, the success rate of human tracking is over 99%. When other people wearing the same color clothes enter into scene, the particular people also can be tracked exactly by using stability of moving direction. Compare to conventional ACM algorithm, success rate of contour extraction can be dramatically improved from 66% to 98% by setting initial contour accurately. In addition, success rate of moving direction is 95% by utilizing time series analysis. In future, the study on particular people is tracked automatically by AR.Drone will be carried out.

6 DISCUSSION

Due to evaluation experiment, the effectiveness of proposed system is proved. However, there are inadequacies also. To control AR.Drone accurately, the success rate of moving direction detection will be improved as much as possible. Currently, the time series analysis is limited in 10 frames. In future, it will be carried out in smaller interval. In addition, because there are many influences such as airflow, inertia, and the accuracy of sensors, it is difficult to control AR.Drone accurately. In future, this matter will be considered in detail.

7 CONCLUSION

In this study, aerial images system is utilized to solve the problems of insufficient tracking capability and limited field of view. With evaluation experiment, the high tracking performance, the high stability, and the effectiveness of proposed system are verified. Also, the moving direction of human can be detected in high accuracy. From now on, flying robot control part will be carried out. High efficiency aerial images system will be expected.

REFERENCES

[1] Takahiro KOIZUMI, Yuichi NAKAMURA, and Shin'chi SATOH, "Video Processing and Retrieval for Finding Lost Item from Personal Eye-View Video", Technical report of IEICE. PRMU 109 (470), 395-399 (2010).

[2] Toshio FUKUDA, Tatsuya SUZUKI, Yasuhisa HASEGAWA, Fumihito ARAI and Masaru NEGI, "Visual Surveillance System with Multiple Cameras in Wide Area Environment", Transactions of the Japan Society of Mechanical Engineers. C, Vol.69, No.680, pp.1011-1018 (2003).

[3] Yoshizawa YUSUKE, Koichi SHINODA and Sadaoki FURUI, "Surveillance Event Detection Using Local and Global Features", the Technical Report of IEICE, PRMU, 110 (27), pp.163-168 (2010).

[4] Hidehito NAKAGAWA, Hitoshi HABE and Masatsugu KIDODE, "Efficient prior acquisition of human existence by using past human trajectories and color of image", the Technical Report of IEICE, PRMU, 108 (484), pp.305-312 (2009).

[5] Yasuhiro AOKI, Yoshio IWAI and Masahiko YACHIDA, Detecting Suspicious Actions Using Particle Filtering", the Technical Report of IEICE, IE, 107 (538), pp.95-102 (2008).

[6] R. T. Collins, "Mean-shift blob tracking through scale space", Proc. IEEE Computer Society Conference on Computer Vision and Pattern Recognition, pp.234-240 (2003).

[7] Masahiro HORIE, Masayuki KASHIMA, Kiminori SATO, Mutsumi WATANABE, Kouzi KUMA and Koichi TOYONAGA, "Automatic Endocardium Contour Tracing Method Using Standard Left Ventricles Shape Model", the Technical Report of IEICE, PRMU, 108 (94), pp.35-40 (2008).

[8] Ryohei TANAKA, Hitoshi YAMAUCHI and Akihiro KANAGAWA, "Object Tracking Using Color Distribution Based on Active Contour Model", Forum on Information Technology, 7 (3), pp.293-294 (2008).

© ISAROB 2013

The Eighteenth International Symposium on Artificial Life and Robotics 2013 (AROB 18th '13),
Daejeon Convention Center, Daejeon, Korea, January 30-February 1, 2013

Semantic Segmentation in Manhattan-like Environments from 2.5D data

Sven Olufs[1] and Markus Vincze[1]

[1] Vienna University of Technology, Automation and Control Institute,
Gusshausstrasse 25-29 / E376, A-1040 Vienna, Austria
(olufs@ieee.org, vincze@acin.tuwien.ac.at)

Abstract: In this paper we propose a novel approach for the robust segmentation of room structure using Manhattan world assumption. First, we estimate the Manhattan-like structure by using an MSAC variant that estimates such a Manhattan system directly from the data. Once the orientation is estimated we extract hypotheses of the room structure by exploiting 2D histograms using mean shift clustering techniques as rough estimate for a pre-segmentation of voxels i.e. their membership to planes of a certain position and orientation. Additionally we use the concept of vanishing points to extract 2D cues from the 2.5D data to improve the segmentation. We apply superpixel over segmentation on the colour input to achieve a dense segmentation. The over segmentation and pre-segmented voxels are combined using graph-cuts for a not a-priori known number of final plane segments with a label minimizing graph cut variant proposed by Delong et al. with polynomial runtime.

Keywords: Segmentation, Manhattan-System, Computer Vision

1 INTRODUCTION

The estimation of semantic room structure, e.g. corridors, doorways or walls, is a vital task for mapping or navigation. With domestic robotics we face the problem of clutter and visually weakly structured environments. The use of 2.5D sensors has become quite popular in the last decade, for instance the use of tilting 3D laser scanners or the Swissranger SR-3000. With the recent release of Microsoft's Kinect structured light sensor, the popularity of 2.5D sensors gained a boost. The Kinect sensor is suitable for the task for two reasons: The sensors are cheaper than laser scanners and they offer an 2D colour image, which can be used for more sophisticated feature extraction.

The challenge with data from 2.5D data is to cope with noise and uncertainty due to the nature of the sensors. For instance, the quality of 2.5D data from the Kinect depends on the reflection properties of the observed surface or the angle of incidence. Since the sensor uses structured light in the infrared spectrum, the sensor is sensitive to sunlight. Within the domestic robotics domain, the environments can be single-coloured walls or furniture without texture, so it can result in few certain and many uncertain estimates. Another issue is that the sensor's depth resolution does not scale linearly with the Kinec.

Many approaches for room structure estimation use the concept of occupancy grids [3] or extensions to 3D, e.g. [4]: The grid contains information on a primitive level if a grid cell corresponds to oder belongs to a wall or ground. At this level, there is no information if certain parts of grid cells with the label "wall" are aligned to other "walls" or if the ground is parallel to other structures, e.g. a table top. This kind of constraints is referred to in the computer vision literature as the so-called *Manhattan world* assumption; The frequently observed dominance of three mutually orthogonal vanishing directions in man-made environments [5, 6, 7, 8]. Many indoor environments can be considered as Manhattan-like since most walls of a room are aligned orthogonally to the ground or quasi Manhattan-like if the walls are not aligned orthogonally to each other. In many cases, furniture is also aligned Manhattan-like to its environment, e.g. a couch or cupboard can be aligned to a wall. Here we emphasize that it is not necessary that the furniture is aligned to all three major axes i.e. even if a table is not aligned to a wall its table surface is usually parallel to the ground.

The novelty of the paper is the use of 2D and 3D features in a unified framework at almost the same runtime as the previous approach in polynomial runtime unlike than common NP hard solutions. The extraction of 2D cues is done in linear runtime and improves the overall precision of the segmentation and also improves the robustness to false matches.

2 OUR APPROACH

The main idea of our approach is to use histograms to extract room structure hypotheses for MRF segmentation rather than using the depth data as voxels. One advantage of using histograms is that it is relatively easy to estimate the Manhattan-like structure within the data if the camera origination is known. One disadvantage is that we lose spatial information about the voxels i.e. post-processing is needed to generate hypotheses on the room structure on all three axes i.e. planes aligned to the X, Y and Z axes. The hypotheses are finally

© ISAROB 2013

evaluated using the 2.5D data in the fashion of RANSAC and pre-segmentation using over segmentation techniques in the source 2D image. In an additional step we extract 2D cues from the 2.5D data using the concept of vanishing points. We use the 2D cues in two ways: Depending on the structure in the image it can be sometime easier to describe which part of an image does *not* belong to a specific Manhattan like structure than sometimes the opposite (at two different stages in the segmentation). We The final segmentation is achieved using an MRF multi-label technique which provides a robust and precise framework for 2D and 3D fusion.

2.1 Estimating Manhattan Geometry

First we estimate the Manhattan System form the 2.5d data with a method that has been proposed by us in [9]. It is based on the idea to RANSAC a valid Manhattan system on the base of normal vectors. The method estimates the relative roll, pitch and yaw to the scene. The method also provides a plane segmentation of Manhattan-like structure, based on a 1D âĂŸâĂŹConnected Components" RANSAC that pre-segments all planes that are orientated to the Manhattan systems i.e. orientated to the X, Y or Z axis. For the sake of simplification, we assume only one system per scene.

2.2 Extracting 2D cues

The basic idea of our approach is to estimate per pixel the probability of the alignment (orientation of the pixel) to the one of the three vanishing points. Instead of using line segments we use straightforward gradients (i.e. orientation and magnitude). In the fashion of the Canny edge detector, we first blur the image using a Gaussian 3x3 kernel and apply a 3x3 Sobel filter on the image to obtain a gradient image. In a next step we calculate the reference orientation of each pixel to its three vanishing points as shown in figure 1 for two pixels. One can see that reference orientation of two vanishing points can be quite similar to each other, e.g. the sample point on the right bottom. In order to avoid artefacts in the estimation step, we calculate the similarity reference angles

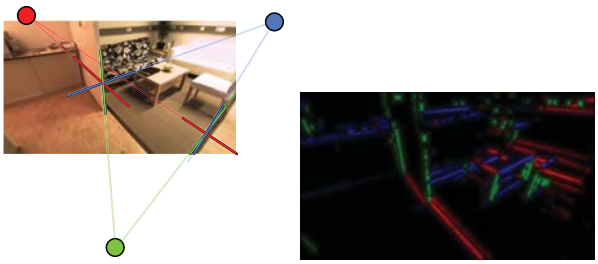

(a) 2D Image with projected vanishing points (b) Colour coded alignments of gradients/pixels to vanishing points

Figure 1: Basic concept of vanishing points in 2D images. The vanishing points are colour coded for better visibility i.e. red=x, green=y and blue=z

in a 3x3 matrix and use it as a additional gain in the estimation step. The estimation per gradient pixel to a vanishing point is a simple winner-takes-it-all method based (fig. 1(b)) on the smallest angle to a reference angle (of the vanishing point) i.e. we assume that every pixel is aligned only to one vanishing point. Finally we convert the value of the smallest angle into a probability by using a Gaussian weighting in a way that 5 degree difference will result in 3 σ.

2.3 Pre-Segmentation

Next, we use the plane hypothesis to pre-segment the individual voxels i.e. assign the voxels to planes and their orientation. This segmentation is done straightforward by re-projecting all hypotheses back into the 3D state space of the voxels. A voxel is assigned to a plane hypothesis if it intersects the plane hypothesis within a certain threshold. Each voxel is assigned only to one (or none, i.e. "undecided") "best fitting" plane using the distance of the plane/voxel intersection to the mean of the voxels as the metric for matching. We count the number of inliers per plane similar to RANSAC. Planes with almost no support $count < 0.05\%$ are then removed from the set and corresponding voxels are freed.

In order to achieve a dense segmentation of the entire image we over segment the colour image using superpixels. The use of superpixels for over segmentation is quite popular in the computer vision literature within the last decade. The main objective is to locally merge pixels into "superpixels" i.e. pixels with similar e.g. colour, texture, appearance or shading. In general we assume that true object boundaries are mostly (but not necessarily) represented by boundaries of the superpixels if the objects size is large enough (e.g. > 5 pixel). In this paper, we use the fast Minimum Spanning Tree based method by Felzenszwalb [10], giving us (by appropriate setting of parameters) 300-500 regions on average. However, any other over-segmentation method can be used.

2.4 MRF based multi-labeling

To label the pixels on a global level, i.e. to take into account prior information about possible plane orientations, 2D geometry and relations between neighbouring superpixels simultaneously, we formulate the problem in a fully probabilistic framework; as searching for a maximum posterior (MAP) configuration of the Markov Random Field [11] for multi-labeling [12]: In a labeling problem we are given a set of observations $\mathcal{P}$ (e.g. voxel and superpixel) and a set of labels $\mathcal{L}$ (e.g plane/orientation hypotheses). The goal is to assign each observation $p \in \mathcal{P}$ a label $f_p \in \mathcal{L}$ such that the joint labeling f minimizes the objective label function $E(f)$. We assume a graph $\mathcal{G} = \langle \mathcal{P}, \mathcal{E} \rangle$ consisting of a discrete set $\mathcal{P}$ of objects and a set $\mathcal{E} \subseteq \binom{|\mathcal{P}|}{2}$ of pairs of those objects.

© ISAROB 2013

An instance of the Max-sum problem is denoted by the tuple $(\mathcal{G}, \mathcal{L})$, where the elements $D_p(f_p)$, $V_{pq}(f_p, f_q)$ and $h_L \delta_L(f)$ of g are of alignment costs or qualities. The quality of a labeling f is defined

$$E(f) = \overbrace{\sum_{p \in \mathcal{P}} D_p(f_p)}^{\text{data cost}} + \overbrace{\sum_{pq \in \mathcal{N}} V_{pq}(f_p, f_q)}^{\text{smooth cost}} + \overbrace{\sum_{L \subseteq \mathcal{L}} h_L \delta_L(f)}^{\text{label cost}}$$

where h_l is the non-negative label cost of label l, and $\delta_L(f)$ is the corresponding indicator function

$$\delta_L(f) = \begin{cases} 1, & \text{if } \exists p : f_p = l \\ 0, & \text{else} \end{cases}$$

A common approach in the computer vision literature is to use three labels [5] for every major axis instead of using multiple labels per major axis. One reason to do so is that the general labeling for more than 3 labels leads often to NP-hard solutions [11, 12]. In this paper we use an MRF multi-label approach proposed by Delong et al. [12] which solves the multi-label problem within polynomial runtime for arbitrary number of labels. The polynomial runtime is achieved by using a different strategy for the multi-labeling than common approaches e.g. using a fixed number of labels: The main idea is to use the MRF to reduce the number of labels by merging them using the $E(f)$ function. The strategy includes starting with a reasonable number of labels e.g. all plane hypotheses and use the *smoothness term* as metric.

2.4.1 Graph entities

We build the graph $\mathcal{G}$ on the over-segmented image i.e. on the superpixels. The use of superpixels significantly reduces the number of objects in the graph compared to building the graph directly on the pixel grid. The superpixels represent objects (the set $\mathcal{P}$ in the graph and edges). The set $\mathcal{E}$, is established between every two neighbouring superpixels. The number of nodes (labels) K is set to the number of observed planes and four "undecided" labels to mark ambiguous label assignments. The "undecided" allow the solver to mark the places where there is *not enough*, information to decide which plane the superpixel belongs to. The individual "undecided" labels are "not_{xy}", "not_{xz}", "not_{yz}" and "undecided". The main idea with "not" labels is that it is sometime easier to estimate where a plane orientation does not belong to than the opposite. The problem is that we have only sparse information at the scale of superpixel labels to determine the actual orientation of a label with a high certainty, like the typical scale space problem in computer vision. One can see that the estimation of the opposite is easier if we use a "higher scale". The "not" labels are estimated using the 2D cues in the "low scale" version and with the "label cost" as the "high scale" i.e. estimating the orientation of a set of labels.
We use an additional parameter to represent weights of edges that connect the superpixels. The calculation of superpixel likelihood is done using simple colour (RGB) histograms and using the Bhattacharyya [13] metric:

$$\rho[p, q] = \sum_{u=1}^{m} \sqrt{p_u q_u}$$

with $\sum_{u=1}^{m} p_u = 1$ and $\sum_{u=1}^{m} q_u = 1$ for u histogram bins of the superpixels p and q. Note that this implementation differs from many other MRF based label methods where the smoothness term is used to describe the likelihood of the neighbouring superpixels instead of using weights in the graph. With Delong et al. [12] approach the smoothness term describes the similarity between individual labels.

2.4.2 Smoothness term

The term $V_{pq}(f_p, f_q)$ describes the smoothness between two labels p, q i.e. the cost to assign q to p. The function itself must be injective i.e. $V_{pq}(f_p, f_q) \neq V_{qp}(f_q, f_p)$ which is necessary for our MRF variant by Delong et al. [12]. In our implementation we set cost function V_{pq} that a label q from a plane hypothesis is set to p of an another hypothesis, if both planes are assigned to the same orientation and they have almost the same position $|pq|$ (e.g. if the plane is y aligned, its the height) and if p has less support by voxels of the plane hypothesis, i.e. inliers, than q:

$$V_{pq}(f_p, f_q) = \begin{cases} 0, & \text{if } p = q \\ 1, & \text{if } p_{orientation} \neq q_{orientation} \\ cost_{pq} \cdot \Delta_{pq} \cdot q_{inliers}, & \text{if } p_{orientation} = q_{orientation} \\ cost_{known}, & \text{if } p = \text{"undecided"} \\ cost_{unknown}, & \text{if } q = \text{"undecided"} \end{cases}$$

with $cost_{pq} \gg cost_{unknown} > cost_{known} \geqq 1$. We use the distance of the plane position of the corresponding labels p, q as weight metric i.e.

$$\Delta_{pq} = \begin{cases} 2.0 - \frac{|pq|}{c} & \text{if } |pq| \leq c \\ 0 & \text{otherwise} \end{cases}$$

for a threshold c. We use $cost_{known} \geqq 1$ since we want to allow the MRF to remove false positives from the graph, i.e. false labeled x-axis oriented planes surrounded by z-axis oriented planes. The condition $p_{orientation} = q_{orientation}$ can combine labels with the same properties while the graph based representation ensures that this is only applied if the source superpixels are "close" to each other in the source image.

2.4.3 Data term

The data term $D_p(f_p)$ encodes the quality of assigning a label f from the set $\mathcal{L}$ to an object/superpixel p in the graph. The quality measures how the superpixel is oriented to a specific plane. We use the pre-segmented labels of the voxels/pixel, i.e. the source pixels within the superpixels p. The data term

© ISAROB 2013

for the "not" labels is given by the 2D cues. For each f_p we sum up the assigned (to vanishing points) gradient values (see figure 1(b)) to the corresponding labels i.e. "not_{xy}", "not_{xz}" and "not_{yz}". The idea is simple, if a gradient pixel is assigned to the z axis, it votes with its gradient value for the "not_{xy}" label. If the gradient is assigned to the x axis it votes for the "not_{yz}" label and y axis votes for the "not_{xz}" label. The overall assumption is that if a segment is assigned to a certain orientation, then it does to contain gradient pixels that are assigned to that axis, see figure 1. We normalize "not_{xy}", "not_{xz}" and "not_{yz}" with the total sum of the *raw* unassigned gradients within f_p. This avoids that false or few matches outvote the "assignment labels" e.g. within textured areas.
The data term for the "assignment labels" is given as follows: For each f_p we count the number of voxels/pixels with the same label as f from the pre-segmentation. Note that the labels f corresponds to the plane hypothesis. Next the number of pixels p_n is normalized to p_m and set as cost to $D_p(f_p)$

$$D_p(f_p) = \begin{cases} W(p_m) \cdot cost_{data}, & \text{if } W(p_m) \geq \lambda \wedge W(p_n) \geq \gamma \\ 0, & \text{otherwise} \end{cases}$$

With $cost_{data} \gg cost_{pq}$ and

$$W(p) = \begin{cases} p \cdot cost_{data}, & \text{if } f_p \text{ is "undecided"} \\ p, & \text{otherwise} \end{cases}$$

where λ and γ are thresholds and $cost_{data}$ is a normalizing constant that can prevent false positives if $cost_{data} > 1$. In our implementation we use $\lambda = 0.1$ and $\gamma = 10$ since we set the "minimum superpixel size" Felzenszwalbs [10] superpixels segmentation to 100 pixels. In our experiments $cost_{data} = 1.5$ which produces fewer, but more certain labels.

2.4.4 Label cost

The label cost term $h_L \delta_L(f)$ is used to penalize each unique label that appears in f within $E(f)$. We use the cost h_L to express the certainty of the label f i.e. a lower cost reflects a higher certainty. Since we use the MRF to minimise the number of labels by fusing labels (=adding the costs of the fused labels), a solution will be used with minimal overall cost. We use the 2D cues to obtain h_L in a similar way we used it for the "not" labels, but using ratios instead of sums. For instance if a label is assigned to the x axis h_L is given as

$$h_L = \frac{sum_x}{sum_y + sum_z + \mu}$$

where *sum* is a function that sums all gradient pixels that are assigned to the corresponding axis and μ the smallest not-zero value that is assumable. The ratio for labels with y or z orientation calculates analog. Please note that we do not use the $\delta_L(f)$ as it was meant to be used in the first place as we distinguish only between three orientations of a plane and "unkown" labels with our 2D cues instead of the individual labels.

3 EXPERIMENTAL RESULTS

We choose a typical home environment (see fig. 2) for data acquisition using the Kinect. The data of all sensors is recorded at 25 frames per second. We recorded a representative set of six tours through our lab with a total length of approximately 320 meters. Three tours have a Manhattan like environment while the other ones represent a quasi Manhattan like environment.

Figure 2 shows sample images for all three tours and their segmentation in comparison with state of the art techniques from Saxena et al. [1] and Saxena et al. [1]. One can see that the combination of MRF and superpixels produces quite precise segmentation if stereo data is available and the superpixels do not contain glossy spots or other overexposed areas. In some case false-matches can appear if a glossy spot on the ground and the wall are to close too each other. The images also show that our parameterization of the segmentation is quite conservative since we want to produce only few false positives.

Our code runs on 2.4 GHz QuadCore PC, while the code is not optimized and uses only one CPU (except for MSAC Manhattan Geometry estimation). The average runtime for one frame is 408ms the clear bottleneck is the superpixel segmentation with 280ms. The next expensive function is the calculation of the Manhattan Geometry (80ms) due to the usage of histograms. Using smaller histograms will result in a lower constant runtime, but will also influence the accuracy negatively. The extraction of 2D cues the thrid third bottleneck with a constant runtime of 20ms followed by the mean shift clustering with 10ms.

4 CONCULSION

In this paper we presented a novel robust method for room structure segmentation in a Manhattan like environment for 2.5D data using 3D and 2D cues. Once the camera

(a) our approach (b) Saxena et al. [1] (c) Hoiem et al. [2]

Figure 2: Segmented sample pictures from our test data: The colour indicates the alignment of a structure to an specific axis. The segmentation is executed on the identical superpixels on all three methods. Please note that the different approaches are using different color coding for the axis, yellow indicates uncertian planes in [1, 2].

© ISAROB 2013

orientation is estimated using MSAC, we calculate the assignment of every voxel to the 3 major axes and we extract plane candidates using histogram voting that are used as priors for a MRF based segmentation. We extract 2D cues from the 2.5D data using the concept of vanishing points and 2D image geometry. We also showed that the segemntion of the MRF can be improved using label cost metric and 2D cues.

The main drawback of our approach is that we depend on Manhattan-like structures which is common with many indoor environments. The extraction of 2D cues depends on the proper estimation of the camera orientation, however this could be overcome by estimating the vanishing points separately like in pure 2D computer vision approaches. Another drawback is that we depend on the output of the superpixel segmentation. Experiments have shown that the use of smaller superpixels is more robust than the usage of large ones, i.e. otherwise the superpixel segmentation tends to group the ground and white walls to one segment. At this stage we do not use multiscale oversegmentation, which would improve the performance of the 2D cues. Right now we kind of abuse the MRF as quasi multiscale by using the "not" labels in a small scale and using it with the label costs in a large scale.

Our next step is to extend the approach with multi-scale over segmentation and to incorporate the 2D cues in the smoothness term of the MRF.

ACKNOWLEDGMENT

The research leading to these results has received funding from the European Community's Seventh Framework Program (FP7/2011-2014) under grant agreement no FP7-ICT-2011-7 288146 (HOBBIT)

REFERENCES

[1] Ashutosh Saxena, Min Sun, and Andrew Y. Ng. Make3d: Learning 3-d scene structure from a single still image. *IEEE Transactions on Pattern Analysis and Machine Intelligence*, 2008.

[2] D. Hoiem, A.A. Efros, and M. Hebert. Recovering surface layout from an image. *IJCV*, 75(1), 2007.

[3] S. Thrun, W. Burgard, and D. Fox. *Probabilistic Robotics*. MIT Press, Cambridge MA, first edition, 2005.

[4] R. B. Rusu, A. Sundaresan, B. Morisset, K. Hauser, M. Agrawal, J. Latombe, and M. Beetz. Leaving flatland: Efficient real-time three-dimensional perception and motion planning. *Journal of Field Robotics, Special Issue: Three-Dimensional Mapping*, 26(10):841–862, 2009.

[5] B. Micusik and J. Kosecka. Piecewise planar city modeling from street view panoramic sequences. In *IEEE Conference on Computer Vision and Pattern Recognition (CVPR)*, 2009.

[6] D. Gallup, J. Frahm, P. Mordohai, Q. Yang, and M. Pollefeys. Real-time plane-sweeping stereo with multiple sweeping directions. In *IEEE Conference on Computer Vision and Pattern Recognition (CVPR)*, 2007.

[7] S. Sinha, D. Steedly, and R. Szeliski. Piecewise planar stereo for image-based rendering. In *International Conference on Computer Vision (ICCV)*, 2009.

[8] A. Gupta, A. A. Efros, and M. Hebert. Blocks world revisited: Image understanding using qualitative geometry and mechanics. In *European Conference on Computer Vision (ECCV)*, 2010.

[9] Sven Olufs and Markus Vincze. Real time manhattanlik structure segmentation from kinect with constrained 1d cc-ransac. In *IEEE International Symposium on Safety, Security, and Rescue Robotics (SSRR2011)*, 2011.

[10] P. Felzenszwalb and D. Huttenlocher. Efficient graph-based image segmentation. *International Journal of Computer Vision*, 59(2), 2004.

[11] R. Szeliski, R. Zabih, D. Scharstein, O. Veksler, V. Kolmogorov, A. Agarwala, M. Tappen, and C. Rother. A comparative study of energy minimization methods for markov random fields with smoothness-based priors. *Pattern Analysis and Machine Intelligence, IEEE Transactions on*, 30(6):1068 –1080, jun. 2008.

[12] A. Delong, A. Osokin, H. Isack, and Y. Boykov. Fast approximate energy minimization with label costs. In *IEEE Conference on Computer Vision and Pattern Recognition (CVPR)*, San Francisco, California, 2010.

[13] D. Comaniciu, V. Ramesh, and P. Meer. Kernel-based object tracking. *IEEE Transactions on Pattern Analysis and Machine Intelligence*, 25:564–575, May 2003.

© ISAROB 2013

The Eighteenth International Symposium on Artificial Life and Robotics 2013 (AROB 18th '13),
Daejeon Convention Center, Daejeon, Korea, January 30-February 1, 2013

Modeling and robust decoupling control for hypersonic scramjet vehicle

Xiaofeng Su[1], Yuefei Jiang[1], Yingmin Jia[1,2]

[1] The Seventh Research Division and the Department of Systems and Control, Beihang University (BUAA),
Beijing 100191, China (e-mail: xfsu@smss.buaa.edu.cn; jyf1214@126.com).
[2] Key Laboratory of Mathematics, Informatics and Behavioral Semantics (LMIB), SMSS, Beihang University (BUAA),
Beijing 100191, China (e-mail: ymjia@buaa.edu.cn).

Abstract: In this paper, the modeling and the robust decoupling control for a generic hypersonic scramjet vehicle are studied. Firstly, the dynamics of the hypersonic vehicle are modeled by applying the Lagrangian approach, which captures the most primary characteristics such as elastic deformation, aerodynamics, aero-heating, variable mass, effect of spherical rotating earth and their inherent interactions. Then, a robust output decoupling controller is designed by using nonlinear dynamic inversion plus the desired proportional integral dynamics, and natural time-scale separation theorem between fast and slow variables. Finally, the nonlinear simulations demonstrate that the controller can eliminate the interaction among the output channels and satisfy the handling quality requirements when the vehicle has parameter uncertainty.

Keywords: HSV modeling, robust output decoupling, dynamic inversion, multitime-scale approach

1 INTRODUCTION

With the historic scramjet-powered Mach 7 and 10 flights of the X-43A in 2004, the research of hypersonic scramjet vehicle (HSV) has seen a resurgence within the aerospace community. This is attributed to the fact that the HSV is viewed as the next critical flying vehicle, which has the ability to easily penetrate and survive against enemy air defenses, promptly reach critical targets at long ranges (i.e., realize rapid global response), and access to space in a manner similar to commercial air travel. Therefore, on one hand, this type of vehicle has great potential as a high-speed, time-saving, and low-cost transport for both commercial and military applications. On the other hand, the modeling and control of the HSV are challenging, due to its severe aero-heating, unconventional propulsion system, much broader flight envelope, and tight interaction among airframe, propulsion, and structure [1, 2].

The modern HSV like NASA X-43 or X-51 has special slender airframe-propulsion lifting-body configuration and operates over a high speed ranging from Mach 5 to Mach 15 within large flight envelope, so that the traditional design approaches are invalid when there exist the manifold interaction among sub-models of the HSV and the complex flight environment. For the modeling issue, several literature [3, 4, 5] have discussed the determinants of the modeling and the interaction of the sub-models. In [3, 4], the inertial dynamics of the model were obtained under the consideration of rigid-body motion, elastic deformation and spherical rotating earth. And McNamara et al [5] focused on the coupling effects among the sub-models of aerodynamics, aero-elasticity and aero-heating based on high fidelity codes. For the decoupling control issue, nonlinear dynamic inversion control method was used in [6, 7] under the condition that the system dynamics were exactly known. Moreover, the stability and performance robustness within the dynamic inversion framework were addressed in [8, 9, 10].

In this work, because of the high computational requirements when applying the precise sub-models of the HSV, some dominating elements and their primary interactions are extracted in the process of modeling. And then, by utilizing the Lagrangian approach, a control-oriented model of the HSV is obtained, in which the effects of inertial dynamics, elastic deformation, aerodynamics, aero-heating, variable mass, and spherical rotating earth are captured. Based on this model, a robust output decoupling controller is designed to enhance the maneuverability of the HSV. Specifically, the dynamics of the vehicle are separated into two time scales according to the natural time-scale separation theorem. In each time-scale loop, an appropriate proportional integral control law is designed in conjunction with the dynamic inversion controller, such that the outputs of the closed-loop system can be robustly decoupled at the steady state with respect to the parameter uncertainty.

2 VEHICLE MODEL

According to [11], the dynamical equations of the HSV are directly presented by using the Lagrangian approach.

$$m\dot{V} - \tilde{S}\dot{\omega} + \int_m \dot{v}dm = \left(\int_m \tilde{v}dm\right)\cdot\omega + mg + F + \Psi_F \quad (1)$$

$$\tilde{S}\dot{V} + J\dot{\omega} + \int_m \tilde{r}\dot{v}dm = \left(2\int_m \tilde{r}\tilde{v}dm - \tilde{\omega}J\right)\cdot\omega - \left(\int_m \tilde{v}dm + \tilde{\omega}\tilde{S}\right)\cdot V + \bar{M} + \Psi_{\bar{M}} \quad (2)$$

© ISAROB 2013

$$[\Lambda]\dot{V} + [\Lambda]\tilde{r}^T\dot{\omega} + [\Lambda]\dot{v} = [\Lambda]\tilde{V}\omega - [\Lambda]\tilde{\omega}\tilde{\omega}r - \int_m \left(\phi_i^2\bar{\omega}_i^2\eta_i\right)dm + Q_e + \Psi_e. \tag{3}$$

The expressions of external forces, moments, and thrust in (1), (2), (3) are extremely complicated, which are determined not only by the velocity and the attitude, but also by the shape and elastic deformation of the HSV. In summary, there are $12+3n$ (n is the number of elastic modes) equations such as: 3 force equations, 3 moment equations, $3n$ elastic deformation equations, 3 trajectory equations, and 3 Euler angle equations. Moreover, the kinematic equations of the HSV are similar as the ones of the regular vehicle. For a vehicle flying over a Mach number ranging from 5 to 15 and a height ranging from 20 to $60km$, the maximum and minimum magnitudes of the Coriolis force $m\omega_{E,I}\times V_r$ are approximately 7.02% and 2.48% of the vehicle weight, and the magnitude of the transport force $m\omega_{E,I}\times(\omega_{E,I}\times R)$ is about 0.35% of the vehicle weight. Finally, the scalar form of the HSV model which is used here are presented in Appendix based on three regular assumptions: i) neglecting the effect of elastic deformation , ii) neglecting the transport item in expression of $\dot{V}$, iii) the vehicle is symmetrical about the ox_Bz_B plane.

3 ROBUST DECOUPLING CONTROLLER

The structure of resulting control law is shown in Fig. 1., in which the nonlinear dynamic inversion theory is applied in two time scales. Because the integral feedback has the ability of eliminating steady-state errors, a desired dynamic (i.e., proportional plus integral feedback dynamic) is applied to solve the robustness problem of the dynamic inversion.

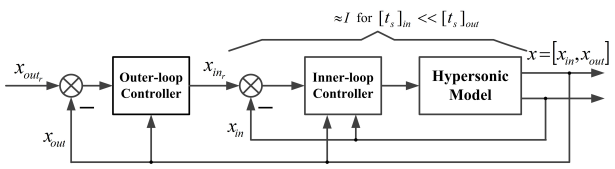

Fig. 1. Two-time scale feedback loop

3.1 Outer-loop Controller design

In the outer loop, the nominal dynamics of slow time scale are placed in the form of (4). The objective of the dynamic inversion in the slow time scale is to realize the decoupling control of the attitude angles and flight trajectory using the rotational rate and flight velocity. And the outputs are chosen to be the system states.

$$\dot{\mathbf{x}}_{out} = \tilde{F}^0(\mathbf{x}_{out}) + \tilde{G}^0(\mathbf{x}_{out})\cdot\mathbf{x}_{in} \tag{4}$$

where $\mathbf{x}_{out} = [\phi \quad \theta \quad \psi \quad x \quad y \quad -h]^T = \mathbf{y}_{out}$, $\mathbf{x}_{in} = [\omega_x \ \omega_y \ \omega_z \ u \ v \ w]^T$. Roll angel ϕ, pitch angle θ, yaw angle ψ are the attitude angels of the body axes relative to the earth axes. x, y are flight displacement along the longitude lines and latitude lines, respectively. h is the altitude of the vehicle. ω_x, ω_y, ω_z are rotational rates of the body axes relative to the inertial axes. u, v, w are the velocities along the body axes related to the earth axes. In practice, because of the parameter uncertainties, the real system is presented as

$$\dot{\mathbf{x}}_{out} = \tilde{F}(\mathbf{x}_{out}) + \tilde{G}(\mathbf{x}_{out})\cdot\mathbf{x}_{in} \tag{5}$$

where $\tilde{F}(\mathbf{x}_{out}) = \tilde{F}^0(\mathbf{x}_{out}) + \Delta\tilde{F}(\mathbf{x}_{out})$, $\tilde{G}(\mathbf{x}_{out}) = \tilde{G}^0(\mathbf{x}_{out}) + \Delta\tilde{G}(\mathbf{x}_{out})$. And the specific expressions of $\tilde{F}(\mathbf{x}_{out})$, $\tilde{F}^0(\mathbf{x}_{out})$, $\tilde{G}(\mathbf{x}_{out})$, and $\tilde{G}^0(\mathbf{x}_{out})$ can be obtained from the Euler angle equations and the trajectory equations. Moreover, the parameter uncertainties in these expressions have the forms as $\omega_E = \omega_E^0 + \Delta\omega_E$, $R_E = R_E^0 + \Delta R_E$, and $\lambda_0 = \lambda_0^0 + \Delta\lambda_0$.

Since the total relative degree is equal to the number of system states, this time scale has no internal dynamics to be considered. Then, the outer-loop control law is given by (6), where the desired dynamics is chosen to have the proportional integral form.

$$\begin{cases} \mathbf{x}_{in} = [\tilde{G}^0(\mathbf{x}_{out})]^{-1}\left\{-[\tilde{F}^0(\mathbf{x}_{out})] + \mathbf{v}_{des}\right\} \\ \mathbf{v}_{des} = \mathbf{k}_{out_1}\cdot(\mathbf{v}_{out} - \mathbf{x}_{out}) + \mathbf{k}_{out_2}\cdot\Omega \\ \dot{\Omega} = \mathbf{v}_{out} - \mathbf{x}_{out} \end{cases} \tag{6}$$

where $\Omega = [\Omega_\phi \quad \Omega_\theta \quad \Omega_\psi \quad \Omega_x \quad \Omega_y \quad \Omega_h]^T$. $\mathbf{k}_{out_i} = [k_{out_\phi i} \ k_{out_\theta i} \ k_{out_\psi i} \ k_{out_xi} \ k_{out_yi} \ k_{out_hi}]^T$, $i = 1,2$ are the desired controller parameters which will be determined. $\mathbf{v}_{out} = [v_\phi \ v_\theta \ v_\psi \ v_x \ v_y \ v_h]^T$ is the virtual input vector. By calculating the determinant of the control matrix $det[\tilde{G}^0(\mathbf{x}_{out})]$, it is concluded that $[\tilde{G}^0(\mathbf{x}_{out})]^{-1}$ exists while the inequality $1/\cos\theta \neq 0$ holds, and it is obviously satisfied.

Substituting the control law (6) into the real system (5), the outer closed-loop system is obtained. Then, the objective is to find the appropriate controller parameters $\mathbf{k}_{out_1}$ and $\mathbf{k}_{out_2}$, so that the equation $\mathbf{y}_{out} = [\ \mathbf{I}\ ]\mathbf{v}_{out}$ (i.e., $\mathbf{x}_{out} = [\ \mathbf{I}\ ]\mathbf{v}_{out}$, where $[\ \mathbf{I}\ ]$ is the identity matrix) is satisfied at the steady state while the system contains parameter uncertainties. Next, setting $\dot{\mathbf{x}}_{out} = \dot{\Omega} = 0$ yields the equilibrium solutions of this system: $\mathbf{x}_{out_e} = \mathbf{v}_{out}$, $\Omega_e = [-\Delta\tilde{f}_1/k_{out_\phi 2} \ -\Delta\tilde{f}_2/k_{out_\theta 2} \ -\Delta\tilde{f}_3/k_{out_\psi 2} \ 0 \ 0 \ 0]^T$. Linearizing about $\mathbf{x}_{out} = \mathbf{x}_{out_e}$ and $\Omega = \Omega_e$ yields the following linear systems: $\Delta\dot{\mathbf{x}}_{out} = [\tilde{A}]_{6\times6}\cdot\Delta\mathbf{x}_{out} + [\tilde{B}]_{6\times6}\cdot\Delta\Omega$, $\Delta\dot{\Omega} = [\tilde{C}]_{6\times6}\cdot\Delta\mathbf{x}_{out} + [\tilde{D}]_{6\times6}\cdot\Delta\Omega$. Then, the characteristic equation of such a linear system is:

$$s^{12} + \tilde{n}_{11}s^{11} + \tilde{n}_{10}s^{10} + \cdots + \tilde{n}_1 s^1 + \tilde{n}_0 = 0$$

where $\tilde{n}_i = \tilde{n}_i(\mathbf{v}_{out}, \mathbf{k}_{out_1}, \mathbf{k}_{out_2}, \Delta)$, $i = 0, \cdots, 11$. Hence, the stability of that linear system is guaranteed, if the eigenvalues of the characteristic equation are less than zero for all allowable $\Delta\tilde{F}$ and $\Delta\tilde{G}$. Moreover, desirable stability margin can be obtained for better dynamic performance by substituting a new variable $s_1 = s + a$ into the original characteristic equation. Therefore, the linear system is stable and the eigenvalues are on the left side of the axis $s = -a$.

© ISAROB 2013

3.2 Inner-loop Controller design

In the inner loop, the control surfaces and vectored thrust are commanded to realize prompt and precise tracking of the flight velocity and rotational angular velocity generated in the outer loop. The most important point is that the slow time scale states in the outer loop are treated as constants in this fast time scale, since they evolve more slowly when compared with fast time scale ones. The real system dynamics of fast time scale are written as

$$\dot{\mathbf{x}}_{in} = F(\mathbf{x}) + G(\mathbf{x}) \cdot \mathbf{u} \tag{7}$$

and $F(\mathbf{x}) = F^0(\mathbf{x}) + \Delta F(\mathbf{x})$, $G(\mathbf{x}) = G^0(\mathbf{x}) + \Delta G(\mathbf{x})$, $\mathbf{x}_{in} = [u\ v\ w\ \omega_x\ \omega_y\ \omega_z]^T$, $\mathbf{u} = [\Phi_x\ \Phi_y\ \Phi_z\ \delta_e\ \delta_a\ \delta_r]^T$. The system states $\mathbf{x}_{in}$ are the same as ones in the outer loop, and $\mathbf{x} = [\mathbf{x}_{in}^T,\ \mathbf{x}_{out}^T]$. The three control surfaces deflection δ_e, δ_a, δ_r are the effective elevator, aileron and rudder deflection. Throttle setting values Φ_x, Φ_y, Φ_z are used to generate vectored thrust. Besides, according to the force equations and moment equations, the expressions of $F(\mathbf{x})$, $F^0(\mathbf{x})$, $G(\mathbf{x})$, and $G^0(\mathbf{x})$ can be obtained. The parameter uncertainties exist not only in ω_E, R_E, λ_0, but also in vehicle mass, moment of inertia, product of inertia, aerodynamic derivatives, and thrust derivatives. Similarly, the desired dynamics of the fast time scale also have proportional integral form, thus inner-loop control law is written as

$$\begin{cases} \mathbf{u} = [G^0(\mathbf{x})]^{-1} \left\{ -[F^0(\mathbf{x})] + \mathbf{k}_{in_1} \cdot (\mathbf{x}_{in_r} - \mathbf{x}_{in}) + \mathbf{k}_{in_2} \cdot \Omega \right\} \\ \dot{\Omega} = \mathbf{x}_{in_r} - \mathbf{x}_{in} \end{cases} \tag{8}$$

where $\Omega = [\Omega_u\ \ \Omega_v\ \ \Omega_w\ \ \Omega_{\omega_x}\ \ \Omega_{\omega_y}\ \ \Omega_{\omega_z}]^T$. $\mathbf{k}_{in_i} = [k_{in_ui}\ k_{in_vi}\ k_{in_wi}\ k_{in_\omega_x i}\ k_{in_\omega_y i}\ k_{in_\omega_z i}]^T$, $i = 1,2$ are the controller parameters to be designed. Besides, matrix $[G^0(\mathbf{x})]^{-1}$ exists if the following inequalities holds.

$$\begin{cases} \Psi^0_{F_x_\Phi_x}(\mathbf{x}) \cdot \Psi^0_{F_y_\Phi_y}(\mathbf{x}) \cdot \Psi^0_{F_z_\Phi_z}(\mathbf{x}) \neq 0 \\ \bar{M}^0_{y_\delta_e}(\mathbf{x}) \left[\bar{M}^0_{x_\delta_r}(\mathbf{x}) \cdot \bar{M}^0_{z_\delta_a}(\mathbf{x}) - \bar{M}^0_{x_\delta_a}(\mathbf{x}) \cdot \bar{M}^0_{z_\delta_r}(\mathbf{x}) \right] \neq 0 \end{cases}$$

Consequently, substituting the controller (8) into the real system (7) yields the inner closed-loop system. Next, get the equilibrium solutions of this closed-loop system by setting $\dot{\mathbf{x}}_{in} = \dot{\Omega} = 0$. Then linearizing about $\mathbf{x}_{in} = \mathbf{x}_{in_e} = \mathbf{x}_{in_r}$ and $\Omega = \Omega_e$ could yield corresponding linear systems: $\Delta\dot{\mathbf{x}}_{in} = [A]_{6\times6} \cdot \Delta\mathbf{x}_{in} + [B]_{6\times6} \cdot \Delta\Omega$, $\Delta\dot{\Omega} = [C]_{6\times6} \cdot \Delta\mathbf{x}_{in} + [D]_{6\times6} \cdot \Delta\Omega$. For the linear system above with uncertainties in ΔF and ΔG, the robust stability of that system is analogously achievable through finding suitable controller parameters $\mathbf{k}_{in_i}(\mathbf{x}_{in_r})$, $i = 1,2$. Furthermore, the desirable stability margin can also be obtained for better dynamic performance.

Remark1: The nonlinear dynamic inversion method is a straight forward approach for designing decoupled feedback systems of nonlinear systems. For the system with parameter uncertainty, the robustness of output decoupling controller can be addressed by using integral terms within the loops.

Remark2: The information of $\mathbf{v}_{out}$ is required in the processing of determining decoupling controller parameters $\mathbf{k}_{out}(\mathbf{v}_{out})$. And this information can be easily obtained from the commands.

Remark3: The linearized model of the nonlinear system has been discussed here, which means that the states convergency can only be achieved in a neighborhood of the equilibrium. Fortunately, this problem can be solved by limiting the change rate of the commands or enhancing the response speed of the systems.

4 SIMULATION RESULTS

A typical nonlinear simulation of the maneuver is shown to examine the effectiveness of the robust output decoupling controller. The data of aerodynamic characteristics and thrust performance in [12] is adopted here. The simulation results of nonlinear system responses to the change of roll angel, velocity and altitude are depicted in Fig. $2-4$, in which the solid line is the response to $v1$ and the dash line is the response to $v2$. It is observed that the change of one output value has no effect on the steady-state values of the others.

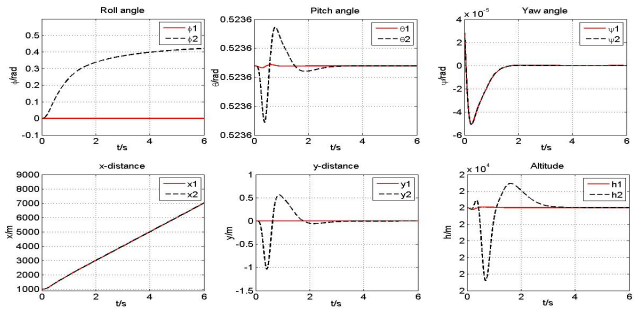

Fig. 2. Responses to the change of roll angle

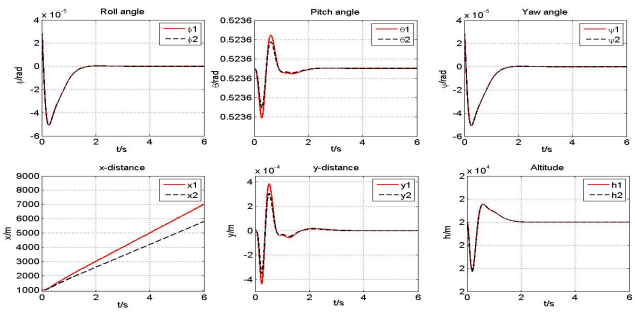

Fig. 3. Responses to the change of velocity

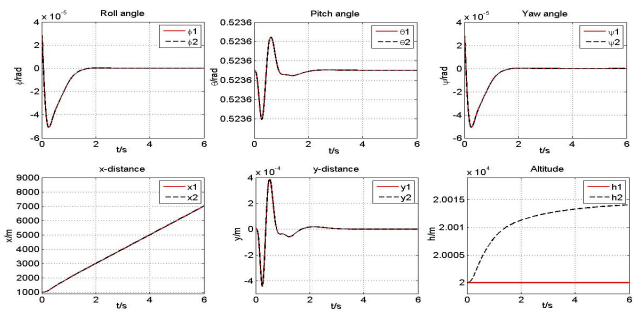

Fig. 4. Responses to the change of altitude

© ISAROB 2013

5 CONCLUSION

In this paper, a multivariable nonlinear strong-coupled HSV model has been developed, which captures the most primary characteristics of this special vehicle. Based on this model, a robust decoupling controller design method, which incorporates a desired proportional integral dynamic with nonlinear dynamic inversion controller, has been proposed. This controller design method mainly addresses two fundamental problems: decoupling of nonlinear system and decoupling robustness. The nonlinear simulation results confirm that the vehicle model equipped with the robust output decoupling controller can provide both steady-state decoupling of the outputs and robustness with respect to parameter uncertainty.

6 APPENDIX

Force equations:

$$\begin{aligned}
\dot{u} &= [\omega_z + \omega_E(T_{31}c\lambda - T_{33}s\lambda)]v \\
&\quad -[\omega_y + \omega_E(T_{21}c\lambda - T_{23}s\lambda]w + gT_{13} + (F_x + \Psi_{F_x})/m \\
\dot{v} &= [\omega_x + \omega_E(T_{11}c\lambda - T_{13}s\lambda)]w \\
&\quad -[\omega_z + \omega_E(T_{31}c\lambda - T_{33}s\lambda)]u + gT_{23} + (F_y + \Psi_{F_y})/m \\
\dot{w} &= [\omega_y + \omega_E(T_{21}c\lambda - T_{23}s\lambda)]u \\
&\quad -[\omega_x + \omega_E(T_{11}c\lambda - T_{13}s\lambda)]v + gT_{33} + (F_z + \Psi_{F_z})/m
\end{aligned}$$

Moment equations:

$$\begin{aligned}
J_{xx}\dot{\omega}_x - J_{xz}\dot{\omega}_z &= J_{xz}\omega_x\omega_y + (J_{yy} - J_{zz})\omega_y\omega_z + \bar{M}_x + \Psi_{\bar{M}_x} \\
J_{yy}\dot{\omega}_y &= (J_{zz} - J_{xx})\omega_x\omega_z + J_{xz}(\omega_z^2 - \omega_x^2) + \bar{M}_y + \Psi_{\bar{M}_y} \\
J_{zz}\dot{\omega}_z - J_{xz}\dot{\omega}_x &= -J_{xz}\omega_y\omega_z + (J_{xx} - J_{yy})\omega_x\omega_y + \bar{M}_z + \Psi_{\bar{M}_z}
\end{aligned}$$

Euler angle equations:

$$\begin{aligned}
\dot{\phi} &= \omega_x + (\omega_z c\phi + \omega_y s\phi)t\theta - (c\theta c\phi + s\theta c\phi t\theta)(v/R) \\
&\quad +(c\theta s\phi + s\theta s\phi t\theta)(w/R) - \omega_E(c\psi s\theta t\theta + c\psi c\theta)c\lambda \\
\dot{\theta} &= \omega_y c\phi - \omega_z s\phi + c\theta(u/R) + s\theta s\phi(v/R) + s\theta c\phi(w/R) \\
&\quad +\omega_E s\psi c\lambda \\
\dot{\psi} &= (1/c\theta)(\omega_z c\phi + \omega_y s\phi) - \omega_E(c\psi t\theta c\lambda - s\lambda) \\
&\quad +s\psi c\theta t\lambda(u/R) + [(s\psi s\theta s\phi + c\psi c\phi)t\lambda - c\phi t\theta](v/R) \\
&\quad +[(s\psi s\theta c\phi - c\psi s\phi)t\lambda + s\phi t\theta](w/R)
\end{aligned}$$

Trajectory equations:

$$\begin{aligned}
\dot{x} &= T_{11}u + T_{21}v + T_{31}w \\
\dot{y} &= T_{12}u + T_{22}v + T_{32}w \\
-\dot{h} &= T_{13}u + T_{23}v + T_{33}w
\end{aligned}$$

where $R = R_E + h$, $\lambda = \lambda_0 + x/R_E$, $s = \sin$, $c = \cos$, $t = \tan$,

$$[T_{ij}] = \begin{bmatrix} c\psi c\theta & s\psi c\theta & -s\theta \\ c\psi s\theta s\phi - s\psi c\phi & s\psi s\theta s\phi + c\psi c\phi & c\theta s\phi \\ c\psi s\theta c\phi + s\psi s\phi & s\psi s\theta c\phi - c\psi s\phi & c\theta c\phi \end{bmatrix}.$$

And u, v, w, ω_x, ω_y, ω_z, ϕ, θ, ψ, x, y, h are the system states. Input control variables are Φ_x, Φ_y, Φ_z, δ_e, δ_a, δ_r, which are included in the expressions of the force, moment and thrust.

7 ACKNOWLEDGMENTS

This work was supported by the National Basic Research Program of China (973 Program, 2012CB821200, 2012CB821201) and the NSFC (61134005, 60921001, 90916024, 91116016).

REFERENCES

[1] Kelkar AG, Vogel JM, Whitmer CE, and et al (2011), Design Tool for Control-Centric Modeling, Analysis, and Trade Studies for Hypersonic Vehicles. Proceedings of the 17th AIAA International Space Planes and Hypersonic Systems and Technologies Conference.

[2] Rodriguez AA, Dickeson JJ, Sridharan S, and et al (2009), Control-Relevant Modeling ,Analysis, and Design for Scramjet-Powered Hy-personic Vehicles. Proceedings of the16th AIAA/DLR/DGLR International Space Planes and Hypersonic Systems and Technologies Conference.

[3] Bilimoria KD and Schmidt DK (1995), Integrated Development of the Equations of Motion for Elastic Hypersonic Flight Vehicles. Journal of Guidance, Control, and Dynamics, 18(1): 73–81.

[4] Meirovitch L and Tuzcu I (2003), Integrated Approach to the Dynamics and Control of Maneuvering Flexible Aircraft. NASA/CR–2003–211748.

[5] McNamara J and Friedmann P (2011), Aeroelastic and Aerothermoelastic Analysis in Hypersonic Flow: Past, Present, and Future. AIAA Journal, 49(6): 1089–1122.

[6] Snell SA (1998), Decoupling Control Design with Applications to Flight. Journal of Guidance, Control, and Dynamics, 21(4): 647–655.

[7] Bajodah AH (2009), Generalised dynamic inversion spacecraft control design methodologies. IET Control Theory and Applicaions, 3(2): 239–251.

[8] Reiner J, Balas GJ, and Garrard WL (1996), Flight Control Design Using Robust Dynamic Inversion and Time-scale Separation. Automatica, 32(11): 1493–1504.

[9] Ito D and Valasek J (2001), Robust Dynamic Inversion Controller Design and Analysis for the X-38. AIAA Guidance, Navigation and Control Conference.

[10] Georgie J and Valasek J (2003), Evaluation of Longitudinal Desired Dynamics for Dynamic-Inversion Controlled Generic Reentry Vehicles. Journal of Guidance, Control, and Dynamics, 26(5): 811–819.

[11] Su XF, Jia YM, Du JP, and et al (2012), Integrated Approach to Hypersonic Vehicle Modeling. Proceedings of the 31th Chinese Control Conference, pp. 1752–1758.

[12] Li HF, Lin P, and Xu DJ (2011), Control-oriented Modeling for Air-breathing Hypersonic Vehicle Using Parameterized Configuration Approach. Chinese Journal of Aeronautics, 24: 81–89.

© ISAROB 2013

The Eighteenth International Symposium on Artificial Life and Robotics 2013 (AROB 18th '13),
Daejeon Convention Center, Daejeon, Korea, January 30-February 1, 2013

Flocking control of multi-agent systems in a limited space

Sharu Jiang, Yingmin Jia, Shichen Long

The Seventh Research Division and the Department of Systems and Control, Beihang University (BUAA), Beijing 100191, China (e-mail: jsrshark@126.com, ymjia@buaa.edu.cn, inuyashalsc@hotmail.com).

Abstract: In this paper, flocking control in a limited space is considered. First, a new conception of safety-value is proposed to evaluate the safety between agents and obstacles in a limited space. Then, a new distributed flocking control protocol called the limited space flocking (LSF) algorithm is designed so as to extend the Olfati-Saber's control protocol to the case of a limited space. The algorithm utilizes control protocols corresponding to the safety-value, so the multi-agent system can automatically change its velocity and structure to pass the limited space both quickly and safely. Finally, simulation results show that the proposed algorithm can greatly improve the average velocity of systems and enhance the safety-value in a limited space.

Keywords: flocking, limited space, LSF algorithm, multi-agent, safety-value

1 INTRODUCTION

Recently, multi-agent systems have drawn increasing attention and many good results on the control protocol design have been obtained in a series of works [1]-[6]. An important issue in the control of multi-agent systems is to design a control protocol in order to achieve flocking behavior of systems. A model introduced by Reynolds in [4] plays an important role in the study of flocking. Reynolds' three heuristic rules (flock centering, collision avoidance and velocity matching [7]) led to the first computer animation of flocking. Since then, there emerge lots of works dealing with the flocking problems [8]-[13]. Particularly, among these works the algorithm proposed by Olfati, Saber [8] had a long-term influence on the later development of the flocking control protocol design because they provided a theoretical and computational framework for design and analysis of scalable flocking algorithms.

Flocking algorithms have wide applications such as self-assembly of connected mobile networks; massive distributed sensing using mobile sensor networks; performing military missions and so on. In some practical cases, for example the control of the air traffic, the space where a system forms flocking is limited. In these situations, by using most algorithms [8]-[13] which may work well in free space, system usually couldn't achieve effective obstacle avoidance and would greatly slow down the average speed. Under the consideration that both the obstacle avoidance and the speed of a system are important standards, in this paper a safety-value is raised to evaluate the safety between agents and obstacles in a limited space and a LSF (Limited Space Flocking) algorithm, which is developed from Olfati-Saber's algorithm [8], is proposed to make the system to pass through a limited space both safely and quickly.

2 PRELIMINARIES

In this section, we provide some basic concepts in graph theory [14]-[16], algebraic graph theory [17], spatially induced graphs (or proximity nets) [18] and make the preparation for us to introduce the LSF algorithm which will be further discussed in the following section.

Consider the following "boids" model of N agents:

$$\begin{cases} \dot{q}_i = p_i \\ \dot{p}_i = u_i \end{cases} \quad i = 1,2,\ldots,N, \tag{1}$$

where q_i is the displacement of agent i, p_i is its velocity, u_i is the behavior rule of agent i

Definition 1 (detection shell [19]). *The detection shell Ω_i of agent i is a region, within which the agent can sense the relative location of neighboring agents.*

we assume that all the Ω_i have the same radius R. Denote the set of agents contained in Ω_i by $N_i(t)$, which can be given as

$$N_i(t) = \{j : \|q_i - q_j\| \leq R\}, \tag{2}$$

where $\|q_i - q_j\|, i, j = 1,2,\ldots,N$ is the relative position vectors.

Definition 2 (neighboring graph [19]). *The neighboring graph, $G = (V,E)$, is an undirected graph consisting of:*

1. *A set of vertices (nodes), $V = \{1,2,\ldots,n\}$, indexed by the agents in the group, and*
2. *A set of edges, $E = \{(i,j) \in V \times V | i \in N_j(t) \text{ or } j \in N_i(t)\}$*

Definition 3 (adjacency matrix). *The Adjacency matrix is a matrix $A = [a_{ij}]$ with nonzero elements satisfying the property $a_{ij} \neq 0 \Leftrightarrow (i,j) \in E$, with its elements:*

$$a_{ij} = \rho_k(\|q_j - q_i\|/R) \in [0,1], \quad j \neq i. \tag{3}$$

where $\rho_k(z)$ is a scalar function which smoothly varies between 0 and 1 [20], and $h \in (0,1)$ is a constant parameter, the fomula of $\rho_k(z)$ is shown below:

$$\rho_k(z) = \begin{cases} 1 & , z \in [0,h) \\ \frac{1}{2}[1 + cos(\pi \frac{(z-h)}{(1-h)})] & , z \in [h,1] \\ 0 & , \text{otherwise} \end{cases} \tag{4}$$

© ISAROB 2013

The use of an indicator bump function leads to an adjacency matrix with 0-1 position-dependent elements.

Definition 4 (α-lattice [1]). *An α-lattice is a configuration satisfying the set of constraints in*

$$\|q_j - q_i\| = d, \quad \forall j \in N_i(t). \tag{5}$$

In reference [8], the conception of virtual agents and a classification were first proposed. Corresponding controls can be given according to different kinds of agents. The physical agent with dynamics $\ddot{q}_i = u_i$ is called an α-agent. The primary objective of α-agent in a flock is to form α-lattice with its neighboring α-agents. In nature, α-agents correspond to birds, bees, fish, and ants. Later, virtual agents β-agents and γ-agents are also introduced, which model the effect of "obstacles" and "collective objective" of a group, respectively. γ-agent can be also called the virtual leader of the system.

The distributed control given by Olfati-Saber [8] is denoted as u_i^{OS} and shown in (6):

$$u_i^{OS} = u_i^{\alpha} + u_i^{\beta} + u_i^{\gamma} \tag{6}$$

where the u_i^{α}, u_i^{β} and u_i^{γ} are the controls related to α-agents, β-agents and γ-agents respectively. The stability of the Olfati-Saber algorithm is proved in [8]. Extended from its theoretical frame, a LSF control protocol is designed to deal with the flocking in a limited space.

3 LSF CONTROL PROTOCOL

In this section we present the LSF control protocol in order to enhance the safety-value and the average speed of systems in limited space. First of all, an index is needed to quantitively describe the safety status of the system. Therefore a new conception called the safety-value should be proposed to evaluate the saftey of agents and obstacles in a limited space.

3.1 Safety-value of system in limited space

When passing through a limited space, a multi-agent system will get greatly compressed by the repulsive force from the obstacles. To get efficient control, we introduce two kinds of safety-values to quantify the safety status of an agent as below.

Definition 5 (obstacle safety). *The Obstacle safety $S_k^o = [s_{k1}^o, s_{k2}^o, \ldots, s_{kN}^o] \in R^N$ is a vector with each element varying between 0 and 1, where N is the number of the agents and $s_{ki}^o < 1$ denote the Obstacle safety between agent i and obstacle k, where i,k are the indices of the agent and the obstacle, respectively. The element s_{ki}^o can be calculated as follows:*

$$s_{ki}^o = f_{thr}\left(\frac{\|\hat{q}_{i,k} - q_i\|}{D_\beta}\right), \tag{7}$$

where the $\hat{q}_{i,k}$ is the location of the β-agent, $\|\hat{q}_{i,k} - q_i\|$ is the real distance between agent i and its β-agent, D_β is the set distance between agent i and its β-agent.

$$f_{thr}(x) = \begin{cases} x & x < 1 \\ 1 & x \geq 1. \end{cases} \tag{8}$$

$s_{ki}^o = 1$ means that agent i is safe with obstacle k. $s_{ki}^o = 0$ means that agent i crashes the obstacle k. Analogously, we can also define the Agent safety to quantify the safety situation among agents:

Definition 6 (agent safety). *The agent safety $S^\alpha = \{s_{ij}^\alpha\} \in R^{N\times N}$ is an array with each element varying between 0 and 1, s_{ij}^α denote the agent safety between agent i and agent j and can be calculated as follows:*

$$S^\alpha = \{s_{ij}^\alpha\}, \quad s_{ij}^\alpha = f_{thr}\left(\frac{\|q_j - q_i\|}{D_\alpha}\right). \tag{9}$$

Here we have to mention that because of the cohesive force from the γ-agent (virtual leader), even in a free space, the system would not form a strict α-lattice, which means the distance between agents may shorter than D_α even when a stable flocking behavior of the system is formed. So there is an agent safety diminishment caused by the cohesive force from the virtual leader (γ-agent) and the S_k^o will stabilize in a matrix with elements slightly smaller than 1.

By using the defined and , we can design the LSF control protocol of system in a limited space.

3.2 LSF algorithm in a limited space

Based on the Olfati-Saber model, we propose an algorithm to improve safety-value and the average speed of a multi-agent system in limited space. Noticed that when a multi-agent system meets a limited space, its structure just can be slightly changed by Olfati-Saber algorithm, accordingly, the key point of the LSF algorithm is to add corresponding control in order to automatically change the formation to greatly enhance the safety-value and speed up the system at the same time. When an agent i get dangerous with obstacle k, namely $s_{ki}^o < 1$, we can introduce two kinds of special α-agents to get more precise control.

Definition 7 (ε_k-agent). *δ_k-agent is a virtual agent, and for obstacle k, agent i of the multi-agent system is a ε-agent when it satisfies:*

1. *$s_{ki}^o < 1$ and $(s_{ki}^o)' > 0$*
2. *There does not exist any j s.t. $s_{kj}^o \geq s_{ki}^o$, $a_{ij} > \lambda_{min}$ and $(p_j \cdot v_\gamma)/\|v_\gamma\| > (p_i \cdot v_\gamma)/\|v_\gamma\|$*

where $(s_{ki}^o)'$ is the derivative of s_{ki}^o with respect to time.

Definition 8 (δ_k-agent). *δ_k-agent is a virtual agent and for obstacle k, agent i of the multi-agent system is a δ_k-agent when it satisfies:*

1. *$s_{ki}^o < 1$*
2. *exists j s.t. $s_{kj}^o \geq s_{ki}^o$, $a_{ij} > \lambda_{min}$ and $p_j \cdot v_\gamma/\|v_\gamma\| > p_i \cdot v_\gamma/\|v_\gamma\|$*

© ISAROB 2013

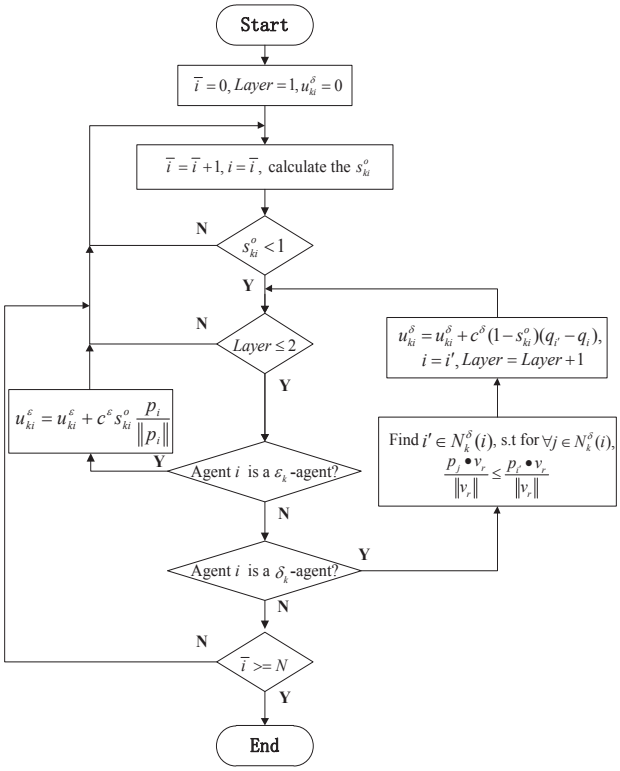

Fig. 1. Flow chart of LSF algorithm 1

where $\lambda_{min} \in \mathbb{R}, 0 < \lambda_{min} \le 1$, v_γ is the velocity of the γ-agent (virtual leader).

The collection of j here is denoted by $N_k^{\delta}(i)$. Notice that an agent can't be ε_k-agent and δ_k-agent at the same time. We present an algorithm to give control to these two kinds of agents respectively. The flow chart of LSF algorithm 1 is displayed in Fig. 1.

Algorithm 1:

It can be inferred from the definition of the ε_k-agent that the ε_k-agents are on the forth front of the system and are heading toward a safer place with an increasing obstacle safety, which makes the effective control to simply be the propulsion along with the same direction. The control u_{ki}^{ε} is obtained in (10):

$$u_{ki}^{\varepsilon} = c^{\varepsilon} s_{ki}^{o} \frac{p_i}{\|p_i\|} \tag{10}$$

where the c^{ε} is a constant coefficient for u_{ki}^{ε}. As to the δ_k-agent, compared to the ε_k-agent, it functions like the follower to the pioneer in the system. δ_k-agent always has agents with higher obstacle safety before it. In order to maximum the effect of changing the structure, enhance the obstacle safety, and securely speed up the velocity, we propel the δ_k-agent to a forefront safer neighboring agent. The specific process is to find $i' \in N_k^{\delta}(i)$, s.t for $\forall j \in N_k^{\delta}(i)$, $p_j \cdot v_\gamma / \|v_\gamma\| \le p_{i'} \cdot v_\gamma \|v_\gamma\|$, then the corresponding control u_{ki}^{δ} is given in (11)

$$u_{ki}^{\delta} = c^{\delta}(1 - s_{ki}^{o})(q_{i'} - q_i) \tag{11}$$

where the c^{δ} is a constant coefficient for u_{ki}^{δ}.

After adding up the control with respect to the obstacles, the result can be expressed in the formulation below:

$$u_i^{\delta} = \sum_k u_{ki}^{\delta}, \quad u_i^{\varepsilon} = \sum_k u_{ki}^{\varepsilon}. \tag{12}$$

The algorithm 1 works well in obstacle avoidance, however, the improvement of the obstacle safety is gained on a little sacrifices of the agent safety, namely the agent safety may drop a little. In order to reduce such sacrifices and make a complement to algorithm 1, we use a complementary algorithm to make some amendment.

Algorithm 2:

When the system is passing through a limited place, the u_i^{θ} can be added to the Algorithm and be gained as follows:

$$u_i^{\theta} = c^{\theta} \sum_j \frac{a(i,j)\Delta s_{i,j}^{\alpha}}{s_{i,j}^{\alpha}} \frac{(q_j - q_i)}{\|q_j - q_i\|}, \tag{13}$$

where $\Delta s_{i,j}^{\alpha} = s_{i,j}^{\alpha}(t) - s_{i,j}^{\alpha}(t - \Delta t)$ is the change of $s_{i,j}^{\alpha}$ from $t - \Delta t$ to t, t is the temporary moment.

The function of u_i^{θ} is like a buffer in the system, when reduction of the ,namely the $\Delta s_{i,j}$ is huge and the $s_{i,j}^{\alpha}$ is low, the u_i^{θ} is fairly considerable. So by adding u_i^{θ}, the reduction of the agent safety can be greatly decreased and then the Algorithm 2 can make complement to the Algorithm 1. In conclusion, the LSF distributed control protocol can be given by the following formula (14):

$$u_i^{LSF} = u_i^{OS} + u_i^{\varepsilon} + u_i^{\theta} \tag{14}$$

where the u_i^{OS} is the control of Olfati-Saber algorithm.

4 SIMULATION RESULT

In this section, we use some simulations to demonstrate the effectiveness of our design method - LSF algorithm. Without loss of generality, we can specify the limited space into a channel, the number of the system N is 25, the width of the channel is 8, and length is 20. The parameters for each kind of agent are set as follows:

$$\begin{array}{lll} c_1^{\alpha} = 1 & , & c_2^{\alpha} = 1, \\ c_1^{\gamma} = 1 & , & c_2^{\gamma} = 1, \\ c_1^{\beta} = 4.5 & , & c_2^{\beta} = 5.8, \\ c^{\delta} = 6.55 & , & c^{\theta} = 7.7. \end{array}$$

and $c^{\varepsilon} = 100.215$. To contrast the control performances between the LSF algorithm and the Olfati-Saver algorithm of multi-agent systems in a limited space, three main qualities of the process of proceeding though the channel are calculated to get further analysis of the two algorithms. $s^o = \min_{k,i}(s_{ki}^o)$ and $s^{\alpha} = \min_{i,j}(s_{ij}^{\alpha})$ can show the safety-value of the system in a limited space, $V_{average}$ is the average velocity of all the agents of the system.

In figure 2 , the blue solid line represents the results of Olfati-Saber algorithm, and the red dotted line represent the results of LSF algorithm. Looking at the Fig. 2, we can see, the LSF algorithm can accelerate the average speed, greatly enhance the s^o and remain the s^{α}.

© ISAROB 2013

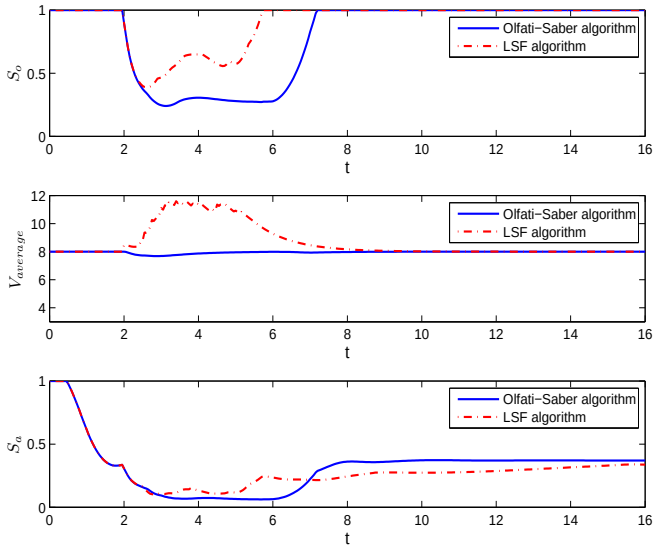

Fig. 2. Contrast figure between two algorithms about $s^o, s^\alpha, V_{average}$

It has been shown that, under the LSF flocking control protocols, the stable flocking behaviors can be achieved and the average speed of the system in a limited space is improved. What's more, the obstacle safety is greatly enhanced and the agent safety basically stays the same. Study of simulation reveals that the LSF control algorithm can speed up the system and improve its safety as the same time.

5 CONCLUSION

In this paper, we study the flocking control for multi-agent systems in a limited space. A new coefficient called the safety-value is introduced to describe the safety between agents and obstacles, On the basis of the safety-value and Olfati-Saber algorithm, a distributed flocking control protocol - LSF algorithm is designed to control the multi-agent system in a limited space. By using local information of each agent, the system can automatically and flexibly change its velocity and structure in order to pass the limited space both quickly and safely. Simulation reveals that the proposed LSF control protocol can greatly improve the velocity of the multi-agent system with even enhanced safety-value.

6 ACKNOWLEDGMENTS

This work was supported by the National 973 Program (2012CB821200, 2012CB821201) and the NSFC (61134005, 60921001, 90916024, 91116016).

REFERENCES

[1] Li Q, Jiang ZP (2009), Global Analysis of Multi-Agent Systems Based on Vicsek's Model. IEEE Trans. Automa. Control, 54(12): 2876-2881.

[2] Lin ZY, Broucke M, Francis B (2004), Local Control Strategies for Groups of Mobile Autonomous Agents. IEEE Trans. Automa. Control 49(4):622-629

[3] Ren W, Beard RW (2005), Consensus Seeking in Multi-agent Systems Under Dynamically Changing Interaction Topologies. IEEE Trans. Automa. Control 50(5):655-661

[4] Reynolds CW (1987), Flocks,Herds,and Schools: A Distributed Behavioral Model. Computer Graphics 21(4): 25-34

[5] Shi H, Wang L, Chu TG, et al (2007), Flocking of Multi-Agent Systems with a Virtual Leader. In: Proceedings of the 2007 IEEE Symposium on Artificial Life, pp. 287-294

[6] Carpin S, Parker LE (2002), Cooperative Leader Following in a Distributed Multi- Robot System. In: Proceedings of IEEE International Conference on Robotics Automation, pp. 2994-3001

[7] Tanner HG (2004), Flocking with Obstacle Avoidance in Switching Networks of Interconnected Vehicles. In: Conference of Robotics and Automation, pp. 3006-3011

[8] Olfati-Saber R (2006), Flocking for multi-agent dynamic systems: Algorithms and theory. IEEE Trans. Automat. Control 51(3): 401-420

[9] Hong Y, Gao L, Cheng D, et al (2007), Lyapunov-based approach to multi-agent systems with switching jointly-connected interconnection. IEEE Trans. Autom. Control 52(5):943-948

[10] Gazi V, Passino KM (2004), A class of attraction/repulsion functions for stable swarm aggregations. Int. J. Control 77(18): 1567-1579

[11] Su H, Wang X, Lin Z (2009), Flocking of multi-agents with a virtual leader. IEEE Trans. Autom. Control 54(2): 293-306

[12] Rimon E, Koditschek DE (1990), Robot navigation functions on manifolds with boundary. Adv. Appl. Math 11(4): 412-442

[13] Gazi V, Passino K (2004), Stability analysis of social foraging swarms. IEEE Trans. Syst., Man, Cybern. B: Cybern. 34(1): 539-557

[14] Bollob s B (1998), Modern Graph Theory. Vol. 184 of Graduate Texts in Mathematics. New York: Springer-Verlag

[15] Diestel R (2000), Graph Theory. Vol. 173 of Graduate Texts in Mathematics. New York: Springer-Verlag

[16] Horn RA, Johnson CR (1987), Matrix Analysis. Cambridge Univ. Press, Cambridge

[17] Godsil C, Royle G (2001), Algebraic Graph Theory, Vol. 207 of Graduate Texts in Mathematics. New York: Springer-Verlag

[18] Olfati-Saber R (2003), Flocking with obstacle avoidance. California Inst. Technol., Control Dyna. Syst., Pasadena, CA, Tech. Rep. 2003-006, Feb

[19] Tanner HG (2004), Flocking with obstacle avoidance in switching networks of interconnected vehicles. In: Conference Robotics and Automation, pp. 3006-3011.

[20] Saber RO, Murray RM (2003), Flocking with obstacle avoidance: cooperation with limited communication in mobile networks. In: Proceedings 42nd IEEE Conf. Decision and Control. Dec, pp. 2022-2028.

© ISAROB 2013

The Eighteenth International Symposium on Artificial Life and Robotics 2013 (AROB 18th '13),
Daejeon Convention Center, Daejeon, Korea, January 30-February 1, 2013

Inverse kinematics in Hyper-redundant robot using Adaptive Neural Network

Chatklaw Jareanpon

Polar Lab, Department of Computer Science, Faculty of Informatics
Mahasarakham University , Thailand
(Tel: 66-86-225-5574, Fax: 66-43-754-359)

chatklaw.j@msu.ac.th

Abstract: The hyper-redundant robot has more degrees-of-freedom. The most difficulty of the hyper-redundant is to finding the inverse kinematic problem. Most of usually used method is Neural Network. However, it is difficult to find the suitable structure and number of node. This paper shows the novel algorithm that can find the suitable structure and number of node depends on the problem. The performance of this algorithm will demonstrated in the computer simulation and compare with the Back-propagation with same structure. The algorithm shows the good performance to adapt the number of node with less error to solve the 8-20 serial link chain hyper-redundant robots.

Keywords: Inverse kinematics, Hyper-redundant robot, Neural Network.

1 INTRODUCTION

The hyper-redundant robot is the robot that has more than the minimum numbers of degrees-of-freedom are termed "many kinematically redundant". The hyper-redundant are used in operation to snakes, elephant trunks, and tentacles. There are a number of very important applications such as obstacle avoidance, manipulated task. However, the most difficulty in Hyper-redundant robot is controlling the inverse kinematics of its.

The different techniques used for solving inverse kinematics can be classified as algebraic that do not guarantee closed form solutions, geometric that usually used the curve and constraint, and iterative. The iterative methods converge to only a single solution. The most learning method that are usually using Neural networks. The Neural Netwoks usually used to solve the problem of inverse kinematics are Back-propagation and Kohonen network. However, the most question of using neural network is "How many are the best number of the nodes? "

In this paper, I proposed a new sequential learning algorithm, which is able to adapt the structure of the network. Using this algorithm, it is possible to find the suitable number of hidden node.

2 HYPER-REDUNDANT ROBOT

Highly redundant manipulators or *hyper degree of freedom (HDOF)* has more degrees of freedom (DOF). A HDOF manipulator can perform manipulation tasks, such as moving in non-convenient environments, and pushing and caging a various sizes and shapes of objects. Due to all-in-one arms, a HDOF manipulator significant enhances the caging method as it, allows caging to perform in a variety of configuration. However, this arm must always maintain a certain shape around an object.

HDOF has been used by several researchers for solving control problems such as kinematic modeling [1], [2] path planning [3], [4], inverse kinematics [5], [6], [7], [8], locomotive gait design [9], [10], obstacle avoidance [11], [12], serpentine locomotion control [13], [14] and sidewinding locomotion control [15] problems.

In our work, we study the shape control of a highly kinematic structure, called a HDOF arm manipulator. The HDOF is composed of serial chain links $l_i, i = 1,....,N$, connected to other with revolute joints $j_i, i = 0,...,N-1$. Each link is a straight rigid part of length L . The link l_1 and link l_N are called the base and the tail, respectively. The angle θ_1 is defined as the angle between link l_1 and x-axis. The set of angle defines the manipulator configuration as shown in Figure 1.

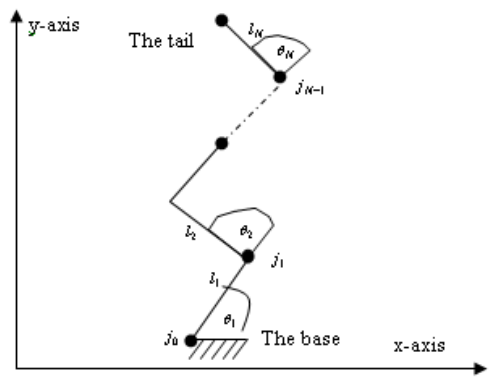

Fig. 1. A hyper degree of freedom (HDOF) structure.

© ISAROB 2013

3 INVERSE-KINEMATICS PROBLEM

A HDOF manipulator has ability to move in highly constrained environment or grasp various sized and shaped objects. HDOF manipulators are categorized into 3 types of mechanisms which are serial rigid, parallel rigid and tentacle-like. A serial rigid robot arm is consisting of links and joints in chain structure. In forward kinematics or direct kinematics, the joint displacement and link parameters are given in order to find the end-effector position. Conversely, the inverse kinematics is to solve for the joint displacement when the end-effector position is given.

The transformation matrix relating i^{th} coordinate system (coordinate of end of link *i*) to the $(i\text{-}1)^{th}$ (coordinate of end of link *i-1*) coordinate system is ${}^{i-1}_{i}T$ given by

$$ {}^{i-1}_{i}T = \begin{bmatrix} \cos\theta_i & -\cos\alpha_i \sin\theta_i & \sin\alpha_i \sin\theta_i & \alpha_i \cos\theta_i \\ \sin\theta_i & \cos\alpha_i \sin\theta_i & -\sin\alpha_i \sin\theta_i & \alpha_i \cos\theta_i \\ 0 & \sin\alpha_i & \cos\alpha_i & d_i \\ 0 & 0 & 0 & 1 \end{bmatrix} \quad (1) $$

where parameters are

a_i = the distance from $\hat{z}_i$ to $\hat{z}_{i+1}$ measured along $\hat{x}_i$

α_i = the angle from $\hat{z}_i$ to $\hat{z}_{i+1}$ measured along $\hat{x}_i$

d_i = the distance from $\hat{x}_i$ to $\hat{x}_{i-1}$ measured along $\hat{z}_i$

θ_i = the angle from $\hat{x}_i$ to $\hat{x}_{i-1}$ measured along $\hat{z}_i$

$\hat{z}_i = \hat{z}_i axis$ of frame *{i}*

$\hat{x}_i = \hat{x}_i axis$ of frame *{i}*

The transformation matrix is divided into two parts which are rotational part and translation part.

$$ {}^{i-1}_{i}T = \left[\begin{array}{ccc|c} & ({}^{i-1}_{i}R) & & ({}^{i-1}_{i}P) \\ \hline 0 & 0 & 1 & 1 \end{array} \right] \quad (2) $$

Transformation matrix form the base frame {0} to link *n* is described by

$$ {}^{0}_{n}T = {}^{0}_{1}T\,{}^{1}_{2}T\,{}^{2}_{3}T \ldots {}^{n-1}_{n}T \quad (3) $$

Since a HDOF manipulator has large number of de grees of freedom (DOF), the inverse kinematics solutio n is not unique. Moreover, the solution of inverse kine matics of the robot arm is difficult to find. The algebr aic and numerical methods are usually employed to sol ve the inverse kinematics problem. The concept of alg ebraic method is to transform the kinematics equations to a high degree polynomial in the tangent of the hal f-angle of joint variable. However, it is complicate in t he nonlinear system.

The numerical methods that are widely used in solv ing for inverse kinematics is the Newton-Raphson itera tion method. Other optimization techniques can also be used. The concept of inverse kinematics problem is si milar to minimization problem where the error between the current position and desired position is minimized. Therefore, nonlinear optimization techniques such as n eural network [16] and genetic algorithm [17] can be applied to this problem.

4 RADIAL BASIS FUNCTION (RBF) NETWORK

The Radial Basis Function (RBF) Networks is a single hidden layer feed forward neural network as shown in Figure 2. Each node of the hidden layer has a parameter vector called the center. This center is used to compare with the network input vector to produce a radial symmetrical response. The response of the hidden layer are scaled by the connection weights of the output layer and then combined to produce the network output. The response of the jth hidden node to input data vector x_i, dimensionality M, is given by (4).

$$ \phi_{ij} = \exp(-\alpha \| x_i - x_j \|^2) \quad (4) $$

where c_j is an M-dimensional center and $\propto$ is a constant which determines the spread factor of the symmetric response of the hidden node. The network output is defined as

$$ \hat{\gamma}_i = \sum_{j-1}^{k} \varphi_{ij} h_j \quad (5) $$

where h_j are the network's second layer connection weights and k is the number of hidden nodes.

The widely used RBF network, may use other functions e.g. piecewise linear, cubic approximation, the thin plate spline, the multiquadratic, and the inverse multiquadratic function in place of the Gaussian.

© ISAROB 2013

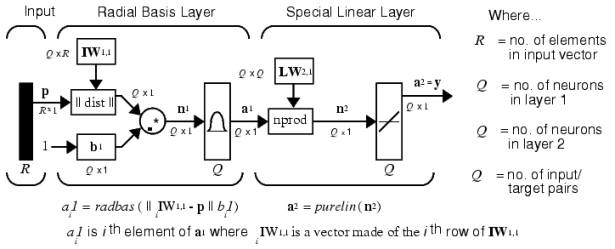

Fig. 2. Architecture of an RBF neural network

The performance of the networks is measured by a Mean-Squared-Error (MSE). The main objective of the training procedure is to approximate the underlying function of the system.

5 THE NEW RBF NETWORK WITH PROPOSED ADAPTIVE STRCUTURE

To determine an appropriate structure for the RBF network, a modified RBF network with adaptive structure is proposed. Initially, in the proposed structure, the radial basis layer has one hidden neuron. Afterward, the network iteratively appends one RBF node to the hidden layer at each training epoch until the error falls beneath an error goal or the maximum number of neurons has been reached. Unlike a traditional network with a fixed structure, the proposed network gradually searches for a minimum number of hidden nodes needed to meet the performance goal. The overall algorithm is given as the following:

- Step 1. Initialize the network using the Structure having a single neuron in the hidden layer.
- Step 2. For each training epoch, feed all input vectors to the network and train the network according to the RBF training algorithm.
- Step 3. Find the input vector in which the network output yields the greatest error.
- Step 4. Add one neuron to the hidden layer with its weight vector equals to the vector obtained from Step 3.
- Step 5. Repeat Step 2 until the performance goal is met or the maximum number of hidden nodes has been reached.

5 EXPERIMENTAL AND RESULT

In this section, experimental results are presented in Table 1 and Figure 3. I try to solve the inverse-kinematics in vary the number of links from the 8 and 20 serial link chains. I will measurement the algorithm in term of the error, time and number of nodes when compares with back-propagation neural network with same structure. The error is calculated from the distance between end-effector and target position. Our experiment is tested on the Core-I7 3.4GHz and 16 GB of RAM.

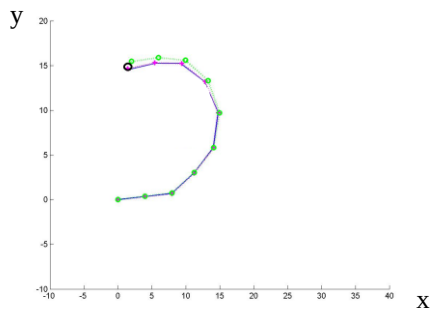

Fig. 3. Comparison between Back-Propagation Neural (Dot line) and our proposed method (solid line) of 9 links serial link chain

Table 1. The comparison between Back-Propagation and Our proposed method

Link	Back-Propagation			Our proposed method		
	Node	err	time (s)	Node	err	time (s)
8	18	1.250	258	18	1.020	260
9	24	3.041	301	24	2.570	284
12	41	3.225	440	41	3.000	365
14	52	4.655	665	52	4.080	556
16	51	4.787	896	51	4.220	803
18	52	5.200	994	52	5.050	925
20	80	6.250	1226	80	6.220	1198

From Table 1, when the number of the link increased, the error and time will increase. Especially, the time is very much consuming.

6 DISCUSSION

Our proposed method is show the performance of finding the suitable number of the node. The proposed method can solve the problem of inverse kinematic. Moreover, we can able to find the suitable number of node for other neural network such as Back-propagation.

In the future, I will try to reduce the time consuming, because the time is abundantly grown when add the number of link.

© ISAROB 2013

REFERENCES

[1] S. Chirikjain and J. Burdisk, "The kinematics of Hyper-Redundant robot locomotion," IEEE Transactions on robotics and automation., vol. 11, no. 6, Dec. 1995.

[2] F. Matsuno and K. Mogi, "Redundancy controllable system and control of snake robots based on kinematic model," Proc. of the 39th IEEE conference on decision and control., pp. 4791-4796, 2000.

[3] H. Poor, An Introduction to Signal Detection and Estimation. New York: Springer-Verlag, 1985, ch. 4.

[4] B. Smith, "An approach to graphs of linear forms (Unpublished work style)," unpublished.

[5] H. Chang, "A closed-form solution for inverse-kinematic of robot manipulators with redundant," IEEE journal of robotics and automation., vol. ra-3, no. 5, Oct. 1987.

[6] Y. Li and H. Leong, "Kinematics control of redundant manipulators using a CMAC neural network combined with genetic algorithm," Robotica., vol. 22, pp. 611-621, 2004.

[7] K. Mathia and R. Saeks, "Inverse kinematics via linear dynamic network," World congress on neural networks, 1994.

[8] Y. Zhau, T. Huang, and Z. Yang, "A new numerical algorithm for the inverse position analysis of all serial manipulators," Robotica., vol. 00, pp. 1-4, 2005.

[9] G. Kulali and et al, "Intelligent gait synthesizer for serpentine robots," Proc. of the 2002 IEEE international conference on robotics and automation., pp. 1513-1518, 2002.

[10] A. Crespi and et al, "An amphibious robot capable of snake and lamprey-like locomotion," Proc. of the 2005 IEEE international conference on robotics and automation., pp. 3035-3039, 2005.

[11] H. Xie, "Real-time collision avoidance for a redundant manipulator in an unstructured environment," Proc. of the 1998 IEEE international conference on intelligent robotics and system., pp. 1925-1930, 1998.

[12] S. Ma and M. konno, "An obstacle avoidance scheme for hyper-redundant manipulators – Global motion planning in posture space –," Proc. of the 1997 IEEE international conference on robotics and automation., pp. 161-166, 1997.

[13] J. Ostrowski and J. Burdick, "Gait kinematics for a serpentine robot," Proc. of the 1996 IEEE international conference on robotics and automation., pp. 1294-1299, 1996.

[14] J. Conradt and P. Varshavskaya, "Distributed central pattern generator control for a serpentine robot," Proc. of the joint international conference on artificial neural network., 2003.

[15] J. Burdick, J. Radford, and S. Chirikjian, "Sidewinding" locomotion gait for hyper-redundant robots,", Proc. of the 1993 IEEE international conference on robotics and automation., pp. 101-106, 1993

[16] K. Mathaia and R. Saeks, "Inverse Kinematics via Linear Dynamic Networks", Proceeding on World Congress on Neural Networks, pp. 47-52, 1994.

[17] Y. Li and A. Hong Lenog, "Kinematics control of redundant manipulators using CMAC neural network combined with a genetic algorithm", Robotica, pp. 611-621, 2004.

© ISAROB 2013

The Eighteenth International Symposium on Artificial Life and Robotics 2013 (AROB 18th '13),
Daejeon Convention Center, Daejeon, Korea, January 30-February 1, 2013

Reduction of Impact when a Humanoid Robot Lands on the Ground

Homare Fujieda, Shingo Okamoto[1], Jae Hoon Lee

Ehime University, Japan
(Tel: 81-89-927-9740, Fax: 81-89-927-9740)

[1]okamoto.shingo.mh@ehime-u.ac.jp

Abstract: The purpose of this research is to reduce the impact force when robot land on the floor by landing motion. First, landing postures of a human were analyzed measuring impacts when the human land on the floor. Through the experimental result on relations between landing postures and the impact forces, it was hypothesized that a human may reduce the impact force by motion control of gravity center of the human, for example to lengthen the time in landing motion. Then a landing robot was developed and the experiment to measure the impact forces was conducted, in order to prove the hypothesis.

Keywords: Humanoid robot, Impact reduction, Passive landing, Active landing, Numerical calculation.

1 INTRODUCTION

Recently, researches about humanoid robots have been well-advanced. In consequence of the well-advance, the humanoid robots became able to practice various motions, such as walking, jumping, and low-speed running. Then, as the development of the humanoid robots is advanced more, the humanoid robots will be needed to behave more intensely for example, like high-speed running. Then, the impact that robots receive in the high-speed running will become a big problem hereafter. This impact may cause various troubles like falling and damage of parts.

The purpose of this research is to reduce the impact when a robot land on the floor by landing motion. Here, we focused on the shifting gravity center of the human in landing on the floor. Then, the experiment to measure the impact was conducted in order to prove that the impact can be reduced by motion control of gravity center of the humanoid robot during landing motion.

2 LANDING OF A HUMAN

2.1 Taking moving images

We took moving images of human's landing by a high-speed camera (CASIO: EX-FH25). Then landing postures when a human lands on the floor was analyzed. Two types of landing, a usual landing and a IR(Impact Reduction)landing, were analyzed. The result of moving images is shown in Figure 1. Through the comparison of two results, it was found that (1) there is no difference between the usual and the IR landing in a touchdown motion and, the human bends his knees more in considering impact reduction than the usual landing. It means that a human shifts slowly down his gravity center when he needs to reduce the impact.

2.2 Measurement of impact

Figure 2 shows the impact force for each landing posture. The period of time from beginning to end of landing motions of the usual and IR landings were 0.480[s] and 0.935[s], respectively. The period of time of IR landing was twice as long as that of usual landing. Then, the impact forces of the usual and IR landings were 2.48×10^3[N] and 1.50×10^3[N], respectively, and that of IR landing decreased by 40 [%] to that of the usual one. From these results, it was hypothesized that a human may reduce the impact by motion control his gravity center, for example, to lengthen the period of time in landing motion.

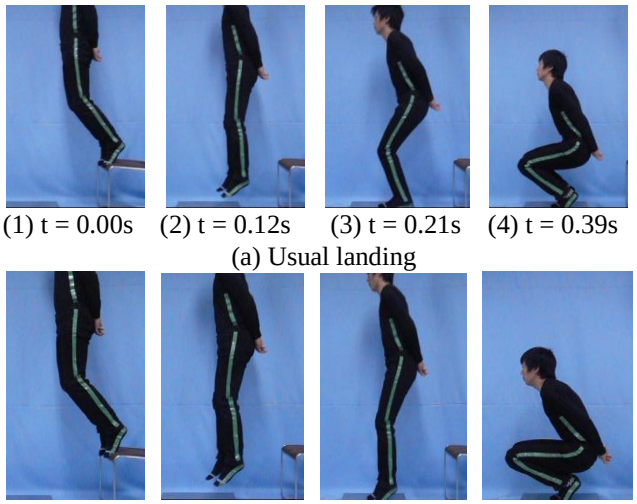

(1) t = 0.00s (2) t = 0.12s (3) t = 0.21s (4) t = 0.39s
(a) Usual landing

(1) t = 0.00s (2) t = 0.12s (3) t = 0.21s (4) t = 0.43s
(b) IR Landing

Fig. 1. Moving images of human's landing

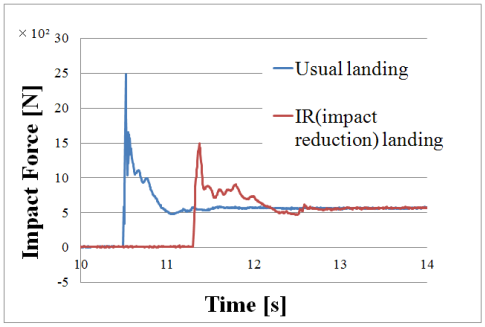

Fig. 2. Impact forces to variable landing postures

© ISAROB 2013

3 CONPUTATIONAL CALCULATION

3.1 Analysis model

An analysis model of a landing robot was designed and the numerical calculation was performed in order to develop the landing robot. Figure 3 shows the analysis model of a landing robot. The analysis model is composed of a foot, an upper body, a shin and a thigh.

The landing robot falls along a rail with a slope in order to diminish the speed in shifting gravity center of the robot so that a motor can control its speed. Then the physical parameters of the lengths, the masses, the inertia moments, the coefficient of viscosity and the spring constant used in the calculation are shown in Table 1.

3.2. Equation of motion

The equation of motion is given by

$$\boldsymbol{M}\ddot{\boldsymbol{Q}} + \boldsymbol{C}\dot{\boldsymbol{Q}} + \boldsymbol{K}\boldsymbol{Q} = \boldsymbol{\tau} - \boldsymbol{G} \tag{1}$$

where $\boldsymbol{Q} = \{u_1 \quad \theta\}^T$, $\boldsymbol{\tau} = \{0 \quad \tau_1\}^T$, $\boldsymbol{M}$ is a inertia matrix, $\boldsymbol{C}$ is a damping matrix, $\boldsymbol{K}$ is a stiffness matrix and $\boldsymbol{G}$ is a gravity vector. The components of matrixes and vector in Eq.(1) are represented as

$$\boldsymbol{M} = \begin{bmatrix} M_{11} & M_{12} \\ M_{21} & M_{21} \end{bmatrix}, \tag{2}$$

where

$$M_{11} = m_1 + m_2 + M_1 + M_2, \tag{3}$$

$$M_{12} = -\{(m_1 + m_2)(L_1 + L_2) + M_1 l_1 - M_2 l_2\} \sin\theta, \tag{4}$$

$$M_{21} = -\{(m_1 + m_2)(L_1 + L_2) + M_1 l_1 - M_2 l_2\} \sin\theta, \tag{5}$$

$$M_{22} = \{(m_2 + M_2)(L_1 + L_2)^2 - 2M_2 l_2 (L_1 + L_2)\} \sin^2\theta + M_1 {l_1}^2 + M_2 {l_2}^2 + J_1 + J_2, \tag{6}$$

$$\boldsymbol{C} = \begin{bmatrix} C_{11} & C_{12} \\ C_{21} & C_{22} \end{bmatrix}, \tag{7}$$

where

$$C_{11} = C_f, \tag{8}$$

$$C_{12} = -\{(m_1 + m_2)(L_1 + L_2) + M_1 l_1 - M_2 l_2\} \dot{\theta} \cos\theta, \tag{9}$$

$$C_{21} = 0, \tag{10}$$

$$C_{22} = 0.5\{(m_2 + M_2)(L_1 + L_2)^2 - 2M_2 l_2 (L_1 + L_2)\} \dot{\theta} \sin 2\theta + 4c_j, \tag{11}$$

$$\boldsymbol{K} = \begin{bmatrix} K_{11} & K_{12} \\ K_{21} & K_{22} \end{bmatrix}, \tag{12}$$

where

$$K_{11} = k_f, \tag{13}$$

$$K_{12} = 0, \tag{14}$$

$$K_{21} = 0, \tag{15}$$

$$K_{22} = 4k_j, \tag{16}$$

$$\boldsymbol{G} = \{G_1 \quad G_2\}^T, \tag{17}$$

where

$$G_1 = (m_1 + m_2 + M_1 + M_2) g \sin\alpha, \tag{18}$$

$$G_2 = -\{(m_1 + m_2)(L_1 + L_2) + M_1 l_1 - M_2 l_2\} g \sin\theta \sin\alpha + (M_1 l_1 + M_2 l_2) g \cos\theta \cos\alpha - 2k_j(\pi - \theta_0), \tag{19}$$

3.3. Passive landing

3.3.1 Calculation method

A computer simulation using the Newmark-β method was performed in a numerical calculation, and Scilab was used as a computer language. Then control torque τ_1 was set at zero in this calculation. The spring constant k_f was given as Eq.(20). These parameters were decided based on the experiment. Then the coefficient of velocity c_f was given as Eq.(3).

$$k_f = 267{,}459(u_1 - h_1 - 0.08)^2 - 1{,}790.1(u_1 - h_1 - 0.08), \tag{20}$$

$$c_f = \beta_2 k_f, \tag{21}$$

The values of β_1 and β_2 were set at 5.15×10^{-2} and 7.50×10^{-1}, respectively. The initial height of the landing robot was set at 0.3[m].

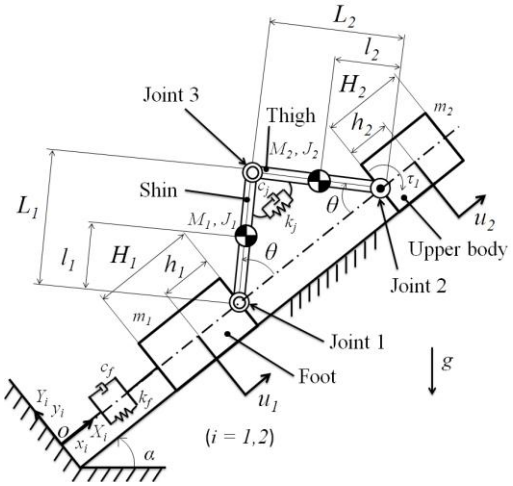

H_1 : Length of the foot, H_2 : Length of the upper body
L_1 : Length of the shin, L_2 : Length of the thigh
h_1 : Length from the joint 1 to the gravity center of the foot
h_2 : Length from the joint 2 to the gravity center of the upper body
l_1 : Length from the joint 1 to the gravity center of the shin
l_2 : Length from the joint 2 to the gravity center of the thigh
m_1 : Mass of the foot, m_2 : Mass of the body
M_1 : Mass of the shin, M_2 : Mass of the thigh
J_1 : Inertia moment of the shin, J_2 : Inertia moment of the thigh
k_j : Spring constant of the joint 3
c_j : Coefficient of viscosity of the joint 3
k_f : Spring constant of the foot
c_f : Coefficient of viscosity of the foot
θ : Rotation angle of the shin(or thigh)
u_1 : Displacement of the foot, u_2 : Displacement of the upper body
τ_1 : Control torque, α : Angle of the slope

Fig. 3. Analysis model of the landing robot

Table 1. Physical parameters of analysis model

m_1 [kg]	2.40	L_1 [m]	2.10×10^{-1}
m_2 [kg]	1.56	L_2 [m]	2.10×10^{-1}
M_1 [kg]	3.10×10^{-1}	l_1 [m]	1.05×10^{-1}
M_2 [kg]	3.10×10^{-1}	l_2 [m]	1.05×10^{-1}
H_1 [m]	1.70×10^{-1}	J_1 [kg•m^2]	2.11×10^{-3}
H_2 [m]	8.00×10^{-2}	J_2 [kg•m^2]	2.11×10^{-3}
h_1 [m]	8.50×10^{-2}	c_j [kg/m•s]	$\beta_1 k_j$
h_2 [m]	4.00×10^{-2}	k_j [kg•m^2/s^2•rad]	3.20

3.3.2 Calculated results

Figure 4 shows the time histories of u_1 and u_2. The experiment of the landing robot was conducted based on this result.

© ISAROB 2013

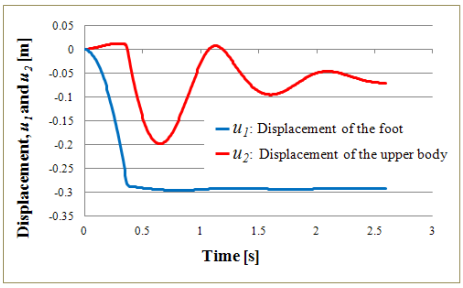

Fig. 4. The calculated time histories of u_1 and u_2 in passive landing

3.4 Active landing

3.4.2 Calculation method

Two types of control method, the proportional control and the proportional-differential control were used. Then the spring constant of the joint 3 k_l and coefficient of viscosity of the joint 3 c_l were set at zero in this calculation.

3.4.3 P control (Proportional control)

The block diagram of an active control for calculation is shown in Figure 5. The control torque τ_1 loaded to the upper body was given by Eq.(22) when the proportional control was used.

$$\tau_1 = k_p(\theta_d - \theta) \quad (22)$$

The calculated result of the proportional control is shown in Fig. 6 when setting at the control gain k_p = 200[N•m/rad], the desired angle of the shin(or thigh) θ_d = 87[deg], and the angle of the shin(or thigh) θ = 87[deg] corresponding to the displacement of the upper body u_2 = 0.2[m]. Then control gain k_d was set at zero in this calculation.

3.4.4 PD control (Proportional-differential control)

The block diagram of an active control for calculation is shown in Figure 5. The control torque τ_1 loaded to the upper body was given by Eq.(23) when the PD control is used. The k_p and k_d denote the control gain.

$$\tau_1 = k_p(\theta_d - \theta) + k_d(\dot{\theta}_d - \dot{\theta}) \quad (23)$$

The calculated result of the PD control is shown in Fig. 6 when setting at the control gain k_p = 200[N•m/rad], the desired angle of the shin(or thigh) θ_d = 87[deg], the desired angular velocity of the shin(or thigh) $\dot{\theta}_d$ = 0[m/s].

3.3.2 Calculated results

Figure 6 shows the comparison of the displacement u_2 of the upper body between the proportional and the PD controls. It was found that the displacement u_2 was stabilized by using the PD control.

4 DESIGN AND DEVELOPMENT OF EXPERIMENTAL SET-UP

4.1. Landing robot

Figure 7 shows a landing robot. The landing robot is composed of a foot, an upper body, the shin and the thigh. Two rotary encoders are installed to measure the rotation angles. The displacement of the foot and the upper body are calculated by them. The torsion springs are attached to the

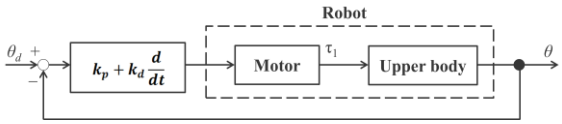

k_d = 0 : P control, $k_d \neq 0$: PD control

Fig. 5. Block diagram of an active control for calculation

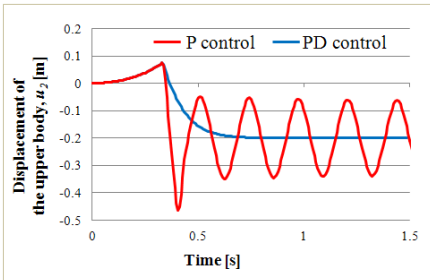

Fig. 6. Comparison of the displacement u_2 of the upper body between the proportional and the proportional-differential controls

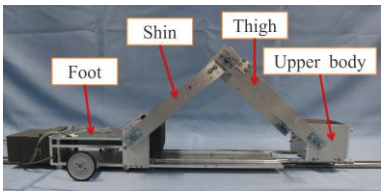

Fig. 7. Landing robot

Fig. 8. Guide flame with a slope

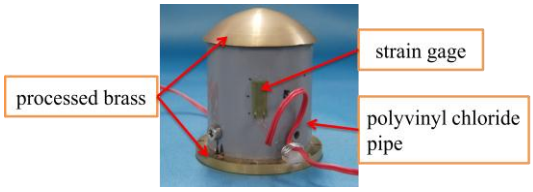

Fig. 9. Force sensor

knee joint to connect the shin and the thigh, in order to give a spring effect that thigh muscles of a human generate.

4.2. Guide flame with a slope

Figure 8 shows a guide flame with a slope. This slope angle can be changed to desired angle. A rail that the landing robot falls along the slope is attached on the guide flame.

4.3. Force sensor

A force sensor to measure the impact which the landing robot is subjected to was developed. Figure 9 shows the force sensor. The force sensor is composed of a polyvinyl chloride pipe, parts of processed brass and strain gages.

© ISAROB 2013

5 EXPERIMENT OF THE LANDING ROBOT

5.1. Passive landing

5.1.1 Experimental method

The initial angle of the shin(or the thigh) was set at θ = 45[deg], and initial height of the landing robot at 0.3[m]. The spring constant of the torsional spring was set at 4.62[kg•m²/s²•rad]. The experiment was conducted in two types of landing condition, (a)a landing with shifting gravity center of the robot and (b)a landing with fixing the distance between the foot and the upper body. Then both the impact forces when the robot lands on the ground and the positions of the moving body were measured to each condition.

5.1.2 Experimental results

Figure 10 shows the impact force on each condition. Figure 11 shows the comparison of u_1 and u_2 between calculation and experimental result. The period of time from beginning to end of landing motions of the (a) and (b) were 0.095[s] and 0.073[s], respectively. The period of time of (a) was 1.3 times as long as that of (b). Then the impact forces of (a) and (b) were 2.84×10^2[N] and 5.81×10^2[N], respectively, and that of (a) decreased by 50 [%] to that of (b). It was found that the impact force when the robot lands on the ground can be reduced by shifting gravity center of the robot. Then the displacement of the foot u_1 and the upper body u_2 in the experiment follow the displacement in calculation. As this result, a validity of the landing robot was confirmed.

5.2. Active landing

5.2.1 Installation of a motor

A motor was installed at the upper body to reproduce effect of the torsion spring. The landing robot installed the motor as shown in Figure 12.

5.2.2 Control method of the motor

The PD control was used for control of the motor. The block diagram of an active control for landing robot is shown in Figure 5. The desired angle θ_d of the shin(or thigh) and the desired angular velocity $\dot{\theta}_d$ of the shin(or thigh) was set at 87[deg] and zero, respectively.

5.2.3 Experimental method

The motor is controlled using the conditions gotten in the experiment. Then both the impact forces when the robot lands on the ground and the positions of the moving upper body are measured, and the control gains so that the motor can reproduce the effect of torsion spring are examined.

5.2.4 Experimental results

The experiment has been being conducted currently.

6 CONCLUSION

The way to reduce the impact when the robot lands on the ground had been studied. The summaries of the results are:

(1) It was hypothesized that a human may reduce the impact by motion control of his gravity center, for example, to lengthen the period of time in landing motion.

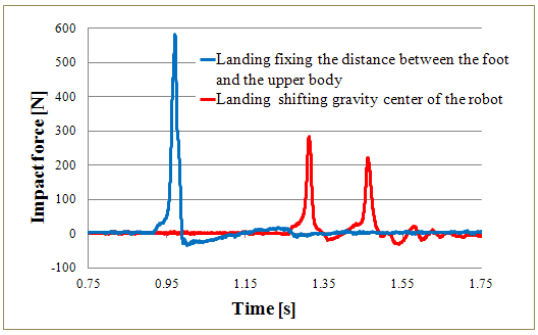

Fig. 10. Impact forces to each condition

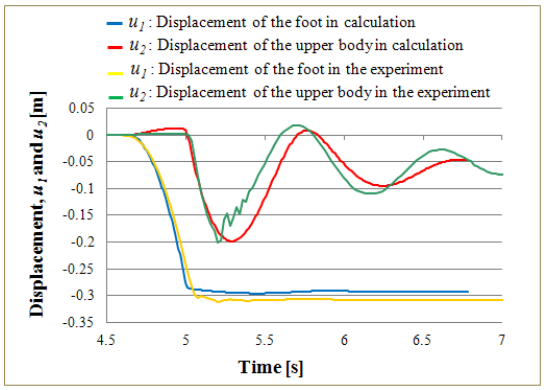

Fig. 11. Comparison of u_1 and u_2 between calculation and experimental result in the passive landing

Fig. 12. The landing robot installed the motor

(2) The analysis model of the landing robot was designed and the control gains k_p and k_d were found in the computational calculation.

(3) The landing robot was designed and developed considering the calculated results.

(4) The experiment of the landing robot with passive landing was conducted. Then the effect of shifting gravity center of the robot in landing motion was confirmed.

The experiment of the landing robot with active landing has been being conducted. For the future, it will be proved that the impact when the robot lands on the ground is reduced by motion control of the robot through the experimental results.

REFERENCES

[1] Tazaki T, Tomita M, Natori T, Shibata M(2002)： Landing impact force reduction on redundant leg biped robot by center of gravity control, vol. IIC-02, no. 15, pp. 1-6

© ISAROB 2013

The Eighteenth International Symposium on Artificial Life and Robotics 2013 (AROB 18th '13),
Daejeon Convention Center, Daejeon, Korea, January 30-February 1, 2013

Cell-production Parts Layout by Virtual Factory System using Reinforcement Learning and MTM

Hidehiko YAMAMOTO [1], Tsuyoshi SUGIMOTO [2], Takayoshi YAMADA [3] ,and Masahiro NAKAMURA [4]

[1, 3] *Department of Human and Information Systems, Gifu University, Japan*
[2] *Graduate School of Engineering, Gifu University, Japan,*
[4]*Lexer Research Inc., Japan*

[1]*yam-h@gifu-u.ac.jp,*
[2]*q3128013@edu.gifu-u.ac.jp*
[3]*yamat@gifu-u.ac.jp*

Abstract: For a cell production system to use a part rack for production environment, the quality of efficiency of the production time varies according to the part placement of the part rack. To solve this problem , we developed Virtual Assembly Cell-production System (VACS) which evaluates the movement distance of operators and decides part placement. In this study, we suggest a new VACS which evaluates not only movement distance of the operators but also up-and-down motion to get parts on the rack. In this VACS, by part placement decision, I adopt reinforcement learning and adopt the MTM as a work evaluation of the up-and-down motion of the rack in this reinforcement learning .

Keywords: Cell-Production , Virtual Factory, Reinforcement Learning, Method-Time Measurement

1 INTRODUCTION

The parts picking up operation which uses a rack in a cell production system has the problem with different production efficiency by the part locations of the rack. To solve this problem, we developed Virtual Assembly Cell-production System(VACS) which optimizes part placement, and visualizes the work process to an operator. [1]

VACS is the system which integrates a virtual production system with a part placement decision system. In the part placement decision system, we decide the most suitable combination of rack and parts. In the virtual production system , we make a shop floor of the cell production by 3DCG, and we visualize the installation process of the production parts based on the combination of the most suitable rack - parts which were decided by a part placement decision system. Thus, we realize the visualized work production, but, VACS decided part placement is based on movement distance. We should add the degree of difficulty of the movement of the operator to evaluate. Therefore, this paper proposes new VACS with reinforcement learning. And we apply this VACS to the assembly cell product line of the PC and inspect the effectiveness.

2 VACS

2.1 VACS

VACS consists of two systems of a part placement decision system and the virtual production system as shown in Fig.1. First, VACS makes the shop floor by the reinforcement learning in a virtual production system. Next, VACS decides the most suitable placement of a part and the rack in a part placement decision system, Finally VACS makes a virtual shop floor by acquiring the most suitable placement by a virtual production system again.

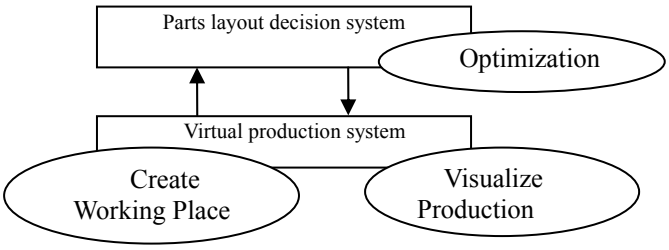

Fig.1 VACS

2.2 Part placement decision system

The part placement decision system uses reinforcement learning based on the workshop which is received from virtual production system, and decides part placement of the cell production. The decision corresponds to the movement distance of the operator and the evaluation of the degree of difficulty of the up and down movement.

In this study, we use Profit Sharing as reinforcement learning, In order to update the value of Profit Sharing, the walk movement that an operator moves between racks, and the work degree of difficulty of the up and down movement when an operator takes a part are

© ISAROB 2013

converted to time value by MTM, and VACS uses this time. We call this time an operating time. The time is decided by conditions such as the weight and height and the part of the operator.

The part placement decision system consists of two modules, namely, the condition making module and the learning module. The condition making module performs reading with various information files, and compiles the data to enable it to learn in a learning module. The learning module performs the pre-decided number of learning times and decides the most suitable part placement by Profit Sharing.

2.3 Condition making module

The condition making module sets a production condition and a learning initial condition of Profit Sharing through the following steps.

Step3-1: Reading of the configuration file

By using the initial conditions, the conditions about production are decided. Reading setting information and decide a condition about the production. The initial conditions are as follows.

Width of the workshop
Depth of the workshop
The size of cart and rack
The number of the steps of the rack
Highest step height of the rack
The lowest step height of the rack
The learning times number
Learning rate
Height of the operator

Step3-2: Read the parts information of the part.

Parts information necessary for product is acquired. The part information to read in this STEP are as follows.

Part name
Size of the part
Ease of grasping the part
Weight of the part

The size of the part data gives 0 or 1, The part which can be held with one hand is 0.The part which is held with both hands is 1.Ease of grasping the part is given as 1～3,which are used as analysis of the up and down movement in movement analysis. As the numbers increase, the degree of difficulty of the grasp rises, and operating times increase. The weight is in kg unit and is used as the analysis of the up-and-down motion.

Step3-3: Setting of the condition of the workshop

The rectangular of the depth and the width that are read in STEP3-1 becomes rectangular. After reading the workshop information, the size of rack parts, carts, and coordinates are set. Fig.2. shows the example of the workshop using this information.

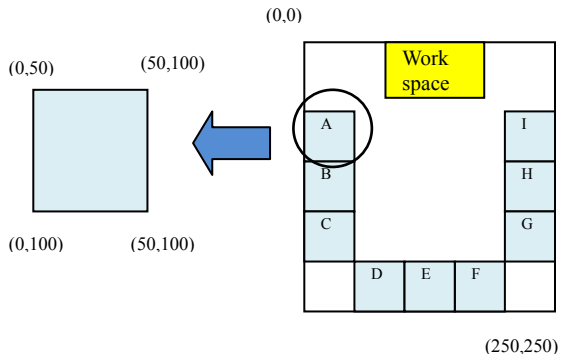

Fig.2 coordinate data

Step3-4: Read order data.

The order data describes the kind of products, outputs, necessary parts information, and the number of the parts. We show an example of order data in Table.1. Table.1 indicates the kind of PC to produce, needed parts and, number of products. For example, in PC 1, one case,one power supply , one motherboard, one unit of CPU,and two memory. Furthermore, a person of order wants to produce PC 1 20.

Table.1 example of order data

Product name	PC1	PC2	
Case	1	1	
Power	1	1	…
Mother board	1	1	
CPU	1	1	
Memory	2	4	
⋮			
Number of products	20	17	

Step3-5: Give the pair of all available placement possibility place - parts an initial value.

This step gives all placement places and pair of the part initial values. The values are the standards which judge the superiority of the state that the part is put is in the part placement. The values are used in later roulette choice.

First, make a table of the values. In the part placement place, the number of L1 - Ln, parts is referred to as part placement possibility place m point, part n unit X1 - Xm, and the table of the value expresses with value ω(Li,Xj). ω (Li,Xj) expresses it how superior it is to place part Xj in the part placement possibility place Li. The table of values of (a number of the parts) × (part placement

possibility place) is shown in Table.2.

Table.2 Values and racks relations

	A	B	C	…
1	ω (A,1)	ω (B,1)	ω (C,1)	…
2	ω (A,2)	ω (B,2)	ω (C,2)	…
⋮	…	…	…	…

A, B… Rack names 1, 2… parts

Step3-6: Calculate the distance of work table and the distance between two points between each placement place.

The step calculates the distance between each necessary part placement for analysis of the walk movement. The distance between two points are caluclated using a Pythagorean formula. For example, (X_A, Y_A) is the coordinate of place A, and B (X_B, Y_B) is the coordinate of place B. The distance between two points is calculated with the following formula.

$$z = \sqrt{(x_B - x_A)^2 + (y_B - y_A)^2} \tag{1}$$

The distance between the two points for all part placement possibility places can be calculated using the above method. In the case where the part placement possibility place to Li - Ln, the distance between pLi-Lj (0i,j <= n) is expressed as D(Li,Lj). The distance between each part placement possibility place that is calculated above is used in the analysis of the walk movement.

2.4 Learning module

The learning module is carried by using Profit Sharing in the following Step.

Step4-1: Make the initial value of the standard value.

For an acquired operating time, the initial value of the standard value to determine whether VACS gives a reward or not is set. As the initial value, the average time value acquired after random parts arrangements is adopted.

Step4-2: Performing part placement based on value (using roulette choice).

The step puts a part using the roulette selection based on the following equation.

$$p(a \mid s) = \frac{\omega(s,a)}{\sum \omega(s,b)} \tag{2}$$

S: placement place a: The part which is chosen
b: The number of total parts

The roulette choice is a method to choose an action according to the ratio of the value. By this method, we calculate the chosen probability of the part in the part placement possibility place and decide the placement sequentially at each placement place.

Step4-3: Using the MTM method and analyzing it.

The step analyzes the picking up operations by the MTM method. The step divides the operations into two operations top and bottom movement and walk movement to move between racks. Fig.3 shows that an operator moves to the front of the rack for the up and down operations. STEP4-3, calculates each up and down time which are needed for produce all products.

Step4-4:Compare the working hour with the conventional smallest working hour.

This step compares the working time taken with the smallest working time of the work simulation. Replace the smallest working time and memorize part placement as the most suitable part placement.

Step4-5: Update the value of each placement.

The step, updates the value of each placement possibility place , by using the following equation.

$$\omega(s,a) \leftarrow \omega(s,a) + \gamma(T - t + 1)r \tag{3}$$

s: placement place a:parts γ : discount rate
r: Reward T: The number of the total parts
t: Part place decision order

Step4-6: Repeat Step4-2 - Step4-5.

As shown in Fig.3 , Step4-2 ～ Step4-5 are repeated. The part placement whose working time is the smallest become the solutions.

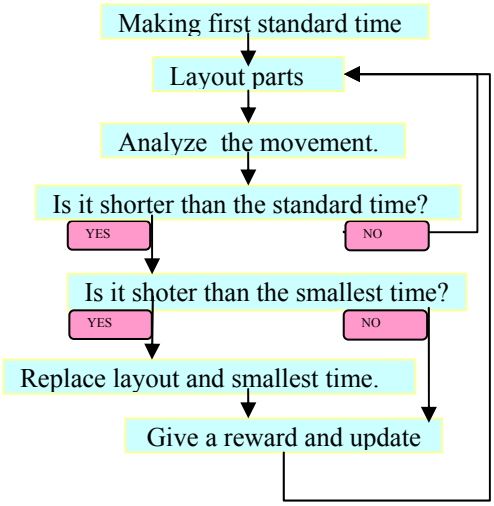

Fig.3 flow of Optimization system

2.5 Virtual production system

The virtual production system makes the shop floor and realizes the visualization of the working process by 3DCG. The virtual production system makes the shop floor including racks and the working table top to use in a part placement decision system. Based on placement decided by a part placement decision system, part on the rack of the shop floor is put. Finally, we input a work process and express a work process with an animation.

3 Application example of VACS

We performed the most suitable placement of the PC part and in the workshop such as Fig.4 using VACS. The simulation performs unevenness by learning ten times to consider it and does the thing which we bought with a little time with the most suitable placement. In addition, we tried it before learning at random to confirm the effect by the learning. As a result, the shortest result, as in Table.3 is adopted as the most suitable placement because there were the fewest the fifth learning results. It was fewer than 141,804, and an effective result was provided. In addition a method of VACS using the reinforcement learning was able to confirm its effectiveness, VACS at minimum time when a value located it before 112,912, learning at random in time for part placement decision using VACS. In addition, we set up a part in a virtual production system and made a virtual shop floor such as in Fig.5 based on the most suitable placement and realized to see the work.

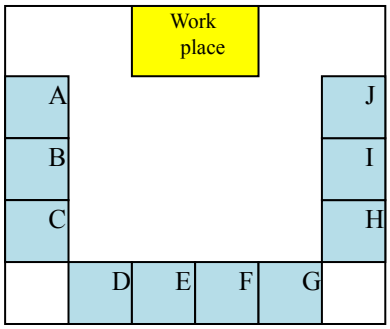

Fig.4 Rack locations

Table .3 Simulation results

Before learning average	181753
Before learning minimum	141804

	1st	2nd	3rd	4th	5th
First standard time	181831	183021	182568	181856	182311
Last standard time	124967	119213	121258	121517	117508
Result time	113227	114726	115559	114917	112912
Update number	38955	52072	42708	33335	60450

	6th	7th	8th	9th	10th
First standard time	182319	182210	182480	181168	181633
Last standard time	119620	119292	117863	117554	118919
Result time	114613	114062	114143	115401	113203
Update number	23407	20029	105376	100089	70012

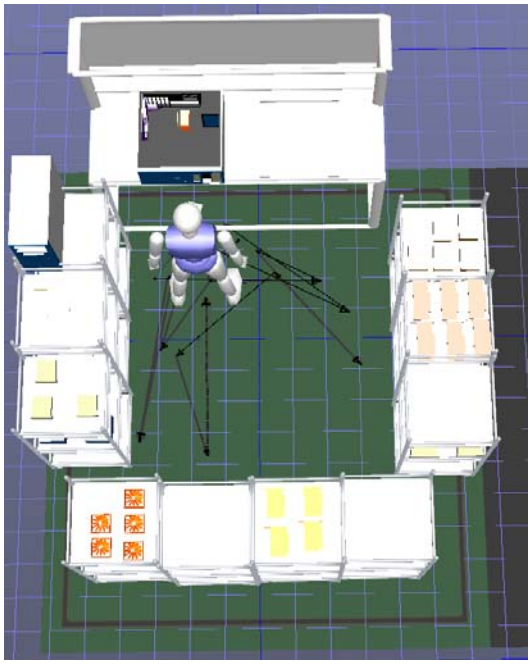

Fig.5 Result of VACS

4 CONCLUSION

VACS, which we suggested reduced the level in the time that the part acquisition took in comparison with random placement from a result for simulation, provided good results, It was shown to be effective for optimization of the part placement of the cell production. In addition, we were able to incorporate the evaluation of the movement analysis using the MTM method in learning by Profit Sharing.

We were able to do part placement of part placement layout decision systems and confirming parts layout by virtual production system by visualizing. In this way, we were able to build VACS where a part placement layout decision system and a virtual production system are linked to each other.

REFERENCES

[1]Hidehiko YAMAMOTO, Takayoshi YAMADA and Masahiro NAKAMURA, Parts Layout Decision for Assembly Cell-Production by GA and Virtual Factory System, Japan Society of Mechanical Engineers , Vol.76, No.764, 994-999(2010-4).

© ISAROB 2013

The Eighteenth International Symposium on Artificial Life and Robotics 2013 (AROB 18th '13),
Daejeon Convention Center, Daejeon, Korea, January 30-February 1, 2013

Gait motion of a six legged real robot employing associatron

Masashi Sakai[1], Masato Hashimoto[1], Tomo Ishikawa[1],
Koji Makino[1], Jin-Hua She[1], Yasuhiro Ohyama[1]

[1] Tokyo University of Technology, Japan
(Tel: 81-42-637-2111 ex.2823, Fax: 81-42-637-2112)

[1] g21110260e@st.teu.ac.jp

Abstract: In this study, we have proposed gait motion algorithm of a six legged robot in order to walk an unpredictable irregular field. The algorithm is adapted to the Associatron. The algorithm has a property that enables the robot to recall an entire pattern from partial information, sequentially. Therefore, the robot can walk in unknown field. First, we verified the proposed algorithm by simulations using ODE (Open Dynamics Engine). It is clear that memorized pattern is recalled from unknown pattern. Secondly, an experiment is performed using the developed real robot. The experiment result proved that the robot is able to select suitable gait motion at the existence of an obstacle.

Keywords: gait motion, real legged robot, Associatron.

1 INTRODUCTION

Legged robots are focused on, because they are able to move in irregular or unpredicted field flexibly [1]. However, the control of the robot is difficult. A lot of researchers study various methods that enable legged robots to walk unpredictable irregular field such as the stricken area. For example, there are mimics insect[2], using neuron[3], subsystems[4], and CPG which is modeled in non-linear trembler system[5]. The other method to walk of the unpredictable irregular field is known as a tire-type, a crawler-type and etc. The one of the advantage of the legged robot is that it can move a center of gravity, and that it can stabilize posture [6].

We have proposed gait motion algorithm of a six legged robot using the property of the Associatron[7][8]. One of the properties of the Associatron is that it can recall an entire pattern from partial information. A mechanism of the memory of the robot is similar to one of an animal. We focus on the Associatron that is associative memory model. The aim of this paper is to implement the gait motion by using the Associatron to the robot. Moreover, the proposed gait motion is applied to a real robot. The validity and possibility of the algorithm are confirmed by simulations and an experiment.

2 SYSTEM

Assume that the robot has six legs, six touch sensors and a position sensing detector (PSD). We deal with static gait motion. The robot is shown in Fig. 1. The size and weight of the robot are 359 x 233 x 313 mm and 2.011 kg (include batteries), respectively.. The robot is similar to an insect. To simplify the discussion, the each leg unit has two actuators. They enable the each leg swing to roll (up-down) and yaw (front-back) direction, respectively. The each touch sensor is installed on each leg in order to detect ground. The PSD sensor is put on the front of the robot to measure the distance between own position and an obstacle. The model numbers of the PSD and the actuator are GPY0A21YK and KRS-784 ICS, respectively.

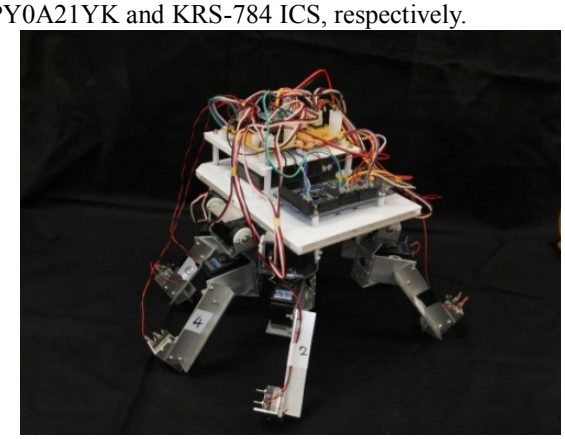

Fig. 1 A six legged robot

3 ASSOCIATIVE MEMORY

First, abstract of the Associatron is introduced. Secondly, proposed algorithm is described. Finally, the motion that we expect is shown.

3.1 Associatron

We adopt the Associatron[9] to the robot. The Associatron is a model for associative memory with a neural network structure. Then, it is a kind of memory algorithm that is similar to animal's brain. The property

© ISAROB 2013

of the Associatron that we utilized is that it can recall an entire pattern from partial information, especially.

Moreover, the orthogonal method of the Associatron [10] is adopted in order to prevent interference.

3.2 Algorithm

We describe the method that the Associatron is applies to gait algorithm. It is possible to recall next angles of all leg from the current angles, touch sensor information and measured distance. The reason is that the Associatron enables to recall the entire pattern from partial pattern.

In order to employ it to the robot, the memorized pattern is divided into present state and next state. The divided pattern is shown in Fig. 2. The memory size is 24 x 24. Gray region means current information (leg's angle, touch sensor state, and distance from obstacle). White one is next angles of the legs. We investigate whether the robot can recall the memorize pattern from unknown or the partial pattern in Sec 4.1.

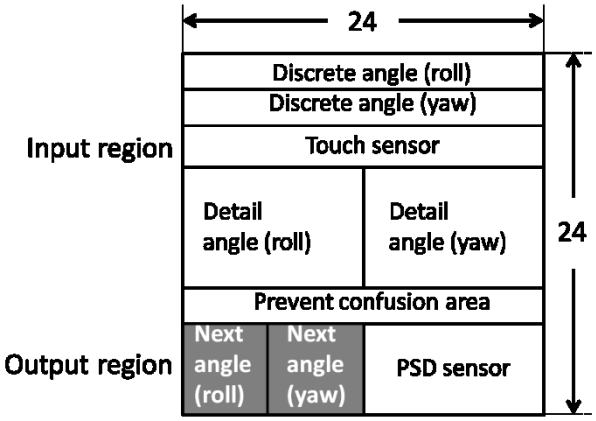

Fig. 2 Structure of the memorized pattern

3.3. Multiple gait motions

The robot must learn multiple gait motion corresponding to various irregular fields. And, the robot has to select the appropriate pattern of the movement, automatically. We consider the case that the Associatron memorized two type motions. The patterns are shown in Fig. 3. One is forward gait motion, when there is no obstacle in front of the robot (black blocks). First, the robot recall the F1.Secondly, it recall F2. Next, F3 and F4 are recalled in sequence. And, the F1 is recalled again. The other is turning gait motion, when there is obstacle (white blocks). Each pattern is repeated, if the value of the PSD sensor that is mounted in the front of the robot is not changed. It is expected that the movement of the robot change another gait motion by existence of obstacle.

Suppose that the robot faces the obstacle, after walking in no obstacle area. In this time, the pattern becomes incomplete. The region of the PSD sensor becomes the values of the obstacles, however the other region remains the pattern of moving forward. Then, we predict following steps:

1.Iincomplete information is recalled (F'-3)

2. Complete information is recalled (T1)

The selecting motion is confirmed by simulations (Sec. 4), and by an experiment (Sec 5).

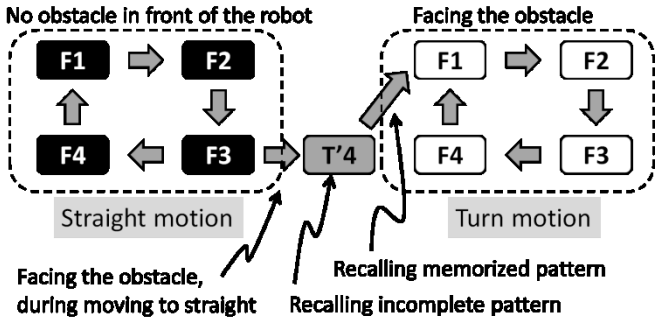

Fig. 3 Selection of the pattern

4 SIMULATION

We verify the proposed algorithm by ODE (Open Dynamics Engine) simulator. ODE is an open source physical simulator[11]. The parameters (weight, size, torque of the actuator and characteristic of the PSD) are same as the real robot.

4.1 Recall the memorized pattern

We confirm whether the robot can recall the memorized pattern from unknown ones. The robot memorizes the eight patterns that are shown in Fig. 3. In the simulations, one hundred different initial poses of the robot is tried. Two initial poses of the robot are illustrated in Fig. 4. Fig. 5 shows the results. Horizontal axis is step. "Step" depicts the number of the recall. Vertical axis means the similarity of the memorized pattern. "100 %" means that the recalled pattern agrees with memorized pattern. The robot can recall the memorized pattern within 10 steps from all performed cases.

It is confirmed that memorized pattern is recalled from unknown pattern.

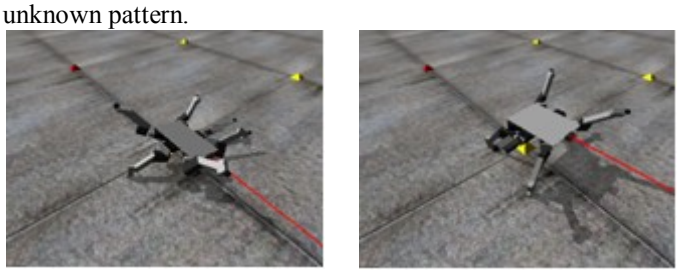

Fig. 4 Initial figures

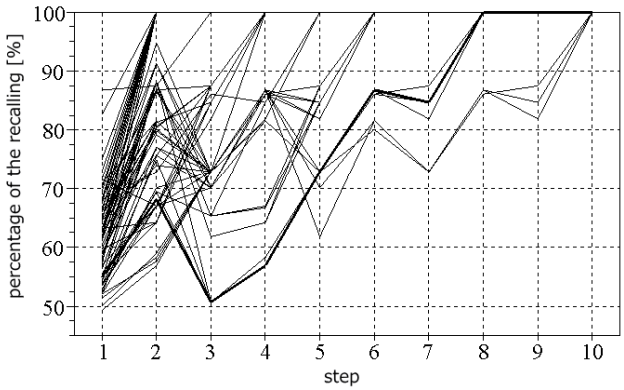

Fig. 5 Recalling the memorized pattern from known patterns

4.2 Multiple gait motion

An obstacle is set in the field. We investigate that the robot can select the motion, corresponding to the obstacles. The initial position and direction are (0,0) and minus direction. The size of the obstacle and the position of the center is 0.95 x 0.22 m and (-1.1, 0.2). The result is shown in Fig. 6. The trajectory of the robot is black line and gray box means the obstacle. Cross symbol shows the position that turning gait motion is selected. The robot moves to straight, during it does not recognize the obstacle. Facing the obstacle, it selects the turning gait motion.

As a consequence, it is clear that the robot is able to autonomously switch to gait motion by existence of an obstacle. This result is called as "basic motion", in order to compare to the other cases.

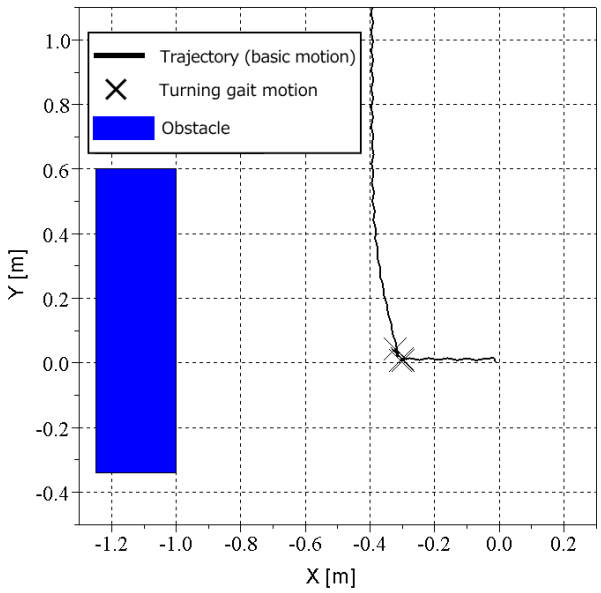

Fig. 6 Trajectory of the robot (basic motion)

4.3 Error of the touch sensor

In the real robot, errors of touch sensor that is set at each leg often occur. The robot that implements the Associatron can walk though the cases occur.

First, the values of some touch sensors are reversed at every step. Fig. 7 shows the trajectories of the robot, in the case that the number of the reversed value of the sensor is changed. When the number of it increases, the movement of the robot is more different from basic motion.

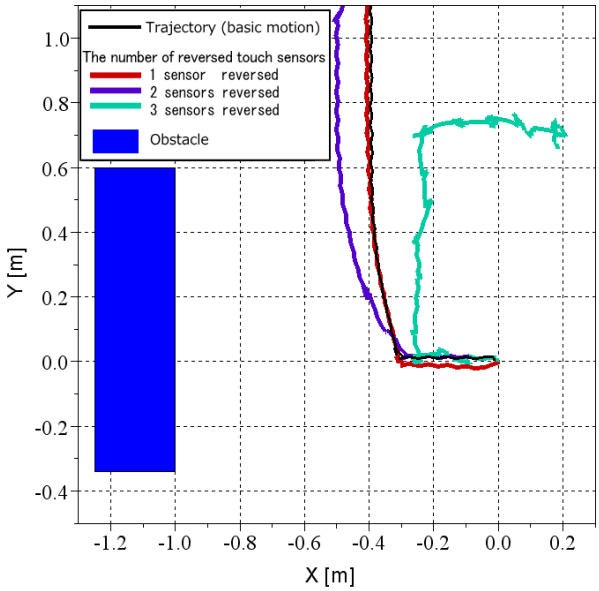

Fig. 7 Influence of reversing some touch sensors

Secondly, the interval that the error occurs is changed (every, 2, 3, 5, 10, and 20 step, respectively). The number of it is two in all simulations. When the interval is longer, the trajectory is more similar to basic motion.

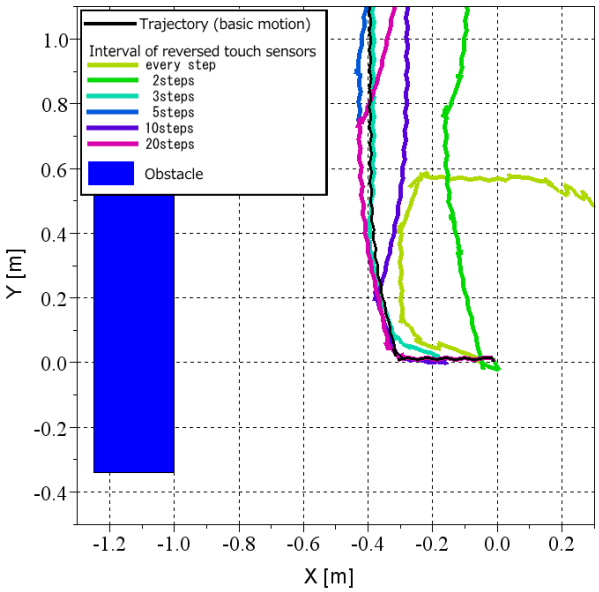

Fig. 8 Influence of the interval

© ISAROB 2013

5 EXPERIMENT

We investigate the validity of the algorithm by an experiment.

5.1 Structure of the experiment

In the system of the experiment, the Arduino Mega is adopted in order to control the robot (controlling of RC servo motor, and sensing touch sensor and PSD). Calculation of the Associatron is executed by the PC. The connection with the Arduino and PC is used by XBee that is a radio communication unit.

5.2 Experiment using a real robot

The experiment is performed at same setting of the simulation of basic motion. The snapshots are illustrated in Fig. 9. The trajectories are shown Fig. 10. Red line is experimental result. It is clear that the trajectory is similar to trajectory of the simulation of the basic motion. As a result, we confirm that the Associatron can be implemented with a real robot.

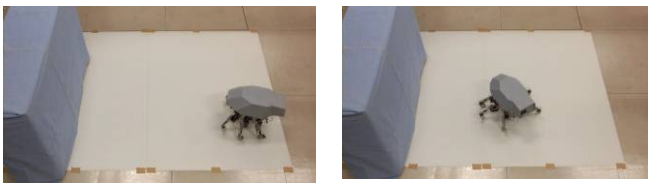

Fig. 9 Snapshots of the robot during the walking

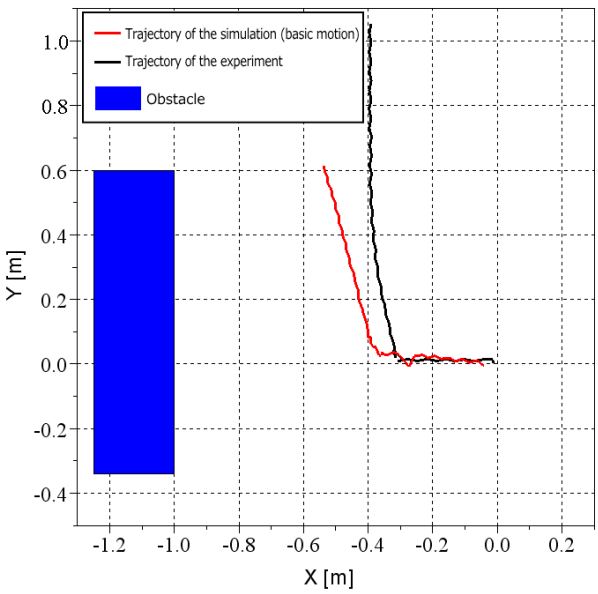

Fig. 10 Trajectories of a simulation and an experiment

6 CONCLUSION

In this paper, we proposed gait algorithm of a six legged robot using the Associatron. Simulations and an experiment of the obstacle avoidance were performed. As a result, the robot was able to select suitable gait motion, automatically. We confirmed that the algorithm was effective to gait motion.

In the future work, we will have the robot learn the motion automatically.

REFERENCES

[1] Maki K. Habib (2007) Bioinspiration and Robotics Walking and Climbing Robots.

[2] Huang Q, Nonami K (2003), Humanitarian Mine Detecting Six-Legged Walking Robot and Hybrid Neuro Walking Control with Position/Force Control, Special Issue on Computational Intelligence in Mechatronic Systems, Mechatronics, Vol.13, No.8-9, pp.773-790

[3] Umar Asif, Javaid Iqbal1 (2011), An Approach to Stable Walking over Uneven Terrain Using a Reflex-Based Adaptive Gait, Journal of Control Science and Engineering, Vol. 2011, pp. 1-12

[4] Hirose, S, Arikawa, K (2000), Coupled and Decoupled Actuation of Robotic Mechanisms, Proc. International Conference on Advanced Robots ICRA'2000, San Francisco, pp.33-39.

[5] Qingjiu Huang, Kenzo Nonami (2002) Neuro-Based Position and Force Hybrid Control of Six-Legged Walking Robot, The Japan Society of Mechanical Engineers pp160-167

[6] Kimura H, Fukuoka Y, Hada Y, Takase K (2002). Three-dimensional adaptive dynamic walking of a quadruped - rolling motion feedback to CPGs controlling pitching motion, IEEE International Conference on Robotics and Automation, ICRA 2002., pp. 2228–2233

[7] Sakai M, Ishikawa T, Hashimoto M, Makino K, She J, Ohyama Y, (2012), Study on Autonomous Gait Motion Using Associative Memory (in Japanese), The 13th SICE System Integration Division Annual Conference (SI 2012), pp. 2758-2759

[8] Sakai M, Sato S, Hirose Y, Makino M, She J, Ohyama Y, (2012), Study on Gait Motion of Six-Legged Robot Using Associative Memory (in Japanese), Robotics and Mechatronics Conference 2012 (ROBOMEC2012) pp. 2A2-V02(1)- 2A2-V02(2)

[9] Nakano K, (1972), Associatron-A Model of Associative Memory, IEEE Trans. Syst. Man & Cyb., SMC-2, No.3, pp. 380 - 388

[10] Iwasaki M, Hashiyama T, Okuma S (2000), Self-Organizing Feature Extraction Using Associative Memory, IEEJ Transactions on Electronics, Information and Systems, Vol. 120, No. 10, pp. 1467-1474

© ISAROB 2013

The Eighteenth International Symposium on Artificial Life and Robotics 2013 (AROB 18th '13),
Daejeon Convention Center, Daejeon, Korea, January 30-February 1, 2013

Reinforcement learning for dynamic environment: a classification of dynamic environments and a detection method of environmental changes

Masato Nagayoshi[1], Hajime Murao[2], and Hisashi Tamaki[3]

[1] Niigata College of Nursing, 240, Shinnan, Joetsu 943-0147, Japan
(nagayosi@niigata-cn.ac.jp)
[2] Faculty of Cross-Cultural Studies, Kobe Univ. 1-2-1, Tsurukabuto, Nada-ku, Kobe 657-8501, Japan
(murao@i.cla.kobe-u.ac.jp)
[3] Graduate School of Engineering, Kobe University, Rokko-dai, Nada-ku, Kobe 657-8501, Japan
(tamaki@al.cs.kobe-u.ac.jp)

Abstract: Engineers and researchers are paying more attention to reinforcement learning (RL) as a key technique for realizing computational intelligence such as adaptive and autonomous decentralized systems. In general, it is not easy to put RL into practical use. In prior research our approach mainly dealt with the problem of designing state and action spaces and we have proposed an adaptive co-construction method of state and action spaces. However, it is more difficult to design state and action spaces in dynamic environments than in static ones. Therefore, it is even more effective to use an adaptive co-construction method of state and action spaces in dynamic environments. In this paper, our approach mainly deals with a problem of adaptation in dynamic environments. First, we classify tasks of dynamic environments and propose a detection method of environmental changes to adapt to dynamic environments. Next, we conducted computational experiments using a so-called "path planning problem" with a slowly changing environment where the aging of the system is assumed. The performances of a conventional RL method and the proposed detection method were confirmed.

Keywords: reinforcement learning, dynamic environment, slowly changing environment, detection of environmental changes, entropy

1 INTRODUCTION

In recent years, artificial systems have become more complicated and large-scaled. The conventional way, in which systems are controlled in a top-down manner mainly by humans, is facing up to the difficulties of not only optimality but also adaptability and flexibility. One of the solutions to this issue is to develop an autonomously adaptive system. Engineers and researchers are paying more attention to Reinforcement Learning(RL)[1] as a key technique of realizing autonomous systems. In general, however, it is not easy to put RL into practical use. Such issues as satisfying the requirement of learning speed, resolving the perceptual aliasing problem, designing reasonable state and action spaces of an agent and adapting dynamic environments must be resolved. In prior research, our approach mainly dealt with the problem of designing state and action spaces and we have proposed a co-construction method of state and action spaces[2]. However, it is more difficult to design state and action spaces in dynamic environments than in static ones. Thus, it may be even more effective to use an adaptive co-construction method of state and action spaces in dynamic environments.

In this paper, our approach deals with problems of adaptation in dynamic environments. Previously, many methods for dynamic environments have been proposed. However the researchers have only referred to the dynamic environment, without focusing on the specific problems that are inherent in a dynamic environment. We make a classification of dynamic environments and propose a detection method of environmental changes to adapt a dynamic environment. In addition, computational experiments are conducted by using a so-called "path planning problem" with a slowly changing environment where the aging of the system is assumed. The performances of a conventional RL method and the proposed detection method are confirmed.

2 Q-LEARNING

Q-learning works by calculating the quality of a state-action combination, namely the Q-value, that gives the expected utility of performing a given action in a given state. By performing an action $a \in \mathcal{A}_{\mathrm{Q}}$, where $\mathcal{A}_{\mathrm{Q}} \subset \mathcal{A}$ is the set of available actions in Q-learning and $\mathcal{A}$ is the action space of the agent. The agent can move from state to state. Each state provides the agent with a reward r. The goal of the agent is to maximize its total reward.

The Q-value is updated according to the following for-

© ISAROB 2013

mula, when the agent is provided with the reward:

$$Q(s(t\text{-}1), a(t\text{-}1)) \leftarrow Q(s(t\text{-}1), a(t\text{-}1)) + \alpha_{\mathrm{Q}}\{r(t\text{-}1) + \gamma \max_{b \in \boldsymbol{\mathcal{A}}_{\mathrm{Q}}} Q(s(t), b) - Q(s(t\text{-}1), a(t\text{-}1))\} \quad (1)$$

where $Q(s(t\text{-}1), a(t\text{-}1))$ is the Q-value for the state and the action at the time step t-1, $\alpha_{\mathrm{Q}} \in [0, 1]$ is the learning rate of Q-learning, $\gamma \in [0, 1]$ is the discount factor.

The agent selects an action according to the stochastic policy $\pi(a|s)$, which is based on the Q-value. $\pi(a|s)$ specifies the probabilities of taking each action a in each state s. Boltzmann selection, which is one of the typical action selection methods, is used in this research. Therefore, the policy $\pi(a|s)$ is calculated as

$$\pi(a|s) = \frac{\exp(Q(s, a)/\tau)}{\sum_{b \in \boldsymbol{\mathcal{A}}} \exp(Q(s, b)/\tau)} \quad (2)$$

where τ is a positive parameter labeled temperature.

3 DYNAMIC ENVIRONMENTS

Dynamic environments are time-varying environments, i.e. when the state transition probability $T(s(t), a(t), s(t+1))$, which is the probability of transition from $s(t)$ to $s(t+1)$ under $a(t)$, changes, or the return function $R(s, a)$, which is the reward at s under a, changes, an "environmental change" has occurred and the environment is a dynamic environment. Hereafter on the premise of time-variance, the state transition probability and the reward function including time t are shown $T_t(s(t), a(t), s(t+1))$ and $R_t(s, a)$ respectively.

The learning becomes difficult when environmental changes occur as in the following formula:

$$\arg\max_{a \in \boldsymbol{\mathcal{A}}} R_t(s(t), a) \neq \arg\max_{a \in \boldsymbol{\mathcal{A}}} R_{t+1}(s(t), a) \quad (3)$$

where the best action changes over time in the states where the agent transits. In particular, in the course of making the action selection probability of the best action larger, environmental changes occur. After such an occurrence, the agent first needs to make the action selection probability of the action smaller, for example if the learning module is Q-learning, in the course of making the entropy of action selection probability $H(s)$:

$$H(s) = -(1/\log|\boldsymbol{\mathcal{A}}_{\mathrm{Q}}|) \sum_{a \in \boldsymbol{\mathcal{A}}_{\mathrm{Q}}} p(a|s) \log p(a|s), \quad (4)$$

the agent needs a process for finding the best action again. This process is the reason for learning difficulties in dynamic environments.

4 CLASSIFICATION OF DYNAMIC ENVIRONMENTS

Until now, Simada et.al.[3] divide 'share states' into 2 types: if the following equation is satisfied, then the state is the 'share sate' of type1, and if not, the state is the 'share state' of type2.

$$\arg\max_{a \in \boldsymbol{\mathcal{A}}} R_i(s, a) = \arg\max_{a \in \boldsymbol{\mathcal{A}}} R_j(s, a) \quad (5)$$

Also, they indicate that determining adaptability to dynamic environments is dependent on the abilities of the "detection of the states of type 1 and type 2" and "reusing and re-studying of learning results".

In this section, previous works are organized by classifying this tasks of dynamic environments more finely.

For the sake of ease, we limit to episodic tasks such as acquiring a series of actions from start states to goal states. In our classification of dynamic environments we use the Boltzmann selection method(Eq.(2)), that is, the agent selects an action with a larger value based on a higher probability.

Here, we assume that each increasing value of the entropy of the action selection probability is given and is caused by environmental changes, as seen in $\dot{H}_{\mathrm{C}}(T, M, t_{\mathrm{E}})$ where t_{E} is the episode, M is the method used, and T is the task.

1. The a) presence or b) absence of the influence of environmental changes:

   If the following formula is satisfied, then the agent can adapt to environmental changes by the learning performance of the method M even if environmental changes occurred.

   $$\forall t_{\mathrm{E}}(\dot{H}_{\mathrm{C}}(T, M, t_{\mathrm{E}}) \leq 0) \quad (6)$$

2. The process of environmental changes:

   In almost all previous works, it is assumed that the cases of
   1) $\exists_1 t_{\mathrm{E}}(\dot{H}_{\mathrm{C}}(T, M, t_{\mathrm{E}}) > 0)$ and $\dot{H}_{\mathrm{C}}(T, M, t_{\mathrm{E}})$ is a repetition of a shape similar to an impulse function. In particular, those tasks in which the characteristic changes momentarily or stages are switched are assumed. On the other hand, 2) $\dot{H}_{\mathrm{C}}(T, M, t_{\mathrm{E}})$ is a continuously small positive value, if the aging of the system or a change of human characteristics is assumed.

3. The timing of the appearance of environmental changes in relation to learning progress:

   It is known that the entropy of the action selection probability approaches 0 in tasks without environmental changes[4]. Here, if the task has no environmental changes, it could be divided into 3 phases based on the entropy of the action selection probability: a prophase $\mathbf{t}_{\mathrm{EB}}$, a metaphase $\mathbf{t}_{\mathrm{EM}}$, and a anaphase of learning $\mathbf{t}_{\mathrm{EL}}$. The task can be classified according to when the appearance of environmental changes $t_{\mathrm{EC}} = \min\{t_{\mathrm{E}}|\dot{H}_{\mathrm{C}}(T, M, t_{\mathrm{E}}) > 0\}$ occurs: i)$\mathbf{t}_{\mathrm{EB}}$, ii)$\mathbf{t}_{\mathrm{EM}}$, or iii)$\mathbf{t}_{\mathrm{EL}}$. Normally, in the case of the task having

© ISAROB 2013

$t_{\mathrm{EC}} \in \mathbf{t}_{\mathrm{EB}}$, it is easy to adapt to environmental changes since the entropy of the action selection probability is large. In the case of the task having $t_{\mathrm{EC}} \in \mathbf{t}_{\mathrm{EL}}$, influences of environmental changes become large since the entropy is small.

Except in b) the absence of influences of environmental changes, it is necessary for researchers to take the remaining $2 \times 3 = 6$ types into consideration. In this paper, we focus on the above 6 types.

In viewing of previous works organized in consideration of the above classification of tasks of dynamic environments, Takahashi et.al.[5] deal with 3 types: i), ii), and iii) in the case of a)1) above by introducing an evaluation index of learning progress in a detection method of environmental changes. Other works deal with the types a)1)ii) and a)1)iii)[3] as above. Thus, it is necessary for researchers to consider tasks of dynamic environments regarding the types other than these above.

5 DETECTION METHOD OF ENVIRONMENTAL CHANGES

The entropy of the action selection probability $H(s)$, shown in Eq.4, becomes smaller in tasks without environmental changes. In contrast, when an environmental change occurs, the entropy becomes larger from the time of the occurrence. Hence, when the entropy $H(s)$ begins to increase, the agent is able to detect the environmental change.

However, Preliminary computational experiments indicate that the entropy of the action selection probability in the state s (Eq.4) shows a range of fluctuations even if in a static environment. In order to decrease false-detections of environmental changes by the influence of the fluctuations, the agent detects the time of the occurrence of the reversal of a downward trend using MACD (Moving Average Convergence / Divergence), which is one of the most popular tools in technical analysis trading. The entropy $H_{\mathrm{D}}^{+}(s)$, after updating the Q-value, is used to refine the detection only when the agent selects an action with the maximal Q-value, if the learning module is Q-learning. Then, a short-term ($n = \theta_{\mathrm{EMAS}}$) EMA (Exponential Moving Average) value and a long-term ($n = \theta_{\mathrm{EMAL}}$) EMA value of the entropy are calculated according to the following equation at a rate of once every θ_t update of $H_{\mathrm{D}}^{+}(s)$.

$$\mathrm{EMA}^{n}(s(t)) = (1-\alpha) \times \mathrm{EMA}_{\mathrm{old}}^{n}(s(t)) + \alpha \times H_{\mathrm{D}}^{+}(s(t)) \tag{7}$$

where $\mathrm{EMA}_{\mathrm{old}}^{n}(s(t))$ is the latest known value of EMA in $s(t)$, $\alpha = 2/(n+1)$ and n are constant numbers expressing the smoothing constant and the average amount of time respectively.

Table 1. Usual parameters of MACD

Parameter	Value	Parameter	Value
θ_{EMAS}	12	θ_{EMAL}	26
θ_{MACD}	9		

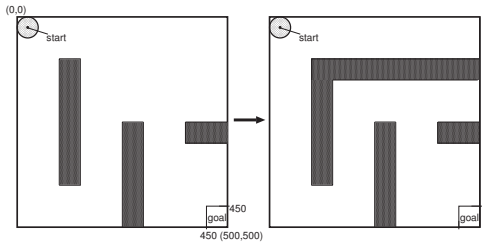

Fig. 1. Dynamic path planning problem.

A MACD (Moving Average Convergence / Divergence) value is calculated according to the following equation, after updating the short-term and the long-term EMA values.

$$\mathrm{MACD}(s) = \mathrm{EMA}^{\theta_{\mathrm{EMAS}}}(s) - \mathrm{EMA}^{\theta_{\mathrm{EMAL}}}(s) \tag{8}$$

In addition, a 'signal' value is a moving average for the latest series of θ_{MACD} values of $\mathrm{MACD}(s)$. In particular, when $\mathrm{MACD}(s)$ becomes larger than the signal value and $\mathrm{MACD}(s) < 0$ and the following formula is satisfied from the condition of $\mathrm{MACD}(s)$ being smaller than the signal value, the agent detects the environmental change.

$$\mathrm{MACD}(s) - \mathrm{MACD}_{\mathrm{old}}(s) > 0.01 \tag{9}$$

where, $\mathrm{MACD}_{\mathrm{old}}(s)$ is the latest known value of MACD(s). Here, the above formula has been added in order to detect environmental changes only when a rapidly increasing trend occurs.

Usual parameters of MACD shown in Table 1 to detect environmental changes are used in the following experiments.

When the environmental change is detected, all Q-values in the detected state are set to the average value of the Q-values in the detected state.

6 COMPUTATIONAL EXAMPLES

Q-learning (hereafter called "QL") and the proposed detection method (hereafter called "PD") are applied to a so-called "path planning problem" with a slowly changing environment where the aging of the system is assumed in a continuous state and action spaces, as shown in Fig. 1. Here, the agent has a circular shape (diameter 50 [mm]), and the continuous space is 500 [mm]×500 [mm] bounded by the external wall, with internal walls as shown in black. One of internal walls is slowly extended to the right from an episode

© ISAROB 2013

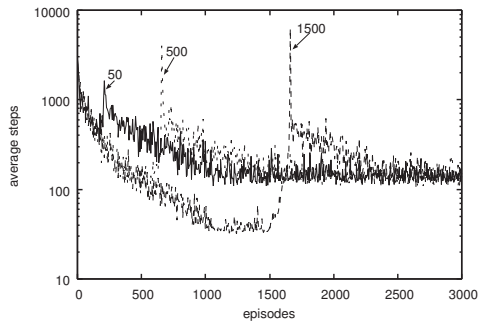

Fig. 2. Required steps of 3 occurrence times of the environmental change by Q-learning.

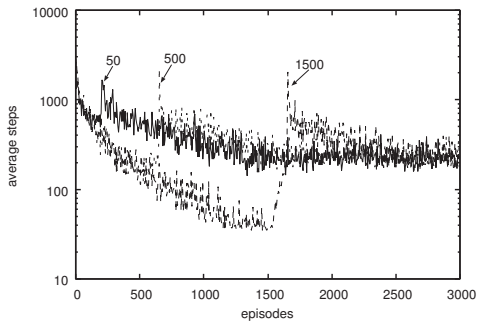

Fig. 3. Required steps of 3 occurrence times of the environmental change by the proposed method.

t_{ES} to an episode t_{EE} as shown in the continuous space pictured on the right of Fig. 1. The agent can observe the center position of itself $(x_{\mathrm{A}}, y_{\mathrm{A}})$ as the input, and decide the direction θ_{A} as the output. The agent moves 25 [mm] in a direction defined by θ_{A} to which gaussian noise has been added.

The positive reinforcement signal $r_t = 10$ (reward) is given to the agent only when the center of the agent arrives in the goal area, and the reinforcement signal is $r_t = 0$ at all other steps. The period from when the agent is located at the starting point to when the agent is given a reward, labeled as 1 episode, is repeated.

After dividing the state space evenly into 20×20 spaces, and the action space evenly into 8 spaces, QL and PD based on QL are compared with 3 occurrence times of the environmental change: $\mathbf{t}_{\mathrm{EB}} = \mathbf{50}$, $\mathbf{t}_{\mathrm{EM}} = \mathbf{500}$, and $\mathbf{t}_{\mathrm{EL}} = \mathbf{1500}$ [episode]. The internal wall is extended to $x = 500$ during 175 [episodes] from the occurrence of the environmental change.

Computer experiments have been carried out with the parameters of Q-learning: $\alpha_{\mathrm{Q}} = 0.1, \tau = 0.1$, and $\gamma = 0.9$. In addition, the rating number θ_t of the detection method is set at 5. All initial Q-values are set at 5.0 as the optimistic initial values[1].

The average number of steps required to accomplish the task was observed during learning over 20 simulations with QL and PD, as described in Fig. 2 and Fig. 3 respectively. The average number of detections was observed during learning over 20 simulations with PD, as described in Fig. 4.

It can be seen from Fig. 2 and Fig. 3 that, 1) when the environmental change occurs later, that is, as the learning progresses, the influence of the environmental change becomes larger, 2) PD has better performances than QL with regard to the influences of the environmental change.

It can be seen from Fig. 4 that, 3) PD has better performances to detect the environmental change as the learning progresses, 4) but PD has few false-detections.

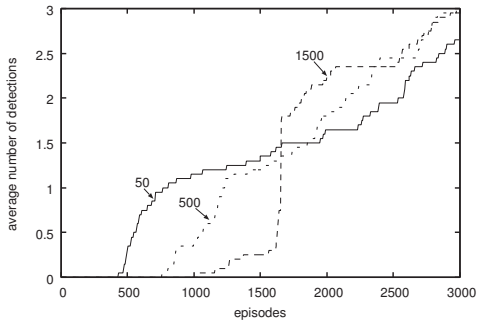

Fig. 4. Number of detections of 3 occurrence times of the environmental change

7 CONCLUSION

We have classified tasks of dynamic environments and proposed the detection method of environmental changes to adapt to dynamic environments. Then, with computational experiments we confirmed that the proposed method has better performances than Q-learning with regard to the influences of the environmental change, and as the learning progresses, detection of the environmental changes improves.

Our future projects include 1) to upgrade the detection method to consider 3 occurrence times of the environmental change, and 2) to apply the adaptive co-construction method of state and action spaces in dynamic environments.

REFERENCES

[1] R.S. Sutton and A.G. Barto (1998), Reinforcement Learning, A Bradford Book, MIT Press.

[2] M. Nagayoshi, H. Murao and H. Tamaki (2012), Developing Reinforcement Learning for Adaptive Co-construction of Continuous High-dimensional State and Action Spaces, Artificial Life and Robotics,**17**(2), 204-210.

[3] S. Shimada and Y. Anzai: "Improving Adaptability of Reinforcement Learning System to Dynamic Environment by Decomposing and Reusing Macro-Operators", J.IEICE, **J84-D-I**(7), 1076/1088 (2001-7)(in Japanese)

[4] M. Nagayoshi, H. Murao, and H. Tamaki (2006), A State Space Filter for Reinforcement Learning, Proc. AROB 11th'06, 615-618(GS1-3).

[5] T. Takahashi and M. Adachi: "Evaluating Progress of Reinforcement Learning Using Recurrence Plots", IEICE Technical Reports, NLP2005-155, 25/30 (2006)(in Japanese)

© ISAROB 2013

The Eighteenth International Symposium on Artificial Life and Robotics 2013 (AROB 18th '13),
Daejeon Convention Center, Daejeon, Korea, January 30-February 1, 2013

Development of Outdoor Mobile Robot for Human Following Navigation

Jae Hoon LEE[1], Kei OKAMOTO[2], Masumi OUE[2], and Shingo OKAMOTO[1]

[1]Graduate School of Science and Engineering, Ehime University, Japan
[2]Faculty of Engineering, Ehime University, Japan
(Tel: 81-89-927-9709, Fax: 81-97-927-9709)

[1]jhlee@ehime-u.ac.jp

Abstract: This paper deals with the development of a mobile robot for human following navigation in outdoor urban environment. Laser scanner and omni-directional camera were installed on the mobile platform for detecting people including a target person. The scan and image data from both sensors was fused into the information for tracking multiple moving objects, i.e. people. System configuration has been designed for effective collaboration between components operating in real-time. In order to follow the target, a motion control method based on the relative distance and velocity between the target and the robot itself. The proposed method was demonstrated through experiments of human following navigation with the developed robot in the outdoor environment of university campus.

Keywords: Human Following, Motion Control, Outdoor Mobile Robot.

1 INTRODUCTION

Over the classical contribution of robots to industry, recent technology is advancing for the future role in human daily life. Also in the case of mobile robot, over the last several decades AGV (Automatic Guided Vehicle) has been its typical application for object transportation in factory automation. However, researches to find applications of the advanced technology recently have been carried out for the innovation of mobile system in human daily life. It has been known that the capability to recognize daily environment and interact with human is fundamentally required for such robot to exist with people and perform service tasks.

So the researches related to human recognition have been actively performed. Most of them use camera sensor to detect human feature [1]. It can provide abundant data in its image but requires complicated algorithms and computing power for processing to extract important information in real time. Besides, stereo camera system is needed for the case to use range information. By using Omni-directional camera with a hyperbolic mirror, a special image of 360-degree field of view in the horizontal plane can be provided. Laser scanner is another alternative sensor to detect the state around the robot, which provides range data of horizontal plane with the time-of-flight information of the laser ray reflected by the rotating mirror. It has been utilized in various applications to mobile navigation such as human detection, map building, positioning, and so on [2].

The objective of this paper is to develop a mobile robot that can follow a target person moving in outdoor environment. For that, a laser scanner and an omni-directional camera have been employed as the primary and the secondary sensor to detect people around the robot, respectively. The information of both sensors and the odometer data of the robot were fused in real time by the filtering algorithm installed in the control system. The system and the proposed method were confirmed through experiments of human following navigation.

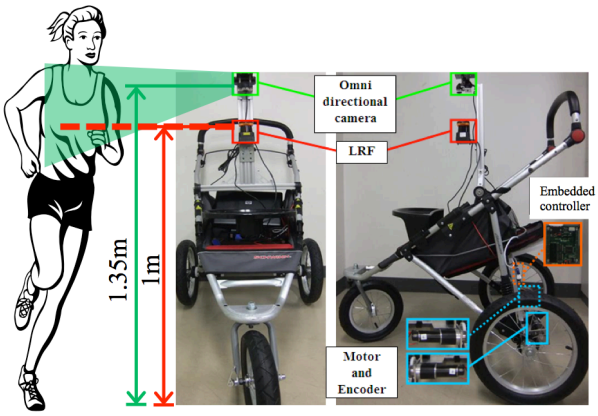

Fig. 1. Mobile robot system

2 DEVELOPMENT OF OUTDOOR MOBILE ROBOT

2.1 Mobile robot system

The mobile robot developed in this research is shown in Fig. 1. Its two active rear wheels rotate independently by two motors and a passive caster was used for the front wheel. An embedded controller is used for the motion control of the robot. The maximum velocity of the robot was designed as 4 [m/s] with the combination of reduction gear and wheel size. The encoders of rear wheels provide the position information with the manner of odometer.

© ISAROB 2013

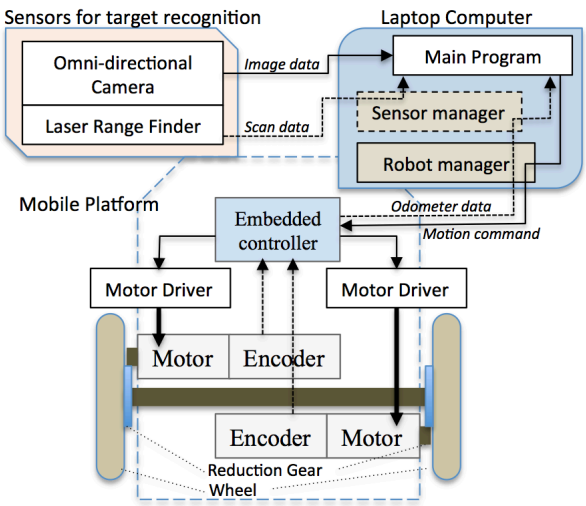

Fig. 2. System block diagram of the mobile robot

2.2 System configuration

The block diagram to show the configuration of the hardware system is given in Fig. 2, which mainly consists of three parts, mobile platform, sensors for target recognition, and laptop computer. The embedded controller in mobile platform is connected to the robot manager of laptop computer. Thus the motion command and odometer data are exchanged with each other. Two sensors, omni directional camera and laser scanner (Laser Range Finder), are installed on the top of the robot with the height of about 1.35 [m] and 1 [m], respectively. Their image and scan data is transferred to the main program in the computer. The capturing frequencies are 30 [fps] for image and 40 [Hz] for scan data, respectively. The sampling time of the odometer data is set to 5 [ms] in the robot. For the management of the large amount of high speed data, sensor manager with ring buffer is employed in the computer. It transfers scan and odometer data as synchronized information. The image data is transferred directly to the user program because of its huge amount. All of them are synchronized and fused with filtering algorithm in the computer.

2.3 Target recognition

In previous research [3, 4], a method to track people with laser scanner and omni directional image. Figure 3 shows the resultant omni directional image in which the laser range data is displayed with red points. This research modified it to recognize the target person. The state of people detected by the robot at time k is defined as

$$x_i(k) = (\ x_i(k) \quad y_i(k) \quad \dot{x}_i(k) \quad \dot{y}_i(k) \quad h_i(k)\ )^T, \quad (1)$$

where the subscript i denotes the number of people. $h_i(k)$ denotes the color state of i-th human, which is extracted from the part of the image.

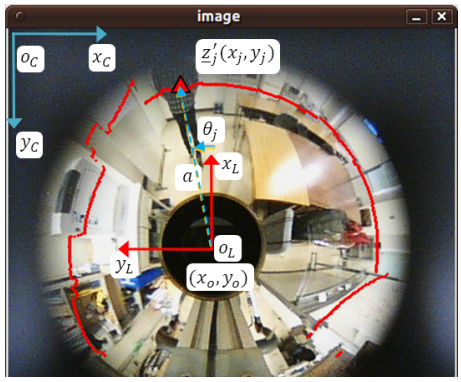

Fig. 3. Omni-directional image with scan data

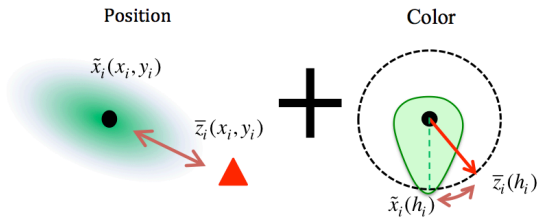

Fig. 4. Data association with position and color information

The association between the predicted state $\tilde{x}_i(k)$ and measurement $\bar{z}_i(k)$ was performed based on Mahalanobis distance considering both position and color as shown in Fig. 4. The state of each person near the robot is estimated with Kalman filtering method [5]. Resultantly the target was selected from the objects recognized by the method.

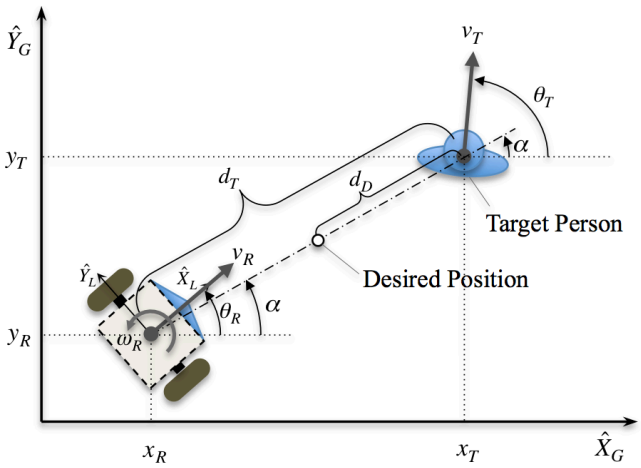

Fig. 5. Schematic representation of motion control for a mobile robot to follow a target person

3 MOTION CONTROL ALGORITHM

3.1 Velocity control for human following

Figure 5 shows the schematic representation of motion control for the robot to follow a target person. For target following navigation, the velocity of the robot should be controlled based on the position relationship between the robot and the target. Besides, the velocity of the target is

also considered at the same time. The desired velocity is realized by controlling both motors of wheels resultantly.

The desired velocity for the robot is computed as follows. The desired linear velocity of the robot is decided based on the velocity of the target person and the relative distance from the robot to target as following.

$$v_D = v_T + K_D(d_T - d_D) \tag{2}$$

where, v_T denotes the velocity of the target person. The distance from target person to robot, d_T is given as

$$d_T = \sqrt{(x_T - x_R)^2 + (y_T - y_R)^2}\ , \tag{3}$$

and its desired distance is defined as d_D. K_D denotes the feedback gain related to control the distance.

The desired angular velocity of the robot is decided based on the moving direction of the target person and the direction from the robot to the target as follows.

$$\omega_D = -K_{\theta 1}(\theta_R - \alpha) + K_{\theta 2}(\theta_T - \alpha) \tag{4}$$

where θ_T denotes the moving direction of the target with respect to the fixed global coordinate. α is the direction from the robot to the target on the global coordinate. $K_{\theta 1}$ and $K_{\theta 2}$ are the feedback gains related to control the moving direction.

3.2 Computer simulation

Computer simulation with the above mentioned algorithm has been carried out. Two results of following a target in linear and sinusoidal motion are given as follows.

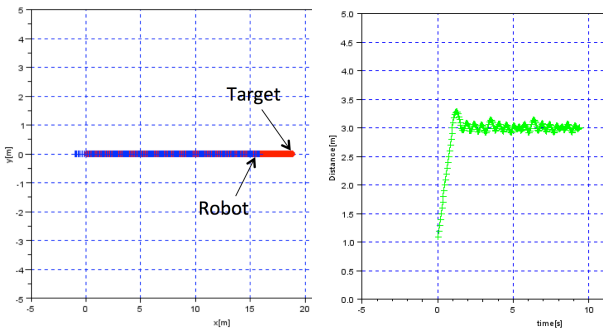

(a) Change of robot's position (left) and distance (right) from the target in linear motion

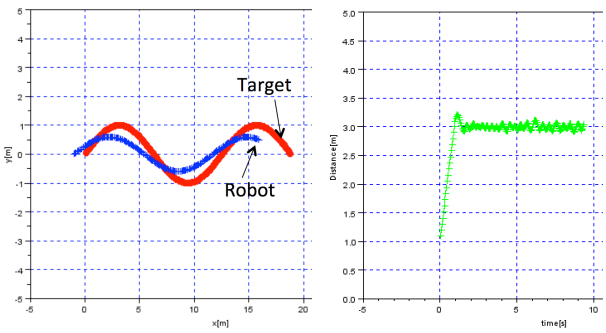

(b) Change of robot's position (left) and distance (right) from the target in sinusoidal motion

Fig. 6. Simulation results of target following control

The target was set to move with the linear velocity of 2 [m/s] in the simulation. The relative distance between robot and target was set to 3 [m]. The left figures of Fig. 6 (a) and (b) show the motion trajectories of both the robot and the target, and the right figures show the change of robot velocity, respectively. It is observed that the robot can follow the target and the distance between them can be controlled in both cases.

4 EXPERIMENT

In order to test both algorithms for people recognition and human following control, experiments with the developed robot system had been carried out.

4.1 People recognition

Experiment of people tracking was performed with the mobile robot in passive running by manual operation. Figure 7 shows an example of tracking three people, in which three people running in front of the robot were recognized robustly.

Fig. 7. Experiment of recognizing running people with the robot system in motion

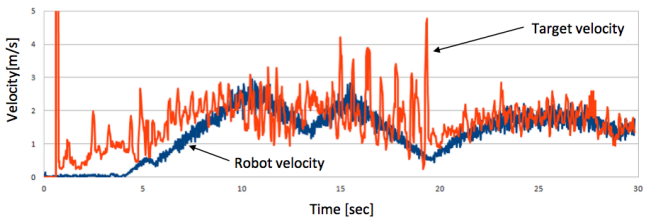

(a) Velocity

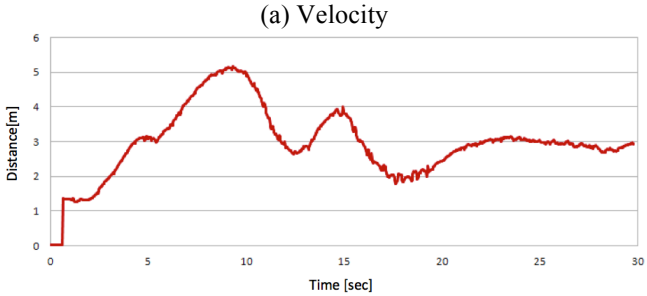

(b) Distance between the robot and the target

Fig. 8. Experimental results of target following control

© ISAROB 2013

(a) Image captured by operator's camera

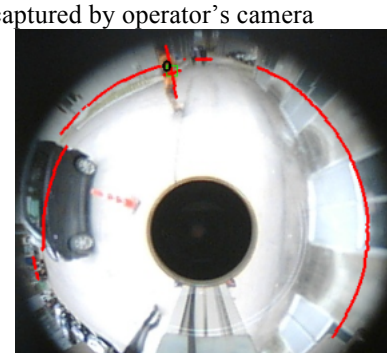

(b) Omni-directional image captured by the robot

Fig. 9. Example 1 of human following experiment

(a) Image captured by operator's camera

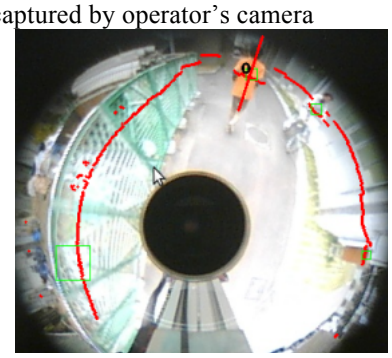

(b) Omni-directional image captured by the robot

Fig. 10. Example 2 of human following experiment

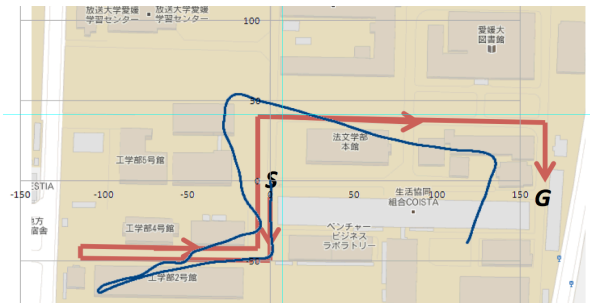

Fig. 11. Motion trajectory of the robot in human following experiment

4.2 Human following

Human following experiment was demonstrated with the developed robot system with the proposed method. The robot could follow the target person without failure during the navigation whose total distance was about 500 [m]. Overall velocity of the robot was changed in the range around 2 [m/s]. It was found that the robot's velocity was controlled according to the target's in spite of its noisy situation as shown in Fig. 8 (a). Besides, the desired distance between the robot and the target was controlled as shown in Fig. 8 (b), though fine tune is also required for more effective motion of fast response. Two representative scenes of the experiment, captured by the omnidirectional camera on the robot and the operator's, are displayed in Fig. 9 and 10. The target person was recognized stably and marked as '0' in the omni directional images. The resultant trajectory measured by odometry is depicted on the map as displayed in Fig. 11, where it shows distortion owing to its natural characteristics.

5 CONCLUSION

Based on people tracking method with both laser scanner and omni directional camera, the robot system that can follow a runner was developed in this research. Through computer simulations and experiments in urban outdoor environment, it was confirmed that the robot with the proposed control could perform human following navigation robustly. As future work, intelligent motion control considering moving and static obstacles will be investigated.

REFERENCES

[1] Sonoura T, Yoshimi T, Nishiyama M, Nakamoto H, Tokura S, Matsuhira N, (2008), Person following robot with vision based and sensor fusion tracking algorithm. Computer Vision, InTech, pp. 519-538

[2] Durrant-Whyte H, Bailey T, (2006) Simultaneous localization and mapping: Part I, IEEE Robotics and Automation Magazine, 13:2, pp. 99-110

[3] Jung EJ, Lee JH, Yi BJ, Yuta S, Noh ST, Marat honer tracking algorithms for a high speed mobile rob ot, Proceedings of International Conference on Intellige nt Robots and Systems (IROS), pp. 3593-3600

[4] Ueda H, Lee JH, Okamoto S, Yi BJ, Yuta S, (2011), People tracking method for a mobile robot with laser scanner and omni directional camera, Proceedings of International Conference on Ubiquitous Robots and Ambient Intelligence (URAI), Incheon, Korea, pp. 503-507

[5] Bar-Shalom Y, Li XR, (1995) Multitarget-Multise nsor Tracking: Principles and Techniques. Vol. 3.

The Eighteenth International Symposium on Artificial Life and Robotics 2013 (AROB 18th '13),
Daejeon Convention Center, Daejeon, Korea, January 30-February 1, 2013

Parameter Estimation Experiment and Development of Decentralized Caster Modules

Kazuyoshi Ohara, Jae Hoon Lee[1], and Shingo Okamoto

Ehime University, Japan
(Tel: 81-89-927-9740, Fax: 81-89-927-9740)

[1]jhlee@eng.ehime-u.ac.jp

Abstract: Parameter estimation method for distributed active caster has been investigated in this paper. By installing multiple active casters to a target object directly, it becomes a mobile system for transportation and can be moved to the goal position automatically. When the system is used to move an object of irregular shape, the position of each caster module should be estimated because it is basic parameter for control. Therefore, a parameter estimation method based on the kinematic model of each caster module and Kalman filter was proposed. The proposed algorithm has been demonstrated by computer simulation and experimental work.
Keywords: Active Caster, Parameter Estimation, Distribute Modular System, Mobile Robot.

1 INTRODUCTION

Object transportation is a well-known application of mobile robot technology. The representative example, AGV(Automatic Guided Vehicles), has been utilized for factory automation in industrial site. It has been used in various factories because of its capability to move a heavy load and autonomous operation. However, a typical AGV has limitation on load capacity owing to its platform size, and sometimes requires special modification for transporting objects with irregular shape. To cope with this problem, a novel device 'active caster system' has been proposed in previous researches [1, 2]. It is a system consists of multiple mobile caster modules that are independent but collaborate with each other. After installing them directly to a target object to move, and operating them by wireless communication, we can move it to the goal position automatically.

While using the active caster system, the actual problem is that the parameters in the kinematic model of the whole system changes according to the shape of the target object and the attachment of multiple casters. It is required to know the attached position of caster modules for collaboration between them. Therefore, the purpose of this research is to propose a method to estimate the attachment position of each caster module for real application. For that, parameter estimation algorithm based on the kinematic model of each caster module and external sensor information was proposed and demonstrated through computer simulation and experiment. Besides, the method of augmented Kalman filter [3] was also applied. The kinematic model of the mobile system with multiple casters is based on the previous researches [2, 4].

2 KINEMATIC MODEL

Double wheel typed caster was adopted for the caster module as shown in Fig. 1. It has two active wheels that rotate independently, which are connected to both ends of an axle that is also connected to the passive joint by a link. So the system configuration with multiple caster modules can be represented as Fig. 1.

Kinematic model between the velocity of the target object and the angular velocities of three joints, a passive joint and two active wheels, are given as follows. Let $\underline{\dot{X}} = \begin{pmatrix} \dot{x} & \dot{y} & \dot{\Phi} \end{pmatrix}^T$ be the velocity vector of target object. And $\underline{\dot{\phi}}_i = \begin{pmatrix} \dot{\theta}_{iL} & \dot{\theta}_{iR} & \dot{\varphi}_i \end{pmatrix}^T$ denotes the angular velocity vector of joints in the caster module.

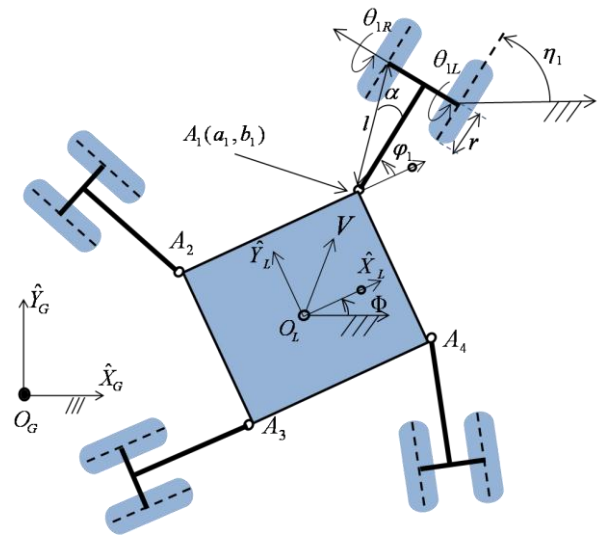

Fig.1. Kinematic model of mobile system with multiple double-wheel-typed casters

© ISAROB 2013

The kinematic relationship between $\underline{\dot{X}}$ and $\underline{\dot{\phi}}_i$ is given as

$$\underline{\dot{\phi}}_i = J_i^{-1}\underline{\dot{X}}. \tag{1}$$

Where J_i^{-1} denotes the inverse Jacobian matrix of *i*-th caster module, and it can be defined as [2]

$$J_i^{-1} = \frac{1}{lrC_\alpha}\begin{pmatrix} lC_{\varphi_i-\alpha} & lS_{\varphi_i-\alpha} & a_i lS_{\varphi_i-\alpha} - b_i lC_{\varphi_i-\alpha} \\ lC_{\varphi_i+\alpha} & lS_{\varphi_i+\alpha} & a_i lS_{\varphi_i+\alpha} - b_i lC_{\varphi_i+\alpha} \\ rS_{\varphi_i} & -rC_{\varphi_i} & -lrC_\alpha - b_i rS_{\varphi_i} - a_i rC_{\varphi_i} \end{pmatrix}. \tag{2}$$

Where a_i and b_i denote the *x* and *y* position of each caster with respect to the moving coordinate on the object. From Eq. (2), it is found that the kinematic relationship is dependent to the attachment position of each caster module.

3 PARAMETER ESTIMATION ALGORITHM

In this section, a parameter estimation algorithm based on the kinematic model is described. The basic idea is to estimate the kinematic parameters based on the difference between the position information from the external sensor and odometry. The error of odometry is mainly depend on the parameters included in the kinematic relationship. So, they can be estimated with the comparison of motion trajectories measured by external sensor. Here, it is assumed that the dimension of each caster module is sufficiently accurate, and the slippage between the wheel and the ground is small to be ignored.

The state vector including the posture of the object at time *k* is defined as

$$x_k = (x(k) \quad y(k) \quad \Phi(k))^T. \tag{3}$$

The state value at time *k+1* is computed with the manner of odometry as

$$x_{k+1} = x_k + \underline{V}_k \Delta t. \tag{4}$$

Where $\underline{V}_k$, the velocity of object, is calculated by Eq. (1) with the angular velocity measured by encoders, which is based on the kinematic relationship of each caster as shown in Eq. (2). The actual position of caster module is defined as a_i and b_i. And its initial position is also represented as a_i^* and b_i^*, respectively as follows.

$$a_i = \delta_{a_i} a_i^*, \tag{5}$$

$$b_i = \delta_{b_i} b_i^*. \tag{6}$$

By changing the parameter δ_a and δ_b, the estimation of real position of each caster module is performed. For parameter estimation, the state vector including δ_a and δ_b is defined as Eq. (7).

$$\hat{x}(k|k) = (x(k) \quad y(k) \quad \Phi(k) \quad \delta_a \quad \delta_b)^T \tag{7}$$

Then, Kalman filter was adopted for parameter estimation as follows[3].

$$P(k+1|k) = F_k P(k|k) F_k^T + Q_k \tag{8}$$

$$K_{k+1} = P(k+1|k) H_{k+1}^T [H_{k+1} P(k+1|k) H_{k+1}^T + R_{k+1}]^{-1} \tag{9}$$

$$\hat{x}(k+1|k+1) = \hat{x}(k+1|k) + K_{k+1}[z_{k+1} - H_{k+1}\hat{x}(k+1|k)] \tag{10}$$

$$P(k+1|k+1) = [I - K_{k+1}H_{k+1}]P(k+1|k) \tag{11}$$

Eq. (8) is state prediction covariance. Kalman gain shown in Eq. (9) is utilized for revising the error by using difference between observation value and prediction value [5]. Then, the state value and the covariance are updated by Eq. (10) and Eq. (11) with Kalman gain, respectively.

Now, the new linearized system matrix, F_{aug} and Gaussian process noise with covariance matrix Q_{aug} takes form Eq. (12). The matrix A is the transition matrix linking the augmented states to the location estimate. The matrix S is a fictitious noise injection on the augmented states to ensure convergence.

$$F_{aug} = \begin{bmatrix} F & A \\ 0 & I \end{bmatrix}, \quad Q_{aug} = \begin{bmatrix} Q & 0 \\ 0 & S \end{bmatrix}. \tag{12}$$

Where,

$$A = \begin{bmatrix} \frac{\partial X_k}{\partial \delta_a} & \frac{\partial X_k}{\partial \delta_b} \\ \frac{\partial Y_k}{\partial \delta_a} & \frac{\partial X_k}{\partial \delta_b} \\ \frac{\partial \Phi_k}{\partial \delta_a} & \frac{\partial X_k}{\partial \delta_b} \end{bmatrix}, \quad S = \begin{bmatrix} s_{11} & 0 \\ 0 & s_{22} \end{bmatrix}. \tag{13}$$

4 COMPUTER SIMULATION

Computer simulation has been performed to verify the performance of the proposed method to optimize the target parameters. Fig. 2 shows motion trajectory of the object adopted in the simulation. It was assumed that while the system, i.e. object with the caster module, is moving along trajectory of dotted line, its position can be observed by external sensor such as a camera installed at the ceiling. At the same time, the position is also computed by odometry with the measured angular velocity of joint and wheels. Because of the difference of parameters, there exists position error between them. Finally, this position error is modified by Kalman filter. Fig. 3 shows the change of the estimated parameters. According to the movement of the system, the parameters a_i^* and b_i^* were changed and approached $\delta_a = 0.3$ and $\delta_b = 0.4$, resultantly.

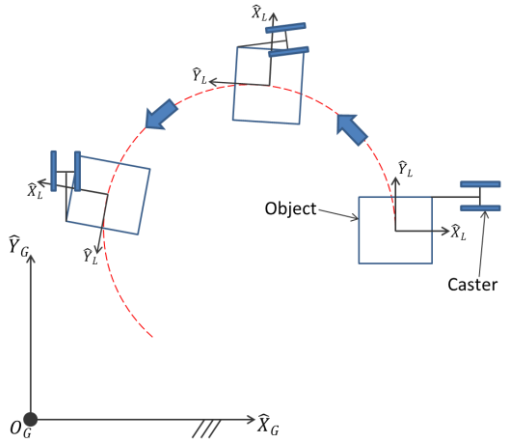

Fig.2. Motion trajectory of the system in simulation

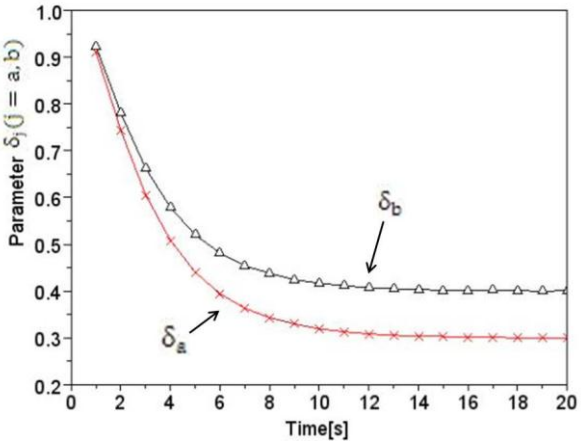

Fig.3. Estimated results of parameters δ_a and δ_b

5 EXPERIMENTS

5.1 Development of experimental caster module

Experimental works were carried out to check the proposed algorithm with real system. For that, a caster module has been manufactured as shown in Fig. 4, which has no actuator at each joint but three encoders to measure angular velocity of each joints. So the system moves manually by human operation.

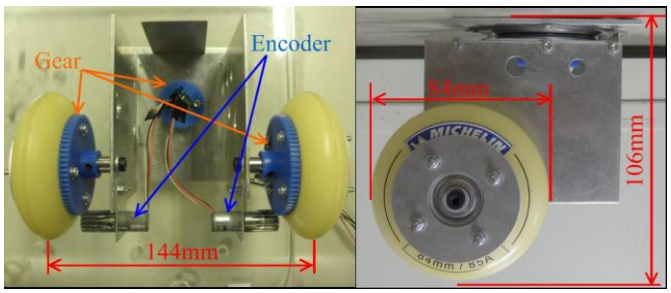

Fig.4. Caster module developed for experiment

5.2 Configuration of experimental system

The configuration of the experimental system and its photograph are shown in Fig. 5 and Fig. 6, respectively. A microcomputer and encoders were used to measure the angular position of passive joint and the angular velocity of both wheels. They can be embodied in a caster module with motors and wireless unit in actual system. In this experiment, the information of each encoder is transferred to the laptop computer for computing odometry. Laser scanner (LRF) is employed as an external sensor to achieve the system position, which is connected to laptop computer through Local Area Network (LAN) communication. In order to achieve the position information by external sensor, scan data from LRF is computed by using Iterative Closest Point (ICP) algorithm. The parameter estimation is carried out in the laptop computer by the algorithm of the previous section with the measured data from LRF and odometry.

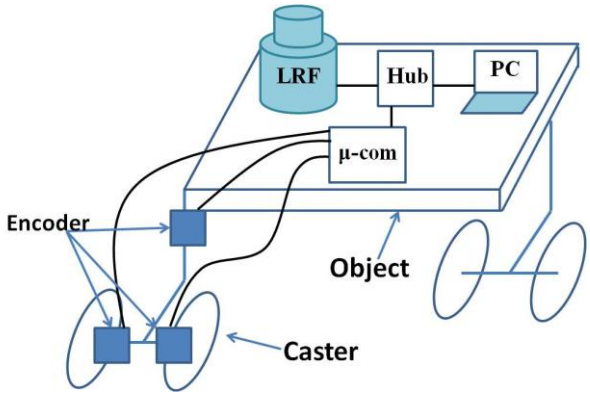

Fig.5. Configuration of the experimental system

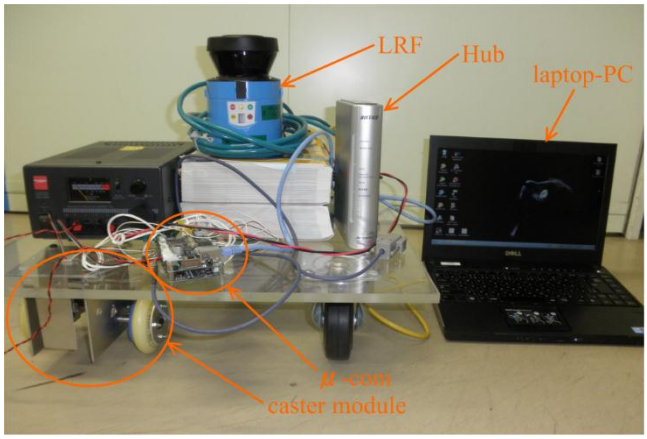

Fig. 6. Photograph of the experimental system

© ISAROB 2013

5.3 Experimental result

In the experiment, the position of active caster was estimated while the system is moved by human manual operation. The initial value of parameter and the true value are defined as imaginary caster position and real caster position as shown in Fig. 7, respectively. The motion trajectory of object center in Fig. 7 is measured by LRF in this experiment. As shown in Fig. 8, the motion trajectory of object center was a semi-circular route in this experiment. Fig. 9 shows the resultant change of parameters which were obtained by the proposed algorithm with the measured data. It was observed that the parameters approach to the real value in company with the motion of system resultantly.

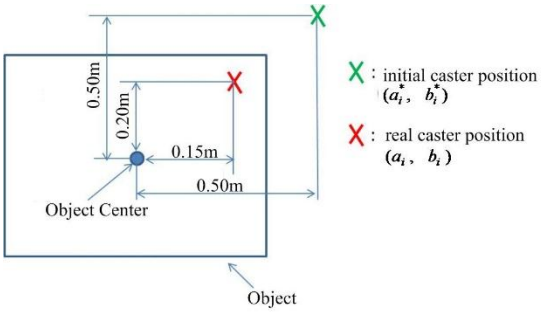

Fig.7. Parameter setting for experiment

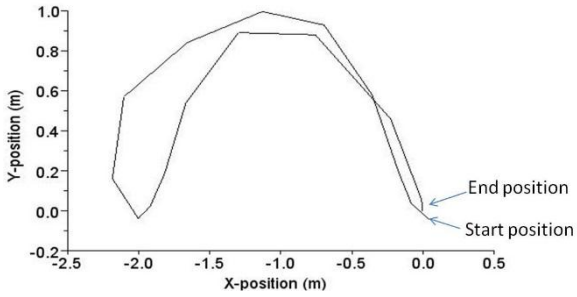

Fig.8. Motion trajectory of the object in experiment

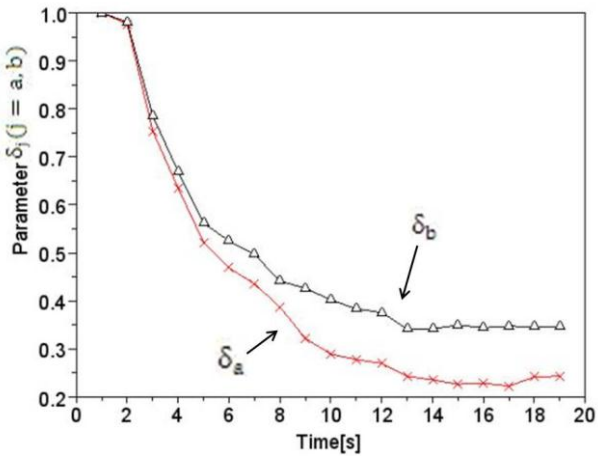

Fig.9. Experimental result on parameters δ_a and δ_b

In order to check the influence of the parameters, both odometry data for the same motion with the estimated value and un-estimated were compared. Fig. 10 shows odometry data of motion trajectories with un-estimated parameters. Fig. 11 shows odometry with estimated parameters, respectively. It is observed that the odometry with estimated parameters shows smaller error that the other. Therefore, the usefulness of the proposed method was confirmed through the experiment.

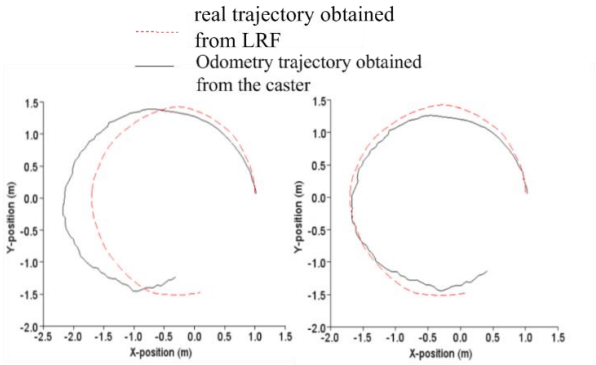

Fig. 10. Motion trajectory by odometry with un-estimated parameters

Fig. 11. Motion trajectory by odometry with estimated parameters

6 CONCLUSION

For real utilization of active caster system, the intelligent method to estimate parameters during its random motion was investigated through computer simulation and experimental works. For real application, redesign of the system with actuators and development of the controller based on wireless communication are now in progress.

REFERENCES

[1] Tomokuni N, Kim BK, Tanikawa T, Ohba K, and Hirai S (2006), Design of the Active Caster for the Actuation Devices of Ubiquitous Robots, 2006 Int. Symposium on Flexible Automation Osaka, Japan, pp.952-955

[2] Lee JH, Kim BK, Tanikawa T, Ohba K (2008), Parameter Identification for an Omni-directional Mobile System with Distributed Mobile Actuator Module, IEEE Int. Conf. on Multisensor Fusion and Integration for Intelligent Systems Seoul, pp.232-234

[3] Larsen TD, Bak M, Andersen NA, Ravn O (1998), Location Estimation for an Autonomously Guided Vehicle using an Augmented Kalman Filter to Autocalibrate the Odometry, Int. Conf. FUSION, pp.245-250

[4] Batlle JA, Barjau A (2009), Holonomy in mobile robots, Robotics and Autonomous Systems 57, pp.433-440

[5] Maeyama S, Ohya A, Yuta S (1997), Retroactive Positioning for a Mobile Robot, J. of Robotics Society of Japan, October 1997, Vol.15 No7, pp.115-121

© ISAROB 2013

The Eighteenth International Symposium on Artificial Life and Robotics 2013 (AROB 18th '13),
Daejeon Convention Center, Daejeon, Korea, January 30-February 1, 2013

Parameter optimization for decoupling controllers of 4WS vehicles

Mingxing Li, Haijing Xu, Yingmin Jia

The Seventh Research Division and the Department of Systems and Control, Beihang University (BUAA), Beijing 100191, China (e-mail: lmx196@126.com, xuhaijing_2005@yahoo.com.cn, ymjia@buaa.edu.cn).

Abstract: In this paper, the performance analysis and parameter optimization for two typical decoupling controllers of the 4WS vehicles are considered. Firstly, a new relationship between velocity and acceleration in effect on the nonlinear performance is established. Then, for the decoupling controller of a quasi-linearized system, the optimized region of parameters is obtained, in which the damping is bigger than one and eigenvalues are smaller than any given negative number. For the decoupling controller of a linearized system, the necessary and sufficient condition that the overshoot and irritating are avoided is deduced by using a new index. And the region, the measurement-error disturbance is attenuated to under any given positive number, is obtained for any expected eigenvalues. Simulation results show that optimized controllers can improve the safety and comfort obviously.

Keywords: 4WS vehicle, controller optimization, decoupling control, nonlinear performance analysis

1 INTRODUCTION

Decoupling control can improve comfort and safety for the vehicles. Thus its application has received a lot of attention in recent years [1]-[13]. Taking yaw rate and lateral speed as states, the decoupling control with velocity-varying and robust performances of the quasi-linearized system is advocated in [1] and [12]-[13]. Based on linearized systems, the diagonal decoupling is achieved in [3]. Taking yaw rate and lateral velocity as states, the diagonal decoupling in [2] and triangular decoupling in [5]-[7] are obtained.

There are high prices to be payed for using the decoupling control laws, e.g., damping and natural frequency are changed, and the desired disturbance attenuation is hard to be ensured. These prices may reduce the safety and comfort. Hence, the following issues are considered in this paper

1. Are the system performance is affected by the same factors with different states?

2. Are there some special decoupling controllers which can ensure the safety and comfort?

The first issue is answered by employing the linear system theory and joint-point locus approach, and the second is solved by optimizing some controller parameters. Models are described in section 2. System performances are analyzed to different states and the relationship to velocity and acceleration is obtained in section 3. Optimization of two decoupling controllers are discussed in section 4, one is used to control quasi-linear model and the other is linear. Simulations are shown in section 5 and conclusions are given in section 6.

2 VEHICLE MODEL

As mentioned in [7], the essential features of 4WS vehicle steering dynamics can be described by the single-track model as shown in Fig.1. If roll, pitch, and vertical dynamics are

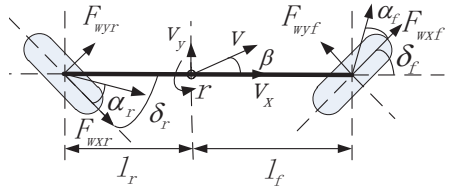

Fig. 1. Single-track model of 4WS vehicles

neglected, then the dynamics can be rewritten as [1]

$$m(\dot{v}_x - rv_y) = \sum_{i=r,l} F_{xi} - f_a \tag{1}$$

$$m(\dot{v}_y + rv_x) = \sum_{i=r,l} F_{yi} + F_y \tag{2}$$

$$J\dot{r} = l_f F_{yf} - l_r F_{yr} + T_z \tag{3}$$

Two typical simplified models can be obtained by linear and quasi-linear methods, which are,

$$\begin{bmatrix} \dot{v}_y \\ \dot{r} \end{bmatrix} = \begin{bmatrix} a_{11} & a_{12} \\ a_{21} & a_{22} \end{bmatrix} \begin{bmatrix} v_y \\ r \end{bmatrix} + \begin{bmatrix} b_{11} & b_{12} & b_{13} \\ b_{21} & b_{22} & b_{23} \end{bmatrix} \begin{bmatrix} \delta_f \\ \delta_r \\ F_l \end{bmatrix} \tag{4}$$

$$\begin{bmatrix} \dot{\beta} \\ \dot{r} \end{bmatrix} = \begin{bmatrix} \tilde{a}_{11} & \tilde{a}_{12} \\ \tilde{a}_{21} & \tilde{a}_{22} \end{bmatrix} \begin{bmatrix} v_y \\ r \end{bmatrix} + \begin{bmatrix} \tilde{b}_{11} & \tilde{b}_{12} & \tilde{b}_{13} \\ \tilde{b}_{21} & \tilde{b}_{22} & \tilde{b}_{23} \end{bmatrix} \begin{bmatrix} \delta_f \\ \delta_r \\ F_l \end{bmatrix} \tag{5}$$

where, F_l is the longitudinal acceleration/braking force. Details of $a_{i,j}$ and $\tilde{a}_{i,j}$ please refer to [1].

***Remark* 1.** *Parameters $b_{11}, b_{12}, b_{21}, b_{22}$ are taken as,*

$$b_{11} = \frac{c_f}{m},\ b_{12} = \frac{c_r}{m},\ b_{21} = \frac{c_f l_f}{J},\ b_{22} = -\frac{c_r l_r}{J} \tag{6}$$

while system (4) are linearized, and taken as

$$\begin{bmatrix} \frac{(1-\gamma)F_{l0}+c_f}{m} & \frac{\gamma F_{l0}+c_r}{m} \\ l_f \frac{(1-\gamma)F_{l0}+c_f}{J} & l_r \frac{\gamma F_{l0}+c_r}{J} \end{bmatrix} \tag{7}$$

while simplified by quasi-linearizing.

***Remark* 2.** *b_{i3}, $\tilde{b}_{i3}$ are almost zeros, and $\tilde{b}_{ij}$, b_{ij} satisfy*

$$\tilde{b}_{1j} = vb_{1j},\ \tilde{b}_{2j} = b_{2j},\ j = 1,2 \tag{8}$$

© ISAROB 2013

3 PERFORMANCE ANALYSIS

Linear and nonlinear performances of systems (4) and (5) are analyzed in this section.

3.1 Linear performance analysis

Stability, frequency and damping performances of systems (4) and (5) around equilibria pairs (v_y^*, r^*)(to system (4)) or (β^*, r^*)(to system (5)), are determined by

$$J(v_y^*, r^*) = \begin{bmatrix} -\frac{c_f^*+c_r^*}{mv} & -v-\frac{c_f^* l_f - c_r^* l_r}{mv} \\ -\frac{c_f^* l_f - c_r^* l_r}{Jv} & -\frac{c_f^* l_f^2 + c_r^* l_r^2}{Jv} \end{bmatrix} \tag{9}$$

$$J(\beta^*, r^*) = \begin{bmatrix} -\frac{c_f^*+c_r^*}{mv} & -1-\frac{c_f^* l_f - c_r^* l_r}{mv^2} \\ -\frac{c_f^* l_f - c_r^* l_r}{J} & -\frac{c_f^* l_f^2 + c_r^* l_r^2}{Jv} \end{bmatrix} \tag{10}$$

Both above matrices have characteristic polynomial as

$$p(s) = \omega_0^2 + 2D_0\omega_0 s + s^2 \tag{11}$$

$$\omega_0^2 = \frac{c_r^* c_f^* l^2 + mv^2(c_r l_r - c_f l_f)}{mJv^2} \tag{12}$$

$$2\omega_0 D_0 = \frac{(c_f^* + c_r^*)J + m(c_f^* l_f^2 + c_r^* l_r^2)}{mJv} \tag{13}$$

Thus (4) and (5) have the same linear performances as shown in [6]. Furthermore, if use a_r to replace l_r and a_f replace l_f, while $v > 0$ and the rear tyre isn't working in decaying region, i.e. rear tyres is driving wheels, then the stability factor $K = c_f a_f - c_r a_r$, and the vehicle is understeering while $K > 0$, neutralsteering while $K = 0$ and oversteering while $K < 0$ [9]. And if denote a_f as a_N with $K = 0$, then

$$a_N c_f - (l - a_N)c_r = 0$$

Thus the vehicle is understeering while $a_N > l_f$ and oversteering while $a_N < a_f$. And if the center of mass trends to rear axle, then the vehicle brings about oversteering, which is a dangerous situation with high velocity. From above analysis, we know

***Remark* 3.** *The damping and frequency of systems (4) and (5) mainly depend on v_x. If v_x is so big that $D_0 < 1$, then oscillation occurs and vehicle performance becomes badly.*

***Remark* 4.** *The handling characteristics may be better while a_f is smaller than a_N in a suitable range.*

3.2 Nonlinear performance analysis

By considering the load distributions and friction coefficient factors in the equilibria, we have

$$F_{ywf} + F_{ywr} = mrv_x,\ F_{ywf} l_f - F_{ywr} l_r = 0 \tag{14}$$

$$F_{ywf} = \mu_f N_f f_f(\alpha_f),\ F_{ywr} = \mu_r N_r f_r(\alpha_r) \tag{15}$$

$$N_f = mgl_r(1-\varepsilon_f)/l,\ N_r = mgl_f(1-\varepsilon_r)/l \tag{16}$$

Then we can get

$$\frac{\mu_f(1-\varepsilon_f)}{\mu} f_f(\alpha_f) = \frac{\mu_r(1-\varepsilon_r)}{\mu} f_r(\alpha_r) = \frac{v_x r}{\mu g} \tag{17}$$

If $\lambda_0 \triangleq \mu_f(1-\varepsilon_f)/\mu$, and $\kappa \triangleq (\mu_r(1-\varepsilon_r))/\mu_f(1-\varepsilon_f)$, then λ_0 corresponds to various road conditions which don't effect the nonlinear performance, whereas κ corresponds to load distributions , and (4) , (5) may have both stable and unstable equilibrium points, and the saddle-node bifurcations with $\kappa \le 1$, while both systems have only globally stable equilibrium points with $\kappa > 1$ [8]. I.e. $\kappa > 1$ can ensure good nonlinear performance. By simply deducing, we know

$$\kappa > 1 \Leftrightarrow \frac{(h_a - h)c_a}{mh} v_x^2 + \dot{v}_x > \frac{l_r l_f(\mu_f - \mu_r)}{l_r \mu_r + l_f \mu_f} g \tag{18}$$

***Remark* 5.** *From formula (18) we know, the velocity and acceleration in the longitudinal direction are very important to handling characteristics. And varying velocity model is more suitable to reflect the actual physical performances of the steering vehicles.*

4 DECOUPLING RESULTS ANALYSIS AND OPTIMIZATION

In this section, decoupling results of quasi-linearization and linearization systems are analyzed and optimized in order to improve vehicle safety and comfort further. As shown in previous section, (4) and (5) have the same location performances, thus we just talk about the system (4).

4.1 Quasi-linearization system

System (4) can be decoupled by decoupling laws [1]

$$u = F^*(x) + G^*(x)\eta,\ \eta = [\eta_1\ \eta_2\ \eta_3]^T \tag{19}$$

Then the quasi-linearization system is decoupled into

$$\begin{bmatrix} \dot{x}_i \\ \ddot{x}_i \end{bmatrix} = \begin{bmatrix} 0 & 1 \\ a_{i1} & a_{i2} \end{bmatrix} \begin{bmatrix} x_i \\ \dot{x}_i \end{bmatrix} + \begin{bmatrix} 0 \\ 1 \end{bmatrix} \eta_i,\ i = 1,2,3 \tag{20}$$

To get good smooth performance and retain the convergence rate, point (a_{1i}, a_{2i}) must be in the following region with any constant $k_{10} > 0$, which is shown in Fig.2,

$$a_{i1} - k_{10}a_{i2} - k_{10}^2 < 0,\ and\ \ a_{i2}^2 + 4a_{i1} > 0 \tag{21}$$

From Fig.2 we know, the feasible region of (a_{1i}, a_{2i}) is smaller, while k_{10} becomes bigger. And linear $a_{i1} - k_{10}a_{i2} - k_{10}^2 = 0$ and quadratic curve $a_{i2}^2 + 4a_{i1} = 0$ have only one intersection point, which is $(-k_{10}^2, -2k_{10})$, i.e. for any $k_{10} > 0$, points (a_{1i}, a_{2i}) which satisfy inequalities (21), always exist.

4.2 Linearization System

In [3], the decoupling controller is

$$\begin{bmatrix} \delta_c \\ \delta_r \end{bmatrix} = \begin{bmatrix} b_{11} & b_{12} \\ b_{21} & b_{22} \end{bmatrix}^{-1} \begin{bmatrix} -a_{12}r - b_{11}\delta_p \\ -k_p r - x_1 \end{bmatrix} \tag{22}$$

$$\dot{x}_1 = a_{21}(a_{CG_m - rv} - q_1\delta_p + k_1 r + x_2) \tag{23}$$

$$\dot{x}_2 = k_0(r - G(V, \delta_p)\delta_p), x_1(0) = x_2(0) = 0 \tag{24}$$

© ISAROB 2013

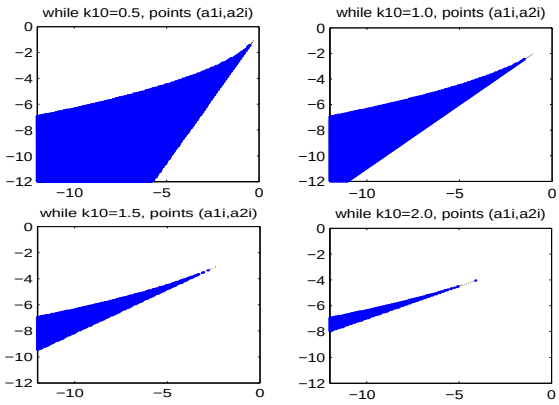

Fig. 2. Regions of (a_{1i}, a_{2i}), with constraints (21)

the controlled linearization system is decoupled into

$$\dot{v}_y = a_{11} v_y \tag{25}$$

$$\begin{bmatrix} \dot{r} \\ \dot{z}_1 \\ \dot{z}_2 \end{bmatrix} = \begin{bmatrix} -(k_P - a_{22}) & 1 & 0 \\ -k_1 & 0 & 1 \\ -k_0 & 0 & 0 \end{bmatrix} \begin{bmatrix} r \\ z_1 \\ z_2 \end{bmatrix} + \begin{bmatrix} b_{21} \\ q_1 \\ k_0 G(v) \end{bmatrix} \delta_p(t) + \begin{bmatrix} 0 \\ a_{21} \\ 0 \end{bmatrix} d(t) \tag{26}$$

The transfer function from $\delta_p(s)$ to $r(s)$ is

$$T_{\delta_p}(s) = \frac{b_{21}s^2 + q_1 s + k_0 G(v)}{s^3 + (k_P - a_{22})s^2 + k_1 s + k_0} \tag{27}$$

The characteristic polynomial is

$$P(s) = s^3 + (k_P - a_{22})s^2 + k_1 s + k_0 \tag{28}$$

To eigenvalues λ_i, there exist $k_{1,i} \in R, i = 1,2,3$, so that

$$T_{\delta_p}(s) = \frac{k_{1,1}}{s - \lambda_1} + \frac{k_{1,2}}{s - \lambda_2} + \frac{k_{1,3}}{s - \lambda_3} \tag{29}$$

Hence, the relationship between $r(t)$ and $\delta_p(t)$ is

$$r(t) = k_1 e^{\lambda_1 t} \delta_P(t) + k_2 e^{\lambda_3 t} \delta_P(t) + k_3 e^{\lambda_3 t} \delta_P(t) \tag{30}$$

Thus, if there were complex λ_i, yaw rate arises overshoot and oscillation. Then the safety and comfort will be worse. So overshoot and oscillation must be avoided.

***Theorem* 1.** *For the cubic equation*

$$ax^3 + bx^2 + cx + d = 0 \tag{31}$$

Roots x_1, x_2, x_3 are real and negative, if and only if $\kappa_0 \leq 0, \frac{b}{a} > 0, \frac{c}{a} > 0$, and $\frac{d}{a} > 0$, where $\kappa_0 = B^2 - 4AC, A = b^2 - 3ac, B = bc - 9ad$ and $C = c^2 - 3bd$.

Proof. From Cardano's formula, the equivalent condition that equation (31) only has real roots is $\kappa_0 \leq 0$. The roots are multiple while $\kappa_0 = 0$, and distinct while $\kappa_0 < 0$. And roots are negative while $\frac{b}{a} > 0, \frac{c}{a} > 0, and\ \frac{d}{a} > 0$ [15]. □

The performance of system (29) is decided by κ_0. By employing theorem 1, all eigenvalues of subsystem (26) not only negative but also smaller than $-k_{20}$ equal to

$$k_P - a_{22} > k_{20},\ k_1 > 3k_{20}^2,\ k_0 > k_{20}^3 \tag{32}$$

$$((k_P - a_{22})k_1 - 9k_0)^2 - 4((k_P - a_{22})^2 - 3k_1)$$
$$(k_1^2 - 3(k_P - a_{22})k_0) < 0 \tag{33}$$

And by complexly deducing, we know a sufficient condition for the norm bound $\|T_d(s)\|_\infty \leq \gamma$ is

$$(k_P - a_{22})^2 - 2k_1 > 0,\ k_1^2 - 2k_0(k_P - a_{22}) - \gamma^{-2} > 0 \tag{34}$$

$$(t_1 t_2 - 9k_0^2)^2 - 4(t_1^2 - 3t_2)(t_2^2 - 3k_0^2 t_1) > 0 \tag{35}$$

The above desired region of k_P, k_0 and k_1 is shown as Fig.3, where $P_0 = (k_P - a_{22},\ k_0,\ k_1)$. From Fig.3 we know, the

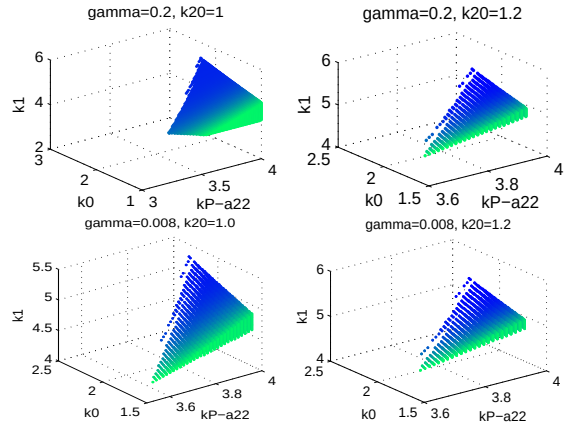

Fig. 3. Regions of P_0 with constraints (32)-(35)

region becomes smaller with k_{20} increasing and γ tending to zeros. Specifically, there aren't k_{20} bigger enough or γ near to zeros closely from over zeros direction, so that the region doesn't exist any longer. Such as, k_0/k_1 is taken as smaller than 1 and $(k_P - a_{22})/k_1$ as a constant, then by choosing a large enough $k_P - a_{22}$, inequalities (32)-(35) can be held.

5 SIMULATION

In this section, effects of optimized controllers are examined. The vehicle model BMW 735i is used [1]. The desired track and lateral acceleration are shown in Fig.4. Fig.5 is the simulation of the decoupled system of [1]. Fig.6 and Fig.7 are the decoupled system of [2]-[3], where Fig.6 is the result without disturbance while Fig.7 is the attenuation result of measurement error disturbance of lateral acceleration as $d(t) = 0.1\sin(26\pi t)$. The output and control signals may be both oscillation, however the output signals may be overshoot, while decoupling controllers are without optimizing, especially when the disturbance exists. But the overshoot and oscillation are avoided, and the output and control signals become more smooth, as the controllers are optimized. Furthermore, arbitrary attenuation of measurement error disturbance is arrived by optimizing k_1. So as Shown in simulation results, the safety and comfort are improved further by optimizing the parameters.

© ISAROB 2013

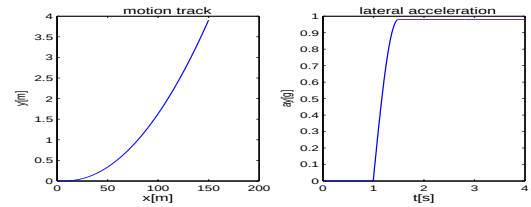

Fig. 4. Desired track and lateral acceleration

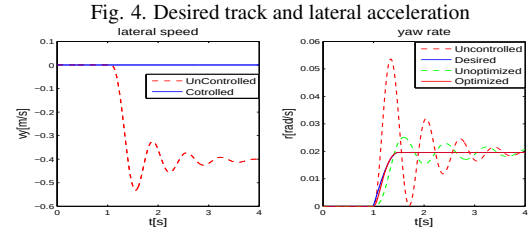

Fig. 5. Steering maneuver of the decoupled system (20)

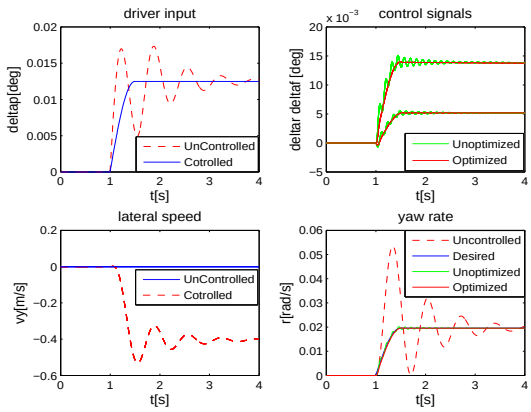

Fig. 6. Steering maneuver of (25)-(26) without disturbing

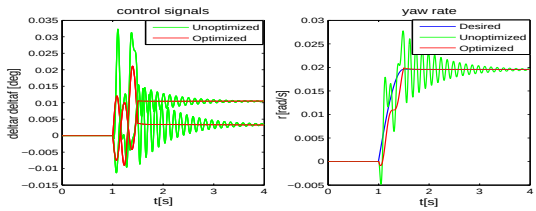

Fig. 7. Steering maneuver of (25)-(26) with disturbing

6 CONCLUSION

The 4WS vehicle performances have been analyzed and a new relationship for nonlinear performance with varying v_x and $\dot{v}_x$ has been given. Specifically, the optimization region of a quasi-linearized system is obtained, in which eigenvalues can be assigned in any desired position and overshoot and oscillation are avoided. Moreover, the necessary and sufficient condition preventing overshoot and irritating of system (25)-(26) is proposed and the optimization region is got, in which any desired H_∞ index γ and specified eigenvalues are achieved with avoiding overshoot and oscillation. And the simulation results show that the comfort and safety for the vehicle driving are improved significantly.

7 ACKNOWLEDGMENTS

This work was supported by the National Basic Research Program of China (973 Program, 2012CB821200, 2012CB821201) and the NSFC (61134005, 60921001, 90916024, 91116016).

REFERENCES

[1] Y.M. Jia(2000), Robust Control with Decoupling Performance for Steering and Traction of 4WS Vehicles under Velocity-Varying Motion, IEEE Transanction on Control System Technology, 8(3): 554-569.

[2] R. Marino and S. Scalzi(2010), Asymptotic Sideslip Angle and Yaw Rate Decoupling Control in Four-Steering Vehicles, Vehicle System Dynamics 48(9): 999-1019.

[3] R. Marino and F. Cinili(2009), Input-Output Decoupling Control by Measurement Feedback in Four-Wheel-Steering Vehicles, IEEE Transanction on Control System Technology, 17(5): 1163-1172.

[4] M.G. Skarpetis, F.N. Koumboulis, F.S. Barmpokas, and G.E. Chamilothoris(2006), Decoupling Control Algorithms for 4WS Vehicles, IEEE 3rd International Conference on Mechatronics, Budapest, pp. 499-504.

[5] J. Ackermann and T. Bünte(1997), Yaw Disturbance Attenuation by Robust Decoupling of Car Steering, Control Engineering Practice, 5(8): 1131-1136.

[6] J. Ackermann(1994), Robust Decoupling of Car Steering Dynamics with Arbitrary Mass Distribution, American Control Conference, Baltimore, 2: 1964-1968.

[7] J. Ackermann, and W.F. Sienel(1993), Robust Yaw Damping of Cars with Front and Rear Wheel Steering, IEEE Transanction on Control System Technology, 1(1): 15-20.

[8] S.W. Shen, J. Wang, P. Shi, and G.L. Premier(2007), Nonlinear Dynamics and Stability Analysis of Vehicle Plane Motions, Vehicle System Dynamics, 45(1): 15-35.

[9] N.J. Reza(2007), Vehicle Dynamics: Theory and Applications, Springer.

[10] B. Catino , S. Santini and M. Bernardo(2003), MCS adaptive control of vehicle dynamics: an application of bifurcation techniques to control system design, 42nd Conference on Decision and Control, pp.2252-2257.

[11] E. Ono, S. Hosoe, H.D. Tuan and S. Doi(1998), Bifurcation in vehicle dynamics and robust front wheel steering control, IEEE Transanction on Control System Technology, 6(3): 412-420.

[12] C.F. Chen, Y.M. Jia(2012), Nonlinear Decoupling Control of Four-Wheel-Steering Vehicles with an Observer, International Journal of Control, Automation, and Systems, pp.697-702.

[13] C.F. Chen, Y.M. Jia(2012), Nonlinear Decoupling Control of Vehicle Plane Motion, *IET*, Acceptted.

[14] H. True(1999), On the theory of nonlinear dynamics and its application in vehicle system dynamics, Vehicle System Dynamics, 31(1): 393-421.

[15] R.S. Irving(2004), Integers, polynomials, and rings: a course in algebra, Springer.

© ISAROB 2013

The Eighteenth International Symposium on Artificial Life and Robotics 2013 (AROB 18th '13),
Daejeon Convention Center, Daejeon, Korea, January 30-February 1, 2013

A method of sharing for common coordinate system by using relative position among the swarm

Makino Koji

Tokyo University of Technology, Japan
(Tel: 81-42-637-2111 ex.2823, Fax: 81-42-637-2112)

rmakino@stf.teu.ac.jp

Abstract: I have proposed a method that the many robots share the common coordinate system using dead-reckoning and observation to other robots without communication and without making the maps, like migration animals. To share the common coordinate system, both position and direction is necessary to be considered. I analyzed the effectiveness of the directional modification method, and confirmed it by simulations. In this paper, the modification of the position is focused on. First, the effectiveness of the method is confirmed by simulations. Secondly, the influence of the coefficient parameter of the positional modification is investigated, when the number of the robots and modification interval are changed. As a result, it is found out that the modification method of the position has optimal values.

Keywords: swarm, migration, common coordinate system

1 INTRODUCTION

A multi robot system that consists of many autonomous robots is drawing attention, because it has various advantages of fault tolerance, scalability and flexibility [1]. In many case, it is desirable that each robots recognizes own position and direction on the same coordinate system. For example, if all the robots recognize the flag position on the common coordinate system, they reach the position exactly (Fig. 1-a). On the other hand, assume that they can't recognize it on the common coordinate system (Fig. 1-b). However, it is difficult to share the common coordinate system. It is called as "localization problem". To solve the problem, GPS, SLAM[2][3], triangulation[4] and probabilistic methods[5][6] have been proposed. GPS is not available in the indoor, in the water, or outside the earth. The other method is necessary to communicate with other robots. Communication conflict occurs, if the large number of the robots exists.

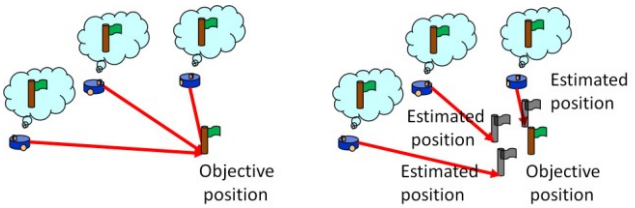

a. on the common coordinate system

b. on different coordinate systems

Fig. 1. Recognition the objective position

I pay attention to the animal of natural world. Migrant animals (bird, animal, fish and insect) often move very long distance. And they can reach their destinations (the lake, the grassland, the river and the sea). They do not communicate position and direction with the others. However, they adjust own velocity to correspond with the others.

I have proposed a method that the many robots share the common coordinate system using dead-reckoning and observation to other robots without communication and without making the maps, like migration animals[7][8][9]. In this paper, the relation between the parameter of the positional modification and optimal value is reported.

2 ROBOT SYSTEM

In the proposed modification method, the robots must move to the same direction and position. In this paper, the control method of the robot swarm that has been proposed is applied [10]. The control method consists of many robots and a supervisor that broadcasts the same command to them (Fig. 1).

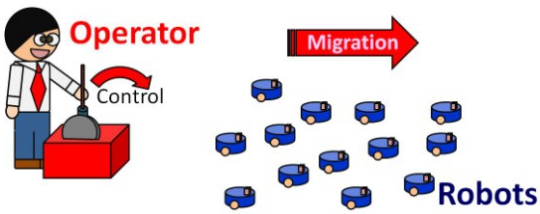

Fig. 2. The manipulation system

The robot has following ability:

- moving in 2-dimensional flat field
- localizing by dead-reckoning
- receiving the broadcast command from the supervisor
- measuring distance and relative velocity of other robots

© ISAROB 2013

where, the each robot does not communicate with each other. And, a general robot can be implemented with these abilities easily.

The robot receives three kinds of force. The force is similar to the force of the 'BOID' [11].

f_{ri} : attractive force to migrate

$$f_{ri} = K(p_r - p_i)$$

f_{ai} : attractive or repulsive force to gather

$$f_{ai} = \sum_{j \in J_{Ai}} \left(\frac{A_1(p_i - p_j)}{|p_i - p_j|^{m1}} - \frac{A_2(p_i - p_j)}{|p_i - p_j|^{m2}} \right)$$

And it decides the velocity by the sum of the forces

$$\dot{p}_i = f_{ri} + f_{ai}$$

In order to migrate, the reference position is changed according to

$$p_r = v_r t$$

The variable and constants are shown in Table 1.

Table 1. Definition of variables and constants

notation	description
$p_i = (x_i, y_i)^T$	absolute position of agent i
$p_r = (x_r, y_r)^T$	absolute position of reference position
$v_r = (v_{xr}, v_{yr})^T$	absolute velocity of reference position
n	number of agents
$K, A_1, A_2, B,$ $m1, m2, m3$	constant value

Fig. 3 shows the simulation result that the robots move by using basic setting without localization error. The basic setting is described in section 4. All the robots migrate together.

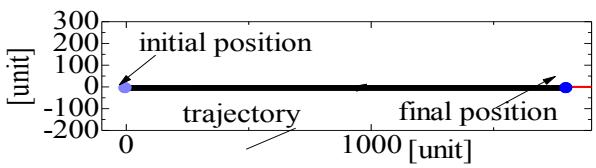

Fig. 3. Trajectories without localization error

3 MODIFICATION METHOD

3.1 Dead-Reckoning error

Dead-reckoning is very simple method to measure the own position and direction. However, the localization error occurs by dead-reckoning error. For example, the robot moves along dash trajectory for localization error in figure, though it tries to move to straight forward. Therefore, the robot estimates a different coordinate system to an initial coordinate system.

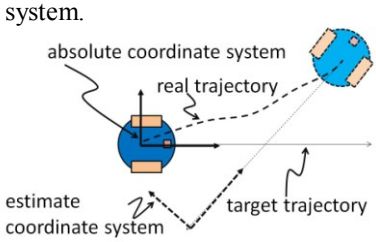

Fig. 4. localization error

Fig. 5 shows the trajectories of the robots. They move the different direction by the dead-reckoning error.

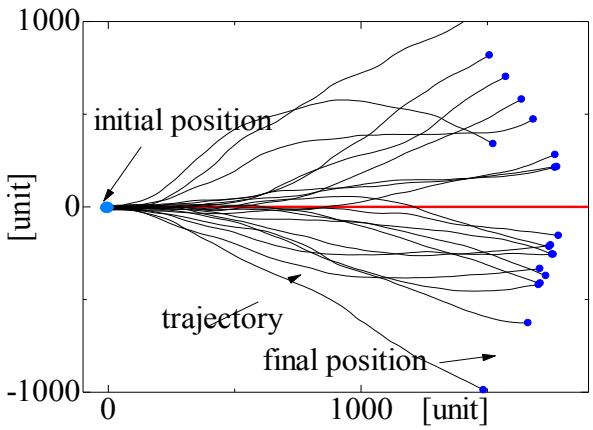

Fig. 5. Trajectories with localization error

3.2 Modification of the direction

The modification method of the direction is described. If all the robots recognize own position on the same coordinate system, they can move to same direction. Each robot modifies adjust own direction to fit direction of other robot, if they move to different direction by the error. The relationship between other and own velocity is illustrated in Fig. 6. The robot can observe relative velocity and can obtain own velocity. Therefore, it is able to calculate $\delta\theta_i$. And, it modifies own direction according to following equation:

$$\theta_i^+ = \theta_i^- + \omega_{dir}\delta\theta_i$$

where, superscript "+" and "–" mean after and before modification.

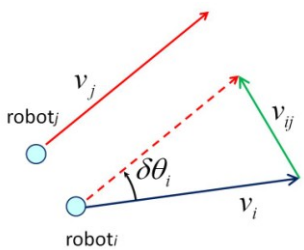

Fig. 6. Modification method of the position

© ISAROB 2013

Fig. 7 shows the trajectories with modification of the direction. All the robots migrate together in spite of the dead-reckoning error. This paper does not focus on the different between average trajectory and target trajectory, because it considers the sharing coordinate system.

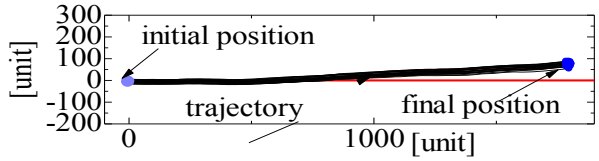

Fig. 7. Trajectories with directional modification without positional one

3.3 Modification of the position

The modification method of the position is described. The robots are not able to gather, if the each robot recognizes different reference position (Fig. 6). The own position is modified by f_{ai} and weight coefficient ω_{pos} as following equation:

$$p_i^+ = p_i^- + \omega_{pos} f_{ai}$$

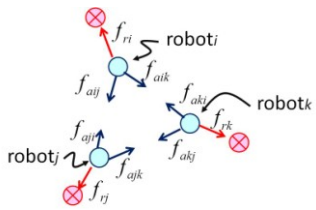

Fig. 8. Modification method of the position

The trajectories with modification of the direction and position are shown in Fig. 8. The trajectories are similar with ones in Fig. 7. The difference whether modification of the position is adopted or not is discussed in section 4.

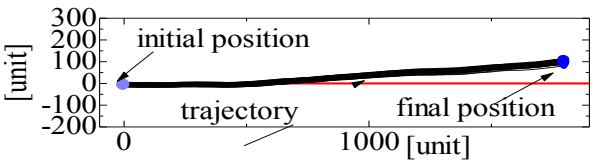

Fig. 9. Trajectories with directional and positional modification

4 SIMULATION

4.1. Setting

Basic setting is shown. The reference velocity is given as $(0.5, 0)^T$ [unit/step]. The dead-reckoning error is set to 2%, and the number of the robot is 20. The interval time between modifications is 20 [step]. The simulations are executed 10 times using different initial random value at the same parameter. The constant parameters K, A_1, A_2, m_1 and m_2 are 0.05, 1, 1, 1 and 2, respectively. The coefficient of the ω_{dir} is employed to 0.5. The optimal value of ω_{dir} is analyzed theoretically and confirmed by the simulation [9].

4.2. Effectiveness of modification of position

The time variant of the direction and position is illustrated in order to confirm the effectiveness of the modification method of the position.

First, standard deviation of the direction is shown in Fig. 10. The result using modification of the position (ω_{pos} = 0.2) is little worse. However, the value is not divergent.

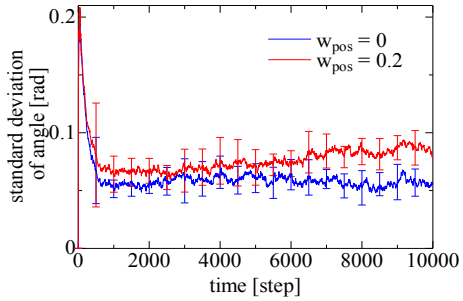

Fig. 10. Standard deviation of the direction

Secondly, Fig. 11 shows standard deviation of the position. The value without modification of the position (ω_{pos}=0) is divergent. On the other hand, the value with positional modification (ω_{pos} =0.2) is converge.

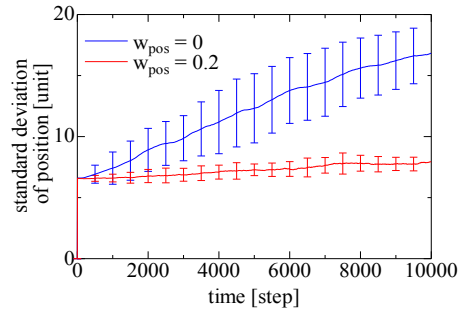

Fig. 11. Standard deviation of the position

Finally, Fig. 12 depicts final positions of the robots with and without modification, respectively. The position without modification is spread. However, the position is gathered using modification.

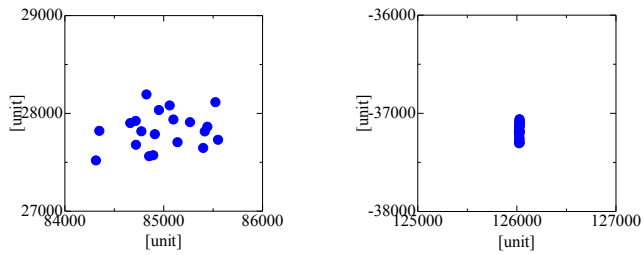

a. without positional modification

b. with positional modification

Fig. 12. Position of the 20 robots after long migration

© ISAROB 2013

The effectiveness of the modification method of the position is confirmed.

4.3. Influence of the parameters

In order to investigate the influence on the error of the position, the coefficient parameter of the modification of the position is changed from 0 to 1 step 0.01.

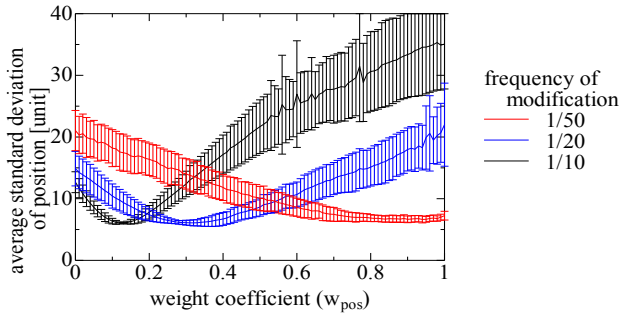

Fig. 13. Standard deviation of the direction changing ω_{pos}

Fig. 13 shows the results using three kinds of the interval times between modifications. Localization error increases, when interval time is long. Larger coefficient parameter is necessary in the case of large error. The robot might have to estimate scale of own error in order to use optimal value.

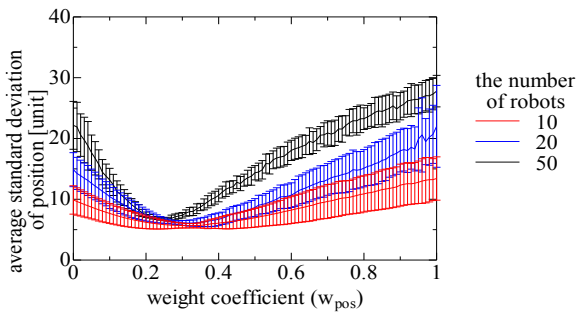

Fig. 14. Standard deviation of the direction various for ω_{pos}

The results using three kinds of the number of the robots (n = 10, 20, 50) is depicted in Fig. 15. The optimal value is the almost same, though the number of the robots is different.

5 CONCLUSION

This paper described the modification method of the direction and position in order to establish the common coordinate system. Both modification of position and direction are effectiveness to sharing direction and position, respectively. Especially, the influence of the coefficient parameter of the modification of the position on the performances is confirmed. I find that optimal parameter depend on the amount of the error, but does not depend on the number of robots.

In the future work, the effectiveness of the positional method is analyzed.

REFERENCES

[1] Y. U. CAO, et al. (1997), Cooperative Mobile Robotics: Antecedentsand Directions, Autonomous Robots, Vol. 4, No. 1, pp. 7-27.

[2] M.W.M.G. Dissanayake, S. Clark P.Newman, H.F. Durrant-Whyte, and M. Csorba (2001), A Solution to the simultaneous localization and map building problem, IEEE Transactions on Robotics and Automation, Vol. 17, No. 3, pp. 229-241.

[3] M. D. Marco, A. Garulli, A. Giannitrapani, and Antonio Vicino (2003), Simultaneous localization and map building for a team of cooperating robots: A set membership approach, IEEE Transactions on Robotics and Automation, Vol. 19, No. 2, pp, 238-249.

[4] KURAZUME, R., NAGATA, S and Hirose, S. (1994), Cooperative positioning with multiple robots, IEEE/RSJ International Conference on Intelligent Robots and Systems (IROS), Vol. 8, pp. 325-344.

[5] Fox, D. ,BURGARD, W, KRUPPA, H and THRUN, S. (2000), A probabilistic approach to collaborative multi-robot localization, Autonomous Robots, Vol. 2, pp. 1250-1257.

[6] IITSUKA, T, MAKINO, K, SHE, J, H and OHYAMA, Y (2010), Cooperative Localization of Autonomous Mobile Robots applied MCL method (in Japanese), 22th SICE Symposium on Decentralized Autonomous Systems, pp. 285-290.

[7] MAKINO, K. and MATSUO, Y. (2007), Method of Coordinate System Merging for Collective Control of Autonomous Mobile Robots (in Japanese), JRSJ, Vol. 25, No. 8, pp. 70-81.

[8] MAKINO, K. SHE, J. H. and OHYAMA, Y. (2010), Establishment of Common Coordinate System by Using Migration of Autonomous Robot Herd, SICE Annual Conference 2010, pp. 404-407.

[9] MAKINO, K. SHE, J. H. and OHYAMA, Y. (2011), Analysis of a Method of Sharing for Common Coordinate System by Migration, SICE Annual Conference 2011, pp. 2484-2487.

[10] MAKINO, K. and MATSUO, Y. (2004), Collective Behavior Control of Autonomous Mobile Robot Herds by Applying Simple Virtual Forces to Individual Robots (in Japanese), JRSJ, Vol. 22, No. 8, pp. 79-90.

[11] Craig W. Reynolds (1987), Flocks, herds and schools: A distributed behavioral model, SIGGRAPH '87 Proceedings of the 14th annual conference on Computer graphics and interactive techniques, pp. 25-34.

© ISAROB 2013

The Eighteenth International Symposium on Artificial Life and Robotics 2013 (AROB 18th '13),
Daejeon Convention Center, Daejeon, Korea, January 30-February 1, 2013

Evaluation of Efficiency of the Symmetry Bias in Grammar Acquisition

R. Matoba[*1], H. Sudo[*1], S. Hagiwara[*1], and S.Tojo[*2]

**1 Toyama National College of Technology*
1-2, Neriya, Ebie, Imizu, Toyama, 933-0293, Japan
(tel:+81-766-86-5283; Fax:+81-766-86-5110)
mail:{rmatoba ,i08323, hagiwara}@nc-toyama.ac.jp

**2 Japan Advanced Institute of Science and Technology*
1-1, Asahidai, Nomi, Ishikawa, 923-1292, Japan
(Tel : +81-0761-51-1372; Fax :+ 81-0761-51-1149)
mail: tojo@jaist.ac.jp

Abstract: The aim of this study is to evaluate the efficacy of cognitive biases in grammar acquisition. So far, we have constructed Iterated Learning Model (ILM) in generation by generation, where a pair of a parent agent and an infant agent resides in a generation, and the infant becomes the parent of the next generation. Then, we have added the effect of such cognitive biases as symmetry bias and mutual exclusivity bias. Thus far, in evaluating results of acquired grammar, the expressivity and the number of grammar rules have been focused on. When we consider the efficacy of cognitive biases, however, we should observe how the infant agent could learn the parent agent's intentions faithfully. Therefore, in this paper, we suggest assessing the difference of linguistic knowledge between a parent agent and an infant agenet, using Levenshtein distance. As a current result, we could observe that the distance becomes further in generations.

Keywords: Cognitive Bias, Levenshtein distance, Grammar Acquisition, Iterated Learning Model.

1. Introduction

It is well known that infants over 18 months old can acquire new words very rapidly, e.g., 7 to 15 words a day [1]. To enable this phenomenal learning, cognitive biases which are constraint to limit possibilities of words-meaning mapping in a situation have suggested [2, 3]. This mapping is considered to be generally difficult as is well known as `gavagai problem' [4], though infants achieve this operation.

So far, we have already reported efficacy of cognitive biases in grammar acquisition using computer simulation [5, 6]. Our model is based on Simon Kirby's Iterated Learning Model [7] where a pair of a parent agent as and an infant agent resides in a generation. In this model, the parent agent is a speaker and the infant agent is a listener. A number of utterances would form a compositional grammar rules in the infant agent's mind, being substrings are chunked. This process is iterated generation by generation, and finally, a certain generation would acquire a compact, limited number of grammar rules. We include cognitive biases into this process. We implement agents with the bias in a virtual world, and make them learn a grammar by computer simulation.

In general, the more grammar is compositional, the higher expressivity and the less number of rules. Therefore, we have evaluated the progress of evolution by these two criteria, so far. However, when we pay attention to the efficacy of cognitive biases, we should observe how the infant agent could acquire the parent agent's intentions correctly. Therefore, we need to assess the difference of linguistic knowledge, consisting of pairs of meanings and utterances, between the parent agent and the infant agent. More precisely, we employed a notion of Levenshtein distance to evaluate two different linguistic knowledge. Applying our suggested distance, we have gotten plausible results of Kirby's ILM to measure the efficacy of cognitive biases.

2. Distance between Two Different Linguistic Knowledge

2.1. Agent's Linguistic Knowledge

According to Kirby's ILM, the parent agent gives the infant agent a pair of a string of symbols as an utterance, and a predicate-argument structure (PAS) as its meaning. The agent's knowledge is a set of a pair of a meaning and a string of symbols, as follows.

S/love(john, mary) → lovejohnmary

Where a speaker's intention is a PAS l*ove(john, mary)* and its utterance becomes `lovejohnmary'; the symbol `S' stands for the category Sentence. After the listener receives a pair of a PAS and an utterance, she/he tries to guess his/her parent's grammar rules,

© ISAROB 2013

as utterances are always paired with their meanings, which are intrinsically compositional. This guessing process consists of the following two operations; `chunk' is to find a common substring, and to substitute it for a new category.

S/read(john, book) → johnreadsbook
S/read(mary, book) → maryreadsbook

↓

S/read(x, book) → N/x readsbook

while `merge' is to unify the identical category names as:

N/mary → mary
N/john → john
B/john → john

↓

N/john→ john

As a result, an infant comes to acquire a set of context-free grammar rules.

2.2. Distance between Two Knowedge

For evaluating the distance of two linguistic knowledge, i.e., the distance between the parent knowledge and the infant one, we employed the edit distance, aka Levenshtein distance, which is a metric for measuring the difference between two sequences of symbols; we count the number of insertion/elimination operations to change one word into the other. For example, the distance between `abc' and `bcd' becomes 2 (erase `a' and insert `d').

All the compositional grammar rules are developed to a set of holistic rules, where one PAS is connected directly to a superficial string excluding intermediate categories, beforehand. Now the comparison between a parent agent and an infant agent takes the following procedure.

1. Pick up a grammar rule (g_p) which is constructed by a pair of a PAS(p_p) and an utterance (u_p) from the parent's knowledge (K_p). Choose a grammar rule (g_c) which PAS (p_c) is most similar to p_p from a child's knowledge (K_c), in terms of Levenstein distance. If there are multiple candidates, all of them are kept for the next process.
2. Focus on an utterance (u_c) of g_c and u_p, and measure a distance (d_1) between u_p and u_c using Levenshtein distance. If there are some, choose smallest one.
3. Normalize d1 from 0 to 1.
4. Carry out 1 to 4 for all grammar rules of K_p. Calculate the sum of all the distances and regard the average of them as the distance of two linguistic knowledge. Thus, in this case, the distance between K_c and K_p is calculated as below.

$$Dist_{K_p to K_c} = \frac{1}{i}\left(\sum^{i} \frac{d_i}{|u_{ci}| + |u_{pi}|}\right)$$

The image of this measuring procedure is show in Fig1.

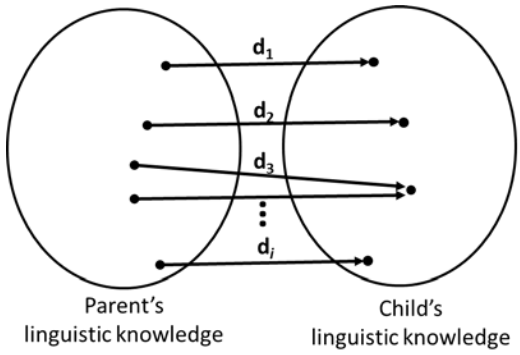

Fig1. Image of measuring procedure

Here, we give a concrete example. Assume that a parent agent has the linguistic knowledge including two rules as below.

rule1: *S/love(pete, mary)* → acd
rule2: *S/hate(mary, john)* → bd

Also, a child agent has

rule3: *love(john, mary)* → abc
rule4: *hate(mary, pete)* → bcd
rule5: *admire(mary, john)* → fcg

Now, pick up rule1 of parent's grammar rule, and search rules which have most similar PAS from the child's knowledge. In this case, rule3 is selected (procedure 1). Considering `acd' and `abc', the elimination of `d' and the succeeding insertion of `b' equate them, i.e., Levenshtein distance of them is 2 (procedure 2). Since the maximum distance is 6, the result of normalization becomes 2/6 (procedure 3). In the case of rule2, rule4 and rule5 are selected in procedure1. In terms of Levenshtein distance, rule4 is selected, and its distance is 1. After the normalization, we obtain 1/5. Therefore, the distance between the knowledge of the child agent and that of the parent agent becomes

$$\left\{\frac{1}{2} \times \left(\frac{1}{3} + \frac{1}{5}\right)\right\} \approx 0.27.$$

3. Experiment and Result

In this section, we show the result of the application of our suggested distance as mentioned in Section 2.2 to Kirby's ILM to testify its plausibility.

3.1 Briefing Experiment of Kirby's ILM

Kirby's ILM employs the following five two-place predicates and five object words:

Predicates: admire, detest, hate, love, like

Objects: gavin, heather, john, mary, pete

where two identical arguments in a predicate like love(john, john) is prohibited. This implies that there are 100 distinct meanings (5 predicates ×five first arguments × 4 second arguments).

Since the number of utterances is limited to 50 in his experiment, the child argent cannot learn the whole meaning space of 100; thus, the child agent comes across the learning bottleneck problem. To obtain the whole possible meanings, the child agent has to generalize his/her own linguistic knowledge by some learning process.

We have carried out this experiment until 100th generation.

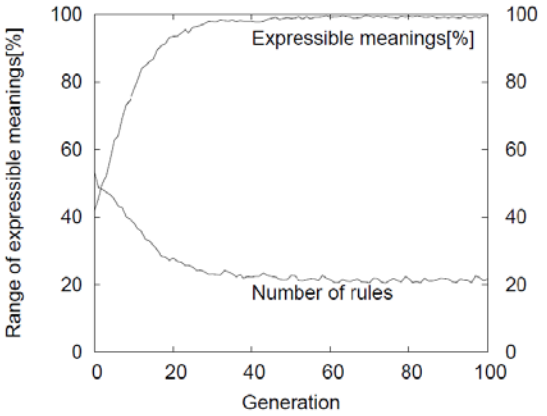

Fig2. Result of Kirby's ILM

The result of this experiment was that the language has low expressivity and a large number of rules in the early stages; however, through generations, the language acquires higher expressivity and the number of rules decreases. We can observe that the more the agent's linguistic knowledge becomes compositional the smaller the number of rules while expressivity persists or improves.

3.2 Application of Distance to Kirby's ILM

In the original experiment, the accomplishment of the learning is evaluated by the number of rules in linguistic knowledge and by the expressivity which is the ratio of the utterable meanings to the whole meaning space. Instead of these two criteria, we employ our own, i.e., the distance between two linguistic knowledge.

Here, we need to distinguish the distance from a parent to his/her offsprings, and that from an infant to his/her ancestors, each of which is shown in Fig. 3 and Fig. 4, respectively.

In Fig. 3, each upward line shows a distance of linguistic knowledge owned by a parent agent to his/her offsprings; the topmost line, for example, shows the distance from the parent agent in the first generation to his/her offsprings in the second, third, ..., and 100th generations. Because the distance becomes larger as the generations go further, the line becomes upward.

In this situation, for example, distance between knowledge of the 2nd generation to the 3rd generation is about 0.39. Also, distance between the 2nd generation to converged generation is about 0.85.

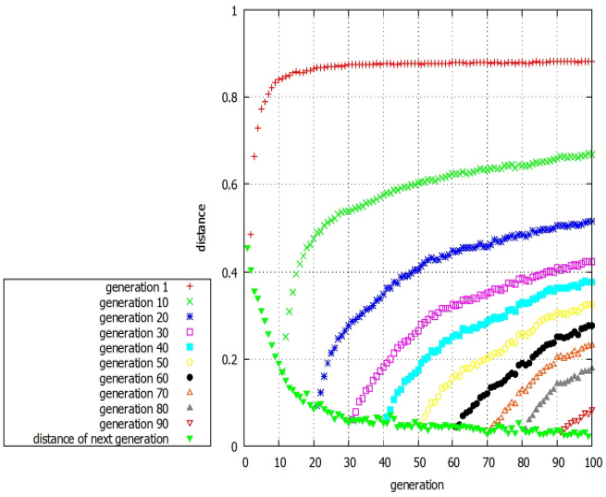

Fig3. distance from ancestor to offspring

In the later stages, linguistic knowledge of the parent agent becomes enough compositional to express the whole meaning world with few grammar rules, then the distance becomes smaller. For example, the distance between the 82nd generation to the 83rd generation is about 0.04. Also, the distance between the 82nd generation to the converged generation is about 0.14. The bottom line in Fig. 3 shows the distance between a generation and its

© ISAROB 2013

immediate follwing generation. We can observe that gradient of early generations is steep though that of the latter generations is flat.

In the early stages, the parent agent does not own compositional linguistic knowledge, i.e., expressivity of the knowledge is low, so the parent agent cannot make utterances with his/her own grammar rules, viz., the parent agent has no choice to make utterances randomly. On the other hand, in the latter stages, the parent acquires enough compositional linguistic knowledge, so the child agent can receive inputs in a regular pattern from the parent agent. Thus, the child agent can acquire similar linguistic knowledge to the parent agent, i.e., the distance of their knowledge is small.

The same tendency can be observed in Fig. 4. The topmost line in Fig. 4 shows the distance from the infant in the 100th generation to his/her ancestors. The further his/her ancestor is the larger the distance becomes, so that each line decreases from left to right. In the similar way, the bottom line in Fig.4 shows the distance between two consecutive generations; this line shows the exactly same tendency in Fig. 3.

5. Conclusion and Future Work

The cognitive biases are known to work to reduce the number of possible interpretations for each word, for first language acquisition. The authors thus far have verified that the function of the cognitive biases work not only in the lexical acquisition but also in the grammar acquisition. For this mission, we have revised Kirby's ILM, and built the cognitive biases into our model.

To evaluate the efficacy of the cognitive biases, however, we reconsidered the two traditional criteria; the expressivity and the number of rules. Although these two criteria are advantageous in evaluating the acquisition speed of compositional language, they cannot evaluate the correctness of meaning; infants in each generation may still misunderstand the mapping between meanings and utterances in such rapid leanings. Therefore, we suggested a criterion to measure the distance between two linguistic knowledge using Levenshtein distance. As a result, the distances between two linguistic knowledge in the early stages are larger because their grammar are not compositional. On the other hand, after grammar becomes enough compositional, the distances become smaller. Our future works include to employ this measuring procedure to our grammar acquisition model and to verify the function of the cognitive biases.

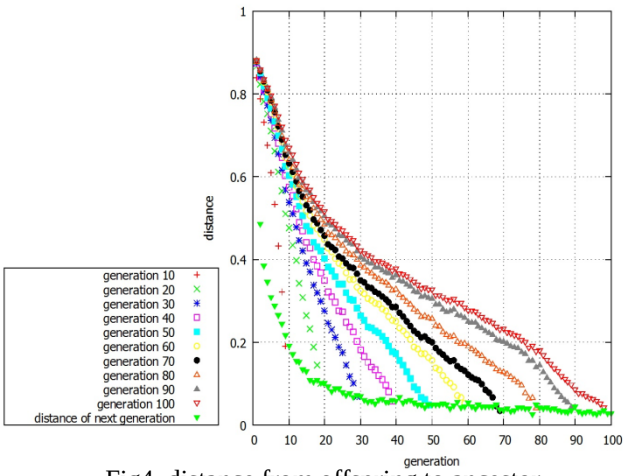

Fig4. distance from offspring to ancestor

Refferences

[1] G. Schafer and K. Plunkett. Rapid word learning by 15-month-olds under tightly controlled conditions. Child Development, Vol. 69, pp. 309{320, 1998.

[2] M. Imai and D. Gentner. Children's theory of word meanings: The role of shape similarity in early acquisition. Cognitive Development, Vol. 9, No. 1, pp. 45~75, 1994.

[3] E. M. Markman. Categorization and naming in children: Problems of induction, MIT Press, Cambridge, 1989.

[4] W.V.O.Quine, Word and Object, MIT Press, Cambridge, MA, 1960.

[5] R.Matoba, M.Nakamura, and S.Tojo, Efficiency of the Symmerty Bias in Grammar Acquisition, Information and Computation, Vol209, Issue 3, Elsevier, pp536-547, 2010.

[6] R.Matoba, M.Nakamura, S.Hagiwara, and S.Tojo, Efficiency of the Cognitive Bias in Grammara Acquisition, CogSci, 2012.

[7] S.Kirby, Learning Bottlenecks and the Evolution of Recursive Syntax, in: T.Briscoe(Ed.), Linguistic Evolution through Language Acquisition, CambridgeUniversity Press, 2002.

© ISAROB 2013

The Eighteenth International Symposium on Artificial Life and Robotics 2013 (AROB 18th '13),
Daejeon Convention Center, Daejeon, Korea, January 30-February 1, 2013

The Evolution of Pre-play Communication in the Interactive Minority Game

Keita Nishimoto[1], Ivan Tanev[2], Katsunori Shimohara[2], Reiji Suzuki[1] and Takaya Arita[1]

[1]Graduate School of Information Science, Nagoya University, Japan
[2]Faculty of Science and Engineering, Doshisha University, Japan

[1]nishimoto@alife.cs.is.nagoya-u.ac.jp

Abstract: Minority Game (MG) is an *N*-person game which represents the collective behavior of agents in an idealized situation in which they have to compete for some finite resource. MG has been studied actively in various fields, but most studies have not focused on the communication among agents. To study the evolution of communication in the MG, we extended the standard MG to a new game named *Interactive Minority Game* (*IMG*) by incorporating the two aspects: a continuous strategy space and a pre-play communication stage. In order to understand basic behaviors of agents in the IMG, we prepare three agents each of which is equipped with a recurrent neural network (RNN) to adjust the tentative strategy value in the pre-play communication stage and evolved the connection weights of each RNN based on the payoff of IMG. As a result, we saw the emergence of various communications such as the adaptive adjustment behavior and oscillation of strategy values of each agent. Moreover, we found the strategy differentiation among agents where two agents adopt "high-risk high-payoff" strategy and the rest one adopts "low-risk low-payoff".

Keywords: Minority Game, Evolution of communication, Multi-agent simulation

1 INTRODUCTION

Minority Game (MG) is an *N*-person game which represents the collective behavior of agents in an idealized situation where they have to compete for some finite resource. Each of *N* agents chooses one out of two alternatives independently, and those who have chosen the minority choice among them win and are awarded a point [1]. Minority Game has been studied actively in various fields because of its simplicity and emergent characteristics (e.g., the emergence of cooperation among agents and the phase transition [2], [3]).

However, most studies have not focused on the communication among agents in the MG. In the real world, people in competitive situations do not make decisions based only on the past record, but also based on communication among them.

We focus on the communication among agents and propose a new model named *Interactive Minority Game (IMG)* [4], where agents make decisions based on dynamic interactions between them instead of the past record. There are several studies to incorporate communication among agents into the MG [5], [6]. Anghel et al. proposed a network-based Minority Game where agents are connected with a random network [5]. Agents employ a two-step decision making procedure and exchange the decision-making information with others through the links. First, each agent predicts what the minority choice will be based on its own strategy table. Then, it selects the agent which has made the most accurate predictions so far from among its neighboring agents including itself, and adopts its prediction as the final choice. As a result of simulations, they discovered that the scale-free imitation network emerged on the random network.

In their model, the information which agents exchange is only a binary decision and one-shot, and thus it cannot be regarded as a dynamic communication. We incorporate *pre-play communication stage* in which agents can modify their intentions continuously and dynamically observing others' intentions before their final decision making.

To incorporate the dynamic communication, we need to change the agents' intentions and payoff from binary to real values. In our model, each agent expresses its intention by strategy value a ($\in$ [-1, 1]) and receives the payoff depending on the value.

As a first step of our study [4], we dealt with the evolutionary dynamics of *social sensitivity* of agents and role switching. This paper focuses on the evolved pre-play communication among agents. We prepare three agents, each of which is equipped with a recurrent neural network (RNN) to adjust the tentative strategy value in the pre-play communication stage. We evolved the connection weights of each RNN with an evolution strategy (ES) based on the payoff of IMG played among these agents.

2 Interactive Minority Game (IMG)

In the MG with *N* (odd) agents proposed by Challet and Zhang [1], the payoff of an agent *i* choosing alternative A_i is calculated as follows:

$$payoff = -A_i \, sgn\left(\sum_{k=1}^{N} A_i\right), \qquad (1)$$
$$\left(A_i \in \{-1,1\}, payoff \in \{-1,1\}\right),$$

© ISAROB 2013

$$sgn(x) = \begin{cases} 1 & \text{if } x > 0, \\ 0 & \text{if } x = 0, \\ -1 & otherwise. \end{cases}$$

We propose the Interactive Minority Game by extending the MG on the following two points. First, we adopt a continuous strategy space instead of a binary one. The payoff of agent i with strategy value a_i is calculated as follows:

$$payoff = -a_i \, sgn\left(\sum_{k=1}^{N} sgn(a_i)\right), \qquad (2)$$
$$\left(a_i \in [-1,1], payoff = [-1,1]\right).$$

This equation represents the situation as follows: The possible signs of the strategy value (positive or negative) correspond to the alternatives in the standard MG. Agents win the game if the sign of their strategy is the minority sign in the group. Furthermore, the strategy's absolute value defines its "intensity". Higher intensity values lead to both higher risk and higher reward. The winning (losing) agents obtain a positive (negative) payoff equal to the absolute value of their strategies.

Secondly, we add a pre-play communication stage before the agents confirm their strategy. During this stage, agents can continuously adjust their strategy. The tentative strategy of agent i at time step t (= 0, 1, .., T - 1) is represented as $a_i(t)$ ($a_i(0) = 0$). Each agent can adjust $a_i(t)$ gradually by ε (t), after observing others' tentative strategies in the previous step. The final decision of agent i : a_i is defined as $a_i(T)$, and used for calculation of payoffs.

$$a_i = a_i(T), \qquad (3)$$
$$a_i(t+1) = a_i(t) + \varepsilon(t),$$
$$(t = 0, 1, \cdots, T-1).$$

Note that if $a_i(t) + \varepsilon(t) > 1 (< -1)$, then $a_i(t + 1) = 1$ (-1). In this study, we focus on the case of $N = 3$, the minimum number of agents for the MG. Fig. 1 shows an example game. The x-coordinate corresponds to the time step t and the y-coordinate represents $a_i(t)$ for each agent.

3 MODEL

3.1 Decision making mechanisms

Every agent is equipped with a recurrent neural network (RNN) to decide $\varepsilon(t)$ at each step. The reason why we choose to use RNNs is to enable agents to make decisions appropriately depending not only on the current inputs, but also on past inputs: RNNs can use their internal memory to process arbitrary sequences of inputs. Each RNN has three layers (5 input units, 6 hidden units, 4 output units), and the units use a sigmoid activation function ($f(x) = 1 / (1 + e^{-x})$). For simplification of the model, RNNs do not have bias units. Two output units in the output layer are recurrently connected to two input units in the input layer.

Every time step, the agent's RNN receives five input values: its own current strategy value, the distance from the strategy values of the other two agents to its own, and the values from the two output units from the previous step. Two units in the output layer generate the values *au* and *ad*, which determine $\varepsilon(t + 1) = \varepsilon(t) + (a_u - a_d) / 100$. The remaining two output units are connected one-to-one to two of input units.

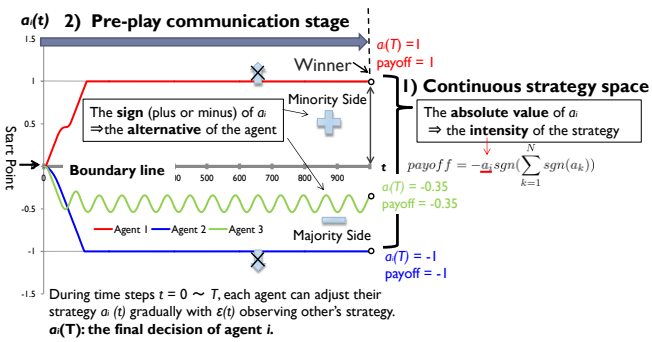

Fig. 1. A trial of IMG (N = 3, T = 1000).

3.2 Evolutionary algorithm

The full set of 54 connection weights in each RNN is encoded in the genotype of each agent and evolved using a simple type of Evolution Strategy (ES). The connection weights do not change during a trial. We assume three independent gene pools, each of which provides one agent in each trial, so the agents that interact in a game trial come from independently evolved gene pools. Each gene pool has n_p individuals.

1. Generating the initial population
   n_p genes are generated in each gene pool using uniform random number U as an initial population.
2. Evaluating individuals' fitness
   We assemble n_p groups of three individuals each of which randomly selected from each gene pool without duplications. Three individuals in each group play IMG and receive the payoff. Individuals picked out from pools are restored to their original pools after the trial. This procedure of group assembly and game trial is repeated R times. The fitness of each individual is defined as an accumulation of fitness over R trials.
3. Creating the next generation

© ISAROB 2013

The population in the next generation of each gene pool is composed as follows: First, we select n_e best individuals from n_p individuals (the elites), and preserve them to the next generation. Then, each of elites contributes two copies of themselves to the next generation, and small random values from a normal distribution N_R with a fixed standard deviation are added to each connection weight in the offspring. Finally, n_p-3n_e individuals with randomly generated genotypes are added to the population. These evolutionary operations for selection and reproduction are performed on each gene pool independently.

4 RESULTS

We evolved the population for 10000 generations. We used the following parameter settings: T = 1000, n_p = 40, n_e = 12, R = 40. Initial connection weights are drawn randomly from a uniform distribution U over [-1, 1], and mutation adds a random number from the normal distribution N_R (0, 0.2^2).

First, we focus on how pre-play communication among agents develops during the early stages of the evolution process. Fig. 2 represents the average fitness of each gene pool and the average fitness of all individuals from the 0th generation to the 99th generation. We see a rapid increase in fitness in all gene pools. The average fitness reached approximately -5 at the 99th generation.

Fig. 3 shows an example communication at the 50th generation. We see that the strategy value of one agent reached the upper limit and that of another agent reached the lower limit, while the remaining agent's value remained near the boundary line between two signs (a_i (t) = 0). We focus on the agent whose strategy value remained near the boundary line. In the situation shown in Fig. 3, the strategies of the other two agents are on the upper and the lower area respectively, and they did not change their strategy values. Thus, the focal agent could not avoid ending up on the majority side, and so its payoff falls below 0 regardless of which side it picks. The optimal behavior thus is to choose a strategy value as close to the boundary line as it can, and receive payoff of near 0. It was often observed in the simulations that the final strategies of the three agents settled on these three positions in the strategy space: the upper limit, the lower limit (high risk and high return strategy) and around the boundary line (low risk and low return strategy). This can be regarded as strategy differentiation among agents.

The average payoff of each agent over R trials becomes near 0, if 1) the final strategy of the agent nearby the boundary line stays very close to it, and 2) its sign splits fifty-fifty between positive and negative. In this scenario, the situation in which the final strategies fall in the same area of the strategy space (yielding payoff far below 0) is avoided. In Fig. 2 we see an increase in average fitness from the initial generation to the 20th generation, likely due to the emergence of the strategy differentiation among agents.

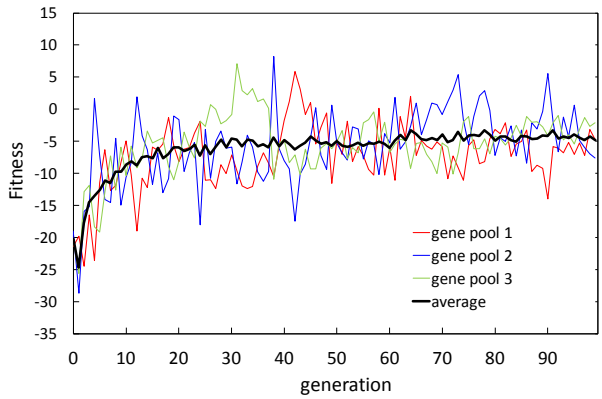

Fig. 2. Evolution of fitness.

Fig. 4 shows a typical communication from the 70th generation in which Agent 1 and Agent 3 can be seen to respond each other's behavior. In Fig. 3, all agents initially lower their strategy values. Agent 3 (at around step 40), and Agent 1 (at around step 80) can be seen to switch their directions and start increasing their strategy values, in order to avoid the situation in which the strategy values of all agents remain negative, in other words, all lose. Once the strategy value of Agent 1 surpasses 0 (at around step 150), Agent 3 switches its direction again correspondingly. The most likely explanation for these behaviors of Agent 1 and Agent 3 is that they changed the increase or decrease in their strategy values in response to the strategy values of the others.

Fig. 5 shows the communication among agents at the 80th generation. We can observe that agents interacted with each other more actively than was the case in the earlier generations. This sort of oscillation was often observed in the simulation.

Next, we classified the types of the pre-play communication among agents into the following three types: (a) Oscillation type (All agents cross the boundary line (a_i (t) = 0) more than one time in the communication stage.) (b) Fork type (All agents do not satisfy the condition of (a), and each strategy value is as follows: one's strategy value is more than 0.8, another's strategy value is more than -0.1 and less than 0.1, and the other's strategy value is less than -0.8), (c) Others. Fig. 6 shows the occurrence rate of each communication type from the 0th generation to the 99th generation. From this figure, we see that the Fork type occurs first, followed by the Oscillation type. We conducted

© ISAROB 2013

ten trials and confirmed this tendency in nine trials among them. This increase in communicative complexity should be worth noting as in the field of animal signaling it has been believed that complex communication cannot be evolved in conflicting situations [7].

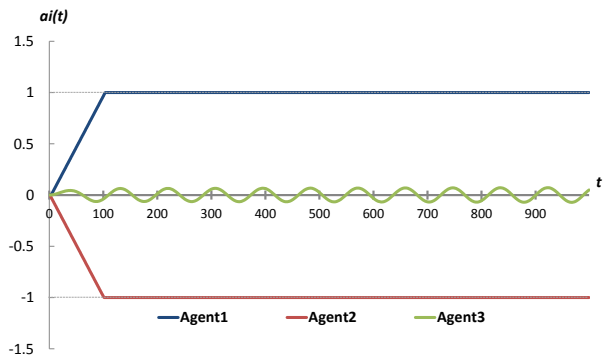

Fig. 3. Communication among agents at the 50th generat ion.

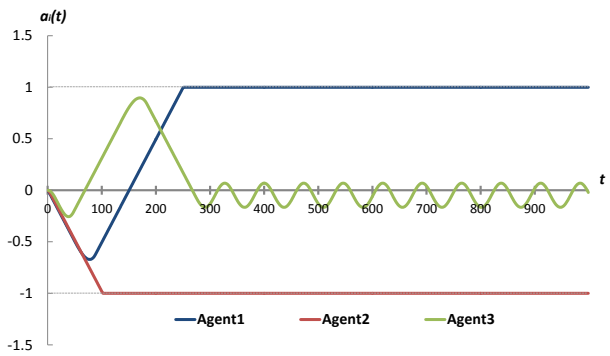

Fig. 4. Communication among agents at the 70th generat ion.

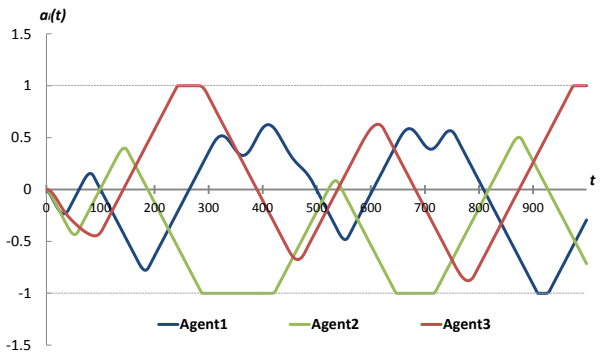

Fig. 5. Communication among agents at the 80th generat ion.

4 CONCLUSIONS

We extended the standard MG to a new game named *Interactive Minority Game (IMG)* by incorporating the two aspects: a continuous strategy space and a pre-play communication stage. As a result of evolutionary simulations in which each agent's RNN evolves based on the payoff of 3-person IMG, we discovered that the strategy differentiation among agents where two agents adopt "high-risk high-payoff" strategy and the rest one adopts "low-risk low-payoff". We also saw the emergence of various communications such as the adaptive adjustment behavior and oscillation of strategy values of agents.

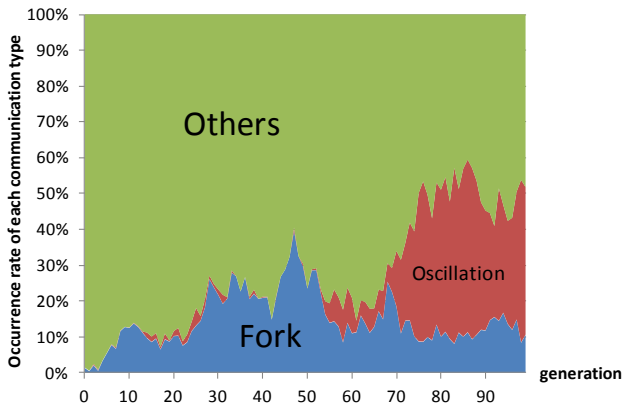

Fig. 6. Occurrence rate of each communication type in each generation.

REFERENCES

[1] Challet D and Zhang YC (1997), Emergence of cooperation and organization in an evolutionary game, *Physica A* 246: 407-418.

[2] Savit R, Manuca R and Riolo R (1999), Adaptive Competition, Market Efficiency, and Phase Transitions, *Phys. Rev. Lett* 82(10): 2203–2206.

[3] Challet D and Marsil M (1999), Phase transition and symmetry breaking in the minority game, *Phys. Rev. E* 60: R6271-R6274.

[4] Nishimoto K et al., Coevolutionary dynamics between roles and social sensitivity in an extended minority game, *Proceedings of ALIFE13*, Michigan, USA, July 19-22, 2012: 226-233.

[5] Anghel M, Toroczkai Z, Bassler KE and Korniss G (2004), Competition in social networks: emergence of a scale-free leadership structure and collective efficiency, *Phys. Rev. Lett.* 92: 058701.

[6] Remondino M and Cappellini A (2005), Minority game with communication of statements and memory analysis: a multi agent based model, *International Journal of Simulation: Systems, Science & Technology* 6(5): 42-53.

[7] Maynard-Smith J and Harper D (2003), *Animal signals*, Oxford University Press, Oxford, U.K.

© ISAROB 2013

The Eighteenth International Symposium on Artificial Life and Robotics 2013 (AROB 18th '13),
Daejeon Convention Center, Daejeon, Korea, January 30-February 1, 2013

A New Decision-Making System of an Agent Based on Emotional Models in Multi-Agent System

ShogoWatada[1], Masanao Obayashi[1], Takashi Kuremoto[1], Kunikazu Kobayashi[2] and Shingo Mabu[1]

[1]Graduate School of Science and Engineering, Yamaguchi University
[2]School of Information Science and Technology, Aichi Prefectural University
m.obayas@yamaguchi-u.ac.jp

Abstract: In this paper, a new behavioral decision method of the robot based on a Markovian emotional model is proposed and it is applied to environmental identification problem. Noting the role of emotion in communication, behaviors of multi-robot implementing the emotional transition model are optimized. The autonomous decentralized robot group with the proposed method is applied to identify an unknown environment. Specially, each robot in this autonomous decentralized system can communicate with other robots located within a certain distance. While searching and exploring the environment, each robot independently generates local topological maps, and uses the map for planning of actions. Finally, the effectiveness of the proposed method is verified using own simulator through evaluating the exploration time and the number of double-visited nodes for different complex environments.
Keywords: decision making system, Markovian emotional model, multi-agent system

1 INTRODUCTION

There exists much literature on the study which focuses on the concept of emotion that animals have, for developing autonomous systems in various fields. Emotion of animals are more attractive from the points of view that it flexibly represents influence from the environment and internal states of them, and that it makes communication with others facilitate. Emotion has been considered as a significant impact on decision making of autonomous robots. There have been many studies of artificial emotion[1 - 4].

The purpose of this study is to optimize the decision making of a robot by introducing emotion to a multi-robot control system. The autonomous decentralized robot group in which each robot has the proposed system is applied to identify an unknown environment. This task is to explore all areas in unknown environment and to generate an accurate map. Getting the map leads to effective determining of behaviors of the robot because it can be used in order to path planning.

Assuming that each robot in the robot group has signal emitting and receiving functions, the robot can communicate with other robots located within a certain distance. While searching and exploring the environment, each robot independently generates local topological maps, and uses the map for planning of actions.

The proposed behavior selection system incorporates with a Markovian emotional model which is represented as a finite state machine, and the emotional state is determined by the internal state and used for behavior selection.

In addition, by optimizing the parameters related to behavior selection and generation of emotional value by a genetic algorithm (GA), one of evolutionary optimization method, the action along objective of the task is selected automatically.

The proposed method is evaluated through an unknown environmental identification problem. The simulation results showed the effectiveness of the proposed method.

The paper is organized as follows. Section 2 describes the proposed Markovian emotional model. In Section 3, the proposed behavior selection system with the Markovian emotional model is described. In Section 4, the simulation results of the proposed method are presented. Finally, Section 5 summarizes the effectiveness of the proposed method and future works.

2 The Markovian emotional model

The Markovian emotional model referenced in this paper is a probabilistic model[5] that consists of finite state machine. It consists of four basic emotions: joy, anger, fear and sadness (Fig.1).

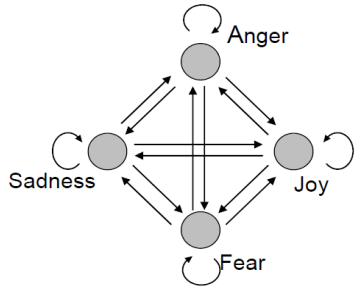

Fig. 1. Topology of Markovian Model

Emotional state transition is given by Eq.1

$$Y_{k+1} = CY_k \quad (1)$$

with emotional state points:

$$\Omega = \{Joy, Anger, Fear, Sadness\}, \quad (2)$$

© ISAROB 2013

where Y_k represents the current emotional state, and C is the emotional state transition matrix, which can be expressed as follows:

$$C = \begin{bmatrix} P_{joy/joy} & P_{joy/anger} & P_{joy/fear} & P_{joy/sadness} \\ P_{anger/joy} & P_{anger/anger} & P_{anger/fear} & P_{anger/sadness} \\ P_{fear/joy} & P_{fear/anger} & P_{fear/fear} & P_{fear/sadness} \\ P_{sadness/joy} & P_{sadness/anger} & P_{sadness/fear} & P_{sadness/sadness} \end{bmatrix}, \quad (3)$$

where $P_{A/B}$ is the probability of transition from state B to state A. Each value $P_{*/*}$ is initially set as basal values $q_{*/*}$, elements of matrix named Q which gives the basal state transition matrix (See Eq. 4). These values $P_{*/*}$ can be changed online by the influence of emotion-inducing factors: $\alpha, \beta, \gamma,$ and δ for joy, anger, fear, and sadness, respectively. These factors vary depending on the internal state and information given by certain other robots and have the role to stimulate each emotion. For example, the probability of state transition from joy to other state expressed by the following equations:

$$\begin{aligned} P_{anger/joy} &= q_{anger/joy} + (\beta - \alpha) q_{anger/joy} \\ P_{fear/joy} &= q_{fear/joy} + (\gamma - \alpha) q_{fear/joy} \\ P_{sadness/joy} &= q_{sadness/joy} + (\delta - \alpha) q_{sadness/joy} \\ P_{joy/joy} &= 1.0 - (P_{anger/joy} + P_{fear/joy} + P_{sadness/joy}) \end{aligned} \quad (4)$$

The emotional state Y is used to determine the behavior.

3 A Behavior Selection System

The proposed behavior selection system is achieved by incorporating the Markovian emotional model described in section 2 into a general action selection system. The overall structure of the system can be shown in Fig.2. The system consists of five modules, cognition, database, emotion, behavior selection, and behavioral system. The cognition module performs recognition and mapping of the environment. The map created by the cognition module is recorded in the database module. Then, the cognition module determines emotion-inducing factors ($\alpha, \beta, \gamma, \delta$). For example, these factors are determined based on remaining battery capacity, the number of frontiers and the emotional state of other robots in communicable area. The emotion module generates and updates the emotional state Y by Eq.1, changing C by emotion-inducing factors determined by the cognition module, and transfers it to the behavior selection module. The behavior selection module determines the behavior selection probability vector X by Eq.5:

$$X_{k+1} = AY_{k+1} + V_{k+1}, \quad (5)$$

where X_{k+1} consists of probabilities of next actions. A expresses the probability transition matrix and is predefined. The parameter vector V that affects instinctive action selection is generated by the cognition module. The reason for adding V is if use of only a simple emotional transition model, it is difficult to realize behavior selections in accordance with the rules. For example, while charging of the battery, the selection probability of the particular behavior increases due to the rise in the transition probability of the joy. However, it will be more efficiency, waiting until the completion of the charging. A behavior is selected stochastically according to the selection probability of each behavior. The behavioral system module generates a control input u taking into account the posture of the robot received from the cognition module to perform the action that has already been decided.

In this model, the policy of behavior selection depends on transition matrices of Q and A. By adjusting the parameters being included in these Matrices, it becomes possible to make various methods for behavior selection.

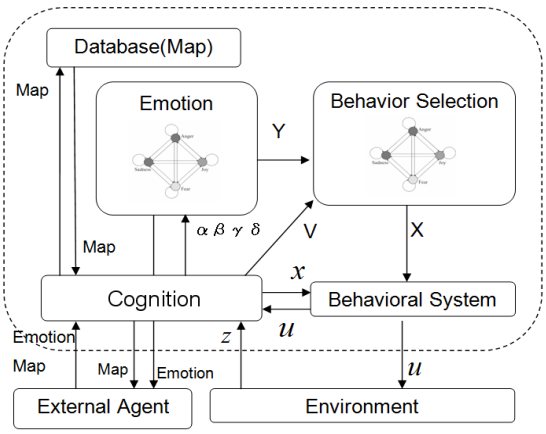

Fig. 2. A behavior selection system proposed here

4 Simulation

The simulation was performed with a simulator which we developed independently. The purpose of the simulation is to identify an unknown environment by multi-agent. In the simulation, a mapping method was simplified under the assumption that the robot is able to exact mapping. So, the environment was represented by a set of cells, and the robot transitioned between cells (Fig.3). First, transition matrices whose value was manually set was used and the proposed system evaluated by the result. Second, GA was introduced to parameter setting, to automatically optimize the behavior selection.

4.1 Common term

The environment was constituted by "Passage" where the robot can reach and "Wall" where the robot cannot

© ISAROB 2013

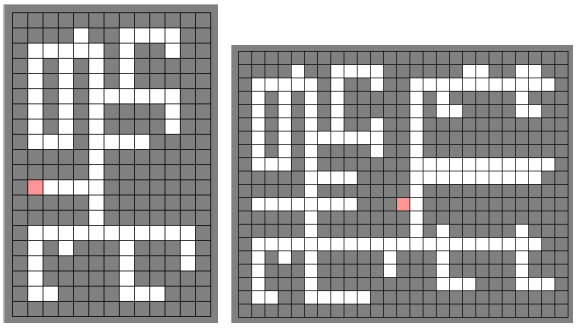

Fig. 3. Environments used for exploration

reach (Fig. 3). The following terms are assumed about robots: i) The robot gets the local coordinate information; ii) The robot can move to four neighboring cells adjacent to the location in the action of one step. However, if the destination is "Wall", it does not change the coordinates; iii) The robot can perceive eight neighboring cells adjacent to the location as the information from the sensor; iv) During the search, the robot creates a local map of its own, and shares the map with other robots exist in the predetermined distance; v) There is a base point in the environment, the robot starts from the base point, and then returns to it; vi) The robot consumes battery by moving, it cannot do *a*ny behavior if there is no amount of battery. When all robots return to the base point and all passages in the environment are visited simulation will be terminated.

Each robot selects one of the following four behaviors "search", "confirmation", "wait" and "return", and determines the destination based on concepts of the behavior. The "search" is an action which sets the most valuable frontier area to destination by referring to the map. At this action, the robot does not select the area which is already mapped by other robots. The worth exploring of the area is determined depending on the distance and the number of unmapped areas around it. The "confirmation" sets the area that the robot has not done mapping in its own to destination even if the area has already been mapped by the other robots. The "return" means to return to the base point by the shortest route which is derived from the map. The robot learns the knowledge about the environment by creating a local map. By doing this, it is possible to calculate the shortest route to the target by using a graph search algorithm.

4.2 The identification simulation of the unknown environment by the proposed method

The simulation which deals with the task for identification of unknown environment by three robots using the proposed method was performed. First the result of simulation for the narrow environment (left in Fig. 3), and then for the wider environment (right in Fig. 3) are

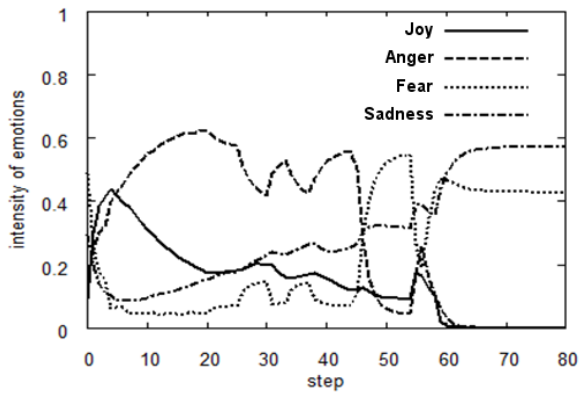

(a) Emotional Intensity vs step

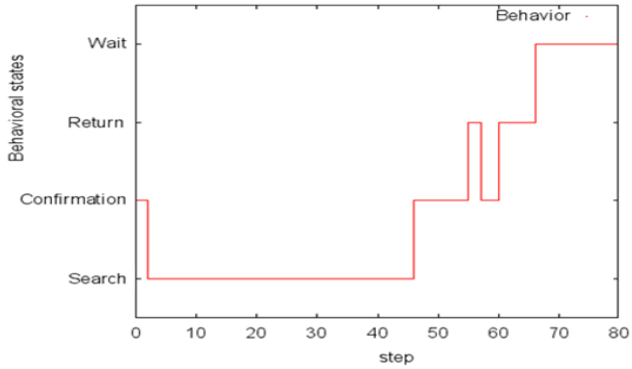

(b)Behavioral state vs step

Fig. 4. Relationship between emotional state and behavioral state

described. In these simulations, Q and A were set manually by trial and error. The emotional state transition of one robot out of three in simulation for narrow environment is shown in Fig. 4(a), and the behavioral state transition is shown in Fig. 4(b). By comparison of state transitions of the emotion and the behavior, it is apparent that the emotional state was reflected to the behavior selection. For example, in the vicinity of step 50, the behavioral state changed from "search" to "confirmation" with increasing the probability of the "Fear". The reason for this is because the robot had finished mapping of all areas in the vicinity of him, and changed the target to the area that was allocated to the other robots.

Next, the simulation was performed for the wider environment. In this case, the robot needs returning to the base point during one trial, for charging battery. At this time, the number of visited areas by each robot was 33, 34, 33, respectively, and this result shows that three robots shared target areas equally.

These results showed that the Markov emotional model worked properly.

4.3 Parameter setting by GA

Next, the transition matrix A and Q were optimized in proposed system by GA. 80 individuals were used. Five environments with different sizes and structures were

© ISAROB 2013

prepared, the four was for learning and the other was for test. Fitness was determined by degree of achievement, the time required for attainment, and the consumption of the battery and such. So the higher the fitness became, the less the energy consumption and the amount of time spent by the end of the task were.

The result performed under five environments using excellent individual parameters in the last generation was compared with the result of the parameters set manually. Fig. 5 shows the average value of the number of steps required to finish the task in 100 trials each. As a result, it was confirmed that the methods for determining the behavior using the parameters optimized by GA was better than those of manual parameter setting.

Then the change in the number of areas which were already visited was observed in the environment 1. As a method for comparison of the proposed method, the search algorithm (named "conventional") was prepared, that determines behavior sequentially from the number of areas not visited yet. Fig. 6 shows the changes in the average number of visited area of 100 trials, respectively, for two types of the proposed methods (settings of parameters by GA or manually) or the conventional method. Stagnation of the change in the graph results from the interruption of the task due to the charging of the battery. Comparing steps required to map all the 149 passages, it is clear from the graph that the proposed method using GA is the smallest. Observing the behavior of robots during the simulation in the conventional method, we found there were inefficient behaviors, for example, multiple agents charged batteries at the same time or set the unreachable area as a destination. On the other hand, in the proposed methods, the robots charged batteries in a timely manner and shared the roles efficiently.

5 CONCLUSION

In this paper, we proposed a method of a robot's behavioral plan using a Markovian emotional model for identifying an unknown environment by multi-agent. The simulation was performed with the simulator which we have developed independently. The results showed that valid action decisions were made by the proposed system. The policy of robot's behavioral decision depends on the parameters being included in basal parameter matrix Q and A. By adjusting these parameters, it is possible to make various plans for determining the robot's behavior. The optimization of the parameters was performed through the use of genetic algorithm. From the results, it became clear that the optimization of the parameters by GA led more

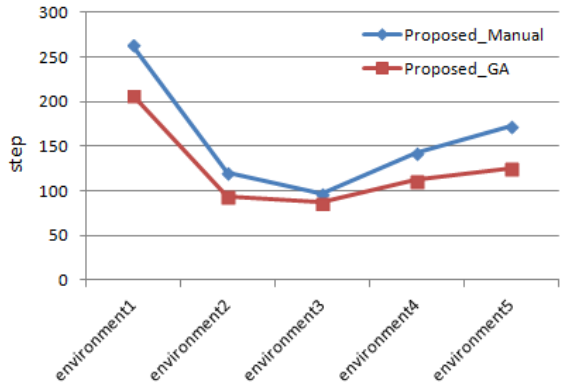

Fig. 5. Average step

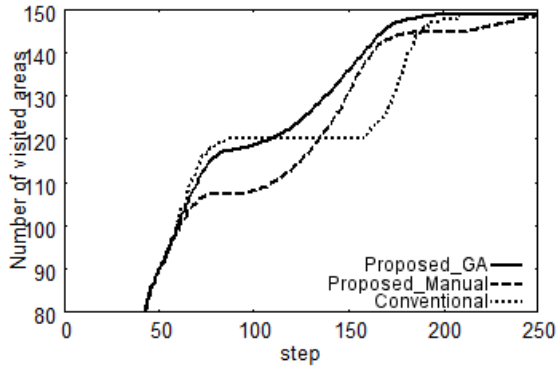

Fig. 6. Average number of areas visited vs step

sophisticated methods of robot's behavioral plan than setting the parameters manually.

In this study, the basis of evaluation was such factor as the search time and so on, however there are various optimal solutions depending on the purpose of the task. By setting the fitness function in line with objectives of those tasks, it is possible to automatically design the methods for determining the behavior of agents in the proposed system. The basal parameters optimized by genetic algorithm were treated as the parameters that were common to all agents. As future works, we think it is possible to find a new optimal solution by giving the different personality to different agent which may be realized by performing different parameter settings for each agent.

REFERENCES

[1] J.Moren, C.Balkenius (2001), A computational Model of Emotional Learning in the Amygdla, Cybernetics and System32(6), pp.611-636

[2] Even Daglarli, Hakan Tameltas, Murat Yesiloglu (2009), Behavioral task processing for cognitive robots using artificial emotions, Neurocomputing 72, pp.2835-2844

[3] Christopher P. Lee-Johnson and Dale A. Carnegie, Senior (2010), : "Mobile Robot Navigation Modulated by Artificial Emotions", CYBERNETICS, VOL. 40, NO. 2, pp.469-480

[4] Francois Michaud (2002), EMIB-Computational Architecture Based on Emotion and Motivation for Intentional Selection and Configuration of Behavior-Producing Modules", Cognitive Science Quarterly

[5] Sajal Chandra Banik, Keigo Watanabe, Kiyotaka Izumi (2008), Improvement of group performance of job distributed mobile robots by an emotionally biased control system", Artificial Life Robotics(12), pp.245-249

The Eighteenth International Symposium on Artificial Life and Robotics 2013 (AROB 18th '13),
Daejeon Convention Center, Daejeon, Korea, January 30-February 1, 2013

Design of a user-support system for finding the other person talking on smart phones

Hiroyuki Nishiyama[1] and Fumio Mizoguchi[1]

[1] Faculty of Sci. and Tech. Tokyo University of Science
2641 Yamazaki, Noda-shi, CHIBA, 278-8510, Japan
(Tel: +81-47122-1106; Fax: +81-47122-1106)
(hiroyuki@rs.noda.tus.ac.jp, mizo@wisdomtex.com)

Abstract: In this paper, we have designed a user-support system for finding the other person using smart phones. When users of this system talk over smart phones, it displays a map on the screen showing locations of both talkers as they share position information (GPS information) via a support server. Using this system, the user can check where to wait for other persons. It also enables the user to search for a lost child or to search for an illiterate person who wandered off and can't return. In our system, the position of searchers is also displayed on the terminal of the person being searched for, so the child or illiterate person can check the searcher's position on the screen of the smart phone in real time while talking.

Keywords: User Support System, Smart Phone, GPS

1 INTRODUCTION

Recently, many multifunctional cellular phone terminals, such as smart phones (e.g., Androids and iPhones), have been developed as a result of the evolution of the computer, network infrastructure, and lightweight battery technology. Thus, the number of users is rapidly increasing [4]. The smart phone is equipped with various sensor systems (e.g., GPS, an acceleration sensor and an infrared sensor). Furthermore, easily programmed applications acquire input from each function. Various research activities and services are provided by a smart phone using such features [1, 2, 3, 6]. Examples are the study of service applications using the GPS function such as car navigation systems and store searching services, so various location-based services have been developed [6]. In addition, one service can locate the person being talked to on a map through advanced mutual registration among users. These services are realized by making maximum use of the GPS function in a smart phone, but the telephone call function is not utilized. A user checks where the other person on the phone or a telephone call location is after completing the telephone call.

We have therefore designed a user-support system for finding the other person using smart phones. When users of this system talk over smart phones, it displays a map on the screen showing locations of both talkers as they share position information (GPS information) via a support server. Using this system, the user can check where to wait for other persons. It also enables the user to search for a lost child or to search for an illiterate person who wandered off and can't return. In our system, the position of searchers is also displayed on the terminal of the person being searched for, so the child or illiterate person can check the searcher's position on the screen of the smart phone in real time while talking.

In this research, we designed a function to manage the position information using the smart phone's GPS, a function to manage a telephone call, and a support server that enables information sharing between smart phones. The function to manage a telephone call records the telephone number of the caller and the called persons. The support server recognizes the connection as a key for the telephone number information and determines the positions by sharing GPS information. A map showing the caller's position and that of the called person is then displayed on the screens of the smart phones during the telephone call.

2 SMART PHONE

In our study, we use HTC Desire SoftBank X06HT as a smart phone (Android phone). The smart phone is similar to a small laptop personal computer. However, a smart phone has a telephone call function, and it is easy to carry because it is small and light. Its display is rather small, and it does not have a keyboard. Moreover, the development of an Android smart phone is comparatively easy because the development language basically conforms to Java in the Android application. In our research, we regard a smart phone as a general portable computer terminal that has a telephone call function, and enable cooperation with the various personal computer terminals that the user uses.

2.1 Communication Facility of the Smart Phone

Some kinds of communication facilities can be used with the smart phone. The wireless LAN is a wireless communications function that can communicated at a maximum speed of 54Mbps, which the computer terminal uses. Its use requires a connection to a wireless LAN router. 3G high speed

© ISAROB 2013

is basically a communication facility intended for the cellular phone, and the wireless communications function can communicate at a speed of 7.2Mbps or less. Its use requires a contract with the communication enterprise, and the cost corresponds to the wire traffic. Bluetooth is a wireless communications function that connects to a computer terminal by a PtoP connection and can communicate at a maximum speed of 2.1Mbps. Connection requires paired setting with a connected terminal (only once).

2.2 API for Telephone Use

By using API [5], the Android application can call another phone and recognize the use state of its own phone. Additionally, API (android.telephony.TelephonyManager) dynamically identifies calling and receiving, and the following information can be collected.

- Ringing State (CALL_STATE_RINGING):

  The ringing state is the state by which a telephone call is received. The calling person's telephone number can be identified.

- Off-hook State (CALL_STATE_OFFHOOK):

  When the telephone receiver is raised in response to a received call, the ringing state changes to the off-hook state. It can be assumed that the smart phone is calling another phone when the idle state changes to the off-hook state.

- Idle State (CALL_STATE_IDLE) :

  A change from the ringing state to the idle state of the standby mode means no response to a call. A change from the off-hook state to the idle state means the telephone call ended.

The API is a function basically intended for receiving; when sending, not much information can be obtained. The obtained information involves calling and ending only, and the telephone number and whether it was possible to talk over the telephone cannot be confirmed. Therefore, it is necessary to acquire information about the calling telephone number and the calling person's response after the end of telephone call by using the API (android.provider.CallLog.Calls) to acquire the vita information prepared for the Android phone.

2.3 GPS Function and API of the Android Phone

The Android phone has a GPS function and a variety of other sensor systems (e.g., acceleration sensor, brightness sensor, and temperature sensor). GPS and each sensor can confirm a change of sensor value by using the sensor manager API (android.location.LocationManager, android.hardware.SensorManager, etc.). It is also possible to

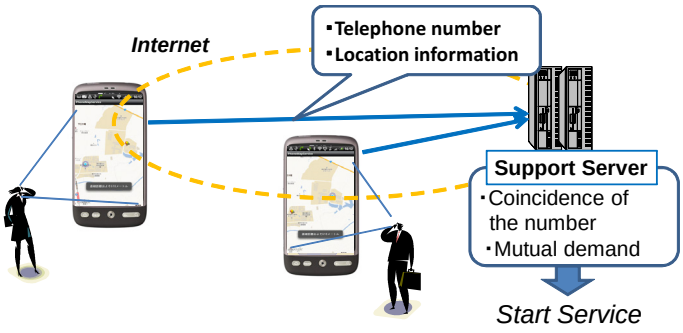

Fig. 1. Illustration of using our system

use android API (com.google.android.maps.*), which displays its location information on a map easily in combination with a Google map.

3 SYSTEM ARCHITECTURE

In our research, we designed a user-support system for finding the other party using smart phones. When users of this system talk over smart phones, the system displays a map on the screen showing locations of both talkers as they share position information (GPS information) via a support server (such as Fig. 1). Using this system, the user can determine where to wait for other persons. In our system, the position of searchers is also displayed on the terminal of the person being searched for, so the user and other person can check each other's position on the smart phone screen in real time while talking.

In this research, we designed a function to manage the position information using the smart phone's GPS, a function to manage a telephone call, and a support server that enables information sharing between smart phones. The function to manage a telephone call records the telephone number of the caller and the called persons. The support server recognizes the connection as a key for the telephone number information and determines the positions by sharing GPS information. A map showing the caller's position and that of the called person is then displayed on the screens of the smart phones during the telephone call.

Figure 2 depicts the structure of the user-support system for finding the other party using smart phones. The modules in this system have the following roles.

- The Telephone Monitor Module monitors the transmission and reception of a telephone. This monitor informs the User Support Module when a telephone call is transmitted or received; it also informs the User Support Module when the call is terminated.

- The User Support Module transmits a request for map-sharing service to the Support Server by using the

© ISAROB 2013

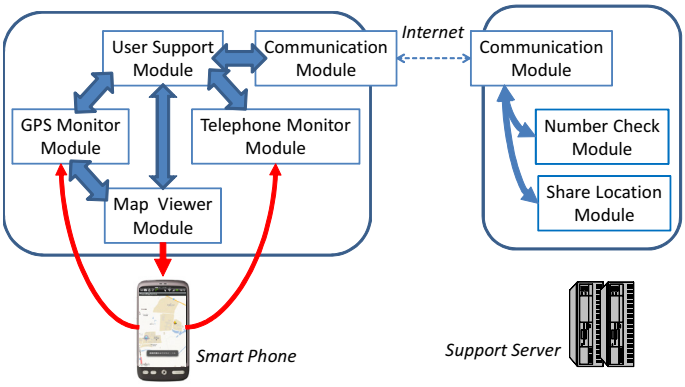

Fig. 2. Structure of the user-support system for finding the other party talking over smart phones

caller's and the called person's telephone number as a key when transmission or reception information is received from the Telephone Monitor Module. During map-sharing service, the partner's GPS information is received from the Support Server, which it then transmits to the Map Viewer Module. This module receives the caller's GPS information from the GPS Monitor Module and transmits it to the Support Server. This module terminates map-sharing service when the telephone call is terminated.

- The GPS Monitor Module continues monitoring own GPS location information during map-sharing service. When location information changes, this module reports the change to the Map Viewer Module and the User Support Module.
- The Map Viewer Module displays a circumference map during map sharing service, and displays the location of the caller and the called party on the map. This module also displays the distance brtween the parties.
- The Communication module functions as an agent between the Smart Phone and Support Server through the Internet.
- The Number Check Module receives the request from the User Support Module of the Smart Phone in the Support Server. This module determines which Smart Phone made the telephone call by detecting the combination of the caller's called party's telephone numbers and starts the map-sharing service.
- The Share Location Module exchanges location information between the Smart Phones engaged in the telephone call during map-sharing service.

4 SYSTEM IMPLEMENTATION

In order to achieve the system depicted in Fig. 2, we implemented each module on the smart phone (Android phone) and a server machine. Each module in the Android phone can be implemented using Android SDK [5] via a computer terminal. Since the programming language is basically similar to Java, we used Java language for implementing all modules.

4.1 User support tool on the Android Phone

The telephone monitor module dynamically monitors the telephone call using the Android telephone API described in section 2.2. When the situation changes, this module sends information to the user support module with additional information (e.g., telephone number).

The GPS monitor module dynamically monitors the location of the smart phone using the Android GPS API described in section 2.3. This module checks location information (latitude and longitude) for every second.

Based on the caller's and called party's location information, the map viewer module creates a map and displays it on the smart phone screen. Map information is created and displayed using the Android GPS API described in section 2.3. The map scale is automatically adjusted so that both parties in the telephone conversation can be indicated on the map.

The user support module consists of the state change rule for starting map sharing service automatically according to the use situation of a user's telephone. By recognizing telephone call transmission or reception, this module requests the support server to initiate the map-sharing service through the communication module. In addition, in the present configuration, the user support module judges whether the service is used for the caller her/himself. After service starts, this module shares location information with the other party through the communication module and the support server.

The communication module exchanges messages with the support server using socket communication (a smart phone becomes the client side of socket communication). This communication can use either Wi-fi or 3G communications.

4.2 Support Server on a Server Machine

The number check module compares the telephone numbers of the caller and the called parties and uses the telephone numbers to specify the intended user. This is possible because the telephone monitor module can identify both the caller's and the called party's telephone number.

The share location module exchanges position information over the smart phones identified by the number check module. This function terminates when the telephone call ends.

The communication module exchanges messages with the support server using socket communication (the Support Server becomes the server side of socket communication).

© ISAROB 2013

(a) Start (b) moving (c) Finding and meeting

Fig. 3. Flow of our system. The users can check the location of the other party on the map while talking and moving, until they find each other and meet.

4.3 Flow of User Support via Map Sharing

By using our user support system, the called party can access the map sharing service during the telephone call as in figure 3. Figure 3 depicts using our user support system to meet a new enrollee at the main front gate of our university. At this time, the new enrollee has arrived at another gate instead of the main gate (Fig3(a)). The user talks to the enrollee over the telephone and moves around the campus (Fig. 3(b)) until finding and meeting the enrollee (Fig. 3(c)).

Figure 3 is displayed on both caller's and the called party's smart phone, so the called party can confirm that the user her/himself approaches talking over the telephone. Moreover, the separation distance can also be displayed, so it is possible to estimate the time of meeting. In general, such service is useful and also enables the user to search for a lost child or for a mentally incapacitated person who has wandered off and can't return by themselves.

5 CONCLUSION

In this paper, we have designed a user-support system for finding the other person using smart phones. When users of this system talk over smart phones, it displays a map on the screen showing locations of both talkers as they share position information (GPS information) via a support server. Using this system, the user can check where to wait for other persons. In our system, we designed a function to manage the position information using the smart phone's GPS, a function to manage a telephone call, and a support server that enables information sharing between smart phones. The function to manage a telephone call records the telephone number of the caller and the called persons. The support server recognizes the connection as a key for the telephone number information and determines the positions by sharing GPS information. A map showing the caller's position and that of the called person is then displayed on the screens of the smart phones during the telephone call. It also enables the user to search for a lost child or to search for an illiterate person who wandered off and can't return. In our system, the position of searchers is also displayed on the terminal of the person being searched for, so the child or a mentally incapacitated person can check the searcher's position on the screen of the smart phone in real time while talking.

REFERENCES

[1] H. Nishiyama and F. Mizoguchi: Design of a User-Support System for Vision Information Using Smart Phone, International Journal of Artificial Life and Robotics, 2012 (to appear).

[2] H. Nishiyama and F. Mizoguchi: Design of a Cognitive User-Support System for Skin Progress Analysis Using a Smart Phone, The 11th IEEE International Conference on COGNITIVE INFORMATICS & COGNITIVE COMPUTING: ICCI*CC 2012, pp.203-210, 2012.

[3] H. Nishiyama and F. Mizoguchi: The Design of Personal Support System in Telephone Correspondence using Smart Phone, 16th International Symposium on Artificial Life and Robotics 2011, pp.745-748, 2011.

[4] Mobile Content Forum: *Smart Phone White Paper 2012*, Impress R&D, 2012. [in Japanese]

[5] Android SDK Guide, http://www.android.com/

[6] Sekai Camera: http://sekaicamera.com/

Epilepsy Diagnosis Using PSO based ANN

Nesibe Yalçın[1], Cihan Karakuzu[1], Gülay Tezel[2]

[1] Bilecik Şeyh Edebali University, Turkey
[2] Selçuk University, Turkey
(Tel: 90-228-214-1412)

[1]nesibe.yalcin@bilecik.edu.tr

Abstract: Electroencephalogram (EEG) is used routinely for diagnosis of diseases occurring in the brain. It is a very useful clinical tool in classification of epileptic attacks and epilepsy diagnosis. In this paper, epilepsy diagnosis by evaluation of EEG records is presented. Artificial Neural Networks (ANN) is used as a classification technique. Particle Swarm Optimization (PSO) method, which doesn't require gradient calculation, derivative information and any solution of differential equations is preferred for ANN training. This training method is compared with back propagation algorithm, which is one of the traditional methods, and the results are interpreted. In case of using the PSO algorithm, the training and test classification accuracies are %99.67 and %100, respectively. PSO based neural network model (PSONN) has a better classification accuracy than back-propagation neural network model (BPNN) for epilepsy diagnosis.

Keywords: Artificial neural networks, back propagation algorithm, EEG, epilepsy diagnosis, particle swarm optimization.

1 INTRODUCTION

Epilepsy disease is a major brain disorder. Particularly, waveforms contained in EEG recorded during the occurrence of epileptic discharges can show similarity with waveforms of some other diseases occurring in the brain. So epilepsy disease cannot be detected easily [1]. EEG signals as shown in Fig. 1. and Fig. 2. are not periodic; their frequency, phase and amplitude continuously change. The changing forms of EEG signals are very complex and difficult to define and interpret [2], [3].

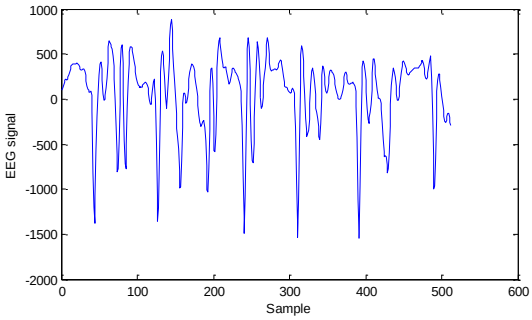

Fig. 1. Example of EEG signal for an epileptic person

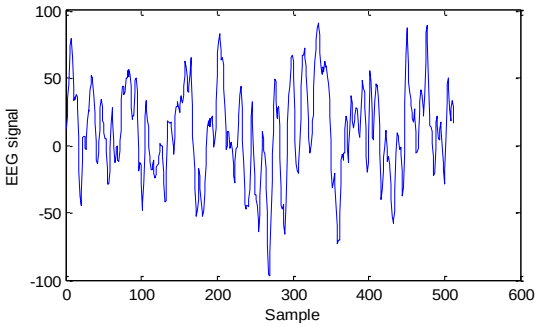

Fig. 2. Example of EEG signal for a healthy person

In recent years, there have been lots of studies using artificial intelligence techniques to recognize EEG signals. ANN as an artificial intelligence technique is used frequently in the classification of EEG signals. In addition to these techniques, heuristic optimization methods are used to increase the success, performance and / or the speed of these techniques. PSO which is one of the heuristic methods is successfully applied to the training of ANN. Because number of PSO parameters is small, PSO studies with real numbers, its realization and implementation are easy [4].

In this work, we aimed to able to diagnose epilepsy whether evaluate automatically EEG records with PSO based ANN. For this purpose, EEG signals taken from epileptic and healthy volunteers are normalized and then classified with ANN. PSO algorithm is used for training of ANN (PSONN) and performance of PSONN is compared with traditional ANN trained using back propagation algorithm (BPNN).

Following this introduction section, the rest of the paper is organized as follows: in the next section, materials and methods used in this study have been mentioned. In the third section, the ANN's trained with back propagation algorithm and the PSO method are emphasized. The fourth section provides information on the applications. The obtained results are presented with tables and the comparisons. The final section summarizes and concludes the results.

© ISAROB 2013

2 MATERIAL AND METHODS

2.1 EEG dataset

In this study, we used publicly available EEG data which is described in [5]. The complete data consists of five sets: Set A and Set B include data that has been taken healthy volunteers with eyes open and closed respectively. Set C and Set D taken from people, having epilepsy disease contain activities which has been measured in the interval has no attack. Set E includes only epileptic attack activities [5, 6].

Set A and Set E have been used in this work. Dataset consists of 1600 segments (800 segments for each class (epileptic and healthy)) and 512 samples for each segment. Dataset has been pre-processed using statistical features which are minimum, maximum, mean and standard deviation of each sample and thus number of samples in each segment has been reduced to 4. Then the new dataset has been normalized into the interval of [0, 1].

2.2 Neural network learned by back propagation (B PNN)

Back propagation [7], is one of error correction algorithms, is used in multi layer and feed forward ANN's training. A multi-layer back propagation network includes an input layer, at least one hidden layer and an output layer. Back propagation algorithm is a supervised learning method and aims to optimize weights and biases between input layer and the output layer depending on output error of the network. Input vector is given to input layer, and then reaches to the final output layer after passing through hidden layers. Each neuron in the network transmits the result to the all neurons of the next layer after receiving the arithmetical addition of the weighted signal from the previous layer's neurons, depending on the activation function.

ANN's training by back propagation is implemented consistently forward computing seen in Fig. 3. and backward computing given in Fig. 4.

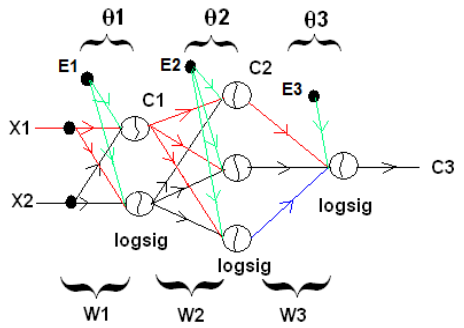

Fig. 3. Forward computing schematic structure

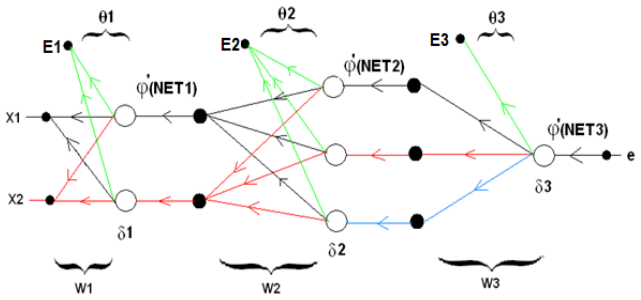

Fig. 4. Backward computing schematic structure (transpose network)

In Fig. 3., X1 and X2 are inputs; C1, C2 and C3 are output vectors of the layers. In Fig. 3. and Fig. 4., W1 and W2 are weight matrixes; W3, θ1, θ2 and θ3 are bias vectors; values of E1, E2 and E3 biases are chosen as 1. NET1, NET2 and NET3 are net input vectors for the related layer. sigmoid activation function φ is preferred for all neurons. φ' is derivative of the activation function. δ1, δ2 and δ3 are local gradient vectors.

2.3 Neural network learned by PSO (PSONN)

Particle swarm optimization (PSO) which is a heuristic method based on social behavior of bird flocking was developed by Eberhart and Kennedy in 1995 [8].

PSO algorithm starts with a set of random particles (candidate solutions for the problem) and then searches for an optimal solution updating its individuals by generations. In each generation, each particle is updated based on two special particles. The first one called "pbest" is the personal best particle for each particle found so far. The other one called "gbest" is a global best particle found so far by any particle in the swarm (population). Fig. 5. illustrates position and velocity updating of a particle.

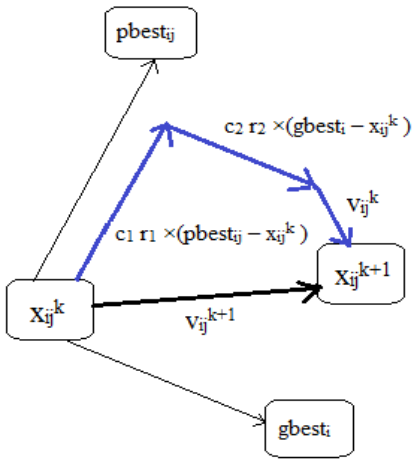

Fig. 5. The velocity and position updating of a particle

© ISAROB 2013

In Fig. 5., v_{ij} and x_{ij} variables are respectively the *j*th (j=1, 2, ..., D) velocity component and the *j*th position component of *i*th (i=1, 2, 3, …, N) particle at generation k. N is the number of particles in the swarm. D is dimension size of the search space. In an improved PSO version, the velocity updating and the position updating are determined by (1) and (2), respectively. In these equations, r_1 and r_2 are two random numbers uniformly distributed in the range of (0, 1). c_1 and c_2 are acceleration constants. w is inertia weight updated using (3) by generations. α variable in (3) is decrease factor and used to decrease linearly inertia weight.

$$v_{ij}^{k+1} = w^k v_{ij}^k + c_1 r_1 (pbest_{ij} - x_{ij}^k) + c_2 r_2 (gbest_i - x_{ij}^k) \quad (1)$$

$$x_{ij}^{k+1} = x_{ij}^k + v_{ij}^{k+1} \quad (2)$$

$$w^{k+1} = \alpha w^k \quad (3)$$

Limitations (V_{min} and V_{max}) defined in (4) determine the minimum and maximum velocity change of a particle during one generation. They are used to supply detailed searching, to allow the particles to escape local minima and to prevent the particles to leave the space research.

$$v_{ij}^{k+1} = \begin{cases} v_{ij}^{k+1}, & V_{min} < v_{ij}^{k+1} < V_{max} \\ V_{min}, & v_{ij}^{k+1} \leq V_{min} \\ V_{max}, & V_{max} \leq v_{ij}^{k+1} \end{cases} \quad (4)$$

In this study, we used PSO for training of ANN to obtain the best classifier model. During the training phase, we computed fitness value of each particle using Mean Squared Error (MSE) by (5) where, S is the number of segments in the training dataset, *e* is the difference between expected and obtained output after presenting *i*th segment (data) to the network. Structure of a particle (P_i) of PSO to train ANN is used as shown by (6).

$$MSE = \frac{1}{2S} \sum_{i=0}^{S} e_i^2 \quad (5)$$

$$P_i = [W1^i{}_{11} W1^i{}_{12} \dots \theta 1^i{}_{11} \dots W2^i{}_{11} W2^i{}_{12} \dots \theta 2^i{}_{11} .. W3^i{}_1 \dots \theta 3^i{}_{11} \dots] \quad (6)$$

Algorithm's pseudo code is as following.

Initialize values for PSO and ANN
Initialize all weights with random values
Do
  for *each particle* ***do***
    Adjust weights according to the particle
    Present training dataset to ANN
    Calculate MSE of the particle
  end for
  fitness value of gbest=min(MSE of all particles)
  if *stop criteria is not provided* ***then***
    Update pbest and gbest particles
  end if
while *stop criteria (maximum generation number or target fitness value of gbest) is provided*
Adjust weights according to gbest particle
Present testing dataset to ANN
Calculate output

3 EXPERIMENTAL STUDIES

In this work, we used EEG dataset belonging to epileptic and healthy volunteers. Then dataset divided to two subsets: training dataset which was formed by 1200 segments (600 epileptic) and test dataset which was prepared as 400 segments (200 epileptic).

PSONN and BPNN models have been developed via Matlab® Software Package without Neural Network Toolbox. Training dataset has been used to train these network models. Each network has been prepared as three layers: an input layer, a hidden layer and an output layer. The different number of particles, generations and neurons in the hidden layer have been used to determine optimum network model. Optimum numbers of these parameters has been experimentally obtained as 30, 200 and 3, respectively.

In order to determine training and test accuracies, the classification threshold value has been selected as 0.4. If output value is lower than this value, the classification result is 0 or healthy else 1 or epileptic.

Initialization values of α and w in (3) are chosen 0.975 and 0.9, respectively [9]. Acceleration constants are $c_1 = c_2 = 2.1$. Limitations are $V_{min} = -0.1$ and $V_{max} = 0.1$. These values provided fast convergence to the target and increased the performance of network models.

Sensitivity, specificity and accuracy statistics are used frequently to determine the success of a classifier. Sensitivity is the proportion of data belonging to epileptic patients; specificity is the proportion of data belonging to healthy people; accuracy is true classification proportion [10]. These statistical measures are calculated by (7), (8) and (9).

$$\text{sensitivity} = \frac{TP}{TP+FN} \quad (7)$$

$$\text{specificity} = \frac{TN}{TN+FP} \quad (8)$$

$$\text{accuracy} = \frac{TP+TN}{TP+FP+TN+FN} \quad (9)$$

© ISAROB 2013

In the above equations, TP (True Positive) is the total number of epileptic patients which are correctly diagnosed, TN (True Negative) is the total number of healthy people which are correctly diagnosed, FP (False Positive) is the total number of epileptic patients which are incorrectly diagnosed, FN (False Negative) is the total number of healthy people which are incorrectly diagnosed.

PSONN is run 30 times for the training set. The classification accuracies and computed results of sensitivity and specificity analysis in the training and test dataset for BPNN and PSONN are given in Table1. The results about PSONNs are based on the best and worst run among 30 runs. The best, worst and average fitness values changing by generations are shown in Fig. 6.

Table 1. Performance of Comparison Networks

Performance Measures	Network Type		
	Best PSONN	Worst PSONN	BPNN
Fitness value of gbest / MSE	0.0041	0.2289	0.0009
Training classification acc.(%)	99.6667	50	99.8333
Test classification acc. (%)	100	50	90.7500
Training sensitivity	1	0.5	0.9967
Training specificity	0.9934	0	1
Testing sensitivity	1	0.5	0.8439
Testing specificity	1	0	1

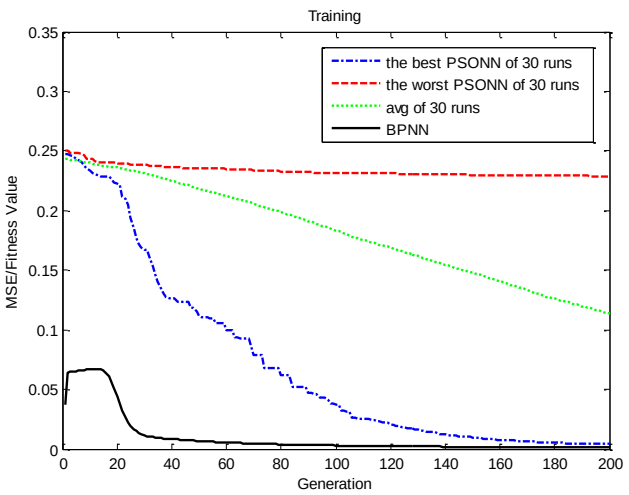

Fig. 6. Training graphics of PSONN and BPNN

4 CONCLUSION

In this work, PSO and back propagation (traditional) algorithms are used to train ANN for epilepsy diagnosis. Comparative results of PSONN and BPNN (traditional ANN) are presented in Table 1. According to table, training performance of BPNN is 99.83% and test performance of BPNN is 90.75%. Training and test classification results of best PSONN are too high (approximately 99.67% and 100%, respectively). The computed results of sensitivity analysis of PSONN are 1 in both the training and test dataset. Thus, it can be said PSONN is more successful than BPNN. PSONN can be adapted for different medical diagnosis problems and other PSO versions can be used to improve the success of the PSO as training algorithm.

This study shows any heuristic optimization method can be used as a learning algorithm to increase ANN's classification success.

REFERENCES

[1] Barışçı N, Müldür S (2003), Classification of epileptic EEG signals using neuro - fuzzy system. Journal of Polytechnic, vol. 6, No:2, pp. 445–449

[2] Toprak IB (2007), Analysis of EEG signals using the wavelet transform and artificial neural network. Süleyman Demirel University Graduate School of Applied and Natural Sciences, M.Sc. Thesis, Turkey

[3] Yazgan E, Korurek M (1996), Medikal Elektronik. ITU, Istanbul, No:15741, pp. 386

[4] Cavuslu MA, Karakuzu C, Karakaya F (2012), Neural identification of dynamic systems on FPGA with improved PSO learning. Applied Soft Computing, vol. 12, pp. 2707–2718

[5] Andrzejak RG, Lehnertz K, Mormann F, Rieke C, David P, Elger CE (2001), Indications of nonlinear deterministic and finite dimensional structures in time series of brain electrical activity: Dependence on recording region and brain state. Physical Review E, 64

[6] Tezel G, Özbay Y (2009), A new approach for epileptic seizure detection using adaptive neural network. Expert Systems with Applications, 36 (2009), pp. 172–180.

[7] Rumelhart D, McClelland J (1986), Parallel Distributed Processing. MIT Press, Cambridge, Mass

[8] Kennedy J, Eberhart RC (1995), Particle swarm optimization. Proc. IEEE int'l conf. on neural networks, IEEE service center, Piscataway, NJ, vol. 4, pp. 1942–1948

[9] Şevkli M, Yenisey MM (2006), A particle swarm optimization for the job shop scheduling problems. itüdergisi/d mühendislik, vol. 5, No: 2(1), pp. 58–68

[10] Özbeyaz A (2010), LS-SVM hyper parameter selection Based on PSO in EMG and EEG signals classification. University of Kahramanmaraş Sütçü Imam, Institute of Natural and Applied Sciences, Msc Thesis, Turkey.

The Eighteenth International Symposium on Artificial Life and Robotics 2013 (AROB 18th '13),
Daejeon Convention Center, Daejeon, Korea, January 30-February 1, 2013

The Effect of the Internal Parameters on Association Performance of A Chaotic Neural Network

Shun Watanabe[1], Takashi Kuremoto[1], Kunikazu Kobayashi[2], and Masanao Obayashi[1]

[1]Yamaguchi University, Japan
[2]Aichi Prefectural University, Japan
(Tel: +81-(0)836-85-9005, Fax: +81-(0)836-85-9016)
[1]{s005we, wu, m.obayas}@yamaguchi-u.ac.jp
[2]kobayashi@ist.aichi-pu-u.ac.jp

Abstract: The chaotic neural network (CNN) proposed by Aihara et al. is able recollect stored patterns dynamically. But there are difficult cases such as a long time processing of association, and difficult to recall a specific stored pattern during the dynamical associations. We have proposed to find the optimal parameters using meta-heuristics methods to improve association performance, for example, the shorter recalling time and higher recollection rates of stored patterns in our previous works. However, the relationship between the different values of parameters of chaotic neurons and the association performance of CNN was not investigated clearly. In this paper, we analyze how the change of values of internal parameters of chaotic neurons affects the characteristics of chaotic neurons when multiple patterns are stored in a CNN. Q-Q plot, least square approximation (LSM), hierarchical clustering (HC), and Hilbert transform (HT) are used to investigate the similarity of internal states of chaotic neurons, and to classify the neurons. Simulation results showed that the different values of the internal parameter yielded different behaviors of chaotic neurons and it suggests the optimal parameter which generates higher association performance may concern with the stored patterns of the CNN.

Keywords: chaotic neural network, Q-Q plot, least squares approximation, hierarchical clustering, Hilbert transform.

1 INTRODUCTION

The chaotic neural network (CNN) proposed by Aihara et al. is well-known as a recurrent neural network which is able to dynamically recollect stored patterns [1]. And CNN is applied to optimization, parallel distribution processing, robotics, and so on. In our previous works, we have proposed some meta-heuristic methods (e.g. genetic algorithm, particle swarm optimization) to determine the optimal parameters of chaotic neurons to realize higher performance of association memory of CNN [2] [3]. However, the causality between the determined parameters and the association ability was not investigated. In this paper, we intend to analyze how the varied internal states of chaotic neurons are yielded by the different parameters of neuron dynamics. The spatiotemporal change of the internal state of each chaotic neuron are observed, and the comparison of these time series data is given by kinds of methods such as Q-Q plot, least squares approximation (LSA), hierarchical clustering (HC), and Hilbert transform (HT). Q-Q plot, LSA, and HC is used to show the similarity between the dynamical changes of the internal states of chaotic neurons of CNN. HT is used to show the synchronization of neurons during association process. Associative simulation showed the change of the internal parameter affected the characteristics of neurons and the optimal parameter may concern with the stored patterns.

2 CHAOTIC NEURAL NETWORK

Aihara et al. 's chaotic neural network (CNN) is a kind of interconnected recurrent artificial neural network which neurons perform chaotic output. The dynamics of a chaotic neuron i of CNN is defined as follows:

$$\eta_i(t+1) = k_f \eta_i(t) + \sum_{i=0}^{N-1} w_{ij} x_j(t) \tag{1}$$

$$\zeta_i(t+1) = k_r \zeta_i(t) - \alpha x_i(t) + a \tag{2}$$

$$y_i(t+1) = \eta_i(t+1) + \zeta_i(t+1) \tag{3}$$

$$x_i(t+1) = \frac{1}{1+e^{-y_i(t+1)/\varepsilon}} \tag{4}$$

Where N is number of chaotic neurons in network, $\eta_i(t)$ and $\zeta_i(t)$ is internal state for the feedback inputs and refractoriness, k_f and k_r is the decay parameter for the feedback input and the refractoriness, w_{ij} is synaptic weights from *j*th neuron to *i*th neuron, α is refractory scaling parameter, a is threshold, $y_i(t)$ is internal state, $x_i(t)$ is chaotic neuron output, ε is steepness parameter. In this paper, the internal states of the chaotic neurons are limited to $y_i(t), i = 0,1,2,\ldots,N-1$ and the internal parameter k_r is investigated in detail.

Hebb learning rule is used to store patterns in CNN, that is, the synaptic weights between two arbitrary neurons is modified as following.

© ISAROB 2013

$$\Delta w_{ij} = \begin{cases} \beta \sum_{m=0}^{M-1} \chi_{mi} \chi_{mj} & if \quad i \neq j \\ 0 & otherwise \end{cases} \tag{5}$$

where $\beta = 1/M$ is learning coefficient, χ_{mi} is ith bipolar value of mth pattern, $m = 0,1,2,\ldots,M-1$.

3 FEATURE EXTRACTION

In this paper, Q-Q plot, least squares approximation (LSA), hierarchical clustering (HC), and Hilbert transform (HT) are used for analyzing the characteristics of the dynamical association in CNN. Firstly, Q-Q plot is used to compare the distribution types of each chaotic neuron internal sates in CNN. Secondly, the curve plotted by Q-Q plot is approximated to a function by LSA. Finally, the approximation errors and approximated parameters are clustered by HC, and the clustered data as the similarity between neurons is shown. Additionally, HT is used to observe the synchronization between internal states of chaotic neuron because the synchronization depends on time, is not able to be represented with the internal state distribution of each chaotic neuron.

3.1. Q-Q plot

Q-Q plot is a graphical method to represent the similarity and it's characteristics between the distributions of two data sets. When the elements of a data set are sorted in ascending order, are plotted on X-dimension in order, and the elements of another data set are plotted on Y-dimension either, then the correlation and the similarity of the two data sets are easily to be observed. If the plotted graph has linearity, it means that their data distributions are similarity. On other hand, if the graph has nonlinearity, it means that their data are not similarity. And the data those are equal to the other, are plotted on a line of the X-Y plane, i.e., a linear function that consists of one gradient coefficient and one bias. In this paper, similarities of all observed internal states of chaotic neurons in CNN are investigated using Q-Q plot.

3.2. Least squares approximation

Least squares approximation (LSA) is a method to find an approximate fitting function using samples of data set. In this paper, linear least square as a LSA method is used to quantitatively measure the plot graph (the sorted data set) in Q-Q plot mentioned in 3.1 section. A polynomial equation of the first degree (linear function) as an approximation function is used to measure the similarity (linearity) between the distributions of two data in Q-Q plot. The advantages of linear function are that squares error is less when the distributions of two data are similar. The similarity of the internal state distributions of neurons is evaluated by LSA here.

3.3. Hierarchical clustering

Hierarchical clustering (HC) is a clustering method that iteratively merges clusters in higher similarity. The method creates the clusters that have a tree-like structure. In this paper, the nearest neighbor method is used in HC and Euclidean distance as the degree of similarity of the internal state is used to classify the chaotic neurons. Shorter Euclidean distance represents higher similarity between two clusters. In this paper, the quantitative values calculated by LSA in Q-Q plot between each chaotic neuron and all are used in HC. So the similarity between the internal state distributions of each neuron are able to be represented in the tree-like structure of HC.

3.4. Hilbert transform

Hilbert transform (HT) is a transform technique to calculate the complex signal from an observed time series signal. In this paper, the complex signal is transformed from the internal state time series signal of each chaotic neuron in CNN. And the synchronization between neurons is observed with the complex signals. The method of HT is defined as follows:

$$y_i(t) \xrightarrow{FT} y_i(\omega) \tag{6}$$

$$y_i(\omega) = \mathrm{Re}[y_i(\omega)] + I\,\mathrm{Im}[y_i(\omega)] \tag{7}$$

$$y'_i(\omega) = \mathrm{Im}[y_i(\omega)] - I\,\mathrm{Re}[y_i(\omega)] \tag{8}$$

$$y'_i(\omega) \xrightarrow{FT^{-1}} y_{iH}(t) \tag{9}$$

where $y_i(t)$ is an observed signal, FT is Fourier transform, I is the imaginary unit, FT^{-1} is inverse Fourier transform, $y_{iH}(t)$ is the signal of HT.

The phase difference $\phi_i(t) - \phi_j(t)$ of two signals ($y_i(t), y_j(t)$) is calculated by the following equation:

$$\phi_i(t) - \phi_j(t) = \tan^{-1} \frac{y_{iH}(t) y_j(t) - y_i(t) y_{jH}(t)}{y_i(t) y_j(t) + y_{iH}(t) y_{jH}(t)} \tag{10}$$

4 COMPUTATER SIMULATIONS

The features of the internal states in CNN are observed when the value of the internal parameter k_r of CNN is different ($k_r = 0.9, k_r = 0.8$). Other parameters of the associative model are set as $N = 100$ (10x10 network), $\zeta_i(0) = 0$, $\eta_i(0) = 0$, $k_f = 0.2$, $\alpha = 10$, $a = 2$, $\varepsilon = 0.015$, $\beta = 0.25$. The stored patterns in CNN are "cross", "star", "triangle", and "wave" as shown in Fig.1. "initial" in Fig.1 means the initial state of CNN in

recollection process. The internal states of chaotic neurons in CNN were observed from $t = 2048$ to $t = 4095$ during a recalling.

The HC results of the case $k_r = 0.9$ (which is the value used in the original paper [1]) and the case $k_r = 0.8$ (which is an optional value used in this simulation) are shown in Fig.2 (a) and (b) respectively.

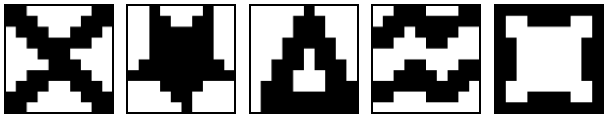

"cross" "star" "triangle" "wave" "initial"

Fig. 1. Stored patterns and initial pattern (width=10, height=10, black: $\chi_{mi} = -1$, white: $\chi_{mi} = +1$).

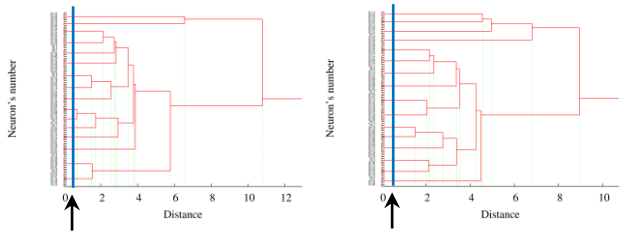

(a) $k_r = 0.9$ (b) $k_r = 0.8$

Fig. 2. The results of hierarchical clustering (HC).

In Fig. 2, 100 neurons are plotted on the vertical axis which orders are according to their clusters. When the distance between the clusters (horizontal axis) is the point with arrows in Fig.2 (a) and (b), the numbers of clusters are the same16, but neurons in those clusters are different when the parameter $k_r = 0.9$ and $k_r = 0.8$. Neurons in 16 clusters yielded by the different parameters are listed in Table 1 (a) and (b) respectively.

Table 1. The results of clustered neurons which internal states were similar during recollection using HC.

(a) $k_r = 0.9$

Cluster's No.	Neuron's No.
C0	23, 32, 45, 55, 66
C1	14, 15, 86
C2	33, 34, 37, 43, 44, 56
C3	3, 4, 20, 30, 31, 59, 70
C4	0, 1, 10, 28, 90
C5	16, 24, 25 53, 58, 68, 85
C6	8, 9, 11, 18, 19, 21, 80
C7	12, 17, 22, 27, 64, 65, 76
C8	46, 47, 52, 57, 84, 95
C9	82, 88, 89, 91, 98, 99
C10	2, 13, 69, 74, 75
C11	7, 42, 51, 60, 61
C12	71, 72, 77, 78, 81, 87
C13	5, 79, 83, 92, 93, 94, 96, 97
C14	6, 29, 38, 39, 40, 41, 48, 49, 50
C15	26, 35, 36, 54, 62, 63, 67, 73

(b) $k_r = 0.8$

Cluster's No.	Neuron's No.
C0	14, 15, 86
C1	71, 72, 77, 78, 81, 87
C2	7, 42, 51, 60, 61
C3	23, 32, 45, 55, 66
C4	46, 47, 52, 57, 84, 95
C5	12, 17, 22, 27, 64, 65, 76
C6	8, 9, 11, 18, 19, 21, 80
C7	5, 79, 83, 92, 93, 94, 96, 97
C8	26, 35, 36, 54, 62, 63, 67, 73
C9	6, 29, 38, 39, 40, 41, 48, 49, 50
C10	2, 13, 69, 74, 75
C11	82, 88, 89, 91, 98, 99
C12	16, 24, 25 53, 58, 68, 85
C13	3, 4, 20, 30, 31, 59, 70
C14	33, 34, 37, 43, 44, 56
C15	0, 1, 10, 28, 90

The phases between the neurons in the same cluster showed no any difference ($\phi_i(t) - \phi_j(t) = 0.0$). Fig. 3 shows some examples of the phase comparison using neuron No.23 in C0 via neuron No. 32, 45, 55, and 66 (The first raw in Table 1 (a) where $k_r = 0.9$), and No. 14 via No. 15, and 86 (The first raw in Table 1 (b) where $k_r = 0.8$). So the value of parameter k_r did not affect the synchronization of the neurons in the same cluster.

Fig. 4 shows the phase differences between the cluster C0 and other clusters (C1-C15). In Fig.4, the horizontal axis indicates the time of recollection, the vertical axis is the phase difference, and the depth axis corresponds to different clusters (from C1 to C15). So we can find that the phase difference happened between the neurons of different clusters. In other word, it can be conclude that the value of parameter k_r affected the synchronization of the neurons in the different clusters.

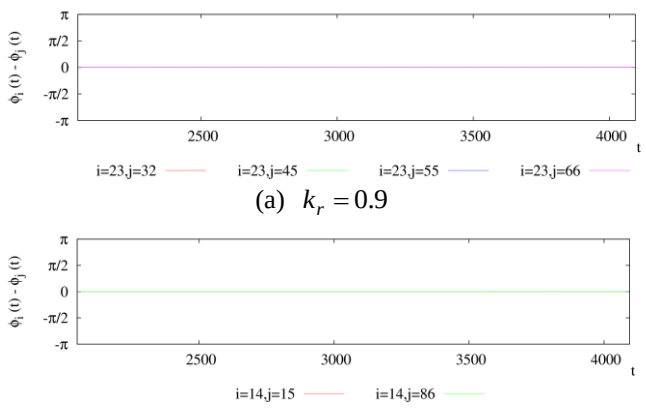

(a) $k_r = 0.9$

(b) $k_r = 0.8$

Fig. 3. The phase differences between the neurons of cluster C0.

© ISAROB 2013

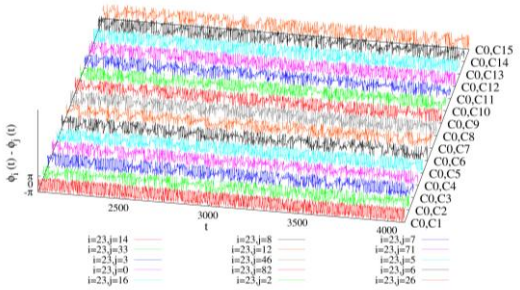

(a) $k_r = 0.9$

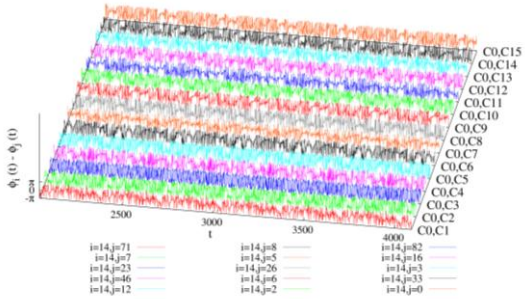

(b) $k_r = 0.8$

Fig. 4. The phase difference between the neurons of different clusters.

The maximum Lyapunov exponent of CNN with $k_r = 0.9$ was 0.290, and CNN with $k_r = 0.8$ was 0.245. Both values of them were positive, nearby zero. These maximum Lyapunov exponent suggested that either the CNN with $k_r = 0.9$ or the CNN with $k_r = 0.8$ were able to generate chaotic associative process, that is, dynamical attracts were available to appear. Table 3 shows the recalling times of the different stored patterns. The CNN with $k_r = 0.9$ which was used in [1] had a higher recalling rates.

Furthermore, to investigate the relationship between the stored patterns and the neuron spatial positions, we listed the output of neurons in 16 clusters, and it was interested that the number of clusters (i.e. 16) equaled to the number of the combination of stored patterns (see Table 4). For example, neuron No. 23, 32, 45, 55, and 66 in C0 when $k_r = 0.9$ and in C3 when $k_r = 0.8$, output "-1" when stored pattern "cross" was recalled. "+1", "+1", "-1" were output corresponding to the recalling of "star", "triangle" and "wave" respectively.

5 Conclusion

In this paper, we investigated the effect of the internal parameter of CNN on the association process. The spatiotemporal change of the internal states of neurons was used to show the difference yielded by the change of the value of the internal parameter. The chaotic neurons were clustered according to their similarity of internal states, and the characterization seemed affected by the parameter values. So these results support our previous works which suggested the importance of the optimal parameter for the dynamic association model CNNs.

Table 3. Recalling times of stored patterns of each CNN.

CNN	"cross"	"star"	"triangle"	"wave"	Total
k_r =0.9	6	2	8	14	30
k_r =0.8	0	7	12	0	19

Table 4. The causality between elements combinations of stored patterns and clustered neurons.

Neuron's output corresponding to the stored patterns (cross, star, triangle, wave)	Neuron's No.	Cluster (k_r 0.9)	Cluster (k_r 0.8)
-1, -1, -1, -1	26, 35, 36, 54, 62, 63, 67, 73	C15	C8
-1, -1, -1, +1	71, 72, 77, 78, 81, 87	C12	C1
-1, -1, +1, -1	33, 34, 37, 43, 44, 56	C2	C14
-1, +1, -1, -1	12, 17, 22, 27, 64, 65,76	C7	C5
+1, -1, -1, -1	16, 24, 25 53, 58, 68, 85	C5	C12
-1, -1, +1, +1	82, 88, 89, 91, 98, 99	C9	C11
-1, +1, -1, +1	8, 9, 11, 18, 19, 21, 80	C6	C6
-1, +1, +1, -1	23, 32, 45, 55, 66	C0	C3
+1, -1, -1, +1	14, 15, 86	C1	C0
+1, -1, +1, -1	46, 47, 52, 57, 84, 95	C8	C4
+1, +1, -1, -1	2, 13, 69, 74, 75	C10	C10
-1, +1, +1, +1	0, 1, 10, 28, 90	C4	C15
+1, -1, +1, +1	5, 79, 83, 92, 93, 94, 96, 97	C13	C7
+1, +1, -1, +1	3, 4, 20, 30, 31, 59, 70	C3	C13
+1, +1, +1, -1	7, 42, 51, 60, 61	C11	C2
+1, +1, +1, +1	6, 29, 38, 39, 40, 41, 48, 49, 50	C14	C9

REFERENCES

[1] Adachi M., Aihara K. (1997), Associative dynamics in a chaotic neural network, Neural Networks, 10(1):83-98

[2] Kuremoto T., Watanabe S., Kobayashi K., Feng. L.-B., and Obayashi M. (2011), Dynamical recollection of interconnected neural networks using meta-heuristics (in Japanese), IEEJ Transactions on Electronics, Information and Systems, 131(8):1475-1484

[3] Kuremoto T., Watanabe S., Kobayashi K., Feng. L.-B., and Obayashi M. (2012), Dynamical recollection of interconnected neural networks using meta-heuristics, Electronics and Communications in Japan, 95(6):12-23

© ISAROB 2013

The Eighteenth International Symposium on Artificial Life and Robotics 2013 (AROB 18th '13),
Daejeon Convention Center, Daejeon, Korea, January 30-February 1, 2013

An estimating method for missing values by using multiple SOMs

Yuui Kikuchi[1], Nobuhiro Okada[1], Yasutaka Tsuji[1], and Kazuo Kiguchi[1]

[1]Kyushu University, Japan
(Tel: 81-92-802-3167)

[1] 2TE11313R@s.kyushu-u.ac.jp

Abstract: Recently, development of information technology grows the importance of data analysis. In actual data, however, instances will sometimes miss some of their values. Then, how to deal such missing values has become one of the important subjects. Estimating and completing the missing values is required when analyzing the instances or attributes including the values. Using a self-organizing map (SOM) is one of such estimating method. This method is available for nonlinear data. In the data which lacks instances which are not including missing values, however, it was difficult to estimate such values by using conventional SOM method. To solve the problem, we propose a new method that uses multiple SOMs for estimating missing values. To evaluate our method, we performed simulation using proposed and other conventional methods. By the simulation results, we showed the advantages of our method.

Keywords: Self-Organizing Map, Data Processing, Missing Value

1 INTRODUCTION

In recent years, collection and accumulation of various data becomes very easy because of development of information technology. Due to this change, the importance of data mining is increasing. Data mining is the work finding the knowledge hid in data. In actual data, however, instances will sometimes miss some of their values for various reasons. Then, how to deal such missing values has become one of the important subjects in data analysis. In general, there are two methods to deal with them. One is the removing instances or attributes including the missing values, and another method is estimating and completing them. The latter method is required when analyzing the instances or attributes including the missing values. Such a method is also applicable to data prediction problems. In this method, at first, the features or the laws of whole data are led from a part of data except for the missing values. Then, the values are estimated basing on the features or the laws.

Prior research on missing values is manifold. Edgar [1] investigated removing method and some estimating method. He investigated their influence in data analysis also. Abe et al [2] compared some statistical-analysis techniques to estimate missing values. Using a self-organizing map (SOM) is one of estimating method. For example, Iwasaki et al [3] studied application SOM to estimating missing values in earthquake data.

The SOM is an artificial intelligence which is proposed by Kohonen [4], and it is applied to data analysis and various field [5]. This method is also available for nonlinear data. The SOM method is very useful, because actual data is frequently nonlinear. The same can be said about missing values estimation. In conventional SOM method, however, only instances which are not including missing values can be used for learning the features or the laws of whole data. Thus, in the data which lacks such instances, it is difficult to estimate missing values by using SOM.

In this paper, to solve the problem, we propose a new method that uses multiple SOMs for estimating missing values. This method can achieve effective estimation even for data which lacks instances not including missing values. Moreover, the system is still available for nonlinear data because of using SOMs. To evaluate our method, we performed simulation of estimating the missing values with incomplete data. From the simulation result, we proved that our method is more effective than some conventional method including a conventional SOM.

2 THE ESTIMATING METHOD BY SOM

In this section, we describe the method to estimate missing values by using conventional SOM. We explain SOM in the sections 2.1-2.3, and the estimating method in the section 2.4.

2.1 A summary of SOM

SOM is the algorithm which makes a map reflecting the features of high-dimensional input vectors. The map consists of neurons latticed in low-dimensional space. Thus, the position of the neuron on the map is expressed with the coordinates in low-dimensions. Each neuron has a reference vector. The reference vectors have same dimensions as input vectors. In algorithm of SOM, the reference vectors

© ISAROB 2013

are updated, whenever an input vector is presented. By repeating updating, a map gradually learns the feature of input vectors. After sufficient learning, the map reflects the features.

2.2 The algorithm of SOM

The algorithm of SOM is described below. For convenience, a number is assigned to each neuron and *i*-th neuron's reference vector is expressed as $\boldsymbol{m}_i$.

Each neuron is initialized by given an initial value to a reference vector. The value is determined at random or based on the result of principal component analysis (PCA).

When the vector $\boldsymbol{x}(t)$ is given as *t*-th input (*t*=1, 2...), a reference vector is updated in the following procedures.

$$||x(t)-m_c(t)|| = \min_i ||x(t)-m_i(t)|| \quad (1)$$

$$m_i(t+1) = m_i(t) + h_{ci}(t)\cdot\{x(t)-m_i(t)\} \quad (2)$$

At fast, a winning neuron which has the reference vector with the greatest similarity to $\boldsymbol{x}(t)$ is chosen from all neurons. The number of a winner is set to c. Then, $\boldsymbol{m}_i(t)$ is updated by equation (2). By updating, $\boldsymbol{m}_i$ is more similar to $\boldsymbol{x}(t)$. $h_{ci}(t)$ is the function of *t* and l_{ci} which is distance in the map from c-th neuron to i-th neuron. An example of $h_{ci}(t)$ using a Gaussian function is shown below.

$$h_{ci}(t) = \alpha(t)\cdot\exp[-l_{ci}^2/\{2\sigma^2(t)\}] \quad (3)$$

$\boldsymbol{m}_i$ of the neuron near a winner on the map changes a lot. As learning proceed, $\alpha(t)$ and $\sigma(t)$ is gradually decrease. In the early stages of learning, a reference vector changes a lot in the wide range on the map. The range and amount of change decrease as learning proceed.

2.3 The map after learning

In this section, we describe the map after learning. To each input vector, a neuron with reference vector which is very similar to it exists. When some two neurons are located close together on the map, their reference vectors are also well alike. Thus, with the position change on the map, the reference vector of the neuron also changes smoothly. By mapping the each input vector to the winning neuron, the relation of inputs in high-dimensional space can be expressed with the coordinates in low-dimensions on the map. The law of each component of input vector is expressed with all neuron's reference vector discretely whether the law is linear or not.

The example of a map after learning is shown in Fig. 1.The features or the laws of two-dimensional input vectors are reflected in the one-dimensional map. The axes in the figure correspond to each component of an input vector (or reference vector). A Fig. 1 shows that the map after learning has the above-mentioned character.

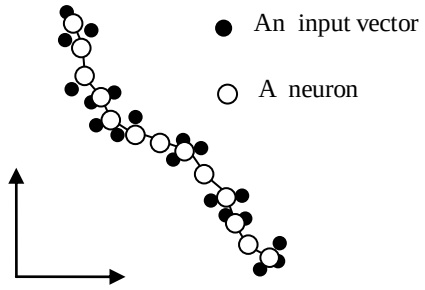

Fig. 1. The input vectors (2 dim) and the map (1 dim)

2.4 The estimating method by conventional SOM

In the method estimating missing values in data by SOM, at fast, instances which are not including missing values are used as input vectors for learning. The laws of each attribute of these instances are learned as the laws in all instances. After learning, the laws expressed with neurons of the map discretely.

Then, to each instance including missing values, the winner is determined. The winner is the neuron which has the reference vector with the greatest similarity to the instance. In the calculation of similarity, the attribute with missing value is excluded from consideration. It is the same also about the corresponding component of the reference vector. After determining the winner to each instance, missing value included in the instance is estimated. The estimated value is the corresponding component of a winner's reference vector.

In this method, however, only instances which are not including missing values can be used for learning. Thus, in the data which lacks such instances, it is difficult to estimate missing values by using SOM.

3 PROPOSED METHOD

In proposed method, a SOM disregarding some attributes are utilized. The SOM learn the relation between only attributes which is not disregarded. In the SOM, the instances including missing values can be used for learning, so long as the attribute with the missing value is disregarded. Thus, the SOM can use more instances than normal one when estimating missing values in data. On the other hand, the SOM can't learn the relation between the disregarded attribute and other attributes. Therefore, the SOM can't estimate missing values in the disregarded attribute.

© ISAROB 2013

We propose the method using multiple disregarding SOMs. The attribute disregarded by a SOM is not disregarded by other SOM. In multiple SOMs method, the relation of all the attributes is learned by the whole of multiple SOMs.

After learning, a missing value is estimated by each SOM. At this time, to one missing value, some estimated values are obtained from some maps. The average of these estimated values is used as a final estimated value.

The concrete way of using the proposed method is explained in section 4.4.

4 SIMULATION

4.1 A summary of simulation

To evaluate the proposed method, we performed simulation of estimating the missing values with incomplete data. In the simulation, the data for benchmark of data analyzing was utilized. The data had no missing values originally. And then we made the data incomplete by removing some values. We applied proposed method, conventional method that uses SOM and other methods to the incomplete data, and compared the results. We evaluated the results based on the average of each error of the estimated value to the original value. The error is a relative error to variance of the attribute with missing value.

In the algorithm of SOM in this simulation, we determined the initial value of reference vectors of neurons based on the result of principal component analysis (PCA). We used equation (3) as $h_{ci}(t)$ when updating a neuron.

4.2. The conventional techniques other than SOM

As the conventional technique for comparing with the proposed one, we adopted the method which used average value, and hot-deck imputation. In the method using average, the average value of an attribute with a missing value is adopted as an estimated value. In the latter method, at fast, the instance with no missing which is most similar to the instance with missing value is determined. In the calculation of similarity, the attribute with missing value is excluded from consideration. After determining the instance, the value which is corresponding missing values is adopted as estimated value.

4.3 The data for validation

In this simulation, we used the iris data which is released as a benchmark of analyzing [6]. The data has 150 instances and 4 attributes (attribute1-attribute4). The data had no missing values originally.

We made the data incomplete by removing some values. At fast, we determined the rate X(%) of the instances including missing values, and then, equally divided the instances into 4 groups at random. In each group, the value of the attribute 1, the attribute 2, the attribute 3, and the attribute 4 was made missed, respectively. These groups call Group1, Group2, Group3, and Group 4, respectively. The group of instances which are not including missing value calls Group0.

We created four kinds of incomplete data (Data1-Data4) by grouping the instances four times to each X (= 10, 20, …, 90).

When X = 90, to each incomplete data, we applied each estimating method, and calculated the average of the error, respectively. Furthermore, we compared proposed method and conventional SOM method when X = 10, 20, …, 90.

4.4 The estimation by proposed method

To estimate missing values by proposed method, we prepared four kinds of disregarding SOMs (SOM-A, SOM-B, SOM-C, and SOM-D) to each group of instances including missing value. SOM-A, SOM-B, SOM-C, and SOM-D disregards attribute1, attribute2, attribute3, and attribute4, respectively.

Then, each SOM learns the relation between attributes which are not disregarded. Each SOM can use more instances for learning than conventional one. For example, SOM-A can use not only instances of Group0, but also instances of Group1 which are including missing values in the attribute1 disregarded by SOM-A.

After learning, each SOM estimate a missing value in the attribute which are not disregarded. For example, the missing value of attribute3 is estimated by SOM-A, SOM-B, and SOM-D which don't disregard attribute3. The average of these estimated values is used as a final estimated value.

4.5 The simulation result

In the following Table 2, we show the simulation result when X = 90. The table 2 shows that the error of the proposed method (multiple SOMs) is the smallest.

In the following Fig. 2, we show the simulation result of estimation by the proposed method (multiple SOMs) and the conventional SOM method when X = 10, 20, …, 90. The Fig. 2 shows that the method using multiple SOMs is more effective than conventional SOM when X is at least 60(%).

© ISAROB 2013

Table 1. The error of estimated value when X = 90

	Data1 (%)	Data2 (%)	Data3 (%)	Data4 (%)	Ave (%)
Multiple SOMs	**32.8**	**36.7**	**35.5**	**31.6**	**34.1**
Conventional SOM	40.3	48.2	56.9	42.6	47.0
Using the average	87.5	88.1	81.7	83.1	85.1
hot-deck imputation	50.0	50.9	54.0	42.8	49.4

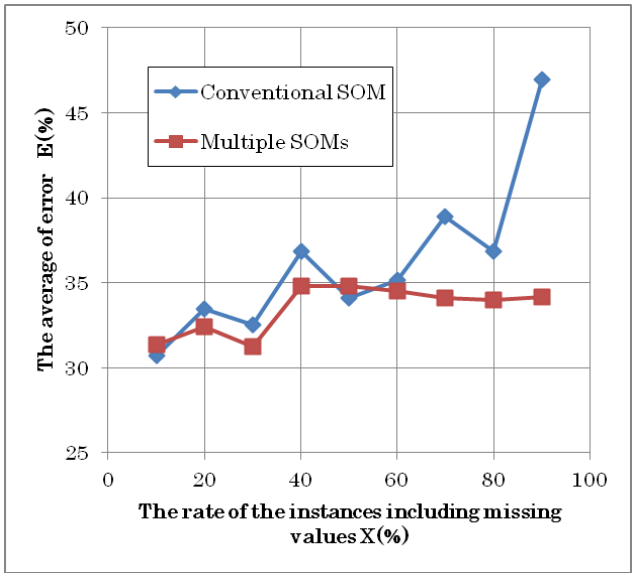

Fig. 2. The input vectors (2 dim) and the map (1 dim)

5 CONCLUSION

From the simulation result, we proved that our method is more effective than some conventional method including a conventional SOM especially in data with many instances including missing values.

In future, we have to perform more simulation in various data and conditions. For example, we have to check whether the proposed method has advantage even if the missing pattern becomes more complex. Moreover, we would like to consider any better method to determine a final estimated value based on some estimated values from each SOM.

REFERENCES

[1] Edgar A, and Caroline R (2004), The Treatment of Missing Values and its Effect on Classifier Accuracy. Classification, Clustering, and Data Mining Applications, Vol. 0, No.7, pp. 639-647

[2] Abe T, Inaba Y, Iwasaki M (2005), The Statistical-Analysis Techniques and Comparison of Software of Incomplete Data (in Japanes). Japanese Society of Computational Statistics, Vol. 18, No. 2, pp. 79-94

[3] Iwasaki T, Genei M (2001), Estimation of the earthquake information with missing by use of a self-organizing map (in Japanese). Technical paper summaries of Architectural Institute of Japan, B-2, p.185

[4] Kohonen T (2005), Self-Organizing Map (in Japanese), Springer-Verlag, Tokyo.

[5] George K (2010) Self-Organizing Maps, Publication In-Tech.

[6] University of California Irvine, Iris Data Set, http://archive.ics.uci.edu/ml/datasets/Iris

© ISAROB 2013

The Eighteenth International Symposium on Artificial Life and Robotics 2013 (AROB 18th '13),
Daejeon Convention Center, Daejeon, Korea, January 30-February 1, 2013

Proposal and evaluation of information gathering methods that consider the MANET's load in a disaster

Keisuke Gohara[1] and Hiroyuki Nishiyama[1]

[1] Graduate School of Science and Technology, Tokyo University of Science,
2641 Yamazaki, Noda-shi, Chiba-ken, Japan
(Tel:+81-47122-1106; Fax:+81-47122-1106)
(j7412610@ed.tus.ac.jp)

Abstract: When a disaster occurs, victims must be rescued quickly and their safety confirmed. However, current information-gathering systems may become unusable if their infrastructures are destroyed. The Mobile Ad Hoc Network (MANET) is a rescue-support system. MANET typically uses the flooding strategy. In flooding, the source node broadcasts the Route Request Control Packet (RREQ) to discover a route to the destination. However, this generates a high number of redundant retransmissions, so flooding places a huge burden on the devices that compose MANET. In this paper, we propose a MANET system that uses location information and the current energy status of the node. By simulating a disaster, we demonstrate that our proposed system outperforms the existing systems in terms of the total number of RREQs and the average power consumption.

Keywords: Mobile Ad Hoc Network, Broadcast, Location Information, Energy Status

1 INTRODUCTION

Recently, growth of mobile devices and the Internet has spurred development of individual information communications. Information communication in disasters such as earthquakes, volcanic eruptions, floods, and terrorism has become more and more important because it is necessary to rescue the victims quickly and confirm their safety. Existing rescue-support systems for disasters use hazard maps and emergency call systems such as 119. Hazard maps anticipate damage and victims' responses. However, damage from disasters may be worse than expected. In this case, systems employing hazard maps would be useless. The emergency call system is regularly used by many people. In the event of a disaster, however, the system may be unusable due to destroyed infrastructure.

The Mobile Ad Hoc Network (MANET) is a current rescue-support system. MANET is a self-configured wireless network formed by a collection of wireless mobile nodes without a fixed infrastructure or a centralized administrator. A rescue-support system using MANET can gather information on victim safety dynamically in a disaster. MANET typically employs a flooding strategy. In flooding, the source node broadcasts the Route Request Control Packet (RREQ) to discover a route to the destination. MANET currently has two problems. The first is the increased number of devices composing MANET. The increase in the number of devices increases the total number of RREQs and degrades the availability of MANET. Second is the difficulty of ensuring electric power. If it is difficult to ensure electric power, the energy status of device must be considered. In this paper, we propose a MANET system that uses location information and the current energy status of the node.

The rest of this paper is organized as follows. Section 2 reviews related work on MANETs. Section 3 provides our proposed system. Section 4 presents the simulation setup and performance evaluation of our proposed system. Finally, section 5 concludes the paper and outlines future work.

2 MOTIVATION

Disseminating routing protocol control packets (e.g., RREQ packets) with blind flooding may entail a huge overhead as mentioned previously. Therefore, increased attention is focused on reducing the routing overhead associated with route discovery by increasing the effectiveness of broadcasting.

2.1 Route discovery using Location Information

In Iwasaki's Location Aided Routing middle (LAR-middle) algorithm [1], mobile nodes use location information obtained from global positioning system (GPS) receivers and transmit RREQ packets in a circle with a diameter of the distance between the source node and the destination node in order to determine the route. This approach effectively reduces the number of broadcast packets, but also reduces the number of communication paths to the destination node and decreases the fraction of packets delivered.

2.2 Route discovery using gossip

Haas et al. proposed an adaptive gossip-based protocol that employs a predefined probability p to forward an RREQ packet if there is the node more than a certain distance from the source ; otherwise it will gossip with probability 1 [2].

© ISAROB 2013

They conducted experiments to demonstate how simple gossiping uses up to 35% fewer packets than flooding for large networks and that the performance of AODV routing relying on a gossip-based search is improved even in a small network of 150 nodes.

2.3 Route discovery using directional gossip

Beradi exploited a directional gossip algorithm to improve the efficiency of route discovery. When a node receives a packet for the first time, it rebroadcasts with a higher gossip probability if the node is estimated to be closer to the destination than the sending node, otherwise it will forward the packet with a lower probability or discard it. However, the algorithm must under the assumptions that any two neighbor nodes can estimate the difference of their current distance from the destination and that such an estimation is done from the inside of the network by using periodic beacons [3].

2.4 Route discovery using energy-based gossip

Nitnaware and Verma introduced the Energy-Based Gossip (EBG) Routing Algorithm [4]. The intermediate nodes forward the RREQ packets with a probability based on the current energy status of that node. If the node 's remaining energy is 80% of the initial energy, then the probability will be set to 0.8, if it is 60% then the probability will be 0.6 and so on. The simulation demonstrates that energy consumption due to routing packets and routing overhead can be reduced 10% to 30%, but they do not consider the RREQ packets dying when the probability is too small.

3 PROPOSED SYSTEM

In our proposed system, RREQ packets are broadcast to the destination node based on the advanced LAR-middle algorithm and the advanced EBG algorithm.

3.1 Advanced LAR-middle algorithm

The Advanced LAR-middle algorithm is a route-discovery algorithm in which the source node receives more communication paths to the destination node than with the LAR-middle algorithm.

First, the source node transmits a RREQ packet to an intermediate node in a circle with a diameter of the distance between the source node and the destination node and in a circle in which the source node can transmit radio. The intermediate node receiving the RREQ packet also transmits the RREQ packet to the node in a circle with a diameter of the distance between the intermediate node and the destination node and in a circle in which the intermediate node can transmit radio. Thus, the source node receives more communication paths (paths through Node E or Node F in Fig.1) to the destination node than with the LAR-middle algorithm by flexibly changing the transfer range.

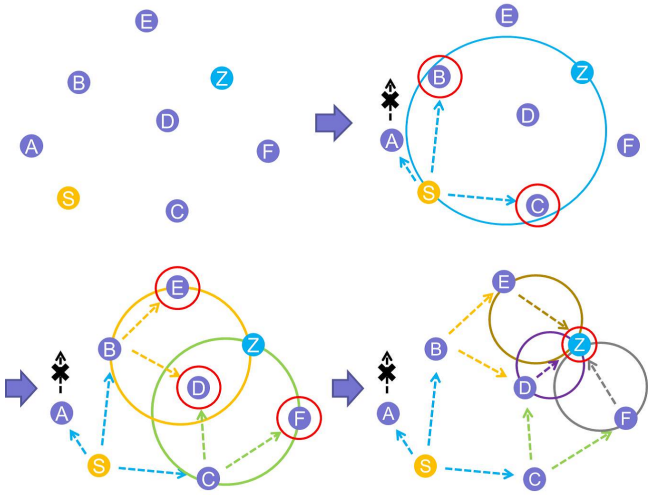

Fig. 1. Advanced LAR-middle algorithm

3.2 Advanced EBG algorithm

The advanced EBG algorithm is a route-discovery algorighm that reduces packet loss more than EBG.

When an intermediate node receives the RREQ packet broadcast from the source node, the intermediate node forwards the RREQ packet with the probability calculated based on the current energy status of that node. The probability of the node i is given by

$$P_i = (1 - \alpha) \times \varphi_i + \alpha$$

where α is the minimum relay probability and φ_i is the percentage of the residual energy of node i. This can prevent a node with little energy from consuming its battery and reduces packet loss more than EBG.

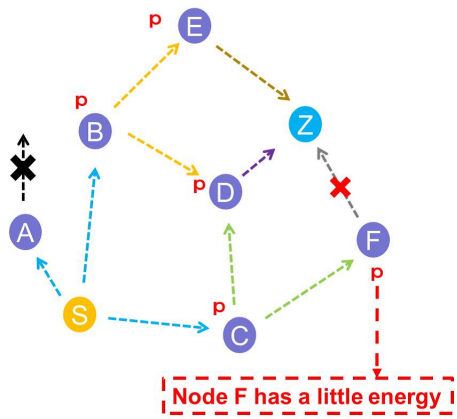

Fig. 2. Advanced EBG algorithm

© ISAROB 2013

3.3 Algorithm for Proposed System

The following is our algorithm for the proposed system.

Algorithm 1 Algorithm for Proposal System

```
Set the threshold k of the distance from the source node to
the distance node;
while each RREQ received by the node do
    Set a random number r between 0.0 and 1.0;
    Obtain the distance h from the node to the distance
    node;
    if h <= k then
        Calculate probability p using remaining energy;
        if r < p then
            Broadcast RREQ;
            Update k to the value of h;
        else
            Drop RREQ;
        end if
    else
        Drop RREQ;
    end if
end while
```

4 PERFORMANCE EVALUATION

We conducted a simulation based on the supposition of a disaster and evaluated our proposed system.

4.1 Simulation Setup

We used network simulator ns-2 [7] to evaluate our proposed system. Network simulator ns-2 is an object-oriented, discrete event-driven network simulator developed at UC Berkeley and USC ISI as part of the VINT project. It is a very useful tool for conducting network simulations involving local and wide-area networks and wireless networks.

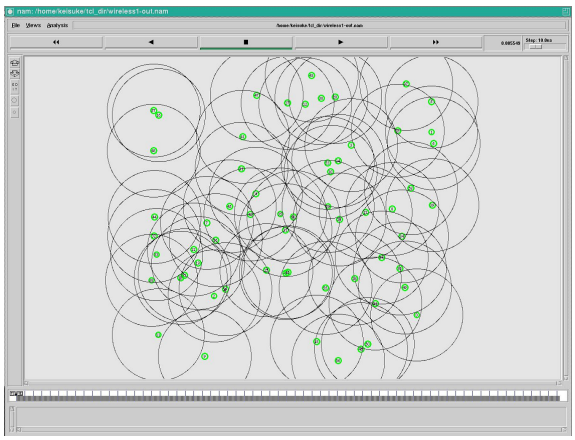

Fig. 3. The network simulator ns-2

This paper uses default radio propagation model ns-2 with a 2Mbps bit rate and transmission range of 250 meters. Our appliction uses the MAC layer protocol IEEE 802.11, and the mobility model is based on the random waypoint model [5] in 1000m $\times$ 1000m. We randomly placed many victim nodes, moving at randomly chosen speeds (uniformly chosen from 1 to 15 m/s) and a rescue node that collects the RREQ packet from victim nodes. Fifty victim nodes transmit the RREQ packet to the rescue node. We set the pause time to zero to achieve the dynamic topology and set the minimal speed to 1 to prevent mobility from going asymptotically to zero. The simulation time was set to 300s. Each data point represents an average of 10 different randomly generated mobility scenarios. Table 1 shows other simulation parameters from the experiment.

Table 1. SIMULATION PARAMETERS

Simulation Parameter	Value
Topology size	$1000m \times 1000m$
Transmitter range	250 meters
Number of nodes	50,60,$\cdots$,100
Simulation time	300 sec
max Speed	15 m/sec
Initial energy	1000 J
Energy consumption during reception	0.1 W
Energy consumption during sending	0.5 W

4.2 Performance Result

We compared our proposed system with existing systems (flooding, LAR-middle, gossip) in four broadcasts of the RREQ packet (the total number of RREQ packets, average energy consumption, packet delivery fraction, and delay time). Also, the minimum relay probability in our proposed system and the relay probability for gossiping are 50%.

Figure 4 depicts the total number of RREQ packets. The results demonstrate that our proposed system uses fewer RREQ packets than existing systems.

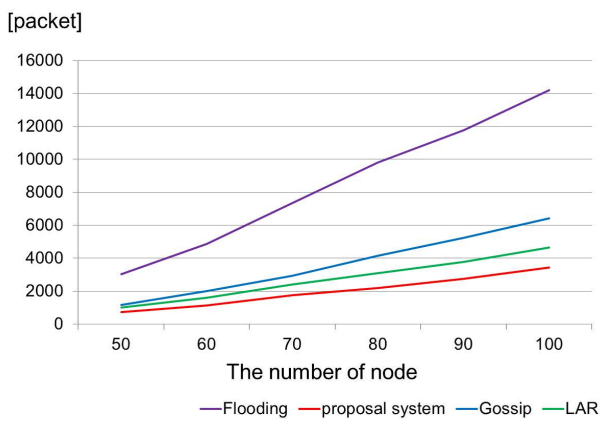

Fig. 4. The total number of RREQ packets

© ISAROB 2013

Figure 5 presents the average energy consumption. The results indicate that our proposed system has lower energy consumption than existing systems and fewer RREQ packets.

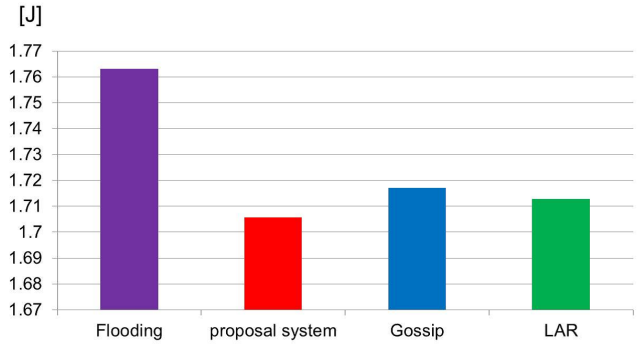

Fig. 5. Average energy consumption

Figure 6 plots the percentage of packet deliveries. Our proposed system delivers more packets than the gossip system but fewer packets than the two other systems.

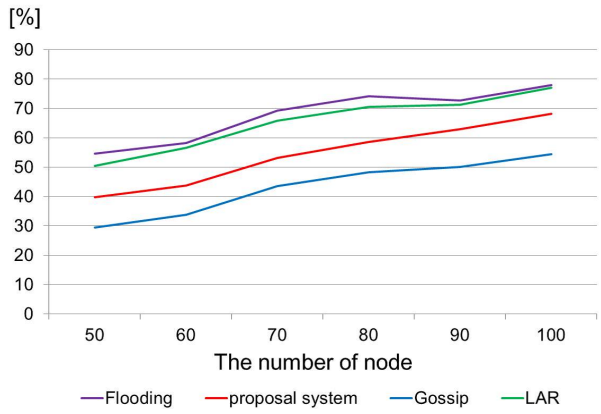

Fig. 6. Packet delivery fraction

Figure 7 plots the packet delay time. Our proposed system has less delay time than the gossip system but more delay time than the two other systems.

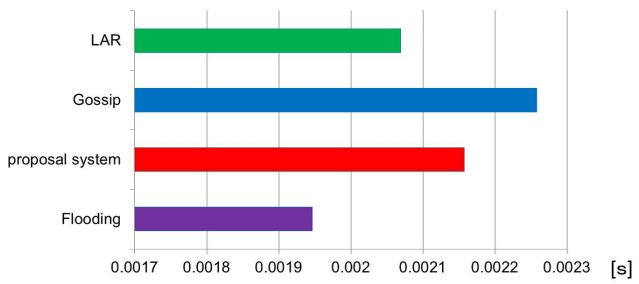

Fig. 7. Delay time

5 CONCLUSION

This paper proposes a MANET routing protocol using location information and current energy status of the node and evaluates the performance of broadcasting RREQ packets based on a supposed disaster. Experiment results proved that the proposed system is superior to the existing systems in the total number of RREQ packets and average energy consumption. However, experiment results also proved that the proposed system is inferior to flooding and LAR-middle algorithms in packet delivery fraction and delay time.

Future work will improve our proposed system's packet delivery fraction and delay time and add a new protocol for sending data to our proposed system to achieve this paper's purpose.

REFERENCES

[1] Midori Iwasaki, Yoshikatu Oota, Hidetomo Suzuki (2009), A Method for Reducing Control Packets of AODV using the Location Information, Information Processing Society of Japan SIG Technical Report , Proceedings of the National Conference 71st(3):125-126.

[2] Z. J. Haas, J. Y. Halpern, and L. Li (2006), Gossip-based ad hoc routing, IEEE/ACM Trans. on Networking, vol.14:479-491.

[3] R. Beraldi (2006), A directional gossip protocol for path discovery in MANETs, in Proc. 26th IEEE Int. Conf. on Distributed Computing Systems Workshops, Lisboa, Portugal, Jul.:82-82.

[4] D. Nitnaware and A. Verma(2010), Energy Based Gossip Routing Algorithm for MANETs, in Proc. 2010 Int. Conf. on Recent Trends in Information, Telecommunication and Computing:23-27.

[5] J. Broch, D. A. Maltz, D. B. Johnson, Y. C. Hu, and J. Jetcheva(1998), A Performance Comparison of Multi-Hop Wireless Ad Hoc Network Routing Protocols, in Proc. 4th Annu. ACM/IEEE Int. Conf. on Mobile Computing and Networking, Dallas, TX, USA,:85-97.

[6] TC Huang, SC Chen, L Tang(2011), Energy-Aware Gossip Routing for Mobile Ad Hoc Networks, High Performance Computing and Communications:955-959.

[7] The Network Simulator - ns (Verision 2). Available: http://www.isi.edu/nsnam/ns/

© ISAROB 2013

The Eighteenth International Symposium on Artificial Life and Robotics 2013 (AROB 18th '13),
Daejeon Convention Center, Daejeon, Korea, January 30-February 1, 2013

Simultaneous Recognition of Multiple Actions using CHLAC features

Kyosuke Masumitsu, Takayasu Fuchida

Kagoshima University, Japan
(Tel: 099-285-3408, Fax: 099-285-3408)
sc108067@ics.kagoshima-u.ac.jp

Abstract: In this study, we propose simultaneous recognition of multiple actions in moving image using sub-space method and CHLAC features. As the CHLAC features are integral value of entire the image, it has the additivity. Thus, when multiple objects exist, it is possible to use the added-feature which is made by adding the each action of the object. But if you use such an added-feature, it becomes difficult to distinguish each action respectively. Then we introduce a method to trace the region of each object in the image. From the computer simulation by using these 8 kinds of moving images, we show that our proposed method can recognize these 8 kinds of actions.

Keywords: CHLAC, Color-HLAC, CLAFIC method, Projection distance method.

1 Introduction

Recently, as the performance of computers improves, the demand of action recognition using features of moving image has risen and different method has been proposed. In recent features descriptor methods, without descripting the features from one only image in the moving image, many methods that utilize time and space that consider the current frame, the previous and the next frame is proposed[1][2][3]. CHLAC(Cubic Higher-order Local Auto Correlation)[3] is one of the amount of image feature. This is what Higher-order Local Auto Correlation[4] is extended and can simultaneously evaluate features of both moving and shape reflected in the camera. This features extraction method is, in general, performed by calculating the frequency of matching between the pixels which has moved in the three binary images obtained by the frame difference from four successive frames in the moving image and the mask patterns prepared in advance. Consequently, the general CHLAC feature has 251 dimensions.

As the CHLAC features have the additivity, when multiple objects exist, it is possible to use the added-feature which is made by adding the each action of the object. It can be simultaneously multiple objects using the added-features, but when the number of object increases, variation becomes enormous and configuring the discriminator is difficult. In previous research which resolves the problem[5], the method using multiple regression analysis has been proposed and it enables simultaneous recognition of multiple moving objects. But in this method, it isn't able to current location of the object and to track the object. So, in this study, we propose the method which traces the region of each object in the image and extract CHLAC features from each object and distinguish the moving.

We used color-information for tracking the objects. We adopted the features which combined Color-HLAC[6] and HLAC for this information.

We used sub-space method to the discrimination of motion. This is one of the pattern recognition methods which utilizes the bias of input vectors and takes relatively small amount of calculation at the time of the identification. So we think that it suits the motion recognition which requires the real-time processing. In this research, we adopt the sub-space method which uses the bias of distribution of the CHLAC features which are extracted for each motion of objects in the movies.

And, we validate the effectiveness of our method through the computer simulations using some movies which include multiple objects in them.

2 extraction of CHLAC features

We will easily explain how to extract CHLAC.

2.1 HLAC feature

HLAC(Higher-order Local Auto Correlation)[4] is the amount of statistical features based on Higher-order correlation the N dimensional autocorrelation for $f(r)$ is expressed as following equation.

$$\mathrm{x}(\boldsymbol{a}_1, \cdots, \boldsymbol{a}_N) = \int f(\boldsymbol{r}) f(\boldsymbol{r} + \boldsymbol{a}_1) \ldots f(\boldsymbol{r} + \boldsymbol{a}_N) dr \quad (1)$$

Here, f is the image which is retrieved in time series and r is the reference position and $\boldsymbol{a}_i$ is the vector that indicates the displacement. Since the correlation between the pixel of interest and its neighboring regions is expected to be high, we usually will not calculate the correlation for

© ISAROB 2013

all areas, but for only neighbor pixels, this feature is usually set as degree$-N = 2$. Consequently, it has 25 dimensions.

2.2 Extraction of CHLAC features

We will extract the features which are used to recognize motion from moving image. First, we convert the moving image to YCbCr color-space in order to remove the illumination variation, and then remove component Y of luminance signal. After this, we perform smoothing processing in order to reduce the noise in the image. Next, we make frame differences from moving image and create the subtraction binary images and then calculate CHLAC feature from its subtraction binary images.

HLAC which we described in sub-section 2.1 is the correlation in the two-dimensional local region, but CHLAC is feature value which introduces the time axis to the local area and then calculates correlation in the local region of $3 \times 3 \times 3$.

In general, degree N is set {0, 1, 2} and the feature has 251 dimensional vector.

3 Tracing the region of the object

In this chapter, we will explain about tracing the region of the object and tracking using color-information.

3.1 Tracing the region of object and tracking

In order to simultaneously recognize each location of multiple objects and motion, we trace the each region of objects. First, we prepare the background image in advance. Next, we extract the subtraction image between the current frame and background image. We divide the whole of subtraction image into the many vertical narrow rectangles and then check the all pixels in each segmented region whether there are any differences. If the different pixel is found in the segmented region, its region becomes a candidate for the presence of the object region and we will check the adjacent pixels of this region.

If the candidate of the object is found in the rectangle which divides the image lengthwise, we divide the candidate region horizontally and explore the region with the subtraction as same as the vertical segmentation.

Moreover, since we use the difference image between two sequential frames in calculating CHLAC feature, we are able to make a more accurate segmentation of the object by examining whether there is a pixel which has motion in the subtraction image within the candidate region of the object. If there is an area of noise, we update the previous pixel value to the current pixel value in order to denoising.

If the presence of the object is confirmed, we register the color-information of the object in order to distinguish between each object of the next frame, and in order to track the object. We have been utilized color-histogram and color-HLAC to the color-feature. Then distinction between objects is performed by Euclidean distance and then we calculate the subtraction between the features quantity of registered object and the features quantity obtained from the current object region. The region which has smallest difference becomes the updated position of the object, and we update the previous feature value.

3.2 Features amount by combining the color-HLAC and HLAC

Color-HLAC is the feature which is extended higher-order local auto correlation to color image. Similarly HLAC, we will consider mask pattern of 3×3 sizes. This is expressed as the combination of each color component in the local region of pixel of interest. In this study, we used 45 dimensional features that have degree {0, 1} only.

In addition, we also added HLAC considering the luminance. Consequently, the feature amount of a combination of the HLAC and color-HLAC becomes 70 dimensions.

4 Motion determination using sub-space method

In this research, we use sub-space method which is the multi-class classification for the input patterns.

4.1 CLAFIC method and projection distance method

Sub-space method is to calculate sub-space of each learning class using bias of distribution of the feature and recognize input pattern by projecting it onto the sub-space.

CLAFIC method is one of the sub-space methods. CLAFIC is, at the time of learning, a method which puts the origin of sub-space on the origin of original feature space and performs KL expansion for each class and then determines sub-space of each class. Then, when an unknown pattern is input, its pattern class is determined as the sub-space class which the length of the projection vector for each class is maximum.

We will describe how to configure the sub-space by this method.

We calculate autocorrelation matrix R_i using CHLAC feature vector $\boldsymbol{x}_{i,j} \in \mathrm{C}_i (1 \leq \mathrm{j} \leq \mathrm{N}_i)$ which belongs to the class C_i as the learning data.

The feature vector is normalized so that its norm becomes 1 using $\boldsymbol{x}_{i,j} / \|\boldsymbol{x}_{N_i}\|$.

$$R_i = \frac{1}{N_i} \sum_{j=1}^{N_i} \boldsymbol{x}_{i,j} \tag{2}$$

Sub-space is composed using eigenvalues $\lambda_{i,j} (\lambda_{i,1} \cdots \lambda_{i,251})$ obtained from the eigenvalue decomposition of the autocorrelation matrix R_i and the corresponding part of the eigenvectors $\boldsymbol{u}_{i,1}, \cdots, \boldsymbol{u}_{i,251}$.

In order to compose the sub-space, we calculate principal component of the consisted sub-space.

© ISAROB 2013

To set the number of principal components, we use a cumulative contribution ratio $a(d_i)$ of the dimension d_i shown in equation (3).

$$a(d_i) = \frac{\sum_{j=1}^{d_i} \lambda_{i,j}}{\sum_{j=1}^{251} \lambda_{i,j}} \tag{3}$$

d_i is selected to satisfy the following conditions,

$$a(d_i) < k_d < a(d_i + 1) \tag{4}$$

where k_d is the threshold and in this study, we use $k_d = 0.998$. After determining d_i, we select the d_i eigenvectors from the top of the value. Then, we calculate projection matrix P_i of sub-space L_i using equation (5).

$$P_i = [\boldsymbol{u}_{i,1}, \cdots, \boldsymbol{u}_{i,di}] \tag{5}$$

In contrast to CLAFIC method, projection distance method is the method which the center of each class is the origin.

While CLAFIC method perform eigenvalue decomposition of autocorrelation matrix obtained by the equation (2), projection distance method calculate average of feature vectors of each class and calculate the variance-covariance matrix R_i according to the following formulas. And sub-space S_i using projection distance method is configured by eigenvalue decomposition of this matrix.

$$\boldsymbol{m}_i = \frac{1}{N_i} \sum_{j=1}^{N_i} \boldsymbol{x}_{i,j} \tag{6}$$

$$R_i = \frac{1}{N_i} \sum_{j=1}^{N_i} (\boldsymbol{x}_{i,j} - \boldsymbol{m}_i)^t (\boldsymbol{x}_{i,j} - \boldsymbol{m}_i) \tag{7}$$

$$S_i = [\boldsymbol{u}_{i,1}, \cdots, \boldsymbol{u}_{i,di}] \tag{8}$$

4.2 Recognition

In this section, we will explain how to identify the unknown pattern $\boldsymbol{q}$ according to each method of CLAFIC method and projection distance method.

Recognition of unknown pattern $\boldsymbol{q}$ using CLAFIC method is executed by calculating the square of the length of $P_i\boldsymbol{q}$ as the degree of similarity between the unknown pattern $\boldsymbol{q}$ and the class C_i by using projection matrix P_i which is determined for each class. Sub-space which projection length is greatest becomes unknown pattern that determines the class of.

$$\begin{aligned} argmax_i\{D_i\} &= \|P_i\boldsymbol{q}\|^2 = \boldsymbol{q}^t P_i \boldsymbol{q} \\ &= \boldsymbol{q}^t \left(\sum_{j=1}^{d_i} (\boldsymbol{u}_{ij}^t \boldsymbol{u}_{ij})\right) \boldsymbol{q} = \sum_{j=1}^{d_i} (\boldsymbol{q}^t \boldsymbol{u}_{ij})^2 \end{aligned} \tag{9}$$

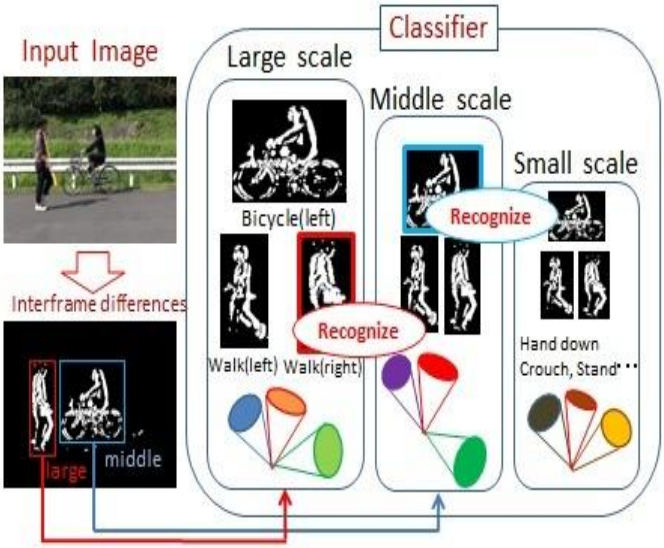

Figure 1. Corresponding to the scaling

In recognition of projection distance method, the total of projection distance to the sub-space is calculated by following:

$$argmin_i\{D_i\} = \sum_{i=1}^{n} \left\{ \|\boldsymbol{q} - \boldsymbol{m}_i\| - \left\| {S_i}^t (\boldsymbol{q} - \boldsymbol{m}_i) \right\|^2 \right\} \tag{10}$$

The class which has smallest D_i is the decision class of the unknown pattern.

4.3 Configuring the discriminator corresponding to the scaling

CHLAC isn't invariant feature quantity to scaling.

Therefore, we configured the sub-space for each scale of object at the time of learning. We configured to determine whether any portion of the scale corresponding to the space according to the size of extracted region of the object (Figure 1).

5 Experiments

To evaluate the effectiveness of our proposed method, we have conducted some experiments.

5.1 Conditions of the experiments

We have set up a camera on the street and have taken the video which was assumed to detect each motion and location of the multiple entering objects. The video was taken with the state of the objects entering the lateral of camera.

We prepared 8 kinds of moving images, such like "bicycle left", "bicycle right", "walk left", "walk right", "crouch", "stand up", "raise hand" and "hand down".

In addition, preparing video such that maximum three objects exist, we have experimented using them.

The experiments were conducted with six subjects. The motion at each scale was learned two per person. Moving images were taken with 30fps and size of them was set to 320×240 pixels.

© ISAROB 2013

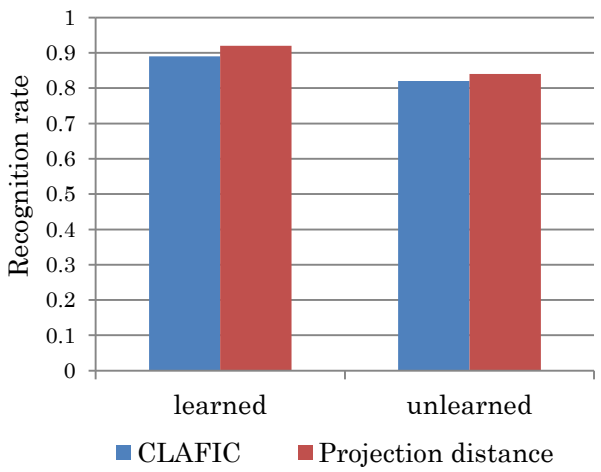

Figure 2. Action recognition rate by each classifier

5.2 Experiment using only objects who were learned

We have carried out an experiment using two videos in which only learned persons exist. Each video has the content that at most three persons are entering.

5.3 Experiment using only objects who were not learned

We have taken two videos which were consists of only persons who were not learned, and conducted an experiment. Each video has the content that at most three persons are entering.

5.4 Result

The success rate of segmentation and object tracking was 95.4%. There was a slight mistake when an object enters and when the object goes out the screen. However, at the time of occlusion between the objects occurred, we have confirmed that detecting the regions of the objects were performed well and also tracking was performed correctly after the occlusion.

The action recognition success rate using each classifier shows at the Figure 2. On the process of identification, mainly erroneous identification occurred when the object entered and went out. In addition, we confirmed that incorrect identification rate didn't change much if an occlusion occurs or not.

6 Conclusion

In this research, we proposed the method for recognizing the location and the motion of multiple objects in moving images captured from a camera which was set on the street. In our proposed method, first, we extract a difference image between one frame image and background image that has been prepared beforehand, and extract regions of objects in the image. Then, we performed the motion recognition by sub-space method that matches the size of each object region. As the feature quantity of the motion recognition, we used CHLAC obtained from the binary image sequence by frame difference. Then, we used CLAFIC method and projection distance method as the classifier. And we utilized a combination of feature quantity color-CHLAC and HLAC.

We have performed two evaluation experiments for videos that have eight types of behavior and at most three people who consist of person and bicycle. For the video of learned objects, the result of CLAFIC method was 89%, and the result of projection distance method was 92%. In addition, for the video of unlearned objects, the result of CLAFIC method was 82%, and the result of projection distance method was 84%.

In this study, we proposed a method that corresponds to the scaling and have confirmed its effectiveness, but we have not been able to respond to changes in speed yet. So, for the future work, we also need to propose a method that corresponds to the action speed of the object. And many type of improved sub-space method are proposed, we are able to consider the implement of variant of sub-space method.

And we think that the accuracy of motion recognition will be improved using the variant of CHLAC[7] which is extended to cross correlation which takes the timing of the motion of an object into consideration.

REFERENCES

[1] Yeffet, L., Wolf, L., Local trinary patterns for human action recognition. In: ICCV, 2009

[2] Nazli, I., Stan, S., Object, Scene and Actions: Combining Multiple Features for Human Action Recognition, ECCV, 2010

[3] T.Kobayashi, and N.Otsu, Three-way auto-correlation approach to motion recognition, Pattern Recognition Letters, Volume 30, Issue 3, pp.212 221, 2009.

[4] N.Otsu and T.Kurita, "A new scheme for practical, flexible and intelligent vision systems", Proc.IAPR Workshop on Computer Vision, pp431-435, 1988.

[5] Y.Simohata, N.Otsu, "Simultaneous Recognition of Multiple Moving Objects Using Cubic Higher-Order Local Autocorrelation", PRMU, 2006.

[6] T.Kurita, T.Kato, I.Fukuda, A.Sakakura, "Sense Retrieval on a Image Database of Full Color Paintings", Information Processing Society of Japan Vol.33, 1992.

[7] T.Matsukawa, T.Kurita, "Action recognition using cu bic cross-correlations features of local motion attribute s", PRMU2009-285, 2010.

© ISAROB 2013

The Eighteenth International Symposium on Artificial Life and Robotics 2013 (AROB 18th '13),
Daejeon Convention Center, Daejeon, Korea, January 30-February 1, 2013

Hand gesture recognition using subunit-based dynamic time warping

Yanrung Wang[1], Atsushi Shimada[1], Takayoshi Yamashita[2], and Rin-ichiro Taniguchi[1]

[1] Kyushu University, Japan
[2] OMRON Corporation, Japan

kenyou@ limu.ait.kyushu-u.ac.jp

Abstract: A subunit-based Dynamic Time Warping (DTW) approach is introduced for hand movement recognition. Two major contributions distinguish the proposed approach from conventional DTW. (1) A set of hand movement subunits is constructed using a data-driven method. The learning is based on subunits instead of the whole hand movement for more efficient learning. (2) A more accurate similarity measure is offered using subunit-to-subunit matching to absorb the difference between two similar sub-sequences belonging to the same subunit, and only keeping the distances between sub-sequences that relate to different subunits. Compared with the conventional DTW approach, the proposed approach is experimentally demonstrated to be both accurate and efficient for locally collected datasets.

Keywords: hand gesture, gesture recognition, subunit

1 INTRODUCTION

Vision-based hand gesture recognition has attracted considerable attention because of its new and fascinating applications such as interactive human-machine interfaces, sign language interpretation, and virtual environments [1]. Features such as appearance, shape, and orientation often play an important role in hand gesture recognition. In this paper, we consider hand gestures as movement trajectories and focus on recognition of the movement trajectories.

Dynamic time warping (DTW) [2] is widely used to recognize movement trajectories, because it simultaneously aligns time-variable data and computes a likelihood of similarity. Generally speaking, there are two major limitations to the use of DTW in hand movement recognition. (1) DTW matching uses information about individual training examples that it is sensitive to variations in training data. Hence, it is difficult to support efficient personalized gesture recognition. (2) DTW is sensitive to noise and unable to distinguish movement trajectories that have similar subsequences, as it requires continuity along the warping path. The use of DTW consequently requires the development of many prototypes to achieve proper performance, leading to an expensive computational load.

To address these issues, we develop an effective recognition approach that combines the use of the DTW distance metric and subunits, widely investigated in the field of sign language [3][4]. Subunits are elementary units in a language and there are far fewer subunits than words in the vocabulary of the language, which is expected to lead to smaller data size in training and a smaller search space in recognition.

2 OVERVIEW OF THE PROPOSED APPROACH

Our system handles color image sequences in real time to recognize numbers from 0 to 9 by the hand movement trajectories. In the training phase, all training data are mapped to sequences of digits between 0 and 7 according to their orientation feature and then segmented into the set of basic motion units according to changes in orientation. Next, subunits are selected via clustering and set as the yielded cluster centers. In this case, each training sequence is mapped to a sequence of subunits. In the testing phase, the test sequence is also represented as a sequence of subunits and then classified according to DP matching between the test sequence and training sequences. Specifically, DTW distance is measured by subunit-to-subunit matching to improve recognition accuracy and online learning is used to adapt the training set to the user's individual habits.

3 HAND MOVEMENT REPRESENTATION

Hand movement trajectories are obtained by detecting the top most point of the hand skin region as the fingertip. To represent these trajectories, we use the orientation feature, which has been shown to provide high accuracy in hand movement recognition in previous work [5]. A hand movement is a spatio-temporal trajectory that consists of fingertip positions $(x_t, y_t), \mathrm{t} = 1,2,\dots,T-1$, where T indicates the length of trajectory. Similar to [5], we calculate the orientation feature according to the positions of fingertips between consecutive frames as follows.

$$\theta_t = arctan\left(\frac{y_{t+1} - y_t}{x_{t+1} - x_t}\right); t = 1,2,\dots,T-1 \tag{1}$$

© ISAROB 2013

The orientation θ_t is quantized into a set of codewords from 0 to 7 by dividing it by 45◦. Therefore, a hand movement can be represented by a sequence of digits according to the yielded codewords as shown in Fig. 1 and the similarity between two movements can be measured by the DTW distance [6]. The Examples of the DTW distance between movements are illustrated in Fig. 2. The examples show that the measurement procedure of adding the current distance to the smallest one can result in similar trajectories being treated as dissimilar, which leads to inaccuracies in hand movement recognition.

4 HAND MOVEMENT SUBUNIT CONSTRUCTION

Motivated by [3] and [4], we consider a hand movement as a sequence of basic motion units, referred to as the common pattern of hand movements, and carry out a self-organization process to select a representative set of motion units from the training set as subunits. All training data are segmented into a set of sub-movements. Clustering is performed for these sub-movements (basic motion units) to find the common pattern of hand movements.

4.1 Motion unit segmentation

Motion unit segmentation can be thought of as a boundary detection problem. The use of trajectory discontinuity and motion speed discontinuity has been shown to be effective in detecting the subunit boundary in sign language recognition [7]. We employ changes in orientation as trajectory discontinuity metrics to detect unit boundaries when the current orientation is very different from that in a neighboring frame or that in the starting frame of the motion unit.

4.2 Subunit clustering

To select a set of representative subunits from all submovements of the training set, we perform k-medoids clustering using the DTW distance metric. The k-medoids algorithm, a variant of k-means clustering, computes medoids instead of centroids as cluster centers to minimize the sum of intra-class distances. To determine the number of clusters, we employ an iterative clustering that selects all sub-movements of the training set as the initial cluster centers and iteratively merges similar clusters until convergence to obtain the "optimal" number of clusters. Furthermore, we use a kmeans-like algorithm for k-medoids clustering [8] to overcome the drawback that partitioning around medoids (PAM, K-medoids) works inefficiently for large data sets because of the complexity.

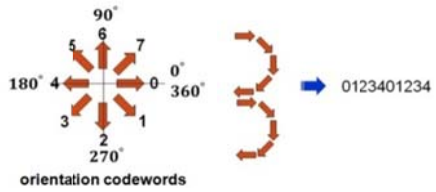

Fig. 1. Orientation codewords and an example of movement representation using orientation codewords

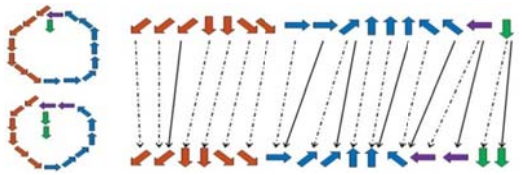

(a) distance between '0' and '0' is 7

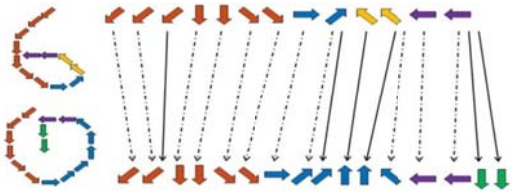

(b) distance between '0' and '6' is 6

Fig. 2. Examples of the DTW distance between movements

The yielded cluster centers are then used as subunits to map the training data to subunit sequences. We build a subunit-to-subunit distance matrix during construction of subunits and use it as a look-up table to speed up the recognition procedure.

5 SUBUNIT-BASED RECOGNITION

We propose two-step submovement-to-subunit and subunit-to-subunit matching in the recognition process to improve the performance of recognition and employ subunit-based learning to overcome sensitivity to variations in the training data.

5.1 Subunit-based learning

Instead of training entire hand movements composed of orientation codewords, we train each movement as a concatenation of subunits. The advantages are as follows. (1) The amount of training materials needed is reduced as all training data are composed of a limited set of subunits. (2) A simplified enlargement of training data is achieved by composing new training data using the existing subunits.

5.2. Submovement-to-subunit matching

Let P_x be a testing sequence and $S = \{s_1, s_2, \dots, s_{|S|}\}$ be a set of $|S|$ subunits constructed from training data. Similar to training sequences, the test sequence P_x is also mapped to a sequence of digits according to changes in

orientation and then segmented into m submovements u_{xi}. We calculate DTW distances between submovement u_{xi} and all subunits to find the nearest subunit s_{xi} and then use these subunits to recompose the testing sequence P_x. The yielded testing sequence $P_x = \{s_{x1}, \dots, s_{xi}, \dots, s_{xm}\}$ is used to perform subunit-to-subunit matching with training data.

5.3. Submovement-to-subunit matching

Hand movement trajectories are recognized through dynamic subunit sequence matching. Let $P_y = \{s_{y1}, \dots, s_{yj}, \dots, s_{yn}\}$ be a training sequence consisting of n subunits. The distance $DTW(P_x, P_y) = D(s_{xm}, s_{yn})$ is calculated as follows.

$$D(s_{xm}, s_{yn}) = \min \begin{cases} D(s_{xi-1}, s_{yj}) + cost \\ D(s_{xi}, s_{yj-1}) + cost \\ D(s_{xi-1}, s_{yj-1}) + cost \end{cases} \quad (2)$$

$$cost = \min \begin{cases} 0 & if\ s_{xi} = s_{yj} \\ dist(s_{xi}, s_{yj}) & if\ s_{xi} \neq s_{yj} \end{cases} \quad (3)$$

Here, $dist(s_{xi}, s_{yj})$ is obtained using the look-up table generated during the construction of subunits.

6 EXPERIMENTS

To test the proposed approach for hand movement recognition and to compare with conventional DTW, we perform evaluations in terms of the recognition rate and average computational time for a locally collected hand movement corpus. Here, the average computation time is the average time taken to calculate the distance.

The constructed corpus contains 10 different classes of hand movement trajectories from 0 to 9, performed by seven subjects in our laboratory environment. Each of the 10 classes of trajectories is repeated 25 times by each subject. To evaluate the performance for datasets of different size, we randomly select 9, 15, and 30 training samples from each class, performed by three subjects, to construct the training set. The other data corresponding to the other four subjects are used as a test set. To obtain results that are more reliable, the construction of subunits and evaluation of recognition performance were repeated five times using different datasets constructed relating to different subjects.

6.1 Evaluation of the recognition rate

Recognition rates classified according to three different sizes of training set are compared in Fig. 3. Compared with conventional DTW, the proposed approach showed a significant improvement when there were only nine training data. The findings indicate that the proposed approach is able to overcome the sensitivity to training data of conventional DTW to offer high recognition accuracy even when there are few training data. The two main reasons for the improvement are as follows.

6.1.1 Increase in the variety of training data

To train each movement as a concatenation of subunits increases the variety of training data such that it is possible to recognize new training patterns not seen in training.

For instance, we might have a training set of three training data $P_y = \{u_{y1}, u_{y2}, u_{y3}\}$, $P_z = \{u_{z1}, u_{z2}\}$, and $P_w = \{u_{w1}, u_{w2}\}$, where u_{yj}, u_{zk}, and u_{wl} are segmented submovements and are clustered into three subunits $s_1 = \{u_{y1}\}$, $s_2 = \{u_{y2}, u_{z1}, u_{w1}\}$ and $s_3 = \{u_{z2}, u_{w2}\}$. According to the yielded subunit set, training data are mapped to sequences of subunits $P_y = \{s_1, s_2, s_3\}$, $P_z = \{s_2, s_3\}$ and $P_w = \{s_2, s_3\}$.

In the example, we only train two training prototypes $s_2 s_3$ and $s_1 s_2 s_3$ for three training data because P_z and P_w are mapped to the same prototype $s_2 s_3$. The reduction of training prototypes improves learning efficiency while maintaining the variety of training data to avoid loss of recognition accuracy. In addition, training patterns that can be represented by the training prototype $s_2 s_3$ are not only P_z and P_w but also $u_{w1} u_{z2}$, $u_{w1} u_{y3}$, and so on. That is, the variety of P_z and P_w is increased to $|s_2||s_3|$ training patterns because of the use of existing subunits that include motion units from the other training data. It is thus also possible to recognize new patterns, even though they are not seen in the training. These merits achieve an improvement of the recognition rate without requiring high computational complexity.

6.1.2 A more accurate similarity measure

The conventional DTW distance metric is sensitive to noise and unable to find movement trajectories that have similar sub-sequences. Therefore, similar trajectories may be treated as dissimilar, leading to inaccurate recognition. As illustrated in Fig. 4, the proposed approach offers a more accurate similarity measure because it absorbs the difference between two similar sub-sequences belonging to the same subunit and only keeps the distances between sub-sequences that relate to different subunits.

6.2 Evaluation of average computation time

The average computation time and the number of training prototypes when using subunit-based learning are given in Fig. 5. The results indicate that a significant improvement in computational complexity was obtained.

© ISAROB 2013

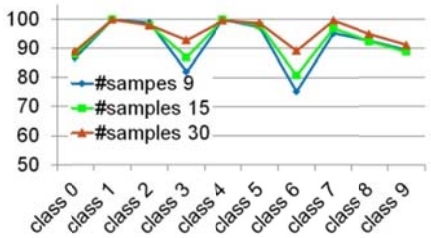

(a) average recognition rate using conventional DTW

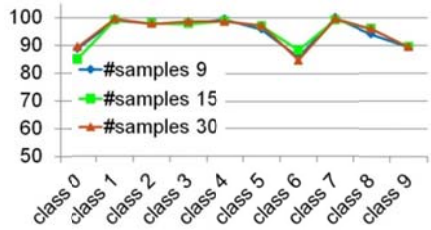

(b) average recognition rate using subunit-based DTW

Fig. 3. Comparison of the recognition rate

The reduction of the number of training prototypes, due to the fact that multiple training data were mapped to single training prototype, was one of the causes of the improvement in computational cost. The major reason for the improvement is that the distance between subunits was rapidly obtained using the lookup table in the procedure of subunit-to-subunit matching. These findings shown in Fig. 3 and Fig. 5 support the claim that the proposed approach improves recognition accuracy while not increasing the computational load.

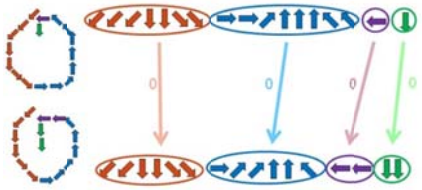

(a) distance between '0' and '0' is 0

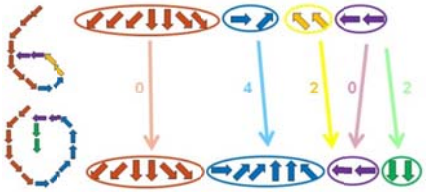

(a) distance between '0' and '0' is 8

Fig. 4. Examples of the subunit-based DTW distance between movements

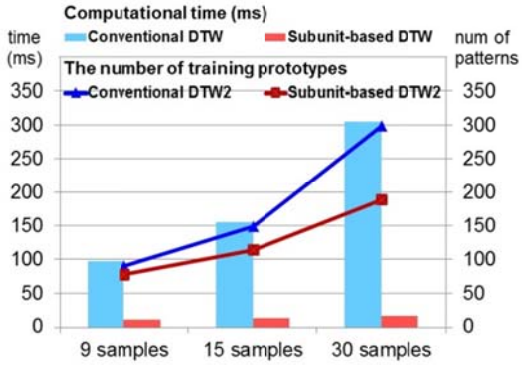

Fig. 5. Average computation time of recognition for different sizes of datasets

7 CONCLUSION

This paper proposes a subunit-based approach to hand movement recognition. In contrast to conventional DTW approaches, we share subunits across hand movements to obtain a smaller training data size and search space to improve recognition performance. In addition, a more robust similarity measure, using subunit-to-subunit matching, is offered. The experimental results demonstrate that the proposed approach is both accurate and efficient for hand movement recognition. Our future research will focus on incremental learning for the subunit itself to support efficient personalized recognition.

REFERENCES

[1] Wachs JP, Kölsch M Stern, et al (2011), Vision-based hand-gesture applications. Commun. ACM 54:60-71

[2] Okada S, Hasegawa O (2008), Motion recognition based on dynamic-time warping method with self-organizing incremental neural network. Proceedings of ICPR'08, pp.1-4

[3] Roussos A, Theodorakis S, Pitsikalis V, et al (2010), Hand tracking and affine shape-appearance handshape subunits in continuous sign language recognition. Proceedings of International Workshop on Sign, Gesture and Activity, ECCV 2010, pp.258-272

[4] Bauer B, Kraiss KF (2002), Towards an automatic sign language recognition system using subunits. In Revised Papers from the International Gesture Workshop on Gesture and Sign Languages in Human-Computer Interaction, vol.14, pp.64-75

[5] Elmezain M, Al-Hamadi A, Michaelis B (2008), Realtime capable system for hand gesture recognition using hidden markov models in stereo color image sequences. The Jour al of WSCG'08, vol.16, no.1, pp.65-72

[6] Cha SH, Shin YC, Shihari SN (1999), Approximate stroke sequence string matching algorithm for character recognition and analysis. In Proceedings of the ICDAR 1999, pp.53-56

[7] Han JW, Awad G, Sutherland A (2009), Modelling and segmenting subunits for sign language recognition based on hand motion analysis. Pattern Recognition Letters 30(6): 623-633

[8] Park HS, Jun CH (2009), A simple and fast algorithm for k-medoids clustering. Expert Systems with Applications 36:3336-3341

The Eighteenth International Symposium on Artificial Life and Robotics 2013 (AROB 18th '13),
Daejeon Convention Center, Daejeon, Korea, January 30-February 1, 2013

Mathematical modeling of mirror based passive moiré target for orientation sensing

M.M. Hasan[1], Satoshi Tanemura[1], and Kenbu Teramoto[1]

[1] Department of Advanced Technology Fusion
Saga University, Japan
E-mail: mahbub_eeekuet@yahoo.com
(Tel: 81-80-39017956)

Abstract: Mirror based passive moiré target has been studied mathematically and numerically. Mathematical model of the passive moiré target at CCD camera sensor plate has been developed mathematical considering its orientations. Based on the mathematical model, the moiré patterns are simulated for the proposed passive target. The simulated resulted are compared to the moiré pattern produced by the existing passive moiré target. From the numerical results, it is found that the proposed passive moiré target exhibits better sensing capacities.

Keywords: Mirror-based moiré passive target, specimen grating, reflected grating, low-frequency moiré pattern.

1 INTRODUCTION

Moiré fringes based sensing technology plays an important role in shape and position control, medicare, biomechanics, liquid wave analysis and sophisticated orientation determination, due to the non-contact nature of the measurement [1-3]. The moiré technique amplifies the small changes into sensible ranges by low cost and simple arrangement. For the position and orientation sensing system, the moiré arrangement which changes its pattern according to the observer position and orientation without using light source is desirable. This type of moiré arrangement is called passive moiré. On the other hand, the moiré sensing systems require lighting arrangement to make grating pattern are called active moiré [4-5]. The research on passive moiré has been reported recently by different authors in which, a moiré target has been proposed by using two same types of specimen gratings attaching in opposite sides of a transparent substrate [6-7]. In this case, the moiré fringes become visible due to interaction of the two gratings which response to the position and orientation. The linear gratings are utilized in these reports and mathematical formulations have been developed for the arrangements. In this report, mirror based passive moiré target has been proposed in which only one specimen grating is required. In the two gratings passive moiré arrangement, two precisely identical gratings should be attached similarly in opposite sides of a substrate. But, the present mirror based one grating arrangement is free from these limitations. To the best of our knowledge, the mathematical or experimental reports on mirror based moiré fringes have not published yet. In this paper, mathematical formulations have been developed based on the orientation of the moiré target. The mathematical relations indicate the intensity of moiré fringes captured by the CCD sensor. The specimen grating function and the reflected grating functions are multiplied to form the moiré pattern. The low frequency term represents the moiré pattern.

The article is organized as follows: in section 2, the mathematical relations have been developed, in section 3, the simulated results from the mathematical relations will be shown, and at last we will draw a conclusion.

2 Mathematical Formulations

For developing mathematical formulation of the moiré fringe, the equation of 2D target plane in three dimension space has been derived. Then the equation of the line that passes through camera image plane point and focal point of the camera (projection line) are also derived. The intersection point of the target plane and projection line has been calculated. This intersection point grating intensity is the image intensity. For calculating the second grating (reflected grating) image intensity the optical ray reflection theory has been used. Then the image intensity function has been multiplied for getting moiré fringes image.

For deriving the mathematical equation consider the fig.1. First the formulations are developed based on target plane origin. Here (x, y, z) is a point on the rotated target plane. The X and Y-axis rotational angles are θ and β respectively. The relation between the rotated plane point (x, y, z) and corresponding before rotation plane point (x', y', z') can be expressed by the following equation:

$$\begin{bmatrix} x' \\ y' \\ z' \end{bmatrix} = \begin{bmatrix} \cos\beta & 0 & \sin\beta \\ \sin\beta\sin\theta & \cos\theta & -\cos\beta\sin\theta \\ -\sin\beta\cos\theta & \sin\theta & \cos\beta\cos\theta \end{bmatrix} \begin{bmatrix} x \\ y \\ z \end{bmatrix} \quad (1)$$

From the fig.1, we can write $z' = 0$ as we consider the

© ISAROB 2013

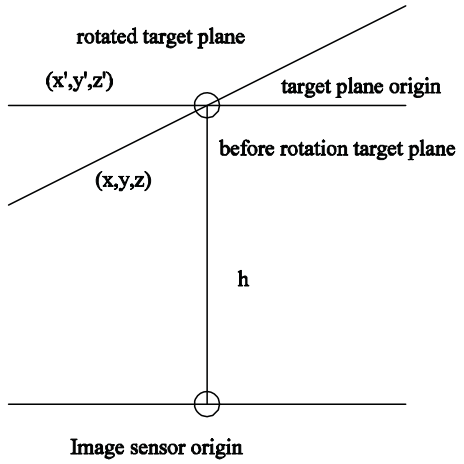

Fig1. One-dimensional moiré target

target plane canter as origin. Putting $z' = 0$ in equation (1), we have:

$$z = \frac{ax - by}{c}; a = \sin\beta\cos\theta; b = \sin\theta;$$
$$c = \cos\beta\cos\theta \qquad (2)$$

This is the equation of the rotated target plane considering origin at target plane centre. But if we consider origin at camera image sensor centre, then we have to modify the equation (2) by the following:

$$z = \frac{ax - by}{c} + h \qquad (3)$$

One dimensional model of camera image scanning process is shown in fig.2. In fig. 2, FOV is the field of view of the camera, f is the focal length of the camera. From fig.2, we can write the following equation:

$$f = \frac{X_{\max}}{\tan(FOV/2)} \qquad (4)$$

The straight line from target plane to image sensor plane passes through focal point $(0,0,f)$ and image sensor plane point (x_i, y_i). So, the equation of the straight line is

$$\frac{x - x_i}{-x_i} = \frac{y - y_i}{-y_i} = \frac{z}{f} \qquad (5)$$

To determine the point of rotated target plane whose intensity are scanned by the image sensor plane point (x_i, y_i), we have to find out the intersection point of equation (3) and (5). After some calculation and simplification, the coordinate of the intersection point on rotated target plane has been evaluated as following:

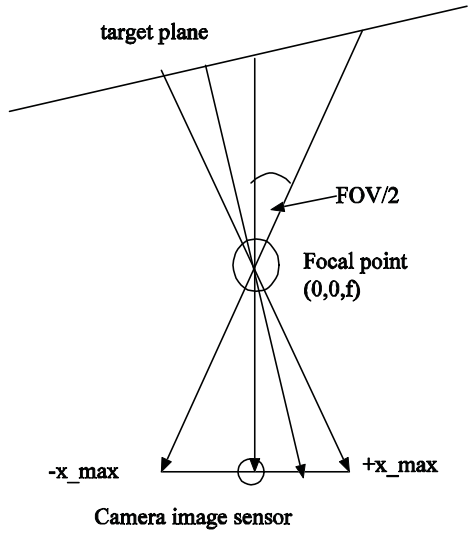

Fig.2: Camera image scanning process

$$x = \frac{cx_i(f - h)}{(cf - by_i + ax_i)}$$
$$y = \frac{cy_i(f - h)}{(cf - by_i + ax_i)} \qquad (6)$$
$$z = \frac{(ax_i - by_i)(f - h)}{(cf - by_i + ax_i)}$$

It is easier to obtain the intensity at point (x, y, z) by finding the before rotation point of point (x, y, z). If before rotation coordinate is (x', y', z'), we are interested in only x' and y'. We can write the expression of x' and y' as following:

$$x' = x\cos\beta + z\sin\beta \qquad (7)$$
$$y' = x\sin\beta\sin\theta + y\cos\theta - z\cos\beta\sin\theta$$

If the target plane grating is Fresnel zone plate (FZP), the intensity of first grating at camera image sensor plane can be expressed by equation(8)

$$G1(x_i, y_i) = \cos\left(\frac{x'^2 + y'^2}{l\lambda}\right) \qquad (8)$$

The second grating is the reflected image of the attached grating (i.e. first grating). The simplified one-dimensional representation of optical ray diagram of target considering Y-axis rotation is shown in fig.3. This figure shows how grating illuminates the camera image sensor plate by reflection. So, from fig.3, it is found that image sensor point A is illuminated by the intensity of grating point B and C. Here, the target rotates around Y-axis and the rotation angle is β.In case of X-axis rotation, the situation is shown in fig.4. From fig.3 and fig.4, the Z-axis rotation will not

© ISAROB 2013

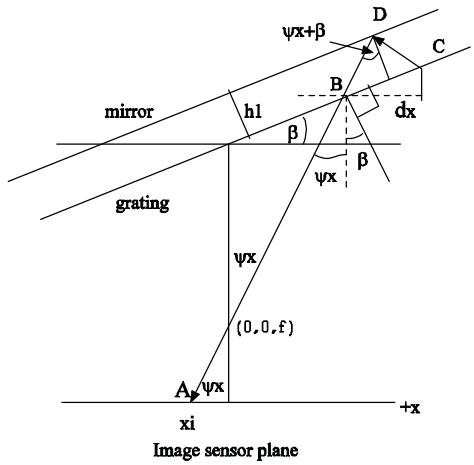

Fig.3: One-dimensional view of reflected grating considering Y-axis rotation

affect on the expression of dx and dy. So, the image sensor point (x_i, y_i) will also illuminated by the point $(x'+\mathrm{dx}, y'+\mathrm{dy})$ of the grating by reflection. If we consider $x'' = x' + dx$ and $y'' = y' + dy$, the equation of the intensity of the reflected grating can be expressed according to the equation

$$G2(x_i, y_i) = \cos\left(\frac{x''^2 + y''^2}{l\lambda}\right) \qquad (9)$$

The equation of the moiré fringes with grating can be expressed by the following equation

$$I(x_i, y_i) = G1(x_i, y_i)G2(x_i, y_i) \qquad (10)$$

we are interesting only in low frequency moiré. So, the captured moiré can be modeled by the equation

$$I(x_i, y_i) = \cos\left(\frac{2x'\mathrm{dx} + 2y'\mathrm{dy} + \mathrm{dx}^2 + dy^2}{l\lambda}\right) \qquad (11)$$

3 Simulated Results

Then numerical experiment has been performed based on the developed mathematical relations for the proposed moiré target. The simulated results for the proposed moiré target have also been compared with the two gratings moiré targets [6]. For numerical experiments, the parameters are selected considering the experimental conditions. The parameters are: field of view of the camera is 20 degree, both width and height of CCD sensor is 24mm, focal length is 30mm. From the simulated results, it is found that three closed contour moiré fringes are produced when distance from CCD to sensor target is 100mm and rotational angles are set to zero, which is shown in fig.5. Two closed contour

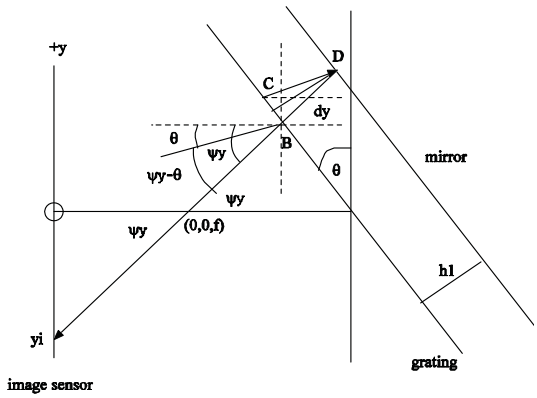

Fig.4: One-dimensional view of reflected grating considering X-axis rotation

moiré fringes are produced in this case for the two grating moiré target which is shown in fig.6. Three closed contour and one open contour moiré fringes are observed when rotation around X-axis is 2 degree $(\theta = 2\,\mathrm{degree})$ which is shown in fig.7. For the 2 degree angular rotation, two closed contour moiré fringes are produced for the two grating moiré target as shown in fig.8. When both X $(\theta = 2\,\mathrm{degree})$ and Y-axis $(\beta = 2\,\mathrm{degree})$ rotational angles are present, the number of contour remains same, but the moiré fringes orientation has been changes according to the ratio of θ and β as shown in fig.9. So, moiré fringes with higher number of contours are observed in our proposed moiré target. As the sensitivity depends on the numbers of contour, the proposed passive moiré target is more sensitive.

4 Conclusion

The moiré patterns produced from the proposed mirror based moiré target are compared with the moiré target described in [6]. For the same values of rotational angles, the proposed moiré target produced more contours moiré pattern, which enhances the sensing capacity and increases sensitivity.

REFERENCES

[1] E.U. Wagemann and T. Haist and M. Schönleber and H.-J. Tiziani, Fast shape and position control by Moiré-filtering and object-adapted fringe projection, Optics Communications,vol. 165, no.1-3, pp.7-10, 1999.

[2] Jinyou Shao and Yucheng Ding and Hongmiao Tian, and Xin Li and Xiangming Li and Hongzhong Liu, Digital moire fringe measurement method for alignment in imprint lithography, vol. 44, no.2, pp. 446-451, 2012.

© ISAROB 2013

[3] Pollyanna F. Gomes and Meinhard Sesselmann and Christina D.C.M. Faria and Priscila A. Araujo and Luci F. Teixeira-Salmela, Measurement of scapular kinematics with the moiré fringe projection technique, vol.43, no.6, pp.1215-1219,2010.

[4] Daniel Post and Bongtae Han and Peter Ifju, High Sensitivity Moire, Springer, 1994.

[5] Chia-Ming Liu and Lien-Wen Chen, Using the digital phase-shifting projection Moiré method and wavelet transformation to measure the deformation of a PMMA cantilever beam, Polymer testing,vol.24, no.5, pp. 576-582,2005.

[6] Glenn P. Tournier, Six degree of freedom estimation using monocular vision and moire patterns, M.Sc thesis, Massachusetts Institute of Technology, 2006.

[7] Eric Feron, Jim Paduano, A passive sensor for position and attitude estimation using an interferometric target, Proc. of 43rd IEEE conference on Decision and Control,vol.2,pp.1663-1669,2004.

Fig.5: Low frequency moiré fringes from proposed target when $\theta = 0, \beta = 0, h = 100mm$

Fig.6: Low frequency moiré fringes from existing target when $\theta = 0, \beta = 0, h = 100mm$

Fig.7: Low frequency moiré fringes from proposed target when $\theta = 0, \beta = 2, h = 100mm$

Fig.8: Low frequency moiré fringes from existing target when $\theta = 0, \beta = 2, h = 100mm$

Fig.9: Low frequency moiré fringes from proposed target when $\theta = 2, \beta = 2, h = 100mm$

© ISAROB 2013

The Eighteenth International Symposium on Artificial Life and Robotics 2013 (AROB 18th '13),
Daejeon Convention Center, Daejeon, Korea, January 30-February 1, 2013

A study about interactive musical editing system for automatic piano : Inferring performance expression by considering tempos

Tomohiro Inoue[1], Eiji Hayashi[2]
[1]Kyushu Institute of Technology Graduate School of Computer Science and Systems Engineering, Japan
[2]Kyushu Institute of Technology Department of Mechanical Information Science and Technology, Japan
(Tel:0948-29-7775)

[1]inoue@mmcs.mse.kyutech.ac.jp
[2]haya@mse.kyutech.ac.jp

Abstract

We developed a system that allows a piano to perform automatically. To enable an automatic piano to play music with the emotional expression that a skilled human pianist can provide, all of the notes in the score must be arranged. The simulation of the emotional expression in an actual performance by a highly skilled pianist would take a great deal of time by a music editor, and in the present research, we structured an interactive music editing system to edit music more efficiently.

The system is based on a concept, "Similar-patterned phrases within the same composition are performed with similar emotional expression," and is composed of two systems: the "searching system of similar-patterned phrases" and the "inferring system of emotional expression in a performance."

In the searching system, we use dynamic programming (DP) matching as the method for searching for similar phrases. In the inferring system, we use Musical Rules Databases that contain information regarding the musical symbols used by pianists for inferring emotional expression in a performance.

Key words: *automatic piano, knowledge database, computer music, DP matching, Music Interface*

1. Introduction

We developed a system that allows a piano to perform automatically. In this system, 90 actuators are installed in the keys and pedals of a grand piano. These actuators perform the key strokes and pedaling during the piano's performance (Fig. 1).

To enable an automatic piano to play music as performed by a human pianist, we must arrange all of the notes in scores. In the case of piano music, the average score contains 1,000 or more notes. Moreover, a skilled pianist is able to play an unfamiliar piece of music by sight, even if the performance is not completely in accord with a specific musical interpretation. In contrast, current computing systems, such as MIDI, cannot truly perform a new piece of music by sight in that they cannot simulate the emotional expression of a human pianist's performance without direction. Therefore, a simulation of the emotional expression in a performance by a highly skilled pianist would take a great deal of time by a music editor. In the present research, we developed an interactive music editing system to edit music more efficiently and to enable the automatic piano to simulate the emotional expression of a skilled human pianist."[1]

This system is composed of a concept that we arrived at by analyzing pianists' expressive tendencies: "Similar-patterned phrases within the same composition are performed with similar emotional expression." In accord with this concept, the editing system is composed of a "searching system of similar-patterned phrases" and an "inferring system of emotional expression in a performance."

In the searching system, we use dynamic programming (DP) matching. This method maps two character strings dynamically and calculates the degree of disagreement of the strings, which is used as an index to determine resemblance.

In the inferring system, we use Musical Rules Databases that are programmed with the musical knowledge of pianists. Their data express the influence of musical symbols numerically. Our interactive musical editing system refers to these databases and infers similar phrases automatically.

Here we describe and evaluate the results of inferring similar phrases when using the parameter called "Step," which determines the tempo.

Fig.1. The automatic piano.

© ISAROB 2013

2. Music Editing Support System

2.1. System architecture

The structure of the music editing support system is shown in Figure 2. The human user edits music via the user's interface on a computer display. The interface edits automatically by referring to the Musical Rules Database which contains information regarding the musical symbols used by pianists. The user's editorial work is greatly reduced and efficient editing becomes possible.

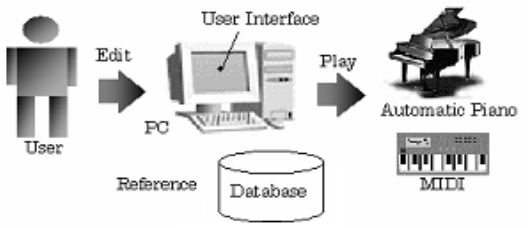

Fig.2. Structure of the editing system.

2.2. Format of performance information

The parameters of the performance information are shown in Table 1.

The data for our automatic piano system are similar to those used by MIDI(Musical Instrument Digital Interface). We defined the performance information by dividing it into two categories: the notes and the pedals. The note information is comprised of the six parameters involved in producing a tone: Key (note), Velo (velocity), Gate, Step, Bar, and Time. "Velo" is the dynamics, given by the value of 1 to 127. "Gate" is the duration of the note in milliseconds (ms). "Step" is the interval of time between notes, and it also depends on the tempo. "Bar" is the vertical line placed on the staff to divide the music into measures.

The pedal information is comprised of four parameters: Key (indicating the type of pedal: Damper or Shifting), Velo (the pedaling quantity), Time (the duration for which the pedal is applied), and Bar.

Table.1. Parameters for automatic piano.

Parameter	Key	Velo	Gate	Step	Time	Bar
Range	21~108	0~127	Depend on Tempo	Depend on Tempo	0~	1~
Unit	–	–	ms	ms	ms	–

2.3. Searching system of similar phrases

2.3.1. Dynamic programming (DP) matching

We used dynamic programming (DP) matching as the method for searching for similar phrases. This method maps two character strings dynamically and calculates the degree of disagreement of the strings, which is used as an index to determine resemblance.

As an example, we'll explain how the resemblance is determined between two strings, "abb" and "aabb." DP matching is applied through the following steps.

Step 1. Draw a route consisting of the strings.

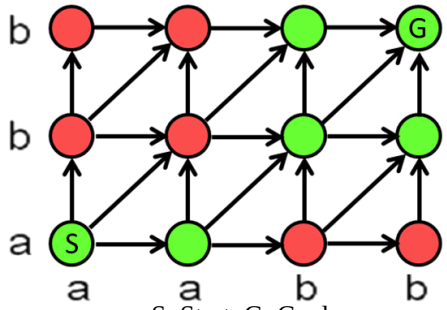

S: Start, G: Goal

Fig.3. A route consisting of the strings.

Step 2. Set the costs for calculating the minimum value.

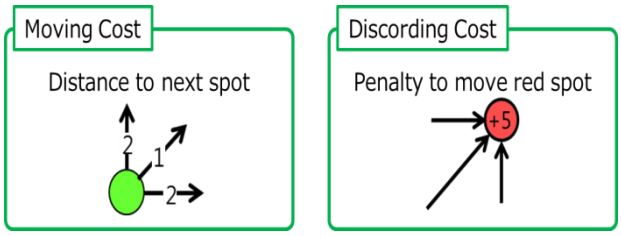

Red spot: Spots composed of different characters

Fig.4. The costs for calculating the minimum value.

Step 3. Calculate the minimum value to achieve the goal.

In this example, the minimum value is 4 and the shortest route is shown by the red arrow.

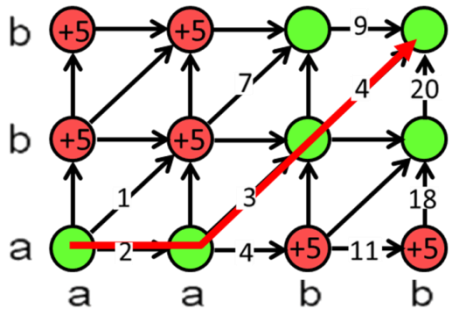

Fig.5. Total costs for reaching the goal.

Step 4. Check the one-to-one correspondence between the strings.

Pursuing the shortest route, we obtain a one-to-one correspondence of the strings. The character string, "abb", is expanded to "aabb" and this string corresponds to "abbb" (Fig.6).

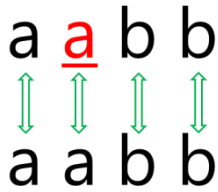

Fig.6. Correspondence between the strings.

© ISAROB 2013

2.3.2. Converting the notes into character strings

For use with the DP matching method, we built a Score Database which contains information regarding the musical score, with a field called "Note Value." The data in this field indicates a particular type of note, e.g., a quarter note, a triplet, and so on. Our interactive musical editing system converts notes into character strings using the "Note Value data." (Fig. 7).

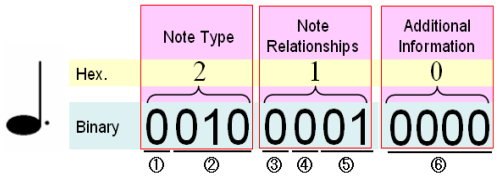

1. Note or Rest (0: Note, 1: Rest)
2. Note Value (000: A whole note, 001: A half note …etc.)
3. Tie (0: No tie, 1~: The number of ties)
4. Ornament (1: This note has an ornament)
5. The number of dots (except that if it is "11" then the note is a tuplet.)
6. Additional Information

   The number of tuplets (Triplets: 0011)

   The type of ornament (Trill: 0101), etc.

Fig.7. Note values.

2.3.3. Process of searching similar phrases

First, we designate an input phrase for searching similar-patterned phrases and we set a threshold for the total costs.

Then, the searching system searches for phrases that resemble the input, using DP matching. Throughout this process, this system outputs all phrases that have a minimum cost less than the threshold as similar-patterned phrases. In our study, we called these phrases Similar Phrases.

These phrases are not edited, so we infer the emotional expression in a performance by using the inferring system.

2.4. The inferring system of emotional expression in a performance

2.4.1. Parameters used in the inferring system

In this example of the inferring system, we use the parameter called "Step," which is the interval of time between notes and which determines the tempo.

Each note, e.g., a quarter note, has an absolute time that depends on the tempo. We called this time the "Phonetic Value."

However, increases and decreases in this time exist in performance by a human pianist: thus, we introduce the parameter "StepRate"

$$\text{StepRate} = \frac{Step[ms]}{Absolute\ Time[ms]} \quad (1)$$

To compare the tendencies of each note, we store this parameter in the relevant Musical Rules Database.

2.4.2. The Musical Rules Databases

The Musical Rules Databases contain the musical knowledge of pianists. We analyzed the MIDI data of performances of highly skilled pianists in order to observe the pianists' expressive tendencies, and we used these tendencies and musical knowledge to build these databases.

Musical Rules Databases are composed of five tables: Dynamics marks, Articulation marks, Symbols of Changing Dynamics or Changing Tempo (symbols that affect the speed of a note or the increase or decrease of the volume), Time signature, and Tempo marks. Each database has data that expresses the influence of musical symbols numerically.

RSoho(60)	番号	記号	VeloRate	GateRate	StepRate	Gate_R_netu	Step_R_netu
1	1	mezzo_staccato	1.00	0.42	0.68	1.00	1.00
2	2	accent	1.00	0.42	0.68	1.00	1.00
3	3	legato	1.00	0.42	0.68	1.00	1.00
4	4	marc.	1.00	0.42	0.68	1.00	1.00
5	11	sf	1.22	0.58	0.70	1.36	1.02
6	5	slur	1.00	0.42	0.68	1.03	1.00
7	12	slur_end	0.95	0.42	0.68	0.95	1.00
8	10	slur_staccato	1.00	0.42	0.68	1.00	1.00
9	6	sostenuto	1.00	0.42	0.68	1.00	1.00
10	7	spiccato	1.00	0.42	0.68	1.00	1.00
11	8	staccato	1.00	0.42	0.68	1.00	1.00

Fig.8. Example of a Musical Rules Database.

2.4.3. The inferring process

Here we explain the process of inferring emotional expressions in a performance, using an example with two phrases: part of the first movement of Beethoven's 'Sonata Pathétique' as an input phrase, and the first movement of his sonata Appassionata as a similar phrase (Fig.9a. and Fig.9b).

Inferring emotional expression in a performance of similar-patterned phrases is accomplished through the following steps.

© ISAROB 2013

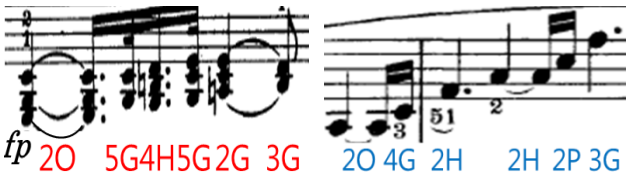

(a) Input phrase (b) Similar phrase

	Musical notations				Musical notations		Position in the bar
No.	Dynamic	Articulation		No.	Dynamic	Articulation	
1	p	fp	⟷	1	pp	slur	
2	p	–	⟷	2	pp	slur	
3	p	–	⟷	3	pp	slur	
4	p	–	⟷	4	pp	slur	Last
5	p	–	⟷	5	pp	slur	First&Before the rest
6	p	–	⟷	6	pp	slur	

(c) Correspondence between the two phrases

Fig.9. Phrases for inferring system.

Step1. Apply the input phrase data to the similar phrase.

We change the similar phrase's value of "StepRate" into the same value of the input phrase considering the correspondence between the two phrases (Fig. 9c).

Step2. Revise by using "Dynamics marks."

We changed the dynamics marks of the input phrase into the same dynamics marks of the similar phrase.

As illustrated in Figure 9c, we changed the dynamics marks "*p*" into "*pp*."

Step3. Revise by using "Articulation marks."

We changed the articulation marks of the input phrase into the same marks of the similar phrase.

As shown in Figure 9c, we changed the articulation marks of all of the notes to "slur."

Step4. Consider the positions of the notes.

"A note before a rest," "First note of a bar" and "Last note of a bar" are all notes with a particulartendency (Fig. 10).

A note with a tendency has these values if the "StepRate" of the standard note is 1. (Fig. 10)

In this case, note No. 4 in the similar phrase must be changed to the value of the "StepRate" by considering this relation.

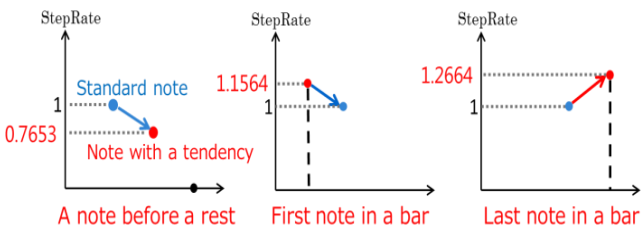

Fig.10. Values of notes with a tendency.

By following the above steps, we obtain results such as those shown in Figure 11. The results provide three values: the "Input phrase," which is non-edited data, the "Result of inferring" and the "Pianist Data," which is the actual emotional expression in a performance by a pianist in the similar phrase.

We have consistently found that the emotional expression represented by the "Result of inferring" resembles the "Pianist Data" more than it resembles the "Input phrase."

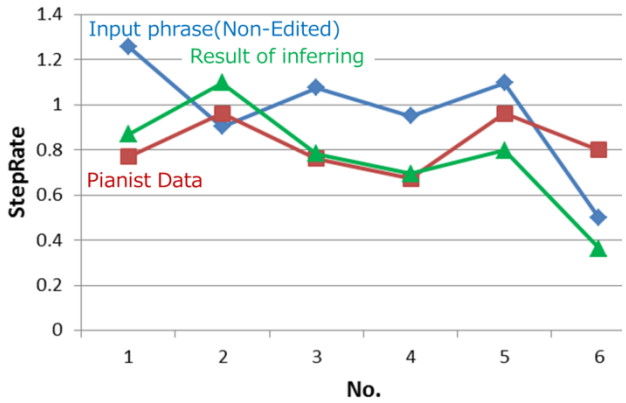

Fig.11. Results of inferring.

3. Conclusions

We developed an interactive musical editing system to edit music more efficiently. This system is composed of a "Searching system of similar-patterned phrases" and an "Inferring system of emotional expression in a performance. The Inferring system infers the emotional expression in a performance of similar phrases by referring to the databases automatically, greatly reducing the time needed for editing. We improved the Inferring system by using StepRate, which is the ratio of the Step to the PhoneticValue and is stored in the Musical Rules Databases.

Moreover, the interactive musical editing system provides edited phrases that resemble the "Pianist Data," which are the actual emotional expressions in a performance by a skilled human pianist.

References

[1] Hayashi, E. et al, "Behavior of piano-action in a grand piano.I", Journal of acoustical Society of America, Vol.105, pp.3534-3544, 1999.

© ISAROB 2013

The Eighteenth International Symposium on Artificial Life and Robotics 2013 (AROB 18th '13),
Daejeon Convention Center, Daejeon, Korea, January 30-February 1, 2013

A simple wall-climbing mechanism for a window cleaning robot

Takafumi Soeda[1], Nobuhiro Okada[2], and Kazuo Kiguchi[1,2]

[1]Kyushu University, Japan
[2]Kyushu University, Japan
(Tel: 81-92-802-3167)

[1]2TE11331E@s.kyushu-u.ac.jp

Abstract: In this paper, a new type of wall climbing robot to clean window is proposed. The developed robot can climb the pane by using a crawler with ordinary suckers. The suckers of the crawler sequentially stick to the window and the robot climb the pane. The robot will be low-cost and simple. The robot was tested to see whether it have performance to climb the window and to carry cleaning equipments. As the result, it was confirmed that the developed robot can move on the window. This paper gives motivation of this development, concept design of this robot, the details of the system, the experimental result, conclusions and future work.

Keywords: robot, window cleaning, crawler, ordinary sucker

1 INTRODUCTION

Recently, the automation of the window cleaning is requested. The number of high-rise building which uses large-scale panes is increasing. And window cleaning has been done by human or by large equipment. They are very dangerous and expensive. It is important that developing safer and cheaper robot to clean the window [1][2].

Many small robots to clean the window have been developed. Such robots can be classified into four types according to the adhesion methods [8]: magnetic, hand-hold, biologically inspired and vacuum suction pad type.

The magnetic method is used magnet for absorbing and wheel for driving [3]. This method has the can steadily absorb the wall and not need electric power for absorbing. However, it has the problem that it is difficult to put the window and that the robot makes the window dirty like stripes by stick slip motion [4] because the frictional force between the magnet and the window. The other, there is a mechanism that adsorbs the wall of iron by permanent magnets and move in itself as wheel [5]. But it is possible to use only for the wall of iron, and can't adopt for window cleaning robot.

The hand –hold method can support very strong adhesion force but it requires special equipment like knobs.

The biologically inspired method does not need no electric power for creating the absorb force. However the possible payload is very small.

The vacuum suction pad type method is a mechanism that adsorbs onto the wall by negative pressure of the vacuum pump, and to run with the wheel for the drive [6][7]. The robot have this mechanism can freely set the adsorption force, easily put the window and easy to control. However, the robot has danger of falling when the trouble is caused in the supply of electrical energy because the vacuum pump of the robot needs the electric power.

Thus, the proposed mechanisms of climbing the wall have the fault respectively, and the development of a new mechanism for wall climbing robot is demanded.

In our laboratory, from such back ground, develop climb the window by rotating a crawler that has general purpose suckers. This robot has the mechanism that climb the wall with an easy mechanism that does adsorb and peel off the glass by the suckers, and the following merits exist.

1. There is no fear of the fall by the electric power cutting.
2. It is suitable for lightening and lowering the cost because the robot has easy mechanism
3. It contributes to conservation of energy because it doesn't need electric energy for adsorb the window.

From the above reason, it is thought that the robot will be lower-cost and simpler than other methods.

We perform some experiment to evaluate this robot.

2 CONCEPT DESIGN OF THE ROBOT

This paper takes the building that has ruggedness o n the wall because it is difficult to adapt by the large-scale cleaning system.

The function demanded from the window cleaning robot is to adsorb outside in the window that is neede d cleaning in some means and to wipe up the window while automatically moving the all aspects of the win dow. For this function, function that moves from objec ted window to another window and that moves with a dsorbing the window are needed.

In the case of the large-scale cleaning system, the hanging crane mechanism must set up in the rooftop t

© ISAROB 2013

o fix the cleaning mechanism to the vicinity of the pa ne, which makes this system more expensive.

On the other hand, small window cleaning robot ne eds to adsorb window and move with adsorbing windo w steadily. Additionally, it also needs the function that wipes all aspects of the window without the lack of wipe and the wipe mark to clean the window perfectly. Then, it is hoped that the robot clean the window wh ile climbing it autonomously.

A small window cleaning robot is needed to move from objected window to another window while getting over the ruggedness, but it is very difficult to develop such function. Then, in this case, we make the approach to develop such function a deferment, and try to achieve to plan that a user set the robot in each window and the robot clean each one window sequentially.

Fig.1 shows the plan that we summarized such idea. We presume that this plan becomes the following procedures.

① The user takes out the robot from the inventory location, and supply to the robot for window cleaning such as water.
② The user adsorbs the robot onto the window and start up the robot. The robot cleans the window autonomously and returns the first position. In this case, the provision of the electrical energy for the robot assumes the power source from indoor by power code which also behaves as a safety rope.
③ The user gets out the robot from the window, and returns it the inventory location.

Thus, we try to trim the weight and to reduce the risk of fal out by using power code from indoor power source an- d combine with the safety rope.

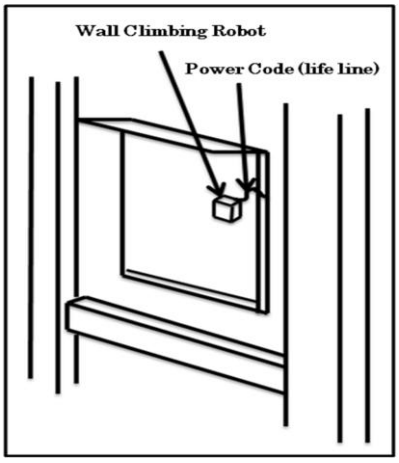

Fig.1. Concept of automated window cleaning

The robot needs the following condition because many robots are needed to carry out such plan and general public use it.

1. The costs about one robot are cheap.
2. It is easy to maintenance.
3. It is a safe for all the people.

Then, we spot the mechanism use the crawler installed s ome ordinary suckers, and climb the vertical pane by adsorb the suckers onto the window and rotate the crawler. The idea suitable to trim weight and to develop cheaper by compared with negative pressure adsorption mechanism an d magnet adsorption mechanism. And it doesn't have the ris k of fall out by electricity failure.

For the above- mentioned reasons, we decided to adopt this mechanism for this plan.

In our laboratory, one robot was made on the basis of this plan [9].The length of the robot that has been made before in the laboratory is 630mm. It is too bi g. In addition, the weight of robot was 4.0kg, it was not working properly. Then, a new smaller robot is developed. The goal was reduced to about 200mm, wh ich is about one-third the size of the robot prior to a size that can easily carry. Sucker which is used in the previous robot was 56mm in diameter. In order to red uce the size of the robot, a sucker diameter of 42mm is selected in ordinary suckers. The size is the smaller one in the ordinary suckers.

Experiment was carried out as shown in Fig.2 in order to know the performance of this sucker. Fig.3 shows the result of the experiment. It can be seen that approximately 8.2kg withstand the load of one suction cup to be used from the experimental result. Design of the robot is performed based on the performance of this sucker.

Fig.2. The outline of a perpendicular load experiment

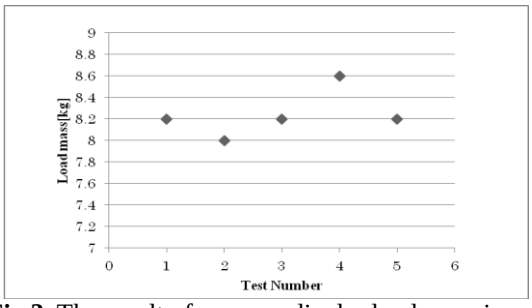

Fig.3. The result of a perpendicular load experiment

3 THE DEVELOPMENT OF THE ROBOT

3.1 The spec of the robot

Fig.4 shows the picture of the developed robot. And Fi g.5 shows the diagrammatic illustration of a wall cleaning robot. This robot is composed of a crawler that has suckers that have a knob, sprocket, and pulley. Then a DC motor is used to drive the crawler.

Total weight of system is 0.8kg. Therefore, the robot can

© ISAROB 2013

afford to have equipment such as cleaning unit because the one of the suckers can hold 8.2kg. The robot's dimensions are 100mm width, 210mm length, and 150mm height. This size is about a third of test model which was made in our earlier study, and the weight is about one-fifth of it. We have refined the concept design so that the size will become suitable to the performance of the suckers. It also contributes in a downsizing of the robot.

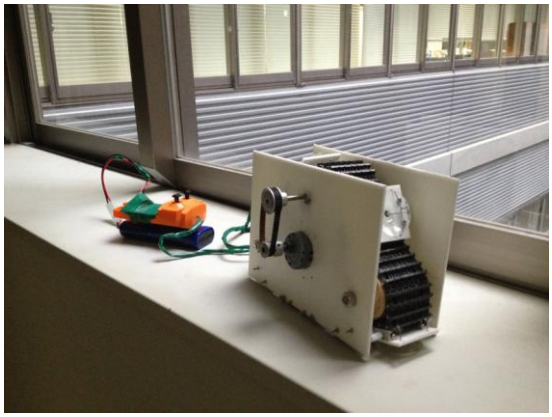

Fig.4. The picture of developed robot

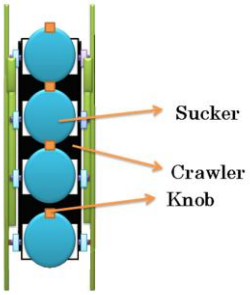

Fig.5. Overall view of robot of climbing the window

3.2. The system of the window climbing

The robot climbs the pane by using a crawler with ordinary suckers. The suckers of the crawler sequentially stick to the window and the robot climb the pane. The suckers are assembled to the crawler so that one or more suckers stick to the window at all times. Total weight of system is 0.8kg and one of the suckers can hold 8.2kg. It means that the robot doesn't fall down if one sucker falls of the window.

Fig.6 shows the outline of the system to climb the pane. When the crawler rotates, the sucker at adsorbing step is pressed to the wall by the rollers moving along the ledge. Then the sucker at holding step keeps absorbing the wall until the roller passes the ledge, also, push the sucker at adsorbing step. The sucker at peeling step peels off when the knob is pushed up by the movement of the crawler.
Thus, the robot keeps absorbing and moves ahead.

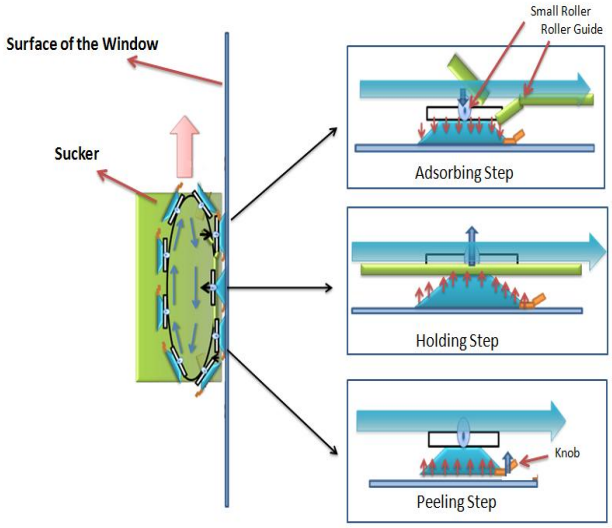

Fig.6. The outline of system

4 EXPERIMENT

In experiment, the robot was adsorbed onto the window and started up. Fig.7 shows the outline of the experiment. Then, we made sure whether the robot could climb the window.

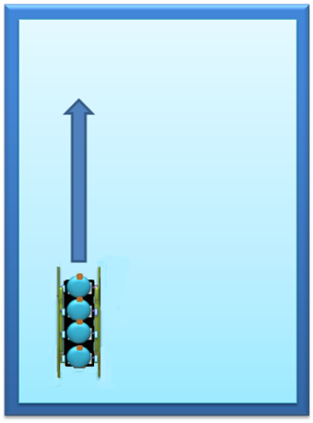

Fig.7. The outline of experiment

5 CONCLUSION

In this paper, the research and development of the window cleaning robot was described as an approach of the window cleaning on the automation. Firstly, we view an idea about the window cleaning using a small wall climbing robot. And propose the robot including the mechanism can climb the pane with simple suckers. Then we actually fabricated the robot and performed an experiment that made sure whether it could climb the window.

Future works are assembling equipments to turn the robot and to control the trajectory of the robot. For exampl e, we try to turn the robot by attach omni-wheel backward of the robot. And try to control the robot by attach the touch-sensitive switch and acceleration sensor to clean the

© ISAROB 2013

window more suitably.

REFERENCES

[1] Furuhashi (2004), Maintenance and structural skill with glass architecture No. 653, pp.182-183

[2]Nishijima, Mizusima (1992), The development of a glass cleaning robot "Canadian Club", Journal of the Japan Society for Mechanical Engineers
Vol. 10 No. 5 pp.596-598

[3]Miyake T (2006), Research and development of w indow cleaning robot WallWalker-Present conditions an d perspective for commercial viability-, JSME Conferen ce on Robotics and Mechatronics, Waseda, Japan

[4]Nakano K, Kikuchi Y (2006), Conditional Expression for the Occurrence of Stick-Slip Motion based on the Coulomb Friction Model, Tribologist Vol.51 pp.131-139

[5]Zui-yuan Qian, Yan-zheng Zhao, Zhuang Fu (2006), Development of Wall-climbing Robots with Sliding Suction Cups, IEEE/RSJ International Conference on Intelligent Robots and Systems, Beijing, China

[6]Hirose S Tsutsumitake H, Development of Disk Rover, Wall-Climbing Robot using Permanent Magnet Disk, Journal of the Robotics Society of Japan Vol. 10 No. 7, pp. 992-997, (1992)

[7]Tsuru K, Yoneda K (2007), Window Cleaning Ro bot with Magnetic Synchronous Drive, Journal of the Robotics Society of Japan Vol. 25 No. 5, pp. 738-744

[8] Young Kouk Song, Chang Min Lee, Ig Mo Koo, et al (2008), IEEE/RSJ International Conference on Inte lligent Robots and Systems

[9]Okada N, Yamanaka K, Kondo E (2009), A Wall Climbing Robot with Simple Suckers, ICCAS-SICE

The Eighteenth International Symposium on Artificial Life and Robotics 2013 (AROB 18th '13),
Daejeon Convention Center, Daejeon, Korea, January 30-February 1, 2013

Topological Graph Based Boundary Coverage Path Planning for a Mobile Robot

Bong Keun Kim, Hideyuki Tanaka, and Yasushi Sumi

Intelligent Systems Research Institute, AIST, Tsukuba, Ibaraki, Japan
(Tel: 81-29-861-3282, Fax: 81-29-861-3493)

bk.kim@aist.go.jp

Abstract: A path planning method for the optimal boundary coverage of building interiors using a mobile robot is proposed. First, the data association problem of indoor modeling caused by localization uncertainties of an information gathering system such as a mobile robot is explained. Then, an expanded obstacle map is proposed to cope with the data association problem, in which the boundaries of the expanded obstacles are utilized as the path of a mobile robot. And also, the path enables a mobile robot to gather information on the obstacles at a certain distance. Next, a topological graph is utilized for the optimization of the travel path. Finally, simulation results are shown to verify the proposed algorithm.

Keywords: Boundary coverage path planning, Expanded obstacle map, Indoor modeling, Topological graph.

1 INTRODUCTION

This paper aims at developing a boundary coverage path planning method which allows a robot to gather ambient information at a certain distance in various structures of indoor environments.

The typical coverage path planning for cleaning and examination of indoor environments is focus on planning the path which allows a robot to pass all accessible area in a given environment. The cell decomposition method is one of the famous approaches for the area coverage path planning. Boustrophedon Cellular Decomposition (BCD) based method carries out optimal coverage of known environments using Reeb graph based critical points [1]. In order to explore surface using UAV, BCD based coverage path planning method was also proposed [2]. In order to solve a boundary coverage problem using multi-robot with an omnidirectional inspection sensor, K. Easton et al. proposed solution of kRPP(k-Rural Postman Problem) using simplified sensor model based graph representation [3]. This approach is most suitable for boundary inspection. But the inspection is not conducted at a certain distance.

On the other hand, the boundary coverage proposed in this paper is for the point cloud generation which expresses environments based on a set of vertices and for gathering information for texture mapping. In order to generate accurate point cloud, a robot should travel via points which allow the robot to collect relative position information of a given environment. And if texture information is collected successively at a regular distance, the frame transform using projective geometry can be reduced and the pixel density of images can be maintained uniformly and finally the image stitching error can be reduced. But the indoor environment with narrow hallways and a complex indoor structure prevents optimal positioning of a mobile robot for collecting ambient information.

Given these considerations, an expanded obstacle map which consists of obstacles with constant offset boundary and a path planning method using a topological graph are proposed to cope with these problems. As a result, a mobile robot can gather environment information at a certain distance continuously and come back to the start location by the minimum traversing distance via all boundaries of obstacles since it navigates the boundary coverage path which is an Eulerian circuit.

The rest of the paper is organized as follows. The following section introduces the data association problem of indoor modeling. Section 3 addresses the algorithm for boundary coverage path planning. Final section sums up with some concluding remarks.

2 DATA ASSOCIATION PROBLEM OF INDOOR MODELING

The point cloud generation using a mobile robot can be summarized as the following three steps.

1. Localization and mapping are conducted based on encoders, a gyroscope, and a horizontal LRF.
2. If the travel distance is long, the position error can be accumulated and it causes a loop closure problem. In order to cope with this problem, the graph SLAM can be utilized for minimizing the accumulated error [4]. As a result, if all the paths of a mobile robot are obtained, the pose of a robot at each sampling time can be calculated.

© ISAROB 2013

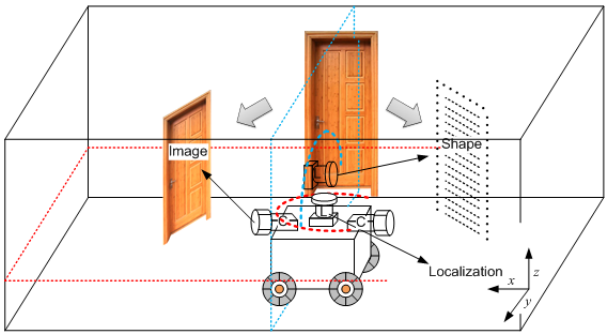

Fig. 1 Indoor modeling using a mobile robot.

3. Integrating the information from a vertical LRF based on a robot pose, the point cloud can be generated.

As a result, in order to generate the point cloud and to gather image information for texture mapping, it is required that a mobile robot navigates along the path on which it can gather ambient information optimally based on the structural characteristics of the surrounding space. Also, in order for reducing the frame transform using projective geometry and keeping the pixel density of visual image uniformly, it is required that image information for texture mapping is gathered continuously at a certain distance. But, the navigation with no regard for changing space disturbs the generation of point cloud with uniform density, and the inaccurate data association between the image and the position data may cause an image stitching problem in the texture mapping.

Fig. 1 shows the scanning patterns of a mobile robot with two laser scanners when it navigates in a corridor for gathering information required for the point cloud generation. The LRF which scans xy horizontal plane can be used for building an obstacle map based on 2D information of the environment. On the other hand, the information from the LRF mounted along z axis is dependent on the robot pose because it gathers information based on line scanning which is vertical to the direction of the robot. That is, since the line scanning is carried out as the blue dot line shown in Fig. 1, the information gathering is seriously affected by the structure of environment and the pose of the robot. Hence, the navigation of the mobile robot should be conducted in order for the second LRF to never miss the boundary of the obstacle.

To cope with these problems, the path planning method for the boundary coverage which allows a robot to gather environment information optimally using a given 2D map is proposed in the next section.

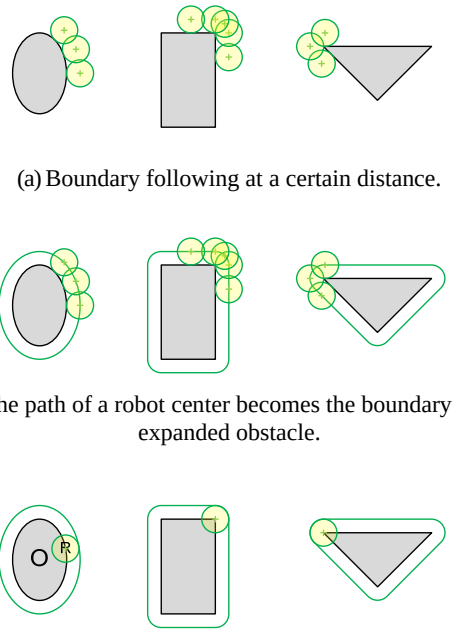

(a) Boundary following at a certain distance.

(b) The path of a robot center becomes the boundary of an expanded obstacle.

(c) Minkowski sum.

Fig. 2 Expanded obstacles.

3 BOUNDARY COVERAGE PATH PLANNING

The boundary coverage path planning method aims at generating the shortest path which allows a robot to travel via all the boundaries of obstacles in various indoor environments. In this paper, the boundaries of obstacles are generated based on expanded obstacles, and then the boundary coverage path is planned by using a topological graph. Hence, the proposed path planning method is composed of the following three steps.

First, expanded obstacles are generated based on the optimal distance which is required for information gathering. If a mobile robot navigates around an obstacle at a certain distance, then the path is generated as shown in Fig. 2 (a). The radius of the robot is the optimal distance. If the center points of the robot are connected, a certain distance offset from the obstacle is generated as shown in Fig. 2 (b). Hence, a robot with optimal sensing area in the obstacle map can be dealt with as a point robot in the expanded obstacle map. This means that if a point robot navigates along the boundary of an expanded obstacle, then the robot can gather environment information optimally. In this paper, an expanded obstacle is calculated by Minkowski sum, which is described by Eq. (1). Fig. 2 (c) shows Minkowski sum for various polygonal obstacles [5].

© ISAROB 2013

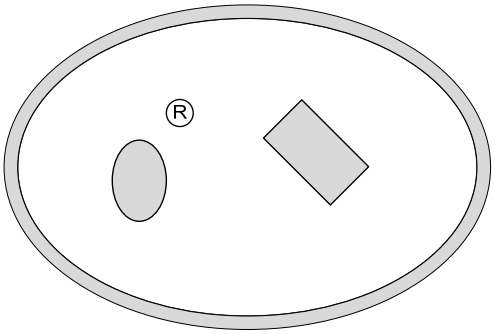

(a) Obstacle map

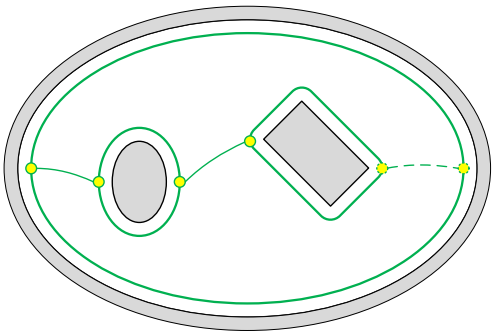

(b) Critical points and edges for disjoint obstacles

Fig. 3 Critical points and edges for disjoint polygonal obstacles.

$$O \oplus R = \{x + y | x \in O,\ y \in R\} \tag{1}$$

Next, the critical points based on Boustrophedon Cellular Decomposition (BCD) [1] are founded and the edges which connect critical points are replaced by the boundaries of expanded obstacles. Then the critical points and the boundaries are utilized as vertices and edges of the topological graph $G = (V, E)$. If expanded obstacles overlap each other and the intersection area doesn't overlap the obstacle, then the intersection points are included in the vertexes of the graph G because the point robot can gather environment information along the intersection boundaries.

Fig.3 (a) shows the expanded obstacle map of inner and outer obstacles. And Fig. 3 (b) shows critical points and edges of the expanded obstacle map. Without loss of generality, if the search is started from the left side, the last two critical points are not included in the vertex of the input graph because they are connected to the boundary of the obstacle which is already connected by other critical point.

Fig. 4 (a) shows the overlap of the boundaries in the expanded obstacle map caused by that two obstacles are located too close in the obstacle map. If the intersection area doesn't overlap the obstacle, then the intersection

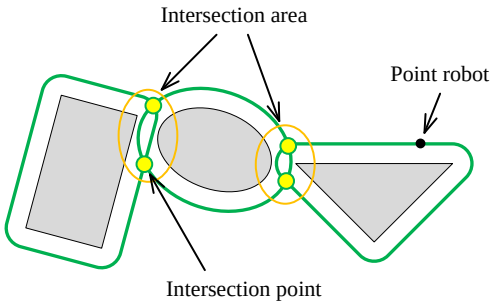

(a) Obstacles with intersection area

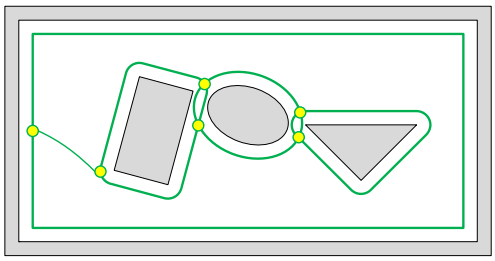

(b) Critical points and edges

Fig. 4 Critical points and edges for overlapping polygonal obstacles.

points are included in the vertices of the graph G because the point robot can gather environment information along the intersection boundary. Fig. 4 (b) shows critical points and edges for overlapping polygonal obstacles.

Finally, the boundary coverage path is calculated by Chinese postman problem with the topological graph [6], which is an Eulerian circuit. Since the Eulerian circuit is an Eulerian path which starts and ends on the same vertex, the obtained path is a closed path traversing via every edge at least once. The boundary coverage path can be obtained by the following linear programming problem:

$$\text{Minimize } z = \sum_{e \in E} (c_e x_e) \tag{2}$$

And the following conditions should be satisfied.

$$\begin{aligned} &x_e \geq 0,\ \ e \in E \\ &w_n \geq 0,\ \ n \in V \\ &\textstyle\sum_{e \in E} a_{ne} x_e - 2w_n = b_n,\ \ n \in V \end{aligned} \tag{3}$$

where c_e is a real number representing the cost of edge e, a_{ne} is 1 if edge e meets node n, and 0 otherwise, x_e is an integer, the number of extra times the edge e is traversed, b_n is 0 when degree of n is even, 1 otherwise, and w_n is an optional integer, which can be thought as adjoining loops to the graph at each node.

© ISAROB 2013

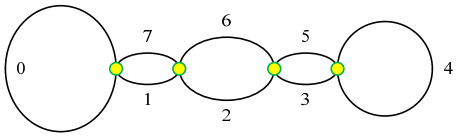

(a) Topological graph for disjoint obstacles.

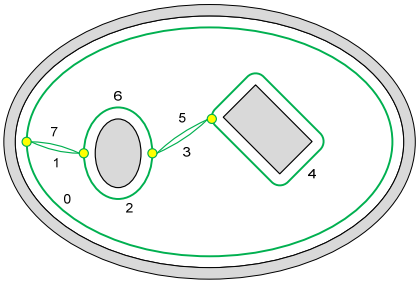

(b) The boundary coverage path for disjoint obstacles.

Fig. 5 Boundary coverage path planning using a topological graph for disjoint obstacles.

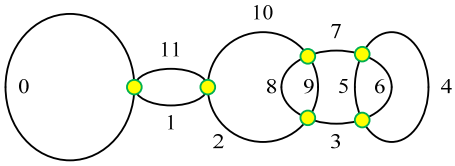

(a) Topological graph for overlapping obstacles

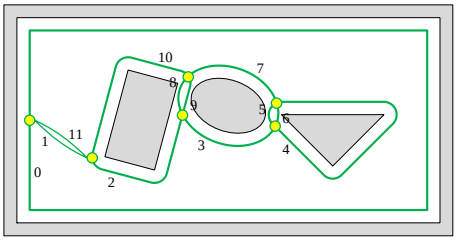

(b) The boundary coverage path for overlapping obstacles.

Fig. 6 Boundary coverage path planning using a topological graph for overlapping obstacles.

As a result, the boundary coverage paths which have the characteristics of an Eulerian circuit are obtained. Fig. 5 shows the result of disjoint polygonal obstacles. Fig. 5 (a) shows the topological graph of the boundary coverage path and Fig. 5 (b) shows the boundary coverage path, in which the gray polygonal area is an obstacle, the green bold line is the boundary of the expanded obstacle, the green thin line is the edge which connects the critical points of disjoint polygonal obstacles, the yellow circle is the critical point, and the number means the order of the path following. Fig. 6 (a) shows the topological graph of the boundary coverage path of overlapping polygonal obstacles. Fig. 6 (b) shows the boundary coverage path.

4 CONCLUSION

In this paper, a mobile robot with cameras and laser scanners for indoor modeling has been introduced and a boundary coverage path planning algorithm using expanded obstacles and topological graphs has been proposed for the information gathering of building interiors at a certain distance. The topological graph based on the critical points and the boundaries of the expanded obstacles was utilized as an input graph for Chinese postman problem for planning the optimal boundary coverage path, which allows a mobile robot to traverse all the boundaries of obstacles at least once. Case study results have been shown for verifying the proposed algorithm.

ACKNOWLEDGMENT

This work was supported by JSPS KAKENHI Grant Number 24300082.

REFERENCES

[1] Mannadiar R, Rekleitis I (2010), Optimal Coverage of a Known Arbitrary Environment. Proc. 2010 IEEE Int. Conf. Robotics & Automation (ICRA 2010), 2010, pp. 5525-5530.

[2] Xu A, Viriyasuthee C, Rekleitis I (2011), Complete Optimal Terrain Coverage Using an Unmanned Aerial Vehicle. Proc. 2011 IEEE Int. Conf. Robotics & Automation (ICRA 2011), 2011, pp. 2513-2519.

[3] Easton K, Burdick J (2005), A Coverage Algorithm for Multi-robot Boundary Inspection. Proc. 2005 IEEE Int. Conf. Robotics & Automation (ICRA 2005), 2005, pp. 727-734.

[4] Grisetti G, Grzonka S, Stachniss C, Pfaff P, Burgard W (2007), Efficient Estimation of Accurate Maximum Likelihood Maps in 3D. Proc. 2007 IEEE/RSJ Int. Conf. Intelligent Robots and Systems (IROS 2007), 2007.

[5] Berg M, Cheong O, Kreveld M, Overmars M (2008), Computational Geometry - Algorithms and Applications, 3rd Ed, 2008.

[6] Edmonds J, Johnson EL (1973), Matching, Euler Tours and the Chinese Postman. Mathematical Programming 5: 88-124.

© ISAROB 2013

The Eighteenth International Symposium on Artificial Life and Robotics 2013 (AROB 18th '13),
Daejeon Convention Center, Daejeon, Korea, January 30-February 1, 2013

Arc/line segments extraction from unknown indoor environment with laser sensor

Rui-Jun Yan[1], Jing Wu[1], Ming-Lei Shao[2], Ji-Yeong Lee[2], and Chang-Soo Han[2#]

[1]Department of Mechatronics Engineering, Hanyang University, Korea
[2]Department of Mechanical Engineering, Hanyang University, Korea
(Tel: 82-031-400-0462)

[#]corresponding author: cshan@hanyang.ac.kr

Abstract: This paper proposed an arc/line extraction algorithm from the unknown indoor environment with a laser sensor. After getting the raw sensor data from laser sensor, the data is divided into different groups by checking the distance of two adjacent points. If the distance is bigger than a limit value, the sensor points in this group will be separated into two groups at these two points. Then the angle of three adjacent points is calculated and compared with another limit value. The group will be split into twos at the middle one of three points if the limiting condition is not satisfied. Moreover, the points in every group are attempted to extracting as a line segment firstly. If the extracted line is not smooth enough, the points in this group are extracted as an arc segment. After the segmenting process, these segments are merged by using the segments merging algorithm. In addition, the experiment results of arc/line extraction in unknown indoor environment by using a HOKUYO laser sensor located on a Pioneer mobile robot are presented.

Keywords: feature extraction, indoor environment, laser sensor and arc/line segments.

1 INTRODUCTION

The extracted segments can be considered as landmarks which take an important effect in the robot localization, navigation, perception and mapping environment. Most experiments, with laser sensor or vision sensor, of robot localization and mapping environment estimate the position of mobile robot using man-made landmarks, like Cup in [1] and Green Circle in [2]. However, it is difficult to put the landmarks into unknown complex environment. The reason of using landmark in these applications to correct the position of mobile robot is its low accuracy with only odometry, integrating the angular velocity and linear velocity over time for measuring the incremental distance and angle.

The data from the laser sensor are a collection of points with angle and distance, which must be extracted as line or arc segment because of the features cannot be identified by points alone. The natural corners are extracted from the natural indoor environment in [3], which are chosen as landmarks applied in the SLAM experiment for realizing the robot localization and mapping environment in [4]. Although the environment is constructed by using the mobile robot and laser sensor successfully, the curves in the experiment are expressed by some line segments which are not very accurate. To express the geometric shape of the feature appropriately, the raw sensor data are extracted as line segments and arc segments in this paper.

Two algorithms about arc/line extraction are proposed in this paper, arc/line segments segmentation algorithm and arc/line segments merging algorithm. Firstly, the sensor data are separated into different groups by checking the distance between two adjacent sensor points. For the data in every group, the angle of three sequential points is compared with a limit value. The group is divided into two groups if the condition is not satisfied. After finish the separation of raw sensor data, the data points in every group are extracted as a line segment or an arc segment. Some segments belong to the same segment actually maybe separated into different parts, which are merged by using the segments merging algorithm if the overlap distance between the segments is long enough.

There are five sections in this paper. The arc/line segments segmentation algorithm is shown in Section 2 and the segments merging algorithm is presented in Section 3. The experiment results prove the feasibility of the proposed in Section 4. Finally, this paper is concluded in the last Section.

2 SEGMENTS SEGMENTATION

The goal of this part is separating the raw sensor data into different groups and extracting the corresponding segments. The distance between point p_i and p_{i+1} is computed for checking whether these two points come from two different objects. If the distance is bigger than a limit value, the data set is divided into two sets. When the sensor points are from several objects, the distance of the end

© ISAROB 2013

points of two data sets from two different objects must be very long.

After finishing the first step, the angle between three sequential points p_i, p_{i+1} and p_{i+2} are calculated in Fig. 1 and compared with another limit value. If the angle is smaller than the restricted condition, the data set is separated into two new sets at the point p_{i+1}. When there is a corner in the environment, the angle between the points from this corner must be smaller and these points should be in two data sets.

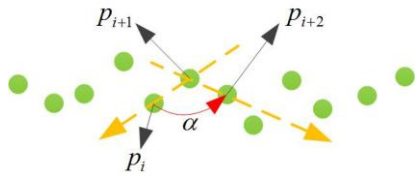

Fig. 1. Calculation of the angle between three sequential points: p_i, p_{i+1} and p_{i+2}

For every group of the sensor data, first of all, the line segments are extracted based on the data in this group. At the same time, the averaged distance between all the sensor points in the group and the extracted line segment is calculated, shown in Fig.2. The detailed calculation of average distance is expressed in Equation 1. After the extraction of line segments, the average distance is compared with a limit average distance. The arc segment is extracted based on the same group of data if the average distance of line segment is bigger than the limit value. The average distance of arc segment is also calculated and compared with the same limit value.

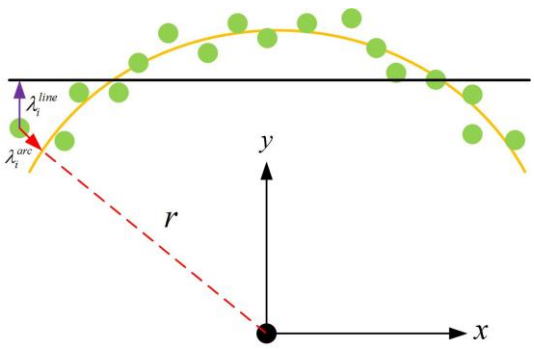

Fig. 2. Average distance between the sensor points and the extracted line or arc segment

$$\lambda_{ave} = \bar{\lambda} = \frac{1}{k}\sum_{i=1}^{k}\lambda_i \qquad (1)$$

If both of the two average distances of the group is bigger than the limit value, the two points with the biggest distance λ_i will be found when the data is extracted as line segment and arc segment separately. By comparing the distance λ of these two points in Fig. 3, this data set is divided into two sets at the point with bigger λ. Moreover, all of these steps are executed repeatedly until the raw sensor data in different groups are extracted as a line or an arc segment successfully.

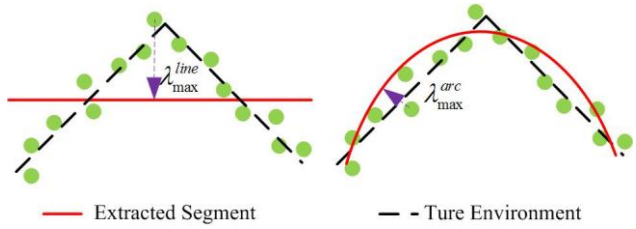

Fig. 3. Two points with biggest distance λ when the sensor data in this group is extracted as line segment and arc segment separately

3 SEGMENTS MERGING

Some segments extracted from raw sensor data by using segments segmentation algorithm maybe belong to the same segment, which should be merged as one segment. If the overlap distance between two line segments or two arc segments is bigger than a limit distance as in Fig.4 and Fig.5, these segments are merged as a new segment based on the sensor data in these two groups. The merging process is the same as the extraction part in the segmentation algorithm.

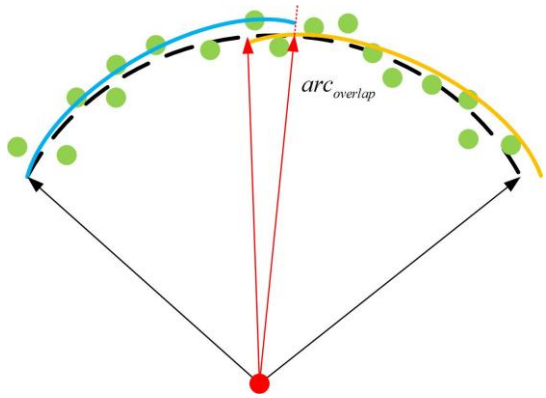

Fig. 4. Overlap distance of two arc segments which belong to the same segment actually

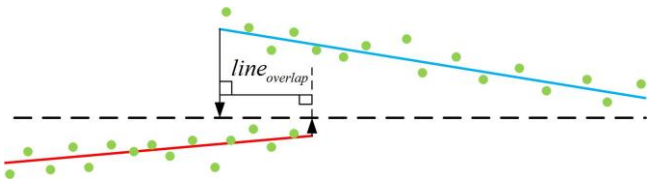

Fig. 5. Overlap distance of two line segments which belong to the same segment actually

© ISAROB 2013

4 EXPERIMENT

4.1 Experiment 1

The experiment 1 is done in the first underground floor of Engineering building #5 in Hanyang University, shown in Fig. 6, including the pictures of real experiment environment. The extracted line segments and arc segments by using the proposed algorithms in environment 1 is presented in Fig. 7. There are three figures of the segments extraction results when the mobile robot moves to different position. The circular objects and walls are extracted as the corresponding arc and line segments successfully. The green dash line in the figures is the range of laser sensor, of which the range is 270 degrees.

Fig. 6. Flow chart and real picture of experiment environment 1

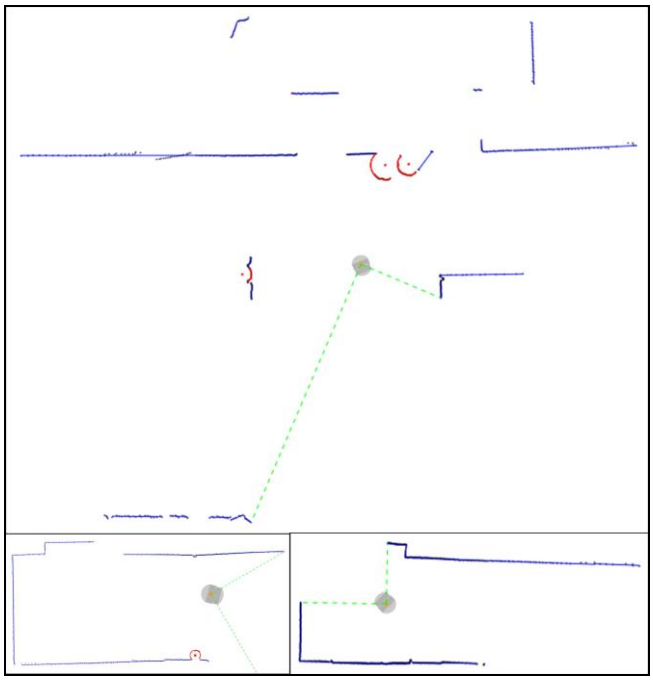

Fig. 7. Extracted arc segments and line segments from environment 1 with the different position of mobile robot

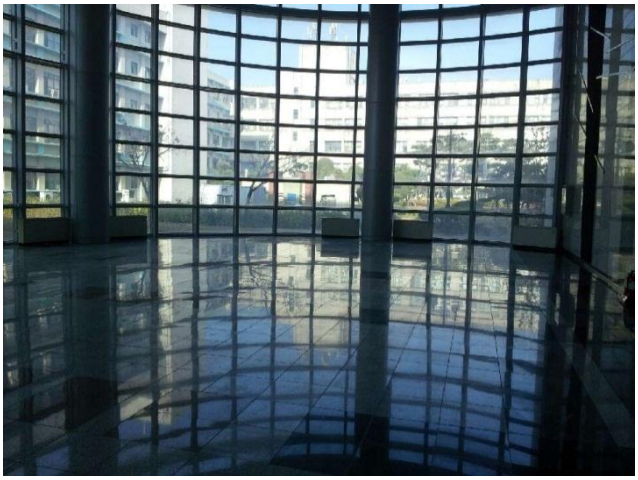

Fig. 8. Real picture of experiment environment 2

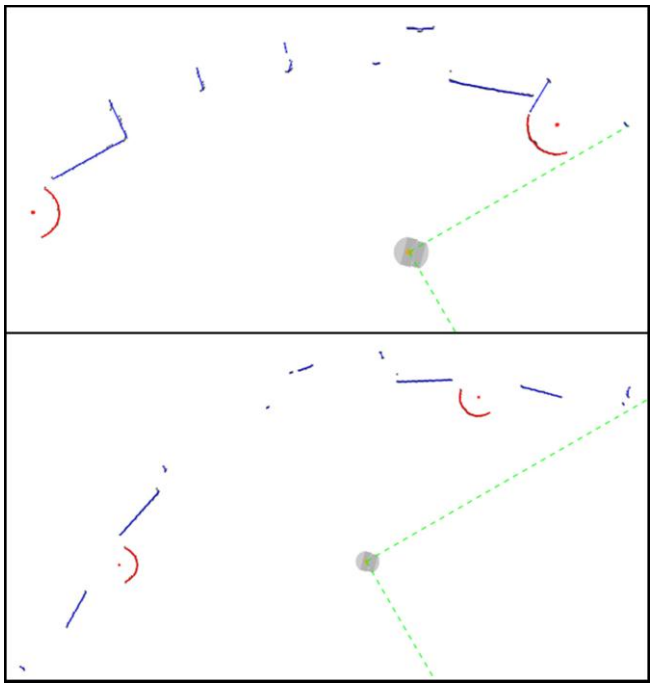

Fig. 9. Extracted arc segments and line segments from envir onment 2 with the different position of mobile robot

4.2 Experiment 2

The experiment 2 is done in the first floor of Engineering building #5 in Hanyang University in Fig. 8, the real picture of experiment. There are some columns and glass in this environment. However, the glass cannot be detected by laser sensor which can be seen in Fig. 9. The grey points in the figure are the raw sensor data and the blue line is extracted line segments. Arc segment is expressed by a red curve with an origin point. The circular columns are extracted as arc segments and glass are extracted as line segments successfully. The bigger grey point with two dash lines stand for the mobile robot and the range of laser sensor.

© ISAROB 2013

5 CONCLUSION

In this paper, the arc/line segments extraction algorithm are proposed, including segments segmentation algorithm and segments merging algorithm. The extracted segments can be chosen as landmarks applied in robot localization, path planning and mapping environment. Two experiments are done for checking the feasibility of proposed algorithm. In the experiments, the objects in unknown complex environment are extracted as line segments and arc segments successfully.

ACKNOWLEDGE

This research was supported by the Ministry of Knowledge Economy, Korea, under the Industrial Foundation Technology Development Program supervised by the Korea Evaluation Institute of Industrial Technology (No. 10038660, Development of the control technology with sensor fusion based recognition for dual-arm work and the technology of manufacturing process with multi-robot cooperation).

REFERENCES

[1] Choi KS and Lee SJ (2010), Enhanced SLAM for a Mobile Robot using Extended Kalman Filter, *International Journal of Precision Engineering and Manufacturing*, Vol. 11, No. 2, pp. 255-264

[2] Mata M, Armingol JM, Escalera A, et al (2001). "A Visual Landmark Recognition System for Topological Navigation of Mobile Robot," *Proceeding of the 2001 ICRA/IEEE International Conference on Robotics and Automation*, Vol. 2, pp. 1124-112

[3] Yan RJ, Wu J, Wang WJ, et al (2012), Natural Corners Extraction Algorithm in 2D Unknown Indoor Environment with Laser Sensor, Proceedings of 12th International Conference on Control, Automation and Systems, Korea, pp.983-987

[4] Yan RJ, Wu J, Lim SJ, et al (2012), Natural Corners-based SLAM in Unknown Indoor Environment, Proceedings of 9th International Conference on Ubiquitous Robots and Ambient Intelligence, Daejeon, Korea, pp. 259-261

© ISAROB 2013

The Eighteenth International Symposium on Artificial Life and Robotics 2013 (AROB 18th '13),
Daejeon Convention Center, Daejeon, Korea, January 30-February 1, 2013

Study on the development of an open motion control platform for a differential mobile robot based on ROS

Jiwu Wang[1], Fangbo Liao[1],Sugisaka Masanori [2]

[1]Department of Mechanical and Electrical Engineering, Beijing Jiaotong University, Beijing, China, 100044
[2]*Alife Robotics Corporation Ltd., 1068-1 Oaza Oshino, Oita*, Japan

Abstract: Robust motion control is prerequisite for an advanced robot. Based on the ROS open source platform, wedeveloped a reliable platform for any differential mobile robot. This platform can be modified according to practical various requirements conveniently. That is, it is an open control platform for any sensors. The developed system has been verified with a mobile robot developed in our lab. The experiment results show its reliability and robustness.

Keywords: mobile robot, motion control

1 INTRODUCTION

Traditional robotic software structure is often determined by the specific hardware. As the variety of the hardware, this led to the difficulty of the common and reusable code platform.ROS (Robot Operation System) is a schedule platform published by Stanford and maintained by Willow Garage with BSD license. Robot developers can build their own app or deploy the shared libs, middleware, and tools provided by ROS. Here a new mobile robot is developed with a completed differential mobile robot based on ROS requirement.

Figure1 shown in the system using differential drive, as a platform of nonholonomic vehicles, two drive wheelsare paralleland a balance wheel realize differential movement and the body balance. Vehicle hardware components include: the two motors, the speed detection unit, the motor drive unit, the motion control unit, the power supply unit, and so on.

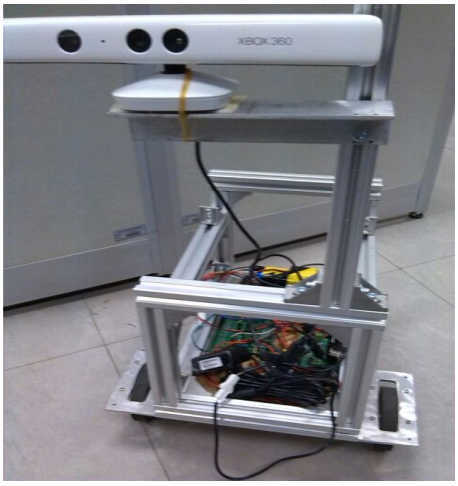

Figure1 Differential drive wheeled mobile robot

Figure2 depicts the relation between translation and rotation. The control of the robot at time t is expressed as linear and angular velocities.

According to planar motion characteristics of the robot, the robot control at time t is expressed as the linear and angular velocities $\begin{Bmatrix} v_t \\ \omega_t \end{Bmatrix}$

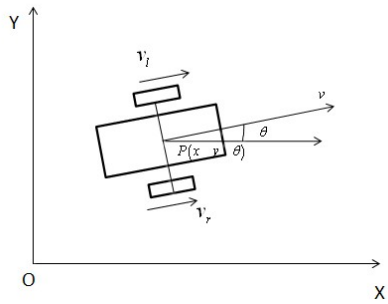

Figure2 Geometric relationships of the vehicle motion

Robot pose P has three degrees of freedom : $\begin{pmatrix} x & y & \theta \end{pmatrix}^T$, The mathematical relationship betweenc ontrol input u_t and pose P is as follows[1] :

$$\begin{bmatrix} x'(t) \\ y'(t) \\ \theta'(t) \end{bmatrix} = \begin{bmatrix} \cos\theta(t) & 0 \\ \sin\theta(t) & 0 \\ 0 & 1 \end{bmatrix} \begin{bmatrix} v(t) \\ \omega(t) \end{bmatrix}$$

2 Motion Analysis

Since the trajectory of the differential mobile robot can be decomposed into three categories : linear, rotary, arc. Therefore, this system facilitates the kinematics conclusion to achieve the control on the three forms of motion[2].

© ISAROB 2013

Linear motion: when the speed of the two differential wheelsequals anddirections are the same, the trajectory of the robot is a straight line： $x(t)=\int_0^t v_r(t)dt$

Rotary motion: when the speed of the two differential wheelsequals and in the opposite direction, the robot moves around the original position： $\theta(t)=\frac{2}{L}\int_0^t v_r(t)dt$

Circular motion: when the directions of the two wheels are identical, speed remains unchanged, and the speed difference is constant, the trajectory of the robot is an arc.

2.1 Prediction model based on control

Suppose the input is $\begin{Bmatrix} v_t \\ \omega_t \end{Bmatrix}$, the state is $x_t=\left(x',y',\theta'\right)^T$ after Δt, also suppose the input is invariant in time Δt, so

$$v=\omega * r$$

$$x_c=x-\frac{v}{\omega}\sin\theta$$

$$y_c=y+\frac{v}{\omega}\cos\theta$$

The pose is as following after Δt

$$x_t=\begin{pmatrix} x' \\ y' \\ \theta' \end{pmatrix}=\begin{pmatrix} x_c+\frac{v}{\omega}\sin(\theta+\omega\Delta t) \\ y_c-\frac{v}{\omega}\cos(\theta+\omega\Delta t) \\ \theta+\omega\Delta t \end{pmatrix}$$

2.2 Robot measurement model based on encoders

For the differential drive robot，robot state is x_t, control input is u_t, measurement is z_t, so the conditional probability of the robot state can be expressed as[3,4]：

$$p(x_t \mid x_{0:t-1}, z_{1:t-1}, u_{1:t})$$

For convenience，we simplify the robot motion process to three stages，shown in figure 3：rotation-translation-rotation，represent the measured motion as：$\left(\delta_{rot1},\delta_{trans},\delta_{rot2}\right)^T$

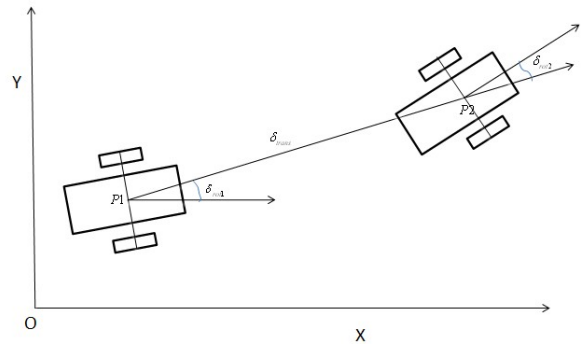

Figure3 vehicle motion analysis

Below is the algorithm to compute x_t:

$$\delta_{rot1}=\arctan(\bar{y}'-\bar{y},\bar{x}'-\bar{x})-\bar{\theta}$$

$$\delta_{trans}=\sqrt{(\bar{x}'-\bar{x})^2+(\bar{y}'-\bar{y})^2}$$

$$\delta_{rot2}=\bar{\theta}'-\bar{\theta}-\delta_{rot1}$$

$$\hat{\delta}_{rot1}=\delta_{rot1}-sample(\alpha_1\delta_{rot1}+\alpha_2\delta_{trans})$$

$$\hat{\delta}_{trans}=\delta_{trans}-sample(\alpha_3\delta_{trans}+\alpha_4(\delta_{rot1}+\delta_{rot2}))$$

$$\hat{\delta}_{rot2}=\delta_{rot2}-sample(\alpha_1\delta_{rot2}+\alpha_2\delta_{trans})$$

$\hat{\delta}_{rot1},\hat{\delta}_{trans},\hat{\delta}_{rot2}$ stand for the true motion，wherein $sample(b)$ represents triangular or Gauss distribution with variance b zero mean，$\alpha_1,\alpha_2,\alpha_3,\alpha_4$ are the robot-specific error parameter，which characterize the robot cumulative error.

So the state $\bar{x}_t$ is computed as:

$$x'=x+\hat{\delta}_{trans}\cos(\theta+\hat{\delta}_{rot1})$$

$$y'=y+\hat{\delta}_{trans}\sin(\theta+\hat{\delta}_{rot1})$$

$$\theta'=\theta+\hat{\delta}_{rot1}+\hat{\delta}_{rot2}$$

Wherein $x_t=\left(x',y',\theta'\right)^T$

2.3 Interface implementation

ROS controls the robot motion through the two messages：cmd_vel message implements the motion control from the high layer to the drive level；Odom message is collection of the motion state.

cmd_vel is of twist data type，twist data type is as the following：

geometry_msgs/Vector3 linear：float64 x，float64 y，float64 z

geometry_msgs/Vector3 angular：float64 x，float 64 y，float64 z

As shown above，Twist message contains two Vector3 type sub messages，in right-handed coordinate system, respectively represent the three directions of the line speed

and the angular velocity. For differential mobile robot , only the translation x and angular z are nonzero because of the freedom degree. The following analyses how the sent message is resolved and implemented:

As mentioned geometric motion analysis, when z is zero, x is the robot translation speed, low-level controller sends two identical channel PWM drive signal, via the motor drive amplifier, the robot pose is :

$$\left(x_i + d_i \cos\theta \quad y_i + d_i \sin\theta \quad \theta\right)$$ 其中

$$d_i = \int_0^t v(t)dt$$

When x is zero, z is the angular speed of the robot, the low-level controller send two channel PWM drive signal with opposite direction and same duty cycle.

The robot pose is $\left[x_i \quad y_i \quad \theta_i - \frac{2d_{Li}}{L}\right]^T$

When x, z are not simultaneously zero, we need to compute the value of v_x and v_y from the known x and known z:

Reverse solution vector U :

$$\begin{bmatrix} v_l(t) \\ v_r(t) \end{bmatrix} = \begin{bmatrix} \frac{1}{2} & \frac{1}{2} \\ -\frac{1}{2}L & \frac{1}{2}L \end{bmatrix} \begin{bmatrix} v \\ \omega \end{bmatrix}$$

Send the velocity command of the two motors, the desired translation velocity angular velocity can be achieved.

Odom message represents the robot state, ROS publishes Odom message to indicate the estimate of the position and velocity, assuming we get $tick(t)$ from the left encoder within measured period $(t, t+\Delta t)$, the applied encoder parameter is η_1 , wheel diameter parameters is η_2 , further computation on these parameter and measured data, we can obtain one side translation and angular velocity,, similarity the right side[5]:

$$\omega_l(t) = \frac{tick(t)}{\Delta t} * \eta_1$$

$$v_l(t) = \frac{tick(t)}{\Delta t} * \eta_1 * \eta_2$$

And Odom message in ROS belongs to nav_msgs/Odometry type , the detail of the nav_msgs/Odometry is as following:

Header header
stringchild_frame_id
geometry_msgs/PoseWithCovariance pose
geometry_msgs/TwistWithCovariance twist

twist is as the previously described, we gain v_l and v_r from the two encoders, and translation and angular velocity can be deduced from the vector U .

The detail of the pose type:

geometry_msgs/Point position: float64 x , float64 y, float64 z
geometry_msgs/Quaternion orientation : float64 x , float64 y, float64 z, float64 w
float64[36] covariance

Therein,the values of x and y in positionare computed as follows:

$$\Delta x = [v_x(t)\cos\theta - v_y(t)\sin\theta] * dt$$

$$\Delta y = [v_x(t)\sin\theta + v_y(t)\cos\theta] * dt$$

$$\Delta\theta = \omega * dt$$

$$x_{i+1} = x_i + \Delta x$$

$$y_{i+1} = y_i + \Delta y$$

$$\theta_{i+1} = \theta_i + \Delta\theta$$

And orientation can be gotten:

odom.pose.pose.orientation
=tf::createQuaternionMsgFromYaw(θ);

3 Experiment design

In order to verify the accuracy of the robot motion, we design two forms of motion to check the constancy of the implemented and the desired results. The two algorithms are respectively translation motion drivex(distance, speed), rotation motion turnx(angle, angularSpeed).

divex(distance, speed)algorithm: send velocity command to robot, record the motion start point:startPose, and update the current pose in real time: CurrentPose, so the distance is:

dx = currentPose.x–startPose.x
dy =currentPose.y–startPose.y
distanceMoved = math.sqrt(dx * dx + dy * dy)

compare the value of distanceMoved and desired distance, controlling the robot to a desired distance can be realized.

Turnx(angle , angularSpeed)algorithm : send angular velocity command cmd_velto robot, record the motion start point:startPose, and update the current pose in real time: CurrentPose, so the rotation angular is:

dx = currentPose.x–startPose.x
dy = currentPose.y–startPose.y
angleTurned = currentAngle + angleOffset–startAngle

whereinangleOffset is offset to $2n\pi$,we can control the robot at desired angular pose through comparing angleTurned and angle.

The Experiment design the trajectory of the robot is square, we evaluate the motion error by comparing the pose of the

start point and the end point.
Design trajectory: square with 1m side length, translation velocity is 0.2m/s, angular velocity is 0.7rad/s.
Pseudo code of test Algorithm :

```
Repeat   4 times:
        divex（1，0.2）
    turnx（radius(90)，0.7）
End repeat
```

The experiment result shows our approach is stable and applicable. Figure4 is the actual trajectory of our robot, from the trajectory we can conclude that our means can construct the desired differential wheeled mobile robot platform.

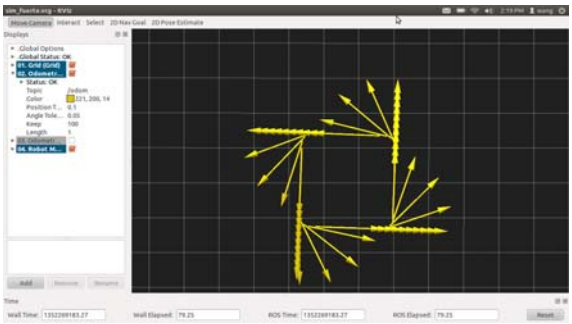

Figure4 vehicle motion analysis

In the next step, some further tests will be carried out, such as navigation with complicated trace, obstacle avoidance etc.

}

REFERENCES

[1] Gregor Klanč ar , DragoMatko, Saš o Blaž ič , A control strategy for platoons of differential drive wheeled mobile robot[J],Robotics and Autonomous Systems 59 (2011) 57－64.

[2] Soonshin Han, ByoungSuk Choi, JangMyung Lee. A precise curved motion planning for a differential driving mobile robot[J]. Mechatronics 18 (2008) 486－494.

[3]Thrun S，Fox D, Burgard Probabilistic Algorithms and theInteractive Museum Tour-guide Robot Minerva[J], InternationalJournal ofRobotics Research,2000,19(1-1)：972-999.

[4]Thrun S, Fox D, Burgard W. Probabilistic Robotics [M]. Massachusetts:MIT Press,2005. 167-193.

[5]Ming Tan, De Xu. Advanced Robot Control [M].Beijing:Higher Education Press,2007. 400-410.

The Eighteenth International Symposium on Artificial Life and Robotics 2013 (AROB 18th '13),
Daejeon Convention Center, Daejeon, Korea, January 30-February 1, 2013

The small eye and tongue module for an android robot head

Dongwoon Choi, Dong-Wook Lee, Duk Yeon Lee, *BYEONG KYU AHN* and Hogil Lee
Department of Applied Robot Technology, Korea Institute of Industrial Technology
(Tel: 81-031-8040-6317; Fax: 81-031-8040-6370)
(cdw / dwlee / proldy / bk.ahn / leehg@kitech.re.kr)

Abstract: In this paper, the small size eye and tongue module for an android robot head are presented. There are narrow spaces inside the android robot head by its human like shape and size, so to use small size parts is very important to design an android robot head. We tried to design an android robot head with 33 D.O.F and human like shape, but as the large numbers of D.O.F and human like shape, it was needed to make small size of each module to achieve our goal. The eye module presented has 2 D.O.F for eyeball and 1 D.O.F for eyelid, so there are roll, pitch motion for eyeball and pitch motion for eyelid like human eye. A gimbal was generally used in robotic eye, but a spherical joint was selected to reduce space occupying by its simple structure. The spherical joint is very simple and can manufacture small one, but it has 3 D.O.F even if there are only 2 D.O.F in eyes, so rotation motion of eye can be occurred. To avoid rotation of eyeball by using spherical joint, spring column was installed in center of eyeball. There has been no active tongue for an android robot or humanoid robot until now. The tongue is very important factor to design human like robot because it can be shown when the robot speaks, so an active tongue give more reality to an android robot when it speaks. Additionally, there are many emotional expressions to use tongue like ridicule, so tongue can help to make more various emotional expressions in android robot research. The tongue module has a flexible silicon complex skin for natural motion and human like looks. It has 2 D.O.F for stick out-put in and bending. The wire and rack gear were used to make that motions. With this small eye and tongue module, an android robot head which is highly sophisticated and more similar to human head can be designed.

Keywords: Android, robot, robot eye, robot tongue

I. INTRODUCTION

As researches in robotics have been developed, the researches of a humanoid robot and an android robot have been increased. An android robot is one of humanoid robots, but it has human likely appearance than one of humanoid robot. Because an android robot has human likely appearance, it can be used generally like a secretary, an announcer, an actor, etc. [1]. The appearance and size of android robots are similar to human, so the inner spaces of them are very narrow and this is one of the hardest things to design an android robot. Especially, in case of a head, there are many actuators to make facial expressions, so securing spaces is the most important to make a face with large numbers of D.O.F. The best method to secure spaces inside head is to reduce the size of each part, but most of parts like actuators, bolts are standardized, so it is not easy to reduce their size. For this reason, to downsize structures by simplification can be one of the best solutions. The eye parts are usually a gimbal which has yaw, pitch joint and they are most complicate and large sized parts in a head. The eye used a gimbal has 2 D.O.F in each eye and it is very common structure as a robotic eye, but it has frame in outside of eye ball and it is not good to downsize [2] [3]. Downsizing an eye means increasing of the number of D.O.F to the android head. Takuya Hashimoto made a female android robot SAYA and its eyes are gimbal type, so it has only 19 D.O.F in head, because eyes take so many spaces [4]. Minoru Hashimoto used artificial muscles to make an android robot face. This face is based on anatomy, so it is very good trial to make an android robot, but it is hard to make and maintain [5]. Jong Won Kwak used polymer artificial muscles to make eyes. These eyes are very small and simple, but it needs separate controller and DC-DC converters, so it is not suitable to our robot [6]. Our android robot has been used in commercial areas, so it is very important factors like maintenance, cost and parts supply, so we tried to develop small but simple structure [7]. To make small and simple eyes, spherical joint and spring column was used. Lorenzo Jamone used spring as a neck joint and bone to make their humanoid robot [8]. From this spring joint, the idea of spring column which prevent a rotation of the spherical joint can be drawn. The spherical joint is the simplest structure to make 2 axis motions, but there is a rotation of axis and using a spring column can hold this rotation. The main role of a tongue to an organism is degustation, but robots don't need to taste, so it is not exist or generally used as a decoration. The android robot has human like appearance, so the tongue is necessary, but it is just a dummy generally. In case of humans, the tongue

© ISAROB 2013

is used when they are speaking, express emotions, so we focused its role to emphasize emotional expression. This is the first trial for android and humanoid robots. Toshiya Kawamura made a robotic tongue to research flexibility and soft motions of robots, but it was made for researches, so its size is too big and appearance is not matched to one of humans [9]. The robotic tongue presented has 2 D.O.F (stick out – put in, bending) and it was made by silicon complex, so it has human like appearance. To make natural bending motions, wires were used and a rack-pinion gear was used to make stick-out and put in motions. This tongue module was designed small size enough to install in a jaw, because there are no actuators for skin in a jaw even if its space is narrow.

II. Hardware design

1. Design of the eye module

The purpose of a presented robotic eye is to make small size, simple structures and easy to maintain. In addition, the size and appearance must be exactly same to human eyes. There are pitch and yaw motions in human eyes and in case of both eyes, the yaw motion is separated but the pitch motion is constrained, so both eyes have 3 D.O.F. In case of the android robot, it has eyelids and they move independently, so the eyes of android robot need 5 D.O.F totally. The gimbal is used generally to make pitch, yaw motions of eyes, but this structure has frame outside of eyes and this is not good structure to miniaturize. In addition, this structure needs standard parts like bearings, bolts, etc. and there is limit to find small parts among them. The simplest structure to make 2 D.O.F is a spherical joint. The spherical joint is consist of only 2 parts, cup and ball joint, so it is very easy to downsize and manufacture, but there is a problem to use for eyes. The joint of spherical joint is not fixed to rotate motion unlike a gimbal or universal joint, so the eyes can rotate. The spring column is used to prevent rotation of eyes. The spring can be used as a joint because it can be bent to any directions. The presented eye ball consists of a cup joint, hollow ball joint and spring column. The spring column is connected with ball and cup joint, and it is located in hollow of ball joint, so the eyeball has only 3 parts but it has 2 D.O.F, small size and the simplest structure (Fig.1). 3 RC servo motors (Dymond D47, HiTec Hs5085mg) are used as actuators to move an eyeball and an eyelid, because RC servo is easy to use and small. The eyelid are designed similar to human eyelid and manufactured by CNC not bending, because the gap between an eyeball and an eyelid is very important to looking, so the gap is just 0.5mm. The eye ball and eyelid is connected to servo motors by ball joints. These parts are assembled as a module, so it is easy to maintain. The module structure is easy to maintain and attach to other face. The size of a presented 3 D.O.F eye module is very small as 64x40x40mm (Fig.2). Because of using small eye modules, more spaces inside of head can be occupied, so 33 D.O.F head can be developed.

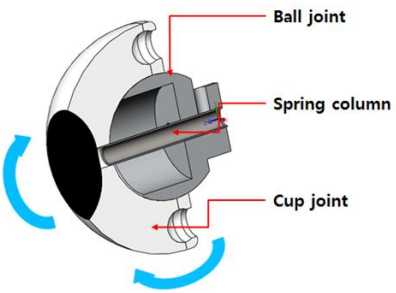

Fig 1 Structure of eyeball

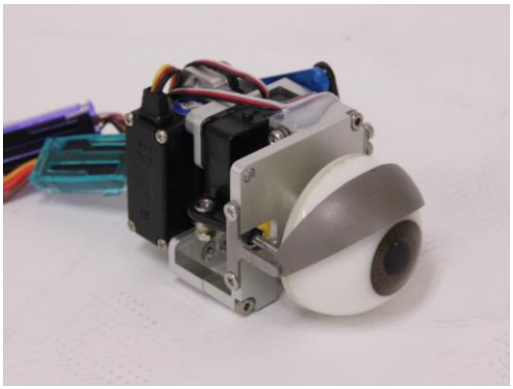

Fig. 2 3 D.O.F eye module

2. Design of the tongue module

A tongue is one of the most complicate parts in human body, so it is very difficult to make human like tongue. The motions of a tongue are divided outside of mouth motions and inside of mouth motions. In case of an android robot, the role of a tongue is only for expressions or as a decoration, so inside of mouth motions are not needed. The outside of mouth motions can be simplified as stick out-put in, bending up-down, bending left-right, so there are 3 D.O.F. The tongue is located in a jaw and the space inside a jaw is very narrow, so 2 D.O.F (stick out-put in, bending

© ISAROB 2013

up-down) is selected for downsizing. The silicon complex is used to make human like appearance and elasticity. There is a plastic bone inside the silicon tong and wires are used to make motions. Three wire holders are attached the bone and by changing of the location of these holders, the bending shape can be adjusted. A rack- pinion gear is used for stick out-put in motion, because it is very simple and cheap. The actuators for tongue are RC servo motors (Dymond D47, Dymond D 60). This robotic tongue is also designed as a module, so it is easy to maintain and apply to other head. The size of this tongue module is small as 100x60x60mm and the range of stick out-put in is 40mm. Fig. 3 shows mechanism of tongue module. These small sized eye modules and tongue module can supply spaces enough to make 33 D.O.F inside an android robot head (Fig.4).

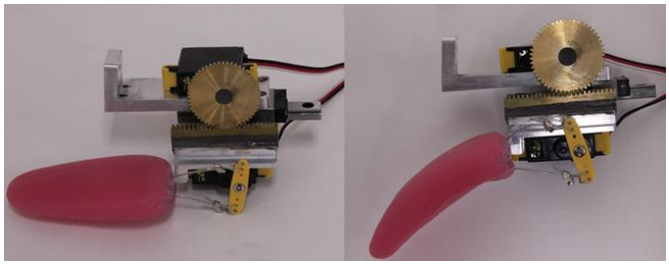

Fig. 3 Tongue module and its mechanism

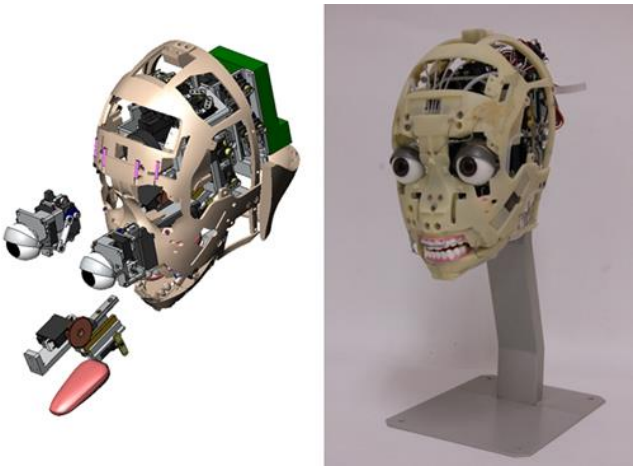

Fig. 4 Assembly of each module and 33 D.O.F head

III. Experiment and result

Experiments were taken to check whether the eye module, tongue module work or not when it is attached to skin and in that time, how the appearance is similar to one of human. There are no cameras in eye module, so accuracy doesn't matter in this device and the RC servo motors used are subminiature analog types, so it is hard to receive data from devices. The most important factor to the android robot is how the android robot is similar to human, so we focused to check its shape when it operated. We attached new eye and tongue modules to our hardware, android robot EveR-3, with new head which has 33 D.O.F and test. Fig. 5 shows yaw and pitch motions of eyeballs and a pitch motion of eyelids. The stick out-put in, bending up-down motions are also checked (Fig.6). All motions with eye, tongue modules are operated without trouble and similar to one of human. The presented eye, tongue modules have small size and simple structure, so the 33 D.O.F android robot head with higher expressions and easy maintenance can be developed.

Fig. 5 Eye motions (default, left, up, down gaze)

Fig. 6 Tongue motion (stick out, bending down)

IV. CONCLUSION

The small and simple eye, tongue modules for new 33 D.O.F android robot head are presented. The android robot needs many actuators to make human like facial expressions, so inside spaces of head are very narrow. In this reason, downsizing of each part is very important to decide its D.O.F. In addition, our android robot has been used in commercial area, so easy maintenance and reliability is very important. To satisfy these needs, small

© ISAROB 2013

and simple eye, tongue modules are developed. The eyes used a spherical joint and spring column and these can make small, simple structure and it is made as a module, so it is easy to maintain. The tongue consists of the silicon complex tong, plastic bone and rack-pinion gear. This tongue is also made as a module and small sized. The small sized RC servo motors are used as actuators. By this eye, tongue modules which are downsized, the android robot head with 33 D.O.F can be developed.

Acknowledgement

This research is supported by Ministry of Culture, Sports and Tourism (MCST) and Korea Creative Content Agency (KOCCA) in the Culture Technology (CT) Research & Development Program 2010

References

[1] H. G. Lee, M. H. Baeg, D. W. Lee, T. G. Lee, and H. S. Park (2006), Development of an Android for Emotional Communication between Human and Machine, Proc. of Int. Symp. on Advanced Robotics and Machine Intelligence

[2] Nobutsuna Endo, Shimpei Momoki, Massimiliano Zecca, Minoru Saito, Yu Mizoguchi, Kazuko Itoh, and Atsuo Takanishi (2008), Development of Whole-body Emotion Expression Humanoid Robot, IEEE International Conference on Robotics and Automation, Pasadena, CA, USA, May, pp.19-23

[3] Chyi-Yeu Lin, Chun-Chia Huang and Li-Chieh Cheng (2011), A Small Number Actuator Mechanism Design for Anthropomorphic Face Robot, IEEE International Conference on Robotics and Biomimetics, Phuket, Thailand Dec. 7-11, pp.633-638

[4] Takuya Hashimoto, Masato Suzuki and Hiroshi Kobayashi (2009), Development of Remote Class Support System and Field Trial using an Android Robot, IEEE International Conference on Mechatronics and Automation , Changchun, China, August 9 – 12, pp.2042-2047

[5] Minoru Hashimoto, Chisaki Yokogawa and Tsugutake Sadoyama (2006), Development and Control of a Face Robot Imitating Human Muscular Structures, IEEE/RSJ International Conference on Intelligent Robots and Systems, Beijing, China, October 9- 15, pp.1855-1860

[6] Jong Won Kwak, Ho June Chi, Kwang Mok Jung, Ja Choon Koo, Jae Wook Jeon, Youngkwan Lee, Jae-do Nam, Youngsun Ryew and Hyouk Ryeol Choi (2005), Journal of Mechanical Science and Technology, Vol 19, No 2, pp. 578~ 588

[7] Dongwoon Choi, Dong-Wook Lee, Duk Yeon Lee, Ho Seok Ahn and Hogil Lee (2011), Journal of Artificial Life and Robotics, Vol 16, No 3, pp.315~ 318

[8] Lorenzo Jamone, Giorgio Metta, Francesco Nori and Giulio Sandini (2006), James: A Humanoid Robot Acting over an Unstructured World, IEEE-RAS International Conference on Humanoid Robots, Dec. 4-6, pp.143-150

[9] Toshiya Kawamura, Tadayoshi Tandai, Hideaki Takanobu (2005), IEEE/RSJ International Conference on Intelligent Robots and Systems, Aug. 2-6, pp.1041-1046

© ISAROB 2013

The Eighteenth International Symposium on Artificial Life and Robotics 2013 (AROB 18th '13),
Daejeon Convention Center, Daejeon, Korea, January 30-February 1, 2013

Design of robotics arm's behavior in imitation animal consciousness: Development of altruistic behavior

Kyoko Tanaka Eiji Hayashi

Department of Mechanical Information Science and Technology
Faculty of Computer Science and Systems Engineering, Kyushu Institute of Technology
680-4, Kawazu, Iizuka-City, Fukuoka Prefecture, Japan

***Abstract*:** Our research has been focused on developing a robot with a "consciousness" like that of a person or an animal to enhance the user affinity of service robots. Our laboratory previously conceived a model of the mechanism of consciousness and action and a related software architecture, called Consciousness-based Architecture (CBA), by which this model can be used to control the action of an artificial animal. Here, we newly theorized a "motivation model" which assumes that certain motives inhere in the actions of sentient beings, and that the motivational processes involved could become part of how a robot determines what action to take. Our motivation model is based on the dopamine-generating mechanism of sentient beings. In the present study, we focus on the altruistic behavior of animals so that the consciousness and behavior of the robot approximate those of an animal. We added altruistic behavior to the CBA and tried to construct a system in which the robot cooperates with the user and chooses altruistic behavior. Our goal is to enhance the user affinity of service robots with this system.

***Keywords*:** CBA, Robot consciousness, Robot consciousness

1. INTRODUCTION

At present, not only industrial robots but also so-called "service" robots are being developed swiftly by many researchers around the world. There are various types of service robot, including business robots, research robots, welfare robots, and domestic robots. The operation of these robots requires not only the basic functions of robots, such as a high level of intellectual activity, but also the function of user compatibility or affinity, so that a user can feel close to the robot as a result of its appearance and behavior. User compatibility implies that the user is easily able to operate the given robot, without getting bored with its use, and can readily develop a sense of closeness with it. One design goal is that the user will ultimately receive from service robots the emotional benefits experienced in relationships with other conscious beings.

Although a robot may gain user compatibility by being genuinely modeled after a face, it is far more challenging to achieve user compatibility through its behavior and actions, including human-like "capricious behavior." The attempt to give robots "consciousness" such as that identified in humans and animals is a part of these requirements.

Our laboratory has studied animals' adjustments to their environments in an attempt to emulate animal behavior. We constructed a hierarchic structural model in which consciousness and behavior were hierarchically related. Based on this model, we developed a software architecture we call Consciousness-based Architecture (CBA). CBA introduces an evaluation function for behavior selection. Here, we elaborate on the evaluation function, using the dopamine-based motivational system as its basis.

For the present study, we developed a robotic arm that has six degrees of freedom, so that the arm could autonomously adjust to a target position. Fig. 1 shows an overview of the robotic arm, which has a hand consisting of three fingers in which a small monocular web camera is installed. The landmark object is detected in the image acquired by the web camera. In a previous study, as an autonomy action experiment, we applied CBA to the robot arm and inspected the arm's behavior. We thus determined that the arm could successfully perform the maneuvers used in the present study.

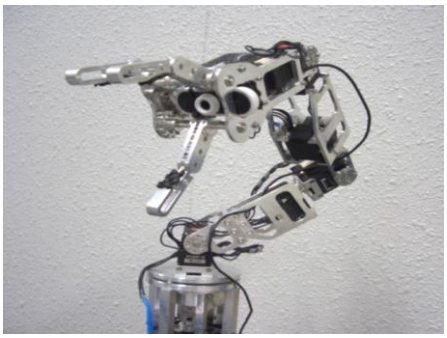

Fig. 1 Overview of robotics arm

© ISAROB 2013

2. SYSTEM STRUCTURE

Figure 2 shows the appearance of the robot arm and its degrees of freedom. The robot arm has 7 levels of flexibility {shoulder (Joint1, Joint2), elbow (Joint3, Joint4), wrist (Joint5, Joint6), and finger (Joint7)} at its full length of 450 [mm]. The hand part has 3 fingers with one level of flexibility; the weight of the main part is about 0.8 kg. A small web camera, installed at the tip of the arm, can recognize the external situation. The web camera and the robot arm's actuator are controlled by USB communication.

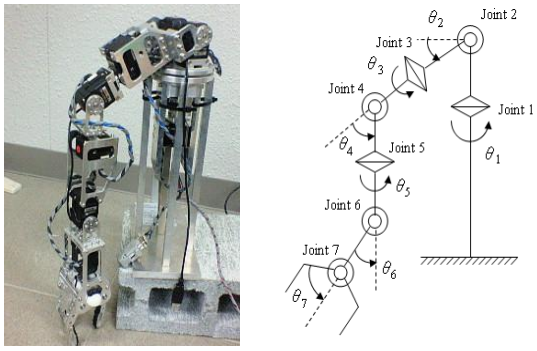

Fig.2 Robot arm and degree of freedom in the robot arm

3. AUTONOMOUS BEHAVIOR

Most robots are pleasing to people because of their unique movements. However, the action choices of robots are very objective in orientation, and we believe action choices that resemble those of subjective human beings and animals are needed to enhance user compatibility. Therefore, we at first considered the structure of a sentient action. When an animal, including a human being, takes an action, it can be represented by a series of steps, such as "Recognition → Comprehension → Motivation → Action." Typically, the action of the robot tends to eliminate motivation and instead engage in the simple flow "Recognition (Comprehension) → Action." Figure 3 shows the ideal series of steps for a robot with both objective and subjective behavior.

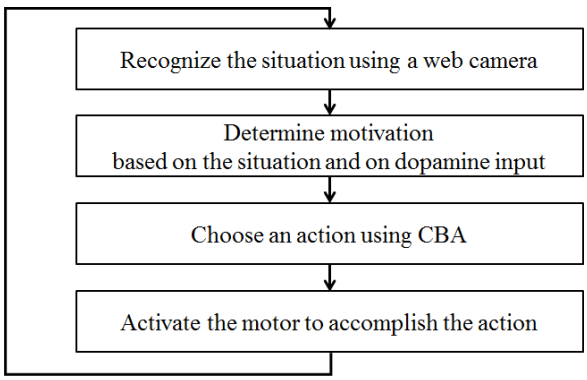

Fig. 3 Flowchart of this system

3.1 Recognize the situation using a web camera

The first step of the "humanized" robot's system would be to recognize a situation. For this purpose we devised a labeling image (Fig. 4), taken by the web camera installed on the robot hand. We programmed the system to divide the image into green, blue, red and flesh-colored blobs and extract the shape, size, and center of gravity position (Fig. 4). From this information and the posture of the robot arm, the robot could recognize the position and its distance from the target-color object. Furthermore, the system memorized the central point for three frames.

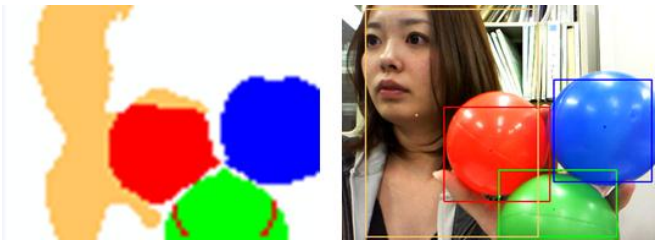

Fig. 4 Simplified image and labeling image

3.2 Determine motivation based on the situation and on dopamine input

When a human and an animal interact, changes occur in the dopamine level in the brains of both the human and the animal. We used the dopamine-generating locus as the model for determining the robot's motivation and copied it for use in the control model. The control model is shown below. In Fig. 5, the graph shows sample changes in ω_n , ζ and T .

Rising $y''+2\omega_n\zeta y'+\omega_n^2 y-\omega_n^2 u_{(t)}=0$

Decaying $y=e^{-t/T}$

ω_n : natural angular frequency
: earliness of a rise in dopamine
ζ : braking rate
: height of the peak of a rise in dopamine
T : time constant : attenuation performance

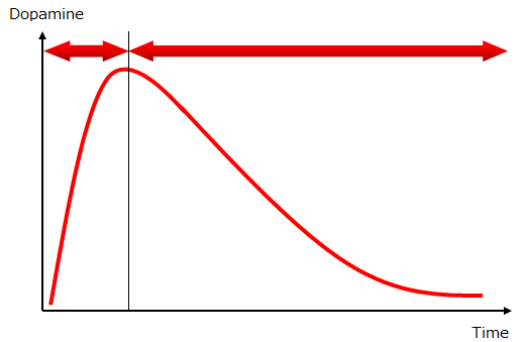

Fig. 5 Dopamine model

© ISAROB 2013

In the control model, dopamine is generated with reference to pleasant or disagreeable stimuli represented in variables.

ω_n and T are determined by the outside environment and the internal state, respectively. Moreover, a robot's motivation is defined by asking for the total of the generated dopamine and calculating the secondary delay response in such a way that the total is considered as the input for the robot's motivation.

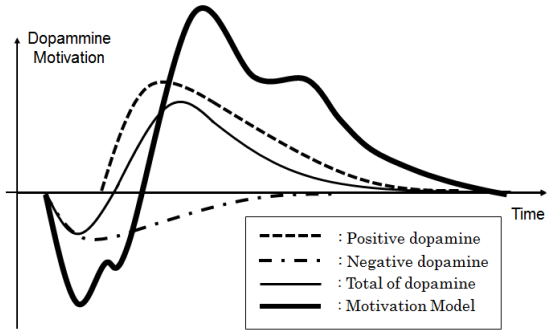

Fig. 6 Motivation model

3.3 Choose an action using CBA

Figure 8 shows a diagram of CBA, which relates consciousness to behavior hierarchically. In this model the consciousness behavior fields are built separately. In a dynamic environment, this model determines the consciousness level appropriate to the environment, and the robot then selects the behavior corresponding to that consciousness level and performs the behavior. When certain behavior corresponding to the consciousness level is discouraged by some external environmental factor, the consciousness level approaches an upper level so that the robot can select an advanced behavior.

Alternately, while operating at upper-level consciousness the robot can choose to perform a low-level behavior. The mechanism of this model is that it selects the optimum behavior within the low-level behaviors, to achieve the robot's goals.

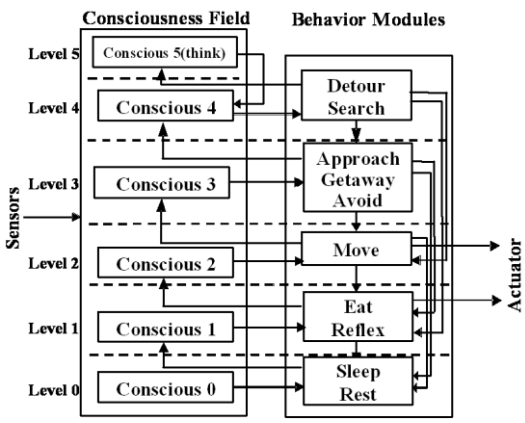

Fig. 7 Consciousness-based Architecture (CBA)

3.4 Activate the motor to accomplish the action

The action level was set up by dividing a robot's motivation by a fixed value. In this way, the actions that could be chosen for each action level were limited. Figure 8 shows the robot's choices in this system.

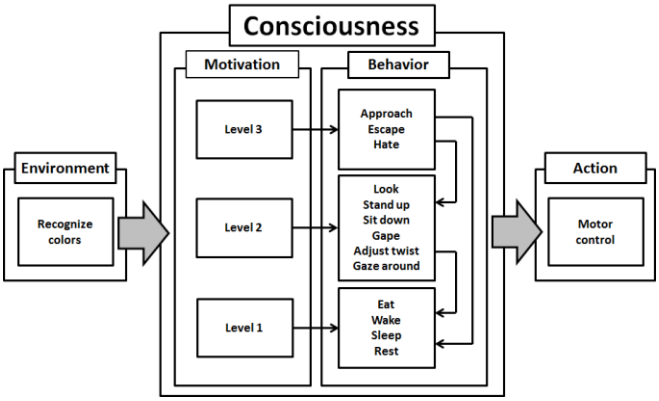

Fig. 8 Choice of action based on motivation

4. ALTRUISTIC BEHAVIOR

Our robot acts in proportion to the value of the motivation. For example, when the robot sees a favorite object, the value of the motivation rises and the robot approaches or catches the object. On the other hand, when the robot sees an object it dislikes, the value of the motivation drops and the robot avoids the object. This behavior of the robot can be considered to be selfish. In the present study, we focus on the altruistic behavior of animals so that the consciousness and behavior of the robot approximate those of an animal. We added altruistic behavior to the CBA so that the robot cooperates with the user, and our goal was to construct a system in which the robot would choose altruistic behavior.

4.1 Flow of imitated action

The altruistic behavior that we added to the CBA is an imitation of the action *sit*, which is a typical command given to a dog. The owner says "Sit." whereupon the dog sits on his hind legs and waits for the owner's direction. The dog acts altruistically during the waiting time, knowing that the appropriate behavior will get him what he wants. In this case, the altruistic behavior includes conquering his desire to simply chase the ball and instead cooperating with his owner. We imitated the *sit* dog command and established an altruistic behavior that the robot could perform, as shown in Fig. 9.

© ISAROB 2013

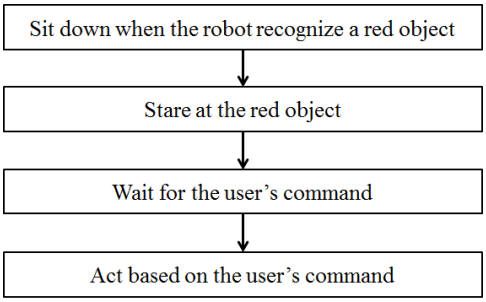

Fig. 9 Flow of altruistic behavior

4.2 Algorithm for altruistic behavior

The robot recognizes the outside situation using the web camera installed on its hand. We programmed the robot to act based on switching from selfish consciousness to altruistic consciousness when the robot sees a red object.

If the robot sees a red object, the robot throws itself into a posture, like the position assumed by a dog when the *sit* command is given. When the user moves the red object, the robot keeps the object in its sight as if it wishes to chase the object. The robot waits until the user gives directions. If the value of the motivation changes while the robot is waiting, the robot doesn't choose its action based on the motivation; instead, it follows the user's direction. If the user brings the object near to the robot, the robot judges that it could catch the object, and it thus tries to catch it. On the other hand, if the user keeps the red object at a distance from the robot, the robot judges that it could not catch the object, and it thus tries waits for the user's direction.

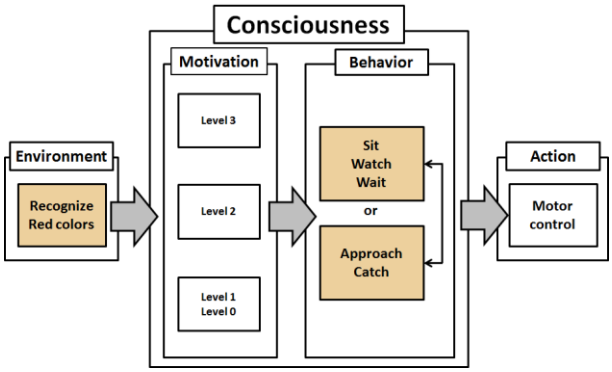

Fig. 10 Choice of altruistic behavior based on altruistic consciousness

5. VERIFICATION EXPERIMENT

We added the system of altruistic behavior to the CBA and verified the subsequent action of the robot experimentally. Figure 11 shows a result of the verification experiment. The robot saw a red object and sat down (A). Then, the robot stared at the red object and waited for the user's direction to catch it (B). If the motivation rose during this time, the robot went on waiting without being selfish (C). The user directed the robot to catch the red object by bringing the subsequent (D). The robot approached the red object (E) and caught it (F).

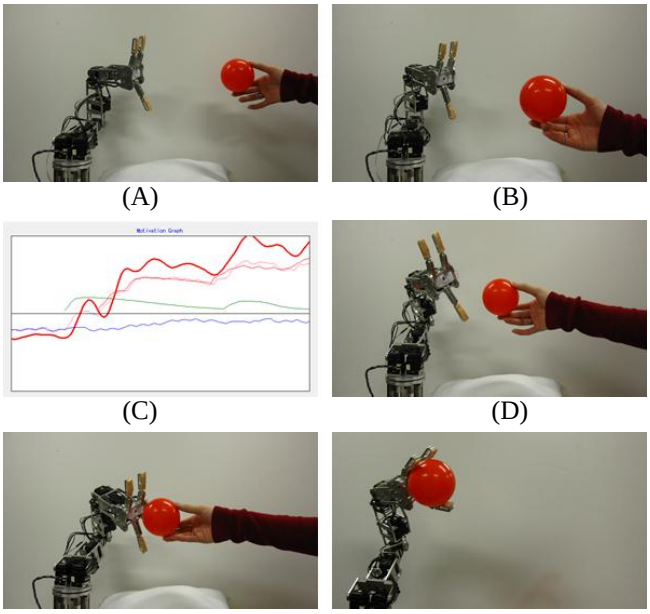

(A) (B) (C) (D) (E) (F)

Fig. 11 The action of a robot arm

6. CONCLUSION

We created a system of altruistic behavior for a robot, which acted based on not selfish consciousness but altruistic consciousness. In this case, the robot cooperated with the user when it saw a red object, as shown in the result of the verification experiment. We thus confirmed the effectiveness of this system.

Our system of altruistic behavior will enable the robot to act sophisticated. For example, when the robot sees an object it does not like as well as a red object, the robot will appear to have difficulty following the user's directions. Eventually we would like the robot to express embarrassment at such a predicament. We believe such behavior would enhance the user affinity of the robot.

7. ACKNOWLEDGEMENT

This research was partially supported by the Ministry of Education and Science,
Sports and Culture, Grant-in-Aid for Scientific Research, 2012.

8. REFERENCES

[1] Kouichirou Kurogi, Kei Ueyama, Eiji Hayashi, Design of robotic behavior that imitates animal consciousness: Emotion expression of robotic arm based on eyeball movement AROB 16th '2011, Bepu, Oita, Japan, 2011

[2]Motoki Yoshida, Eiji Hayashi, Design of robotic behavior that imitates animal consciousness: Construction of the user-recognition system, AROB 17th '2012, Beppu, Oita, Japan, 2012

© ISAROB 2013

The Eighteenth International Symposium on Artificial Life and Robotics 2013 (AROB 18th '13),
Daejeon Convention Center, Daejeon, Korea, January 30-February 1, 2013

Network Based Multiple Mobile Robots with Subsumption Architecture Supporting Swarm Behaviors

Maki K Habib[1], Fusaomi Nagata[2], Akimasa Otsuka[2] and Keigo Watanabe[3]

[1]The American University in Cairo, Egypt
[2]Tokyo University of Science, Yamaguchi, Japan
[3]Okayama University, Yamaguchi, Japan

[1]maki@ieee.org

Abstract: This paper presents the use of dynamic sampling period to evaluate the basic behavior performance of network-based multiple mobile robots system with cooperative swarm behaviors. Network-based subsumption architecture with PC server is proposed to minimize the total cost for designing multiple mobile robots system by maximizing the group performance of robots with limited hardware and software capabilities rather than optimizing the behavior performance of a individual robot. This enables to develop high-level group behavior architecture such as a complex schooling behavior. Such capability is based on decomposing a complex behavior into simple and basic behaviors that are organized into layers of subsumption architecture. Finally, this paper, the basic performance of the network-based subsumption architecture is experimentally evaluated in association with the measurement of the dynamic sampling period.

Keywords: Multiple mobile robots, Subsumption architecture, Swarm intelligence, Group behaviors.

1 INTRODUCTION

Nature continually aspire the development of new ideas and system. Many simple biological species influence directly the development of new multi robot systems. Some of these species include insects such as ants [1 - 4], bees, wasps, and termites [5]. A multi robot system is a widely progressive research fields that went from simulation, prototyping and recently real applications [`1, 6]. It represents a team of robots that are either heterogeneous or homogeneous in their physical structure and functionality. The importance of multi robot systems is reflected in its high task reliability, fault tolerance and flexibility, spatially distributed, cost effective by using simpler individual structures, high application demand and the research challenges facing it [6, 22].

While robotics community witness recognizable progress in research and developments in the field of multi robot systems and its applications, there are still many research challenges which need to be addressed and efficiently solved by applying new innovative techniques. These research challenges may include: task allocation, cooperative mapping and localizations, sensor integration and real time sensory information fusion, real time based control architectures, local and global behaviors, resources utilization and deadlock solving, heterogeneous and distributed intelligence (think, reason, decide and learn), effective reconfigurable modular functionality, autonomy and cooperation, awareness and coordination, inter process communication and human machine interface, etc. [1aa, 1a, 1b].

The application areas of multi robot systems may cover areas such as, military and security, underwater and space exploration, hazardous environments, service robotics in both public and private domains, entertainment, and so forth, can benefit from the use of multi-robot systems. In these challenging application domains, multi-robot systems can often deal with tasks that are difficult, if not impossible, to be accomplished by an individual robot. The following paragraph highlights some examples of the work in the field of multi robot systems.

Parsons and Canny proposed an algorithm for planning the motions of several mobile robots which share the same workspace containing polygonal obstacles [7]. Each robot has an ability of independent translational motion in two dimensions. The algorithm computes a path for each robot which avoids all obstacles in the workspace as well as the other robots. Barman et al. developed an extensible facility for multiple mobile robots [8]. The system consists of nine radio-controlled mobile robots, two CCD color video cameras, a video transmitter and tuner, radio controllers, and so on. Software for tracking control is described. Kube and Zhang examined the problem of controlling multiple behavior-based autonomous robots [9], [10]. Based on observations made from the study of social insects, they proposed five simple mechanisms used to invoke group behavior in simple sensor based mobile robots. They also constructed a system of five homogeneous sensor-based mobile robots with capability of achieving simple collective task. Noreils described architecture for cooperative and autonomous mobile robots [11]. The cooperation is composed of two phases. One is the collaboration where a task is decomposed into subtasks. The other is the coordination where robots coordinate their activities to fulfill the initial task using the notion of coordinated protocols. This architecture showed benefits of modularity, robustness and programmability.

In addition, Azarm and Schmidt presented a novel approach to do conflict-resolution for multiple mobile robots [12]. A framework for negotiation is developed by using the online motion planning, which permits quick decentralized and parallel decision-making. The key

© ISAROB 2013

objective of the negotiation procedure is dynamic assignment of robot motion priorities. The performance was evaluated experimentally using only two mobile robots. Bennewitz and Burgard considered the problem of path planning for teams of mobile robots [13] using a decoupled and prioritized approach to coordinate the movements of the mobile robots in their environment. The proposed algorithm computes the paths for the individual robots in the configuration-time space. To estimate the risk of colliding with other robots, it uses a probabilistic model of the robots motions. Guo and Parker proposed a distributed and optimal motion planning algorithm for multiple robots, in which computation cost was decomposed into two modules, i.e., path planning and velocity planning [14]. The D* search method was applied in both modules, based on either geometric formulation or schedule formulation. The algorithm was implemented and tested in a group of Nomad 200 indoor robots. Parker outlined the project that demonstrated a team of 100+ heterogeneous robots solving an indoor reconnaissance and surveillance task [15]. The focus was the impact of heterogeneity on the collaborative solution approach that the robot team must take. Pimentel and Campos addressed the problem of multi-mobile robot cooperation with strict communication constraints which are considered indispensable for successful task execution [16]. The problem is modeled as a minimization of an energy functional which accounts for network connectivity, other relevant robot and task requirements in order to select locally optimal actions for each robot.

Antonelli et al. presented two experimental case studies performed using a multi-robot system made of six Khepera II mobile robots [17]. The experiments are aimed at testing the performances and the robustness of a behavior-based technique, called the null-space-based behavioral control (NSB). The NSB approach was developed to control a generic team of autonomous vehicles and it was implemented on a centralized architecture to control a platoon of autonomous mobile robots at a kinematic level. Also, the experimental validation of the NSB in the presence of static and dynamic obstacles was evaluated with a team of grounded mobile robots [18].

In this paper, network-based subsumption architecture with PC server is proposed to minimize the total cost for designing multiple mobile robots system by maximizing the group performance of robots with limited hardware and software capabilities rather than optimizing the behavior performance of individual robot. This enables to develop high-level group behavior. A server supervisory control with networked-based subsumption architecture is implemented and tested to realize a schooling behavior by relying only on information from the PSD sensors. Further, the dynamic sampling period is introduced to evaluate the basic performance of developed system.

2 MOBILE ROBOT WITH SIX PSD SENSORS

A. Basic Hardware

Figure 1 shows the developed mobile robot [19], [20]. The robot is an omnidirectional mobile robot with three wheels driven by DC motors and six PSD (Position Sensitive Detector) sensors.. It is produced by TosaDenshi LTD. A MicroConverter ADuC814ARU provided by Analog Devices is mounted on the control board of the mobile robot. In order to measure the distance to any object in real time, $\boldsymbol{d}_i(k) = [d_{i1}(k)...d_{i6}(k)]^T$ is the distance vector of the i-th mobile robot at the discrete time k. The PSD sensor is mainly composed of LEDs, electrical resistances and photodiodes, and can calculate the distance to an object through triangulation technique. Figure 2 shows the measurement graph of the PSD sensor, In order to cope with the problem of narrow directivity, the required number of the PSD sensor was decided to be six. In order to reduce the dead zone angle in the sensor view, more PSD sensors is required. Besides, each robot has a Bluetooth wireless device to communicate with the PC server.

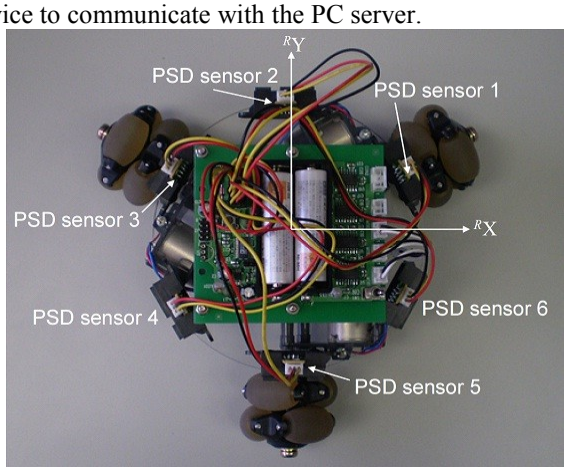

Fig. 1. The mobile robot with three wheels and six PSD sensors.

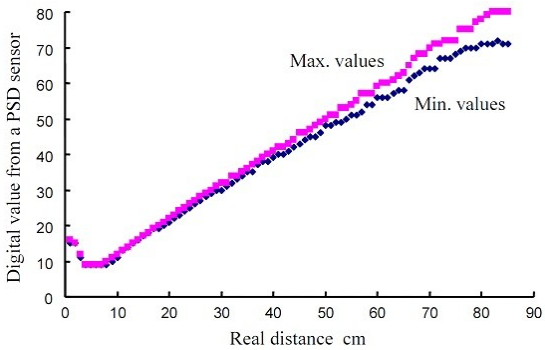

Fig.2. Shows the functional graph of PSD distance measurements.

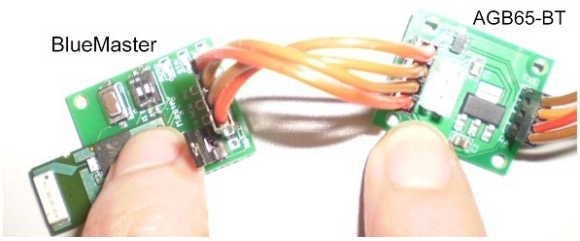

Fig.3. Bluetooth module through a serial interface AGB65-BT.

The Bluetooth is connected to each mobile robot through serial port to support data communication, so that text codes can be transmitted to and received from the Bluetooth

module called BlueMaster through a serial interface AGB65-BT as shown in Fig. 3. The small Bluetooth device is provided by Asakusagiken Co., Ltd. The AGB65-BT is connected to the serial port of MicroConverter ADuC814ARU mounted on a mobile robot.

B. Kinematic Control of Three-Wheeled Mobile Robot

Next, the kinematic control method of the mobile robot is explained. Figure 4 illustrates the kinematic model of the mobile robot in robot coordinate system $\Sigma R(\mathrm{O} - {}^{R}\mathrm{X}^{R}\mathrm{Y})$. ω_i (i = 1, 2, 3) is the angular velocity of each wheel. Also, by using the radius r of each wheel, $v_{ri} = r\omega_{ri}$ is the forward velocity of each wheel. If the position and orientation vector of the robot is given by $[x_r \quad y_r \quad \phi_r]^T$, then the velocity is represented by $v_r = [\dot{x}_r \quad \dot{y}_r \quad \dot{\phi}_r]^T$. The following kinematic relation is obtained from Fig. 3 [21].

$$\begin{pmatrix} \omega_1 \\ \omega_2 \\ \omega_3 \end{pmatrix} = \frac{1}{r} \begin{pmatrix} -\frac{1}{2} & \frac{\sqrt{3}}{2} & L \\ -\frac{1}{2} & \frac{\sqrt{3}}{2} & L \\ 1 & 0 & L \end{pmatrix} \begin{pmatrix} \dot{x}_r \\ \dot{y}_r \\ \dot{\phi}_r \end{pmatrix} \qquad (1)$$

where L is the distance between the center O of the robot and the center of each wheel. By using Eq. (1), the robot can be controlled kinematically, i.e., the is desired behavior designed by $v_r = [\dot{x}_r \quad \dot{y}_r \quad \dot{\phi}_r]^T$ can be performed by making three wheels rotate with the angular velocity vector $\boldsymbol{\omega} = [\omega_1 \ \omega_2 \ \omega_3]^T$. As special cases, Table 1 shows the basic velocity components to move in the direction of each PSD sensor. When designing the schooling mode using multiple mobile robots, the six basic velocities are used. The important point is that the direction of velocity, a mobile robot generates in ΣR, depends on the ratio $\dot{x}_{ri} : \dot{y}_{ri}$. The velocity norm can be arbitrarily changed as $\alpha\omega = [\alpha\omega_1 \ \alpha\omega_2 \ \alpha\omega_3]^T$ with a scalar α.

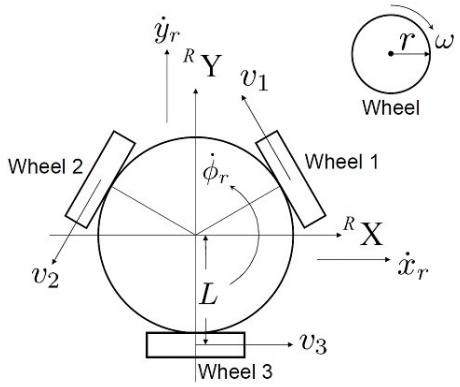

Fig. 4. Kinematics of the mobile robot with three wheels.

Table 1
Velocity components to move in the direction of each PSD sensor.

i	1	2	3	4	5	6
$\dot{x}_{ri}$	$\sqrt{3}$	0	$-\sqrt{3}$	$-\sqrt{3}$	0	$\sqrt{3}$
$\dot{y}_{ri}$	1	2	1	-1	-2	-1

3 NETWORK-BASED MULTI ROBOT SYSTEM

A. Software Development Environment and Its Limitation

The software development environment of the selected mobile robot using a free C language has two limitations since we are using robots with limited capabilities. The first is having limited memory and communication overhead, the flash ROM of the mobile robot is only 8 kB, so that it is difficult to deal with huge amount of state information. The second is, the mathematical functions within the standard library such as "exp ( )" is not supported by the complier while the computation resources is not enough to realize advance behavior. Thus, for example, it is impossible to directly program potential field technique supporting navigation and planning. In order to cope with such limitations of the software development environment, a n efficient strategy was adopted to have two levels of behaviors. The first level of behaviors constitutes simple reflexive swarm behaviors implemented directly on the mobile robot itself. The other level of behaviors represents a complex set of smarm behaviors implemented on a PC server expressing a supervisory control scheme. In the server control mode, each mobile robot collects all sensory information from the six PSD sensors and transmits it to the PC server, $\boldsymbol{d}_i(k) = [d_{i1}(k)...d_{i6}(k)]^T$ through Bluetooth communication. The subscript i denotes the identification number of a robot. Then the server decides and returns a simple swarm command/behavior to the robot while considering the overall swarm behavior (current and next). By means of the proposed supervisory control of the PC server, a complex swarm behavior can be executed be deciding the selection of such behavior by the PC server according to the situation needs and decompose it into sets of simple behaviors that are sent to each robot to execute. In addition, functions demanding high computation, such as potential field technique, can be placed at the PC server side where the Windows Visual Studio runs (representing the software development environment).

B. Server Supervisory Control Based on Subsumption Architecture

The proposed PC server based supervisory control is designed coordinate the required behavior for multiple homogeneous mobile robots each with three wheels and six PSD sensors. This system is used to support study needs of fourth year students at Tokyo University of Science, Yamaguchi, such as, to learn the subsumption control architecture for schooling behavior. The subsumption control architecture was first proposed by Brooks [23]. Students can practically know the basic concept and effectiveness of subsumption control architecture which provides a method for structuring reactive systems from lower level to higher level using layered sets of rules, i.e., reactive behaviors according to the change in the situation within robot's environment. Accordingly, the PC server returns a set of simple behavior associated with short execution time, e.g., 200 ms to the corresponding robot. Nine kinds of the most simply subdivided reaction behaviors, i.e., reflex actions, are implemented for the mobile robots as tabulated in Table 2. When a set of behavior codes and an execution time is transmitted from the PC server to a mobile robot, the mobile robot conducts the motion exactly within the specified execution time.

© ISAROB 2013

Three agents called "Avoid objects ", "Turn to left or right" and "Move forward " are designed as a composite of a set of basic behaviors/commands/actions A_i (i = 0, 1, 2, ... , 8) shown in Table 2 that are used to realize a schooling behavior.

4 SUBSUMPTION ARCHITECTURE IMPLEMENTED ON PC SERVER

The software development environment is Windows Visual Studio C#, which is used to develop and implement high level software architecture such as subsumption control architecture according to application requirements and can be adapted based on robot's hardware capabilities. Subsumption is an efficient way to decompose complex behavior into a set of simple behaviors. Based on sensory information, only one behavior is selected as a highest priority when a new set of sensory information is presented. Figure 5 shows the subsumption control architecture implemented on the supervisory PC server. The controller includes the three agents. The upper level agent has a higher priority to be dispatched. This section introduces the three kinds of agents and the corresponding output command codes from the list shown in Table 2. The nine commands shown in Table II are simple and basic motions but important reflex actions for each mobile robot to consequently produce the competences relevant to the three agents. The PC server receives PSD sensory information $\boldsymbol{d}_i(k)(1 \le i \le N)$ from all mobile robots periodically every dynamic sampling period, in which N is the number of the available mobile robots. By analyzing $\boldsymbol{d}_i(k)$, the controller dispatches the current execution to one of the three agents for the i-th mobile robot according to triggering priority.

In the schooling mode, all mobile robots try regularly move along the inner of a circular fence keeping the distance to both the fence and other mobile robots. This mode enables the robots to behave like carps in a Japanese artificial circular pond.

TABLE 2
The basic list of simple reactive behaviors/commands/Actions that can be executed at the robot side together with the corresponding motion.

Cmd. code	Corresponding motion
0	Halt at the position
1	Move to the direction of PSD sensor 1
2	Move to the direction of PSD sensor 2
3	Move to the direction of PSD sensor 3
4	Move to the direction of PSD sensor 4
5	Move to the direction of PSD sensor 5
6	Move to the direction of PSD sensor 6
7	Rotate to clockwise direction
8	Rotate to counterclockwise direction

Figure 6 and 7 show the layout configuration and the experimental scene of schooling behavior respectively, in which multiple mobile robots are controlled based on the subsumption control architecture incorporated in the PC server associated with supervisory control capability as shown in Fig. 5. It was confirmed from the experiment that the multiple mobile robots performed the desirable schooling behavior successfully.

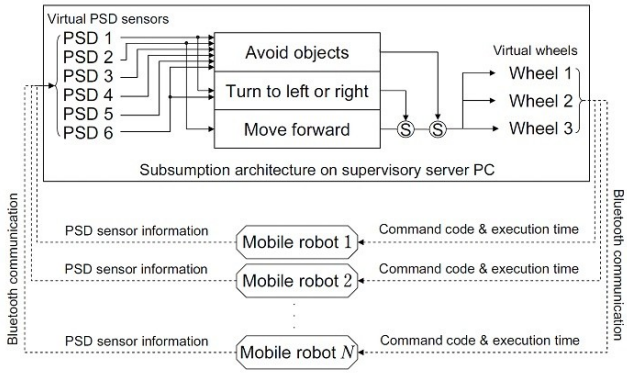

Fig. 5. Network-based subsumption architecture for a schooling behavior, which is implemented on a PC server.

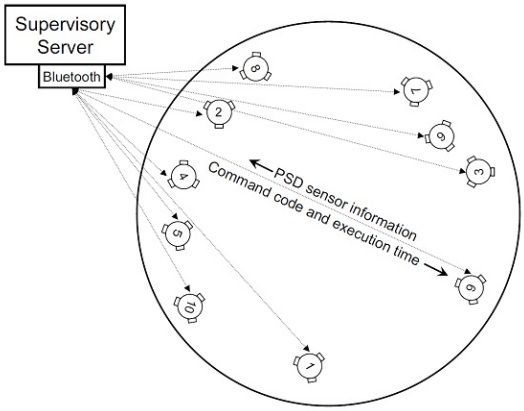

Fig. 6. Layout configuration of the developed system.

Fig. 7. Experimental school behavior demonstration.

To coordinate the relation between each robot and the PC server, there is an agent dispatcher supervises the controller shown in Fig. 4. The dispatcher does not immediately move the execution right to a higher priority agent when a lower priority agent is running, because each agent works as a simple reactive behavior every sampling period according to the sensory information. Instead of this, whenever a reaction behavior is executed during a specified execution time, the dispatcher checks and updates the activity of each agent and gives the next execution right to a newly updated active agent with the highest priority.

5 DYNAMIC SAMPLING PERIOD

The dynamic sampling period is an important factor to evaluate the performance of the multiple mobile robots

© ISAROB 2013

system. The dynamic sampling period is defined for a PC server as a variable time starting from submitting a command packet to a mobile robot until receiving a response packet including the new sensory information. Figure 9 shows the handshake process to measure the sampling period $T_k = t_{k+1} - t_k$. The processor time t_k at the discrete time k in the PC server is used as a timestamp to synchronize the time between the PC server and each mobile robot. The processor time t_k can be obtained by referring the Windows parameter "int smillisec = Environment.TickCount;" in a timer interrupt process at the PC server side. The size of the packet used in Bluetooth communication between the PC server and a mobile robot is 30 bytes. When a command packet is transmitted from the PC server to a mobile robot, necessary information about the command is written at the offset positions from byte 0 to 11. On the other hand, when returning to the PC server from the mobile robot, the sensory information of the six PSD sensor are set at the offset positions starting from byte 12 to 29. It should be noted that the execution time in Fig. 4 is set to 0 ms in this measurement process. It is observed experimentally that there exists some time dispersion around 62.4 ms and the resolution of the time dispersion is about 15.6 ms. The timer interval of Microsoft Visual C# used in the measurement.

6 CONCLUSION

In this paper, network-based subsumption architecture has been presented to realize high level behavior such as, schooling behavior using only information from PSD sensors. Experimental results showed interesting behavior among the multiple mobile robots, such as following, avoidance, and schooling. Further, how to simply measure the dynamic sampling period has been introduced to evaluate the basic performance of network-based multiple mobile robots system. The dynamic sampling period is defined for the PC server as the variable time. It is expected that the dynamic sampling period becomes one of important criterion for network-based multiple mobile robots system.

REFERENCES

[1] Asama, H, Habib, M K, Endo, I, Ozaki, K, Mastumoto, A Ishida, Y, "Functional distribution among multiple mobile robots in an autonomous and decentralized robot system", IEEE Robotics and Automation 1991 conf. (ICRA 1991), USA, pp.1921-1926.

[2] Moffet, M W, "Cooperative Food Transport by an Asiatic Ant," National Geographic Research, 4(3), 1988, 386-394.

[3] Anderson, C and Franks, N R., "Teams in animal societies," Behavioral Ecology, 12(5), 2001, 534-540.

[4] Gautrais, J., Theraulaz, G., Deneubourg, J.L., and Anderson, C., "Emergent polyethism as a consequence of increased colony size in insect societies," Journal of Theoretical Biology, 215, 2002, 363-373.

[5] Mori, H, Saito, Y, and Tho, Y P, "Cooperative group predation in a sit and wait cheyletid mite," Experimental and Applied Acarology, 23, 1999, 643-651.

[6] Chow, M-Y, Chiaverini, S, and Kitts, C, "Introduction to the Focused Section on Mechatronics in Multirobot Systems," IEEE/ASME Transactions on Mechatronics, VOL. 14, No. 2, 2009, pp.133 – 140.

[7] Parsons, D and Canny, J, "A motion planner for multiple mobile robots," in Proc. IEEE International Conference on Robotics and Automation, Cincinnati, OH, USA, May, 1990, 8–13.

[8] A. R. Barman, A R, Kingdon, S J, Little, J J, et al, "DYNAMO: Real-time experiments with multiple mobile robots," Intelligent Vehicles Symposium, Tokyo, Japan, July, 1993, 261–266.

[9] Kube, C R and Zhang, H, "Collective robotic intelligence," in Proc. The Second International Workshop on Simulation of Adaptive Behavior, 1992, 460–468.

[10] Kube, C R and Zhang, H, "Collective robotics: From social insects to robots," Adaptive Behavior, vol. 2, no. 2, 1993, 189–219.

[11] Noreils, F R, "An architecture for cooperative and autonomous mobile robots," in Proc. IEEE International Conference on Robotics and Automation, Nice , France, May, 1992, 2703–2710.

[12] Azarm, K and Schmidt, G, "Conflict-free motion of multiple mobile robots based on decentralized motion planning and negotiation," in Proc. IEEE International Conference on Robotics and Automation, Albuquerque, NM , USA, April, 1997, 3526–3533.

[13] Bennewitz, M and Burgard, W, "A probabilistic method for planning collision-free trajectories of multiple mobile robots", Proc. of the Workshop Service Robotics - Applications and Safety Issues in an Emerging Market at the 14th European Conference on Artificial Intelligence, Berlin, Germany, August, 7 pages, 2000.

[14] Guo, Y and Parker, L E, "A distributed and optimal motion planning approach for multiple mobile robots", Proc. IEEE International Conference on Robotics and Automation, Washington, DC, USA, 2002, 2612–2619.

[15] Parker, L E, "The effect of heterogeneity in teams of 100+ mobile robots," Multi-Robot Systems: From Swarms to Intelligent Automata, Volume II, Kluwer Academic Publishers, 2003, 205–215.

[16] Pimentel, B and Campos, M, "Cooperative communication in ad hoc networked mobile robots," in Proc. IEEE/RSJ International Conference on Intelligent Robots and Systems, Las Vegas, NE, Oct., 2003, 2876–2881.

[17] Antonelli, G, Arrichiello, F, Chakraborti, S and Chiaverini, S, "Experiences of formation control of multi-robot systems with the null-spacebased behavioral control," in Proc. IEEE International Conference on Robotics and Automation, Roma, April, 2007, 1068–1073.

[18] G. Antonelli, F. Arrichiello and S. Chiaverini, "Experiments of formation control with multirobot systems using the null-space-based behavioral control," IEEE Transactions on Control Systems Technology, Vol. 17, No. 5, pp. 1173–1182, 2009.

[19] F. Nagata, T. Yamashiro and K. Watanabe, "Cooperative swarm control for multiple mobile robots using only information from PSD sensors," Artificial Life and Robotics, vol.16, no. 1, pp. 116–120, 2011.

[20] N. Kitahara, F. Nagata, A. Otsuka, K. Sakakibara, K. Watanabe and M. K. Habib, "A proposal of experimental education system of mechatronics," in Proc. of 17th International Symposium on Artificial Life and Robotics, Beppu, Oita, Japan, January, pp. 166–169, 2012.

[21] K. Watanabe, Y. Shiraishi, S. G. Tzafestas, J. Tang and T. Fukuda, "Feedback control of an omni-directional autonomous platform for mobile service robots," Journal of Intelligent & Robotic Systems, vol. 22. nos. 3/4, pp. 315–330, 1998.

[22] Asama, H , Ishida, Y, Ozaki, K, Habib, MK, Matsumoto, A, Kaetsu, H, and Endo, I "Communication system between multiple robotic agents.," the 1992 Japan-USA Symposium on Flexible Automation Part 1(of 2), 1992, 647-654.

[23] R. A. Brooks, "A robust layered control system for a mobile robot," IEEE Journal of Robotics and Automation, vol. 2, no. 1, pp. 14–23, 1986.

The Eighteenth International Symposium on Artificial Life and Robotics 2013 (AROB 18th '13),
Daejeon Convention Center, Daejeon, Korea, January 30-February 1, 2013

A precision position arrangement of the SCARA robot by H_∞robust control

Yasuyuki Hirofuji, Zhang Feifei, Masanori Ito

Tokyo University of Marine Science and Technology, Japan
(Tel:+81-3-5245-7422, Fax: +81-3-5245-7422)

Abstract: The SCARA (Selective Compliance Assembly Robot Arm) robot is playing an active role in many manufacturing stages of electrical machinery, electronic components etc. In those days, improvement of productivity is becoming important subject. And it will be realized with improvement in a capacity utilization rate, and industrial accident prevention, development of the technology for speed up of motion, accuracy of operation, or abnormality detection. Especially speed, accuracy and safety are most important items for it. We applied modern control theory, such as H_∞ robust control and confirmed the performance with experiments.

Keywords: H∞Robust Control SCARA Robot

1 INTRODUCTION

Currently, the control method of industrial robots, such as a SCARA robot is PID control, which is classified as a classical control. As PID control is relatively simple and easy to use, it is widely used in various situations and not limited. On the other hand, modern control theory is not so used in the field with the reason of difficulty to use because of its stringency and complexity. However, various control theory have been studied and many advanced control theory have been established until now.

As the factors that cause to parameter change of SCARA robots, some mass change at the time of holding the work, posture change, interference from other joints, and aging of the device are pick-upped. Modern control is different from classical control, such as PID control, and able to handle multiple-input multiple-output systems. With applying the H_∞ robust control, robust stabilization for parameter variations, disturbance from peripheral inhibitory effect can be expected. Then it is possible to improve the performance such as high-precision positioning with smooth operation of the arm, stabilization of the system, and reduction of maintenance.

2 CONTROLLED OBJECT

In this study, we used a SCARA robot (very small) YX-XG series by Yamaha Motor CO. Ltd.

Table 1. Spec. of controlled object

Shaft X length	45(mm)
Shaft Y length	75(mm)
Motor capacity	30(W)
Maximum rotation	8000(rpm)
Reduction ratio	1/50

The mass of each joint, the moment of inertia, friction coefficient are identified with experiment.

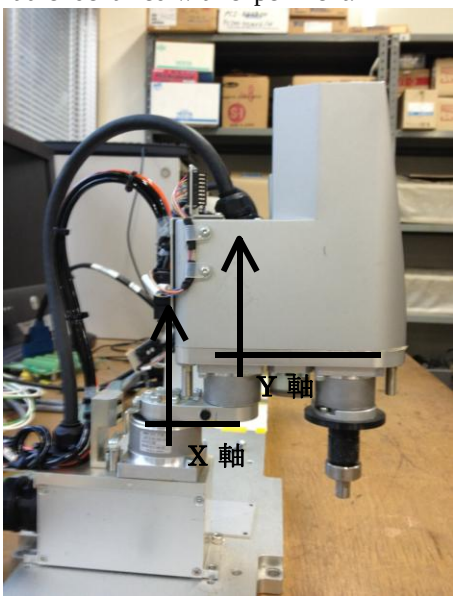

Fig. 1 SCARA Robot

3 H_∞ROBUST CONTROL

Control design to stabilize the closed-loop system including the control target is to minimize the H_∞ norm of the closed-loop transfer function between the input and output.

The actual system is complex, and it can't be represented with a single transfer function. So, we adopted the method to estimate the uncertainly from the difference between actual and model system.

Model for this design is that of the nominal plant. Real systems are included in the plant.

Therefore, on the design of the controller, instead of thinking the actual system, we considered the collection of

© ISAROB 2013

this plant model, to guarantee the stability and control, also ensures the stability and control to the real system.

4 SCARA ROBOT MODELING

At first, from the experiment, we calculated mass, moment of inertia of each axis and the friction coefficient including a motor and load.

Equation of motion and the transfer function of the motor is as follows,

$$J\ddot{\theta} + D\dot{\theta} = J\dot{w} + Dw = kV \quad (1)$$

$$G(s) = w(s)/V(s) = k/(Js + D) \quad (2)$$

θ : Angle of rotation of the arm

J : Moment of inertia of the base of the arm

D : Coefficient of friction of the arm

V : Input voltage

k : Motor parameters

Time constant : $T = J/D$ (3)

Gain : $g = k/D$ (4)

$$D = V \times 50 \times 50 \times k/A \quad (5)$$

Fig.2 and 3 are the output data of the angular velocity of each arm when input to the X-axis is 0.25 (V), and input to the Y-axis is 0.5 (V),

From measured data graph, we can read Time constant: T, the Gain: g, and calculate the unknown J and D.

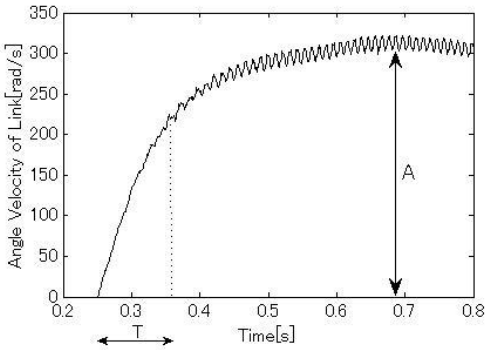

Fig. 2 Experiment x

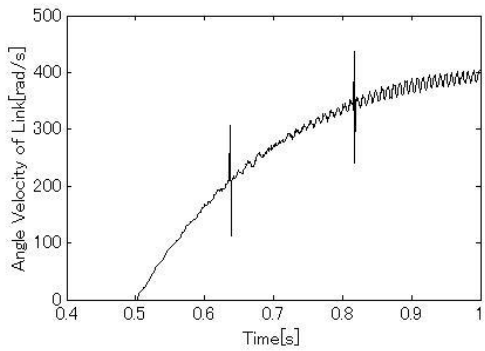

Fig. 3 Experiment y

Next, from the moment of inertia calculation, mass can be estimated as follows,

$$Jy = Dy \times Ty \quad (6)$$

$$Jy = Iy + My(\frac{h}{2})^2 \quad (7)$$

Unknown parameters can be obtained with those processes.

$$Mx = 1.5(kg)\ My = 2.4(kg)$$
$$Jx = 0.04(kgm^2)\ Jy = 0.02(kgm^2)$$
$$Dx = 0.486\ Dy = 0.226$$

From those data, we can fix model of target.

The transfer function from the input voltage to the rotation angle of each of the X-axis, Y-axis of controlled object is as follows.

$$P_x = \frac{89.39s + 5959}{s^3 + 187.1s^2 + 4755s} \quad (8)$$

$$P_y = \frac{159.8s + 6561}{s^3 + 175.6s^2 + 4253s} \quad (9)$$

5 DESIGN OF H∞ROBUST CONTROLLER

Using MATLAB, we designed a H∞ robust controller. The design procedure is as follows,

1) Selection of nominal model
2) Formulation as a mixed sensitivity problem
3) Configuration of the general plant
4) H∞ robust controller design

First, for the step 1) each transfer function of X axes and, Y axes uses.

Next, in order to design a H∞ control system, the problem of determining the controller K is considered to minimize following evaluation function.

.

$$\left\| \begin{matrix} W_1 PK(1+PK)^{-1} \\ W_2(1+PK)^{-1} \end{matrix} \right\|_\infty \rightarrow \text{Minimization}$$

Fig. 4 Evaluation function

As shown in the Fig.5, it corresponds to the transfer function from W1 to z, and from W2 to z.

© ISAROB 2013

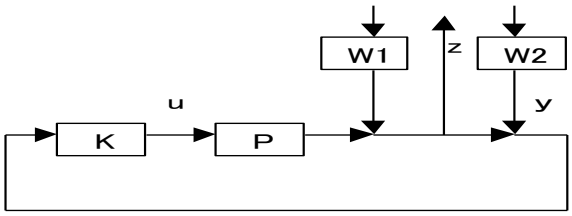

Fig. 5 Mixed sensitivity problem

Then, as shown in the following figure, we configure the general plant.

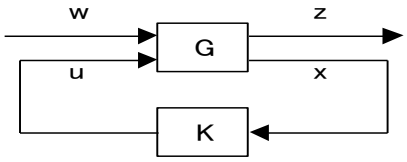

Fig. 6 General plant

· How can we choose the weighting function?

It was depicted as follows. The frequency response variation were estimated on bode diagram, and so as to cover this, it was determined with the low-order transfer function on the graph. At this time, we determine the weighting function as shown in the broken line with approximation. Then, at the same time we draw the Bode plots of the variation and weight, and make sure that the top of the Bode plot of weight variation. In addition, as the control is not performed in a high frequency band, we set the frequency as high as possible and increase the gain of the variation. Then vibration input is reduced.

In Fig.7, P is solid line, W1 is broken line, and W2 is alternate long and short dash line.

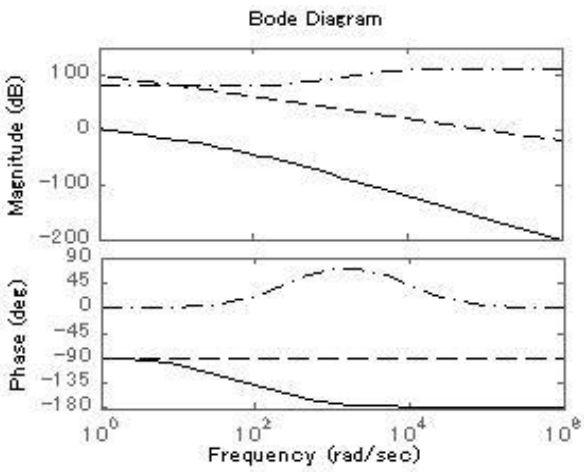

Fig. 7 Bode diagram

$$K = \left[\begin{array}{c|c} A_k & B_k \\ \hline C_k & D_k \end{array}\right]$$

$$A_k = \begin{bmatrix} 0.001603 & -0.3104 & -0.5645 & 1.529e+004 \\ 0.004666 & -1.545 & -57.34 & 3.452e+004 \\ -0.4592 & 166.4 & 141.8 & -3.899e+006 \\ -2.64e-005 & 0.0003646 & 0.02252 & -279.8 \end{bmatrix}$$

$$B_k = \begin{bmatrix} -9.008e-005 \\ -0.0002033 \\ 0.02296 \\ -5.725e-005 \end{bmatrix}$$

$$C_k = \begin{bmatrix} -7.997 & 1577 & 6319 & -7.508e+007 \end{bmatrix}$$

$$D_k = \begin{bmatrix} 0.4422 \end{bmatrix}$$

6 RESULTS OF EXPEREMENT

We performed comparative experiments of H_∞ controller and PID controller. Confirming the robustness, we experimented to change positioning speed. Fig. 8 to 11 are the results of PID control. Fig 12 to 15 are the results of H_∞ control. On each control, we experimented with different positioning speed at 1.4 seconds to three times, four times, five times. The horizontal axis is Time (s). The vertical axis is angle of each link (rad.). Solid line is the target angle. The dotted line is the measured angle

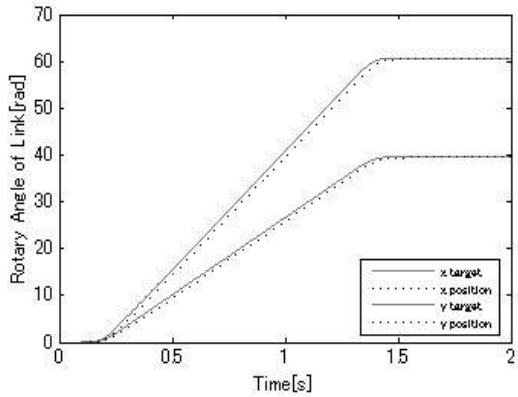

Fig. 8 Experiment result of PID control (1.4sec)

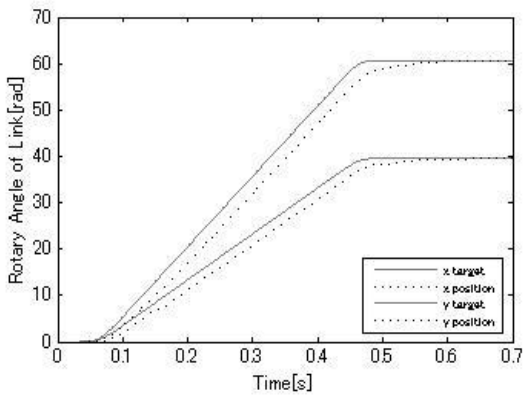

Fig. 9 Experiment result of PID control (0.47sec)

© ISAROB 2013

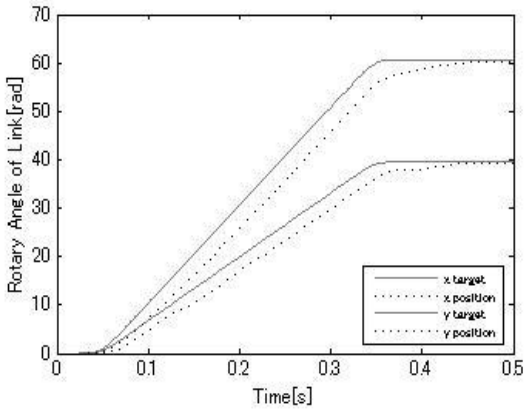

Fig. 10 Experiment result of PID control (0.35sec)

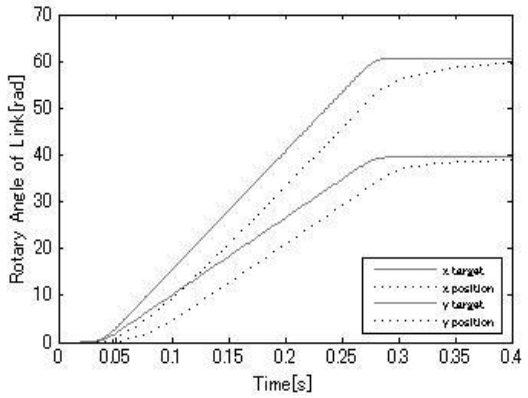

Fig. 11 Experiment result of PID control (0.28sec)

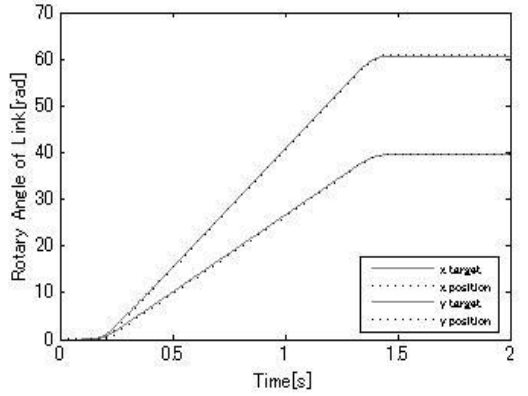

Fig. 12 Experiment result of H ∞ control (1.4sec)

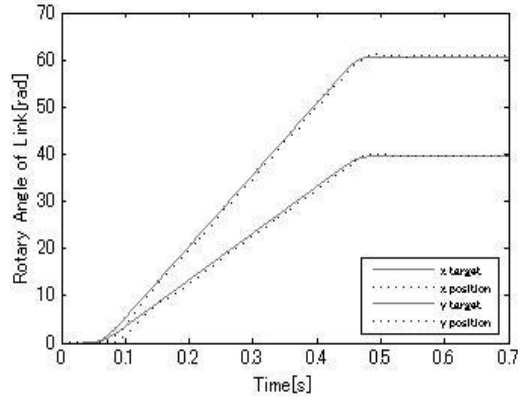

Fig. 13 Experiment result of H ∞ control (0.47sec)

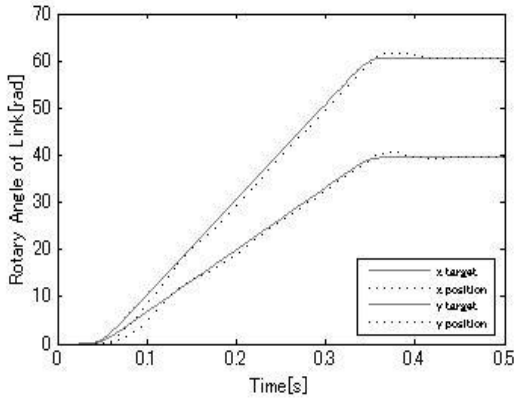

Fig. 14 Experiment result of H_∞ control (0.35sec)

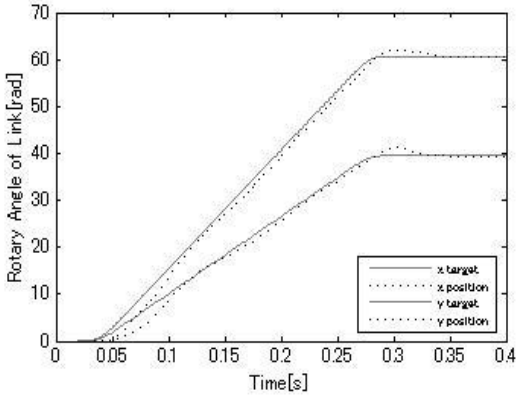

Fig. 15 Experiment result of H ∞ control (0.28sec)

7 CONCLUSION

In this study, we applied H_∞ robust control to SCARA robot, in order to confirm the possibility of control performance improvement. We performed comparative experiments of H_∞ controller and PID controller with actual device, and the following conclusions were obtained.

1) To get faster operation speed of SCARA robot, robust H_∞ control obtained good results in target joint angle tracking capability and we confirmed the robust stability. In addition, for the parameter variations due to load fluctuation or change in the attitude of the arm, the stability could be confirmed as well.

2) Based on the results of this study, we want to expand the control to multi-input multi-output system from the single-input single-output system.

REFERENCES

[1] Y. Liu (2002), Linear robust control
[2] Hideki Kimura (2000), H∞control

The Eighteenth International Symposium on Artificial Life and Robotics 2013 (AROB 18th '13),
Daejeon Convention Center, Daejeon, Korea, January 30-February 1, 2013

Hybrid control with adaptive and state feedback control for Robot Hand

Kazuma.Funahashi, Hiroki.Goto, Feifei.Zhang and Masanori.Ito

Tokyo University of Marine Science and Technology,
2-1-6 Echujima, Koto-ku, Tokyo 135-8533, JAPAN
(Tel : 81-3-5245-7422; Fax : 81-3-5245-7422)

kazuma9@hotmail.co.jp

Abstract: In this research, we aimed to get an optimum control performance for any kinds of system with the combination of adaptive and state feedback control which are one of modern control theory. Here we used "Gifuhand" which is a hand type robot of 5 fingers as an experimental device. It is optimum experimental device for the purpose of this research to develop the control method which does not spoil controllability under any condition. Because it is the structure imitating human's hand and it is possible to be applied in various scenes. The results of performance such as robustness and accuracy are satisfiable.

Keywords: robot hand, adaptive control, state feedback control, hybrid

1 INTRODUCTION

An adaptive control is expected as next-generation of control method with its very high robustness and easiness for actual use. For example, there is no necessity of parameter tuning in a design phase, and controllability can be maintained to status change of the target in the control process.

However, on the other side it has weak points. Since there exist much computational complexity, the reaction tends to be overdue and the offset is inevitable for system operation.

A state feedback control has the features that are possible to extend to the formula of various optimizations, such as type 1, and type 2 and has very high controllability with adjusting precisely in a design phase except low robustness.

In this research, we propose a hybrid control method which is combined each strong point of above mentioned two control theory, and have high performance such as no offset, saving time and effort of design and maintaining high robustness.

The validity of control and the robustness of adaptation proposed control method were confirmed with the experiments of position control for the robot hand of 5 fingers, 16 DOF and 20 joint and called "Gifuhand" and comparison with conventional method.

2 CONTROL DESIGN

The feature of the proposed control method is to make a good input to make a set variable follow while it replies the optimum gain and an integral gain for every sampling period with a pole assignment method applying the discrete numeric model of the system which is it obtained with iterative least squares technique and the eigenvalue specified beforehand to integral type servo system of discrete state feedback.

Hereinafter, the block diagram of a control system is shown in. Fig.1

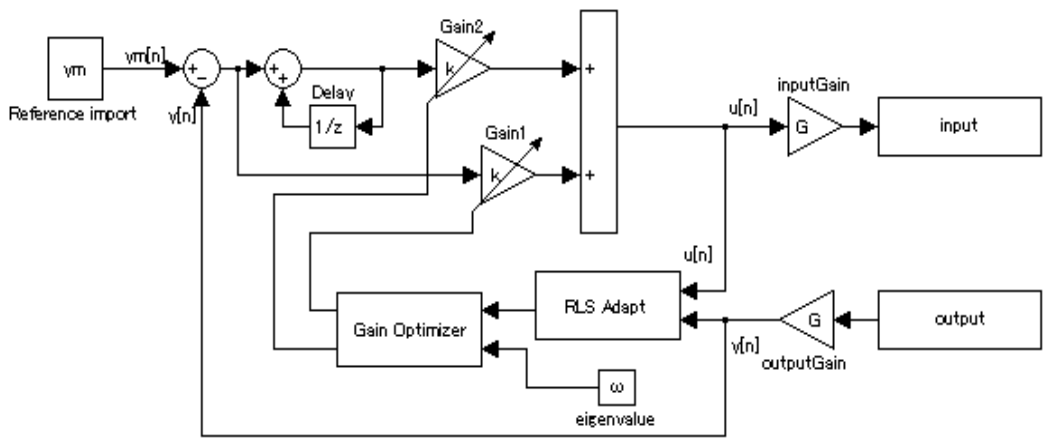

Fig.1 Block diagram of hybrid system

© ISAROB 2013

2.1 Discrete-time model

In a basic adaptive control (the RLS method), they perform optimum control with following steps that it calculating the coefficient of the input and output of the difference equation of a system with a least-squares method and substituting them to the equation and a desired value for the future.

To apply this method, we designed control system based on the difference equation using adaptive control in this experiment.

And we designed difference equation as quadratic system considering for the time and effort for a design, accuracy of control, computational complexity, and etc, in the difference equation of the system. Eq.(1)

$$y[n+1] = a_1 y[n] + a_2 y[n-1] + b_1 u[n] + b_2 u[n-1] \quad ..(1)$$

And in order to extend an Eq.(1), a discrete state Eq.(2.1) ~ (2.3) is made to correspond as follows.

$$X[n+1] = AX[n] + Bu[n] \quad ..(2.1)$$

X and y are the followings.

$$X[n] = \begin{bmatrix} x_1[n] \\ x_2[n] \end{bmatrix} \quad ..(2.2)$$

$$y[n] = x_2[n] \quad ..(2.3)$$

From Eq.(1) and Eq.(2.1) ~ (2.3), a state variable and A and B can be found uniquely. Each Eq.(3.1) ~ (3.3) can be derived.

$$x_1[n] = a_2 y[n-1] + b_1 u[n-1] \quad ..(3.1)$$

$$x_2[n] = y[n] \quad ..(3.2)$$

$$A = \begin{bmatrix} 0 & a_1 \\ 1 & a_2 \end{bmatrix}, B = \begin{bmatrix} b_1 \\ b_0 \end{bmatrix} \quad ..(3.3)$$

The integration clause of a discrete integration type servo system is added into the state equations Eq.(1) and Eq.(2.1) ~ (2.3). The results are Eq.(4.1) ~ (4.2).

$$X[n+1] = AX[n] + Bu[n] \quad ..(4.1)$$

$$A = \begin{bmatrix} 0 & a_1 & 0 \\ 1 & a_2 & 0 \\ 0 & \Delta & 1 \end{bmatrix}, B = \begin{bmatrix} b_1 \\ b_0 \\ 0 \end{bmatrix} \quad ..(4.2)$$

Here X[n] is given from the following equations. And a desired value is given to a state variable in order to converge on it.

$$X[n] = \begin{bmatrix} \hat{x}_1[n] \\ \hat{x}_2[n] \\ W[n] \end{bmatrix} \quad ..(4.3)$$

$$\hat{x}_1[n] = x_1[n] \quad ..(4.4)$$

$$\hat{x}_2[n] = x_2[n] - y_m[n] \quad ..(4.5)$$

$$W[n] = W[n-1] + \Delta(y[n] - y_m[n]) \quad ..(4.6)$$

Here Δ is a sampling period. Eq.(4.6) integrates with the difference of the present output and a target output for every sampling period, and, finally suppress offset

2.2 Control systems

Eq.(5) is given to Eq.(4.1) ~ (4.6) as an input. With a pole placement method and eigenvalue ω, the value of k is calculated, respectively. Eq.(6.1) ~ (6.3).

$$u[n] = -[k_1 \quad k_2 \quad k_3]X[n] \quad ..(5)$$

$$k_1 = \frac{b_0 b_1(a_2 - a_1 + \Omega_1) - b_0^2(\Omega_2 - a_2) + b_1^2(\Omega_3 + a_1 + 1)}{-b_0 b_1^2(1 + a_1) + b_1 b_0^2(a_2 - a_1) + a_2 b_0^3 - b_1^3} \quad ..(6.1)$$

$$k_2 = \frac{-b_1 k_1 + a_1 + 1 + \Omega_3}{b_0} \quad ..(6.2)$$

$$k_3 = \frac{\Omega_2 - a_2 + b_1 k_2 - (a_1 b_1 - a_2 b_0)k_1}{b_1} \quad ..(6.3)$$

Here each Ω is given from Eq.(7.1) ~ (7.3).

$$\Omega_1 = \omega_0\omega_1 + \omega_1\omega_2 + \omega_2\omega_0 \quad ..(7.1)$$

$$\Omega_2 = \omega_0\omega_1\omega_2 \quad ..(7.2)$$

$$\Omega_3 = \omega_0 + \omega_1 + \omega_2 \quad ..(7.3)$$

Since it is a discrete system, the system is stabilized while all eigenvalues are between -1 and 1. However, in this study, all ω are set to 0, in order to save the time and effort of a control design.

2.3 Identification

In calculating a_1, a_2, b_0 and b_1, a iterative least squares mean method (the RLS method) is used. θ[n] and φ [n] are defined as follows.

$$\theta^T[n] = [a_2 \quad a_1 \quad b_1 \quad b_0] \quad ..(8.1)$$

$$\varphi^T[n] = [y[n-1] \quad y[n-2] \quad u[n-1] \quad u[n-2]] \quad ..(8.2)$$

And the value of θ is presumed with iterative least squares mean technique. At every sampling period, this calculation is repeated and each value is derived.

The algorithm is as follows.

$$\theta[n] = \theta[n-1] + \frac{P[n-1]\varphi[n]}{1 + \varphi^T[n]P[n-1]\varphi[n]}\varepsilon[n] \quad ..(9.1)$$

$$\varepsilon[n] = y[n] - \varphi^T[n]\theta[n-1] \quad ..(9.2)$$

$$P[n] = P[n-1] - \frac{P[n-1]\varphi[n]\varphi^T[n]P[n-1]}{1 + \varphi^T[n]P[n-1]\varphi[n]} \quad ..(9.3)$$

$$\theta^T[0] = [1 \quad 1 \quad 1 \quad 1] \quad ..(9.4)$$

$$P[0] = I \quad ..(9.5)$$

3 EXPERIMENTAL SYSTEM

The Gifuhand consists of a thumb and four fingers. The thumb and a finger are modularized for every joint, and unitized for every finger, respectively. The thumb has 4 joint and 4 DOF and other fingers have 4 joint and 3 DOF. It has a total of 20 joint 16 DOF for single hand. This is almost equal to man's DOF of hand, and can imitate a motion of man's hand. In addition, as for an each finger, the 4th joint is connected to the 3^{rd}joint with a parallel link mechanism.

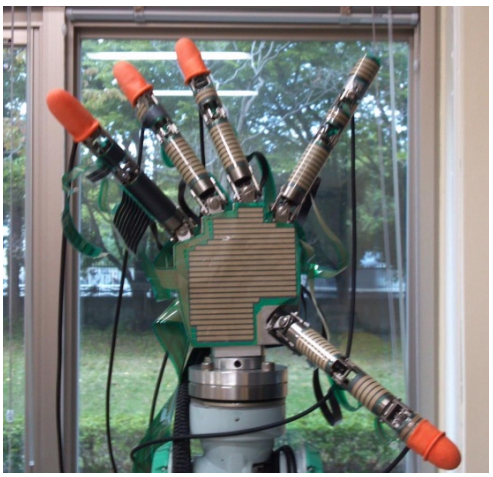

Fig.2 Photo of robot hand

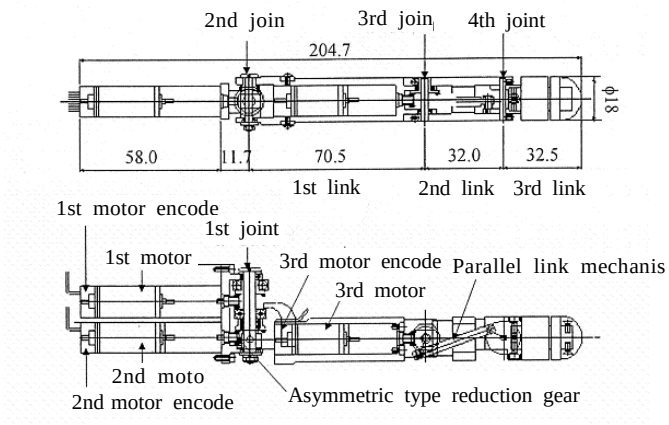

Fig.3 Finger mechanism & size

Fig.2 is the photo of the hand and Fig.3 is the mechanism of the little finger of the experimental device.

Moreover, in this experiment, in order to move a robot hand, a visual C ++ is used for programing and a D/A board, an A/D board, an encoder counter board, and 16-channel power amplifier are used as interface.

The specification of the third joint of the finger used in this experiment is introduced in Table 1.

Table 1 Specifications of robot hand

Speed reduction	148.48:1
Encoder resolution	3.79×10^{-2}[deg]
Max torque	0.20[Nm]
Frequency characteristic	7.0[Hz]
Rating output	1.2[W]
Idling speed	17700[Rpm]
Starting current	673[mA]
Rotor moment-of-inertia	$0.286 gcm^2$

4 RESULTS AND EVALUATION

The experiments were done for sampling period is 0.01second. All eigenvalues were set to 0.The joint which was used for the experiment was a root joint of a little finger. We gave order to this joint to move 60 deg within 1 sec to the direction of grasping. In every experiment, we set the data of control parameter obtained with pre-operation as initial value. (a_1=1, a_2=0.1, b_0=0, b_1=0)

In this experiment we compared following three methods

(1) Conventional adaptive control
(2) Hybrid control which we are proposed
(3) Hybrid control under loading

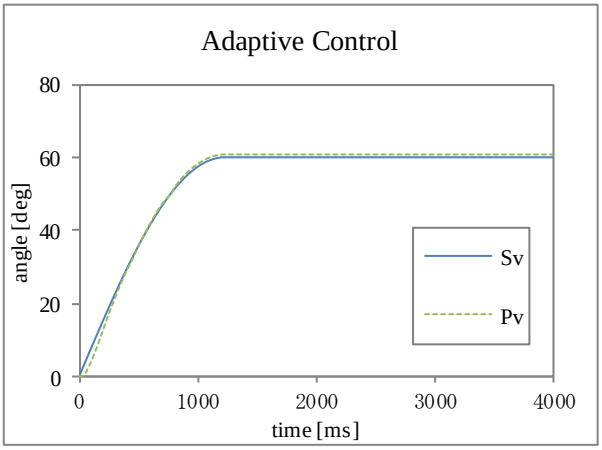

Fig.4 Adaptive control

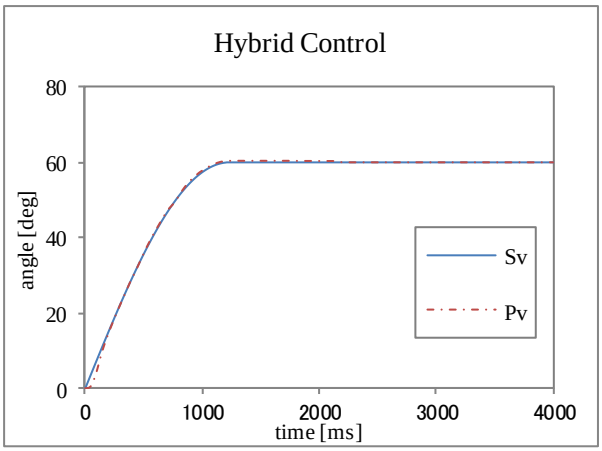

Fig.5 Hybrid control

© ISAROB 2013

Fig.4 is the result of conventional adaptive control. Input is a solid line, and output is a dotted line.

Although the outputs follow to the input stably, the small offset error occurs. The detail is shown in Fig.6.

Fig.5 is the result of the Hybrid control. Input is a solid line, and output is a chain line.

Although there is some overshooting of about 2 seconds, it has a high traceability to the change of input. The detail is shown in Fig.6.

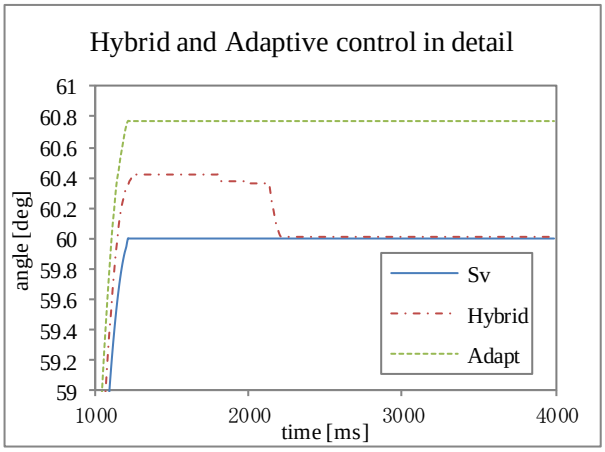

Fig.6 Hybrid and Adaptive in detail

Fig.6 shows the enlarged comparison of the conventional method and a hybrid method. Input is a solid line, Hybrid output is a chain line and conventional output is a dotted line.

This shows the overshoot of Hybrid control is 0.4deg and offset error is very small (0.01deg) and offset error of conventional adaptive control is about 0.8 deg.

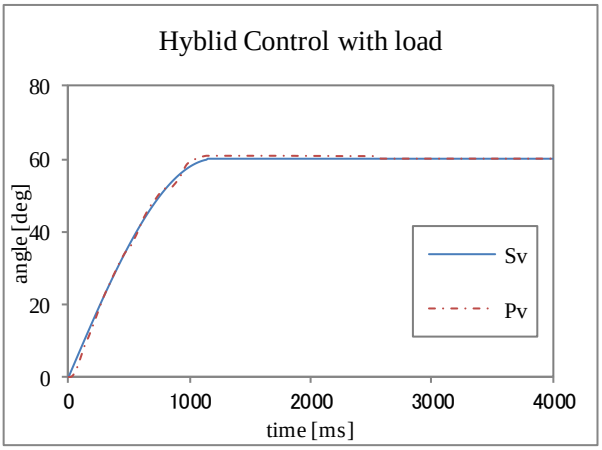

Fig.7 Hybrid control with load

Fig.7 is the result of the Hybrid control under 1kg load. Input is a solid line, and output is a chain line.

Since the load of 1kg is hung to the fingertip, the load moment changes with the motion of finger. It is a kind of hard condition for control. However it shows high robustness that the speed change and shock of motion was not so large to the big change of moment.

5 CONCLUSION

This study showed that hybrid control has high robustness and easiness for adjustment, and higher controllability and accuracy than conventional adaptive control. In particular, the problem of the steady-state error which was a problem until now was solved, and precise control was also attained. Moreover, it can be said that it is very effective in the equipment used for various uses like a robot hand with very high robustness.

However, the shortage of speed which comes from the numerousness of the computational complexity of adaptive control is remained yet. Although this problem is being solved with evolution of a computer, still, it is not enough for high speed control. Solving of this problem will become a future subject.

REFERENCE

[1] System Identification for Control, Shuuichi Adachi, Tokyo Denki Univ Press.

[2] Theory ＆ Practice of Adaptive Control Systems, I. D. Landau and M. Tomizuka, OHM Co. Ltd.

[3]Design of Multirate Digital Servo Systems, Junnichi Hara, Graduate school of Information Sciences, Tohoku University, Instrument and control engineers, vol.67, No.3, 2001, (PP.466~472)

[4]Auto-Tuning of Digital Controllers for DC servo motors, Hiromitsu HIKITA, The Japan Society for Precision Engineering, vol.192, No.192-17, 2000

© ISAROB 2013

The Eighteenth International Symposium on Artificial Life and Robotics 2013 (AROB 18th '13),
Daejeon Convention Center, Daejeon, Korea, January 30-February 1, 2013

Hexa-Quad Transformation Control for Hexapod Robot Based on Support Polygon Pattern

Addie Irawan[1], Yee Yin Tan[2], Mohd Syakirin Ramli[3], Mohd Riduwan Ghazali[4] and Kenzo Nonami[5]

[1,2,3,4]Robotics & Unmanned System (RUS) Group, Faculty of Electrical & Electronics Engineering, University Malaysia Pahang, Malaysia

[5]Division of Artificial Systems Science, Department of Mechanical Engineering, Chiba University, Chiba, Japan

[1]addieirawan@ump.edu.my, [2]yeeyin1228@gmail.com, [3]syakirin@ump.edu.my, [4]riduwan@ump.edu.my, [5]nonami@faculty.chiba-u.jp

Abstract: This paper presents a leg reconfigurable technique to optimize the multi-legged robot operation and walking performances. A hexapod-to-quadruped (Hexa-Quad) transformation technique is proposed to optimize hexapod legs on certain situation that need some legs to be disabled as a leg to do other tasks/operations. By separating two legs from the others, hexapod robot is able to be configured as quadruped robot configuration. Quadruped robot configuration is stand within dynamically and statically stable criteria if compare to the hexapod robot that has only statically stable criteria. Thus, it is very crucial to have a stable transformation technique during walking and operation session. Therefore Hexa-Quad is proposed with reference to the defined support polygon that based on its body area. A real-time based model of hexapod robot (4-DOF/leg) control architecture with Hexa-Quad transformation is designed and verified using separated 3D simulators.

Keywords: Hexa-Quad Transformation, center of mass, support polygon

1 INTRODUCTION

Multi-legged robot or so called active suspension vehicle (ASV) has significant advantages if compare to the wheel type robot especially on facing irregular and mountainous terrain. The advantages of multi-legged or legged robot can be seen obviously on inspired life living form; legged creatures. Raibert in his book has mentioned that only about half of the earth 's landmass is accessible to existing wheeled and tracked vehicles ,whereas a much larger fraction can be reached by animals on foot[1].

In multi-legged robot research and development, several studies have been done to achieve good adaptability, function, high flexibility and extensibility with extreme and unknown terrain. The progress emphasized in all expects and hierarchy of multi-legged system such as system mechanism, structure design/configuration, software development/control technique and electronics unit design. In control technique level, reconfiguration technique is one of the important parts in legged robot control, which is emphasized on recovery action [2] and multi-tasking. Therefore stability become a main point in this research that involving center of mass (CoM) of the legged robot and its support polygon. The larger the *support polygon* developed by the robots the bigger the probability for the robot to remain upright without overturning when it stops walking at any moment during the walking period, and this is called statically stable walking or static stability. Static stability occurs when CoM lies completely within the support polygon and the polygon's area is greater than zero, and hence static stability requires at least three points of ground contact [3]. Robot's CoM represented a significant aid in maintaining the stability[4] and as additional source of information in identified process and stability indicator. Moreover, CoM is calculated to provide critical to access rehabilitation success in pathology detection and in describing gaits[5]. In reconfiguration aspect, the CoM's of legged robot is will be reallocated since the changing of in the structure or leg configuration of the robot.

Therefore in this study, control technique on hexapod configuration to quadruped configuration for a hexapod robot (Hexa-Quad) is proposed. Hexapod is one of the statically stable configurations of multi-legged robot that has potential to be reconfigured into less than six legs such as quadruped and bipedal configuration. Transforming hexapod to bipedal configuration is considered as critical configuration for hexapod unless there have a special design on leg configuration and robot body's shape itself (other than common hexapod's body shapes; square, trapezium, round or hexagon body). The quadruped configuration is selected since this configuration is in between statically and dynamically stable and suitable for any common shape of hexapod robot's body. Static stability assumes the vertical projection of the CoM always remain

© ISAROB 2013

inside the support polygon with an adequate stability margin during all phase of movements [6]. On the other hand, dynamically stable depends on the stability during the robot is moving which demands on active actuation to maintain the balance and performing faster motion [7]. Quadruped legged robot configuration also practical on performing locomotion for complex terrain, due to the amount of researches that have been done on practical walking and motion control such as reported in [8-10].

CONRO from Polymorphic Robotics Laboratory of USC Information Science Institute is one of the examples of hexapod robot that performing proposed hormone-based distributed control to implement its gait reconfiguration between caterpillar and spider gait mode [2]. Shen *et. al.* mentioned that the number of supported leg must meet the stability criteria according to the number of leg that available for walking used. In this article, the focus will be on the proposed Hexa-Quad transformation with two different forms namely center legs disable (CLD) and side legs disable (SLD). The form is decided based on common application for the hexapod robot such as converting legs to the free manipulators. The proposed transformation technique is created by inspired from the CoB and leg shoulder angle symmetrical concept proposed previous in [11]. The proposed transformation was modeled and applied on hexapod robot real-time model with 4 degree of freedom (DOF) and verified using separated 3D model developed previously in [12].

2 HEXA-QUAD TRANSFORMATION TECHNIQUE

Most of the proposed transformation techniques for multi-legged walking robot are due to the specific configuration of the robot itself. In this study, the transformation is proposed for general hexapod robot configuration with any number of DOF legs. The proposed Hexa-Quad transformation technique is designed by considering the support polygon or stability area of the robot as shown in **Fig. 1** and **Fig.2**. The larger the support polygon developed by the robots the bigger the probability for the robot to remain upright without overturning when it stops walking at any moment during walking period, and this is called statically stable walking or static stability [3].

Therefore in proposed Hexa-Quad transformation technique, two forms of transformation are proposed by considering the support polygon and CoM as shown in **Fig.1**; center legs disable (CLD) and side legs disable (SLD). *Disable* here mean the legs are disable from walking command and separated from walking sequence.

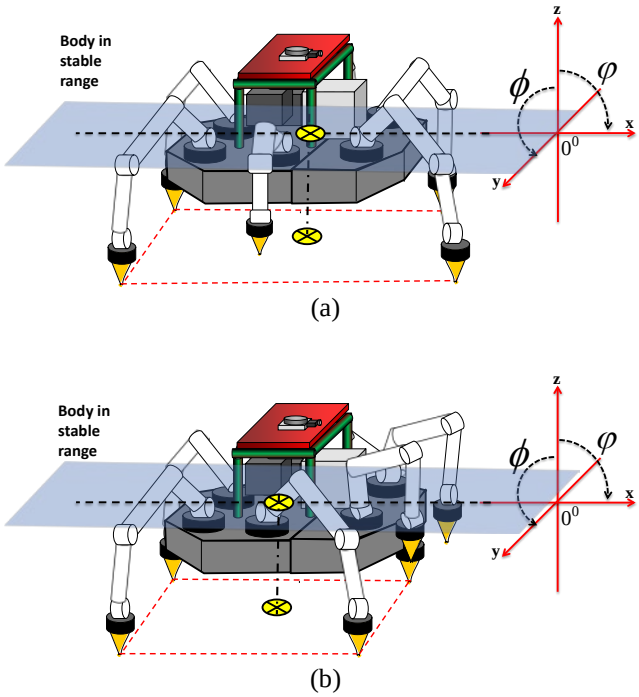

Fig 1. The proposed form of Hexa-Quad transformation; (a) CLD form, (b) SLD form.

CLD is realized by lifting up two center legs as in *sit down mode*. This form is not critical to control if compare to the SLD (**Fig.1(b)**) that required a proper initial standing position for other legs. Therefore, this proposed technique introduced separated calculation for CLD and SLD as shown in **Fig.2** and **Fig.3** respectively.

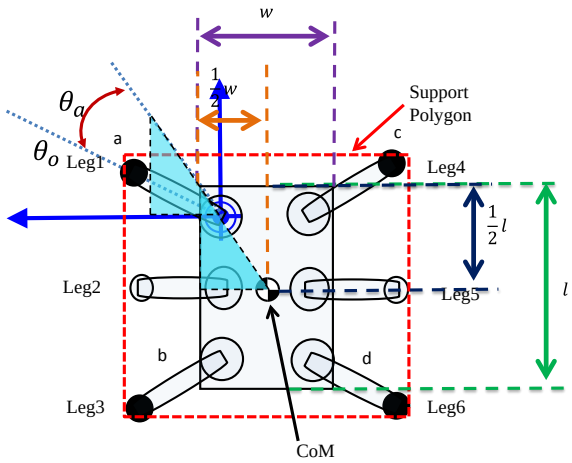

Fig. 2. Shoulder angle determination for CLD transformation mode.

As shown in **Fig.2**, the CoM is at the center of the body (CoB) of the robot and the support polygon is followed by the shape of the standing legs. The shape of support

polygon is depends on the number of touching leg on the ground (red dotted line) as shown in **Fig.2** and **Fig.3**. Thus the new angle of shoulder for each supporting legs (enabled legs) (θ_a) after transformation can be determined by using is the length (l) and width (w) of the robot body as follows;

$$\theta_a = 0.5\tan^{-1}\left(\frac{l}{w}\right) - |\theta_{n_o}| = 0.5\tan^{-1}\left(\frac{x_o}{y_o}\right) - |\theta_{n_o}| \quad (1)$$

where the area of robot's body $l \cong 2w$, x_0 is the vertical length from the center of the robot body while y_0 is the horizontal length from the center of the body and θ_{n_o} is an initial value for each shoulder. This rule is applied with reference to the shoulder-based coordination system [13] and CoB-based symmetrical approach[11]. Therefore, in this situation, the stability of the Hexa-Quad is achieved which CoM is within the support polygon and the area of the polygon is greater than zero. It is different to the SLD form mode whereby side legs are disabled from walking used and other legs initial angle for each shoulder is reset using **Eq.(1)**. As shown in **Fig.3**, example situation of two side legs (leg 1 and leg 4) is disabled and other four legs (leg 2,3,5 and 6) is reinitialized by using **Eq.1**. The full proposed Hexa-Quad transformation flow is illustrated via finite state machine (FSM) as shown in **Fig. 4.**

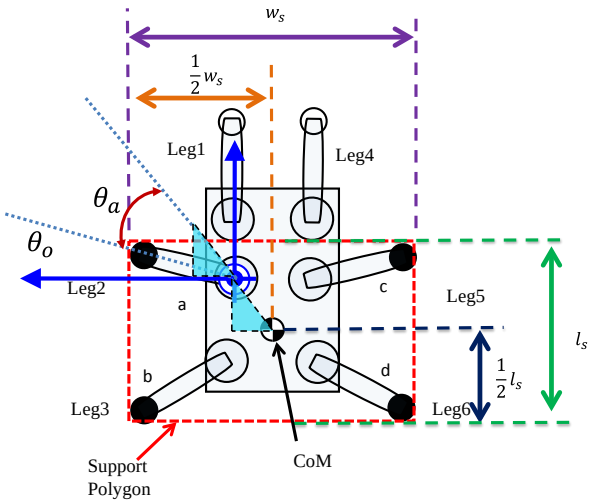

Fig. 3. Shoulder angle determination for SLD transformation mode.

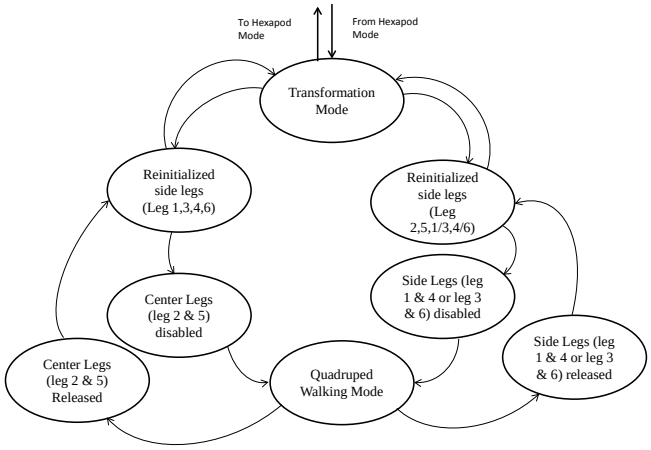

Fig. 4. FSM of proposed Hexa-Quad transformation for hexapod robot model.

3 WALKING PATTERN AND SHOULDER-BASED COORDINATION SYSTEM

Shoulder-based coordination system (SCS) was established implemented in the previous progresses for hexapod configuration such reported in [13,11] but not for quadruped configuration. For this transformation walking pattern, the combination of transverse and trot gait patterns [14] are used for the quadruped walking algorithm. The sequences of the legs for quadruped and hexapod walking are presented in finite state machine (FSM) as shown in **Fig 5 (a)**. On hexapod configuration or hexapod mode (see **Fig. 5(b)**), tripod walking gait pattern is used since it performs fastest walking with minimum area of support polygon in hexapod robot stability.

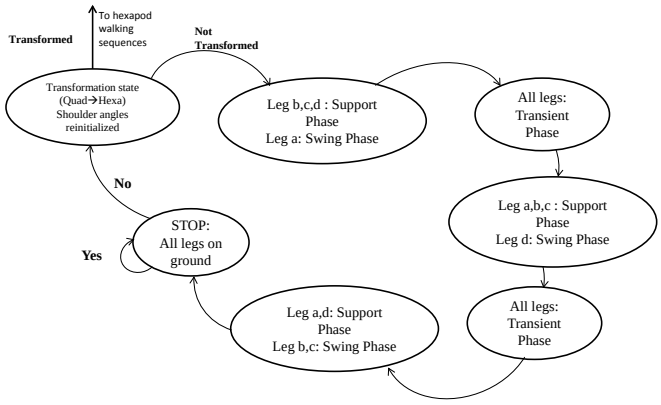

(a)

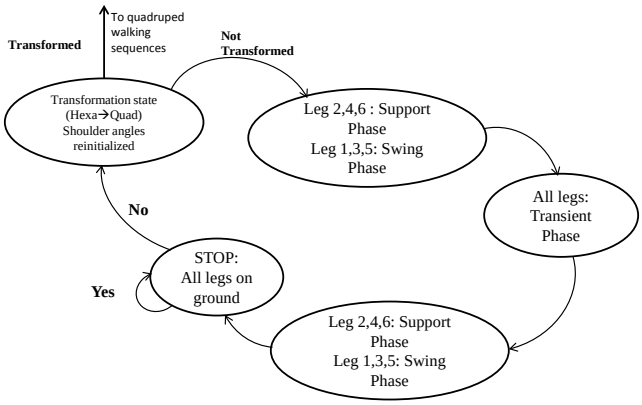

(b)

Fig. 5: FSM for (a) traverse and trot gait pattern and (b) tripod gait pattern in proposed model of hexapod robot with Hexa-Quad transformation.

As shown in **Fig. 5**, in transformation state, θ_a is changed and used on both x and y position of leg on the next sequences. x and y for each n-leg are part of moving frame and kinematics element for each link on each leg as shown in **Fig.6**. Both positions including vertical leg position (z) is determined differently in each support and swing phase by using **Eq.2** and **Eq.3** respectively.

(Support Phase – Step and push on the ground) $0 \le t \le \frac{T_c}{2}$

$$x_{s_n}(t) = x_{0_n} + \frac{S_o}{4}\left(\frac{2t}{T_c} - \frac{1}{2\pi}\sin\left(\frac{4\pi t}{T_c}\right)\right)\cos\theta_{a_n}$$
$$y_{s_n}(t) = y_{0_n} + \frac{S_o}{4}\left(\frac{2t}{T_c} - \frac{1}{2\pi}\sin\left(\frac{4\pi t}{T_c}\right)\right)\sin\theta_{a_n}$$
$$z_{s_n}(t) = z_{0_n} \qquad (2)$$

(Swing Phase) $0 \le t \le \frac{T_c}{2}$

$$x_{s_n}(t) = x_{0_n} + \frac{S_o}{2}\left(1 - \cos\left(\frac{2\pi}{T_c}t\right)\right)\cos\theta_{a_n}$$
$$y_{s_n}(t) = y_{0_n} + \frac{S_o}{2}\left(1 - \cos\left(\frac{2\pi}{T_c}t\right)\right)\sin\theta_{a_n} \qquad (3)$$
$$z_{s_n}(t) = z_{0_n} + H_0 \sin\left(\frac{2\pi}{T_c}t\right)$$

where

T_c = walking cycle time (s),
t = update time (real-time) (s),
t_{ex} = additional period for applying extra force (s),
S_0 = distance of foot placement for one cycle (m), and
H_0 = height of leg lift from the initial position (m).

Both **Eq.2** and **Eq.3** were created to realize the motion shape as shown in **Fig. 6**. This motion shape is important for the force control implementation on each robot foot for walking on irregular terrain. As shown in **Fig.6**, (1) leg standing up, (2) swing phase (first step), (3) support phase, and (4) swing phase (next step).

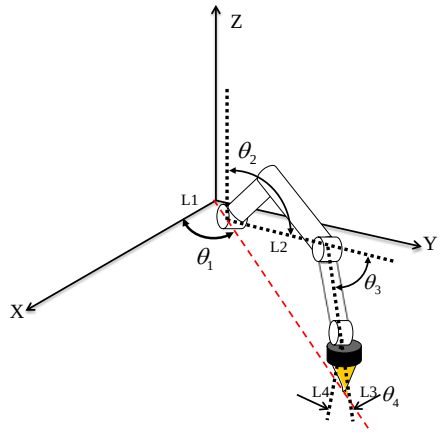

Fig. 6. SCS trajectory kinematics motion for a 4-DOF leg of hexapod robot model

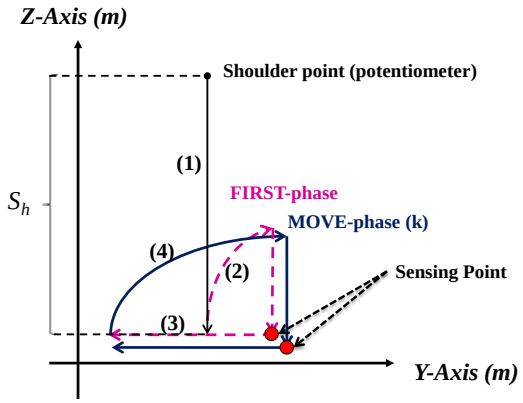

Fig. 7. A leg motion shape used in proposed model Hexa-Quad robot

4 SIMULATION AND RESULT

In this study, several simulations running have been done to analyze the potential of the proposed method to be implemented in the real system. The first simulation in done on CLD method by simulating the real-time system model with the 3D model that designed separately [12] as shown in **Fig.8**. On **Fig.8** it shows that center legs (Leg 2 and 5) are disabled after robot stop walking with hexapod mode. In this case of transformation, side legs become main legs that functional for quadruped mode walking. The initial angle of each main leg for quadruped mode doesn't change much due to the calculation using **Eq.1**.

© ISAROB 2013

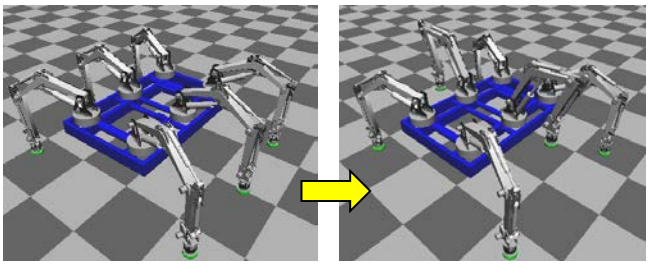

(a) (b)

Fig. 8. 3D model simulation result for CLD transformation, (a) hexapod walking stop, (b) center legs disabled

It is different to the SLD transformation whereby certain steps of initialization need to be done on the main legs that will be used for quadruped mode walking. As shown in **Fig. 9**, center legs (Legs 2 and 5) and side legs are reinitialized (**Fig. 9(b)** and **(c)**) to appropriate angle before another side legs (Leg 1 and 4) are flipped to the front and disabled (**Fig. 9(d)**). This procedure of transformation to make sure robot are in stable range and overturning avoidance.

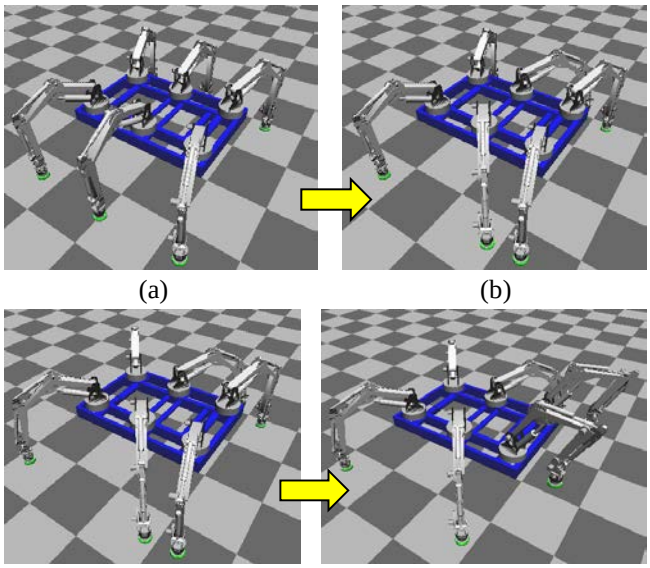

(a) (b)

(c) (d)

Fig. 9. 3D model simulation result for SLD transformation, (a) hexapod walking stop, (b) center legs shoulder angle reinitialized, (c) side legs shoulder angle reinitialized, (d) target legs disabled.

Quadruped mode walking is verified by simulating the performance of robot CoB [12] with comparison to the hexapod walking mode as shown in **Fig.10**. CoB representing body way point shows that both modes perform almost same results with the same omnidirectional angles inputs.

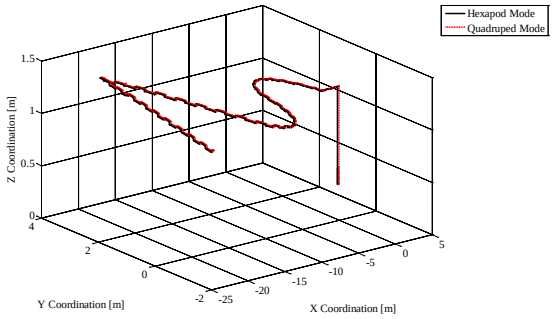

Fig.10 Omnidirectional walking simulation results for both hexapod and quadruped walking mode.

5 CONCLUSION

The performance of proposed Hex-Quad transformation technique has been presented. Through the series of simulations, it was shown that the proposed method performed stable reconfiguration on hexapod robot system to quadruped configuration with proposed reinitializing calculation. On the next step progress, the proposed method will be customized and applied on real-time hexapod system walking on actual environment.

6 ACKNOWLEDGEMENT

I would like to thanks to Research and Innovation Centre, University Malaysia Pahang on funding support on this research project. Also deep appreciation and thanks to my former supervisor, Prof. Kenzo Nonami from Chiba University, regarding his support on this research studies. Last but not least, also thanks to my students and associate researchers that involved in this research project.

REFERENCES

[1] Raibert MH (1986) Legged Robots That Balance. MIT Press,
[2] Wei-Min Shen, Salemi B, Will P (2002) Hormone-I nspired Adaptive Communication and Distributed Contr ol for CONRO Self-Reconfigurable Robots. IEEE Trans actions On Robotics and Automation 18 (5):700-712
[3] Siegwart R, Nourbakhsh IR (2004) Introduction to autonomous mobile robots. MIT Press, Massachusetts I nstitute of Technology Cambridge, Massachusetts
[4] Muscolo GG, Recchiuto CT, Laschi C, Dario P, Ha shimoto K, Takanishi A A method for the calculation of the effective Center of Mass of humanoid robots In: 11th IEEE-RAS International Conference on Humanoid Robots (Humanoids), 2011 Bled, Slovenia, 2011. pp 3 71 - 376
[5] Cotton S, Murray AP, Fraisse P (2009) Estimation

of the Center of Mass: From Humanoid Robots to Human Beings IEEE/ASME Transactions on Mechatronics 14 (6):707-712

[6] Shugen M, Takashi T, Hideyuki W (2005) Omnidirectional Static Walking of a Quadruped Robot. IEEE Transactions On Robotics 21 (2)

[7] Freyr H (1997) Locomotion for difficult terrain. Royal Institute of Technology, Stockholm, Sweden,

[8] Raibert M, Blankespoor K, Nelson G, Playter R, TheBigDogTeam BigDog, the Rough Terrain Quadruped Robot. In: Proceeding of 17th World Congress, The International Federation of Automatic Control, Seoul, Korea, 2008.

[9] Hirose S (1984) A Study of desing and control of a quadrupped walking vehicle. International Journal of Robotics Research 3 (2):113-133

[10] Byl K (2008) Metastable Legged-Robot Locomotion. Massachusetts Institute of Technology, Massachusetts Institute of Technology Cambridge, Massachusetts

[11] Irawan A, Nonami K Force Threshold-Based Omni-directional Movement for Hexapod Robot Walking on Uneven Terrain. In: 2012 Forth International Conference on Computational Intelligence, Modelling and Simulation (CIMSiM), Kuantan, Pahang, Malaysia, 2012. vol 127-132. IEEE Computer Society,

[12] Ohroku H, Irawan A, Nonami K (2009) A 3D modeling for Hydraulic-drive Hexapod Walking Robot using 3D Geometric Technique with distributed Numerical Model. International Journal of Automation, Robotics and Autonomous Systems 9 (1)

[13] Irawan A, Nonami K (2011) Compliant Walking Control for Hydraulic Driven Hexapod Robot on Rough Terrain. Journal of Robotics and Mechatronics 23 (1):149-162

[14] Tsujita K, Tsuchiya K, Onat A (2001) Adaptive gait pattern control of a quadruped locomotion robot. Paper presented at the IEEE/RSJ International Conference on Intelligent Robots and Systems, 2001, Maui, USA,

© ISAROB 2013

The Eighteenth International Symposium on Artificial Life and Robotics 2013 (AROB 18th '13),
Daejeon Convention Center, Daejeon, Korea, January 30-February 1, 2013

Design of a special cam-based high speed manipulator system

Jing Wu[1], Rui-Jun Yan[1], Kyoosik Shin[2], Chang-Soo Han[2#]

[1]Department of Mechatronics Engineering, Hanyang University, Korea
[2]Department of Mechanical Engineering, Hanyang University, Korea
(Tel: 82-031-400-0462)

[#]corresponding author: cshan@hanyang.ac.kr

Abstract: In this paper, we develop a mechanism that mainly used a special cam and gearbox to utilize a DC servo motor powerfully and speedily for a linkage manipulator. The mechanisms can be charged slowly, store the energy in a spring and release it on demand using a click mechanism. By compared the motions with many cams, we designed our special cam that can output an explosive movements. Two torsion springs, used as elastic elements, are located on the manipulator axis which is connected to the main link and the mechanism. Consider about the output of a manipulator, we choose to implement a four bar linkage design for the motion and force control. The manipulator's mathematic models are built for purposed of analysis and control.

Keywords: High-speed manipulator, series-elastic actuation (SEA), five bar linkage, explosive movements.

1 INTRODUCTION

Since robots work in place of humans in many fields, the developing of high-performance robots has increased rapidly, such as those in industry fields, automobile assembly plants, precision works, etc. Depends the development of multiple motors, about the high speed robot, one interesting and challenging research topic is the energy saving problems.

However, multitudinous of techniques are proposed in many aspect to achieve the high speed motions. For a manipulator, the motion of high-speed could consist of three patterns, 1) Fast-forward (FF); 2) Fast-reverse (FR); 3) Fast forward and reverse (FFR). There is a developed golf robot [1] whose swing simulates human motion is proposed in order to reach ultra Fast-forward speed. Imitate to human motion ability, this robot consists of a shoulder joint with a high-power direct-drive motor and a wrist joint with a low-power direct-drive motor to realize ultrahigh-speed dynamic manipulation using a dexterous mechanism. The most representational Fast-reverse technique is utilized in jumping robot. It is generally known that the high power humanoid is desired for application of running or jumping motions. The dynamic motion of jumping is characterized by large instantaneous forces and short duration [2], depends of those conditions, some jumping structures used springs both in improve the velocity and energy conservation [3]. The crucial factor in a high speed manipulator is the motor.

There is a relatively large robots related to using high-speed mechanisms or methods for manipulators for different applications and different scales. In the following subsections, we will review the principles of how these existing robots address the challenges of high-speed problem in manipulators.

By the literature survey the general classification is given in Fig. 1. Five common high-speed structures are introduced in this figure, (i) the spring systems [4], (ii) the cam system [5], [6], (iii) four-bar spring linkage system [5], [7], (iiii) the electric system [8], (iiiii) hydraulic system. Every structure has their advantages and disadvantages. The most skillful spring system is applied in gums, combine of kinds of springs and the bullet,

2 DESIGN OF HIGH-SPEED MANIPULATOR

The driving principle of this system is described.

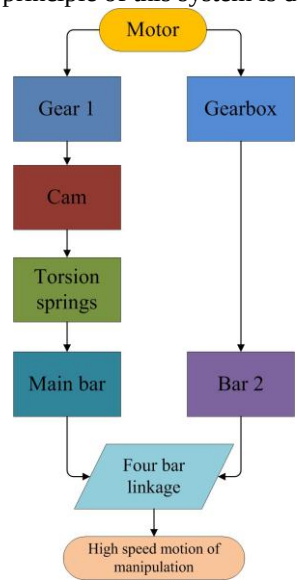

Fig. 1. The illustration of motion flow chart

© ISAROB 2013

High-speed structure	Advantage	Disadvantage	The figures of existing structure
Spring system	Simple construction Low cost, Energy saving Light weight	Nonlinear control	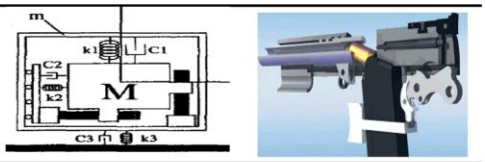
Cams system	Construction simple Realize high speed motion, Motion can stack up	Easy abrade Short journey distance Invariance time/angel Processing difficulty	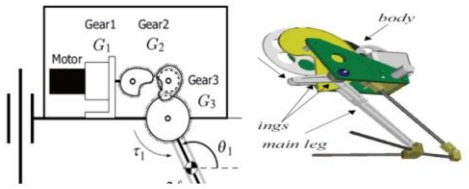
Four-bar spring-linkage system	Small abrade Easy fabrication High precision	Trajectory fixed High speed will cause the large vibration, Design Complexity	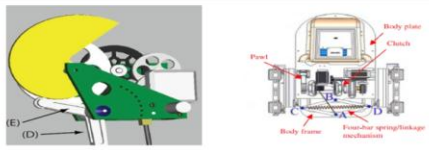
Electric system	Easy to control Variance time or angle Light weight	Energy-intensive	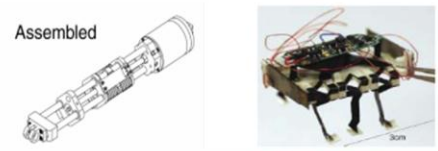
Hydraulic system	Regulation of output	Finishing movement has big impulsion, Complicated structural. Big size/volume High cost	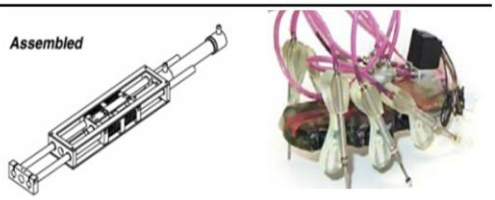

Fig. 2. Classification of the existing high-speed manipulators

2.1 Mechanical design

The mechanisms can be charged slowly, store the energy in a spring and release it on demand using a click mechanism. This mechanical principle is used by several small animals and insects.

By compared the motions with many cams, we designed our special cam that can output an explosive movements. The manipulator, consisting of a four bar linkage structure connected by springs and travels quickly using this special cam that is mounted on actuator which are connect by gears. The shape of the cam has been specifically designed to yield a constant torque on the motor through a three stage gearbox system.

Two torsion springs, used as elastic elements, are located on the manipulator axis which is connected to the main link and the mechanism. To charge these two springs, a small DC motor actuates the special cam and rotates the main link lever manipulator by a constant angle (can been calculate by the given cam parameters) for one charge cycle.

Consider about the output of a manipulator, we choose to implement a four bar linkage design for the motion and force control. Using this design offers the possibility to modify the rotating angle by adjustment the parameters of the special cam and the trajectory of the manipulator tip by adjustment of the gear ratio.

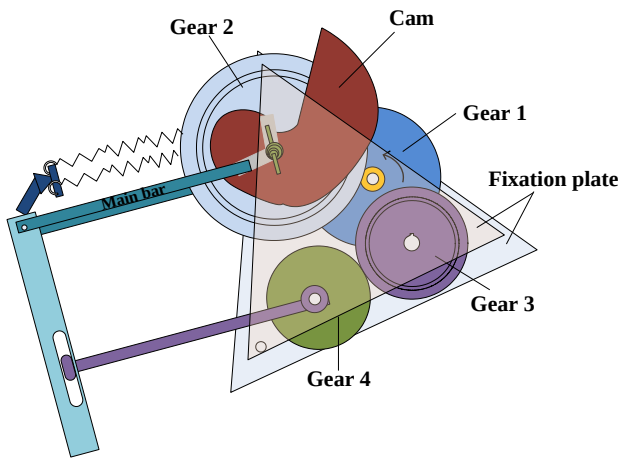

Fig. 3. The mechanical design of the high speed structure.

The structure for connect the main link and the torsion springs:

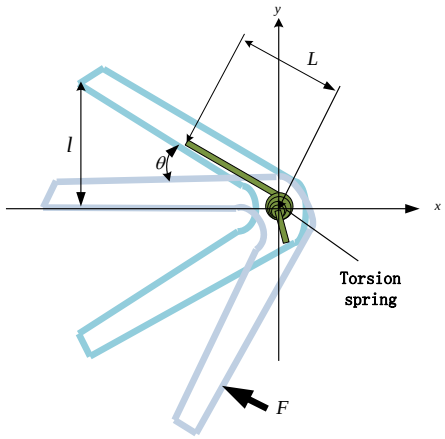

Fig. 4. The torsion spring fixing mechanism

2.2 Kinematic model

Mechanical design and kinematic analysis are introduced in this paper.

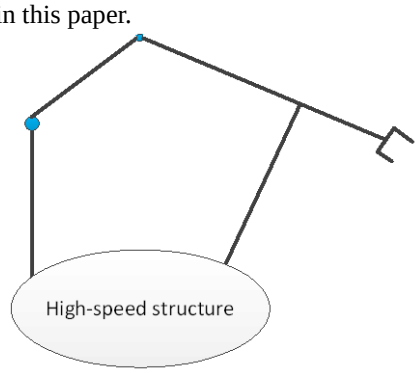

Fig. 5. The kinematic model of the high speed structure.

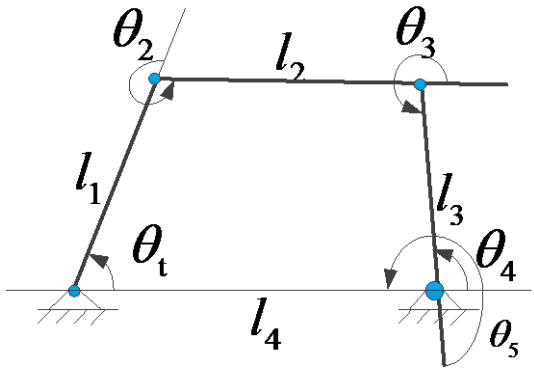

Fig. 6. The four bar linkage structure.

For the input of the motor, we have :

$$\omega_2 = \frac{R_1 z_1}{z_2}\omega_m \Rightarrow \dot{\underset{\rightarrow}{\phi}}_2 = \frac{R_1 z_1}{z_2}\omega_m \tag{1}$$

For the gear1 and gear2, we get:

$$\begin{bmatrix} x \\ y \end{bmatrix} = \begin{bmatrix} \cos(Iw\bullet\phi) & -\sin(Iw\bullet\phi) \\ \sin(Iw\bullet\phi) & \cos(Iw\bullet\phi) \end{bmatrix} \begin{bmatrix} S_o + S \\ e \end{bmatrix} \tag{2}$$

S_0, S and e are parameters of cam.

If clockwise, $Iw = +1$; anticlockwise, $Iw = -1$.

k_1 and k_2 are parameters of torsion spring.

For the Torsion springs, we know that

$$\underset{\rightarrow}{\theta}_t = \frac{F}{k_1}\begin{bmatrix} x \\ y \end{bmatrix} = \frac{k_2}{k_1}\begin{bmatrix} (S_o + S)\cos(Iw\bullet\phi) & -e\sin(Iw\bullet\phi) \\ (S_o + S)\sin(Iw\bullet\phi) & e\cos(Iw\bullet\phi) \end{bmatrix}\underset{\rightarrow}{\phi} \tag{3}$$

Where, the force is calculated

$$F = k_2 \underset{\rightarrow}{\phi} \tag{4}$$

So, we get:

$$\begin{aligned} \dot{\underset{\rightarrow}{\theta}}_t &= \frac{k_2}{k_1}\begin{bmatrix} x \\ y \end{bmatrix}\dot{\underset{\rightarrow}{\phi}} + \frac{k_2}{k_1}\underset{\rightarrow}{\phi}\begin{bmatrix} \dot{x} \\ \dot{y} \end{bmatrix} \\ &= \frac{k_2}{k_1}\begin{bmatrix} (S_o + S)\cos(Iw\bullet\phi) & -e\sin(Iw\bullet\phi) \\ (S_o + S)\sin(Iw\bullet\phi) & e\cos(Iw\bullet\phi) \end{bmatrix}\underset{\rightarrow}{\phi}\bullet\dot{\underset{\rightarrow}{\phi}} \\ &+ \frac{k_2}{k_1}\underset{\rightarrow}{\phi}\begin{bmatrix} -(S_o + S)\sin(Iw\bullet\phi) & -e\sin(Iw\bullet\phi) \\ (S_o + S)\cos(Iw\bullet\phi) & e\sin(Iw\bullet\phi) \end{bmatrix}\dot{\underset{\rightarrow}{\phi}} \end{aligned} \tag{5}$$

2.3 Dynamic model

The manipulator's mathematic models are built for purposed of analysis and control. The dynamic model is built and many simulation models are built for testing the velocity and explosive force of the manipulator.

Suppose the system is in balance, we have,

$$\underset{\rightarrow}{T}_t^* = \underset{\rightarrow}{0} \tag{6}$$

In this redundant actuator system, suppose there are two independent joint 1 and 4, the equation between the independent joint and the dependent joint is:

$$\underline{\dot{\phi}_P} = \left[G_a^P\right]\underline{\dot{\phi}_a} \tag{7}$$

The equation of the dynamic model as,

$$\begin{bmatrix} 1 & g_4^t \\ 0 & -h_{tt}^4 \end{bmatrix}\begin{pmatrix} T_t \\ T_4 \end{pmatrix} = \begin{pmatrix} T_t^* \\ 0 \end{pmatrix} \tag{8}$$

Here,

$$\begin{aligned} \left[G_a^P\right] &= \begin{bmatrix} g_t^2 \\ g_t^3 \\ g_t^4 \end{bmatrix} \\ &= \frac{1}{l_2 l_3 \sin_3}\begin{bmatrix} -l_3 l_4 \sin_{t+2+3} \\ l_4(l_2 \sin_{t+2} + l_3 \sin_{t+2+3}) \\ l_2(l_3 \sin_3 + l_4 \sin_{t+2}) \end{bmatrix} \end{aligned} \tag{9}$$

$$\begin{aligned} h_{tt}^4 &= \frac{\partial}{\partial\theta_t}(g_t^4) \\ &= \frac{l_4 \cos_{t+2}(1 + g_t^2)\sin_3 - l_4 \sin_{t+2}\cos_3 g_t^3}{l_3(\sin_3)^2} \end{aligned} \tag{10}$$

© ISAROB 2013

The testing results show that the requirements with respect to velocity, acceleration, working space and energy are successfully achieved.

3 CONCLUSION

This mechanism witch is designed to be characterized as high speed manipulator could also form the propulsion system of a jumping robot or be used for self deployment of sensors. Our future research can combining some more degree of freedom manipulator and developed as a biomimetic arm that may attach more applications.

ACKNOWLEDGEMENT

This research was supported by the MKE (The Ministry of Knowledge Economy), Korea, under the 'Advanced Robot Manipulation Research Center' support program supervised by the NIPA (National IT Industry Promotion Agency). (NIPA-2012-H1502-12-1002)

REFERENCES

[1] Maruyama T, Xu CQ, Ming A and Shimojo M (2006), Motion Control of Ultra-High-Speed Manipulator with a Flexible Link Based on Dynamically Coupled Driving, Journal of Robotics and Mechatronics, Vol. 18, No.5, pp.598-607

[2] Urata J, Nakanishi Y, Okada K and Inaba M (2010), Design of High Torque and High Speed Leg Module for High Power Humanoid, in Proceedings of International Conference on Intelligent Robots and Systems, pp. 4497-4502

[3] Wang M, Zang XZ, Fan JZ and Zhao J (2008), Biological Jumping Mechanism Analysis and Modeling for Frog Robot, pp.181-188

[4] Shimoda S, Kubota T and Nakatani I (2002), New Mobility System Based on Elastic Energy under Microgravity. in Proceedings of International Conference on Robotics and Automation, pp. 2296-2301

[5] Mirko K, Martin F, Andr G, et al (2008),A miniature 7g jumping robot, in Proceedings of International Conference on Robotics and Automation, pp.373-378

[6] Okada M and Murakami K (2007), Robot Communication Principal by Motion Synchronization using Orbit Attractor, pp. 2564-2569

[7] Reddy N. S., Ray R, Shome S.N. (2011), Modeling and Simulation of a Jumping Frog Robot, in Proceedings of International Conference on Mechatronics and Automation, pp.1264-1268

[8] Jerry E. Pratt, Benjamin T. Krupp (2004), Series Elastic Actuators for legged robots, Storage and Retrieval for Image and Video Databases,

The Eighteenth International Symposium on Artificial Life and Robotics 2013 (AROB 18th '13),
Daejeon Convention Center, Daejeon, Korea, January 30-February 1, 2013

Estimating the clothes characteristics with the image and depth sensors for developing virtual fitting room

Yuka Mastuba[1], Jehan Jung[2], Hiroyuki Funaya[1], Kazushi Ikeda[1], Rammohan Mallipeddi[2], and Minho Lee[2]

[1]Nara Institute of Science and Technology, Japan
[2]Kyungpook National University, Republic of Korea
[1](Tel: 81-743-72-5984, Fax: 81-743-72-5989)
[2](Tel: 82-53-950-6436, Fax: 82-53-950-5505)

[1]{yuka-m,hiroyuki-fn,kazushi}@is.naist.jp
[2]{jjhan,mallipeddi,mholee}@knu.ac.kr

Abstract: Creating physically simulated animations of real clothes is needed for virtual fitting rooms. In this paper, we propose a method for estimating the parameters of real clothes using the motion data obtained from a commercial RGB-depth sensor. Our method determines the parameters using simulated annealing so that the distance between the spatiotemporal trajectories of the real and the computer-simulated shapes of clothes. Here, the shapes of the clothes are expressed by several points identified by a feature-selection algorithm. In our experiments, the method showed a good reconstruction of motions of a skirt.

Keywords: clothes characteristics, optimization, simulated annealing, virtual fitting room

1 INTRODUCTION

A virtual fitting room (VFR) enables customers to see their fashion coordinates in online clothing shops by displaying computer graphics. VFRs have been in need and developed recently because the main reason of customers' hesitancy in buying stuff online is that they could not try on them [1]. One example of VFR is H&M's online dressing room [2] which allows customers to change various clothes on a fashion model and see the coordination. Digital fashion ltd is a similar service but different from the H&M's in that they prepare a special studio where the fashion models in clothes are captured from all directions [3].

Although all those systems have been developed and commercialized, there are still some limitations: 1. they provide only the clothes sold in a shop, 2. displayed models including garments are static although dynamics of the clothes also influences the purchase decision, and 3. an expensive studio is need to register garments with sufficient information. To make a dynamic model of garments and to create animations, their physical parameters should be estimated.

There are several systems that estimate the physical parameters of fabrics. Kawabata Evaluation System is a standard tool for a thorough evaluation of textile fabrics deformability. Although it gives the behaviors of a fabric in tension, shear, bending, compression and friction [4], the system requires a special and expensive device to measure the characteristics of the fabric.

Bhat et al., for example, used video images to estimate the static and dynamic parameters of fabrics [5]. Their system swings a swatch of a fabric using a robot arm, extracts features from video images and estimates the parameters of the fabric using an optimization algorithm. Hasler et al. proposed a similar system using clothes silhouette [6]. Their approaches generatively estimate the true parameters of clothes using swatches and applied them to generate animations. The systems have to prepare the same swatch as the given real cloth in advance that seems not realistic.

The essential difficulty of this problem lies on the estimation of the physical parameters of clothes. The conventional systems estimate them from the movement of swatches for known forces. To avoid this difficulty, we estimate the parameters used in a 3D physical simulator, instead. A 3D physical simulator generates computer graphics according to given physical models. It uses not necessarily a cloth model according to the material mechanics but a simpler one. In that case, we need to estimate only the parameters in the simulator.

Our system estimates the parameters in the simulator by comparing the real trajectory of clothes with the simulated one. This idea makes it possible to employ any cloth model in the simulator. The trajectory of the clothes is measured using a commercial-use depth and image sensor, Kinect™ [7], so that it is affordable at home.

© ISAROB 2013

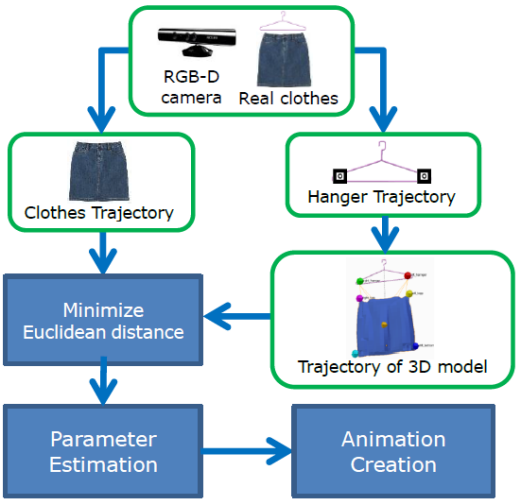

Fig. 1. The procedure of our method

The detail of system is shown in Section 2 and its effectiveness was confirmed by experiments in Section 3 and 4. Section 5 gives our conclusion.

2 METHOD

Our goal is to generate realistic 3D CG animations based on the measurement of real clothes. To accomplish this goal, our proposed method estimates the parameters of clothes in a simulator by minimizing the distance between the measured trajectory of clothes and the simulated one of clothes. The term "trajectory" means time-series data of 3D locations of five feature points of a cloth captured frame by frame in our system. The five feature points are defined as the four corners and the center point of real clothes

One point of our method is that we need not to know the force to clothes a priori. The force is measured through the trajectory of the hanger that produces the movement of the clothes (Fig. 1). Hence we can swing the hanger by human hand. The hanger has two markers so that we can easily measure the trajectory from the depth and image sensor. Note that we have to click the center point of markers for detection in the first frame at this time. After the second frame, our system can track the markers using the AR toolkit [8] and OpenCV [9].

The measurement of clothes should be marker-less since clothes have no common markers. Hereafter, we consider the cases of a skirt and a T-shirt for clothes (Fig. 2). We use the depth image as a silhouette because some kinds of clothes are difficult to extract feature points from the surface. In the case of skirt, after eliminating the background from the depth image, we extract the four corners of the skirt using the Harris corner detector, therein we rotate 45 degrees clockwise so that the corners have the

Fig. 2. The experiment condition for measuring. Yellow and green lines present the vertical position of hanger.

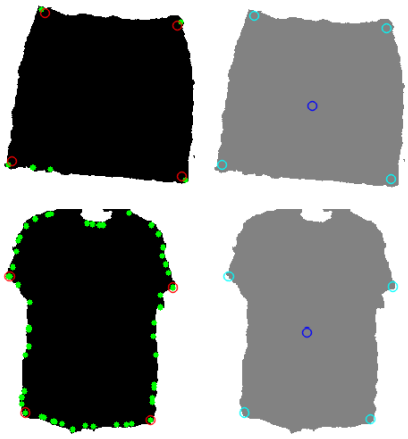

Fig. 3. The result of Harris corner detection and Dijkstra algorithm.

maximum/minimum x-/y-coordinate. In the case of a T-shirt, the leftmost and rightmost points in the original coordinate correspond to the left-top and right-top points, respectively (Fig. 3).

We add the center point as a feature point, which is defined as the max-min distant point from the four corners. Here, the distances are calculated as the lengths of geodesics and minimized using the Dijkstra algorithm [10].

Our system compares the measured trajectories of the feature points with the simulated ones. The simulated trajectories are synthesized using a physical simulator, Blender [11]. Blender has a cloth simulation function that has six parameters (Table 1).

The parameters $\boldsymbol{\theta}$ of the simulator are adapted so that the two sets of trajectories match. Here, the distance of the two sets is defined as the Euclidean distance,

$$D(R,S) \equiv \frac{1}{N}\sum_{n=1}^{N}\frac{1}{M}\sum_{i=1}^{M}\|r_{in} - s_{in}\|_2. \qquad (1)$$

Table 1. Parameters in cloth simulation function

parameter	Description
Mass	The mass of the cloth material
Struct	Overall stiffness of the cloth
Bend	Wrinkle coefficient (higher creates more large folds)
Spring	Damping of cloth velocity (higher creates more smooth, less jiggling)
Air	Have normally some thickness which slows falling things down
Velocity	Help with the cloth wobbling problem

Table 2. The definition of parameter values

parameter	value			
	initial	*minimum*	*maximum*	*interval*
Mass	1.0	0.15	10.0	0.5
Struct	30.0	5.0	80.0	15.0
Bend	20.0	0.1	150.0	10.0
Spring	3.0	0.0	25.0	4.0
Air	5.0	1.0	10.0	5.0
Velocity	0.95	0.9	1.0	0.01

where r_{in} and s_{in} denote the position of the ith feature point (a corner or the center point) in the nth frame. Because, the function D is no-convex, our system minimizes it with a simulated annealing method, that is, perturbs the parameters randomly within a range depending on a decreasing temperature. The perturbation is accepted with a probability also depending on the temperature.

The details of the setting are as below.

The perturbation range v_i of ith parameter θ_i was set to

$$v_i = \theta_{si} \tan\left\{\pi\left(p_1 - \frac{1}{2}\right)\right\} \cdot \mu {T_t}^{\sigma}, \qquad (2)$$

where θ_{si} is the standard value of the perturbation range of θ_i, p_1 represents a random number between 0 and 1, and μ and σ are gain factors. The temperature T_t at the tth iterations is set to

$$T_t = \frac{T_{t-1}}{(1+\beta t)^{\alpha}}, \qquad (3)$$

where T_0 is the initial value and α, β are gain factors.

The probability that the perturbations are accepted depends on the change of the distance,

$$change = \mathrm{D}\big(\mathrm{R}, \mathrm{S}(\boldsymbol{\theta}_t)\big) - D\big(\mathrm{R}, \mathrm{S}(\boldsymbol{\theta}_t + \boldsymbol{v})\big) \qquad (4)$$

where $\boldsymbol{\theta}_t$ is the parameter vector at the tth iteration, and v is the perturbation range vector. Then, the parameter vector is updated according to

$$A = \min(1, exp\{(change \cdot \gamma)/T_t\})$$
$$\begin{cases} \boldsymbol{\theta}_{t+1} = \boldsymbol{\theta}_t + v & if\ p_2 \le A \\ \boldsymbol{\theta}_{t+1} = \boldsymbol{\theta}_t & otherwise \end{cases} \qquad (5)$$

where p_2 is also a random number between 0 and 1, and γ is a factor.

3 EXPERIMENT

The effectiveness of our method was confirmed by experiments. In the first experiment, we evaluated the accuracy of the estimation of the center point. In the second experiment, we evaluated the estimation error of our method. The six parameters $\boldsymbol{\theta}$ for a cloth simulation function in the 3D physical simulator, Blender, are Mass, Structural, Bending, Spring, Air and Velocity (Table 1). Their initial, minimum, maximum and interval values were set as shown in Table 2 according to the preset parameters in Blender and our preliminary experiments.

The parameters for the simulated annealing, the starting temperature, the maximum loop count and the temperature decrement parameters (α, β) were set to 1000, 350, and (0.003, 1.0), respectively. Other parameters in (2) ware set to $\mu = 0.1$ and $\sigma = 0.6$. These values were chosen so that the annealing algorithm can search all parameter space within the maximum iteration count.

4 RESULTS

The result of the first experiment showed that the estimated center point had errors of 1.9 cm (4.30 % of the clothes width) on average from the measured center point using an additional marker for the ground truth. This value is accurate enough compared to the estimation error of the corners shown in the second experiment below.

In the second experiment, a short-and-hard skirt was used (Fig. 5). The annealing method reduced both the maximum and mean Euclidean distances in the swung direction (Fig. 6).

The animation in 3D simulator was also considered reasonable and proper by looks. We made another animation of human walking motion in which a human model wore on the optimized clothes (Fig. 7).

5 CONCLUSION

This paper proposed a method for generating realistic 3D CG animations using a depth image sensor and a 3D physical simulator. We successfully captured the motion of clothes as trajectories and optimized the physical

© ISAROB 2013

parameters by comparing the real and simulated motions. Our method will work as a part of VFR system by combining to other techniques such as a body measurement system [12].

At this time, however, our system cannot treat occlusion that occurs due to bends. We need to change feature points to cope with this problem to make our system applicable to various clothes.

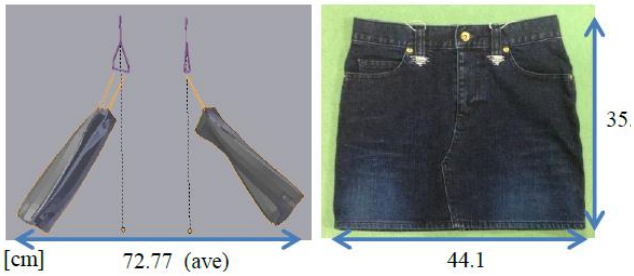

Fig. 5. The detail of clothes used for experiment

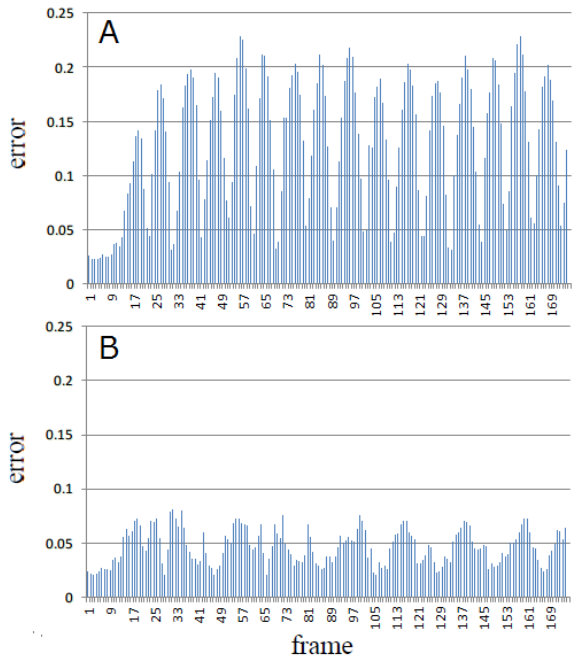

Fig. 6. Errors before (A) and after (B) the optimization experiment. The maximum errors in all frames are 0.2290 (A) and 0.0807 (B), the average errors are 0.1276 (A) and 0.0467 (B), respectively.

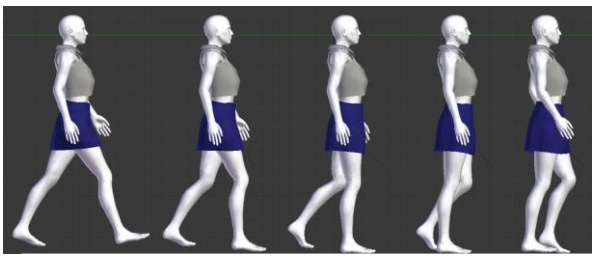

Fig. 7. The animation of human walking motion

REFERENCES

[1] Brian Beck, Key Strategic Issues in Online Apparel Retailing, yourfit.com, 2000, Version 1.0

[2] H&M: http://www.hm.com/

[3] digital fashion ltd: http://www.digitalfashion.jp/

[4] Kawabata S (1980), The standardization and analysis of hand evaluation. Textile Machinery Society of Japan

[5] Bhat K, Twigg C, Hodgins J, Khosla P, Poppvic Z, Seitz S (2003), Estimating cloth simulation parameters from video. In Proceedings of the 2003 ACM SIGGRAPH/Eurographics symposium on Computer Animation (SCA 2003), pp.37-51

[6] Hasler N, Asbach M, Rosenhahn B, Ohm J.-R, Seidel H.-P (2006), Physically based tracking of cloth. In Proceedings of VMV 2006, Aachen, Germany, pp.49-56

[7] Microsoft Kinect™: http://www.microsoft.com/en-us/kinectforwindows/

[8] ARToolkit: http://www.hitl.washington.edu/artoolkit/

[9] OpenCV: http://opencv.org/

[10] Plagemann C, Ganapathi V, Koller D, Thrun S (2010), Real-time identification and localization of body parts from depth images. In Proceedings of ICRA, Alaska, USA

[11] Blender: http://blender.org/

[12] Weiss A, Hirshberg D, Black M.-J (2011), Home 3D body scans from noisy image and range data. IEEE International Conference on Computer Vision, Barcelona, pp.1951-1958

© ISAROB 2013

The Eighteenth International Symposium on Artificial Life and Robotics 2013 (AROB 18th '13),
Daejeon Convention Center, Daejeon, Korea, January 30-February 1, 2013

Spatial operation using skeletal recognition for virtual 3D work space

Yusuke Saito[1] and Hiroyuki Nishiyama[1]

[1] Graduate School of Science and Technology, Tokyo University of Science,
2641 Yamazaki, Noda-shi, Chiba-ken, Japan
(Tel:+81-47122-1106; Fax:+81-47122-1106)
(j7412611@ed.tus.ac.jp)

Abstract: 3D desktop application software for the general environment as well as professional work environment has been increasing. However, the input method for existing applications requires large-scale facilities and special equipment. This study proposes an operation method using skeletal recognition technology with depth information only. In addition, the method compares placement and specifying rotation tasks with the wheel mouse to verify its operability and to evaluate its efficiency and usability. The efficiency of the method, excluding the adjustment and some usability aspects was found to be good, but the overall efficiency was poor compared with using a mouse because the operation of the space is unstable and the estimated position of the skeleton was inaccurate.

Keywords: 3D operation, Input device, Skeletal recognition, kinect

1 INTRODUCTION

In recent years, there have been improvements in working environments and applications that use 3D space represented on a 2D plane screen. 3dsMax[1] and GoogleEarth[2] are current examples. However, a virtual 3D work environment like this increases the degrees of freedom required for operation compared to a 2D workspace. Several operations in space have been studied to resolve these problems. However, these studies had to employ hand-held devices, large-scale systems with a marker at the site, or a camera in a room.

This paper proposes an operation method using skeletal recognition technology[4]. this technology can acquire the depth of an object by a single infrared sensor device.[3] With the skeletal recognition technology for virtual 3D workspace on the computer, at operation in real 3D space that is no tabletop surface, 3D coordinate of the dominant hand corresponds to the transition, we suggest a technique employing a complex device consisting of a 2D cursor and a 3D cursor. With respect to efficacy, we create tasks that mimic the operation of placement and of rotation in workspace virtual 3D, participants did the experiment compared with the mouse wheel, to consider and feeling its efficiency also.

[1] 3dsMax, http://usa.autodesk.com/
[2] GoogleEarth, http://www.google.com/intl/en/earth/index.html
[3] Kinect, http://www.xbox.com/en-US/kinect

2 RELATED WORK

Interfaces suitable for a 3D virtual working environment have been proposed. These include the Globe Fish and the Globe mouse[1], which decouple translation and rotation at the device level and Wii Remote[5], which achieves high degrees of freedom in space by employing infrared and tilt sensors. Operating in virtual 3D space requires much zooming and rotation, even for simple point of view (POV) and objects. However, input devices have a limited number of buttons, which hinders scalability for these mode changes to perform complex tasks in a virtual 3D work environment.

On the other hand, operations with the body have been actively researched. Examples include Kimura et al.[2] who designed and implemented a gesture-interface system for a wide-view electronic workspace and gesture operation in a large space called the "g-stalt"[6]. In addition, Nancel et al.[3] conducted a comparative study considering input devices and differences between the dimension of the method of manipulation.

In this study, we selected operation on a tabletop surface and in space for a comparative evaluation and implemented operations in space with skeletal recognition assuming that a two-button click of the mouse is a pseudo hand gesture. During the evaluation, we decided to use only mouse buttons because hand gesture recognition accuracy can be a factor.

© ISAROB 2013

3 DESIGN PRICIPLES

3.1 Operation target

This study seeks to implement POV and object manipulation with reference to manipulations in 3D space of modeling software Metasequoia[4].

- Changing the POV (camera control)
  - Vertical and parallel movement of the POV
  - Changing POV in the depth direction
  - Moving POV along a curve (Rotating the scene)
- Changing object positions
  - Vertical and parallel movements of the object
  - Rotating to change the object orientation

Operations on a tabletop surface, such as mouse movement, are restricted to a plane, and be forced to change view when adjusting or moving the depth of the object in the above operation. However, for operation in space, if both objects and the target point are displayed on the screen, there will be less need to change the POV before moving the target point of the object.

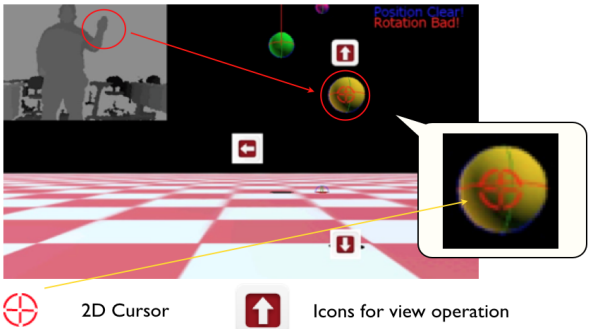

Fig. 1. Example of complex cursor.

3.2 Proposed method

In operation in space, it is difficult to control the point of view (POV) with only a 3D cursor. Therefore, we sought to design a system suitable for controlling objects with a 3D cursor and controlling the POV with a 2D cursor. Figure1 illustrates an example of using a complex 3D and 2D cursor. The user move objects and specify the direction directly with a 3D cursor. The 2D cursor controls the POV until the arrow is reached.

3.3 Systemflow

3.3.1 Skeletal information acquiring module

This module employs a depth sensor to obtain the distance between the sensor and something in sight of the sensor. Thus, it is able to acquire rate of positions for the 2D image of each skeletal site, by orthogonal projection that 3D position converted to 2D image.

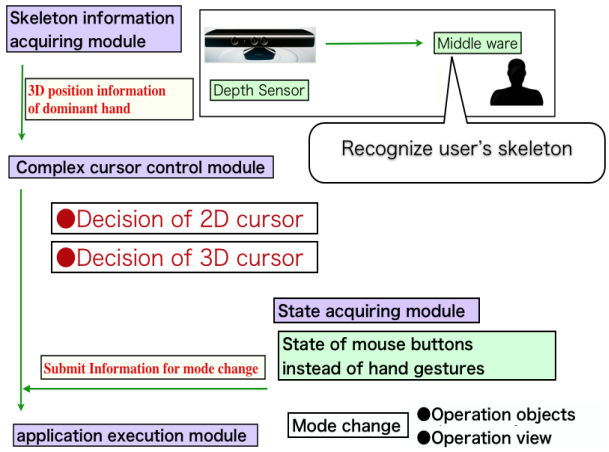

Fig. 2. Systemflow

3.3.2 Complex cursor control module

The position of the 2D cursor is determined by multiplying rate of 2D position that is determined by the orthogonal projection of the 3D hand and the screen size. tmpX(tmpY) is referred to as ratio of the dominant position in the image depth for the x (y) axis, and the position is represented by equation (1).

$$2DCusorPosition(X,Y) = (tmpX \times DisplayWide, tmpY \times DisplayHeight) \quad (1)$$

The position of the 3D cursor is determined by the position of the 2D cursor and the distance from the sensor to the dominant hand. In particular, *SD* is the distance from the work field to the sensor, *HD* is the distance between the dominant hand and the sensor, *HS* is the sensitivity of the movement distance in virtual space and the real operating distance of the hand, and equation (2) represents the position.

$$3DCusorDepth = \{(SD \times 2) - HD\}^{HS} \quad (2)$$

3.3.3 State-acquiring module

Information for switching operation mode is needed when working with objects and viewpoints. In this system, we assume that an object is clicked when the 3D cursor touches the object and that the POV is clicked when the 3D cursor is not touching the object.

3.3.4 application-execution module

This module reflects the complex cursor and the mode change process of the state-acquiring module in this application.

[4]Metasequoia, http://www.metaseq.net/metaseq/

© ISAROB 2013

4 EXPERIMENT

Participants continuously perform the two tasks of placing an object in the specified location and turning the object to the specified direction. They performed these tasks using both the proposed method and the mouse wheel, with placement distance and difficulty of angle adjustment divided into three levels. The difficulty of adjusting the setting angle is divided into three levels, beginning from the easiest: less than 45 degrees, sideways, and diagonal front. As representing the efficiency, not only in the overall time for consecutive task, it took time to adjust location and direction of the object, to reach the goal and such as measuring the number of errors.

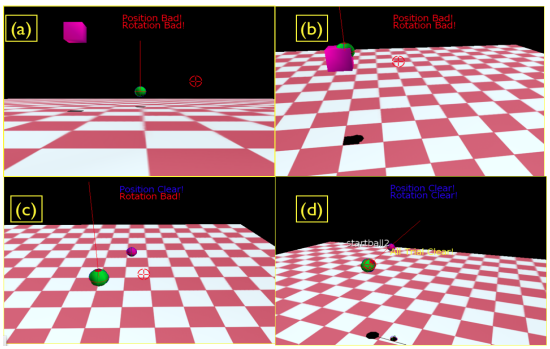

Fig. 3. Set of tasks.

4.1 Consecutive tasks

In the placement task, participants transported the green sphere to the target (purple cube). Immediately after the start, the POV is located just in front of the object. Verifying the target area requires pulling some of the POV, it has become random whether the left or right (figure3(a)). When the controlled object remains in the range of the target for 1.0 seconds, we assume the object position is stable (figure3(b)). When the rotation task is specified, the target (purple cube) will disappear when the placement task is completed (figure3(c)). Purple spheres that has become random whether the left or right indicate the direction in which the occurrence of the specified. As with objects, the consecutive task is considered completed when the red light indicating the direction of the object intersects the sphere and is stable for 1.0 second (figure3(d)).

4.2 Experiment environment

To measure the performance efficiency, we recorded the time to first pass through the destination, to adjust placement, to fit the direction completely, to adjust the direction, and to complete both tasks. In this experiment, participants performed three consecutive tasks after some practice. We recruited nine participants (one female), ranging in age from 20 to 24 years old. All are right-handed daily computer users. None are colorblind. We measure each of Operation time and number of overshoots for each of 486 trials: $2interface \cdot 3distance \cdot 3rotation \cdot 9participants \cdot 3replications$.

We asked questions based on the five-point Likert scale. We ask that question a total of 10 times per participant in the entire experiment: each distance of placement task, each difficulty of rotation adjustment, and each of 2 interfaces. Participants rated the usability in each operation object and POV and in each of the two tasks, and of fatigue. We also encouraged comments after every question.

In both the mouse and the proposed control methods, the distance between the participant and the screen was a uniform 3[m]. Depth sensors are placed as near 1.3 [m] is about space and work from the sensor. The mouse had a wheel and was made by Logicool, using a kinect depth sensor. The system and the trial were implemented on the XNA framework using C# language.

4.3 Results and Consideration

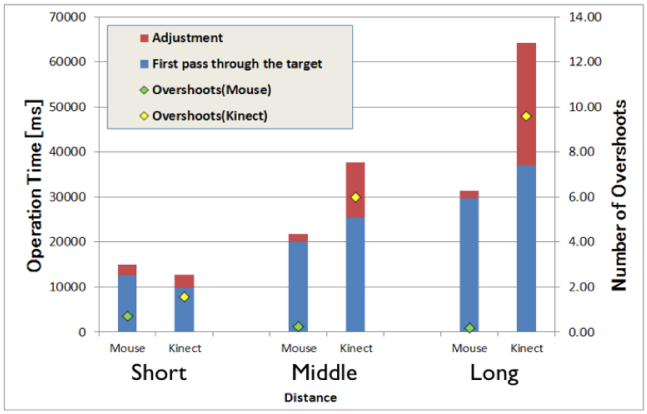

Fig. 4. Operation time : Placement task.

4.3.1 Operation Time

Figure4 and Figure5 presents the operation time for each task. First, in placement task, when placement distance is short, the average time has reduced by 23% compared to using the mouse (average 9,673[ms] vs. 12,492[ms]). However, as the distance increased, the time for moving to the target and the time for adjustment increased because time is lost in the proposed

© ISAROB 2013

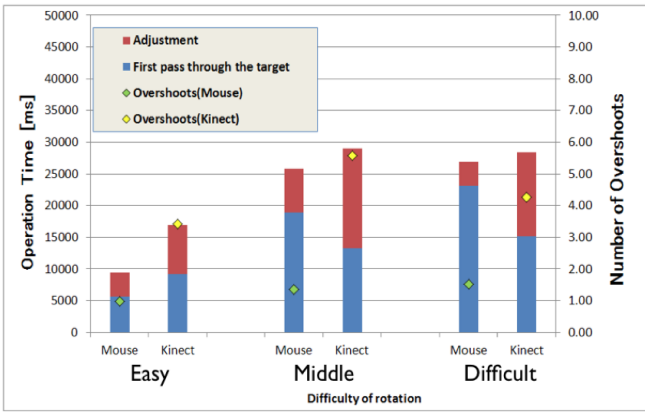

Fig. 5. Operation time : Rotation task.

method from the time the participant presses the button to change the perspective until he/she moves the 2D cursor to the icon to change the POV. Second, the number of overshoots increases considerably as the distance increases. Cursor shaking instability is a possible cause. Third, the overall efficiency using our method to specify a rotation task is less than that using mouse. However, as regards suitable time in the approximate direction, our method is not affected by the complexity of direction. This can be specified directly in spatial orientation, which means that users can easily suited to a complex direction.

4.3.2 Operability

To evaluate the operability, participants evaluated ease of controlling the object and POV on a five-point scale with 5 being comfortable and 1 being uncomfortable; fatigue was rated on a similar scale with 5 being most fatiguing. The proposed method was harder to use for moving the object (mouse 327 points vs. proposed method 284 points). In comments, some participants say that moving the object to the target was easy, but it could seem difficult due taking a long time to adjust and the instability of the complex cursor. And, there were no significant differences between the mouse and the proposed method for vertical and lateral control of the POV (339 points vs. 304 points) or for scene rotation (319 points vs. 301 points). This indicates that 2D feedback such as with an arrow icon is more efficient. About tiredness, The standard deviation of the proposed method is also greater than that of the mouse (3.57 points vs. 7.87 points). Some participants didn't feel tired, and were able to control the object and direction smoothly in space.

4.3.3 Cause of cursor shaking instability

We will now address the issue of specific shaking instability of skeletal recognition that is considered to have the greatest impact on efficiency and usability. In placement and rotation tasks, the cursor became unstable when approaching the goal, and this did not simply seem to relate to holding the hand steady in space. When skeletal positions closely overlapped, the middleware 's estimated 3D coordinates became inaccurate, and the tracking of the hand 's 3D position information became unstable in the final stages.

5 SUMMERY AND FUTURE WORK

In this study, we designed and implemented a method of controlling virtual 3D objects and POV based on skeletal recognition. The proposed system used a complex cursor composed of 2D and 3D cursors. Experiments compared the complex cursor and mouse cursor with respect to efficiency and usability. In addition, using skeletal recognition technology in virtual 3D space clarified the issues that require precise operation. The future direction of this study will include designing an algorithm to account for the instability of the skeletal position recognition and improving the POV control in virtual space.

REFERENCES

[1] Froehlich, B et al.(2006), The globefish and the globe mouse: two new six degree of freedom input devices for graphics applications. In: ACM Conference on Human Factors in Computing Systems (CHI), pp. 191—199. ACM Press

[2] Kimura, A et al.(2005), Design and Implementation of Wide-view Electronic Working Space, In: Proceedings of Interaction 2005, pp. 143-150

[3] Nancel, M et al.(2011), Mid-air Pan-and-Zoom on Wall-sized Displays. In: ACM Conference on Human Factors in Computing Systems (CHI), pp. 177-186, ACMPress

[4] J. Shotton et al(2011), Real-time human pose recognition in parts from a single depth image. In Proc. CVPR

[5] WiiRemote, http://wii.com/

[6] Zigelbaum, J. et al.(2010), g-stalt: a chirocentric, spatiotemporal, and telekinetic gestural interface. In Proc. TEI '10, pp.261-264, ACM

© ISAROB 2013

The Eighteenth International Symposium on Artificial Life and Robotics 2013 (AROB 18th '13),
Daejeon Convention Center, Daejeon, Korea, January 30-February 1, 2013

Breast Cancer Palpation Training System Using Five-Fingered Haptic Interface Robot and GPGPU

Takamitsu Kawai[1], Tetsuya Mouri[2], Takahiro Endo[2], and Haruhisa Kawasaki[2]

[1]Organization for Research and Community Development, Gifu University, Japan
[2]Department of Human and Information Systems, Gifu University, Japan
(Tel: 81-58-293-2675, Fax: 81-58-293-2675)

[1]takawai@gifu-u.ac.jp

Abstract: As the number of breast cancer patients grows, teaching more medical students is highly demanded than ever. However, seeking for real patients and actually having a training session with them are very difficult due to the nature of the training involving touching their body. Our approach to this problem is to develop a virtual breast cancer palpation training system that can completely eliminate the need for real human patients for the training. Our training system uses HandHIRO, a five-fingered haptic interface robot to create haptic sensations of the deformations of a virtual breast including tumors. The deformations of the virtual breast are entirely computed on a GPU using an FEM and the computational results are rendered both haptically using a HandHIRO and graphically using a 3D display system with a half mirror. In this paper, the design and implementation of our training system and preliminary experimental results are presented.

Keywords: breast cancer palpation, haptic interface robot, 3D display, deformable body simulation, FEM, GPGPU

1 INTRODUCTION

Training environments for breast cancer palpation that are easily accessible by medical users have been greatly in demand reflecting the increasing number of breast cancer patients. Creating a virtual human breast model utilizing VR technologies such as haptic interfaces and 3D displays can completely eliminate the need for real human patients. Based on this idea, we have been developing a virtual training system for breast cancer palpation.

Takaiwa et al. [1] created a breast cancer palpation simulator based on a real off-the-shelf breast training model and a pneumatic parallel manipulator to create force feedback. Jeon et al. [2] created an augmented reality system based on a real silicone breast model and a PHANToM haptic device. Although these systems create realistic haptic sensations utilizing real breast models, they are required to replace the breast model when simulating breasts of different geometry. Moreover, they do not simulate multi-fingered touch sensations. The basic idea of our training system is to create a complete virtual model of a breast as a deformable body and simulate its deformation in realtime. The haptics are rendered for each finger individually by a five-fingered haptic interface robot called HandHIRO (Endo et al. [3]) and the graphics are rendered by a 3D display system with a half mirror. The simulator is based on an FEM (Finite Element Method) with a corotational formulation. Our system allows the user to specify the stiffness for each finite element to place tumors with arbitrary shapes and position, up to the mesh resolution. Introducing GPGPU (General Purpose computing on Graphics Processing Units) technologies, the simulator runs entirely on a GPU. The use of GPUs allows us to simulate large-scale models in realtime that are intractable to conventional CPU implementations. These features enable the user to quickly change the virtual models without lengthy offline precomputations. This means that the users can train using a wide variety of virtual patients with different medical conditions.

This paper presents the design and implementation of our training system featuring the HandHIRO, 3D display system, and a GPU-based FEM simulator. Preliminary experimental results are also presented.

2 SYSTEM OVERVIEW

Fig. 1. shows the overview of our training system. It is comprised of a HandHIRO installed at the bottom, and a 3D display based on a LCD (Liquid Crystal Display) attached at the top, and a half mirror in between. As shown in **Fig. 2.,** a user wearing a pair of 3D shutter glasses sits down in front of the half mirror and sees the 3D images of a female chest including breasts which are projected on the half mirror as a stereoscopic image. At the same time, all the five fingers of the user are connected to the HandHIRO that is placed behind the half mirror so that he/she can receive haptic sensations for each finger individually, while seeing his/her own hand through the half mirror. The 3D images of the deformed virtual breast generated by a PC with GPUs

© ISAROB 2013

are overlaid on top of their own hand, thereby a mixed reality effect is created. This effect is expected to enhance the user's training experience.

2.1 HandHIRO: five-fingered haptic interface robot

Fig. 3. shows the appearance of HandHIRO. HandHIRO is a five-fingered haptic interface robot that features the ability to present high-precision three-directional forces to each of the user's five fingertips individually. HandHIRO has many DOFs: 15 DOFs for the haptic hand and 6 DOFs for the interface arm. Thanks to this arm, HandHIRO can be used in a large workspace. A user connects his/her five fingertips to HandHIRO through passive spherical permanent magnet joints. These joints will automatically come off when excessive amount of forces are exerted, thereby HandHIRO allows to touch a virtual object with five fingers in a safe manner. **Fig. 4.** shows an example of graphics rendering of a virtual breast. The white spheres represent the user's five fingertips. As the user pushes the breast, dents are made and reaction forces are given to the user through HandHIRO. The breast deforms in realtime in response to the movements of the user's fingertips.

3 DEFORMABLE BODY SIMULATION FOR VIRTUAL BREAST CANCER PALPATION

Many parts of a human body, including organs and/or tissues are modeled as a deformable body. We focus on simulating the breast part only as a deformable body. Deformable body simulation is generally a difficult task since deformable bodies have infinite DOFs. Therefore, usually we have to discretize the deformable body using numerical methods such as FEM. Our past breast palpation simulator (Daniulaitis et al. [4]) is also based on an FEM. It realized realtime simulation of a deformable body based on precomputation of the body's displacement and reaction forces: the deformations of the entire body and the reaction forces are precomputed for unit displacements for each vertex of the FE model. At runtime, the deformation of the entire body and the reaction forces for each finger are computed as a linear combination of these precomputed displacements, given a set of contact points. The drawback of this method is the need for the lengthy precomputation and lack of dynamics. Our method simulates the dynamics of a deformable body in realtime using GPGPU and at the same time interacts with HandHIRO for haptic rendering so that more realistic results can be obtained on the fly.

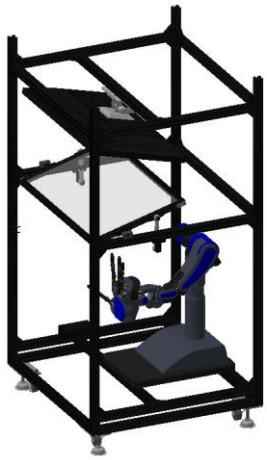

Fig. 1. Proposed breast cancer palpation training system

Fig. 2. Actual use of our training system

Fig. 3. HandHIRO, five-fingered haptic interface robot

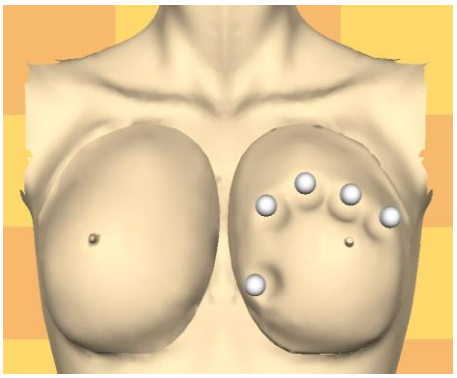

Fig. 4. Deformations of breast by multiple fingertips

© ISAROB 2013

3.1 Simulation algorithm overview

Our simulation algorithm is comprised of (1) collision detection and response and (2) FEM computation. The first step for the algorithm is to receive the current position of fingertips from HandHIRO and perform collision detection between the fingertip spheres and the deformable body surface. If a collision is detected, its contact forces are computed and used as boundary conditions for the FEM. At the same time, the contact forces will be sent to HandHIRO for haptic rendering. Finally, the time step in the simulator is proceeded and the next time step's physical states are calculated.

3.2 Corotational FEM

In our simulator, the deformation of breast is simulated using an FEM based on a corotational formulation on the GPU (Allart et al. [5], Parker and O'Brien [6], Nesme [7]). The corotational formulation accounts for geometric nonlinearities of the deformations. It can avoid so-called "inflation" artifacts when subject to large deformations. The idea of corotational FEM is to rotate the stiffness matrix by a rotational matrix that brings it to the original coordinate space before deformation. This eliminates the bad influence of the rotational component of the deformation to the linear strain that leads to an inflation effect. The system of ordinary differential equations is solved by implicit time integration based on backward Euler scheme for stability. The backward Euler scheme updates the velocity using the acceleration at the end of the time step. This requires to solve a system of linear equations at every time step. This is done by a conjugate gradient solver.

3.3 Modeling fingertip contact

HandHIRO has 5 fingers and each fingertip is modeled as a rigid sphere. The spheres and the deformable body need to avoid interpenetration. We employ a penalty method for simplicity. Proximity is checked for each sphere center against all the vertices within the deformable mesh. If the distance is less than the sphere radius r, then the vertex is considered in contact and proceeds to penalty force computation. This process is efficiently done on the GPU in parallel. The penalty force is given by

$$F = -k_s d - k_e v \qquad (1)$$

where d is the penetration depth and v is the rate of change of the penetration distance, k_s and k_e are a spring constant and a damping constant, respectively. For each sphere, all the penalty forces exerted on the sphere are applied to the deformable body as external forces at each contact point. The penalty forces for each sphere are summed and converted into one 3D force vector for haptic rendering. Note that in some cases we observed some noticeable vibrations due to the penalty force when a sphere and the deformable body collide. To suppress these vibrations, we apply a low-pass filter for the computed forces.

3.4 GPGPU: General Purpose computing on GPUs

The entire FEM and collision detection and response are implemented based on GPGPU by CUDA technology (NVIDIA [8]). In the GPU kernels, shared memory is extensively utilized to maximize memory bandwidth utilization. Most of vectors in the algorithms are mapped to a vertex buffer object and made interoperable with OpenGL. This allows direct graphics rendering of the computational results by GPU without copying the results back to the CPU memory.

4 EXPERIMENTAL RESULTS

A preliminary evaluation was conducted using a PC with Intel Xeon E5606 2.13GHz, 48GB main memory, and NVIDIA Tesla C2075 for running GPGPU, and NVIDIA Quadro 2000 for stereoscopic 3D graphics rendering with NVIDIA 3D vision technology. The frequency of the haptic control loop is kept to 1 [kHz] and the graphics frame rate is set to 30 [Hz].

4.1 Constructing a virtual breast model

A virtual breast model was constructed as follows: A real silicone palpation training model was first scanned. Then after the data is cleaned up, it is processed with mesh generation software to generate a triangular surface mesh and a tetrahedral volumetric mesh. **Fig. 5.** shows the breast model represented with a surface mesh (6004 triangles). A volumetric mesh (44208 tetrahedra, 9097 nodes) is constructed from the surface mesh. According to Krouskop [9], the Young's modulus of the entire breast except the tumor part is set to E=19000 [Pa] and the tumor is set to 107000 [Pa], so that the tumor part can be felt stiffer than other parts of the breast. **Fig. 5.** also shows the size and location of the tumor used in this experiment. The tumor's radius is set to 1.5 [cm] and is located on the x axis at x = 0.125 [m]. Only one of the breasts (the one on the right hand side in the **Fig. 4.**) is modeled by an FEM and simulated. Other body parts are static and not included in the simulation. The base part of the breast is given Dirichlet boundary conditions to fix the breast part on top of the chest part.

© ISAROB 2013

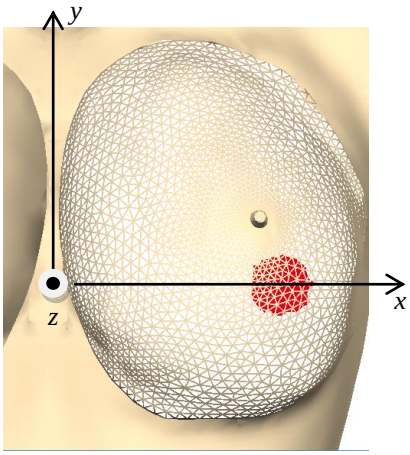

Fig. 5. Tetrahedral mesh and tumor (red part: E=107000 [Pa]). E=19000 [Pa] for the rest of the mesh.

4.2 Results from virtual breast palpation

A virtual palpation session was conducted using the constructed model. Although the user can generally use up to 5 fingers simultaneously, here we show only the results of 1 finger case for simplicity. The palpation is done using his/her index finger by periodically repeating a push/pull motion along z direction (in **Fig. 5.,** $+z$ points towards the reader) translating his/her hand along the x axis from the left to the right, and then from the right to the left (repeat this 2 times). **Fig. 6.** shows the changes in the index finger's x position (dotted line) and the corresponding z component of the target reaction forces (solid line) that are computed by the computational module. These target forces are sent to the HandHIRO and rendered to the user's fingertip. As shown in the figure, the reaction force becomes noticeably high at positions around x = 0.12 [m]. This means that, around this location, the user should be receiving significant reaction forces in $+z$ direction and feeling the existence of the tumor. The position x = 0.12 [m] approximately corresponds to the x position of the tumor that is predefined as shown in **Fig. 5.** This verifies that the location of the tumor is reasonably well represented, thus showing the effectiveness of our system.

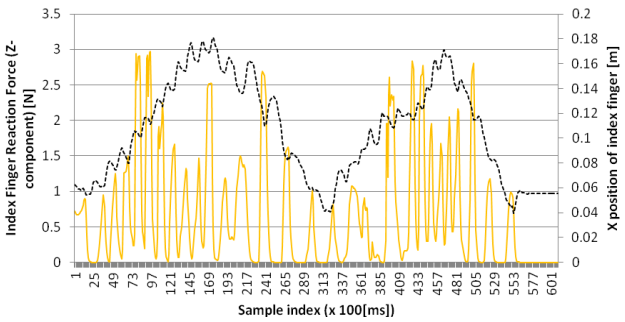

Fig. 6. X-component of index fingertip position vs. Z-component of reaction force of index fingertip measured in a virtual palpation session

5 CONCLUSION

We have discussed the implementation of our virtual breast cancer palpation training system based on a five-fingered haptic interface robot HandHIRO, a 3D display, and GPGPU. The deformation of breast is modeled using a corotational FEM and is computed on a GPU. This enables large-scale realtime simulation of the deformations of a virtual breast. The preliminary experimental results show that our system can simulate the physical behavior of a breast and is effective for breast cancer palpation training.

ACKNOWLEDGMENTS

This paper was supported by the Ministry of Internal Affairs and Communication R & D Promotion Programme (SCOPE) and Grant-in-Aid for Scientific Research from JSPS, Japan ((B) No. 23360184).

REFERENCES

[1] Takaiwa M, Noritsugu T (2007), Development of breast cancer palpation simulator using pneumatic parallel manipulator. SICE Annual Conference, 2007, pp.823-827

[2] Jeon S, Knoerlein B, Harders M, et. al. (2010), Haptic simulation of breast cancer palpation: a case study of haptic augmented reality. 9th IEEE International Symposium on Mixed and Augmented Reality (ISMAR), 2010, pp. 237-238

[3] Endo T, Kawasaki H, Mouri T, et al. (2011), Five-fingered haptic interface robot: HIRO III. IEEE Transaction of haptics, 4(1):14-27

[4] Daniulaitis V, Alhalabi O, Kawasaki H, et al. (2004), Medical palpation of deformable tissue using physics-based model for haptic interface Robot (HIRO). Proc of 2004 IEEE/RSJ Internatinoal Conference on Intelligent Robots and Systems, pp. 3907-3911

[5] Allart J, Courtecuisse H, Faure F (2011), Implicit FEM solver on GPU for interactive deformation simulation. In GPU Computing Gems Jade Edition. Elsevier. 2011, pp. 281-294

[6] Parker EG, O'Brien JF (2009), Real-time deformation and fracture in a game environment, In: Fellner D, Spencer, S (ed) Symp. on Computer Animation (2009) ACM, New York, pp. 156-166

[7] Nesme M, Marchal M, Promayon E, et al. (2005), Physically realistic interactive simulation for biological soft tissues, Recent Res. Developments Biomech 2 (2005) pp. 1-22

[8] NVIDIA Corporation, CUDA toolkit documentation. http://docs.nvidia.com/cuda/index.html

[9] Krouskop TA, Wheeler TM, Kallel F, et al. (1998), Elastic moduli of breast and prostate tissues under compression. Ultrason. Imaging, 20, 1998, pp. 260-74

© ISAROB 2013

The Eighteenth International Symposium on Artificial Life and Robotics 2013 (AROB 18th '13),
Daejeon Convention Center, Daejeon, Korea, January 30-February 1, 2013

ALife approach for body-behavior predator-prey coevolution: body first or behavior first?

Takashi Ito[1], Marcin L. Pilat[2], Reiji Suzuki[3] and Takaya Arita[4]

[1,2,3,4]Graduate School of Information Science, Nagoya University
Furo-cho, Chikusa-ku, Nagoya 464-8601, Japan
[1]takashi@alife.cs.is.nagoya-u.ac.jp, [2]marcin.pilat@gmail.com, [3]reiji@nagoya-u.jp, [4]arita@nagoya-u.jp

Abstract: We present the results of morphology-behavior predator-prey coevolution in a 3D physically simulated environment. The morphology and behaviors of virtual creature predators and prey are evolved using a genetic algorithm and random one-on-one encounters in a shared environment. We analyze the evolutionary dynamics on the basis of quantitative characterization of morphology and behavior. Specifically, we pose and answer the question: Which precede the other, morphology or behavior, during the evolutionary acquisition of predator and prey strategies?

Keywords: Coevolution, Predator-prey, 3D physical simulation, Artificial life

1 INTRODUCTION

Prey-predator interactions are the key element of ecological systems [1]. Predation pressures in food chains shape diversity and functions of organisms [2]. Many predators employ various strategies capturing their prey and at the same time, many prey employ various protective mechanisms against their predators. These strategies arose through the coevolution between predators and prey. Furthermore, in the coevolution, morphology and behavior have been tightly coupled in each species. Therefore, the process can be regarded as double coevolution of morphology-behavior and predator-prey couplings (Fig. 1).

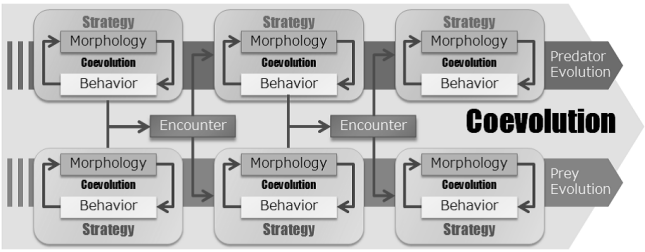

Fig. 1. Double coevolution of morphology-behavior and predator-prey.

The purpose of this study is to understand the process and dynamics of strategy emergence in the context of this double coevolution. We performed double coevolution of morphology-behavior and predator-prey by using a simple predator-prey scenario in a 3D physically simulated environment. Predator-prey coevolution has been studied mainly in mathematical biology using mathematical methods typically to analyze the change in population size of each species [4]. However, these studies have not focused or have not been able to focus attention on coevolution of morphology and behavior of individual virtual creatures. On the other hand, virtual creature models in Artificial Life, following the pioneering study [5], allow us to analyze the morphology and behavior coevolution.

In our previous study as a first step, we observed the emergence of various morphological and behavioral prey defensive strategies. This paper focuses on the morphology-behavior coevolution in terms of the evolution of strategies. Specifically, we pose a question: *Which preceded the other, morphology or behavior, during the evolutionary acquisition of new strategies?* We attempt to answer it by analyzing two example cases of evolutionary experiments: acquiring a new strategy as the first move or the countermove against the new strategy of the other species.

2 MODEL

We used the Morphid Academy open-source simulation system [6] to evolve virtual creatures in a 3D physically simulated environment (Fig. 2). The presented coevolution of predators and prey provides the example of simulating several agents in a shared environment of Morphid Academy in a coevolutionary context.

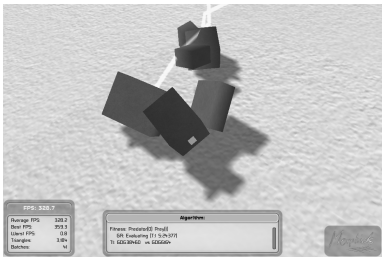

Fig. 2. Virtual creatures in Morphid Academy.

The agents are virtual creatures comprised of several 3D rectangular solid body parts connected with simple hinge

© ISAROB 2013

joints. Their physical phenotype is developed from a directed graph (Fig. 3). The nodes represent body parts and the links represent joints. The genotype graph undergoes evolution based on a genetic algorithm, and the phenotype tree represents the connected body parts. We termed the root body part as the *torso*, and all the other parts as *limbs*.

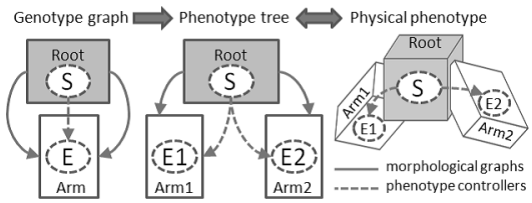

Fig. 3. The development from genotype to phenotype.

The controller of a virtual creature is a recurrent neural network embedded in body nodes. There are three types of neurons: input, calculation and output. The input neurons represent sensory information from the environment, the computational neurons process the input and the results are fed into the output neurons as joint effectors that power the joints, making the creature move. The creature sensor detects other living agents nearest to the virtual creature within a sensing range r . This virtual creature model is a simplification of Sims' Blockies model [5] and is fully described in [6]. The simplification in body and neural structure decreases the evolutionary search space and has been demonstrated to perform well for various evolutionary task.

Two populations are concurrently evolved, representing the predators and the prey. A steady-state genetic algorithm is used with tournament selection of size 3. Fitness of each agent is calculated from the result of an encounter between a randomly selected predator-prey pair. For each tournament, one or two individuals with the best fitness can produce a child through one of the genetic operators of copy, crossover or grafting. The child replaces the worst performing of the 3 individuals. Mutation is applied to the resulting child individual and includes: mutation of the morphological node or link parameters, addition of morphological nodes, and the addition or removal of morphological links.

The fitness of each agent is calculated after the encounter through a fitness function. The fitness of a predator is defined by Eq. 1. It gets 5000 if it has captured the prey and gets another maximum of 5000 points proportional to the early capturing. Otherwise, its fitness is proportional to the distance gained towards the prey, based on the initial distance r_0 and the final distance r_n.

$$F_{pred} = \begin{cases} 5000 + 5000 \times \frac{t-t_n}{t} & \text{(caught)} \\ 5000 \times \frac{r_0 - r_n}{r_0} & \text{(missed, } r_0 \geq r_n) \\ 0 & \text{(missed, } r_0 < r_n) \end{cases} \quad (1)$$

The fitness of the prey is defined by Eq. 2. If it escaped from its predator without caught in the simulation time steps, it gets 5000 and gets another maximum of 5000 fitness points proportional the distance it moved l_n. Otherwise, the fitness is calculated according to the ratio of the time the prey escaped during t_n over the time limit t.

$$F_{prey} = \begin{cases} 5000 + 5000 \times \frac{l}{l_n} & \text{(escaped, } l_n \leq l) \\ 10000 & \text{(escaped, } 0 \leq l < l_n) \\ 5000 \times \frac{t-t_n}{t} & \text{(being caught)} \end{cases} \quad (2)$$

The random predator and prey are positioned above the simulation plane and allowed to free-fall due to gravity during a stabilization phase. Once they are stable from movement and resting on the ground surface, the evaluation encounter begins and lasts for S simulation time steps. Capturing is defined as the predator touching the torso of the prey with any of the predator's body parts. A captured creature is disabled and cannot be sensed.

We calculated several indices to characterize the morphology or behavior of the creatures quantitatively. As for the morphology, we used these four indices: volume (*VOL*), center of the mass (*COM*), agent body width (*WID*) and number of body parts (*NUM*). Comparing morphology and behavior, it is more difficult to characterize the latter quantitatively because, in general, the behavior heavily depends on the former, and is too complex to know what kind of indices will clearly represent the progress of coevolution in a 3D physical simulation environment. We decided to use these two simple indices: the maximum output of sensory neurons (*SEN*) and the average output of effector neurons (*EFF*), which are intended to approximately represent the sensitivity to the environment and the mobility, respectively. These indices do not depend directly on the morphology of the agents. In order to answer the question posed in Introduction, concerning the evolutionary order of morphology and behavior, we use the idea of cross-correlation methods.

3 RESULTS

We evolved predator and prey populations, each of size $i = 30$ and initially random individuals, for $g = 10000$ tournaments. Each evaluation of an encounter was performed for $S = 100000$ simulation time steps with an initial distance $r = 700$ between the agents. For each tournament, a child was created by asexual copy (probability of 40%), crossover (30%), or grafting (30%). Mutation of the child was performed with prob. of 80% with each mutation able to apply small changes to the whole genome (prob. of 5% per gene). The vision radius of predators was 5000 while the prey were only able to see within 500 distance units. Therefore, the predator can sense the prey much earlier than the prey.

In previous studies, we classified the evolved prey's defensive strategies into two types, each with an assortment

© ISAROB 2013

of evolved morphologies and behaviors: *Runaway Strategy* which involves fleeing from the predator and *Guard Strategy* which relies on their morphologies and typically stationary behavior to provide protection from predation [7]. It is easy to detect the emergence of the Guard Strategies as they tend to evolve with a sharp increase in the fitness. Therefore, we investigate the relationship between morphology and behavior evolutions by focusing on the course of the evolution of Guard Strategies. To control the movement of prey and to promote the emergence of Guard Strategies, we used the modified fitness function of the prey (Eq. 2) and the environmental parameter $l = 100$.

We performed 30 trials. Among them, the prey evolved some Guard Strategy to prevent the predator from capturing it in 17 trials and the prey did not evolved any defensive strategies in the other trials. We used 12 results with a sharp increase in fitness for analysis out of the 17 results. Fig. 4 shows a typical evolution in which Guard Strategy emerged. It is shown that firstly, the predator fitness increased, and at the same time, the prey fitness decreased. At some point, the prey increased the fitness sharply by evolving a strong defensive strategy.

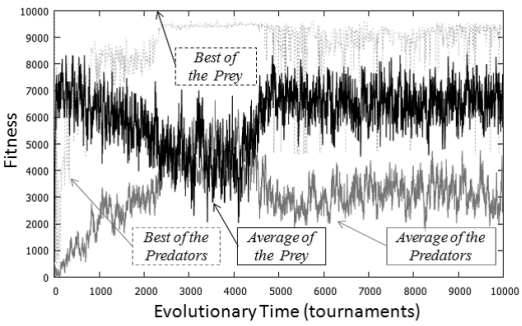

Fig. 4. Fitness change in a typical predator-prey coevolution. The prey evolved strong Guard Strategies at 4500 evolutionary time step.

Fig. 5 shows the changes in a morphological index, VOL, a behavioral index, EFF and the fitness of the prey in the same evolution with the one shown in Fig. 4. We see a certain tendency that when the fitness value increased, the morphological index also increased, but the behavioral index decreased.

3.1 Morphology first or behavior first?

Next, we investigate the evolutionary order relation between morphological and behavioral evolutions by repeatedly calculating the cross-correlation between the evolutionary sequences of index and another index with a changed time-lag. We performed 12 trials and calculated 8 cross-correlation (4 morphological indices $\times$ 2 behavioral indices) per trial and obtained 96 cross-correlation coefficients in total. Fig. 6 shows a result of the coefficient between VOL as a morphological index and EFF, SEN as behavioral indices for a typical trial. Note that we used the absolute value of the coefficient in order to calculate the result in Fig. 6. The maximum time-lag was set to 500 evolutionary time steps before and after the emergence of Guard Strategy and focused on in analysis, which was identified by the maximum increase in fitness of the prey. The time-lag maximizing the coefficient can be used to estimate the evolutionary order of the two indices. If it is positive or negative, the behavioral changes precede the morphological changes or vice versa, respectively. In this way, we see from Fig. 6 that EFF change preceded VOL change, and on the other hand, VOL change preceded SEN change, which means that the evolutionary order between morphological and behavioral indices depends on which index was used for calculation even in one trial. We thus classified all 96 cases into the cases in which morphology changes preceded the behavior changes and the reverse cases by checking if the time-lag maximizing the coefficient is positive or negative. Table 1 shows the results. It shows a weak tendency for morphological change to precede behavioral change.

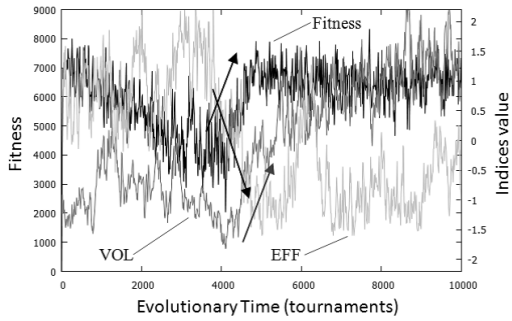

Fig. 5. Fitness and two indices change of the prey in the evolution shown in Fig. 4.

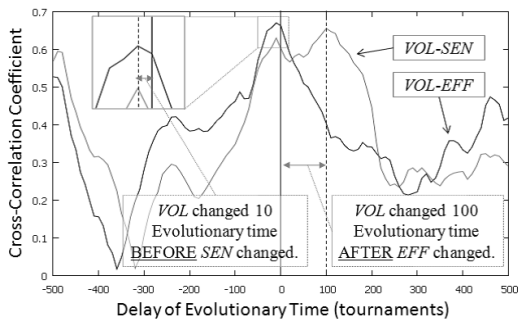

Fig. 6. Cross-correlation coefficients with evolutionary time-lags.

The tendency of morphology evolution to precede the behavior evolution might partly depend on the evolved strate-

© ISAROB 2013

Table 1. Frequency of the evolutionary order (precursor).

Morphology	Simultaneous	Behavior
41.6%	17.7%	31.3%

gies. This paper focused on the emergence of Guard Strategies in the prey evolution. They rely heavily on their morphology and do not need specific behavior. Therefore, the increase in fitness during the emergence of these strategies tends to depend on a few mutations which modify the morphology giving a greater fitness. On the other hand, the behavior is less important for these strategies, and therefore, the behavior modification adapting to the new morphology tends to follow the morphological evolution.

It was also shown that the morphological or behavioral indices tended to change in advance of the change in fitness by using the same cross-correlation based method. This result is reasonable because morphology and behavior emergences did not occur simultaneously as shown in the first experiment, and in order to increase the fitness, some morphology might need corresponding behavior or vice versa.

3.2 By morphology or by behavior?

The previous analysis treated evolutionary change in the traits only of the prey. Here, we focus on the evolution of predator strategies responding to the emergence of new prey strategies.

We calculated the cross-correlation coefficient value between the same indices of the predator and of the prey. Fig. 7 shows the frequency of the cases in which the cross-correlation was more than 0.4 in all trials. We see a clear tendency that the cross-correlation coefficient for behavior indices was larger than that for morphological indices. In other word, they tend to respond to new strategies of the opponent by changing behavior and not by changing morphology.

This might be due to the difficulty of morphological change. In general, a morphological change tends to be drastic, and thus non-adaptive without the corresponding change in behavior. By contrast, a behavioral change has a greater tendency to lead to a small improvement for the strategy.

4 CONCLUSION

We presented the results of evolutionary experiments showing morphological and behavioral changes under a predator-prey coevolutionary scenario in a 3D physically simulated environment. We defined the indices to characterize the morphology or behavior of the creatures quantitatively and analyzed their dynamics in order to answer the question: Which preceded the other, morphology or behavior, during the evolutionary acquisition of new strategies? The answer is summarized as follows. Morphology tends

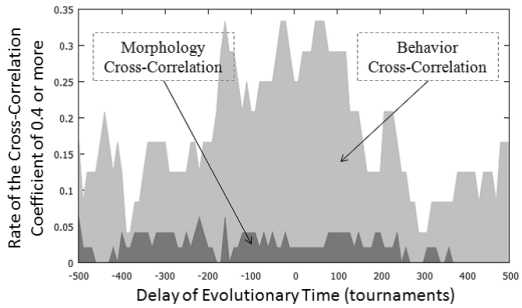

Fig. 7. Frequency of the cases in which the cross-correlation coefficient was more than 0.4 with evolutionary time-lags.

to precede behavior in the independent emergence of new strategies and behavior tends to precede morphology in the response to the new strategies of the opponents. This difference might indicate that the former and the latter were driven mainly by big changes and small changes, respectively.

In general, there is an obvious asymmetry between predator and prey at the inter-species level. The results shown in this paper indicate that an asymmetry between morphology and behavior at the intra-species level does produce complex dynamics in the coevolution between predators and prey.

REFERENCES

[1] P. Legreneur, M. Laurin and V. Bels, "Predator-prey interactions paradigm: a new tool for artificial intelligence," *Adaptive Behavior*, 20 (1), 3-9, 2012.

[2] A. A. Agrawal, "Phenotypic plasticity in the interactions and evolution of species," *Science*, 294 (5541), 321-326, 2001.

[3] M. Edmunds, *Defence in Animals: A Survey of Anti-predator Defences.* Longman Group Limited, 1974.

[4] J. Murray, *Mathematical Biology I: An Introduction.* Springer-Verlag, 2003.

[5] K. Sims, "Evolving virtual creatures," in *21st Annual Conf. on Computer Graphics and Interactive Techniques (SIGGRAPH 94)*, 15-22, 1994.

[6] M. L. Pilat and C. Jacob, "Creature academy: A system for virtual creature evolution," in *Proc. of the IEEE Cong. on Evolutionary Computation (CEC 2008)*, 3289-3297, 2008.

[7] T. Ito, M. L. Pilat, R. Suzuki and T. Arita, "Emergence of defensive strategies based on predator-prey coevolution in 3D physical simulation," in *Proc. of the 6th Int. Conf. on Soft Computing and Intelligent Systems, and the 13th Int. Symp. on Advanced Intelligent Systems 2012 (SCIS-ISIS2012)*, 890-895, 2012.

© ISAROB 2013

The Eighteenth International Symposium on Artificial Life and Robotics 2013 (AROB 18th '13),
Daejeon Convention Center, Daejeon, Korea, January 30-February 1, 2013

Application of an actor–critic method to a robot using state representation based on distance between distributions

Manabu Gouko

Dept. of Mechanical Engineering and Intelligent Systems,Faculty of Engineering,
Tohoku Gakuin University, Japan
(Tel&Fax: 81-97-594-0181)

gouko@tjcc.tohoku-gakuin.ac.jp

Abstract: In this study, an actor–critic learning method was applied to a mobile robot. The method adopts a state representation based on distances between probability distributions. This state representation is less affected by the environment i.e., sensor signals maintain an identical state even under certain environmental changes. A simulation was performed and verified that the mobile robot can learn action relationship in the suite state using the actor–critic method.

Keywords: Reinforcement learning, actor–critic method, state representation, mobile robot

1 Introduction

Over the past few decades, several researches have been conducted on autonomous robots. Given the wide variety of external environments, robot's adaptability has become primarily importance. In a robot system, it is important to determine how the outside environment is processed as a state from sensor information.

In a previous study, a state representation was developed on the basis of noisy sensor data using distances between probability distributions[1]. This state representation is insensitive to the environment, i.e., sensor signals maintain an identical state even under certain environmental changes. Sensor signals are assumed to be expressed by probability distributions, and states are defined in terms of distances between distributions.

In the previous study, reinforcement learning to the autonomous mobile robot was applied using the proposed state representation. Then, by repeated trial and error, it was confirmed that the robot can learn a suitable state–action relationship that helps it to perform a given task. Specifically, the robot was trained by *Q*-learning method to move forward along walls. However, *Q*-learning cannot usually be applied to discrete state and action spaces. In such cases, the discrete state and the action of the robot must be defined prior to robot learning.

In this study, an actor–critic method was applied to a mobile robot, which uses the proposed state representation. Actor–critic is a reinforcement learning algorithm that can process a continuous state and action space, demanding the need to define the discrete state and action prior to robot learning.

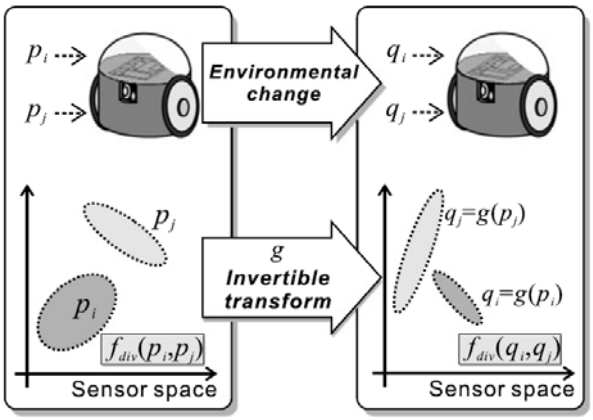

Fig. 1. State representation using distance between distributions [1].

A simulation was performed and verified that the mobile robot can learn action relationship in the suite state using the actor–critic method. The robot's ability to perform the moving task was confirmed.

2 State representation using distance between distributions

In this section, the proposed state representation was defined. In theoretical information and statistics, the distance between two probability distributions is expressed in several ways. *f*-divergence (*f*-div) is a family of measures introduced by Csiszár and Shields [2] that includes the well-known Kullback–Leibler divergence. The *f*-div of probability distribution $p_i(x)$ from $p_j(x)$ is defined as

$$f_{div}\big(p_i(x), p_j(x)\big) = \int p_j(x)\, f\left(\frac{p_i(x)}{p_j(x)}\right) dx, \qquad (1)$$

© ISAROB 2013

where $f(y)$ is a convex function defined for $y > 0$ and $f(1) = 0$. Qiao and Minematsu [3] proposed that *f*-div is invariant to invertible transforms and showed that all invariant measures are of the *f*-div form. Furthermore, they applied the invariant of measures to speech recognition [4].

3 Mobile Robot Application and Behavior Learning

Subsection 3.1shows how the proposed state representation is applied to a mobile robot. Subsection 3.2 describes behavior learning by the actor–critic method.

3.1 Mobile Robot Application

Figure 2 shows the autonomous mobile robot, named e-puck, used in our experiments.

The robot has eight infrared distance sensors. In our experiments, I used the six sensors labeled in Fig. 2. The next section describes an experiment in which the mobile robot performs a wall-following task. It was assumed that the robot's sensors respond only to differences in the wall color and not to wall position. Figure 3 shows how the state representation is acquired. First, while a robot moves in time Δt, each sensor memorizes M data. Next, the distances between the distributions of each sensor's data are calculated. In this study, the sensor distribution $i\ (1, \cdots, i, \cdots I)$is assumed to be Gaussian with mean μ_i and standard deviation σ_i. I used the Bhattacharyya distance (*BD*), a widely used measure of *f*-div, as the distance between two distributions. The *BD* between the distributions of the sensors i and j ($p_i$andp_j) is given by the following formula

$$BD(p_i, p_j) = \frac{1}{4}\frac{(\mu_i - \mu_j)}{\sigma_i^2 + \sigma_j^2} + \frac{1}{2}\ln\frac{\sigma_i^2 + \sigma_j^2}{2\sigma_i\sigma_j}. \quad (2)$$

BD is calculated from the sensor signal distributions acquired by the moving robot from time $t - \Delta t$ to t. The state vector at time t contains distances and is defined as follows:

$$\boldsymbol{v} = [\boldsymbol{v}_{1,2}, \boldsymbol{v}_{1,3}, \boldsymbol{v}_{1,4}, \boldsymbol{v}_{1,5}, \boldsymbol{v}_{1,6}, \boldsymbol{v}_{2,3}, \boldsymbol{v}_{2,4}, \boldsymbol{v}_{2,5}, \boldsymbol{v}_{2,6}, \boldsymbol{v}_{3,4}, \boldsymbol{v}_{3,5}, \boldsymbol{v}_{3,6}, \boldsymbol{v}_{4,5}, \boldsymbol{v}_{4,6}, \boldsymbol{v}_{5,6}]^{\boldsymbol{T}}, \quad (3)$$

where $\boldsymbol{v}_{i,j}$ is $BD(p_i, p_j)$. In this formulation, when an object is outside the sensing range of a sensor and the distribution is 0, the distance between distributions cannot be calculated. In such a situation, the distance between the distributions of that sensor and other sensors is set to 0.

3.2 Behavior learning by actor–critic method

This subsection explains behavior learning using reinforcement learning [5]. In the reinforcement learning framework, a robot learns a suitable state–action mapping without prior knowledge of its dynamics or environment.

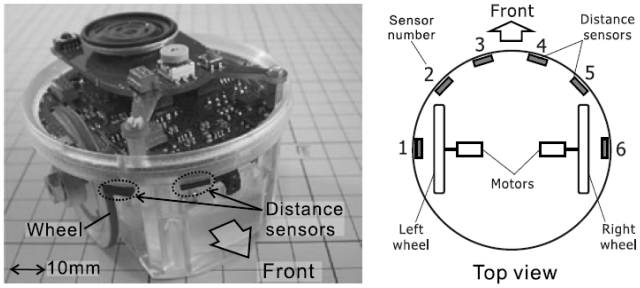

Fig. 2. Autonomous mobile robot e-puck and its infrared distance sensors [1].

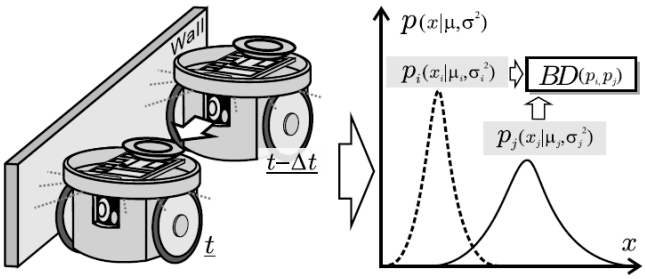

Fig. 3. Proposed state representation using e-puck. While a robot moves in time Δt, Mdata are memorized by every sensor. Next, the distances between the distributions of each sensor's data are calculated [1].

The actor–critic learning method is applied, which is a reinforcement learning algorithm that can handle a continuous state and action spaces. This method needs a critic, which estimates a reward expectation from a state. It also needs an actor as a controller. The actor outputs a motor commanding response to the state.

4 Experimental Result and Discussions

In this section, I present and discuss the experimental r esult. The robot executed behavior learning and obtaine d state–action mapping. After the learning process, the sensor signal was artificially transformed and the robot can perform a task using the acquired mapping was ver ified.

The robot was then placed in the experimental environment shown in Fig. 4.

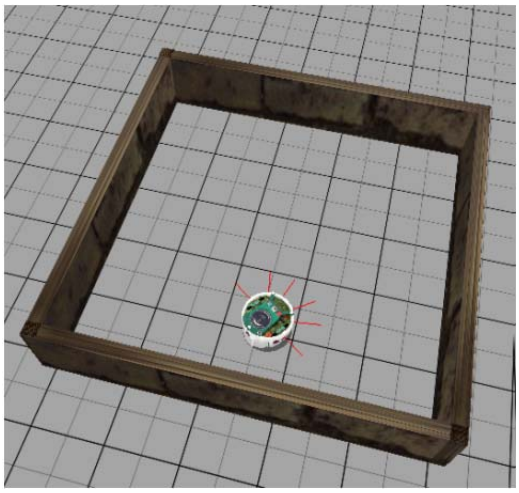

Fig. 4. Experimental environment.

Behavior learning was assessed in a wall-following task. When all conditions given below were satisfied at time t, the reward was defined as follows,

$$r_t = x_{t,6} - x_{t,3} + m_l + m_r \,. \tag{4}$$

Here $s_{t,6}$ and $s_{t,3}$ are signal outputs by sensors 6 and 3, respectively, and m_l and m_r are the respective motor commands of the left and right wheel. In this experiment, Δt was set to 1 sec and M was set to 20.

The learning time was 10,000 steps (one step = Δt). The robot was placed near the wall at every 500 steps during learning. After learning, I confirmed the success of the learning behavior. Figure 5 shows the obtained reward data for the three nonlinear transformations shown below (Equations 5, 6, and 7).

$$x'_{t,i} = 10x_{t,i} - 5 \quad (\mathrm{i} = 1, \cdots, 6) \tag{5}$$

$$x'_{t,i} = \sqrt{x_{t,i}} \quad (\mathrm{i} = 1, \cdots, 6) \tag{6}$$

$$x'_{t,i} = x_{t,i}^2 \quad (\mathrm{i} = 1, \cdots, 6) \tag{7}$$

In this figure, the total rewards accumulated over 200 steps are normalized by the total rewards obtained by the robot with normal sensor signals.

The performance of the robot using our proposed state representation showed minimal degradation. Note that these nonlinear transformations did not correct for physical environmental changes. The results indicate that the proposed state representation model is applicable to all invertible transformations, including nonlinear transformations.

5 Conclusions

In this study, I applied an actor–critic learning method to a mobile robot. The method uses a proposed state representation based on distances between probability distributions. This state representation is insensitive to the environment,

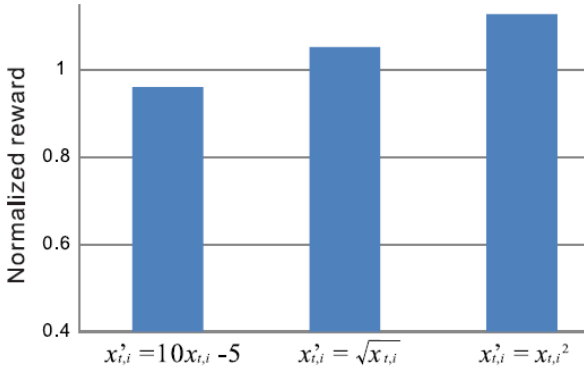

Fig. 5. Normalized rewards.

i.e., sensor signals maintain an identical state even under certain environmental changes. A simulation was performed and verified that the mobile robot can learn action relationship in the suite state using the actor–critic method.

Acknowledgements

This research was partially supported by the Ministry of Education, Science, Sports and Culture, Grant-in-Aid for Young Scientists (B), 24700196, 2012.

References

[1] Gouko M. and Kobayashi Y. (2012) A State Representation Model for Robots Unaffectedby Environmental Changes. International Journal of Social Robotics, DOI:10.1007/s12369-012-0164-9.

[2] Csiszár I, Shields PC (2004) Information theory and statistics: a tutorial. Now, Boston

[3] Qiao Y. and Minematsu N. (2008) *f*-divergence is a generalized invariant measure between distributions. In: Proceedings of 10th annual conference of the international speech communication association, pp 1349–1352.z

[4] Qiao Y. and Minematsu N. (2010) A study on invariance of *f*-divergence and its application to speech recognition. IEEE TransSignal Process, 58 (7): 3884–3890.

[5] Sutton RS, Barto AG (1998) Reinforcement learning: an introduction. The MIT Press, Cambridge.

© ISAROB 2013

Color Halftoning Using the Error Diffusion Method by the Edge Adjustment and the False Colored Limit

Kazuya Kadoya[1], Ken-ichi Tanaka[2]

Meiji University, Japan[1,2]
(Tel: [1]090-7724-0425 , [2]090-2146-7873)

[1]ce11025@meiji.ac.jp, [2]tanaken@meiji.ac.jp

Abstract: In the device that the usable number of the colors and density of printer or facsimile communication are limited, the digital halftoning is an important technique. When you use error diffusion method for mix of color and monochrome images, false color appear in monochrome parts. The images were evaluated using the Mean Squere Error. The image evaluation of MSE had rise. And so the evaluation with the monitor, a very good value was in this way provided. Full-color images grayscale is not contaminated and black and white images, images of the experimental results of different patterns, without compromising the quality of the original error diffusion method, we solve the problem.

Keywords: color halftoning, error diffusion method, grayscale

1 INTRODUCTION

Digital halftoning [1] includes many methods. For example, there are the applications of the combination optimization problem, dither method, the error diffusion method [2]. Error diffusion method is applied easy for color image halftoning, and has already been put to practical use.

However, as for the problems of the error diffusion method, a domain of the grayscale [3] is that a color unrelated at all occurred when the image in a part of the color image is processed though it is necessary for white and black to express a domain of the gray scale. In other words it means that a false color [4] occurred.

Among others, there is a problem that this processing scatters an error, some outline parts become dim. we suggested the new error diffusion method that we emphasized an edge, Contrast adjustment and limited a false color, to solve these two problems.

2 TECHNIQUE

We will show a method used in this experiment here.

2.1 The emphasis of the edge

The emphasis of the edge used a Gaussian [5] filter with unsharp mask on this occasion again.

The unsharp mask is a method to add the difference share with the original image after shading off an image once. When blur the image, equation (1) used a Gaussian filter using a Gaussian functions.

$$f(x,y) = \frac{1}{2\pi\sigma^2} exp\left(-\frac{x^2+y^2}{2\sigma^2}\right) \qquad (1)$$

σ of the Gaussian coefficient assumed it 1 then.

2.2 The adjustment of the contrast

The adjustment of the contrast adjusted the bright place becomes brighter, the dark place becomes darker with the sigmoid tone curve [6] called the highlight shadow to darken to apply to a variety of original images.

In this study is adjusting the contrast by Equation (2) to coordinate the contrast.

$$\text{Before processing} = 128 \times \left(\frac{After\ processing}{128}\right)^C \qquad (2)$$

This expression (2) supports only numerical value to 0-128 of the brightness before the processing. The subsequent brightness changes the degree of the increase rate symmetrically.

Not only a hue improves by doing contrast adjustment, but also the place that brightness is remarkable and is high or is low becomes easy to make a hit for the halftoning of the false color limit.

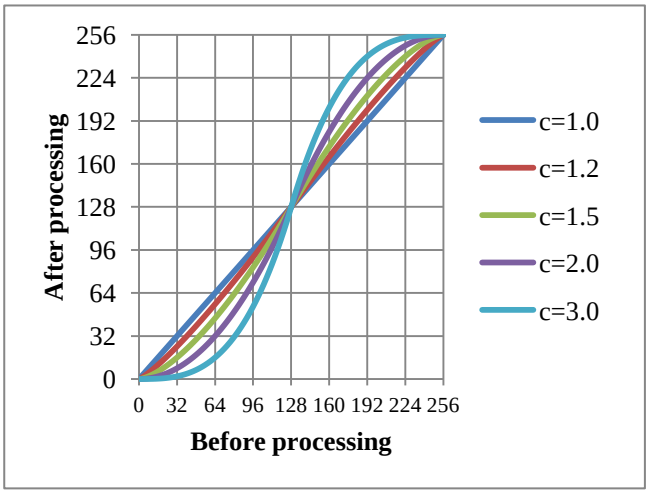

Fig. 1. The illustration of something

© ISAROB 2013

2.3 False color limit

2.3.1 Basic concept of error diffusion method

Fig.2 shows basic concept of the error diffusion me thod. Data f (n) is assumed that the value within the r ange of -1 ~ +1 is taken.

A. Data f (k) in n=k is read.Value g(k) ,which the qua ntization error is added, is given as follows,

$$g(k) = f(k) + e(k-1) \quad (3)$$

where, if k is equal to zero, quantization error $e(k-1)$ is equal to zero. This is because that n is greater that zero.

B. The values $g(k)$ are compared with threshold (=0) and binary number $H(k)$ is obtained as follows.

$$H(k) = \begin{cases} +1 (g(k) \geq 0) \\ -1 (g(k) < 0) \end{cases} \quad (4)$$

C. Quantization error $s(k)$ which generated between $g(k)$ and $H(k)$ is given as follows.

$$s(k) = g(k) - H(k) \quad (5)$$

D. Value $g(k+1)$, which the quantization error $e(k)$ i s added, given as follows.

$$g(k+1) = f(k+1) + e(k) \quad (6)$$

E. Ass data $\{f(n)\}$ are quantized by a similar process that consisting of the procedure 2~4, mentioned ab ove. Output binary number $\{H(n)\}$ is obtained.

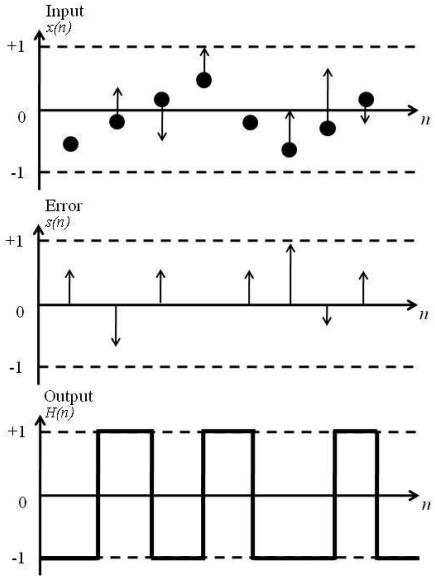

Fig. 2. Basic concept of error diffusion method

2.3.2 Extension to color image

The color image is composed by the combination o f each Red, Green, and Blue (three primary colors). At the color image the case of Windows Bit Map, the t hree primary colors of R, G and B has density inform ation of 0-255 respectively. Therefore, the color data is first divided into each primary color element. And, pr ocessing similar to the case of a monochrome image i s done. Each primary color results are united at the en d. Then, the color image can be treated.

In this study used error diffusivity of Floyd & Stei nberg which we showed in table 1. The pixels that sc attered an error by scattering an error in the pixel that does not perform threshold processing become easy to exceed the threshold. In addition, the scanning assume d it raster scanning.

Table 1. Floyd & Steinberg

g(-1,0)=0	g(0,0)=0	g(1,0)=7/16
g(-1,1)=3/16	g(0,1)=5/16	g(1,1)=1/16

2.3.3 New concept of error diffusion method

When the level of the original image color components R is equal to G, we keep that R is equal to G in the same position of the halftoning image. When the level of the original image color components R is equal to B, we keep that R is equal to B in the same position of the halftoning image. When the level of the original image color components B is equal to G, we keep that B is equal to G in the same position of the halftoning image. In case of a full-color image is constructed in grayscale, Halftone images should not be generated in colors that are quit irrelevant in black and white images.

Figure 3 shows relations of Red, Green, Blue, Cyan Magenta and Yellow.

Table 2 shows the list of the false color limit.

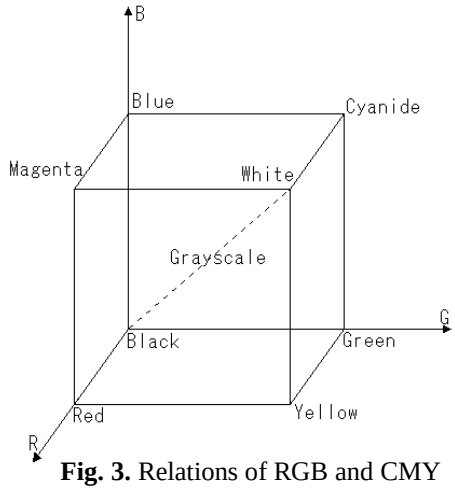

Fig. 3. Relations of RGB and CMY

Table 2. False color limit

Input data	The color that I can output	False color
R=G=B	White, Black	Red, Green, Blue, Cyanide, Magenta, Yellow
R=G	White, Black, Blue, Yellow	Red, Green, Cyanide, Magenta
R=B	White, Black, Green, Magenta	Red, Blue, Cyanide, Yellow
B=G	White, Black, Red, Cyanide	Green, Blue, Magenta, Yellow

© ISAROB 2013

2.4 Evaluation method

It is a picture evaluation of the halftoning about the color image.

The valuation basis of a color image carries out convolution of the Gaussian filter to the RGB ingredient of the quantized image, and to create a pseudo-color image is represented. In this study, minimizing the mean squared Euclidean distance in RGB color space of the image and the original image.

The MSE is defined as the equation (7).

$$MSE = \frac{1}{MN}\sum_{i=0}^{M-1}\sum_{j=0}^{N-1}\{f'(i,j) - f(i,j)\}^2 \qquad (7)$$

In $f(i,j)$ in original image, $f'(i,j)$ decoding image, M and N show the size of the image.

It may be said that a high quality image was provided if a MSE level is small.

3 EXPERIMENTAL RESULT

Comparing the processed image with conventional and suggestion method error diffusion method.

At first the right half compared it with an image of "Balloon" which became the grayscale. Fig 4 shows the results.

The left image of Fig 4 is the image which it processed by the conventional error diffusion method. The right image is the image which it processed by the error diffusion method of the proposed method.

Proposed method understands that a false color does not occur. The grayscale area is the error diffusion processing is not only black and white.

Table 3 shows an evaluation value for this image. 63 people were monitored. Good results were obtained with the monitor and MSE.

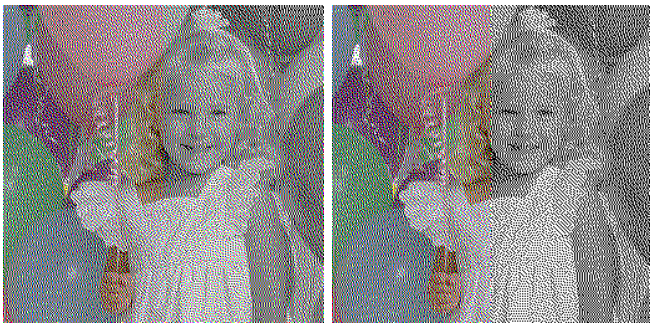

(a) Conventional method (b) Proposed method

Fig. 4. Comparison image of "Balloon" image

Table 3. "Grayscale Balloon" experimental results

	MSE	Monitor[people]
Conventional method	57.4170	1
Proposed method	56.1591	62

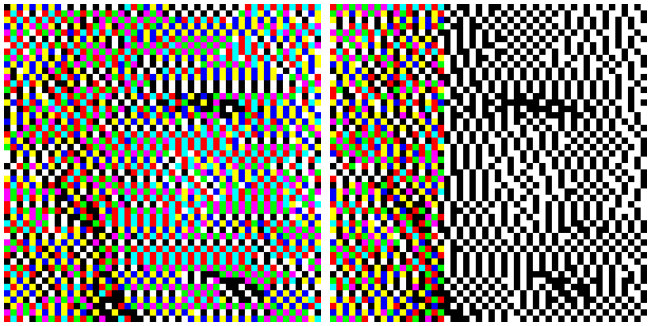

(a) Conventional method (b) Proposed method

Fig. 5. Enlargement of the right eye

Fig 5 shows an enlargement of the right eye of girl having Balloon in Fig 4.

In this study compare it with six kinds of original images "Aerial" "Airplane" "Balloon" "Earth" "Mandrill" "tulip". Table 4 shows an evaluation value for each image.

Good results were obtained with the monitor and MSE.

There were not many differences of the value of MSE. However, the difference of the number of people with the monitor was clearly.

Here is an example "Balloon" and "Mandrill" image shows the results.

Fig 6 shows the original image. Fig 7 shows an image subjected to unsharp mask and contrast adjustment. Fig 8 shows an image of the conventional error diffusion method. Fig 9 shows images of the proposed error diffusion method.

The left image "Balloon", the right image "Mandrill" images show.

Table 3. Experimental results

		MSE	Monitor [people]
Aerial	conventional method	232.1830	5
	proposed method	197.6562	58
Airplane	conventional method	227.3057	2
	proposed method	188.3521	61
Balloon	conventional method	57.4170	1
	proposed method	56.1591	62
Earth	conventional method	103.9658	7
	proposed method	94.1132	56
Mandrill	conventional method	382.2701	2
	proposed method	355.2142	61
Tulip	conventional method	420.8529	3
	proposed method	409.8079	60

© ISAROB 2013

(a) Ballon (b) Mandrill

Fig. 6. Original image

(a) Ballon (b) Mandrill

Fig. 7. Unsharp mask and contrast adjustment images

(a) Ballon (b) Mandrill

Fig. 8. The conventional error diffusion method

(a) Ballon (b) Mandrill

Fig. 9. The proposed error diffusion method

4 CONCLUSION

The advantages of unsharp mask

- It was improvement that "large part of the change in gradation blurred" is defect of error diffusion method.
- Easy to handle.

The advantages of contrast adjustment

- Easier to hit when you try to limit false color.
- An objective visual evaluation increase.

The advantages of false color limit

- False color is eliminated.
- An objective visual evaluation increase.
- The grayscale is expressed more beautifully.

Good images were provided visually by taking above-mentioned process.

In the future, we will try to do a thing as a variety of value. For example, there are Gaussian coefficients and contrast adjustment coefficients. We want to obtain a good image and more.

REFERENCES

[1] T. Umemura, H. Aguirre, K. Tanaka, "Multi-Level Image Halftoning Technique with Genetic Algorithms," IEICE transactions on fundamentals of electronics, communications and computer sciences E85-A, no.8, pp.1892-1897 (2002).

[2] K. Miyake, M. Saito, "An Evaluation Method for the Images Obtained by Multi-Level Error Diffusion," J. Imag .Sci. Technol. 42, 155-120 (1998).

[3] R. W. Floyd, L. steinberg "An adaptive algorithm for spatial gray-scale," Prpc. Soc. Inf Disp., 17, pp.75-77 (1976).

[4] K. Tanaka, "Error Diffusion Method for Color Images without False Color," The Institute of Image Information and Television Engineers, 33(51), pp45-48 (2009).

[5] F. Catté, P.-L. Lions, J.-M. Morel, and T. Coll, "Image selective smoothing and edge detection by nonlinear diffusion" in SIAM J.Numer. Anal., vol. 29, pp. 182–193 (Feb. 1992).

[6] K. Tanaka and H. Arai, "Color Halftoning without Generation of False Color," IWAIT2011, (2011)

© ISAROB 2013

The Eighteenth International Symposium on Artificial Life and Robotics 2013 (AROB 18th '13),
Daejeon Convention Center, Daejeon, Korea, January 30-February 1, 2013

The three optimization methods of searching the effective combination dither matrix

Shohei Niinuma and Ken-ichi Tanaka

Meiji University, Japan
(Tel:044-934-7562)

ce11068@meiji.ac.jp

Abstract: In this paper, we proposed the dither matrix for color image with optimization methods. A dither method displays a grayscale picture that is expressed two colors. They are black and white values. Thereby, in a picture, although it is two values, in view of a distant view, it seems that there is a monochrome shade. I used three methods that are Genetic Algorithm (GA), Simulated Annealing (SA), and taboo searching (TS). The criterion of comparing data is cost E that is the evaluation value of reproduction of gray image. And it is addition of evaluated value of gray level and evaluated value of contrast.

Keywords: Dither method,GA,SA,TS.

1 INTRODUCTION

Dither method [1] is the methods used by digital halftoning. Nowadays, There are some popularly methods of dither matrix. Bayer dither, mesh dither, and so on. These methods are actually good on a viewpoint of image quality. However, there is difference of evaluation value for using different images. In addition, conventional methods, Bayer dither for example, are not really optimal combination on a viewpoint of combinational optimization problem.

In this paper, we proposed the dither matrix for color image with optimization methods. I used three methods that are Genetic Algorithm (GA) [2],[3],[4], Simulated Annealing(SA) [5], and taboo searching(TS) [6]. Processing procedure is follows,

(1) The color image is composed of eight bits respectively of red, green, blue, and becomes 24 bits in total. Therefore, the color image is dividing into a red element, a green element, a blue element.

(2) And, the divided each element is optimized severally.

(3) The optimized element is synthesized and the color halftoning image is made.

The criterion of comparing data is cost E that is the evaluation value of gray level. And it is addition of cost E_m and cost E_c. Individuals that have small cost E are prior carried over.

2 DITHER METHOD

Organized dither method, as shown in Fig.1. below, the original image dither matrix (or Dither pattern) called intentional noise $D(i;\ j)i;\ j\ =\ 0;\ 1;\ldots\ldots;N\text{-}1$ are added, and then quantized. Now, the original image is shown as $f(n_1,n_2)\ n_1,\ n_1 = 0,1,\ldots\ldots,\mathrm{M}-1$ of M×M. The handling of Fig.2. is equivalent with choosing the threshold as expression (1).

$$f(n_1,n_2) = \begin{cases} 1 & f(n_1;n_2) \geq p \\ 0 & f(n_1;n_2) < p \end{cases} \quad (1)$$

But

$$i = n_1\ mod\ N \quad (2)$$
$$j = n_2\ mod\ N \quad (3)$$

In this case, it is the operation method, and A $mode\ B$ means the rest that divided, A in B.

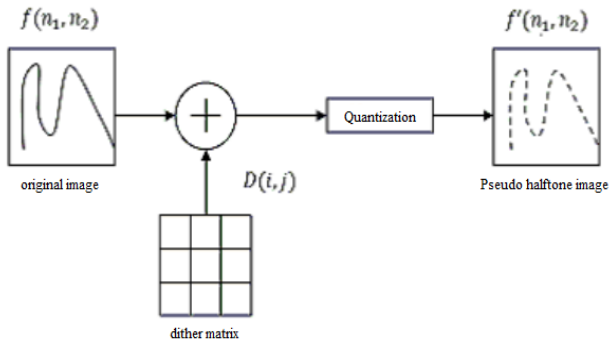

Fig. 1. Principle of the organized dither method

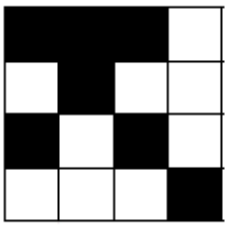

Fig. 2. Threshold change image

© ISAROB 2013

3 OPTIMIZATION METHODHOD

3.1 Genetic Algorithm

In this study, individuals are themselves. Elements of individuals are threshold level of gray level from 0 to 255. The threshold levels are Equation.1. "I[x]" is position x of the matrix. "i" is numerical number from 0 to 15. The numeral numbers of elements of Table 1 are "i" of equation (1).

The same number is not set in the same individual. GA is to convert grouping and to search what combination of elements is the optimal combination. In this study, the operation of GA which shows is as below.

(1) The matrices which have elements set in at random are prepared

(2) Set up solution of cost function E. Cost function E is the addition of cost E_m and cost E_c. Cost E_m is evaluated value of gray level. Cost E_c is Evaluated value of contrast. Equation of cost function E is as below.

(3) The individuals of next generation are decided by using the tournament method.

(4) Selecting two individuals and doing single point Crossover.

(5) Two elements of the individual which is selected at random are exchanged.

(6) Running over from (2) to (5) until the numbers of generations reach the generation number.

The number of individual is 200, the number of generation is 40, the probability of shakeout is 0.1 and the probability of mutation evolution is 0.01.

Single point Crossover is exchanging the position of elemental number from 0 to X of individual. The position of elemental number X is selected at random.

If the same elements are in the same individual, empty number of element sets one of duplicative element.

3.2 Simulated Annealing

In this paper, the algorithm of SA is as below.

(1) An individual that have matrices which is set elements in at random is prepared.

(2) New individual is made by changing element of the individual which is made at operation (1).

(3) Comparing two individuals

(4) New individual is made by exchanging element of the individual getting better evaluated value

(5) Running over from (3) to (4) until the satisfaction of the conditions.

In this study, the conditions are that temperature is under number which is set at hand or evaluated value of SA is better than Bayer method.

3.3 Taboo searching

The method of taboo searching is as below.

(1) The matrices which have elements set in at random are prepared (it is named individual A)
(2) Making some individuals based the individual A
(3) Evaluating and comparing these individuals
(4) The best evaluated value individual (it is named individual B) is selected by these individuals
(5) If combination of individual A and B has be selected before, return to operation (2)
(6) Comparing individual A and individual B
(7) If individual A is better than individual B, return to operation (2)
(8) If individual B is better than individual A, making some individuals based the individual B
(9) Running over from (3) to (8) until numbers of repeat time surpass numbers of generations

4 FLOW CHART

Figure 3 shows the steps from original image to halftone image.

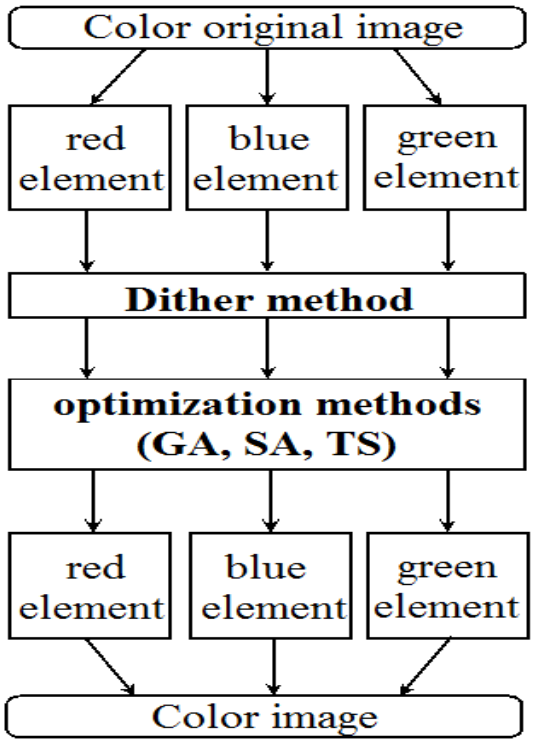

Fig. 3. Flow of optimized halftone image

5 EXPERIMENTAL RESULT

The following shows experimental results that was used this time. The picture is "Balloon" and "Mandrill" and "Parots" Using. In this study, I used the panmagic square dither because panmagic square dither was better than the bayer dither. Evaluation was performed by comparing the values of E. visually good Pseudo-gray image is given that by reducing the Evaluation value of contrast E_c and the Evaluation of the tone reproduction E_m. From the above, the evaluation value is represented by Expression (4).

$$E = \alpha_m E_m + \alpha_c E_c \quad (4)$$

An above expression's "α_m" and "α_c" are Weighting coefficients."α_m" and "α_c" is related to the following.

$$\alpha_m + \alpha_c = 1 \quad (5)$$

Changes in the tone reproduction and contrast of the image obtained according to the weighting coefficients.

Table 1. Experimental results using GA

Image name	E_m	E_c	E
Blue element "Balloon"	7.4926	127.6042	103.5820
Green element "Balloon"	6.5050	127.1885	103.0519
Red element "Balloon"	6.8001	127.2975	103.1981
Blue element "Mandrill"	16.5764	123.7008	102.2760
Green element "Mandrill"	16.2016	124.0656	102.4928
Red element "Mandrill"	13.8551	125.0254	102.7914
Blue element "Parrots"	8.5978	125.8586	102.4065
Green element "Parrots"	9.2138	126.0804	102.7071
Red element "Parrots"	8.5727	126.0877	102.5848

Table 2. Experimental results using SA

Image name	E_m	E_c	E
Blue element "Balloon"	6.9416	127.0003	102.9885
Green element "Balloon"	7.0533	127.2086	103.1775
Red element "Balloon"	6.8086	127.3100	103.2097
Blue element "Mandrill"	16.6493	123.7304	102.3142
Green element "Mandrill"	16.4153	123.7034	102.2458
Red element "Mandrill"	14.2207	125.1569	102.9696
Blue element "Parrots"	9.1002	125.8621	102.5097
Green element "Parrots"	8.6757	126.1537	102.6581
Red element "Parrots"	8.4334	126.0297	102.5104

Figure.4 shows the original image used in the experiment. The blue element of the original image was shown in Figure 5 and the green element of the original image was in Figure 6, the red element of the original image was in Figure 7. In addition, Figure 8 shows a synthesis of three elements. And Figure.9 shows an image using a panmagic square dither. Finally, Table 4 shows the evaluation of the best things in GA and SA and TS, which were compared with the panmagic square dither method's images.

Fig. 4. Original image

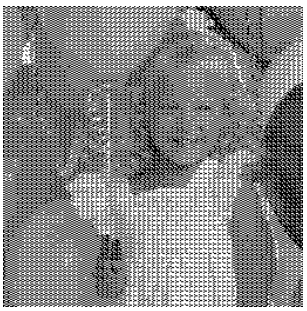

Fig. 5. Blue element

© ISAROB 2013

Table 3. Experimental results using TS

Image name	E_m	E_c	E
Blue element "Balloon"	9.0856	126.9960	103.4139
Green element "Balloon"	11.2213	127.2162	104.0172
Red element "Balloon"	8.7723	127.3087	103.6014
Blue element "Mandrill"	18.4120	123.9069	102.8079
Green element "Mandrill"	17.5246	124.0483	102.7435
Red element "Mandrill"	14.3682	125.1369	102.9832
Blue element "Parrots"	10.4983	125.8647	102.7915
Green element "Parrots"	11.6400	126.2159	103.3007
Red element "Parrots"	10.7327	126.1812	103.0915

Fig. 6. Green element

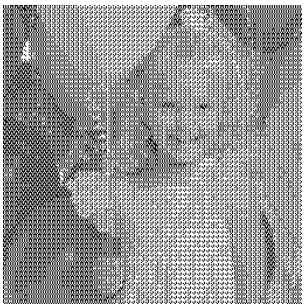

Fig. 7. Red element

Fig. 8. Synthetic image

Fig. 9. panmagic image

Table 4. Comparison of evaluation values about each element in "Balloon"

	Blue element	Green element	Red element
panmagic square dither	103.3915	103.5731	103.3127
The optimized value	102.9885	103.0519	103.1981

4 CONCLUSION

By using optimization techniques, in this study, obtained more good evaluation value than the conventional evaluation. Then, in the three methods, considering both calculation time and the evaluation value, we think that SA is the most good in the three methods. Because SA spent the shortest time in three method as the calculation and got good evaluation values on the average. Then, we obtained some opinions that this technique has better than conventional method in visually. In the future we would like to strive to improve the assessment by changing the input values during optimization. In addition, We would like to shorten the time of optimization about GA,SA and TS.

REFERENCES

[1] Tsuneyasu Kato and Ken-ichi Tanaka, "The optimal method of searching the effective combination of dither matrix" ARTIFICIAL LIFE AND ROBOTICS No.16 pp140.(2011)

[2] D.E.Goldberg, "Genetic Algorithm in Search, Optimization, and Machine Leaming", Addison-Wesley, Reading, Mass(1989)

[3] S.Kirtpatrick, C.D.Gelatt and M.P.Vecchi, "Optimization by Simulated Annealing", Science, vol.220, pp.671-680(1983)

[4] T.Umemura, H.Aguirre,and K.Tanaka,"Multi-Level Image Halftoning Technique with Genetic Algorithms", IEICE Trans. Fundamentals, Vol.E85-A, No.8, pp.1892-1897,Aug 2002

[5]K. Tanaka, "halftone processing of images for SA" Journal of ITEJ, Vol.61 No.6 pp828-837 (2007)

[6] F.Glover. "Tabu search II". ORSA Journal on Computing, 2:4-32,(1989)

© ISAROB 2013

The Eighteenth International Symposium on Artificial Life and Robotics 2013 (AROB 18th '13),
Daejeon Convention Center, Daejeon, Korea, January 30-February 1, 2013

Inverse halftoning of color image using unsharp mask

Hiroki Matsuo[1] and Ken-ici Tanaka[2]

Meiji University, Japan
(Tel: 044-934-7562)

[1]ce11082@meiji.ac.jp
[2]tanaken@meiji.ac.jp

Abstract: The inverse halftoning is image restoration technique to make the grayscale image from binary image that is processed by digital halftoning. Inverse halftoning techniques need the removal of the noise. This is because the noise is added to reconstruct the pseudo grayscale image using black and white. In inverse halftoning image, important information also blurred when the noise in inverse halftoning image is reduced. In other hand, when the edge in inverse halftoning image is left, reducing the noise becomes insufficient. The goal of the inverse halftoning technique that can reduce the noise on inverse halftone image and that can emphasize the edge on inverse halftoning image. Therefore we propose inverse halftoning to emphasize the edge using unsharp mask. As a result of using unsharp mask, SNR became higher than conventional method and became easy to look visually.

Keywords: inverse halftonig, unsharp mask, canny method.

1 INTRODUCTION

The inverse halftoning is processing that restores the image made binary by the half tone processing to former gray-scale image. Inverse halftoning displays the pixel value with 0 (white) or 255 (black) bordering on a threshold value from 0 to 255. And, when the image is made binary, it is an expression technique as mixing the noise, and doing the one that is not a continuous step, etc. using the mistake of eyes of man who shows it. The one that is called the dither method and a random dither as a past technique is enumerated in the half tone processing. And, because the noise is mixed when the half tone was processed, it is necessary to remove it though the inverse halftoning returns the image made binary thus to former step value. Even perfection has not lived yet as a past technique of the inverse halftoning though the restoration of the image of the level that is only these past techniques can expect though a smoothing filter, a median filter, and gaussian filter, etc. are proposed. Because there is an evil such as growing dim of the edge part of the image to remove even the high frequency elements ,in a word, necessary information in the image other than the noise when it tries to obtain a smooth image by the inverse halftoning. Oppositely, the removal of the noise becomes insufficient when it tries to emphasize the edge part of the image, and the great result is not obtained so much as restoration accuracy of the image. The removal of the noise and the emphasis of the edge relate closely in the restoration of the image like this, and the design of processing where it can be difficultly achieved is expected as for doing the two highly accurate at the same time.

Therefore, we removed the noise by a mean filter and the gaussian filter, and performed unsharp mask to the edge part. From this, we are aiming that get the highly precise reconstruction image which satisfied both removal of the noise and emphasis of the edge.

2 INVERSE HALFTONING

Inverse halftoning is processing to return to the gradation of original image which is binarized by halftoning, and to become easy to look visually. Representative inverse halftoning processing includes a smoothing filter, a gaussian filter, a median filter.

In this paper, halftoning image is used Floyd & Steinberg..

2.1 Smoothing filter

The Smoothing filter is processing to let the mean of attention pixel and the pixel of the eight pixels of neighboring pixels be a pixel value of a new attention pixel. Fig. 1 shows that pixel (x,y) with a focus on nine pixels can be expressed as following equation..

$$f'(x,y) = f(x,y) * M(x,y) \qquad (1)$$

Here, * is the convolution of the above equation, M(x,y) is the mask of Fig. 2, f(x,y) is the attention pixel and the neighboring pixels, f'(x,y) represents a new pixel that.

© ISAROB 2013

(-1,1)	(0,1)	(1,1)
(-1,0)	(0,0)	(1,0)
(-1,-1)	(0,-1)	(1,-1)

Fig. 1. operator

1	1	1
1	1	1
1	1	1

$\times \frac{1}{9}$

Fig. 2. smoothing filter

2.2 Gaussian filter

Gaussian filter is a process of determining the weighting factor of the neighborhood surrounding the pixel of interest using a Gaussian distribution. Gaussian distribution can be expressed as follows.

$$f(x,y) = \frac{1}{\sqrt{2\pi}\sigma}\exp\left(-\frac{x^2+y^2}{2\sigma^2}\right) \qquad (2)$$

In this paper, σ=0.53. Gaussian filter is obtained by convolving a mask that obtained by calculating the above equation as 3 × 3 pixels and attention pixel. Because Gaussian distribution is a normal distribution, the sum of the coefficients is always 1. Therefore, the pixel values before and after remains unchanged, so it can be folded in the coefficients.

2.3 Median filter

Median filter is a processing of decreasing order of pixel values in the neighborhood surrounding the pixel of interest, and let the value of middle be attention pixel.

2.4 Unsharp mask

Unsharp mask, when interpreted literally, "Sharp eliminate" becomes a means, but it is actually sharpen the image processing. Unsharp masking is often used to correct blurry images. Unsharp mask algorithm is as follows.

Means to sharpen the image is that increasing the difference between the pixel values of adjacent pixels. Applying a blur to the contrary is a process that continuous gradation is smoothly. Plus the blurred images to original image minus the difference and original image then can get a large picture of the difference gradation. This is a basic algorithm of unsharp mask. However, when the entire image to be processed, it is too sharp, and sharpens the noise, the picture may become ugly. Therefore, unsharp mask determine "quantity" and "Range" and "threshold", and processes into the portion which fulfilled conditions.

"Quantity" specifies the percentage K of change in pixel value. K is determined how much a sharp is used. " Quantity" can be expressed as follows.

$$f'(x,y) = f(x,y) + \big(f(x,y) - g(x,y)\big) * K \qquad (3)$$

Here, f(x,y) is the image before blurring, g(x,y) is the image blurred.

"Range" specifies the range of processing in pixel value. when the range is small, processing is only reflected in neighboring pixels. But, when the range is large, processing is reflected in far pixel. Therefore, an effect becomes large, so that the range is large. In this paper, we perform an operation on nine pixels of 3 × 3.

"Threshold" specifies processing, when there is the gradation difference that is how much. If the threshold is high, the noise can be cut neatly, but cut it to the edge when too high. On the contrary, when the threshold is too low, a noise is left and becomes the dirty image. Therefore, it is necessary to determine the appropriate threshold. However, it cannot isolate the noise and the edge with one threshold, because inverse halftoning image has much noise. Therefore, this paper describes unsharp mask only edge part by canny method.

2.5 Canny method

Canny method is a method to detect edge that is t hinned by combining the Sobel filter and Gaussian filt er. Canny method algorithm is processing of the image smoothing; the calculation of the gradient direction ed ge strength, edge thinning process is performed in the order of Hysteresis thresholding. Each step of the Can ny method is described as follows.

- Image smoothing

  Performed by the Gaussian smoothing filter to the input image image, and reduce the effects of noise.

- The calculation of the gradient direction edge strength

  After obtaining the derivative in each direction by Sobel filter, the strength and direction of each pixel are calculated. Sobel filter to calculate differential value of the horizontal fx and vertical fy by convoluting the mask in Fig. 3,4 and the attention pixel. Edge intensity E and gradient direction θ obtained by the following equation is obtained from fx and fy.

$$e = \sqrt{fx^2 + fy^2} \qquad (4)$$

$$\theta = \frac{fy}{fx} \qquad (5)$$

The gradient direction θ calculates the pixel edge direction in 3 × 3, can be classified into four directions, as shown in Fig. 5,6,7. Four-way can be classified by splitting in the range of θ is calculated.

$$\begin{cases} 0° \text{ direction}: -0.4142 < \theta \le 0.4142 \\ 45° \text{ direction}: \quad 0.4142 < \theta < 2.4142 \\ 90° \text{ direction}: \quad |\theta| \ge 0.4142 \\ 135° \text{ direction}: -2.4142 < \theta \le -0.4142 \end{cases}$$

© ISAROB 2013

Here, the red line in Fig. 5,6,7,8 is the direction of an edge pixel, the black pixels is adjacent pixels in the vertical direction of the edge pixels.

- Edge thinning

  Proccess of edge thinning slim thickened edge by Gaussian filter. Comparing the pixel value of pixels adjacent vertical edges as in Fig. 5,6,7,8, and edge value to 0 if pixel value of edge is not max. Then, edge can be made thin.

- Hysteresis thresholding

  Two thresholds are set as high value and as low values. High threshold is detected as edge pixel, and low threshold is detected as there is no edge pixel. When a lower threshold than under a high threshold, attention pixel is detected as edge pixel if edge pixel exists in the neighborhood and attention pixel is detected as there is no edge pixel if edge pixel doesn't exist in the neighborhood. In this paper, high threshold to 128, low threshold to 20.

-1	0	1
-2	0	2
-1	0	1

Fig. 3. Horizontal direction fx

-1	-2	-1
0	0	0
1	2	1

Fig. 4. Vertical direction fx

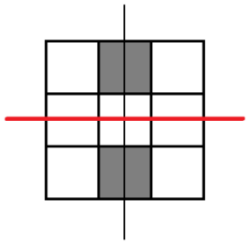

Fig. 5. 0^0 direction

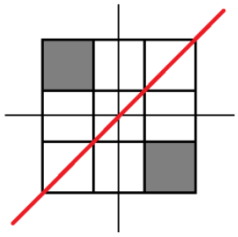

Fig. 6. 45^0 direction

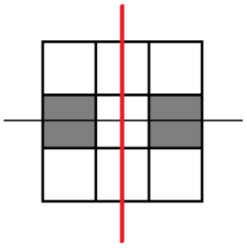

Fig. 7. 90^0 direction

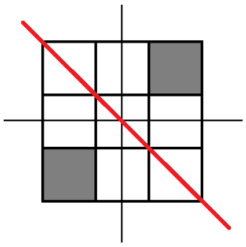

Fig. 8. 135^0 direction

3 PROCESS OF PROPOSAL METHOD

Fig. 9 shows the experimental procedure in this paper. The unsharp mask gradates processing use that smoothing filter, gaussian filter, a combination of three filter median filter. As a result of having inspected it with six pieces of images, the best thing is to use Gaussian filter twice. Therefore, gradate processing uses Gaussian filter twice in this paper.

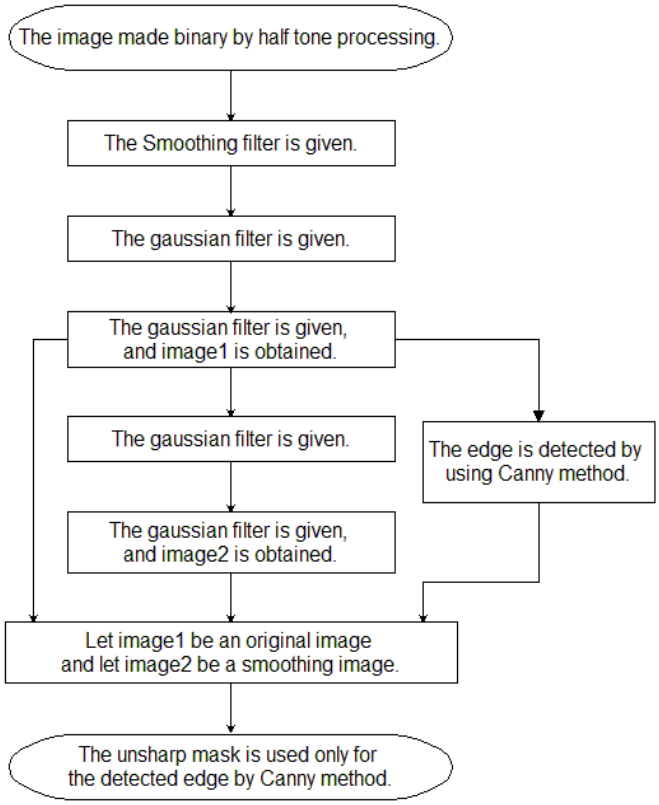

Fig. 9. Process of inverse halftonig

4 EXPERIMENTAL RESULT

We tested it in a procedure of Fig. 9 and verified the most suitable value of the unsharp coefficient K. Verification is used a representative sample images, "Airplane", "Lenna", "Milkdrop", "Parrots", "Pepper", "Sailboat".

Experiment is used SNR as a method for evaluation of the accuracy of image reconstruction. SNR can be calculated as follows.

$$\mathrm{SNR} = 10\log_{10}\frac{\sqrt{\sum f(x,y)^2}}{\sqrt{\sum(f(x,y)-f'(x,y))^2}} \quad [dB] \qquad (6)$$

Here, f(x,y) is the original image, f'(x,y) is the processed image.

Fig. 10 shows that coefficient of variation of 6 images of images corresponding to SNR as a graph. SNR can't use as an evaluation function for inverse halftoning. So, coefficients K should be constant for any image. After we computed the mean of coefficient K when SNR of each image was the highest, and handling it, it was shown in table 1. Table 1 shows SNR when the coefficient K is average, comparison between maximum SNR and the SNR

© ISAROB 2013

when the coefficient K is average, SNR of the conventional method. The conventional method used the good following combinations of Halftoning image affinity by Floyd & Steinberg.

$$\begin{cases} \text{1st : smoothing filter} \\ \text{2nd : gaussian filter} \\ \text{3rd : gaussian filter} \end{cases}$$

"Airplane" and "Sailboat" is greatest difference between SNR of the conventional method and SNR of the proposal method in Table 1. Therefore, we show a disposal result of two images in Fig. 11,12,13,14,15,16.

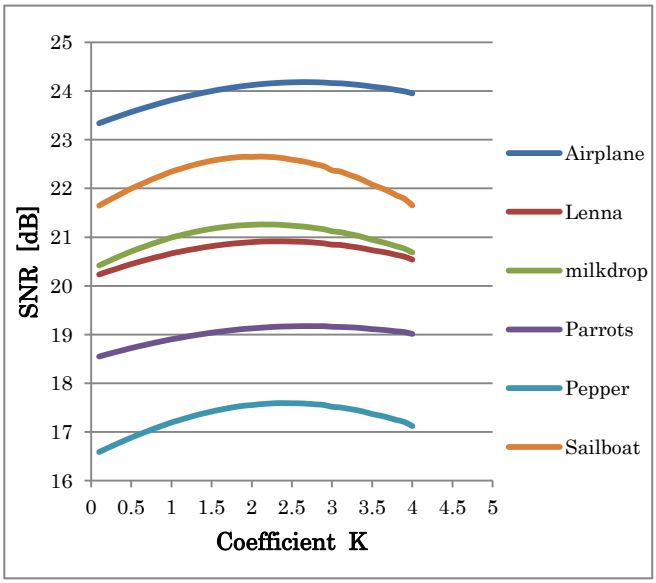

Fig. 10. Coefficient K corresponding to SNR

Fig. 11. Original image Airplane

Fig. 12. Original image Sailboat

Fig. 13. Unsharp mask

Fig. 14. Conventional method

Fig. 15. Unsharp mask

Fig. 16. Conventional method

5 CONCLUSION

In this paper, inverse halftoning was applied unsharp mask, it was confirmed that it is possible to restore some level of any image. In addition, the maximum difference between difference between the average and maximum values of the coefficient K wasn't little difference that was 0.04[dB]. Comparing the proposed method and the conventional method, SNR of each images are 0.5 [dB] higher, and became easy to look visually.

REFERENCES

[1] J.Z.C Lai and J.Y. Yen (1998), Inverse error-diffusion using classified vector quantization. IEEE Trans. Image Process

[2] John Canny(1986) , A Computational Approach To Edge Detection.

[3] Naoto Suzue, and shinishi yoshida (2009), Edge Feature for Monochrome Image Retrieval.

Table 1. Average value of the coefficient K and conventional method

	unsharp mask			conventional method
	Average value of the coefficient K	*SNR [dB]*	*Difference between the average and maximum values of the coefficient K*	*SNR [dB]*
Airplane	2.41	24.18	0	23.36
Lenna		20.92	0	20.36
milkdrop		21.25	0.01	20.75
Parrots		19.17	0	18.65
Pepper		17.59	0	16.79
Sailboat		22.62	0.04	21.51

© ISAROB 2013

The Eighteenth International Symposium on Artificial Life and Robotics 2013 (AROB 18th '13),
Daejeon Convention Center, Daejeon, Korea, January 30-February 1, 2013

Development of mobile robot navigation system using simplified map based on place recognition

Satoshi Yamanaka [1], Kazuyuki Morioka [2]

[1,2] *Dept. of Electrical Engineering, School of Science and Technology, Meiji University*, Japan

[1] ce11093@ meiji.ac.jp, [2] morioka@isc.meiji.ac.jp

Abstract: This paper introduces a mobile robot navigation system using simplified hybrid maps based on occupancy grid maps of important places and relationships among them. In order to achieve autonomous navigation with the hybrid maps, additional information, such as waypoints in important places with occupancy grid maps, are learned in SLAM process. Also, navigation system based on state transition between inside and outside of the important places is proposed. Finally, experimental results with actual robot systems in indoor environments are shown.

Keywords: Mobile robot navigation, Hybrid map, Position estimation

1 INTRODUCTION

Recently, various kinds of robots, such as cleaning robots, have been available in human living environments. In order to perform mobile robot navigation, environmental maps for robots are needed. Generally, most of studies for robot navigation use detailed occupancy grid maps representing all the environments that the mobile robots will move[1]. However, such global metric maps based on occupancy grids are not necessarily required for the purpose of navigation. At least, humans do not need such grid maps for navigation. Then, a number of navigation approaches consider using simple maps. Especially, hybrid maps that combine metric and topological maps have been widely proposed[2]. This study assumes the hybrid maps with geometrical relations between important places via straight lines are enough for representing the simple environments that consist of straight lines such as corridors. Then, this study aims to achieve autonomous navigation of the mobile robot using the hybrid maps at indoor environment.

2 SIMPLIFICATION OF THE MAP

2.1 Hybrid map

The robot's navigation in this study is performed using a hybrid environmental map as shown in Fig.1. In the hybrid map, occupancy grid maps are generated using FastSLAM[3] at important places with complicated shapes like crossing points among corridors. On the other hand, at the places with simpler shapes, such as corridors, detailed maps are not generated and only geometrical relationships between important places are learned. Then, the map representation does not lose necessary global relationships among important places as maps for robot navigation. In order for the robot to learn the map, we previously proposed a novel SLAM algorithm based on acquisition and matching of images in each important place[4]. Also, integration of occupancy grid maps in revisit places and etc. was added to the proposed SLAM algorithm. As the results

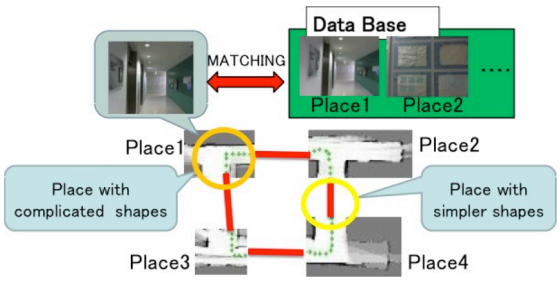

Fig.1 Outline of the proposed SLAM and hybrid map

of the proposed SLAM algorithm, exact geometrical relationships between important places are required. In other words, the robot has to judge whether the important place is visited for the first time or not in the SLAM process. Then, geometrical relationships between the place and the other places must be obtained. In order to recognize revisit or not, images are acquired at a fixed intervals in the important places and SURF features of the images are stored in databases. And, image features newly acquired in each place are compared with image features stored in the databases. According to matching results, "new" or "revisit" is recognized. Thus, the geometrical relationship between important places is recognized. In this study, two cameras are attached to the robot around the height of human's eyes (about 160 cm) in order to capture images. Cameras are set to right and left directions. This is because we can see specific information of each place, such as room numbers, information maps, etc. on walls or doors around the height of human eyes. These are easy to extract as image features and effective for image matching. The hybrid map is generated by the above method.

2.2 Information acquisition for navigation

The hybrid map simply expresses relationships among important places and occupancy grid maps of each important place. In order to perform autonomous mobile robot navigation with this map, additional information is required. For example, how to move in the important places should be considered. When the robot enters in the

© ISAROB 2013

important places, robot positions and orientations must be accurately estimated in the coordinate system of each occupancy grid map. Waypoints in the each occupancy grid map are also required for going to the other place. Just learning relationships among important places are not enough for navigation because distances among places are also required for actual navigation. Then, in order to use the proposed hybrid map for navigation, the robot acquires the following information and adds the information to the hybrid map while map generation process with the proposed SLAM algorithm.

A) **Waypoints**: A starting point and a terminal point based on geometrical relationships among places, and relay points in the grid maps are used as waypoints for navigation. These points are called bridge points as shown in Fig.2. Relay points are defined as the middle waypoints between bridge points. The robot moves toward a bridge point via a relay point first in each place. A relay point is set in a position where the robot changed its heading 70 degrees in each place during map learning process.

B) **Gate**: Gates in each important place are straight lines for judging moving out from the place. The lines are calculated from the LRF scan data on bridge points.

C) **Distance between places**: It can be roughly calculated by odometry while map learning process.

D) **Acquisition positions of database images**: Images stored in database are mentioned in Chapter 2.1. Position of the robot in each place is estimated according to acquisition positions of database images.

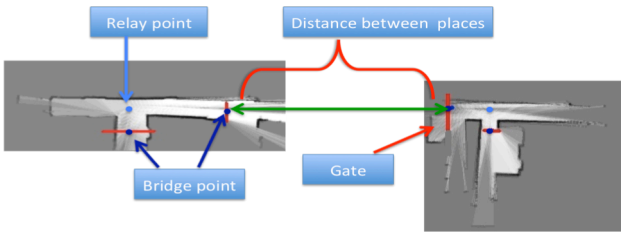

Fig.2 Information acquisition for robot navigation

3 NAVIGATION SYSTEM

In this chapter, navigation system using the hybrid map is explained. In order to perform navigation using the hybrid map, it is necessary to change localization and moving methods according to robot conditions. In the navigation system, robot conditions based on places are divided into three states: Inside, Outside A and Outside B. Details of the navigation system are explained as follows. Finally, the configuration of the system is shown.

3.1 Robot's state transition

The definition of three states in a navigation system is shown below. State transition diagram is shown in Fig. 3.

Inside: The robot is in a place under localization.

Outside A: The robot is out from a place through a gate. Its movement distance from the gate is less than distances between the last place and next places.

Outside B: Movement distance of the robot from the previous gate exceeds distances between the last place and next places before localization in a next place.

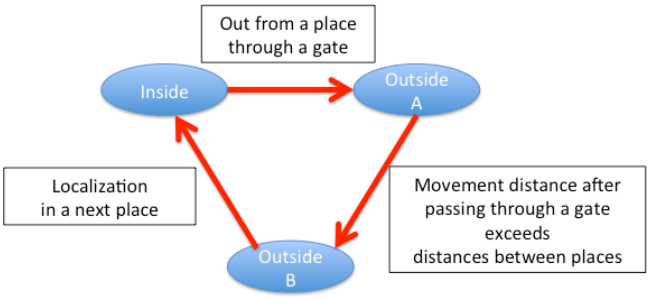

Fig.3 State transition diagram

3.2. Localization

Localization in three states is described below.

Inside: Localization is performed with particle filter using scan data of LRF and the grid map of each place.

Outside A: In this study, courses between places are assumed as corridors. First, position relationships between the robot and gates are calculated, when a robot state has just transited from Inside to Outside A. Coordinate system after transition to Outside A is defined according to relationships between the robot and the gate (Fig. 4). And, navigation along wall is performed. Moving distances along walls are also calculated from base information.

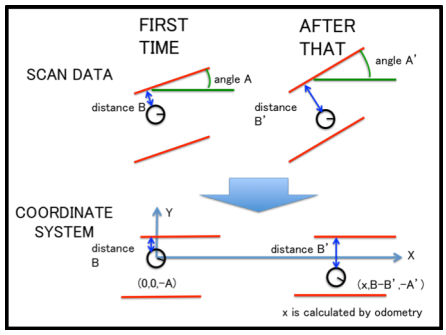

Fig4. Wall following method

Outside B: When a moving distance along walls exceeds distances between places memorized in the hybrid map, a state of the robot transits to Outside B. In this state, there are possibilities that the robot is in next places. Then, recognition of a place number and accurate localization in the place should be performed in this state. First, the rough self-position of the robot in the place is estimated by image matching with database images of places stored in the hybrid map. Next, the accurate self-position of the robot in the place is estimated by ICP matching with the grid map of the place. Details of this process are explained below. As described above, rough position estimation based on image matching is performed. Since images in the robot are captured in short sampling rate, successive captured images match same one of database images. In that case, an image with the highest voting rate can be regarded as the most similar image with one of database images. It is considered

© ISAROB 2013

that the position of the robot is the closest to the acquisition position of database image. Then, the acquisition position of database image is exploited as the position, where the image with the highest voting rate is captured, as shown in Fig.5. In addition, recognition of the place number is also achieved from image matching. However, this position estimation is too rough to control the robot. So, accurate position estimation based on the scan data of LRF and a grid map is also performed. ICP matching[5] between the grid map and the scan data of LRF is performed. Rough position estimation results based on image matching are used as initial positions of ICP matching. The accurate self-position of the robot in the place is estimated from this matching. Although several images are saved in database as representing the places in the hybrid map, the first database image matched with one of successive captured images is only used for position estimation in each place. When the accurate self-position of the robot in the place is estimated, the state transits from Outside B to Inside. Image matching method in this position estimation is similar with the method of recognition of relationships between places for the hybrid map generation[4] except the followings.

Step2. All feature points in captured images from two cameras of the robot are not saved in a database. If features extracted in one image are less than 20, the image is deleted as out of matching.

Step3. Two votes are given for the image when Euclid distance between features is the smallest in order to find the nearest image with the corresponding database image. In this voting, two votes are needed for compatibility with calculation of the voting rate.

Step4. The images with more than 10% share of the voting rate in the databases are regarded as candidates of matching images.

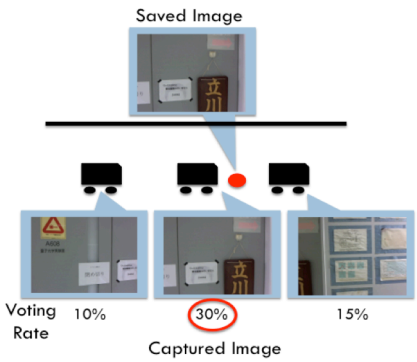

Fig.5 Image matching in Outside B

3.3. Navigation

A destination place number, a current place number and a rough self-position of the robot in the current place are given as initial information. Then, autonomous movement of the robot is carried out from the current place to the destination place. First, global path planning is performed using relationships of places. The shortest path is calculated by the Dijkstra method from the initial information. Path planning includes places transition from the current place to the destination place. Then, the robot moves according to the determined path. In navigation, the same movement is performed in Outside A and Outside B. Movement methods in Inside and Outside (including Outside A and Outside B) are shown below. The configuration of the navigation system actually used in this study is shown in Fig. 6.

Inside: First, the robot moves to a relay point in each place. Next, the robot moves toward a bridge point connected to the next place.

Outside: The robot keeps moving along a wall.

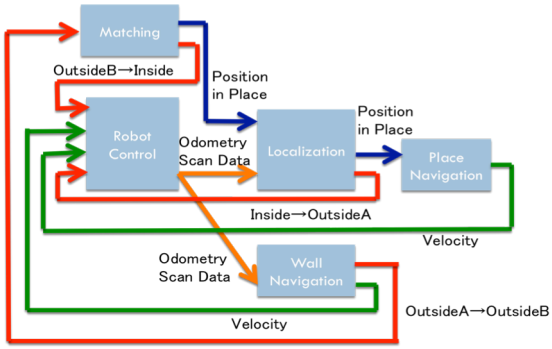

Fig.6 Navigation system

4 EXPERIMENT

4.1 Experiment setup

In this study, the mobile robot carries two cameras (Logicool® HD Pro Webcam C910) (Fig.7(b)) around the height of human's eyes and one LRF (HOKUYO electrical machinery UTM-30LX) (Fig.7(c)) ahead of the robot as shown in Fig.7(a). The experimental environment is one floor of university buildings (Fig.8). In this study, four corners or intersections are defined as important places in a hybrid map by a human operator before map learning. Also, in advance, the robot moved manually by a controller and the hybrid map was generated.

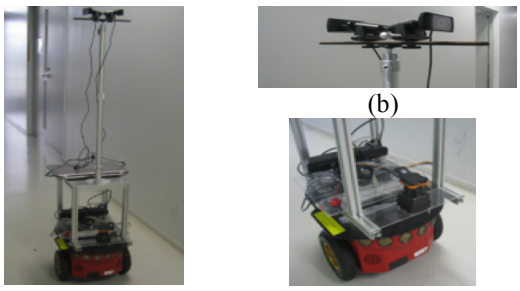

(a) (b) (c)

Fig.7 Mobile robot with LRF and camera

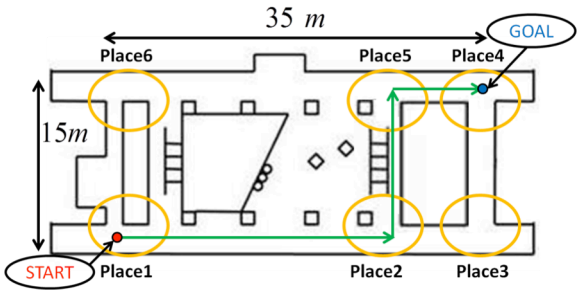

Fig.8 Experimental environment

© ISAROB 2013

4.2 Experiment method

In this experiment, it was tested whether autonomous navigation of the mobile robot could be actually achieved using the hybrid map. Followings are given to the robot in advance as initial information.

1) Initial place number
2) Rough initial position of the robot in the current place
3) Destination place number

After ICP matching based on the rough position to estimate for an exact position in the initial place, the robot starts movement. Each parameter setup is as follows. In localization with the particle filter, the number of particle was set to 30. In ICP algorithm, the maximum loop count was set to 500 times. Also, when the distance between each point of one point group and the nearest point of another point group to the point was shorter than 600 mm, the nearest point was considered a corresponding point.

4.3 Experimental result

In the example, the robot is placed at place "1" at first and the destination place is place "4". As a result of the Dijkstra method, the robot moved from place "1" through place "2" and place "5" to place "4". At place "2", place "5" and place "4", image matching and ICP matching was performed when the robot state is Outside B. Fig.9 shows images captured by the robot during the navigation, matched database images in the places of the hybrid map and voting rate in the case of the highest voting rate in image matching at place "2" and place "5". The result of ICP matching at place "2" and place "5" is shown in Fig.10. In this figure, red points represent grids whose occupation probabilities are over 50 percent in the occupancy grid map of each place, blue points represent scan data of LRF at robot position estimated roughly by image matching, and green points represent scan data of LRF at accurate robot position corrected by ICP matching. The result of state transition in navigation is shown in Fig.11. Fig.9 shows these two images are comparatively similar. That means place recognition based on image matching was successful. Fig.10 shows ICP matching in the initial rough place was also successful since the suitable position is searched by image matching. As a result, localization of the robot was achieved and navigation to the destination place was successful, carrying out a state transition as shown in Fig.11.

Fig.9 Matching image of navigation

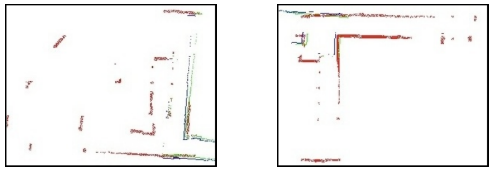

Fig.10 ICP matching of navigation

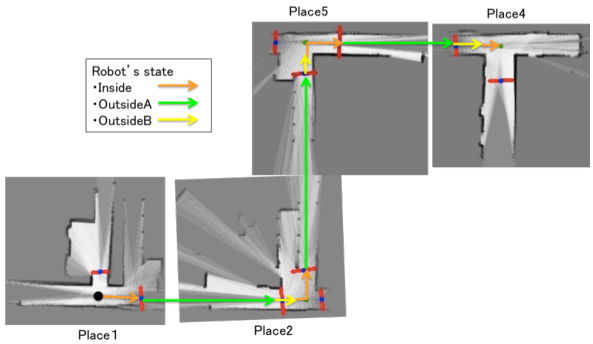

Fig.11 State transition of navigation

5 CONCLUSIONS

The navigation system using the hybrid map was developed. And, autonomous navigation using the hybrid map was achieved. Experimental results showed validity of the hybrid map and the navigation system. The experiment of the map generation and navigation in more complicated environment is conducted from now on, and detailed evaluation of the approach should be performed.

REFERENCES

[1] Ato Araki, Kentaro Takemura, Junichi Ido et al, "Generating Individual Maps for Mobile Robots from Universal 3D Environment Map", Journal of the Robotics Society of Japan, Vol.28, No.1, pp.106-111, 2010

[2] Kurt Konolige, Eitan Marder-Eppstein, and Bhaskara Marthi "Navigation in Hybrid Metric-TopologicalMaps", International Conference on Robotics and Automation (ICRA), pp.3041-3047, 2011

[3] D. Haehnel, D. Fox, W. Burgard et al, "A highly efficient FastSLAM algorithm for generating cyclic maps of large scale environments from raw laser range measurements", In Proc. of the Conference on Intelligent Robots and Systems (IROS), pp.206-211, 2003

[4] Satoshi Yamanaka, Kazuyuki Morioka, "Mobile robot navigation using hybrid simplified map with relationships between places and grid maps", In Proc. 10th IFAC Symposium on Robot Control (SYROCO), 2012

[5] F.Lu, E.Milios, "Robot Pose Estimation in Unknown Environments by matching 2D Range Scans", Journal of Intelligent and Robotic Systems, Vol.18, pp.249-275, 1997

© ISAROB 2013

The Eighteenth International Symposium on Artificial Life and Robotics 2013 (AROB 18th '13),
Daejeon Convention Center, Daejeon, Korea, January 30-February 1, 2013

Real-time 3D-Shape Reconstruction System in Intelligent Space Based on Networked Vision Sensors

Takashi Ishimaru [1], Kazuyuki Morioka [2]

[1,2] *Dept. of Electrical Engineering, School of Science and Technology, Meiji University,* Japan

[1] ce11008@ meiji.ac.jp, [2] morioka@isc.meiji.ac.jp

Abstract: In recent years, intelligent spaces based multi-viewpoint cameras and range image sensors have been developed. Especially, real-time human 3D shape reconstruction system with multiple sensors in intelligent space is considered in this study. In order to achieve application of human shape reconstruction in intelligent space, it is necessary to integrate several kinds of sensors efficiently. This paper focuses on roles and functions required to each sensor node, and proposes systematic structures with RT-component for sensor integration.

Keywords: Intelligent Space, 3D-Shape Reconstruction, RT component

1 INTRODUCTION

Intelligent space is a platform, which organically integrates various sensors, computers and robots via network[1]. Especially, intelligent spaces, which multiple cameras and range image sensors are distributed, have been widely proposed. These systems aim to achieve various applications, such as supporting mobile robot navigation or human tracking with position estimation. In addition to human positions estimation, 3D shapes of humans can be reconstructed by cooperation of image sensors. Positioning and shape reconstruction of humans in intelligent space are promising for human-system interaction. In this study, real-time 3D shapes recognition systems in intelligent spaces are considered. This paper focuses on sensor nodes configuration in 3D-shape reconstruction systems for a target person by integrating image data captured by distributed sensors.

In order to acquire 3D shape of a target human in intelligent space, it is important how to process sensor data from sensors contributed to 3D shape reconstruction. However, intelligent space is a platform including various kinds of sensors. There are various kinds of sensors for contributing 3D shape reconstruction in intelligent spaces. Then, intelligent spaces require the system configuration for integrating various sensors effectively. This paper considers how to assign roles between intelligent space and application of 3D shape reconstruction. Especially, this paper proposes the system configuration that consists of hierarchical sensor nodes in intelligent space and application of 3D shape reconstruction independent of sensors. In the intelligent space side, various kinds of sensor data is integrated through a network as shown in Fig.1. This figure means that all sensor nodes provide same kinds of sensor data to application. In order to provide same kinds of sensor data, two or more sensors are hierarchically integrated for sensor nodes. On the other hand, the application side is independent to kinds of distributed sensors. Then, software configuration of application can be simple. Also, the configuration for accepting additional sensors or new sensors should be required for intelligent spaces as platform of various sensors integration. This paper describes followings. At first, integration methods for configuring sensor nodes from distributed sensors are described. And, an application of 3D shape recognition system for accepting sensor nodes is described. Finally, a total system including sensor nodes and application is shown.

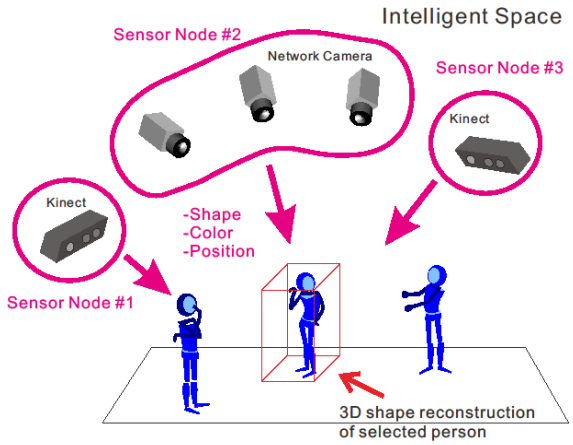

Fig 1. 3D shape reconstruction system

2 APPLICATION IN INTELLIGENT SPACE

As mentioned above, the intelligent space is a platform for integrating various sensors via network. Sensor data is integrated in order to achieve applications with networked sensors. The 3D shape reconstruction in this paper is also one of the applications in intelligent space. Sensors distributed in the intelligent space are not necessarily exploited only for the purpose of 3D shape reconstruction. These sensors should afford the other applications. This means that output of distributed sensors must not depend on the specific application. So, each sensor in intelligent space cannot provide suitable information for the application. On the other hand, the application should not include processes

© ISAROB 2013

that depend on kinds of sensors, so that the application can accept different sensors added in intelligent space. The 3D shape reconstruction application needs following elements from distributed sensors. The first is 3D point cloud data of a target human. The second is color information corresponding to 3D points. The last is a target position in the intelligent space. Some sensors, such as Kinect sensors, can provide these elements by themselves. The other sensors, such as cameras or LRFs, cannot provide them. However, the sensors such as cameras or LRFs can provide same kinds of elements by integrating several sensors. In the proposed application, sensor nodes integrating several sensors are considered in order to provide information of same form to applications. Such same form information from sensor nodes will make the applications that flexibly accept several kinds of sensors in the intelligent space.

In this study, a system based on networked cameras and Kinect sensors is developed, because information required for 3D shape reconstruction can be easily acquired. Also, the system includes different kinds of sensors. Then, the system will show flexible acceptance of different sensors. As mentioned above, Kinect sensors can provide information required for 3D shape reconstruction. A standalone Kinect sensor can be regarded as a sensor node in 3D shape reconstruction application. On the other hand, raw data obtained by cameras cannot be directly used for 3D shape reconstruction. This raw data should be changed into the same data format in order to be accepted by 3D shape reconstruction application. In this case, a sensor group integrating several cameras can be regarded as a sensor node in the application. In this study, a system design based on RT component is performed.

3 SENSOR NODE COMPONENT

At first, every sensor data acquired in intelligent space should be generalized so that it becomes same data formats for 3D shape reconstruction application. For this purpose, processing in each sensor is integrated and wrapped in order to generalize data formats for 3D reconstruction application. Specifically, RT-component[2] based sensor nodes including several sensors are developed for 3D shape reconstruction application. In this application, three elements mentioned in Section.2 are same data formats for 3D data reconstruction. Therefore, same data formats from sensor nodes must be accepted and processed in 3D shape reconstruction application. Design and development of components of sensor nodes, which output same data formats, are explained below. Especially, sensor nodes based on cameras or Kinect sensors are described.

3.1 Component based on Kinect

A sensor node to output the same data format using a Kinect sensor is configured as follows.

Kinect sensors can acquire RGB image data and depth image data respectively. A target human on the image is tracked using depth data and human posture pattern. 3D point clouds of human can be also acquired from depth data around the target human position. Since Kinect sensors can RGB data in synchronization with the depth data acquired with the infrared camera, color information corresponding to 3D point clouds can be acquired. Then, data required for 3D shape reconstruction application is acquired by each standalone Kinect sensor. This means that each Kinect sensor can be regarded as a sensor node for 3D shape reconstruction application.

In addition, in order to integrate data between sensors nodes in intelligent space, each sensor node must be geometrically calibrated in common world coordinates. Each distributed Kinect has calibrated manually in advance in this system. Internal parameters and external parameters can be obtained by calibration in each sensor.

Although 3D point clouds obtained from a Kinect sensor are numerical values in a camera coordinate system of each Kinect sensor, 3D point clouds are transformed to world coordinates with internal and external parameters. Then, suitable data integrated in 3D shape reconstruction application is acquired by a sensor node by a Kinect sensor.

3.2 Component based on several cameras

Color information of a target human can be acquired with one camera. However, 3D point clouds and human positions in world coordinates cannot be acquired using one camera. Therefore, two or more cameras should be integrated for satisfying minimum requirements of 3D shape reconstruction application. Such integrated cameras can be treated as a sensor node to output the same data formats with a sensor node based on a Kinect sensor. Then, the application built on the platform of intelligent space should have following functions. That is a dynamical configuration of a sensor node according to kinds of applications.

A sensor node component including several cameras is explained below. First, this component obtains images from several cameras. Next, 3D point clouds of a target human are calculated using images from cameras connected to this component. Also, color information corresponding to the point is obtained from images.

Image processing methods in this component are as follows. At first, in order to obtain a human region in each camera image, background subtraction is performed between input images and a background image. Geometrical calibration of each camera is performed in advance in the similar way with Kinect sensors. Camera parameters obtained by calibration can be used for a volume intersection method integrating several camera images. Calculation results of the volume intersection method are regarded as 3D point clouds of a target human.

Details of the volume intersection method in the developed component are as follows. First, a 3D point in world coordinate system is transformed into a pixel position on image coordinate system of each camera. It is judged whether the transformed position is inside a human region in the image of each camera.

This judgment is applied to all cameras in a sensor node. When the transformed positions exist in human regions of all cameras, the 3D point is recorded as one of the points representing a target human. At this time, color information corresponding to that point is also recorded. This

© ISAROB 2013

calculation is applied to points in a given cuboid around human position. These processes are implemented using GPU. Then, data formats for 3D shape reconstruction application can be obtained in real-time with a sensor node based on several cameras. These data formats are same with a sensor node based on a Kinect sensor. That is, this component based on cameras is acceptable as a distributed sensor node in 3D shape reconstruction application.

3.3 Data integration through a network

Two sensor node components mentioned above output data of same formats. A 3D shape reconstruction system is achieved by integrating them.

However, processing performance of sensor nodes was decreased when integrating them through a network. For example, a sensor node component based on Kinect can generate 3D point clouds and color information at about 100 milliseconds cycle. This loop cycle is sufficient performance for real-time 3D shape reconstruction. On the other hand, when integrating this component to the other component through a network for data sharing, a processing loop cycle decreases to 600 milliseconds. This degradation makes sensor node performance worse in the viewpoints of real-time 3D shape reconstruction.

In order to stabilize tracking human moving at natural speed, it is important to keep short processing cycle. Therefore, the following components are added for integration of sensor nodes through a network. First, the data compression components and decoding components are prepared among sensor node components and 3D shape reconstruction application. These components are efficient for short loop cycle of each sensor node component. In this study, several compression methods are evaluated toward executing a loop at about 100 milliseconds cycle in sensor node components.

As a result of evaluation, image data including color information is compressed with JPEG of high compression ratio because color information does not greatly affect the accuracy of shape reconstruction. Since 3D point clouds affect to reconstruction accuracy of human, PNG was adopted for them. PNG is lossless compression, so 3D shape reconstruction application can obtain data calculated in each sensor node without any changes.

4 FLEXIBILITY OF THE SYSTEM

4.1 Application integrating distributed sensor nodes

Each distributed sensor node component outputs following data formats as mentioned above. The first is 3D point cloud data of a target human. The second is color information corresponding to 3D points. The last is a target position in the intelligent space. 3D shape reconstruction application receives these from sensor node components through a network. This application execute following processes. First, this application integrates the 3D points on the world coordinate sent from sensor nodes. And, color information is put to a corresponding 3D point. Then, integrated 3D shapes are displayed using OpenGL. The range of reconstruction does not need to be the whole intelligent space. It is enough for this application to reconstruct around a target human. This makes processing time of integrating data short. So, this is efficient for real-time shape reconstruction.

4.2 Real time reconstruction through a network

The information acquired by each distributed sensor is unified through a network. When the data volume transmitted is excessive, it has bad influence on processing of each component. As an example, if a component based on Kinect passed a network, it was investigated what bad influence it would have to the processing. The result of the influence is shown in Table 1.Table 1 expresses comparison of the processing time at one cycle in a component based on Kinect. The top of a table is a case where it processes independently without unifying data. The middle of a table is a case where the data through a network is unified. The lower berth of a table is a case where data integration which uses the compression component explained in Section 3.3 is performed. Data was compared in this table. Time of the case not compressed and time of the case compressed is compared. The case of data compressed is 14 times as quick as the case of data not compressed. This has influence good for the performance of 3D shape reconstruction application.

Table 1. Processing time in a component based on Kinect

	Time of one cycle
Case of only component	20[ms]
Case of not compressed	831[ms]
Case of compressed	60[ms]

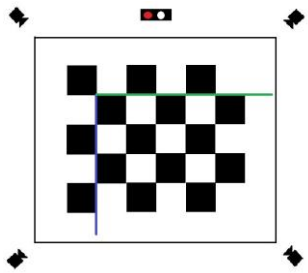

Fig 2. Sensors placements in an initial intelligent space

4.3 Flexible system and 3D shape reconstruction

In the proposed system, output of each distributed sensor node is the same format for the application.

This means that same frameworks to all sensor nodes are adopted in this system. The following advantages of the proposed system can be explained from this viewpoint. Even if a new sensor node is added to the system, the sensor node is easily integrated to the application. This makes the system more scalable. In order to show the advantages of the proposed system, addition of a new sensor node in this system is performed.

First, an initial intelligent space as shown in Fig. 2 was configured. In this space, four USB cameras and one Kinect sensor, which are geometrically calibrated in the common world coordinate, have been installed. Four USB cameras are integrated and it is regarded as one distributed sensor

© ISAROB 2013

node. One Kinect is also regarded as a distributed sensor node. Fig. 3 shows the experiment environment seen from the Kinect sensor installed in intelligent space. Each line on this figure expresses an axis of the world coordinate set in advance. The blue line is the X-axis on the world coordinate. The green line is the Y-axis. The red line is the Z-axis. Each voxel size in 3D shape reconstruction is set as 1cm x 1cm x 1cm.

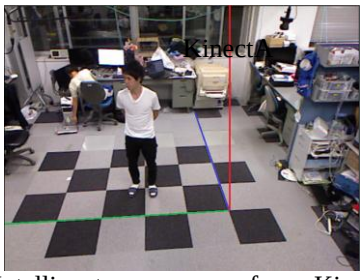

Fig 3. Intelligent space seen from KinectA

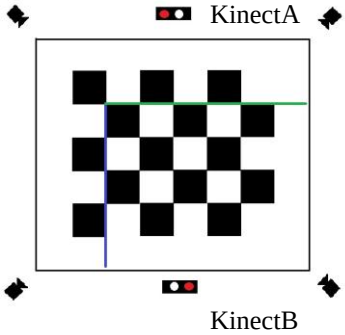

Fig 4. An intelligent space with an additional sensor

Next, the system as shown in Fig. 4 was configured. In this system, a sensor node based on one Kinect is added to the initial intelligent space as shown in Fig.2. Fig.5 shows 3D shape reconstruction results in the initial intelligent space of Fig. 2. Fig.5 (a) is the result of seeing a target human from a front viewpoint. Fig.5 (b) is the result of seeing a target human from a back viewpoint.Fig.6 shows 3D shape reconstruction results in the improved intelligent space of Fig. 4.
The viewpoints of 3D shape reconstruction results are same with Fig. 5.These results show that shapes of Fig.6 are more accurate. Since the new sensor node was installed so that dead angles in intelligent space might be reduced, these results were previously expected. Generally, optimal placements of sensor nodes depend on scales or shapes of environments or purposes of the applications. When building such systems, developers usually configure the systems by trials-and-errors of sensor nodes placements. On the other hand, the proposed system configuration, which means integration of same format data from distributed sensor nodes, can contribute to flexibly adding new sensor nodes or new kinds of sensors to the systems. This data integration platform is required for intelligent spaces configured with various kinds of sensors. This also means that the intelligent spaces evolve according to addition of new sensors.

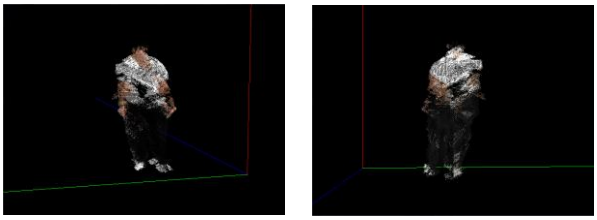

(a)Front viewpoint (b)Back viewpoint

Fig 5. 3D shape reconstruction at environment of Fig2

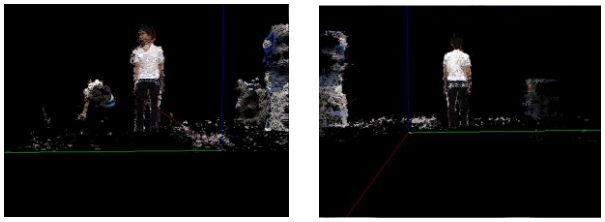

(a)Front viewpoint (b)Back viewpoint

Fig 6. 3D shape reconstruction at environment of Fig4

5 CONCLUSION

In this paper, a flexible system configuration for the 3D shape reconstruction application in intelligent space was proposed.
The proposed system was based on sensor nodes with same functions respectively. And each sensor node integrated several sensors in order to achieve the same function for the application.
Sensor nodes and the application were implemented as RT components. Then, an experiment for adding a new sensor to the system was performed. Accuracy of 3D shapes of target humans depend on placements of sensors. The results show that a system for satisfying a purpose of the application is easily constructed with the proposed platform of sensor integration.

REFERENCES

[1] Joo-Ho Lee, Hideki Hashimoto, "Intelligent Space - concept and contents", Advanced robotics, Vol.16, No.3, pp.265-280, 2002

[2] Noriaki ANDO, Takashi SUEHIRO, Kosei KITAGAKI, Tetsuo KOTOKU, Woo-Keun Yoon, "RT-Middleware: Distributed Component Middleware for RT (Robot Technology)", 2005 IEEE/RSJ International Conference on Intelligent Robots and Systems (IROS2005), pp.3555-3560, 2005

© ISAROB 2013

The Eighteenth International Symposium on Artificial Life and Robotics 2013 (AROB 18th '13),
Daejeon Convention Center, Daejeon, Korea, January 30-February 1, 2013

Using a GA-based Extension Recognized Method for Fault Diagnosis in Car Engines

Meng-Hui Wang*, Pi-Yun Chen

National Chin-Yi University of Technology, Taiwan
(TEL: +886-4-23924505, FAX: +886-4-23924419)

*wangmh@ncut.edu.tw

Abstract: Due to the passenger's security, the recognized hidden faults in car engines are the most important work for a maintain engineer, so they can regulate the engines to be safety and improve the reliability of automobile systems. In this paper, we will present a novel fault recognized method based on the genetic algorithm (GA) and the extension theory, and also applies this method in the fault recognition of a practical car engine. The proposed recognized method has been tested on the practical tested records of the Nissan CEFIRO 2.0 engine and also compared with other traditional classified methods. Experimental results are of great effective for the hidden faulting recognition of car engine, the proposed method also suits application in other industrial apparatus.

Keywords: genetic algorithm (GA), extension theory, fault diagnosis, pattern recognition.

1. INTRODUCTION

Car is an important tool in human life currently, and the traffic accident has become a part of human life. An engine fault not only damages the engine itself but also causes a break in the car system. Usually, the component module of the engine generates natural loss and improper maintenance that will make the engine oil consumption to increase gradually and let the thickness of exhaust to be increased. The cylinder vibration and the temperature of engine exhaust will come to abnormal situation. The type of the hidden defect is due to the gradual formation, so it is difficult to recognize in the normal inspection. So how to detect engine fault signs early, and to immediately repair or remove them, is very necessary.

In the past, various pattern clustering techniques, including, expert systems (ES) [1], fuzzy clustering [2] and neural networks (NN) [3] have been extensively used in pattern recognition. Combinations of personal computers (PC), expert and fuzzy systems bring up possibilities of automating recognition. However, it is hard to use these rule-based methods to acquire pictorial knowledge and hard to maintain the database of decision rules. A limitation of the MNN approach is the inability to produce linguistic output, because it is difficult to understand the content of network memory.

To overcome the limitations of the ES and MNN mentioned above, a new recognition method, based on the GA and extension theory, is presented for fault diagnosis of car engine in this paper. The extension theory concept was first proposed by Cai in 1983 [4]. Now extension theory has been used in the research field of artificial intelligence (AI) and its relevant sciences. Experimental results show that the GA-based extension recognized method not only has a high accuracy and much suitable as a practical solution of diagnosis problem [5].

2. SUMMARY OF EXTENSION THEORY

There are two main points in extension theory that are matter-element model and extension set [6]. The hard core of extension theory is two theoretical pillars that include matter-element theory and the theory of extension set.

2.1 Matter-element theory

In extension theory, a matter-element uses an ordered triad as the basic element for describing things as follows:

$$R = (N, c, v) \tag{1}$$

Where N represents the matter, c the characteristics; v is N's measure of the characteristics c, where v can be a value or an interval. A multi-dimensional matter-element is defined as follows:

$$R = (N, C, V) = \begin{bmatrix} R_1 \\ R_2 \\ \cdots \\ R_n \end{bmatrix} = \begin{bmatrix} N, c_1, v_1 \\ c_2, v_2 \\ \cdots\ \cdots \\ c_n, v_n \end{bmatrix} \tag{2}$$

2.2 Summary of extension set

Definition1.Let U be a space of objects and x a generic element of U, then an extension set $\tilde{E}$ in U is defined as a set of ordered pairs as follows:

$$\tilde{E} = \left\{ (x, y) \middle| x \in U, y = K(x) \in (-\infty, \infty) \right\} \tag{3}$$

Where $y = K(x)$ is called the correlation function for extension set $\tilde{E}$. The $K(x)$ maps each element of U to a membership grade between $-\infty$ and ∞. The extended membership function is shown in Fig.1. When $K(x) > 0$, it indicates the degrees to which x belongs to

© ISAROB 2013

x_0. When $K(x)<0$ it describes the degree to which x does not belong to x_0. When $-1<K(x)<0$, it is called the extension domain, which means that the element x still has a chance to become part of the set if conditions change.

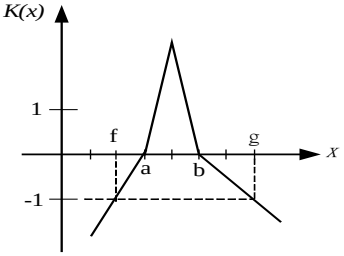

Fig. 1. The extended membership function

2.3 The basic theory of genetic algorithm

The best-known evolutionary algorithm (EA) is the genetic algorithm (GA), which transposed the notion of evolution in Nature to computers and imitates natural evolution and selection [8,9].The genetic algorithm generally includes the following five parts:

1. Gene coding:
   Combining all genes into a chromosome of sequence 0 and 1.
2. Fitness function:
   It describes the capability of a certain individual gene to reproduce and is usually equal to the proportion of the individual's genes in all genes of the next generation.
3. Selection mechanism:
   It is the intentional manipulation by chromosome of the fitness of individuals in a population to produce a desired evolutionary response.
4. Crossover:
   A process in which chromosomes exchange genes through the breakage and reunion of two chromosomes.
5. Mutation:
   A change in a gene resulting in new or rearranged hereditary determinants, mutations are rare, random events in which the base sequence of the gene is changed.

3. GA-BASED EXTENSION RECOGNIZED METHOD

In this paper, the proposed recognized method involves a combination of the genetic algorithm (GA) and extension theory. The extension theory provides a means for distance measurement in the classification process. The genetic algorithm has the ability to search for an optimal solution within a wide space.

3.1 The training stage

The chromosomes propagate next generation of chromosomes to combine the matter-element models in the proposed method. Setting *Patterns*= $\{p_1, p_2,\ldots p_n\}$ with *i-th* as follow: $p_{ij}=\{c_1,c_2,\ldots,c_k\}$.In the patterns, *i* is the total number of genes, and *j* is the type of pattern. Using the proposed method can be simply described as follows:

Step1: Set the epoch, the crossover rate C_r, the mutation rate m_u, the tolerance of error rate E_r, and the chromosome rate R_a.

Step2: Find the gene of lower limit and upper limit value.

$$v_a^j = \min(c_{kn}^j) \tag{4}$$

$$v_b^j = \min(c_{kn}^j) \tag{5}$$

$$v^j = < v_a^j, v_b^j > \tag{6}$$

k is number of characteristic.

v_a is the upper limit, and v_b is lower limit.

Step3: Produce new gene of lower limit and upper limit value with chromosome rate. The chromosome rate is produced with random generator.

$$v_a^j - R_a \le G_L^j \le v_a^j + R_a \tag{7}$$

$$v_b^j - R_a \le G_L^j \le v_b^j + R_a \tag{8}$$

Step4: The genes make up the chromosome.

$$chrom = \{G_L^{11}, G_L^{11}, G_L^{12}, G_L^{12}, ..., G_L^{jk}\} \tag{9}$$

The amount of gene in a chromosome is calculated by the function 2*k*j.

Step5: Building the matter-element model from gene.

$$R_j = \begin{bmatrix} N, c_1, < G_L^1, G_U^1 > \\ c_2, < G_L^2, G_U^2 > \\ \vdots \quad \vdots \\ c_n, < G_L^k, G_U^k > \end{bmatrix} \quad j = 1,2,...,m \tag{10}$$

Step6: Input the training of data that is the value of gene.

$$x^j = \{c_1, c_2, ..., c_k\} \tag{11}$$

Step 7: Calculate the correlation function.

$$z^k = (G_L^k + G_U^k) \tag{12}$$

$$K_{nk} = \sum_{i=1}^{n} \left[\frac{\left| x_{nk}^j - z_{jk} \right| - (G_U^{jk} - G_L^{jk})/2}{\left| (G_U^{jk} - G_L^{jk})/2 \right|} + 1 \right] \tag{13}$$

Step8: Normalizing the value of correlation function for the matter-element model to be between 1 and -1.

Step9: Input the next training of data to repeat Step6 to Step8.

Step10: Input the next matter-element model, and repeat Step5 to Step9.

Step11: Calculate the fitness function.

$$Fitness = \frac{N_r}{N_a} \tag{14}$$

N_r is the right amounts, and N_a is the total mounts.

Step12: The selection of the parental chromosomes put into the mating pool, and the genes implement crossover mechanism.

Step13: Let the next generation of chromosomes to

replace the chromosomes, and implement mutation mechanism.

Step14: Calculate the correct rate.

$$E_r = (1 - Fitness) \times 100\% \quad (15)$$

Step15: Until the training is finished. If training process is not finished; otherwise go to Step3.

4. FAULT DIAGNOSIS OF CAR ENGINE

The tested object of this research is the engine of the Nissan Cefiro2.0 as shown in Fig. 2, the engine temperature is working between *80~95℃*, and the base configuration of the engine has about 1.0mm spark-plug gap. In the experiment time, the car is parked gear when the engine is the normal condition or the fault tests condition.

Fig. 2. The engine of Nissan Cefiro 2.0

4.1 The tested configuration

The back pressure is received on digital storage oscilloscope by using pressure transmitter; the exhaust temperature was received by temperature sensor. The exhausted component was received by exhaust gas analyzer. The experimental structure is shown in Fig. 3, the signals of engine are all delivered by the sensors to the diagnosis system, and then the detailed records of signals can be easy designed by a LabView8.5 software [12], the typical windows of fault diagnostic software are also shown in Fig. 4. Here, the fault types are divided into 16 kinds (including no fault), and there are 8 characteristics to be the input data. The components of engine exhaust include HC (ppm), CO (%) and CO_2 (%), and this study separately installed the temperature sensor in T_1, T_2, T_3 and T_4, so that we can promptly monitoring the temperature for every exhaust position to speculated engine fault.

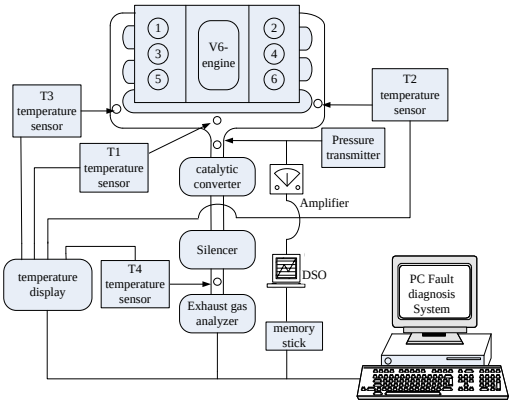

Fig. 3. The experimental structure

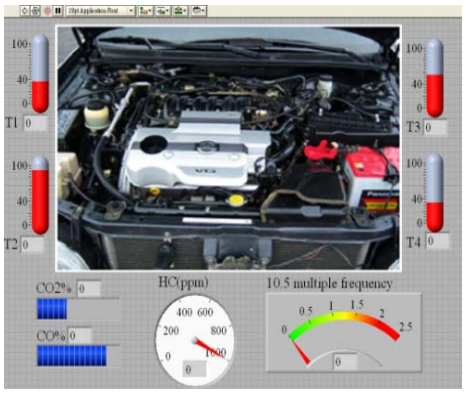

Fig. 4. The LabView recorder of the fault diagnosis system

4.2 Testing results and discussion

In this paper, we use 208 sets of tested data according to the reference [13] to test the practicability of the proposed method. In the training stage, the training data are 160 sets, and the other data (48 sets) are used to test pattern. The input data of a fault diagnosis system would unavoidably contain some uncertainties and noise. The sources of error include environmental noise, transducers, human mistakes, etc., which could lead to data uncertainties. To take the noise and uncertainties into account, 1,800 sets of testing data were created by adding ±5% to ±15% of random, uniformly distributed error to the training data to appraise the fault-tolerant abilities of the proposed method. To take into account the noise and uncertainties, and 48 sets of testing data were created by adding ±5% to ±20% of random, uniformly distributed, error to the training data to appraise the fault-tolerant abilities of the proposed method. The reason is the input data of engine system would contain some noise and uncertainties. Table 1 shows recognition results of different methods, we can find, when using the multilayer neural network (MNN) and k-means-based method to diagnose the faults of engine, the maximum accuracy of the MNN-based method is 95% and the accuracy is 85% in k-means-based method. The accuracy of the proposed diagnostic method is 98%, and the accuracy of the proposed method is quite high and batter than the other methods. The input data of a fault diagnosis system would unavoidably contain some uncertainties and noise.

The sources of error include environmental noise, transducers, human mistakes, etc., which could lead to data uncertainties. To take the noise and uncertainties into account, 1,800 sets of testing data were created by adding ±5% to ±20% of random, uniformly distributed error to the training data to appraise the fault-tolerant abilities of the proposed method. The test results using different numbers of added errors are given in Table 2. Usually, the error-containing data indeed degrade the recognition capabilities in proportion to the number of errors added. This table shows that these methods all bear remarkable tolerance to the errors contained in the

© ISAROB 2013

data. The proposed method shows good tolerance to the added errors, and has high accuracy rates of 65% in extreme error of ±20%.Usually, the error containing data indeed degrade the recognition capabilities in proportion to the amounts of error added.

Table 1. Diagnosis performances of method compare

Method	Training time	Accuracy rate (%)
Proposed method	1000	98%
K-means method	N/A	85%
MNN-I (8-8-16)	1000	62%
MNN-II (8-10-16)	1000	80%
MNN-III (8-15-16)	1000	95%

Table 2. Diagnosis performances of proposed method

Noise percentage (%)	Accuracy rate (%)
± 0%	98%
± 5%	95%
± 10%	87%
± 15%	77%
± 20%	65%

5. CONCLUSIONS

This paper presents a novel fault diagnosis method based on the GA and extension theory for car engine. The calculation of the proposed recognized method is fast and very simple. It can be easily implemented by PC software. When a diagnosed data input the proposed diagnosis system, the proposed recognized method will output the possibility of all fault types. It provides useful information to engine fault diagnosis and maintenance. Test results shows that the proposed method cannot only diagnose the main fault types; it can also detect useful information for future trends and multi-fault analysis by the relation degrees. Moreover, the proposed method has a significantly high degree of diagnosis accuracy and shows good tolerances to errors added.

REFERENCES

[1] E. Styvaktakis et al, "Expert system for power quality disturbance classifier," *IEEE Transactions on Power Delivery*, **22** (3) (2007) 1979-1989.

[2] Tovar et al, "Fuzzy neural modeling via clustering and support vector machines," *IEEE 22nd International Symposium on Intelligent Control*, (2007) 24-29.

[3] B. Kerezsi, and I. Howard, "Vibration fault detection of large turbine generators using neural networks," *IEEE International Conference on Neural Networks*, **l** (1) (1995) 121-126.

[4] W. Cai, "The extension set and incompatibility problem," *Journal of Scientific Exploration*, **l** (1) (1983) 81-93.

[5] M. H. Wang, "A novel extension method for transformer fault diagnosis, "*IEEE Transactions on Power Delivery*, **18** (1) (2003) 164-169.

[6] W. Cai, "Extension theory and its application, journal of scientific exploration,"**44** (7) (1999) 673-682.

[7] B. Das, "Fuzzy logic-based fault-type identification in unbalanced radial power distribution system, "*IEEE Transactions on Power Delivery*, **21** (1) (2006) 278-285.

[8]Renner G,Ekárt A. "Genetic algorithms in computer aided design."*Computer-Aided Design*, **35** (8) (2003) 709-726.

[9] S. Jesús Aguilar-Ruiz, Raúl Giráldez, and José C. Riquelme, "Natural encoding for evolutionary supervised learning, "*IEEE Transactions on Evolutionary Computation*, **11**(4) (2007) 466-479.

[10] M. H. Wang, Y. F. Tseng, H. C. Chen, and K. H. Chao, "A novel clustering algorithm based on the extension theory and genetic algorithm, "*Expert Systems with Applications*,**1**(36) (2009) 8269-8276.

[11]Hwang S. F, He R. S. "A hybrid real-parameter genetic algorithm for function optimization." *Advanced Engineering Informatics*, **20** (1)(2006) 7-21.

[12] Xuejun, Xiang Ping, Xia Yang, Sheng. Liu, "Real-time digital simulation of control system with LabVIEW simulation interface toolkit, "*Control Conference*, (2007) 318-322.

[13] Y. Y. Chen, "An artificial neural network model for the diagnosis of automotive engine, "*National Chung Hsing University* (2006)

The Eighteenth International Symposium on Artificial Life and Robotics 2013 (AROB 18th '13),
Daejeon Convention Center, Daejeon, Korea, January 30-February 1, 2013

Design of a rehabilitation robot suit with hardware-based safety devices - Proposal of the basic structure -

Yoshihiro Kai[1], Satoshi Kitaguchi[1], Wenlong Zhang[2] and Masayoshi Tomizuka[2]

[1] Tokai University, Japan
[2] University of California, Berkeley, USA

[1]kai@tokai.ac.jp

Abstract: Safety is one of the most important issues in rehabilitation robot suits. We present a new rehabilitation robot suit equipped with two hardware-based safety devices. The robot suit assists a patient's knee joint. The safety devices consist of only mechanical components without actuators, controllers, or batteries. We expect that the safety devices guarantee the safety even if the computer does not work. We call one device the "velocity-based safety device" and the other device the "torque-based safety device". The velocity-based safety device can switch off the motor of the robot suit if the device detects an unexpected joint angular velocity. Also, the torque-based safety device can switch off the motor if the device detects an unexpected joint torque.

Keywords: Human-machine cooperative systems, Human-welfare robotics, Rehabilitation robot, Robot suit, Safety device.

1 INTRODUCTION

In gait rehabilitation of patients with neurological diseases such as spinal cord injury, stroke, and traumatic brain injury, physical therapists often assist the patient leg movement by using a treadmill and a partial body-weight support system [1]. In Japan, the number of aged people is rapidly increasing [2]. Predictably, it is expected that elderly patients who need gait rehabilitation will increase, that the physical therapists' burdens will increase and that the time that can be allotted to gait rehabilitation of each patient will become insufficient. In order to relieve the therapists from manually moving the legs of the patients, rehabilitation robot suits are needed that can assist the patient leg movement [3], [4].

In the design of rehabilitation robot suits, safety consideration for patients is one of the most important issues. Computer-aided control techniques can improve the safety of the robot suits [5], [6]. However, the computer may break down, which makes the software-based safety measure inadequate. Therefore, a robot suit with hardware-based safety devices would be desirable to guarantee safety even under breaking down of the computer.

Emergency switches and joint limiters are often used as hardware-based safety devices [7], [8]. When the computer does not work, emergency switches are useful for stopping the robot suits. Also, joint limiters can prevent the hyperextension of the patient's joints. However, the patient and/or the physical therapists may not be able to push the emergency switch in case of emergency. Joint limiters involve risks such as (1)the robot suit may move the patient's leg at an unexpected high velocity and (2) the robot suit may provide an unexpected high torque to the patient's joint, before the patient's joint is stopped by the joint limiter, as mentioned in section 2.

In this paper, we present a new rehabilitation robot suit with two hardware-based safety devices – "velocity-based safety device" and "torque-based safety device". The robot suit assists a patient's knee joint. The safety devices consist of only mechanical components without actuators, controllers, or batteries. The velocity-based safety device can switch off the motor of the robot suit if the device detects an unexpected joint angular velocity. Also, the torque-based safety device can switch off the motor if the device detects an unexpected joint torque. The safety devices can work even if the computer does not work.

This paper is organized as follows. In section 2, we briefly describe the safety problems in rehabilitation robot suits and two hardware-based safety devices. In section 3, we explain the basic structure and mechanism of the rehabilitation robot suit with two hardware-based safety devices. Section 4 concludes this paper.

2 REHABILITATION ROBOT SUIT WITH HARDWARE-BASED SAFETY DEVICES

We consider a rehabilitation robot suit which assists a patient's knee joint. The robot suit is controlled by a computer.

Assume that the computer of the robot suit breaks down. If an unexpected high velocity of the motor occurs, the patient's foot may collide with the ground at high speed as shown in Fig.1(a). If the motor generates an unexpected

© ISAROB 2013

high torque, the patient may feel pain as shown in Fig.1(b). Therefore, we present a rehabilitation robot suit equipped with two safety devices (velocity-based safety device and torque-based safety device).

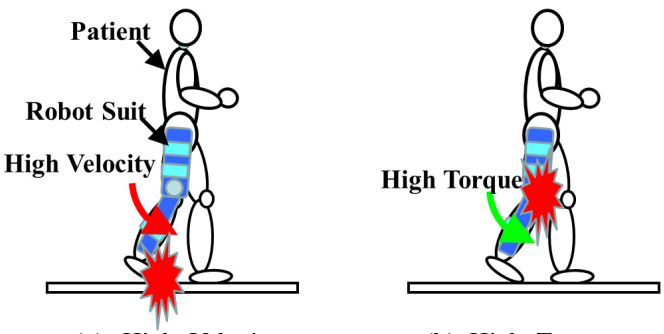

(a) High Velocity (b) High Torque

Fig. 1. Problems in computer failure

The characteristics of the velocity-based safety device are as follows:

(1) If the angular velocity of the motor exceeds a preset threshold level, then the safety device can switch off the motor. We call the preset threshold level the "detection velocity level".

(2) The detection velocity level is adjustable.

By (1), we can expect that the velocity-based safety device prevents from moving the patient's leg at a high speed. Furthermore, by (2), we can adjust the detection velocity level according to the requirement of each patient's gait exercise.

Also, the characteristics of the torque-based safety device are as follows:

(3) If the torque which the robot suit provides to patient's knee exceeds a preset threshold level, then the safety device can switch off the motor. We call the preset threshold level the "detection torque level".

(4) The detection torque level is adjustable.

By (3), we can expect that the torque-based safety device prevents from providing an unexpected high torque to the patient. Furthermore, by (4), we can adjust the detection torque level according to the requirement of each patient's gait exercise.

3 BASIC STRUCTURE & MECHANISM

3.1. Basic Structure

Fig.2 shows the rehabilitation robot suit with the velocity-based safety device and the torque-based safety device. The robot suit is worn on a patient's leg by two thigh braces and a calf brace.

Fig.3 shows the basic structure. A motor is mounted on *Frame A*. The motor torque is transmitted to *Calf Brace* via *Worm Gear*, *Worm Wheel*, *Shaft A*, *Plate A*, *Torsion Spring*, *Gear C, Gear D*, *Shaft B*, and *Frame B*. The velocity-based safety device consists of *Gear A*, *Rotary Dumper*, *Bar*, two *Springs*, two *Pins*, and two *Switches*.

Fig.4 shows the details of velocity-based safety device. *Gear A* is attached to *Shaft A*. *Gear B* meshes with *Gear A*. *Rotary Dumper* is connected to *Gear B*. Bar is connected to the axis of *Rotary Dumper*. *Bar* is also attached to two *Springs*. The ends of the *Springs* are connected to *Frame A* by two *Pins*.

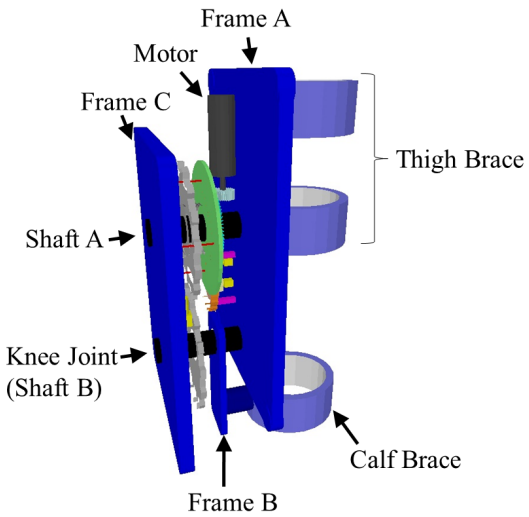

Fig. 2. The rehabilitation robot suit with safety devices

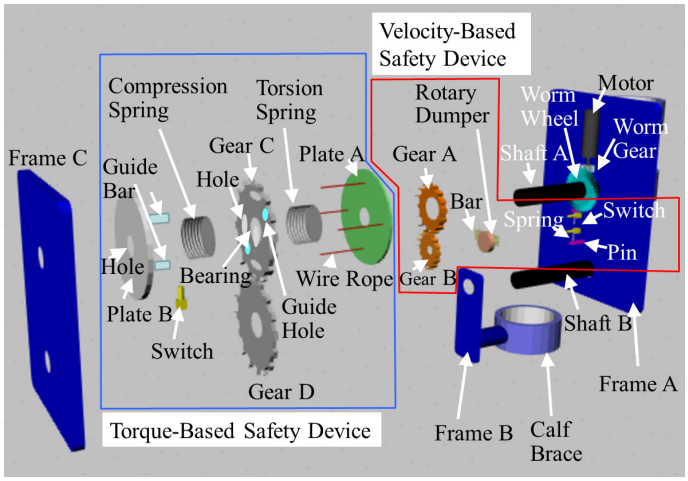

Fig. 3. The basic structure

© ISAROB 2013

Next, we explain the structure of torque-based safety device by using Fig.3. *Plate A* is attached to *Shaft A*. The *Torsion Spring* is directly installed between *Plate A* and *Gear C*. Four *Wire Ropes* are connected to *Plate A* and *Plate B* through 4 *Holes* of *Gear C*. *Gear C* is attached to *Shaft A* via *Bearing*. *Compression Spring* is installed between *Plate B* and *Gear C*. *Shaft A* is inserted to *Hole* of *Plate B*. Two *Guide Bars* attached to *Plate B* are inserted to two *Guide Holes* of *Gear C*. By the geometric restriction, *Plate B* and *Gear C* can rotate around *Shaft A* together, and *Plate B* can slide along *Shaft A* when *Plate B* is pulled by four *Wire Ropes*.

3.2. Mechanism

(1) Velocity-based Safety Device

Fig.5 shows the mechanism which mechanically detects the unexpected robot suit motion on the basis of the angular velocity of the motor. The damping torque by *Rotary Damper* and the spring torque by *Springs* act on *Bar*, when *Gear B* is rotated by the motor. As the motor velocity increases, the damping torque increases. If the motor velocity exceeds the detection velocity level, *Bar* rotates by the torque difference between the damping torque and the spring torque and switches off the motor. Also in the opposite direction, *Bar* can switch off, as shown in Fig.6. The detection velocity level is adjustable by changing the attachment positions of *Springs* as shown in Fig.7.

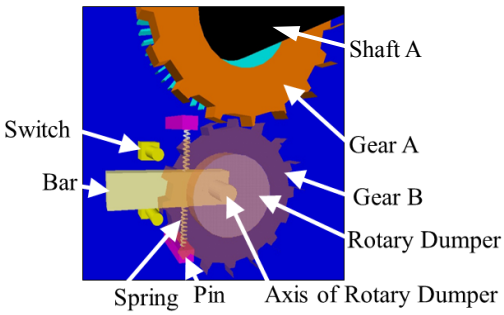

Fig. 4. The velocity-based safety device

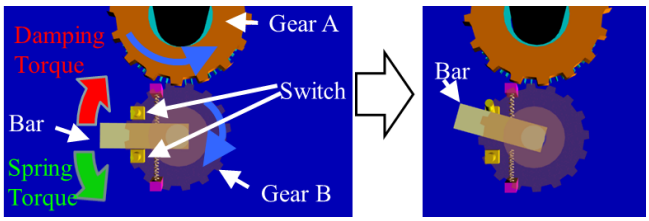

Fig. 5. The switch-off mechanism in the velocity-based safety device

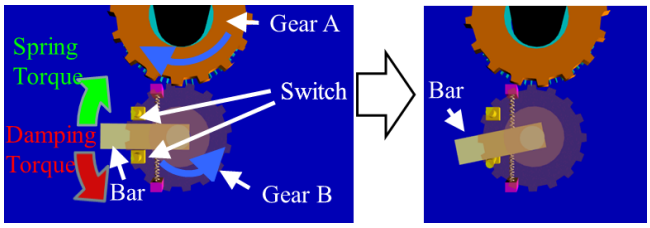

Fig. 6. The switch-off mechanism in the velocity-based safety device (in the opposite direction)

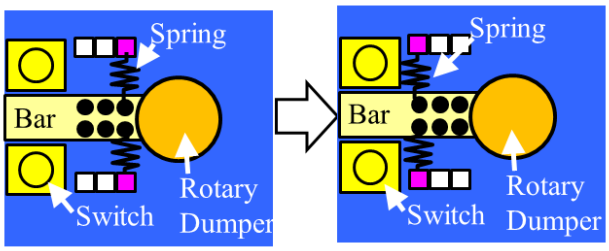

Fig. 7. Setting of the detection velocity level

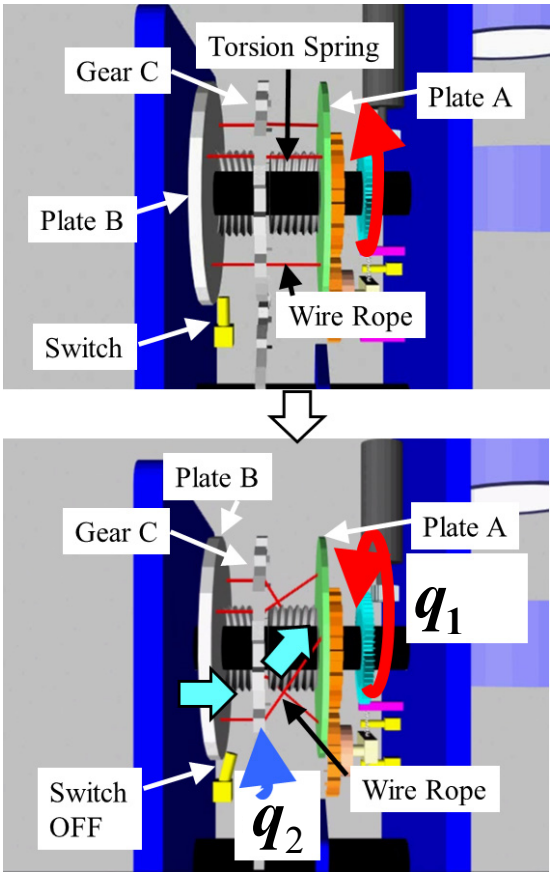

Fig. 8. The switch-off mechanism in the torque-based safety device

© ISAROB 2013

(2) Torque-based Safety Device

Fig.8 shows the mechanism which mechanically detects the unexpected robot suit motion on the basis of the torque which the robot suit provides to patient's knee. When the torque acts on *Torsion Spring*, the angle difference (q_1-q_2) between *Plate A* and *Gear C* generates (q_1: the angle of *Plate A*, q_2: the angle of *Gear C*) and *Plate B* is pulled by four *Wire Ropes*. If the torque exceeds the detection torque level, *Plate B* switches off the motor. Also in the opposite direction, *Plate B* can switch off as shown in Fig.9. The detection torque level is adjustable by changing the attachment position of *Switch* as shown in Fig.10.

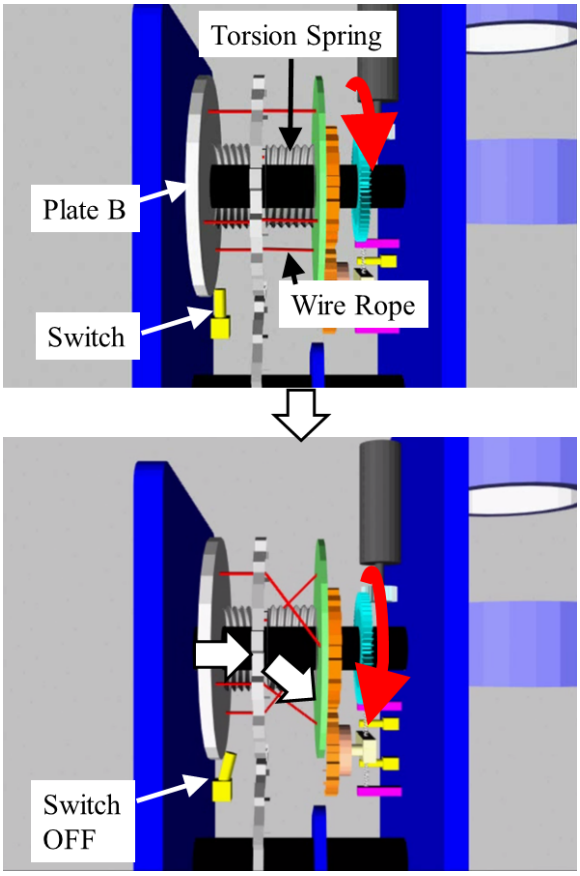

Fig. 9. The switch-off mechanism in the torque-based safety device (in the opposite direction)

4 CONCLUSION

We presented a new rehabilitation robot suit with two hardware-based safety devices (velocity-based safety device and torque-based safety device). In the future, we will build the robot suit and experimentally examine the usefulness of the two hardware-based safety devices.

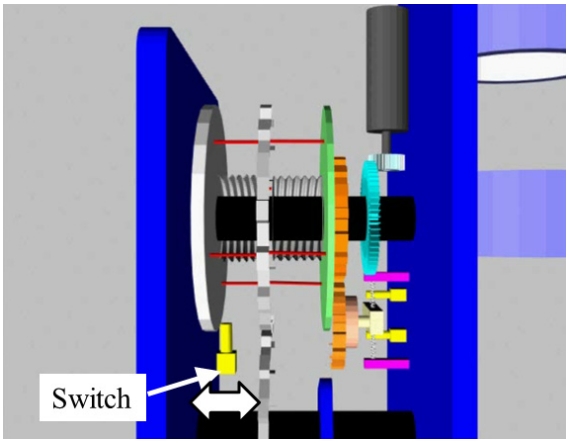

Fig. 10. Setting of the detection torque level

ACKNOWLEDGMENT

This work was supported by Overseas Research Visit Program of Tokai University (2012).

REFERENCES

[1] Kelly P Westlake1 and Carolynn Patten (2009), Pilot study of Lokomat versus manual-assisted treadmill training for locomotor recovery post-stroke, Journal of NeuroEngineering and Rehabilitation 2009, 6:18.

[2] Cabinet Office, Government of Japan (2011), Annual Report on the Aging Society: 2010 (Summary), Cabinet Office Japan, 2011, pp.2-5.

[3]Robert Riener (2012), Technology of the Robotic Gait Orthosis Lokomat, Neurorehabilitation Technology, 2012, pp.221-232.

[4]Kenta Suzuki, Gouji Mito, Hiroaki Kawamoto, Yasuhisa Hasegawa, Yoshiyuki Sankai (2010),"Intention-Based Walking Support for Paraplegia Patient with Robot Suit HAL", Climbing and Walking Robots, 2010, pp.383-408.

[5] Kong K, Bae J, Tomizuka M (2012), A Compact Rotary Series Elastic Actuator for Human Assistive Systems, IEEE/ASME TRANSACTIONS ON MECHATRONICS, VOL. 17, NO. 2, 2012, pp.288-297.

[6] Bae J, Kong K, and Tomizuka M (2011), Control Algorithms for Prevention of Impacts in Rehabilitation Systems, 2011 IEEE/ASME International Conference on Advanced Intelligent Mechatronics (AIM2011), pp.128-133.

[7] Kawamoto H., Lee S., Kanbe S., Sankai Y., "Power Assist Method for HAL-3 using EMG-based Feedback Controller", Proc. of Int'l Conf. onSystems, Man and Cybernetics (SMC2003), 2003, pp.1648-1653.

[8] Feng Chen, Yong Yu, Yunjian Ge, Jian Sun and Xiaohong Deng, A PAWL for Enhancing Strength and Endurance during Walking Using Interaction Force and Dynamical Information", Climbing and Walking Robots: towards New Applications, 2007, pp.417-428.

© ISAROB 2013

The Eighteenth International Symposium on Artificial Life and Robotics 2013 (AROB 18th '13),
Daejeon Convention Center, Daejeon, Korea, January 30-February 1, 2013

Through-Wall Imaging for a Metallic Cylinder by Dynamic Differential Evolution

Chung-Hsin Huang[1]
Department of Information Technology and Mobile Communication, Taipei College of Maritime Technology, New Taipei City, Taiwan, R.O.C.
e-mail: havehuang@hotmail.com

Chi-Hsien Sun[2]
Department of Electronic and computer engineering, National Taiwan University of Science and Technology, Taiwan, R.O.C.
e-mail:laisingsun@yahoo.com.tw

Ping-Chieh,Chiang[3]
Department of Electrical Engineering
National Taiwan University of Science and Technology, Taiwan, R.O.C.
e-mail:cfes2579@hotmail.com

Lung-Fai Tuen[4]
Electrical Engineering Department, Tamkang University, New Taipei City, Taiwan, R.O.C.
e-mail:justintuen@pchome.com.tw

Ching-Lieh Li[5]
Electrical Engineering Department, Tamkang University, Taipei County, Taiwan, R.O.C.
e-mail: chingliehli1@gmail.com

Pin-Ru, Lai[6]
Electrical Engineering Department, Tamkang University, Taipei County, Taiwan, R.O.C.
e-mail: cynically6667@livemail.tw

Abstract— **Through wall imaging for estimating shape of a metallic cylinder is proposed. The ability of dynamic differential evolution (DDE) stochastic searching algorithm for shape reconstruction of 2-D conducting targets hidden behind a homogeneous building wall is demonstrated by using simulated backscattered fields. After an integral formulation, a discretization using the method of moment (MoM) is applied. The through-wall imaging (TWI) problem is recast as a nonlinear optimization problem with an objective function defined by the norm of a difference between the measured and calculated scattered electric field. Thus, the shape of metallic cylinder can be obtained by minimizing the objective function. Simulations show that DDE can successfully reconstruct the through-wall imaging for a metallic cylinder.**

Keywords- Inverse Scattering, Dynamic Differential Evolution.

I. INTRODUCTION

Through-wall imaging (TWI) consists of imaging objects hidden behind an obstacle by using electromagnetic (EM) waves at the microwave frequencies. This problem is of great interest, as the aim of detecting and localizing hidden objects is shared in many applicative contexts (i.e., both military and civilian) such as in search and rescue, security, peacekeeping, and law enforcement operations [1]-[3].

The focus of the present work is on the reconstruction using inverse scattering approach. Among the inverse scattering approaches, several numerical reconstruction methods have been applied for through-wall imaging. General speaking, two main kinds of approaches have been developed. The first is based on local searching schemes such as the contrast source inversion (CSI) [4]. Recently, subspace-based optimization method (SOM) [5]-[6] has been proposed to solve inverse scattering problems. However, for a gradient-type method, it is well known that the convergence of the iteration depends highly on the initial guess. If a good initial guess is given, the speed of the convergence can be very fast. On the other hand, if the initial guess is far away from the exact one, the searching tends to get fail [7]. In general, they tend to get trapped in local minima when the initial trial solution is far away from the exact one. Thus, some population-based stochastic methods, such as genetic algorithms (GAs) [8], differential evolution (DE) [9],[10] and particle swarm optimization (PSO) [11]-[13] are proposed to search the global extreme of the inverse problems to overcome the drawback of the deterministic methods for TWI or buried problems.In our knowledge, there are still no numerical results by the DDE algorithm for metallic cylinder scatterers hidden behind a homogeneous wall. The DDE algorithm is used to recover the shape of the scatterer. The outline of the paper is as follows. In Section II, we describe the forward scattering for TWI. Section III and IV present inverse problem and dynamic differential evolution (DDE), respectively. Two numerical examples are presented in Section V. Section VI is the conclusion.

II. FORWARD PROBLEM

Let us consider a two-dimensional slab structure as shown in Fig.1, where (ε_i, σ_i) $i = 1,2,3,$ denote the permittivities and conductivities in each region. Here the permeabilities of all three regions are assumed to be μ_o and a conducting cylinder is buried in region 3. In our simulation, a priori information is assuming that scatterer is a metallic cylinder. The cylinder is of an infinite extent in the z direction, and its cross-section is described in polar coordinates in the x, y plane by the equation $\rho = F(\theta)$ (i.e., the object is of a star-like shape.) is illuminated by an incident plane wave whose electric field vector is parallel to

© ISAROB 2013

the z axis (i.e., TM polarization). We assume that the time dependence of the field is harmonic with the factor exp($j\omega t$). Let E_{inc} denote the incident field form region 1 with incident angle θ_1 as follow:

$$E_{inc} = E_1^+ e^{jk_1 \cos\theta_1 y} e^{-jk_1 \sin\theta_1 x} \hat{z} \quad (1)$$

At an arbitrary point (x, y) (or (r, θ) in polar coordinates) in regions 3 the scattered field, $E_s = E - E_i$, can be expressed as

$$E_s(x,y) = -j\,\omega\mu_0 \int_c G(x,y,F(\theta'),\theta')\, J_s(\theta') \sqrt{F(\theta)+F'(\theta)}\, d\theta \quad (2)$$

Where $J_s(\theta')$ is the induced surface current density, which is proportional to the normal derivative of the electric field on the conductor surface. $F(\theta)$ is the shape function, and $F'(\theta)$ is the differentiation of $F(\theta)$. c is cross section for detect domain. Note that G_1 and G_3 denote the Green's function which can be obtained by tedious mathematic manipulation for the line source in region 3. More detail on subgriding FDTD can be found in [9]

The direct scattering problem is to calculate the scattered electric fields while the shape and location of the scatterer are given. The shape function $F(\theta)$ of the scatterer is described by the trigonometric series in the direct scattering problem

$$F(\theta) = \sum_{n=0}^{N/2} B_n \cos(n\theta) + \sum_{n=1}^{N/2} C_n \sin(n\theta) \quad (3)$$

where *Bn* and *Cn* are real coefficients to expand the shape function.

III. INVERSE PROBLEM

For the inverse scattering problem, the shape of the metallic cylinder is reconstructed by the given scattered electric field

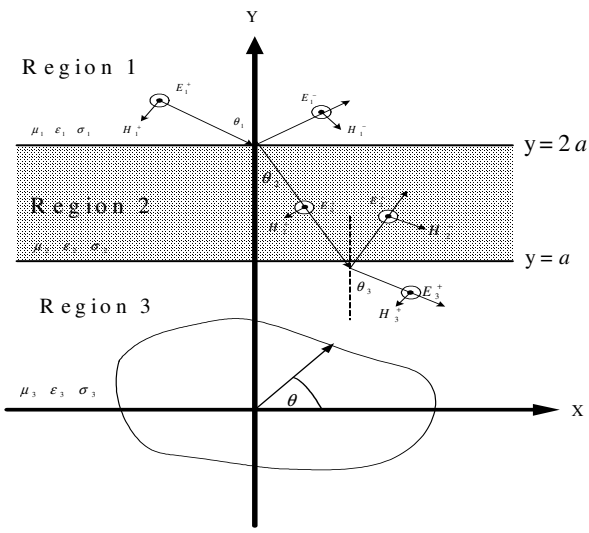

Fig. 1. Geometrical configuration of the problem.

measured at the receivers. This problem is resolved by an optimization approach, for which the global searching scheme DDE is employed to minimize the following objective function (*OF*):

$$OF = \left\{ \frac{1}{M_t} \sum_{m=1}^{M_t} \left| E_s^{\exp}(\bar{r}_m) - E_s^{cal}(\bar{r}_m) \right|^2 / \left| E_s^{\exp}(\bar{r}_m) \right|^2 \right\}^{1/2} \quad (4)$$

Where E_z^{exp} and E_z^{cal} are experimental electric fields and the calculated electric fields, respectively.

IV. EVOLUTIONAL ALGORITHMS

Dynamic Differential Evolution

DDE algorithm starts with an initial population of potential solutions that is composed by a group of randomly generated individuals which represents shape function of the cylinders. Each individual in DDE algorithm is a *D*-dimensional vector consisting of *D* optimization parameters. The initial population may be expressed by $\{x_i : \ i = 1, 2, \cdots, Np\}$, where *Np* is the population size. After initialization, DDE algorithm performs the genetic evolution until the termination criterion is met. DDE algorithm, like other EAs, also relies on the genetic operations (mutation, crossover and selection) to evolve generation by generation.

The key distinction between a DDE algorithm and a typical DE [12] is on the population updating mechanism. In a typical DE, all the update actions of the population are performed at the end of the generation, of which the implementation is referred as static updating mechanism. Alternatively, the updating mechanism of a DDE algorithm is carried out in a dynamic way: each parent individual will be replaced by his offspring if the offspring has a better objective function value than its parent individual does. Thus, DDE algorithm can respond the progress of population status immediately and to yield faster convergence speed than the typical DE. Based on the convergent characteristic of DDE algorithm, we are able to reduce the numbers of cost function evaluation and reconstruct the microwave image efficiently.

V. NUMERICAL RESULT

We illustrate the performance of the proposed inversion algorithm and its sensitivity to random noise in the scattered field. Consider a lossless three-layer structure ($\sigma_1 = \sigma_2 = \sigma_3 = 0$) and a perfectly conducting cylinder buried in region 3. The permittivity in each region is characterized by, $\varepsilon_1 = \varepsilon_0$, $\varepsilon_2 = 8.0\varepsilon_0$ and $\varepsilon_3 = \varepsilon_0$ respectively, as shown in Fig. 1. The incident angles equal to 45°, 90° and 315°, respectively. The frequency of the incident wave is chosen to be 3GHz. The width of the second layer is 0.1 m. There are seven measurement points are equally separated on a circle of radius 3m about center at

© ISAROB 2013

equal spacing in region 1. Thus there are totally 21 measurements in each simulation. The number of unknowns is set to be 7 (i.e., N+1=7). To save computing time, the number of unknowns is set to be 7. Moreover, to avoid inverse crime, the discretization number for the direct problem is two times that for the inverse problem in the simulation. In forward problem, the shape function $F(\theta)$ is discretized to 30. Reconstruction is carried out on an Intel PC (3.4 GHz/ 4G memory /500 G). The software is developed on FORTRAN VISION 6.0 in WINDOWS XP system environment. The search range for the unknown coefficient of the shape function is chosen to be from 0 to 0.1. The operational coefficients for the DDE algorithm are set as below: The crossover rate *CR*=0.8. Both parameters λ and ξ are set to be 0.8. The population size *Np* is set to be 70. It should be noted that the termination criterion is set to 2000 generations in our simulation based on our empirical rule.

In the first example, the shape function is chosen to be $F(\theta) = (0.025 + 0.015\cos 3\theta)$ (unit:m). The reconstructed shape function for the best population member is plotted in Fig.2 with the shape error shown in Fig.3. It is observed that DDE algorithm can be quickly achieved within 150 generation to minimize the relative errors of the shape and has good convergences. The typical CPU time for each example is about 2 minutes. Here, the shape function discrepancy is defined as

$$DF = \{\frac{1}{N'}\sum_{i=1}^{N'}[F^{cal}(\theta_i) - F(\theta_i)]^2 / F^2(\theta_i)\}^{1/2} \times 100\% \quad (5)$$

where N' is set to 1000. The relative error is about 0.01%.

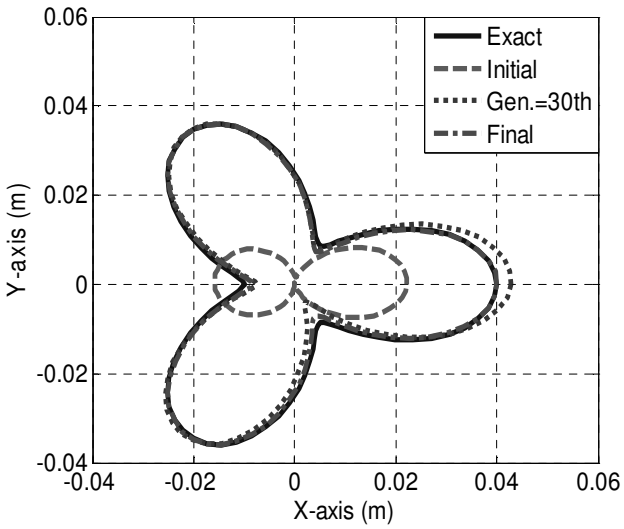

Fig. 2. The reconstructed cross section of the cylinder of the example at different generations.

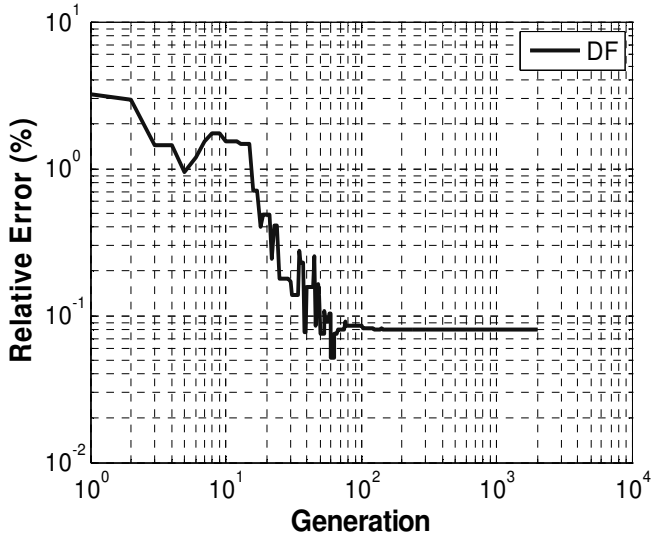

Fig. 3. Shape function error at different generations

IV. CONCLISIONS

In this paper, a computational approach to microwave imaging of homogeneous dielectric scatterer with arbitrary cross section in time domain has been presented. Scattering fields are obtained by FDTD method. The subgridding scheme is employed to closely describe the shape of the cylinder for the FDTD method. The approach has been formulated as a global nonlinear optimization problem and NU-SSGA has been applied. It has been shown that the location, shape and permittivity of the dielectric object can be successfully reconstructed even when the dielectric object with fairly large permittivity

ACKNOWLEDGEMENT

This work was supported by National Science Council, Republic of China, under Grant NSC 101-2221-E-229-001-

REFERENCES

[1] F. Soldovieri, R. Solimene, A. Brancaccio, and R. Pierri, "Localization of the interfaces of a slab hidden behind a wall," *IEEE Transactions on Geoscience and Remote Sensing*, vol. 45, no. 8, pp. 2471–2482, Aug. 2007.

[2] M. Dehmollaian, K. Sarabandi, "Refocusing Through Building Walls Using Synthetic Aperture Radar," *IEEE Transactions on Geoscience and Remote Sensing*, vol. 46, pp. 1589-1599, 2008.

[3] Y. Wang and A. E. Fathy, "Advanced System Level Simulation Platform for Three-Dimensional UWB Through-Wall Image" *IEEE Transactions on Geoscience and Remote Sensing*, vol. 50, pp. 1986-2000, 2012.

[4] Abubakar, A. and P. M. van den Berg, "The contrast source inversion method for location and shape reconstructions," *Inverse Problems*, Vol. 18, No. 2, 495-510, Mar. 2002.

[5] Chen, X., "Subspace-based optimization method for solving inverse scattering problems," *IEEE Transactions on Geoscience and Remote*

© ISAROB 2013

Sensing, Vol. 48, 42-49, 2010.

[6] Ye, X., X. Chen, Y. Zhong, and K. Agarwal, "Subspace-based optimization method for reconstructing perfectly electric conductors," *Progress In Electromagnetic Research*, PIER 100, 119-128, 2010.

[7] T. Moriyama, Z. Meng, and T. Takenaka, "Forward-backward time-stepping method combined with genetic algorithm applied to breast cancer detection", *Microwave and Optical Technology Letters*, Vol. 53, No. 2, pp.438-442, 2011.

[8] C. H. Sun, C. L. Li, C. C. Chiu and C. H. Huang, "Time Domain Image Reconstruction for a Buried 2D Homogeneous Dielectric Cylinder Using NU-SSGA.", *Research in Nondestructive Evaluation*, Vol. 22, No.1, pp. 1-15, Jan. 2011.

[9] M. Dehmollaian, "Through-Wall Shape Reconstruction and Wall Parameters Estimation Using Differential Evolution," *IEEE Geoscience and Remote Sensing Letter,* Vol. 8, 201-205, 2011.

[10] C. H. Sun, C. C. Chiu, W. Chien and C. L. Li, "Application of FDTD and Dynamic Differential Evolution for Inverse Scattering of a Two-Dimensional Perfectly Conducting Cylinder in Slab Medium", *Journal of Electronic Imaging.* Vol. 19, 043016, Dec. 2010.

[11] C. H. Sun, C. C. Chiu and C. L. Li, "Time-Domain Inverse Scattering of a Two- dimensional Metallic Cylinder in Slab Medium Using Asynchronous Particle Swarm Optimization.", *Progress In Electromagnetic Research M.* PIER M Vol. 14, pp. 85-100. Aug. 2010.

[12] C. C. Chiu, C. H. Sun and Y. S. Fan "Shape Reconstruction of 2-D Perfectly Conducting Cylinder Targets Using the Particle Swarm Optimization." *Imaging Science Journal.* Vol. 60, No 2, pp. 83-89, Apr. 2012.

[13] C. C. Chiu, C. H. Sun and W. L. Chang "Comparison of Particle Swarm Optimization and Asynchronous Particle Swarm Optimization for Inverse Scattering of a Two- Dimensional Perfectly Conducting Cylinder.", I*nternational Journal of Applied Electromagnetics and Mechanics* Vol. 35, No.4, pp. 249-261,Apr. 2011

© ISAROB 2013

The Eighteenth International Symposium on Artificial Life and Robotics 2013 (AROB 18th '13),
Daejeon Convention Center, Daejeon, Korea, January 30-February 1, 2013

Analysis of Effects of Exercises on Middle-aged and Elderly Arthritics by Thermal Imagery and Automatic Auxiliary Diagnosis

[1,a]Chin-Lun Lai* [2,b]Tsung-Ching Lin and [1,c]Tung-Lin Yang
[1]Institute of Information and Communication Engineering, Oriental Institute of Technology, Taipei, Taiwan
[2]Department of Physical Medicine and Rehabilitation, Far Eastern Memorial Hospital, Taipei, Taiwan

Email: [a]fo001@mail.oit.edu.tw, [b]tclin0331@gmail.com, [c]maniya.ntcb@msa.hinet.net,

Abstract: In this paper, an automatic infrared thermal image analysis method is proposed to analyze the rehabilitation effects, after simple exercise intervention, on middle-aged and elderly osteoarthritic patients, while an automatic CV diagnosis criteria for distinguishing the patients from the healthy persons is also established, to assist medical personnel's diagnoses and suggestions. To approach this goal, the questionnaires from the Western Ontario and McMaster Universities are also used as basis for evaluating physiological changes before and after rehabilitative exercises and the data analyzed may also be used as the reference for subsequent exercise adjustment by the subject. Experimental results shows that the proposed method performs well in automatic judgement of degenerative arthritis hence can be a good reference for clinical diagnosis.

Keywords: Infrared thermal imaging, osteoarthritic, automatic diagnosis , WOMAC

1 INTRODUCTION

Some chronic diseases occur with age increasing and Osteoarthritis (OA) is just one of the most common ones. Degenerative gonitis is also referred to as knee osteoarthritis which is the most common joint disease across the world. It has gradually spread from the elderly to the young in recent years. The main symptom is articular cartilage damaged. Therefore some people hold that the degenerative arthritis is joint weak and degeneration and the degenerative joints are vulnerable to pain, hydrarthrosis and swelling resulting in the range of motion decreased. The arthritis may occur to various parts of the whole body, in particular to the weight bearing joint or joints with a large range of motion, such as cervical vertebra, lumbar vertebra, hip joints, knee joints and hand joints. Such symptoms will significantly affect daily motions of the patient, such as waking tread, surmounting obstacles, walking up and down the stairs, change from sitting to standing, etc. In the past, such physiological conditions relied on X-ray examination. The result is accurate while the issue of radiation dose exists. Infrared imaging is also called temperature-difference photographing and is a detection technique for observing shell temperature distribution using the infrared radiation photographing principle. The local heat balance will be affected when a human being contracts a disease or the physiological condition is abnormal and clinically the tissue temperature will increase or decrease accordingly. Thus the measurement of body temperature variation is one of the important indicators for clinical disease diagnosis. And then many studies focus on the application and limitation of exploring biomedicine via thermal imagery [1]. For example: evaluation of hand osteoarthritis and rheumarthritis, effect of lesion of nerves around the sole of the diabetics' foot soles on blood circulation [2-3]. The detection methods above are based on symptoms such as inflammatory responses, swell, fever, pain etc. These pathological processes will affect blood vessels and surrounding tissues. But, the heat radiation is the energy diffused naturally from the body temperature and can be remotely sensed to form thermal imagery data and analyzed. Hence the thermal image can be used to diagnose diseases occurring to body surface or proximity of body surface without invasive behavior or radiation dose problem, which is a highly safe physiological exploring approach. Thus great importance has gradually been attached to the approach in the medical circle. It is required that attention shall be paid to the operating errors when the thermal image assessment diagnosis is used for conditions. The errors will not be decreased unless the operating conditions for infrared thermograph are complied [4]. It is attributed that the experimental environment, equipment and physiological condition of the subject at the moment will affect the result. In addition, the assessment scale for OA patients is used in the study the Western Ontario and McMaster Universities Osteoarthritis Index (WOMAC) [5]. However, the assessment scale can only objectively reflect the conditions of the patient after exercise and a thermal imager is required for pathological detection in combination with the assessment scale. The heat generated can be used for detecting the skin surface temperature indicating pain intensity by the thermal imager since the area below the

© ISAROB 2013

patella is most sensitive to pain for the arthritic [6]. Besides, it will be very difficult to distinguish from other arthritis or symptoms and the temperature detected by the thermal imager may approximate the temperature of a normal subject if no change is observed or only slight stenosis of articular cavity is noted on the X-ray film for the initial degenerative arthritis. In such a case, it is difficult to judge the subject as an arthritic or a healthy person. Hence, the paper presents a set of rehabilitation exercise method to induce the difference between an arthritic and a healthy person after exercise and calculate the center point [7] of patch below the patella with the image captured automatically by the thermal imager. Compare the difference (if any) between the skin surface temperate of the experimental group and control group after the temperature of the area is obtained, and the rehabilitation effect after exercise for two weeks. Then overlap the two different images (visible image and thermal image), adjust the contrast after overlapping [8], to allow the location of local abnormal temperature to be more easily observed on the overlapped image. With such detections, the medical personnel are able to judge the patients' conditions even more accurate and quicker.

The paper will introduce methods in the following section, the third section will present and discuss and experimental results, the fourth section will present conclusions and suggestions.

2 Experimental Methods

According to the bibliography, it is known that the infrared thermal image can be used to detect degenerative arthritis. But the detection effect of the person with slight symptom is not necessarily significant compared with that of a healthy person. Therefore, the study is conducted in cooperation with a doctor from the rehabilitation division. Annular oil pressure resistance training movement as induced to detect the difference between the degenerative arthritics and healthy persons, and collected data as the basis for establishing an automated auxiliary discrimination program, in order to make the process more clear, the flow chart for the system operation is showed as the Fig. 1 below and then the function of each block is described as follows:

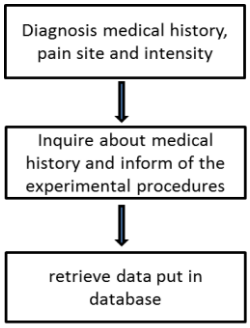

Fig. 1. Collected data System Diagram.

Step 1: Doctor diagnosed the medical history, pain site and severity of the patient and delivered the statistical study data to the study personnel for photographing the pain site.

Step 2: The study personnel are required to inform the subject of precautions in advance. The subject shall stay in the isolation room for 15 minutes prior to the start of the first-week exercise. Apply a patch with diameter of about 2cm to the central point of the knee patella as the locating point and photograph the temperature before the first-time exercise. The subject shall do warm-up exercises first and then take rehabilitation exercise under the direction of the coach in the fitness center (annular oil pressure resistance training, eight apparatus in total, one minute for each apparatus, and three circles in total). Take note of the exercise effect of each subject at all times. The subjects will be lead to the isolation room for experiment following exercise. They shall also stay in the isolation room for 15 minutes before the experiment, understand the experiment procedures to be performed and fill in the WOMAC questionnaires. All procedures will be performed at a room temperature of about 23±1℃. In addition, be sure to make infrared image measurement after the body temperature reaches the balance state to avoid temperature errors caused by heat accumulation. Maintain low humidity for the body and prevent the measurement being influenced by the convection and heat radiation.

Step 3: Repeat the steps in A and B above , retrieve the Image Data of the experimental group and the control group and input them to the data base. Then write computer identifying programs based on the images in the database. The flow chart for the automatic computer identifying system operation is showed as the Fig .2 below the automatic identifying program is as follows:

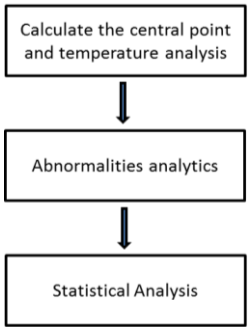

Fig. 2. Automatic computer identifying System Diagram.

© ISAROB 2013

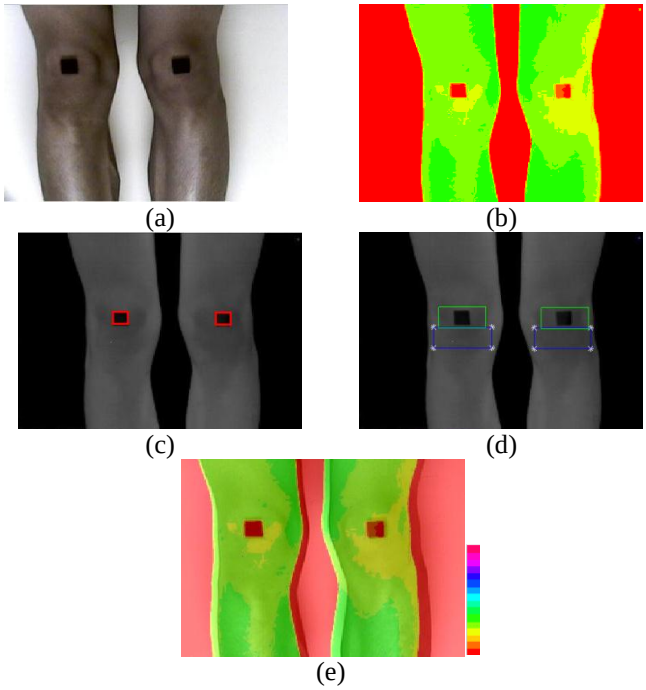

Fig. 3. (a) Original visual image, (b) thermal image, (c) the black patch marked as 2 cm, applied to the center of the patella, the red box for confirming the patch's registration with the central point, and the stance during photographing, (d) the blue box for calculating the temperature below the patella, (e) the overlapped image is convenient for identifying the variation of skin surface.

Step 4: Reference [16], set the black patch as the desired object, calculate the central point of the patch, in addition, stick the patch with diameter about 2cm to the central point of the knee patella as the positioning point to confirm that the positions of the thermal image and visible image are consistent the mark displays as a red block on the thermal imager shown in Fig. 3(b). Therefore, it is easy to identify the registration of the two images. Finally, adjust the thermal imager to the optimal angle and height for photographing the knee joints. Fig. 3(c) is for confirming whether the patch is selected, whether the standing position for photographing is excessively close to or away from the camera. The range of the black patch will be beyond the red box and affect the judgment if the standing position for photographing is excessively close to the camera. Calculate the temperature of the feet down from the central point of the patch. The blue box below the central point (below the patella) can be simply defined as:

$$S(x, y) = I(c + d, r + i) < k\,. \qquad (1)$$

The green box in Fig. 3(d) is the patch range set, variables c and r are the central points of the patch, d is the distance between the upper and the lower end of the central point, i is the distance between the left end and the right end of the central point, k is the value of background pixel. Record the coordinate value of the previous point if the pixel of the following point is less than the pixel value of k point. Repeat the above steps for four times to obtain the average temperature, maximum temperature and minimum temperature of the pixel sum in the blue box.

Step 5: The coordinates of the central points from the two images shown in Fig. 3(a) and Fig. 3(c) subtract and the resulting new central point is exactly the distance between the two cameras shown in Fig. 3(e). Perform image overlapping for conveniently viewing the abnormal sites on the skin. Finally, retrieve the temperatures of the experimental group and the control group before and after exercise and find out the difference.

Step 6: Input the collected data of subjects to the database and apply Gaussian distribution statistical data to the experimental group and control group. Normalize the derived average value and standard deviation to determine the probability of each observed value in the data distribution as the basis for inferring whether the data from a certain population. In the database, one-point density function is applied per 0.01℃ for the data of ten groups of patients and ten groups of healthy persons collected based on the average value and standard deviation. The curve derived is distributed as shown in Fig. 4 (the red points on the left and right curves are the actual temperatures of ten subjects). The two curves significantly show the temperature difference between the arthritics and healthy persons. In addition, collect the data of four subjects with condition unknown and input it to the database (purple round points) as probability for testing the system prognosis, which can assist the medical personnel in diagnosis.

3 Experimental Results

In order to achieve the expected results of the study, listed t he following precautions: infrared thermal imager, subjects information, shooting distance, and environmental factors.

A. Subject Information

The study is approved by Institutional Review Board for coo perating with the doctor from rehabilitation division of Far E astern Memorial Hospital.

B. Operating Way

The sequences: wait for 15 minutes, stand by the foot mat, researchers subjects paste patch to automate capture images show the temperature of the subjects, and analysis belongs to which part of the ethnic groups with a probability value.

In WOMAC questionnaires for evaluating pain intensity (knee pain, stiff degree, motion difficulty) from patients with objective conditions, the pain intensity of second time is weaker than that before and after the exercise of first time and the second time and the temperature before and after exercise decreases significantly. Therefore it is determined that the rehabilitation exercise can generate rehabilitation effects as shown in Table 1. The result of experimental numerical analysis shows that partial subjects are not easily judged as arthritics due to the fact that their temperature

© ISAROB 2013

differences before exercise are not significant. Therefore, the temperatures after induced rehabilitation exercise are used to plot the normal distribution curve in the form. The temperature of the left foot is higher than that of the right foot among all subjects, which may relate to footedness. Therefore, the temperatures of left feet are uniformly adopted for the distribution curve for more convenient difference distinguishing as show in Table 2. Observe the Normal distribution curve established with the experimental group and control group in Fig. 4 if the prediction demonstrates that the method after simple exercise is able to identify the range value for the difference temperature between the patients and healthy persons. It is assumed that a subject with condition unknown is measured to be 33.17℃ as shown in Table 3. It is predicted that the probability of the subject in the database range for degenerative arthritics accounts for 25.30% while the probability of healthy persons accounts for 0.10%. But the probability of patients is much higher than that of healthy persons. Hence the subject is judged as an arthritic finally. And the temperature is within the range of patient database and partial area is within the range of healthy persons. Hence the part is also judged as error rate.

Table 1. Differences after Exercise

Arthritic	First Detection	Second Detection
WOMAC(pain intensity)	12.66	10.92
Temperature before exercise (left/right)	32.44/33.85	30.78/32.92
Temperature after exercise (left/right)	31.93/33.84	30.48/32.80

Table 2. Characteristics of the study participants

	Degenerative Arthritis	Without Degenerative Arthritis
Quantity	10	10
Age	66.8±14.2	20.8±3.2
Average temperature before exercise (left foot)	32.44	28.41
Average temperature before exercise (right foot)	31.93	28.30
Average temperature after exercise (left foot)	33.85	29.35
Average temperature after exercise (right foot)	33.84	29.28
Grade	Grade Ⅰ-Ⅱ	Grade 0

Table 3. Analysis of System auxiliary Discriminant

Temperature	Probability of Patient	Probability of Healthy Person	Cross Error Rate
29.35	5.20e-06%	47.46%	5.20e-06%
30.19	1.64e-04%	24.21%	1.64e-04%
33.17	25.30%	0.16%	0.16%
33.85	50.12%	0.03%	0.03%

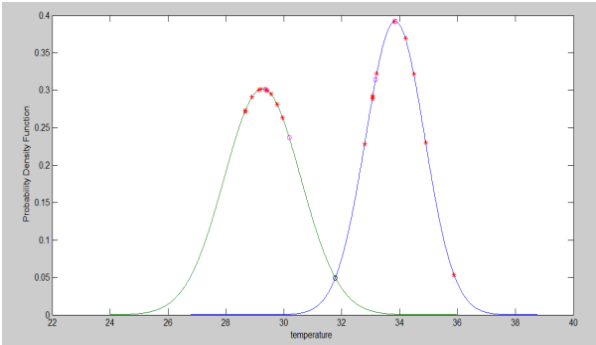

Fig. 4. Normal distribution of subjects

4 Conclusions And Suggestions

The experiment result verifies the following arguments. The thermal imager can be used to detect the difference between the degenerative arthritics and healthy persons after rehabilitation exercise and it is obviously observed that the rehabilitation exercise is significantly helpful for the patients. In addition, the questionnaire assessment also shows that the pain index of the patients involved in rehabilitation is decreasing.

REFERENCES

[1] L. J. JIANG, E. Y. K. NG, A. C. B. YEO, S. WU, F. PAN, W. Y. YAU, J. H. CHEN, and Y. YANG, "A perspective on medical infrared imaging," *Journal of Medical Engineering & Technology*, vol. 29, no. 6, pp. 257-267, 2005.

[2] S. Bagavathiappan, J. Philip, T. Jayakumar, B. Raj, PN. Rao, M. Varalakshmi, and V. Mohan, "Correlation between Plantar Foot Temperature and Diabetic Neuropathy: A Case Study by Using an Infrared Thermal Imaging Technique," *Journal of Diabetes Science and Technology*, vol. 4, pp. 1386-1392, November 2010.

[3] N. Borojevic, D. Kolaric, S. Grazio, F. Grubisic, S. Antonini, I. A. Nola, and Z. Herceg, "Thermography of Rheumatoid Arthritis and Osteoarthritis," *ELMAR*, pp. 293-295, Zadar, Croatia, September 2011.

[4] N. Kakuta, S. Yokoyama, and K. Mabuchi, "Human thermal models for evaluating infrared images," *IEEE Trans. on Engineering in Medicine and Biology Magazine*, vol. 21, no. 6, pp. 65-72, 2002.

[5] S. McConnell, P. Kolopack, and A. M. Davis, "The Western Ontario and McMaster Universities Osteoarthritis Index (WOMAC): A review of its utility and measurement properties," *Arthritis Care & Research*, vol. 45, no. 5, pp. 453-461, October 2001.

[6] Anna E. Denoble, Norine Hall, Carl F. Pieper, and Virginia B. Kraus, "Patellar Skin Surface Temperature by Thermography Reflects Knee Osteoarthritis Severity," *Departments of Medicine*, pp. 69-75, October 2010.

[7] F. Essannouni, R. Oulad Haj Thami, D. Aboutajdine, and A. Salam, "Simple noncircular correlation method for exhaustive sum square difference matching," *Optical Engineering*, vol. 46, no. 10, October 2007.

[8] G. Schaefer, R. Tait, and S. Y. Zhu, "Overlay of thermal and visual medical images using skin detection and image registration," *Int. Conf. of Engineering in Medicine and Biology Society, 2006. EMBS '06*, New York City, USA, pp. 965-967, 2006.

© ISAROB 2013

The Eighteenth International Symposium on Artificial Life and Robotics 2013 (AROB 18th '13),
Daejeon Convention Center, Daejeon, Korea, January 30-February 1, 2013

Enhancing electrical communication through reconstructed nanowire electrodes for implantable enzymatic biofuel cell (EBFC)

Deby Fapyane[1], Soo-Jin Lee[1], Duhyun Lim[2], Jou-Hyeon Ahn[2] and In Seop Chang[1]

[1]School of Environment Science and Engineering, Gwangju Institute of Science and Technology (GIST), 261 Cheomdan-gwagiro, Buk-Gu, Gwangju 500-712, Republic of Korea; Telephone: 82-62-715-3278
[2] Department of Chemical and Biological Engineering, Gyeongsang National University, Jinju 660-701, Republic of Korea

Corresponding author: ischang@gist.ac.kr

Abstract: Enzymatic biofuel cell (EBFC) is a promising continuous energy supply powered by abundant and essential components in human physiological fluid; glucose and oxygen, for powering implanted device. Important aspects in BFC are establishing efficient electron transfer pathways between enzyme redox center and electrodes and maintaining enzyme stability. In this study we characterized of electron transport from enzyme as core of BFC to the nanowire by edge-immobilization (EI) and sidewall-immobilization (SI). Through immobilization in both aspects of nanowire surface, electrical transport through edge is responsible for efficiency meanwhile sidewall immobilization benefits for enzyme stacking compartment. We also studied the functional group exist in nanowire may act as bridge to individual nanowire. Nanowire which is lacking of EWG diminished electron transport enhancement between C-C bonds through resistance barrier. Further study which factor limiting and enhancing electrical transport through pristine and constructed carbon nanotube is still being assessed.

Keywords: Implantable EBFC, carbon nanotube network, electrical communication, reconstructed nanowire

1 INTRODUCTION

Enzymatic biofuel cell (EBFC) is a system which generates electrical power from conversion of substrate through redov reaction in the enzyme redox center ((Mano, Mao et al. 2003; Soukharev, Mano et al. 2004; Cracknell, Vincent et al. 2008; Moehlenbrock and Minteer 2008). Being able to generate micropower, EBFC has been drawing out the attention for real application and developed the power source for implanted devices (MacVittie, Halamek et al. 2012) by using human essential compound; glucose and oxygen. As near future promising power source, EBFC is expected to be able to power developed implanted devices such as pacemakers, neuron stimulator and implanted neurophysiological monitoring devices (Justin, Yingze et al. 2004; MacVittie, Halamek et al. 2012).

Before Heller and Cosnier's group conducting the real application of implanted enzymatic in plant and animal, EBFC was less attractive due to its low voltage which thermodynamically limited by the potential of enzymes substrate (MacVittie, Halamek et al. 2012). Based on the EBFC main limitation, many studies had been conducted to overcome the critical points of EBFC which is the communication between enzyme and electrode (Ferreira, Iost et al. 2012). Achieving the high current and power density of EBFC is the main objective of the electrodes construction.

Conductive nanowires have been studied as a matrix for electrode architecture of EBFC. Nanowire such as carbon nanotubes (CNTs) are able to act as enhancement factor of electrical communication between enzyme and electrode superficial (Ferreira, Iost et al. 2012) and also as enzyme stacking compartment due to its large surface area. However, like other nanoparticle characteristic, CNTs also carry concerning drawback as electrode matrix where it is accompanied by high charge transfer resistance (Wang 2006) and electrolyte diffusion limitation due to its hydrophobicity. Hence, optimization of nanowire condition is practically needed to enhance electron transfer efficiency.

In this study we assessed the electrical network through CNTs in the EBFC system. Nanowire network are built in the edge-edge (E-E), edge-sidewall (E-S) and sidewall-sidewall (S-S) to support EBFC performance. Utilization of pristine carbon nanotube (CNTs) with its native high electrical conductivity needs to be improved to achieve maximal use of nanowire network through reconstructed electrical network with chemical functionalization. Acid treatment creates defect sites for activating –COOH functional groups in carbon nanotube to enhance electron transport from and to individual nanowire as –COOH is an electron withdrawing group (EWG). We also assessed the characteristic of electron transport from enzyme (glucose oxidase, GOX) as core of BFC to the nanowire as supporting material to avoid ambiguous interpretation of over-potential occurrence during electron transport.

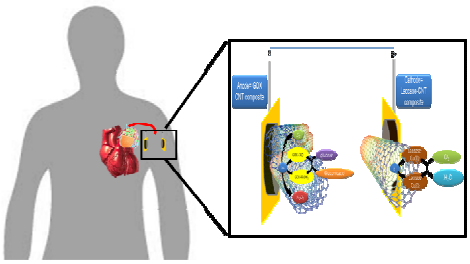

Scheme1. Near future application of implanted BFC in human powering implanted medical devices

© ISAROB 2013

2. MATERIAL AND METHOD

2.1. Material

Glucose oxidase from *Aspergillus niger (type VII-S, 192 U/mg)*. Laccase from *Trametes versicolor (13.6 U/mg)*, *β*-D Glucose, 1-pyrenebutanoic succinimidyl ester, N-(-3-dimethylaminoprophyl) N'-ethylcarbodiimide, 2-thioethanol, cystamine sodium diphosphate and disodium phosphate and Si/Au wafer as substrate from Sigma Aldrich. Pristine, purified and acid treated multi walled carbon nanotube (MWNTs) was provided from Gyeongsan National University, Gyeongsan, South Korea. Phosphate buffer solution (PBS, 100 mM, pH 7.0) was prepared as supporting electrolyte for BFC performance. D-glucose solutions (10mM) prepared at least a night before to allow mutarational equilibrium. All solutions were prepared with deionized water.

2.2. Method

Characterization of enzyme immobilization as Edge-immobilization (EI) and sidewall-immobilization (SI) were constructed by covalent bonding and utilizing heterobifunctional polymer, respectively. Each immobilization method was evaluated through XPS (Thermo Fisher Scientific, U.K) spectroscopy. Characterization of each CNT material was done by FTIR (JASCO, U.S.A), Raman spectroscopy (Andor, U.S.A) and XPS. All electrochemical measurements for EBFC performance were performed in PBS buffer at 37°C.

Electrochemical method was performed using three electrodes system (BAS-EC epsilon, U.S.A) consists of Si/Au wafer, platinum and Ag/AgCl as working, counter and reference electrode respectively. Anode (CNT-GOX) and cathode (CNT-laccase) composites were placed in one membraneless compartment biofuel cell. Stirring and aeration was done for cathode reaction during performance test with electrolyte flow 0.1mL/min. A surface area of 0.196 cm^2 used for calculation of the current and power density.

3. RESULT AND DISCUSSION

3.1. Vertically and horizontally aligned CNTs

Direct electron transport can be achieved by enzyme immobilization in the edge of CNT shown at potential of FAD as glucose oxidase redox center, which was -0.4 V (against Ag/AgCl). EI enzyme wiring achieved electron transfer with K_s value of 1620.5/s whereas SI enzyme K_s is 953.6/s. Furthermore, SI enzyme wiring contributed to the over-potential happened in the electron transport from redox center to the electrode characterized by cathodic peak at -0.3 V instead of -0.4 V (**Fig.1**).

However, SI produced 1.5 times higher current EI indicating, more load of enzyme in the sidewall than in the edge which can be confirmed through nanowire diameter-length ratio. Through immobilization in both aspects of nanowire surface, electrical transport through edge is responsible for efficiency meanwhile sidewall immobilization benefits for enzyme stacking compartment

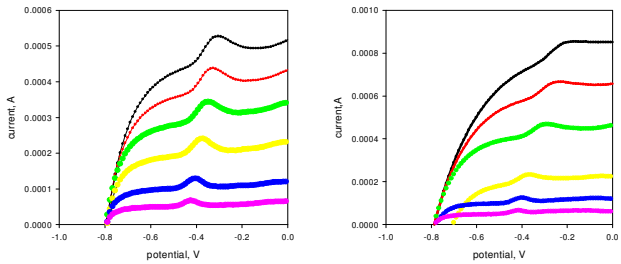

Fig. 1. Cyclic voltammograph of vertically (left) and horizontally (right) aligned CNT for GOX immobilization

3.2. XPS profile

Each immobilization method was evaluated through XPS which showed the emerge peak of C=O bonding in the 286.25 eV for horizontally aligned CNTs showing carbonyl groups mainly present in the edge of CNTs which will react with amine group of enzyme. In the other hand, we can observe increase of π-π* stacking point in the 291 eV or also called satellite peak as the result of heterobifunctional polymer use for sidewall modification

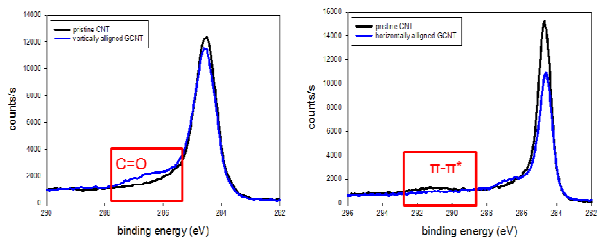

Fig. 2. XPS spectra of vertically (left) and horizontally (right) aligned CNTs on Si/Au wafer

3.3. Reconstructed nanowire with functionalization

Nanowire network are built in the edge-edge (E-E), edge-sidewall (E-S) and sidewall-sidewall (S-S) to support EBFC performance. Utilization of pristine carbon nanotube (CNTs) with its native high electrical conductivity needs to be improved to achieve maximal use of nanowire network through reconstructed electrical network with chemical functionalization.

Acid treatment creates defect sites for activating –COOH functional groups in carbon nanotube to enhance electron transport from and to individual nanowire as –COOH is an electron withdrawing group (EWG). As expected, higher current was achieved for higher degree of functionalized nanowire approximately increased 50% every 4h of strong acid treatment (**Fig. 3)**

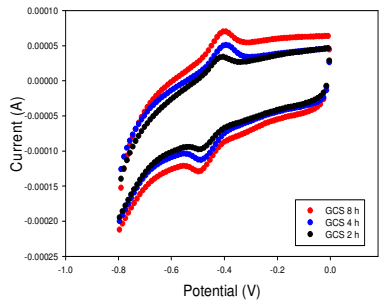

Fig. 3. Current enhancement after acid treatment

© ISAROB 2013

3.4. Performance of EBFC

Constructed network of CNT disk increased current and power density of BFC. By utilizing 4800 U of glucose oxidase, constructed nanowire current density was 863.00±49.33 μA/cm^2 while non-constructed network showed 67% of performance which was 583.58±49 μA/cm^2. Fig. 4. showed the performance of reconstructed and pristine CNTs-enzyme in EBFC. Reconstructed nanowire resulted 30% higher power density compared with pristine CNTs composites.

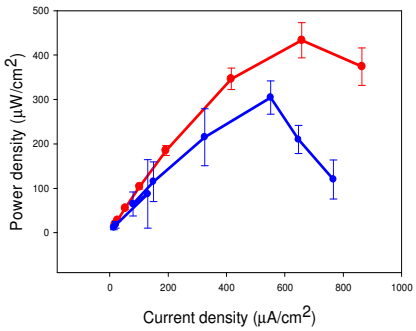

Fig. 4. I-V curve of reconstructed CNTs-GOX (red) and pristine CNTs-GOX anode composites operated in EBFC system with reconstructed CNTs-Laccase as cathode

Measurement of impedance by EIS revealed that non-functionalized CNT disk has less conductivity (3mm thick; 15,000 Ω) by higher resistance than functionalized CNT disk (3 mm thick; 9,000Ω). We suggest that functional group acts as bridge to individual nanowire which is lacking of EWG diminished electron transport enhancement between C-C bonds in CNT junction through resistance barrier. Advance assessment for the factor which limiting and enhancing electrical transport through pristine and constructed carbon nanotube is still being assessed.

4. CONCLUSION

We successfully examined the effect of enzyme stacking site to nanowire interface. Edge of CNTs is more active to enhance the electrical communication rather than sidewall. However, sidewall of CNTs is important site for enzyme stacking compartment.

Reconstructed nanowire by functionalization to make edge-like site in the sidewall will accommodate the enhancement of electrical communication by minimizing resistance between nanowire interfaces

Further factor relating to EBFC operation which affects composites performance such as electrolyte diffusion barrier and its chance to decrease the electron transfer is still being assessed.

5. REFERENCES

[1] Mano, N., F. Mao, and A. Heller, *Characteristics of a miniature compartment-less glucose-O2 biofuel cell and its operation in a living plant.* Journal of the American Chemical Society, 2003. **125**(21): p. 6588-6594.

[2] Soukharev, V., N. Mano, and A. Heller, *A four-electron O2-electroreduction biocatalyst superior to platinum and a biofuel cell operating at 0.88 V.* Journal of the American Chemical Society, 2004. **126**(27): p. 8368-8369.

[3] Moehlenbrock, M.J. and S.D. Minteer, *Extended lifetime biofuel cells.* Chemical Society Reviews, 2008. **37**(6): p. 1188-1196.

[4] Cracknell, J.A., K.A. Vincent, and F.A. Armstrong, *Enzymes as working or inspirational electrocatalysts for fuel cells and electrolysis.* ChemInform, 2008. **39**(41): p. no-no.

[5] MacVittie, K., et al., *From "Cyborg" Lobsters to a Pacemaker Powered by Implantable Biofuel Cells.* Energy & Environmental Science, 2012.

[6] Justin, G.A., et al. *Biofuel cells: a possible power source for implantable electronic devices*. in *Engineering in Medicine and Biology Society, 2004. IEMBS '04. 26th Annual International Conference of the IEEE*. 2004.

[7] Ferreira, F., et al., *Intravenous Implantable Glucose/Dioxygen Biofuel Cell with Modified Flexible Carbon Fiber Electrodes.* Lab on a Chip, 2012.

[8] Wang, P., *Nanoscale biocatalyst systems.* Current Opinion in Biotechnology, 2006. **17**(6): p. 574-579.

© ISAROB 2013

The Eighteenth International Symposium on Artificial Life and Robotics 2013 (AROB 18th '13),
Daejeon Convention Center, Daejeon, Korea, January 30-February 1, 2013

Object Tracking Based on Adaboost Classifier and Particle Filter

Chin-Lun Lai[1] , Li-Yin Lee[2]
[1,2]Communication Engineering Department, Oriental Institute of Technology, Taipei, Taiwan

[1]fo001@mail.oit.edu.tw
[2]990130108@mail.oit.edu.tw

Abstract: In this paper, a hybrid structure combining adaboost classifier and particle filter is proposed to automatically detect and track the pedestrian targets. The adaboost detection process is adopted first to target candidate objects, and then the particle filter is applied for confirming and tracking of targets. Experiment results show that via the proposed method, the drawback of the current particle filters which requires specifying an object to be tracked in advance can be overcome, while performing good also in cases of target missing, occlusion, and identifying the previously appeared objects.

Keywords：object tracking, adaboost detection, particle filter

1 INTRODUCTION

Application of object tracking has always been an important issue in computer vision or image processing applications. In the early stages, object tracking had been applied to air traffic control. Recently, it has often been applied to with security monitoring related fields. There are various types of methods for object tracking. Generally, these methods can be divided into time domain methods and space domain methods. Time domain methods include such as motion estimation[1] or optical flow, etc., while space domain methods include k-means, mean-shift, kalman filter, and particle filters [2].

In a time domain system, the target must be able to show time differences. In other words, the target has to move so that judgments can be made. In a space domain system, judgments are made based on image characteristics of the targets. And usually judging methods based on characteristic information are more complex and diversified.

However, if only a time domain method is applied, the only thing that can be confirmed is that whether the target is moving or not. It is difficult to find out if this target is the interest one. Methods like k-means and mean-shift require manual settings and object size changes are not allowed. Kalman filter is used for linear systems thus is not appropriate for real-world systems which are usually no-linear systems. On the other hand, particle filter is a good solution for target tracking but is only applicable when the scene is known and possible locations of the target are preset[2]. However, adding the adaboost algorithm helps to solve this issue [3]. Therefore, this study proposed a combined structure with adaboost detection and particle filtering method to resolve the problems mentioned above for the pedestrian tracking problems.

2 SYSTEM FRAMEWORK

The proposed system framework is shown in figure 1 and the detailed steps are described as follows:

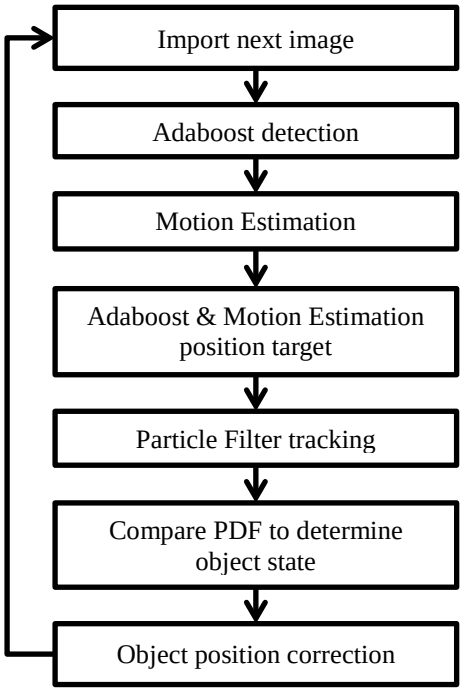

Fig. 1. system framework

© ISAROB 2013

2.1 Adaboost detection

To improve the prediction rate and reduce the error rate, four adaboost cascades were combined to form the initial conditions for pedestrian detection. The types of the four cascades were upper body, lower body, front side of whole body, and back side of whole body. All four cascades were objects or parts of objects, resolving the issue of imprecise detection with only one cascade.

The training sequences included 2094 positive samples and 1333 negative samples. The width and height were 10 and 24 (pels), using all upright rectangle feature and 45 rotated rectangle feature [4].

Two of the four cascades were used to detect upper body and lower body. Therefore, whole body normalization was required. An upper body includes head and shoulders. Thus, a bounding box may contain head and shoulders. And in the cascade training, the size was 22x20, with the shape being close to a square. Since humans' upper bodies are rectangles, it is necessary to normalize bounding boxes for upper bodies as follows:

$$\mathrm{BBox}_{\mathrm{up(x)}} = \mathrm{upbody(x)} + \frac{\mathrm{upbody(w)}}{4} \quad (1a)$$

$$\mathrm{BBox}_{\mathrm{up(w)}} = \frac{3}{4} \times \mathrm{upbody(w)} \quad (1b)$$

$$\mathrm{BBox}_{\mathrm{up(h)}} = \sqrt{2} \times \mathrm{upbody(h)} \quad (1c)$$

where $BBox_{up}$ is the normalized bounding box and *upbody* is the bounding box detected using adaboost. Parameters for upbody, (x, y, w, h), represent the x-coordinate, y-coordinate, width, and height, respectively.

Similarly, as for the lower body training, the size was 19x23. Thus whole body normalization was performed by (2) as follows.

$$\mathrm{BBox}_{\mathrm{low(y)}} = \mathrm{lowbody(y)} - \frac{1}{2}\mathrm{lowbody(h)} \quad (2a)$$

$$\mathrm{BBox}_{\mathrm{down(h)}} = \sqrt{2} \times \mathrm{lowbody(h)} \quad (2b)$$

where $BBox_{low}$ is the normalized bounding box and *lowbody* is the bounding box detected using adaboost.

2.2 Motion estimation

By adopting adaboost, many candidate targets were found hence further filtering was required to remove the misjudged ones. It can be done by adding simple motion estimation process. First, binary threshold for three continuous images was calculated. And then morphology erosion and closing, with 3x3 and 5x5 masks, were applied to these 3 images to obtain a binary image using OR gate, in order to determine the moving range of an object.

2.3 Adaboost & motion estimation

After applying motion estimation to the normalized bounding boxes, the areas of the bounding boxes are calculated. The bounding boxes of small sizes were considered as noises, while the centers of those which were not noises were obtained.

With a given size threshold, the bounding boxes with areas over the average were removed. Among the bounding boxes left, the one with the smallest area was considered as the most possible target. Then, target positioning was performed with the most possible bounding box. And the positioning information, including the center and the range of the target, was sent to the particle filter.

2.4 Particle filter tracking

Ones the object was confirmed, the particles of the particle filter are initialized using the positioning information of the object to perform particle filter tracking[2]. The re-sampling method adopted was the systematic method[5]. The new model was based on the average of the two previous models.

After that, the PDF of the target at *t-1* was compared with that at *t* through the corresponding correlation coefficient. If the difference was too large, the target was considered disappeared or lost. In that case, adaboost was applied again for re-positioning.

2.5 Adaboost & particle filter correction

In order to prevent particle distribution from being too scattered due to large changes of PDF of the target, adjustments needed to be made based on the adaboost detection results when applying particle filter. In continuous images of the target, the functions of the size and the distance were supposed to be continuous. Therefore, by referencing continuous sizes and distances from adaboost and particle filter, targets of abnormal sizes were removed and targets of large distances were repositioned according to corresponding adaboost information while particle filter was reinitialized.

3 EXPERIMENTAL RESULTS AND DISCUSSIONS

Two detection results with different scenes are shown in figure 2. It is noted that, in figure 2(a)(c), squares with different colors represent the adaboost detection results corresponding to different training database, where red, green, blue, and cyan squares resulted from upper bodies, lower bodies, front/back of whole body, and sideways of whole body respectively.

© ISAROB 2013

In figure 2(b)(d), the red squares are generated from (a) and (c) after filtering, while the blue points and green ellipses represent the particles and average statuses of particles respectively.

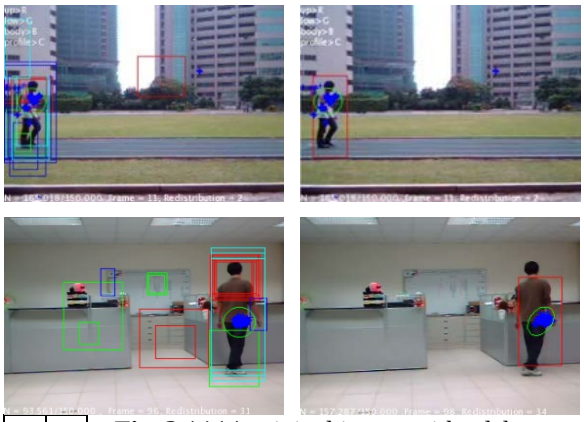

a	b
c	d

Fig. 2.(a)(c) original image with adaboost detection results, and (b)(d): the corresponding final detection result and target location of particles.

Figure 3 shows the number of detection and that of false alarm for each method in scene1.

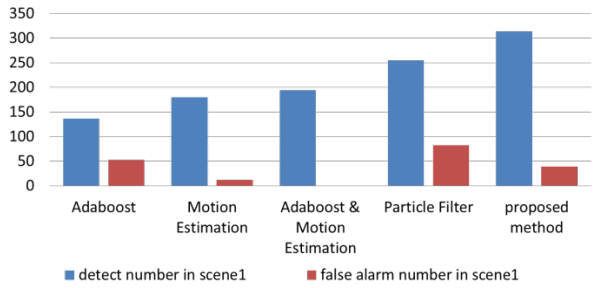

Fig. 3. Detection and false alarm results of compared algorithm in test scene 1.

Figure 4 shows the number of detection and that of false alarm for each method in scene2.

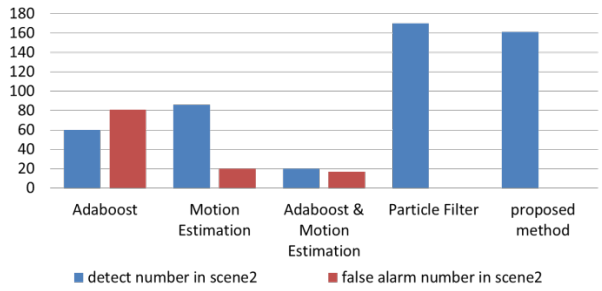

Fig. 4. Detection and false alarm results of compared algorithm in test scene 2.

The statistical result of the detection and false alarm rate is shown in Table 1 to illustrate the efficiency differences between the proposed method and the current tracking methods. The detection rate is defined as: the number of successful tracking of the object in the 507 images (there're a total of 701 images from the videos for the two testing scenes, and after the ones with the target disappearing were removed, a total of 507 images were left).

Table 1. The detection rate and false alarm rate of compared algorithms in test scenarios

Method	Detection rate	False alarm rate
Adaboost[3]	0.4065	0.1572
Motion Estimation[1]	0.5341	0
Adaboost & Motion Estimation	0.5756	0.0356
particle filter[2]	0.7566	0.2433
proposed method	0.9139	0.1483

According to Table 1, compared with other algorithms, the detection rate of the proposed method was higher and the false alarm rate was lower. However, its performances in other experiment scenes weren't all as outstanding. For example, in a scene with complex environment and weak lights, as shown in figure 5, tracking was not possible. The reason was the high error rate and low accuracy of adaboost, making successful positioning impossible. In the future, before adaboost is applied, preprocessing using histogram equalization can be done to reduce issues caused by weak lights and low contrast. In addition, by increasing the number of negative sample for cascade training, more features which don't belong to the object can be learned to break the limitation of this system.

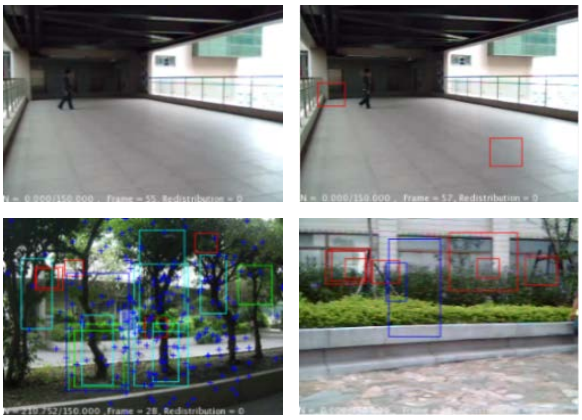

a	b
c	d

Fig. 5. Failure positioning examples. (a)(b) low contrast conditions, and (c)(d) complex environment. In both cases the adaboost results low detection rate and high false alarm.

© ISAROB 2013

4 CONCLUSIONS

An efficient and effective pedestrian tracking method is proposed to overcome the drawbacks of the existing methods based on particle filter. With adaboost appended, the positioning information can be obtained in advance for particle filter initiation while the tracking results can be adjusted automatically. Via this structure the limitation of having to specifying target positions in advance manually is broken and it also solved issues such as object disappearing, object being masked, form changes, and object re-appearing. Therefore, this method can be applied in various scenes thus can be widely applied in different areas with high efficiency.

Like other current methods, the issue of bad performances in detection and tracking in a complex environment still exists with the object tracking method proposed by this study. In the future, we will add a preprocessing step of image enhancement before target detection and increase the number of negative samples in the sample for cascade training, to solve the issue above, so this system can be applied more widely with efficiency.

REFERENCES

[1] Saxena V., Grover S., and Joshi S.(2008), A real time face tracking system using rank deficient face detection and motion estimation. Cybernetic Intelligent Systems, 2008, pp.1-6

[2] Katja Nummiaro, Esther Koller-Meier, and Luc Van Gool.(2002), An Adaptive Color-Based Particle Filter", Image and Vision Computing, 2002, pp.1-22

[3] Viola, P., and Jones M.(2001), Robust Real-Time Face Detection. Computer Vision, ICCV 2001. vol 2, 2001, pp. 137-154

[4] Lienhart R., and Maydt J.(2002) An Extended Set of Haar-like Features for Rapid Object Detection", Image Processing, vol. 1, 2002, pp.I-900 - I-903

[5] Gordon N, Salmo D J, and Smith A F M(1993), Novel approach to nonlinear/ non-Gaussian Bayesian state estimation, IEE Proceedings F Radar and Signal Processing, 1993, pp.107-113

The Eighteenth International Symposium on Artificial Life and Robotics 2013 (AROB 18th '13),
Daejeon Convention Center, Daejeon, Korea, January 30-February 1, 2013

A metaheuristic for huge scale quadratic assignment problems

Hatsumi Nakaura[1], Fubito Toyama[1], Hiroshi Mori[1], Kenji Shoji[1], and Juichi Miyamichi[1]

[1]Graduate School of Engineering, Utsunomiya University, Japan
(Tel: 81-28-689-6244, Fax: 81-28-689-6244)

[1]hatsumi.nakaura@gmail.com

Abstract: The quadratic assignment problem (QAP) is one of the most difficult problems in the NP-hard class. Many metaheuristics have been proposed for the QAP. To evaluate the performance of these algorithms, QAPLIB which is a library of QAP instances is used. But QAPLIB does not have large scale QAP instances. QAPLIB cannot be used to evaluate the performance for large scale instances. Thus, these metaheuristics have been only applied to small scale QAP instances. It is difficult to apply these algorithms to large scale QAP instances because the number of combinations is huge. In this paper, we propose a metaheuristic approach for large scale QAP. The computational results showed that the proposed method outperformed conventional methods for huge scale QAP instances.

Keywords: Combinatorial optimization, Metaheuristics, Quadratic Assignment Problem, Tabu search

1 INTRODUCTION

The quadratic assignment problem (QAP) [1] is one of the most difficult problems in the NP-hard class [2]. In the QAP, n facilities have to be assigned to n locations at minimum cost when a $n \times n$ distance matrix and a $n \times n$ flow matrix are given. A solution is generally defined as a permutation of $\{1, 2, ..., n\}$, and the evaluation value of the solution is calculated using the two matrices. QAP has a large number of applications, including printed circuit design, facility layout, network design, and others.

Many metaheuristics have been proposed for the QAP [3][4]. To evaluate the performance of these algorithms, QAPLIB which is a library of QAP instances is used. But QAPLIB does not have large scale QAP instances. QAPLIB cannot be used to evaluate the performance for large scale instances. Thus, these metaheuristics have been only applied to small scale QAP instances. It is difficult to apply these algorithms to large scale QAP instances because the number of combinations is huge. 2-opt local search which uses the best improvement strategy is incorporated into the most of previous methods. 2-opt local search finds a better solution in a neighborhood of a current solution. The neighborhood is defined as the set of all solutions that can be reached from the current solution by swapping two elements in a permutation. Therefore, the number of solutions in the set of neighborhood is $n(n-1)/2$, where n represents the size of the problem. The computational cost of calculating neighborhood is $O(n^2)$. But after once evaluation values of the neighborhood are calculated, the computational cost of it can reduce to $O(n)$ by the difference value list between the current solution and the neighborhood solutions. If the problem size n is small, the first calculation of evaluation values of neighborhood solutions does not consume much time. But if the problem size n is huge, its calculation consumes huge time. Therefore it is hard to apply 2-opt local search to huge scale QAP instances. On the other hand, Genetic algorithms (GA) are often used for the QAP. GA works effectively for the problems in which the size of instances, n, is around 100. However, it is hard to apply GA to huge scale QAP instances (n is over 1000) because it takes too much time for GA to converge. Moreover, in order to improve search ability, most algorithms based on GA use hybrid GA (Memetic algorithm [5]) with 2-opt local search [6]. Therefore, GA cannot be applied for huge scale QAP because it is difficult even to apply 2-opt local search.

In this paper, a metaheuristic approach is proposed for the huge scale QAP. Robust Tabu Search (RoTS) [7] and the construction of difference value list are performed simultaneously in the proposed method. The construction of difference value list means to calculate evaluation values of the neighborhood solutions. Moving current solution is generally performed after the construction of the difference value list. But it is performed using the difference value list which is not constructed completely in the proposed method. The difference value list is constructed gradually while RoTS is performed. The proposed method can search for a relatively good solution in short time. Thus, it appears to be an appropriate algorithm for huge scale QAP instances.

In our experiments, the proposed method was compared to a fast local search and RoTS. The problem size n used in our experiments was set from 1000 to 10000. The

© ISAROB 2013

computational results showed that the proposed method outperformed the local search and RoTS for huge scale QAP instances.

2 QUADRATIC ASSIGNMENT PROBLEM

The QAP [7] is one of the most difficult problems in the NP-hard class. In the QAP, n facilities have to be assigned to n locations at minimum cost when a $n \times n$ distance matrix, and a $n \times n$ flow matrix are given. A solution is generally defined as a permutation of {1, 2, …, n}, and the evaluation value of the solution is calculated using the two matrices as follows:

$$F(\pi) = \sum_{i=1}^{n} \sum_{j=1}^{n} a_{ij} b_{\pi(i)\pi(j)} \tag{1}$$

where π is a permutation of {1, 2, …, n}, a_{ij} is an element of flow matrix and b_{kl} is an element of distance matrix. The element a_{ij} represents the flow quantity between the facilities i and j. The element b_{kl} represents the distance between the locations k and l. If the facilities i and j are assigned to locations k and l, the part of permutation will be $\pi(i)=k$, $\pi(j)=l$. If π is the permutation that minimizes the objective expression (1), it is the optimum solution of the problem.

The most of benchmark instances of QAP are shown in QAPLIB. The largest instance in QAPLIB is tai256c in which the size n is 256. We set the size n from 1000 to 10000 for our experiments as larger instances than QAPLIB's.

3 PROPOSED ALGORITHM

The proposed algorithm is composed of two steps; the construction of the difference value list and Robust Tabu Search (RoTS). In the construction step, a gain between current solution and a 2-opt neighborhood solution which is randomly selected is calculated. Then its value is assigned to an element of the difference value list. 2-opt neighborhood is defined as a solution obtained by swapping two elements in a current solution. Therefore, in 2-opt neighborhoods, the number of neighborhood solutions is $n(n-1)/2$ (n: size of the problem). The difference value list (gain list) is defined as follows:

$$\Delta = \begin{bmatrix} * & \delta_{0,1} & \delta_{0,2} & \delta_{0,3} \\ * & * & \delta_{1,2} & \delta_{1,3} \\ * & * & * & \delta_{2,3} \\ * & * & * & * \end{bmatrix} \tag{2}$$

where $\delta_{i,j}$ represents a gain value obtained by subtracting the evaluation value of a current solution from the evaluation value of a neighborhood solution obtained by swapping two elements i and j in the current solution. At the beginning of a search, any gain values have not been calculated. Therefore the elements of the difference value list do not have the value. In the construction step, if swap elements 1 and 2 are first selected to obtain a neighborhood solution, gain value $\delta_{1,2}$ is calculated. Then the difference value list is shown as follows.

$$\Delta = \begin{bmatrix} * & * & * & * \\ * & * & \delta_{1,2} & * \\ * & * & * & * \\ * & * & * & * \end{bmatrix} \tag{3}$$

Once a gain was assigned to the difference value list, the same two swap elements are not selected for the assignment process. When a current solution moves to a neighborhood solution, the assigned gain value is updated in the RoTS step. The computational cost required to calculate a gain is $O(n)$ and the cost of update a gain is $O(1)$.

The RoTS step is executed only if the assigned gain was a negative value which means the exchange makes current solution better. In the RoTS step, current solution moves to 2-opt neighborhoods within the limit of the difference value list. The tabu tenure which is the parameter of the RoTS is changed according to the number of assigned elements in the difference value list.

The pseudocode for the proposed method is shown in Fig. 1. n in Fig. 1 is the size of a problem, π is a permutation of current solution, π_{best} is a permutation of the best solution found so far, P is a set of pairs of elements which indicates the position of a permutation, and Δ is the difference value list: When $p=\{i,j\}$, $\Delta(p)=\delta_{i,j}$. After initializing P at the first double loop (lines 4－8 in Fig. 1.), P becomes as follows:

$$P = \{\{0,1\},\{0,2\},...,\{0,n\},...,\{n-1,n\}\} \tag{4}$$

The while loop between line 9－21 of Fig.1 is the main loop. The construction of the difference value list is performed in the first step of the main loop (line 10－14). The RoTS is applied in the next step (line 15－20). The construction of the difference value list and RoTS are repeated until some criterion is satisfied. In the construction step, first, a pair $p=\{i,j\}$ is selected randomly from the set P. Then the gain value, $\delta_{i,j}$ is calculated by SwapGain(π, p). In SwapGain(π, p), a difference value (gain value) between current solution and a 2-opt neighborhood solution obtained by swapping i and j of current solution is calculated. This gain value is assigned to the difference value list Δ. Then, the selected pair p is eliminated from the set P. The RoTS is performed if $\Delta(p)<0$ or $P=\emptyset$. Otherwise the performance of the RoTS is skipped. $\Delta(p)<0$ means the evaluation value of the neighborhood solution obtained by swapping pair p is better than current evaluation value. This skipping strategy can make the current solution better. The other condition to perform the RoTS, $P=\emptyset$, means the difference value list is constructed completely. Therefore, after the difference value

© ISAROB 2013

list was completed, the proposed method works the same as the RoTS. When the termination criterion was satisfied, the best solution, π_{best}, found in the search is returned.

```
Procedure Proposed Algorithm
begin
  generate a random solution π
  π_best := π;
  P := ∅;
  for i := 1 to n−1 do
    for j := i+1 to n do
      P := P∪{{i,j}};
    endfor
  endfor
  while (termination criterion not satisfied) do
    if P≠∅ then
      select p from P randomly;
      Δ(p) := SwapGain(π, p);
      P := P−{p};
    endif
    if Δ(p)<0 or P=∅ then
      π := TabuSearch(π, Δ);
      if π<π_best then
        π_best := π;
      endif
    endif
  endwhile
  return π_best;
end
```

Fig. 1. Process of proposed algorithm

4 EXPERIMENTAL RESULTS

To evaluate the performance of the proposed method, we compare the performance of the proposed method with those of other methods on huge scale QAP instances. The size of huge instances used in our experiments was set from 1000 to 10000. The flow matrix and the distance matrix were asymmetric and their diagonals had non-zero elements. Values of these matrices were decided randomly between 0 and 99. Simple RoTS and 2-opt Local Search (2-opt-F) which uses first improvement strategy were applied to compare the performance. In simple RoTS, the complete difference value list is constructed at the beginning of search. In 2-opt Local Search using first improvement strategy, a current solution moves to 2-opt neighborhood obtained randomly if its gain value is better than that of current solution. The 2-opt-F does not make difference value list. Thus it does not consume much time to construct the difference value list and the convergence speed is very fast. A proposed algorithm without any conditions to execute RoTS is also tested for comparison of the performance of the proposed algorithm. In this method, RoTS is always executed after a gain value is assigned to the difference value list (even though $\Delta(p)>0$). We call this method "Proposed Algorithm (unconditional)". In the experiment, the parameters of RoTS were the same as those used in the literature [7].

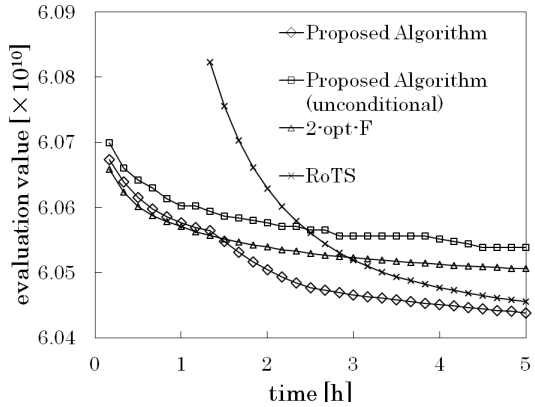

Fig. 2. Variation in evaluation value of best solution for n=5000 instance

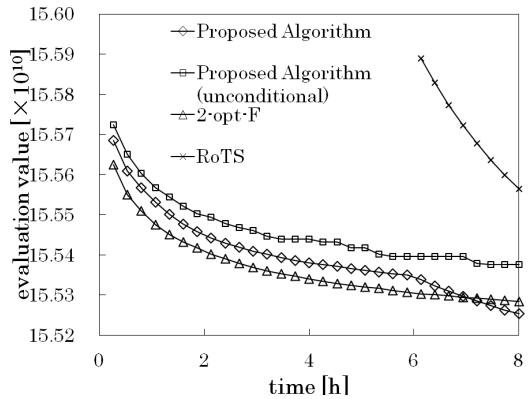

Fig. 3. Variation in evaluation value of best solution for n=8000 instance

First solutions are all the same for the methods on each instance. The experiment is executed on the same computer whose CPU is Intel Xeon X5650 2.67GHz and main memory has 64GB capacity. We used gcc4.4.6 as the compiler with –O3 option.

The results are shown in Table 1. n shows a size of instances, Time shows the the maximum run time, Best value shows the best evaluation values from all of 4 methods. "Deviation from best value" defined as the result of subtracting the "best value" from the evaluation values obtained by each method. Lower values are better than higher values, and 0 is the best value of 4 methods. As shown in Table 1, the proposed algorithm shows the best performance in 7 instances. Therefore the proposed algorithm is definitely very effective method for the huge scale QAP instances.

Fig. 2 and Fig. 3 show the changes in the evaluation value of the best solution against processing time for the

© ISAROB 2013

Table 1. Performance comparison to other methods

n	Time [h]	Best value	Deviation from best value			
			Proposed Algorithm	Proposed Algorithm (unconditional)	2-opt-F	RoTS
1000	1	2376195206	0	8.34×10^{6}	7.68×10^{6}	6.14×10^{5}
2000	2	9577858020	3.98×10^{4}	2.57×10^{7}	2.42×10^{7}	0
3000	3	21657258081	0	5.94×10^{7}	4.84×10^{7}	6.73×10^{6}
4000	4	38593328252	0	8.90×10^{7}	6.54×10^{7}	8.37×10^{6}
5000	5	60438065514	0	1.01×10^{8}	6.81×10^{7}	1.70×10^{7}
6000	6	87132554267	0	1.33×10^{8}	7.50×10^{7}	6.43×10^{7}
7000	7	118734259691	0	1.30×10^{8}	8.57×10^{7}	1.41×10^{8}
8000	8	155253875423	0	1.22×10^{8}	3.03×10^{7}	3.12×10^{8}
9000	9	196707554616	4.32×10^{7}	1.14×10^{8}	0	6.40×10^{8}
10000	10	242888642072	1.05×10^{8}	1.74×10^{8}	0	9.72×10^{8}

Table 2. Time to complete the difference value lists

n	Time [h]	Time rate [%]
1000	9.20×10^{-3}	0.920
2000	0.109	5.44
3000	0.294	9.78
4000	0.736	18.4
5000	1.37	27.5
6000	2.36	39.3
7000	3.81	54.4
8000	5.96	74.5
9000	-	-
10000	-	-

instances of n=5000 and n=8000, respectively. The horizontal axis represents the processing time and the vertical axis represents the evaluation value for the best solution obtained with each method. As shown in Fig. 2 and Fig. 3, the proposed method seems to find good solutions in shorter times than the previous method and the unconditional proposed method. The above results confirmed that the condition ($\Delta(p)<0$) to execute RoTS is an important factor to search huge QAP efficiently.

The time to complete the difference value lists on the proposed method is shown in Table 2. Time rate means the ratio of completion time to whole search time. On the instances of n=9000 and n=10000, the difference value lists were not completed until the ends of searches.

5 CONCLUSION

In this paper, we proposed an algorithm for huge scale QAP instances. The proposed algorithm is based on random 2-opt selection and Robust Tabu Search. Experimental results show the effectivities of the proposed algorithm for huge scale QAP instances. In order to use proposed algorithm effectively, the conditions to execute RoTS are required.

REFERENCES

[1] Koopmans TC, Beckman M. (1957), Assignment problems and the location of economic activities. Econometric 25:53-76

[2] S. Sahni, T. Gonzalez (1976), P-Complete Approximation Problems. Journal of the ACM 23(3):555-565

[3] A. S. Ramkumar, S. G. Ponnambalam, N. Jawahar et al (2008), Iterated fast local search algorithm for solving quadratic assignment problems. Robotics and Computer-Integrated Manufacturing 24:392-401

[4] Nilgun Fescioglu-Unver, Mieczyslaw M. Kokar (2011), Self Controlling Tabu Search algorithm for the Quadratic Assignment Problem. Computers & Industrial Engineering 60:310-319

[5] Moscato P. (2002), Memetic Algorithms. In: Handbook of Applied Optimization, P. M. Pardalos and M. G. C. Resende (eds), Oxford University Press, New York, pp. 157-168

[6] P. Merz, B. Freisleben (2000), Fitness landscape analysis and memetic algorithms for the quadratic assignment problem. IEEE Transactions on Evolutionary Computation 4:337-352

[7] E. D. Taillard (1991), Robust taboo search for the quadratic assignment problem. Parallel Computing 17:443-455

© ISAROB 2013

The Eighteenth International Symposium on Artificial Life and Robotics 2013 (AROB 18th '13),
Daejeon Convention Center, Daejeon, Korea, January 30-February 1, 2013

Competition-based Particle Swarm Optimizer for Solving Numerical Optimization Problems

Sheng-Ta Hsieh and Bo-Han Chen

Department of Communication Engineering, Oriental Institute of Technology, Taiwan
(Tel: +886-2-7 738-0145 Ext. 2325, Fax: +886-2-7738-7411)

fo013@mail.oit.edu.tw

Abstract: In this paper, a new variant of particle swarm optimizer is proposed for solving numerical optimization problems. The main difference between proposed method and common PSO is the swarm structure. In general, the PSO has only one swam and each particle of the swarm will share their information for guiding other particles toward to potential solution space. The proposed method is to separate swarm into two sub-swarm. The size of two sub-swarms will be adjusted according to their performance. It can drive increased the diversity of the particles and prevent particle to fall into the local optimum. For testing the performance of proposed method, fifteen of CEC 2005 test functions were selected for experiments. From the result, it can be observed that the proposed method performs better than SPSO2011.

Keywords: computational intelligence, optimization, particle swarm optimizer, population.

1 INTRODUCTION

In last 3 decades, evolutionary algorithms were applied for solving variety of real world problems. Since 1975, John Holland proposed the first evolutionary based optimizer, genetic algorithm (GA)[1]. More and more optimizer was then proposed, such as, ant colony optimization (ACO)[2], particle swarm optimization (PSO)[3], differential evolution (DE)[4], and artificial bee colony algorithm (ABC)[5], etc. The main feature of PSO is it has simply equations to generate new moving vector and has and very few parameters to be set. The Particle swarm optimization (PSO) was introduced by Kennedy and Eberhart in 1995. The PSO Simulated foraging behavior of birds or fishes to solve optimization problems. Particles of the swarm will move in a D-dimensional space according to new moving vector. The positions of particles represent potential solutions. Each particle will have chance to share their better experience (global best solution, *Gbest*) for guiding other particle toward to unsearched or potential solution space. The global best solution is selected from the best performance of the personal best solutions (*Pbest*) of all particles. Both of the *Gbest* and *Pbest* will then guide particles' for searching optimal solution.

In last decade, more and more variants of PSO have been proposed to improve PSO's efficiency and make it much robust. Omran *et al.* introduced a hybrid of particle swarm optimization and differential evolution [6]. Chen and Yeh presented a new search strategy [7]. They keep only personal best position for providing moving vector but no global best position. It will make vector update much simply, and reduce computational consumption. But is will also decrease particles' ability for deep search. Some methods were focus on parameters adjustment. Due to different setting of parameters will affect optimizer's performance directly. In [8] Bratton and Kennedy proposed two kinds of topology type which are *Gbest* and *Lbest* topology. The *Gbest* type is for solving uni-modal problems; and *Lbest* type is much suitable for solving multi-modal problems. Ghosh *et al.* proposed hierarchical dynamic neighborhood PSO [9]. It will arrange particles for define their neighborhood under a dynamic hierarchical structure. Neighborhoods of a particle will changes constantly according to their solution quality. The changing of the arrangement (relationship of particle's neighborhoods) can preserve particle's diversity for easier finding optimal solution.

In general, the main advantage of PSO is fast convergence, but the weakness is easier to fall into local optimum. Due to particles will toward around global optimal solution. In order to overcome this situation, Blackwell and Branke proposed multi-swarm PSO[10], which divided population into several sub-swarms. Each swarm has its own parameters and will perform evolution independently. After a few generations, sub-swarm will perform information sharing. Since there are more than one global optimal solution, It can avoid particles form fall into local optimum.

In order to further improve PSO's performance, a competition-based particle swarm optimizer is proposed. The population is separated as two sub-swarms. After several generations, performance of two sub-swarms will

© ISAROB 2013

take into comparison. The swarm size will be adjusted according competition results.

The paper is organized as follows: In Section II, a simply introduce of standard PSO will be described. Section III presents the detail of proposed method. Section IV presents the experiments including test functions and parameter settings. Finally, the conclusion is described in Section V.

2 PARTICLE SWARM OPTIMIZATION

2.1. Original PSO

Since the original PSO proposed in 1995[3], researchers are focus on improve its solution searching ability and applied it on various applications. In order to extend its ability of exploration and exploitation, Shi and Eberhart [11] introduced *inertia weight* into the original PSO, for enhancing particles' search abilities and drive particle keep closer on potential solution space. The modified PSO (with inertia weight) will make PSO much robust and increase its searching performance.

In PSO, particle's movement are represented by position vector x and velocity v. The new velocity for particle i is generated by equation (1). Then, the ith particle's new position will be updated by equation (2).

$$\begin{aligned} v_{id}(t+1) &= w \times v_{id}(t) + c_1 \times r_1 \times (pb_{id}(t) - x_{id}(t)) \\ &+ c_2 \times r_2 \times (gb_{id}(t) - x_{id}(t) \end{aligned} \tag{1}$$

$$x_{id}(t+1) = x_{id}(t) + v_{id}(t+1) \tag{2}$$

Where, d denotes dimension, gb is the global best particle, and pb is the personal best particle. The w represents inertia weight, c_1 and c_2 are acceleration coefficients, r_1 and r_2 are random number between [0, 1].

The velocity update equation is consists of three parts, including the previous velocity, personal experience and social experience. They are controlled by inertia weight and two acceleration coefficients respectively.

3 COMPRTITION-BASED PARTICLE SWARM OPTIMIZATION

In this paper, competition-based particle swarm optimizer is proposed for solving numerical optimization. For the proposed method, the population is divided into two sub-swarms. Either of sub-swarm will apply different parameters setting.

3.1 Sub-Swarm Setting

The velocity update of proposed is listed as follows.

Velocity update for Sub-swarm1:

$$\begin{aligned} v_{id}(t+1) &= w \times v_{id}(t) + c_1 \times r_1 \times (pb_{id}(t) - x_{id}(t)) \\ &+ c_2 \times r_2 \times (lb^1_{id}(t) - x_{id}(t)) \end{aligned} \tag{3}$$

Velocity update for Sub-swarm2:

$$\begin{aligned} v_{id}(t+1) &= w \times v_{id}(t) + c_1 \times r_1 \times (pb_{id}(t) - x_{id}(t)) \\ &+ c_2 \times r_2 \times (lb^2_{id}(t) - rpb_{id}(t)) \end{aligned} \tag{4}$$

and the inertia weight is assigned according following equation.

$$w = (w_1 - w_2) \times \frac{(MAX_FEs - FEs)}{MAX_FEs} + w_2 \tag{5}$$

Where, MAX_FEs is the maximum fitness evaluations, the c_1 and c_2 are acceleration coefficients, and r_1 and r_2 are random number between $[0,1]$.The lb^s is the local best solution of s_{th} sub-swarm, and pb is the personal best particle. The rpb is the random selected neighborhood pb, and rpb is not equal the current pb. The w_1 and w_2 denotes the lower and upper bound of inertia weight. The w for sub-swarm1 will decrease linearly, and the w for s ub-swarm2 is generated randomly. The range of two sub-swarms are set as [0.4, 0.9] and [0.45, 0.75] respectively.

3.2 Information Exchange and Sub-swarm Size Adjustment

In general, each sub-swarm will perform its own solution search process independently. After several generations, the sub-swarm with better performance will share its own *gbest* information to other sub-swarms. The pseudo code of information exchange is given as follows:

```
If   lbf^1 < lbf^2
     count = count + 1;
else
     count = count - 1;
End

If   count == 10
     lb^2 = lb^1;
     count = 0;
     regrouping = regrouping + 1;
elseif
     count  == -10
     lb^1 = lb^2;
     count = 0;
     regrouping = regrouping - 1;
End
```

*lbf denoted fitness value of local best particle.

In order to provide better sub-swarm has much resource to keep finding better solutions, the sub-swarm size will be adjustment according its performance. Thus, after several generations, the better sub-swarm will have a new joined particle and the worse sub-swarm will reduce one. However, in order to keep sub-swarm's basic ability and to prevent all

© ISAROB 2013

the particles of worse swarm be removed. The minimum sub-swarm size is set 10. The pseudo code of sub-swarm size adjustment is given as follows:

```
If regrouping == 20
    If   np2  > 10
    {regrouping sub-swarm}
    End
    regrouping =  0;
Elseif   regrouping == -20
    If   np1 > 10
    {regrouping sub-swarm}
    End
    regrouping =  0;
End
```

3.3 Flowchart of the CSPSO

The procedure of the CSPSO is given as follows:

Step 1: Initial population.

Step 2: Divide population into two sub-swarms.

Step 3: Calculate Fitness value for each sub-swarm.

Step 4: Perform solution search by two sub-swarms.

Step 5: Update each swarm local best particle(*lb*) and personal best particle(*pb*).

Step 6: Determine condition for information exchange (local best position).

Step 7: Determine condition for regrouping sub-swarms.

Step 8: Stop evolution if meet the stop condition, else jump to step 4.

TABLE 1. TEST FUNCTIONS

f	**Test Functions**
f_1	Shifted Sphere Function (f_1)
f_2	Shifted Schwefel's Problem 1.2 with Noise in Fitness (f_4)
f_3	Schwefel's Problem 2.6 with Global Optimum on Bounds (f_5)
f_4	Shifted Rosenbrock's Function (f_6)
f_5	Shifted Rotated Griewank's Function without Bounds (f_7)
f_6	Shifted Rastrigin's Function (f_9)
f_7	Shifted Rotated Weierstrass Function (f_{11})
f_8	Schwefel's Problem 2.13 (f_{12})
f_9	Expanded Extended Griewank's + Rosenbrock's Function (f_{13})
f_{10}	Hybrid Composition Function 1 (f_{15})
f_{11}	Rotated Hybrid Composition Function 2 (f_{18})
f_{12}	Rotated Hybrid Composition Function 2 with a Narrow Basin for the Global Optimum (f_{19})
f_{13}	Rotated Hybrid Composition Function 2 with the Global Optimum on the Bounds (f_{20})
f_{14}	Rotated Hybrid Composition Function 3 with High Condition Number Matrix (f_{22})
f_{15}	Rotated Hybrid Composition Function 4 without Bounds (f_{25})

4 EXPERIMENTAL RESULTS

In order to test proposed method and compare it to standard particle swarm optimization (SPSO2011) [12], fifteen test functions of the CEC 2005 [13], which includes included uni-model functions (f_1 ~ f_3), multi-model functions (f_4 ~ f_8), expanded functions (f_9), and hybrid composition functions (f_{10} ~ f_{15}), are listed in Table 1. The global optimum, initialization and search range of the 18 test functions are listed in Table 2. All algorithms are implemented by MATLAB 2010a and are executed on platform with Intel Core i3-2120 and 4GB RAM.

TABLE 2. THE GLOBAL OPTIMUM, INITIALIZATION RANGE AND SEARCH RANGE OF TEST FUNCTIONS.

f	**Global Optimum**	**Initialization**	**Search Range**
f_1	0	$[-100, 100]^D$	$[-100, 100]^D$
f_2	0	$[-100, 100]^D$	$[-100, 100]^D$
f_3	0	$[-100, 100]^D$	$[-100, 100]^D$
f_4	0	$[-100, 100]^D$	$[-100, 100]^D$
f_5	0	$[-100, 100]^D$	$[-100, 100]^D$
f_6	0	$[-32, 32]^D$	$[-32, 32]^D$
f_7	0	$[-0.5, 0.5]^D$	$[-0.5, 0.5]^D$
f_8	0	$[-100, 100]^D$	$[-100, 100]^D$
f_9	0	$[-3,1]^D$	$[-3, 1]^D$
f_{10}	0	$[-5,5]^D$	$[-5, 5]^D$
f_{11}	0	$[-5, 5]^D$	$[-5, 5]^D$
f_{12}	0	$[-5, 5]^D$	$[-5, 5]^D$
f_{13}	0	$[-5, 5]^D$	$[-5, 5]^D$
f_{14}	0	$[-5, 5]^D$	$[-5, 5]^D$
f_{15}	0	$[-2, 5]^D$	$[-2, 5]^D$

All the test functions are set as 30-dimension and executed for 25 times. Both the population size of SPSO

© ISAROB 2013

2011 and proposed method are set as 40, and the maximum fitness evaluations (FEs) are set 300,000. The details of related parameters are listed in Table 3.

TABLE 3. PARAMETER SETTINGS

Algorithm	**Proposed Method**	**SPSO 2011**
Inertia weight	[0.4,0.9] for sub-swarm 1 [0.45,0.75] for sub-swarm 2	0.7213
Population size	40	
Dimensions	30	
c_1, c_2	1.1931	
Max FEs	300,000	
Run	25	

The experimental results are listed in TABLE 4 which includes mean and standard deviation of 15 selected test functions of 25 independent runs. The better performance of two PSO variants is shown in bold. From the results, it can be observed that the proposed method perform better in most test functions, especially in the hybrid problems.

TABLE 4. EXPERIMENT RESULTS FOR 30-D PROBLEMS

Algorithms / Functions	**SPSO 2011**	**Proposed method**
f_1	1.3717e-027 (1.7744e-028)	**2.0195e-030** **(9.8934e-030)**
f_2	**6.0104e+001** **(3.4593e+001)**	1.0867e+002 (1.4697e+002)
f_3	4.7958e+003 (8.2740e+002)	**3.8486e+003** **(1.8659e+003)**
f_4	3.9496e+002 (2.8910e+002)	**6.6767e+001** **(2.4387e+002)**
f_5	4.8127e+003 (4.4511e+001)	**2.1846e-002** **(1.6000e-002)**
f_6	**6.2365e+001** **(1.4530e+001)**	7.0721e+001 (1.5324e+001)
f_7	**2.9061e+001** **(1.2393e+000)**	3.8296e+001 (1.0916e+000)
f_8	9.1062e+005 (1.2477e+005)	**8.7510e+005** **(1.3349e+005)**
f_9	1.0825e+001 (1.1886e+000)	**5.5308e+000** **(1.3665e+000)**
f_{10}	4.5201e+002 (4.9538e+001)	**3.4388e+002** **(3.1475e+001)**
f_{11}	9.2079e+002 (2.2923e+001)	**8.2431e+002** **(3.3237e+000)**
f_{12}	9.1608e+002 (1.3797e+001)	**8.2650e+002** **(5.9936e+000)**
f_{13}	9.1667e+002 (9.0488e+000)	**8.2615e+002** **(3.4888e+000)**
f_{14}	9.1363e+002 (1.6512e+001)	**5.3446e+002** **(8.6952e+001)**
f_{15}	9.9539e+002 (9.5791e+000)	**2.1832e+002** **(5.3872e+000)**

5 CONCLUSION

In this paper, a new variant of PSO is proposed for solving numerical optimizations. The two sub-swarms will increase population's diversity for prevent particles from fall into local optimum. In the experimental results, fifteen test functions of CEC 2005 are selected. In order to test the performance of proposed method, the SPSO 2011 is taken into comparison. From the results, it can be observed that the proposed method is able to explore better solutions.

ACKNOWLEDGEMENT

This work was supported in part by National Science Council of Taiwan, Taiwan, R.O.C. under Grant NSC 101-2221-E-161-011.

REFERENCES

[1] J. H. Holland , Adaptation in Natural and Artificial Systems , University of Michigan Press, 1975

[2] A. Colorni, M. Dorigo, and V. Maniezzo, "Distributed optimization by ant colonies," in *Proc.* of the 1st European Conference on Artificial Life, pp. 134-142, 1991.

[3] J. Kennedy and R. Eberhar, "Particle Swarm Optimization," in *Proc.* of *IEEE Int. Conf. on Neural Network*, pp. 1942-1948, 1995.

[4] R. Storn and K. Price, "Differential evolution—A simple and efficient heuristic for global optimization over continuous spaces," *Journal of Global Optimization*, vol. 11, pp. 341–359, 1997.

[5] D. Karaboga, "An idea based on honeybee swarm for numerical optimization," *Technical Report* TR06, 2005.

[6] M. G. H. Omran , A. P. Engelbrecht and A.Salman, " Differential Evolution Based Particle Swarm Optimization," in *Proc.* of *IEEE Swarm Intelligence Symposium*, pp.112-119, 2007.

[7] C. H. Chen and S. N. Yeh "Personal Best Oriented Constriction Type Particle Swarm Optimization," in *Proc.* of *IEEE Conference on Cybernetics and Intelligent Systems*, pp.1-4, 2006.

[8] D. Bratton and J. Kennedy "Defining a Standard for Particle Swarm Optimization," in *Proc.* of *IEEE Swarm Intelligence Symposium*, pp.120-127, 2007.

[9] P. Ghosh, H. Zafar, S. Das and A. Abraham, "Hierarchical dynamic neighborhood based Particle Swarm Optimization for global optimization," in *Proc.* of *IEEE Congress on Evolutionary Computation (CEC)*, pp.757-764, 2011.

[10] T. M. Blackwell and J. Branke, "Multiswarms, Exclusion, and Anti-Convergence in Dynamic Environments," in *Proc.* of *IEEE Transactions on Evolutionary Computation*, vol. 10/4, pp. 51-58, 2004.

[11] Y. Shi, and R. Eberhart, " A modified particle swarm optimizer", in *Proc.* of *Conference on Evolutionary Computation: IEEE Press. Piscataway.* , pp.69 –73, 1998.

[12] [Online]. Available: http://particleswarm.info

[13] [Online]. http://www.ntu.edu.sg/home/EPNSugan

© ISAROB 2013

The Eighteenth International Symposium on Artificial Life and Robotics 2013 (AROB 18th '13),
Daejeon Convention Center, Daejeon, Korea, January 30-February 1, 2013

Elitist Differential Evolution for solving Numerical Optimization Problems

Sheng-Ta Hsieh, Huang-Lyu Wu, Tse Su

Department of Communication Engineering Oriental Institute of Technology Taiwan
(Tel: +886-2-7738-0145 Ext. 2325, Fax: +886-2-77380145)

fo013@mail.oit.edu.tw

Abstract:
In this paper, an elitist strategy is proposed for enhancing solution searching performance of Differential Evolution (DE). Also, a new variant of mutation for DE is proposed to improved population's exploration and prevent particles form fall into local optimum. In the experiments, 10 hybrid composition functions of CEC 2005 test functions are selected for testing performance of proposed method and compare it with 4 DE variants. From the results, it can be observed that the proposed method exhibits better than related works.

Keywords: Differential Evolution, elitist, optimization, population.

1 INTRODUCTION

In last four decades, more and more heuristic-based algorithms were proposed for solving numerical optimization, such as genetic algorithm (GA) [1] and particle swarm optimizer (PSO) [2], etc. In 1996, the concept of original differential evolution (DE) was proposed by Storn and Price [3]-[6]. The DE algorithm is a powerful population-based optimizer with simply concept to be implemented.

Due to there are many parameters in DE need to be decide before apply it on solving optimization problems. These parameters are very sensitive to different type of problems. Thus, in order to increase robust of DE, researchers are aiming to fine tune these parameters in last decade [8]-[12]. Similar to PSO, particles in DE will be moved according new moving vector, which is generated by variety mutation and crossover strategies. The selection will then be performed to preserve better particles for next generations.

In 2006, Brest *et al.* proposed self-adaptive differential evolution (jDE) [13], which is focus on adjust control parameters, such as crossover rate and scale factor, etc. In 2009, Huang and Suganthan proposed a DE variant named SaDE [14]. The trail vector generating strategies in SADE will change according to current solution search status for dealing with different kinds of problems. It is archived by analyzing the better and worse vectors to provide useful clue for selecting mutation strategy in next generation. Furthermore, the related parameters such as scale factor, crossover and population size, etc. will also self-adjust according current status. In the same year, Zhang and Sanderson proposed adaptive differential evolution named JADE [15]. The mutation strategy in JADE is refer to DE/current to best/1. Due to the particles will toward to around the global best particle due to the natural of current to best/1 mutation. It will make particles' convergence in early stage. Thus, in JADE, DE/current to best/1 is modified as DE/current to *pbest*. The *pbest* is selected form several better target vectors randomly. It will keep particles' diversity and improved DE's robust. Besides, the selected and unselected trail vector will also be recorded as a reference for parameters adjustment in next generation.

Recently, Islam et al. proposed a new variant of DE named MDE_pBX [16]. They proposed a new mutation strategy named DE/current to gr_best/1 for solving early convergence. The gr_gebest is a better target vector form *q* randomly selected target vectors. It can also prevent particles be clustered around the global best particle and avoid particle fall into local optimal. On the other hand, the crossover in MDE_Pbx is to random select two target vectors from *p* better vectors for information exchange. The *p*% value will decrease linearly by generations. It will enhance DE's convergence (deep search) in last stage of solution search process. However, a smaller population will decrease solution searching ability and diversity of DE/current to gr_best/1.

In this paper, a new variant of DE is proposed for solving numerical optimization problems. The proposed elitist strategy is referred to the DE/current to best/1 mutation, and to replace the *best particle* with *elitist particles*. It's an efficient way to solving early convergence

© ISAROB 2013

problem and can avoid particles from fall into local optimum. Besides, the two of elitist particles will be randomly selected for crossover to discover more potential solution space. Finally, the scale factor is adjusted by Gaussian distribution.

This paper is consisted of five sections. The basic concept of differential evolution (DE) is described in section 2. The detail of proposed method is introduced in section 3. The experiments are presented in section 4. Finally, the conclusions are described in section 5.

2 Differential Evolution

Differential Evolution (DE), in recent years, is one of the popular optimizers. Its main advantages include have a few parameters, simply structure and fast convergence, etc. The DE is a population-based optimization algorithm. The members of population in DE are called parameter vectors. Particles' movement is according to trial vectors. The five common mutation strategies are listed as follows.。

1. DE/rand/1

$$V_{i,G} = X_{r1,G} + F(X_{r2,G} - X_{r3,G}) \tag{1}$$

2. DE/best/1

$$V_{\mathrm{i,G}} = X_{\mathrm{best,G}} + F(X_{r1,G} - X_{r2,G}) \tag{2}$$

3. DE/current to best/1

$$V_{\mathrm{i,G}} = X_{i,G} + F\left(X_{best,G} - X_{i,G}\right) + F(X_{r1,G} - X_{\mathrm{r2,G}}) \tag{3}$$

4. DE/rand/2

$$V_{\mathrm{i,G}} = X_{r1,\mathrm{G}} + F(X_{r2,G} - X_{r3,G}) + F(X_{r4,G} - X_{r5,G}) \tag{4}$$

5. DE/best/2

$$V_{\mathrm{i,G}} = X_{\mathrm{best,G}} + F(X_{r1,G} - X_{r2,G}) + F(X_{r3,G} - X_{r4,G}) \tag{5}$$

where i, r_1, r_2, r_3, r_4, r_5 denote current selected particle and five random selected particles of population, respectively. And $\mathrm{i} \neq r_1 \neq r_2 \neq r_3 \neq r_4 \neq r_5$.The G represent current generation, X_{best} denote best particle of population and F denote scale factor where $F \in (0,1)$.

Unlike GA, the mutation process is executed before crossover. Due to the mutation in DE is main approach to explore better solutions in solution space. Thus, either mutation is adopted for generating new trail vector; the crossover will be performed by following equation.

$$\mathrm{u_{j,i,G}} = \begin{cases} \mathrm{V_{j,i,G}}\ , \text{if } (\mathrm{rand_{i,j}}[0,1) \leq \mathrm{CR} \text{ or } \mathrm{j} = \mathrm{j_{rand}}) \\ \mathrm{X_{j,i,G}}\ , \text{otherwise} \end{cases} \tag{6}$$

where $\mathrm{CR} \in (0,1)$ denotes crossover rate, j denotes dimension. While the random number is smaller than or equal to CR, the trial vector ($\mathrm{u_{j,i,G}}$) will inherit mutated vector ($\mathrm{V_{i,G}}$). Otherwise, the trial vector ($\mathrm{u_{j,i,G}}$) will duplicate current particle's moving vector ($\mathrm{X_{i,G}}$). Finally, the selection in DE is performed by following equation.

$$X_{\mathrm{i,G+1}} = \begin{cases} u_{i,G}\ , \text{if } f(u_{i,G}) \leq X_{\mathrm{i,G}} \\ X_{\mathrm{i,G}}\ , otherwise \end{cases} \tag{7}$$

3 PROPOSED METHOD

3.1 DE/current to elitist/1

In this paper, a new mutation structure is proposed, named DE/current to elitist/1. The vector update equation is listed as follows.

$$\mathrm{V_{i,G}} = \mathrm{X_{i,G}} + \mathrm{F}\left(\mathrm{X_{Elitist,G}} - \mathrm{X_{i,G}}\right) + \mathrm{F}\left(\mathrm{X_{r1,G}} - \mathrm{X_{r2,G}}\right) \tag{8}$$

where $\mathrm{X_{i,G}}$ denotes target vector, $\mathrm{V_{i,G}}$ represents donor vector, scale factor must be a positive integer between 0 and 1. The $\mathrm{X_{r1,G}}$ and $\mathrm{X_{r2,G}}$ are two random selected particles, and $\mathrm{X_{Elitist,G}}$ is the first E% better particles of population. Note that the $\mathrm{X_{i,G}}$ must not be the same as $\mathrm{X_{Elitist,G}}$. Thus, the selected elitist particle will be different for current selected particles. It can avoid particles are guided to the same position (global best particle) and can prevent particles fall into local optimum or early convergence.

3.2. Current to real-random

In this paper, there are two mutation strategies are proposed for deal with complex problems, especially the problems contain many local optimum solutions in solution space. In previous sub-section, the elitist mutation is introduced. In order to prove particles higher ability to jump out from local optimum, the DE/current to real-rand/1 is then proposed.

In traditional DE/current to rand/1, the random selected particle is belonging to current population. It seems a reasonable way to generate random vector. In fact, after several generations, particles will get closer to search specific area. The random selected particles may not be able to provide useful information to help other particles, which could trap in local optimum, to jump out to unsearched solution space. The proposed DE/current to real-rand/1 is listed as follows.

$$V_{i,G} = X_{i,G} + F\left(X_{T,G} - X_{Elitist,G}\right) + F\left(X_{r1,G} - X_{r2,G}\right) \tag{9}$$

where $X_{T,G}$ is a random generated particle, which is not belonging to current. If particles can find one or more solutions to update the global best solution in k consecutive generations, the DE/current to real-rand/1 will be activated to generate potential moving vectors. It will allow more

potential solutions to be found during the solution exploration, and find unsearched solution space. In this paper, the *k* is set as 50.

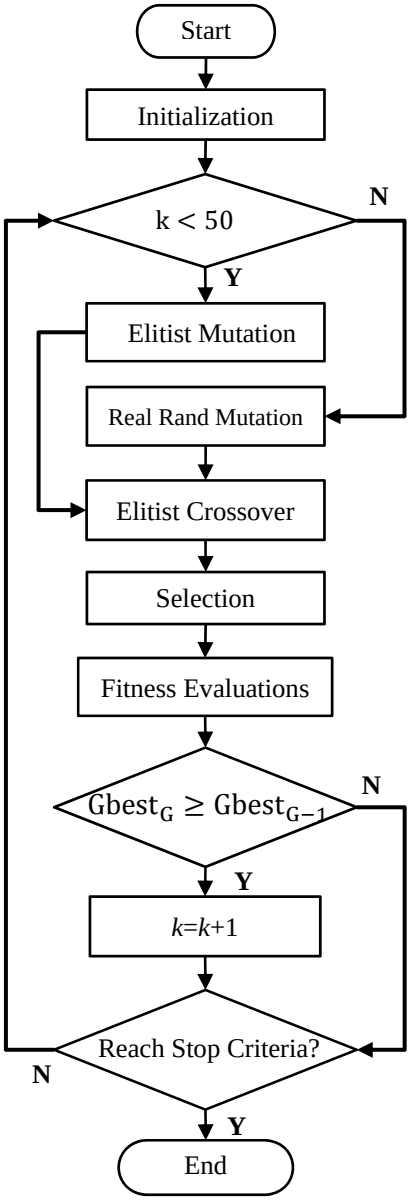

Fig. 1. Flowchart of this paper

3.3. Elitist crossover

In original DE, crossover is to combine mutated particle and random selected particle to produce new particles. In fact, the random selected particle could contain poor information and may not be able to generate better particle. In this paper, one of the *C*% better particles will be selected for join crossover with the mutated particle. It will increase particles' deep searching ability and speed up convergence.

3.4 Parameter adjustment

In this paper, the scale factor will be adjusted in each generation and will be generated by following equation.

$$F = \mathrm{Gaussian}(F_u, 0.1) \tag{10}$$

where the F_u is set as 0.5 in initial stage. After that, the F_u will be generated according to following equation.

$$F_u = (1 - u_F) * F_u + F_u * \mathrm{mean}_L(R) \tag{11}$$

where u_F is a random generated number between 0.5 and 1. And the $mean_L(R)$ [17] is used to adjust *F* value, where *R* is survival rate in current generation.

3.5 Flowchart of proposed method

The flowchart of proposed is presented in figure 1 and the procedure of proposed method is listed as follows.

Step 1：Initialization and set the generation number G=0.

Step 2：If *k* >= 50 then execute step 3.1, else execute step 3.2

Step 3.1：DE/current to elitist/1, to generate mutated vector by (8)

Step 3.2：DE/current to real-rand/1, to generate mutated vector by (9)

Step 4：Elitist Crossover

Step 5：Selection by (7)

Step 6: Fitness Evaluations.

Step 7：Repeat step 2 to step 6, until meet the stop criteria.

4 EXPERIMANTS RESULTS

4.1. Test functions

In order to test the performance of proposed method and compare it with other variants of DE, ten hybrid composition functions, which are f_{16} ~ f_{25} of CEC 2005 [18], are selected for experiments. All the test functions are set as 30 dimensions. The global optimum, initialization range and search range of ten test functions are listed in table 1.

TABLE 1. GLOBAL OPTIMUM AND SEARCH RANGE OF TEST FUNCTIONS

Functions	Global Optimum	Initialization Range	Search Range
f_1~ f_2	0	$[-5, 5]^D$	$[-5, 5]^D$
f_3~ f_5	0	$[-5, 5]^D$	$[-5, 5]^D$
f_6~ f_8	0	$[-5, 5]^D$	$[-5, 5]^D$
f_9	0	$[-5, 5]^D$	$[-5, 5]^D$
f_{10}	0	$[2, 5]^D$	No Boundary

4.2. Parameters Settings

In the experiments, the population size for all DE variants are set as 100, each approaches are executed for 25 independent runs, and the maximum fitness evaluations (FEs) are set as 300,000. For fair comparison, the original parameters setting of jDE variants are adopted. For the basic DEs, which include DE/Rand/1, DE/best/1, and DE/Current to best/1, both the mutation and crossover rate

© ISAROB 2013

are set as 0.9. For the proposed method, the F_u is set as 0.5, *CR* is set as 0.9, *E* is set as 15 and *C* is set as 25.

4.3. Experimental Results

The experiment results are listed in table 2 which presents the mean, standard deviation, and average computation time of 25 runs of the five variants of DE approaches on the 10 test functions with 30 dimensions. The best results among the five methods are shown in bold.

From the results, the proposed method performed with better results on most test functions can be observed. The jDE [13] performed best result on function 1 and 2.

TABLE 2. EXPERIMENT RESULTS

Methods	Results	f_1	f_2	f_3	f_4	f_5
Rand/1	Mean	2.8143E+02	3.4813E+02	8.3249E+02	8.3518E+02	8.3087E+02
	Std.	3.1917E+01	5.6843E+01	5.2431E+00	7.4596E+00	4.6088E+00
Best/1	Mean	9.1785E+02	9.6942E+02	1.3100E+03	1.3252E+03	1.3051E+03
	Std.	4.0104E+01	5.7750E+01	2.8452E+01	1.9686E+01	3.0350E+01
Current to best/1	Mean	1.4592E+02	1.8311E+02	8.1645E+02	8.1639E+02	8.1642E+02
	Std.	4.6975E+01	4.8953E+01	2.5121E-01	4.3215E-01	3.5078E-01
jDE	Mean	**1.0541E+02**	**2.0837E+02**	8.1738E+02	8.1738E+02	8.1740E+02
	Std.	**2.4564E+01**	**4.8086E+01**	5.9315E-01	5.2053E-01	5.2154E-01
Proposed Method	Mean	1.8257E+02	2.5625E+02	**8.1600E+02**	**8.1605E+02**	**8.1606E+02**
	Std.	1.9297E+01	3.6249E+01	**2.9137E-02**	**7.4758E-02**	**5.6439E-02**
Methods	**Results**	f_6	f_7	f_8	f_9	f_{10}
Rand/1	Mean	8.6260E+02	7.8090E+02	8.6636E+02	2.1275E+02	2.1236E+02
	Std.	1.0110E+00	1.7051E+02	1.3069E+00	1.6850E+00	1.2230E+00
Best/1	Mean	1.4328E+03	1.5227E+03	1.4392E+03	1.4446E+03	1.4577E+03
	Std.	2.6894E+01	1.0783E+02	2.9659E+01	1.7320E+01	1.4929E+01
Current to best/1	Mean	8.6570E+02	5.0009E+02	8.7159E+02	2.1098E+02	2.1086E+02
	Std.	4.7043E+00	2.6955E-01	2.7118E+00	7.7643E-01	5.4458E-01
jDE	Mean	8.5873E+02	5.0109E+02	8.6621E+02	2.1080E+02	2.1118E+02
	Std.	9.7320E-01	1.5504E+00	1.4459E+00	6.6982E-01	7.4161E-01
Proposed Method	Mean	**8.2198E+02**	**5.0001E+02**	**8.3194E+02**	**2.0925E+02**	**2.0904E+02**
	Std.	**1.8666E+01**	**1.2824E-02**	**1.4056E+01**	**1.7458E-01**	**3.4315E-01**

5 CONCLUSION

In this paper, two mutation strategies are proposed, which are DE/current to elitist/1 and DE/current to real-rand/1, to replace DE's mutation process. The DE/current to elitist/1 can produce more potential particles for improving particles' searching abilities, and can easier to find the global optimal solution. The DE/current to real-rand/1 can prevent particles from fall into the local optimum.

The experimental results proved that the proposed method can find better solutions than four DE variants. Ten hybrid composition functions were adopted for testing through a reasonable average. Form the results; it can be observed that the proposed has high ability to solve complex numerical optimization problems.

ACKNOWLEDGEMENT

This work was supported in part by National Science Council of Taiwan, Taiwan, R.O.C. under Grant NSC 101-2221-E-161-011.

REFERENCES

[1] J. H. Holland, "*Adaptation in Natural and Artificial Systems*, University of Michigan Press," Ann Arbor, MI, 1975.

[2] J. Kennedy and R. C. Eberhart, "in: Particle Swarm Optimization," in *Proc.* of 1995 IEEE International Conference on Neural Networks, vol. 4, pp. 1942–1948, 1995.

[3] R. Storn and K. V. Price, Differential evolution−A simple and efficient adaptive scheme for global optimization over continuous spaces, ICSI, Berkeley, CA, Tech. Rep. TR-95-012. [Online]. Available:http://http.icsi.berkeley.edu/~storn/litera.html

[4] R. Storn and K. Price, "Differential evolution−A simple and efficient heuristic for global optimization over continuous spaces," J. Global Optim.,vol. 11, no. 4, pp. 341-359, Dec. 1997.

[5] K. Price, R. Storn, and J. Lampinen, Differential Evolution—A Practical Approach to Global Optimization. Berlin, Germany: Springer-Verlag,2005.

[6] R. Storn and K. V. Price, "Minimizing the real functions of the ICEC 1996 contest by differential evolution," in Proc. IEEE Int. Conf. Evol. Comput.,Nagoya, Japan, 1996, pp. 842-844.

[7] J. Liu and J. Lampinen, "On setting the control parameters of the differential evolution method," in Proc. 8th MENDEL, R. Matoušek and P. Ošmera, Ed.s, 2002, pp. 11–18.

[8] J. Liu and J. Lampinen, "A fuzzy adaptive differential evolution algorithm,"Soft Comput., Fusion Found. Methodologies Appl., vol. 9, no. 6,pp. 448–462, Jun. 2005.

[9] J. Liu and J. Lampinen, "Adaptive parameter control of differential evolution,"in Proc. 8th MENDEL, R. Matoušek and P. Ošmera, Eds., 2002,pp 19–26.

[10] J. Rönkkönen and J. Lampinen, "On using normally distributed mutation step length for the differential evolution algorithm," in Proc. 9th MENDEL, Brno, Czech Republic, 2003, pp. 11–18.

[11] M. M. Ali and A. Törn, "Population set based global optimization algorithms: Some modifications and numerical studies," Computers and Operations Research, Elsevier,vol. 31, no. 10, pp. 1703–1725,Sep. 2004.

[12] W. Gong, Z. Cai, C. X. Ling, and H. Li, "Enhanced differential evolution with adaptive strategies for numerical optimization," IEEE Trans. Syst.,Man, Cybern. B, Cybern., vol. 41, no. 2, pp. 397–413, Apr. 2011.

[13] J. Brest, S. Greiner, B. Boškovi ́c, M. Mernik, and V. Žumer, "Selfadapting control parameters in differential evolution: A comparative study on numerical benchmark problems," IEEE Trans. Evol. Comput., vol. 10,no. 6, pp. 646-657, Dec. 2006.

[14] A. K. Qin, V. L. Huang, and P. N. Suganthan, "Differential evolution algorithm with strategy adaptation for global numerical optimization,"IEEE Trans. Evol. Comput., vol. 13, no. 2, pp. 398–417, Apr. 2009.

[15] J. Zhang and A. C. Sanderson, "JADE: Adaptive differential evolution with optional external archive," IEEE Trans. Evol. Comput., vol. 13, no. 5,pp. 945-958, Oct. 2009.

[16] S.M. Islam, S. Das, S. Ghosh, S. Roy, P.N. Suganthan, "An Adaptive Differential Evolution Algorithm With Novel Mutation and Crossover Strategies for Global Numerical Optimization," IEEE Trans. Syst., Man, Cybern. B, Cybern., vol. 42, no. 2, pp. 482–500, Apr. 2012.

[17] Evans, M., N. Hastings, and B. Peacock. Statistical Distributions. 2nd ed., Hoboken, NJ: John Wiley & Sons, Inc., 1993, pp. 147–148

[18] http://www.ntu.edu.sg/home/EPNSuga

© ISAROB 2013

The Eighteenth International Symposium on Artificial Life and Robotics 2013 (AROB 18th '13),
Daejeon Convention Center, Daejeon, Korea, January 30-February 1, 2013

Artificial Bee Colony Algorithm with Crossover Strategies for Global Numerical Optimization

Sheng-Ta Hsieh and Jhih-Sian Chen
Department of Communication Engineering Oriental Institute of Technology, Taiwan
(Tel: +886-2-7738-0145 Ext.2325, Fax: +886-2-7738-7411)

fo013@mail.oit.edu.tw

Abstract: In this paper, a new variant of artificial bee colony (ABC) algorithm is proposed for solving numerical optimization problems. In order to increase population's solution searching ability, the crossover operation of genetic algorithm (GA) is involved to produce new potential offspring. In the experiment, the CEC 2005 test functions are adopted for test proposed method and compared it to related works. From the results, it can be observed that the proposed method performed better performance than two variants of ABC approaches.

Keywords: artificial bee colony, crossover, genetic algorithm, optimization.

1 INTRODUCTION

In order to deal with complicate real-world optimization problems, more and more researchers are focus on creating new optimizers or improving its performance. Such as Genetic Algorithm (GA) [1], Ant Colony Optimization (ACO) [2], Particle Swarm Optimization (PSO) [3] and Differential Evolution(DE) [4] etc.

Artificial bee colony algorithm was first proposed by Karaboga [5]-[6] in 2005. It simulated Bees' forage behavior. Then, Tereshko and Loengarov [7] proposed the foraging model for ABC algorithm.

The ABC algorithm is consisted of three basic elements, employed bees, onlooker bees and scouts bees. The employed bee, onlooker bee will try to find food. While employed and onlooker bees cannot find any food, then, the scout bee will start over for following food searching process and looking for new food source.

In recent years, more and more researchers are studying ABC algorithms either enhancement or applications. In 2010, Banharnsakun *et al*. proposed distributed population [9], which divide whole population into several small sub-populations. Each sub-population will perform its own solution search process in parallel. The sub-swarm will exchange their information after several iterations for improving solution quality and improving solution searching process. In 2011, Bi and Wang proposed FMABC [8], which introduced a free search algorithm to replace traditional roulette wheel for selecting onlooker bees. Further, it also combined an opposition-based strategy to replace scouts bee. Both strategies will speed up solution searching process. In the same year, Guo *et al*. proposed GABCS [10] which refer to PSO moving behavior to modify bees' moving vector. Also, a mutated strategy is involved to generate new bees for increasing bees' solution searching ability. In 2012, El-Abd proposed an interesting ABC variant named GOABC [11], which introduced a opposition-based learning and involved generalized concept into ABC for enhancing optimizer's performance. The GOABC exhibit good results on solving both uni-modal and multi-modal test functions.

However, an optimizer may has higher ability for solving uni-modal problems due to its deep search approach, but it could make optimizer has a weak ability on widely search for solving multi-modal problems, and vice versa. In other word, for the deep and widely search ability, improved one will worsen the other one. Thus, how to make choose a suitable strategy to deal with current problem will be an important issue of optimizer improvement.

In order to enhance ABC optimizer's solution searching ability. In this paper, the crossover of GA is involved into to generate more potential individual. Also, the elitist strategy is involved to speed up convergence.

This paper is consisted of five sections. The basic concept of ABC algorithm is described in section 2. The detail of proposed method is introduced in section 3. The experiments are presented in section 4. Finally, the conclusions are described in section 5.

© ISAROB 2013

2 ARTIFICIAL BEE COLONY

2.1 Introduction to ABC algorithm

Artificial bee colony (ABC) algorithm is a novel optimizer which simulated Bees' forage behavior in solution space and try to looking for optimal solution in reasonable computational consumption In ABC, there are 2 kinds of bees, employed and onlooker bees, are response for finding food source (also named solutions). The employed bees are going to explore new food and onlooker bees are response for better food source. The food searching process will be performed by following equation.

$$v_{ij} = x_{ij} + \emptyset_{ij} \times \left(x_{ij} - x_{kj}\right) \tag{1}$$

where both i and k are random integer, whose range are between $[1, \mathrm{s}]$, and i is not equal to k. The s denotes population size. In other word, i and k are random selected bees. The j is also a random integer whose range is between $[1, \mathrm{D}]$. The D denotes dimension. $\emptyset_{\mathrm{ij}}$ is a normal distribution number which is between [-1, 1], x denotes current food source and v is the new food source.

Onlooker bees will then select a food source according to equation (2) and perform food searching process by equation (1).

$$p_i = \frac{fit_i}{\sum_{n=1}^{\mathrm{SN}} fit_n} \tag{2}$$

where fit_i is fitness value and i denotes the i_{th} bee. The fitness value will be updated by following equation.

$$fit_i = \begin{cases} \frac{1}{(1+f_i)}, & if\ f_i \geq 0 \\ 1 + \mathrm{abs}(f_i), & if\ f_i < 0 \end{cases} \tag{3}$$

where f_i represents objective value of i_{th} bee. After several generations, if there is no better food source be found. The scout bees will take over the food search process and try to looking for new food source (better solutions) by following equation.

$$x_i^{rand} = x_i^{min} + rand(0,1)(x_i^{max} - x_i^{min}) \tag{4}$$

where x^{rand} denotes random selected bee, and x^{min} and x^{max} present minimal and maximal boundary of search range respectively.

The procedure of ABC algorithm is listed as follows.

Step 1: Initialization for generated food source randomly.
Step 2: Calculate fitness value for each food source.
Step 3: Employed bees looking for new food source by (1) and evaluate x_i and v for select better food source.
Step 4: Calculate probability of fitness value by (2).
Step 5: Onlooker bees will select food source by roulette wheel and keep looking for better food by (1).
Step 6: Evaluate x_i and v for select better food source.
Step 7: Record the best food source.
Step 8: If no better be found in limited generations, use (4) to find new food source.
Step 9: Repeat step 3 to 8, until terminal condition is reached

3 PROPOSED METHOD

In order to enhance ABC optimizer's solution searching ability. In this paper, the crossover of GA is involved into to generate more potential individual. Also, the elitist strategy is involved to speed up convergence.

3.1 Crossover

In genetic algorithm, crossover is going to produce offspring by re-combine parents' information. In this paper, multi-point crossover is involved to generate new individual for searching potential/unsearched solution space.

The multi-point crossover will applied on random selected dimension and perform information exchange for selected bees. Thus, it will drive bees toward to right direction and perform deep and widely search. The same as GA, the crossover rate Cr is also set.

In order to prevent solution from fall into local optimum, the multi-point crossover will not perform every generation but every g generations.

3.2. Elitist strategy

The elitist strategy is to select the best bee for guide other bees toward to right direction and perform solution search for finding better food source. Thus, the equation (1) is modified as following equation.

$$v_{ij} = x_{ij} + \emptyset_{ij} \times \left(x_{ij} - x_j^{best}\right) \tag{5}$$

where x^{best} is the best bee of population in current generation.

Although the elitist strategy will speed up convergence of solution searching process, it could also make all the bees are clustered in a small area of solution space. In order to avoid this situation, the elitist strategy will not be activated every generation but by an activation rate Er.

3.3. Procedure of proposed method

The procedure of proposed method is listed as follows.

Step 1: Initialization for generated food source randomly.
Step 2: Calculate fitness value for each food source.
Step 3: If the random value is smaller than Er, jump to step 5, else execute step 4.
Step 4: Employed bees looking for new food source by (1)

© ISAROB 2013

and evaluate x_i and v for select better food source.

Step 5: Employed bees looking for new food source by (5) and evaluate x_i and v for select better food source.

Step 6: Calculate probability of fitness value by (2).

Step 7: Onlooker bees will select food source by roulette wheel and keep looking for better food. If the random value is smaller than *Er*, use (5), else use (1).

Step 8: Evaluate x_i and v for select better food source.

Step 9: If the random value is smaller than Cr, perform crossover, else jump to step 10.

Step 10: Record the best food source.

Step 11: If no better be found in limited generations, use (4) to find new food source.

Step 12: Repeat step 3 to 11, until terminal condition is reached

4 EXPERIMENT RESULTS

4.1 Test functions

In order to test the performance of proposed method and compare it with other variants of ABC, the twenty five test function of CEC 2005 [12] are selected which include uni-modal functions (f_1 ~ f_5), multi-modal functions (f_6 ~ f_{12}), expanded functions (f_{13} ~ f_{14}) and hybrid composition functions (f_{15} ~ f_{25}). All the test functions are set as 30 dimensions. In order to easier compare the performance between optimizers, the error e between the real global optimum f^* and function value f found by optimizer will be presented. Thus, the bias of CEC 2005 test functions is not involved.

$$e = f - f^* \tag{6}$$

The search range and global optimum of all test function is listed in Table 1.

TABLE 1. GLOBAL OPTIMUM AND SEARCH RANGE OF CEC 2005 TEST FUNCTIONS

Test Functions	Global Optimum	Search range
F_1 ~ F_6	0	$[-100, 100]^D$
F_7	0	$[0, 600]^D$
F_8	0	$[-32, 32]^D$
F_9 ~ F_{10}	0	$[-5, 5]^D$
F_{11}	0	$[-0.5, 0.5]^D$
F_{12}	0	$[-100, 100]^D$
F_{13}	0	$[-3, 1]^D$
F_{14}	0	$[-100, 100]^D$
F_{15} ~ F_{24}	0	$[-5, 5]^D$
F_{25}	0	$[-2, 5]^D$

TABLE 2. EXPERIMENT RESULTS

Algorithms	Results	F_1	F_2	F_3	F_4	F_5
ABC	Mean	**0.00E+00**	6.00E+03	8.81E+06	3.04E+04	1.26E+04
	Std.	**0.00E+00**	2.87E+03	2.50E+06	6.74E+03	1.45E+03
GOABC	Mean	**0.00E+00**	2.72E+03	6.15E+06	3.18E+04	1.20E+04
	Std.	**0.00E+00**	9.13E+02	2.07E+06	6.52E+03	1.61E+03
Proposed Method	Mean	**0.00E+00**	**2.98E+02**	**1.89E+06**	**9.59E+03**	**3.21E+03**
	Std.	**0.00E+00**	**1.57E+02**	**6.83E+05**	**2.86E+03**	**6.63E+02**
Algorithms	**Results**	F_6	F_7	F_8	F_9	F_{10}
ABC	Mean	**5.17E+00**	4.70E+03	2.08E+01	2.89E-11	3.89E+02
	Std.	**7.93E+00**	1.74E-12	4.65E-02	1.41E-10	5.59E+01
GOABC	Mean	8.46E+00	**3.29E+03**	2.08E+01	**0.00E+00**	3.48E+02
	Std.	1.23E+01	**2.22E+02**	4.05E-02	**0.00E+00**	5.63E+01
Proposed Method	Mean	1.93E+01	4.70E+03	**2.04E+01**	**0.00E+00**	**8.73E+01**
	Std.	1.89E+01	5.75E-13	**4.81E-02**	**0.00E+00**	**2.10E+01**
Algorithms	**Results**	F_{11}	F_{12}	F_{13}	F_{14}	F_{15}
ABC	Mean	2.83E+01	1.27E+04	1.10E+00	1.31E+01	1.85E+01
	Std.	1.44E+00	5.83E+03	1.50E-01	1.31E-01	5.47E+01
GOABC	Mean	2.97E+01	8.43E+03	**8.08E-01**	1.30E+01	2.94E+01
	Std.	1.47E+00	3.86E+03	**1.48E-01**	1.13E-01	6.29E+01
Proposed Method	Mean	**2.37E+01**	**2.84E+03**	8.59E-01	**1.26E+01**	**4.00E+00**
	Std.	**1.09E+00**	**2.19E+03**	1.85E-01	**1.35E-01**	**1.96E+01**
Algorithms	**Results**	F_{16}	F_{17}	F_{18}	F_{19}	F_{20}
ABC	Mean	3.43E+02	2.75E+02	9.24E+02	9.22E+02	9.21E+02
	Std.	3.99E+01	3.61E+01	6.32E+00	5.19E+00	6.95E+00
GOABC	Mean	3.47E+02	3.75E+02	9.25E+02	9.23E+02	9.25E+02
	Std.	3.05E+01	4.30E+01	6.00E+00	4.39E+00	6.20E+00
Proposed Method	Mean	**1.64E+02**	**2.07E+02**	**9.08E+02**	**9.08E+02**	**9.04E+02**
	Std.	**2.93E+01**	**5.82E+01**	**1.45E+00**	**2.12E+00**	**7.96E+00**
Algorithms	**Results**	F_{21}	F_{22}	F_{23}	F_{24}	F_{25}
ABC	Mean	5.00E+02	1.12E+03	5.34E+02	**2.00E+02**	**1.02E+03**
	Std.	3.68E-03	4.41E+01	6.08E-04	**8.76E-13**	**7.47E+00**
GOABC	Mean	5.00E+02	1.09E+03	**5.33E+02**	2.33E+02	1.26E+03
	Std.	1.09E-12	4.63E+01	**7.86E-04**	2.97E+01	1.17E+01
Proposed Method	Mean	**5.00E+02**	**9.43E+02**	5.34E+02	2.56E+02	1.23E+03
	Std.	**4.62E-13**	**2.18E+01**	3.23E-04	3.29E+01	2.00E+01

© ISAROB 2013

4.2 Parameter settings

In order to fair comparison, all the parameters are according to their original settings. The population size of proposed method is referring to [11]. The crossover will be activated every 300 generations, and the crossover rate is set as 0.5. The maximum Fitness Evaluations (FEs) are set as 300,000.

4.3 Experiment results

Table 2 presents the mean, standard deviation, and average computation time of 25 runs of the 3 variants of ABC approaches on the 25 test functions with 30 dimensions. The best results among the three approaches are shown in bold.

From the results, the proposed method performed with better results on most test functions can be observed. The proposed method surpasses all other algorithm in solving all functions and a significant improvement on the results of functions 2, 4, 5, 15 and 22. The Proposed method performed the same best result as the ABC [5] and GOABC [11] on function 1. The Proposed method performed the same best result as the GOABC on function 9.

5 CONCLUSIONS

In this paper, both the crossover and elitist strategy are involved into ABC algorithm for solving numerical optimizations. The crossover can produce more potential individuals for improving bees' searching abilities, for easier to find the global optimal solution. It also makes ABC more robust, prevents bees from falling into the local optimum.

The experimental results proved that the proposed method can find better solutions than other ABC variants. Twenty five test functions were adopted for testing through a reasonable average. Form the results; it can be observed that the proposed has high ability for solving uni-modal functions, multi-modal functions, expanded functions and hybrid composition functions.

ACKNOWLEDGEMENT

This work was supported in part by National Science Council of Taiwan, Taiwan, R.O.C. under Grant NSC 101-2221-E-161-011.

REFERENCES

[1] J. H. Holland, "*Adaptation in Natural and Artificial Systems*, University of Michigan Press," Ann Arbor, MI, 1975.

[2] M. Dorigo, V. Maniezzo, and A. Colorni, "Ant System: Optimization by a colony of cooperaing agents," *IEEE Trans. on SMC*, pp. 29-41, 1996.

[3] J. Kennedy and R. C. Eberhart, "in: Particle Swarm Optimization," in *Proc.* of 1995 IEEE International Conference on Neural Networks, vol. 4, pp. 1942–1948, 1995.

[4] R. Storn and K. Price, "Differential evolution – a simple and efficient daptive scheme for global optimization over continuous spaces," *Technical report*, International Computer Science Institute, 1995.

[5] D. Karaboga, "An idea based on honeybee swarm for numerical optimization," Technical Report TR06, 2005.

[6] D. Karaboga and B. Akay, "Artificial bee colony (ABC), harmony search and bees algorithms on numerical optimization," in Innovative Production Machines and Systems Virtual Conference, 2009.

[7] V. Tereshko and A. Loengarov, "Collective Decision-Making in Honey Bee Foraging Dynamics," *Computing and Information Systems Journal*, vol. 9, No 3, ISSN 1352-9404, 2005.

[8] X. Bi and Y. Wang, "An improved artificial bee colony algorithm," in *Proc.* of 2011 3rd International Conference on Computer Research and Development (ICCRD), vol.2, pp.174-177, 2011.

[9] A. Banharnsakun, T. Achalakul and B. Sirinaovakul, "Artificial bee colony algorithm on distributed environments," in *Proc.* of 2010 Second World Congress on Nature and Biologically Inspired Computing (NaBIC), pp.13-18, 2010.

[10] P. Guo, W. Cheng and J. Liang , "Global artificial bee colony search algorithm for numerical function optimization," in *Proc.* of 2011 Seventh International Conference on Natural Computation (ICNC), vol.3, pp.1280-1283, 2011.

[11] M. El-Abd, "Generalized opposition-based artificial bee colony algorithm," in *Proc.* of 2012 IEEE Congress on Evolutionary Computation (CEC), pp.1-4, 2012.

[12] http://www.ntu.edu.sg/home/EPNSugan

© ISAROB 2013

The Eighteenth International Symposium on Artificial Life and Robotics 2013 (AROB 18th '13),
Daejeon Convention Center, Daejeon, Korea, January 30-February 1, 2013

Microwave Imaging of Dielectric Cylindrical Target Using Dynamic Differential Evolution and Self-Adaptive Dynamic Differential Evolution

Ching-Lieh Li[1]
Electrical Engineering Department, Tamkang University,
New Taipei City, Taiwan, R.O.C.
e-mail:li@ee.tku.edu.tw

Chi-Hsien Sun[2]
Department of Electronic and Computer Engineering, National Taiwan University of Science and Technology
E-mail:laisingsun@yahoo.com.tw

Chung-Hsin Huang[3]
Department of Information Technology and Mobile Communication, Taipei College of Maritime Technology, New Taipei City, Taiwan, R.O.C.
e-mail: havehuang@hotmail.com

Lung-Fai Tuen[4]
Electrical Engineering Department, Tamkang University,
New Taipei City, Taiwan, R.O.C.
e-mail: justin_tuen@hotmail.com

Huang-Wei Wong[5]
Electrical Engineering Department, Tamkang University,
New Taipei City, Taiwan, R.O.C.
e-mail: mayday72001@hotmail.com

Abstract: The inverse problem under consideration is to reconstruct the characteristic of scatterer from the scattering E field. Dynamic differential evolution (DDE) and self-adaptive dynamic differential evolution (SADDE) are stochastic-type optimization approach that aims to minimize a cost function between measurements and computer-simulated data. These algorithms are capable of retrieving the location, shape and permittivity of the dielectric cylinder in a slab medium made of lossless materials. The finite-difference time-domain (FDTD) is employed for the analysis of the forward scattering. Numerical results indicate that both optimization methods are reliable tools for inverse scattering applications. In the particular case of small-scale problems investigated in this paper, SADDE outperforms the DDE a little in terms of reconstruction accuracy.

Keywords: ***Inverse Scattering, Differential Evolution, Optimization.***

1 INTRODUCTION

The inverse scattering scattering problem of unknown objects has many applications including microwave imaging, ground penetrating radar, nondestructive evaluation, and biomedical engineering. Numerous inverse problem techniques for 2-dimensional or 3-dimensional targets were reported [1]-[10].

For example, single frequency plane waves at a fixed angle were used in [1] to illuminate the perfect electric conductors (PEC), and the observation domain was located in the far zone. Upon using a linear distributional model, the unknown parameters were retrieved. A Kirchhoff-based approximation was employed in [2] to retrieve the shape of 2-D dielectric cylinders from aspect-limited multi-monostatic backscattering data. The Tikhonov regularized Gauss-Newton framework was implemented in [3] to reconstruct the boundary and the inhomogeneity parameters of 2-D scatterers. For the breast cancer application, the shape and the location of a 3-D breast cancer tumor-like were retrieved using the spherical harmonic decomposition approach [4]. The gradient descent optimization method and the Method of Moments (MoM) were combined to determine the coefficients of the spherical harmonic decomposition. A lossless dielectric 2-D object with irregular shape was simulated nondestructive evaluation [5]. However, these papers are focused on frequency-domain.

As compared to frequency-domain approach, the interaction of the entire medium in the time domain with the incident field needs to be considered. In contrast, time-domain approaches can exploit causality to limit the region of inversion, potentially reducing the number of unknowns. The genetic algorithm (GA) was reported as a fast and very effective technique for shape reconstruction problems [6]. In this method, the shape of the scattering object was retrieved upon solving cost function. However, large amount of computation load was generally needed. Improvements in the GA were reported in [7] where good reconstruction results were demonstrated using fewer searching time. Optimization methods, such as the synchronous particle swarm optimization (SPSO)

© ISAROB 2013

techniques were reported in [8] where the shape of 2-D PEC target was reconstructed using the asynchronous particle swarm optimization (APSO). In the 2010, the dynamic differential evolution (DDE) was first proposed to deal with the shape reconstruction of homogeneous dielectric cylinders under time domain [9]. The DDE algorithm is a potentially trend to obtain the global optimum of a functional whatever the initial guesses are. In recent decade years, some papers have compared different algorithm in inverse scattering [10]-[15]. To the best of our knowledge, there is still no comparative study about the performances of SADDE and DDE to inverse scattering problems is also investigated. I n this paper, the computational methods combining the FDTD method [16] and the DDE and SADDE is presented. The forward problem is solved by the FDTD method. The shape of scatterer is parameterized by closed cubic spline expansion. The inverse problem is formulated into an optimization one and then the global searching scheme DDE and SADDE is used to search the parameter space. In section II, the subgridding FDTD method for the forward scattering are presented. In sections III and IV, the inverse problem and the DDE and SADDE of the proposed inverse problem are given, respectively. In V section, the numerical result of the proposed inverse problem is given. Finally, in VI section some conclusions are drawn for the proposed time domain inverse scattering.

.2 FORWARD PROBLEM

Let us consider a two-dimensional metallic cylinder buried in a slab medium as shown in Figure 1. The cylinder is parallel to z axis, while the cross-section of the cylinder is arbitrary. The object is illuminated by a Gaussian pulse line source located at the points denoted by Tx and reflected waves are recorded at those points denoted by Rx. The computational domain is discretized by Yee cells. It should be mentioned that the computational domain is surrounded by the optimized perfect matching layers (PML) absorber to reduce the reflection from the environment-PML interface [17].

The direct scattering problem is to calculate the scattered electric fields while the shape and location of the scatterer are given. The shape function $F(\theta)$ of the scatterer is described by the trigonometric series in the direct scattering problem

$$F(\theta)=\sum_{n=0}^{N/2}B_n\cos(n\theta)+\sum_{n=1}^{N/2}C_n\sin(n\theta) \qquad (1)$$

where *Bn* and *Cn* are real coefficients to expand the shape function.In order to closely describe the shape of the cylinder for both the forward and inverse scattering procedure, the subgridding technique is implemented in the FDTD code; More detail on subgriding FDTD can be found in [16].

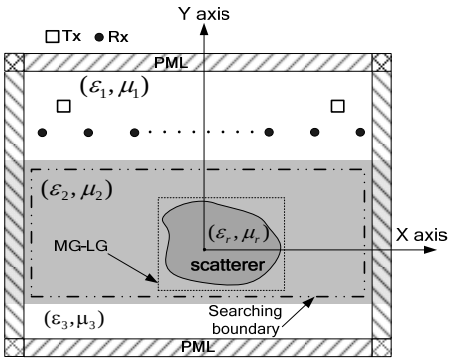

Fig. 1. Geometrical configuration of the problem.

3 INVERSE PROBLEM

For the inverse scattering problem, the shape and location of the perfectly conducting cylinder are reconstructed by the given scattered electric field measured at the receivers. This problem is resolved by an optimization approach, for which the global searching DDE and SADDE is employed to minimize the following objective function (*OF*):

$$OF=\frac{\sum_{n=1}^{N_i}\sum_{m=1}^{M}\sum_{q=0}^{Q}\left|E_z^{exp}(n,m,q\Delta t)-E_z^{cal}(n,m,q\Delta t)\right|}{\sum_{n=1}^{N_i}\sum_{m=1}^{M}\sum_{q=0}^{Q}\left|E_z^{exp}(n,m,q\Delta t)\right|} \qquad (2)$$

Where E_z^{exp} and E_z^{cal} are experimental electric fields and the calculated electric fields, respectively. The N_i and M are the total number of the transmitters and receivers, respectively. Q is the total time step number of the recorded electric fields.

4 EVOLUTIONAL ALGORTHEMS

DDE algorithm starts with an initial population of potential solutions that is composed by a group of randomly generated individuals which represents the center position and the geometrical radiuses of the cylinders. Each individual in DDE algorithm is a *D*-dimensional vector consisting of *D* optimization parameters. The initial population may be expressed by $\{x_j:\ j=1,\ 2,\cdots,Np\}$, where *Np* is the population size. After initialization, DDE algorithm performs the genetic evolution until the termination criterion is met. DDE algorithm, like other EAs, also relies on the genetic operations (mutation, crossover and selection) to evolve generation by generation. The mutation operation of DDE algorithm is performed by arithmetical combination of individual. For each parameter vector x_j of the parent generation, a trial vector v_j is generated according to following equation:

$$(V_j^{g+1})_i=(X_j^g)_i+F\cdot[(X_{best}^g)_i-(X_j^g)_i]+\lambda\cdot[(X_{r1}^g)_i-(X_{r2}^g)_i],$$

$$r1, r2 \in [0, N_p - 1],\ r1 \neq r2 \qquad (3)$$

where F and λ are the scaling factors associated with the vector differences $(X^g_{best} - X^g_j)$ and $(X^g_{r1} - X^g_{r2})$, respectively. The disturbance vector V due to the mutation mechanism consists of parameter vector X^g_j, the best particle X^g_{best} and two randomly selected vectors. SADDE are based on DDE scheme. Each vector is extended with its own λ, F and *CR* values. Therefore the control parameters are self-adjusted in every generation for each individual according to the following scheme:

$$F_{i,G+1} = \begin{cases} F_l + rand_1 * F_u, & if \quad rand_2 < 0.1 \\ F_{i,G+1}, & otherwise \end{cases} \qquad (4)$$

$$\lambda_{i,G+1} = \begin{cases} \lambda_l + rand_3 * \lambda_u, & if \quad rand_4 < 0.1 \\ \lambda_{i,G+1}, & otherwise \end{cases} \qquad (5)$$

$$CR_{i,G+1} = \begin{cases} rand_5, & if \quad rand_6 < 0.1 \\ CR_{i,G+1}, & otherwise \end{cases} \qquad (6)$$

where *rand1, rand2, rand3, rand4, rand5* and *rand6* are uni form random numbers with thin values uniformly between 0 and 1. And F_l, F_u, λ_l and λ_u are the lower and the upper limits of F and λ, respectively .Both F_l and λ_l are set to 0.1 and both F_u and λ_u are set to 0.9. Based on the self-adaptive concept, the F, λ and CR parameters adjust automatically while the time complexity does not increase. More details about the SADDE algorithm can be found in [18]. It should be noted that the value of Fourier series used to describe the shape of the cylinder will be determined by the DDE and SADDE scheme.

5 NUMERICAL RESULT

As shown in Figure 1, the problem space is divided in 68×68 grids with the grid size $\Delta x = \Delta y = 5.95$ mm. The dielectric cylinder is buried in lossless slab medium ($\sigma_1 = \sigma_2 = \sigma_3 = 0$). The transmitters and receivers are placed in free space above the homogeneous dielectric. The permittivities in region 1, region 2 and region 3 are characterized by $\varepsilon_1 = \varepsilon_0$, $\varepsilon_2 = 6\varepsilon_0$ and $\varepsilon_3 = \varepsilon_0$, respectively, while the permeability μ_0 is used for each region, i.e., only non-magnetic media are concerned here.

The scatterer is illuminated by plane waves with the electric field polarized along the axis, while the time dependence of the field is of a one derivative Gaussian pulse. The cylindrical object is illuminated by a transmitter at two different positions, N_i=2, which are located at the (-143mm, 178.5mm) and (143mm, 178.5mm), respectively. The scattered E fields for each illumination are collected at the eight receivers, *M*=8, which are equally separated by 47.8mm along the distance of 48mm from the interface between region 1 and region 2.

For the example, the dielectric cylinder with shape function $F(\theta) = 29.75 + 5.95\cos(4\theta)$ mm and the relative permittivity of the object is $\varepsilon_r = 3.5$ is considered. The final reconstructed shapes by SADDE and DDE at the 300 th generation are compared to the exact shape in Figure 2. The r.m.s. error of shape function for SADDE and DDE are about 2.31% and 2.51% in the final generation, respectively. The relative error for permittivity by SADDE and DDE are both less than 1%.The R.M.S. error of the reconstructed shape $F^{cal}(\theta)$ and the relative error for permittity with respect to the exact values versus generations are shown in Figure 3. It is clear that the SADDE a little bit outperforms DDE for this example.

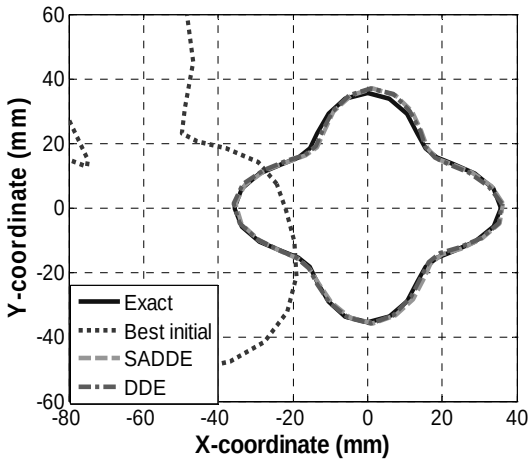

Fig. 2. The reconstructed shapes of the cylinder for example by DDE and SADDE, respectively.

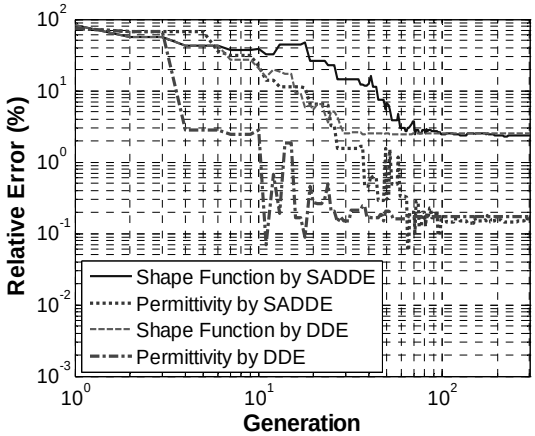

Fig. 3. Error value versus generation for example by DDE and SADDE, respectively.

6 CONCLUSION

In this paper, we study the time domain inverse scattering of an arbitrary cross section dielectric cylinder. Numerical results show that result by SADDE in accurate reconstruction. Finally, SADDE leads to more precise reconstruction results for the same population size and total number of iterations. It should be mentioned that this comparative study is indicative and its conclusion should not be considered generally applicable in all inverse scattering problems.

ACKNOWLEDGEMENT

This work was supported by National Science Council, Republic of China, under Grant NSC 101-2221-E-032-029-.

REFERENCES

[1] C. C. Chiu and P. T. Liu, "Image Reconstruction of a Perfectly Conducting Cylinder by the Genetic Algorithm," *IEE Proceeding-Microwaves Antennas and Propagation*, vol. 143, pp. 249-253, June 1996.

[2] A. Brancaccio and G. Leone, "Multimonostatic shape reconstruction of two-dimensional dielectric cylinders by a Kirchhoff-based approach," *IEEE Transactions on Geoscience and Remote Sensing*., vol. 48, no. 8, pp. 3152–3161, Aug. 2010.

[3] Naik, J. Eriksson, P. de Groen, and H. Sahli, "A nonlinear iterative reconstruction and analysis approach to shape-based approximate electromagnetic tomography," *IEEE Transactions on Geoscience and Remote Sensing.*, vol. 46, no. 5, pp. 1558–1574, May 2008.

[4] M. El-Shenawee and E. Miller, "Spherical harmonics microwave algorithm for shape and location reconstruction of breast cancer tumor," *IEEE Trans. Med. Imag.*, vol. 25, no. 10, pp. 1258–1271, Oct. 2006.

[5] C. H. Huang, C. L. Liu, C. C. Chiu, Y. D. Wu, T. Wysocki and B. J Wysock, "Electromagnetic Transverse Electric-Wave Inverse Scattering of a Two-dimensional Dielectric Object by Genetic Algorithm," *Electromagnetics* Vol. 27, No. 5, pp. 241-251, June 2007.

[6] X.-M. Zhong, C Liao and W. Chen, "Image reconstruction of arbitrary cross section conducting cylinder using UWB pulse, " *Journal of Electromagnetic Waves Application*,, vol. 21, No. 1, pp. 25-34, 2007

[7] C. H. Sun, C. L. Li, C. C. Chiu and C. H. Huang, "Time Domain Image Reconstruction for a Buried 2D Homogeneous Dielectric Cylinder Using NU-SSGA.", *Research in Nondestructive Evaluation*, Vol. 22, No.1, pp. 1-15, Jan. 2011.

[8] C. C. Chiu, C. H. Sun and W. L. Chang "Comparison of Particle Swarm Optimization and Asynchronous Particle Swarm Optimization for Inverse Scattering of a Two- Dimensional Perfectly Conducting Cylinder.", *International Journal of Applied Electromagnetics and Mechanics* Vol. 35, No.4, pp. 249-261,Apr. 2011.

[9] C. H. Sun, C. C. Chiu, C. L. Li, and C. H. Huang, "Time Domain Image Reconstruction for Homogenous Dielectric Objects by Dynamic Differential Evolution," *Electromagnetics.* Vol. 30, No. 4, pp. 309-323, May. 2010.

[10] A. Semnani, M. Kamyab, and I. T. Rekanos, "Reconstruction of One-Dimensional Dielectric Scatterers Using Differential Evolution and Particle Swarm Optimization," *IEEE Geoscience and Remote Sensing Letters*, Vol. 6, No. 4, pp. 671-675, Oct. 2009.

[11] I. T. Rekanos, "Shape Reconstruction of a Perfectly Conducting Scatterer Using Differential Evolution and Particle Swarm Optimization," *IEEE Transactions on Geoscience and Remote Sensing*, Vol. 46, No. 7, pp. 1967-1974, Jul. 2008.

[12] M. Pastorino, "Stochastic Optimization Methods Applied to Microwave Imaging: A Review," *IEEE Transactions on Antennas and Propagation*. Vol. 55, No. 3, pp. 538-548, Mar. 2007.

[13] P. Rocca, M. Benedetti, M. Donelli, D. Franceschini and A. Massa, "Evolutionary optimization as applied to inverse scattering problems," *Inverse Problems*. Vol. 925 pp. 1–42, 2009.

[14] C. H. Sun, C. C. Chiu and C. L. Li, "Time-Domain Inverse Scattering of a Two- dimensional Metallic Cylinder in Slab Medium Using Asynchronous Particle Swarm Optimization.", *Progress In Electromagnetic Research M.* PIER M Vol. 14, pp. 85-100. Aug. 2010.

[15] C. C. Chiu and W. C. Hsiao "Comparison of Asynchronous Particle Swarm Optimization and Dynamic Differential Evolution for Partially Immersed Conductor." *Waves in Random and Complex Media.* Vol. 21, No.3, pp. 485-500, Aug. 2011.

[16] A. Taflove and S. Hagness, "*Computational Electrodynamics: The Finite-Difference Time-Domain Method*," Artech House, Boston, MA, 2000

[17] M. W. Chevalier, R. J.Luebbers and V. P. Cable, "FDTD local grid with material traverse," *IEEE Transaction on Antennas and Propagation*, vol. 45, No. 3, March 1997.

[18] C. C. Chiu, C. H. Sun, C. L. Li and C. H. Huang, "Comparative Study of Some Population-based Optimization Algorithms on Inverse Scattering of a Two- Dimensional Perfectly Conducting Cylinder in Slab Medium" *IEEE Transactions on Geoscience and Remote Sensing*. (in press)

© ISAROB 2013

The Eighteenth International Symposium on Artificial Life and Robotics 2013 (AROB 18th '13),
Daejeon Convention Center, Daejeon, Korea, January 30-February 1, 2013

Application of Natural Language Processing for Information Retrieval

Su Mei Xi[1], Dae Jong Lee[2], Young Im Cho[3]

[1]Department of Information, Shandong Polytechnic University, Jinan, 250353, China
[2]College of Electrical and Computer Engineering, Chungbuk National University, Cheong Ju, 361-763, Korea
[3]College of Information Technology, Suwon University, San 2-2, Bongdam-eup, Hwaseong-si, 445-743, Korea

[1]xiyanzi_79@sina.com.cn
[2]bigbell@chungbuk.ac.kr
[3]ycho@suwon.ac.kr

Abstract: Through a comprehensive analysis of using natural language processing in information retrieval, we compared the effects with the various natural language techniques for information retrieval precision in this paper. This is for the tasks of more suitable as well as accurate results of natural language processing.

Keywords: natural language processing, information retrieval, phrase identification, stemming

1 INTRODUCTION

Many researchers have been trying to use natural language processing (NLP) in information retrieval, but the result is not satisfactory. Less complex basic natural language processing techniques with small calculated consumption and simple implementation help a small for information retrieval, which including stop words removal, word segmentation, stemming etc. But some techniques are still recommended in the information retrieval experimental platform, which can improve the retrieval effect such as stop words removal and stemming etc. Senior high complexity of natural language processing techniques with high calculated consumption and low precision can't help the information retrieval even harmful to it, which including parsing, phrase identification, named entity recognition, concept extraction, anaphora resolution and WSD etc [1].

Therefore, in this paper, through a comprehensive analysis of using natural language processing in information retrieval, we will compare the effects with the various natural languages. This paper is organized as follows: Firstly we introduce the application of natural language processing in information retrieval, and secondly we compare the effectiveness of NLP for IR precision, and third, we discuss and finally we conclude of natural language processing in information retrieval.

2 Application of NLP in Information Retrieval

2.1 Application of Basic NLP Technique

2. 1. 1 Stop Word Removal

Stop word refers to the word that lack actual meaning and appear lot of times in the document, such as most of English prepositions, and articles etc. Because stop word removal technique has no substantial help to improve the retrieval effect actual information retrieval systems such as Web search engines often do not use this technique. Moreover, using this technique could not lead to good results in dealing with some queries. The classic example is the query of "to be or not to be". So stop word also has been reserved as index item in most actual retrieval system.

2.1.2 Word Segmentation

Word segmentation is a special problem in information retrieval of Asian languages such as Chinese and Japanese. Most of European languages need not word segmentation. Word segmentation technique is widely used in Chinese information retrieval systems.

Peng et al have made word segmentation and retrieve experiments in the Chinese data set of TREC5 and TREC6 [2]. Their experiments showed that word segmentation accuracy and retrieval effect is not the monotonous directly proportional. The best retrieval effect can be obtained when word segmentation accuracy is 70% or so. If the Word segmentation accuracy is too high, it may lead to decline in retrieval effect.

2. 1. 3 Stemming

Stemming can make the same stem word match the different form word. Commonly used methods include rule-based stemming (e.g. Porter Stemmer) and dictionary-based stemming (e.g. KSTEM).

Strzalkowski and Vauthey applied the stemming method of dictionary-assisted in their retrieval system. The

© ISAROB 2013

unreasonable states were improved in the results of stemming and the retrieval precision has 6% to 8% increase [3]. The corpus-based stemming approach improved the retrieval precision slightly to the Porter stemmer and KSTEM put forward by Xu and Croft [4].

In practice, stemming technique was widely used in information retrieval system for its high availability although it can only improve the retrieval effect a little.

2. 1. 4 Part-of-Speech Tagging

It has no obvious usage about part-of-speech tagging to information retrieval. The biggest problem is that we do not know how to use it in retrieval even if it has a very high accuracy .

One approach is that only index the certain parts-of-speech. Kraaij and Pohlmann studied the importance of the different part-of-speech words to retrieval [5]. Their result is that 58% are noun, 29% are verb and 13% are adjective among the document words that useful to retrieval. It can be found that 84% are noun among the useful words if we only focus on those fronts of documents. Arampatzis et al only used nouns to complete the experiment and the result showed that there was 4% improvement compared with using all words [6].

Another use is to separate the different parts of speech of words. Let the words that have the same part of speech in the query and document can be matched. Using TREC7 and TREC8 data sets, Su Qi and others examined the retrieval effect of this use to the SMART system [7].The results show that if we can tag the words that have the same form but different part of speech we will improve retrieval accuracy and decrease the matching noise. The words that have the same meaning, the same stemming and different parts of speech have no match, leading to the decline of retrieval recall.

2.2 Application of Advanced NLP Technique

Advanced natural language processing technique include parsing, phrase identification, named entity recognition, concept extraction, anaphora resolution and word sense disambiguation etc.

2. 2. 1 Phrase Identification

Phrase identification technique used in information retrieval mixed the results, largely depending on the specific recognition technology, the phrase type and the matching strategy[8,9,10]. Nie and Dufort made the phrase as an additional unit to combine with the traditional word-based index. They placed the phrases and words in different vectors, calculated the similarity of the query and document and then added their weights[11].

2. 2. 2 Named Entity Extraction

Named entity is a special phrase that identified a concept or entity, such as proper nouns, place names, organization name and so on. Obviously, the named entities express more accurate information than the general phrases.

But the application of named entity in information retrieval has not obtained the direct effect to retrieval. On the one hand it existing error in the named entity recognition technique itself, on the other hand, researchers have also confused that how to match the named entity.

2. 2. 3 Concept Extraction

Concept is a more general special phrase than named entity. Named entity identifies a concept, so we can consider it belong to the concept. Concept also includes other phrases that not belong to the named entity.

2. 2. 4 Anaphora and Co-references

An anaphora and co-references technique is to find the actual things for the pronoun or the unknown phrase that appeared in the document. This technique seems to have contributed to the information retrieval since it is able to eliminate the unclear expression in the document. However, the truth is not the case. Anaphora and co-references also can not improve information retrieval effect. On the one hand anaphora resolution still has more errors, the other hand pronoun and the unknown phrase does not actually affect the results of information retrieval[12].

2. 2. 5 Word Sense Disambiguation

Voorhees used the word sense disambiguation technique in treating word sense as an index item. It is found that some queries can indeed benefit from the word sense index, however more decline after individually analyzing retrieval results of each query. Almost all the declines are because of the match fails of those words should be matched between queries and documents, since word sense index is used.

Then what word sense disambiguation accurate could help the information retrieval? The answer is 90% which is given by Sanderson[13]. In his experiment he found that the improvement of succeeded disambiguation for retrieval would be offset by the negative effects of failed disambiguation if there was 20% to 30% error rate of word sense disambiguation.

Stokoe et al used Semcor corpus which released with WordNet training the word sense disambiguation system. The words of failed disambiguation would be assigned to the meaning of the highest frequency appeared in the WordNet[14]. Although the accuracy of the word sense disambiguation was only 62%, the experimental results which completed in TREC9 data show that this

© ISAROB 2013

disambiguation method can relatively improve the retrieval effect 45%. However, their retrieval results are still worse than the best result of TREC9 even if there is more improvement about retrieval accuracy because the performance of the benchmark system used in their experiments is poor.

Kim et al used a particular Word Sense Disambiguation technique. They only consider the 25 most original word meanings of a word in the WordNet and then assign a meaning to a word, which can insure the accuracy of WSD[15].

2.3 Adding Natural Language Processing Technique into Language Model

The nature of the language model is to determine the relevance between the query and document by computing the probability of generating the query from the document.

Kumaran and Allan joined the stemming technique in the language model. They thought that Stemming can be seen as smoothing [16]. They proposed a generative model. In this model, they thought that it can be divided into two steps from d to w. Firstly, d generates c, and then c generates w. This assumption comes from the writer writing. When writers select the words they usually think to a meaning and then select the word with correct form. Experimental results show that the average retrieval accuracy of the new model has increased about 10%.

2.4 The Application Effect of NLP Technique in Information Retrieval

TREC5 NLP evaluation results show that query expansion, phrase identification, terminology, and stemming and other natural language processing Techniques used in information retrieval can obtain better effect than the word-based retrieval system. These systems that applied these technologies are still not better than the systems based on statistical [17].

Manning analyzed the roles of natural language processing techniques in Web Retrieval. In fact, Web retrieval technique has gained more progress through Web link analysis techniques and AnchorText.

2.5 The Application of NLP Resources in Information Retrieval

Natural language processing resources refer to the dictionary like WordNet and HowNet. Smeaton experimented with WordNet after the failure that using natural language technique to retrieval experiment such as parsing. In addition, as mentioned above, WordNet is commonly tools used in word sense disambiguation.

Natural language processing resources are constructed manually or revised manually after generated by machine. It has a very high accuracy and it is suitable to be used in information retrieval. We should use it according to the actual situation for different problems.

3 Comparison of Different NLP Techniques Applied in IR Systems

TREC NLP evaluation results (table1 and table2) show that phrase identification, terminology, and stemming and other natural language processing Techniques used in information retrieval can obtain better effect than the word-based retrieval system.

Table 1. The experimental results of basic NLP techniques used in IR systems

	TREC-5		TREC-6	
	Avg.Prec.	R.Prec.	Avg.Prec.	R.Prec.
Stop word removal	No use	null	No use	null
Word segmentation	0.3721	0.3988	0.5044	0.5072
Stemming	0.328	0.356	0.273	0.304
Part-of-speech tagging	0.4632	0.4804	0.2692	0.2712

Most of the trial had no good effect, which try to use natural language processing in information retrieval, even had some little help, it was not satisfied for people. Researchers have analyzed, and draw conclusions that it was need to be optimized that natural language processing for information retrieval tasks.

Table 2. The experimental results of advanced NLP techniques used in IR systems

	TREC-5		TREC-6	
	Avg.Prec.	R.Prec.	Avg.Prec.	R.Prec.
Phrase identification	0.2347	0.2939	0.2434	0.2574
Named entity extraction	0.2860	0.2835	0.1961	0.2014
Concept extraction	0.2613	0.2545	0.3346	0.3321
Anaphora co-references	0.2998	0.2876	0.3261	0.3211
Word sense disambiguation	0.3291	0.1994	0.2426	0.1980

4 CONCLUSION

For a long time, the development of natural language processing is to be applied to the tasks which need precise results such as machine translation, so the role of natural

© ISAROB 2013

language understanding may be larger in the question answering system, automatic abstract and information extraction. In face, in these tasks, we have achieved good results through the interaction between the NLP and IR. The results of TREC also show that Natural language processing can improve the effect of these tasks.

It can be seen in table 3 that the tasks of longer length of the query are more suitable for using natural language processing, such as information extraction and question answering system etc. It is conceivable that the tasks of shorter length results more need to use natural language processing because of the need for syntactic and semantic processing in order to ensure its accuracy. Therefore, compared to the document retrieval, information extraction and question answering system are more suitable for the use of natural language processing.

Table 3. Classification of Document Retrieval, Passage Retrieval, Question Answering, and Information Retrieval according to query length and result length

Query length / Result length	Short	Medium	Long
Short			QA/ IE
Medium		PR	
Long	DR		

REFERENCES

[1] Ricardo Baeza-Yates, "Challenges in the Interaction of Information Retrieval and Natural Language Processing". In: Proceedings of 5th International Conference on Intelligent Text Processing and Computational Linguistics , CICLing 2004 , Seoul , Korea , February 15-21 , pp.445-456, 2004.

[2] Fuchun Peng , Xiangji Huang , Dale Schuurmans and Nick Cercone, "Investigating the Relationship between Word Segmentation Performance and Retrieval Performance in Chinese IR", In: Proceedings of 19th International Conference on Computational Linguistics, pp.72-78, 2002.

[3] Tomek Strzalkowski and Barbara Vauthey, "Information retrieval using robust natural language processing", In: Proceedings of the 30th annual meeting on Association for Computational Linguistics, pp.104-111,1992.

[4] J Xu and W. B. Croft , "Corpus-based stemming using cooccurrence of word variants", ACM Transactions on Information Systems (TOIS) , vol.16,no.1, pp.61-81, 1998.

[5] W. Kraaij and R. Pohlmann, "Viewing stemming as recall enhancement", In: Proceedings of the 19th Annual International ACM SIGIR Conference on Research and Development in Information Retrieval ,ACM Press, pp.40-48, 1996.

[6] A. T. Arampatzis , Th. P. van der Weide , C. H. A. Koster and P. van Bommel , "Text Filtering using Linguistically-motivated Indexing Terms". Technical Report CSI-R9901, Computing Science Institute, University of Nijmegen , Nijmegen , The Netherlands ,1999.

[7] Qi Su,Hongying Zan, "Effects of POS Tagging on Performance of IR Systems", Journal of Chinese Information Processing, vol.19,no.2 , pp.58-65,2005.

[8] Thorsten Brants, "Natural Language Processing in Information Retrieval", In: Proceedings of 20th International Conference on Computational Linguistics , Antwerp, Belgium, pp.1-13, 2004.

[9] M. Mit ra , C. Buckley , A. Singhal , and C. Cardie, "An analysis of statistical and syntactic phrases", In : Proceedings of the RIAO97 , pp.200-216,1997.

[10] S. E. Robert son and S. Walker, "Okapi/ Keenbow at TREC28", In: Proceedings of the 8th Text Retrieval Conference, NIST Special Publications 500-246, Gaithersburg , pp.151-162, 1999.

[11] Jian-Yun Nie and J ean-Francois Dufort, "Combining words and compound terms for monolingual and cross-language information retrieval", In: Proceedings of Information. Beijing, pp.453-458, 2002.

[12] James Allan, "Natural Language Processing for Information Retrieval", tutorial presented at the NAACL/ANL P language technology joint conference in Seattle ,Washington , April 29 , 2000.

[13] M. Sanderson, "Word Sense Disambiguation and Information Retrieval", In: Proceedings of the 17th Annual International ACM SIGIR Conference on Research and Development in Information Retrieval , ACM Press, pp.49-57,1994.

[14] Christopher Stokoe , Michael P. Oakes and John Tait , "Word Sense Disambiguation in Information Retrieval Revisited", In: Proceedings of the 26th Annual International ACM SIGIR Conference on Research and Development in Information Retrieval, ACM Press , pp.159-166, 2003.

[15] Sang-Bum Kim , Hee-Cheol Seo and Hae-Chang Rim, "Information Retrieval using Word Senses : Root Sense Tagging Approach", In: Proceedings of the 27th Annual International ACM SIGIR Conference on Research and Development in Information Retrieval,ACM Press, pp.258-265, 2004.

[16] James Allan and Giridhar Kumaran, "Stemming in the Language Modeling Framework", In: Proceedings of the 26th Annual International ACM SIGIR Conference on Research and Development in Information Retrieval (poster) ,ACM Press , pp.455-456,2003.

[17] Canhui Wang , Min Zhang , Shaoping Ma, "A Survey of Natural Language Processing in Information Retrieval", Journal of Chinese Information Processing, vol.21,no. 2,pp.40, 2007.

AUTHOR INDEX

Notation of session name: PL: Plenary Speech, IS: Invited Speech, ISP: Invited Session on Playware, GS: General Session, OS: Organized Session PS: Poster Session

A

Adachi	Yuto	OS6-1	**P-12** / 130
		OS6-6	**P-13** / 152
Adaniya	Yoshiaki	OS12-1	**P-28** / 258
Ahn	Byeong-kyu	GS15-2	**P-17** / 508
Ahn	Jou-Hyeon	PS1-13	**P-19** / 594
Aikawa	Masaru	OS2-4	**P-27** / 49
Aoki	Kenji	OS2-2	**P-27** / 41
Arita	Takaya	GS2-1	**P-21** / 316
		GS2-2	**P-21** / 320
		GS11-2	**P-23** / 448
		GS17-4	**P-25** / 551
Asada	Taro	OS8-1	**P-24** / 176
		OS8-2	**P-24** / 180
		OS8-3	**P-25** / 186
		OS8-4	**P-25** / 192
Ayano	Hideki	OS6-4	**P-13** / 142

B

Bin Ambar	Radzi	OS7-4	**P-24** / 168
		OS7-5	**P-24** / 172
Boku	Kanu	OS8-1	**P-24** / 176

C

Cao	Jihao	GS5-2	**P-18** / 364
Chamnongthai	Kosin	OS6-1	**P-12** / 130
		OS6-6	**P-13** / 152
Chang	In seop	PS1-13	**P-19** / 594
Chang	Jhih-Cheng	OS10-2	**P-14** / 218
Chang	Yi-Chang	OS10-3	**P-15** / 222
Chen	Bo-Han	PS1-16	**P-19** / 605
Chen	Jhih-Han	OS11-5	**P-17** / 254
Chen	Jhih-Sian	PS1-18	**P-20** / 613
Chen	Kuo-Kung	OS10-7	**P-15** / 238
Chen	Pi-Yun	OS10-1	**P-14** / 214
		PS1-9	**P-19** / 578
Chen	Po-Yu	OS10-7	**P-15** / 238
Chiang	Huann-Keng	OS10-3	**P-15** / 222
Chiang	Ping-Chieh	PS1-11	**P-19** / 586
Cho	Young Im	PS1-20	**P-20** / 621
Choi	Dongwoon	GS15-2	**P-17** / 508
Choi	Taeyong	PS1-7	**P-19**
Christensen	David J.	ISP3	**P-12** / 9
Chung	Cheng-Yun	OS11-1	**P-16** / 242
Ciou	Wei-Yi	OS11-2	**P-17** / 246
Cui	Chengyou	OS1-1	**P-22** / 21
		OS1-2	**P-23** / 25

D

Do	Shaodong	GS15-1	**P-17**

E

Endo	Takahiro	GS17-3	**P-25** / 547

F

Fapyane	Deby	PS1-13	**P-19** / 594
Fu	Yu-Fen	OS10-2	**P-14** / 218
Fu	Yu-Yi	OS10-1	**P-14** / 214
		OS10-2	**P-14** / 218
Fuchida	Takayasu	GS1-1	**P-16** / 304
		GS13-1	**P-26** / 476
Fujieda	Homare	GS8-4	**P-17** / 412
Fujiwara	Kei	OS4-7	**P-14**
Fujiwara	Takeshi	GS3-3	**P-27** / 333
Fukami	Kazuhiko	OS9-4	**P-15** / 210
Funahashi	Kazuma	GS16-2	**P-26** / 525
Funamoto	Satoshi	OS3-1	**P-13** / 53
Funaya	Hiroyuki	GS17-1	**P-25** / 539
Furutani	Hiroshi	OS2-1	**P-27** / 37
		OS2-2	**P-27** / 41
		OS2-3	**P-27** / 45
		OS14-1	**P-28** / 296
		OS14-2	**P-28** / 300
Furuya	Naoki	OS5-6	**P-24** / 122

G

Gao	Xiang	GS3-3	**P-27** / 333
Ghazali	Mohd Riduwan	GS4-2	**P-20** / 346
		GS16-3	**P-26** / 529
GO	Sou	GS6-1	**P-25** / 371
Gohara	Keisuke	GS12-4	**P-18** / 472
Gornev	Evgeny S.	PS1-6	**P-19**
Goto	Hiroki	GS16-2	**P-26** / 525
Gouko	Manabu	PS1-1	**P-18** / 555
Guo	Jr-Hung	OS10-5	**P-15** / 230

H

Habib	Maki K.	GS15-4	**P-18** / 516
Hagiwara	Shingo	GS11-1	**P-23** / 444
Han	Chang-Soo	GS14-3	**P-16** / 500
		GS16-4	**P-26** / 535
Han	Kun-Young	OS1-3	**P-23** / 29
		OS1-4	**P-23** / 33
Hanada	Masaki	OS5-3	**P-23** / 110
		OS5-7	**P-24** / 126

© ISAROB 2013

Hanada	Masaki	OS9-1	**P-15** / 197
		OS9-2	**P-15** / 202
Hara	Yusuke	OS4-5	**P-14** / 93
Hasan	Md. Mahbub	GS13-3	**P-26** / 484
Hashimoto	Masato	GS9-2	**P-21** / 420
Hattori	Tetsuo	OS13-1	**P-22** / 276
		OS13-2	**P-22** / 280
		OS13-3	**P-22** / 284
		OS13-4	**P-22** / 288
		OS13-5	**P-22** / 292
Hayashi	Eiji	GS13-4	**P-26** / 488
		GS15-3	**P-17** / 512
Higuchi	Kohji	OS6-1	**P-12** / 130
		OS6-6	**P-13** / 152
Hikasa	Shigeki	OS3-4	**P-13** / 65
Hiraishi	Kunihiko	GS4-1	**P-20** / 342
Hirofuji	Yasuyuki	GS16-1	**P-26** / 521
Hsia	Kuo-Hsien	OS11-2	**P-17** / 246
Hsieh	Sheng-Ta	PS1-16	**P-19** / 605
		PS1-17	**P-20** / 609
		PS1-18	**P-20** / 613
Huang	Chung-Hsin	PS1-11	**P-19** / 586
		PS1-19	**P-20** / 617
Huang	Tzu-Hsuan	OS12-3	**P-28** / 268
		OS12-4	**P-28** / 272
Hung	Chung-Wen	OS11-4	**P-17** / 250
		OS11-5	**P-17** / 254

I

Iimura	Ichiro	GS1-3	**P-16**
Ikeda	Kazushi	GS17-1	**P-25** / 539
Ikeda	Masaaki	OS3-4	**P-13** / 65
Ikeda	Satoshi	OS14-1	**P-28** / 296
		OS14-2	**P-28** / 300
		OS2-3	**P-27** / 45
Imai	Masatoshi	OS13-5	**P-22** / 292
Imai	Yoshiro	OS13-2	**P-22** / 280
		OS13-4	**P-22** / 288
		OS13-5	**P-22** / 292
Imaike	Kenichi	OS7-5	**P-24** / 172
Imamura	Hiroki	GS5-1	**P-18** / 360
Inoue	Hirofumi	OS4-1	**P-14** / 78
Inoue	Tomohiro	GS13-4	**P-26** / 488
Irawan	Addie	GS16-3	**P-26** / 529
Ishikawa	Tomo	GS9-2	**P-21** / 420
Ishimaru	Takashi	PS1-8	**P-19** / 574
Ito	Hiroshi	OS4-6	**P-14** / 97
Ito	Kazuyuki	GS1-2	**P-16** / 308
Ito	Masanori	GS3-2	**P-27** / 329
		GS5-2	**P-18** / 364
		GS16-1	**P-26** / 521
		GS16-2	**P-26** / 525
Ito	Takao	OS2-3	**P-27** / 45
		OS14-1	**P-28** / 296
		OS14-2	**P-28** / 300
Ito	Takashi	GS17-4	**P-25** / 551
Iwasaki	Hideo	OS4-6	**P-14** / 97
Iwasaki	Shinya	OS5-7	**P-24** / 126
		OS9-2	**P-15** / 202
Izumi	Tetsuya	OS13-1	**P-22** / 276
Izumi	Tetsuya	OS13-2	**P-22** / 280
		OS13-3	**P-22** / 284

J

Jang	Jaeho	GS5-3	**P-18** / 367
Jareanpon	Chatklaw	GS8-3	**P-17** / 408
Javidi	Bahram	OS13-3	**P-22** / 284
Jessen	Jari Due	ISP1	**P-12** / 1
Jia	Yingmin	GS8-1	**P-17** / 400
		GS8-2	**P-17** / 404
		GS10-3	**P-21** / 436
Jiang	Ganwen	GS7-3	**P-21** / 391
Jiang	Sharu	GS8-2	**P-17** / 404
Jiang	Yuefei	GS8-1	**P-17** / 400
Jin	Hu	OS1-1	**P-22** / 21
Jin	Xing	GS3-2	**P-27** / 329
Jung	Jehan	GS17-1	**P-25** / 539

K

Kadoya	Kazuya	PS1-2	**P-18** / 558
Kai	Yoshihiro	PS1-10	**P-19** / 582
Kajikawa	Tatsuyoshi	OS6-1	**P-12** / 130
		OS6-6	**P-13** / 152
Kamiura	Moto	OS4-3	**P-14** / 85
Karakuzu	Cihan	GS12-1	**P-18** / 460
Kashima	Masayuki	GS7-3	**P-21** / 391
Kawabata	Yuma	GS4-4	**P-20** / 356
Kawai	Takamitsu	GS17-3	**P-25** / 547
Kawakami	Yusuke	OS13-1	**P-22** / 276
		OS13-2	**P-22** / 280
Kawano	Hiromichi	OS13-1	**P-22** / 276
		OS13-3	**P-22** / 284
Kawano	Yoshihiro	OS5-6	**P-24** / 122
Kawasaki	Haruhisa	GS17-3	**P-25** / 547
Khomyakov	Ilya A.	PS1-6	**P-19**
Kiguchi	Kazuo	GS6-4	**P-25** / 383
		GS12-3	**P-18** / 468
		GS14-1	**P-16** / 492
Kikuchi	Yuui	GS12-3	**P-18** / 468
Kim	Bong Keun	GS14-2	**P-16** / 496
Kim	Hyogon	GS5-3	**P-18** / 367
Kim	Jinwook	GS1-2	**P-16** / 308
Kim	Yeon-Seob	GS9-3	**P-22**
Kitaguchi	Satoshi	PS1-10	**P-19** / 582
Ko	Chia-Nan	OS10-1	**P-14** / 214
		OS10-2	**P-14** / 218
Kobayashi	Koichi	GS4-1	**P-20** / 342
Kobayashi	Kunikazu	GS11-3	**P-23** / 452
		GS12-2	**P-18** / 464
Koga	Hiroyuki	OS7-2	**P-24** / 160
Koga	Kiminobu	OS2-1	**P-27** / 37
Koike	Hisashi	GS4-3	**P-20** / 352
Kondo	Takao	OS4-6	**P-14** / 97
Kori	Hiroshi	OS4-6	**P-14** / 97
Koro	Chikoto	OS8-4	**P-25** / 192
Koyamada	Koji	OS4-4	**P-14** / 89
Krasnikov	Andrey G.	PS1-6	**P-19**
Kubota	Yuchi	GS2-2	**P-21** / 320
Kuremoto	Takashi	GS11-3	**P-23** / 452

© ISAROB 2013

Kuremoto	Takashi	GS12-2	**P-18** / 464
Kurogi	Tatsuma	OS2-3	**P-27** / 45
		OS14-1	**P-28** / 296
		OS14-2	**P-28** / 300
Kutsuna	Daisuke	OS13-2	**P-22** / 280
Kwak	Youngjoo	OS9-3	**P-15** / 206
		OS9-4	**P-15** / 210

L

Lai	Chin-Lun	PS1-12	**P-19** / 590
Lai	Chin-Lun	PS1-14	**P-19** / 597
Lai	Li-Chun	OS10-5	**P-15** / 230
		OS10-6	**P-15** / 234
Lai	Pin-Ru	PS1-11	**P-19** / 586
Lee	Dae Jong	PS1-20	**P-20** / 621
Lee	Dongwook	GS15-2	**P-17** / 508
Lee	Duckyeon	GS15-2	**P-17** / 508
Lee	Hee-Hyol	OS1-1	**P-22** / 21
		OS1-2	**P-23** / 25
		OS1-3	**P-23** / 29
		OS1-4	**P-23** / 33
Lee	Hogil	GS15-2	**P-17** / 508
Lee	Jae Hoon	GS4-3	**P-20** / 352
		GS8-4	**P-17** / 412
		GS10-1	**P-20** / 428
		GS10-2	**P-20** / 432
Lee	Ji-Yeong	GS14-3	**P-16** / 500
Lee	Jongwon	GS5-3	**P-18** / 367
Lee	Ju-Jang	GS1-4	**P-16** / 312
		GS9-3	**P-22**
Lee	Li-Yin	PS1-14	**P-19** / 597
Lee	Minho	GS17-1	**P-25** / 539
Lee	Soo-Jin	PS1-13	**P-19** / 594
Lee	Sukwoo	GS5-3	**P-18** / 367
Li	Ching-Lieh	PS1-11	**P-19** / 586
		PS1-19	**P-20** / 617
Li	Lu	OS1-3	**P-23** / 29
Li	Mingxing	GS10-3	**P-21** / 436
Liao	Fangbo	GS14-4	**P-16** / 504
		GS15-1	**P-17**
Liao	Yi-Lin	OS10-5	**P-15** / 230
		OS11-1	**P-16** / 242
Lien	Shao-Fan	OS11-2	**P-17** / 246
Lim	DuHyun	PS1-13	**P-19** / 594
Lin	Ben-Zhong	OS11-3	**P-17**
Lin	Chien-Chou	OS11-3	**P-17**
Lin	Sheau-Wen	OS10-6	**P-15** / 234
Lin	Tsung-Ching	PS1-12	**P-19** / 590
Lin	Wen-Bin	OS10-3	**P-15** / 222
		OS10-7	**P-15** / 238
Lin	Yung-Chin	OS11-1	**P-16** / 242
Liu	Guan-Yu	OS10-1	**P-14** / 214
Long	Shichen	GS8-2	**P-17** / 404
Lu	Cunwei	OS12-1	**P-28** / 258
Lu	Yi-Yu	OS10-7	**P-15** / 238
Lund	Henrik Hautop	ISP1	**P-12** / 1
		ISP3	**P-12** / 9

M

Ma	QinLian	OS2-1	**P-27** / 37
Mabu	Shingo	GS11-3	**P-23** / 452
Mackin	Kenneth J.	OS5-5	**P-24** / 118
		OS5-7	**P-24** / 126
		OS9-2	**P-15** / 202
Maeyama	Shoichi	OS3-1	**P-13** / 53
		OS3-2	**P-13** / 57
Magnússon	Arnþór	ISP3	**P-12** / 9
Makino	Koji	GS9-2	**P-21** / 420
		GS10-4	**P-21** / 440
Mallipeddi	Rammohan	GS17-1	**P-25** / 539
Marti	Patrizia	ISP2	**P-12** / 5
Masumitsu	Kyosuke	GS13-1	**P-26** / 476
Masunari	Saki	OS13-3	**P-22** / 284
Matoba	Ryuichi	GS11-1	**P-23** / 444
Matsuba	Yuka	GS17-1	**P-25** / 539
Matsui	Yosihiro	OS6-4	**P-13** / 142
Matsunaga	Nobutomo	GS6-3	**P-25** / 379
Matsuo	Hiroki	PS1-4	**P-19** / 566
Matsushita	Haruna	OS13-2	**P-22** / 280
Minami	Mamoru	OS3-6	**P-13** / 73
Miura	Asaki	ISP4	**P-12** / 17
Miya	Takuya	OS5-6	**P-24** / 122
Miyachi	Hideo	OS4-4	**P-14** / 89
Miyake	Shuhei	GS3-3	**P-27** / 333
Miyamichi	Juichi	PS1-15	**P-19** / 601
Mizoguchi	Fumio	GS11-4	**P-23** / 456
Moghadam	Mikael	ISP3	**P-12** / 9
Mohd Tumari	Mohd Zaidi Bin	GS4-2	**P-20** / 346
Mori	Hayao	OS9-1	**P-15** / 197
Mori	Hiroshi	PS1-15	**P-19** / 601
Mori	Kazuma	OS5-7	**P-24** / 126
		OS9-2	**P-15** / 202
Morioka	Kazuyuki	PS1-5	**P-19** / 570
		PS1-8	**P-19** / 574
Moritoh	Yoshio	OS13-4	**P-22** / 288
Motonaka	Kimiko	OS3-2	**P-13** / 57
Mouri	Tetsuya	GS17-3	**P-25** / 547
Murao	Hajime	GS9-4	**P-22** / 424
Murata	Takayuki	GS6-2	**P-25** / 375
Murata	Yu	OS4-3	**P-14** / 85
Murayama	Yoriko	OS4-6	**P-14** / 97

N

Nabekura	Kazuki	GS6-3	**P-25** / 379
Nagai	Isaku	OS3-4	**P-13** / 65
		OS3-5	**P-13** / 69
Nagai	Yasuo	OS5-3	**P-23** / 110
Nagata	Fusaomi	GS15-4	**P-18** / 516
		OS3-3	**P-13** / 61
Nagata	Yuichi	GS3-1	**P-26** / 325
Nagatomo	Makoto	OS2-3	**P-27** / 45
		OS14-1	**P-28** / 296
		OS14-2	**P-28** / 300
Nagayoshi	Masato	GS9-4	**P-22** / 424
Naitoh	Ken	OS4-1	**P-14** / 78
		OS4-2	**P-14** / 81
Nakamura	Kazunori	OS12-2	**P-28** / 264

© ISAROB 2013

Nakamura	Masahiro	GS9-1	**P-21** / 416
Nakamura	Yoshikazu	OS3-5	**P-13** / 69
Nakanishi	Yuu	OS8-2	**P-24** / 180
		OS8-3	**P-25** / 186
Nakano	Kazushi	OS6-4	**P-13** / 142
		OS6-5	**P-13** / 146
Nakashima	Naotoshi	GS3-1	**P-26** / 325
Nakaura	Hatsumi	PS1-15	**P-19** / 601
Nakayama	Shigeru	GS1-3	**P-16**
Narukawa	Kyoko	GS3-2	**P-27** / 329
Niinuma	Shohei	PS1-3	**P-19** / 562
Nishimoto	Keita	GS11-2	**P-23** / 448
Nishiyama	Hiroyuki	GS5-1	**P-18** / 360
		GS11-4	**P-23** / 456
		GS12-4	**P-18** / 472
Nishiyama	Hiroyuki	GS17-2	**P-25** / 543
Nogami	Tsuyoshi	OS4-2	**P-14** / 81
Nomura	Shin-ichiro M.	OS4-7	**P-14**
Nonami	Kenzo	GS16-3	**P-26** / 529
Nunohiro	Eiji	OS5-1	**P-23** / 101
		OS5-2	**P-23** / 106
		OS5-7	**P-24** / 126
		OS9-1	**P-15** / 197
		OS9-2	**P-15** / 202
		OS9-3	**P-15** / 206

O

Obayashi	Masanao	GS11-3	**P-23** / 452
		GS12-2	**P-18** / 464
Obu	Yuka	OS5-6	**P-24** / 122
Ohara	Kazuyoshi	GS10-2	**P-20** / 432
Ohshiro	Masanori	OS5-1	**P-23** / 101
		OS5-2	**P-23** / 106
Ohyama	Yasuhiro	GS9-2	**P-21** / 420
Okada	Nobuhiro	GS6-4	**P-25** / 383
		GS12-3	**P-18** / 468
		GS14-1	**P-16** / 492
Okajima	Hiroshi	GS6-3	**P-25** / 379
Okamoto	Kei	GS10-1	**P-20** / 428
Okamoto	Shingo	GS4-3	**P-20** / 352
		GS8-4	**P-17** / 412
		GS10-1	**P-20** / 428
		GS10-2	**P-20** / 432
Okazaki	Naonobu	GS3-4	**P-27** / 338
Okumura	Katuhiro	OS7-2	**P-24** / 160
Olufs	Sven	GS7-4	**P-21** / 395
Ono	Isao	GS3-1	**P-26** / 325
Ono	Yosuke	GS6-4	**P-25** / 383
Orlov	Sergey N.	PS1-6	**P-19**
Otsuka	Akimasa	GS15-4	**P-18** / 516
		OS3-3	**P-13** / 61
Oue	Masumi	GS10-1	**P-20** / 428
Oya	Masahiro	OS7-1	**P-24** / 156
		OS7-2	**P-24** / 160
		OS7-3	**P-24** / 164

P

Pacheco	Moises	ISP3	**P-12** / 9
Park	Jonggeol	OS9-1	**P-15** / 197
		OS9-3	**P-15** / 206
Park	Jonggeol	OS9-4	**P-15** / 210
Park	Sangdeok	GS5-3	**P-18** / 367
Park	Sooyoung	OS9-3	**P-15** / 206
Peng	Gang	GS1-3	**P-16**
Pilat	Marcin L.	GS17-4	**P-25** / 551

R

Ramli	Mohd Syakirin	GS16-3	**P-26** / 529

S

Saealal	Muhammad Salihin	GS4-2	**P-20** / 346
Sagara	Shinichi	OS7-4	**P-24** / 168
		OS7-5	**P-24** / 172
Saito	Yusuke	GS17-2	**P-25** / 543
Sakai	Masashi	GS9-2	**P-21** / 420
Sakamoto	Makoto	OS2-1	**P-27** / 37
		OS2-2	**P-27** / 41
		OS2-3	**P-27** / 45
		OS14-1	**P-28** / 296
		OS14-2	**P-28** / 300
Sakamoto	Naohisa	OS4-4	**P-14** / 89
Sakurai	Naoko	GS3-3	**P-27** / 333
Sano	Shigenori	GS4-4	**P-20** / 356
Sapaty	Peter S.	IS1	**P-12**
Sato	Kiminori	GS7-3	**P-21** / 391
Sato	Tomoaki	OS6-1	**P-12** / 130
		OS6-6	**P-13** / 152
Sato	Yusuke	OS4-7	**P-14**
Sawada	Kenji	OS6-2	**P-13** / 134
		OS6-3	**P-13** / 138
Serikawa	Seiichi	GS7-1	**P-21** / 387
Shao	Ming-Lei	GS14-3	**P-16** / 500
She	Jin-Hua	GS9-2	**P-21** / 420
Shih	Chia-Hung	OS10-6	**P-15** / 234
Shimada	Atsushi	GS13-2	**P-26** / 480
Shimohara	Katsunori	GS11-2	**P-23** / 448
Shimokakimoto	Tomoya	ISP4	**P-12** / 17
Shin	Kyoosik	GS16-4	**P-26** / 535
Shin	Seiichi	OS6-2	**P-13** / 134
		OS6-3	**P-13** / 138
Shintaku	Satoshi	OS6-5	**P-13** / 146
Shoji	Kenji	PS1-15	**P-19** / 601
Shu	Panfeng	OS7-1	**P-24** / 156
		OS7-3	**P-24** / 164
Shu	Qingyu	OS13-3	**P-22** / 284
Soeda	Takafumi	GS14-1	**P-16** / 492
Stienstra	Jelle T.	ISP2	**P-12** / 5
Su	Juhng-Perng	OS11-2	**P-17** / 246
Su	Kuo-Lan	OS10-2	**P-14** / 218
		OS10-5	**P-15** / 230
		OS10-6	**P-15** / 234
		OS11-1	**P-16** / 242
Su	Tse	PS1-17	**P-20** / 609
Su	Xiaofeng	GS8-1	**P-17** / 400
Sudo	Hiroki	GS11-1	**P-23** / 444
Suetake	Yusuke	OS7-3	**P-24** / 164
Sueyoshi	Kenji	OS2-2	**P-27** / 41
Sughimura	Noritsugu	GS2-1	**P-21** / 316
Sugimoto	Tsuyoshi	GS9-1	**P-21** / 416

© ISAROB 2013

Sugisaka	Masanori	GS14-4	**P-16** / 504
		GS15-1	**P-17**
Sugita	Kaoru	OS12-2	**P-28** / 264
		OS12-3	**P-28** / 268
		OS12-4	**P-28** / 272
Sumantri	Bambang	GS4-4	**P-20** / 356
Sumi	Yasushi	GS14-2	**P-16** / 496
Sun	Chi-Hsien	PS1-11	**P-19** / 586
		PS1-19	**P-20** / 617
Suzuki	Kenji	ISP4	**P-12** / 17
Suzuki	Reiji	GS2-1	**P-21** / 316
		GS2-2	**P-21** / 320
		GS11-2	**P-23** / 448
		GS17-4	**P-25** / 551

T

Tabuse	Masayoshi	OS8-1	**P-24** / 176
		OS8-2	**P-24** / 180
Tabuse	Masayoshi	OS8-3	**P-25** / 186
Tachibana	Katsunori	GS1-2	**P-16** / 308
Takatsuka	Kayoko	GS3-4	**P-27** / 338
Tamaki	Hisashi	GS9-4	**P-22** / 424
Tamoto	Kazuyuki	OS2-4	**P-27** / 49
Tamura	Hiroki	GS6-1	**P-25** / 371
		GS6-2	**P-25** / 375
Tan	Yee Yin	GS16-3	**P-26** / 529
Tanaka	Hideyuki	GS14-2	**P-16** / 496
Tanaka	Ken-ichi	PS1-2	**P-18** / 558
		PS1-3	**P-19** / 562
		PS1-4	**P-19** / 566
Tanaka	Kyoko	GS15-3	**P-17** / 512
Tanemura	Satoshi	GS13-3	**P-26** / 484
Tanev	Ivan	GS11-2	**P-23** / 448
Taniguchi	Rin-ichiro	GS13-2	**P-26** / 480
Tanimoto	Hiro	OS3-6	**P-13** / 73
Tanno	Koichi	GS6-1	**P-25** / 371
		GS6-2	**P-25** / 375
Tanoue	Michihito	GS3-4	**P-27** / 338
Teramoto	Kenbu	GS13-3	**P-26** / 484
Tezel	Gülay	GS12-1	**P-18** / 460
Thi Aung	Kathy	GS1-1	**P-16** / 304
Ting	Ying-Yao	OS10-4	**P-15** / 226
Tobe	Takahiro	OS4-2	**P-14** / 81
Tojo	Satoshi	GS11-1	**P-23** / 444
Tomita	Shigeyuki	GS3-4	**P-27** / 338
Tomizuka	Masayoshi	PS1-10	**P-19** / 582
Toyama	Fubito	PS1-15	**P-19** / 601
Tsuji	Yasutaka	GS12-3	**P-18** / 468
Tsujino	Kazuhiro	OS12-1	**P-28** / 258
Tsukamoto	Seiji	OS9-1	**P-15** / 197
Tuen	Lung-Fai	PS1-11	**P-19** / 586
		PS1-19	**P-20** / 617

U

Uchida	Yasuo	OS2-3	**P-27** / 45
		OS14-1	**P-28** / 296
		OS14-2	**P-28** / 300
Uchiyama	Naoki	GS4-4	**P-20** / 356

V

Vincze	Markus	GS7-4	**P-21** / 395

W

Wada	Hideki	OS7-2	**P-24** / 160
Wahab	Yasmin Binti Abdul	GS4-2	**P-20** / 346
Wang	Huan-Sheng	OS10-4	**P-15** / 226
Wang	Jeong Hyeon	GS1-4	**P-16** / 312
Wang	Jiwu	GS14-4	**P-16** / 504
		GS15-1	**P-17**
Wang	Meng-Hui	PS1-9	**P-19** / 578
Wang	Yanrung	GS13-2	**P-26** / 480
Watada	Shogo	GS11-3	**P-23** / 452
Watanabe	Keigo	GS15-4	**P-18** / 516
		OS3-1	**P-13** / 53
		OS3-2	**P-13** / 57
		OS3-4	**P-13** / 65
		OS3-5	**P-13** / 69
Watanabe	Mutsumi	GS7-3	**P-21** / 391
Watanabe	Shun	GS12-2	**P-18** / 464
Wong	Huang-Wei	PS1-19	**P-20** / 617
Wu	Chang-Hong	OS11-3	**P-17**
Wu	Huang-Lyu	PS1-17	**P-20** / 609
Wu	Jing	GS14-3	**P-16** / 500
		GS16-4	**P-26** / 535

X

Xi	Su Mei	PS1-20	**P-20** / 621
Xu	Haijing	GS10-3	**P-21** / 436

Y

Yaginuma	Takumi	GS5-2	**P-18** / 364
Yalçın	Nesibe	GS12-1	**P-18** / 460
Yamaba	Hisaaki	GS3-4	**P-27** / 338
Yamada	Takayoshi	GS9-1	**P-21** / 416
Yamaguchi	Daisuke	OS5-4	**P-23** / 114
Yamaguchi	Takashi	OS5-1	**P-23** / 101
		OS5-2	**P-23** / 106
		OS5-3	**P-23** / 110
		OS5-7	**P-24** / 126
		OS9-1	**P-15** / 197
		OS9-2	**P-15** / 202
		OS9-3	**P-15** / 206
Yamaguchi	Takuya	OS7-4	**P-24** / 168
Yamamori	Kunihito	OS2-1	**P-27** / 37
		OS2-2	**P-27** / 41
		OS2-4	**P-27** / 49
Yamamoto	Hidehiko	GS9-1	**P-21** / 416
Yamanaka	Satoshi	PS1-5	**P-19** / 570
Yamasaki	Kazuko	GS2-3	**P-21** / 324
		GS3-3	**P-27** / 333
Yamashita	Takayoshi	GS13-2	**P-26** / 480
Yamawaki	Akira	GS7-1	**P-21** / 387
Yan	Mingmin	GS6-1	**P-25** / 371
Yan	Rui-Jun	GS14-3	**P-16** / 500
		GS16-4	**P-26** / 535
Yang	Jun	GS2-3	**P-21** / 324
Yang	Tung-Lin	PS1-12	**P-19** / 590

Yanou	Akira	OS3-6	**P-13** / 73
Yanovich	Sergey I.	PS1-6	**P-19**
Yokomichi	Masahiro	OS2-3	**P-27** / 45
		OS14-1	**P-28** / 296
		OS14-2	**P-28** / 300
Yokota	Masao	OS12-2	**P-28** / 264
		OS12-3	**P-28** / 268
		OS12-4	**P-28** / 272
Yoshinaga	Tsunehiro	OS2-3	**P-27** / 45
		OS14-1	**P-28** / 296
		OS14-2	**P-28** / 300
Yoshitomi	Yasunari	OS8-1	**P-24** / 176
		OS8-2	**P-24** / 180
		OS8-3	**P-25** / 186
		OS8-4	**P-25** / 192
Yoshizaki	Saya	OS8-4	**P-25** / 192
Yoshizawa	Kousuke	GS3-3	**P-27** / 333

Z

Zaytsev	Nikolay A.	PS1-6	**P-19**
Zengin	Aydin Tarik	GS6-3	**P-25** / 379
Zhang	Feifei	GS3-2	**P-27** / 329
		GS5-2	**P-18** / 364
		GS16-1	**P-26** / 521
Zhang	Feifei	GS16-2	**P-26** / 525
Zhang	Wenlong	PS1-10	**P-19** / 582
Zhang	Yu-an	OS2-1	**P-27** / 37
Zheng	Zeyu	GS2-3	**P-21** / 324
		GS3-3	**P-27** / 333
Zhou	Bo	OS7-1	**P-24** / 156
Zhuo	Jinxin	OS7-1	**P-24** / 156
		OS7-3	**P-24** / 164
Zhu	Yonghu	OS12-1	**P-28** / 258

Springer

springer.com

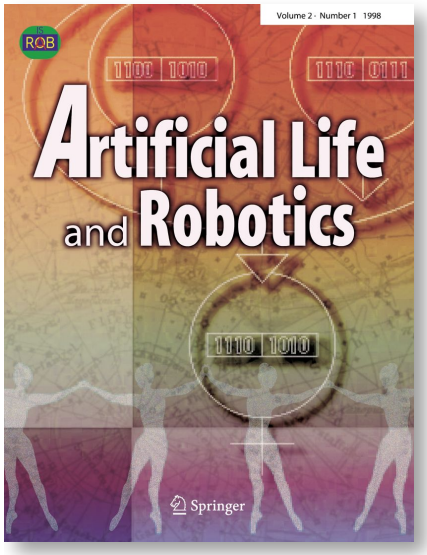

4 issues/year

Electronic access

- springerlink.com

Subscription information

- springer.com/librarians

Artificial Life and Robotics

Editor-in-Chief: Hiroshi Tanaka

- **Publishing body: International Symposium on Artificial Life and Robotics.**
- **Presents the development of new technologies concerning artificial life and robotics, especially computer-based simulation and hardware.**
- **Publishes technical papers and authoritative state-of-the-art reviews.**
- **Covers a broad multidisciplinary field.**

This is an international journal publishing original technical papers and authoritative state-of-the-art reviews on the development of new technologies concerning artificial life and robotics, especially computer-based simulation and hardware.
The journal covers a broad multidisciplinary field, including such areas as artificial brain research, artificial intelligence, artificial life, artificial living, artificial mind research, brain science, chaos, cognitive science, complexity, computer graphics, evolutionary computations, fuzzy control, genetic algorithms, innovative computations, intelligent control and modeling, micromachines, micro-robot world cup soccer tournament, mobile vehicles, neural networks, neurocomputers, neurocomputing technologies and applications, robotics, robus virtual engineering, and virtual reality. It also covers hardware-oriented issues.
Publishing body: International Symposium on Artificial Life and Robotics

On the homepage of **Artificial Life and Robotics** at **springer.com** you can

- Read the most downloaded articles for free
- Sign up for our Table of Contents Alerts
- Get to know the complete Editorial Board
- Find submission information